Graham K. Taylor
Michael S. Triantafyllou
Cameron Tropea
Editors

Animal Locomotion

The Physics of Flying
The Hydrodynamics of Swimming

Springer

Animal Locomotion

Graham K. Taylor, Michael S. Triantafyllou, and
Cameron Tropea (Eds.)

Animal Locomotion

Springer

Dr. Graham K. Taylor
University of Oxford
Dept. Zoology
South Parks Road
OX1 3PS Oxford
UK
E-mail: graham.taylor@zoo.ox.ac.uk

Prof. Michael S. Triantafyllou
Massachusetts Institute of Technology
Dept. Mechanical Engineering
Center for Ocean Engineering
Massachusetts Avenue 77
02139-4307 Cambridge
Massachusetts
USA
E-mail: mistetri@mit.edu

Prof. Cameron Tropea
TU Darmstadt
FB 16 Maschinenbau
FG Strömungslehre und
Aerodynamik
Petersenstr. 30
64287 Darmstadt
Germany
E-mail: ctropea@sla.tu-darmstadt.de

ISBN 978-3-642-11632-2 e-ISBN 978-3-642-11633-9

DOI 10.1007/978-3-642-11633-9

Library of Congress Control Number: 2010922310

Typesetting: Data supplied by the authors

Production: Scientific Publishing Services Pvt. Ltd., Chennai, India

Cover Design: WMX Design, Heidelberg, Germany

Printed in acid-free paper

9 8 7 6 5 4 3 2 1

springer.com

Preface

The physical principles of swimming and flying in animals are intriguingly different from those of ships and airplanes. The study of animal locomotion therefore holds a special place not only at the frontiers of pure fluid dynamics research, but also in the applied field of biomimetics, which aims to emulate salient aspects of the performance and function of living organisms. For example, fluid dynamic loads are so significant for swimming fish that they are expected to have developed efficient flow control procedures through the evolutionary process of adaptation by natural selection, which might in turn be applied to the design of robotic swimmers. And yet, sharply contrasting views as to the energetic efficiency of oscillatory propulsion – especially for marine animals – demand a careful assessment of the forces and energy expended at realistic Reynolds numbers. For this and many other research questions, an experimental approach is often the most appropriate methodology. This holds as much for flying animals as it does for swimming ones, and similar experimental challenges apply – studying tethered as opposed to free locomotion, or studying the flow around robotic models as opposed to real animals.

This book provides a wide-ranging snapshot of the state-of-the-art in experimental research on the physics of swimming and flying animals. The resulting picture reflects not only upon the questions that are of interest in current pure and applied research, but also upon the experimental techniques that are available to answer them. Doubtless, many new questions will present themselves as the scope and performance of our experimental toolbox develops over the coming years.

While there has been great progress in identifying the principles and role of vorticity shedding and control in fish swimming, much remains to be done in terms of understanding the three-dimensional structure of the vortical patterns and the energetics of the flow. These developments will also drive work on sensing and control. Observations and flow visualization with living fish and experimentation with robotic fish-like swimming devices are unique tools in exploring the properties of the flow structures produced by fish. Some of the more pertinent questions in this regard are addressed in the opening article by George Lauder *Swimming hydrodynamics: ten questions and the technical approaches needed to resolve them*. The field of micro-organism swimming is equally intriguing and is a field that will grow rapidly in the near future. Hence, while they fall outside the strict scope of “animal locomotion”, bacteria find a place in this book – not least because of the insight they yield into the effects of collective behaviour in swimming micro-organisms more generally.

Turning now to flying, the emphasis in experimental research has shifted in recent years from an exploratory quest to identify "novel" mechanisms of unsteady lift production - clap and fling, leading-edge vortices, rotational mechanisms, wake capture - to more detailed examinations of the underlying flow physics. This shift has been enabled in large part by the widespread availability of Particle Image Velocimetry (PIV), which has allowed new questions to be asked, for example, about the detailed wake structures of birds and bats, or of the importance of tandem wing interactions and aeroelastic deformation in insects. This aspect of the field is addressed directly with a review article from Geoff Spedding and Anders Hedenström *PIV Based Investigations of Animal Flight*. Other more classical techniques, such as smoke visualization and direct force or pressure measurements retain an important role in cases where PIV is impractical or uninformative, and all feature in this book accordingly.

Many fundamental questions remain, and many more will doubtless arise, as an ever wider range of species and systems is studied. Here in a single volume are measurements from multiple species of swimming and flying organisms – from bacteria to fish, and from insects to birds and bats. This presentation offers a glimpse of the future possibilities opened by comparative experimental approach which asks not only how the fluid dynamic principles operate, but also how they vary systematically with fluid medium, scale, form and function.

This book assembles articles previously published in two special issues of Experiments in Fluids: **Animal Locomotion: The Hydrodynamics of Swimming** (Vol. 43, No. 5, November 2007) and **Animal Locomotion: The Physics of Flying**

(Vol. 45, No. 4, May 2009) with the addition of a review article contributed by George Lauder (DOI: 10.1007/s00348-009-0765-8, October 2009). The editors hope that this condensed version of the current state-of-the-art in the field will be appreciated by the readers and, of course, we welcome any feedback or suggestions for future publishing efforts.

Graham K. Taylor
Oxford University, Department of Zoology, UK
graham.taylor@zoo.ox.ac.uk

Michael Triantafyllou
MIT, Mechanical and Ocean Engineering, USA
mistetri@triant.mit.edu

Cameron Tropea
Technische Universität Darmstadt, Mechanical Engineering, Germany
ctropea@sla.tu-darmstadt.de

Table of Contents

Part I: The Hydrodynamics of Swimming

Part II: The Physics of Flying

PART I

The hydrodynamics of swimming

Swimming hydrodynamics: ten questions and the technical approaches needed to resolve them

George V. Lauder

Abstract Recent experimental and computational studies of swimming hydrodynamics have contributed significantly to our understanding of how animals swim, but much remains to be done. Ten questions are presented here as an avenue to discuss some of the arenas in which progress still is needed and as a means of considering the technical approaches to address these questions. 1. What is the three-dimensional structure of propulsive surfaces? 2. How do propulsive surfaces move in three dimensions? 3. What are the hydrodynamic effects of propulsor deformation during locomotion? 4. How are locomotor kinematics and dynamics altered during unsteady conditions? 5. What is the three-dimensional structure of aquatic animal vortex wakes? 6. To what extent are observed propulsor deformations actively controlled? 7. What is the response of the body and fins of moving animals to external perturbations? 8. How can robotic models help us understand locomotor dynamics of organisms? 9. How do propulsive surfaces interact hydrodynamically during natural motions? 10. What new computational approaches are needed to better understand locomotor hydrodynamics? These ten questions point, not exclusively, toward areas in which progress would greatly enhance our understanding of the hydrodynamics of swimming organisms, and in which the application of new technology will allow continued progress toward understanding the interaction between organisms and the aquatic medium in which they live and move.

G. V. Lauder (✉)
Museum of Comparative Zoology, Harvard University,
26 Oxford Street, Cambridge, MA 02138, USA
e-mail: glauder@oeb.harvard.edu

1 Introduction

The study of swimming hydrodynamics has attracted considerable attention in recent years as engineers and biologists, both separately and together, have focused on the remarkable diversity in design and locomotor performance of aquatic organisms. A great deal of progress has been made, as evidenced by the chapters in this volume and by the number of review papers and books presenting our current understanding of how aquatic organisms interact with their fluid environment. Many of these recent overviews (e.g., Dabiri 2009; Fish and Lauder 2006; Fish et al. 2008; Lauder 2006; Lauder and Tytell 2006; Lauder and Madden 2007; Shadwick and Lauder 2006; Triantafyllou et al. 2005; Triantafyllou et al. 2000) have focused on the results from recent studies of aquatic locomotor dynamics, and present current information on swimming organisms. Here, I will take a different approach and structure this essay around a selection of the key questions that remain, and emphasize the techniques and approaches needed to address these questions going forward. I will present only limited data for each topic, and instead focus on discussing for each question the concepts and approaches relevant to broader issues in swimming hydrodynamics.

The ten questions presented below are certainly not the only possible ones that might be discussed, but these questions can serve as a starting point for thinking about new directions for the next years of research. For each question I first assess briefly the current state of research, and then address some of the technical approaches that are needed to address these questions. Some of the needed experiments or computations are feasible now, but others will require the development of new technologies or the further application of techniques just now becoming available to biologists and engineers studying aquatic locomotor systems.

G.K. Taylor, M.S. Triantafyllou, and C. Tropea (Eds.): Animal Locomotion, pp. 3–15.
springerlink.com

2 Ten questions for swimming hydrodynamics

2.1 What is the three-dimensional structure of propulsive surfaces?

Without an understanding of the three-dimensional shape of the propulsive surfaces of aquatic animals, and how these shapes can deform during propulsion (see Question 2 below), it is difficult to imagine how we will make substantial further progress in understanding the hydrodynamics of swimming organisms. While some organisms probably can be treated reasonably by two-dimensional analyses, either experimental or computational, in my view we have effectively reached the limit of progress using two-dimensional views and computational techniques (Lauder et al. 2007; Tytell et al. 2008). It is now important that we move to a full three-dimensional understanding of the shape of swimming animals, and to understand how deformation of propulsive surfaces takes place during locomotion.

One would think that numerous data files would be available on the three-dimensional shapes of animals such as jellyfish, fish, and marine mammals. And yet, until very recently, almost no data existed to document the geometry of complex biologic propulsive surfaces. Even now there are surprisingly few data sets with full three-dimensional shape information. Most studies of locomotion in fishes and marine mammals, e.g., treat the body two-dimensionally, either by considering a horizontal slice of a swimming animal, or a vertical plane through a flapping appendage.

This situation is beginning to change, and both computational fluid dynamics (Borazjani and Sotiropoulos 2009; Bozkurttas et al. 2009; Liu et al. 1997; Wolfgang et al. 1999; Zhu et al. 2002) and experimental fluid mechanical analyses (Bartol et al. 2005; Cooper et al. 2008; Lauder and Madden 2007; Lauder and Madden 2008; Weber et al. 2009) are beginning to incorporate a full three-dimensional animal geometry. A public database of such biologic geometries is still lacking, and would be a valuable resource for scientists. Such a database could be created through micro-CT (Computed Tomography) scanning of a diversity of whole organisms and individual propulsive surfaces, which would permit detailed reconstruction of body surface shape (as well as many internal bone and cartilage elements).

While the streamlined shape of marine mammal bodies and flukes in cross-section is well known (Fish 2004; Fish et al. 2008) and the streamlined shape of most fish bodies is well understood (Hertel 1966; Hoerner 1965; Webb 1975), it is not generally appreciated that the fins of fishes are often not at all streamlined, and in fact resemble the basic design of insect wings in forming a textured surface. In fact, textured surfaces are a prominent feature of the fins of ray-finned fishes, and these propulsive surfaces are far from smooth (Fig. 1). The fins of most fishes consist of jointed bony or cartilage fin rays with a thin collagenous membrane extending between them. This results in a "bumpy" surface structure, the implications of which have never been investigated. The biomechanical properties of fish fin rays and the remarkable bilaminar design have been analyzed (Alben et al. 2007; Geerlink and Videler 1987; Lauder and Madden 2007), but the effect of the uneven fin surface (with fin rays that may extend as much as 1 mm above the membrane on each side) on flow control during swimming has not been studied. It is also noteworthy that different fins present the textured surface at different orientations to incoming flow. For example, the bumpy surface of fin rays in the caudal fin are oriented at a relatively low angle of attack to freestream flow, while the dorsal and anal fin rays can be nearly orthogonal to incoming flow depending on the extent to which fish erect these fins. Three-dimensional reconstructions of fin geometry would be a first step toward computational fluid dynamic analyses of the effects of surface structure.

There is also considerable variation in cross-sectional geometry along the body of fish when viewed in three dimensions, and this is another area that has received relatively little attention. Figure 1 shows a series of body cross sections resulting from a micro-CT scans of a bluegill sunfish (*Lepomis macrochirus*) where the change in sharpness of the upper and lower body margins is evident, and suggests the possibility of considerable change in flow separation along the body during undulatory locomotion. Also noteworthy in the posterior sections is the textured surface structure of the dorsal and caudal fins.

2.2 How do propulsive surfaces move in three dimensions?

If little is known about the three-dimensional structure of animal locomotor surfaces, then even less is known about how these control surfaces move in three dimensions.

Although it might seem, in the year 2010, that the three-dimensional motions of aquatic animal appendages or bodies should have been well studied, in fact there are extremely few papers in which the three-dimensional conformation of propulsive surfaces has been measured through time. The lack of data on the motion of appendages through time and space is a serious constraint on both computational and experimental analyses of animal locomotion in water, as without this information analyses are necessarily simplified into two dimensions.

Figure 2 shows three different views of one position of the pectoral fin of a bluegill sunfish at the mid-fin beat time (near the transition time from outstroke to instroke) during steady locomotion at one body length per second

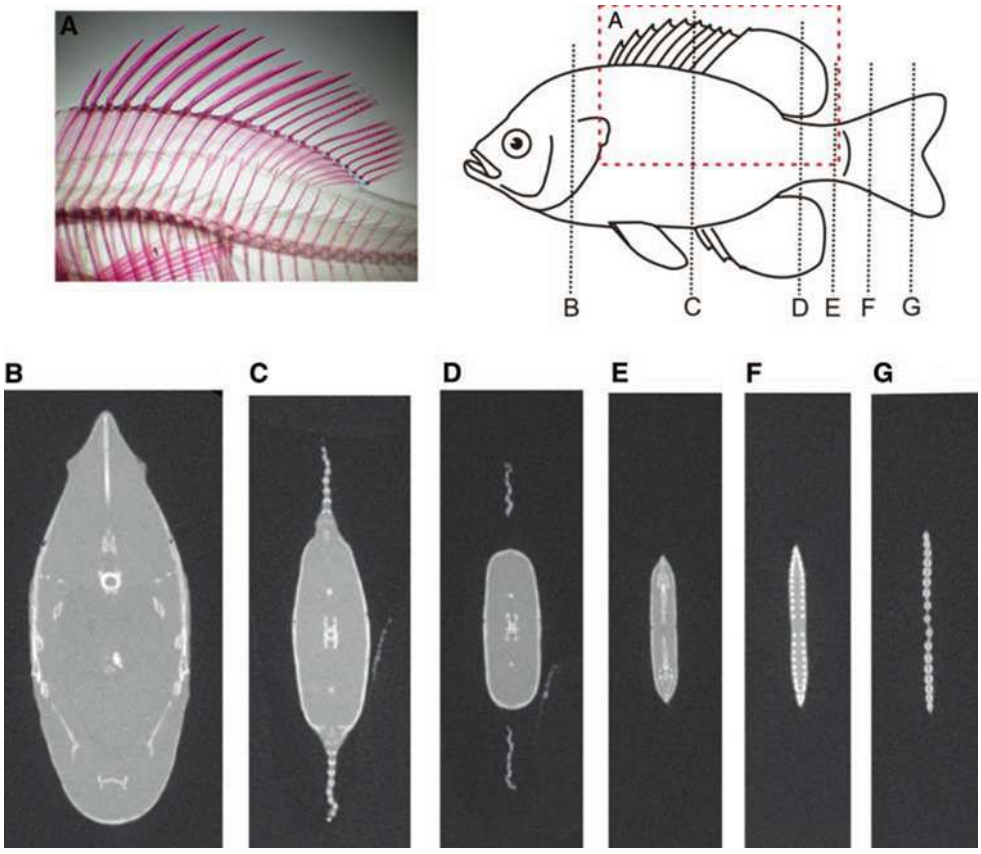

Fig. 1 Anatomy of a bluegill sunfish to illustrate changes in cross-sectional shape down the body and the non-streamlined textured surfaces of the fins. Bluegill image in *upper right* shows the location of anatomic features. **a** cleared and stained image of the dorsal fin region of a bluegill sunfish (bones are stained *red*, and muscle and skin have been cleared) to show the bony spines and rays that support the thin fin membrane. **b–g** micro-CT sections through a bluegill sunfish to illustrate changes in shape down the body. Note the relatively rounded shape of the body until the tail region where sections are flat with sharp upper and lower edges. Fin surfaces are bumpy (see sections **c** and **g**) with projecting fin rays. All micro-CT images are shown at the same scale

(approximately 10 cm/sec in this case). The conformation of the fin is complex and involves cupping of the upper and lower margins to form two simultaneous leading edges, a wave of bending that travels from root to tip, and chordwise deformation, which changes through time (Lauder et al. 2006; Lauder and Madden 2007). Given the complex kinematics of this pectoral fin, using a flat-plate model or a highly simplified representation of the fin that does not allow for changes in fin area through time or chordwise or spanwise dimensional changes is not likely to lead to advances in our understanding of pectoral fin propulsion. This accurate representation of the three-dimensional motion through time of a fish pectoral fin was critical to using computational fluid dynamics to understand the mechanism of thrust production by the sunfish pectoral fin (Bozkurttas et al. 2009). Accurate three-dimensional kinematic data of propulsor and body surface deformation through time are key elements of computational fluid dynamic modeling.

However, data such as those shown in Fig. 2 are difficult to obtain. Multiple synchronized high-speed cameras with reasonable resolution (1 K by 1 K at least) are needed to obtain three-dimensional kinematics when there is considerable deformation and folding of moving appendages. Often the propulsive surfaces of swimming animals are either not well marked naturally, or are difficult to place clear markers on to facilitate quantification of motion. Ideally, up to several hundred points would be measured at each time step to give an accurate representation of surface deformation, and a measurement frequency of five to ten times the movement frequency will be needed to capture transient components of three-dimensional motion. And, once some system of identifying points has been developed, the job of digitizing the x, y, and z locations in space and through time begins. None of this is trivial. And although computer-assisted quantification techniques are increasingly being developed for insects (e.g., Fontaine et al. 2009; Wang et al. 2008) to reduce the manual work needed to reconstruct three-dimensional propulsor conformations, these approaches have not yet yielded a bounty of three-dimensional kinematic data for swimming animals.

The three-dimensional motions of swimming animal propulsors are the result of a complex fluid–structure interaction, complex in part due to the (mostly unstudied) non-linear material properties of biologic propulsors. The observed motion will be a function of the material properties of the body and appendages (which change along the chordwise and spanwise directions), interacting dynamically with fluid-generated forces. Quantification of three-dimensional motion could thus also be used to test fluid–structure interaction computational models which, if correct in a particular case, should be able to predict the resulting movement pattern.

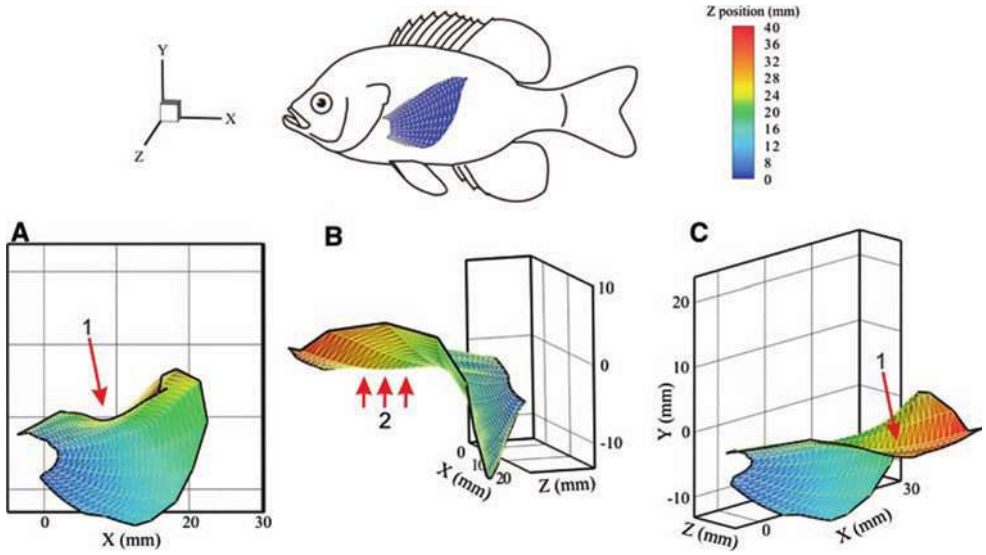

Fig. 2 Three views of a single time during the fin beat cycle (just after the transition from fin outstroke to instroke) to illustrate bending and conformational changes in a fish pectoral fin. The three fin images are color coded by z-position, which indicates the distance of the fin element from the body. Note the bent and cupped shape of the fin at this time. Arrow #1 points to the wave of bending that travels from root to tip of the fin, while arrows labeled #2 point to the region of the fin surface that generates thrust during the outstroke

For swimming fishes, examples of three-dimensional data on fins include efforts to quantify the curvature of fish fin rays in three dimensions during a variety of natural locomotor movements (Lauder et al. 2006; Standen and Lauder 2005; Standen and Lauder 2007; Standen 2008; Taft et al. 2008), and these data have proven very useful for understanding how the structure of fish fin rays (Alben et al. 2007; Lauder and Madden 2007) deforms under in vivo locomotor conditions. In addition, it is clear that fish propulsive surfaces frequently undergo substantial changes in area during both the movement cycle at one swimming speed, and also when compared across changes in speed or locomotor behavior (Tytell et al. 2008). So analyses of fish locomotion very much need to account for area changes in fins during motion. I am not aware of any three-dimensional experimentally obtained kinematic data for swimming mammals.

2.3 What are the hydrodynamic effects of propulsor deformation during locomotion?

Although quite a few papers have investigated the effects of flexibility on aquatic locomotor performance (e.g., Alben et al. 2004; Alben 2008; Blondeaux et al. 2005; Bozkurttas et al. 2006; Shen et al. 2003; Shoele and Zhu 2009), we still lack basic information on how flexible natural biologic systems are and hence on how much changes in flexibility affect locomotor parameters such as thrust generation and efficiency. Only limited three-dimensional data are available for swimming fishes, and some two-dimensional estimates of fluke camber changes through the tail stroke are available for marine mammals (Fish and Lauder 2006; Fish et al. 2008).

For example, one form of natural flexibility in motion is the cupping and bending motions of pectoral fins in swimming fishes (e.g., Fig. 2). One possible benefit of this motion is the control of both positive and negative lift forces during the outstroke and instroke, as the production of simultaneous up and down forces could act to minimize center of mass oscillation (Lauder and Madden 2007). Another example of the control of propulsor deformation is the caudal fin (tail) of swimming fishes. Researchers as early as Bainbridge (1963) noticed the substantial change in fish fin shape during the tail beat (also see Lauder 1989; Lauder 2000), and this has been quantified for swimming fishes and related to the vortical flow patterns shed by the tail (Tytell 2006). In addition, Flammang and Lauder (Flammang and Lauder 2008; Flammang and Lauder 2010) showed that these conformational changes in tail shape are actively produced with intrinsic musculature, and caudal fin shape change varies greatly in concert with the type of maneuver being performed by the swimming fish.

Changes in fin area with swimming speed (Standen and Lauder 2005; Standen and Lauder 2007; Tytell et al. 2008) have obvious implications for hydrodynamic force production, and the evidence is now clear that swimming fishes actively adjust their fin area as speed changes. However, the pattern of fin area change with speed can differ considerably between species, with swimming trout and bluegill sunfish showing different patterns of fin area change as speed increases.

Radially symmetrical jellyfish greatly simplify the problem of quantifying body deformation, and recent studies of jellyfish hydrodynamics have shown in detail how the flexible body moves to produce thrust and generate specific wake vortex patterns (Dabiri et al. 2005; Dabiri et al. 2006).

The study of propulsor deformation and its possible hydrodynamic consequences is one area in which a robotic approach (see Question 8 below) can be extremely useful,

permitting controlled alterations in flexibility of elements scaled to the naturally observed bending of biologic tissues during movement. Study of a range of flexible propulsors in a flapping robotic apparatus allowing measurement of efficiency and energy consumption simultaneously with wake dynamics will allow more definitive statements about the hydrodynamic consequences of flexibility than is now possible.

Additionally, a computational fluid dynamic approach can be used to investigate models of varying flexibility to compute resulting changes in efficiency and wake dynamics. Examples of this approach applied to fish pectoral fins allowed the conclusion that structural flexibility of pectoral fin rays may increase both thrust and efficiency (Shoele and Zhu 2009; Zhu and Shoele 2008).

2.4 How are locomotor kinematics and dynamics altered under unsteady conditions?

Fish often move in an unsteady manner. And even when the time-averaged center of mass velocity is constant, the motion of individual propulsors is dynamic. So understanding the hydrodynamics of aquatic animal locomotion requires understanding how body motions and induced flows change with time. This in turn requires both time-resolved kinematics and experimental fluid dynamic data.

Only in the past ten years has there been increasing focus on investigating the fluid dynamics of unsteady locomotor behaviors such as maneuvering locomotion. There are still no experimental analyses of maneuvering fluid dynamics or changes in propulsor conformation during maneuvers by aquatic mammals. Most analyses of acceleration or other unsteady behaviors such as braking, stopping, or backing up have occurred in fishes, where particle image velocimetry and kinematic analysis have demonstrated the considerable changes in wake dynamics and the shape and area of propulsive surfaces that accompany maneuvers (Flammang and Lauder 2009; Shirgaonkar et al. 2008; Tytell 2004). The study of unsteady locomotor dynamics is an area of swimming hydrodynamics that is very much in need of further analysis.

One unsteady behavior in fishes that has received a great deal of attention from fish biologists and neurobiologists is the so-called c-start escape response. In this behavior, the fish rapidly (5–30 ms) bends its body into a c-like shape during stage 1, followed by a strong tail movement during stage 2 to move the center of mass away from the stimulus (Wakeling 2006). This behavior is controlled by a well-understood neuronal network, and has been the subject of nearly a thousand papers over the years. But virtually nothing is known about the fluid dynamics of this cannonical unsteady locomotor behavior.

Figure 3 shows one result from the analysis by Tytell and Lauder (2008) who quantified the fluid dynamics of the escape response in bluegill sunfish. The rapid pattern of body bending during the c-start escape produces three distinct vortical flows, nearly orthogonal to each other. Summing the estimated forces along the direction of the escape response calculated from particle image velocimetry data produced an estimate for body momentum that was not significantly different from that calculated from the body motion itself. Generally similar flow patterns were also found by Epps and Techet (2007) in their study of rapid turning maneuvers. A great deal of more experimental study is needed on rapid locomotor behaviors, which are frequently exhibited by fishes and which form a very important part of their natural locomotor repertoire.

Another key area of unsteady swimming hydrodynamics is the behavior exhibited by fishes swimming in turbulent flows. Although natural turbulence in streams may be hard to replicate in a laboratory setting, it is possible to generate controlled turbulence using cylinders in a flow. Producing a Karman street and inducing fish to swim there reveals a number of novel locomotor modes (Liao et al. 2003a, b; Liao 2004) that had not previously been observed by fishes swimming steadily in the typical laboratory setting. The control system used by fishes to interact with turbulent flows is mostly unknown, although there is a great deal of information about individual fish sensory systems (Collin and Marshall 2003; Coombs and Van Netten 2006; Webb et al. 2008). Analyses of aquatic animals swimming in well-characterized unsteady flows is just in its infancy, and a great deal more research is needed in this area.

2.5 What is the three-dimensional structure of aquatic animal vortex wakes?

There are now numerous reconstructions, using data from two-dimensional planar particle image velocimetry, of the vortex wakes shed by swimming animals. Examples include simplistic views of the vortex wake produced by the tail of swimming fishes (Lauder and Drucker 2002; Nauen and Lauder 2002a; Videler 1993; Wilga and Lauder 2004), pectoral fin vortex rings (Drucker and Lauder 1999; Drucker and Lauder 2000), and more sophisticated estimates of the vortical patterns shed by the tail as well as dorsal and anal fins (Tytell 2006; Tytell et al. 2008) of swimming fishes. These data have been generated using time-resolved particle image velocimetry, with framing rates up to 1000 Hz, which gives good resolution of the evolution of the wake in a single plane. Some progress has also been made in understanding the vortical wake and patterns of wake momentum using stereo particle image velocimetry which results in three velocity components for a single plane (Nauen and Lauder 2002b; Sakakibara et al.

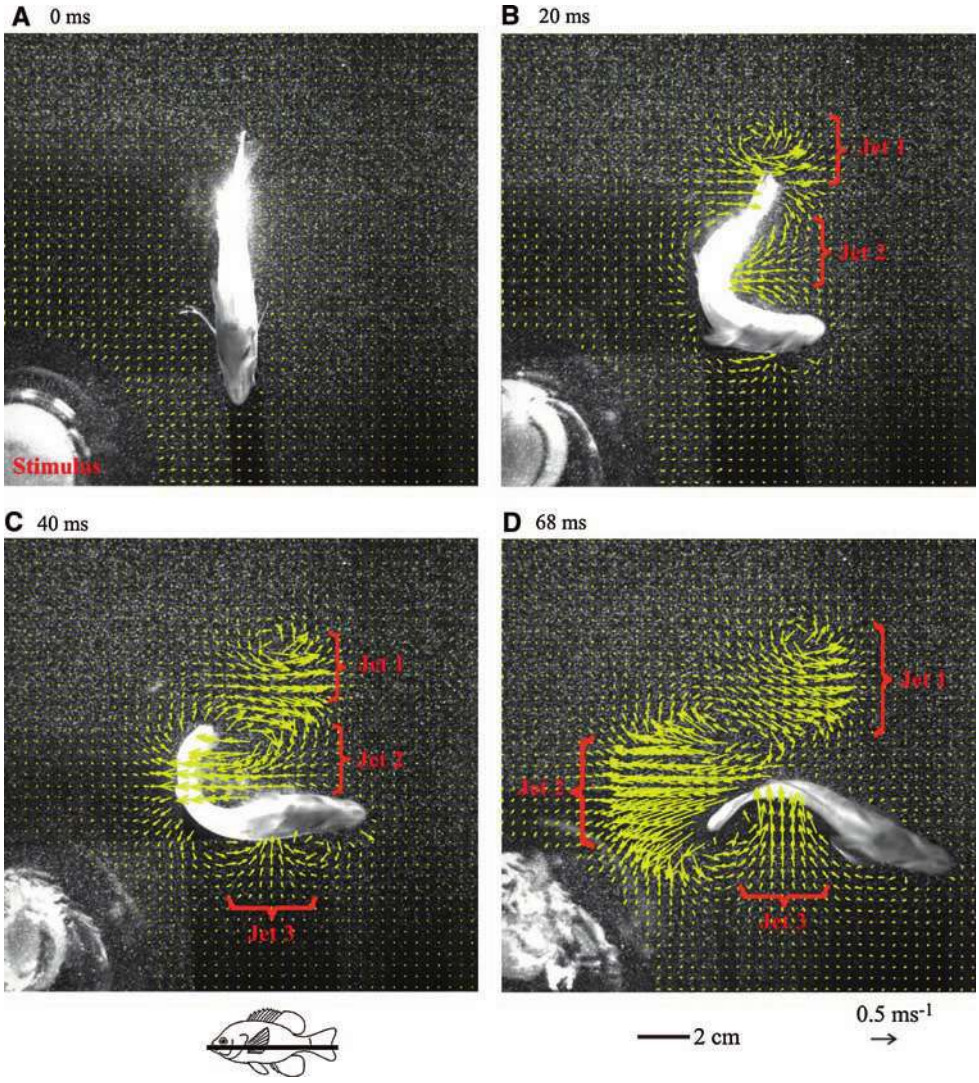

Fig. 3 Wake flow patterns (yellow velocity vectors) generated by a bluegill sunfish exhibiting a c-start escape response to show the unexpected hydrodynamic patterns that can emerge from unsteady locomotor behaviors. Each rapid c-start produces *three* nearly orthogonal jet flows (labeled Jet 1, Jet 2, and Jet 3) as the fish bends its body during the escape. The stimulus is visible in the lower left of each image, and the laser light sheet intersected the mid-body region. Image from Tytell and Lauder (2008)

2004; Willert 1997), but a key future goal should be to use more technically sophisticated methods to estimate the three-dimensional structure of wake vorticity.

There are unavoidable difficulties in using planar data to reconstruct three-dimensional structures, especially when freely swimming fishes are studied. Phase averaging is possible, although difficult, because each fin beat is slightly different both in the timing and excursion of fin and body motion, and fishes rarely swim in a constant absolute position (Lauder and Madden 2007; Lauder and Madden 2008). Extrapolating from data obtained in one plane to a three-dimensional vortex structure is also challenging. To some extent, these difficulties can be mitigated by using a scanning approach in which the laser light sheet is scanned rapidly through the moving fin (Brücker and Bleckmann 2007; Lauder and Madden 2007; Zhang et al. 2008), or reorienting the laser light sheet into orthogonal orientations to evaluate vorticity in multiple planes (e.g., Drucker and Lauder 1999). Such approaches have permitted considerable progress in reconstructing vortex dynamics and analyzing momentum fluxes associated with the moving body and propulsors, and inaccuracies have been at least reduced by using time-resolved particle image velocimetry which provides a high-sample rate of flow dynamics (200–1000 Hz) relative to the frequency of body and appendage motion (typically 1–10 Hz).

Nonetheless, future advances in understanding locomotor dynamics would be greatly aided by the ability to reconstruct the full three-dimensional flow pattern generated by moving organisms. Technically, this is just now becoming feasible, but there are as yet no examples of volumetric data showing the full three-dimensional vortex wake structure behind a swimming body or moving animal surface. The technology to generate such data is just now available, with tomographic, holographic, or defocusing approaches becoming more common, and allowing the calculation of all three velocity components within a volume at an instant in time, thus providing a snapshot of the

full wake structure (Hain et al. 2008; Pereira et al. 2000; Svizher and Cohen 2006; Troolin and Longmire 2008; Wieneke 2008).

2.6 To what extent are observed body and propulsor deformations actively controlled?

The extent to which observed body and propulsive surface deformations are primarily active, passive, or a complex interaction between the two, is one of the most difficult questions facing investigators studying the locomotor dynamics of swimming organisms. This is a non-trivial question, and addressing this issue comprehensively requires not just approaches from fluid mechanics, but also the use of electrophysiological techniques such as electromyography to determine when muscles are active to power locomotion.

Because most swimming animals have bodies and/or moving propulsive surfaces with intrinsic muscles that can be activated to varying degrees, the stiffness of the body and surfaces can be altered from moment to moment. And, changes in body stiffness often accompany changes in speed of swimming animals (e.g., Long 1998; Long and Nipper 1996). Bony fish, in particular, possess fin architectures that allow them to control the stiffness of their appendages by activating muscles at the base of the fin, even though no muscle tissue resides within the fin itself (Alben et al. 2007; Geerlink and Videler 1987; Lauder 2006; Lauder and Madden 2006). This makes interpreting observed correlations between movement and wake-flow patterns very difficult.

There is at least one situation in which it is possible to conclusively state that animals are actively moving their bodies and appendages: if motion occurs into external flow so that body motion opposes the direction of flow. Alben et al. (2007: Fig. 8) show an example of this from the sunfish pectoral fin during a maneuver. But in almost all cases, the observed deformation will be neither clearly actively generated nor purely a passive result of flow-induced pressure on the surface.

At least two distinct approaches can be taken to the problem of determining the extent of active versus passive control of surface deformation. First, measurements can be made of muscle activity patterns during swimming to determine if the appendages or body regions under analysis are being activated by the animal's musculature as the appendages move into oncoming fluid. In addition, muscle activity recordings will show if an animal is resisting fluid loading on the body or appendages even though they are being deformed by fluid forces. Examples of such data for fishes are given in Flammang and Lauder (2008, 2009) for fish tail function, and muscular control of fish body deformation is reviewed in Shadwick and Lauder (2006).

Second, a computational approach is possible. Generating a coupled fluid–structure model for a particular appendage will allow computing both flows and shapes of the appendage with a prescribed root movement pattern. The computed and predicted movement patterns can then be compared to the body and appendage motions observed during natural locomotion (Zhu and Shoele 2008).

Progress in addressing this question will depend in part on our ability to generate a much greater array of data on the material properties of biologic tissues, and data on how these properties can be actively controlled. Most important will be the development of new methods for determining the in vivo stiffness of tissues of swimming animals, and how stiffness changes during movement of the body and appendages.

2.7 What is the response of the body and appendages to external perturbations?

Despite the many analyses of propulsion in aquatic animals ranging from jellyfish to a diversity of fishes to marine mammals, very few papers have attempted to perturb directly the freely swimming animal with a controlled stimulus. And yet such perturbations could be exceptionally informative about the instantaneous mechanical properties of the moving body or fins, and also reveal many aspects of both the hierarchical locomotor control system and the dynamics of body stability.

Webb (2004b) conducted an exemplary study of the responses of fishes to jets of water impinging on their body, and showed that the fish species studied appeared to be more sensitive to roll disturbances and attempted to correct for roll torques more rapidly than for yaw or pitch torques; also see Webb (2006, 2004a) for more general discussions of fish stability. But further experiments are needed to assess how aquatic animals maintain stability and to understand the role that different sensory systems play in regulating stable body posture.

Figure 4 shows an example of an experimental arrangement used to perturb swimming bluegill sunfish. A synthetic jet vortex generator was used to produce a single vortex ring that propagated toward the swimming fish. This jet is visualized by filling the cavity in the vortex generator with dye, and jets can be aimed at both pectoral fins (Fig. 4a) and the caudal fin (Fig. 4b, c). If the impinging vortex ring is not too strong, fish do not attempt to escape, and fins exhibit a passive response to the vortex jet. In this case, the strength of the vortex ring impacting the swimming fish was determined to be in the range of forces generated by fish fins during locomotion: fin and vortex impulses ranged from 0.1 to 1.0 mNs.

Another type of perturbation can be achieved by altering the viscosity of the liquid in which animals move, either by altering viscosity directly by adding polymers or by changing the temperature (Horner and Jayne 2008; Hunt

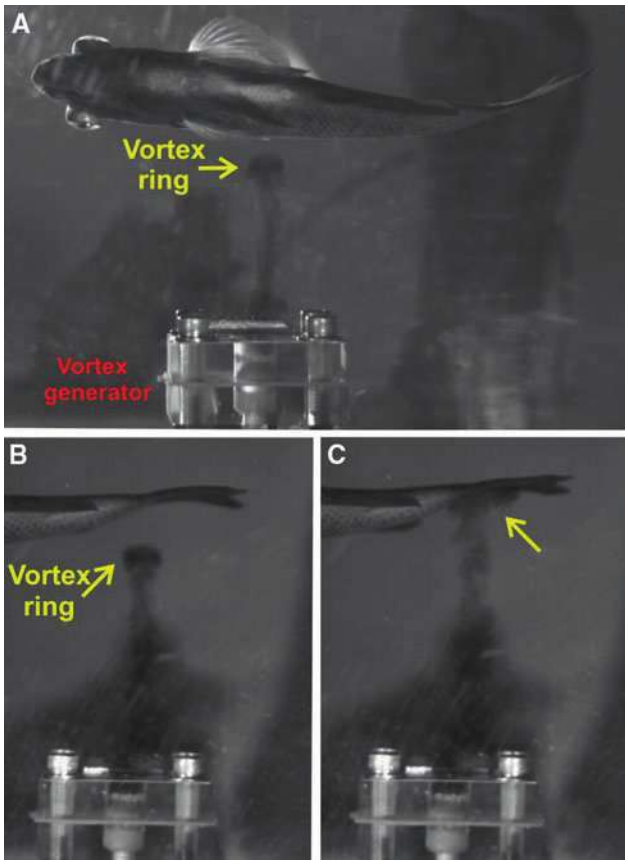

Fig. 4 Vortex perturbations of a freely swimming bluegill sunfish. Images are individual frames from 500-Hz digital videos of generated vortices impacting the fish during locomotion. **a** The sunfish (18 cm in length) and the vortex generator used to perturb the fish which is freely swimming in a recirculating flow tank at 0.5 L/s. A small vortex (48 mN impact force) is about to hit the fish just posterior to the center of mass. **b** A small vortex ring moving toward the fish near the tail fin. **c** Impact of this vortex ring 28 ms later on the tail. The original movie clearly shows rapid and passive deflection of the tail within 10 ms resulting from vortex impact

von Herbing and Keating 2003; Johnson et al. 1998). Studies of this kind promise new insights into the regulation of locomotor dynamics in swimming animals by greatly extending the parameter space within which animals must perform locomotor actions.

Perturbation studies of swimming animals are still in their infancy, and a great deal more remains to be done, especially in the development of controlled systems for generating appropriate stimuli that induce a response (either active or passive) in the swimming animal, and in methods of analyzing responses of animals to stimuli.

2.8 How can robotic models help us understand locomotor dynamics?

The last 10 years have seen a rapid increase in the development of robotic devices that can swim (e.g., Bandyopadhyay 2002; Kato 2000; Long et al. 2006; Tan et al. 2007; Triantafyllou and Triantafyllou 1995). In some cases, robotic animal-like swimmers are developed to answer engineering questions about underwater propulsion. But robotic models have an important role to play in helping biologists understand how aquatic animals function to move effectively. Robotics can inform biology in many useful ways. One key area in which robotic swimming devices are useful is in allowing isolation of individual factors that might influence propulsion. For example, comparative analyses of fish locomotion are hampered by the fact that species of fishes differ in many mechanical attributes. If one is interested in the effect of fish tail shape on propulsion, a comparison can be done between fish of different species that have different tail shapes, but there are many other features of these species that will differ also. Similarly, if one is interested in how changes in fish body or fin flexibility alter propulsive efficiency, a comparison could be made between different species that differ in flexibility, but these species will also differ in many other attributes, any of which could affect propulsion. The many ways in which species differ from each other make it very difficult to isolate individual components and thus to investigate key biomechanical questions to better understand aquatic locomotion.

Robotic models are a great advantage in allowing isolation of individual components of design, but this can also come at the cost of simplifying the biology to such an extent that key features of animal design are lost. However, it is possible to undertake a range of studies from simple physical models of propulsion to more highly biomimetic robotic devices that allow one to investigate fundamental questions about propulsion with much greater control than can be achieved using live animals.

As one example of this approach, an overview of a diversity of robotic approaches from our recent research on fish propulsion is shown in Fig. 5 (Lauder et al. 2007). We have attempted to range from the study of simple flexible plastic foils where we can easily change material properties and shapes (even though these systems are not as biologically realistic) to more highly biomimetic designs with fish pectoral fin robots that closely resemble the pectoral fins of live fishes (Tangorra et al. 2007). Even complex fish locomotor surfaces such as a ray wing can be modeled simply using a two-actuator system to understand basic properties of surface deformation and its effect on propulsion. One critical feature of these robotic test platforms is that they are self-propelling: they generate propulsive forces and swim against oncoming flow on a low-friction air carriage so that they can be studied easily using standard kinematic and fluid dynamic approaches (Lauder et al. 2007). The ability to study robotic models under conditions of self propulsion is critical to understanding the body and fin motions and how wake-flow patterns are produced.

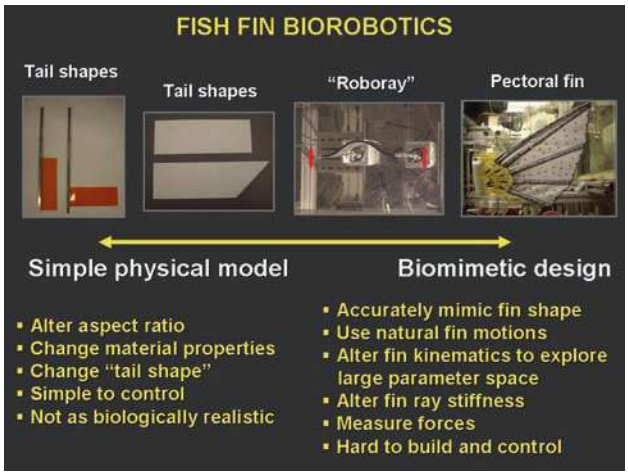

Fig. 5 Diagrammatic overview of one approach to fish biorobotics that includes both simple physical models (flapping flexible plastic foils—on the left) and more highly biomimetic models of fish and their fins (biomimetic pectoral fin—on the right). Simple physical models with one or two actuators allow easy alteration of flexibility and shape to model fish tail diversity, while more complexly actuated designs permit study of motion similar to that in freely swimming fishes. Some positive and negative aspects of each extreme approach are listed

Robotic test platforms have many advantages: control of specific structural parameters such as flexibility, precise motion control, direct measurement of force (difficult in freely swimming fishes), and exploration of a wider parameter space of motion than seen in live animals. Robotic devices also facilitate three-dimensional kinematic studies and correlated hydrodynamic analyses, as the location of the locomotor surface can be known accurately. And, individual components of a natural motion (such as outstroke vs. instroke of a flapping appendage) can be programmed separately, which is certainly difficult to achieve when working with a live animal.

2.9 How do propulsive surfaces interact hydrodynamically during natural motions?

One aspect of aquatic animal propulsion that is clearly evident in fishes, and to a lesser extent in marine mammals, is the possibility that the different control surfaces used for locomotion can interact with each other hydrodynamically. The idea of hydrodynamic interactions among propulsive surfaces is an old one, but recently this idea has received more attention. One aspect of this question is the extent to which flow encountered by the trailing edge of the swimming animal is altered by body motions upstream, and this has been a topic of some discussion for swimming fishes (Lauder and Tytell 2006; Müller et al. 2001; Tytell and Lauder 2004). But the possibility of hydrodynamic interactions between flapping appendages (acting as two individual foils) has also been a topic of interest, although most research to date has been on insect wings during flight (Birch and Dickinson 2003; Lehmann et al. 2005; Lehmann 2008; Lehmann 2009; Usherwood and Lehman 2008). There is certainly a great deal more that could be studied on the interesting topic of hydrodynamic interactions among propulsive surfaces of swimming animals.

Experimental studies of live fishes have shown that upstream fins such as the dorsal and anal fins actively generate vortex wakes that travel downstream and encounter the tail (Drucker and Lauder 2001; Standen and Lauder 2007), and that the tail experiences greatly altered flows that are quite different from the free stream. This has clear implications for locomotor efficiency, as well as for the hydrodynamic mechanisms that are involved in lift and thrust production during swimming. One computational study (Akhtar et al. 2007) analyzed a range of phase relationships between the flapping dorsal fin and tail of swimming bluegill sunfish, and compared the biologic values to the values of thrust and efficiency calculated for a diversity of parameter values. Interestingly, the optimal computed phase difference of 48° is different than the observed 108° observed during swimming sunfish. This result is still unexplained, but suggests that fish are subject to constraints on fin shapes, location, and movement patterns that limit their ability to move propulsive surfaces in a hydrodynamically optimal fashion.

2.10 What new computational approaches are needed to better understand locomotor hydrodynamics?

There is only so much that can be learned from experimental studies of live animals. Data that are important for understanding hydrodynamic mechanisms and flow physics, such as surface pressure distributions, are extremely hard to obtain on freely swimming animals. Small localized transducers can be attached (see, e.g., the classic papers by DuBois et al. 1976; Dubois and Ogilvy 1978), but data from one point on the swimming animal gives only a very general impression of the forces exhibited by the surface as a whole.

A computational approach, particularly when married with experimental analysis of live animals and robotic devices, permits exploration of a large parameter space, alteration of movement patterns, and a focused investigation of hydrodynamic mechanisms underlying locomotor performance. And computational approaches are an excellent way to simplify biologic structures and movement patterns, and compare them to more canonical engineering solutions such as heaving and pitching foils.

There have been a number of recent computational fluid dynamic analyses of aquatic locomotion, which involve study of either whole body deformations (Borazjani and Sotiropoulos 2008; Borazjani and Sotiropoulos 2009;

Carling et al. 1998) or propulsive surfaces such as pectoral fins (Bozkurttas et al. 2009; Mittal et al. 2006; Ramamurti et al. 2002). To date no study that I am aware of has included both moving fish bodies and fins together. Since fish fins are actively moved by intrinsic musculature (Lauder 2006) and shed their own vortex wake, computational approaches to fish locomotion in the future could certainly be extended by incorporating both body and fin motions. The computational studies of Borazjani and colleagues (2008; 2009) in particular show how understanding difficult issues in comparative hydrodynamics can be greatly enhanced by a computational approach, as they were able to directly compare computationally fish swimming in an anguilliform versus carangiform locomotor mode, something that would not be possible to achieve by studying live fishes.

Computational approaches also have recently contributed considerably to the analysis of experimental data, as evidenced by recent work on a Lagrangian approach to wake dynamics and identification of an "upstream wake" (Dabiri 2005; Peng and Dabiri 2008a; Peng and Dabiri 2008b).

Future contributions of computational approaches are likely to be enhanced by the development of more sophisticated internal body models of swimming animals (e.g., Bowtell and Williams 1991; Bowtell and Williams 1994) and then coupling these to fluid dynamic model for a comprehensive analysis of body and control surface inputs and outputs during swimming. However bright the prospects for such an approach, this work will be challenging, as full three-dimensional analyses of all propulsive surfaces will be needed, as will knowledge of the dynamic material properties of the body and moving surfaces. As noted above, acquiring time-varying geometries on moving organisms is not a simple task, although recent techniques such as proper orthogonal decomposition (POD) allow simplification of the movement pattern, once acquired, for subsequent computational analysis (Bozkurttas et al. 2009). An additional challenge will be the ability to run computational analyses at Reynolds numbers high enough to reflect the speeds and sizes of most adult swimming organisms, in the range of 5,000 to 20,000.

3 Conclusions

There are many unresolved questions in the study of the swimming hydrodynamics of animals, and the papers collected in this volume exemplify many of the new avenues of research that will lead to future advances. In this contribution, I have gathered together ten key questions that in my view might, especially for students contemplating research in this area, guide plans for future studies of swimming hydrodynamics. Addressing even a portion of one of these questions could form the basis for thesis research or even the focus of an entire research program for several years.

There are certainly many other possible questions that could be addressed, and in the interest of brevity I have omitted many interesting areas of research. But I believe that if, in the next decade, we are able to make as much progress as we have in the past one, the field of swimming hydrodynamics will have demonstrated remarkable innovation and growth that promises many new discoveries about how swimming animals interact with their fluid environment.

Acknowledgments This work was supported by an ONR-MURI Grant N00014-03-1-0897, and by ONR grant N00014-09-1-0352. We thank Drs. Rajat Mittal for many helpful discussions on bio-inspired propulsion. Many thanks to members of the Lauder and Tangorra Laboratories for numerous helpful discussions, and to Timo Gericke for constructing the vortex generator.

References

Akhtar I, Mittal R, Lauder GV, Drucker E (2007) Hydrodynamics of a biologically inspired tandem flapping foil configuration. Theor Comput Fluid Dyn 21:155–170

Alben S (2008) Optimal flexibility of a flapping appendage in an inviscid fluid. J Fluid Mech 614:355–380

Alben S, Shelley M, Zhang J (2004) How flexibility induces streamlining in a two-dimensional flow. Phys Fluids 16:1694

Alben S, Madden PGA, Lauder GV (2007) The mechanics of active fin-shape control in ray-finned fishes. J Roy Soc Interface 4:243–256

Bainbridge R (1963) Caudal fin and body movements in the propulsion of some fish. J Exp Biol 40:23–56

Bandyopadhyay PR (2002) Maneuvering hydrodynamics of fish and small underwater vehicles. Int Comp Biol 42:102–117

Bartol IK, Gharib M, Webb PW, Weihs D, Gordon MS (2005) Body-induced vortical flows: a common mechanism for self-corrective trimming control in boxfishes. J Exp Biol 208:327–344

Birch JM, Dickinson MH (2003) The influence of wing-wake interactions on the production of aerodynamic forces in flapping flight. J Exp Biol 206:2257–2272

Blondeaux P, Fornarelli F, Guglielmini L, Triantafyllou MS, Verzicco R (2005) Numerical experiments on flapping foils mimicking fish-like locomotion. Phys Fluids 17:113601

Borazjani I, Sotiropoulos F (2008) Numerical investigation of the hydrodynamics of carangiform swimming in the transitional and inertial flow regimes. J Exp Biol 211:1541–1558

Borazjani I, Sotiropoulos F (2009) Numerical investigation of the hydrodynamics of anguilliform swimming in the transitional and inertial flow regimes. J Exp Biol 212:576–592

Bowtell G, Williams TL (1991) Anguilliform body dynamics—modelling the interaction between muscle activation and body curvature. Phil Trans R Soc Lond B 334:385–390

Bowtell G, Williams TL (1994) Anguilliform body dynamics—a continuum model for the interaction between muscle activation and body curvature. J Math Biol 32:83–91

Bozkurttas M, Dong H, Mittal R, Madden P, Lauder GV (2006) Hydrodynamic performance of deformable fish fins and flapping foils. AIAA paper 2006-1392

Bozkurttas M, Mittal R, Dong H, Lauder GV, Madden P (2009) Low-dimensional models and performance scaling of a highly deformable fish pectoral fin. J Fluid Mech 631:311–342

Brücker C, Bleckmann H (2007) Vortex dynamics in the wake of a mechanical fish. Exp Fluids 43:799–810

Carling JC, Williams TL, Bowtell G (1998) Self-propelled anguilliform swimming: simultaneous solution of the two-dimensional Navier–Stokes equations and Newton's laws of motion. J Exp Biol 201:3143–3166

Collin SP, Marshall NJ (2003) Sensory processing in aquatic environments. Springer Verlag, New York

Coombs SA, Van Netten SM (2006) The hydrodynamics and structural mechanics of the lateral line system. In: Shadwick RE, Lauder GV (eds) Fish biomechanics volume 23 in fish physiology. Academic Press, San Diego, pp 103–139

Cooper LN, Sedano N, Johansson S, May B, Brown JD, Holliday CM, Kot BW, Fish FE (2008) Hydrodynamic performance of the minke whale (*Balaenoptera acutorostrata*) flipper. J Exp Biol 211:1859–1867

Dabiri JO (2005) On the estimation of swimming and flying forces from wake measurements. J Exp Biol 208:3519–3532

Dabiri JO (2009) Optimal vortex formation as a unifying principle in biological propulsion. Ann Rev Fluid Mech 41:17–33

Dabiri JO, Colin SP, Costello JH, Gharib M (2005) Flow patterns generated by oblate medusan jellyfish: field measurements and laboratory analyses. J Exp Biol 208:1257–1265

Dabiri JO, Colin SP, Costello JH (2006) Fast-swimming hydromedusae exploit velar kinematics to form an optimal vortex wake. J Exp Biol 209:2025–2033

Drucker EG, Lauder GV (1999) Locomotor forces on a swimming fish: three-dimensional vortex wake dynamics quantified using digital particle image velocimetry. J Exp Biol 202:2393–2412

Drucker EG, Lauder GV (2000) A hydrodynamic analysis of fish swimming speed: wake structure and locomotor force in slow and fast labriform swimmers. J Exp Biol 203:2379–2393

Drucker EG, Lauder GV (2001) Locomotor function of the dorsal fin in teleost fishes: experimental analysis of wake forces in sunfish. J Exp Biol 204:2943–2958

Dubois AB, Ogilvy CS (1978) Forces on the tail surface of swimming fish: thrust, drag and acceleration in bluefish (*Pomatomus saltatrix*). J Exp Biol 77:225–241

DuBois AB, Cavagna GA, Fox RS (1976) Locomotion of bluefish. J Exp Zool 195:223–235

Epps B, Techet A (2007) Impulse generated during unsteady maneuvering of swimming fish. Exp Fluids 43:691–700

Fish F (2004) Structure and mechanics of nonpiscine control surfaces. IEEE J Oceanic Eng 29:605–621

Fish F, Lauder GV (2006) Passive and active flow control by swimming fishes and mammals. Ann Rev Fluid Mech 38:193–224

Fish FE, Howle LE, Murray MM (2008) Hydrodynamic flow control in marine mammals. Integr Comp Biol 48:788–800

Flammang BE, Lauder GV (2008) Speed-dependent intrinsic caudal fin muscle recruitment during steady swimming in bluegill sunfish, *Lepomis macrochirus*. J Exp Biol 211:587–598

Flammang BE, Lauder GV (2009) Caudal fin shape modulation and control during acceleration, braking and backing maneuvers in bluegill sunfish, *Lepomis macrochirus*. J Exp Biol 212:277–286

Fontaine EI, Zabala F, Dickinson MH, Burdick JW (2009) Wing and body motion during flight initiation in *Drosophila* revealed by automated visual tracking. J Exp Biol 212:1307–1323

Geerlink PJ, Videler JJ (1987) The relation between structure and bending properties of teleost fin rays. Neth J Zool 37:59–80

Hain R, Kähler C, Michaelis D (2008) Tomographic and time resolved PIV measurements on a finite cylinder mounted on a flat plate. Exp Fluids 45:715–724

Hertel H (1966) Structure, form and movement. Reinhold, New York, NY

Hoerner SF (1965) Fluid-dynamic drag. Hoerner Fluid Dynamics, Bakersfield, California

Horner AM, Jayne BC (2008) The effects of viscosity on the axial motor pattern and kinematics of the African lungfish (*Protopterus annectens*) during lateral undulatory swimming. J Exp Biol 211:1612–1622

Hunt von Herbing I, Keating K (2003) Temperature-induced changes in viscosity and its effects on swimming speed in larval haddock. In: Browman HI, Skiftesvik A (eds) The big fish bang. Institute of Marine Research, Bergen, pp 23–34

Johnson TP, Cullum AJ, Bennett AF (1998) Partitioning the effects of temperature and kinematic viscosity on the c-start performance of adult fishes. J Exp Biol 201:2045–2051

Kato N (2000) Control performance in the horizontal plane of a fish robot with mechanical pectoral fins. IEEE J Oceanic Eng 25:121–129

Lauder GV (1989) Caudal fin locomotion in ray-finned fishes: historical and functional analyses. Amer Zool 29:85–102

Lauder GV (2000) Function of the caudal fin during locomotion in fishes: kinematics, flow visualization, and evolutionary patterns. Amer Zool 40:101–122

Lauder GV (2006) Locomotion. In: Evans DH, Claiborne JB (eds) The physiology of fishes, 3rd edn. CRC Press, Boca Raton, pp 3–46

Lauder GV, Drucker EG (2002) Forces, fishes, and fluids: hydrodynamic mechanisms of aquatic locomotion. News Physiol Sci 17:235–240

Lauder GV, Madden PGA (2006) Learning from fish: kinematics and experimental hydrodynamics for roboticists. Int J Automat Comput 4:325–335

Lauder GV, Madden PGA (2007) Fish locomotion: kinematics and hydrodynamics of flexible foil-like fins. Exp Fluids 43:641–653

Lauder GV, Madden PGA (2008) Advances in comparative physiology from high-speed imaging of animal and fluid motion. Ann Rev Physiol 70:143–163

Lauder GV, Tytell ED (2006) Hydrodynamics of undulatory propulsion. In: Shadwick RE, Lauder GV (eds) Fish biomechanics volume 23 in fish physiology. Academic Press, San Diego, pp 425–468

Lauder GV, Madden PGA, Mittal R, Dong H, Bozkurttas M (2006) Locomotion with flexible propulsors I: experimental analysis of pectoral fin swimming in sunfish. Bioinsp Biomimet 1:S25–S34

Lauder GV, Anderson EJ, Tangorra J, Madden PGA (2007) Fish biorobotics: kinematics and hydrodynamics of self-propulsion. J Exp Biol 210:2767–2780

Lehmann F-O (2008) When wings touch wakes: understanding locomotor force control by wake wing interference in insect wings. J Exp Biol 211:224–233

Lehmann F-O (2009) Wing–wake interaction reduces power consumption in insect tandem wings. Exp Fluids 46:765–775

Lehmann F-O, Sane SP, Dickinson M (2005) The aerodynamic effects of wing-wing interaction in flapping insect wings. J Exp Biol 208:3075–3092

Liao J (2004) Neuromuscular control of trout swimming in a vortex street: implications for energy economy during the Karman gait. J Exp Biol 207:3495–3506

Liao J, Beal DN, Lauder GV, Triantafyllou MS (2003a) Fish exploiting vortices decrease muscle activity. Science 302:1566–1569

Liao J, Beal DN, Lauder GV, Triantafyllou MS (2003b) The Kármán gait: novel body kinematics of rainbow trout swimming in a vortex street. J Exp Biol 206:1059–1073

Liu H, Wassersug RJ, Kawachi K (1997) The three-dimensional hydrodynamics of tadpole locomotion. J Exp Biol 200:2807–2819

Long J (1998) Muscles, elastic energy, and the dynamics of body stiffness in swimming eels. Amer Zool 38:771–792

Long JH, Nipper KS (1996) The importance of body stiffness in undulatory propulsion. Amer Zool 36:678–694

Long JH Jr, Koob TJ, Irving K, Combie K, Engel V, Livingston N, Lammert A, Schumacher J (2006) Biomimetic evolutionary analysis: testing the adaptive value of vertebrate tail stiffness in autonomous swimming robots. J Exp Biol 209:4732–4746

Mittal R, Dong H, Bozkurttas M, Lauder GV, Madden PGA (2006) Locomotion with flexible propulsors II: computational modeling and analysis of pectoral fin swimming in sunfish. Bioinsp Biomimet 1:S35–S41

Müller UK, Smit J, Stamhuis EJ, Videler JJ (2001) How the body contributes to the wake in undulatory fish swimming: flow fields of a swimming eel (*Anguilla anguilla*). J Exp Biol 204:2751–2762

Nauen JC, Lauder GV (2002a) Hydrodynamics of caudal fin locomotion by chub mackerel, *Scomber japonicus* (Scombridae). J Exp Biol 205:1709–1724

Nauen JC, Lauder GV (2002b) Quantification of the wake of rainbow trout (*Oncorhynchus mykiss*) using three-dimensional stereoscopic digital particle image velocimetry. J Exp Biol 205: 3271–3279

Peng J, Dabiri JO (2008a) An overview of a Lagrangian method for analysis of animal wake dynamics. J Exp Biol 211:280–287

Peng J, Dabiri JO (2008b) The 'upstream wake' of swimming and flying animals and its correlation with propulsive efficiency. J Exp Biol 211:2669–2677

Pereira F, Gharib M, Dabiri D, Modarress D (2000) Defocusing digital particle image velocimetry: a 3-component 3-dimensional DPIV measurement technique. Application to bubbly flows. Exp Fluids 29:S78–S84

Ramamurti R, Sandberg WC, Lohner R, Walker JA, Westneat M (2002) Fluid dynamics of flapping aquatic flight in the bird wrasse: three-dimensional unsteady computations with fin deformation. J Exp Biol 205:2997–3008

Sakakibara J, Nakagawa M, Yoshida M (2004) Stereo-PIV study of flow around a maneuvering fish. Exp Fluids 36:282–293

Shadwick RE, Lauder GV (2006) Fish biomechanics. In: Hoar WS, Randall DJ, Farrell AP (eds) Fish physiology, vol 23. Academic Press, San Diego

Shen L, Zhang X, Yue D, Triantafyllou MS (2003) Turbulent flow over a flexible wall undergoing a streamwise travelling wave motion. J Fluid Mech 484:197–221

Shirgaonkar AA, Curet OM, Patankar NA, MacIver MA (2008) The hydrodynamics of ribbon-fin propulsion during impulsive motion. J Exp Biol 211:3490–3503

Shoele K, Zhu Q (2009) Fluid–structure interactions of skeleton-reinforced fins: performance analysis of a paired fin in lift-based propulsion. J Exp Biol 212:2679–2690

Standen EM (2008) Pelvic fin locomotor function in fishes: three-dimensional kinematics in rainbow trout (*Oncorhynchus mykiss*). J Exp Biol 211:2931–2942

Standen EM, Lauder GV (2005) Dorsal and anal fin function in bluegill sunfish (*Lepomis macrochirus*): three-dimensional kinematics during propulsion and maneuvering. J Exp Biol 205:2753–2763

Standen EM, Lauder GV (2007) Hydrodynamic function of dorsal and anal fins in brook trout (*Salvelinus fontinalis*). J Exp Biol 210:325–339

Svizher A, Cohen J (2006) Holographic particle image velocimetry measurements of hairpin vortices in a subcritical air channel flow. Phys Fluids 18:014105–014114

Taft N, Lauder GV, Madden PG (2008) Functional regionalization of the pectoral fin of the benthic longhorn sculpin during station holding and swimming. J Zool Lond 276:159–167

Tan G-K, Shen G-X, Huang S-Q, Su W–H, Ke Y (2007) Investigation of flow mechanism of a robotic fish swimming by using flow visualization synchronized with hydrodynamic force measurement. Exp Fluids 43:811–821

Tangorra J, Anquetil P, Fofonoff T, Chen A, Del Zio M, Hunter I (2007) The application of conducting polymers to a biorobotic fin propulsor. Bioinsp Biomimet 2:S6–S17

Triantafyllou MS, Triantafyllou GS (1995) An efficient swimming machine. Sci Amer 272:64–70

Triantafyllou MS, Triantafyllou GS, Yue DKP (2000) Hydrodynamics of fishlike swimming. Ann Rev Fluid Mech 32:33–53

Triantafyllou M, Hover FS, Techet AH, Yue D (2005) Review of hydrodynamic scaling laws in aquatic locomotion and fish swimming. Transactions of the ASME 58:226–237

Troolin D, Longmire E (2008) Volumetric 3-component velocity measurements of vortex rings from inclined exits. In: 14th international symposium on applications of laser techniques to fluid mechanics. Lisbon, Portugal, pp 1–11

Tytell ED (2004) Kinematics and hydrodynamics of linear acceleration in eels, *Anguilla rostrata*. Proc Roy Soc Lond B 271:2535–2540

Tytell ED (2006) Median fin function in bluegill sunfish, *Lepomis macrochirus*: streamwise vortex structure during steady swimming. J Exp Biol 209:1516–1534

Tytell ED, Lauder GV (2004) The hydrodynamics of eel swimming. I. Wake structure. J Exp Biol 207:1825–1841

Tytell ED, Lauder GV (2008) Hydrodynamics of the escape response in bluegill sunfish, *Lepomis macrochirus*. J Exp Biol 211:3359–3369

Tytell ED, Standen EM, Lauder GV (2008) Escaping flatland: three-dimensional kinematics and hydrodynamics of median fins in fishes. J Exp Biol 211:187–195

Usherwood JR, Lehman F-O (2008) Phasing of dragonfly wings can improve aerodynamic efficiency by removing swirl. J Roy Soc Interface 5:1303–1307

Videler JJ (1993) Fish swimming. Chapman and Hall, New York

Wakeling JM (2006) Fast-start mechanics. In: Shadwick RE, Lauder GV (eds) Fish biomechanics volume 23 in fish physiology. Academic Press, San Diego, pp 333–368

Wang H, Ando N, Kanzaki R (2008) Active control of free flight manoeuvres in a hawkmoth, *Agrius convolvuli*. J Exp Biol 211:423–432

Webb PW (1975) Hydrodynamics and energetics of fish propulsion. Bull Fish Res Bd Can 190:1–159

Webb PW (2004a) Maneuverability–general issues. IEEE J Oceanic Eng 29:547–555

Webb PW (2004b) Response latencies to postural disturbances in three species of teleostean fishes. J Exp Biol 207:955–961

Webb P (2006) Stability and maneuverability. In: Shadwick RE, Lauder GV (eds) Fish biomechanics volume 23 in fish physiology. Academic Press, San Diego, pp 281–332

Webb JF, Fay RR, Popper A (2008) Fish bioacoustics. Springer Verlag, New York

Weber PW, Howle LE, Murray MM, Fish FE (2009) Lift and drag performance of odontocete cetacean flippers. J Exp Biol 212:2149–2158

Wieneke B (2008) Volume self-calibration for 3D particle image velocimetry. Exp Fluids 45:549–556

Wilga CD, Lauder GV (2004) Hydrodynamic function of the shark's tail. Nature 430:850

Willert C (1997) Stereoscopic digital particle image velocimetry for application in wind tunnel flows. Meas Sci Technol 8:1465–1479

Wolfgang MJ, Anderson JM, Grosenbaugh M, Yue D, Triantafyllou M (1999) Near-body flow dynamics in swimming fish. J Exp Biol 202:2303–2327

Zhang W, Hain R, Kähler C (2008) Scanning PIV investigation of the laminar separation bubble on a SD7003 airfoil. Exp Fluids 45:725–743

Zhu Q, Shoele K (2008) Propulsion performance of a skeleton-strengthened fin. J Exp Biol 211:2087–2100

Zhu Q, Wolfgang MJ, Yue DKP, Triantafyllou GS (2002) Three-dimensional flow structures and vorticity control in fish-like swimming. J Fluid Mech 468:1–28

A potential-flow, deformable-body model for fluid–structure interactions with compact vorticity: application to animal swimming measurements

Jifeng Peng · John O. Dabiri

Abstract This paper presents an approach to quantify the unsteady fluid forces, moments and mass transport generated by swimming animals, based on measurements of the surrounding flow field. These goals are accomplished within a framework that is independent of the vorticity field, making it unnecessary to directly resolve boundary layers on the animal, body–vortex interactions, or interactions among vortex lines in the wake. Instead, the method identifies Lagrangian coherent structures in the flow, whose dynamics in flows with compact vorticity are shown to be well approximated by potential flow concepts, especially the Kirchhoff and deformation potentials from deformable body theory. Examples of the application of these methods are given for pectoral fin locomotion of the bluegill sunfish and undulatory swimming of jellyfish, and the methods are validated by analysis of a canonical starting vortex ring flow. The transition to a Lagrangian approach toward animal swimming measurements suggests the possibility of implementing recently developed particle tracking (vis-à-vis DPIV) techniques for fully three-dimensional measurements of animal swimming.

J. Peng · J. O. Dabiri
Department of Bioengineering,
California Institute of Technology,
Pasadena, CA 91125, USA

J. O. Dabiri (✉)
Graduate Aeronautical Laboratories,
California Institute of Technology,
Pasadena, CA 91125, USA
e-mail: jodabiri@caltech.edu

1 Introduction

A distinguishing feature of animal swimming in real fluids is the generation of vorticity and the shedding of vortices into the wake. It is for this reason that much of the experimental work on animal swimming has been approached from a perspective that aims to quantify vorticity dynamics (e.g. Drucker and Lauder 1999, 2001; Wilga and Lauder 2004; Bartol et al. 2005; Dabiri et al. 2005; Stamhuis and Nauwelaerts 2005). The standard tool for flow field measurements is digital particle image velocimetry (DPIV), which quantifies the velocity field of the flow in an Eulerian frame of reference, i.e. instantaneously and at fixed locations in space. The vorticity field is then immediately deduced by numerically taking the curl of the measured velocity field.

These wake studies have been complemented by theoretical tools that, in principle, enable the quantification of instantaneous forces and moments created by the animal, given knowledge of the surrounding flow field. However, with the exception of purely steady flows, these methods require either measurement of the boundary layers on the animal, the replacement of the animal body with an equivalent system of image vorticity, or measurements on the surface of a control volume with length scales an order of magnitude larger than the animal itself (Wu 1981; Noca 1997, 1999). Each of these options is difficult to achieve in practice. Therefore, the state-of-the-art in the field is the calculation of time-averaged forces, in which unsteady effects like added-mass tend to cancel when integrated over a swimming cycle (Daniel 1984).

The study of body–vortex interactions, such as those occurring due to incident vortices from upstream or generated by the head of the animal (e.g. Gopalkrishnan et al. 1994; Liao et al. 2003; Beal et al. 2006), is also

G.K. Taylor, M.S. Triantafyllou, and C. Tropea (Eds.): Animal Locomotion, pp. 17–26.
springerlink.com

limited by practical obstacles to quantitative flow visualization. The velocity and vorticity fields cannot usually be well resolved at the interface between the animal and the surrounding fluid while maintaining a full-field view of the flow (see Anderson et al. 2001, for a notable exception). Together these limitations represent a potential show-stopper to more detailed and quantitative analyses of animal swimming.

In general, the challenge of analyzing flow measurements is related to the need to identify consistent boundaries in the flow on which to evaluate the equations of motion. The aforementioned theoretical tools rely on either the fluid–solid boundary represented by the animal surface, or a virtual, fluid–fluid boundary used to define a control volume. Recent applications of Lagrangian, particle-tracking flow analyses have demonstrated that in many unsteady flows there exist physically meaningful, fluid–fluid boundaries that act as barriers to fluid transport. The Lagrangian coherent structures (LCS) defined by these real fluid–fluid boundaries are currently studied for their kinematic properties and have been used primarily to better understand transport and mixing processes or to identify fluid structures in turbulence (e.g. Haller 2000, 2001, 2002; Green et al. 2006).

This paper examines the dynamic properties of LCS and shows that these properties can be used to deduce the forces and moments on a swimming animal. A distinguishing feature of this approach is that it does not appeal to the vorticity dynamics in the flow. Instead, it is shown that potential flow concepts from deformable body theory can be used to approximate the LCS dynamics when the vorticity field is sufficiently compact (i.e. bounded spatially). The LCS tend to appear away from the surface of the animal body but not at prohibitively large distances away. Together these properties make it possible to determine instantaneous, unsteady forces and moments created by swimming animals without the need to resolve boundary layers on the animal, to construct equivalent image vorticity systems, or to use far-field control volume analyses. In addition, the known transport properties of LCS enable quantification of mass transport that is induced by the animal during locomotion.

Recent implementation of these methods in studies of the bluegill sunfish pectoral fin and the entire body of a free-swimming jellyfish are highlighted to demonstrate the capabilities and limitations of the present approach. To be sure, the methods presented here are more generally applicable than animal swimming. However, the study of animal swimming provides a robust test of the method in flows characterized by unsteady fluid–structure interactions and complex vorticity dynamics. Validation using direct numerical simulations of a starting vortex ring formed by a piston-cylinder apparatus demonstrates the capabilities of the method in a more canonical flow and helps to put these results in the context of traditional fluid mechanics analyses.

Section 2 presents the experimental and analytical methods that constitute this vorticity-free approach to the study of animal swimming. Examples of the resulting measurements, taken from recent contributions by the authors and coworkers, are presented in Sect. 3 along with a validation of the method using direct numerical simulations of vortex ring formation by a piston-cylinder apparatus. Finally, Sect. 4 suggests a path forward that addresses issues such as three-dimensional flow, in situ animal measurements, and measurement validation.

2 Experimental and analytical methods

2.1 Identification of Lagrangian coherent structures

The first step in the vorticity-free approach to swimming measurements is to identify the LCS from which fluid dynamic forces and moments will be deduced. Haller (2001) and Shadden et al. (2005, 2006) identify LCS as ridges of local maxima in the finite-time Lyapunov exponent (FTLE) field of a given flow. The FTLE measures the maximum linearized growth rate of the distance between initially adjacent fluid particles. To determine this quantity, fluid particles are tracked over a finite time interval. Since the available information regarding the velocity field $\mathbf{u}$ is typically given in an Eulerian frame (e.g. DPIV), the particle trajectories $\mathbf{x}(t)$ are determined by numerical solution of the ordinary differential equation

$$\dot{\mathbf{x}}(t) = \mathbf{u}(\mathbf{x}(t), t), \tag{1}$$

with the initial position of the fluid particle used as the initial condition. The flow map, which maps fluid particles from their initial location at time t_0 to their location at time $t_0 + T$ can be expressed as

$$\varphi_{t_0}^{t_0+T}(\mathbf{x}) : \mathbf{x}(t_0) \rightarrow \mathbf{x}(t_0 + T), \tag{2}$$

where $\varphi_{t_0}^{t_0+T}(\mathbf{x}) = \mathbf{x}(t_0 + T)$ describes the current location of a fluid particle advected from the location $\mathbf{x}(t_0)$ at time t_0 after a time interval T. A given infinitesimal perturbation $\delta\mathbf{x}_0$ (i.e. fluid particle separation) at time t_0 is transformed to $\delta\mathbf{x}$ by the relation

$$\delta\mathbf{x} = \nabla\varphi_{t_0}^{t_0+T}(\mathbf{x})\delta\mathbf{x}_0, \tag{3}$$

where $\nabla\varphi_{t_0}^{t_0+T}(\mathbf{x})$ is the deformation gradient tensor and defined by

$$\nabla\varphi_{t_0}^{t_0+T}(\mathbf{x}) = \frac{d\varphi_{t_0}^{t_0+T}(\mathbf{x})}{d\mathbf{x}}. \tag{4}$$

The magnitude of the mapped perturbation is defined by the symbol $\|\delta\mathbf{x}\|$ and given by

$$\|\delta\mathbf{x}\| = \sqrt{\langle\delta\mathbf{x}_0, [\nabla\varphi(\mathbf{x})]^*\nabla\varphi(\mathbf{x})\delta\mathbf{x}_0\rangle}, \tag{5}$$

where [ ]* denotes the transpose of matrix [ ]. The inner product can be written in summation form as

$$\begin{aligned}&\langle\delta\mathbf{x}_0, [\nabla\varphi(\mathbf{x})]^*\nabla\varphi(\mathbf{x})\delta\mathbf{x}_0\rangle \\ &\quad= \sum_i\sum_j\sum_k (\delta\mathbf{x}_0)_i([\nabla\varphi(\mathbf{x})]^*)_{ik}(\nabla\varphi(\mathbf{x}))_{kj}(\delta\mathbf{x}_0)_j\end{aligned} \tag{6}$$

Let the symmetric matrix Δ be defined as the Cauchy–Green deformation tensor:

$$\Delta = [\nabla\varphi_{t_0}^{t_0+T}(\mathbf{x})]^*\nabla\varphi_{t_0}^{t_0+T}(\mathbf{x}), \tag{7}$$

and let $\lambda_{\max}(\Delta)$ be the maximum eigenvalue of the Cauchy–Green deformation tensor. Note from Eq. 5 that $\sqrt{\lambda_{\max}(\Delta)}$ gives the maximum stretching of $\delta\mathbf{x_0}$ (i.e. the maximum separation of fluid particle pairs initially located at $\mathbf{x}(t_0)$) when $\delta\mathbf{x_0}$ is aligned with the eigenvector associated with $\lambda_{\max}(\Delta)$; hence

$$\|\delta\mathbf{x}\|_{\max} = \sqrt{\lambda_{\max}(\Delta)}\|\delta\mathbf{x}_0\|. \tag{8}$$

The finite-time Lyapunov exponent $\sigma_t^T(\mathbf{x})$ is then defined as:

$$\sigma_t^T(\mathbf{x}) = \frac{1}{|T|}\ln\sqrt{\lambda_{\max}(\Delta)} = \frac{1}{|T|}\ln\left\|\frac{\delta\mathbf{x}(T)}{\delta\mathbf{x}(0)}\right\|. \tag{9}$$

Shadden et al. (2005) showed that the ridges of local maxima in the FTLE field act as material lines in the flow and, furthermore, are nearly perfect barriers to fluid transport when computed in the limit as T becomes very large. Shadden et al. (2005) also derived an estimate for the fluid flux across an LCS that is deduced from finite-time data (i.e. finite T in Eq. 9) and showed that, for practical purposes, this quantity is often negligible. Hence, the LCS are treated as ideal material lines in practice. The absolute value $|T|$ is used instead of T in Eq. 8 because FTLE can be computed for $T > 0$ and $T < 0$. The material line is called a repelling LCS ($T > 0$) over the time interval if infinitesimal perturbations away from this line grow monotonically under the linearized flow. The material line is called an attracting LCS ($T < 0$) if it is a repelling LCS over the interval in backward time. In the parlance of dynamical systems, repelling and attracting LCS reveal stable and unstable manifolds, respectively.

The FTLE field can be calculated from a time-series of discrete velocity field data typical of DPIV measurements. The flow map is determined by integration of the velocity field and the FTLE can be calculated from the flow map. There are currently at least two software packages available for the calculation of FTLE fields from DPIV-type velocity field data. MANGEN, a package developed by F. Lekien and C. Coulliette, is a C-language program previously implemented by Shadden et al. (2005, 2006) and is available for download at http://www.lekien.com/~francois/software. A MATLAB package for FTLE calculation has been developed by the authors (Peng and Dabiri 2007) and is available for download at http://dabiri.caltech.edu/software.

The extraction of LCS curves from FTLE fields can be accomplished by a variety of ad hoc methods including thresholding or gradient searches of the FTLE field to identify local maxima. Shadden (2006) derives more rigorous criteria than these; however, for practical purposes, identification of LCS boundaries from well-resolved FTLE fields is relatively insensitive to the implemented method of extraction.

Figure 1 shows the forward-time and the backward-time FTLE fields computed for a steadily propagating vortex ring generated by a piston-cylinder apparatus (Shadden et al. 2006). The corresponding repelling and attracting LCS identified by the ridges of high FTLE values are shown in Fig. 2. The increasingly sinuous nature of the repelling (attracting) LCS near the front (rear) of the vortex ring is the result of perturbations from an ideal, unperturbed vortex

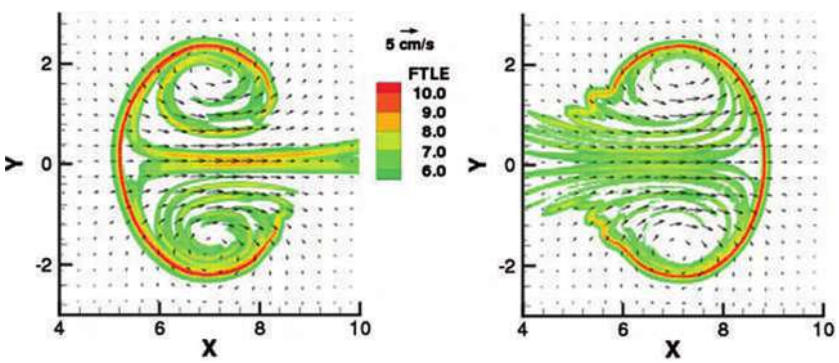

Fig. 1 Contour plot of forward-time (*left*) backward-time (*right*) FTLE fields for vortex ring propagating from *left* to *right*. LCS are identified by the ridge of high FTLE values (*red*)

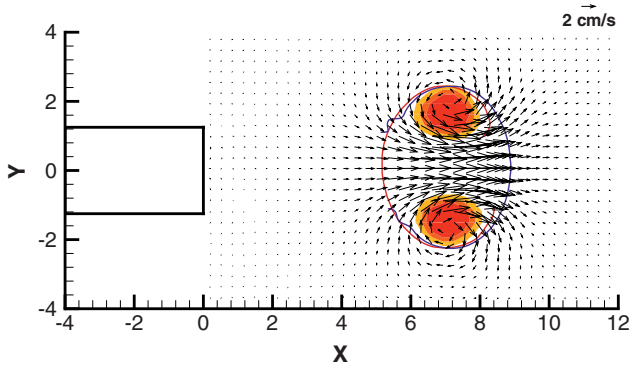

Fig. 2 Vortex ring generated by piston-cylinder apparatus. Vortex ring propagates from *left* to *right*. *Red curve*, forward-time LCS; *blue curve*, backward-time LCS; *filled contours*, vorticity magnitude; *black rectangle*, outline of downstream end of cylinder

ring configuration with connected stable and unstable manifolds (i.e. connected streamlines emanating from the rear and front stagnation points, respectively; see Shadden et al. 2006). Increasing detail of this sinuous structure is revealed with increasing integration time $|T|$.

2.2 The potential flow hypothesis

Given the geometry and kinematics of the LCS in the flow, we aim to use these structures to deduce dynamics (i.e. forces and moments) of the corresponding flow field. The present method takes advantage of the fact that the LCS represents a slip boundary in the flow on which a no through-flow condition holds, since the LCS is a material line. If we hypothesize that the shear stresses on and outside the LCS boundary are negligible, then the flow external to the LCS can be solved as a linear homogenous boundary value problem with nonhomogenous boundary conditions, i.e. a solution of Laplace's equation for the velocity potential ϕ.

The potential flow hypothesis is valid, for example, when all of the vorticity in the flow is enclosed by the LCS, as in the isolated vortex ring flow shown in Fig. 2 (Shadden et al. 2006). If the potential flow hypothesis holds, we can immediately make use of existing theory for the dynamics of deformable bodies in potential flow in order to deduce the forces and moments on the LCS. These forces and moments can be related unambiguously to the dynamics of the animal in the flow. The following section outlines the governing equations of motion.

2.3 Equations of motion

Galper and Miloh (1995) have previously derived the equations of motion for a deformable body in an arbitrary potential flow field. We make direct use of these equations presently, where the LCS structure is treated as a deformable body. It is important to note that there exist no a priori restrictions on which segments of the repelling and attracting LCS can be used to construct the deformable body, as long as (1) the segments form a closed curve and (2) the aforementioned potential flow hypothesis is satisfied. Nonetheless, certain combinations of the LCS provide more information regarding the fluid dynamics than others; hence, the choice should be made judiciously (see next section).

Let $\mathbf{U}_1 = \nabla\phi_1(\mathbf{X}, t)$ represent the ambient flow field surrounding the LCS, where ϕ_1 is the velocity potential of the ambient flow and $\mathbf{X}$ is the position vector measured relative to the laboratory frame of reference. The outward-facing unit normal to the LCS is denoted $\mathbf{n}$; the position vector relative to the LCS centroid, $\mathbf{x}$; and the instantaneous surface of the LCS, $S(\mathbf{x}, t) = 0$. The velocity potential that arises due to the presence of the LCS in the flow is given by

$$\phi_2 = \mathbf{U}_2 \cdot \mathbf{\Phi} + \mathbf{\Omega} \cdot \mathbf{\Psi} + \phi_d + \phi_0 \tag{10}$$

where $\mathbf{U}_2$ is the linear velocity of the LCS centroid in the laboratory frame and $\mathbf{\Omega}$ is the angular velocity of the principal axes of the LCS. The harmonic functions $\mathbf{\Phi}, \mathbf{\Psi}, \phi_d$, and ϕ_0 represent, respectively, the translational Kirchhoff potential, rotational Kirchhoff potential, deformation potential, and additional potential associated with the ambient flow. These potentials satisfy the boundary conditions listed below:

$$\frac{\partial\mathbf{\Phi}}{\partial n} = \mathbf{n}|_S; \quad \frac{\partial\mathbf{\Psi}}{\partial n} = \mathbf{x}\times\mathbf{n}|_S; \quad \frac{\partial\phi_d}{\partial n} = -\frac{\partial S/\partial t}{|\nabla S|}\Big|_S; \quad \frac{\partial\phi_0}{\partial n} = -\mathbf{U}_1\cdot\mathbf{n}|_S \tag{11}$$

where each is evaluated on the LCS surface $S(t)$. In addition, $\phi_2 \to 0$ as $|\mathbf{x}| \to \infty$. The fluid dynamic force $\mathbf{F}$ and moment $\mathbf{M}$ (per unit fluid density) acting on the LCS are given by

$$\mathbf{F} = \frac{\mathrm{d}}{\mathrm{d}t}\int_S \phi\mathbf{n}\,\mathrm{d}S - \int_S \nabla\phi(\nabla\phi\cdot\mathbf{n})\mathrm{d}S + \frac{1}{2}\int_S (\nabla\phi)^2\mathbf{n}\,\mathrm{d}S \tag{12}$$

$$\begin{aligned}\mathbf{M} = {} & \frac{\mathrm{d}}{\mathrm{d}t}\int_S \phi\mathbf{x}\times\mathbf{n}\,\mathrm{d}S + \mathbf{U}_2 \\ & \times\int_S \phi\mathbf{n}\,\mathrm{d}S - \int_S \mathbf{x}\times\mathbf{U}_1(\nabla\phi\cdot\mathbf{n})\mathrm{d}S \\ & + \frac{1}{2}\int_S (\nabla\phi)^2(\mathbf{x}\times\mathbf{n})\mathrm{d}S\end{aligned} \tag{13}$$

where $\phi = \phi_1 + \phi_2$. The following sections consider the application of these governing equations to two common classes of animal swimming measurements in which we will assume that ambient flow and LCS rotation are negligible, i.e. $\mathbf{U}_1 = \mathbf{\Omega} = \phi_0 = 0$.

2.3.1 Inertial frame; single appendage measurements

When studying the dynamics of single appendages in an inertial frame, we must account for the combined dynamical effect of the appendage and the vorticity that it generates. The LCS captures this by delineating an 'effective appendage' boundary that interacts with irrotational fluid surrounding the appendage–vortex system. Specifically, the effective appendage is given by the closed boundary formed by the intersection of the forward- and backward-time LCS curves (cf. Figs. 1 and 2). If the deformation of the effective appendage is small relative to its translation through the fluid, i.e. $\phi_d << \mathbf{U}_2 \cdot \mathbf{\Phi}$, then Eq. 12 reduces to

$$\mathbf{F} = \frac{\mathrm{d}}{\mathrm{d}t} \int_S (\mathbf{U}_2 \cdot 2\mathbf{\Phi})\mathbf{n}\, \mathrm{d}S \tag{14}$$

The balance of this fluid dynamic force and the external force $\mathbf{F}_{\text{ext}}$ applied by the animal to the appendage leads to a temporal change in the momentum of the effective appendage:

$$\mathbf{F} + \mathbf{F}_{\text{ext}} = \frac{\mathrm{d}}{\mathrm{d}t}(V_{\text{LCS}}\mathbf{U}_2) \tag{15}$$

or, equivalently,

$$\frac{\mathrm{d}}{\mathrm{d}t}(V_{\text{LCS}}(\mathbf{I} + \mathbf{A}_{\text{LCS}})\mathbf{U}_2) = \mathbf{F}_{\text{ext}} \tag{16}$$

where V_{LCS} is the volume of fluid displaced by the LCS, $\mathbf{I}$ is the identity matrix, and $\mathbf{A}_{\text{LCS}}$ is the added-mass tensor of the LCS (i.e. $\mathbf{A}_{\text{LCS}} = -\int_S \mathbf{\Phi} \cdot \mathbf{n}\, \mathrm{d}S$; Lamb 1932). Since the external force $\mathbf{F}_{\text{ext}}$ is applied by the animal, an equal and opposite locomotive force $\mathbf{F}_{\text{L}}$ is exerted by the fluid on the animal, i.e. $\mathbf{F}_{\text{L}} = -\mathbf{F}_{\text{ext}}$.

2.3.2 Non-inertial frame; whole animal measurements

It is often necessary to measure animal swimming in a non-inertial frame; for example, when tracking free-swimming animals over distances longer than a stationary measurement window will permit. In these cases, the LCS centroid velocity $\mathbf{U}_2$ in Eq. 10 cannot be determined by visual inspection. However, if a closed curve surrounding the entire animal body can be constructed from the measured LCS, then the locomotive force generated at the animal–fluid interface becomes an internal force in the system and Eq. 12 reduces to a simplified expression for $\mathbf{U}_2$:

$$\frac{\mathrm{d}}{\mathrm{d}t}\left[V_{\text{LCS}}(\mathbf{I} + \mathbf{A}_{\text{LCS}})\mathbf{U}_2 - \int_S \phi_d \mathbf{n}\, \mathrm{d}S\right] = 0 \tag{17}$$

The deformation potential ϕ_d can be determined by using a standard boundary value problem solver (e.g. MATLAB) with the boundary condition specified in Eq. 11. The problem then becomes purely kinematic, in which the animal body velocity $\mathbf{U}_{\text{body}}$ can be deduced from its weighted contribution to the velocity of the LCS centroid, i.e.

$$\mathbf{U}_{\text{body}} = \frac{\mathbf{U}_2 V_{\text{LCS}} - \mathbf{U}_{\text{fluid}} V_{\text{fluid}}}{V_{\text{body}}} \tag{18}$$

where V_{body} is the volume of the animal body (assumed neutrally buoyant), and the subscript fluid refers to properties of the fluid enclosed by the LCS.

It is important to note that, unlike the previous section in which deformation of the effective appendage was neglected, whole body calculations based primarily on either the repelling or attracting LCS can have a substantial contribution from the deformation potential ϕ_d in Eq. 17. This is because the lobular portions of the LCS may be included in the deformable body in these cases. In the previous section, the deforming, lobular portions of both the repelling and attracting LCS were eliminated from the analysis when the LCS were intersected to determine the effective appendage boundary.

3 Results

3.1 Bluegill sunfish pectoral fin locomotion

The analysis presented in Sect. 2.3.1 was applied by Peng et al. (2007) to DPIV measurements of the bluegill sunfish pectoral fin. The animals were swum in a flume so that they could be observed in an inertial frame of reference. Since measurements were taken in a transverse plane, i.e. with ambient flow normal to the measurement plane, Eq. 16 could be used to deduce the lateral and lift components of the locomotive force $\mathbf{F}_{\text{L}}$ (but not the thrust component). Figure 3 shows a snapshot of the computed forward- and backward-time FTLE fields and the resulting LCS structure that comprises the effective appendage boundary. These FTLE fields are not resolved as sharply as the vortex ring calculations shown in Fig. 1. This is due to the shorter integration time $|T|$, the result of a shorter duration of available DPIV measurements. Nonetheless, the effective appendage is reconstructed without much difficulty.

Figure 4 plots the measured lateral and lift forces deduced from the vorticity-free analysis. For comparison, the steady force level determined using the vorticity method of Drucker and Lauder (1999) is also plotted. The time-averaged force computed using the vorticity method is sensitive to the time at which the vorticity field is evaluated and the vorticity threshold used to identify the spatial extent of the shed vortex. We selected an instant near the end of the fin downstroke and included all vorticity above the background noise level in the calculation. The result is provided for qualitative comparison with the present vorticity-free method. As shown in Fig. 4, the present method provides detailed information regarding the transient fluid dynamic forces, in addition to the time-averaged dynamics. To be sure, this particular data set is limited by a lack of measurement data before the start of the fin downstroke at time $t = 0$. Hence, at the beginning of the fin motion there is insufficient data to compute the backward-time FTLE and the corresponding repelling LCS, which locates the front boundary of the effective appendage. Since it is not possible to evaluate the locomotive forces until this portion of the effective appendage geometry is revealed, the peak force generation during the early downstroke is not captured in the analysis and the corresponding time-averaged force over the downstroke may be underestimated. Nevertheless, the transient force dynamics that are captured agree with observations of instantaneous animal body kinematics (Peng et al. 2007).

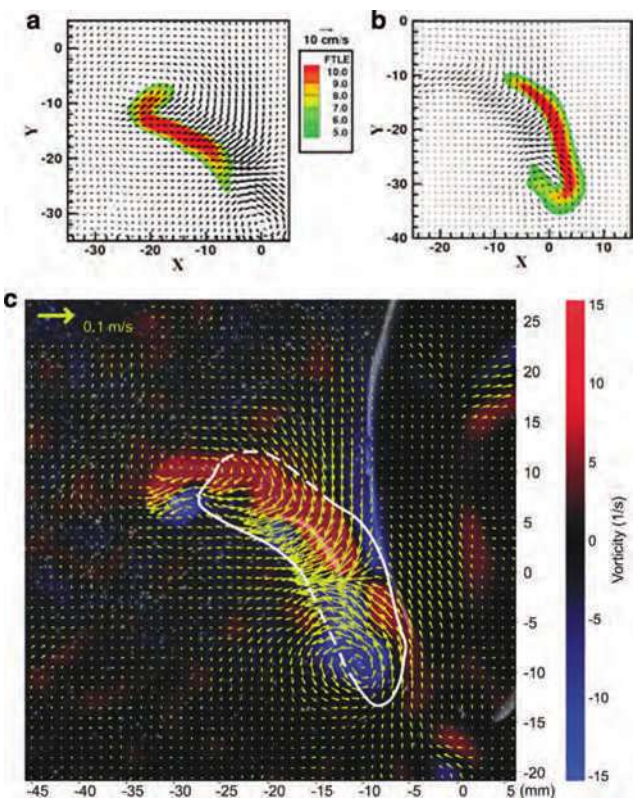

Fig. 3 FTLE fields and LCS for the flow generated by a bluegill sunfish pectoral fin. **a** Backward-time FTLE field; **b** forward-time FTLE field. Position coordinates are specified in millimeters. **c** Boundary of the effective appendage derived from the repelling and attracting LCS. *Solid curves* on the *left* and *right* show the attracting and repelling LCS, respectively. *Broken curves* are splines connecting the LCS. The fin (the curved feature with high brightness inside the LCS curves) can be seen embedded inside the effective appendage

3.2 Jellyfish undulatory locomotion

The analysis presented in Sect. 2.3.2 was applied to DPIV measurements of free-swimming *Aurelia aurita* medusae

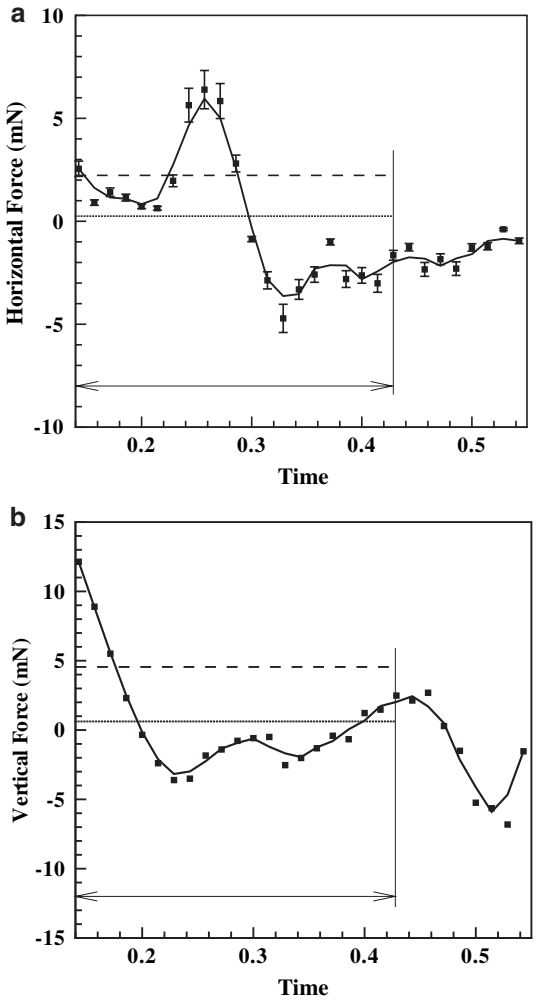

Fig. 4 Measured locomotive forces in **a** horizontal and **b** vertical directions. Time is normalized by the duration of the fin stroke cycle. *Squares*: vorticity-free method. *Error bars* indicate uncertainty from measurement and evaluation. For comparison, the steady horizontal and vertical force levels determined using the vorticity method of Drucker and Lauder (1999) are shown in *dashed lines*, and the time average of the instantaneous data over the same interval is given by the *solid horizontal lines*. The interval over which the time averages are taken is indicated by the *arrows*

(i.e. jellyfish). This species of jellyfish swims via full body undulations that create vortex rings of alternating rotational orientation during the swimming cycle (Dabiri et al. 2005). The animals were observed in an inertial frame in order to validate the non-inertial analytical methods. Figure 5 shows a snapshot of the forward-time LCS structure. Deformation of the lobular portions of the LCS (i.e., the two elongated lobes) upstream of the animal makes a substantial contribution to Eq. 17. Figure 6 compares the measured LCS centroid velocity $\mathbf{U}_2(t)$ to that predicted by Eq. 17; the agreement is reasonable, and it appears that the discrepancies are due to three-dimensional flow effects that cannot be captured by the two-dimensional DPIV measurements.

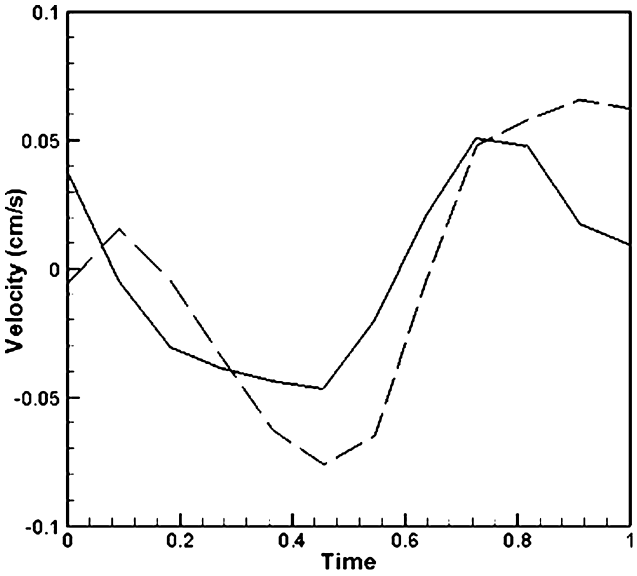

Fig. 6 Velocity of the LCS surrounding a free-swimming jellyfish. *Solid line*: directly measured velocity of the LCS; *dashed line*: vorticity-free method. Velocity is plotted as the instantaneous velocity minus the average velocity over the swimming cycle. Time is normalized by the duration of the swimming cycle

3.3 Validation of the potential flow hypothesis

To test the potential flow hypothesis and associated analytical method, we analyzed direct numerical simulations of vortex ring formation by a piston-cylinder apparatus. Details of the numerical model, which is similar to the experiment shown in Fig. 2, are described in a separate study (Shadden et al. 2007). The forward-time FTLE fields are shown for four frames in Fig. 7. The LCS extracted from the forward- and backward-time FTLE fields are plotted in Fig. 8, showing the temporal evolution of the flow. As in the case of the bluegill sunfish pectoral fin data, the backward-time LCS structure could not be identified until a finite time after flow initiation, since no data exists before that time. In Fig. 9, the total fluid momentum determined by the present vorticity-free method (i.e. spatial integration of the fluid potential in Eq. 12) is compared with a direct evaluation of this quantity from the DNS over the time interval $0.4T_S < t < T_S$, where T_S is the duration of the piston stroke. The agreement is very good. Since the numerical data set provides a vorticity field that is well resolved even near the solid boundaries, we can also compute the instantaneous first moment of vorticity in the flow in order to determine the fluid momentum by a vorticity approach (Wu 1981). This result is also close to the DNS calculation, as expected since the effect of nozzle exit overpressure, which may not be captured by the vorticity approach, has decayed by the time $t = 0.4T_S$.

As mentioned previously, the vorticity-free analyses implemented presently rely on the assumption that there is no vorticity on or external to the LCS boundary, so that the shear stresses on the LCS surface are negligible. This hypothesis can be tested directly based on the measured velocity field data, by integrating the shear stress tensor $\boldsymbol{\tau}$ on the surface $S(t)$ of the LCS and comparing this with the computed locomotive force $\mathbf{F}_\mathrm{L}$. The ratio $\frac{\int_S \boldsymbol{\tau}\cdot\mathbf{n}\,\mathrm{d}S}{\mathbf{F}_\mathrm{L}}$ is evaluated in Fig. 10 for DPIV measurements of the pectoral fin

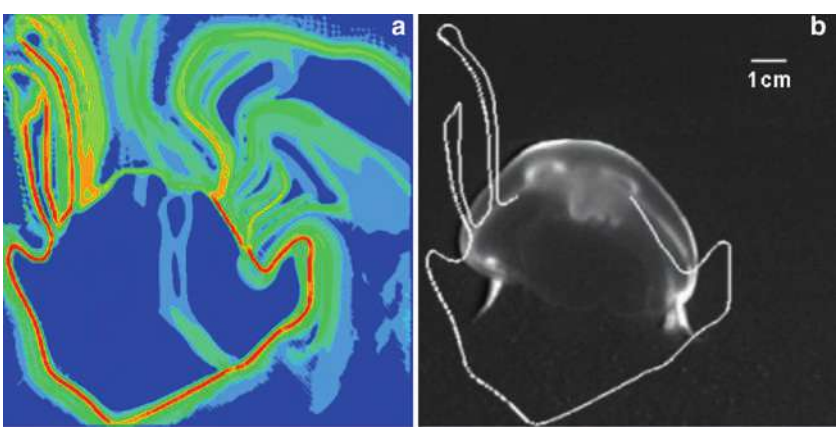

Fig. 5 **a** Shows the forward-time FTLE field of the flow around a free-swimming jellyfish. **b** Shows the LCS derived from the FTLE at the same instant. The image of the jellyfish is overlayed for reference

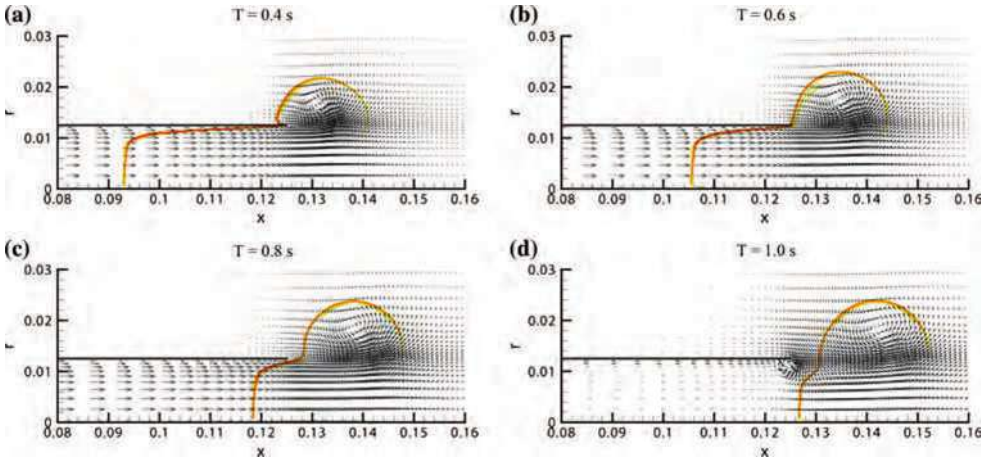

Fig. 7 Velocity field and the forward-time FTLE for direct numerical simulation of a vortex ring generated by a piston-cylinder apparatus. The longitudinal (x) and radial (r) axes are plotted in meters. The ridge of highest FTLE values is shown in *red*. The cylinder wall is indicated by the *black horizontal line*

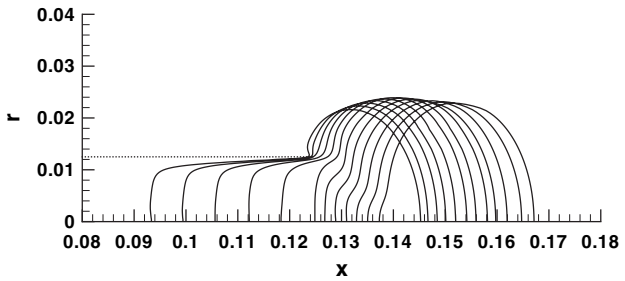

Fig. 8 Temporal evolution of the vortex boundary, shown as *solid lines*. The vortex moves from *left* to *right*. *Dotted line*: cylinder wall

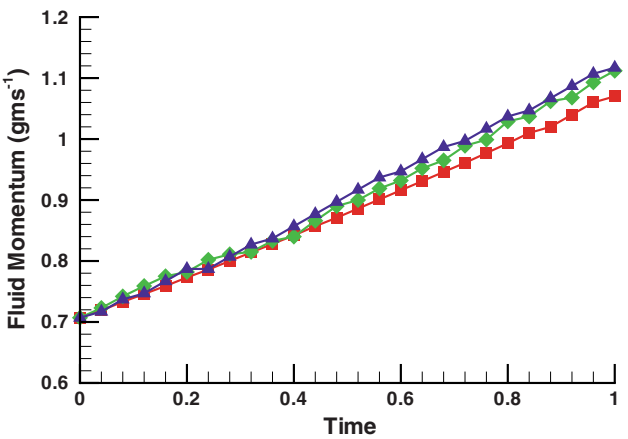

Fig. 9 Comparison of total fluid momentum. *Red squares*: direct DNS calculation; *green diamonds*: vorticity-free method; *blue triangles*: vorticity method. Time $t = 0$ corresponds to 0.4 normalized time units after flow initiation

and the free-swimming jellyfish from the previous sections. Figure 10 shows that in both cases the shear on the LCS is small relative to the locomotive force, consistent with the potential flow hypothesis. The local peak in the pectoral fin data is attributable to vorticity outside the dorsal edge of the LCS, as seen in Fig. 3c. This vorticity external to the LCS causes the potential flow hypothesis to break down locally. The quantitative effect of non-compact vorticity on the validity of the potential flow hypothesis is an issue of ongoing study.

4 Discussion

The ability of the present methods to deduce unsteady fluid forces and moments makes them a valuable complement to existing techniques for quantitative studies of animal swimming. The vorticity-free approach can benefit from the wealth of theoretical tools developed for the study of potential flows, such as Hamiltonian formulations for optimization (e.g. Galper and Miloh 1995). From the perspective of an experimentalist, these methods possess the practical advantage that vorticity dynamics need not be resolved exactly. Furthermore, Haller (2002) showed that the geometry and kinematics of the LCS are robust to localized measurement errors (which will appear in the computed fluid particle trajectories), whereas the integrals that must be evaluated in common vorticity formulations are not.

To be sure, the present approach requires the extraction of fluid particle trajectories, data that we have derived here from Eulerian, DPIV data. In principle, it would be more efficient to extract these trajectories empirically, as in particle-tracking velocimetry (PTV) techniques. However, PTV methods are most effective in flows with relatively low seeding densities, typically at least an order of magnitude less than DPIV. Computing the FTLE fields would then require substantial interpolation of the measured fluid particle trajectories. One potential advantage of this approach, however, is that three-dimensional PTV can be implemented with substantially greater ease than an equivalent DPIV technique. Furthermore, PTV has experienced significant refinements recently (Pereira et al. 2006; Ouellette et al. 2006). The extraction of three-dimensional fluid

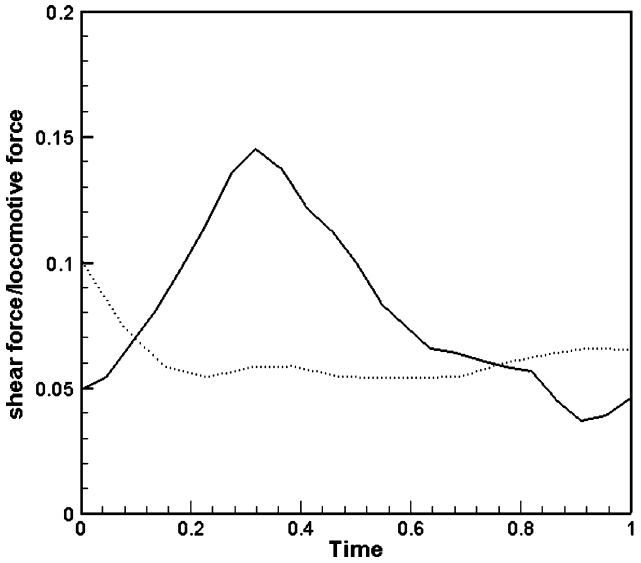

Fig. 10 Ratio of the shear force on LCS surface to the magnitude of the locomotive force. *Solid line*: bluegill sunfish pectoral fin; *dotted line*: free-swimming jellyfish

dynamics from animal swimming measurements may be facilitated by the use PTV within the context of a Lagrangian, vorticity-free method of analysis.

Perhaps the greatest challenge for animal swimming measurements lies in quantitative validation of the results. Fluid dynamic force and moment measurements cannot usually be validated directly in these cases; at best, they can be shown consistent with known requirements for locomotion of a particular animal (e.g. balancing negative buoyancy) or with measured body kinematics (i.e. linear and angular position, velocity and acceleration). Simultaneous measurements of body and flow kinematics will ultimately be required in order to confirm the conclusions of fluid dynamic studies currently being undertaken in the field.

Finally, we reiterate that the methods developed here are very general. Immediate applications of this vorticity-free perspective to animal swimming can be found in studies of C- and S-starts; labriform, carangiform, and anguilliform locomotion; and jet propulsion. Animal flight can be studied under this same paradigm, as can bluff-body flows and fluid–structure interactions more broadly. The transport properties of LCS have recently been studied within the context of animal swimming (Franco et al. 2007), resulting in new physical insights into the coupling of mass and momentum transport during animal swimming.

Acknowledgments The authors are grateful for collaborations on this work with J.E. Marsden, S.C. Shadden, G.V. Lauder, P.G. Madden, M. Rosenfeld, E. Franco, D.N. Pekarek, and K. Katija. This research is supported by a grant from the Ocean Sciences Division, Biological Oceanography Program at NSF (OCE 0623475) to J.O.D.

References

Anderson EJ, McGillis WR, Grosenbaugh MA (2001) The boundary layer of swimming fish. J Exp Biol 204:81–102

Bartol IK, Gharib M, Webb PW, Weihs D, Gordon MS (2005) Body-induced vortical flows: a common mechanism for self-corrective trimming control in boxfishes. J Exp Biol 208: 327–344

Beal DN, Hover FS, Triantafyllou MS, Liao JC, Lauder GV (2006) Passive propulsion in vortex wakes. J Fluid Mech 549:385–402

Dabiri JO, Colin SP, Costello JH, Gharib M (2005) Flow patterns generated by oblate medusan jellyfish: field measurements and laboratory analyses. J Exp Biol 208:1257–1265

Daniel TL (1984) Unsteady aspects of aquatic locomotion. Am Zool 24:121–134

Drucker EG, Lauder GV (1999) Locomotor forces on a swimming fish: three-dimensional vortex wake dynamics quantified using digital particle image velocimetry. J Exp Biol 202:2393–2412

Drucker EG, Lauder GV (2001) Wake dynamics and fluid forces of turning maneuvers in sunfish. J Exp Biol 204:431–442

Franco E, Pekarek DN, Peng J, Dabiri JO (2007) Geometry of unsteady fluid transport during fluid-structure interactions (in press)

Galper A, Miloh T (1995) Dynamic equations of motion for a rigid or deformable body in an arbitrary non-uniform potential flow field. J Fluid Mech 295:91–120

Gopalkrishnan R, Triantafyllou MS, Triantafyllou GS, Barrett D (1994) Active vorticity control in a shear-flow using a flapping foil. J Fluid Mech 274:1–21

Green MA, Rowley CW, Haller G (2006) Detection of Lagrangian coherent structures in 3D turbulence. J Fluid Mech 572:111–120

Haller G (2000) Finding finite-time invariant manifolds in two-dimensional velocity fields. Chaos 10:99–108

Haller G (2001) Distinguished material surfaces and coherent structures in three-dimensional fluid flows. Physica D 149:248–277

Haller G (2002) Lagrangian coherent structures from approximate velocity data. Phys Fluids 14:1851–1861

Lamb H (1932) Hydrodynamics. Dover, New York

Liao JC, Beal DN, Lauder GV, Triantafyllou MS (2003) Fish exploiting vortices decrease muscle activity. Science 302:1566–1569

Noca F, Shiels D, Jeon D (1997) Measuring instantaneous fluid dynamic forces on bodies, using only velocity fields and their derivatives. J Fluid Struct 11:345–350

Noca F, Shiels D, Jeon D (1999) A comparison of methods for evaluating time-dependent fluid dynamic forces on bodies, using only velocity fields and their derivatives. J Fluid Struct 13:551–578

Ouellette NT, Xu HT, Bodenschatz E (2006) A quantitative study of three-dimensional Lagrangian particle tracking algorithms. Exp Fluids 40:303–313

Peng J, Dabiri JO (2007) An overview of a Lagrangian method for analysis of animal wake dynamics. J Exp Biol (in press)

Peng J, Dabiri JO, Madden PG, Lauder GV (2007) Non-invasive measurement of instantaneous forces during aquatic locomotion: a case study of the bluegill sunfish pectoral fin. J Exp Biol 210:685–698

Pereira F, Stuer H, Graff EC, Gharib M (2006) Two-frame 3D particle tracking. Meas Sci Tech 17:1680–1692

Shadden SC (2006) A dynamical systems approach to unsteady systems. Ph.D. Thesis, California Institute of Technology

Shadden SC, Lekien F, Marsden JE (2005) Definition and properties of Lagrangian coherent structures from finite-time Lyapunov exponents in two-dimensional aperiodic flows. Physica D 212:271–304

Shadden SC, Dabiri JO, Marsden JE (2006) Lagrangian analysis of entrained and detrained fluid in vortex rings. Phys Fluids 18:047105

Shadden SC, Katija K, Rosenfeld M, Dabiri JO, Marsden JE (2007) Transport and stirring induced by vortex formation (submitted)

Stamhuis EJ, Nauwelaerts S (2005) Propulsive force calculations in swimming frogs. II. A vortex ring approach. J Exp Biol 208:1445–1451

Wilga CD, Lauder GV (2004). Biomechanics: hydrodynamic function of the shark's tail. Nature 430:850

Wu JC (1981) Theory for aerodynamic force and moment in viscous flows. AIAA J 19:432–441

Wake visualization of a heaving and pitching foil in a soap film

Florian T. Muijres · David Lentink

Abstract Many fish depend primarily on their tail beat for propulsion. Such a tail is commonly modeled as a two-dimensional flapping foil. Here we demonstrate a novel experimental setup of such a foil that heaves and pitches in a soap film. The vortical flow field generated by the foil correlates with thickness variations in the soap film, which appear as interference fringes when the film is illuminated with a monochromatic light source (we used a high-frequency SOX lamp). These interference fringes are subsequently captured with high-speed video (500 Hz) and this allows us to study the unsteady vortical field of a flapping foil. The main advantage of our approach is that the flow fields are time and space resolved and can be obtained time-efficiently. The foil is driven by a flapping mechanism that is optimized for studying both fish swimming and insect flight inside and outside the behavioral envelope. The mechanism generates sinusoidal heave and pitch kinematics, pre-described by the non-dimensional heave amplitude (0–6), the pitch amplitude (0°–90°), the phase difference between pitch and heave (0°–360°), and the dimensionless wavelength of the foil (3–18). We obtained this wide range of wavelengths for a foil 4 mm long by minimizing the soap film speed (0.25 m s^{-1}) and maximizing the flapping frequency range (4–25 Hz). The Reynolds number of the foil is of order 1,000 throughout this range. The resulting setup enables an effective assessment of vortex wake topology as a function of flapping kinematics. The efficiency of the method is further improved by carefully eliminating background noise in the visualization (e.g., reflections of the mechanism). This is done by placing mirrors at an angle behind the translucent film such that the camera views the much more distant and out-of-focus reflections of the black laboratory wall. The resulting high-quality flow visualizations require minimal image processing for flow interpretation. Finally, we demonstrate the effectiveness of our setup by visualizing the vortex dynamics of the flapping foil as a function of pitch amplitude by assessing the symmetry of the vortical wake.

F. T. Muijres · D. Lentink (✉)
Experimental Zoology Group, Wageningen University,
6709 PG Wageningen, The Netherlands
e-mail: david.lentink@wur.nl

F. T. Muijres
Department of Theoretical Ecology, Lund University,
Ecology Building, S-223, 62 Lund, Sweden

1 Introduction

Marine fish that live and hunt in the water column (pelagic piscivorous fish) are both fast and efficient swimmers. Many of such fish, like tuna, have slender tails (caudal fins) and propel themselves primarily with their tail beat; hence they are referred to as thunniform swimmers (e.g., Sfakiotakis et al. 1999). Thunniform swimmers operate at a Reynolds number of 1,000 and up (Webb and Weihs 1986). The fluid mechanics of the heaving and pitching tails is governed by the generation and shedding of vortices (e.g., Triantafyllou et al. 1993; Sfakiotakis et al. 1999). These vortices influence swimming performance through their interactions with the tail. The nature of these vortex interactions depend on the foils kinematics and are not fully understood (Lentink et al. 2007). To better understand the vortex dynamics of thunniform swimmers, scientists often model the tail with a simple, non-flexible, pitching and heaving foil (Fig. 1) (Triantafyllou et al. 1993). Studying such simple foil geometry, kinematics and

G.K. Taylor, M.S. Triantafyllou, and C. Tropea (Eds.): Animal Locomotion, pp. 27–35.
springerlink.com

Fig. 1 The tail (caudal fin) of a thunniform swimmer (e.g., tuna and many sharks) forms the main source of propulsion. The tail can be effectively approximated as a heaving and pitching foil

dynamics is a fair first approximation of thunniform swimmers.

Here we present a novel experimental setup for studying such a flapping foil in a soap film tunnel. Soap films provide an important advantage compared with conventional setups using digital particle image velocimetry (DPIV): the vortical flow can be visualized and filmed time and space resolved without image correlation. Gharib and Derango (1989) illustrated the effectiveness of such setups for studying many types of two-dimensional flows. Rutgers et al. (2001) developed a simple and high quality soap tunnel (driven by gravity) that has eliminated many of the challenges of earlier designs (e.g., Gharib and Derango 1989; Couder et al. 1989). Georgiev and Vorobieff (2001) improved this setup for low flow speeds. Couder et al. (1989) studied vibrating cylinders in a static soap film, they were probably the first to actively drive an object similar to a flapping foil in a soap film. Zhang et al. (2000) studied freely flapping flags in a soap film tunnel, such fluid-structure interactions are also relevant for understanding anguilliform swimming of fish larvae, eels and swimming snakes. To our knowledge we were the first to actively flap a foil in a soap film tunnel (Lentink et al. 2007).

A soap film consists of a thin sheet of water stabilized by soap molecules on the surfaces. The soap molecules give the film elasticity, which mediates the propagation of disturbances through the film in the form of elastic Marangoni waves (Couder et al. 1989). Couder et al. (1989) and Chomaz and Costa (1998) showed that the in-plane dynamics of thin soap-films dominate the out-off-plane dynamics if the film speed is significantly lower than the Marangoni wave speed (elastic Mach number significantly smaller than 1). Hence "sub-sonic" soap-films can be regarded as 2D fluids. Chomaz and Costa (1998) further showed that a soap film obeys the 2D incompressible Navier–Stokes equations provided that the elastic Mach number is significantly lower than 1 and the initial film thickness variations are small. In the same paper Chomaz and Costa show that the vorticity field in the film is correlated to thickness variations of the soap-film. Rivera et al. (1998) showed that the correlation between the thickness and vorticity field in the wake of a grid of cylinders, generating 2D turbulence, remains strong well beyond 19 cylinder diameters downstream (region of interest 50 mm downstream; cylinder diameter 2.7 mm). Here we will study the vortical flow generated by a flapping foil less than 10 chord lengths downstream. Hence we may expect a particular strong correlation between the vorticity and thickness field. Thickness variations in a soap film can be visualized by illuminating the soap film with monochrome light, which results in interference fringes (Rutgers et al. 2001). Filming these fringes time and space resolved enables the quantitatively study of vortex dynamics in soap-films. This makes slow and uniform soap-films ideally suited for studying two-dimensional vortex dynamics at sub-sonic speeds.

Here we quantitatively describe our set-up and illustrate its effectiveness for studying the topology of the vortical wake of a harmonically flapping foil. We chose a dimensionless wavelength and flapping amplitude of the foil that is relevant for thunniform swimmers. Subsequently we qualitatively study the symmetry of the vortical wake of the flapping foil as a function of pitch amplitude.

2 Dimensionless parameterization of a flapping foil

The kinematics of a two-dimensional foil can be described using different dimensionless variables; we chose an approach inspired by the work of Williamson and Roshko (1988). We have published this approach (Fig. 2) elsewhere (Lentink et al. 2007). We describe the harmonic kinematics of a heaving and pitching foil with a dimensionless wavelength λ^*, dimensionless amplitude A^*, geometric angle of attack amplitude (or pitch angle) $A_{\alpha,\mathrm{geo}}$ and Reynolds number Re. The dimensionless wavelength λ^* represents the number of chord lengths travelled forward during one full flap period of the foil:

$$\lambda^* = \frac{U_\infty}{fl}, \tag{1}$$

in which U_∞ is the free stream velocity, f the flapping frequency and, l the foil length. The dimensionless

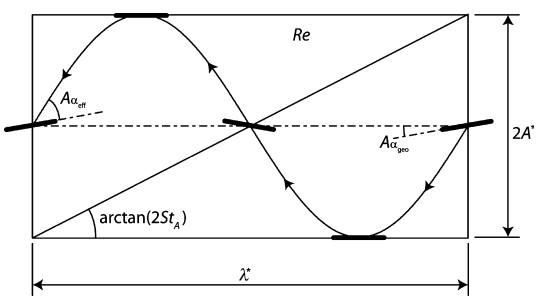

Fig. 2 A graphical representation of the non-dimensional parameters of a sinusoidally flapping foil: dimensionless wavelength, λ^*, dimensionless heave amplitude, A^*, amplitude-based Strouhal number, St_A, geometrical angle of attack amplitude, $A_{\alpha,\mathrm{geo}}$ effective angle of attack amplitude, $A_{\alpha,\mathrm{ef}}$ and the stroke-averaged Reynolds number, Re (adapted from Lentink et al. 2007)

amplitude A^* represents the amplitude of the foil excursion A with respect to the foil length l:

$$A^* = \frac{A}{l}. \tag{2}$$

The amplitude-based Strouhal number St_A is equal to the ratio of dimensionless amplitude A^* and dimensionless wavelength λ^*, and scales with the maximum induced angle of attack at mid-stroke (see Fig. 2; Eq. 4):

$$St_A = \frac{A^*}{\lambda^*}. \tag{3}$$

The effective angle of attack amplitude $A_{\alpha,\text{eff}}$ is equal to the angle of attack amplitude induced by the flapping foil minus the geometric angle of attack amplitude, $A_{\alpha,\text{geo}}$ (the pitch amplitude):

$$A_{\alpha,\text{eff}} = \arctan(2\pi St_A) - A_{\alpha,\text{geo}}. \tag{4}$$

The time-averaged velocity U_{ave} of the flapping foil can be approximated as follows (Lentink and Gerritsma 2003):

$$U_{\text{ave}} \approx \sqrt{U_\infty^2 + (4Af)^2}. \tag{5}$$

Based on this average velocity we define the time-averaged Reynolds number, Re that represents the relative importance of inertia versus viscosity in the flow:

$$Re = Re_\infty \sqrt{1 + (4St_A)^2}, \text{ in which } Re_\infty = \frac{U_\infty l}{v}, \tag{6}$$

note that v is the kinematic viscosity.

3 Flapping foil mechanism

The foil is a flat plate and its kinematics is generated with a mechanism that can generate nearly perfect sinusoidal heave and pitch kinematics. Our first mechanism generated kinematics with a small asymmetry because the design is based on a crank-shaft mechanism (Lentink et al. 2007). Here we present and describe an improved flapping mechanism that can generate symmetric sinusoidal kinematics.

The foil has a thickness t of 0.2 mm and length l of 4 mm (relative thickness 5%). It is made out of a thin piano-steel wire bend into an "L" shape. The horizontal part of the "L" functions as the foil (in the soap film), while the vertical part is mounted to the flapping mechanism (Fig. 4b). The foil is mounted such that its axis of rotation is located at approximately 1/4 foil length behind the leading edge. The leading edge of the foil is naturally rounded as a result of bending the wire, while the trailing edge is more or less blunt (flat) as a result of cutting the wire.

The harmonic heave and pitch kinematics of the foil are generated by two coupled mechanisms. A single mechanism consists of a high-inertia constant-RPM spinning disk (aluminum) that drives a light-weight sled (aluminum) of which a schematic is shown in Fig. 3. The disk is connected with a pin (brass) to a rod (carbon fiber tube) that is connected to the sled. Simple Nylon and Brass bearings and proper lubrication resulted in a smoothly running mechanism that can generate both a sine (translation of rod) and cosine (translation of sled). The frequency of these harmonics is determined by the disk's RPM, while the radius at which the pin connects the disk to the rod (and hence the sled) determines the amplitude of the harmonic. Both the heave and pitch amplitude can be varied independently (at the same frequency), because we used two coupled disk-sled mechanisms to generate both the heave and pitch kinematics, which we further explain in Fig. 4.

The mechanism allows presetting the heave amplitude (0–6 chord lengths), the geometrical pitch amplitude (0°–90°) and the phase difference between pitch and heave (0°–360°). The mechanism is driven by a reduced electric motor (water cooled) that spins at moderate frequencies (4–25 Hz). Additionally we can also preset the stroke plane angle of the flapping foil with respect to the free-stream velocity of the soap-film, which is relevant for flapping flight, e.g., insects (David 1978).

We determined how accurate the mechanism can generate harmonic kinematics by tracking the foil in the soap film tunnel with our high speed video. For our error

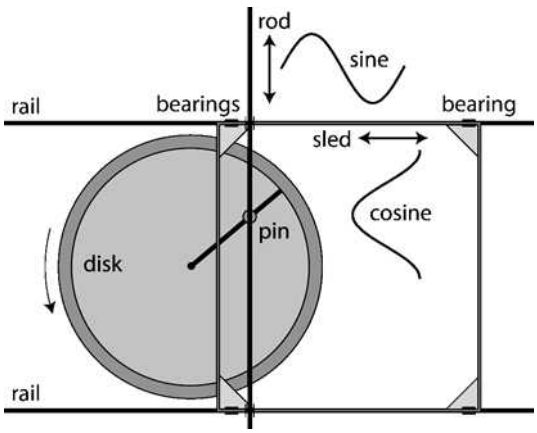

Fig. 3 Working principle of our flapping mechanism. The spinning disk (constant RPM) is connected to the rod (by a pin fixed with bearings), and the rod is connected to the sled that slides over two (horizontal) rails. The rod moves up and down with a sine, while the sled moves left and right with a cosine. The cosine of the sled is used to drive the heave of the foil while the sine of the rod drives the pitch of the foil. We use one such mechanism to generate the heave kinematics (using the sleds cosine) and another one to generate the pitch kinematics (using the rods sine). We coupled the disks of both mechanisms such that they operate at the same frequency, phase locked (Fig. 4)

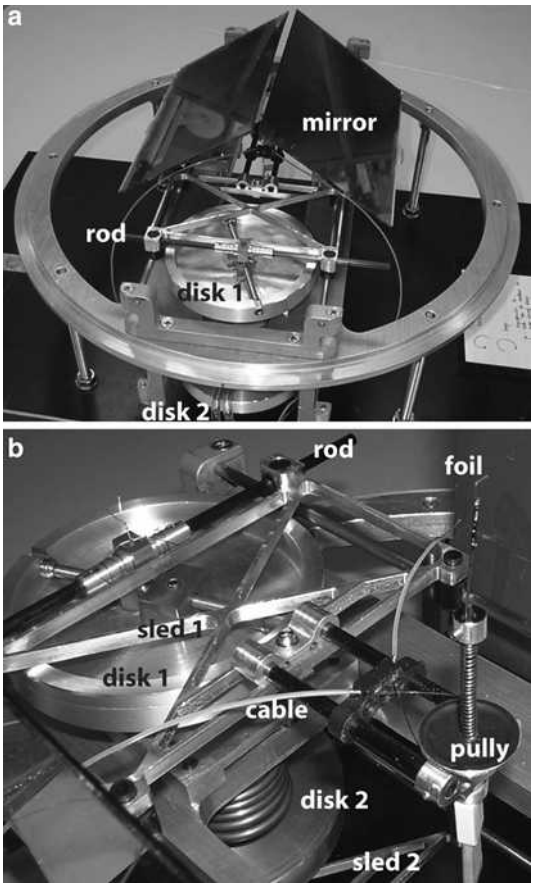

Fig. 4 Overview of flapping mechanism (**a**) and detailed photo (**b**) (the upper part of the mechanism is indicated with "1", the lower part with "2"). The flap mechanism consists of two rotating disks driven by an electric motor (water cooled). The upper disk (see **b**) is connected to a sled such that it generates the harmonic stroke kinematics (Fig. 3). We mounted the foil on the upper sled. The lower disk is connected to the lower sled with a rod that drives the harmonic pitch kinematics of the foil. The pitch kinematics is transferred by 0.2 mm piano steel wires, which slide through a flexible Teflon tube, to the upper sled were they connect to a pulley on which the foil is mounted. The whole mechanism is shielded by two mirrors set at an approximate angle of 45°

analysis we considered three flap periods to determine the error in heave amplitude (ε_A), pitch amplitude ($\varepsilon_{A\alpha}$), heave-pitch phase-difference (ε_φ) and frequency (ε_f) (Fig. 5). We determined the error using a best fit method (cftool Matlab 7, method: least squares, algorithm: trust-region) for kinematics generated at different heave amplitudes (1 and 4 chord lengths), pitch amplitudes (0°, 45°, 60°) and frequencies (4–21 Hz), see Table 1. The heave-pitch phase-shift is set to 90° [Read et al. (2003) showed that a flapping foil produces maximal thrust for such a phase shift]. We normalized the data with respect to these input variables in our error analysis. The variable range considered (Table 1) comprises the most extreme cases that we can obtain with our setup. Hence our error analysis can be considered a

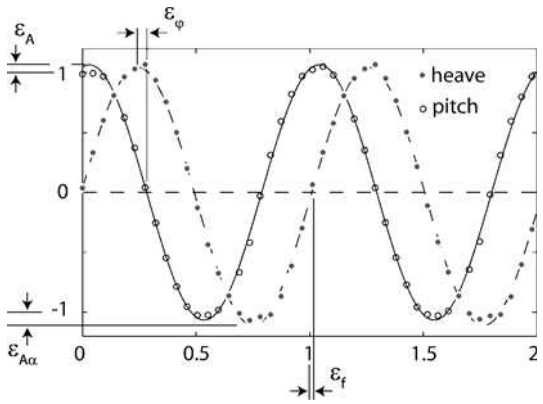

Fig. 5 Measured pitch and heave kinematics fitted with sine and cosine functions to determine the accuracy of our mechanism (note that we made the kinematics dimensionless with respect to the frequency (here 23 Hz), amplitude (here 1*l*) and geometric angle of attack amplitude (here 60°) in Table 1). The subsequent error indicators are the heave amplitude error ε_A, the pitch amplitude error, $\varepsilon_{A\alpha}$ the phase error, ε_φ and the frequency error ε_f

worst case analysis. We found that the mechanism accurately produces harmonic (sinusoidal) pitch and heave kinematics (Fig. 5). The maximum (local) deviation from ideal sinusoidal kinematics occurs at maximum excursion and is less than 5%, but this is an extreme value, it is typically less than 2%. Hence our new mechanism does not produce perfectly sinusoidal kinematics (as any other mechanism would) but it does generate significantly more sinusoidal kinematics than our earlier design (Lentink et al. 2007).

The average root mean square error (RMSE) of the present mechanism is small for both the pitch and heave kinematics (<0.02), Fig. 6. The results of the error analysis for the four flap variables are given in Fig. 6, they represent simply the difference between the intended value and the observed value of the flap parameters. Within one image sequence of three periods (part of a run of orders of magnitude more periods) we did not find significant fluctuations. Hence, the errors in Fig. 6 represent the resolution at which we can predetermine the parameters of the mechanism that define the flap kinematics. From this analysis we conclude that the harmonics generated with our mechanism can be preset reasonably accurately (under worst case conditions) with errors close to 0.05. Note that the frequency error is particular low, less than 0.01. Further

Table 1 Variables used in error analysis (Fig. 6)

f [s^{-1}]	A [mm]	$A_{\alpha,geo}$ [°]	symbol
20.0	4	60°	
23.0	4	60°	
20.4	16	0°	
20.6	16	45°	
4.5	16	60°	

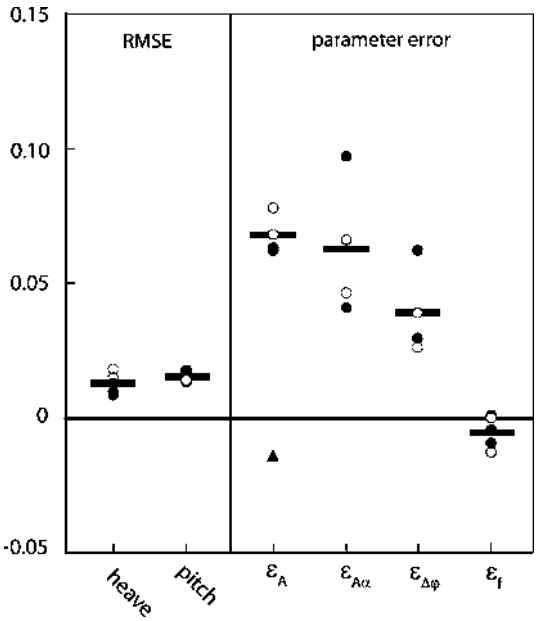

Fig. 6 Error analysis of the kinematics generated by the mechanism compared with ideal harmonic kinematics [*black lines* indicate average; *filled circles* indicate individual measurements and correspond to Table 1; *triangle* not part of average (measured at 4.5 Hz)]. *Left*, RMSE for both heave and pitch kinematics, showing that the kinematics are indeed harmonic. *Right*, mean relative errors in heave amplitude ε_A, pitch amplitude $\varepsilon_{A\alpha}$, phase ε_φ (with respect to the maximum phase error 360°) and frequency ε_f. All errors are of order 0.05 (5%) or less. At low frequency (4.5 Hz) we found that the amplitude error (but not the other errors) is significantly lower than at high frequency ($\sim$20 Hz). We expect that this is due to the inertial loading on the mechanism

note that phase shifts (errors) do not influence the symmetry of the foils kinematics provided that this shift is constant, as found for our mechanism. We found that such phase shifts are due to a misalignment of the top and bottom disk in the mechanism (Fig. 4).

4 Soap film tunnel

Our soap film tunnel generates a constant velocity soap film that runs between two wires, driven by gravity. We based our design (Fig. 7) on the simple and effective soap tunnel designed by Rutgers et al. (2001) and Georgiev and Vorobieff (2001). The frame of the current design is made out of cast iron and steel and is therefore more rigid than our first light weight soap tunnel build out of glass fiber tubes (Lentink et al. 2007). Our soap solution consists of tap water and 3% Dawn dishwasher detergent (Dawn "Manual pot and pan detergent", Professional line, USA). In the current literature there is still considerable controversy with respect to the exact viscosity of soap-films (Rutgers et al. 1996). One of the most extensive studies to date has been performed by Martin and Wu (1995), they

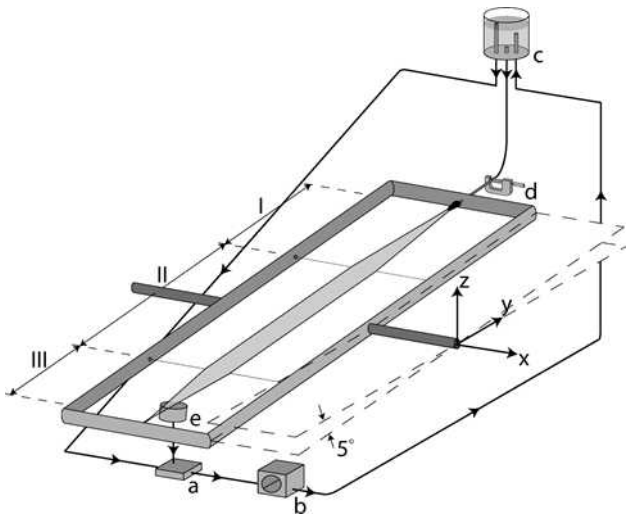

Fig. 7 The soap film tunnel consists of a frame that spans two Nylon tunnel "walls". The frame is set at an inclination of 5°. The tunnel has a diverging section (*I*), a test section (*II*) in which the foil is placed in the film, and a convergent section (*III*). The main components of the soap tunnel are: the main reservoir (*a*), a medical pump (*b*), a constant-height reservoir (*c*), a valve (a micrometer that constricts the tubing) (*d*) and a drain (*e*)

determined that the kinematic viscosity of a soap-film consisting of a 4% Dawn soap solution (Dawn "Manual pot and pan detergent", Professional line, USA) is in the order of 10^{-6} m^2 s^{-1}, we adapt this value in our study. We stored the soap solution in a 1-l reservoir (Fig. 7a) and pumped it with a peristaltic pump (1,000 Mity Flex, Fig. 7b) into a 2 m high, constant height, "overflow" reservoir (Fig. 7c). The soap solution then flows from the reservoir through tubing into a valve (Fig. 7d) that regulates the mass flow. From the valve the soap solution flows to two parallel 1 mm thick nylon wires that gradually diverge (Fig. 7, section I), which results in a stable flowing soap-film. The two Nylon wires run parallel (separation: 0.06 m) along the test section (Fig. 7, section II), in which the flow velocity is approximately constant in flow direction. The flapping foil is inserted in this test section. The soap film continues flowing from the test section along two converging wires (Fig. 7, section III) into the drain (Fig. 7e) from where the film flows into the main reservoir, which completes the cycle.

The soap film speed and thickness can be controlled by two parameters once the Nylon wires are fixed to the frame: first, the valve (control of mass flow) and second, the tilt angle of the film with respect to the horizon (preset of gravitational component in flow direction). Reducing the flow at the valve results in slower and thinner films, while reducing the tilt angle results in slower and thicker films. Super-critical film speeds, at elastic Mach numbers (ratio of film speed over elastic wave speed) of order one, can be obtained at large tilt angles (up to 90°) when the valve is

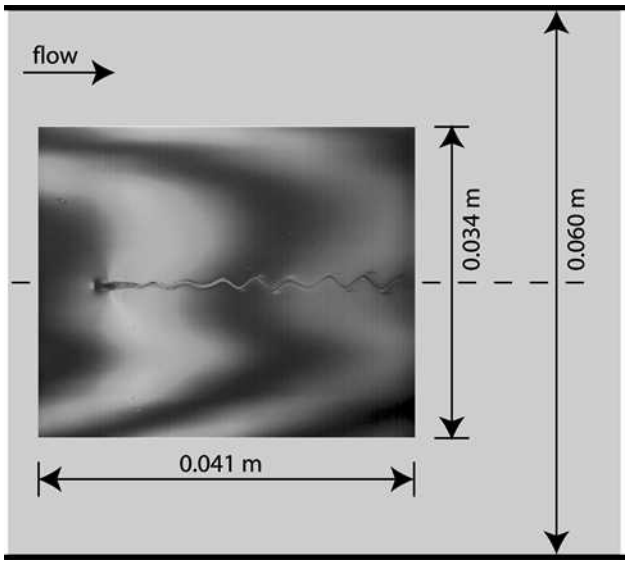

Fig. 8 Foil in the test section of the soap film tunnel (34 × 41 mm). The non-flapping foil generates small vortices downstream. Nylon wires (1 mm thick) that bound the test section are indicated with thick horizontal lines

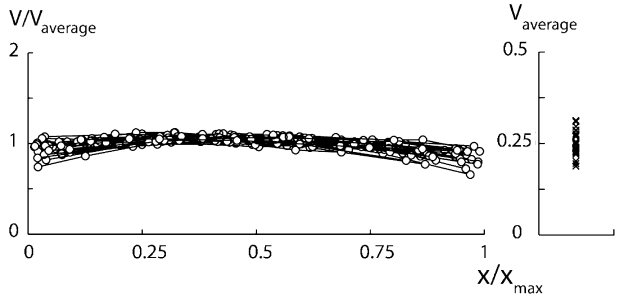

Fig. 9 The normalized (plug-like) velocity profiles as measured in the soap tunnel. We chose velocities at which no flow separation would occur in the test section; on average we obtained our slowest films without separation at 0.25 m s^{-1}

wide open (Rutgers 1999). Under "supersonic" conditions, at flow speeds up to 4 m s^{-1} and higher, "shockwaves" can occur in the film (Rutgers 1999; Wen et al. 2003). Such flows are not relevant for fish and should be avoided, also because flows at high elastic Mach numbers do not correlate with transonic and supersonic fluid dynamics in air or water (Wen and Lai 2003). For studying subsonic flows, our goal, tilt angles need to be low. For a tilt angle of 5° (at low mass flow, not measured) we obtained a thick film (not measured) with an average speed of 0.25 m s^{-1}, which is 50% slower than "The slowest soap-film tunnel in the Southwest" (Georgiev and Vorobieff 2002). At lower speeds, typically lower than 0.15 m s^{-1}, flow separation starts to occur at the end of the test section near the Nylon wires. For every run we tuned our valve to obtain the lowest possible speed without flow separation. Our optimally tuned soap-films produced nice plug-like velocity profiles in the test section (Fig. 8). Note that we measured the velocity profile over a width of 34 mm, compared with the 60 mm width of the test section (Figs. 8, 9). These profiles were obtained by tracking small pollutants in the soap film, which we filmed with a RedLake® MotionPro digital high speed video. Pollutant tracking was performed manually with a dedicated Matlab program. We tracked pollutants (diameter of order 10 pixels) over the full width of the camera image (of order 1,000 pixels), which resulted in good tracking accuracy (better than 1%). The measured velocity profiles in the area of investigation in the test section are shown in Fig. 9. The velocity profiles are reasonably flat, while the average film speed is non-constant over a time period of several hours. Hence we measured the velocity profile several times during a measurement cycle to account for these slow fluctuations in our experiments. We always determined the average velocity over the whole heave excursion (twice the amplitude) in order to obtain good average velocities for the non-dimensional variables that depend on this velocity (dimensionless wavelength and Reynolds number).

5 Visualization setup

The flapping foil in the soap film generates shear layers that roll up into vortices. The resulting vorticity field correlates strongly with thickness variations in the soap-film (Rivera et al. 1998). We visualize the thickness variations by illuminating the film with monochromatic light of a sodium lamp (SOX, wavelength 590 nm,) and film the reflected interference fringes at high speed (Fig. 10). The intensity of the reflected light changes from light to dark and vise versa for thickness variations that approach a quarter of the wavelength of the light source (Fig. 10). To acquire both a high spatial and temporal resolution a RedLake® high speed digital camera is used to record the interference fringes in the soap film. The camera settings are: resolution of 1,280 × 1,024 pixels at 500 frames per second. To eliminate intensity fluctuations in the recordings we used a special 30 kHz SOX lamp (Philips) (Palmer and Beach 1995). We further improved the image quality by reducing the background reflections (noise) viewed by the camera through the translucent soap film. The light reflected by the mechanism formed the main source of noise in the images. After trying several alternative solutions (e.g., spray painting the mechanism black, shielding it with black paper, etc.) we found that putting mirrors (at an angle of approx. 45°) between the mechanism and film worked best (Fig. 4). These mirrors reflect the little light from the distant, out of focus, black laboratory wall into the camera, which resulted in negligible image noise.

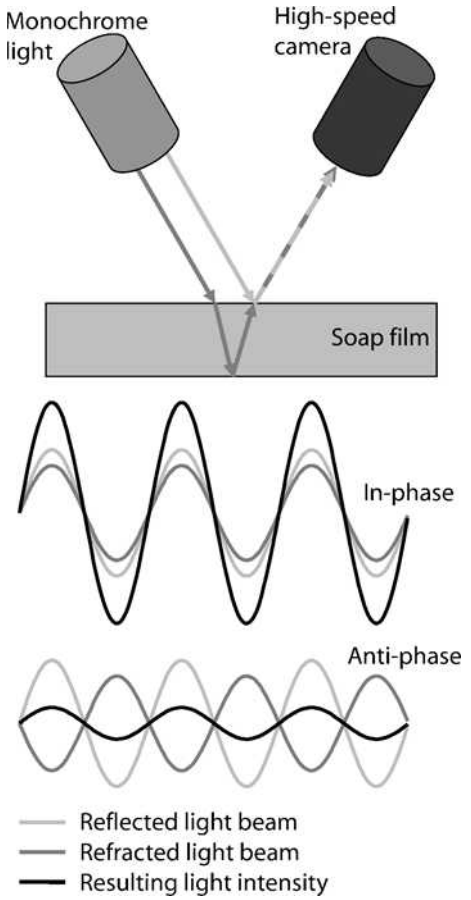

Fig. 10 Interference fringes reflected by a soap film that is illuminated with a monochromatic light source. We capture these fringes with digital high-speed video

6 Vortex wake symmetry of a flapping foil

The heave and pitch variables of our flapping foil setup can be set as follows; $A^* = 0–6$, $A_{\alpha,\mathrm{geo}} = 0°–90°$, $\lambda^* = 3–18$ and the phase difference between heave and pitch can be set between 0° and 360°. The Reynolds number of the foil in our soap tunnel is of order thousand. The ranges of these parameters are representative for thunniform swimmers (including the Reynolds number; Webb and Weihs 1986). The caudal fin and its beat are approximated with a flat plate and harmonic kinematics. We focus our experimental study on how foil kinematics affects vortex wake symmetry. Several CFD studies have shown that the vortex wake and the corresponding forces generated by a symmetrically flapping foil can be asymmetric (e.g., Lewin and Haj-Hariri 2003; Lentink and Gerritsma 2003). Symmetry is relevant for thunniform swimmers because force asymmetries can result in net turning moments, which complicate straight swimming in fish. Here we show how a soap tunnel could potentially be used to effectively explore the parametric space of a flapping foil to identify asymmetric vortical wakes. For this study we focus on the influence of pitch amplitude on wake symmetry for a fixed amplitude $A^* = 3$ and dimensionless wavelength $\lambda^* = 11$ at a Reynolds number of order 1,000 while varying the geometric angle of attack $A_{\alpha,\mathrm{geo}} = [0°, 15°, 25°, 45°]$. Recently we have made a much broader parametric study with our soap tunnel that will be published elsewhere.

We assess the wake symmetry by making series of 99 triggered photos at a fixed flap phase. We then high-pass filter the individual images and subsequently calculate the average filtered image (Fig. 11) for four phases; 0°, 90°, 180° and 270°. If the vortex wake is symmetric, then the vortical fields must be anti-symmetric for 180°-out-of-phase triggered images (Fig. 11). We developed a simple procedure that enables a graphical check for wake symmetry: we add two 180°-out-of-phase locked images using different RGB channels. The first phase is represented by an orange image and the second by a mirrored pink image. If the two wakes overlap they produce a red image (Fig. 11) and one can assess wake symmetry by eye. We did this for all four pitch angles and found that wake symmetry strongly depends on pitch angle for the heave amplitude and dimensionless wavelength considered (Fig. 11).

Our experiments show that high effective angles of attack result in large vortices and wakes. When the effective angle of attack becomes small, an array of small vortices are generated along the foils path, similar to (but larger than) the wake shed by the non flapping foil at the same speed (Fig. 8). The vortex wake asymmetry is most likely due to non-linear near-vortex-wake interactions, as found by Williamson and Roshko (1988) for vibrating cylinders. How the vortex interactions in the wake and the interactions with the foil induce the wake asymmetry is largely unclear. In some cases the asymmetry is due to vortex merging or tearing (Lentink et al. 2007), but not for the foil kinematics considered here as we did not observe such vortex interactions. There are two sources of imperfections in the experimental setup that could potentially result in wake asymmetry: first flow asymmetry, because our plug like velocity profiles are slightly asymmetric. We do not expect this to result in the wake asymmetry, because wake asymmetry also occurs in close to perfectly symmetrical CFD simulations (e.g., Lewin and Haj-Hariri 2003). The influence of flow asymmetry could, however, be tested in future CFD studies. Second asymmetries in the kinematics generated by the mechanism, these are however small, we again note that wake asymmetry also occurs for close to perfectly symmetrical kinematics in CFD simulations (e.g., Lewin and Haj-Hariri 2003). Note, however, that the symmetry of the tail beat kinematics of fish and the background flow in which they swim in their habitat is not perfectly symmetric either (a detailed study of the level of symmetry of both swimming kinematics and background

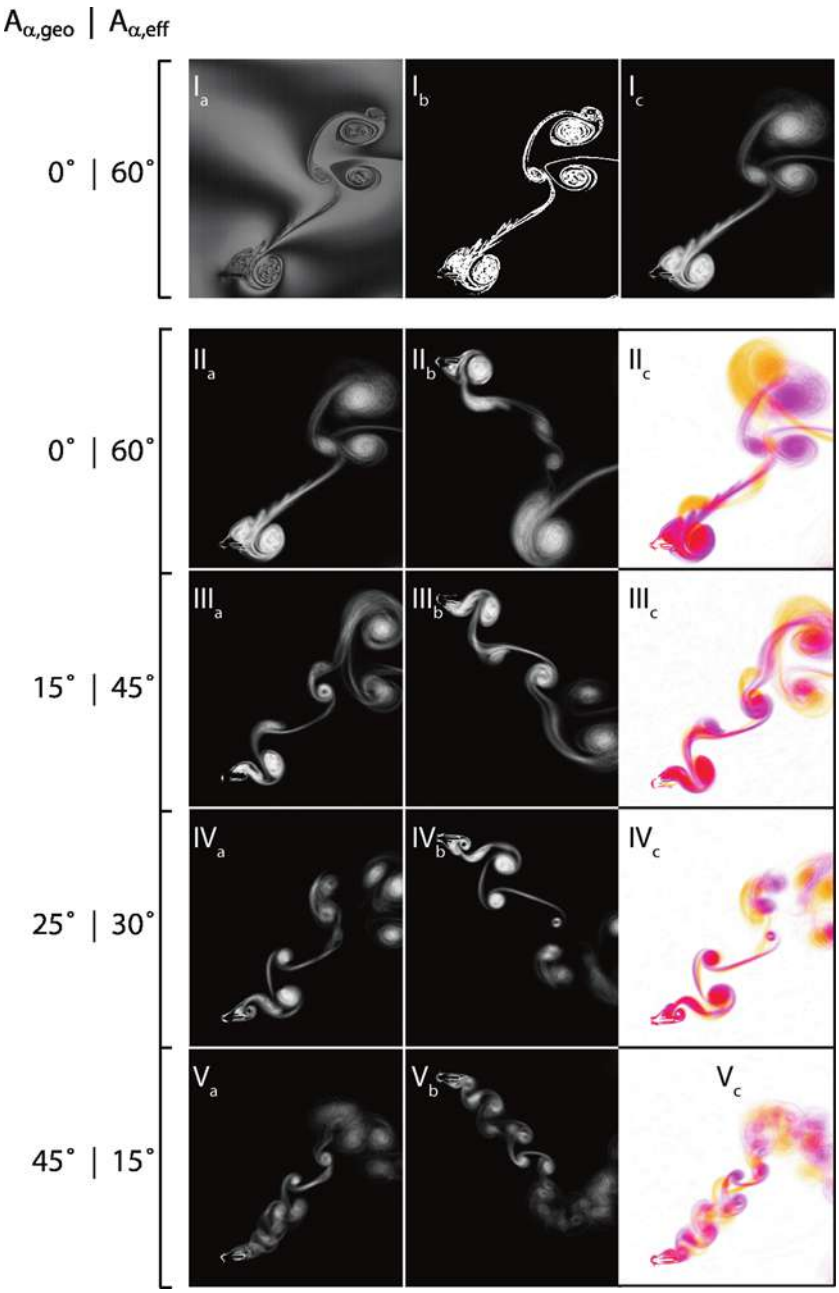

Fig. 11 Wake visualization of a flapping foil in a soap film. We first filter the raw images (I_a) using the Matlab 7.0 gradient and median (3×3) filter (I_b) and than average 99 subsequent filtered frames (I_c), these 99 images were all shot at the same flapping phase. We then assess the symmetry of the wake as a function of the geometric angle of attack ($A_{\alpha,geo}$); note that the resulting effective angle of attack is also indicated ($A_{\alpha,eff}$): *II–V*. The symmetry of the wake can be assessed qualitatively by comparing the average images at the start of the up- and down stroke (indicated with *a*, *b*). We subsequently reflect the upstroke wake "*b*" with respect to the horizontal centerline, in *orange*, and add it to the downstroke wake "a" in *pink*. Hence the overlapping parts of the wake become *red* (*c*)

flow does not exist to our knowledge). Finally despite small asymmetries in our setup we found both symmetric and asymmetric wake patters while varying the geometric angle of attack amplitude in our experiment. Hence we conclude that we found experimental evidence for vortex wake asymmetry generated by a (to good approximation) symmetrically flapping foil in a soap tunnel. This finding is similar to findings by others in three-dimensional water tunnels (e.g., Jones et al. 1996) and two-dimensional CFD simulations (e.g., Lewin and Haj-Hariri 2003).

7 Concluding remarks

We presented a novel soap tunnel setup to effectively study the vortex dynamics of a pitching and heaving foil. The visualization of the vortex dynamics is based on the strong correlation between the vorticity field and thickness variations in the soap film. A high-frequency monochromatic SOX lamp enabled us to film the resulting interference fringes (due to thickness variations) of the soap film at high speed–time and space resolved.

The soap film can flow as slow as 0.25 m s^{-1} in our setup, 50% slower than previously published setups (Georgiev and Vorobieff 2002), which is essential for operating at both high and low dimensionless wavelengths. Low stride lengths are obtained when the mechanism flaps at maximum frequency. The mechanism itself generates accurate and symmetric harmonic kinematics at all frequencies. We can preset the parameters of the harmonics (the heave amplitude, pitch amplitude, phase difference and flap frequency) with an error close to 5% or less.

To analyze the flow, we filtered and subsequently averaged a large series of images (n = 99). We then compared the average filtered images shot at a constant-phase with similar images shot at a 180° phase difference. We demonstrated the usefulness of such an approach for assessing the wake symmetry qualitatively. We could not find any reliable numerical method to assess the wakes asymmetry quantitatively; to our knowledge this is an open question.

The main advantage of our setup is that it facilitates a detailed and efficient study of the vortex wakes generated by flapping foils. The experiments are time-efficient—they only take 10 min per run, which is much faster than numerical simulations of similar flows on a high-end PC, which can take up to 30 days. Hence our experimental approach is ideally suited for a time-efficient study of the different vortex wake modes in the large parametric space of a flapping foil.

The main restrictions of our method are: it is limited to low Reynolds numbers, has a simplistic foil geometry and a fixed kinematics pattern (harmonic, two-dimensional), and the flow fields in the soap film are intrinsically two-dimensional. Within these constraints one can, however, use the results obtained with our setup as an efficient first order approximation of the more complicated three-dimensional flows generated by swimming animals such as thunniform swimmers. Interestingly we found, like others, asymmetric wakes for symmetric foil kinematics. The question emerges if thunniform swimmers encounter such wake modes during straight swimming.

Acknowledgments We thank Johan van Leeuwen for supporting both D.L. and F.T.M.; Mees Muller and Ulrike Müller for their help; Jos van den Boogaard, Eric Karruppannan, Evert Janssen and Henk Schipper for helping us with the design and construction of the soap tunnel and flapping mechanism; Bas van Oudheusden for co-supervising F.T.M. at the TU Delft. We thank Marc van Geest for help with some of the preliminary experiments. Finally we would like to thank Maarten Rutgers for advice and great soap (Dawn from the USA rocks).

References

Chomaz JM, Costa M (1998) Thin film dynamics. In: Kuhlmann HC, Rath HJ (eds) Free surface flows, vol 391. CISM courses and lectures, pp 44–99

Couder Y, Chomaz JM, Rabaud M (1989) On the hydrodynamics of soap films. Physica D 37:384–405

David CT (1978) The relationship between body angle and flight speed in free-flying *Drosophila*. Physiol Entomol 3:191–195

Georgiev D, Vorobieff P (2002) The slowest soap-film tunnel in the Southwest. Rev Sci Instrum 73:1177–1184

Gharib M, Derango P (1989) A liquid film (soap film) tunnel to study two-dimensional laminar and turbulent flows. Physica D 37:406–416

Jones KD, Dohring CM, Platzer MF (1996) Wake structures behind plunging airfoils: a comparison of numerical and experimental results. AIAA 78:1–9

Lentink D, Gerritsma M (2003) Influence of airfoil shape on performance in insect flight. AIAA 3447:1–17

Lentink D, Muijres FT, Donker-Duyvis FJ, van Leeuwen JL (2007) Vortex-wake interactions of a flapping foil that models animal swimming and flight. J Exp Biol (submitted)

Lewin GC, Haj-Hariri H (2003) Modelling thrust generation of a two-dimensional heaving airfoil in a viscous flow. J Fluid Mech 492:339–362

Martin B, Wu XL (1995) Shear flow in a two-dimensional couette cell: a technique for measuring the viscosity of free-standing liquid films. Rev Sci Instrum 66:5603–5608

Palmer GT, Beach AD (1995) Sodium vapour discharge lamps with high-frequency electronic ballast for machine vision systems illumination. Meas Sci Technol 6:1634–1635

Read DA, Hover FS, Triantafyllou MS (2003) Forces on oscillating foils for propulsion and maneuvering. J Fluid Struct 17:163–183

Rivera M, Vorobieff P, Ecke RE (1998) Turbulence in flowing soap films: velocity, vorticity, and thickness fields. Phys Rev Lett 81:1417–1420

Rutgers MA (1999) Flowing soap films: a platform for 2D non-linear dynamics experiments. Department of Physics, The Ohio State University, Columbus

Rutgers MA, Wu X-I, Bhagavatula R, Petersen AA, Goldburg WI (1996) Two-dimensional velocity profiles and laminar boundary layers in flowing soap films. Phys Fluids 8:2847–2854

Rutgers MA, Wu XL, Daniel WB (2001) Conducting fluid dynamics experiments with vertically falling soap films. Rev Sci Instrum 72:3025–3037

Sfakiotakis M, Lane DM, Davies JBC (1999) Review of fish swimming modes for aquatic locomotion. J Ocean Eng 24:237–252

Triantafyllou GS, Triantafyllou MS, Grosenbaugh MA (1993) Optimal thrust development in oscillating foils with application to fish propulsion. J Fluids Struct 7:205–224

Webb PW, Weihs D (1986) Functional locomotor morphology of early-life-history stages of fishes. Trans Am Fish Soc 115:115–127

Wen CY, Lai JY (2003) Analogy between soap film and gas dynamics. I Equations and shock jump conditions. Exp Fluids 34:107–114

Wen CY, Chang-Jian SK, Chuang MC (2003) Analogy between soap film and gas dynamics. II Experiments on one-dimensional motion of shock waves in soap films. Exp Fluids 34:173–180

Williamson CHK, Roshko A (1988) Vortex formation in the wake of an oscillating cylinder. J Fluid Struct 2:355–381

Zhang J, Childress S, Libchaber A, Shelley M (2000) Flexible laments in a flowing soap film as a model for one-dimensional flags in a two-dimensional wind. Nature 408:835–839

A harmonic model of hydrodynamic forces produced by a flapping fin

David N. Beal · Promode R. Bandyopadhyay

Abstract The hydrodynamic control laws of unsteady fins inspired by swimming and flying animals are considered. A controller based on cycle-averaged forces requires a bandwidth lower than the flapping frequency, with correspondingly slow reactions to disturbances or commands in order to avoid undesirable feedback from the oscillating fins. A harmonic model of the periodic thruster forces was empirically found using a mechanical fin flapping in roll and pitch in hover, in uniform flow, and under various kinematic conditions. A multi-fin vehicle could use this model to account for the dominant non-linearities and minimize undesirable motions through coordinated control of individual fins.

1 Introduction

The flight of birds and the swimming of dolphins, penguins, and fish have long inspired human imagination and invention. Despite having been proven effective in nature, biologically inspired designs have often been set aside in favor of less complex technologies such as wheeled vehicles or propeller-driven, steady-fin-controlled underwater vehicles. When the required operating envelope is limited, these designs have performed admirably. But outside of the designed operating regimes, such as performing low-speed maneuvers or station-keeping in a surf zone, these engineered designs are often inefficient, or even inept. This has led to a renewed interest in the application of biology inspired technology in recent years (Licht et al. 2004; Bandyopadhyay 2004, 2005).

The studies of insects, fish, penguins, and the elemental forms abstracted from these animals are particularly relevant to undersea vehicle applications. Ellington (1984) and Dickinson et al. (1999) identified delayed stall as the primary mechanism used by rigid-winged insects in flight. Later work by Read et al. (2003) identified a large plateau of 50–60% efficiency with a two-dimensional heaving and pitching foil, and demonstrated the potential for the flapping fin as a maneuvering thruster through bias of the pitch motion sinusoid. With this foundation in place, researchers such as Licht et al. (2004) and Kato et al. (2005) began developing prototype flapping-fin powered vehicles.

The Naval Undersea Warfare Center (NUWC) has developed a prototype six-fin biorobotic vehicle that has demonstrated independent swimming maneuvers in all six degrees-of-freedom (Bandyopadhyay et al. 2008). A single instrumented fin, flapping sinusoidally in roll and pitch, was used to generate an empirical thruster model for a hovering vehicle. The cycle-averaged force magnitude was found to be proportional to the frequency and roll amplitude squared. The direction of the mean vectored thrust was a function of pitch bias alone and remained in the plane normal to the fin span zero-roll position. The controller, as discussed in Menozzi et al. (Menozzi A, Leinhos H, Beal DN, Bandyopadhyay PR Open loop engineering control of a multi-fin biorobotic underwater vehicle, IEEE JOE submitted), was able to use the six fins to produce force and moment vectors in any direction. The controller was based on an underdetermined linear combination of the cycle-averaged forces generated by the fins, minimized for energy and within a constrained space considering the restrictions of the actuator

D. N. Beal (✉) · P. R. Bandyopadhyay
Autonomous Systems and Technology Department,
Naval Undersea Warfare Center, Newport, RI, USA
e-mail: bealdn@npt.nuwc.navy.mil

P. R. Bandyopadhyay
e-mail: bandyopadhyaypr@npt.nuwc.navy.mil

G.K. Taylor, M.S. Triantafyllou, and C. Tropea (Eds.): Animal Locomotion, pp. 37–44.
springerlink.com

design. Although effective in demonstrating several maneuvers, this controller made no attempt to stabilize the vehicle wobble caused by the unsteady nature of the fin forces, and was bandwidth-limited when station-keeping. Using intuitive fin coordination, the vehicle was able to perform certain maneuvers without undesirable forces and moments, such as flapping the fore and aft fins out-of-phase in order to swim forward or backward smoothly. This demonstrated the potential to cancel or reduce higher harmonic motions, but no algorithm was developed to do this for an arbitrary force and moment vector.

A control system that utilizes a cycle-averaged model of the forces produced by a flapping fin must be limited in bandwidth to the flapping frequency to prevent the controller from reacting to the inherent unsteady forces created by the fin motion. Higher bandwidth control requires taking into account the instantaneous forces produced by the fin. Breaking the periodic forces into Fourier coefficients enables a small data set to model the fin-generated forces with reasonable accuracy (Videler 1993). A thruster model based on these harmonic coefficients would enable the controller to reduce vehicle wobble and increase response bandwidth.

2 Materials and methods

Fourier coefficients for a rolling and pitching rigid fin were empirically found for a range of motion parameters in both hover and cruise. These coefficients were made dimensionless through the mean wing velocity, as discussed below.

2.1 Apparatus

An abstracted penguin-like flapping apparatus was tested over a wide range of parametric motions in order to study the forces produced and power expended in hover and cruise. The apparatus was evaluated primarily as a maneuvering thruster intended to supplement, rather than supplant, the primary cruising thruster of a hypothetical submersible. Hence, the system was tested in its capacity to vector forces in directions perpendicular as well as parallel to a vehicle axis.

Two servomotors were used to flap the fin in roll (a sweeping motion) and in pitch (a feathering motion). The flapping apparatus was mounted to a tow carriage in the NUWC low-speed testing tank, a facility with an overall length of 27 m and a cross-section 0.90 m deep and 1.22 m wide. The apparatus was attached to the carriage through a six-axis load cell, as shown in Fig. 1. Torque sensors attached to the output shaft of the roll and pitch motors

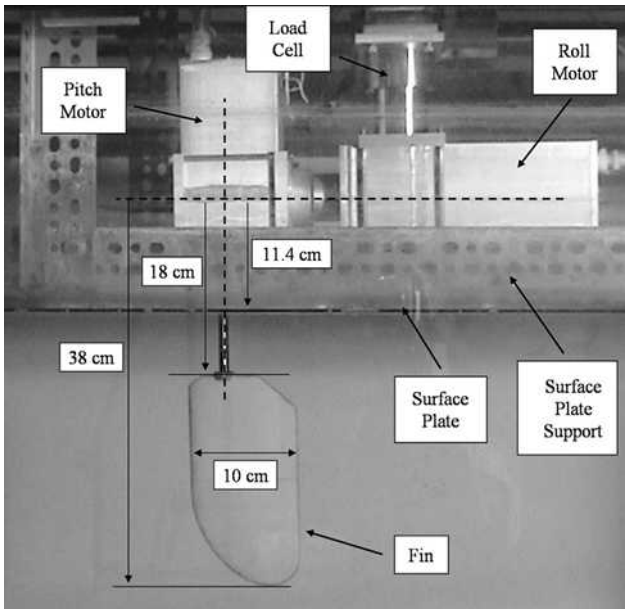

Fig. 1 Annotated diagram of the flapping fin apparatus mounted to the tow carriage

were used to calculate hydrodynamic power, a measurement independent of the specific actuators used. A computer on the tow carriage performed the motion control and data collection functions. A horizontal Plexiglas plate was used to reduce surface effects and air entrainment in the vortex wake of the fin. The fin shaft oscillated within a slot in the plate. The fin was rigid, with a 20 cm span, 10 cm chord, a NACA 0012-64 cross-section with zero camber, and with an 18 cm arm between the roll axis and the inside of the fin span.

The fin flapping motion was a combination of sinusoids in roll and pitch, with the following independent parameters: carriage speed U_∞, frequency ω (in rad/sec), roll and pitch amplitudes ϕ_0 and θ_0, and the DC bias to the pitch sinusoid θ_{bias}, as shown in Fig. 2. The roll and pitch motions were held 90° out of phase and were defined as

$$\phi(t) = \phi_0 \sin(\omega t), \tag{1}$$

and

$$\theta(t) = \theta_0 \cos(\omega t) + \theta_{\text{bias}}. \tag{2}$$

The fin was tested under a variety of motion parameters for hover (U_∞ = 0) and at three speeds (U_∞ = 0.47, 0.85, and 1.30 m/s). The frequency was varied between 0.75 and 1.50 Hz; with roll amplitudes of 30° and 40°, and pitch amplitudes between 15° and 65° (within the limitations of the apparatus); pitch biases were between 0° and −45° for the hover tests, and between 0° and 25° at speed.

The directions of thrust and lift are defined as in Fig. 2, where positive thrust is in the positive x-direction and

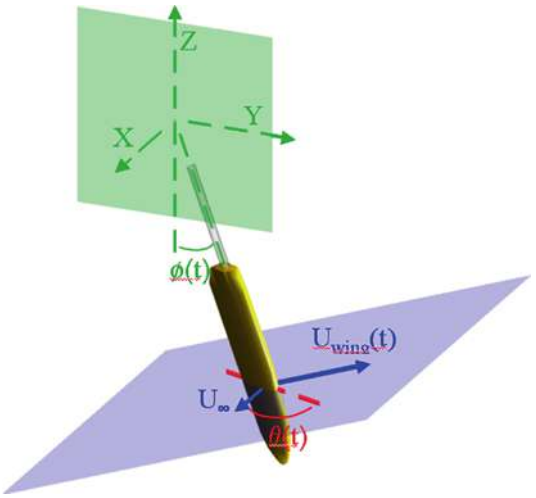

Fig. 2 The roll motion ϕ sweeps the fin through an arc in the y–z plane, whereas the pitch θ feathers the fin into the sweep velocity U_{wing}. In this paper, thrust and C_T are in the positive x-direction, whereas positive lift and C_L are in the positive y-direction

perpendicular to the plane of foil roll motion. In these experiments, this plane of foil sweep is always perpendicular to the carriage velocity and the uniform flow. The errors in the force measurements are ±0.25 N, and power is within ±0.39 W.

2.2 Analysis

Fourier coefficients were found using a least-squares fit to the cycle-averaged forces. Define y as a vertically–oriented vector containing the instantaneous force and t as a vector containing the corresponding times, where $t = 0$ is defined as from Eq. (1). Matrix x was set up as columns of the harmonics:

$$x = \begin{bmatrix} 1 & \sin(\omega t) & \cos(\omega t) & \sin(2\omega t) & \cos(2\omega t) & \cdots & \cos(5\omega t) \\ \vdots & \vdots & \vdots & \vdots & \vdots & \vdots & \vdots \\ 1 & \vdots & \vdots & \vdots & \vdots & \vdots & \vdots \end{bmatrix}. \tag{3}$$

The Fourier coefficients were then found by multiplying y by the pseudo-inverse of x. A fit with the first five harmonics was seen to produce a reasonable approximation of the experimental data, as shown in Fig. 3. The amplitudes and angles of each harmonic were then found using the sine and cosine coefficients of that harmonic. Note that the cosine-coefficients are in phase with the roll velocity, whereas the sine-coefficients are in phase with the roll position and out of phase with the acceleration. Harmonic coefficients were found for the thrust (streamwise) and lift (transverse) forces.

For cruise, the input motion parameters for frequency, roll amplitude, and carriage speed were reduced using the Strouhal number

$$St = \frac{2f\phi_0 R_{\text{avg}}}{U_\infty}, \tag{4}$$

where f is the frequency in Hz and R_{avg} is the radius that defines the center of swept area of the fin:

$$R_{\text{avg}} = \sqrt{r_o^2 + r_i^2}/2, \tag{5}$$

where r_o and r_i are the distances from the roll axis to the tip and inner edge of the span, respectively.

The Fourier coefficients were normalized using the mean wing velocity over a half-cycle, the density of the fluid, and the plan-form area of the fin:

$$C_{F,\text{wing}} = \frac{F}{\frac{1}{2}\rho \bar{U}_{\text{wing}}^2 A_{\text{Planform}}}, \tag{6}$$

where F is the harmonic coefficient and, for a sinusoidal roll motion,

$$\bar{U}_{\text{wing}} = \frac{2}{\pi}\phi_0 \omega R_{\text{avg}}. \tag{7}$$

The Fourier coefficients can be more easily compared between tests with vastly different motions and force amplitudes using $\bar{U}_{\text{wing}}$ rather than U_∞; this also avoids problems with $U_\infty = 0$.

Hydrodynamic power was calculated using the instantaneous torques and velocities of the two motors:

$$\bar{P}_{\text{hydro}} = \overline{-\tau_\phi(t)\dot{\phi}(t) - \tau_\theta(t)\dot{\theta}(t)}, \tag{8}$$

where τ_ϕ and τ_θ are the instantaneous roll and pitch torques, respectively. Mean power was then normalized by wing velocity to calculate the coefficient of power:

$$C_{P,\text{wing}} = \frac{\bar{P}_{\text{hydro}}}{\frac{1}{2}\rho \bar{U}_{\text{wing}}^3 A_{\text{Planform}}}. \tag{9}$$

3 Results and discussion

For clarity of discussion, the results have been split between the hovering and cruising experiments. While hovering, the non-dimensional forces reduce to functions of pitch amplitude and pitch bias alone. Although the cruising data are dependent on Strouhal number as well, similar trends are seen. The normalized Fourier coefficients for the third harmonic were below 1.0, and those for the fourth and fifth harmonics were below 0.5; hence, the

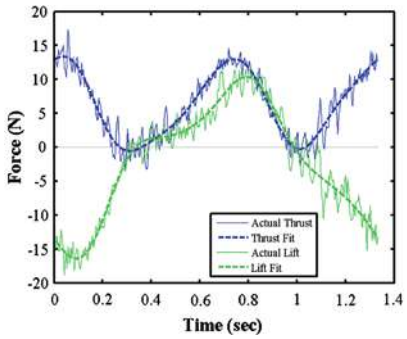

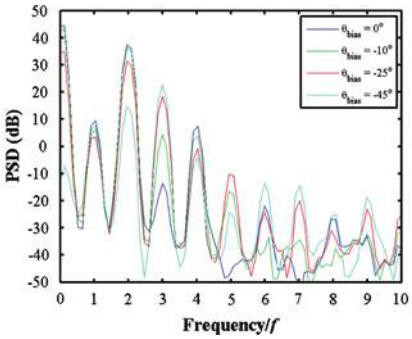

Fig. 3 Example showing unfiltered thrust and lift data against the fit using the first five harmonics of the primary flapping frequency (left), for $\phi_0 = 40°$, $\theta_0 = 45°$, $f = 0.75$ Hz, $\theta_{\text{bias}} = -10°$, $U_\infty = 0$ m/s. The harmonics are shown using the power spectral density estimate via Welch's averaged, modified periodogram method for thrust (*right*), for $\phi_0 = 40°$, $\theta_0 = 45°$, $f = 0.75$ Hz, $\theta_{\text{bias}} = 0$ to $-45°$, $U_\infty = 0$ m/s

discussion focuses on the first and second harmonics, which are of similar magnitude as the mean forces.

3.1 Hover

The first Fourier coefficients of lift and thrust are the cycle-averaged forces produced during the test. The use of wing velocity as the dimensional parameter collapsed the data from roll amplitude and frequency, allowing the representation of the data as functions of pitch amplitude and bias only. As shown in Fig. 4, 5, and 6, the mean force shifts between pure thrust and pure lift as the pitch bias changes from 0° to −45°. The magnitude of the mean force for a bias of −45° is roughly three-quarters of that for 0°, illustrating a loss in effectiveness as the swimming "gait" transitions from a flapping motion to a paddling or rowing motion.

Data from tests with a 45° pitch amplitude and zero pitch bias show a strong second harmonic cosine in thrust roughly equal in amplitude to the mean thrust, as shown in Fig. 4. This is due to a thrust peak during the high roll velocity portion of each side-to-side sweep and a momentary loss of thrust generation while the roll velocity is low at the roll limits. Additionally, there is a strong first harmonic in lift roughly in anti-phase with the roll velocity due to the fluidic drag resisting the roll motion of the fin.

The second harmonic cosine transitions from the thrust to the lift direction as the pitch bias is decreased from 0° to −45°. Meanwhile, the first harmonic is little changed, so that when the mean force is exactly in lift at a pitch bias of −45°, the lift trace exhibits both the first and second harmonics on top of the DC component. This implies that beneficial mean forces are entirely due to the second harmonic—with the first harmonic representing losses—even during a paddling-style motion. Further study visualizing the vorticity in the wake may be useful to support this assertion.

When the pitch amplitude is increased to 55° and 65° (see Figs. 5, 6, respectively), the normalized Fourier coefficients generally decrease. At zero bias, the first harmonic cosine diminishes the most, from (−3 to −2.2) to (−1.3) as the pitch amplitude increases from 45°–55° to 65°, respectively. This corresponds to the reduction in the coefficient of power, as shown in Fig. 7, from (3–2.2) to (1.3) for increasing pitch amplitude. The similarity between the magnitudes of the first harmonic cosine and the coefficient of power supports the assertion that the first harmonic cosine largely represents losses and implies that higher pitch amplitudes are generally more efficient for hover. However, as pitch bias changes from zero, this benefit is lost, as the first cosine increases to a value similar to that seen at a pitch amplitude of 45°.

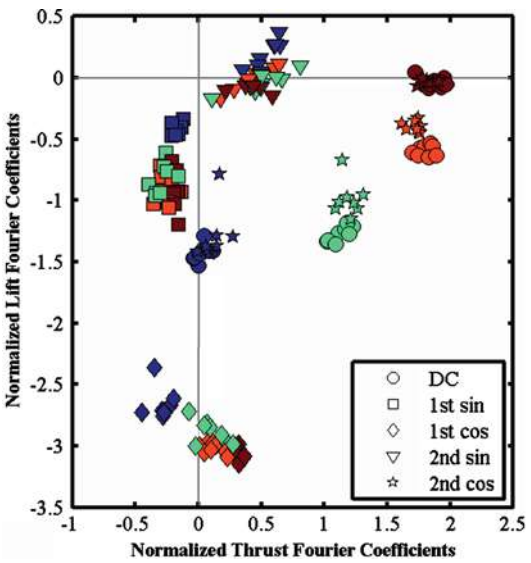

Fig. 4 Normalized lift and thrust Fourier coefficients for hover, 45° pitch amplitude. The color of each point denotes the bias to the pitch sinusoid: *red* 0°, *orange* −10°, *green* −25°, and *blue* −45°. Forces were normalized by the mean absolute wing velocity, fluid density, and plan-form area

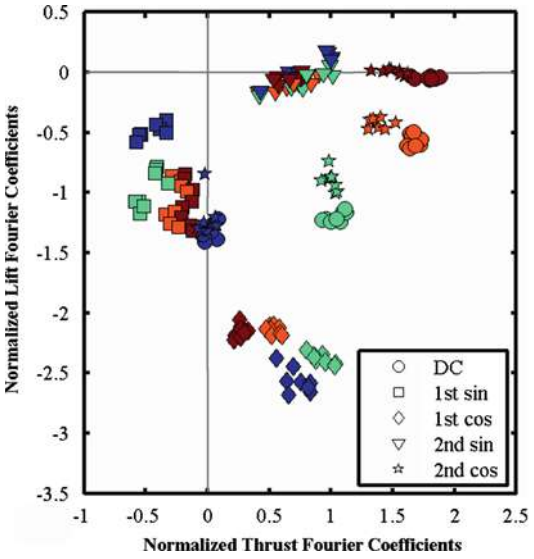

Fig. 5 Normalized lift and thrust Fourier coefficients for hover, 55° pitch amplitude. The color of each point denotes the bias to the pitch sinusoid: *red* 0°, *orange* −10°, *green* −25°, and *blue* −45°. Forces were normalized by the mean absolute wing velocity, fluid density, and plan-form area

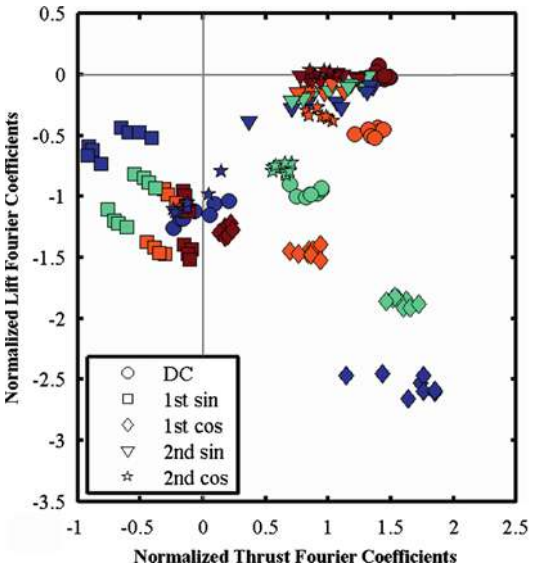

Fig. 6 Normalized lift and thrust Fourier coefficients for hover, 65° pitch amplitude. The color of each point denotes the bias to the pitch sinusoid: *red* 0°, *orange* −10°, *green* −25°, and *blue* −45°. Forces were normalized by the mean absolute wing velocity, fluid density, and plan-form area

The hovering tests show that the non-dimensional thrust and lift forces are dependent on pitch amplitude and pitch bias alone. Operating at a pitch amplitude of 45°, a reasonable estimate of the instantaneous forces could be modeled using the mean component, first harmonic cosine, and second harmonic cosine alone. A controller could be

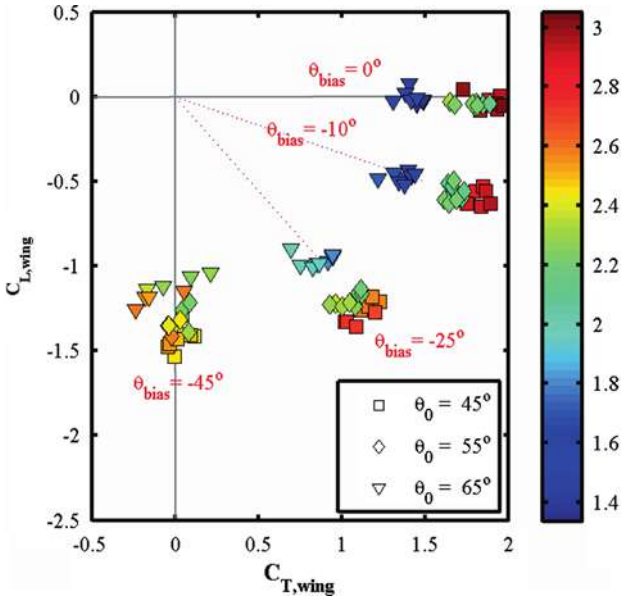

Fig. 7 Thrust and lift coefficients for hover, showing mean components only. *Color* represents the coefficient of power based on wing velocity, fluid density, and plan-form area

designed to balance the undesirable oscillatory forces of multiple fins while producing the desired mean forces through the control of wing velocity, pitch amplitude, pitch bias, and the phase between individual fin motions. This could be similar to what Menozzi et al. (Menozzi A, Leinhos H, Beal DN, Bandyopadhyay PR Open loop engineering control of a multi-fin biorobotic underwater vehicle, IEEE JOE submitted) did with the cycle-average forces, but instead of simply searching an under-determined space for the desired combined force and moment vectors with minimized energy, this would search an over-determined space to minimize a cost function related to harmonics forces as well.

Alternatively, the unsteady component of measured acceleration could be subtracted through a hydrodynamic model of the vehicle hull in a form of feedback linearization, enabling the controller to react to external disturbances with a higher bandwidth, but not suppressing wobble.

3.2 Cruise

Although the results of the cruising studies are more complicated than those for hover, many of the general trends found above are still relevant. The non-dimensional forces are completely described using the Strouhal number, pitch amplitude, and pitch bias. The maximum Strouhal number achievable for a given pitch amplitude was limited by the roll motor, which was incapable of supplying the torque necessary for high Strouhal number motions at low pitch amplitude.

The zero harmonic results (see Fig. 8) show that the mean thrust coefficient reaches a maximum of approximately 1.5 for high Strouhal numbers and decreases as Strouhal number is decreased or as pitch amplitude or pitch bias is increased. The mean lift coefficient is zero when the pitch bias is zero due to symmetry; it increases with pitch bias and decreases with Strouhal number, but does not change significantly with pitch amplitude.

At speed, the mean lift force is a function of the fin's bias both to the oncoming flow and to the component created by the flapping motion seen above with hover. In other words, the mean lift consists of components due to U_∞^2 as well as $\bar{U}_{\text{wing}}^2$. Normalizing by $\bar{U}_{\text{wing}}^2 = \left(\frac{2}{\pi}\phi_0 \omega R_{\text{avg}}\right)^2 + U_\infty^2$ reduces the mean lift coefficients to functions of pitch bias alone, with coefficients of 0.01 ± 0.02, 0.49 ± 0.07, and 1.04 ± 0.12 for pitch biases of 0, 10, and 25°, respectively. This uniform flow effect on lift is not relevant for the harmonic forces, however, as this is inherently a steady effect. Since it is desired to normalize all forces identically, $\bar{U}_{\text{wing}}$ from Eq. (7) is used for all numbers and plots in this paper except for those in this paragraph.

Due to the uniform flow effect on pitch bias, pure mean lift forces (without any mean thrust) were seen for pitch biases lower than 45° in all cases. Indeed, pure mean lift loads were seen for biases of 10° or 15° in many cases where the carriage speed was high. Additionally, all of the tests have a higher coefficient of lift when generating a pure-lift force than they do a coefficient of thrust when generating a pure-thrust force at 0° bias. This is a reverse of the situation seen for hover, since the flow aids in the production of maneuvering forces.

Figure 9 shows the first harmonic coefficient amplitudes for thrust and lift. The first harmonic in the thrust direction is negligible when the pitch bias is 0°, but increases as the pitch bias increases. The first harmonic in lift is a strong function of pitch amplitude alone, increasing from coefficients less than two for $\theta_0 = 65°$ to coefficients greater than six for $\theta_0 = 15°$. The coefficient of power again matches well with the first harmonic in lift, implying that this drives the power losses.

The second harmonic coefficients again shift from the thrust direction into the lift direction as the bias angle is increased, although the rate of this change is strongly dependent on pitch amplitude, as shown in Fig. 10. The magnitudes are similar to those seen in hover.

Although some similar trends are seen in cruise as in hover, a look-up table would likely be needed for proper real-time modeling of the periodic forces. It may be possible to simplify the model by separating the effects of uniform flow and the flapping motion on the mean lift forces produced by a pitch bias angle.

4 Conclusions

The unsteady forces produced by a fin flapping in roll and pitch can be adequately described using the Fourier

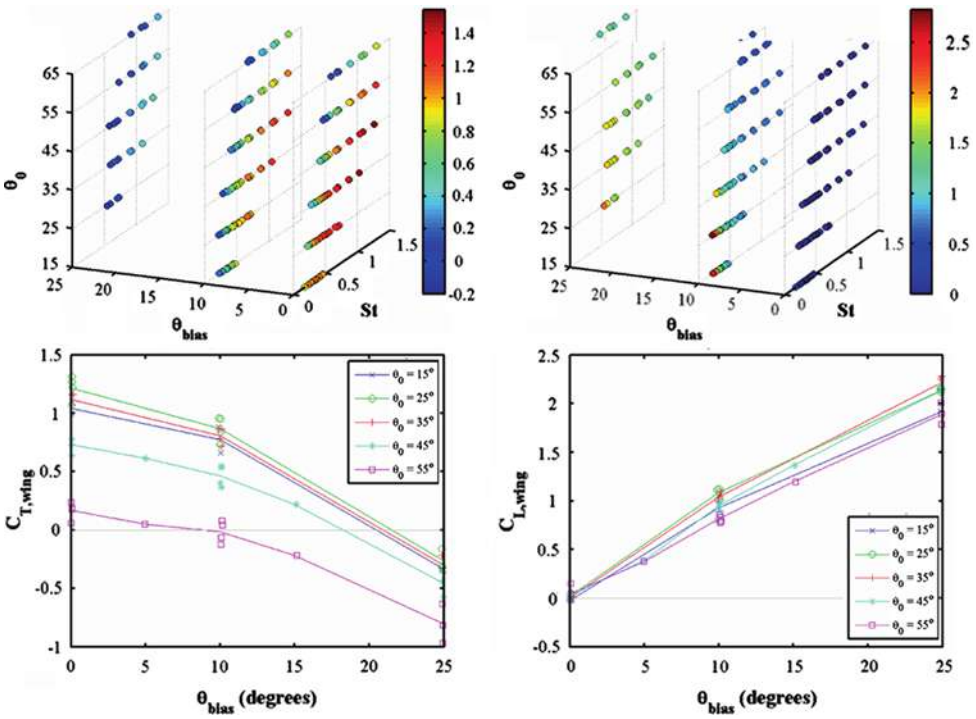

Fig. 8 Coefficients of zero harmonic for thrust (*left*) and lift (*right*), for cruise ($U_\infty > 0$). The *lower plots* limit results to tests between $St = 0.45$–0.55 to more clearly illustrate trends. Some thrust values are negative for a bias of 25°, representing a drag- and lift-producing motion. Values with a thrust coefficient of less than −0.2 were removed from the *upper plots* in order to better visualize the data

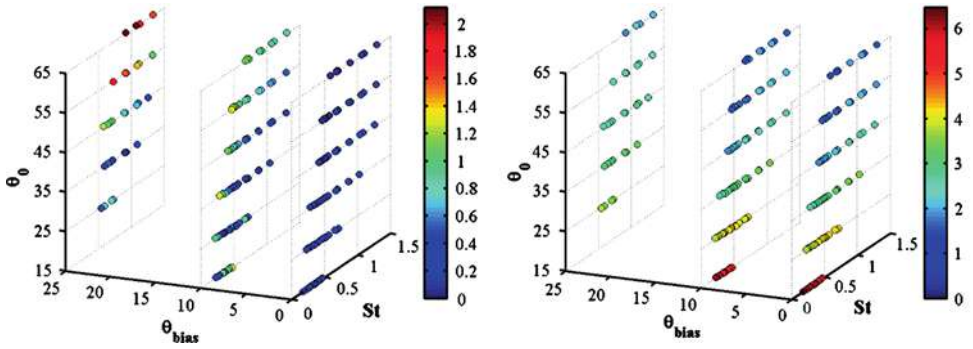

Fig. 9 Coefficients of first harmonic for thrust (*left*) and lift (*right*), for cruise ($U_\infty > 0$), where the *color scale* denotes the amplitude of the combined sine and cosine coefficients

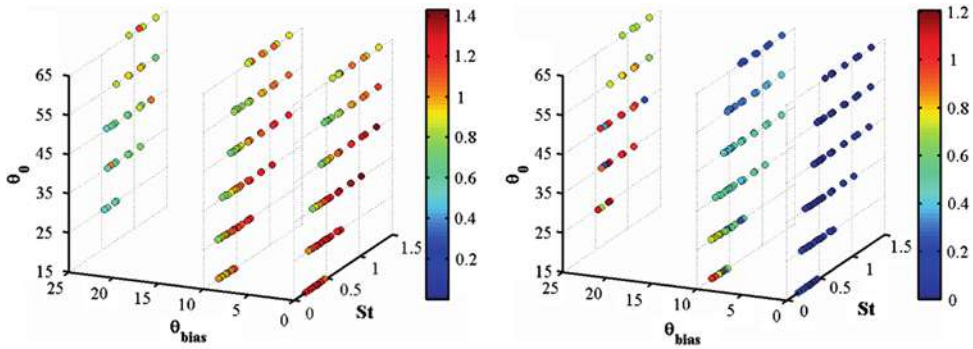

Fig. 10 Coefficients of second harmonic for thrust (*left*) and lift (*right*), for cruise ($U_\infty > 0$), where the *color scale* denotes the amplitude of the combined sine and cosine coefficients

coefficients for the first five harmonics. Experiments revealed characteristics inherent to a fin thruster in hover as follows:

1. The mean absolute wing velocity, pitch amplitude, and pitch bias completely describe the fin motion parameters, forces, and power.
2. The mean-vectored force shifts from the thrust to the lift direction as the pitch bias changes from 0° to −45°.
3. The coefficient of the first harmonic cosine is nearly identical to the coefficient of power, and it decreases faster than the mean force as the pitch amplitude is increased from 45° to 65°. This coefficient represents the losses due to the roll velocity in the fluid.
4. The coefficient of the second harmonic cosine follows the magnitude and direction of the mean force as it vectors with pitch bias. Analysis of the wake may be useful in understanding this effect.

During cruise:

1. The bias angle needed to produce a pure-lift mean force is significantly less than that for hover because a portion of the mean lift in cruise is dependent on the flow speed.
2. As with hover, the coefficient of the first harmonic is nearly the same as the coefficient of power.
3. As with hover, the second harmonic magnitude and direction transitions from the thrust to the lift direction as pitch bias increases.

This harmonic model enables the controller to act at a higher bandwidth in order to improve the reaction time to disturbances or commands, as compared to a cycle-averaged force model alone. The proposed model accounts for some of the nonlinearities present in the instantaneous fin forces that become linearized in a cycle-averaged controller. A fin-powered submersible could use such a harmonic model to minimize undesirable unsteady vehicle motions.

Acknowledgments This work was sponsored by the Cognitive and Neuroscience Division of the Office of Naval Research (ONR 34, Program Officer Dr. Thomas McKenna) and the ONR/NUWC ILIR Program (Program Officer Mr. Richard Philips). Additionally, the authors would like to thank Dr. Alberico Menozzi and Mr. Henry Leinhos for discussions regarding the integration of the harmonic model into the NUWC biorobotic vehicle autopilot.

References

Bandyopadhyay PR Guest (ed) (2004) Special issue on biology-inspired science and technology for autonomous underwater vehicles. IEEE JOceanic Eng 29(3)

Bandyopadhyay PR (2005) Trends in biorobotic autonomous undersea vehicles. IEEE J Oceanic Eng 30:109–139

Bandyopadhyay PR, Beal DN, Menozzi A, Boller M (2008) Underwater vehicles close performance gaps with nature via exploitation of the high-lift principles of swimming and flying animals IEEE J Oceanic Eng 211(2) (in press)

Dickinson MH, Fritz-Olaf L, Sane SP (1999) Wing rotation and the aerodynamic basis of insect flight. Science 284:1954–1960

Ellington CP (1984) The aerodynamics of hovering insect flight, IV. Aerodynamic mechanisms. Phil Trans R Soc Ser B 305:79–113

Kato N, Liu H, Morikawa H (2005) Biology-inspired precision maneuvering of underwater vehicles–part 3. Intl J Offshore Polar Eng 15(2):81–87

Licht S, Polidoro V, Flores M, Hover FS, Triantafyllou MS (2004) Design and projected performance of a flapping foil AUV. IEEE J Oceanic Eng 29(3):786–794

Read DA, Hover FS, Triantafyllou MS (2003) Forces on oscillating foils for propulsion and maneuvering. J Fluids Struct 17:163–183

Videler JJ (1993) Fish swimming. Chapman & Hall, London

Flowfield measurements in the wake of a robotic lamprey

Marcus Hultmark · Megan Leftwich · Alexander J. Smits

Abstract Experiments are reported on the hydrodynamics of a swimming robotic lamprey under conditions of steady swimming and where the thrust exceeds the drag. The motion of the robot was based on the swimming of live lampreys, which is described by an equation similar to that developed for the American eel by Tytell and Lauder (J Exp Biol 207:1825–1841, 2004). For steady swimming, the wake structure closely resembles that of the American eel, where two pairs of same sign vortices are shed each tail beat cycle, giving the wake a 2P structure. Force estimates suggest that the major part of the thrust is produced at or close to the end of the tail.

1 Introduction

Eels, snakes and lampreys are anguilliform swimmers, in that a large part of the body undulates during locomotion. In contrast to carangiform swimmers, such as trout and mackerel, where only the caudal part of the body generates thrust, the flowfield dynamics of anguilliform swimmers is not well understood. In particular, it is not clear what parts of the body are engaged in thrust and drag production.

A recent study by Tytell and Lauder (2004) investigated the wake structure developed by a steadily swimming American eel using Particle Imaging Velocimetry (PIV). It was found that for every tail beat two same sign vortices were created. They also found that the most striking feature of the wake is the size and strength of the lateral jets and the notable absence of substantial downstream flow (Tytell and Lauder 2004). This wake structure, with two vortices per tail beat, has also been noted by Müller et al. (2001). A stopping-starting vortex is produced each time the tail reaches a lateral maximum and changes direction. As to the secondary vortex, Müller et al. (2001) suggested that it was created as a result of a phase difference between the body and the tail. In contrast, Tytell and Lauder suggested that when the tail starts to move after changing direction, a low pressure region is created that sucks fluid laterally. When this fluid is shed from the tail it stretches the first vortex and creates a new, same-sign, vortex.

Tytell (2004) found that the American eel swims steadily at a Strouhal number of 0.32 and that the Strouhal number increased slightly when the eel was swimming at lower speeds. The Strouhal number St is a non-dimensional frequency defined by

$$St = \frac{Af}{U}, \tag{1}$$

where f is the frequency of the tail oscillation, A is its peak-to-peak amplitude, and U is the swimming speed.

Triantafyllou et al. (1993) investigated the optimal frequency of a two-dimensional pitching airfoil using linear stability analysis on the mean wake profile, under conditions of maximum efficiency. They argued that the frequency of optimal efficiency is found at the frequency of maximum amplification. They found that the Strouhal number for maximum efficiency was between 0.25 and 0.35 with a most likely value of 0.30. Strouhal number for the most fish in steady swimming have also been reported

M. Hultmark · M. Leftwich · A. J. Smits (✉)
Mechanical and Aerospace Engineering, Princeton University, Princeton, NJ 08540, USA
e-mail: asmits@princeton.edu

Present Address:
M. Hultmark
Chalmers University of Technology, 41296 Gothenburg, Sweden

G.K. Taylor, M.S. Triantafyllou, and C. Tropea (Eds.): Animal Locomotion, pp. 45–52.
springerlink.com

to be close to the predicted value for optimal efficiency (Triantafyllou et al. 1993).

A recent study by Buchholz and Smits (2007) investigated the flow field in the wake of a pitching flat plate, taken as a simplified tail of a fish without heave. Buchholz and Smits found that the wake consisted of three-dimensional vortex loops linked together in a complicated vortex chain (see Fig. 1). It was found that the width of the wake increased with increasing *St*, and that two modes of wake structure exist. For lower Strouhal numbers a single vortex is shed each half cycle, and a vortex of opposite sign is shed in the next half cycle. This structure was found for Strouhal numbers between 0.2 and 0.25, and it is shown in Fig. 1. Following Williamson and Roshko (1998), this is described as a 2S structure because two single vortices are shed each cycle. As the Strouhal number increases, the wake broadens and two vortices of opposite sign are shed each half cycle, that is, it resembles a 2P structure (Buchholz and Smits 2007).

Kern and Koumoutsakos (2006) investigated the thrust production of an anguilliform swimmer by numerical simulation and found that the anterior half of the body had no contribution to the thrust. While the majority of the thrust was produced at the tail, there was also some thrust produced by the posterior part of the body. Lighthill's inviscid elongated body theory (Lighthill 1971) predicts the efficiency of a carangiform swimmer to be much higher than the efficiency of an anguilliform swimmer, but this model assumes that thrust is produced only at the trailing edge (that is, right at the tail).

Here, we are interested in the hydrodynamics of lamprey locomotion. Lampreys (*Ichthyomyzon unicuspis*) are jawless fish (see Fig. 2) that resemble eels in their swimming motion. Lampreys are one of the simplest vertebrates and their behavior may give insight on the locomotion of higher vertebrates. As the lamprey swims, we see a complex behavior that involves rhythmic output from each spinal segment or functional group of motoneurons. This output derives from the central pattern generator (CPG) neural circuitry that periodically activates muscles and muscle groups. Periodic CPG bursting must be coordinated to maintain the proper phase relationships among the muscles, a task performed by the intersegmental coordinating system. The muscles must then move the limbs and/or body parts through the water. The resulting motions cause mechanical reaction forces on the body, depending upon task and environment, and body movements in turn generate sensory feedback signals to the CPG that can reshape and retime the rhythm or its components to produce appropriate muscle forces and velocities. In terms of the body hydrodynamics, we aim to understand the wake structure, the forces acting on the body, and the possible feedback between the CPG and the hydrodynamics, specifically through neuromast organs located on the exterior of the body.

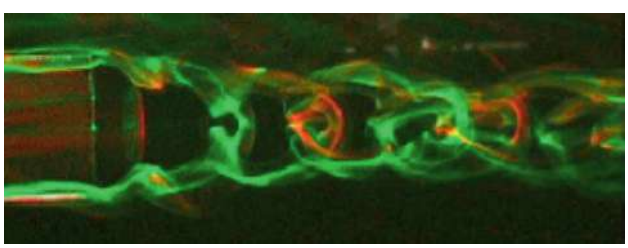

Fig. 1 Flow visualization of the wake produced by a flapping rectangular plate at a Strouhal number of 0.23. Flow is from *left* to *right*. The *red* and *green* dyes originate on opposite sides of the plate. From Buchholz and Smits (2007)

Fig. 2 The silver lamprey, *Ichthyomyzon unicuspis*, © Clifford Kraft

Because of the difficulties involved in working with live lampreys, a robotic lamprey is used to study the flowfield. The kinematics of the body motion are based on the study of live animals. PIV is used to examine the flowfield over the body and the structures in the wake in steady swimming, and where the thrust exceeds the drag. By integrating the flowfield, estimates of the resultant force are made, which can then be used to investigate the relative contributions made by different parts of the body.

2 Experiment

The swimming motions of live lampreys were studied at the University of Maryland. The animals were filmed while swimming in a small water channel ($110 \times 20 \times 20$ cm) using a DRS Lightning RDT/1 high speed digital video camera with Midas 2.0 (Xcitex, Cambridge, MA, USA) at 60 frames per second. The camera was mounted above the channel and was able to capture up to five tail beats before the fish swam out of view. The film clips of the swimming lamprey were analyzed using a custom Matlab R2006b program that finds the centerline of the lamprey body at every instant.

A recent study by Tytell and Lauder (2004) investigated the kinematics of a steadily swimming American eel and described the motion of the eel centerline by an exponentially growing traveling wave. That is,

$$y(s) = Ae^{[\alpha(s/L-1)]} \sin\left[\frac{2\pi}{\lambda}(s - Vt)\right] \quad (2)$$

where y is the lateral position of the midline, s is the coordinate following the midline, A is the tail beat

Table 1 Parameters for Eq. 2

	Amplitude, A	Growth rate, α	Body wavelength, λ	Wave speed, V
Lamprey	0.089	2.18	0.642	1.404
Eel	0.069	2.76	0.604	1.878

The eel parameters are taken from Tytell and Lauder (2004)

amplitude, α is the amplitude growth rate, L is the body length, λ is the wave length, t is time and V is the wave speed. It was found here that Eq. 2 also describes lamprey motion accurately, and therefore Eq. 2 was fitted to the points of the centerline with a correction for a possible angle of the lamprey relative to the camera. The lampreys moved at a steady swimming speed between 0.5 and 1.5 L/s. The parameters are given in Table 1 where a comparison with Tytell and Lauder's (2004) results on the American eel are also given.

The kinematics of the live animal swimming was used to generate the motion of the robotic lamprey. The robot consists of 13 Hitech HS-945MG Coreless Ultra Torque servomotors (see Fig. 3) connected together by rigid links. Each servomotor is controlled through a BasicX microcontroller mounted in the "head" of the robotic lamprey. A custom Matlab program converts the coordinates given by Eq. 2 to coordinates based on the angle at each point. This is uploaded by BasicX to the microprocessor. When a given servomotor is actuated, the shaft of the servomotor will move to the specific angular position and hold that position as long as the actuation is unchanged. In this way a traveling wave is generated along the robot body at the desired wave speed.

The robot is powered by 12 rechargeable 2,500 mAh AA batteries, each 1.2 V, connected in two groups of six batteries connected in series to give an output voltage of 7.2 V for the servomotors.

A foam skeleton was wrapped around the servomotors to create a more realistic cross-section and a smoother exterior. A waterproof skin covered the foam skeleton. The skin was made of Cementex vulcanizeable natural Latex with low ammonium content (#80 VLA). A model form was painted with three to five layers of liquid latex. Each layer was allowed to dry before applying the next layer. The skin was then vulcanized for 20 h at room temperature. The skin of the robotic lamprey captures the general form of the animal without anal or dorsal fins. The foam skeleton trapped air inside the robot to help make it neutrally buoyant. Weights were added inside the tail of the robot to make fine adjustments on balance and buoyancy. The total length of the robot was $L = 1.14$ m, with a typical cross-section measuring 38 mm $\times$ 97 mm.

Fig. 3 The image shows the 13 servomotors comprising the robotic lamprey. Each servomotor is connected to its neighbours by rigid links

The flow over the body of the robot and in the wake were investigated using PIV in a plane containing the body motion. The experiments were conducted in a closed loop, free surface water channel with a test section that is 0.46 m wide, 0.3 m deep, and 2.5 m long (see Fig. 4). Upstream of the 5:1 contraction is one honeycomb and three screens. The front part of the robot was held in the test section at mid-depth by a frame mounted on an air-bearing sled free to move in the streamwise direction. The steady swimming condition was set by matching the flow speed in the channel to the swimming speed of the robot (neglecting the friction in the air-bearing system). Surface waves were eliminated by mounting a clear acrylic plate so that it was in contact with the free surface.

Silver coated hollow ceramic spheres with a diameter of 100 μm were used as seeding particles (Potters Industries Inc. Conduct-O-Fil AGSL150 TRD). A Spectra Physics 2020 Argon laser was used to create a light sheet using an optical fiber delivery system and a Powell lens (Oz Optics Ltd). The sheet thickness was typically 1.5 mm (1/e thickness). A Redlake MotionXtra HG-LE camera was used to capture the PIV images. The camera has a resolution of 1,128 $\times$ 752 pixels and can capture a total of 1,263 frames at up to 1,000 fps. It is equipped with a Burst Record on Command (BROC) function that allows it to take a specified number of images at every trigger signal with an adjustable frequency. The camera could also be used with an external triggering device and a Stanford Research Systems DG535 Digital Delay/Pulse Generator was used to control the camera timing and generate image pairs with a time delay of 8 ms between images. Exposure times were typically 3 ms.

3 Results

The actual motion of the robotic lamprey is compared with the input according to Eq. 2 in Fig. 5. The motion of the robot surface is filtered by the presence of the foam skeleton and the flexible, waterproof skin, but it is clear that the largest discrepancies occur near the tail. To minimize this discrepancy, the length of the last rigid segment was minimized and a short, flexible section was added to the tail.

Figure 6 shows the instantaneous velocity fields in the wake of the robotic lamprey under conditions where thrust and drag are matched so that the robot is swimming

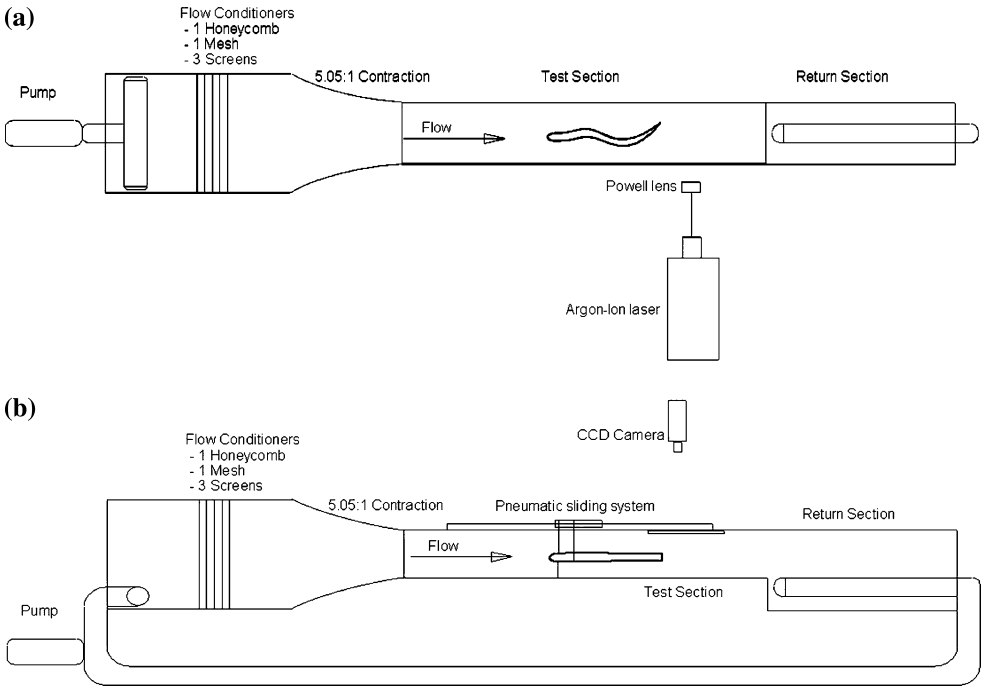

Fig. 4 Sketch of the water channel showing the laser sheet and camera arrangements. **a** *Top* view and **b** *side* view

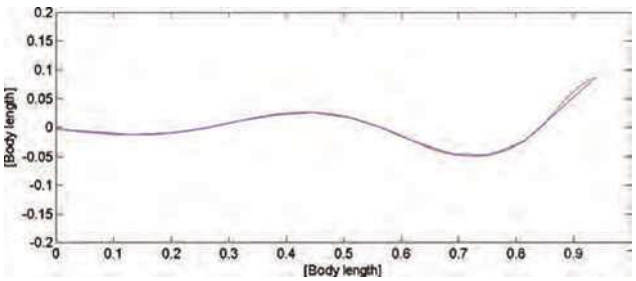

Fig. 5 Comparison between lamprey (*red line*) and robot waveforms (*blue line*). The robotic lamprey motion is the approximation due to 13 connected segments

steadily (flow speed of 9.5 cm/s, and $St = 0.65$). The Strouhal number at which the robotic lamprey swims steadily is between 0.6 and 0.65. This can be compared with a living lamprey which typically swims steadily at a Strouhal between 0.3 and 0.35. The discrepancy is probably due to the higher drag associated with the robot, so that the robot tail beat frequency needs to be higher to develop a larger thrust required to balance the increased drag. It is noted that the Reynolds number of the robot based on length of the robotic lamprey is approximately 1.15×10^5 where the live animal typically has a Reynolds number around 6×10^4. No attempt was made to match Reynolds number. Figure 7 shows the wake at the same conditions but the flow fields are phase-averaged over 35 periods. The phase averaged velocity fields contain less noise than the instantaneous ones but the principal features are the same,

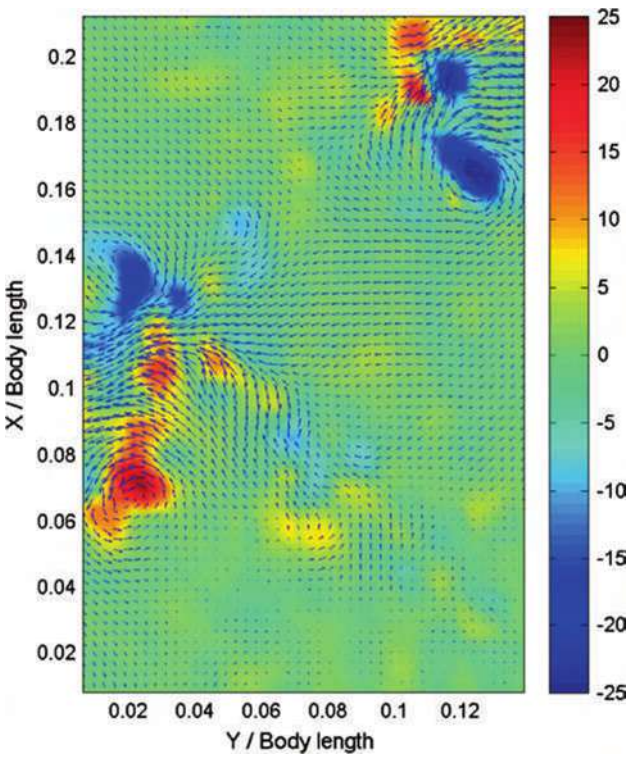

Fig. 6 Example of instantaneous velocity and vorticity fields in the wake of the steady swimming robot. The vectors represent the velocity field with the convective velocity subtracted, and the *background color* represents the out-of-plane vorticity. The flow is from *top* to *bottom*, and the tail of the robot is just out of the picture at the *top*

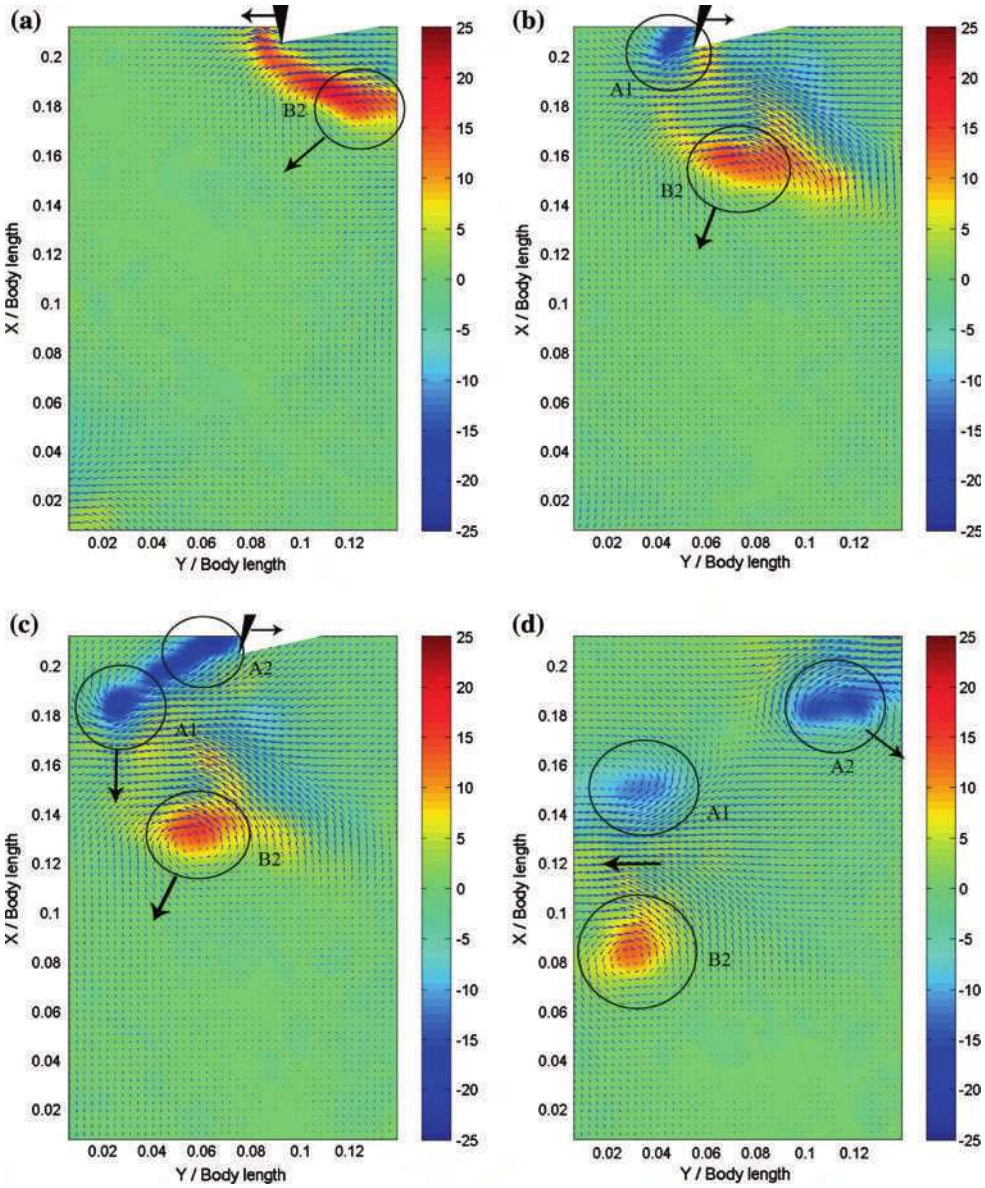

Fig. 7 Phase-averaged velocity and vorticity fields in the wake of the steady swimming robot. The vectors represent the velocity field with the convective velocity subtracted, and the *background color* represents the out-of-plane vorticity. The flow is from *top* to *bottom*, and the tail of the robot is indicated by the *small black* wedge near the *top* of each image

indicating that the motion of the robotic lamprey is highly repetitive.

The data show that two same sign vortices are created at every tail beat. In Fig. 7a the tail is moving to the left, transporting positive vorticity from the last tail beat. In Fig. 7b the tail has just passed its extrema and is moving to the right. A stopping-starting vortex is created with negative vorticity (A1, the primary vortex), and the vorticity that was transported from the other side of the wake has separated from the tail and is moving downstream and to the left. A "jet" marked by an arrow, is induced between the two vortices. When the tail has moved further to the right (Fig. 7c), the primary vortex is stretched out and a secondary vortex can be distinguished (A2). The vortex seen in Fig. 7a is the secondary vortex from the last tail beat (B2). The primary vortex (A1) is completely separate from the secondary vortex (A2) and shed directly in the wake (see Fig. 7d). At a steady swimming speed, the primary and the secondary vortex from the tail beat 180° earlier (A1 and B2) align in the streamwise direction so that they induce a jet between them normal to the direction of forward motion (see Fig. 7d). In the same figure it can be seen that the secondary vortex (A2) is transported by the tail to the other side of the wake where it will have the same role as B2 had earlier.

The flowfield generated by the robot may be compared to the results obtained by Tytell and Lauder (2004) (see Fig. 8a). The similarities in the structure of the two wakes are striking. The two counter-rotating vortices and the induced lateral jet are apparent in both wakes, and the magnitude and distribution of the vorticity is very similar, including the trail of vorticity from the tail to the primary

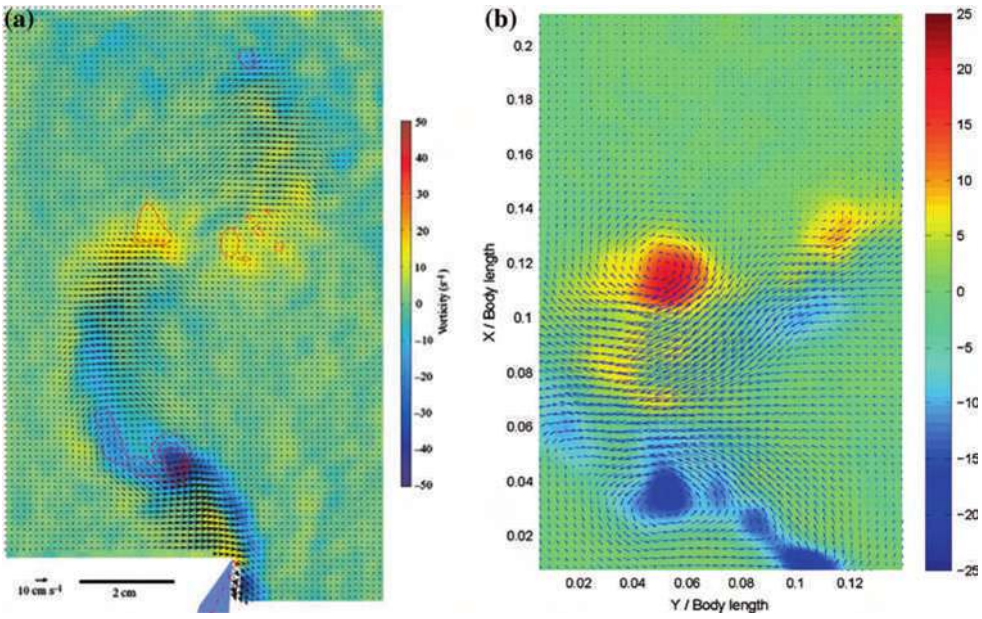

Fig. 8 Phase averaged velocity fields in the wake of **a** an American eel, taken from Tytell and Lauder (2004). **b** The robotic lamprey. Both represent the field at the same phase of motion

vortex and the area of positive vorticity on the right hand side. However, the wake of the robotic lamprey spreads more quickly, primarily because the robot is operating at a higher Strouhal number than the eel (0.65 compared to 0.32).

For cases where the thrust is greater than the drag, the jet induced between the primary and secondary vortices will have a component in the streamwise direction. Figure 9 shows the wake of the robotic lamprey when the thrust exceeds the drag, with the arrow indicating the direction of the induced jet (flow speed of 9.5 cm/s, and St = 0.65). To estimate the direction of the resultant force on the robot as a function of Strouhal number, the momentum flux, $\rho\vec{U}(\vec{n}\cdot\vec{U})$, was integrated over a control volume bounded by the half wake (see Fig. 6) for each image. The integration was done in the symmetry plane corresponding at the middle of the robot, and all out-of plane motions were neglected. The results were summed for an entire cycle to find the time-averaged force direction. The Strouhal number was varied by changing the free stream velocity at a constant tail beat frequency f = 0.56 Hz and amplitude A = 15 cm. The results are shown in Fig. 10. The angle is defined positive downstream so that the net momentum flux in the downstream direction increases as the Strouhal number increases (flow speed decreasing). For a freestream velocity of 9.5 cm/s (corresponding to the results given in Figs. 6, 7), the resulting angle is 0.38°, confirming that this condition closely approximates the condition of steady swimming. At higher Strouhal numbers, where the thrust exceeds the drag, the wake is wider than in steady swimming because the convection velocity of the vortices is lower while their induced velocity is not reduced as much. This is the same behavior Buchholz and Smits (2007)

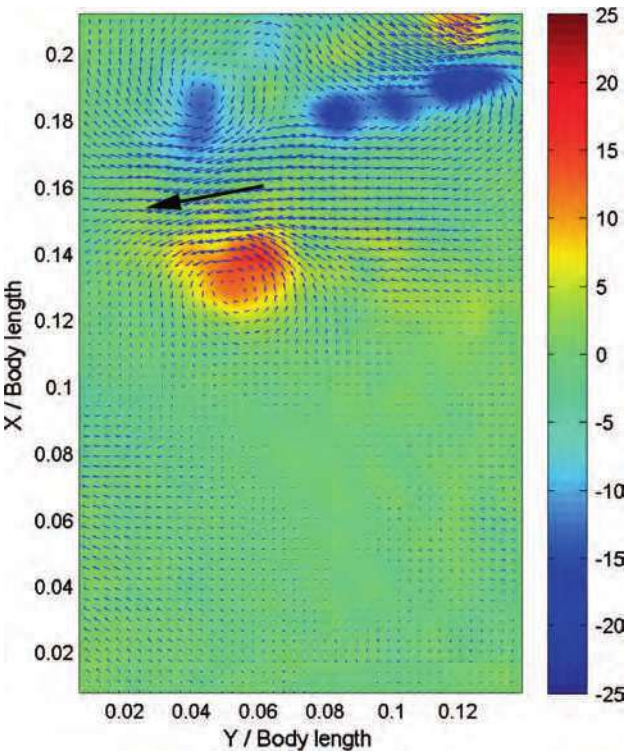

Fig. 9 An example of the phase-averaged velocity and vorticity fields in the wake of the robot when the thrust exceeds the drag

found in the wake of a flat plat at increased Strouhal number.

Figure 11 shows the instantaneous velocity and vorticity fields along the body of the robot. A relatively low level of vorticity are seen in the region near the body, and it seems to be confined to the boundary layer rather than being shed and convected downstream, so that it is unlikely to

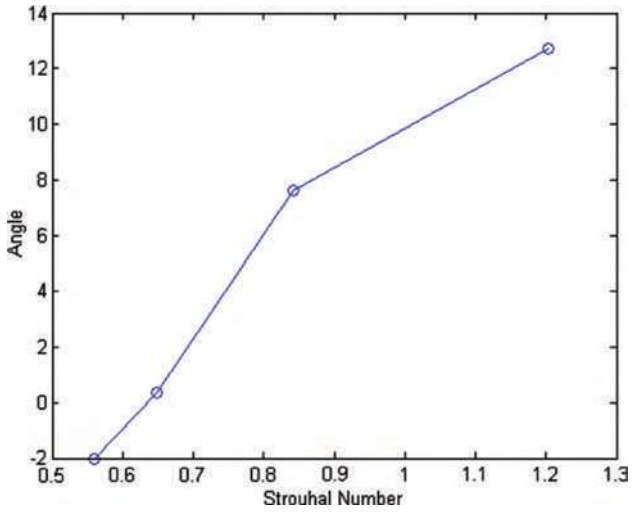

Fig. 10 Angle of force vector plotted against the Strouhal number. *Positive values* indicate that the resultant force acts to accelerate the robot

contribute significantly to the thrust. The side-to-side motion of the robot generates alternating favorable and unfavorable pressure gradients along the body, and this causes the vortical region to expand as the robot moves to the right in Fig. 11b. When the tail changes directions, the pressure gradients change signs and the region of vorticity becomes thinner, as seen in Fig. 11c.

To further determine if thrust is produced in this region, the momentum flux may be integrated over the boundaries of a two-dimensional control volume containing the wake and parts of the tail. By varying the size of the box to include progressively more of the body, the net force acting on particular parts of the body may be identified (subject to the restrictions on the analysis, particularly the assumption of two-dimensionality). Figure 12 shows the results using two different starting points for the control volume. Where the two volumes overlap it is clear that the forces in this region match. The tip of the tail is at $x/L = 0$, where x is positive upstream. Because this method estimates the total force produced by the sections downstream, it is the slope of the curve that indicates the resultant force production at a specific point rather than the absolute value. The slope is steep around $x/L = 0$ which suggests that this part of the body is responsible for the majority of the force production. Between $x/L = 0.01$ and $x/L = 0.1$ the force is approximately constant, suggesting that the thrust produced in this region is balanced by the local drag contribution. At x-locations upstream of $x/L = 0.1$ the slope is negative which implies that the drag produced is greater than the thrust.

4 Conclusions

Particle image velocimetry was employed to obtain the instantaneous flowfield in the wake behind a robotic lamprey while swimming in a water channel, as well as over the body of the robot. Two same-sign vortices are produced for every tail beat and a jet is induced between the primary vortex produced from one tail beat and the secondary vortex produced from the previous tail beat. This jet is normal to the direction of forward motion while the robot is

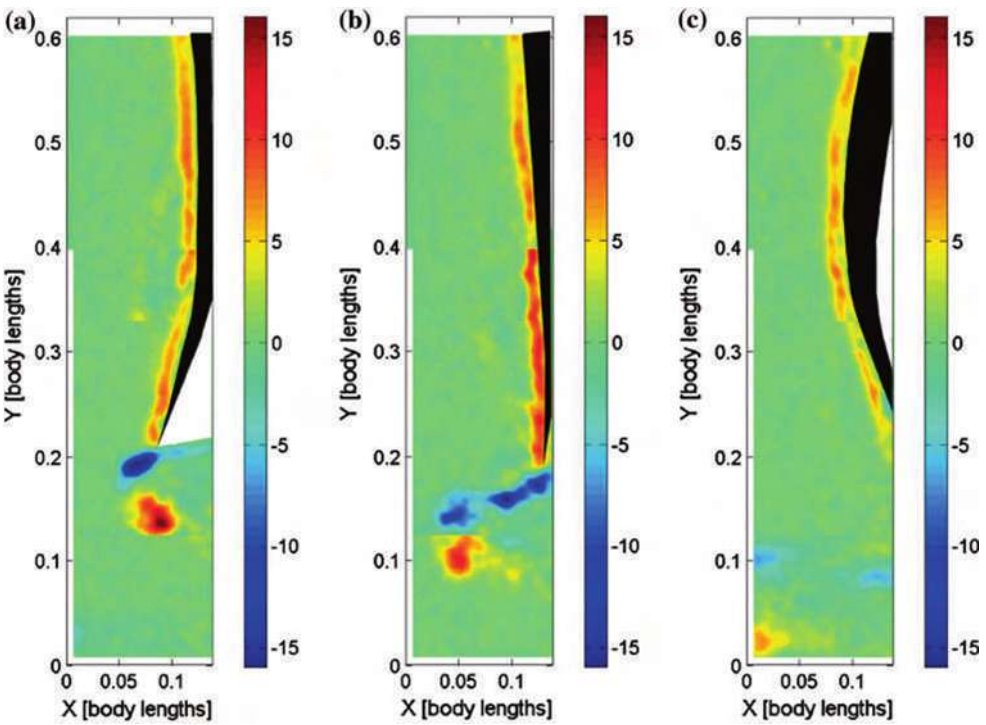

Fig. 11 Phase-averaged velocity and vorticity fields along the body and in the wake for a steadily swimming robot. The*vectors* represent the velocity field with the convective velocity subtracted, and the *background color* represents the out-of-plane vorticity. The flow is from *top* to *bottom*, and the body of the robot is indicated by the *black shape*

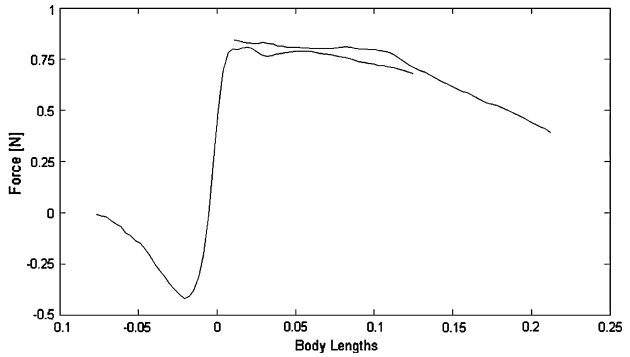

Fig. 12 The force produced from the wake to different x/L locations along the body ($x/L = 0$ is the tip of the tail). The *blue curve* is derived using one control volume only, and the *red curve* is derived from combining two control volumes to extend the domain

swimming steadily. When the thrust exceeds the drag the induced jet has a streamwise component.

The wake of the robotic lamprey appears to be similar to the wake produced by anguilliform fish. In particular, the 2P wake structure produced at steady swimming is very similar to that observed for the American eel by Tytell and Lauder (2004).

The velocity and vorticity fields along the body suggest that net thrust production occurs primarily at, or close to, the tail. This conclusion was supported by estimates of the resultant force using a control volume approach, which indicated that although some thrust is produced by the posterior part of the body, it is almost balanced by the local drag contribution.

Acknowledgments This study was supported by NIH CNRS Grant 1R01NS054271. Dr. Eric Tytell helped guide our research through many useful discussions and access to data and research methods. Our interactions with Professors Avis Cohen and Phil Holmes continue to be invaluable. The first robotic lamprey was built by Annora Bell and Ed Sheldon, and it was subsequently improved by Steve Batis.

References

Buchholz JH, Smits AJ (2007) On the evolution of the wake structure produced by a low aspect ration pitching panel. J Fluid Mech 546:433–443

Kern S, Koumoutsakos P (2006) Simulations of optimized anguilliform swimming. J Exp Biol 209:4841–4857

Lighthill MJ (1971) Large-amplitude elongated-body theory of fish locomotion. Proc R Soc Lond B 179:125–138

Müller UK, Smit J, Stamhuis EJ, Videler JJ (2001) How the body contributes to the wake in undulatory fish swimming: flow fields of a swimming eel (anguilla anguilla). J Exp Biol 204:2751–2762

Triantafyllou GS, Triantafyllou MS, Grosenbaugh MA (1993) Optimal thrust development in oscillating foils with application to fish propulsion. J Exp Biol 7:205–224

Tytell ED (2004) The hydrodynamics and eel swimming ii: effects of swimming speed. J Exp Biol 207:3265–3279

Tytell ED, Lauder GV (2004) The hydrodynamics and eel swimming 1: wake structure. J Exp Biol 207:1825–1841

Williamson CHK, Roshkol A (1998) The hydrodynamics and eel swimming ii: effects of swimming speedvortex formation in the wake of an oscillating cylinder. J Fluid Struct 2:355–381

Impulse generated during unsteady maneuvering of swimming fish

Brenden P. Epps · Alexandra H. Techet

Abstract The relationship between the maneuvering kinematics of a Giant Danio (*Danio aequipinnatus*) and the resulting vortical wake is investigated for a rapid, 'C'-start maneuver using fully time-resolved (500 Hz) particle image velocimetry (PIV). PIV illuminates the two distinct vortices formed during the turn. The fish body rotation is facilitated by the initial, or "maneuvering" vortex formation, and the final fish velocity is augmented by the strength of the second, "propulsive" vortex. Results confirm that the axisymmetric vortex ring model is reasonable to use in calculating the hydrodynamic impulse acting on the fish. The total linear momentum change of the fish from its initial swimming trajectory to its final swimming trajectory is balanced by the vector sum of the impulses of both vortex rings. The timing of vortex formation is uniquely synchronized with the fish motion, and the choreography of the maneuver is addressed in the context of the resulting hydrodynamic forces.

1 Introduction

When it comes to maneuvering performance, fish can swim circles around underwater vehicles. A conventional, propeller-driven underwater vehicle turns by sweeping a circular arc, about ten vehicle lengths in diameter, and this requires about fifteen times the amount of time it would take to cruise forward one vehicle length. In contrast, a fish, such as the Giant Danio (*Danio aequipinnatus*), can turn in a space that is approximately one third of its body length and requires only about half the time it takes to swim one body length. This performance is enhanced by the well-choreographed formation and control of large-scale wake vortices by the fish body and fins.

Maneuvers and fast-starts are defined classically as either 'C' or 'S' types. Typically, three stages of each maneuver are considered: in stage one (the preparatory stage) a straight swimming fish bends into a C or S shape; in stage two (the propulsive stage) the fish sweeps its tail in the reverse direction; and in the final, variable stage, the fish exits the turn either swimming straight ahead or coasting (Weihs 1973; Webb 1978). Classical hydrodynamic analyses by Lighthill (1971) and Weihs (1972) assert that as the body bends, unsteady (added mass) forces oppose this motion and apply a net angular moment on the fish, thus turning the body. When the fish whips its tail aft to straighten its body, it generates a propulsive force parallel to the direction of the anterior portion of the fish body.

In fast-starting maneuvers, the fish is essentially stationary at the onset of the turn and exits the maneuver with a non-zero velocity. This is in contrast to the case where a fish has an initial non-zero forward velocity and then turns to swim along another trajectory. When the fish has an initial forward velocity, turning can be initiated by simply reorienting the head or tail to achieve a lifting force which causes a moment on the body. Blake and Chan (2006) offer physical models to describe these two cases in the context of powered versus unpowered turns.

Researchers use qualitative and quantitative experimental techniques to better understand fish maneuvering performance (e.g., Weihs 1972; Harper and Blake 1990; Wolfgang et al. 1999). An excellent review of the kinematics and performance of fast-starting is presented by Domenici abd Blake (1997). Research on the maneuvering

B. P. Epps · A. H. Techet (✉)
Department of Mechanical Engineering,
Massachusetts Institute of Technology, Cambridge, MA, USA
e-mail: ahtechet@mit.edu

G.K. Taylor, M.S. Triantafyllou, and C. Tropea (Eds.): Animal Locomotion, pp. 53–62.
springerlink.com

of fish-like swimming mechanisms also extends to the robotic realm, from biomimetic studies with robotic fish (e.g., Triantafyllou et al. 2000; Bandyopadhyay 2002) to simple flapping foils and fins (e.g., Freymouth 1988; Albhorn et al. 1991, 1997; Tobias 2006).

Flow visualization helps researchers studying live fish better understand the overall vortical wake structure. McCutchen (1977) presents shadograph images of a maneuvering Zebra Danio (*Brachydanio rerio*) which show two wakes generated during burst-and-coast swimming maneuvers, and he suggests that these wakes may be modeled as vortex rings. Müller et al. (1999) and Wolfgang et al. (1999) use particle imaging velocimetry (PIV), both at 30 Hz or less, to quantitatively visualize the wake of maneuvering Zebra and Giant Danio, respectively. Müller et al. (1999) present a very thorough analysis of the maneuvering wake, as well. In addition to the PIV results, Wolfgang et al. (1999) presented a panel method numerical simulation of a maneuvering fish, showing good agreement with the experiments.

Dye visualization experiments by Tobias (2006) show that for a simple double flap motion of a NACA 0030 foil, with a 2:1 aspect ratio, a single vortex ring could be formed (see Fig. 1). Tip and trailing edge vortices are shed in a horseshoe shape that eventually pinches off into a single, discrete vortex ring. Similar looking vortex rings are reported in the wake of swimming fish by McCutchen (1977), in his shadowgraphs of maneuvering fish, and also by Drucker and Lauder (1999) through PIV experiments on steady swimming fish.

Modeling the wake of a maneuvering fish as a simple vortex ring makes the analysis straightforward; an algebraic expression predicts impulse of the ring. Thus, by inspecting the wake generated by a maneuvering fish, one can deduce the impulse imparted on the body during the maneuver.

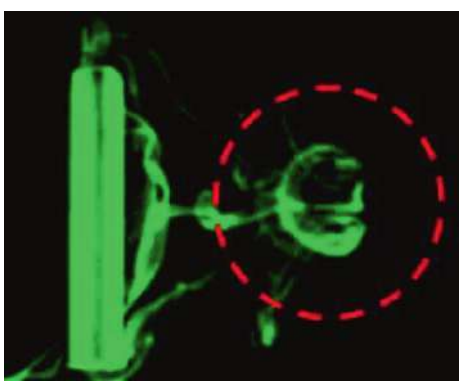

Fig. 1 Dye visualization of a foil that has flapped once to the right on the page and back to the position shown in a continuous motion, as viewed from behind the trailing edge. The foil is a NACA0030 with 2:1 aspect ratio. The overall flap took 3.2 s and had a maximum heave of approximately one chord length, maximum angle of attack of 20°, and 0° phase shift between heave and pitch. Courtesy, Tobias (2006)

Since the typical maneuver time of the Giant Danio is less than one half of one second, it is desirable to revisit the problem of the maneuvering fish with high-speed PIV capable of frame rates over 100 Hz. Thus fully time-resolved PIV is used here to illustrate the vortical evolution and circulation as a function of time over the duration of the maneuver. 'C' starts and turns are investigated to capture the instantaneous flow field with enhanced spacial and temporal resolution over prior published results. Using the simple vortex ring model, the circulation and impulse is calculated for each vortex generated by the fish. The overall body kinematics and momentum through the turn are compared with the vortex evolution and impulses to develop an enhanced understanding of fish maneuvering.

2 Materials and methods

The experimental study with maneuvering fish was performed using the Giant Danio (*Danio aequipinnatus*) in a small tank, in which the fish were allowed to swim freely. The four fish ranged in length from 5.0 to 7.5 cm and mass from 1.6 to 5.6 g. Results presented herein are for a larger adult fish that had a mass of 4.3 g and had an overall length, height, and beam of 7.4, 1.9 and 0.83 cm, respectively. The fish were constrained to swim in a 15.6 cm $\times$ 12.5 cm working area, with 8 cm deep water. The maneuvers considered were those in response to visual and auditory stimuli; a slender rod was introduced into the aquarium near the wall and tapped the floor of the tank, triggering an evasive maneuver.

The flow features were characterized using a high-speed implementation of PIV (Raffel et al. 2002). The tank was seeded with silver coated, neutrally buoyant, hollow glass spheres (average diameter 93 μm). The particles were illuminated using a low-powered, near-IR diode laser. The Lasiris Magnum diode laser produced a maximum output of 500 mW at 810 nm, and was fitted with optics to produce a 10° fan of light. The horizontal light sheet was imaged using an IDT XS-3 CCD camera with an 85 mm Nikkon lens which viewed up from the bottom of the tank (see Fig. 2). The high-speed camera imaged at 500 frames/s (fps), yielding a time-step between frames of 0.002 s. The image resolution was 1,260 $\times$ 1,024 pixels and the field of view was 15.33 cm $\times$ 12.46 cm, giving a 82.2 px/cm zoom. The laser sheet was positioned 3.5 cm from the bottom of the tank. Many runs were performed, but only those where the fish was positioned such that the light sheet was at its mid-plane (i.e., approximately along the lateral line of the fish) were processed. Since the fish were allowed to swim freely, it was a significant challenge to ensure that

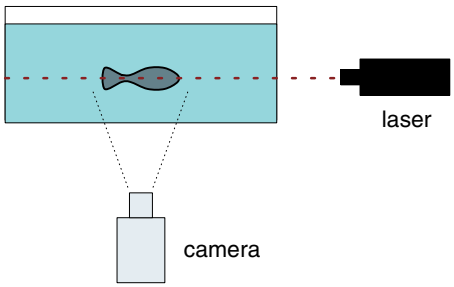

Fig. 2 Experimental PIV setup used for maneuvering studies. The high speed camera viewed up through the bottom of a glass aquarium, and the laser sheet was oriented horizontally at the midplane of the fish

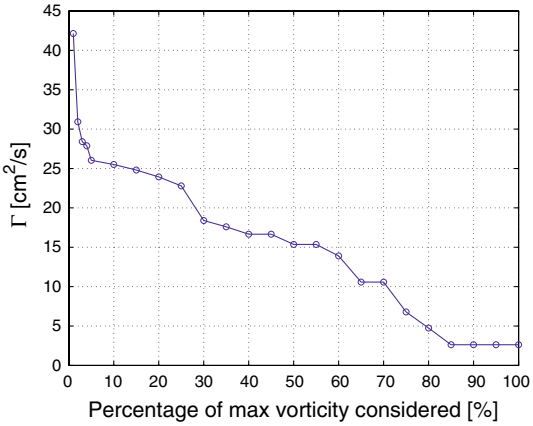

Fig. 3 Plot of circulation computed by Stokes theorem (Eq. 1) versus the threshold percentage of the maximum vorticity used to bound the vortex, for vortex 1A at time $t = 0.120$ s, as shown in Fig. 5. For reference, the values at 1, 5, and 25% are 53.1, 23.2, and 20.0 cm^2/s, respectively

the light sheet illuminated the mid-plane of the body. Luckily, however, the fish did not actively try to elude the near-IR light sheet as they typically do with green lasers.

The time-series of particle images were processed using the LaVision DaVis 7.1 software package. A multi-pass, cross-correlation processing algorithm, with a final interogation window size of 32 × 32 pixels and 50% overlap was used for processing all of the images. The output was a velocity field of 79 × 64 vectors, with approximately 38 vectors along the length of the fish body. The velocity field was postprocessed in Matlab to determine vorticity and circulation, as well as the body trajectory.

Circulation of each vortex was computed by evaluating Stokes theorem numerically

$$\Gamma = \sum_{i,j} \omega_{i,j} \delta A \tag{1}$$

where $\omega_{i,j}$ is the curl of the velocity field at point (i, j), and $\delta A = (16 \text{ px})^2 = 0.0379 \text{ cm}^2$ was the box size. The circulation computed depends on the area defined to be the vortex: the more area considered, the higher the total circulation. Gharib et al. (1998) overcome this by defining the vortex to reside within an isovorticity line of some fixed level. To calculate the circulation of the vortices in the fish wake presented herein, an isovorticity line equivalent to 25% of the maximum vorticity is chosen for each vortex. Given our field of view and PIV spatial resolution, this percentage yielded the most accurate and repeatable results.

Figure 3 is an example of the circulation calculated as a function of percentage of the maximum vorticity considered. These data were computed for the first vortex formed by the fish during its maneuver, 0.120 s after the start of the turn, corresponding to the fifth frame of Fig. 5. The plot shows that, as the vorticity threshold decreases towards 5% of the maximum vorticity in that vortex, the circulation steadily increases, but beyond the 5% level, the circulation blows up, due to summing low-level vorticity over a large area of the ambient fluid. For this example, the 25% vorticity threshold level yields a circulation of 22.8 cm^2/s, whereas using a threshold of 5% would yield 26.0 cm^2/s, or approximately 14% more circulation. Using a threshold of 1% yields 53.1 cm^2/s, a 129% difference from a baseline 5% threshold level, which introduces unacceptable error. Using a 25% vorticity threshold admittedly introduces a 10–15% uncertainty on circulation calculations, but it limits the region of interest to the vortices formed by the fish. For Fig. 5, only vorticity levels greater than 10 1/s have been shown, which is consistent with the 25% vorticity threshold used in all circulation calculations.

3 Results and discussion

This paper focuses on a representative C-start maneuver, in which the fish makes a 105° clockwise turn in 0.25 s. In this powered turn, the fish is barely moving at the onset, but increases its speed tenfold by the end of the maneuver. The kinematics, vortex circulation, and timing will be discussed.

An overview of this C-start is presented in Fig. 4. Here, mid-line body traces of the fish at 0.012 s intervals (every 6th frame) are shown. These mid-lines are determined manually by inspecting the fish body position in the PIV image sequence. Initially, the fish is moving towards the top of the frame with a velocity of 1.4 cm/s (0.18 L/s). The body proceeds to coil up into a C shape over the first 0.1 s of the maneuver. Then the tail rapidly reverses direction and sweeps aft (to the left and upwards in Fig. 4), before the fish extends straight along its new trajectory at time 0.25 s. The final velocity of the fish is 14.6 cm/s (1.98 L/s).

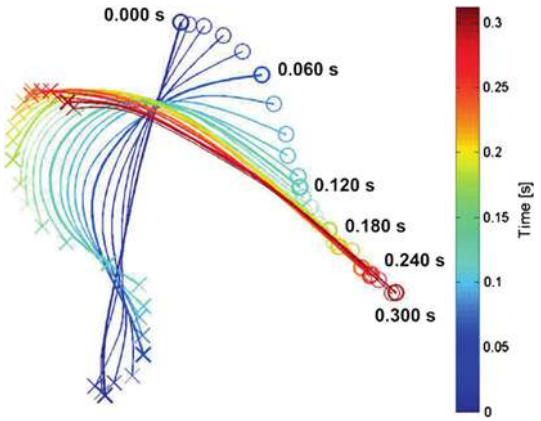

Fig. 4 Body midline tracings of a 105° single-bend C-start. The head is marked with an "o" and the tail with an "x". The *colorbar* is offered to help discern the beginning of the turn from the end; the *darkest blue* trajectory represents the initial body position, and the *darkest red line* shows the final body mid-line at the end of the turn

3.1 Vortical wake structure

An overview of the vortex formation throughout the maneuver is presented in Fig. 5. This figure shows twelve instantaneous vorticity fields, which were calculated from their respective velocity fields, as determined by the PIV algorithm. The images shown are 15 frames (0.030 s) apart. The vorticity contours are overlayed on digitized projections of the fish's body determined from the image sequence.

Figure 5 shows the formation of four distinct vortices during the maneuver, as well as a patch of vorticity which appeared to pinch off from the third vortex. In the axi-symmetric vortex ring model, it is assumed that the two pairs of opposite-signed vortices are each the cross-section of a toroidal-shaped vortex ring. To facilitate discussion of the two rings, these vortices are labeled vortex 1 and vortex 2. Further, the first side of each ring shed is labeled side A, and the second, side B. Without 3D imaging, it is unclear what roll the small patch of vorticity between the two rings plays in the overall wake structure. Thus, the following is a discussion of the generation of vortices 1A, 1B, 2A, and 2B only.

The sequence shown in figure 5 begins at the onset of the maneuver. Over the first 30 frames (0.060 s), a strong vortex pair develops at the tail, as the tail pushes against the fluid. The clockwise (blue) side, vortex 1A, is shed first, at time $t = 0.036$ s, followed by vortex 1B, which is shed at $t = 0.092$ s. This first vortex pair is configured in a jet-like arrangement; its impulse is a result of the net forcing by the fish on the water at that location. The inertia of the fluid resists the motion of the fish, and a vortex ring is generated. The reaction force, acting on the caudal peduncle and tail, far from the fish center of mass, applies a clockwise moment on the fish, which augments the anterior body rotation as the fish curls up into the C shape. Henceforth, vortex 1 is referred to as the "maneuvering" vortex.

As the fish body flexes into a 'C' shape, it draws its head and tail together, pushing and pulling the surrounding fluid and thus, imparting circulation into the flow around the body. Eventually, body-bound vorticity is shed into the wake in a second vortex pair; we refer to vortex two as the "propulsive" vortex. Vortex 2A is shed first at $t = 0.150$ s, and vortex 2B, the clockwise side, is shed subsequently at $t = 0.250$ s, between the ninth and tenth PIV frames shown in Fig. 5. This counter-rotating vortex pair also resembles a jet, indicating again a net force by the fish on the fluid at that location. The reaction thrust is in the direction of the fish's final trajectory, which serves to stop the body rotation and to propel the fish forward.

Since the fish body is reflective and textured, the PIV software can track the body using its cross-correlation algorithm, just as it can track other particles in the fluid. By the body boundary conditions, the velocity field should be continuous and smooth along the body. Given a smooth and continuous velocity field, its curl can be computed; this is equivalent to the vorticity of a fluid particle or equivalent to twice the rotation rate of a discrete portion of the fish body. For the image sequence used herein, considering all the frames, a continuous velocity field is evident except in the shadow regions. Calculations of vorticity for the time series show that body rotation is "shed" into the fluid during the maneuver in a continuous fashion.

It is useful to note that the laser illuminates the fluid from the left in the PIV images, such that data in the shadow to the right of the fish must be considered with care. Most notably, vortex 2B (labeled in Fig. 5) appears out of the shadow region, just prior to time $t = 0.180$ s, as the fish body moves out of the way from obstructing the laser sheet. Despite being unable to image the formation of vortex 2B, the entire vortex is in full view by the time it is shed, so the calculation of its impulse is still possible.

3.2 Maneuver kinematics

The kinematics of the fish motion are now compared with the timing of vortex shedding. From the fish position data presented in Fig. 4, the velocity of the head, caudal peduncle, and tail tip are calculated for each time step in both the local body-tangent ($V_{\parallel}$) and body-normal ($V_{\perp}$) directions. For each body location, the tangential direction is defined positive towards the head, and the normal direction is defined positive towards the center of the C-shape.

Figure 6 shows several kinematic parameters plotted over the duration of the maneuver; the time at which each

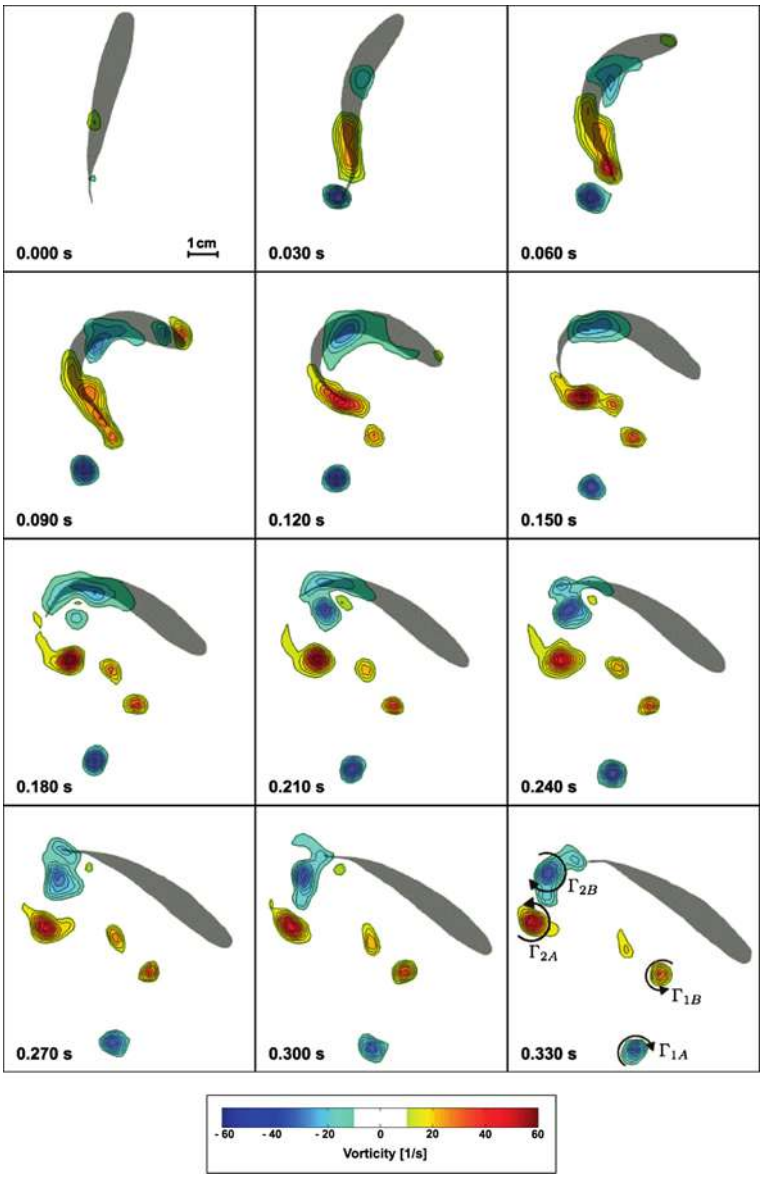

Fig. 5 Sequence of instantaneous vorticity fields determined using PIV for a 105° C-start. Every 15th frame is presented ($\triangle t = 0.030\,\mathrm{s}$). Anticlockwise (positive) vorticity is shown in *red* and clockwise (negative) in *blue*. Ambient vorticity of less than 10 L/s has been removed for clarity. The four vortices shed during the maneuver are labeled Γ_{1A}, Γ_{1B}, Γ_{2A}, and Γ_{2B}

vortex is shed from the tail is indicated by the dashed vertical lines. The angular velocity (θ') and acceleration (θ'') of the anterior body, taken from the head to one third of the body length, are shown in Fig. 6a and b. The body-tangent ($V_{\parallel}$) and body-normal ($V_{\perp}$) velocities of the head, caudal peduncle, and tail are shown in Fig. 6c–f.

The timing of both anterior body rotation and of vortex shedding closely follows the body-normal motion of the caudal peduncle. This makes sense, because added mass forcing on the peduncle, far from the center of mass, applies a moment on the flexed fish body. This moment, carried through the body by the fish musculature, acts to turn the anterior portion of the fish. Wolfgang et al. (1999) show that vorticity is shed at the caudal peduncle and manipulated by the tail fin. Thus, it is reasonable that the shedding of vortices would follow the motion of the caudal peduncle perpendicular to itself.

Figure 6 shows that for stage one of the maneuver, the rotation of the anterior body follows the body-normal velocity of the caudal peduncle. The angular velocity (θ') of the anterior body increases monotonically in the clockwise (negative) sense while the body-normal velocity ($V_{\perp}$) of the caudal peduncle is positive (i.e., as the fish coils up into the C-shape). Angular velocity reaches its maximum at time 0.060 s, as the caudal peduncle reverses direction. At this time, the angular acceleration changes from negative to positive and the body-normal velocity of the caudal peduncle is zero.

The timing does not synchronize as well for stage two of the maneuver. This is because the fish does not recoil from

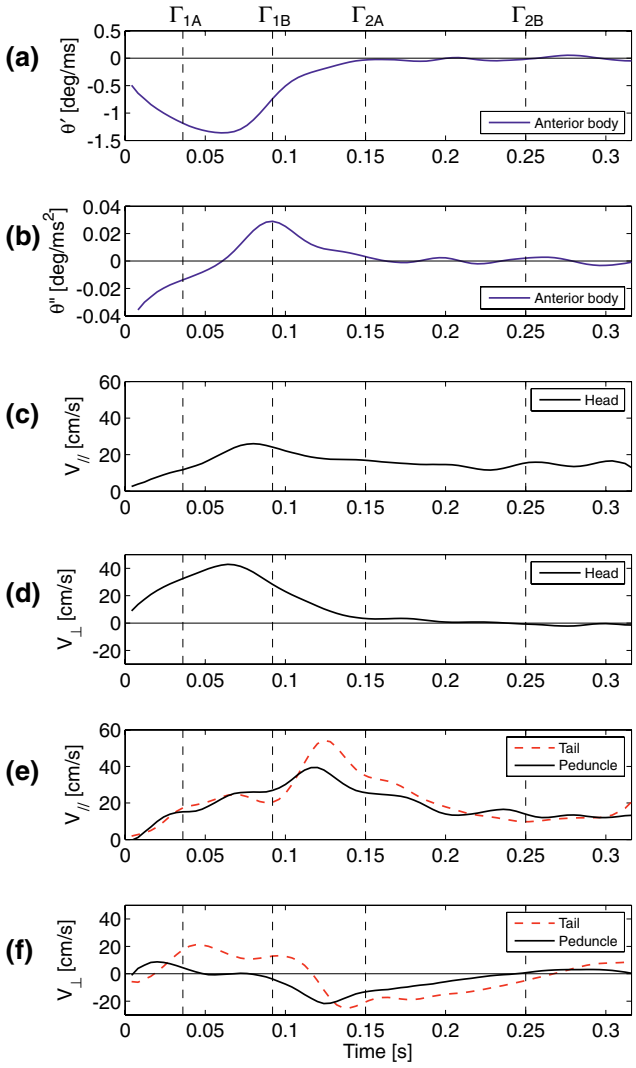

Fig. 6 Kinematic analysis of the maneuver: **a** Anterior body (head to 1/3 of length) angular velocity, θ' (positive anticlockwise), **b** anterior body angular acceleration, θ'', **c** Body-tangential head velocity, $V_{\parallel}$, **d** body-normal head velocity, $V_{\perp}$, **e** body-tangential tail and caudal peduncle velocities, $V_{\parallel}$, and **f** body-normal tail and caudal peduncle velocities, $V_{\perp}$. all body-tangential $(V_{\parallel})$ and body-normal $(V_{\perp})$ velocities are in local coordinate systems for each body part. Body-tangentail is instantaneously tangent to the midline at the body part, positive towards the head. Body-normal is positive towards the inside of the C-shape. *Dashed lines* show times when vortices are shed

the C-shape in the same manner as it forms it. Instead, the posterior of the fish unrolls, as the anterior portion rotates and progresses forwards (see Fig. 4). Thus, the negative body-normal peduncle and tail velocities serve to both stop the anterior body rotation as well as provide forward thrust.

A similar correlation between the body-normal motion of the caudal peduncle and the timing of vortex shedding is seen. Vortex 1A is shed at 0.036 s, just prior to the time when the body-normal velocity of the caudal peduncle reaches zero. For a short time, the body-normal velocity at the caudal peduncle remains zero; the motion of the peduncle is tangential only as it traverses the face of what will be the maneuvering vortex. Vortex 1B is shed at 0.092 s, as the caudal peduncle body-normal velocity becomes negative. A patch of secondary vorticity forms as the fish sweeps its tail through the middle portion of the turn. Between times 0.10 and 0.15 s, the motions of the tail and peduncle are predominantly tangential as they follow their paths from the points of release of vortex 1B to 2A. The timing of vortex shedding in stage two does not quite synchronize with the motion of the caudal peduncle. Vortex 2A is shed at 0.150 s, while the peduncle is still unrolling and has negative body-normal velocity. However, vortex 2B is shed when the body-normal velocity of the caudal peduncle again reaches zero at time 0.250 s. At this point the fish has finished forming the second vortex pair, which results in the final forward motion of the fish along its new trajectory.

3.3 Circulation

The circulation of the vortices over time is presented here in the context of the maneuvering choeography. The circulation of each vortex is evaluated using Stokes theorem with a 25% vorticity threshold, as discussed in Sect. 2. Figure 7 shows the evolution of circulation in each of the four vortices over time as well as the rotation of the fish body. When determining the circulation and body rotation, a digitized projection of the fish is overlaid on the vorticity field, such that vorticity can be identified as body-bound or free. Only vorticity that is free from the body is considered in the circulation of the vortices. Body "vorticity" is integrated and reported as "body rotation".

In maneuvers when the fish has little to no initial forward velocity, such as this one, the predominant forcing on the fluid can evidenced in topological flow changes. For the maneuvering fish discussed herein, the rotation of the posterior body and subsequent tail motions act to create vortices 1B and 2A. After vortex 2A is shed at time 0.150 s, the anticlockwise body rotation goes to zero. The sum of the circulations of vortices 1B and 2A at time $t = 0.150$ seconds is $13.2 + 47.9 = 61.1$ cm^2/s.

As the fish coils up into the C-shape, three distinct regions of circulation appear: clockwise vortex 1A, posterior body anticlockwise rotation, and anterior body clockwise rotation. Despite the three dimensionality of our flow, at $t = 0.056$ s, the total circulation is almost zero: $\Gamma_{\text{tot}} = -23.7 + 60.2 - 33.9 = 2.6$ cm^2/s. The total circulation is computed at each time step. The average and standard deviation of the total instantaneous circulation were 9.4 and 6.2 cm^2/s, respectively. Vorticity that may have formed at the fish's nose, could not be imaged due to laser setup.

The circulation data in Fig. 7 supports the use of a vortex ring model for maneuvering fish. Vortex rings have the same circulation at any azimuthal position, so a counter-rotating pair made by taking a cross-section should have equal and opposite circulation. Indeed, the two vortex pairs (1A and 1B) and (2A and 2B) exhibit excellent symmetry in both size and circulation over the duration of the turn. The two traces of circulation over time in Fig. 7 match quite well and reinforce the assertion by researchers such as McCutchen (1977) and Drucker and Lauder (1999) that the vortex ring model is quite applicable in fish maneuvering. At the conclusion of the maneuver (t = 0.250 s), the circulation of vortices 1A and 1B are Γ = −18.8 and 12.2 cm^2/s, and the circulation of vortices 2A and 2B are Γ = 33.8 and −34.6 cm^2/s, respectively.

The uncertainty in these circulation computations is on the order of 15% and comes from three main sources of error: vorticity thresholding, sampling error, and PIV error. The predominant source of error is in the thresholding used to define the vortex. Since the vortex ring model assumes that all circulation is concentrated at or near the core of the vortex ring, counting vorticity far from the core is not appropriate. Thus, choosing the level at which to threshold is a balancing act between including all of the points that constitute the vortex, but not including points far from the centroid. For the example discussed in Sect. 2, a 14% error resulted from thresholding at the 25% level as opposed to the 5% level, but a 129% was prevented error by not summing large areas of low-level vorticity unrelated to the maneuver.

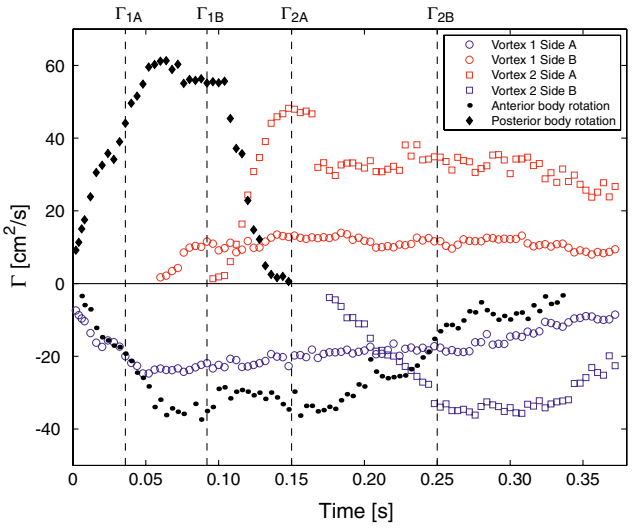

Fig. 7 Circulation as a function of time for each vortex formed during the maneuver, computed using Eq. 1 with a 25% threshold. Counterclockwise (positive) circulation is represented by the red markers for both vortex 1 and 2; clockwise (negative) circulation is indicated in blue. The *closed*, *black circles* and *diamonds*, *filled diamond* represent the body rotation generated by the anterior and posterior fish body, respectively. *Dashed lines* show times when vortices are shed

The second source of error comes from the limited sample size available for circulation calculations. The circulation is computed in Matlab by identifying the vortex core, and then running an algorithm which searches for all neighboring points which meet the threshold requirement. To assess repeatability, the authors performed this computation multiple times on any given frame and were always able to repeat their results to within 5% variation. Finally, error in the PIV velocity field, which propagates through circulation computations, is also a factor in the overall error. As an example, consider the circulation of vortex 2A, plotted over time in Fig. 7 (red squares). From time 0.25 to 0.30 s, Γ_{2A} should be approximately constant, but it has a mean value of 33.3 cm^2/ s and standard deviation of 1.8 cm^2/s. Error in circulation due to PIV error is on the order of 5%.

3.4 Comparison of fluid impulse with fish impulse

In order to better understand how the fluid impulse balances the fish's overall change in momentum, classical vortex ring theory is used. The impulse of a vortex ring moving steadily ahead is

$$\underline{I}_0 = \rho\Gamma\frac{\pi D^2}{4}\underline{e}_z \tag{2}$$

where Γ is the circulation, D is the diameter from core to core, and $\underline{e}_z$ is the axial direction normal to the plane of the vortex. If the ring is instead a toroid, then the additional impulse associated with the thickness of the vortex core is

$$I_1 = \rho\Gamma\frac{\pi D^2}{4}\left[\frac{3}{4}\frac{d^2}{D^2}\right] \tag{3}$$

where d is the diameter of the vortex core (Saffman 1995).

Figure 7 shows that the circulation of the vortices decreases after they are released from the body. Consequently, the circulation must be evaluated immediately after each vortex is shed from the fish. In other words, the circulation of vortex 1 must be computed immediately after it is shed, which is always several time-steps before vortex 2 is shed. To compute the circulation of vortex 1 listed in Table 1, the circulation is averaged over the four time-steps following the shedding of vortices 1A and 1B. This procedure is also repeated for vortex 2. Thus, the values listed in Table 1 average out any small variations in time (or measurement) or differences between the two sides of the vortex ring.

The added impulse (added mass times velocity) of a vortex ring is given by (Dabiri 2005):

Table 1 Table of vortex quantities for the maneuvering and propulsive vortex rings: circulation, Γ vortex ring diameter, D vortex core diameter, d vortex ring axial diameter, S vortex ring propagation speed, U_v impulse of a concentrated vortex ring, I_0 impulse associated with a finite core diameter, I_1 added mass impulse, I_a total impulse, I_v angle the impulse makes with the positive x-axis (to the right on the page, in a lab-fixed cartesian reference frame), β maximum wake velocity, V and time to form the vortex, t

	"maneuvering" vortex	"propulsive" vortex
Γ (Eq. 1)	17	34 cm^2/s
D	1.40	1.84 cm
d	0.84	1.03 cm
S	1.26	1.66 cm
U_v	13.5	14.2 cm/s
I_0 (Eq. 2)	25	91 gcm/s
I_1 (Eq. 3)	7	21 gcm/s
I_a (Eq. 4)	19	45 gcm/s
I_v (Eq. 5)	51	157 gcm/s
β	−27	167°
V	16.7	20.0 cm/s
t	0.092	0.250 s

$$I_a = \rho c_{11} \frac{\pi D^2}{4} S U_v \tag{4}$$

where c_{11} is the added mass coefficient, S is the diameter of the vortex ring in the direction of propagation, and U_v is the velocity of propagation of the ring. Dabiri (2005) reports $c_{11} = 0.72$ for a mechanically generated vortex ring. The total impulse of a vortex ring then becomes

$$\underline{I}_v = (I_0 + I_1 + I_a)\underline{e}_z \tag{5}$$

The results of the wake analyses are presented in Table 1. Determining the longitudinal vortex diameter (S) via the procedure outlined in Dabiri (2005) proves quite challenging, due to the three-dimensionality of the fish wake. The vortex ring axial diameter is $S \approx 0.9D$ for both vortices over a range of frames. All magnitudes of the impulse (I_0, I_1, and I_a) are tabulated, and they all act along the same line. The angle this impulse vector makes with the positive x axis (to the right on the page in a lab-fixed cartesian reference frame) is given by β.

The vector sum of the impulse of the two vortex rings should balance the net change in linear momentum of the fish

$$\underline{I}_f = (m + m_{11})\triangle \underline{V} \tag{6}$$

where $m = 4.3$ g and m_{11} are the fish mass and added mass, and $\triangle \underline{V}$ is the change in swimming velocity of the fish. The fish initial and final swimming velocities are computed manually by locating a morphological feature of the fish in images five frames apart and computing $\triangle V_x = 10.3$ cm/s and $\triangle V_y = -10.9$ cm/s.

Since only the initial and final stages of the turn are considered, where there is no longer any body rotation, the added mass is calculated for a fish moving straight ahead without undulation. A lower bound for m_{11} can be made by assuming the fish is a rigid slender body of revolution, for which the ratio of the added mass to the mass of a neutrally buoyant body is $\frac{m_{11}}{m_f} = \left(\frac{r}{l}\right)^2 \ln\left(\frac{r}{l}\right)$, where r is the maximum body radius, and l is the body length (Newman 1977). Taking r to be the half-breadth of the fish, the added mass is 0.9% of the fish mass. An upper bound for m_{11} is 20% of the fish mass, which was the value found by Webb (1982) for fast-starts of trout. Webb (1982) also reports that other researchers have found values for m_{11} in-between 1 and 20%.

To balance the overall change in momentum of the fish, one must account for *both* the propulsive and maneuvering vortices. The impulse of the individual vortices is listed in Table 1, and the net impulse on the fluid and on the fish is reported in Table 2. For perfect agreement, the magnitudes of the impulses should be equal, and the angle β should equal 180° minus α. For this trial, the magnitude of the change in momentum of the fish was between 65 and 78 gcm/s. If the "maneuvering" vortex is ignored in the momentum balance, then the resulting fluid impulse would be greater than 91 gcm/s (I_0, listed in Table 1), which is an overestimation of the magnitude. Further, if the maneuvering vortex was not generated during stage 1, the fish would be unable to effectively generate body rotation, since the moment on the fish would be negligible.

There is not perfect alignment in the direction of fluid and fish impulses (see Table 2). Since the line of action of the fish impulse was −47°, the fluid impulse should act at 133° from the horizontal. However for this trial, the fluid impulse acts approximately 172° from the horizontal. This discrepancy is most likely due to the curvature of the fish body over the duration of the turn. When the fish has non-zero forward swimming speed, curvature allows the body to act as a lifting surface (i.e., a rudder) to steer the fish through the water. A steady-moving, cambered hydrofoil experiences a moment about its quarter-chord, even though it does not shed trailing edge vorticity. Similarly, the fish will change its swimming direction without any measurable effect on the circulation imparted to the wake.

4 Conclusion

This paper presents fully time-resolved PIV data, with high spatial resolution, for a maneuvering fish. The Giant Danio used in these experiments performs a 105° 'C'-maneuver during which it generates two distinct vortex rings, indicated by counter-rotating pairs of vortices. The data presented for the circulation of each shed vortex, over time,

Table 2 Impulse comparison: fuid impulse assuming concentrated vortexrings, I_0; fluid impulse assuming finite core diameter rings, $I_0 + I_1$; fluid impulse using the total impulse, I_v; angle thefluid impulse makes with the positive x-axis (to the right on the page,in a lab-fixed cartesian reference frame), β; fish impulse usingthe lower bound for added mass, $I_{f,l}$; fish impulse using theupper bound for added mass, $I_{f,u}$; angle the fish impulse makeswith the positive x-axis, α

Fluid impulse	
I_0	66 gcm/s
β	172°
$I_0 + I_1$	81 gcm/s
β	172°
I_v	108 gcm/s
β	174°
Fish impulse	
$I_{f,l}$	65 gcm/s
$I_{f,u}$	78 gcm/s
α	−47°
$180 - \alpha$	133°

All fluid impulse values are themagnitude of the vector sum of the impulses of the two ring vortices

shows good symmetry in the vortex pairs, confirming our assertion that each vortex pair can be treated as a ring, similar to that formed by the foil in Fig. 1. This is clearly a three-dimensional problem, warranting further investigation using three-dimensional flow measurement techniques such as stereo PIV (e.g., Sakakibara et al. 2004). However, the trade-offs between resolving three-dimensional effects and the rapid time scales of the maneuver make a case for both high speed and 3D flow measurement techniques.

Fish are clearly adapted as graceful swimmers with an excellent capacity for rapid-maneuvering. Through the combination of PIV visualizations (Fig. 5) and kinematic data (Fig. 6), it is shown that the formation and shedding of the vortices corresponds well with the motions of the caudal peduncle. This is in agreement with Wolfgang et al. (1999) who showed that for a swimming Giant Danio, vorticity is shed at the caudal peduncle and is manipulated by the tail fin.

Several researchers have sought to determine a robust starting point for stage two of a maneuver. As detailed in Domenici and Blake (1997), this transition from stage one to stage two has been thought of in several different ways: (a) the change in direction of the tail motion (i.e., $V_\perp$ of the peduncle becoming negative) (Webb 1978), (b) the change in turning direction of the anterior body midline (from clockwise to anticlockwise in our case) (Domenici and Blake 1997), (c) the onset of forward propulsion (Foreman and Eaton 1993), and (d) the onset of contralateral electomyographic signal (Jayne and Lauder 1993). Domenici and Blake (1997) also note that these four definitions are not necessarily synonymous. In our data, for example, the change in direction of the caudal peduncle motion (a) occurs at time $t \approx 0.08$ s, whereas the change in turning direction of the anterior body midline (b) does not happen until $t = 0.150$ s, and the head body-parallel velocity is non-zero (c) at the start of the maneuver.

An alternate, or perhaps even synonymous, definition to those above may arise if the timing of vorticity generation in the fish wake is considered. When the first vortex has been fully shed (i.e., vortex 1B is released from the tail), the fish is no longer putting energy into the turning phase of the maneuver (stage one), nor into the maneuvering vortex. For the case presented here, vortex 1B is shed at time $t = 0.092$ s, just moments after the change in direction of the caudal peduncle lateral motion, which occurs at $t = 0.078$ s. At this time the peduncle region is moving in a predominately tangential direction, and the tail is just beginning to change directions. The timing of vortex shedding used to determine the transition from stage 1 to stage 2 correlates well with the definition of transition suggested by Webb (1978). The current assessment of the vortex wake does not necessarily agree with criteria (b) by Domenici and Blake (1991) or (c) by Foreman and Eaton (1993), and without EMG data, and cannot compare with (d) by (Jayne and Lauder 1993).

Taking into account solely the linear momentum of the fish into and out of the turn, it has been shown that the net impulse of the *two* vortex rings is close to the total change in momentum of the fish. In this particular maneuver, the initial velocity is quite low, and thus the fish body is not able to use its initial forward momentum to significantly aid in the turn. Were the fish moving at a sufficiently high initial velocity, such that slight changes in body orientation away from the forward motion could generate a lifting force on either the anterior or posterior sections of the body and thus a turning moment, the need for this "maneuvering" vortex might be lessened. The transitions between maneuvering stages become important when only considering one of the vortices or certain segments of the turn. Here, the question arises as to which parts of the turn should be considered when determining scaling laws: should the entire turn be considered (using both the maneuvering and propulsive vortex), or only the formation of the final vortex ring?

Triantafyllou et al. (2005) suggests that a scaling law can be determined using the time to develop a full vortex ring as the principal parameter controlling rapid maneuvering and fast-starting, in a similar fashion to the Strouhal law for steadily flapping foils and the formation number in impulsive started jets by Gharib et al. (1998). In order to determine scaling laws for maneuvering fish, considering the maneuver from stage one through stage three taking into account only the linear momentum of the fish's body at

the beginning and end of the turn, there will be cases where both the first "maneuvering" vortex jet as well as the second "propulsive" vortex jet may need to be considered in order to balance the total change in momentum of the fish. There may also be cases where the first vortex is negligible or non-existent due to the initial conditions of the turn.

Acknowledgments Support from the MIT SeaGrant program is gratefully acknowledged, as is Tadd Truscott for his assistance with the PIV setup and handling of the live fish.

References

Albhorn B, Harper DG, Blake RW, Ahlborn D, Cam M (1991) Fish without footprints. J Theor Biol 148:521–533

Albhorn B, Chapman S, Stafford R, Blake RW, Harper DG (1997) Experimental simulation of the thrust pahses of fast-start swimming fish. J Exp Biol 200:2301–2312

Bandyopadhyay P (2002) Maneuvering hydrodynamics of fish and small underwater vehicles. Integ Comp Biol 42:102–117

Blake RW, Chan KHS (2006) Models of the turning and fast-starting swimming dynamics of aquatic vertebrates. J Fish Biol 69:1824–1836

Dabiri JO (2005) On the estimation of swimming and flying forces from wake measurements. J Exp Biol 208:3519–3532

Domenici P, Blake RW (1991) The kinematics and performance of the escape response in the angelfish (*Pterophyllum eimekei*). J Exp Biol 156:187–205

Domenici P, Blake RW (1997) The kinematics and performance of fish fast-start swimming. J Exp Biol 200:1165

Drucker EG, Lauder GV (1999) Locomotor forces on a swimming fish: three-dimensional vortex wake dynamics quantified using digital particle image velocimetry. J Exp Biol 202:2393–2412

Foreman MB, Eaton RC (1993) The direction change concept for reticulospinal control of goldfish escape. J Neurosci 13:4101–4133

Freymouth P (1988) Propulsive vortical signature of plunging and pitching airfoils. AIAA J 26:881–883

Gharib M, Rambod E, Shariff K (1998) A universal time scale for vortex ring formation. J Fluid Mech 360:121–140

Harper DG, Blake RW (1990) Fast-starts of rainbow trout *Salmo gairdneri* and northern pike *Esox lucius* during escapes. J Exp Biol 148:128–155

Jayne BC, Lauder GV (1993) Red and white muscle activity and kinematics of the escape response of bluegill sunfish during swimming. J Comp Physiol A 173:495–508

Lighthill M (1971) Large-amplitude elongated-body theory of fish locomotion. Proc Roy Soc Lond B 179(1055):125–138

McCutchen CW (1977) Froude propulsive efficiency of a small fish, measured by wake visualization. In: Pedley T (ed) Scale effects in animal locomotion, Chap 22. Academic, London, pp 339–363

Müller UK, Stamhuis EJ, Videler JJ (1999) Hydrodynamics of unsteady fish swimming and the effects of body size: Comparing the flow fields of fish larve and adults. J Exp Biol 203:193–206

Newman J (1977) Marine hydrodynamics. MIT, Cambridge

Raffel M, Willert C, Kompenhans J (2002) Particle image velocimetry: a practical guide. Springer, New York

Saffman P (1995) Vortex dynamics. Cambridge University Press, Cambridge

Sakakibara J, Nakagawa M, Yoshida M (2004) Stereo-piv study of flow around a maneuvering fish. Exp Fluids 36:282–293

Tobias D (2006) Kinematics and vortical wake patterns of rapidly maneuvering fish and flapping foils. Batchelor's Thesis. MIT, Cambridge

Triantafyllou MS, Triantafyllou GS, Yue DKP (2000) Hydrodynamics of fish-like swimming. Ann Rev Fluid Mech 32:33–53

Triantafyllou MS, Hover FS, Techet AH, Yue DKP (2005) Review of hydrodynamic scaling laws in aquatic locomotion and fishlike swimming. Appl Mech Rev 58(4):226–237

Webb P (1978) Fast-start performance and body form in seven species of teleost fish. J Exp Biol 74:211–226

Webb PW (1982) Fast-start resitance of trout. J Exp Biol 96:93–106

Weihs D (1972) A hydrdynamical analysis of fish turning manoeuvres. Proc Roy Soc Lond B 182(1066):59–72

Weihs D (1973) The mechanism of rapid starting of slender fish. Biorheology 10:343–350

Wolfgang M, Anderson J, Grosenbaugh M, Yue D, Triantafyllou M (1999) Near-body flow dynamics in swimming fish. J Exp Biol 202:2303–2327

Do trout swim better than eels? Challenges for estimating performance based on the wake of self-propelled bodies

Eric D. Tytell

Abstract Engineers and biologists have long desired to compare propulsive performance for fishes and underwater vehicles of different sizes, shapes, and modes of propulsion. Ideally, such a comparison would be made on the basis of either propulsive efficiency, total power output or both. However, estimating the efficiency and power output of self-propelled bodies, and particularly fishes, is methodologically challenging because it requires an estimate of thrust. For such systems traveling at a constant velocity, thrust and drag are equal, and can rarely be separated on the basis of flow measured in the wake. This problem is demonstrated using flow fields from swimming American eels, *Anguilla rostrata*, measured using particle image velocimetry (PIV) and high-speed video. Eels balance thrust and drag quite evenly, resulting in virtually no wake momentum in the swimming (axial) direction. On average, their wakes resemble those of self-propelled jet propulsors, which have been studied extensively. Theoretical studies of such wakes may provide methods for the estimation of thrust separately from drag. These flow fields are compared with those measured in the wakes of rainbow trout, *Oncorhynchus mykiss*, and bluegill sunfish, *Lepomis macrochirus*. In contrast to eels, these fishes produce wakes with axial momentum. Although the net momentum flux must be zero on average, it is neither spatially nor temporally homogeneous; the heterogeneity may provide an alternative route for estimating thrust. This review shows examples of wakes and velocity profiles from the three fishes, indicating challenges in estimating efficiency and power output and suggesting several routes for further experiments. Because these estimates will be complicated, a much simpler method for comparing performance is outlined, using as a point of comparison the power lost producing the wake. This wake power, a component of the efficiency and total power, can be estimated in a straightforward way from the flow fields. Although it does not provide complete information about the performance, it can be used to place constraints on the relative efficiency and cost of transport for the fishes.

E. D. Tytell (✉)
Department of Biology, University of Maryland,
College Park, MD 20742, USA
e-mail: tytell@umd.edu

1 Introduction

Fishes are often assumed to be highly efficient swimmers. After all, many species routinely swim or migrate over very long distances, including fishes of such diverse shapes and sizes as eels, tunas, many sharks, and river fishes like trout (Helfman et al. 1997). Natural selection has had hundreds of millions of years (Helfman et al. 1997) to tune the design of these fishes. One would naturally imagine that efficient swimming would be an important design criterion, particularly for these migratory or long-distance swimmers. Therefore, biologists and engineers have been eager to examine the efficiency of undulatory swimming, with a goal of determining the best fish body shapes and swimming modes, and to extract design principles for the construction of highly efficient underwater autonomous vehicles.

This goal, however, is based on a fallacy. Natural selection has *not* produced optimal swimming performance. Selection merely results in performance that is good enough that an animal can avoid dying or being eaten long enough to reproduce (Garland 1998). "Good enough,"

G.K. Taylor, M.S. Triantafyllou, and C. Tropea (Eds.): Animal Locomotion, pp. 63–74.
springerlink.com

also, is determined within a multitude of conflicting demands. Evolutionary history, feeding, migration, and sexual displays, among many other factors, all simultaneously influence an organism's fitness. Not only this, but the conditions under which selection happens are constantly changing, as predators and prey evolve together and the environment changes. Even though any one fish species is not optimal (or even necessarily very good), the differences among species may provide useful hints for the design of underwater vehicles.

However, it would be wise not to assume that fish swimming is highly efficient—it might not be, particularly in comparison to propeller-based propulsion at steady speeds. For a migrating fish, an independent and possibly more important criterion than efficiency is energy consumption. The hydrodynamic energy consumption rate P_{total} is composed of two components,

$$P_{\text{total}} = UT + P_{\text{waste}}, \tag{1}$$

where UT is the useful power, the product of swimming velocity U and the thrust force T, and P_{waste} is the wasted power. For the purposes of this review, P_{waste} is assumed to be only the power used to produce a wake (P_{wake}); metabolic power wasted converting chemical energy into mechanical energy is ignored. Propulsive efficiency, in turn, is conventionally defined as

$$\eta = UT/P_{\text{total}}. \tag{2}$$

Based on these definitions, P_{total} could be large, even if η is close to one. For example, a fish with high drag might put 99% of its locomotory energy to forward propulsion, but end up using more total energy than a very streamlined fish that wastes 50% of its output.

Together, however, propulsive efficiency and total energy output provide a useful way of comparing the swimming performance of different fishes and underwater vehicles. While natural selection cannot be said to produce optima, different species of fishes presumably differ in propulsive efficiency or total power consumption. In particular, one would expect migratory fishes, like trout, and eels, to be better swimmers than fishes that generally stay put, like bluegill sunfish—although the criteria that determine "better" are unknown. As an evolutionary question, it would be interesting to examine those criteria. How does hydrodynamic performance factor into the shape changes over the evolutionary history of fishes? For example, trout and eels, two very differently shaped fishes, both swim long distances—is one body shape more efficient or more power-conserving than the other? Or are other factors, unrelated to swimming, more important in determining body shape? As an engineering question, it would also be useful to compare swimming performance among different types of self-propelled systems. If one wanted to design a submarine, would it be better be shaped like a trout, an eel, or a conventional propeller-based underwater vehicle?

The recent availability of high-resolution, high-speed particle image velocimetry (PIV; Willert and Gharib 1991) systems has made it possible and relatively straightforward to measure the fluid flow in a two-dimensional plane around swimming fishes (e.g., Anderson et al. 2001; Müller et al. 1997; Nauen and Lauder 2002a; Tytell and Lauder 2004). This measurement technique has raised the possibility of estimating the thrust or drag on a swimming fish from the flow in its wake. To date, however, such estimates have been problematic (Schultz and Webb 2002).

In this review, the differences among wakes of several swimming fishes are first demonstrated, using examples from swimming eels (Tytell 2004a; Tytell and Lauder 2004), along with rainbow trout and bluegill sunfish (E. D. Tytell, unpublished data). These differences are examined by looking at the net momentum flux in each wake. Because thrust is problematic to estimate in general, the wake power is instead studied. Although it is only one component of the total power, this review demonstrates how it can be used to bracket the possible performance envelopes of different fishes for future comparative studies.

1.1 Swimming modes

The fishes examined in this review span much of the range of the standard classification of swimming modes (Breder 1926). Eels are termed anguilliform swimmers, and are understood to undulate with about one complete wave on their bodies, with a substantial undulation amplitude even close to the head. Bluegill sunfish, in contrast, are termed carangiform swimmers, and bend through about half of a wave, which only reaches a substantial amplitude in the posterior third of their bodies. Trout are called subcarangiform, which is intermediate between the eel and the bluegill.

Additionally, the fish span a range of body shapes. Eels are elongate, with a fairly constant oval cross-section and no physical demarcation between the "tail" and "body." Bluegill, in contrast, have a highly flattened body with a fairly separate tail (caudal fin), joined by a narrow region termed the caudal peduncle. Trout, again, are intermediate, with a fusiform body and separate tail, but less narrowing at the caudal peduncle than bluegill.

Figure 1 shows examples of the kinematics and body shape for each fish. Although the eel moves its anterior body more than the other fishes, all fishes have some head motion. In fact, the modes are more similar than they are different (Lauder and Tytell 2006). Specifically, both the

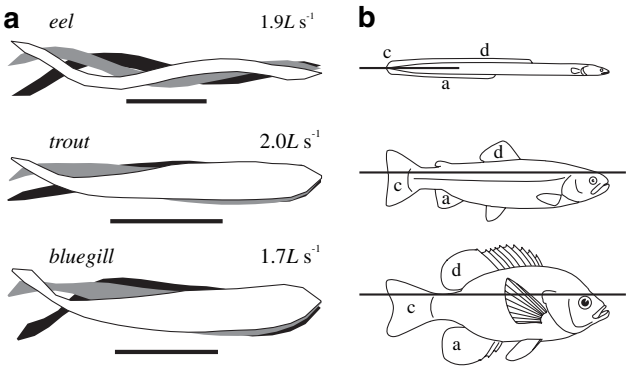

Fig. 1 Kinematics and body shapes for each of the example fishes. **a** Silhouettes of the fishes swimming at approximately the same length (*L*) specific speeds [eel data from Tytell (2004a); trout and bluegill from E. D. Tytell, unpublished data]. Tracings are shown for three instants, separated by the same amount of time, between maximum lateral tail tip excursion on either side. *Scale bars* are all 5 cm. **b** Line drawings of the fishes, showing the differences in body shape. Approximate positions and extents of the PIV measurement planes are shown with a *thick line*. For reference, the median fins are identified by *letter* (*c* caudal fin, *d* dorsal fin, *a* anal fin). In the eel, the three fins are joined. The dorsal and anal fins are shown fully erect, but are often lowered during steady swimming, particularly at higher speeds

angle of the tail and amplitude of its motion, which together probably determine the majority of the thrust (Lighthill 1960), are very similar for all of the modes. Despite the similarities in the kinematics, the differences in three-dimensional body shape (Fig. 1b) may result in different wake flow (Tytell 2006).

2 Wake flow

Early observations of the flow in the wake of swimming fishes showed the presence of a reverse von Kármán vortex street (Anderson 1996; McCutchen 1977; Müller et al. 1997; Rosen 1959). Sets of staggered vortices are arrayed in the wake, with jets in between them pointing laterally and along the swimming direction (axially), away from the animal. This structure is indicative of thrust production (Koochesfahani 1989; Triantafyllou et al. 1993). Eels were later shown to have a somewhat different wake structure, with two pairs of counter-rotating vortices shed per tail beat (Müller et al. 2001; Tytell and Lauder 2004), and very little net axial flow.

Examples for these two types of wake during swimming at about 1.9 body lengths (*L*) per second are shown in Fig. 2. The eel wake is modified from Tytell (2004a) and the bluegill wake is from previously unpublished data, gathered in the same flow tank under similar conditions and analyzed using the same custom Matlab PIV code (Mathworks, Natick, MA, USA; see Tytell and Lauder 2004, for a detailed explanation of methods). All animal procedures were approved by the Harvard University Institutional Animal Care and Use Committee.

The flow in the eel's wake (Fig. 2a) is concentrated into jets with predominately lateral flow, and are separated by pairs of same-sign vortices or a shear layer (e.g., between jets 1 and 2 in Fig. 2a). In contrast, flow in the wake of a bluegill sunfish (Fig. 2b) contains jets with a distinct axial component (particularly the fully formed jet 2; Fig. 2b), and the jets are separated by a single vortex.

Why are the wakes so different? In both cases, the animals were swimming quite steadily, holding station against the flow (38 cm s^{-1} for the eel; 27 cm s^{-1} for the bluegill) while drifting <1 cm in the laboratory frame of reference over four tail beats. Thus, for both fishes, the net force remains close to zero when averaged over many tail beats. This does not mean, however, that the net force is necessarily zero at any specific instant in time. If thrust is produced in a much more pulsatile way than drag, then it may periodically overwhelm the drag, resulting in a center-of-mass acceleration and a corresponding momentum flux in the wake. This effect will be termed "temporal separation" of thrust and drag.

If thrust and drag are separated temporally, then the center-of-mass speed should fluctuate. Center of mass was therefore estimated on the basis of height and width profiles by assuming the fish's bodies have a constant density and oval cross-section. Figure 3 shows the instantaneous center-of-mass speed and the tail position. Velocities were determined from video using the technique detailed in Tytell and Lauder (2004), which is based on a smoothing-spline method evaluated in Walker (1998). Both framing rate and magnification were the same for all data (250 frames per second, and about 300 pixels per body length), which should result in comparable error on the velocity estimates (Walker 1998).

All three species show velocity oscillations at least at twice or possibly at four times the tail beat frequency. Eels maintain the smoothest velocity trace (Fig. 3a), with root-mean-squared (RMS) velocity fluctuations about the mean of about 0.03 L s^{-1} (5 mm s^{-1}) for this sequence, consistent with their nearly zero-momentum wakes. Trout have fluctuations of 0.07 L s^{-1} (10 mm s^{-1}) (Fig. 3b). Bluegill have the largest oscillations, ~0.09 L s^{-1} (15 mm s^{-1}) about the mean (Fig. 3c), which suggests that their wakes should show corresponding fluctuations in net momentum.

A second possible reason that the wakes differ may be because of the differences in body shape. Over the course of many tail beats, the fish maintain a consistent orientation to the oncoming flow, indicating that the average forces through a tail beat must integrate to zero over the body's surface. This does not mean, however, that the force is necessarily zero at any given point on the body. In particular, for the bluegill and trout, the anterior body

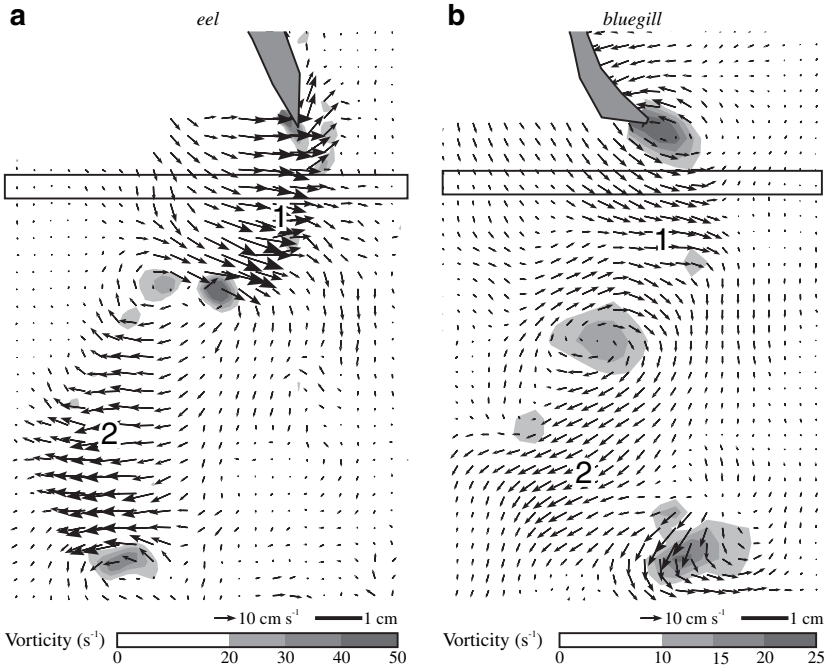

Fig. 2 Representative wake vector fields for the eel (**a**), modified from Tytell and Lauder (2004), with an additional flow field for the bluegill sunfish (**b**). Fluid flow direction and magnitude is indicated with *arrows*. In panel **a**, every other vector is skipped for clarity. *Scale bars* and *scale vectors* are shown below and are the same for both panels. Vorticity magnitude is given with shades of *gray*; note that the scales are different for panels **a** and **b**. The outline of the tail is shown in *gray* at the top of each panels. Due to the shadow from the tail, some vectors could not be calculated and are not shown. The position of downstream velocity transects is indicated by a *box*, and the jets are identified with the *numbers* 1 and 2

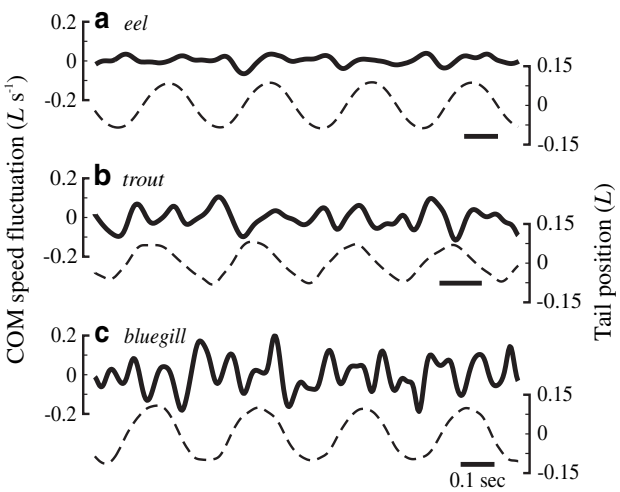

Fig. 3 Representative traces of the fluctuations of the axial center-of-mass speed around the mean swimming speed (*solid line*, *left axes*) and the lateral position of the tail tip relative to the mean body position (*dashed line*, *right axes*), for each of the three fishes. Each trace is from a swimming speed of ~1.9 L s^{-1}. *Horizontal scale bars* are all 0.1 s

probably contributes most of the drag and relatively little thrust, while the tail contributes mostly thrust with relatively little drag. The body drag appears not to strongly affect the flow encountered by the tips of the tail, because low-momentum flow from the body does not separate, but rather converges on the center line as the peduncle narrows (Anderson et al. 2001; Nauen and Lauder 2001). This effect will be termed "spatial separation" of thrust and drag. For the eel, in contrast, spatial separation of forces is probably much less significant, with much of the body contributing to both thrust and drag. Simulations of anguilliform swimming by Kern and Koumoutsakos (2006) support this idea. Their calculations indicated that substantial thrust in eels may be produced by segments anterior to the tail (Kern and Koumoutsakos 2006), unlike in carangiform swimmers.

2.1 Control volume analysis

To examine both spatial and temporal separation of forces, it is best to use a standard control volume analysis (see any fluid dynamics textbook; e.g., Shames 1992) in a cubic region surrounding the fish. The animal produces forces, first, by altering the pressure locally, and second, by changing the fluid momentum. The total force is estimated by integrating the pressure over the surface of the volume and the momentum flux through the surface.

One substantial challenge of these analyses is that techniques like PIV cannot measure pressure directly. The standard way to deal with this issue is to place the sides of the control volume sufficiently far away from the fish that local changes in pressure are converted to fluid acceleration and the pressure on the sides of the control volume is ambient. This method has two problems. First, measurement techniques are often limited in spatial resolution. Examining a large area thus means fewer measurements directly in the wake, where the flows are complex. Second, the further away measurements are made, the more diffuse the wake becomes due to both viscous and turbulent effects (see Tytell and Ellington

2003, for a detailed discussion of these effects). More precision is thus necessary for measurements in the far wake than for those in the near wake.

However, because fishes are self-propelled, they may not require such large control volumes. The net force is close to zero, and so any local pressure changes will be small and will be distributed in the wake quite rapidly. Consider the changes in velocity shown in Fig. 3. Peak acceleration for the bluegill is around 2,000 mm s^{-2}, corresponding to a force of about 150 mN for the ~70 g fish. Remember, this force is not thrust, but a rough estimate of the peak net force. If all of this force is due to pressure applied to an actuator surface swept out by the tail over a tail beat, then the pressure change on that surface would be well under 1% of ambient. Thus, due to the very low-net forces on a self-propelled body, pressure changes even in the near wake can safely be neglected.

For the control volume analysis, the remaining effect is momentum flux through the sides of the volume. If the sides and the top and bottom are placed parallel to the mean flow and sufficiently far from the wake, they will have zero flux. In the end, the only planes that matter are the transects upstream and downstream of the fish.

Since the fluid density and mean flow speed are constant, the momentum flux through these planes is proportional to the average net fluid velocity added by the fish. Transects across the wake were therefore estimated in a 5 mm thick box spanning the wake, placed 10 mm downstream from the average tail position (examples shown in Fig. 2). Single transects were produced by averaging the PIV vectors along the axial thickness of the box, which helped to reduce noise. If necessary, transects were angled to be perpendicular to the swimming angle of the fish to compensate for any small angle that might have been present. Swimming angle was <2° on average.

The net momentum flux is the difference between the flux through the upstream and downstream planes of the control volume. For trout and bluegill, upstream flow was measured directly and upstream transects were estimated analogously to the wake transects, but placed 10 mm upstream from the head. For eels, upstream flow could not be measured directly, because the animals would not swim consistently with their heads in the laser light sheet (Tytell and Lauder 2004). Instead, the laser light sheet was positioned to view flow around the posterior two thirds of the eels' bodies (Fig. 1), and flow entering the control volume was estimated from the average flow field measured without an animal present.

Figure 4 shows net fluid flow in the eel wake during swimming at 1.9 $L\ s^{-1}$, corresponding to a Reynolds number of 80,000 based on body length. Figure 4a shows transects at three phases, with the left half of the tail beat (thin solid lines) superimposed on the mirror image of the right half (thin dashed lines) to show the symmetry of the tail beat. Phase-averaged flow profiles are shown with thick lines. In the 410 flow fields analyzed in this sequence, the net velocity averaged across the transect never deviated more than 9% from the mean flow speed (indicated by the bars on the right in Fig. 4). The mean velocity in the phase-averaged profiles (triangles on the right of Fig. 4a), in turn, was less than the measurement error, and thus indistinguishable from zero. At each point in time, therefore, measurements suggest that the eel wake has close to zero net momentum (as Tytell 2004a found through a different method).

The lack of net momentum, however, does not mean that the eel wake is strictly momentumless. Momentumless wakes are a special class of wakes produced by self-propelled bodies, when the thrust and drag forces are identically equal (Tennekes and Lumley 1972). Such wakes scale differently than drag or thrust wakes (Afanasyev 2004; Sirviente and Patel 2000; Tennekes and Lumley 1972). The wake structure is very sensitive to any deviation from precisely zero net force (Meunier and Spedding 2006). The eel's wake averaged over a full tail beat (Fig. 4b) is reminiscent of the classic mean velocity profile in a momentumless jet (Tennekes and Lumley 1972) and has a similarly strong sensitivity to small deviations from zero-net force (Tytell 2004b). The eel's wake, though turbulent, differs from experimental studies of self-propelled turbulent jets (Finson 2006; Naudascher 1965; Sirviente and Patel 2000) in that the vortices are more coherent and the time scales are longer. Thus, the eel's wake is probably not truly momentumless, particularly in how wake velocity and turbulence scale with distance from the fish, because net momentum fluctuates around zero (indicated by the bars in Fig. 4a), and the center-of-mass velocity oscillates accordingly. However, it is possible that general conclusions from these jet studies, such as the spatial separation of thrust and drag profiles suggested by Sirviente and Patel's (2000) results, can be applied to the eel's wake.

Trout and bluegill wakes, in contrast, clearly do contain net momentum (Fig. 5), at least in the plane in which PIV was conducted. At nearly every point in the cycle, the phase-averaged wakes for both fishes have non-zero momentum flux (Fig. 5a, c). Bluegill have a wake with net momentum above zero at almost every phase in the tail beat cycle (ranging from –2 to 11% of the free-stream momentum flux; Fig. 5c) and on average throughout the tail beat (about 5% of free stream; Fig. 5d). Trout have less net momentum than bluegill, with some instantaneous transects near zero (range –4–13% of free stream; bars on right in Fig. 5a). The average wake for trout (Fig. 5b) also resembles a momentumless wake profile, with one center peak with momentum above free-stream and two side lobes with momentum below free-stream (Tennekes and Lumley

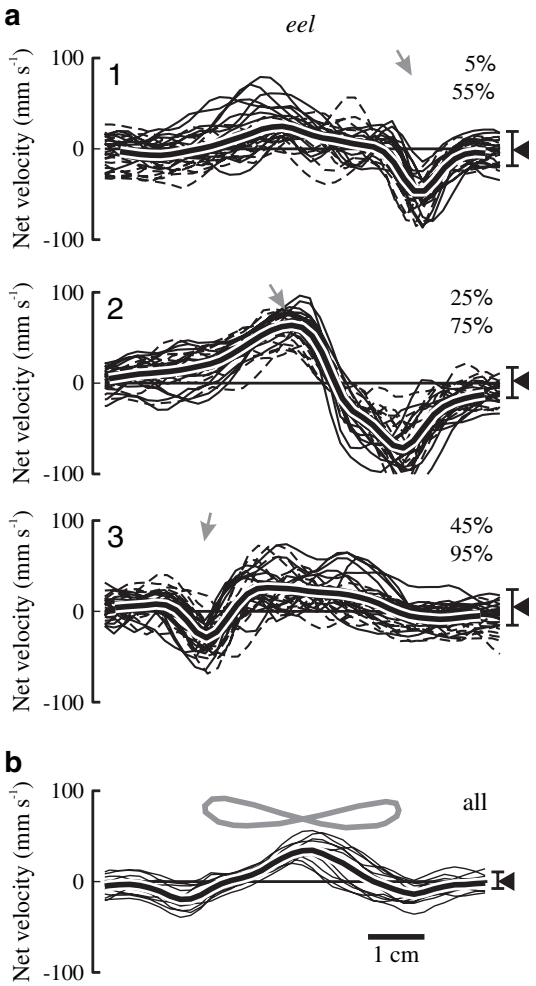

Fig. 4 Transects of axial velocity in the eel's wake during swimming at 1.9 L s^{-1} in a region 10–15 mm downstream of the tail, showing axial velocity (*thin lines*), the phase averaged transect (*thick line*), and the position and angle of the tail (*gray arrows* or *line*). The *bar* on the right indicates the range of mean velocities taken from each transect, and mean velocity across the phase averaged transect is shown with a *triangle*. **a** Transects at particular phases (given by percentages in the *upper right*) during the tail beat cycle. Transects in which the tail is moving from *right* to *left* (*solid lines*) have been mirrored and superimposed on left-to-right transects (*dashed lines*), centering on the tail position. The lateral tail position and angle is indicated with a *gray arrow*. The overall phase average is shown with a *thick line* outlined in *white*. **b** Mean transects over the entire tail beat. Transects are centered on the mean tail position, and the path of the tail is shown in *gray*. The mean over all tail beats is shown with a *thick line* outlined in *white*. *Scale bar* at bottom is 1 cm and is valid for all plots

1972), but the net momentum is nonetheless slightly above zero (about 2% of the free-stream momentum flux).

These transects are examples of the differences between anguilliform, subcarangiform, and carangiform wakes, and have not been subjected to the statistical analysis necessary to discern real differences between the classes of wakes independently from differences among these particular individuals. However, the general structure is consistent with previous, more detailed results (Drucker and Lauder 2001; Nauen and Lauder 2002b).

Why do the bluegill and trout wakes have net momentum? Although both animals have a fluctuating center-of-mass velocity (Fig. 3b, c), temporal separation of thrust and drag does not appear to be the cause of the net momentum in their wakes. If this were the case, one would expect the instantaneous momentum flux (Fig. 5a, c) to dip below zero at some times during the cycle and the average wake profiles (Fig. 5b, d) to have momentum integrals close to zero. Since neither effect is apparent, the more likely explanation is spatial separation of thrust and drag. Experimentally, the PIV plane was generally somewhat above or below the fish's midline (Fig. 1b). In bluegill, the upper and lower lobes of the caudal fin move faster and over a larger amplitude that the center of the fin (Lauder 2000; Tytell 2006), resulting in higher fluid velocities (Fig. 6) and likely more thrust than the center of the fin. Additionally, the body's drag will impact the upper and lower lobes of the tail less than the center. The drag reduces fluid momentum around the body, but, because flow does not separate on the body (Anderson et al. 2001; Nauen and Lauder 2001), the narrowing at the caudal peduncle will tend to cause the low-momentum fluid to converge on the fish's center line. Thus, if the measurement plane is somewhat off-center, the tail may appear to produce a thrust wake. In reality, thrust may genuinely be higher at the tail tips than at the center, due to the higher angle of attack of the tips (Lauder 2000; Tytell 2006) and possibly because of thrust enhancement due to interaction with vortices from the dorsal and anal fin (Drucker and Lauder 2001; Tytell 2006; Zhu et al. 2002), resulting in even more pronounced spatial separation of thrust and drag. However, streamwise tip vortices (Tytell 2006) may also reduce the thrust. A well-centered measurement plane might show a drag wake, but such detailed measurements have not been done. The best measurement would be a stereo-PIV (Prasad 2000) plane aligned perpendicular to the flow in the fish's wake.

2.2 Estimating thrust

Could these wake transects nonetheless be used to estimate thrust? For the eel, the challenge is extracting the thrust magnitude from a nearly zero momentum wake. This may be possible by measuring the height of the central peak in the average wake profile (Fig. 4b). Sirviente and Patel (2000) found that the peak in a momentumless wake close to the body has nearly the same maximum velocity and width as the thrust wake alone, and thus could be used to estimate the thrust force. However, it is not clear whether the same procedure could be used with the eel data to

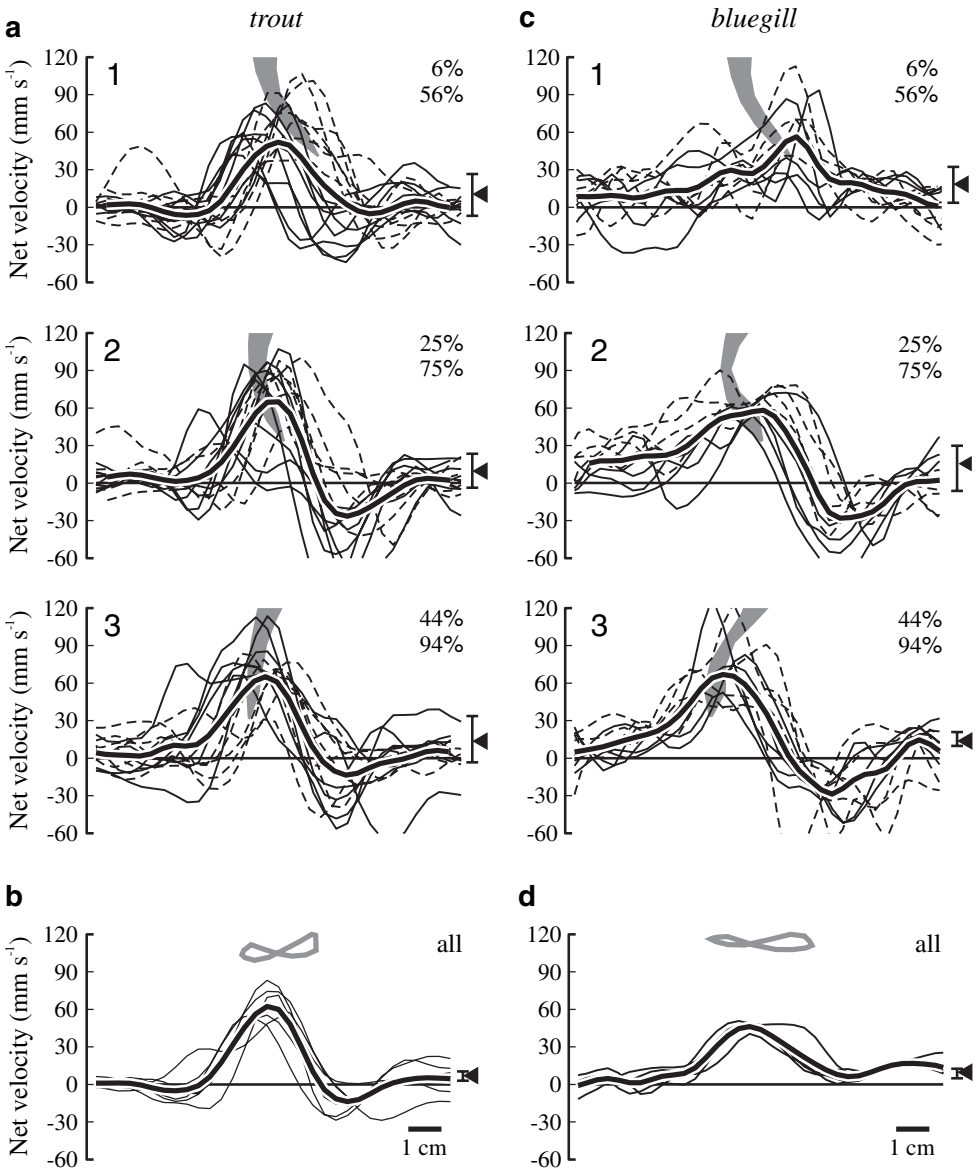

Fig. 5 Transects through the trout and bluegill wakes during swimming at 2.0 and 1.7 L s^{-1}, respectively. Format of the plots is the same as in Fig. 4. **a, c** A silhouette of the tail is shown in *gray*

extract average thrust from an average wake profile, given that the turbulence in the wake is much more structured than in truly momentumless wakes (Meunier and Spedding 2006).

For the trout and bluegill, the challenge is different; the difficulty is in the spatial separation of thrust and drag. The velocity profile of a transect in a single plane (Fig. 5c, d) provides an estimate of the net force per unit height in that plane. Close to the tips of the tail, the net force is likely to be primarily thrust. However, thrust will not be homogeneous over the height of the tail, though, because the center moves slower and over a smaller amplitude than the tips (Lauder 2000; Tytell 2006) and hence has a lower angle of attack. Figure 6 shows that fluid velocities, and thus probably forces, at the upper and lower lobes of the fin are about twice those at the center. Thus, it would be best to make measurements of momentum flux at the tips and the center of the tail over a range of speeds in which the tail beat amplitude varies. These measurements could be used construct an empirical relationship between tail beat amplitude and momentum flux per unit height, which could then be used to estimate the total thrust at a single speed.

An alternative approach, used by many researchers, is to extract forces on the basis of the vortical structure of the wake (Drucker and Lauder 1999; Müller et al. 2001, 1997; Nauen and Lauder 2002a; Tytell 2004a). In this approach, vortices in the wake like those in Fig. 2b are assumed to link up in three dimensions to form a chain of linked vortex rings (e.g., Nauen and Lauder 2002a) or a series of separate

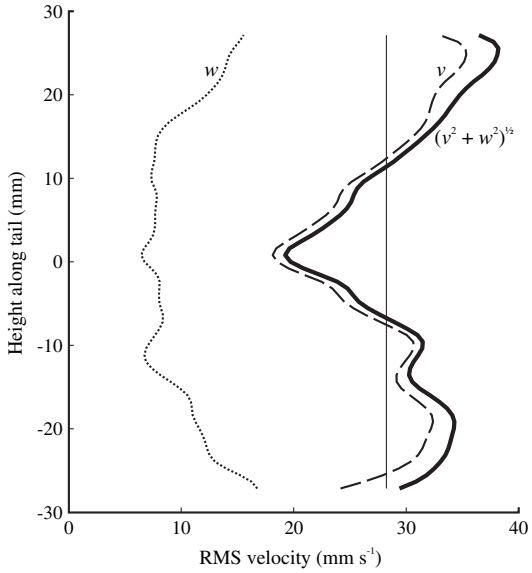

Fig. 6 Flow velocities in a transverse plane through the wake of the bluegill sunfish at different levels along the height of the tail (modified from Tytell 2006). Root-mean-squared (*RMS*) velocities are taken over the course of five tail beats, with lateral (*V*) velocities in the *dashed line*, vertical (*W*) velocities in the *dotted line*, and total velocities in the transverse plane in the *thick solid line*. The *thin vertical line* indicates the mean absolute velocity over the height of the tail. Note that the fluid flow at the upper and lower lobes of the tail has almost twice the velocity of the flow at the centerline

but interacting rings (e.g., Tytell and Lauder 2004). The standard expression for the impulse of an isolated, steadily traveling vortex loop (Batchelor 1973) is then used to estimate forces. This approach, though relatively common, has several potential deficiencies. First, the vortex rings are neither isolated nor steady. Recent work by Dabiri (2005, 2006) indicates that unsteady vortex rings have added mass, like that for solids, which can substantially alter the forces estimated by assuming an isolated, steadily moving vortex ring (Dabiri 2005). The effect of the linkage or interaction between the rings is unknown. Second, the rings are most likely not circular (Tytell 2006), and thus transmit forces to the fluid less efficiently than circular or even oval-shaped rings would (Lighthill 1970). Finally, turbulence can break up the assumed vortex structure, resulting in an underestimate of forces (Spedding et al. 1984; Tytell and Ellington 2003) unless all vortical structures are taken into account (Rosén et al. 2004). Validating this approach has been difficult. Drucker and Lauder (1999) found a good agreement between their thrust estimates for pectoral fin swimming (during which the fish holds its body straight) and the drag measured on an anesthetized fish. Nauen and Lauder (2002a), in contrast, did not find very good agreement. More experiments are necessary to validate this approach, probably using simulation or physical models (such as in Krueger and Gharib 2003; Tytell and Ellington 2003).

3 Wake power

A different approach, requiring fewer assumptions about the structure and temporal evolution of the wake is to estimate the net energy flux, or wake power, added by the fish. This approach was first advocated for biological research by Schultz and Webb (2002). To produce thrust, the fish that is not 100% efficient adds energy to the fluid in the form of the kinetic energy of the wake. PIV methods can conveniently measure the kinetic energy flux through a control volume surrounding the fish. In a low-turbulence flow tank, the upstream input is simply $1/2\rho hwU^3$, where U is the flow speed, h is the height of the fish, w is the width of the wake. Wake flow velocities can then be represented as $(U + u, v, w)$ where u, v, and w are the axial, lateral, and vertical fluid velocities produced by the fish, respectively. The net wake power is thus

$$P_{\text{wake}} = \frac{1}{2}\rho U \int \left[(U+u)^2 + v^2 + w^2 - U^2\right] \mathrm{dS}, \qquad (3)$$

where S is the downstream surface of the control volume. Simplifying the expression in the brackets to $2Uu + u^2 + v^2 + w^2$ helps to reduce round-off error when $U >> u$.

Due to the use of standard two-dimensional PIV, vertical (w) velocities were not measured. For bluegill, the only fish for which such data exist, the w component is a fairly small fraction of the total velocity (data from Tytell 2006 replotted in Fig. 6). In this case, w is about 35% of v, on average, while u and v themselves are of comparable magnitude (e.g., see the flow field in Fig. 2b). Therefore, we assume that vertical velocities make a similarly small contribution to the total power in all three species of fish, and use a simplified form for power:

$$P'_{\text{wake}} = \frac{1}{2}\rho hU \int (2Uu + u^2 + v^2)\mathrm{dy}, \qquad (4)$$

where y is the coordinate of lateral position.

Equation (4) requires an assumption about the 3D profile of the wake, but makes no assumptions about the physics or temporal evolution of the wake, unlike the approaches described in §2.2. As written, the equation assumes uniform flow over the height of the wake, clearly an invalid assumption (as Fig. 6 shows). In the data used for this review, measurement planes were generally slightly above or below the dorso-ventral center line of the fish (Fig. 1), which appear to be the best level to make single-plane measurements, because those are where the mean intersects the measured velocities (Fig. 6). Planes at higher levels may overestimate the power. Measurement planes for the eel were well-centered at the dorso-ventral midline,

although they did not extend all the way anteriorly to the head (Fig. 1). Wake profiles at different levels are unknown for eels, but with a tapered and quite flexible caudal fin (Fig. 1b), it is likely that flow speeds will decrease away from the midline. Thus, the values from eels are probably also overestimates.

In all of these cases, it would be better to have parallel planes at multiple levels to assess the contribution of spatial variation in flow along the height of the fin. However, even one plane can provide useful information, although the data have to be regarded with appropriate caution, as indicated above.

Data analyzed included the entire American eel *(Anguilla rostrata*) data set from Tytell (2004a), consisting of 274 steady tail beats from three eels (body lengths from 20 to 23 cm) at swimming speeds from 0.5 to 2 L s^{-1}. Also analyzed were unpublished data including 27 tail beats from one trout (*Oncorhynchus mykiss*), body length 14 cm, swimming at 1, 2, and 2.5 L s^{-1}, and 31 tail beats from two bluegill sunfish (*Lepomis macrochirus*), lengths 15 and 16 cm, swimming at 1.25–2 L s^{-1}. Reynolds number ranges were from 20,000 to 80,000 for the eel, 20,000 to 50,000 for the trout, and 30,000 to 50,000 for the bluegill.

To compare the fishes, the data were normalized to produce a power coefficient C_P, analogous to a drag coefficient, by dividing by $\frac{1}{2}\rho SU^3$ (Krueger 2006; Schultz and Webb 2002; Tytell 2004a), where S is the wetted surface area for each species. The surface area was estimated from body width and height measurements, assuming an oval cross-section and including the caudal fin area. For eels, the estimated area was 0.18 L^2; for trout, 0.54 L^2; and for bluegill, 0.69 L^2 (close to the values estimated by Webb 1992). Note that this estimate does not include the dorsal or anal fins (Fig. 1). The wetted area (i.e., twice the lateral projected area) of these fins decreases with swimming speed: for bluegill, at the lowest speeds, they make up at most 0.10 L^2 (according to measurements in Standen and Lauder 2005), for trout they are about 0.006 L^2 (Standen and Lauder 2007), and for eels they are ~0.02 L^2 (E. D. Tytell, unpublished data).

Figure 7 shows mean wake power coefficients from eels, trout and bluegill at a range of swimming speeds. Eels maintain about the same power coefficient, about 0.004, over their range of swimming speeds, but with a fairly large spread (SD = 0.002). Below speeds of 2 L s^{-1}, both trout and bluegill have substantially higher power coefficients than eels (trout, 0.03; bluegill, 0.04). In the one high-speed swimming sequence from trout, the wake power coefficient dropped to 0.007.

This review is meant to demonstrate a technique of comparing swimming performance, and conclusions regarding differences between species should be considered tentative. With so few data, it is not possible to perform the appropriate statistical analyses to distinguish real differences among species from random variability among individuals. Nonetheless, the data do show some interesting trends. Bluegill sunfish waste the most energy during steady swimming, as might be expected, because they live in ponds or other relatively still bodies of water where they do not typically spend much time swimming steadily (Hartel et al. 2002). They may be better adapted to low-speed swimming and maneuvering, in which strict power conservation is not an important factor (Webb 2006). Trout have comparable power coefficients to bluegill at low and moderate speeds, but show a marked decrease in the wasted power coefficient at the highest speed examined, possibly reflecting their specialization for high-speed burst swimming, particularly while swimming upstream in rivers (as is known for a closely related species, Standen et al. 2004). Eels, often considered to be inefficient (Lighthill 1970), waste relatively much less power than bluegill or trout at the same swimming speeds.

The wake power is only one component of the total power (Eq. 1), but it can be used to set bounds on the useful power and the efficiency. For example, eels are generally thought to be less efficient than carangiform swimmers like trout (Lighthill 1970; but see van Ginneken et al. 2005). For the current data to be consistent with this hypothesis, the trout must, counterintuitively, expend much more total energy than the eel. Since it already wastes more energy, relative to its body shape, than the eel, it must expend even more useful energy overcoming drag, so that the wasted portion makes up a small fraction of the total. At the same speeds, the trout's wake power coefficient is about eight times larger than the eel's; to have the same propulsive efficiency at these speeds as the eel, its drag (=thrust) coefficient must also be eight times larger. Thus, it seems unlikely that trout are more efficient than eels at low swimming speeds, which is consistent with the metabolic data of van Ginneken et al. (2005).

In contrast, if one wanted to argue that the cost of transport for the trout was less than that for the eel swimming at the same speed, then the trout's drag coefficient would have to be much less than the eel's. In fact, if the eel's drag coefficient was less than the difference in the wake power coefficients, then the trout could never have a lower cost of transport. Of course, trout tend to swim faster than eels, and particularly tend to swim in bursts at high speeds, which could mean that their average cost of transport during intermittent swimming may be lower or equal to that of an eel swimming steadily at a low speed.

Webb has made a number of estimates of the drag and power output of swimming fishes, using a variety of techniques. He estimated the drag on swimming trout by measuring the maximum sustained swimming speeds of trout with artificially increased drag coefficients (Webb

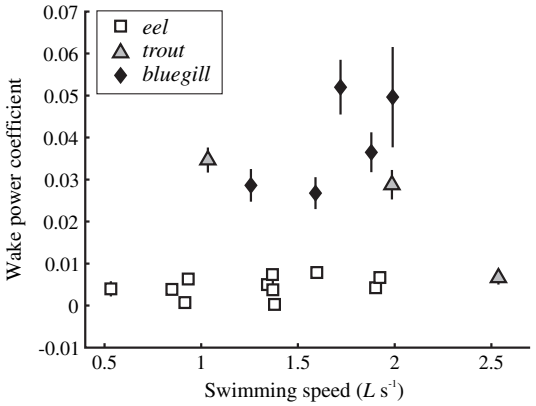

Fig. 7 Net wake power coefficients against swimming speed for eels (*white squares*), modified from Tytell (2004a), with additional data from bluegill (*black diamonds*) and trout (*gray triangles*) superimposed. *Error bars* indicate standard error. Where they are not visible, the symbol is larger than the *error range*

1971). In his study, he estimated a drag (=thrust) coefficient of ~0.05 over speeds from 1 to 2 L s^{-1}. Together with the data in Fig. 7, this would indicate that trout have a hydrodynamic propulsive efficiency of about 60% at low speed, but about 85% at high speed. Webb (1992) also estimated useful power coefficients for both trout and bluegill sunfish using Lighthill's (1971) elongated body theory. This method suggested that the bluegill has a lower thrust power coefficient at low speeds than trout, but that they both approach 0.01 at higher speeds. Elongated body theory may not fully account for the forces in swimming (Tytell 2004a), but its underestimate is unlikely to be dramatically different for trout than bluegill. Thus, together with the current PIV data, these data suggest that bluegill are both more efficient and have a lower cost of transport than trout at low speeds, but that the trout is dramatically more efficient at higher speeds. These data seem to reflect the lifestyle and habitats of the fishes: still water and slow, irregular swimming for bluegill, but moving streams and fast burst swimming for trout.

One must be careful not to read too much into data like these. It is easy to construct "Just So" stories (after Kipling's 1907 stories for children) that explain exactly why the power coefficients should be the way they are. More data from more species are necessary to resolve genuine functional differences between body forms and swimming modes.

Krueger (2006) recently described a similar approach to the one used here. He described a different mechanism for measuring the wake power, which would avoid some of the problems of PIV. In particular, his method would account for all three components of velocity over the entire downstream plane, thus avoiding any assumptions about the 3D structure of the wake. However, he also concludes that without some other way of estimating thrust, wake power can only be used to provide bounds for the efficiency, in the same way as was done in this study.

4 Conclusions and prospectus

Do trout swim better than eels? This review has demonstrated several problems with both the question itself and a number of ways of evaluating it. First, the question itself is somewhat ill-posed. "Better" depends on the metric used—propulsive efficiency, total power use, or power wasted are important metrics, but they need not all be good under the same conditions. Additionally, swimming performance depends on the conditions under which it is measured. Fig. 7 suggests that eels and trout may waste similar amounts of power—but only when swimming at their preferred speeds. When trout are forced to swim artificially slowly, they seem to be more wasteful than eels. Bluegill, in turn, waste substantial energy during steady swimming (Fig. 7), but, under natural conditions, they rarely swim steadily, so they may not be very well adapted for steady power conservation.

Second, given a particular metric and conditions to measure it, it is still challenging to estimate performance of swimming fishes. Making three-dimensional flow measurements around swimming fishes is not straightforward. In particular, there is no currently feasible method for measuring the flow in a full 3D volume around the swimming fish. PIV, the standard technique, can only measure flow in a plane, although stereo-PIV, which can measure all three components of flow in a plane (Prasad and Adrian 1993; Willert 1997) is becoming more feasible in biological applications (e.g., Nauen and Lauder 2002b). Using stereo-PIV planes perpendicular to the swimming direction as the upstream and downstream boundaries of a control volume would avoid many of the assumptions about 3D flow structure that were necessary in the current analysis.

However, the primary issue is not methodological. Fish are, by definition, self-propelled, which makes it challenging to separate thrust and drag forces (Schultz and Webb 2002). Despite this challenge, there are several avenues remaining to be explored as possible routes for comparing hydrodynamic swimming performance among fishes and underwater vehicles.

1. Temporal separation of forces. Although it was not possible with the limited data used for this review, the fluctuating center-of-mass velocity in carangiform swimmers (Fig. 3) may provide information on the relative magnitude of thrust and drag. In fishes with

relatively large fluctuations in velocity, like the bluegill, the thrust may temporally overwhelm the drag to such an extent that the net force at certain phases in the tail beat cycle is composed primarily of thrust.

2. Spatial separation of forces. Measurements of momentum flux at the tips of the tail may provide information on the thrust force, without much of an effect from the drag on the fish's body (Fig. 5d), particularly in fishes with narrow caudal peduncles like the bluegill sunfish used as an example here, or the mackerel (Nauen and Lauder 2002a) or tuna. Full stereo PIV planes behind the swimming fish, perpendicular to the flow, may provide the best information.
3. Zero-momentum wake profiles. For fishes like the eel, which maintain effectively zero axial momentum in their wakes, the velocity profile in the wake may provide information on the thrust and drag forces simultaneously. The near wake of a self-propelled jet can be used to extract both the individual profiles of thrust and drag wakes (Sirviente and Patel 2000). Whether the time-average of a highly structured wake from an oscillating propulsor (as in Fig. 4b) can be used in the same way will have to be confirmed by simulations or physical models.
4. Wake power. In the absence of effective methods to extract thrust, the wake power (wasted power), can be used to place bounds on the relative performance of different fishes. Particularly if there are a priori hypotheses about fish performance based on habitat or lifestyle (i.e., that trout are more efficient than eels), the wake power can be used effectively to constrain if not disprove such hypotheses (trout would have to have a surprisingly large drag coefficient to be more efficient than eels, at least at swimming speeds $<2\ L\ s^{-1}$).

These methods may provide a framework for addressing relative performance as it becomes more feasible to perform comparative studies of swimming in many different fishes.

Comparative studies of the performance of many different fishes, examining many different performance metrics under many different conditions will provide the best route to extracting design principles for undulatory swimming. Only by comparing fishes with different evolutionary histories can one begin to disentangle all the competing adaptive pressures that were involved in producing the body shapes and swimming modes of fishes today. Such comparisons, while challenging, may ultimately provide the best framework for understanding the performance of fishes and biomimetic submarines.

Acknowledgments Many of the ideas in this review developed from a discussion with Rajat Mittal. Data were taken with funding from National Science Foundation grants to George V. Lauder (grant numbers IBN9807021 and IBN0316675). Support is currently provided by the National Institutes of Health (grant number 5 F32 NS054367).

References

Afanasyev YD (2004) Wakes behind towed and self-propelled bodies: asymptotic theory. Phys Fluids 16:3235–3238. doi:10.1063/1.1768071

Anderson EJ, McGillis WR, Grosenbaugh MA (2001) The boundary layer of swimming fish. J Exp Biol 204:81–102

Anderson JM (1996) Vortex control for efficient propulsion. Ph.D. Dissertation, Dept Ocean Eng, Mass Inst Tech

Batchelor GK (1973) An introduction to fluid dynamics. Cambridge University Press, Cambridge

Breder CM (1926) The locomotion of fishes. Zoologica 4:159–297

Dabiri JO (2005) On the estimation of swimming and flying forces from wake measurements. J Exp Biol 208:3519–3532. doi:10.1242/jeb.01813

Dabiri JO (2006) Note on the induced Lagrangian drift and added-mass of a vortex. J Fluid Mech 547:105–113. doi:10.1017/S0022112005007585

Drucker EG, Lauder GV (1999) Locomotor forces on a swimming fish: three-dimensional vortex wake dynamics quantified using digital particle image velocimetry. J Exp Biol 202:2393–2412

Drucker EG, Lauder GV (2001) Locomotor function of the dorsal fin in teleost fishes: experimental analysis of wake forces in sunfish. J Exp Biol 204:2943–2958

Finson ML (2006) Similarity behaviour of momentumless turbulent wakes. J Fluid Mech 71:465–479

Garland T (1998) Conceptual and methodological issues in testing the predictions of symmorphosis. In: Weibel ER, Taylor CR, Bolis L (eds) Principles of animal design. Cambridge University Press, Cambridge

Hartel KE, Halliwell DB, Launer AE (2002) Inland fishes of Massachusetts. Massachusetts Audobon Society, Lincoln, MA

Helfman GS, Collette BB, Facey DE (1997) The diversity of fishes. Blackwell Science, London

Kern S, Koumoutsakos P (2006) Simulations of optimized anguilliform swimming. J Exp Biol 209:4841–4857. doi:10.1242/jeb.02526

Kipling R (1907) Just so stories. Doubleday, Garden City, NY

Koochesfahani MM (1989) Vortical patterns in the wake of an oscillating airfoil. AIAA J 27:1200–1205

Krueger PS (2006) Measurement of propulsive power and evaluation of propulsive performance from the wake of a self-propelled vehicle. Bioinsp Biomimet 1:S49–S56. doi:10.1088/1748-3182/1/4/S07

Krueger PS, Gharib M (2003) The significance of vortex ring formation to the impulse and thrust of a starting jet. Phys Fluids 15:1271–1281. doi:10.1063/1.1564600

Lauder GV (2000) Function of the caudal fin during locomotion in fishes: kinematics, flow visualization, and evolutionary patterns. Am Zool 40:101–122

Lauder GV, Tytell ED (2006) Hydrodynamics of undulatory propulsion. In: Shadwick RE, Lauder GV (eds) Fish biomechanics. Academic, San Diego, pp 425–468

Lighthill J (1960) Note on the swimming of slender fish. J Fluid Mech 9:305–317

Lighthill J (1970) Aquatic animal propulsion of high hydromechanical efficiency. J Fluid Mech 44:265–301

Lighthill J (1971) Large-amplitude elongated-body theory of fish locomotion. Proc R Soc Lond B 179:125–138

McCutchen CW (1977) Froude propulsive efficiency of a small fish, measured by wake visualisation. In: Pedley TJ (ed) Scale effects in animal locomotion. Academic, London, pp 339–363

Meunier P, Spedding GR (2006) Stratified propeller wakes. J Fluid Mech 552:229–256. doi:10.1017/S0022112006008676

Müller UK, Smit J, Stamhuis EJ, Videler JJ (2001) How the body contributes to the wake in undulatory fish swimming: flow fields of a swimming eel (*Anguilla anguilla*). J Exp Biol 204:2751–2762

Müller UK, van den Heuvel B-LE, Stamhuis EJ, Videler JJ (1997) Fish foot prints: morphology and energetics of the wake behind a continuously swimming mullet (*Chelon labrosus* Risso). J Exp Biol 200:2893–2906

Naudascher E (1965) Flow in the wake of self-propelled bodies and related sources of turbulence. J Fluid Mech 22:625–656

Nauen JC, Lauder GV (2001) Locomotion in scombrid fishes: visualization of flow around the caudal peduncle and finlets of the chub mackerel *Scomber japonicus*. J Exp Biol 204:2251–2263

Nauen JC, Lauder GV (2002a) Hydrodynamics of caudal fin locomotion by chub mackerel, *Scomber japonicus* (Scombridae). J Exp Biol 205:1709–1724

Nauen JC, Lauder GV (2002b) Quantification of the wake of rainbow trout (*Oncorhynchus mykiss*) using three-dimensional stereoscopic digital particle image velocimetry. J Exp Biol 205:3271–3279

Prasad AK (2000) Stereoscopic particle image velocimetry. Exp Fluids 29:107–115

Prasad AK, Adrian RJ (1993) Stereoscopic particle image velocimetry. Exp Fluids 15:49–60

Rosén M, Spedding GR, Hedenstrom A (2004) The relationship between wingbeat kinematics and vortex wake of a thrush nightingale. J Exp Biol 207:4255–4268. doi:10.1242/jeb.01283

Rosen MW (1959) Waterflow about a swimming fish. US Naval Ordnance Test Station, China Lake, CA. Tech Publ 2298, pp 1–96

Schultz WW, Webb PW (2002) Power requirements of swimming: do new methods resolve old questions? Integr Comp Biol 42:1018–1025

Shames IH (1992) Mechanics of fluids, 3rd edn. McGraw-Hill, New York

Sirviente AI, Patel VC (2000) Wake of a self-propelled body, Part 1: momentumless wake. AIAA J 38:611–619

Spedding GR, Rayner JMV, Pennycuick CJ (1984) Momentum and energy in the wake of a pigeon (*Columba livia*) in slow flight. J Exp Biol 111:81–102

Standen EM, Hinch SG, Rand PS (2004) Influence of river speed on path selection by migrating adult sockeye salmon (*Oncorhynchus nerka*). Can J Fish Aquat Sci 61:905–912. doi:10.1139/F04-035

Standen EM, Lauder GV (2005) Dorsal and anal fin function in bluegill sunfish (*Lepomis macrochirus*): three-dimensional kinematics during propulsion and maneuvering. J Exp Biol 208:2753–2763. doi:10.1242/jeb.01706

Standen EM, Lauder GV (2007) Hydrodynamic function of dorsal and anal fins in brook trout (*Salvelinus fontinalis*). J Exp Biol 210:325–339. doi:10.1242/jeb.02661

Tennekes H, Lumley JL (1972) A first course in turbulence. MIT, Cambridge, MA

Triantafyllou GS, Triantafyllou MS, Grosenbaugh MA (1993) Optimal thrust development in oscillating foils with application to fish propulsion. J Fluids Struct 7:205–224

Tytell ED (2004a) The hydrodynamics of eel swimming. II. Effect of swimming speed. J Exp Biol 207:3265–3279. doi:10.1242/jeb.01139

Tytell ED (2004b) Kinematics and hydrodynamics of linear acceleration in eels, *Anguilla rostrata*. Proc R Soc Lond B 271:2535–2541. doi:10.1098/rspb.2004.2901

Tytell ED (2006) Median fin function in bluegill sunfish, *Lepomis macrochirus*: streamwise vortex structure during steady swimming. J Exp Biol 209:1516–1534. doi:10.1242/jeb.02154

Tytell ED, Ellington CP (2003) How to perform measurements in a hovering animal's wake: physical modelling of the vortex wake of the hawkmoth *Manduca sexta*. Philos Trans R Soc Lond B 358:1559–1566. doi:10.1098/rstb.2003.1355

Tytell ED, Lauder GV (2004) The hydrodynamics of eel swimming. I. Wake structure. J Exp Biol 207:1825–1841. doi:10.1242/jeb.00968

van Ginneken V, Antonissen E, Müller UK, Booms R, Eding E, Verreth J, van den Thillart G (2005) Eel migration to the Sargasso: remarkably high swimming efficiency and low energy costs. J Exp Biol 208:1329—1335. doi:10.1242/jeb.01524

Walker JA (1998) Estimating velocities and accelerations of animal locomotion: a simulation experiment comparing numerical differentiation algorithms. J Exp Biol 201:981–995

Webb PW (1971) The swimming energetics of trout. I. Thrust and power output at cruising speeds. J Exp Biol 55:489–520

Webb PW (1992) Is the high cost of body caudal fin undulatory swimming due to increased friction drag or inertial recoil? J Exp Biol 162:157–166

Webb PW (2006) Stability and maneuverability. In: Shadwick RE, Lauder GV (eds) Fish biomechanics. Academic, San Diego, pp 281–332

Willert CE (1997) Stereoscopic digital particle image velocimetry for application in wind tunnel flows. Meas Sci Tech 8:1465–1479

Willert CE, Gharib M (1991) Digital particle image velocimetry. Exp Fluids 10:181–193

Zhu Q, Wolfgang MJ, Yue DKP, Triantafyllou MS (2002) Three-dimensional flow structures and vorticity control in fish-like swimming. J Fluid Mech 468:1–28

Time resolved measurements of the flow generated by suction feeding fish

Steven W. Day · Timothy E. Higham · Peter C. Wainwright

Received: 20 February 2007 / Revised: 25 August 2007 / Accepted: 15 September 2007 / Published online: 12 October 2007

Abstract The majority of aquatic vertebrates are suction feeders: by rapidly expanding the mouth cavity they generate a fluid flow outside of their head in order to draw prey into their mouth. In addition to the biological relevance, the generated flow field is interesting fluid mechanically as it incorporates high velocities, is localized in front of the mouth, and is unsteady, typically lasting between 10 and 50 ms. Using manometry and high-speed particle image velocimetry, this is the first study to quantify pressure within and outside the mouth of a feeding fish while simultaneously measuring the velocity field outside the mouth. Measurements with a high temporal (2 ms) and spatial (<1 mm) resolution were made for several feeding events of a single largemouth bass (*Micropterus salmoides*). General properties of the flow were evaluated, including the transient velocity field, its relationship to pressure within the mouth and pressure at the prey. We find that throughout the feeding event a relationship exists for the magnitude of fluid speed as a function of distance from the predator mouth that is based on scaling the velocity field according to the size of the mouth opening and the magnitude of fluid speed at the mouth. The velocity field is concentrated within an area extending approximately one mouth diameter from the fish and the generated pressure field is even more local to the mouth aperture. Although peak suction pressures measured inside the mouth were slightly larger than those that were predicted using the equations of motion, we find that these equations give a very accurate prediction of the timing of peak pressure, so long as the unsteady nature of the flow is included.

S. W. Day (✉)
Department of Mechanical Engineering,
Rochester Institute of Technology,
76 Lomb Memorial Dr, Rochester, NY 14623, USA
e-mail: steven.day@rit.edu

T. E. Higham
Department of Organismic and Evolutionary Biology,
Concord Field Station, Harvard University,
100 Old Causeway Road, Bedford, MA 01730, USA

P. C. Wainwright
Section of Evolution and Ecology,
University of California, One Shields Avenue,
Davis, CA 95616, USA

1 Introduction

Most aquatic vertebrates, including fish, feed by generating a flow of water outside the head that acts to draw the prey into the mouth, a behavior known as suction feeding. The flow is interesting from a fluid mechanical perspective as it includes high spatial gradients of velocity and pressure and dramatic temporal accelerations with the entire prey capture lasting $\sim$10 ms for many species. As is the case with locomotion through a fluid medium, feeding involves some direct fluid-structure interactions. Forces are a function of the biomechanical forces within the fish and the fluid mechanical pressure within mouth. The speed of cranial expansion is a function of the biomechanical kinematics within the animal and also the volumetric flow rate of the fluid. Force and speed of fish movement are related through muscle physiology and gearing within the animal, and pressure and fluid speed are related through the governing equations of fluid mechanics. As an example, an attempt by a fish to increase the speed of mouth opening increases the required force through interaction of the fluid field; increased fluid speeds lead to increased magnitude of generated pressures.

G.K. Taylor, M.S. Triantafyllou, and C. Tropea (Eds.): Animal Locomotion, pp. 75–86.
springerlink.com

Species of fish exhibit variations in suction feeding behavior, including some with relatively large mouths that swim rapidly towards the prey when feeding and some that have small mouths and hold their body still while drawing the prey into the mouth, as have been investigated by Norton and Brainerd (1993), Norton (1991), and Higham et al. (2007). Individuals within a given species can modulate aspects of this feeding behavior with musculoskeletal control, including the speed with which they open the mouth and the maximum size of the mouth opening. For example, Nemeth (1997) demonstrated that more aggressive feedings (i.e. faster mouth opening) are employed when feeding on more evasive prey. Extensive research by Aerts et al. (1987), Aerts (1990), Lauder (1980), Liem (1973), Carroll et al. (2004), and Svanback et al. (2002) has investigated the musculoskeletal basis of suction feeding and Muller et al. (1982), Ferry-Graham et al. (2003), and van Wassenbergh et al. (2006) have devoted some attention to the study of the generated fluid flow.

Initial investigations into the fluid mechanics of suction feeding based on mathematical models using potential flow theory include those by Drost et al. (1988), Muller et al. (1982), Weihs (1980) and van Leeuwen and Muller (1984b). Earlier empirical studies included qualitative flow visualization by Muller and Osse (1984), van Leeuwen and Muller (1984a) and quantitative measurements of speed by particle streaking at a few locations in front of the fish Lauder and Clark (1984). Recent studies by our group, including Day et al. (2005) and Higham et al. (2005, 2006a), used particle image velocimetry (PIV) to resolve the flow field in front of two species of fish with sufficient spatial and temporal resolution to quantify the distribution of fluid speed as a function of distance in front of the fish and investigated the effect of swimming speed (or "ram speed"), mouth size, and time of mouth expansion on this flow. Nauwelaerts et al. (2007) used PIV to investigate the effect of substrate on water flow patterns generated by sharks.

This fluid flow field as described by distributions of velocity and pressure is central to the suction feeding event because it imparts all of the forces that act to draw the prey into the predator's mouth. The traditional view is that pressure within the mouth drives the velocity field and the forces imparted onto the prey are caused by drag and the acceleration reaction force, both of which are a consequence of the generated velocity field. Recently, Wainwright and Day (2007) proposed that there are three forces that the flow can exert onto a prey item: drag, acceleration reaction, and the pressure gradient force. Drag and the acceleration reaction are caused by the relative motion of the fluid and prey, both of which are a result of the velocity field. The pressure gradient force (Batchelor (1967) is, however, a direct result of gradients of pressure within the flow field and would be present even in the absence of the prey. While the characteristics of the velocity field in front of a fish's mouth have been investigated previously, and it is assumed that there is a pressure gradient within this flow field, no study has empirically determined the difference in pressure between the prey and predator's mouth. It is supposed that a strong gradient of pressure exists as the result of fluid velocity varying in both space, being higher at the mouth aperture and decreasing with distance from the mouth, and in time.

The generated flow is very local to the fish's mouth and ephemeral, typically lasting 10–50 ms. The predator must manipulate the timing and location of the feeding to locate a small region of influence near the prey, some of which are very evasive. Suction feeding success depends heavily on the details of these water flow patterns and how the fish uses them to capture prey as has been described in Nyberg (1971), van Leeuwen and Muller (1984b) and Weihs (1980). Thus, a clear understanding of the time-course of the suction flow and the spatial region over which it operates is required before it will be possible to fully interpret the extensive morphological and behavioral diversity that exists among suction feeding species.

Manometry has frequently been used to measure the magnitude of negative pressure generated within the mouth cavity of feeding fish, for examples see Lauder (1980), van Leeuwen and Muller (1983), Sanford and Wainwright (2002) and Higham et al. (2006b). Peak sub-ambient pressure within the mouth is still the most common metric of suction feeding performance, but is only related to the prey through the flow field within, see van Wassenbergh et al. (2006), and outside the head. One way of conceptualizing this flow field is as follows: the feeding fish uses its musculoskeletal apparatus to pull against the volume of water within its mouth, thereby generating a sub-ambient "suction" pressure. The flow both within and outside the mouth is then driven by the gradient of pressure between the ambient surroundings and the sub-ambient pressure within the mouth. Because the pressure changes suddenly and resulting fluid accelerations are high, the fluid momentum is substantial and velocity as a function of time is temporally delayed as compared to the pressure. Experimentally, the measurement of pressure involves considerably less apparatus than measurements of velocity, so that many authors, such as Wainwright et al. (2006), Norton and Brainerd (1993), van Leeuwen and Muller (1983) and Carroll et al. (2004), have presented measurements of the timing and magnitude of maximum sub-ambient intra-oral pressure (aka suction pressure) within a variety of species of suction feeding fish.

In Day et al. (2005) and Higham et al. (2005), we used particle image velocimetry to investigate the flow field generated by bluegill and largemouth bass. In the current

study we couple manometry with the PIV method used in prior studies in order to empirically determine the temporal relationship between the velocity field in front of suction feeding largemouth bass and pressure at two critical locations, within the mouth and at the prey. We demonstrate that, while substantial fluid velocities are confined to a region near the mouth of the fish, the sub-ambient pressures extend an even smaller distance into the flow. We describe the temporal patterns of velocity and pressure and demonstrate directly that maximum sub-ambient pressures occur before peak fluid speeds. We show that, although the velocity field varies with time, the distribution of fluid velocity in front of the fish is still a function of only the instantaneous gape and fluid speed at the mouth. We are able to demonstrate the effectiveness of applying the momentum equation to predict the relationship between the generated velocity field outside the mouth and pressure within the mouth and to demonstrate the contribution of fluid momentum to pressure within the mouth.

2 Materials and methods

2.1 Experimental animals

One largemouth bass, *Micropterus salmoides* Rafinesque, with a standard length of 18.5 cm was used in this study. The fish was caught in Yolo County, near Davis, CA and housed in a 100 l aquarium. The fish was fed a variety of squid (*Loligo*) and live ghost shrimp (*Palaemonetes*) daily. All fish maintenance and experimental procedures used in this research followed a protocol approved by the University of California, Davis Animal Care and Use Committee. Six feeding sequences were analyzed for this individual. The low inter-individual variance with respect to fluid speed–pressure relationships found in a previous study using this species (Higham et al. 2006b) suggests that using a single individual is a valid approach for measuring the relationship between the fluid velocity field in front of the feeding fish and pressures within the mouth. All values are reported as the mean ± standard deviation for these six feedings.

2.2 Experimental setup

Experiments were conducted in a 200 l experimental aquarium that was integrated with a PIV system. Digital particle image velocimetry (DPIV) is a well-established technique (Adrian 1991) that measures the nearly instantaneous velocity field within an illuminated plane of the fluid field using light scattered from particles seeded into the fluid. This method is very versatile and ideally suited for non-uniform transient flows. Similarly, miniature pressure transducers developed for blood vessel catheterization are commercially available. Details of both the PIV and the manometry system used in these experiments follow.

2.2.1 *Particle image velocimetry*

The illumination used in this experiment consists of an Innova I-90 continuous argon-ion laser with an output power of ~3 W (Coherent, Inc., Santa Clara, CA, USA). A matched set of a single cylindrical and spherical lens created a collimated light sheet about 10 cm wide and was focused to a waist thickness of approximately 1 mm within the measurement region. The laser sheet was directed upwards by a mirror located below the tank and passed into the aquarium through the tank bottom (Fig. 1). The resulting sheet was parallel to the sagittal plane (plane of symmetry) of an approaching fish. After traversing the depth of the tank, a mirror near the surface of the tank reflected the laser sheet back down within the same plane as the upward directed sheet, but angled towards the posterior of the fish. In this experiment, the downward directed sheet illuminated the fluid field above the upper lip of the fish that was in the shadow of the upward directed beam, but the methods may be useful for illuminating the flow in the shadow of any opaque object. Additionally, most of the flow field is illuminated by both the "upward" and the "reflected" sheets, thereby nearly doubling the amount of scattered light.

The seed particles used for light scattering were nominally 14 μm silver-coated glass beads manufactured for light scattering in reflective paints (Potter Industries, Inc., Carlstadt, NJ). The particles are hollow and have an

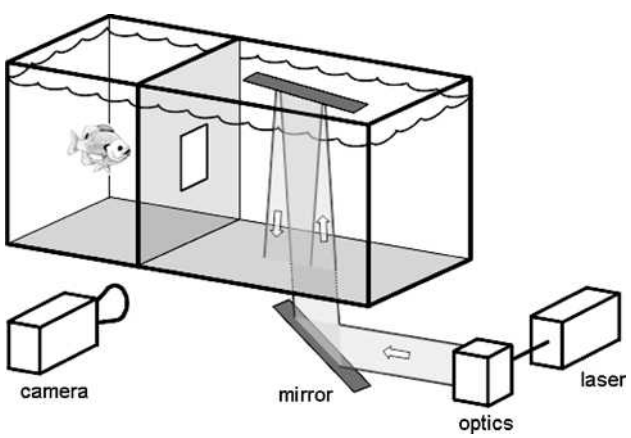

Fig. 1 Schematic of the experimental setup, showing experimental tank, position of laser sheet, optics, mirrors, camera, fish prior to a feeding, tank divider and door

average specific gravity of approximately 1.05 which, when used in fresh water, results in a calculated settling velocity of 5e – 4 mm/s (Durrani and Greated 1977). In practice, it was apparent that a fraction of the particles settled out of the flow within 10–15 min, so we suspect that the density of the particles is variable.

The scattered light was imaged and collected by a NAC Memrecam ci digital high-speed video camera (Tokyo, Japan) through an f/1.2 c-mount video lens. The Memrecam is a high speed CMOS based camera with full resolution (512 × 462 pixels) at 500 frames per second. As the laser was not shuttered or pulsed, a mechanical shutter that is built into the camera was used to give an exposure time of 1/3,000 s. This was sufficiently short to prevent blurring and long enough to provide adequate signal (∼1 mJ/image).

2.2.2 *Manometry*

Two pressure transducers were used in these experiments. The first, hereafter referred to a p_{mouth}, was surgically implanted into the fish skull. The second, referred to as p_{prey}, was attached to the prey mount and so moved with the prey up until the point of ingestion. Typically, as the prey moved into the mouth aperture, the prey mount wire contacted the upper lip of the fish so that the prey came off the mount and was carried into the mouth as the mount and transducer remained in the mouth aperture (see Fig. 2c, d).

In order to implant the mouth transducer, the fish was anesthetized by submerging it in a 0.3 g l^{-1} solution of buffered MS-222 (Carroll et al. 2004). Once anesthetized, as determined by a cessation of gill ventilation and lack of a response to tactile stimulation, the fish was positioned in clean water in a dissection tray and a 15 gage (1.8 mm) biopsy needle was forced through the neurocranium of the fish caudal to the ascending process of the pre-maxilla but rostral to the braincase. The needle emerged within the buccal cavity just lateral to the midline. A plastic cannula was constructed from PE-90 tubing and threaded into the needle (0.034” ID, 0.050” OD). The end of the cannula that was inside the buccal cavity had been flared prior to the procedure, enabling the cannula to be pulled up against the dorsal surface of the cavity with its opening positioned about 1–2 mm away from the buccal wall. A small sleeve of Tygon tubing (Cole-Parmer, Vernon Hills, IL, USA) was friction fit to the cannula where it protruded from the head of the fish to prevent it from sliding into to the skull. A Millar SPR-407 micro catheter-tipped pressure transducer (Millar Instruments, Inc., Houston, TX, USA) was threaded into the cannula and held in place by inserting the tip of the cannula into a piece of silicon sealant that had previously been allowed to set around the pressure transducer cable. The tip of the pressure transducer was positioned such that it was flush with the buccal cavity or slightly dorsal to the opening of the cannula. Surgery took no more than 15 min. The experiment began within 2–4 h after surgery.

The Millar SPR-407 is a solid state strain gauge type pressure transducer designed for intravenous measurements in small laboratory animals. The tip of the probe is cylindrical with a diameter of 0.67 mm and length ∼5 mm. The sensor is located on the side of this cylinder and measures about 0.5 × 2 mm. The flange of the cannula that housed the transducer was designed to lay flush with the interior of the mouth. The transducer was recessed slightly in the cannula. The sensing element was exposed by a short fluid path to pressure in the buccal cavity so that it measures the static pressure outside the cannula and has a frequency

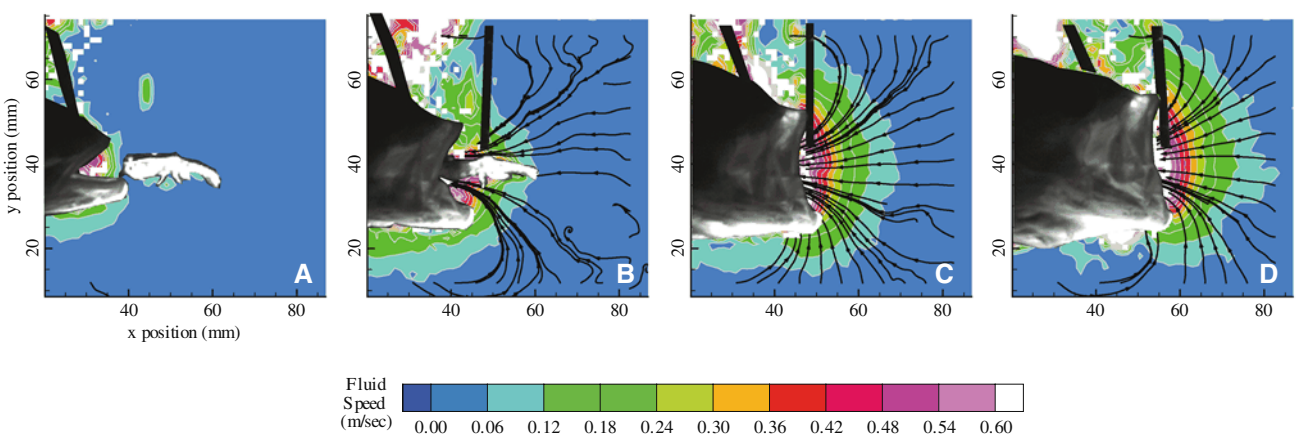

Fig. 2 PIV measurements in front of a bass feeding on a live, but mounted ghost shrimp at four instants during the feeding. Times are measured from the time that mouth opening began, the time of each is **a** 6 ms, **b** 18 ms, **c** 28 ms, **d** 50 ms. The position of the predator and prey are both shown as overlays onto the calculated velocity field. The contour levels represent the magnitude of fluid speed and direction is parallel to the streamlines. The cannula that holds the mouth pressure transducer is clear as a black object protruding from the fish head. A second cannula that houses the pressure transducer located at the prey is also seen in the image

response of 10 kHz. Pressure transducers were calibrated prior to the surgery by placing them into a sealed flask. The pressure within the flask was varied over a range of –60–0 kPa using a vacuum pump and was measured with a commercial (World Precision Instruments, Sarasota, FL, USA) pressure transducer that came with an NIST (National Institute of Standards and Testing) certificate of calibration. The voltage output of the transducer is a linear function of pressure ($r^2 = 0.99$).

The transducer at the prey was housed in and protected by a short length of stainless steel tubing in order to both maintain the position of the transducer and to protect it when contacted by the feeding fish. The tubing was attached with glue and thread to the prey mount, so that the open and exposed end of the housing was just above the prey. Thin plastic tubing (PE-90) connected the top of the stainless tubing to a syringe located outside the tank. This was used to purge the cannula before each feeding.

The output of the mouth and prey pressure transducers were sent to linear op-amp based amplifiers with gains of 10 and 25 respectively. The amplified voltages were on the order of 1 V and were recorded at a sampling rate of 5 kHz using a National Instruments analog to digital converter (ADC) and LabView software (DAQPad-6070E National Instruments, Austin, Texas). Since the baseline pressure varied depending on the depth of the fish, we refer to pressure in this paper as the difference between the instantaneous pressure and the baseline value prior to the feeding event. Both the camera and ADC have a circular buffer, so that when armed they are continually acquiring data until triggered. In these experiments the pressure and video recordings were synchronized by using an external manual button to trigger both devices.

2.3 Experimental protocol

The fish was easily trained over the course of several days to reliably feed within the laser sheet. Prior to beginning the experiment, the fish was confined to one end of the tank by a physical barrier. The prey was suspended and positioned in the laser sheet and the camera field of view by a flexible (0.15 in. diameter) wire inserted under the exoskeleton, so that the shrimp generally remained alive and initiated an escape in response to the approaching predator. To keep the predator motivated, unrestrained prey were occasionally introduced during feeding sessions. The fish was confined to one end of the tank until a trap door was opened at the beginning of each experiment (Fig. 1). The fish swam through the door and towards the prey, suspended in the measurement region. The fish's movement is not confined in any direction, but due to the relative location of the trap door and prey, generally swam down the midline of the tank and located the center of its mouth at the laser sheet. A standard 30 Hz camcorder (Sony, Inc., Tokyo, Japan) recorded an anterior view of the fish in order to determine the relative position of the laser sheet and the mouth of the feeding fish. Only those trials for which the laser sheet was located less than 10% of the mouth diameter from the center line of the fish were analyzed.

2.3.1 PIV processing

Images were transferred from NAC proprietary format into a series of TIFF images. The entire sequence from the beginning of mouth opening until mouth closure lasted from 20 to 150 images (40–300 ms) depending on the speed of the event. An adaptive mesh cross-correlation algorithm created by Scarano and Riethmuller (1999) was used to calculate fluid velocities from image pairs, each pair consisting of two successive images from the high-speed video sequence. This is an iterative algorithm that includes resolution refinement, discreet window offsets, and deformation. All of the measurements for this work used an initial interrogation window size of 64×64 pixels and two refinement steps for a final resolution of 16×16 pixels. Two additional refinement steps are applied with no further refinement, but iterative offset and deformation. The final image interrogation used 16×16 pixel interrogation regions with 50% overlap, so that the measurement grid spacing was eight pixels, corresponding to approximately 1.3 mm for the camera field of view (7×5 cm). Each image pair lead to a simultaneous measurement of two components (u and v) of velocity at every location on a regularly spaced i, j ordered measurement grid with overall dimensions of $i = 53$ and $j = 70$. In addition to two components of velocity, the algorithm returned the signal-to-noise ratio (SNR) for each correlation. During all refinement steps, vectors falling below a fixed SNR or neighboring mean criterion are removed and replaced by interpolation. In the final interrogation step, removed vectors are not replaced. The majority of vectors lying within interrogation regions located on the fishes body are invalidated, but >95% of vectors lying in front of the fish pass the validation criteria.

Determining the uncertainty of correlation-based PIV methods complicated, but well studied. Generally, uncertainty increases as a result of poor seeding in that region of the image, high velocity gradients, solid boundaries that scatter light, and particle displacements that are large relative to the size of the interrogation region, as is described in Adrian (1997). The following two-step validation scheme was implemented.

First, vectors with a signal-to-noise ratio (SNR) of less than 2.0 were removed, without replacement, and no

smoothing was applied to the final velocity field. Some spurious measurements that are not representative of fluid particle displacement still passed the SNR validation criterion. The second step of the validation scheme deals with these spurious vectors. For velocities extracted from a transect extending away from the mouth along the centerline of the fish, measurements both directly on the transect (i, j) and at 2 grid points above (i, $j + 2$) and 2 grid points below (i, $j - 2$) were considered at each horizontal position. Measurements located 2 grid points away from the primary measurement location are used because these do not overlap the primary measurement region. The neighboring points in the i direction were not used for validation because of the very steep gradients of fluid velocity in the horizontal direction. If at least two of the three measurements considered had not been removed based on the SNR criterion (step one of the validation scheme), then the mean of the remaining measurements was used as the value of speed for that given position along the transect.

This validation scheme resulted in the removal of some measurements near the mouth for all sequences. Measurements near the mouth were the most likely to fail the validation scheme because particle displacements (high fluid speed), velocity gradients, and occasional glare from the predator were all highest in this region. The camera frame rate and spatial resolution used for the measurements placed an effective upper bound of measured fluid speed at approximately 1.5 m/s, corresponding to 16 pixel displacement between images. For the majority of feedings, all measurements greater than 2–3 mm from the mouth passed the validation procedure and measurements further than 5 mm from the mouth were validated for all feedings.

2.3.2 Data analysis

The position of the eye and upper and lower jaws were manually identified and measured for each frame of the acquired video sequence using Image J (NIH, Washington, DC, USA). The x, y position of each was used to calculate several kinematic variables using and Excel spreadsheet. The position of the center of the mouth was defined as the midpoint between the upper and lower jaw tips. Gape was the distance from tip of the upper jaw to tip of the lower jaw and Peak Gape (PG) was the maximum value of gape during the feeding. Ram speed was calculated as the horizontal component of the temporal derivative of eye position. The measurements of horizontal position were smoothed with a three-point moving average before calculating derivative quantities. The onset of mouth opening and the onset of peak gape are defined as the time at which the mouth has opened to 20 and 95% of its maximum value, respectively. The time between these is referred to as time to peak gape, TTPG.

This extraction of speed along the centerline of the fish from the vector field output by the PIV algorithm was automated with a custom program written in Visual Basic because the absolute position of the fish, and therefore positions of the transects varied during the feeding. The program probed the PIV velocity data, accounting for both the angle of the fish and the position of mouth as determined from manual digitization.

In Day et al. (2005), we showed that the profiles of speed in front of the fish scale with the magnitude of fluid speed at the mouth and the size of the mouth at the time of peak fluid speed. In this study, the profile of speed along the centerline throughout the feeding event was scaled by dividing spatial dimensions (x) by the magnitude of instantaneous gape (G) and speeds by the magnitude of fluid speed at a distance of 1/2 gape in front of the fish. The speed at this relative position is used throughout as a reference because at this location fluid speed is substantial and the PIV measurements meet the validation criteria described above, and is referred to as $FS_{1/2\ gape}$ from here on. Profiles of scaled speed were compared to one another to see if the function of fluid speed holds true throughout the duration of the feeding.

The pressure transducer located at the prey mount moves towards the mouth during the feeding, resulting in pressure measurements as a function of time and position in front of the fish. For each acquired data point, the magnitude and distance between the mouth aperture and transducer were recorded. In a manner similar to our scaling of the velocity field, the acquired pressures at the prey are scaled. The magnitude of each measurement of pressure at the prey, p_{prey}, was divided by the instantaneous pressure in the fish mouth, p_{mouth}, and the spatial position of each was divided by the instantaneous gape. This results in a distribution of scaled pressure as a function of non-dimensional position ($x^* = x/G$) in front of the mouth. Is should be remembered that the profile of pressure versus distance was not acquired at a single instantaneous time for each feeding, but is the compilation of single point measurements taken over the period of the feeding. Nonetheless, each is scaled by the instantaneous pressure in the fish mouth and instantaneous gape.

Finally, the measured distribution of the velocity in front of the fish was used to calculate a predicted pressure within the buccal cavity according to the momentum equation along the centerline of the fish. We integrated the differential form of one-component of the momentum equation (Eq. 1) along a path extending from a point far away from the fish and ending at the mouth aperture in order to find the relationship between p_{mouth} and $p_{ambient}$ (Eq. 2).

$$\frac{dp}{dx} = -\rho\left(\frac{\partial u}{\partial t} + u\frac{\partial u}{\partial x}\right) \quad (1)$$

$$p_{\text{mouth}} - p_{\text{ambient}} = \int_{x_{\text{ambient}}}^{x_{\text{mouth}}} \frac{dp}{dx}dx = \int_{x_{\text{ambient}}}^{x_{\text{mouth}}} \rho\left(\frac{\partial u}{\partial t} + u\frac{\partial u}{\partial x}\right)dx \quad (2)$$

Implementation of the momentum equation directly on the raw PIV data leads to high uncertainty because of the derivative terms, so we instead first fit a function to the empirical data and then applied the equation to this function. The spatial distribution of fluid speed is specified by a polynomial fit to the empirical data. The curve-fit for the time course of fluid speed is based on the form of equation 11 from Muller et al. (1982) with parameters manually adjusted to agree with the empirical data for that particular feeding. This implementation resulted in a function of predicted pressure at the mouth aperture that was arrived at independently of the measured p_{mouth}. This predicted pressure was compared to the measured p_{mouth} in order to validate the utility of this relationship.

3 Results

The suction feeder creates a velocity and pressure field that both have high spatial and temporal gradients. Speeds are highest near the mouth (1.5 ± 0.36 m/s) and decrease as a function of distance away from the mouth. There is a general shape of contour lines of constant velocity throughout the feeding that we describe as the top of a mushroom (Fig. 2). This pattern is symmetric about the long-axis of the fish. The size of the pattern varies in proportion to the diameter of the mouth and the magnitude of velocity at the mouth varies throughout the feeding. Both the size of the affected region and magnitude of fluid speed are highest at a time shortly after reaching peak gape. The fish continues to ingest water throughout the duration of the feeding, even as the mouth is closing, as shown in Figs. 2 and 3.

3.1 Temporal pattern

There is a general temporal pattern of generated fluid speed, gape, and the recorded pressures (see Fig. 3 for a representative sequence). All times are given as both the absolute time (relative to the beginning of mouth opening) and as a fraction of TTPG, the time between beginning of mouth opening and peak gape, as the relative timing of events scales in proportion of the total duration of the feeding. Maximum sub-ambient pressure in the mouth (–5.7 ± 1.9 kPa) occurs

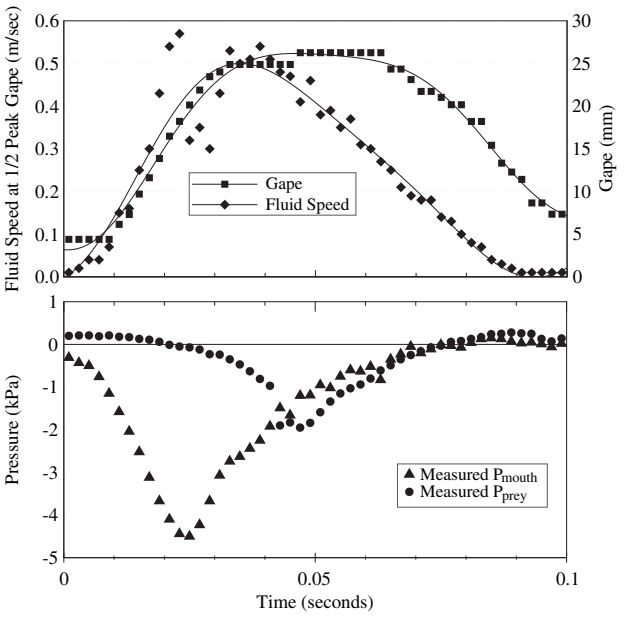

Fig. 3 Relative time course of fluid speed compared to gape distance and pressures within and outside the mouth for the representative sequences. Fluid speed is measured at a constant distance in front of the fish equal to 1/2PG. This is a moderate speed feeding (time to open mouth ~25 ms). The relative timing of events is similar for all recorded feedings. Peak fluid speed occurs slightly before the onset of peak gape. The pressure within the mouth, p_{mouth} reaches is maximum sub-ambient pressure during mouth opening and has already decayed significantly by the time of mouth opening. The pressure at the prey, p_{mouth}, is near ambient, but gradually decreases as both fluid speed increase and the prey moves closer to the predator's mouth. Near 48 ms, the prey enters the mouth. The transducer and mouth are in contact with the upper lip of the fish, so the transducer remains in the aperture until the end of the feeding. During this time, the pressure measured near the mouth aperture and within the buccal cavity are nearly equal

at a time (24 ± 18 ms, 58 ± 18%*TTPG*) when the mouth is still opening and has typically decayed to approximately 1/2 the peak amplitude at the onset of peak gape (38 ± 21 ms, 100 ± 0%*TTPG*), consistent with Sanford and Wainwright (2002). Peak fluid speed (1.50 ± 0.36 m/s) reached a maximum just after (38.3 ± 20.3 ms, 113 ± 41%*TTPG*) the onset of peak gape, consistent with Day et al. (2005) and Higham et al. (2006a). Peak gape is maintained for some time (25 ± 9.7 ms) before the mouth begins to close. At the end of peak gape (0.63 ± 0.20 m/s), as indicated by the mouth diameter having reached it's maximum and then decreased to 95% of its maximum size, fluid speed at the mouth has decreased to a fraction (32 ± 28%) of the maximum speed for that feeding. The pressure at the prey is initially very small and decreases exponentially as a result of both the flow speed increasing and the prey moving towards the mouth. At the time when the prey is at the mouth opening (48 ms in this feeding), the pressure transducer is located in the mouth aperture and remains there for the duration of the feeding

after the prey is drawn off the wire and ingested. The transducer located at the prey, p_{prey}, records a nearly identical pressure as p_{mouth}. It should be emphasized that for all feedings that we recorded, the second transducer, p_{prey}, is located at the aperture only after peak gape and not during mouth expansion.

3.2 Spatial pattern

After creating a non-dimensional distance (x^*) and speed (SS, scaled speed) by dividing all measured distances (x) by the instantaneous mouth diameter and dividing all fluid speeds (FS) by the fluid speed at a reference location located at a distance 1/2 of gape ($x^* = 1/2$) in front of the fish ($FS_{1/2\ gape}$), the velocity profile along the centerline for all feedings collapse to one empirical relationship (Fig. 4; Eq. 3). At all times during the feeding, fluid speed decays with distance in front of the feeding fish, being equal to approximately 25% the speed at the mouth at a distance of 1/2 the mouth diameter and 5% at one mouth diameter. Because the spatial distribution of velocity scales in proportion to the mouth diameter, the spatial distribution of absolute velocity is dependent on gape diameter and the magnitude of fluid speed generated at the mouth (Day et al. 2005). The feeding *Micropterus* can modulate both of these, so that there is significant feeding-to-feeding variation. A fourth order polynomial fit to the data assembled for all feedings is given as

$$\begin{aligned} FS(x^*) = FS_{mouth}\,(&0.215x^{*4} - 1.26x^{*3} \\ &+ 2.73x^{*2} - 2.63x^* + 1) \end{aligned} \quad (3)$$

The magnitude of fluid speed and gape vary throughout the feeding. After normalization based on FS at the mouth and the mouth diameter, both measured as a function of time, transects of scaled speed in front of the fish have a very similar shape at all times during the feeding (Fig. 5), suggesting that Eq. 3 is an appropriate description of the spatial pattern of the velocity throughout the feeding.

3.3 Pressure outside the mouth

For most feedings, the onset of mouth opening occurs when the prey is approximately one mouth diameter in front of the fish and the prey enters the mouth of the fish slightly before the onset of peak gape (40 ± 16 ms, 58 ± 18% *TTPG*). This allows for measurements of the pressure in front of the fish during this period as the transducer attached to the prey moved towards the mouth. The distribution of pressure decays even more dramatically than

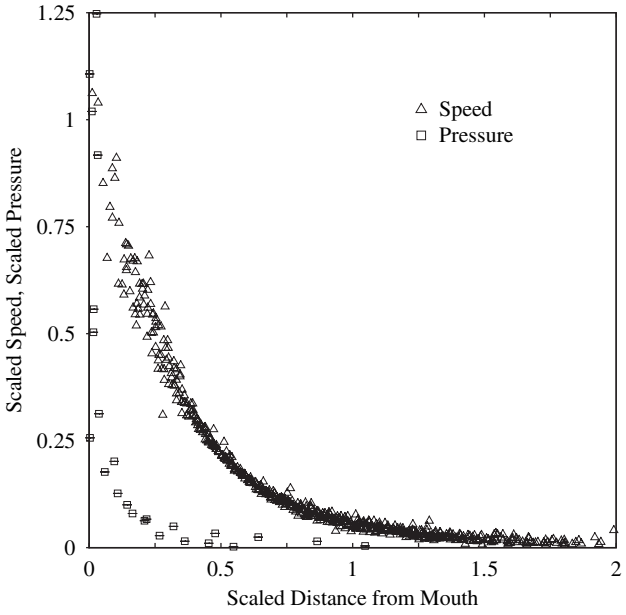

Fig. 4 Profiles of scaled speed and pressure along the centerline in front of the fish. Additionally, measurements from the pressure transducer located at the prey are presented. As the prey moved towards the predator during each feeding, the distance from mouth to prey was calculated and scaled by the instantaneous gape. The magnitude of pressure was scaled by the magnitude of measured pressure within the mouth cavity at that instant in time. Note that the decay of pressure in front of the fish is even more dramatic than that of fluid velocity. There is a very steep pressure gradient very near the mouth and substantially less away from the mouth

velocity in front of the fish (Fig. 4). The pressure is approximately 10% the pressure within the mouth at a distance of 1/4 gape, and 5% at 1/2 gape, thereby only influencing a region that is extremely local to the fish mouth. The spatial gradient of pressure is steepest at the mouth aperture and very small at a distance more than 1/4 gape from the fish.

3.4 Model results

The existence of a general form of the spatial pattern of fluid speed (Eq. 3) based on fluid speed at the mouth (FS_{mouth}) and the mouth aperture (G), allows a mathematical function for the spatio-temporal pattern of fluid speed in front of the fish so long as FS_{mouth} and G are specified as a function of time. The resulting spatio-temporal pattern of fluid speed along a line extending away from the fish's mouth is shown in Fig. 6 for a representative feeding.

Predictions of the pressure within the mouth based on the solution of Eq. 2 both neglecting (steady form) and including (unsteady form) the temporal derivative of velocity are compared in Fig. 7 for this same representative

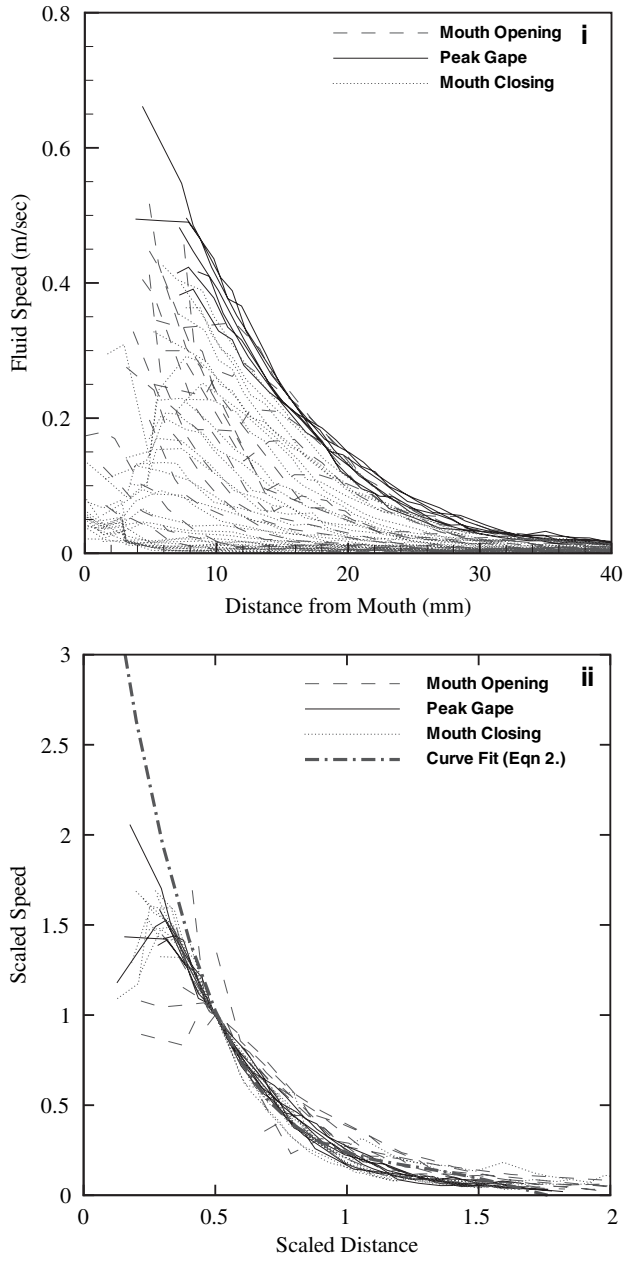

Fig. 5 Profiles of speed (**a**) and scaled speed (**b**) measured along the centerline at all times during the feeding, including mouth opening, the duration of peak gape and mouth closure. **a** Both the magnitude and size of the velocity profile vary during the feeding. **b** The same data as in **a**, but after scaling. The distance in front of the fish was scaled by the mouth diameter at the time of velocity measurement. Magnitudes of velocities were scaled by the FS measured at a distance of 1/2 gape at that time (FS1/2 gape). Variations in mouth size and the speed of flow at the mouth have a very significant effect on the absolute speeds in front of the fish, but the scaled profiles are similar at all times during the feeding

feeding. For all feedings, the time of peak sub-ambient pressure predicted based on the unsteady form of the model (25 ± 18 ms, 61 ± 19%*TTPG*) agreed well with the empirical data (24 ± 18 ms, 58 ± 18%*TTPG*), as shown in Fig. 8. The steady form (30 ± 19 ms, 77 ± 21%*TTPG*) predicted peak pressure to occur later than the unsteady form, and always after it was measured (Figs. 7, 8). The unsteady form predicts greater magnitude of sub-ambient pressures than the steady form (–3.9 ± 1.1 kPa vs. –3.2 ± 1.0 kPa). For some feedings there is very good agreement between the magnitude of predicted and measured (–5.7 ± 1.9 kPa) mouth pressures but the predicted pressure is smaller magnitude than the observed for most feedings (as is the case for the feeding shown in Fig. 7).

4 Discussion

The simultaneous measurement of fluid speed and pressure presented here is one of the first empirical attempts to bridge the relationship between pressure and fluid speed in the complex, unsteady flow field that characterizes suction feeding. During suction feeding, the affected flow is confined to a region close to the mouth of the fish and the size of this region varies in direct proportion to mouth diameter throughout the feeding. The area of substantial fluid speed forms a three-dimensional shaped region similar to the top of a mushroom. This result is consistent with models by Muller and Osse (1984) and the empirical findings of Ferry-Graham et al. (2003) and Day et al. (2005) for other species. This study also shows that the area of affected pressure is confined to an even smaller region than the area affected by the velocity field. The pressure gradient force, as opposed to velocity-based forces such as drag, has recently been proposed to be the dominant forces in many suction feeding scenarios by Wainwright and Day (2007). This study underscores the conclusion of previous studies that the predator must locate the prey in very close proximity to its mouth in order to have any effect on the prey.

Day et al. (2005) showed that a single polynomial fit to empirical data describes the distribution of fluid speed in front of the fish and showed that this relationship holds true at the time of peak fluid speed across a wide range of mouth size and fluid speed in a bluegill. Here we show that a similar polynomial function (Eq. 3) can be used to describe the spatial distribution of fluid speed at all times during the feeding for the largemouth bass. Velocity profiles scaled by the instantaneous gape and instantaneous fluid speed all fit one generalized function well. This result is consistent with previous findings that peak fluid speeds measured at three locations along the centerline transect all occurred nearly simultaneously with one another and with the onset of peak gape (95% opening) Higham et al. (2006b). Further, this allows a description of the velocity field using only two parameters, the mouth diameter and fluid speed, which are specified as functions of time.

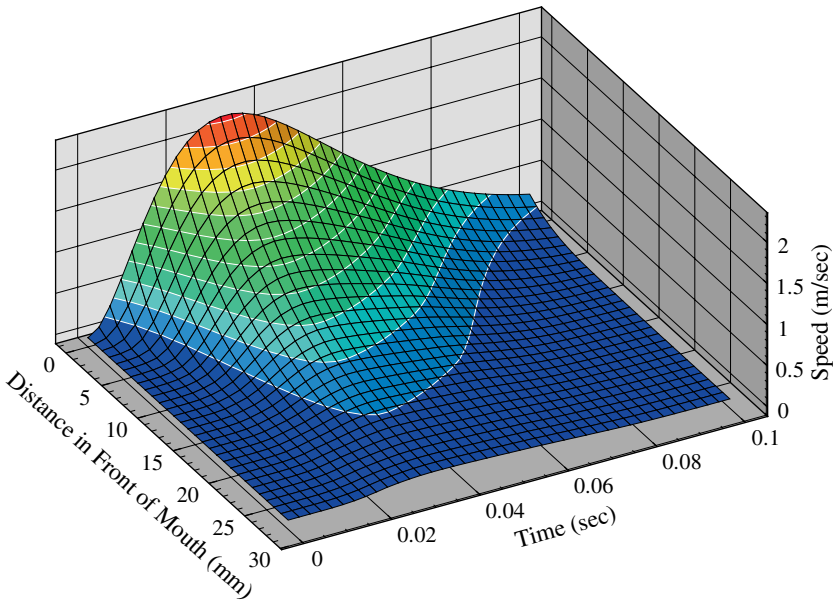

Fig. 6 Curve fit to the spatio-temporal pattern of fluid speed along the centerline transect in front of the feeding fish. Fluid speed in front of the fish is always given (Eq. 3) as $FS(x^*) = FS_{mouth}\ (0.215x^{*4} - 1.26x^{*3} + 2.73x^{*2} - 2.63x^* + 1)$. FS_{mouth} is the fluid speed at the mouth (distance equals 0) and is specified as a function of time and is based on the form of equation 11 from Muller et al. (1982)

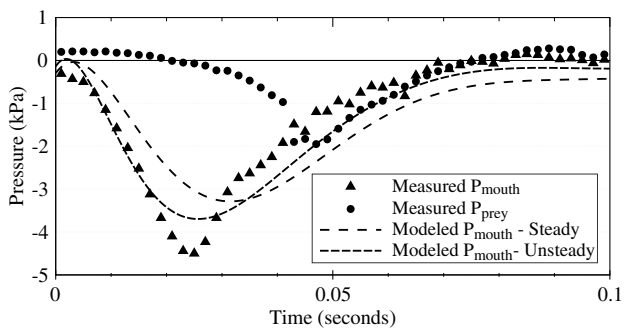

Fig. 7 The *symbols* show measured pressures within the mouth and in front of the fish. The *dashed lines* show predictions of pressure at the mouth aperture calculated by applying Eq. 3 to the time sequence of measured speeds along the centerline

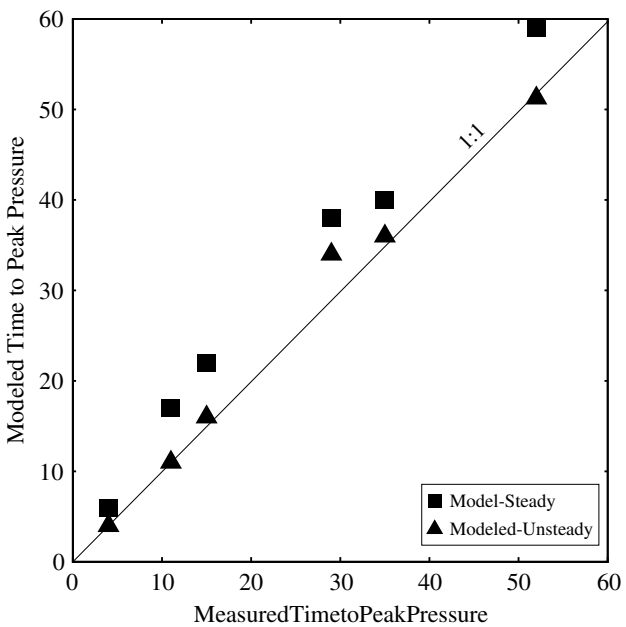

Fig. 8 Comparison of the time to peak pressure, as predicted by both the steady and unsteady models, plotted versus the measured peak pressure

Fluid speed was not constant during the course of the feeding event, increasing from zero to peak fluid speed in 40 ± 18 ms. The time of peak fluid speed occurred near the onset of peak gape (38 ± 21 ms). The synchronization of fluid speed and gape is potentially a very effective feeding strategy because the fish simultaneously maximizes flow-induced forces acting on the prey and the space over which the flow occurs. One mechanism that can facilitate this that continued expansion of the posterior portion of the buccal and opercular cavities after peak expansion of the anterior portion prolongs the period of volumetric expansion of the total mouth past peak gape. A distinct delay in the posterior expansion (as measured by suspensory and opercular abduction) relative to gape was shown consistently throughout feedings of three species of centrarchid fishes by Lauder (1980). The anterior-to-posterior delay of expansion of major functional components of the head has been shown to hold true across a wide range of taxa by Lauder (1982). The second is that the opening of the opercular slits allows fluid to continue to flow into and through the mouth, driven only by fluid momentum, after volumetric expansion of the buccal cavity has ceased. At the beginning of the feeding, when the opercular slits are closed, the volumetric flow rate into the mouth aperture is exactly equal to the instantaneous volumetric expansion of the combined buccal and opercular cavities. After the opercular slits are open, the flow into the mouth is equal to any remaining expansion of the mouth cavity in addition to

the volumetric flow rate out of the opercular slits. After the mouth has reached full expansion, the velocity of the fluid cannot continue to increase. However, the flow will continue on its own momentum, slowing due to losses, while the mouth is held open. It is likely that both the anterior-to-posterior expansion and timing of opercular opening contribute to the observed temporal relationship between fluid speed and gape.

Although a relationship between the velocity and pressure field through the equations of motion necessarily exists, the relationship in this particular flow is complicated. According to van Leeuwen and Muller (1983) "*Flow patterns cannot be derived from the pressure regime as the process is essentially unsteady (Muller, 1982).*" As a result of statements to this effect and support from numerical models that show that the magnitude of generated buccal pressure is very sensitive to the shape of the mouth cavity van Wassenbergh et al. (2006), measurements of pressure within the mouth are only related to the velocity field in front of the fish with great caution. This is, however, problematic when trying to study and evaluate feeding performance because the purpose of the predator is to exert forces on the prey and these forces are a result of the flow outside the mouth and the mechanism for doing this is to directly affect the fluid within the mouth. We have shown in Higham et al. (2006b) that the magnitude of peak fluid speed is correlated to the magnitude of peak suction pressure.

This study quantifies the degree to which the time course of buccal pressure is affected by the unsteady nature of the flow. When the unsteady terms are included in the relationship between the velocity field and pressure, the prediction of pressure at the mouth leads to excellent temporal agreement with the measured buccal pressure. Exclusion of these terms (a quasi-steady assumption) leads to slightly lower magnitude and temporal latency of the prediction.

In this study we have demonstrated that in at least one species of fish, there is a clear relationship between pressure within the mouth and fluid speed outside the head. We propose that because of properties and characterization of this flow field, measured pressures within the mouth could, in fact, be used to derive the flow outside the fish. This is primarily due to the fact that there is a general function for the velocity distribution in front of the fish that is valid for all times during the feeding and over a wide range of behavioral variations, as was shown in Day et al. (2005) and Higham et al. (2006a). By accounting for only two variables, i.e. mouth size and fluid speed at the mouth, we can characterize velocity in front of the fish. Assuming that mouth size is known as a function of time, the pressure at the mouth aperture can be used to predict the velocity at the mouth aperture or vice versa. In this study, we have demonstrated the latter. Our measurements demonstrate that the pressure at the mouth aperture is very nearly the same as at the posterior location of p_{mouth} for all times after the onset of peak gape, which is perhaps one reason why our prediction of the pressure at the mouth aperture agrees well with the measured pressure.

Although the predictions of the timing of peak pressure agree well with observations, the magnitude of estimated pressure was always lower than observed. This could be due to radial movement of the mouth walls resulting in streamline curvature, losses at the mouth opening, or viscous losses both within and outside the mouth, none of which are accounted for in the integration of one-dimensional form of the momentum equation given in Eq. 2.

The flow field is characterized by high spatial and temporal gradients of velocity. The local acceleration near the mouth aperture is on the order of 50 gs and even higher in some species, such as the bluegill, as was shown in Day et al. (2005). Both the spatial gradients of velocity and accelerations contribute to pressure gradient within the flow field, which Wainwright and Day (2007) have shown exerts substantial forces on the prey. This study represents a significant advance in understanding the relationship between pressure and velocity in this dynamic fluid flow because it measures both simultaneously and demonstrates good temporal agreement between the fluid velocity external to the fish and the pressure measured within the fish mouth. In addition to the intra-oral pressure, this inclusion of pressure experienced by the prey is a novel perspective on this flow. The study confirmed the localized and short lasting generated velocity field described previously and demonstrated that substantial gradients of pressure are only present in an even smaller region in front of the fish. Despite the spatial and transient nature of the flow, a fairly simple pattern of fluid speed exists throughout the feeding and the fluid velocity field outside the fish can be successfully related to pressure within the mouth.

In conclusion, we find that the equations of motion can, in fact, be used to relate pressure measured inside the mouth cavity, to the flow field outside the mouth, at least up until the time when the opercula are opened at the back of the head. This is the first such demonstration for suction feeding fishes and establishes an important physical linkage between the pressures that are generated during expansion of the head and the flow that results and is used to capture prey. Our understanding of the fluid mechanics of suction feeding has advanced considerably in recent years, but as yet there has not been a detailed treatment of the mechanics of internal expansion of the oral cavity and how this pattern relates to flow entering the mouth. These results are an important step in this direction that will lead to a greater understanding of how internal head movements can be regulated to control flow in front of the fish.

Acknowledgments This research was supported by NSF grants IOB-0444554 and 0610310.

References

Adrian RJ (1991) Particle imaging techniques for fluid mechanics. Annu Rev Fluid Mech 23:261–304

Adrian RJ (1997) Dynamic ranges and spatial resolution of particle image velocimetry. Meas Sci Technol 8:1393–1398

Aerts P (1990) Variability of the fast suction feeding process in *Astatotilapia elegans* (Teleostei, Cichlidae)—a hypothesis of peripheral feedback control. J Zool 220:653–678

Aerts P, Osse JWM, Verraes W (1987) Model of jaw depression during feeding in *Astatotilapia elegans* (Teleostei, Cichlidae)—mechanisms for energy-storage and triggering. J Morphol 194:85–109

Batchelor GK (1967) An introduction to fluid mechanics. Cambridge

Carroll AM, Wainwright PC, Huskey SH, Collar DC, Turnigan RG (2004) Morphology predicts suction feeding performance in centrachid fishes. J Exp Biol 207:3873–3881

Day SW, Higham TE, Cheer AY, Wainwright PC (2005) Spatial and temporal patterns of water flow generated by suction-feeding bluegill sunfish *Lepomis macrochirus* resolved by particle image velocimetry. J Exp Biol 208:2661–2671

Drost MR, Muller M, Osse JWM (1988) A quantitative hydrodynamical model of suction feeding in larval fishes: the role of frictional forces. Proc R Soc Lond Ser B 234:263–281

Durrani TS, Greated CA (1977) Laser systems in flow measurements. New York

Ferry-Graham LA, Wainwright PC, Lauder GV (2003) Quantification of flow during suction feeding in bluegill sunfish. Zoology 106:159–168

Higham TE, Day SW, Wainwright PC (2005) Sucking while swimming: evaluating the effects of ram speed on suction generation in bluegill sunfish *Lepomis macrochirus* using digital particle image velocimetry. J Exp Biol 208:2653–2660

Higham TE, Day SW, Wainwright PC (2006a) Multidimensional analysis of suction feeding performance in fishes: fluid speed, acceleration, feeding accuracy and the ingested volume of water. J Exp Biol 209:2713–2725

Higham TE, Day SW, Wainwright PC (2006b) The pressures of suction feeding: the relation between buccal pressure and induced fluid speed in centrarchid fishes. J Exp Biol 209:3281–3287

Higham TE, Hulsey CD, Rican O, Carroll AM (2007) Feeding with speed: prey capture evolution in cichlids. J Evol Biol 20:70–78

Lauder GV (1980) The suction feeding mechanism in sunfishes (*Lepomis*): an experimental analysis. J Exp Biol 88:49–72

Lauder GV (1982) Patterns of evolution in the feeding mechanism of actinopterygian fishes. Am Zool 22:275–285

Lauder GV, Clark BD (1984) Water flow patterns during prey capture by teleost fishes. J Exp Biol 113:143–150

Liem KF (1973) Modulatory multiplicity in the feeding mechanism in cichlid fishes, as exemplified by the invertebrate pickers of Lake Tanganyika. J Zool Soc Lond, pp 93–125

Muller M, Osse JWM (1984) Hydrodynamics of suction feeding fish. Trans Zool Soc Lond 37:51–135

Muller M, Osse JWM, Verhagen JHG (1982) A quantitative hydrodynamical model of suction feeding in fish. J Theor Biol 95:49–79

Nauwelaerts S, Wilga C, Sanford C, Lauder G (2007) Hydrodynamics of prey capture in sharks: effects of substrate. J R Soc Interface 4(13):341–345

Nemeth DH (1997) Modulation of buccal pressure during prey capture in *Hexagrammos decagrammus* (Teleostei: Hexagrammidae). J Exp Biol 200:2145–2154

Norton SF (1991) Capture success and diet of cottid fishes—the role of predator morphology and attack kinematics. Ecology 72:1807–1819

Norton SF, Brainerd EL (1993) Convergence in the feeding mechanics of ecomorphologically similar species in the Centrarchidae and Cichlidae. J Exp Biol 176:11–29

Nyberg DW (1971) Prey capture in largemouth bass. Am Midl Nat 86:128–144

Sanford CPJ, Wainwright PC (2002) Use of sonomicrometry demonstrates the link between prey capture kinematics and suction pressure in largemouth bass. J Exp Biol 205:3445–3457

Scarano F, Reithmuller ML (1999) Iterative multigrid approach in PIV image processing with discrete window offset. Exp Fluids 26:513–523

Svanback R, Wainwright PC, Ferry-Graham LA (2002) Linking cranial kinematics, buccal pressure, and suction feeding performance in largemouth bass. Physiol Biochem Zool 75:532–543

van Leeuwen JL, Muller M (1983) The recording and interpretation of pressures in prey-sucking fish. Neth J Zool 33:425–475

van Leeuwen JL, Muller M (1984a) A quantitative study of flow in prey capture by rainbow trout, *Salmo gairdneri*, with general consideration of the actinopterygian feeding mechanism. Trans Zool Soc Lond 37:171–227

van Leeuwen JL, Muller M (1984b) Optimum sucking techniques for predatory fish. Trans Zool Soc Lond 37:137–169

van Wassenbergh S, Aerts P, Herrel A (2006) Hydrodynamic modelling of aquatic suction performance and intra-oral pressures: limitations for comparative studies. J R Soc Interface 3:507–514

Wainwright PC, Day SW (2007) The forces exerted by aquatic suction feeders on their prey. J R Soc Interface 4:553–560

Wainwright PC, Huskey SH, Turingan RG, Carroll AM (2006) Ontogeny of suction feeding capacity in snook, *Centropomus undecimalis*. J Exp Zool A 305A:246–252

Weihs D (1980) Hydrodynamics of suction feeding fish in motion. J Fish Biol 16:425–433

Powered control mechanisms contributing to dynamically stable swimming in porcupine puffers (Teleostei: *Diodon holocanthus*)

Alexis M. Wiktorowicz · Dean V. Lauritzen · Malcolm S. Gordon

Abstract Balances of multiple varying forces must be the basis for the unusually great dynamic stability of swimming pufferfishes. We used high-speed digital video recordings to study biomechanics and kinematics of rectilinear swimming at different speeds of five porcupine puffers in a water tunnel. We measured critical swimming speeds (U_{crit}); fin biomechanics, kinematics, and coordination; recoil movements; and gait changes. Major propulsors were pectoral fins at lower speeds; dorsal, anal, and caudal fins at higher speeds. Precise coordination of fin movements produced small recoil movements at speeds below U_{crit}. The unusual body shape probably contributes to unconscious stability control.

1 Introduction

Swimming postures and trajectories shown by the derived bony fishes belonging to three major families of the Order Tetraodontiformes are unusually smooth and dynamically well controlled. These fishes are all rigid-bodied, median and paired fin (MPF) swimmers. These features are readily observed in the field, in environments varying in intensities of water movement and turbulence, and in aquaria. The families are the tropical boxfishes (including trunkfishes and cowfishes; Ostraciidae), smooth pufferfishes (puffers; Tetraodontidae), and spiny puffers (Diodontidae). Major features of swimming biomechanics and kinematics have been described for one or more species in each of the families (Ostraciidae: Gordon et al. 2000; Hove et al. 2001; Tetraodontidae: Gordon et al. 1996; Plaut and Chen 2003; Diodontidae: Arreola and Westneat 1996).

This paper is part of an effort to experimentally determine the hydrodynamic bases for the smooth and precise swimming performances of these fishes. Both unconscious and powered control mechanisms (Fish and Lauder 2006; Webb 2006) are involved (Gordon et al. 2000; Bartol et al. 2003, 2005). Among the puffers, fin and body movements serve as powered control mechanisms, and integumentary ornamentation (e.g., spines) and skin compliance properties are possible mechanisms for unconscious control (Brainerd 1994; Gordon et al. 1996; Arreola and Westneat 1996).

This paper describes major features of swimming biomechanics and kinematics in a previously unstudied species of spiny puffer, *Diodon holocanthus* (family Diodontidae) (Fig. 1). We made digital high-speed video recordings of five puffers swimming at different speeds in a water tunnel. Like other members of Diodontidae this species swims smoothly, but achieves its stability using substantially different patterns of body and fin movements, as compared with the only other species in its family whose fin kinematics have been studied (the burrfish, *Chilomycterus schoepfii*; Arreola and Westneat 1996). Major morphological differences between the species are their body shapes and the fact that *D. holocanthus*' spines are long, straight, and lie flat while *C. schoepfii*'s are short, curved and stand erect.

Swimming patterns in the two diodont species are both different from patterns shown by the tetraodont smooth puffers, which seem to show less within group variability (Tetraodontidae; Gordon et al. 1996; Plaut and Chen 2003). All of these patterns are again different from the patterns

A. M. Wiktorowicz · D. V. Lauritzen · M. S. Gordon (✉)
Department of Ecology and Evolutionary Biology,
University of California-Los Angeles,
Los Angeles, CA 90095-1606, USA
e-mail: msgordon@ucla.edu

G.K. Taylor, M.S. Triantafyllou, and C. Tropea (Eds.): Animal Locomotion, pp. 87–97.
springerlink.com

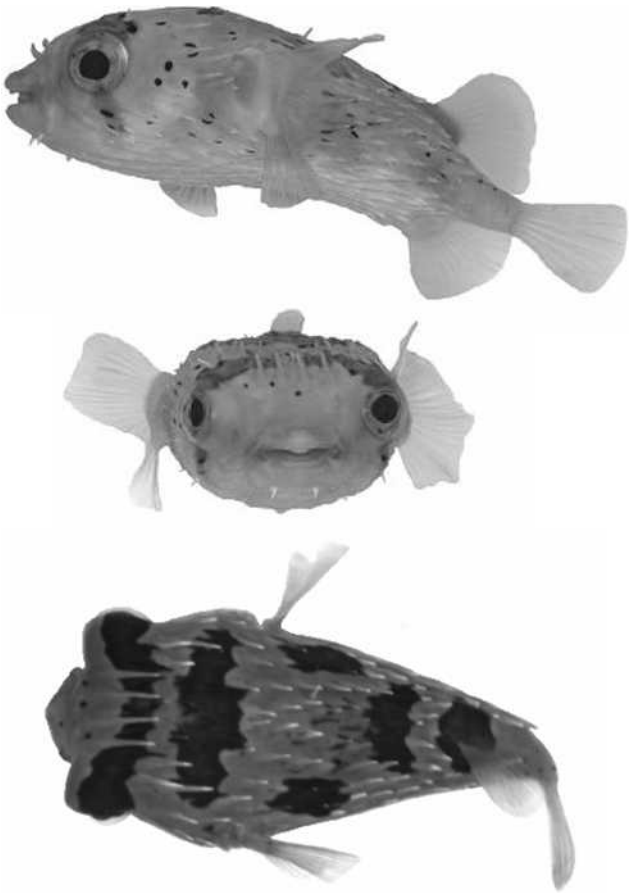

Fig. 1 *Diodon holocanthus* in lateral, anterior, and dorsal perspectives

shown by the ostraciid tropical boxfishes (Gordon et al. 2000; Hove et al. 2001). The array of these differences justifies changing the definitions used by students of fish locomotion to characterize what have been (loosely) termed tetraodontiform and ostraciiform locomotion.

2 Experiments

2.1 Animals

Five porcupine puffers were purchased from a fish supplier. The masses of the fish were 159 ± 38 g (SD, $N = 5$); mean lengths were 16.8 ± 1.6 cm (total length, *TL*, SD, $N = 5$), 14.5 ± 1.4 cm (body length, *BL*, SD, $N = 5$). These mean lengths are at the lower length range for the adults of this species. They were captured in various locations in Mexico, Belize, Brazil, and the Indo-Pacific. They were held separately in individual aerated flow-through aquaria. Maintenance followed standards of UCLA's Animal Research Committee (protocol #2003-057-11). Photoperiods were 12 h:12 h L:D; water temperatures and salinities were 27 ± 2°C and 27 ± 3‰, respectively. Fish were fed mussels, clams, squid, and shrimp.

2.2 Water tunnel

High-speed digital video recordings were made of fish swimming over a range of steady swimming speeds in a 2,625 l volume closed circuit, temperature-controlled water tunnel (Engineering Laboratory Design, Inc., Lake City, MN). The working section was made of clear acrylic plexiglas (100 × 30 × 37.5 cm). To produce laminar flow the section was bounded upstream by a large Venturi constriction section, a 7.6 cm-long precision, round cell, polycarbonate plastic honeycomb section, three stainless steel perforated plates, and four high porosity stainless steel screens. The section was bounded downstream by a high porosity stainless steel screen and acrylic plexiglas flow-directing channels. Water velocities of 6.5–56 cm/s were generated by two computer-controlled, enclosed impeller, stainless steel centrifugal pumps. Water temperatures and salinities were the same as for fish maintenance. Water temperatures were controlled via two thermostated external chillers circulating cold fresh water through two stainless steel countercurrent heat exchangers.

2.3 Videography

Digital high-speed video recordings of swimming fish were made at 125 frames/s (fps) using two electronically synchronized Redlake Motionscope HR500 high-speed cameras. Camera computer memories permitted continuous filming of 2 s sequences. Lateral and ventral views were recorded simultaneously. A 45° front surface mirror was placed directly under the working section so that a camera placed to the side of the section could record ventral views. Illumination was by a 250 W Mini-Pro Berkeley Colortran stage light and two incandescent lamps. The top and back of the section were covered in black fabric to provide clearer, high-contrast images. Sequences used for analyses were those in which the fish swam in the upstream half of the section, near the center (to minimize possible wall effects).

2.4 Protocols

Fish were fasted 24 h prior to swimming experiments to limit potential variability in swimming performance caused by digestion. A flashing green LED light housed in a hollow plastic tube connected to a bicycle light was used to condition fish to swim in the camera field. The LED lure and was removed when the fish approached and several seconds were allowed to pass before capturing the video to eliminate possible interference from residual water turbulence.

Fish were placed in the working section of the water tunnel and maintained at zero current speed for 1 h where their swimming behaviors were observed, after which flow speed was increased to 0.5 BLs^{-1}. They swam for 15 min at this speed to acclimate before filming commenced. Fish were filmed for five 2 s duration sequences at the current speed, after which speeds were increased by 0.5 $BL\ s^{-1}$ (total time spent at each speed was 30 min). This procedure was repeated until the fish could swim no faster, fatigued, and became pinned against the downstream screen. More than thirty-five 2 s sequences per fish were filmed at swimming speeds of 0.5–3.5 $BL\ s^{-1}$.

Critical swimming speeds (U_{crit}) were measured according to standard protocols (Brett 1964) by increasing swimming speed by 0.5 $TL\ s^{-1}$ increments every 10 min until fish fatigued and were pinned against the watertunnel's downstream screen. Critical swimming speeds were calculated from the equation:

$$U_{crit} = U_i + (U_{ii} \times t_{ii}/t_i)$$

U_i highest swimming speed at which fish swam for duration of experiment; U_{ii} speed increment; t_{ii} length of time fish swam at fatigue speed; t_i time increment.

U_{crit} measurements were repeated 2–3 times per fish with at least 48 h separating each trial.

2.5 Video analyses

Video sequences were transferred from the computer memories of the high-speed cameras to a Dell Dimension 4600 computer via an ULead Video Studio frame-grabber. Each sequence was 256 frames in length (2.048 s). These were edited with Virtual Dub1.5.10 (Avery Lee, Concord, CA).

Landmarks were identified and marked using Image J, a National Institutes of Health (NIH) imaging program. Fifteen measurements of physical landmark positions were made for either all frames or every second frame in sequences of lateral views; nine measurements were made for either all frames or every second frame in sequences of ventral views. Various technical reasons made it necessary to do this.

Landmarks in lateral views were: lower jaw tip; dorsal insertion of left pectoral fin; anterior/posterior insertions of dorsal and anal fins; dorsal/ventral insertions of caudal fins; outer tips of those caudal fin rays; distal tips of the leading edges on the pectoral, dorsal, and anal fins; and the trailing edges of the dorsal and anal fins. The same landmarks were used in ventral views, minus the four on the dorsal fins and the dorsal edges of the caudal base and fin. Based on the movements of these landmarks, kinematic parameters were calculated using a series of custom-written algorithms in two programs (Mathematica 3.0 and Matlab 6.0.0.42a Release 12). Parameters included pectoral, dorsal, anal, and caudal fin beat frequencies; fin beat amplitudes; body angles of attack; and rotational (yaw, pitch, roll) and translational (surge, heave, sideslip) recoil movements. More than 16,700 frames were digitized.

To determine propulsor kinematics and coordination we analyzed sequences from all five fish at 5–7 speeds per fish (some fish swam at higher speeds than others). Three of the highest quality sequences were selected per speed per fish, for a total of 120 video sequences. Ventral views were used to measure angular positions of the pectoral, anal, and caudal fins. Angular positions, instead of distance, were used to avoid allometric differences between fish. Fin positions were calculated as the angles between the lines joining the insertions and the leading edge tips of each fin, and a line drawn between the tip of the jaw and anterior anal fin insertion. In ventral views the anal fin obscured the dorsal fin, but posterior views showed that the dorsal and anal fins [the dorsal-anal (DA) fin complex; usage following Hove (2001)] always beat synchronously. Movements of the DA complex were therefore quantified based only on anal fin movements.

Median fin-beat cycles were defined as starting from and returning to the maximum (left or right) lateral excursion. Pectoral fin-beat cycles began with the fins pressed against the body (maximally adducted), moving away (abducting) from the body to a maximum point of excursion and returning (adducting) to the original position.

We also measured the amplitudes of fin tip positions during single fin-beat cycles for each fin at all swimming speeds by converting the Cartesian coordinates to polar coordinates. Maximal DA and caudal fin movements to the right and left were assigned to +90° and –90°, respectively; maximal pectoral adductions and abductions were assigned to 0° and ±180° respectively, positive representing the right fin and negative representing the left fin. Fin beat frequencies (Hz) were determined by taking the Fourier transform of the amplitudes, $\theta(t)$, and locating the frequency at which the transform variable, $\theta\hat{}(s)$, was the largest. A Fourier transform was needed as fin beats were often too noisy to allow for the traditional method of hand counting number of beats/time. The dominant frequency was 2.5 Hz.

Phase lags between fins were calculated to determine oscillation patterns/multiple fin coordination and to determine whether these values varied over swimming speed. If two fins move at the same frequency, their phase lags can range from 0° (synchrony) to 180° (asynchrony) to 360° (synchrony) (Denny 1988). The relative positions of the fins during fin beat cycles were used to calculate phase lags by determining the position of one fin at the time of maximum abduction of another fin. Significant changes in

fin beat frequencies, amplitudes, and phase lags allowed for the identification of gait transitions.

2.6 Determination of centers of mass and buoyancy

In previous studies the centers of mass and buoyancy were determined on sacrificed fish. However, the fish used in these experiments were trained and needed for further studies, so we used an alternative, harmless method. Traditional and alternative methods were compared on puffers that had died naturally and were found to produce identical results.

The position of the center of mass was determined by locating the point at which an anesthetized fish on a lightweight tray balanced on a fulcrum (Bierman et al. 2004). Individual fish were placed on a styrofoam tray that had centimeter markings. With the fish's rostrum placed at 0 cm, the tray was moved across the fulcrum until it balanced, and the position (cm from nose) was recorded. In ventral views this was identical to the point at which the body midline intersected a virtual line connecting the left and right pectoral fin bases.

To assure that the center of buoyancy was on the same plane as the center of mass, the center of buoyancy was measured as the center of mass when the fish was submerged (Weihs 1993). This was determined by suspending an anesthetized fish in water by a string that was lightly secured to the dorsal, caudal, and anal fin bases. Digital pictures documented the positions of the fish's body as it was suspended by each fin base in turn. Digital overlay allowed the strings to be intersected, revealing the position of the center of buoyancy.

2.7 Recoil movements

Six possible recoil motions exist for a rigid body resulting from propulsor movements, three translational and three rotational. Translational recoil is movement in a plane containing the center of mass (heave, surge, and sideslip). Rotational recoil is rotary movement around an axis that passes through the center of mass (pitch, yaw, and roll). Recoil motions should, in principle, be measured at the center of mass.

In lateral views pitch was estimated as the angle from the horizontal subtended by a virtual line connecting the snout tip to the middle of the caudal base (estimated by connecting the upper and lower caudal bases) relative to the center of mass. In ventral views yaw was estimated as the angle subtended by a virtual line connecting the center of mass and the snout tip, with respect to the direction of motion of the fish. The side-to-side movements of a virtual line connecting the jaw and anal fin origin seen in ventral views of the swimming fish were used to measure sideslip. Heave and surge were measured from *y*- and *x*-motions, respectively of the virtual center of mass seen in the side view. Roll was examined through the clear posterior section of the water tunnel, but it was not quantified as high quality video was difficult to collect.

2.8 Statistical analysis

Mean values of measured kinematic parameters for each speed were calculated for each fish. Pectoral fin sample means were compared using a two-tailed paired sample Student's *t*-test. Least squares linear regressions were used where appropriate to describe the relationships between kinematic averages and swimming speed. Results were considered significant if $p < 0.05$. Analyses were performed using Matlab 6.0.0.42a Release 12 and Stata 9.3. Values are presented ±1 standard error of the coefficient or mean (SE and SEM, respectively), or standard deviation (SD).

3 Results and discussion

3.1 General morphology

The center of mass was located at 34.4 ± 0.3% *TL* (SD) posterior of the snout tip and the center of buoyancy was at 39.0 ± 0.4% *TL* (SD). Both centers were located on the midline, the center of buoyancy was above the center of mass.

Figure 1 shows the body shape and the positions/sizes of the fins of *D. holocanthus* in lateral, anterior, and dorsal views. The lateral profile is airfoil shaped, the antero-ventral portion possibly generating significant lift as the fish moves through the water. On occasion the lateral profile can resemble the prolate spheroid that occurs more often in smooth puffers, depending on the individual fish. The body cross-section anteriorly is ovoid, with no sharp angles or keels. It is markedly wider than it is deep (major axis is horizontal).

Brainerd (1994) showed that the antero-ventral skin of the porcupine puffer is extremely pliable and distensible, which is an important part of the basis for the species' ability to swallow fluid to inflate itself into a sphere when alarmed. In smooth puffers the same area of the integument significantly stretches and deforms as the fishes swim faster, changing their lateral profiles (Gordon et al. 1996). This was not seen in either the burrfish (Arreola and Westneat 1996) or the porcupine puffer. In both of the diodont species this resistance to deformability is likely due to the presence of the embedded rigid spines.

3.2 Critical swimming speed

Porcupine puffers achieved a mean U_{crit} of 3.6 ± 0.3 *TL* s^{-1} (SD). This value falls within the usual range for other median and paired fin (MPF) swimmers. It is lower than the speeds achievable by some ostraciid tropical boxfish (*Ostracion meleagris*: 3.2–4.6 *TL* s^{-1}; Gordon et al. 2000) and some triggerfish, but similar to speeds attained by some parrotfish (parrotfish, *Scarus schlegeli*: 2.8–3.7 *TL* s^{-1}; triggerfish, *Rhineacanthus aculeatus*: 3.2–5.0 *TL* s^{-1}; Korsmeyer et al. 2002). It is also comparable to speeds attained by many species of body and caudal fin (BCF) swimmers (Hove et al. 2001; Webb 2006).

3.3 Swimming biomechanics and gaits

Past descriptions of tetraodontiform locomotion state that puffers propel themselves using only oscillations of their dorsal and anal fins (Breder 1926; Lindsey 1978). More recent quantitative observations of smooth puffers (Gordon et al. 1996; Plaut and Chen 2003), burrfish (Arreola and Westneat 1996), and porcupine puffers (this paper) show that these generalizations are incomplete. Porcupine puffers, in this respect, use each fin at some speed, but most importantly their caudal fins beat actively at most speeds. Table 1 compares the major features of swimming kinematics in the two species of diodont puffers, the smooth puffers, and in tropical boxfish (Arreola and Westneat 1996; Gordon et al. 1996; Plaut and Chen 2003; Hove et al. 2001).

Porcupine puffers are multi-propulsor swimmers that use varying combinations of their pectoral, dorsal, anal, and caudal fins. They have at least four gaits (Table 1): (1) pectoral–dorsal–anal fin dominant (PDA); (2) all fins (pectoral, dorsal, anal, and caudal fins); (3) median fins only (here we define median fins as the dorsal, anal, and caudal fins); and (4) burst and coast swimming (rapid body undulations coupled with any combination of median fin beats).

3.3.1 Pectoral fin movements

The pectoral fins are used only for hovering (0 *BL* s^{-1}; from observations) and at low swimming speeds (0.5–1.5 *BL* s^{-1}; Figs. 2, 4). Left and right fin movements are not significantly different ($p > 0.05$) except when fish independently move them for posture correction. Forward strokes (abduction) begin with the leading edge moving anteriorly and laterally away from the body. This initiates a sequence of undulatory individual ray movements, and ends with the anterior-lateral excursion of the trailing edge. Observations made of both pectoral fins reveal one or the other can beat as the fish hover or swim at speeds up to 0.5 *BL* s^{-1}, but more often the pectoral fins undulate together continuously and alternately (left fin moving forward while right fin moves backward, and vice versa).

From 0.5 to 1.0 *BL* s^{-1} the pectoral fins predictably beat continuously and alternately (Fig. 2). At 1.5 *BL* s^{-1} there is a combination of fin usage and non-usage (gait transition, see gait section for details). Continuously alternating movements persist, but with rapidly decreasing amplitudes as speeds increase. Beyond 2.0 *BL* s^{-1} the pectorals are fully adducted to the sides of fish and do not participate in thrust generation (Fig. 4) which is unlike most pufferfish.

Table 1 Fin beat patterns and gait comparisons reported for pufferfish and boxfish

	Pectoral	Dorsal/anal	Caudal	Gaits
D. holocanthus	Alt, stop at 2.0 *BL* s^{-1}	+, used at all speeds	– with DAC (peduncle), forms c-shape, used at all speeds	4; PDA dominant, all fins, median fins only, median fins/ CBC
C. schoepfii (Arreola and Westneat 1996)	Alt, used at all speeds	+, used at all speeds	– with DAC (peduncle), forms c-shape, used at all speeds	± paired and median fins
A. meleagris and *A. nigropunctatus* (Gordon et al 1996)	Alt, used at all speeds	+, used at all speeds	Stationary except at CBC	N/A
T. schoutedeni (Plaut and Chen 2003)	Alt, used at all speeds	+, used at all speeds	Stationary except at CBC	N/A
O. meleagris (Hove et al 2001)	+ and –, used at all speeds	+, used at all speeds	Stationary except at CBC	3; PA dominant, DA dominant, CBC dominant

Alt alternate, + in phase, – 180° out of phase, *P* pectoral, *D* Dorsal, *A* Anal, *C* caudal, ± subtle phase difference; *CBC* caudal burst and coast swimming

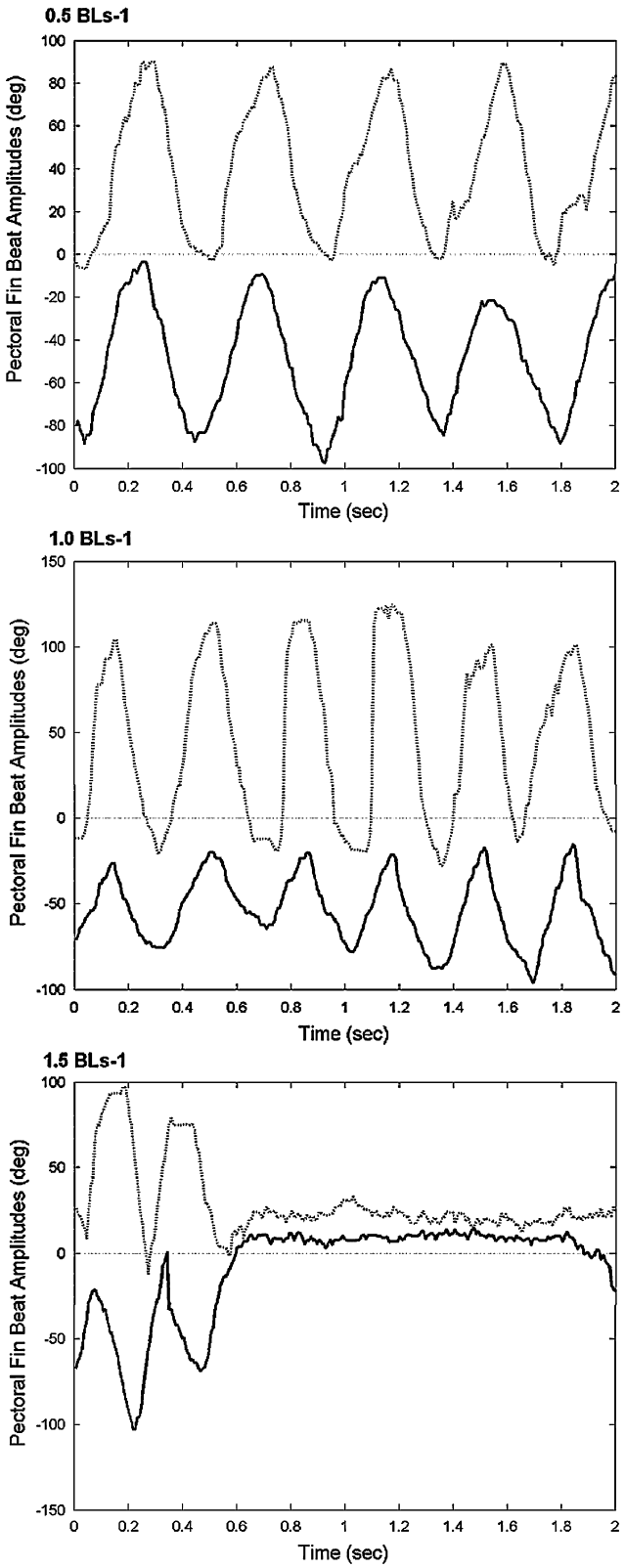

Fig. 2 Left (*solid*) and right (*dashed*) pectoral fin beat patterns of *D. holocanthus* at speeds 0.5–1.5 *BL* s^{-1}

Even in the closely-related burrfish the pectoral fins are used at all speeds (Table 1; Arreola and Westneat 1996).

3.3.2 Dorsal and anal (DA) complex movements

The leading edges of the dorsal and anal fins also initiate movements. DA fins are observed to undulate to manage trim control while the fish hover at 0 *BL* s^{-1}, but from 0.5 to 3.5 *BL* s^{-1} the fins steadily oscillate back and forth laterally, in phase. Fin rays appear to be kept fairly stiff and straight under all conditions.

3.3.3 Caudal fin movements

At very slow speeds (hovering and 0.5 *BL* s^{-1}) the caudal fin appears to move passively. At 1.0 *BL* s^{-1}, as the peduncle initiates lateral movements, the caudal fin begins its excursions with the outermost rays leading (Fig. 3). The middle rays lag. This creates a cupped shape span-wise, while the fin curves chord-wise. At 1.5 *BL* s^{-1}+, the rays of the tail appear to stiffen and straighten out the tail, although not completely. Seen especially at high speeds (2.0 *BL* s^{-1}+), the caudal peduncle beats out of phase with the leading rays, which in turn are in phase with the DA complex.

Among tetraodont fishes only *D. holocanthus* and *C. schoepfii* have been documented to actively use their caudal fins for thrust at cruising speeds. Kinematic data for *A. meleagris, A. nigropunctatus*, *T. schoutedeni*, and *O. meleagris* (Gordon et al. 1996; Plaut and Chen 2003; Hove et al. 2001) show that the caudal fins of these other fishes are rarely used prior to burst and coast swimming. In *D. holocanthus* and *C. schoepfii* the caudal fin moves actively throughout the range of swimming speeds. In *D. holocanthus* the caudal peduncle clearly moves out of phase with the DA complex and the caudal fin itself (Fig. 3). Since the body anterior to the caudal peduncle is rigid, these dramatic caudal fin excursions can only be initiated from the peduncle. Although Arreola and Westneat (1996) did not study caudal peduncle kinematics, personal observations of *C. schoepfii* suggest the fish also actively moves its caudal peduncle. Past descriptions of tetraodontiform locomotion state that the caudal fin remains stationary except for occasional fluttering movements caused by vortices shed by the anterior fins/body.

3.3.4 Gaits

The porcupine puffers have four gaits:

1. During hovering (0 *BL* s^{-1}) and at 0.5 *BL* s^{-1} puffers move by using varied combinations of all fins

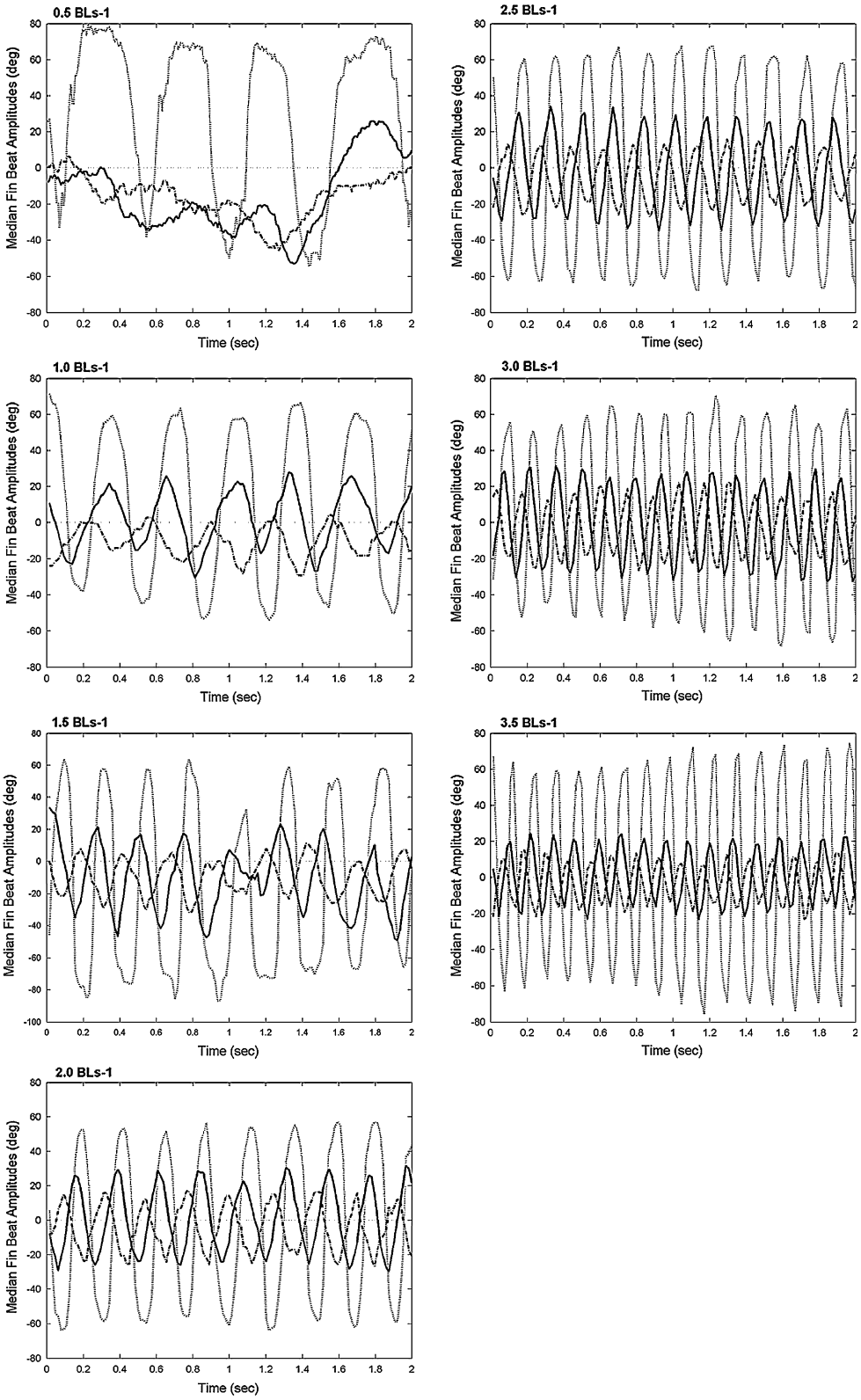

Fig. 3 Anal (*light dashed*), caudal base (*dark dashed*), and caudal fin (*solid*) fin beat patterns for *D. holocanthus* from 0.5 to 3.5 *BL* s^{-1}. Dorsal fin patterns are represented by the anal fin

(Figs. 2, 3, 4, 5), though the pectoral and dorsal-anal fins dominate (PDA dominant gait). This is largely due to the fish changing its trajectory and turning; at these speeds its pectoral fins are the major executors of turns and the dorsal and anal fins serve as minor thrust generators. The caudal fin is mostly used as a rudder as

shown by its weak fin beat trajectories (Fig. 3; 0.5 *BL* s^{-1}) and from observations (caudal peduncle was curved as fish carried out turns).

2. Pectoral, dorsal, anal, and caudal fin beats become regular as swimming speeds increase due to the fish rectilinearly swimming. Only between 1.0 and 1.5 *BL* s^{-1} are all fins continuously coordinated (all fins gait). At 1.5 *BL* s^{-1} there is a marked gait transition, indicated by intermittent pectoral fin beats.
3. At 2.0 *BL* s^{-1} and beyond, the pectoral fins remain close to the body and do not beat (Fig. 4), except for occasional minor fluttering of the trailing edges. From 2.0 to 3.5 *BL* s^{-1} the median fin only gait is seen, where only the DA complex and the caudal fin are used for propulsion.

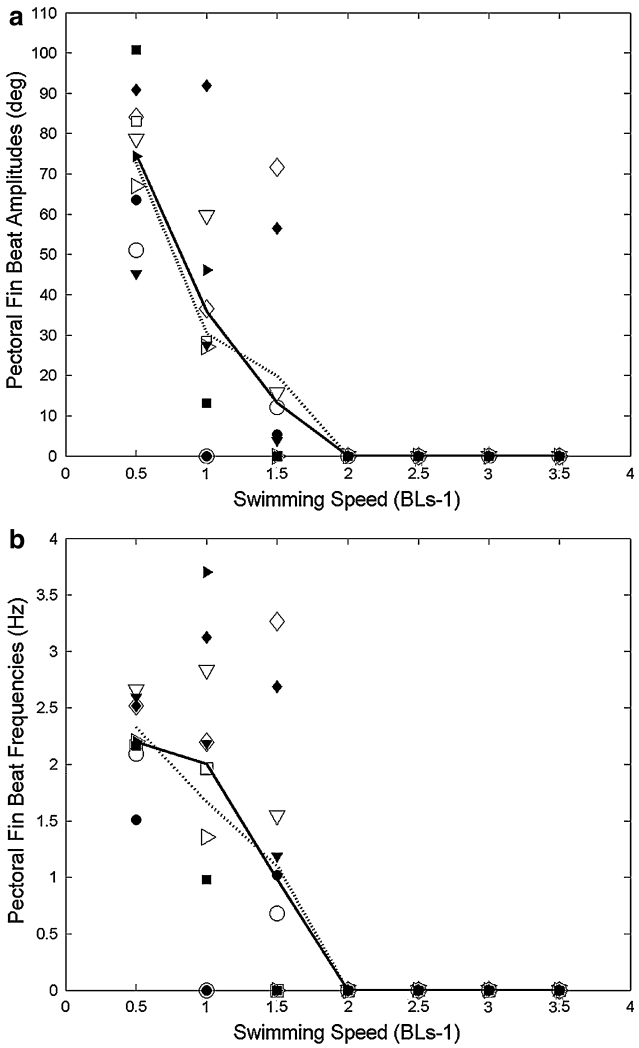

Fig. 4 Average left (*filled symbols*) and right (*open symbols*) pectoral fin beat amplitude and frequency. Each symbol represents an average for each fish ($N = 3$); total averages over all fish ($N = 5$) shown by lines (*solid*, *dashed*)

4. At speeds above 3.5 *BL* s^{-1} (from observations) fish are unable to steadily maintain their positions using only median fin movements; they add strong body undulations, marking the median fin/caudal burst and coast gait (CBC). Pectoral fins occasionally are used to correct trajectories.

These gait patterns are similar to those found by Hove et al. (2001) in boxfish but differ drastically from the more subtle gait changes of *C. schoepfii* (Table 1; Arreola and Westneat 1996). The boxfish, *O. meleagris*, have three gaits: pectoral-anal fin dominant (PA; 0–1 *TL* s^{-1}), anal-dorsal fin dominant (AD; 1–5 *TL* s^{-1}), and caudal burst and coast (CBC, 5+ *TL* s^{-1}). During the PA gait the boxfish are changing their trajectories, moving their left and right pectoral fins either synchronously (in phase) or asynchronously (180° out of phase), while beating their anal fins at variable frequencies. This seemingly chaotic gait is likely associated with the numerous turns executed and for supporting the weight of the fish in water (Hove et al. 2001; Webb 1993). The next gait (AD gait) is used over the largest part of the boxfish's swimming range. This is characterized by linearly-increasing frequencies and amplitudes of the anal, dorsal, and pectoral fin beats (though the latter increases at a slower rate and its amplitude plateaus above 3 *TL* s^{-1}). The final gait (CBC gait) is marked by the recruitment of the otherwise quiescent caudal fin in the burst and coast swimming mode. Here the fins that were active previously are aligned with the body axis (dorsal and anal) or adducted (pectoral) to reduce drag.

The gait transitions of *C. schoepfii* can at best be described as subtle (Arreola and Westneat 1996); distinct fin usages seen in *D. holocanthus* and *O. meleagris* are not present. Instead, variable phase relationships between the fins are necessarily used to mark the three gait transitions (<2 *SL* s^{-1}, 2–4 *SL* $s^{-1}$and 3–6 *SL* s^{-1}; standard length; identical to *BL* in this study). *C. schoepfii* is the only puffer shown to execute continuous fin movements of all fins over its entire swimming range.

3.4 Median and paired fin kinematics

Frequencies and amplitudes of median and caudal fin movements are linearly related to swimming speeds over substantial ranges (Fig. 5). Interestingly, theoretical amplitude maximums were never reached (180° for pectoral fins, +90° and –90° for the median fins), possibly due to structural constraints on the fins and fin bases.

Among individual fish, pectoral fin beat frequencies are more variable than dorsal, anal, and caudal fin beat frequencies (Figs. 4, 5). Amplitudes and frequencies of the left and right pectoral fins are not significantly different

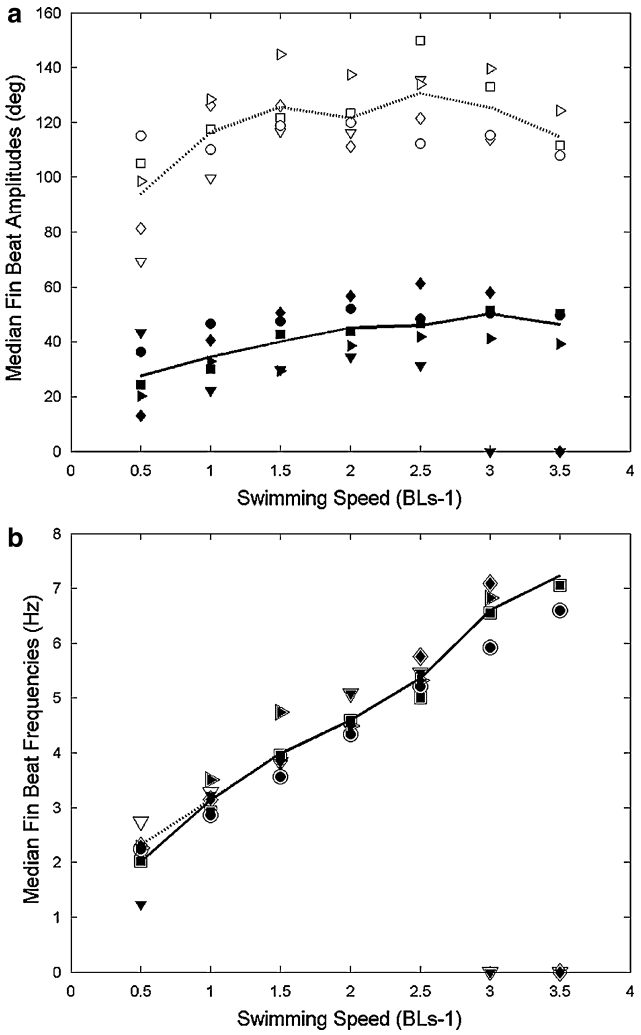

Fig. 5 Average anal (*open symbols*) and caudal (*filled symbols*) fin beat amplitude and frequency. Each symbol represents averages for individual fish; total averages are shown by *lines* (anal = *dashed*, caudal = *solid*)

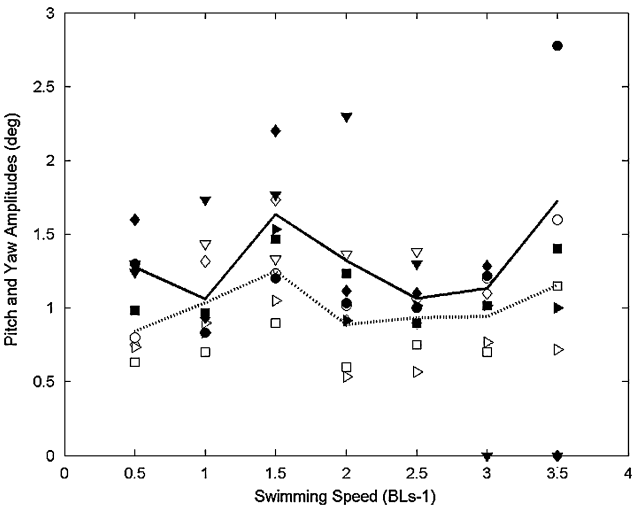

Fig. 6 Average pitch (*open symbols*) and yaw (*filled symbols*) amplitudes. Each symbol represents averages for individual fish; total averages are shown by *lines* (pitch = *dashed*; yaw = *solid*)

($p > 0.05$). At 0.5, 1.0, 1.5 *BL* s^{-1} pectoral fin beat frequencies range from 1.5 to 2.7, 0 to 3.7, and 0 to 3.3 beats s^{-1} respectively. Pectoral fin beat frequencies are inversely related to speed (least squares regressions: $y = -0.82x + 2.36$, right fin; $y = -0.83x + 2.39$, left fin). Average amplitudes at 0.5, 1.0, and 1.5 *BL* s^{-1} range from 45 to 101°, 0 to 92°, and 0 to 72° respectively (regressions: $y = -21.35x + 60.27$, right fin; $y = -22.11x + 61.92$, left fin).

Beat frequencies for the DA complex increase at nearly the same rate (regression: $y = 1.64x + 1.46$; $p < 0.01$; SE 0.07) as caudal fin beat frequency (regression: $y = 1.71x + 1.27$; $p < 0.01$; SE 0.08). DA and caudal fin beat amplitudes increase with speed and range from 69–115° to 108–150°, and 13–43° to 39–61° respectively (DA complex regression: $y = 7.51x + 104.25$; $p < 0.05$; SE 2.83; caudal fin regression: $y = 7.21x + 27.22$; $p < 0.01$; SE 1.74). No refractory periods are observed at the points of direction change during fin beat cycles of any of the median and paired fins, indicating constant thrust production in both directions at all speeds. This is similar to kinematically-derived constant thrust production seen in *C. schoepfii* (Arreola and Westneat 1996).

3.5 Recoil movements and angles of attack

Puffers swim horizontally at all speeds except when hovering; angles of attack at very low speeds are variable. Pitch and yaw values are small at all speeds and do not vary significantly with speed (Fig. 6). Pitch and yaw amplitudes range from 0.5 to 1.7° (regression: $y = 0.03x + 0.94$; $p > 0.05$; SE 0.06) and 0.8–2.8° (regression: $y = 0.04x + 1.21$; $p > 0.05$; SE 0.09), respectively. No roll is detectable. Translational recoil movements (heave, surge, sideslip) are undetectable above noise levels at all speeds (<1 mm displacements).

Compared to values found by Hove et al. (2001) for boxfish (pitch = 0.004; yaw = 0.013), porcupine puffers show similarly low, but somewhat larger values for pitch and yaw. These recoil values are especially interesting as boxfish have rigid keels and ornaments on their bony carapaces that act as continuous generators of vorticity that changes position as angles of attack change (Bartol et al. 2002). These moving vortices are integral to maintaining stable swimming (Bartol et al. 2003, 2005; Weihs 1993; Webb 2000). All puffers lack such rigid protuberances, yet *D. holocanthus* is as stable a swimmer as the boxfish. Our study shows that porcupine puffers rely primarily on their

coordinated fin movements to minimize recoil, and possibly on their body shapes.

4 Conclusions

The classical definitions of tetraodontiform and ostraciiform swimming developed initially by Breder (1926) and used subsequently by many others did not take into account the impact of changes in speed on the variations and complexities of swimming patterns and gaits in these groups. The more recent results cited here lead us to suggest that the term tetraodontiform swimming be restricted to the smooth puffers (family Tetraodontidae), which seem to show little within group variation in swimming biomechanics and kinematics. The diodont puffers appear to have substantial within group variability in these respects. It is probably best to describe MPF swimming in the diodont context as stable swimming with varying combinations of all fins, at all speeds.

Destabilizing forces caused by the recoil movements that are linked to BCF modes of swimming significantly increase drag on fishes (Lighthill 1971; Webb 1975). Smaller recoil movements occur in fishes using rigid-bodied MPF swimming modes. This is specifically the case for the tropical boxfishes (Gordon 2000; Hove et al. 2001; Bartol et al. 2003, 2005).

Hanke and Bleckmann (2004) showed that the wakes of swimming smooth puffers attenuate quickly and show no substantial lateral motions. Until now no direct recoil measurements have been made on pufferfishes. *D. holocanthus*' insignificant recoil movements further demonstrate stable MPF swimming.

Recent results demonstrate that both unconscious and powered control mechanisms play major roles in the control of swimming posture and trajectory in both BCF and MPF swimmers (Fish and Lauder 2006; Standen and Lauder 2007). *D. holocanthus* achieves high postural and trajectory stability through powered mechanisms that include thrust production and dampening of yawing forces generated by the side-to-side motions of the DA complex, countered by out of phase movements by the caudal peduncle/fin. The pectoral fins at low speeds probably control pitch and are used for maneuvering and posture correction (personal observation). The lack of a refractory period in DA oscillations and the constant phase relationship between the DA and caudal fins suggest that constant thrust is generated at all speeds by the median fins. Nothing is known about the directions of the thrust vectors developed by these fins. At higher swimming speeds the trailing edges of the pectoral fins of *D. holocanthus* flutter in what may be powered movements. The lower parts of these edges extend below the body. These movements may also contribute to stability control, such as the pelvic fins of brook trout (Standen and Lauder 2007).

Unconscious control mechanisms may be a significant part of the basis for smooth, stable swimming by the porcupine puffer and require further examination. The lateral profile of the body implies that, under many conditions, flows over the body generate significant lift that could counteract sinking tendencies that might result if the fish is slightly negatively buoyant. The broad, normally flat-bottomed, anterior section of the body may act to produce significant drag that would resist pitching tendencies that could result from small asymmetries in paired fin positions and areas.

Acknowledgments We thank Devin Conroy, Jon Valencia, Moi Yue Kouch, and Kennedy Wheatley for their administrative and logistical support for this project. We also thank Rick Klufas and John Milligan of the UCLA Life Sciences machine and electrical shop for fabrication of the LED lure and for help with water tunnel maintenance, and Eric Cohen (Sea Dwelling Creatures, Inc., Los Angeles, CA) for providing the porcupine puffers. Thanks to Felicia Coleman and staff, Florida State Univ. Marine Laboratory, St. Teresa, FL for logistic support. Funding from the Department of Ecology and Evolutionary Biology's Bartholomew Research Fund at UCLA made this work possible.

References

Arreola VI, Westneat MW (1996) Mechanics of propulsion by multiple fins: kinematics of aquatic locomotion in the burrfish (*Chilomycterus schoepfi*). Proc R Soc Lond Ser B 263:1689–1696

Bartol IK, Gharib M, Weihs D, Webb PW, Hove JR, Gordon MS (2003) Hydrodynamic stability of swimming in ostraciid fishes: role of the carapace in the smooth trunkfish *Lactophrys triqueter* (Teleostei: Ostraciidae). J Exp Biol 206:725–744

Bartol IK, Gordon MS, Gharib M, Hove JR, Webb PW, Weihs D (2002) Flow patterns around the carapaces of rigid-bodied, multi-propulsor boxfishes (Teleostei: Ostraciidae). Integr Comp Biol 42:971–980

Bartol IK, Gharib M, Webb PW, Weihs D, Gordon MS (2005) Body-induced vortical flows: a common mechanism for self-corrective trimming control in boxfishes. J Exp Biol 208:327–344

Bierman HS, Schriefer JE, Zottoli SJ, Hale ME (2004) The effects of head and tail stimulation on the withdrawal startle response of the rope fish (*Erpetoichthys calabaricus*). J Exp Biol 207:3985–3997

Brainerd EL (1994) Pufferfish inflation: functional morphology of postcranial structures in *Diodon holocanthus* (Tetraodontiformes). J Morphol 220(3):243–261

Breder CM (1926) The locomotion of fishes. Zoologica (NY) 4:159–297

Brett JR (1964) The respiratory metabolism and swimming performance of young sockeye salmon. J Fish Res Board Can 21:1183–1226

Denny MW (1988) Biology and the mechanics of the wave swept environment. Princeton University Press USA

Fish FE, Lauder GV (2006) Passive and active flow control by swimming fishes and mammals. Annu Rev Fluid Mech 38:193–224

Gordon MS, Plaut I, Kim D (1996) How puffers (Teleostei: Tetraodontidae) swim. J Fish Biol 49:319–328

Gordon MS, Hove JR, Webb PW, Weihs D (2000) Boxfishes as unusually well-controlled autonomous underwater vehicles. Physiol Biochem Zool 73(6):663–671

Hanke W, Bleckmann H (2004) The hydrodynamic trails of *Lepomis gibbosus* (Centrarchidae), *Colomesus psittacus* (Tetraodontidae) and *Thysochromis ansorgii* (Cichlidae) investigated with scanning particle image velocimetry. J Exp Biol 207:1585–1596

Hove JR, O'Bryan LM, Gordon MS, Webb PW, Weihs D (2001) Boxfishes (Teleostei: Ostraciidae) as a model system for fishes swimming with many fins: kinematics. J Exp Biol 204:1459–1471

Korsmeyer KE, Steffensen JF, Herskin J (2002) Energetics of median and paired fin swimming, body and caudal fin swimming, and gait transition in parrotfish (*Scarus schlegeli*) and triggerfish (*Rhinecanthus aculeatus*). J Exp Biol 250:1253–1263

Lighthill MJ (1971) Large-amplitude elongated-body theory of fish locomotion. Proc R Soc Lond Ser B 179:125–138

Lindsey CC (1978) Form, function and locomotory habits in fish. In: Hoar WS, Randall DJ (eds) Fish Physiology, Vol VII, Locomotion. Academic, New York pp 1–100

Plaut I, Chen T (2003) How small puffers (Teleostei: Tetraodontidae) swim. Ich Res 50:149–153

Standen EM, Lauder GV (2007) Hydrodynamic function of dorsal and anal fins in brook trout (*Salvelinus fontinalis*). J Exp Biol 210:325–339

Webb PW (1993) The effect of solid and porous channel walls on steady swimming of steelhead trout, *Oncorhyncus mykiss*. J Exp Biol 178:97–108

Webb PW (1975) Hydrodynamics and energetics of fish propulsion. Bull Fish Res Board Can 190:1–158

Webb PW (2006) Stability and maneuverability, In: Shadwick RE, Lauder GV (eds) Fish biomechanics. Elsevier and Academic, Amsterdam, pp 281–332

Webb PW (2000) Maneuverability versus stability? Do fish perform well in both? 1st international symposium on aqua bio-mechanisms/international seminar on aqua bio-mechanisms vol 1:21–29

Weihs D (1993) Stability of aquatic animal locomotion. Cont Math 141:443–461

Fluid dynamics of self-propelled microorganisms, from individuals to concentrated populations

Luis H. Cisneros · Ricardo Cortez · Christopher Dombrowski · Raymond E. Goldstein · John O. Kessler

Received: 13 February 2007 / Revised: 16 July 2007 / Accepted: 21 August 2007 / Published online: 6 October 2007

Abstract Nearly close-packed populations of the swimming bacterium *Bacillus subtilis* form a collective phase, the "Zooming BioNematic" (ZBN). This state exhibits large-scale orientational coherence, analogous to the molecular alignment of nematic liquid crystals, coupled with remarkable spatial and temporal correlations of velocity and vorticity, as measured by both novel and standard applications of particle imaging velocimetry. The appearance of turbulent dynamics in a system which is nominally in the regime of Stokes flow can be understood by accounting for the local energy input by the swimmers, with a new dimensionless ratio analogous to the Reynolds number. The interaction between organisms and boundaries, and with one another, is modeled by application of the methods of regularized Stokeslets.

L. H. Cisneros · C. Dombrowski · R. E. Goldstein · J. O. Kessler (✉)
Department of Physics, University of Arizona,
1118 E. 4th St., Tucson, AZ 85721, USA
e-mail: kessler@physics.arizona.edu

L. H. Cisneros
e-mail: cisneros@physics.arizona.edu

C. Dombrowski
e-mail: dombrows@gmail.com

R. Cortez
Department of Mathematics, Tulane University,
6823 St. Charles Ave., New Orleans, LA 70118, USA
e-mail: rcortez@tulane.edu

R. E. Goldstein
Department of Applied Mathematics and Theoretical Physics,
Centre for Mathematical Sciences, University of Cambridge,
Wilberforce Road, Cambridge CB3 0WA, UK
e-mail: R.E.Goldstein@damtp.cam.ac.uk

1 Introduction

The fluid dynamics of fast, large self-propelled objects, ranging from krill to whales, mosquitoes to eagles, is extensively studied and intuitively understood (Childress 1981). In these cases the Reynolds number *Re* ranges from somewhat >1 to enormous. At the other end of the spectrum are microscopic swimmers: bacteria, uni- and multicellular algae, and protists: which, although capable of swimming many body lengths per second, live in the regime $Re \ll 1$. While the essential features of the swimming of individual organisms of this type are known (Lighthill 1975; Berg 2003), the manner in which the flows associated with locomotion couple many such swimmers to each other and to nearby surfaces are only now being fully explored. Flows generated cooperatively by flagella of unicellular organisms and by those of multicellular organisms can also drive significant advective transport of molecular solutes associated with life-processes (Solari et al. 2006, 2007; Short et al. 2006).

In this paper we provide experimental and theoretical insights into the remarkable collective dynamics of a particular bacterial system, expanding on our original reports (Dombrowski et al. 2004; Tuval et al. 2005). Much microbio-hydrodynamical research has focused on the morphologically similar swimming bacteria *Escherichia coli*, *Salmonella typhymurium* and *Bacillus subtilis*. The chief results described in this paper are derived from our investigations of fluid dynamical phenomena driven by individual and collective swimming of *B. subtilis*.

G.K. Taylor, M.S. Triantafyllou, and C. Tropea (Eds.): Animal Locomotion, pp. 99–115.
springerlink.com

Individual cells of these generally non-pathogenic soil bacteria are rod-shaped (Fig. 1). Their length ranges from 2 to 8 μm, depending on nutrition and growth stage. In typical experiments they are approximately 4 μm long and somewhat less than 1 μm in diameter. They are peritrichously flagellated: the helical flagella, their means of propulsion, are distributed randomly over the cell body, emerging from motors that are fixed within the cell membrane. The shafts are able to rotate at various rates, typically on the order of 100 Hz. The flagella themselves are complex polymeric structures approximately 20 nm in diameter, with a length of 10–15 μm, considerably greater than a cell's body, and a helical pitch of $\sim$2–4 μm. They are attached to the motors by a flexible hook which acts as a universal joint. When a bacterial cell swims smoothly forward, hydrodynamic interactions between the many helical flagella cause the formation of a propulsive bundle within which they co-rotate. The swimming speed of an individual is approximately 11% of the helix wave speed (Magariyama et al. 1995, 2001). The motors are fueled by proton gradients; their direction of rotation is reversible. Spontaneous reversals may occur as a function of the surrounding concentration of chemicals and of other factors and can play a major role in chemotaxis (Berg 1993, 2003). The cell bodies are not polar. The flagellar bundle can form at either end of a cell, whether *E. coli* (Turner and Berg 1995) or *B. subtilis* (Cisneros et al. 2006), an important aspect of group locomotion discussed later.

A single swimming bacterium has associated with it an extensive flow field which is produced entirely by drag forces on the fluid, exerted forward by the cell body and backward by the flagella. No wake remains behind moving cells or cell groups. When a cell stops rotating its flagella, all motion of the fluid and of the cell ceases. Motor boats are not analogs. The viscous forces are described by Slender Body Theory and extensions of Faxén's and Stokes' laws (Pozrikidis 1997). A key feature of these dynamics is that for an isolated swimmer the net propulsive force of the flagella must equal the opposing drag force of the body connected to the flagella, taking into account the effect of nearby surfaces or other organisms. While the creeping flow equations are linear and time reversible, in real world situations these features are only approximate or worse. Deviations from the ideal occur when flows affect boundary conditions such as location and orientation of nearby cells, the speed and directionality of flagella beating and the deformation of nearby interfaces. Some of these situations apply to the phenomena discussed in this paper, e.g., the effect of flows generated by the bacteria on their own spatial distribution and motional dynamics, which then modify the flows. A full accounting for these effects is necessary for a complete theory of the collective dynamics, but this is not yet at hand. The basic phenomenology of this collective behavior and its quantification by particle imaging velocimetry (PIV) are described in Sects. 2 and 3.

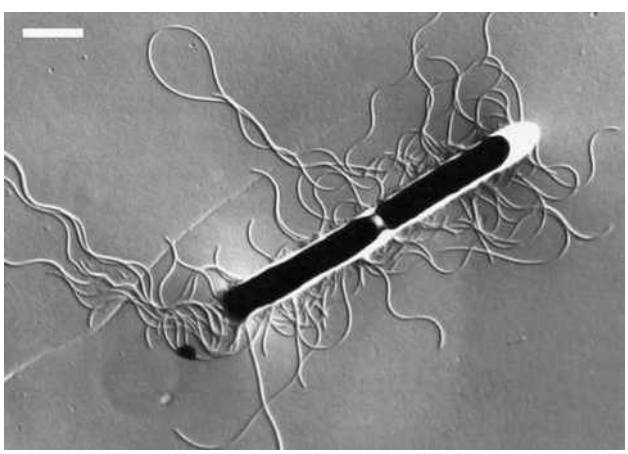

Fig. 1 Two *Bacillus subtilis* cells about to separate after cell division. Flagella can be seen emerging from the body. Many of them have been broken during sample preparation for this transmission electron micrograph. *Scale bar* is 1 μm

The swimming trajectories of living organisms can be modified by local shear and vorticity. For example, we describe in Sect. 4, that *B. subtilis* tend to swim upstream in a shear flow. Should we ascribe this to hydrodynamic interactions that passively orient cells which simply continue to rotate their flagella? Or perhaps might we infer that, when bacteria experience shear stress, they "want" to swim upstream? In Sect. 4 we show one example of this phenomenon, adequate for the purpose of demonstrating its importance for recruiting individuals into groups of co-directionally swimming cells. However, the specific recorded trajectories of more than 60 cells show wide variations in detail. There may be many microscopic origins for the recruitment of cells into correlated groups leading eventually to the collective behavior, but inferences concerning fundamentals of micro-bio-hydrodynamics require experiments designed to disentangle the physics from the biology.

Microorganisms use, exude, and respond to the presence of biologically significant molecules. Chemical interactions provide an avenue for change of the collective dynamic. Emission of molecules involved in signaling, and exudates of biopolymers that may radically change the viscosity of the embedding fluid, are both involved in quorum sensing (Miller and Bassler 2001) and the formation of biofilms (Kolter and Greenberg 2006). Before occurrence of these radical events, subtle chemical interactions can influence the biology and modify the behavior of individual cells. Even at low concentrations, polymer exudates modify the properties of the suspension. For instance, we observe that in slightly aged cultures of still normally motile bacteria, passive marker particles, as well as the bacteria themselves,

can be coupled by polymer strands of cellular origin. We have observed (unpublished) that the water/air interface can accumulate bacterially-synthesized polymer surfactants that trap and immobilize bacteria arriving there. A nominally free surface becomes a stiff, no-slip boundary. We infer that the bacteria are immobilized because the flagellar motors are too weak to overcome the implied yield stress. Vigorously shaking a culture bounded by such an interface frees the bacteria. After shaking stops, the newly unoccupied surface soon becomes again populated by bacteria stuck in the inferred interfacial layer of polymer, while in the bulk fluid many cells swim normally, some attached to each other by polymers, forming immobile multicellular clumps. In biofluid mechanics, before reaching definitive conclusions about mechanisms involving free surfaces: *caveat emptor*.

On a larger scale, response to chemical gradients can initiate behavior that creates striking hydrodynamic flows (Figs. 2 and 3). For instance, respiration of *B. subtilis* depletes dissolved oxygen in the fluid medium. Transport from an interface between the aqueous suspension of these cells and the surrounding air replenishes it. Bacteria swim up the resultant gradient of oxygen concentration. In a shallow suspension the cells swim upward, toward the air. Accumulation at the interface results in an unstable gradient of mean fluid density, since the bacteria are approximately 10% denser than water. Such convective dynamics also occur with swimming cells of algae (Pedley and Kessler 1992; Hill and Pedley 2005), plants that swim upward, toward light, and/or because of orientation of the cells in the earth's gravitational field. The initial volume fraction is typically fairly low in these situations, $\approx 10^{-3}$ or less. Theoretical approaches can therefore use Navier–Stokes equations that include a smoothed gravitational body force proportional to the local concentration of organisms and their mass density. An additional equation models transport of organisms due to swimming and advection by the flow (Hillesdon et al. 1995; Hillesdon and Pedley 1996; Tuval et al. 2005).

These unstable stratifications evolve in the usual manner by a Rayleigh–Taylor instability which, in turn, can lead to highly concentrated populations (Dombrowski et al. 2004, Tuval et al. 2005) (Fig. 2). These concentrated accumulations of cells support the collective dynamics discussed here, which were first reported in a more qualitative manner some time ago (Kessler and Wojciechowski 1997; Kessler and Hill 1997). Closely related phenomena, jets and whirls, that occur near the edges of bacterial cultures that grow and expand on wet agar surfaces have been reported (Mendelson et al. 1999). Likewise, such phenomena can be seen in concentrated bacterial populations trapped in suspended thin aqueous films (Wu and Libchaber 2000; Sokolov et al. 2007). Models of various types have been proposed to address these phenomena, from very simple discrete-particle dynamics not involving hydrodynamics (Vicsek et al. 1995) to continuum models based on

Fig. 2 *Bacillus subtilis* cells concentrated at a sloping water/air interface. This meniscus is produced by an air bubble in contact with the glass bottom of a bacterial culture 3 mm deep. Near the *top* of the image bacteria have accumulated, forming a monolayer of cells perpendicular to the air/water/glass contact line. Their lateral proximity and the adjacent surfaces immobilize them. Toward the *bottom* of the image the fluid becomes progressively deeper; the swimming cells exhibit collective dynamics. The accumulation occurs because bacteria swim up the gradient of oxygen produced by their consumption and by diffusion from the air bubble. The *black specs* are spherical latex particles 2 μm in diameter

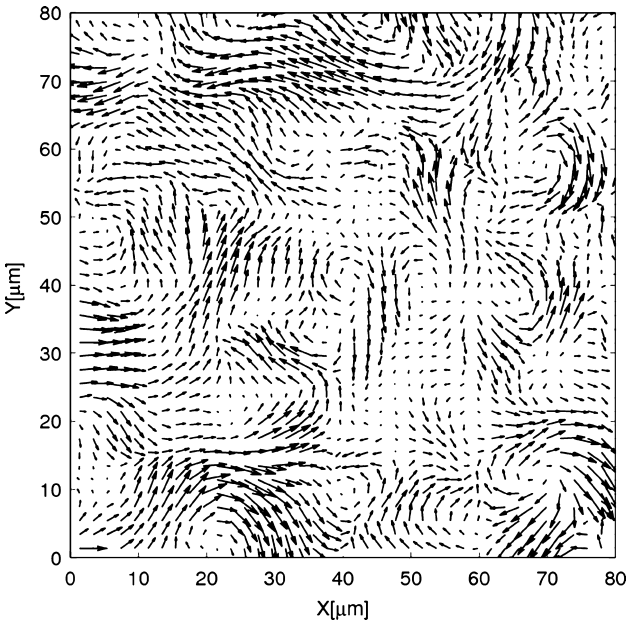

Fig. 3 One randomly chosen instant of the bacterial swimming vector field estimated by PIV analysis. The *arrow* in the extreme lower left corner represents a magnitude of 50 μm/s. The turbulent appearance of the flow is evident here

ideas from liquid crystal physics (Toner and Tu 1995; Simha and Ramaswamy 2002a), two-fluid models (Lega and Mendelson 1999; Lega and Passot 2003), numerical studies of idealized swimmers (Hernandez-Ortiz et al. 2005) and hydrodynamic models (Aranson et al. 2007). The emerging consensus is that hydrodynamic interactions between the bacteria are sufficient to account for the observed collective behavior, although some models suggest that steric interactions alone in a collection of self-propelled objects will produce the collective dynamics (Sambelashvili et al. 2007).

In Sects. 5 and 6 we describe some further mathematical aspects of modeling individual swimming dynamics and collective motions in bacterial systems. These results give insight into the details of flows and forces in the neighborhood of surfaces, and between nearby groups of cells. In particular, the great reduction in flow between closely-spaced organisms is argued to play an important role in the observed dynamics of the collective state, and forms the basis for a heuristic model for the locomotion of coherent groups of swimming cells. Section 7 outlines scaling arguments for turbulent-like behavior at low *Re* through the introduction of a new dimensionless quantity reflecting the power input from swimming organisms. The discussion in Sec. 8 highlights a number of important open questions for future work.

2 Collective phenomena: the Zooming BioNematic (ZBN)

The ZBN collective phase, occurs when the bacterial cells are very concentrated, i.e., nearly close-packed. They form codirectionally swimming domains that move chaotically, giving the appearance of turbulence. As is shown in Sect. 7, these regions may move at speeds larger than the average speed of single organisms. Maintenance of a sustaining environment is required when working with suspensions of living organisms. *Bacillus subtilis* require oxygen for swimming. The dynamics of the ZBN phase, driven by swimming, continue unabated for hours, suggesting that an adequate supply of oxygen and nutrients is available to the bacteria. Molecular transport into the bacterial suspension from the adjacent air involves molecular diffusion and also advection by collectively generated streaming. Bacteria consume $\sim 10^6$ molecules of O_2 per second per cell. As the solubility of oxygen is $\sim 10^{17}$ molecules/cm^3, and the concentration of cells is $\sim 10^{11}$ cm^{-3}, in absence of transport into the suspension the oxygen would be gone in about one second. During experiments on the ZBN, the typical depth of the suspension is $L \sim 5 \times 10^{-3}$ cm. With the diffusion coefficient of O_2 in water $D = 2 \times 10^{-5}$ cm^2/s, the diffusion time, L^2/D is also of order 1 s. A scale for collective velocity is $V \sim 4 \times 10^{-3}$ cm/s (Fig. 17 below), so that the advection time is again approximately 1 s. This fortuitous combination of characteristic times implies "just in time" oxygen delivery. The Péclet number, $P_e = VL/D$, which measures the relative importance of advection and diffusion, is therefore of order unity for a small molecule such as oxygen; it can be considerably greater for larger molecules. The complex and quite fascinating details of the transport processes of food, waste products, and of molecular signals need extensive investigation, another example of the convolution of biology and fluid dynamics. The biochemistry of metabolism and sensory processes also plays a major role. Recent work (Solari et al. 2006; Short et al. 2006) describe investigations on diffusive transport necessarily augmented by advection due to the motion of flagella. There, the context is an aspect of the origin of multicellularity in a family of algae. In a sense, the collective behavior of a bacterial population converts it too into a type of multicellular "individual" (Shapiro and Dworkin 1997).

The volume of a single *B. subtilis* is $\sim 1.5 \times 10^{-12}$ cm^3. Since the bodies are rod-shaped, concentrated populations, e.g., $n - 10^{11}$ cm^{-3}, tend to form domains within which the self-stacked cell bodies are approximately parallel. The entire high concentration region consists of such domains separated by regions of disalignment (Figs. 2, 3). All the cells in one domain swim in the same direction, so that, unlike the analogous liquid crystals, the domains move and are dynamically polar. The cell bodies have no intrinsic polarity; on any one cell, the propelling flagella can flip to either end of the rod-shaped body. This appears to be one mechanism for quorum polarity: individual organisms joining the swimming direction of the majority. A domain is thus characterized by coherence of body alignment and polarity, hence coherence of swimming direction. The domains zoom about; they spontaneously form and disintegrate, giving the appearance of internally maintained turbulence. The next section describes PIV measurements of spatial and temporal correlations of velocity, vorticity and polar alignment.

The dynamical system of cells and water is driven by rotation of the helical flagella that emerge from the bodies of the bacteria. The flagella propel (force) the fluid phase backward; they exert an equal and opposite force on the bodies from which they emerge. Since the flagella are typically three times longer than the cell bodies, the flow generated by the flagella of a particular cell exerts a backward drag on the bodies of several cells located behind that particular one. Flows in the interior of domains are therefore rather small; propulsion arises mostly at the periphery. Further discussion and relevant calculations follow in Sects. 5 and 6, which also present results on cohesive hydrodynamic interactions.

3 Coherence of polar and angular order: a novel use of PIV

Our experiments were conducted with *B. subtilis* strain 1085B suspended in terrific broth (TB) (Ezmix Terrific Broth, Sigma; 47.6 g of broth mix and 8 ml of glycerin in 1 l of distilled water). Samples were prepared by adding 1 ml of –20°C stock to 50 ml of TB and incubating for 18 hours in a shaker bath at 37°C and 100 rpm. Then, 1 ml of bacteria suspension (concentration of around 10^9cells/cm^3) was mixed with 50 ml of fresh TB and incubated for another 5 h.

A single drop of suspension was placed on a glass-bottomed petri dish to be observed with an inverted microscope using a 20× bright field objective. This magnification is sufficient to observe individual cells and produce a reasonably wide field of view. Additional water reservoirs were placed in the closed chamber to induce high humidity and avoid evaporative flows at the edge of the drop. The sessile drop is imaged from below through the bottom of the petri dish and near the contact line, where dimensions of the medium are close to a thin layer and self-concentration mechanisms provide very high accumulations of cells (Dombrowski et al. 2004). Videos were obtained using a high-speed digital camera (Phantom V5) at a rate of 100 frames per second and with a resolution of 512 × 512 pixels. Sets of 1,000 frames were subsequently obtained from each of those videos and processed with a commercial particle-imaging-velocimetry system (DANTEC Flow Manager) in the cinemagraphic mode. The PIV system can estimate the most probable displacement of small rectangular regions in the image by implementing a simple pattern matching algorithm between two consecutive images (Willert et al. 1991; Keane et al. 1992). A sampling grid of 42 × 42 windows, each 16 pixels wide with 25% overlap, was chosen. Each window represents 2.7 μm. Given the displacement of these small evaluation regions at a given frame rate, a discrete velocity field is returned for each time step. The observed system is a layer with a sloping upper surface, varying in thickness from "zero" to ∼200 μm. These measurements are projections of a three-dimensional field into the plane defined by the area of view and the optical depth of field.

Measurement of the coherence lengths and times that characterize the dynamics of the ZBN can be done by the implementation of a PIV analysis either on the recorded motion of passive tracer particles or on the suspended bacteria themselves. The data presented here uses the latter technique. Passive tracer data is too sparse when the concentration of tracer particles is sufficiently low so as not to affect the basic phenomena. On the other hand, optical problems arise in the highly concentrated ZBN phase. The close-packed cells scatter light, producing distortion and diffraction effects that reduce the quality of the image.

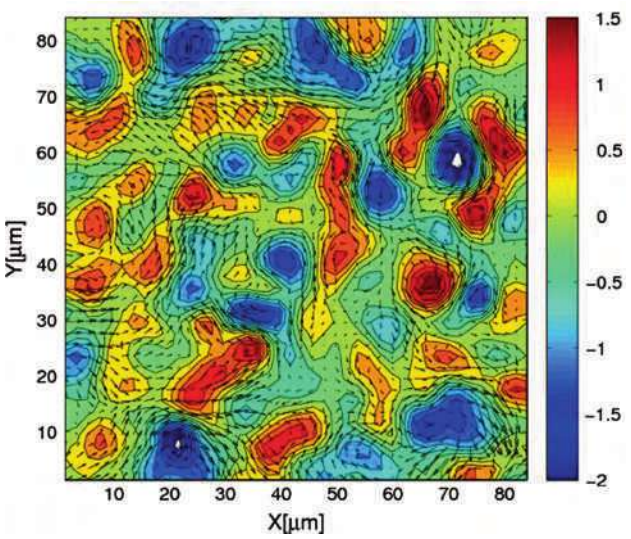

Fig. 4 Vorticity of the swimming velocity vector field shown in Fig. 3. *Color bar* indicates vorticity in seconds^{-1}. The graphing method discretizes vorticity levels

Individual cells are difficult to resolve in this setup. Though more work is needed to increase precision of velocity measures, analysing these diffuse images with PIV captures well the overall dynamics of the system in a quantitative way. A snapshot of the velocity field is shown in Fig. 3; the corresponding vorticity is in Fig. 4.

The motion of the suspension appears turbulent. Coherent regions, surges, plumes and jets occur intermittently. These domains of aligned motility are hundreds of times larger than bacterial dimensions, remaining coherent for a second or longer. Observed cinemagraphically, the leading segments of such plumes often roll-up into spirals, then disperse, either spontaneously or due to interactions with neighboring coherent regions. These observations relate to the trajectories, the paths of groups consisting of hundreds or thousands of bacteria. PIV provides only a quasi-instantaneous snapshot of streamlines associated with a derived velocity field.

Correlation functions were estimated from the quantitative data. The temporal correlation function of velocity is defined as the following statistic over the vector field $\mathbf{v}(\mathbf{x},t)$:

$$J_v(\mathbf{x},t) = \frac{\langle \mathbf{v}(\mathbf{x},s+t)\cdot\mathbf{v}(\mathbf{x},s)\rangle_s - \langle \mathbf{v}(\mathbf{x},s)\rangle_s^2}{\langle \mathbf{v}^2(\mathbf{x},s)\rangle_s - \langle \mathbf{v}(\mathbf{x},s)\rangle_s^2}. \quad (1)$$

The space correlation function is defined as

$$I_v(r,t) = \frac{\langle \mathbf{v}(\mathbf{x}+\mathbf{r},t)\cdot\mathbf{v}(\mathbf{x},t)\rangle_{\mathbf{x},\theta} - \langle \mathbf{v}(\mathbf{x},t)\rangle_{\mathbf{x}}^2}{\langle \mathbf{v}^2(\mathbf{x},t)\rangle_{\mathbf{x}} - \langle \mathbf{v}(\mathbf{x},t)\rangle_{\mathbf{x}}^2}, \quad (2)$$

where $\langle\cdot\rangle_s$ is the average over time frames and $\langle\cdot\rangle_{\mathbf{x}}$ indicates the average over space coordinates $\mathbf{x} = (x, y)$. The

first term in (2) is also averaged over all angles θ of $\mathbf{r}$. Then $I_v(r)$ depends only on the magnitude $r \equiv |\mathbf{r}|$.

Similar definitions are used for the correlation of the vorticity scalar field $\Omega(\mathbf{x}, t)$,

$$J_\Omega(\mathbf{x},t) = \frac{\langle \Omega(\mathbf{x},s+t)\Omega(\mathbf{x},s)\rangle_s - \langle \Omega(\mathbf{x},s)\rangle_s^2}{\langle \Omega^2(\mathbf{x},s)\rangle_s - \langle \Omega(\mathbf{x},s)\rangle_s^2} \tag{3}$$

and

$$I_\Omega(r,t) = \frac{\langle \Omega(\mathbf{x}+\mathbf{r},t)\Omega(\mathbf{x},t)\rangle_{\mathbf{x},\theta} - \langle \Omega(\mathbf{x},t)\rangle_{\mathbf{x}}^2}{\langle \Omega^2(\mathbf{x},t)\rangle_{\mathbf{x}} - \langle \Omega(\mathbf{x},t)\rangle_{\mathbf{x}}^2}. \tag{4}$$

Using these measures on the PIV data, we obtain 1,000 different curves for I_v and I_Ω, one for each time realization, and $42 \times 42 = 1{,}764$ curves for J_v and J_Ω, one for each possible discrete coordinate in the PIV sampling grid. We further calculate averages of these sets to show the overall mean behavior of the correlation functions. Graphs are shown in Fig. 5. Comparison of the average plots with plots of individual cases show that, in light of the prevalence of positive and negative correlations, averaging does not provide good insights into dynamic events. The oscillations of correlation are somewhat reminiscent of vortex streets at high *Re*.

These analyses reveal correlation lengths of velocity on the order of 10 μm, which is about a typical vortex radius in Fig. 4. We also observe anticorrelation extending for more than 70 μm and coherence in time that persists for at least a second, suggestively close to the advection time mentioned at the end of Sect. 1. While these measures define some characteristic length and time scales of the system, these curves do not provide information on the continuity and dominance of extensive coherence of alignment and collective polar motion. A novel method of analysis of the velocity field, using the streamlines derived from PIV (Dombrowski et al. 2004) was employed to provide that insight.

The local velocity of domains of concentrated bacteria correlates with the direction of the axis of the cell bodies. In this way, the direction of the associated streamlines averaged over suitably chosen areas can provide a measure of the orientation of a local director vector, traditionally used to characterize liquid crystalline phases. In this context, the swimming co-direction defines the polarity of coherent behavior absent from standard liquid crystalline order (de Gennes and Prost 1993). Spatially rapid deviations of streamline directions from the local average provide a quantitative measure of the end of coherence within the projected plane. They may signal the occurrence of orientational singularities, such as excursions into the orthogonal dimension or the presence of boundaries that define unrelated regions of coherence that collide or fold into each other. Relatively low angle deviations of the director provide data on the splay and bend parameters that occur in the analysis of the liquid crystal free energy.

We now introduce a new method of analysis which consists of defining a scalar field to measure the level of

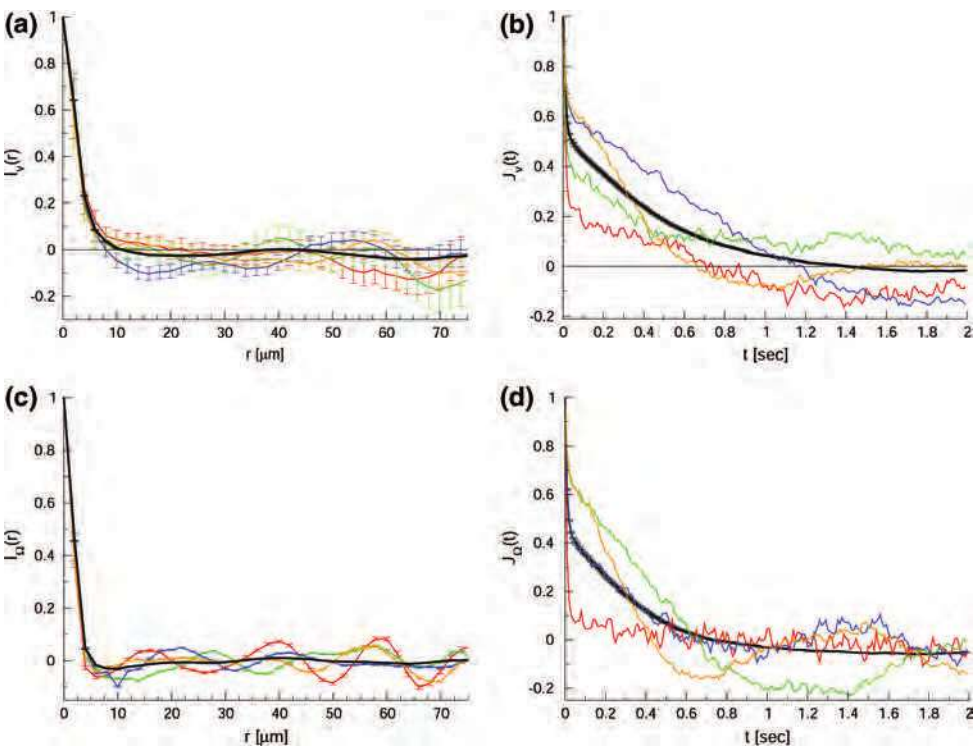

Fig. 5 Correlation functions from PIV analysis. (**a**) Spatial correlation function of velocity $I_v(r)$. Four examples, corresponding to four different times, are shown in colors; the black trace is the average over 1000 time realizations. (**b**) Temporal correlation function of velocity $J_v(t)$. Four examples corresponding to four particular locations in the field of view are shown in colors. Black is the average over space. Plots of the vorticity spatial correlation $I_\Omega(r)$. (**c**) and temporal correlation $J_\Omega(t)$. (**d**) are shown for four examples and, again in *black*, for the average. The oscillations in **c** correspond to alternation in the handedness of vorticity, as shown in Fig. 4. *Error bars* in **a** and **b** indicate typical statistical uncertainties

coherent directional motion in the velocity field. The obvious choice is a local average $\Phi_R = \langle \cos\theta \rangle_R$ of the cosine of the angle between adjacent unit vectors of velocity, averaged over a small region defined by R. This average over the measured velocity field $\mathbf{v}_{ij}(t)$ is

$$\Phi_R(i,j,t) = \frac{1}{N_R} \sum_{(l,m)\in B_R(i,j)} \frac{\mathbf{v}_{ij}(t) \cdot \mathbf{v}_{lm}(t)}{|\mathbf{v}_{ij}(t)||\mathbf{v}_{lm}(t)|}, \quad (5)$$

where $B_R(i,j)$ is a quasi-circular region of radius R, centered at (i,j), containing N_R elements. When $\Phi_R \sim 1$ the vectors inside the region B_R are nearly parallel. Values close to zero indicate strong misalignment. Negative values imply locally opposing streamlines. Resolution and noise level are determined by the choice of R.

Standard correlation functions based on the velocity field, as in Fig. 5, hide information on the contiguousness of correlations. Analyzing the streamline field in this novel way exhibits the global continuity of angular and polar correlations. The extent of the resultant sinuous domains depends on the choice of the averaging area $\sim R^2$. Large values of R produce a strong smoothing of the local data, which may hide the details of the chaotic nature of flow by means of statistical cancellations. Hence, small values of R should be preferred. But on the other hand, too small values of R produce results that are more sensitive to noise in the raw data or that are biased by the specific shape of the averaging region, and the particular geometry of the grid chosen for the PIV analysis. Figure 6 shows the extent of continuous domains, derived from one data set, using different values of R. The regions colored dark red corresponds to $0.8 < \Phi_R < 1$, which selects regions of high coherence. Inside these domains all velocities are parallel within an angle slightly lower than 37°.

For liquid crystals, the conventional order parameter involves $\langle \cos^2\theta \rangle$, thereby avoiding polarity. For the domains of coherent directional motion considered here, we can define an order parameter as

$$P_R(t) = \langle \Phi_R(t) \rangle, \quad (6)$$

where this average extends over the entire area, i.e., all elements of the PIV image at time t. This quantity can be treated as a time series. We find that $P_R(t)$ displays a stationary value with random fluctuations. Figure 7 shows histograms of these order parameters. This method of analysis will be used to determine the onset of the ZBN phase as a function of cell concentration n.

What is the distribution of values of Φ_R in the whole field of view for each time step? What fraction of the total area in the level map of Φ_R do they span? This approach asks for the probability of finding any given level of coherence in the flow, or the portion of the total that is spanned by each contour level in Fig. 6. These area fraction distributions are

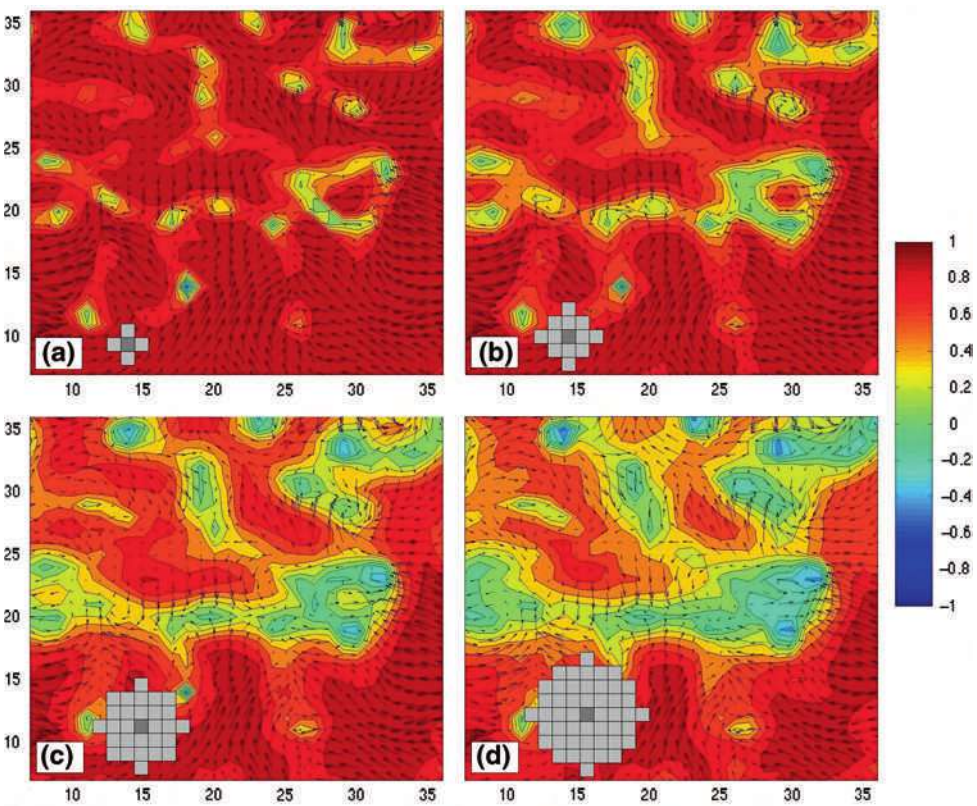

Fig. 6 Instantaneous coherence measure Φ_R (Eq. 5) for $R = 1$ (**a**), $R = 2$ (**b**), $R = 3$ (**c**) and $R = 4$ (**d**). Axes and R are in PIV grid units ($\simeq 2$ μm each). *Grey boxes* in the lower left corner indicate, in each case, the size and shape of the local averaging region used to estimate the measure. The *color bar* on the right indicates scale levels for values of Φ_R. The plotting method discretizes the countour levels. Note the near absence of *dark blue* regions, which would indicate counterstreaming

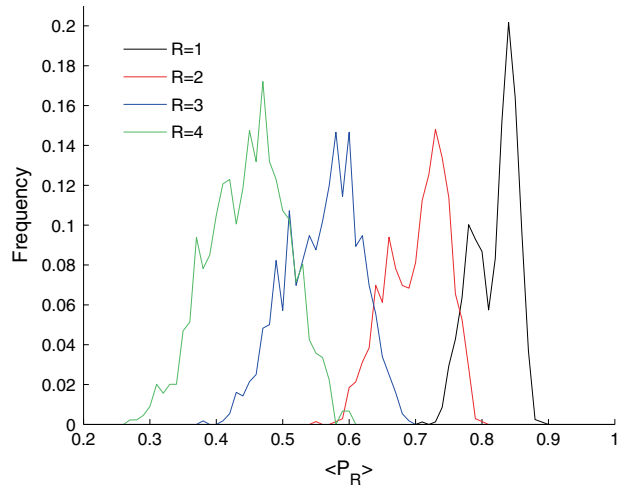

Fig. 7 Histograms of the order parameter $P_R(t)$ for different values of R, the radius of the sampling area. Each one is generated with 1,000 time steps. The skewing of the distributions becoming two-peaked at low R (high resolution) may indicate bimodality in the coherent phase, or an approximately aligned transient phase

shown in Fig. 8 for four values of R. The data set in [−1, 1] is partitioned in bins of size 0.2. We see an obvious shift of the center of the distribution when R is changed. It is interesting that each distribution is basically constant, concluded by seeing that fluctuations (error bars) are typically small, meaning that the fraction of the system with a particular coherence level stays more or less the same over time. Given the three-dimensional volume-filling nature of the bacterial population, this average temporal stability of projected coherent area implies zero net divergence of swimmers. The up/down rate of departure is matched by incomers.

Another possibility is that the whole dynamics is limited to a very narrow layer and is therefore quasi-two-

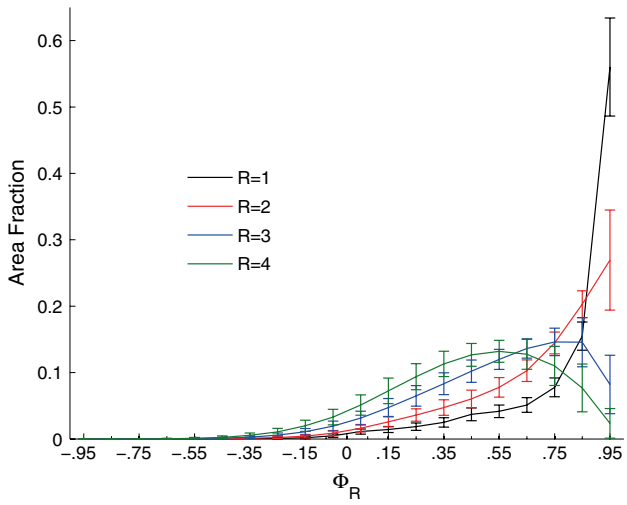

Fig. 8 Area fraction of coherent regions distributed over the whole range of Φ_R, averaged over 1,000 time frames. *Error bars* indicate standard deviation in each case

dimensional. But this is not the case, for we have observed that cells and clumps of cells or passive tracers tumble and move in and out of the focal plane, clearly proving that the dynamics is three-dimensional. Dynamics of recruiting and dropping of individuals into and out of phalanxes could be related to the topological details, with clear implications for mixing and transport phenomena. We expect that this observation will eventually provide a significant link to a more complete analysis.

4 Recruiting into ZBN domains

The recruiting of swimmers into a co-directionally swimming domain of cells, a phalanx, depends on several mechanisms. We have discovered, as discussed below, that individual cells of *B. subtilis* have a strong tendency to swim upstream in a shear flow. Similar observations have been made recently (Hill et al. 2007), in which upstream swimming of *E. coli* was found immediately adjacent to a surface. In contrast, our finding is not restricted to motion on the surface bounding a fluid, but simply in close enough proximity to be in a region of shear. In the context of the ZBN, shear flows can emerge from groups of co-directionally swimming cells, for a tightly knit group of propagating cells generates a backwash flow field, a lateral influx, and a flow forward, in the swimming direction. These flows, which are due to incompressibility, are shown in Sect. 5 (Figs. 12 and 13 below). They provide a mechanism for recruiting more individuals into a phalanx. Another organizing/recruiting mechanism occurs when one of these bacteria encounters an obstacle. It can flip the propelling flagella from “back” to “front”, resulting in reversal of locomotion, without turning the bacterial cell body (Cisneros et al. 2006). This action may be a behavioral manifestation of flagellar dynamics and orientational instability. Paradoxically, it can aid polar alignment in groups, just because the individual cells are not themselves polar. Individual mis-oriented cells can react by joining a colliding “obstacle”, a moving phalanx of others.

Swimming bacteria were suspended in Poiseuille flows within flat microslides (Vitrodynamics) with a 0.1 mm lumen. A fine motion linear actuator (Newport 850G) was used to depress a non-sticking syringe (Hamilton Gastight #1702) to produce a continuous and smooth fluid flow. This flow was coupled through a micropipette ($\sim$50 μm) which is inserted into one side of the flat microslide. The velocity profile was determined by tracking 2 μm fluorescent particles (Bangs Labs) near the focal plane. By comparing the out-of-focus beads with their images at known distances from the focal plane, the depth and velocity of the tracer particles can be used to determine the 3D velocity field and the shear. Cell trajectories in these experiments were visualized by tracking the position of both ends of cells

through a sequence of images in the plane of focus. The vector orientation of a cell was determined from the distance between the ends of the cell and the angle of the connecting line segment. The angle and length give the projection of the cell body in the plane of focus. Velocity of the cells is calculated from the change in position of the cell from one frame to the next. This velocity represents the speed and direction that the cell is moving in the lab reference frame. Due to the external shear stress experienced by the cell the velocity vector does not necessarily point in the same direction as its orientation. Data were obtained on 65 individual tracks that exhibit these characteristics, each modified by idiosyncratic details.

Figure 9 shows one representative trajectory. Reading from right to left, the trajectory consists of a downstream segment with the cell oriented across the flow, an upstream segment, and then again downstream. This behavior may be entirely hydrodynamic or it may be a behavioral response to differential shear stress. Orientation of the cell transverse to the swimming direction occurs in many cases, but not all. When it does, it implies the dissolution of the flagellar bundle, with individual flagella emerging approximately perpendicular to the body axis, as if driven by the fluid "wind" in which they operate. Our optical resolution is insufficient to ascertain whether the cell bodies and flagella are at different levels in the shear field, a possible explanation of the phenomenon. The interactions of cells with shear, the deconvolution of cell path lines and fluid stream lines and analysis of cell body orientation in relation to swimming direction are current endeavors covering many such observations.

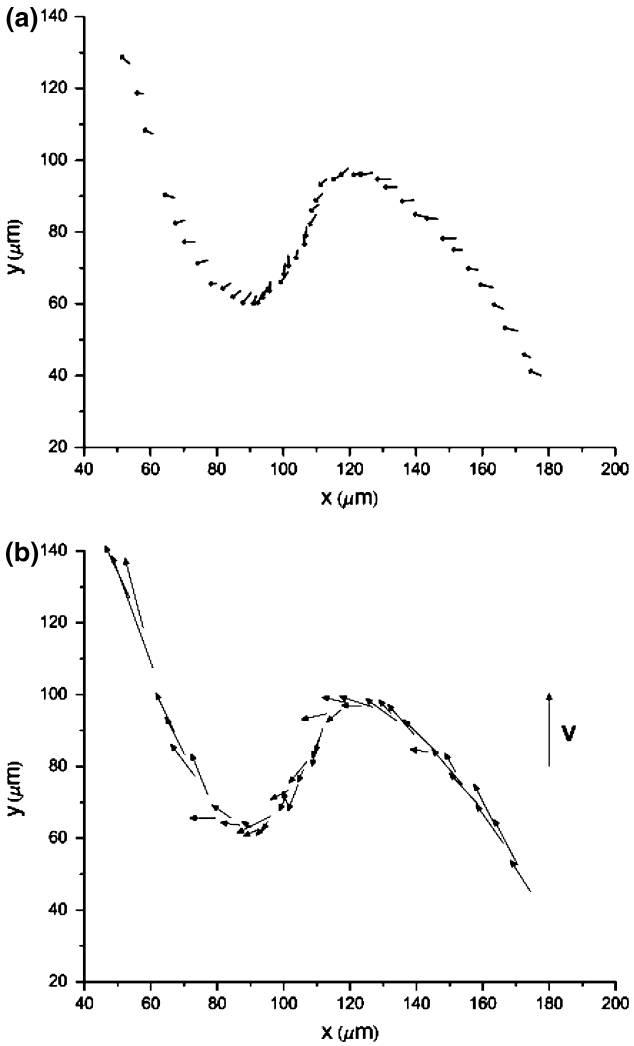

Fig. 9 Upswimming of bacteria in a shear flow. **a** Trajectory and orientation of a particular bacterial cell swimming in a flow, with velocity in the $+y$ direction, and shear $dV_y/dz \sim 1.0\ s^{-1}$. The *small arrows* show the apparent swimming direction and the projection of the body size on the plane of observation. **b** Trajectory of the velocity vectors in the laboratory reference frame. Vector on right indicates fluid flow direction. The velocity of the bacterium can be transverse to its orientation

5 Modeling self-propelled microorganisms

There is a long history of models for the swimming of individual microorganisms, dating back to classical works on flagellated eukaryotes (Taylor 1952), ciliates (Blake 1971a), and bacteria (Ramia et al. 1993). Very recent work has addressed the complex circular swimming of individual *E. coli* near surfaces (Lauga et al. 2006), where the specific interactions between helical flagella and a boundary are crucial. In this section we wish to return to the very simplest of models to examine the nature of flows in concentrated populations. In the creeping flow regime where $Re \ll 1$, featuring linearity, superposition and time independence, a simple model of a self-propelled organism consists of two parts, a "body" **B** and an attached extendable "thruster" **T** that emerges from **B**. When forces within **B** provide an incremental backward push to **T**, the resulting increment of motion generates a surrounding field of fluid velocity. The motion of **B** is "forward" with velocity $\mathbf{V}_B$ relative to the surrounding stationary fluid; the motion of **T** is backward with velocity $\mathbf{V}_T$. The velocity with which **T** emerges from **B** is $\mathbf{v}_r$. Hence, since **T** is attached to **B**,

$$\mathbf{V}_T = \mathbf{v}_r - \mathbf{V}_B.$$

When the respective drag coefficients are R_B and R_T, force balance is achieved when

$$F_B = R_B|\mathbf{V}_B| = R_T|\mathbf{v}_r - \mathbf{V}_B| = R_T|\mathbf{V}_T| = F_T, \tag{7}$$

where F_B and F_T are the forward and backward force magnitudes on the fluid. A schematic diagram of swimmers and velocities is shown in Fig. 10, where the sphere and the

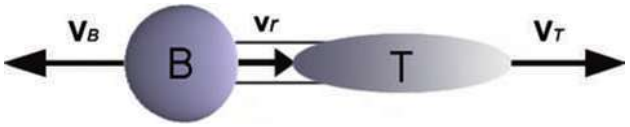

Fig. 10 Diagram of a model swimmer showing V_B and V_T relative to the fluid, and the velocity $\mathbf{v}_r$ of **T** out of **B**

ellipsoid indicate, respectively, **B** and **T**. The rotation rate of the flagella helix, times the helix pitch, times an efficiency factor, is represented by $\mathbf{v}_r$.

For bacteria, **T** represents the rotating bundle of helical flagella. An increment of motion consists of a slight turn of the bundle during an increment of time. For the simplified case presented here, we ignore rotation. This model generates the salient features of the fluid flow field that surrounds a self-propelled organism or, by superposition, a group of organisms. This model does not intend to elucidate the development over time of the locomotion of one or more swimmers, as in the models of Hernandez-Ortiz, et al. (2005), Saintillan and Shelley (2007), and the asymmetric stresslet of model of Cortez et al. (2005). Rather, it produces an instantaneous field of flow over the entire available space, as required by the time independence of Stokes flow. We re-emphasize that since the increment of linear displacement between B and T models an incremental turn of the propelling bundle of flagellar helices, it is inappropriate to consider an actual finite elongation of the organism followed by retraction of T to its original position. Calculation of the flow field of one or more organisms requires enforcement of no-slip conditions at bounding surfaces and at surfaces of the organisms. The computational model presented below considers **B** a sphere and **T** a rod of finite diameter. Forward and backward velocities, calculated by force balance, are used to specify $\mathbf{V}_B$ and $\mathbf{V}_T$.

6 Flows and forces

Each organism consists of one sphere (body **B**) of radius a_B and a cylinder (flagellum bundle **T**) of length ℓ, radius a_T along the z-axis, as depicted in Fig. 11. The figure also shows an infinite plane wall which will be included in some

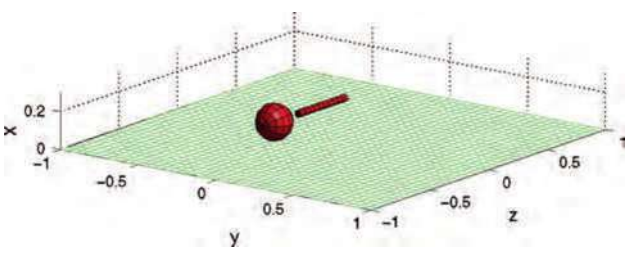

Fig. 11 Perspective view of the sphere-stick model and the wall

of our computations. When the wall is present, it is located at $x_w = 0$. The head has velocity $(0,0,V_B)$ and the tail has velocity $(0,0,V_T)$.

The approximate balance of forces is achieved as follows. The drag force on an isolated sphere moving at velocity $(0, 0, V_B)$ is

$$\mathbf{F}_B = R_B \mathbf{V}_B = 6\pi\mu a_B V_B(0,0,1), \tag{8}$$

where μ is the fluid viscosity and R_B represents the drag coefficient for the sphere. The force required to move a cylinder of length ℓ and radius a_T along its axis with velocity $(0, 0, V_T)$ is

$$\mathbf{F}_T = R_T \mathbf{V}_T = \frac{4\pi\mu\ell}{\ln(\ell^2/a_T^2) - 1} V_T(0,0,1), \tag{9}$$

where R_T is the drag coefficient of the cylinder. Force balance requires $\mathbf{F}_B + \mathbf{F}_T = 0$ which yields

$$V_T = -\frac{3}{2}\frac{a_B}{\ell}\left[\ln(\ell^2/a_T^2) - 1\right] V_B. \tag{10}$$

Given the instantaneous velocities of the head and tail of the organism, our goal is to compute the surface forces that produce these velocities at all the surface points. For this we use the method of Regularized Stokeslets (Cortez 2001; Cortez et al. 2005). Briefly, the method assumes that each force is exerted not exclusively at a single point, but rather in a small sphere centered at a point $\mathbf{x}_k$. The force distribution is given by

$$\mathbf{F}(\mathbf{x}) = \mathbf{F}_k \phi(\mathbf{x} - \mathbf{x}_k), \tag{11}$$

where ϕ is a smooth narrow function (like a Gaussian) with total integral equal to 1. The limit of $\phi(\mathbf{x})$ as the width (given by a parameter ε) approaches zero is a Dirac delta $\delta(\mathbf{x})$. The role of the function ϕ is to de-singularize the velocity field that results from the application of a single force. For example, given a force $\mathbf{F}_k\phi(\mathbf{x})$ centered at $\mathbf{x}_k$ and using the regularizing function

$$\phi(\mathbf{x}) = \frac{15\varepsilon^4}{8\pi(|\mathbf{x}|^2 + \varepsilon^2)^{7/2}}, \tag{12}$$

the resulting velocity is

$$\mathbf{u}(\mathbf{x}) = \left(\frac{1}{8\pi\mu}\right)\frac{\mathbf{g}_k}{(|\mathbf{x} - \mathbf{x}_k|^2 + \varepsilon^2)^{3/2}}, \tag{13}$$

where

$$\mathbf{g}_k = [|\mathbf{x} - \mathbf{x}_k|^2 + 2\varepsilon^2]\mathbf{F}_k + [\mathbf{F}_k \cdot (\mathbf{x} - \mathbf{x}_k)](\mathbf{x} - \mathbf{x}_k). \tag{14}$$

This is called a Regularized Stokeslet (Cortez 2001; Cortez et al. 2005). For a collection of N forces distributed on a discrete set of points covering the surfaces of the

sphere and cylinder, the resulting velocity obtained by superposition is

$$\mathbf{u}(\mathbf{x}) = \left(\frac{1}{8\pi\mu}\right)\sum_{k=1}^{N}\frac{\mathbf{g}_k}{(|\mathbf{x}-\mathbf{x}_k|^2+\varepsilon^2)^{3/2}}. \quad (15)$$

Equation (15) is the relationship between the forces exerted by the organisms on the fluid and the fluid velocity when there are no walls bounding the flow. This formula is used as follows: the surfaces (sphere and cylinder) of all organisms are discretized and an unknown force is placed at each point of the discretization. We assume that the velocities of all spheres and all cylinders are known to be $\mathbf{V}_B$ and $\mathbf{V}_T$ (they can be different for different organisms). Then Eq. 15 is used to set up and solve a linear system of equations for the surface forces of all organisms simultaneously. For N surface points per organism and M organisms, the size of the linear system is $3NM \times 3NM$. This ensures that the velocity on any one organism that results from the superposition of the Stokeslets on all organisms exactly equals the given boundary condition.

For the computations with flow near an infinite plane wall, the boundary conditions of zero flow at the wall are enforced using the method of images. The image system required to exactly cancel the flow due to a singular Stokeslet was developed by Blake (1971b). It requires the use of a Stokeslet, a dipole and a doublet outside the fluid domain, below the wall. This image system does not enforce zero flow at the wall when using the regularized Stokeslets in Eq. (15). However, the image system can be extended to the case of the regularized Stokeslet through the use of regularized dipoles and doublets. The details, discussed in Ainley et al. (2007), show that for any value of $\varepsilon > 0$, the system of images for the regularized Stokeslet exactly cancels the flow at the wall and reduces to the original system derived by Blake as $\varepsilon \to 0$. The result of the images is a variation of Eq. (15) but the procedure to determine the forces is as before.

We consider first a single organism moving parallel to an infinite plane wall. The table below shows the dimensionless parameters used. Since the cylinder is simply a way of representing the effect of the flagellum bundle and the sphere is a simplification of the cell body, the specific dimensions of these elements do not exactly correspond to the organism. However, for a model motor rotating at 75 Hz and a helical flagellum with pitch 3 μm, the wave speed is 225 μm/s. The observed swimming speed of an organism is about 11% of the wave speed, or about 25 μm/s. Thus, the length scale used for the dimensionless parameters was L = 25 μm so that the dimensionless sphere speed is 1. A cell body of radius 2.5 μm has dimensionless radius 0.1, and so on. All parameters except for V_T were chosen as dimensionless values representative of the problem. The cylinder velocity V_T was computed using Eq. (10).

Parameter	Description
a_B = 0.1	Radius of the sphere
a_T = 0.02	Radius of the cylinder
ℓ = 0.4	Length of the cylinder
V_B = –1.0	Velocity of the sphere
V_T = 1.8718	Velocity of the cylinder

In all simulations presented here, the discretizations resulted in 86 points per sphere and 88 points per cylinder. This give a maximum discretization size (longitudinal or latitudinal distance between neighboring particles) of h = 0.0524. The regularization parameter was set to ε = 0.0571 which is slightly larger than the discretization size. This is a typical choice based on accuracy considerations (Cortez et al. 2005).

Figure 12 shows the fluid velocity in a plane parallel to the wall and through the organism, and the flow in a plane through the organism and perpendicular to the wall. The contour lines are at 5, 10, 25, 50, 75 and 90% of the maximum speed. Those contours reveal the extent of the fluid disturbance created by an organism. Figure 13 shows the streamlines of the instantaneous velocity field, revealing circulation patterns.

Consider now two organisms next to each other prescribed to move parallel to an infinite plane wall and to each other. The parameters are the same as those used in the previous example. Just as in the case of a single organism, the flow pattern suggests that the flow tends to "push" the organisms toward the wall and toward each other. This can be quantified by computing the total forces exerted by the organisms on the fluid in order to move parallel to the wall and to each other. Figure 14 shows the velocity field and the resulting forces exerted on the fluid by each of the two organisms. It is apparent that there is a component of the force pointing away from the wall, indicating that this component is needed to counteract the attraction effect of the wall in order to keep the organisms moving parallel to it. Similarly, the component of the force pointing away from the neighboring organism is required to counteract the attraction induced by the flow field, as noted in earlier work (Nasseri and Phan-Thien 1997). These results agree with experiments (Sokolov et al. 2007) showing that two bacteria swimming near each other, co-directionally, continue for long distances in these parallel paths.

We next compute the flow around several organisms placed in a common plane above the wall. The velocity is determined in that plane in order to visualize the effect of

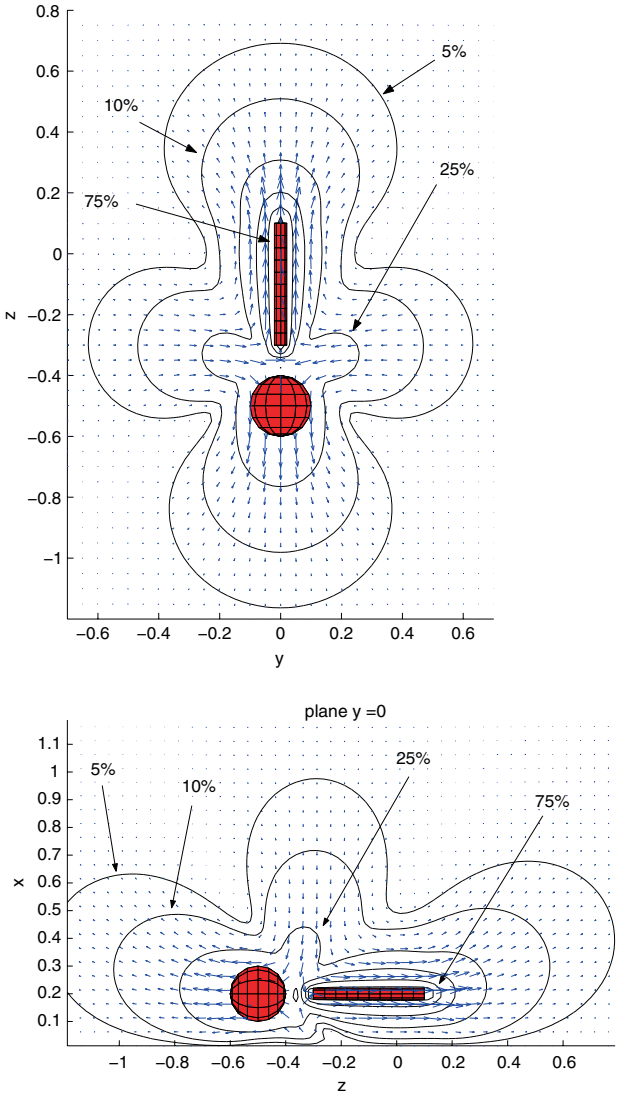

Fig. 12 Plan and side views of velocity field around one organism near a wall. The *numbers* indicate contours where the fluid speed is 5, 10, 25, 50, 75 and 90% of the maximum speed. The infinite plane wall is located at $x = 0$

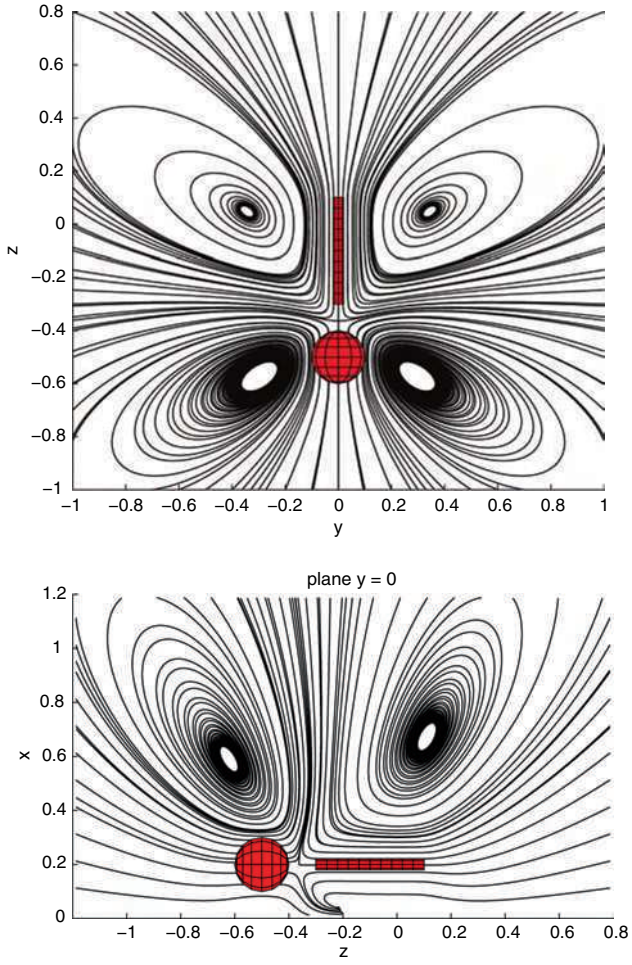

Fig. 13 Streamlines of the velocity field around one organism near a wall. Plan and side views

the prescribed motion of the group. Figure 15 shows the velocity around the organisms and a close-up view of the flow between some of them, while Fig. 16 shows the streamlines for the same configuration. The computed geometries and magnitudes of the flows generated by the locomotion provide some understanding of the forces between swimming organisms and between organisms and adjacent no-slip surfaces. The forces on each swimmer (Fig. 14) show the attraction of the cells to each other and to the nearby plane.

Additional computations show that in the absence of the plane, the vertical components vanish (by symmetry), and the horizontal attractive components diminish. The attractive force is due to transverse flow toward the organism axis (Fig. 12), required by conservation of volume: the body propels water forward, the tail pushes water backward, leaving a central region of inflow due to lowered pressure. In the absence of the nearby plane, the influx is weaker because of cylindrical symmetry. The same influx can be seen toward the centers (between body and tail) of organisms which are members of a multi-organism phalanx (Fig. 15). Transverse flows between the body of a follower and the tail of a preceder are also seen in the upper image of Fig. 15. Whether a sum over transverse flows in a 3D domain consisting of many close-packed organisms provides net radial cohesion remains to be seen.

Figures 15 and 16 also show the flows that penetrate or surround a group. It is evident that there is very little front-to-back penetration of fluid. The exchange is mostly lateral. The leading heads push water forward, the tail-end cells push water backward, generating much of the collective forward propulsion. The low velocities of flow in the interior (lower panels of Figs. 15 and 16) imply compensating forces and relatively little advective communication

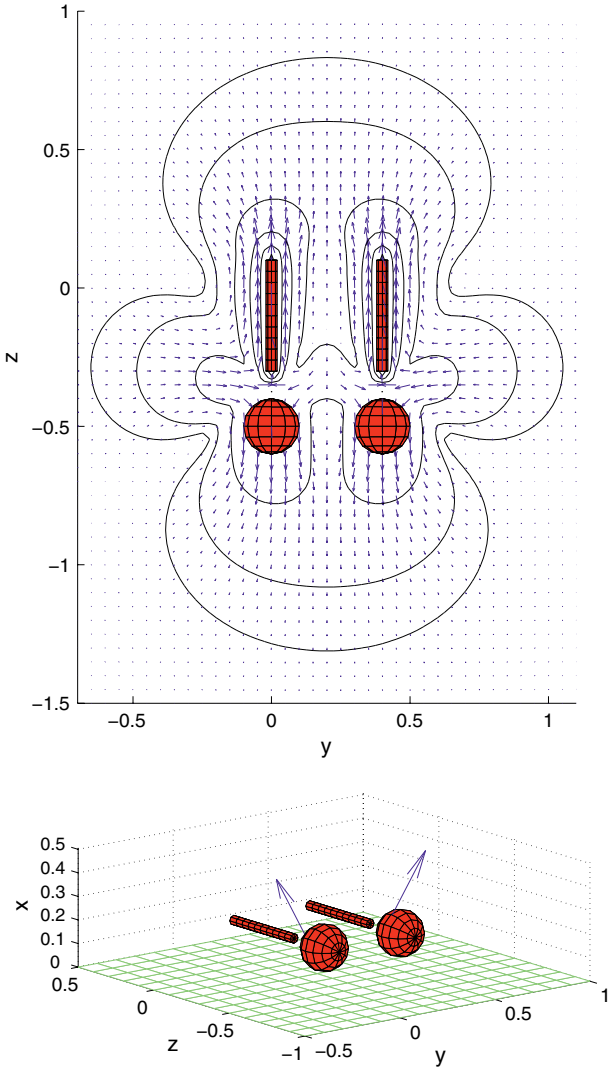

Fig. 14 Velocity field around two organisms near a wall and resultant forces exerted by each organism on the fluid in order to move parallel to the wall and to each other. The forces are (2.72, –1.71, –0.22) $|\mathbf{F}_B|$ (*left organism*) and (2.72, 1.71, –0.22) $|\mathbf{F}_B|$ (*right organism*), where $\mathbf{F}_B$ is the drag on the sphere given by Eq. 8

between cells, as discussed in the introduction. Similar calculations performed on groups of ten cells, and on staggered pairs show that the associated interior flows are weak, but vortical regions, as in Fig. 16, or even more spectacular, can significantly enhance transport of suspended particles or molecules.

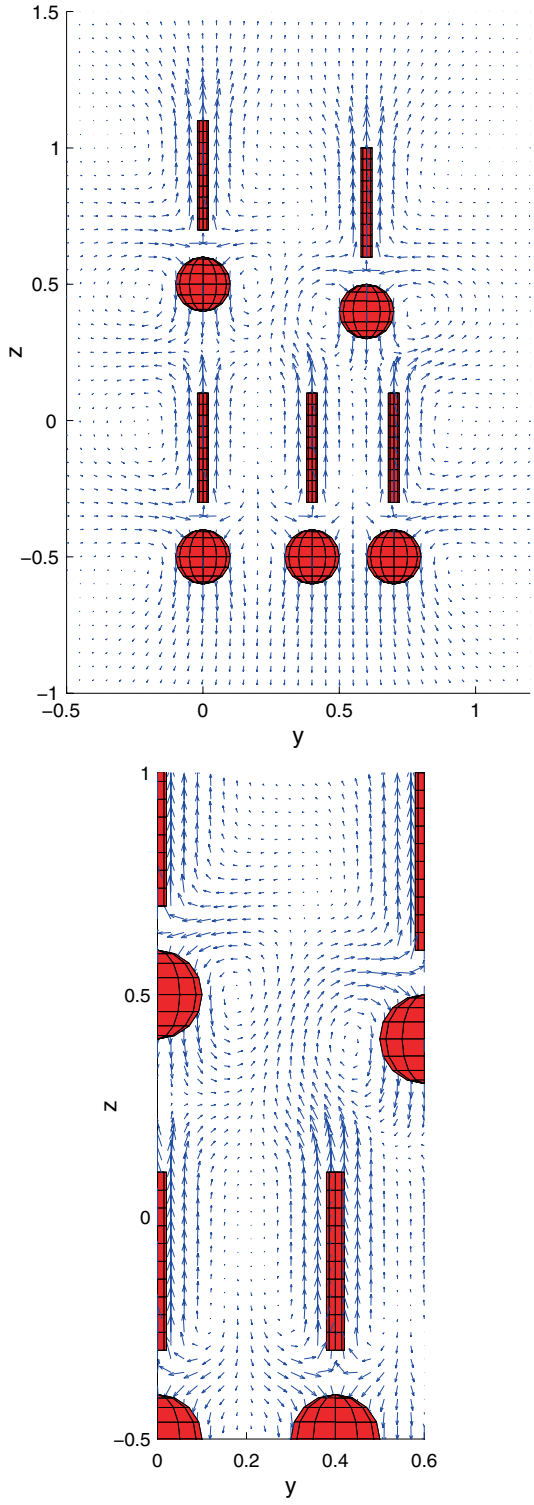

Fig. 15 Velocity field around several organisms above a wall (*top*) and a closer view of the velocity between them (*bottom*)

7 Turbulence at $Re \ll 1$?

To the casual observer, the ZBN phase of a concentrated suspension of swimming *B. subtilis* appears turbulent. More quantitatively, the analysis of the collective dynamics, using PIV based on the motion of the bacteria can reveal not only the correlation functions discussed earlier, but the entire distribution of velocities. Such statistical information can form the basis of analysis of the energy flows in these systems, from the "injection" scale of

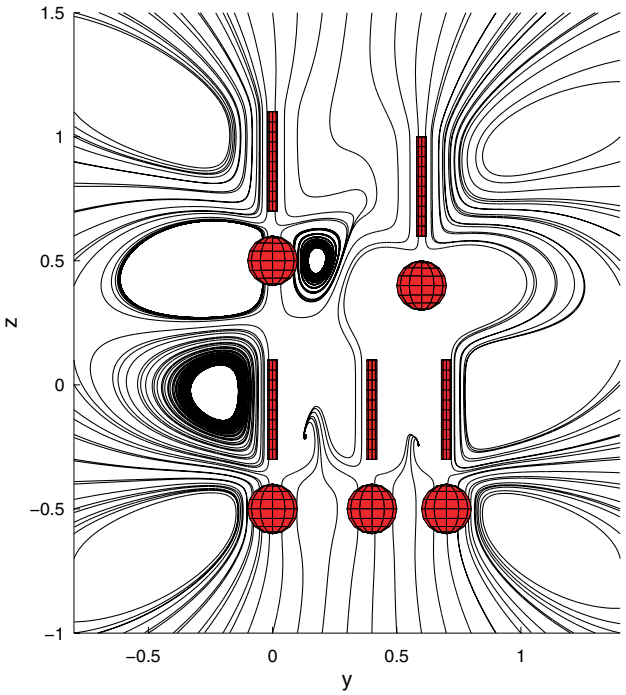

Fig. 16 Streamlines of the velocity field around several organisms near and above a wall. The flow is the same as that in Fig. 15

individual bacteria up to the system size. In this section we briefly discuss that velocity distribution and offer some dimensional analysis regarding an effective Reynolds number for these flows.

One important feature of the ZBN is that the collective speeds of coherent subpopulations of bacteria can be greater than the swimming speeds of individual cells. The distribution of speeds of uncorrelated cells of *B. subtilis* was shown to be approximately Maxwellian over an entire population (Kessler and Hill 1997). The swimming speed of individual cells can vary greatly even over observation times as short as one second (Kessler et al. 2000). When these locomoting cells form a phalanx, they all have approximately the same velocity. The histogram of speeds from our PIV studies, over the entire data set, regardless of angles between streamlines, is again approximately Maxwellian (Fig. 17, black curve). Can the analysis be improved by selecting data over only those regions where the angles between streamlines are smaller than some specified value, i.e., for regions of directional coherence? Does greater co-directionality correlate with a lesser variation in speeds within a domain? Using three thresholds of Φ, 0.8, 0.9 and 0.95, we obtain histograms of the speeds found in progressively more co-linear regions (Fig. 17, red, blue, green curves). These distributions are not Maxwellian; there is a finite lower threshold. This threshold measures the minimum speed required for coherence, for the swimming organisms to form a phalanx. The tail of the distributions at maximum velocity does not change appreciably for different values of Φ, indicating an upper limit of speed for these particular bacteria, a limit likely associated with physical constraints on the mechanism of propulsion. It is significant that the most probable value of the speed, the peak of the distribution, increases with higher values of Φ, and that the width of the distributions does not decrease. Speeds are greater in regions of greater coherence. The spread of velocities occurs because the histograms include data for many coherent domains.

Let us turn now to the question of how to understand the existence of a turbulent dynamic at a formally low *Re*. Considering the suspension as a simple fluid, the conventional Reynolds number, the ratio of inertial and viscous forces, is

$$Re = \frac{UL}{\nu},$$

where ν is the kinematic viscosity, the mean collective velocity $U \sim 5 \times 10^{-3}$ cm/s, $L \sim 10^{-2}$ cm is a typical correlation length (Fig. 5). Thus, $Re \ll 1$ for the typical value $\nu \sim 10^{-2}$ cm^2/s. An increase of ν due to suspension effects further decreases *Re*. How can the quasi-turbulence be sustained?

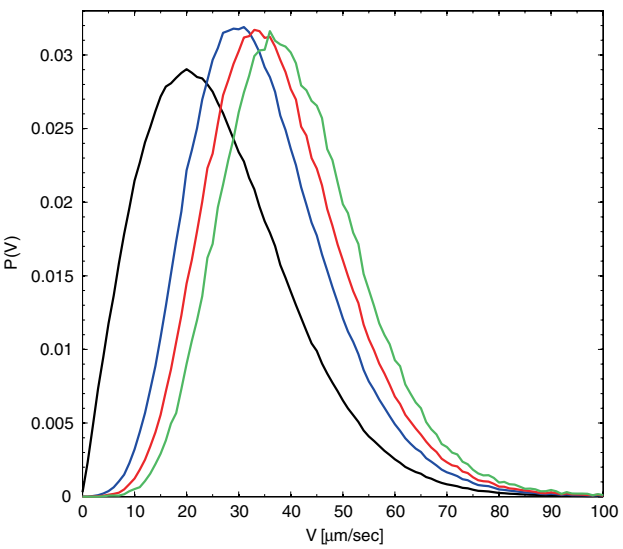

Fig. 17 Experimentally observed distribution of velocities as a function of their angular spread. Within localities where angular spread is defined by Φ (Eq. 5) with $R = 2$, velocity distributions are plotted as histograms for $\Phi_2 > -1.0$, *black*; $\Phi_2 > 0.8$, *blue*; $\Phi_2 > 0.9$, *red* and $\Phi_2 > 0.95$, *green*. These plots imply that improved collective co-directionality correlate with higher mean speeds and displacement of lower thresholds of probability to higher speeds. The *black histogram* includes measurements of the magnitudes of all velocities, codirectional or not; it is approximately Maxwellian. Its lower mean than the *colored curves* indicates that the collective codirectional locomotion of cells is associated with speeds that are on average higher than those for uncorrelated ones

One can analyze the observed dynamics by considering the force or power densities produced by the swimming organisms. A suitable dimensionless ratio can be constructed from the Stokes force that a single bacterial cell must exert to move itself at velocity $\mathbf{v}$,

$$\mathbf{f} = c\mu a\mathbf{v}, \tag{16}$$

where a is a characteristic length scale for the cell, μ is the viscosity of the medium and c is a geometrical factor of order 10^1 (for a sphere in an infinite medium $c = 6\pi$). If there is a concentration of n cells per unit volume the force density is

$$F_n = cn\mu av. \tag{17}$$

On the scale of the coherent structures, the viscous dissipation force density in the collective phase is estimated as

$$F_\mu = \frac{\mu U}{L^2}, \tag{18}$$

where $\mu U/L$ is the collective shear stress. Then, based on these arguments, we define the dimensionless "Bacterial swimming number" Bs,

$$Bs = \frac{F_n}{F_\mu} = cna^3\left(\frac{L}{a}\right)^2\left(\frac{v}{U}\right). \tag{19}$$

For the nearly close-packed ZBN phase, $n \sim 10^{11}$ cm^{-3}. Taking the velocity ratio of order unity, a of order 10^{-4} cm, and $L \approx 10^{-2}$ cm, the observed correlation length, $Bs \sim 10^4$. This "alternative Reynolds number" explains the possibility of a turbulent dynamics when $Re \ll 1$. The large magnitude of Bs sweeps away details on the assumptions of parameters values. Note that even though the fluid dynamics is produced by the motion of flagella, so energy is injected locally into the system, the perceived turbulence is associated with large scales when compared with the cell-flagella complex.

This result can also be obtained via the standard non-dimensionalization of the Navier–Stokes equation with an included force/volume exerted by the swimming organisms. This appears as the divergence of the deviatoric stress tensor $\mathbf{\Sigma}$, where a typical form of stress tensor would be $\mathbf{\Sigma} \sim cn\mu a^2 v\sigma$, where again a is a characteristic size of the swimmer, and where the dimensionless tensor $\boldsymbol{\sigma}$ encodes the internal orientations of the swimmers. Hence, the fluid flow $\mathbf{u}$ is described by

$$\rho\frac{D\mathbf{u}}{Dt} = -\nabla p + \mu\nabla^2\mathbf{u} + cn\mu a\gamma\mathbf{v}, \tag{20}$$

where ρ is the mean density of the suspension, we have introduced the local velocity $\mathbf{v}$, and γ is a function that models the propulsive force of one organism. γ accounts for the fact that a single organism exerts on the fluid equal and opposite forces, displaced by approximately one organism length. Eq. 20 applies only to the case of rather low concentrations of bacteria. Dividing this equation by the term $\mu U/L^2$ delivers a new dimensionless number Bs', based on stresses, as the magnitude of the forcing term:

$$Bs' = cn\mu a\gamma\frac{|\mathbf{v}|}{\mu U/L^2}\gamma = cnL^2 a\gamma\left(\frac{v}{U}\right). \tag{21}$$

This dimensionless ratio is similar in spirit to Bs, except that now U and L ought to arise out of (20) as parameters that give a particular scale to the system. Note that both Bs and Bs' are essentially geometric factors, the viscosity having cancelled (Tuval et al. 2005). Avoiding vectorial aspects of these arguments, a power-based ratio Bsp can be defined as $F_n v/F_\mu U$, yielding

$$Bsp = cna^3\left(\frac{L}{a}\right)^2\left(\frac{v}{U}\right)^2. \tag{22}$$

Observing that $v/U \sim 1$, we note that $Bs \simeq Bsp$.

We now sketch the outline of a model that uses the results of experiments together with an extrapolation of the calculation results in the previous section, e.g., Figs. 15 and 16. To estimate the collective velocity U of a phalanx, we consider a cylinder of aligned co-directionally swimming bacteria each swimming with the mean velocity $\mathbf{v}$ (Fig. 18). The propulsion of the cylindrical domain is due to the forces exerted on the fluid by the flagella emerging from one or more layers of cells at the rear of the cylinder. The bodies of cells at the front push fluid forward. Transverse flows enter and leave the side of the cylinder, with presumably a net volume conserving, and perhaps temporarily stabilizing influx. The concentration of bacteria per area is $n^{2/3}$, the area is πR^2, and S layers of cells contribute the force f (Eq. 16). Assuming the drag of the cylinder is $C\mu LU$, we find

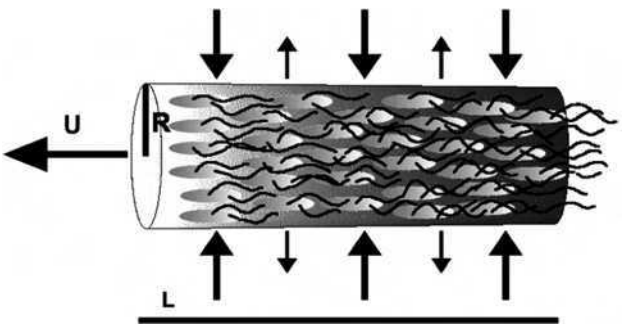

Fig. 18 Schematic diagram of a phalanx, a coherent domain of cells swimming to the left with collective velocity $\mathbf{U}$. *Arrows* indicate direction of transverse fluid flow as in Figs. 15 and 16 due to the collective motion inside the domain

$$U = \left(\frac{\pi c}{C}\right)\left(\frac{SR^2 a n^{2/3}}{L}\right)v. \quad (23)$$

This result is independent of the fluid viscosity. For $R = 10^{-3}$cm, $L = 10^{-2}$ cm, $a = 10^{-6}$ cm, $n^{2/3} = 2 \times 10^7$ cm^{-2} and $S\pi c/C = 10$, we obtain a phalanx moving faster than an individual, $U = 1.8v$, indicating that a more formal version of this approach may prove useful.

8 Discussion

This paper has described how hydrodynamics and biological behavior of a concentrated population of swimming microorganisms can combine to produce a collective dynamic, the ZBN, with interacting nematic-like domains that exhibit quorum polarity of propagation with spatial and temporal correlation. Relevant experiments on individual cell motility, and a novel approach for understanding locomotion and for calculating the flows that surround swimmers, provide ingredients for a realistic theoretical model of this complex two-phase system. Dimensional analysis demonstrates that the observed speeds of the collective domains are plausible, and that the occurrence of "turbulent" dynamics at $Re \ll 1$ can be understood by considering the input of (swimming) energy from the occupants of the fluid.

We demonstrate that the results of PIV, obtained from high frame rate video microscopy images of the swimming cells, i.e. under difficult circumstances, can provide useful data on velocity and vorticity distributions, the latter exhibiting a rather satisfying alternation of signs, somewhat like vortex streets. It should be remembered that the PIV data were obtained from the bacteria, the motile suspended phase, not from added tracers in the water. Moreover, we have developed a novel measure of angular alignment (and deviation), based on the velocity vector field. That analysis shows the remarkable spatial extent of continuous alignment, as well as singular regions of defects. Whereas averages over many quasi-instantaneous correlations of vorticity and velocity show decays of order one second, the alignment data exhibits remarkable stability.

Transport of biologically significant molecules, for cell-cell communication, supply of nutrients and elimination of wastes, and for respiration can be greatly enhanced by the chaotic advection that accompanies the intermittent collisions, reconstitution and decay of the zooming domains. We have proposed a heuristic model of the formation of propagating coherent regions whose ingredients are the transverse flows and inward forces that accompany swimming (Fig. 14), up-flow swimming in shear flows (Sect. 4), flipping of flagella at obstacles (Cisneros et al. 2006), and, of course, geometrically determined stacking (steric repulsion).

What determines the breakup of domains? Extrapolating from Fig. 15 and calculations, not shown here, for phalanxes comprising more swimmers, the flow inside a domain is quite weak. The supply of oxygen to the interior cells (note Fig. 16) would be insufficient to maintain average levels of concentration. The interior cells will therefore swim transversely, up the gradient of oxygen concentration, or swim ever more slowly; both scenarios imply breakup. The swimming velocity distribution of individual cells is approximately Maxwellian, and very oxygen dependent (Kessler and Wojciechowski 1997). The uniform speed of cells in phalanxes is therefore quite remarkable. The decay time of averaged correlations is about one second (Fig. 5) and oxygen supply times (Sect. 1) are about the same. This would seem to be more than a coincidence. There are other possible contributors to the decay of coherence. Interior cells may begin tumbling in search of a more favorable chemical environment; phalanxes that collide break up; the head end of elongated domains, as in Fig. 18, may buckle (we occasionally observe very explicit cases of roll-up); instability of nematics (Simha and Ramaswamy 2002b) may also be a factor. The problem of understanding this intermittency clearly demands further work.

Acknowledgments This research has been supported by DOE W31-109-ENG38 and NSF PHY 0551742 at the University of Arizona, NSF DMS 0094179 at Tulane, and the Schlumberger Chair Fund in Cambridge. We should like especially to thank Matti M. Laetsch for her contributions to Section 4, David Bentley for help with Fig. 1, and T.J. Pedley for discussions and comments on the manuscript.

References

Ainley J, Durkin S, Embid R, Boindala P, Cortez R (2007) The method of images for regularized stokeslets. submitted

Aranson IS, Sokolov A, Kessler JO, Goldstein RE (2007) Model for dynamical coherence in thin films of self-propelled microorganisms. Phys Rev E 75:040901

Berg HC (1993) Random walks in biology. Princeton University Press, Princeton

Berg HC (2003) *E. coli* in motion. Springer, New York

Blake JR (1971a) A spherical envelope approach to ciliary propulsion. J Fluid Mech 46:199–208

Blake JR (1971b) A note on the the image system for a stokeslet in a no-slip boundary. Proc Camb Philol Soc 70:303–310

Childress S (1981) Mechanics of swimming and flying. Cambridge University Press, Cambridge

Cisneros L, Dombrowski C, Goldstein RE, Kessler JO (2006) Reversal of bacterial locomotion at an obstacle. Phys Rev E 73:030901

Cortez R (2001) The method of regularized Sokeslets. SIAM J Sci Comput 23:1204–1225

Cortez R, Fauci L, Medovikov A (2005) The method of regularized Stokeslets in three dimensions: analysis, validation and application to helical swimming. Phys Fluids 17:1–14

de Gennes PG, Prost J (1993) The physics of liquid crystals. Oxford University Press, Oxford

Dombrowski C, Cisneros L, Chatkaew S, Goldstein RE, Kessler JO (2004) Self-concentration and large-scale coherence in bacterial dynamics. Phys Rev Lett 93:098103

Hernandez-Ortiz JP, Stoltz CG, Graham MD (2005) Transport and collective dynamics in suspensions of confined swimming particles. Phys Rev Lett 95:204501

Hill NA, Pedley TJ (2005) Bioconvection. Fluid Dyn Res 37:1–20

Hill J, Kalkanci O, McMurry JL, Koser H (2007) Hydrodynamic surface interactions enable *Escherichia coli* to seek efficient routes to swim upstream. Phys Rev Lett 98:068101

Hillesdon AJ, Pedley TJ, Kessler JO (1995) The development of concentration gradients in a suspension of chemotactic bacteria. Bull Math Biol 57:299–344

Hillesdon AJ, Pedley TJ (1996) Bioconvection in suspensions of oxytactic bacteria: linear theory. J Fluid Mech 324:223–259

Keane RD, Adrian R (1992) Theory of cross-correlation analysis of PIV images. Appl Sci Res 49:191–215

Kessler JO, Hill NA (1997) Complementarity of physics, biology and geometry in the dynamics of swimming micro-organisms. In: Flyvbjerg H et al. (eds) Physics of biological systems. Springer Lecture Notes in Physics, Springer, Berlin 480:325–340

Kessler JO, Wojciechowski MF (1997) Collective behavior and dynamics of swimming bacteria. In: Shapiro JA, Dworkin M (eds) Bacteria as multicellular organisms. Oxford University Press, New York, pp 417–450

Kessler JO, Burnett GD, Remick KE (2000) Mutual dynamics of swimming microorganisms and their fluid habitat. In: Christiansen PL, Srensen MP, Scott AC (eds) Nonlinear science at the dawn of the 21st century. Springer Lecture Notes in Physics Springer, Berlin 542:409–426

Kolter R, Greenberg EP (2006) Microbial sciences the superficial life of microbes. Nature 441:300–302

Lauga E, DiLuzio WR, Whitesides GM, Stone HA (2006) Swimming in circles: motion of bacteria near solid boundaries. Biophys J 90:400–412

Lega J, Mendelson NH (1999) Control-parameter-dependent Swift–Hohenberg equation as a model for bioconvection patterns. Phys Rev E 59:6267–6274

Lega J, Passot T (2003) Hydrodynamics of bacterial colonies: a model. Phys Rev E 67:031906

Lighthill MJ (1975) Mathematical biofluiddynamics. SIAM, Philadelphia

Magariyama Y, Sugiyama S, Muramoto K, Kawagishi I, Imae Y, Kudo S (1995) Simultaneous measurement of bacterial flagellar rotation rate and swimming speed. Biophys J 69:2154–2162

Magariyama Y, Sugiyama S, Kudo S (2001) Bacterial swimming speed and rotation rate of bundled flagella. FEMS Microbiol Lett 199:125–129

Mendelson NH, Bourque A, Wilkening K, Anderson KR, Watkins JC (1999) Organized cell swimming motions in *Bacillus subtilis* colonies: patterns of short-lived whirls and jets. J Bact 181:600–609

Miller MB, Bassler BL (2001) Quorum sensing in bacteria. Ann Rev Microbiol 55:165–199

Nasseri S, Phan–Thien N (1997) Hydrodynamic interaction between two nearby swimming micromachines. Comput Mech 20:551–559

Pedley TJ, Kessler JO (1992) Hydrodynamic phenomena in suspensions of swimming microorganisms. Ann Rev Fluid Mech 24:313–358

Pozrikidis C (1997) Introduction to theoretical and computational fluid dynamics. Oxford University Press, New York

Ramia M, Tullock DL, Phan-Thien N (1993) The role of hydrodynamic interaction in the locomotion of microorganisms. Biophys J 65:755–778

Saintillan D, Shelley MJ (2007) Orientational order and instabilities in suspensions of swimming micro-organisms. Phys Rev Lett 99:058102

Sambelashvili N, Lau AWC, Cai D (2007) Dynamics of bacterial flow: emergence of spatiotemporal coherent structures. Phys Lett A 360: 507–511

Shapiro JA, Dworkin M (1997) Bacteria as multicellular organisms. Oxford University Press, New York

Simha RA, Ramaswamy S (2002a) Hydrodynamic fluctuations and instabilities in ordered suspensions of self-propelled particles. Phys Rev Lett 89:058101

Simha RA, Ramaswamy S (2002b) Statistical hydrodynamics of ordered suspensions of self-propelled particles: waves, giant number fluctuations and instabilities. Physica A 306:262–269

Short MB, Solari CA, Ganguly S, Powers TR, Kessler JO, Goldstein RE (2006) Flows driven by flagella of multicellular organisms enhance long-range molecular transport. Proc Natl Acad Sci (USA) 103:8315–8319

Sokolov A, Aranson IS, Kessler JO, Goldstein RE (2007) Concentration dependence of the collective dynamics of swimming bacteria. Phys Rev Lett 98:158102

Solari CA, Ganguly S, Kessler JO, Michod RE, Goldstein RE (2006) Multicellularity and the functional interdependence of motility and molecular transport. Proc Natl Acad Sci (USA) 103:1353–1358

Solari CA, Kessler JO, Goldstein RE (2007) Motility, mixing, and multicellularity. Genet Program Evolvable Mach 8:115–129

Taylor GI (1952) The action of waving cylindrical tails in propelling microscopic organisms. Proc R Soc London A 211:225–239

Toner J, Tu Y (1995) Long-range order in a two-dimensional dynamical XY model: how birds fly together. Phys Rev Lett 75:4326–4329

Turner L, Berg HC (1995) Cells of *Escherichia coli* swim either end forward. Proc Natl Acad Sci (USA) 92:477–479

Tuval I, Cisneros L, Dombrowski C, Wolgemuth CW, Kessler JO, Goldstein RE (2005) Bacterial swimming and oxygen transport near contact lines. Proc Natl Acad Sci (USA) 102:2277–2282

Vicsek T, Czirok A, Ben-Jacob E, Cohen I, Shochet O (1995) Novel type of phase transition in a system of self-driven particles. Phys Rev Lett 75:1226–1229

Willert CE, Gharib M (1991) Digital particle image velocimetry. Exp Fluids 10:181–193

Wu TY, Brokaw CJ, Brennen C (1975) Swimming and flying in nature. Plenum, New York

Wu XL, Libchaber A (2000) Particle diffusion in a quasi-two-dimensional bacterial bath. Phys Rev Lett 84:3017–3020

Swimming by microscopic organisms in ambient water flow

M. A. R. Koehl · Matthew A. Reidenbach

Abstract When microscopic organisms swim in their natural habitats, they are simultaneously transported by ambient currents, waves, and turbulence. Therefore, to understand how swimming affects the movement of very small creatures through the environment, we need to study their behavior in realistic water flow conditions. The purpose of the work described here was to develop a series of integrated field and laboratory measurements at a variety of scales that enable us to record high-resolution videos of the behavior of microscopic organisms exposed to realistic spatio-temporal patterns of (1) water velocities and (2) distributions of chemical cues that affect their behavior. We have been developing these approaches while studying the swimming behavior in flowing water of the microscopic larvae of various bottom-dwelling marine animals. In shallow marine habitats, the oscillatory water motion associated with waves can make dramatic differences to water flow on the scales that affect trajectories of microscopic larvae.

1 Introduction

Studies of swimming organisms are usually done in still water or in a flume in which unidirectional flow is adjusted so that an animal swimming steadily upstream maintains its position in the working section of the tank. In contrast, organisms swimming in nature can be buffeted by unsteady ambient water motions. The smaller or more weakly swimming the organism, the greater the effect of environmental water motion on its trajectory. When microscopic organisms swim in their natural habitats, they are simultaneously transported by ambient currents, waves, and turbulence. Therefore, to understand how swimming affects the movement of very small creatures through the environment, we need to study their behavior in realistic water flow conditions. However, measuring the swimming behavior of an individual microscopic organism (e.g., instantaneous velocity of the organism, beating of cilia or appendages) requires high-magnification imaging of that organism.

The purpose of the work described here was to develop a series of integrated field and laboratory measurements at a variety of scales that enable us to record high-resolution videos of the behavior of microscopic organisms exposed to realistic spatio-temporal patterns of water velocities and distributions of water-borne chemical cues that affect their behavior. We used microscopic larvae of marine animals to study the effects of ambient water flow on trajectories of very small swimming organisms.

1.1 Swimming by microscopic planktonic larvae of benthic marine animals

Many bottom-dwelling marine animals disperse to new sites by producing microscopic planktonic larvae that are dispersed by ocean currents. Where those larvae settle back down onto the substratum can affect not only the population dynamics of those species, but also the structure of the benthic communities into which they recruit (reviewed by Roughgarden et al. 1991; Ólafsson et al. 1994; Rothlisberg and Church 1994; Palmer et al. 1996). When competent larvae (larvae old enough to be capable of undergoing

M. A. R. Koehl (✉) · M. A. Reidenbach
Department of Integrative Biology,
University of California, 3060 VLSB,
Berkeley, CA 94720-3140, USA
e-mail: cnidaria@socrates.berkeley.edu

G.K. Taylor, M.S. Triantafyllou, and C. Tropea (Eds.): Animal Locomotion, pp. 117–130.
springerlink.com

metamorphosis into the bottom-dwelling form) move from the water column to the substratum, they pass through the benthic boundary layer. A number of studies conducted in flumes with unidirectional currents have shown that turbulent flow in the benthic boundary layer affects the delivery of larvae to the substratum (reviewed in Nowell and Jumars 1984; Butman 1987; Eckman et al. 1990; Abelson and Denny 1997; Crimaldi et al. 2002; Koehl and Hadfield 2004; Koehl 2007). Many shallow coastal sites where larvae recruit into benthic communities are exposed to waves, yet our knowledge of how ambient water motion affects rates of larval settlement has been based on studies in steady currents. Boundary layers are thinner in waves and shear stresses along the bottom are higher than in unidirectional flow at the same free-stream velocity (Charters et al. 1973; Nowell and Jumars 1984). However, net horizontal transport across a habitat in back-and-forth, wave-dominated flow is slow, even though instantaneous velocities in waves can be high (e.g., Koehl and Powell 1994).

Experiments done in still water have shown that dissolved chemical cues can induce the larvae of many types of benthic marine animals to undergo metamorphosis into the bottom-dwelling form (reviewed by Hadfield and Paul 2001). These chemical cues are released by organisms living on the substratum, such as adults of the same species as the larvae, their prey, or bacterial biofilms. A few behavioral studies of swimming competent larvae have shown that these chemical cues can also induce downward motion in still water (Hadfield and Koehl 2004) and in a unidirectional ambient water current (Tamburri et al. 1996). However, the low magnification of the video records of larval trajectories in those studies did not reveal whether such downward motion was due to active swimming or passive sinking, nor did those experiments reveal the spatial distributions in the water of the chemical cues inducing the changes in larval trajectories.

We used larvae of the nudibranch *Phestilla sibogae* and of the tube worm, *Hydroides elegans*, both of which swim with cilia, to investigate the effects of ambient water flow on the motion through the environment of swimming microscopic organisms.

2 Materials and methods

To investigate how swimming by microscopic organisms interacts with ambient water motion to determine the movement of the organisms in their natural habitats, we studied how the larvae of benthic marine animals move from the water column to the substratum to settle into suitable habitats. We have focused on the larvae of the sea slug, *Phestilla sibogae*, which settle onto the substratum in response to a water-borne species-specific metabolite of their prey, *Porites compressa*, the abundant coral that forms reefs in shallow habitats in Hawaii (Hadfield 1977; Hadfield and Koehl 2004; Koehl and Hadfield 2004). To study the interaction of swimming larvae with ambient water flow, we measured water velocities and mass transport on a variety of scales to determine realistic conditions under which to measure the swimming responses of individual larvae.

2.1 Field measurements of water flow

Our first step in determining how ambient water flow affects the motions of swimming larvae was to measure water velocities in the field in the habitats in which the larvae make their way from the water column to the substratum. For the larvae of *Phestilla sibogae*, we measured water velocities above coral reefs in Kaneohe Bay on the island of Oahu, HI (N21°27′, W157°47′).

As is typical of Hawaiian reefs, the dominant coral species at our study sites was *Porites compressa*. We measured water velocities above *P. compressa* throughout the tidal cycle, when water depth above the reef ranged between 0.10 and 0.80 m. On the days when we measured water velocities, water temperatures were 23–26°C, mean wind speeds were 6.6–6.8 m s^{-1}, and maximum wind speeds were 9.2–10.8 m s^{-1} (weather station in Kaneohe Bay of the Hawaiian Institute of Marine Biology, University of Hawaii).

Water velocities were measured using a Sontek SP-AV10M01 Acoustic Doppler Velocimeter (ADV) with a measurement volume of $\sim$0.25 cm^3 and a sampling rate of 25 Hz. A cable from the ADV was run to a boat anchored nearby, where the data were recorded on a laptop computer. Water velocities were recorded for periods of 3 min at heights of 4 and 8 cm above the surface of the reef. The distance of the sampling volume above the reef was measured both by the ADV and by ruler (see Finelli et al. 1999), and these distances agreed in all cases. The ADV was held in position by a rigid scaffolding placed not to interfere with the flow being recorded.

Our field measurements revealed that the shallow coastal habitats in which the larvae of *P. sibogae* must make their way from the water column to a coral reef are characterized by turbulent, wave-driven flow. Some examples of our field water velocity data are shown in Figs. 1 and 2. How are microscopic larvae transported in such flow? How does such water flow disperse the dissolved chemical cues released by the coral *P. compressa* that induce the larvae to settle onto the substratum? We addressed these questions in a series of laboratory flume experiments.

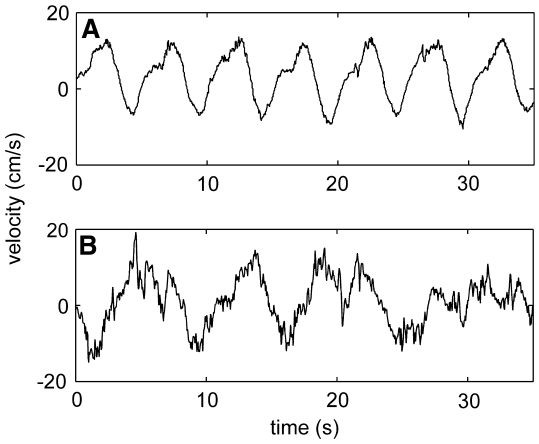

Fig. 1 Comparison of horizontal velocities measured using LDA at a height of 2 cm above the top of the *P. compressa* "reef" in the laboratory wave-current flume (*top graph*), and measured using ADV at a height of 2 cm above the top of a living *P. compressa* reef in Kanehoe Bay, HI (*lower graph*). In both cases the mean water depth above the top of the reef was ∼25 cm. The flume is diagrammed in Fig. 3

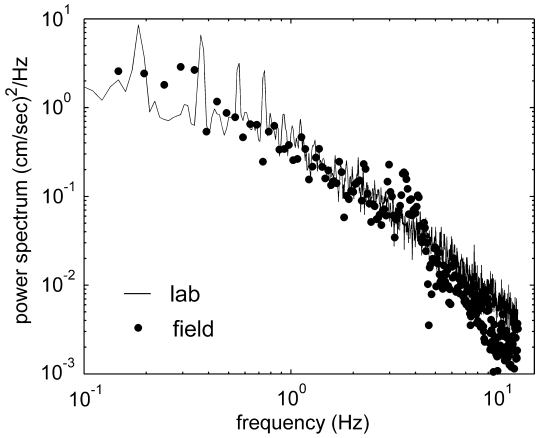

Fig. 2 Comparison of the power spectra for vertical velocity fluctuations measured using LDA at a height of 2 cm above the top of the *P. compressa* "reef" in the laboratory wave-current flume (*black line*), and measured using ADV at a height of 2 cm above the top of a living *P. compressa* reef in Kanehoe Bay, HI (*black circles*). These are data from the same flow records plotted in Fig. 1. In both cases the mean water depth above the top of the reef was ∼25 cm

2.2 Wave-current flume

Our field measurements of water velocities above coral reefs were used to design the water flow in a wave-current flume (12.5-m long by 1.2-m wide) that could produce both a mean current and surface waves (Fig. 3). A steady re-circulating water current was produced by a centrifugal pump commanded by a digital frequency controller. Waves could be generated simultaneously by a paddle-type wavemaker that was driven by a servo motor and linear actuator (Pidgeon 1999). The wavemaker paddle produced waves at a single frequency (which could be adjusted) that propagated in the direction of water motion. A sloping, broad-crested weir at the downstream end of the tank minimized reflection of wave energy, since the flow over the weir was supercritical.

A section of coral "reef" was constructed in the wave-current flume from skeletons of the branching, reef-forming coral *Porites compressa* (provided by M. Hadfield, State of Hawaii collecting permit #1999–2005, after they had been used in other experiments). Left-over coral skeletons, rather than living corals, were used both to minimize the impact of this study on wild populations of *P. compressa*, and to avoid the difficulty of maintaining healthy corals in the laboratory. Baird and Atkinson (1997) found little difference between the overall drag, Re_*, roughness length scale, and mass transfer coefficients of living *P. compressa* and of their skeletons, thus our use of coral skeletons to study water flow over reefs is justified. The skeletons of coral heads (typically about 15 cm tall) were packed together tightly, as they are in the field, such that the constructed reef completely covered the floor of the test section of the flume (1.8-m long and 1.2-m wide). The coral skeletons used in the flume had branch widths and inter-branch spacings of approximately 1 cm (Reidenbach et al. 2006). The total water depth in the flume for all experiments was 40 cm, with the depth of water above the canopy being on average 25 cm.

2.3 Measurements of water velocities in the flume using Laser Doppler Anemometry

A Dantec two-component Laser Doppler Anemometer (LDA), operated in forward scattering mode, was used to measure streamwise, u, and vertical, w, velocities. The

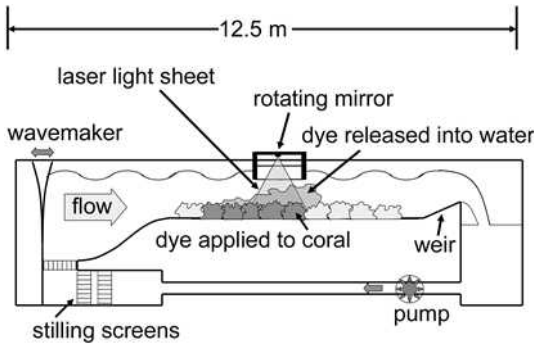

Fig. 3 Diagram of the wave-current flume (details given in the text). Planar-laser induced fluorescence was used to image the flux of Rhodamine 6G dye from the surfaces of the coral under a combined wave-current flow. Examples of velocity measurements and a turbulence spectrum used in this flume are shown in Figs. 1 and 2, respectively

LDA optics were coupled with a laser (Coherent Innova 90), operated at a wavelength of 514.5 nm. The measurement volume was 0.1 mm in the vertical and streamwise directions, and 1 mm in the cross-channel direction. Velocity measurements in the horizontal and vertical directions were made by detecting the Doppler frequency shift of laser light scattered by small particles moving with the fluid. The LDA system was positioned by a 3-axis motorized rail-bearing traverse with positioning in the vertical direction to a precision of 50 μm. Velocities were acquired above the top of the coral canopy (z = 0 defined at the tip of the uppermost branch of the coral) at heights z = 0.2, 0.4, 0.7, 1.0, 2.0, 4.0, 6.0, 8.0, 10.0, 15.0, 20.0, 30.0, 40.0, 50.0, 75.0, and 100.0 mm. Velocity measurements at each height above the canopy were collected at 50 Hz for 30 min. The free-surface displacements of the air–water interface in the flume directly over the LDA measurement volume was simultaneously measured using a capacitance wave height gauge (Richard Brancker Research Ltd., Model WG-30).

2.4 Comparison of water flow in the field and in the flume

Although water flow over coral reefs in Kaneohe Bay was more variable than in the laboratory wave-current flume, the small-scale features of the flow that should affect the movement of larvae and of dissolved cues above a reef were reproduced quite well in the flume. The peak velocities and periods of waves in the flume (Fig. 1a) fell within the ranges of those measured in the field (Fig. 1b), although the waves were more regular in the flume. While large-scale, low-frequency flow features in the field could not be replicated in the flume, the turbulence structure of field and flume flow were very similar (Fig. 2).

2.5 Effects of waves on fine-scale flow

Our LDA measurements of velocity profiles along coral surfaces in the flume revealed that the superposition of waves onto a unidirectional current can have dramatic consequences to water motion at the fine spatial scales encountered by larvae swimming in the water near a coral reef. Examples of such LDA measurements are shown for the case of a unidirectional current (Fig. 4a) and a wave-dominated current (Fig. 4b). The root-mean-squared (rms) velocity for a unidirectional current over the coral increased logarithmically away from the canopy, as expected for a turbulent boundary layer (i.e., Gross and Nowell 1983). In contrast, the profile of the rms velocities for the wave-dominated case revealed drastically different flow structure. A very steep gradient in rms velocities, as well as in peak velocities, occurred very near the surface of the coral. Due to the oscillatory nature of the flow, which is caused by strong pressure gradients that oscillate with the period of the wave forcing (Sleath 1987), water parcels must be quickly diverted around the coral structure, causing accelerations in the flow and ultimately inducing much higher velocities immediately adjacent to the coral roughness elements (Lowe et al. 2005). While flow diversion around the coral also occurred in unidirectional flows, the flow directly adjacent to the coral was much slower than in waves because a thicker boundary layer developed due to the lack of an oscillating pressure in the flow field.

The higher velocities near the coral due to wave action had the effect of increasing both the fluid shear stress imposed on the coral and the turbulent motions near the coral surfaces. Peak Reynolds stresses measured near the surfaces of the coral under the oscillatory flow were

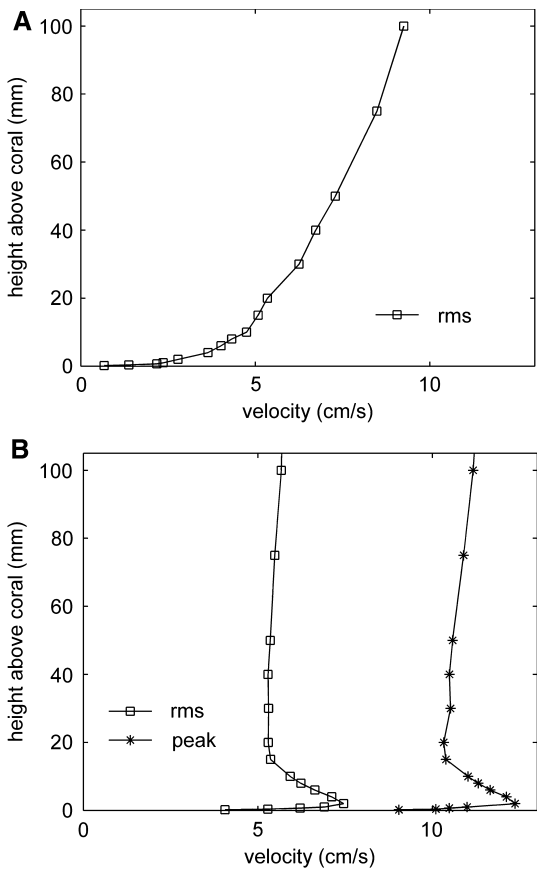

Fig. 4 Root-mean-squared (rms) water velocity profiles, calculated from LDA measurements made above a coral "reef" in a wave-current flume for a unidirectional current with a free-stream velocity of 9.7 cm/s (**a**), and for a wave-dominated flow with a background mean current (**b**). In this example, the wave period was 3s, and the peak freestream horizontal velocity in the downstream direction attained during each wave was 11.3 cm/s, while the peak horizontal velocity near the corals was 12.4 cm/s

$\langle u'w' \rangle_{max}/U^2_{rms}$ = 0.04 ± 0.005 while that for the unidirectional flow were 0.008 ± 0.001, indicating a five-fold increase in turbulence due to waves. While these flow dynamics may be small in scale relative to the depth of the water column, they can have a dramatic effect on a microscopic larva attempting to settle onto the reef.

2.6 Planar laser-induced fluorescence (PLIF) measurements of chemical cues leaching from corals

To investigate how realistic wave-driven water flow affects the dispersal of the dissolved chemical cues that affect larval behavior, we measured the fine-scale instantaneous distributions of chemicals released from a reef in the wave-current flume. Rhodamine 6G fluorescent dye was used as an analogue for dissolved substances, such as larval settlement inducer, released by the corals. This is justified because the Schmidt numbers (Sc = {kinematic viscosity of the fluid}/{molecular diffusivity of the dissolved substance}) for chemicals dissolved in water are quite high. The Sc of Rhodamine 6G in water is 1,250 (Barret 1989). Although we do not yet know the Sc's of settlement inducer released by corals, even if it were an order of magnitude different from that of the dye, the fine-scale patterns of concentration distribution of the two would be quite similar because molecular diffusivity is so low relative to water's kinematic viscosity.

To mimic the release of dissolved inducer from the corals, we painted coral skeletons with a mixture of equal volumes of a solution of Rhodamine 6G dye (500 ppm in fresh water) and gelatin powder (Difco Laboratories Bacto-Gelatin). A layer 1-mm thick of this dye-gelatin solution was painted onto the surfaces of the coral skeletons. A strip along the midline of the coral "reef" 1.2-m long (parallel to the flow direction) and 0.20-m wide was painted in this manner and allowed to set in air for 30 min. These coated corals were then placed into the water in the flume. As the gelatin slowly dissolved, the dye was released into the water to simulate dissolved substances leaching from living corals. For each experiment, coated corals could be exposed to water flow in the flume for approximately 10 min before uneven wear of the dye coating along the surfaces of the corals occurred.

Planar laser-induced fluorescence (PLIF) was used to determine the fine-scale spatial and temporal structure in the water above the reef of the concentrations of dye released from the corals. By illuminating a thin slice of the water column with a sheet of laser light (1-mm thick) that caused the rhodamine dye to fluoresce, we could measure concentrations of this analogue for inducer on a spatial scale relevant to the ambits of microscopic swimming larvae (Fig. 5). Our PLIF system consisted of a laser, imaging optics to expand and focus the laser light, a scanning mirror to produce a sheet of light, and a digital CCD camera to record the dye fluorescence in the flowing water. Laser light was emitted by an Argon-Ion laser (Coherent Innova 90) at an output of 1 watt. The laser beam was first expanded using a 3× laser expander (Melles Griot) to minimize transmission losses and then focused using a 2 m focusing lens. A light sheet was created using a moving-magnet optical scanning mirror (Cambridge Technology model 6800HP). As the dye passed through the laser light sheet, the fluoresced dye was imaged with a CCD camera (Silicon Mountain Design with 1024 by 1024 pixels and 12 bit resolution) fitted with a Micro-Nikkor 55 mm flat-field lens to reduce curvature effects at the image edges. A filter on the receiving optics, with a center frequency of 555 nm and bandwidth of 30 nm, was used to remove laser and ambient light wavelengths, leaving only emitted light from the fluorescing dye. Pixel brightness was proportional to dye concentration (calibration procedures described in Crimaldi and Koseff 2001). Raw images were processed to remove biases in the data, including varying pixel dark response, varying pixel response to fluorescence intensity, slow background changes in pH and temperature, lens and optics aberrations, and laser attenuation due to the background dye concentrations, as described in Crimaldi and Koseff (2001).

Each image (of an area in the flume 21 × 21 cm), was exposed by a single laser scan with a total integration time

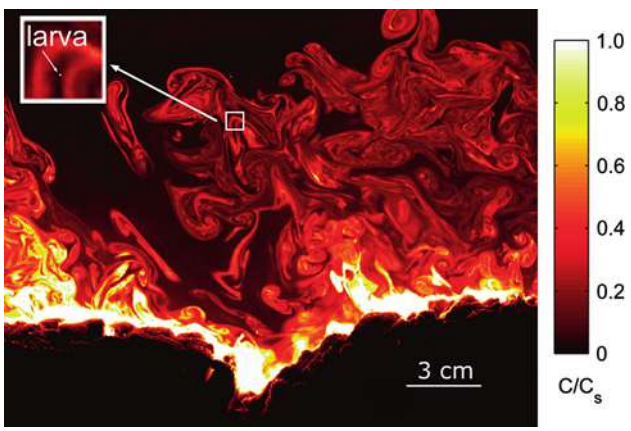

Fig. 5 Planar laser-induced fluorescence (PLIF) image of chemical flux from the surfaces of two *P. compressa* coral heads (which appear *black* at the *bottom* of the image) in the "reef" on the floor of the wave-current flume. The inset image is a ×5 magnification of the portion of the scalar field indicated by the *white box*. The *white dot* in the inset indicates the size of a larva relative to the dye filaments. The color scale bar indicates dye concentration, which is normalized by C_s, the concentration along the surface of the coral. Mean flow was from right to left with a mean current of 7.8 cm/s and a superimposed wave with a period of 5 s and orbital wave velocity amplitude of ±11 cm/s

of 30 ms. The advection of dye during this integration time was much smaller than the typical pixel dimension of 200 μm, thus ensuring accurate mapping of the scalar structure onto the pixel. Images were collected at a rate of 10 Hz. Typically, 100–500 sequential images were taken during each experiment sequence.

By using PLIF to examine the instantaneous spatial distribution of dissolved inducer in the water moving above a reef on the fine spatial scale relevant to a microscopic larva, we learned that filaments of inducer swirl around in inducer-free water. Therefore, we reasoned that as larvae swim or sink through the water, they move into and out of inducer filaments (see insert in Fig. 5), rather than encountering a continuous diffuse concentration gradient as has been assumed in models of larval settlement in response to aromas from the substratum (e.g., Eckman et al. 1994). How do brief encounters with settlement inducer affect the swimming of larvae of *P. sibogae*?

2.7 Rapid reactions of larvae to encounters with filaments of inducer

The larvae of *Phestilla sibogae* swim by beating cilia along the edges of a two-lobed swimming organ, the "velum" (Fig. 6a). To determine how larval swimming is affected by brief encounters with filaments of dissolved inducer, we had to record the action of the cilia and the velum of individual larvae as the animals moved into and out of inducer filaments, hence the animals had to be viewed using a microscope. Because the field of view of a microscope is small, we could not follow the velar actions of freely swimming larvae. Instead, we used videomicrography to record the actions of the velar lobes of individual larvae tethered in a small flume (mini-flume) that moved water past each larva at the velocity of water motion relative to an untethered swimming larva, $\sim$0.2 cm s^{-1} (Hadfield and Koehl 2004).

The Plexiglas "mini-flume" had a working section that was small enough (3-cm wide $\times$ 3-cm deep $\times$ 14.5-cm long) to permit a larva to be viewed using a microscope so that ciliary beating and the position of the velum could be discerned. We videotaped individual larvae (60 frames s^{-1}) using a SPI Minicam mounted on the ocular of a Wild stereomicroscope. A steady flow rate of filtered sea water through the flume was maintained by a constant-head tank, arrays of screens were used to create a flat velocity profile across the middle of the working section where the larva was positioned, and velocity was adjusted by raising or lowering the constant-head tank with a lab jack. The mini-flume was designed to be a flow-through system so that background levels of dye and chemical cues would not build up over the course of an experiment. Water velocity past a larva in the mini-flume was measured by videotaping the movement of small neutrally buoyant particles carried in the moving water. The microscope was focused on the mid-line of the flume (where the larva was positioned) and only particles in sharp focus were digitized and used to calculate water velocities (using SCION Image software) to avoid errors due to parallax.

An individual larva was tethered by using Vaseline® to stick its hydrophobic shell to the tip of a fine stainless steel insect pin (0.24-mm diameter) and was held in a fixed position in the mini-flume in the field of view of the microscope. The pin and larva were gently lifted from the larval culture dish and positioned with a micromanipulator in the mini-flume so that the larva could "swim" into the flow (i.e., the water flow relative to the tethered larva was the same as the water flow relative to a freely swimming larva) (Fig. 6a).

Tethered larvae were exposed to filaments of test solutions (filtered sea water, or various concentrations of chemical inducer released by the coral, *P. compressa*) labeled with 0.05 or 0.1% fluorescein that were carried past them in the flowing water (Fig. 6b) (Hadfield and Koehl 2004). These filament encounters were designed to mimic the exposure to inducer filaments that a freely swimming larva would encounter in the turbulent flow above a coral reef (Fig. 5). We estimated the time course of encounters with odor filaments by a larva above a coral reef using a computer simulation of larval motions (due to swimming, ambient waves, and turbulence) through the changing concentration fields recorded in PLIF videos (e.g., Fig. 5) (Koehl et al. 2007). Swimming velocities measured for untethered larvae in still water in aquaria (Hadfield and Koehl 2004) were used in these simulations. Our calculations indicated that a larva moving through the water passes into and out of filaments of inducer, and that larvae close to the reef encounter filaments more often than do larvae higher above the reef (Koehl et al. 2007). We simulated swimming through an inducer filament in the mini-flume by gently releasing (using a syringe pump, Sage Instruments model No. 351) a narrow filament of test solution into the water through a syringe needle (bore diameter of 0.5 mm) positioned by a micromanipulator perpendicular to the flow upstream from the larva. The needle was higher in the water column than the larva, so the larva did not experience the wake of the syringe. The filament of test solution was carried downstream across the tethered larva by the water flowing in the mini-flume, as though the larva were swimming through the filament. Video records of these fluorescein-labeled filaments showed that before they reached a larva, the momentum induced by the filament-releasing system was damped out.

We videotaped the instantaneous responses of larvae, including cessation and resumption of beating of velar

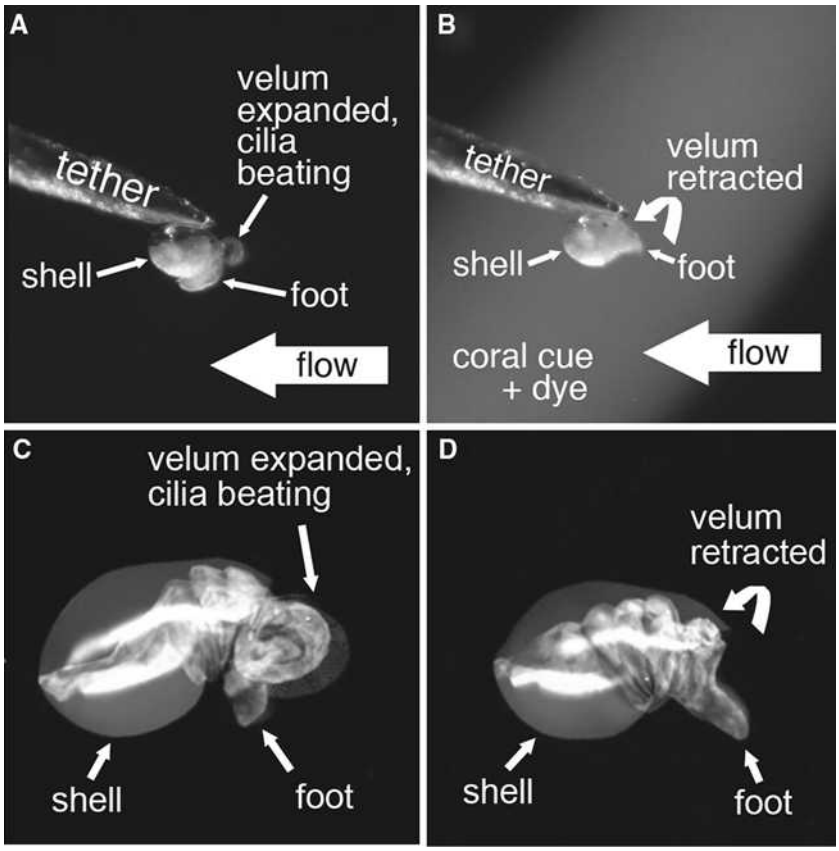

Fig. 6 Side views of a larva of *Phestilla sibogae*. **a**, **b** are frames of a video taken of a larva tethered in a small flume in which water was moved past the larvae at the same speed and opposite direction as the swimming velocity of the larva (video made using a SPI Minicam mounted on the ocular of a Wild dissecting microscope). The tether was a fine insect pin (diameter 0.24 mm). **c**, **d** are diagrams of larvae in the same postures as shown in **a**, **b**, respectively. When the tethered larva was "swimming" in filtered seawater, its velum was extended and its velar cilia were beating (video frame in **a** and diagram in **c**). When a tethered larva encountered a filament of inducer from *P. compressa* (labeled with fluorescien dye), it stopped beating its cilia and retracted its velum into the shell, but left its foot protruding out of the shell (video frame in **b** and diagram in **d**)

cilia, and partial or complete retraction or re-extension of the velum or foot. Using frame-by-frame analyses of these video records, we measured (to the nearest 0.017 s) the time lag between the onset or cessation of these behaviors and the time when the edge of a filament encountered or left the chemoreceptive organ of a larva (Hadfield et al. 2000). The mini-flume permitted us to expose larvae to different temporal patterns of inducer encounters and different concentrations of the chemical cue. We found that swimming competent larvae of *P. sibogae* did not respond to fluorescein dye alone, but that they stopped beating their cilia and retracted their velum into the shell when they encountered inducer above threshold concentration, and they re-expanded the velum and resumed ciliary beating upon exiting an inducer filament (Hadfield and Koehl 2004). If they had not been tethered, the larvae would have sunk through the water when the velum was retracted.

Our high-magnification records of what larvae did during brief encounters with inducer filaments revealed that they kept the foot protruded out of the shell when the velum was retracted. This observation explains why larvae moving downwards in coral inducer in still water traveled more slowly than both swimming larvae and than sinking dead, fully retracted larvae (Hadfield and Koehl 2004): the high drag on the foot of a larva sinking in response to inducer slows down its rate of descent. The foot of a competent *P. sibogae* larva is sticky, thus a larva with its foot extended from the shell can adhere to a surface on which it lands (Hadfield and Koehl 2004; Koehl and Hadfield 2004). Past analyses of larval settlement onto surfaces have often relied on sinking velocities measured for dead or anesthetized larvae (e.g., Butman et al. 1988), but our *Phestilla* results illustrate the importance of knowing the postures and behaviors of larvae before assuming that living larvae move like passive, dead ones.

How do the instantaneous behavioral responses of larvae of *P. sibogae* to brief encounters with filaments of coral inducer affect their motion relative to a coral reef in nature? To address that question, we must put microscopic larvae (whose responses to inducer were measured in the mini-flume, and whose swimming and sinking velocities were measured in still water in aquaria, Hadfield and Koehl 2004) back into the wave-driven ambient flow over a coral reef.

2.8 Simultaneous measurements of water velocities (particle image velocimetry, PIV) and of scalar concentrations (PLIF)

Microscopic organisms such as larvae are carried along by the water in which they are swimming, Because they are so small, such organisms are transported across the habitat by

net current flow, and are carried around locally in turbulent eddies. Those turbulent eddies also carry the filaments of chemical cues to which the larvae react (Fig. 5). The only way that a microscopic organism can move *relative to the water and chemical cues* around it is to swim or sink. In contrast, the organism moves *relative to the substratum* both by swimming or sinking and by being carried by the ambient water flow. Therefore, to determine the temporal pattern of inducer encounters by a larva or the trajectory of a microscopic animal relative to the substratum, we must simultaneously measure both the fine-scale velocity vector field of the flow and the fine-scale patterns of concentration of dissolved inducer in the water.

Instantaneous velocity vector fields of turbulent flowing water can be measured using particle image velocimetry (PIV; technique described in detail in e.g., Cowen and Monismith 1997). A method which combines measurements of planar laser-induced fluorescence and particle image velocimetry can be used to simultaneously measure inducer concentration and velocity structure in two dimensions. For our PLIF imaging, we used a laser with an output wavelength of light at 488 nm to excite fluorescein dye (mean excitation at 490 nm) leaching from coral skeletons, as described above for rhodamine. A sheet of laser light (produced with a scanning moving-magnet mirror, as described above) illuminated a thin slice through the water column in the flume, and the fluorescein dye in that slice emitted light at a mean wavelength of 520 nm. We recorded the dye motions in the flume using a digital camera (Redlake motionscope with 480 × 420 pixel resolution) fitted with an optical bandpass filter of 520 ± 10 nm (Andover Corp.) so that only emitted light from the fluorescent dye was imaged. This laser sheet was scanned to illuminate the imaging field every 0.02 s, with a wait period of 0.02 s between each scan. A second laser with an output wavelength of light at 532 nm was simultaneously used for our PIV imaging. This second laser illuminated silver-coated glass spheres (11 μm in diameter, Potter Industries) carried in the water moving in the flume, but did not excite the fluorescein dye. The second laser was also pulsed at 0.02 s intervals, but only during the time periods when the PLIF laser was not being scanned. The pulsed laser passed through a 30° cylindrical lens to create a light sheet that was aligned along the same two-dimensional plane as the PLIF laser. Particle motions illuminated by the PIV laser were recorded using a second Redlake motionscope digital camera (Fig. 7a). Both cameras were aligned so that they imaged the same field. Images of particle trajectories were analyzed with PIV software (MatPIV 1.6.1) to calculate a velocity vector in every subwindow (16 by 16 pixels), and these vector fields were superimposed on the simultaneously recorded scalar concentration field (Fig. 7b). Such data permits us to assess the instantaneous water flow and inducer concentration encountered by a microscopic larva at any defined position in the portion of the water column that we have imaged.

2.9 Putting data from different scales together to determine larval trajectories through the environment

A computer simulation of the transport of larvae relative to the substratum can be conducted using data measured at the

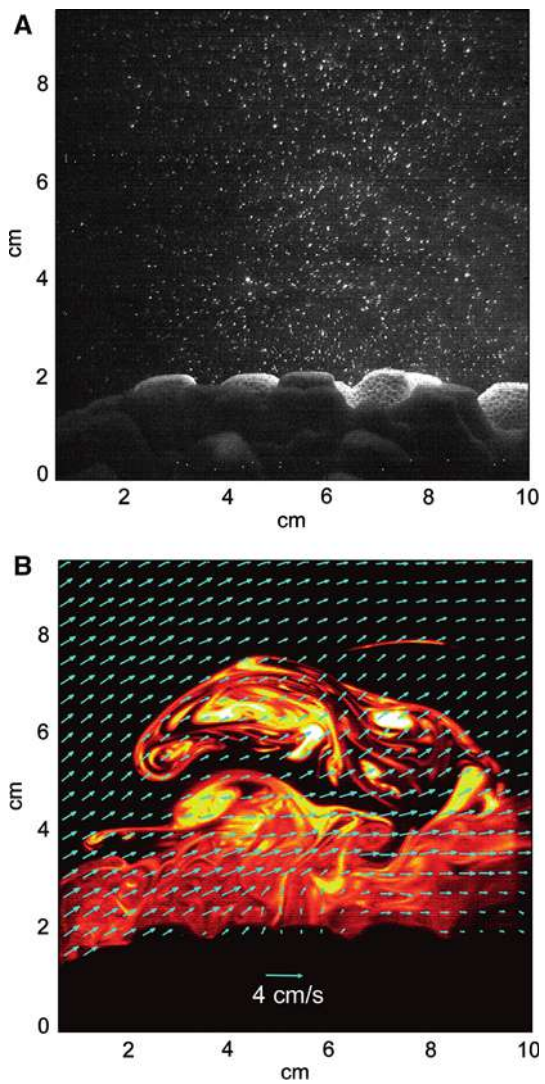

Fig. 7 Example of simultaneous PIV and PLIF measurements over *P. compressa* coral in wave-dominated flow in a flume. The flow was oscillatory with a mean freestream velocity (from left to right in the image) of U = 10 cm/s. Images shown here were collected when the oscillatory flow was beginning to reverse the current from right to left. **a** Frame of a PIV video. **b** PLIF image of dye concentrations recorded 0.02 s after the image shown in **a**. The velocity vectors of water motion that occurred during this interval are shown in *blue*

different spatial scales described above. Larvae can be simulated by behavioral algorithms (based on microscope observations on the scale of micrometers of larvae in the mini-flume) and can be assigned swimming and sinking velocities (measured on the scale of millimeters to centimeters s for freely swimming larvae in aquaria). These simulated larvae can be placed randomly in the PLIF/PIV data (scale of 0.1 mm's to cm's) recorded in a wave-flume, in which water flow and coral reef structure measured in the field on the scale of centimeters to meters was mimicked. A larva sinks or swims, depending on the concentration of inducer in the pixel in which it is located in the PLIF video frame. The vector sum of the swimming (or sinking) velocity of a microscopic larva and of the water velocity in the PIV subwindow in which the larva is located predicts where that animal will be in the next frame of the PLIF video of the scalar (i.e., inducer) field. By repeating such calculations for successive frames of the PLIF/PIV videos, the trajectories of larvae swimming and sinking in the turbulent, wave-driven, inducer-laden water above a coral reef can be determined.

2.10 Larval swimming near surfaces in water currents and waves

When swimming animals encounter surfaces, their behavior can be altered. For example, in still water, the swimming behavior of microscopic larvae of the marine tube worm, *Hydroides elegans*, changes if they touch a surface covered with biofilm (The mechanisms responsible for these behavioral changes are not yet understood.). Surfaces in marine habitats are first colonized by biofilms of bacteria and other microorganisms; then larvae of larger animals recruit onto the biofilmed substratum (e.g., reviewed by Koehl 2007). Videos of larvae of *H. elegans* in dishes of still water showed that they continued to swim when over clean glass surfaces, but spent more time crawling on the substratum than swimming above biofilmed surfaces (J. Zardus, M. Hadfield, T. Cooper, M. A. R. Koehl, unpublished data). Contact with biofilms in still water also induces the larvae of *H. elegans* to undergo metamorphosis (Unabia and Hadfield 1999). If these larvae are being carried past the substratum by ambient water flow, how do contacts with biofilmed surfaces affect their trajectories?

Hydroides elegans are abundant members of the "fouling communities" that grow on man-made structures, such as ships and docks, in warm-water harbors worldwide. To study the trajectories of the microscopic larvae of *H. elegans* in realistic flow conditions, we first measured water flow across surfaces in Pearl Harbor, HI, where *H. elegans* are abundant. Our measurements of water velocity profiles (using a small electromagnetic flow meter, Marsh-McBirney Model 523) adjacent to dock surfaces, showed that the flow oscillated due to wind chop superimposed on slow ambient currents (Fig. 8a).

We videotaped the behavior of competent larvae of *H. elegans* near different substrata in the "mini-flume" described above. An array of screens upstream from the working section was used to produce a velocity profile similar to that measured in Pearl Harbor, and a plunger upstream of the screens was used to superimpose velocity oscillations on the net downstream water motion in the flume to simulate the wind chop measured in the field (Fig. 8b). Water velocity profiles were measured as a function of time by digitizing (Matplotlib 0.83) videos (60 fps) of the paths of neutrally buoyant marker particles carried in the water.

Competent larvae of *H. elegans* were placed in the upstream reservoir of the flume and were carried by the moving water through the working section of the flume. By working in the mini-flume, we were able to make high-magnification videos in which individual larvae could be followed (Fig. 9). The water was not recirculated through the flume so that we only recorded the first encounters of larvae with a test substratum. We videotaped the larvae (60 fps) and digitized their trajectories using Matplotlib 0.83.

3 Results and discussion

3.1 Putting data from different scales together to determine larval trajectories through the environment

Our computer simulation of the transport of larvae *Phestilla sibogae* relative to the substratum was an

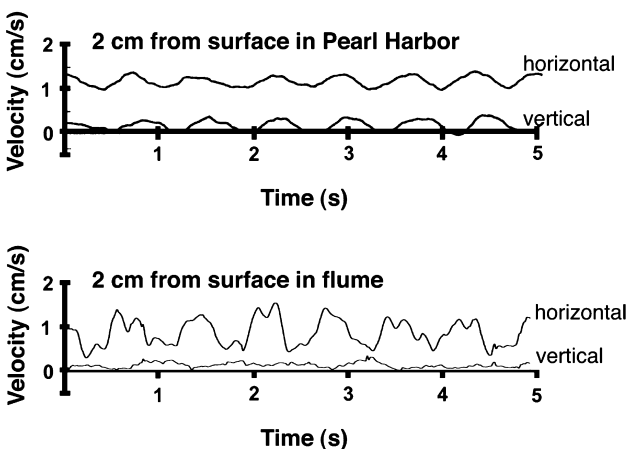

Fig. 8 Water velocities measured as a function of time 2 cm above surfaces covered with the tube worm *Hydroides elegans* in Pearl Harbor, HI (**a**), and in the lab in the working section of the "mini-flume" in which larval behaviors can be recorded

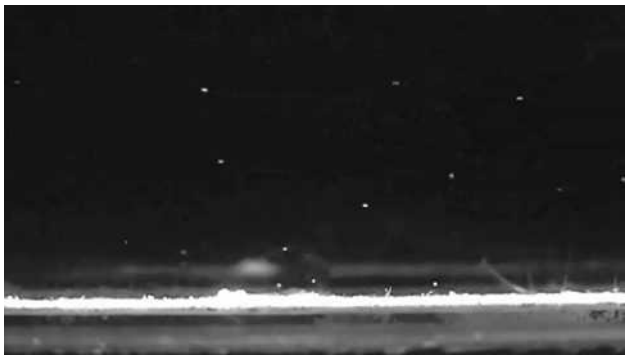

Fig. 9 Frame of a video of competent larvae of the tube worm *Hydroides elegans* swimming in wave-driven flow near a surface covered with a biofilm in a small wave-current flume. The larvae, which look like white dots, are about 100-μm long. The magnification was chosen to achieve the largest field of view in which the larvae were still big enough to be clearly visible

individual-based model that coupled behavioral algorithms [measured for microscopic larvae exposed to realistic patterns of encounters with coral odor (Hadfield and Koehl 2004)] with fine-scale patterns of time-varying instantaneous flow velocities and odor concentrations [measured above a coral reef in a flume (Reidenbach et al. 2007) exposed to wavy, turbulent water movement like that measured in the field (Koehl and Hadfield 2004)]. Our calculations revealed that the simple behavior of sinking during brief encounters with odor filaments can enhance the rate of larval settlement onto a reef by about 20% (Koehl et al. 2007). Thus, we learned that the behavioral responses of slowly moving microscopic larvae to chemical cues can affect their trajectories in the environment, even in turbulent, wave-driven ambient water flow.

Is it worth the effort to measure fine-scale time-varying velocity and odor distributions under field flow conditions? Past analyses of larval settlement in response to odors assumed a constant, diffuse concentration gradient of dissolved chemical cues from the benthos (e.g, Crisp 1974; Eckman et al. 1994). When we used the diffuse time-averaged odor concentration gradient measured above our reef in the flume to calculate larval transport rates, we overestimated larval transport by about 15% compared with rates we calculated using the time-varying instantaneous filamentous pattern (Koehl et al. 2007). Many studies of larval settlement assumed that larvae are transported in the benthic boundary layer like passive, negatively buoyant particles (e.g., Hannan 1984; Butman 1987). When we ran our model with the assumption that larvae sink continuously like passive particles, we over-estimated the rate of transport of larvae to the substratum compared with rates we calculated using the behavior measured for larvae of *Phestilla sibogae* that sink only while in coral odor above a threshold concentration (Koehl et al. 2007). Thus, our calculations indicate that ignoring time-varying, fine-scale flow and odor distributions or instantaneous larval responses can lead to overestimates of the rates of transport of larvae to the substratum.

3.2 Larval swimming near surfaces in water currents and waves

H. elegans larvae in still water swim along helical paths (Fig. 10a). Such helical swimming has been shown to enable organisms in still water to navigate relative to odors, light, and gravity (e.g., reviewed in McHenry and Strother 2003). However, we found that when *H. elegans* were swimming in the miniflume in water flow like that encountered near surfaces in harbors, they were carried distances of a cm or more (i.e., $\geq$100 body lengths) relative to the substratum for each turn of the helix (Fig. 10b, c) (M. A. R. Koehl, D. Sischo, T. Cooper, T. Hata, and M. Hadfield, unpublished data). Furthermore, when the oscillations due to wind chop were added to the slow currents typical of harbors, larval trajectories were more varied and showed more vertical motion (Fig. 10c) than in flow without the wind chop (Fig. 10b). The importance of helical swimming in navigation by larvae carried by turbulent or wave-driven ambient water motion has not yet been determined.

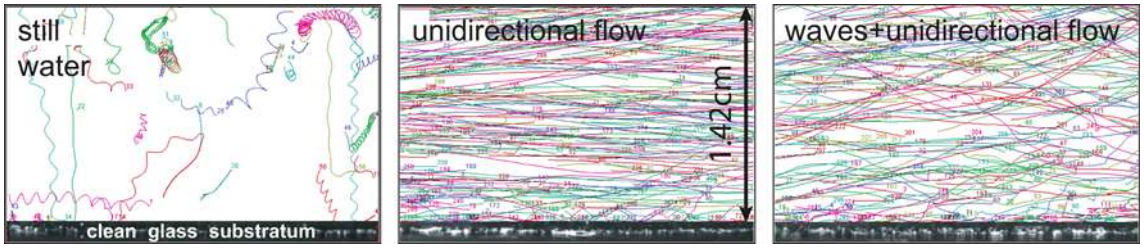

Fig. 10 Digitized trajectories of competent larvae of *H. elegans*. Each colored line shows the path of an individual larva. Larvae in still water swam along helical paths (*left panel*), but were carried downstream in a unidirectional water current (*middle panel*), or were carried in a slow current plus small waves (typical of wind chop in harbors) (*right panel*). The larvae had more variable trajectories with more vertical motion when waves were superimposed on the current

By producing small-scale flow in the miniflume that was similar to water motion measured in the field, we were also able to record the behavior of individual larvae of *H. elegans* as they encountered the substratum under realistic flow conditions (Koehl, Sischo, Cooper, Hata, and Hadfield, unpublished data). We learned that when competent larvae of *H. elegans* contacted the flume floor, they appeared to "hop" along the bottom, touching down two–three times per centimeter that they moved downstream. The touchdown durations of larvae that contacted biofilmed surfaces were longer than for larvae that contacted clean glass, the duration of a larva's contact with the substratum was shorter in flowing water than in still water, and the variation in touchdown time was greater in waves than in unidirectional flow. Our results indicate flowing water and contact with biofilmed surfaces have dramatic consequences for the trajectories of larvae of *H. elegans.*

3.3 Ambient water flow affects the motion of swimming microscopic organisms

Studies of swimming are often done in still water or in unidirectional currents in flumes. However, when microscopic organisms swim in their natural habitats, they simultaneously are being transported by ambient currents, waves, and turbulence. Therefore, to understand how swimming affects the movement of very small creatures through the environment, we need to study their behavior in realistic water flow conditions. However, quantifying the swimming behavior (e.g., ciliary beating, body trajectory) of an individual microscopic organism requires high-magnification imaging of that organism over time, which is very difficult in their natural habitats or in a large flume. In this paper, we have described a series of integrated field and laboratory measurements at a variety of scales that have enabled us to record high-resolution videos of the behavior of microscopic marine larvae exposed to realistic spatio-temporal patterns of water velocities and of chemical cues that affect their behavior.

We found that the oscillatory water motion associated with waves can make dramatic differences to water flow on the scale of microscopic larvae (Reidenbach et al. 2007). Although shallow marine habitats are often exposed to waves or wind chop, most flume studies of the effects of water flow on larval settlement onto the substratum have been done in unidirectional flow (reviewed in Abelson and Denny 1997; Koehl 2007). Fortunately, the tools are now available to produce in the laboratory more realistic water flow, based on field measurements on the spatio-temporal sales relevant to larval swimming.

Not only do ambient currents affect the trajectories of microscopic organisms by carrying them across the habitat, but water movement also can stimulate them to change their swimming behavior. For example, some larvae curtail their swimming in rapid water currents (e.g., lobsters, Rooney and Cobb 1991; polychaetes, Pawlik and Butman 1993). Similarly, snail larvae were induced to sink when high turbulence dissipation rates were produced in a tank by oscillating screens (Fuchs et al. 2004). Some types of larvae orient their locomotion relative to the direction of ambient water flow or shear (e.g., barnacles, Crisp 1955; bivalves, Jonsson et al. 1991; bryozoans, Abelson 1997). Larvae that have landed on a surface can stay or they can reject the surface and resume swimming (reviewed by Krug 2006); the larvae of some species of barnacles resume swimming after landing more often in rapidly moving water than they do in slow flow (Mullineaux and Butman 1991; Jonsson et al. 2004; Larsson and Jonsson 2006). As these studies illustrate, laboratory swimming studies conducted in still water may not reveal ecologically relevant behaviors for those animals that alter their locomotion in response to water movement in the environment.

3.4 Swimming by microscopic organisms can affect their transport by ambient water flow

Whether marine larvae are simply transported like passive particles by moving water or actively seek suitable habitats has long been debated (e.g., reviewed by Butman 1987; Woodin 1991; Jumars 1993; Koehl 2007). Evidence has been accumulating that, although microscopic organisms such as larvae are small and swim slowly relative to ocean currents, their locomotory behavior can affect where they are transported by ambient water flow.

As described above, we found that the behavior of sea slug larvae that are being carried in realistic wave-driven water flow near surfaces can affect their transport to the surfaces (Koehl et al. 2007). Similarly, the swimming of bivalve larvae in unidirectional flow in flumes affects their transport to the bottom. (Tamburri et al. 1996; Finelli and Wethey 2003). In addition, studies of ascidian larvae, which are large enough to be seen and tracked by investigators in the field under natural flow conditions, have shown that larval swimming responses to light and gravity affect their transport across the habitat and their settlement onto the substratum (reviewed in Young 1990; Worcester 1994; Koehl et al. 1997).

Not only can the behavior of larvae affect their transport across the benthic boundary layer, but their locomotion also can affect their horizontal transport over long distances. Large-scale water movements in the ocean carry marine larvae between sites and from offshore waters to the coast (e.g., reviewed by Roughgarden et al. 1991; Rothlisberg et al. 1995; Shanks 1985). The vertical position

of larvae in the water column can determine where they are carried, since water at different depths can move in different directions. Thus, the vertical swimming or sinking behavior of larvae can affect their horizontal transport despite how slowly they locomote relative to ambient water currents (e.g., Cronin and Forward 1986; Shanks 1985; Epifanio et al. 1989; Bingham and Young 1991; Rothlisberg et al. 1995; Tankersley and Forward 1994; Tankersley et al. 1995; Queiroga and Blanton 2005). Many lab studies have documented the behavioral responses of larvae to environmental cues (e.g., light, gravity, pressure, salinity), as well as the endogenous rhythms of such behaviors and the ontogenetic changes in swimming, and have related these responses to where larvae are carried by currents (e.g., Forward and Cronin 1980; Forward et al. 1995; Tankersley and Forward 1994; Tankersley et al. 1995; and others reviewed by Chia et al. 1984; Young and Chia 1987; Young 1995). However, some larvae swim too weakly for such mechanisms to be important to their dispersal (e.g., Stancyk and Feller 1986), while others are such strong swimmers that they can actively move horizontally in spite of ambient currents (e.g., crabs, Luckenbach and Orth 1992; lobsters, Katz et al. 1994).

4 Conclusions

Studies of swimming are often done in still water or in unidirectional currents in flumes. However, the motion of microscopic organisms swimming in their natural habitats cannot be understood without considering how ambient water flow affects their trajectories and the transport of chemical cues that induce behavioral responses. In shallow marine habitats, the oscillatory water motion associated with waves can make dramatic differences to water flow on the scale of microscopic organisms such as larvae.

Acknowledgments This research was supported by National Science Foundation grant # OCE-9907120 (MK), Office of Naval Research grant # N00014-03-1-0079 (MK), The Virginia G. and Robert E. Gill Chair (MK), a MacArthur Foundation Fellowship (MK), a Stanford Graduate Fellowship (MR), and a Miller Postdoctoral Fellowship (MR). We thank M. Hadfield for the use of facilities at the Kewalo Marine Laboratory, University of Hawaii, for collaborating with us on work involving living larvae, and for providing coral skeletons (State of Hawaii collecting permit #1999–2005). We thank J. Koseff for the use of facilities at the Environmental Fluid Mechanics Laboratory, Stanford University, and for collaborating with us on wave-flume experiments, and M. Stacey for the use of flume facilities in the Department of Civil and Environmental Engineering, University of California, Berkeley. D. Sischo (supported by a National Institutes of Health MBRS RISE grant) and T. Hata took the minflume videos from which Figs. 9 and 10 were made. We are grateful to R. Chock, T. Cooper, A. Faucci, N. George, S. Jackson, and M. O'Donnell for technical assistance, and to G. Rangan for making the diagrams in Fig. 6c and d.

References

Abelson A (1997) Settlement in flow: upstream exploration of substrata by weakly swimming larvae. Ecology 78:160–166

Abelson A, Denny MW (1997) Settlement of marine organisms in flow. Annu Rev Ecol Syst 28:317–339

Baird ME, Atkinson MJ (1997) Measurement and prediction of mass transfer to experimental coral reef communities. Limnol Oceanogr 42:1685–1693

Barret TK (1989) Nonintrusive optical measurements of turbulence and mixing in a stabily stratified fluid. University of California, San Diego PhD Dissertation

Bingham BL, Young CM (1991) Larval behavior of the ascidian *Ecteinascidia turbinata* Herdman; an in situ experimental study of the effects of swimming on dispersal. J Exp Mar Biol Ecol 145:189–204

Butman CA (1987) Larval settlement of soft-sediment invertebrates: The spatial scales of pattern explained by active habitat selection and the emerging role of hydrodynamic processes. Oceanogr Mar Biol Ann Rev 25:113–165

Butman CA, Grassle JP, Busky EJ (1988) Horizontal swimming and gravitational sinking of *Capitella* sp. 1 (Annelida: Polychaeta) larvae: implications for settlement. Ophelia 29:43–58

Charters AC, Neushul M, Coon D (1973) The effect of water motion on algal spore adhesion. Limnol Oceanogr 18:884–896

Chia F, Buckland-Nicks SJ, Young CM (1984) Locomotion of marine invertebrate larvae: a review. Can J Zool 62:1205–1222

Cowen EA, Monismith SG (1997) A hybrid digital particle tracking velocimetry technique. Exp Fluids 22:199–211

Crimaldi JP, Koseff JR (2001) High-resolution measurements of the spatial and temporal scalar structure of a turbulent plume. Exp Fluids 31:90–102

Crimaldi JP, Thompson JK, Rosman JH, Lowe RJ, Koseff JR (2002) Hydronamics of larval settlement: The influence of turbulent stress events at potential recruitment sites. Limnol Oceanogr 47:1137–1151

Crisp DJ (1955) The behavior of barnacle cyprids in relation to water movement over a surface. J Exp Biol 32:569–590

Crisp DJ (1974) Factors influencing the settlement of marine invertebrate larvae. In: Grant PT, Mackie AM (eds) Chemoreception in marine organisms. Academic, London p 177

Cronin TW, Forward RB Jr (1986) Vertical migration cycles of crab larvae and their role in larval dispersal. Bull Mar Sci 39:192–201

Eckman JE, Savidge WB, Gross TF (1990) Relationship between duration of cyprid attachment and drag forces associated with detachment of *Balanus amphitrite*. Mar Biol 107:111–118

Eckman JE, Werner FE, Gross TF (1994) Modeling some effects of behavior on larval settlement in a turbulent boundary layer. Deep Sea Res 41:185–208

Epifanio CE, Masse AK, Garvine RW (1989) Transport of blue crab larvae by surface currents off Delaware Bay, USA. Mar Ecol Prog Ser 54:35–41

Finelli CM, Hart DD, Fonseca DM (1999) Evaluating the spatial resolution of an acoustic Doppler velocimeter and the consequences for measuring near-bed flows. Limnol Oceanogr 44:1793–1801

Finelli CM, Wethey DS (2003) Behavior of oyster larvae (*Crassostrea virginica*) larvae in flume boundary layer flows. Mar Biol 143:703–711

Forward RB Jr, Cronin TW (1980) Tidal rhythms of activity and phototaxis of an estuarine crab larva. Biol Bull 158:295–303

Forward RB Jr, Tankersley RA, De Vries MC, Rittshof D (1995) Sensory physiology and behavior of blue crab (*Callinectes sapidus*) postlarvae during horizontal transport. Mar Freshw Behav Physiol 26:233–248

Fuchs HL, Mullineaux LS, Solow AR (2004) Sinking behavior of gastropod larvae (*Ilyanassa obsoleta*) in turbulence. Limnol Oceanogr 49:1937–1948

Gross TF, Nowell ARM (1983) Mean flow and turbulence scaling in a tidal boundary layer. Cont Shelf Res 2:109–126

Hadfield MG (1977) Chemical interactions in larval settling of a marine gastropod. In: Faulkner DJ, Fenical WH (eds) Marine natural products chemistry. Plenum, New York, pp 403–413

Hadfield MG, Koehl MAR (2004) Rapid behavioral responses of an invertebrate larva to dissolved settlement cue. Biol Bull 207:28–43

Hadfield MG, Meleshkevitch EA, Boudko DY (2000) The apical sensory organ of a gastropod veliger is a receptor for settlement cues. Biol Bull 198:67–76

Hadfield MG, Paul VJ (2001) Natural chemical cues for settlement and metamorphosis of marine-invertebrate larvae. In: McClintock JB, Baker BJ (eds) Marine chemical ecology. CRC Press, Boca Raton,pp 431–461

Hannan CA (1984) Planktonic larvae may act as passive particles in turbulent near-bottom flows. Limnol Oceanogr 29:1108–1116

Jonsson PR, Andre C, Lindegarth M (1991) Swimming behavior of marine bivalve larvae in a flume boundary-layer flow. Evidence for near-bottom confinement. Mar Ecol Prog Ser 79:67–76

Jonsson PR, Berntsson KM, Larsson AI (2004) Linking larval supply to recruitment: flow-mediated control of initial adhesion of barnacle larvae. Ecology 85:2850–2859

Jumars PA (1993) Concepts in biological oceanography. Oxford University Press, New York, p 348

Katz CH, Cobb JS, Spaulding M (1994) Larval behavior, hydrodynamic transport, and potential offshore-to-inshore recruitment in the American lobster *Homarus americanus*. Mar Ecol Prog Ser 103:265–273

Koehl MAR (2007) Minireview: Hydrodynamics of larval settlement into fouling communities. Biofouling 23:1–12

Koehl MAR, Hadfield MG (2004) Soluble settlement cue in slowly moving water within coral reefs induces larval adhesion to surfaces. J Mar Syst 49:75–88

Koehl MAR, Powell TM (1994) Turbulent transport of larvae near wave-swept rocky shores: does water motion overwhelm larval sinking. In: Wilson H, Shinn G, Stricker S (eds) Reproduction and development of marine invertebrates. Johns Hopkins University Press, Baltimore, pp 261–274

Koehl MAR, Powell TM, Dobbins EL (1997) Effects of algal turf on mass transport and flow microhabitat of ascidians in a coral reef lagoon. Proc 8th Int Coral Reef Symp 2:1087–1092

Koehl MAR, Strother JA, Reidenbach MA, Koseff JR, Hadfield MG (2007) Individual-based model of larval transport to coral reefs in turbulent, wave-driven flow: effects of behavioral responses to dissolved settlement cues. Mar Ecol Prog Ser 335:1–18

Krug PJ (2006) Defense of benthic invertebrates against surface colonization by larvae: A chemical arms race. In: Fusetani N, Clare AS (eds) Marine molecular biotechnology, Springer, Berlin, pp 1–53

Larsson AI, Jonsson PR (2006) Barnacle larvae actively select flow environments supporting post-settlement growth and survival. Ecology 87:1960–1966

Lowe RL, Koseff JR, Monismith SG (2005) Oscillatory flow through submerged canopies: 1. Velocity structure. J Geophys Res 110, Art. No. C10016

Luckenbach MW, Orth RJ (1992) Swimming velocity and behavior of blue crab (*Callinctes sapidus* Rathbun) megalopae in still and flowing water. Estuaries 15:186–192

McHenry MJ, Strother JA (2003) The kinematics of phototaxis in larvae of the ascidian *Aplidium constellatum*. Mar Biol 142:173–184

Mullineaux LS, Butman CA (1991) Initial contact, exploration, and attachment of barnacle (*Balanus amphitrite*) cyprids settling in flow. Mar Biol 110:93–103

Nowell ARM, Jumars PA (1984) Flow environments of aquatic benthos. Ann Rev Ecol Syst 15:303–328

Ólafsson EB, Peterson CH, Ambrose WG Jr (1994) Does recruitment limitation structure populations and communities of macroinvertebrates in marine soft sediments: the relative significance of pre- and post-settlement processes. Oceanog Mar Biol Ann Rev 32:65–109

Palmer MA, Allan JD, Butman CA (1996) Dispersal as a regional process affecting the local dynamics of marine and stream benthic invertebrates. Trends Evol Ecol 11:322–326

Pawlik JR., Butman CA (1993) Settlement of a marine tube worm as a function of current velocity: interacting effects of hydrodynamics and behavior. Limnol Oceanogr 38:1730–1740

Pidgeon EJ (1999) An experimental investigation of breaking wave induced turbulence. Stanford University PhD Dissertation

Queiroga H, Blanton J (2005) Interactions between behaviour and physical forcing in the control of horizontal transport of decapod crustacean larvae. Adv Mar Bio 47:107–214

Reidenbach MA, Koseff JR, Monismith SG, Steinbuck JV, Genin A (2006) The effects of waves and morphology on mass transfer within branched reef corals. Limnol Oceanogr 51:1134–1141

Reidenbach MA, Koseff JR, Monismith SG (2007) Laboratory experiments of fine-scale mixing and mass transport within a coral canopy. Phys Fluids 19:075107

Rooney P, Cobb JS (1991) Effects of time of day, water temperature, and water velocity on swimming by postlarvae of the American lobster, *Homarus americanus*. Can J Fish Aquatic Sci 48:1944–1950

Rothlisberg PC, Church JA (1994) Processes controlling the larval dispersal and postlarval recruitment of Penaeid prawns. In: Sammarco PW, Heron ML (eds) Coastal and estuarine studies. American Geophysical Union, Washington, pp 235–252

Rothlisberg PC, Church JA, Fandry CB (1995) A mechanism for near-shore concentration and estuarine recruitment of postlarval *Penaeus plebeius* Hess (Decapoda, Penaeidae). Est Coast Shelf Sci 40:115–138

Roughgarden J, Pennington JT, Stoner D, Alexander S, Miller K (1991) Collisions of upwelling fronts with the intertidal zone: The cause of recruitment pulses in barnacle populations of central California [USA]. Acta Oecol 12:35–52

Shanks AL (1985) Behavioral basis of internal-wave-induced shoreward transport megalopae of the crab *Pachygrapsus crassipes*. Mar Ecol Prog Ser 24:289–295

Sleath JF (1987) Turbulent oscillatory flow over rough beds. J Fluid Mech 182:369–409

Stancyk SE, Feller RJ (1986) Transport of non-decapod invertebrate larvae in estuaries: an overview. Bull Mar Sci 39:257–268

Tamburri MN, Finelli CM, Wethey DS, Zimmer-Faust RK (1996) Chemical induction of larval settlement behavior in flow. Biol Bull 191:367–373

Tankersley RA, Forward RB Jr (1994) Endogenous swimming rhythms in estuarine crab megalopae: Implications for flood-tide transport. Mar Biol 118:415–423

Tankersley RA, McKelvey LM, Forward RB (1995) Responses of estuarine crab megalopae to pressure, salinity and light: Implications for flood-tide transport. Mar Biol 122:391–400

Unabia C, Hadfield MG (1999) The role of bacteria in larval settlement and metamorphosis of the polychaete *Hydroides elegans*. Mar Biol 133:55–64

Woodin SA (1991) Recruitment of infauna: positive or negative cues? Amer Zool 31:797–807

Worcester SE (1994) Adult rafting versus larval swimming: Dispersal and recruitment of a botryllid ascidian on eelgrass. Mar Biol 121:309–317

Young CM (1990) Larval ecology of marine invertebrates: a sesquicentennial history. Ophelia 32:1–48

Young CM (1995) Behavior and locomotion during the dispersal phase of larval life. In: McEdward LR (ed) Ecology of marine invertebrate larvae. CRC Press, Boca Raton, pp 249–278

Young CM, Chia FS (1987) Abundance and distribution of pelagic larvae as influenced by predation, behavior and hydrographic factors. In: Giese AC, Pearse JS, Pearse VB (eds) Reproduction of marine invertebrates. Blackwell, Palo Alto, pp 385–463

Water-walking devices

David L. Hu · Manu Prakash · Brian Chan · John W. M. Bush

Abstract We report recent efforts in the design and construction of water-walking machines inspired by insects and spiders. The fundamental physical constraints on the size, proportion and dynamics of natural water-walkers are enumerated and used as design criteria for analogous mechanical devices. We report devices capable of rowing along the surface, leaping off the surface and climbing menisci by deforming the free surface. The most critical design constraint is that the devices be lightweight and non-wetting. Microscale manufacturing techniques and new man-made materials such as hydrophobic coatings and thermally actuated wires are implemented. Using high-speed cinematography and flow visualization, we compare the functionality and dynamics of our devices with those of their natural counterparts.

Electronic supplementary material The online version of this article (doi:10.1007/s00348-007-0339-6) contains supplementary material, which is available to authorized users.

D. L. Hu · J. W. M. Bush (✉)
Department of Mathematics,
Massachusetts Institute of Technology,
Cambridge, MA, USA
e-mail: bush@math.mit.edu

Present Address:
D. L. Hu
The Courant Institute, New York University,
New York, NY, USA

M. Prakash
Center for Bits and Atoms,
Massachusetts Institute of Technology,
Cambridge, MA, USA

B. Chan
Department of Mechanical Engineering,
Massachusetts Institute of Technology,
Cambridge, MA, USA

1 Introduction

Nature has much to teach us about innovative, optimal and versatile designs. Since its inception, biomimetics has grown increasingly interdisciplinary, merging biology with nanotechnology, engineering and applied mathematics. The interface of these fields has led to the invention of diverse devices and materials, from gecko-inspired tape (Geim et al. 2003) to a dolphin-skin-inspired torpedo shell (Fish 2006). Biomimetic robots are now being built to emulate birds (Dickinson et al. 1999), fish (Triantafyllou et al. 2000) and turtles (Long et al. 2006); some recent developments are reported in this issue. In this paper, we present a few relatively modest devices capable of a form of locomotion that has been largely neglected in biomimetics: walking on water.

Nearly three centuries ago, the biologist Ray (1710) reported with amazement the ability of certain insects (*Mesovelia*) to run from land across the water surface without slowing. Recently, progress has been made towards the classification of the various means of walking on water (Bush and Hu 2006) and the development of the first water-walking devices based on nature's designs (Hu et al. 2003; Suhr et al. 2005; Song et al. 2006; Floyd et al. 2006). Unlike devices inspired by swimming and flying creatures, water-walking devices must contend with the additional challenge of staying atop the water surface. We identify in this paper a minimum number of design principles relevant for water-walkers and apply these principles in the construction of a number of water-walking devices.

G.K. Taylor, M.S. Triantafyllou, and C. Tropea (Eds.): Animal Locomotion, pp. 131–140.
springerlink.com

We begin with a review of previously built biomimetic water-walking devices. Water-walkers can be classified as large or small according to the magnitude of the Baudoin number $Ba = \frac{Mg}{\sigma P}$, where Mg is the creature's weight, σ P its maximum supporting surface tension force, P its contact perimeter and $\sigma = 70$ dynes/cm the surface tension of water (Baudoin 1955; Bush and Hu 2006). Large water-walkers ($Ba > 1$) cannot rely on surface tension for static support. Certain lizards and shorebirds can dash across water by slapping the surface with their feet, thereby supporting their weight with a combination of fluid inertia, buoyancy and added mass forces (Glasheen and McMahon 1996b). A machine capable of running on water in a manner similar to the basilisk lizard is being developed by Floyd et al. (2006). However, this feat is beyond the capabilities of humans due to their inherent power limitations (Glasheen and McMahon 1996a). Man may only walk on water using flotation devices, which are generally plodding and cumbersome. The first such device resembled floating cross-country skis and was implemented by fifteenth century ninja (Heishichiro et al. 1966); a similar design was envisioned by Leonardo da Vinci (1478–1518).

Small water-walkers ($Ba < 1$) can reside at rest on the water surface, supported by surface tension. Their means of locomotion have inspired the devices reported here. The most common water-walking insect is the water strider, which propels itself by rowing with its long middle legs. The water strider has a key adaptation common among water-walking insects: its legs are covered with a dense mat of hair that renders them effectively non-wetting (Andersen 1976; Gao and Jiang 2004; Bush et al. 2007). The first biomimetic water strider leg was designed by Shi et al. (2005) by means of electrochemical deposition of gold aggregates. The first mechanical water strider was reported by Hu et al. (2003) and is detailed in Sect. 3. Recently, Suhr et al. (2005), Song et al. (2006) constructed a new generation of biomimetic water striders capable of turning and remote-controlled motion on the water surface. A thermally actuated mechanical water strider is reported in Sect. 3.

In addition to propelling themselves laterally along the free surface, many water-walking insects and spiders can leap vertically. The dynamics of leaping off the free surface was first studied by Suter and Gruenwald (2000) in the context of the fisher spider. Theoretical work on jumping off the free surface was reported by Li et al. (2005), who considered the dynamics of a floating spring-mass system and examined the dynamical importance of compression length and spring stiffness. In Sect. 4, we describe the first mechanical device capable of leaping off the water surface.

It would seem obvious that an insect must move its legs in order to propel itself. However, in the presence of a meniscus, some water-walking insects can move simply by deforming the free surface: by maintaining certain fixed postures, they can ascend fluid menisci in a quasi-static manner (Hu and Bush 2005). Baudoin (1955) first observed this type of motion in *Dryops*, which ascends a fluid meniscus by arching its back. He showed that bent metal strips do likewise if he bent the strips so that they have the same curvature as the meniscus. Floating hexagons also propel themselves quasi-statically into a tessellation, as shown by Whitesides and Grzybowski (2002). In Sect. 5 we present a simple design for a mechanized meniscus climber.

In Sect. 2, we enumerate the physical constraints that guided us in designing our devices. Thereafter, we report the designs of our mechanical water-walkers and accompanying descriptions of the insects that inspired them. In Sect. 3, we present a mechanical rower based on the water strider *Gerris*; in Sect. 4 a leaper based on the springtail *Podura aquatica*; and in Sect. 5 a mechanical meniscus climber based on the beetle larva *Pyrrhalta*.

2 Design principles

We have based the design of our small water-walking devices on the following fundamental principles. First and foremost, the device must be hydrophobic in order to prevent its penetrating and adhering to the free surface (Bush et al. 2007). Second, it must be sufficiently lightweight to reside at rest on the free surface. Since water-walking insects are more dense than water, they cannot rely exclusively on buoyancy forces for weight support; instead, their weight Mg must be supported by curvature forces: $Ba = \frac{Mg}{\sigma P} < 1$. Thirdly, we require that the driving leg never be completely wetted during its stroke. In nature, this is accomplished by a dense mat of hairs that preclude the intrusion of water onto the driving leg; contact with the water is limited to the hair tips. In our devices, complete wetting is discouraged by the use of water-repellent materials. Finally, where possible, the devices have been designed to resemble their natural counterparts, having the same number of limbs and body proportions.

These design constraints for the mechanical water-walkers may be satisfied by maintaining dynamic similarity with their natural counterparts. The driving leg can be modeled as a cylinder of radius w and length L striking the free surface with a peak speed U, rowing frequency f, and applied force per unit length F. Buckingham's Theorem (McMahon and Bonner 1985) indicates that this reduced insect-fluid system for a given impact geometry is uniquely prescribed in terms of six dimensionless groups: the Reynolds number $Re = Uw/\nu$, Bond number $Bo = \rho g w^2/\sigma$, Weber number $We = \rho U^2 w/\sigma$ and Strouhal number $St = (wf)/U$, aspect ratio $\lambda = w/L$ and Andersen number

F/σ, where v and ρ are the viscosity and density of water and where F. These dimensionless groups relate the relative magnitudes of the propulsive forces used by the water-walker (Bush and Hu 2006). All designs were aimed at achieving dynamic similarity between the mechanical device and its natural counterpart, and so matching these dimensionless groups.

3 Rowing

The biomimetic device in Fig. 1 was inspired by the most common of water-walking insects, the water strider. The water strider's typical gait consists of a sculling motion of its middle legs against the free surface; this gait involves two phases. The first is a propulsive phase in which it drives its central pair of legs backwards against the free surface (Andersen 1976; Hu et al. 2003). The next is a recovery phase in which the strider recocks its legs for the next stroke as it glides to a stop. By varying the strength and angle of the driving stroke, the water strider either glides across the surface or leaps vertically.

Robostrider (R1), originally reported in Hu et al.(2003), is a self-contained device that rows without breaking through the water surface. The body plan is detailed in Fig. 1. Measuring 13 cm from leg tip-to-tip, it is comparable in size to the world's largest water strider, *Gigantometra gigas* (Tseng and Rowe 1999). Despite its size, its aluminum frame makes it sufficiently lightweight (0.35 g) to be supported by surface tension, as indicated by its Baudoin number in Table 2. Like its natural counterpart, R1 sits on the water surface on its front and back pairs of legs. The legs are cut from hydrophobic stainless steel wire (0.2 mm gauge), and the body from aluminum sheet (thickness 0.13) cut from a beverage can.

R1 is driven by its middle legs that are actuated by the lightweight pulley apparatus detailed in the inset of Fig. 1. The middle legs are attached to the axis of a nylon pulley (radius $R_1 = 0.09$ cm). An elastic band (9 cm length, elastic modulus $k = 3{,}100$ dynes per unit strain) is anchored on one end to the pulley, on the other end to the rear of the body. The device is loaded by winding the pulley; when released, the tension of the elastic band rotates the pulley, driving the rowing leg tips in a circular motion of radius $R_2 = 1$ cm. It is critical that the leg tips do not penetrate the surface during the stroke; subtle tuning of the orientation of the driving legs is thus generally required. The total force applied by R1's legs can be readily calculated for this simple system: using a torque balance on the driving leg, the total force may be written $2F = F_e R_1/R_2$ where the force F_e provided by the elastic band is given by Hooke's law, $F_e = k\varepsilon$ where k is the elastic modulus and ε the maximum strain. A rubber band of elastic modulus 3,100 dynes per unit strain and maximum strain 1.5 was chosen that produced a force per length of the driving legs of 30 dynes/cm. Since this force per unit length is less than 2σ, curvature forces adequately resist the submergence of the driving leg.

The dynamics of R1 was studied using high-speed video at 500 fps (Fig. 2). Its dynamics are characterized in Tables 1 and 2. The maximum distance travelled by R1 with a fully wound pulley was 20 cm, or five leg strokes (Fig. 2c). Flow visualization using thymol blue showed that R1 generates a wake containing vortices similar in form to, but less coherent than, those generated by water striders (Fig. 2b; Hu et al. 2003). Generally, the leg tips did

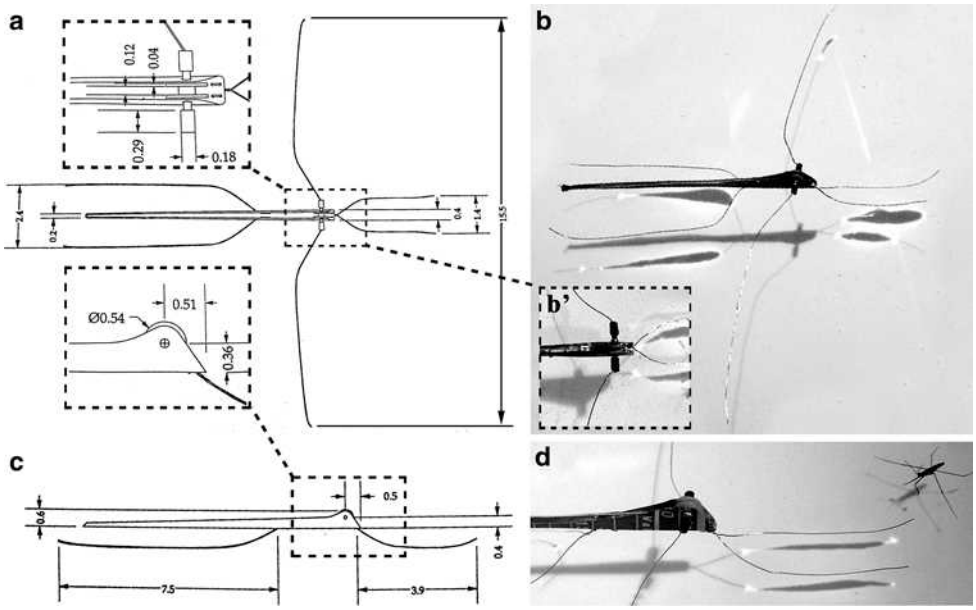

Fig. 1 Schematic diagrams of Robostrider 1 (R1) in plan (**a–b**) and side views (**c–d**). Insets detail the pulley and elastic string driving mechanism. At rest, R1 sits on the free surface on its pairs of front and hind legs. During locomotion, an elastic thread wrapped around the pulley rotates the central driving legs in a circular rowing motion that propels the device forward. All units in cm

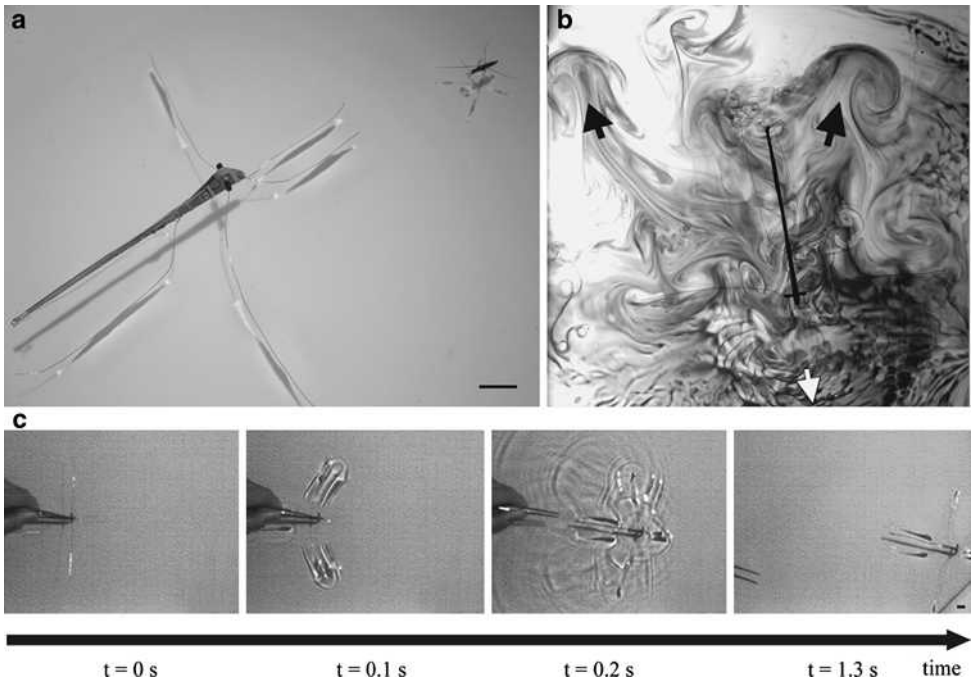

Fig. 2 **a** R1 facing its natural counterpart, *Gerris remigis*. R1 is 9 cm long and is powered by an elastic band running down its length. **b** R1 generates dipolar vortices in its wake, as visualized using thymol blue. The direction of R1 and its vortices are indicated by the *white* and *black arrows*, respectively. **c** High-speed video frames of R1's motion during five rowing strokes. R1 is released by hand (at *left* in **c**). The device is lit from above; consequently, shadows are cast by surface deformations associated with static menisci (**a**) or waves generated by the driving stroke (**c**). *Scale bars* 1 cm

Table 1 Physical parameters describing the geometry and dynamics of the water strider and its mechanical counterparts (R1 and R2)

	Leg radius w (cm)	Leg length L (cm)	Body weight Mg (dyn)	Leg speed U (cm/s)	Leg frequency f (1/s)	Leg perimeter P (cm)	Applied force/unit length F (dyn/cm)
Strider	0.006	0.6	4.5	27	100	2.2	60
R1	0.009	4.3	350	20	60	50	30
R2	0.025	1.2	70	5	5	10	20

Table 2 Dimensionless groups characterizing the geometry and dynamics of the water strider and its mechanical counterparts (R1 and R2)

	Leg aspect ratio $\lambda = \frac{w}{L}$	Reynolds $Re = \frac{Uw}{\nu}$	Bond $Bo = \frac{\rho g w^2}{\sigma}$	Weber $We = \frac{\rho U^2 w}{\sigma}$	Strouhal $St = \frac{wf}{U}$	Andersen $An = \frac{F}{\sigma}$	Baudoin $Ba = \frac{\mathrm{Mg}}{\sigma P}$
Strider	0.01	16	5×10^{-4}	6×10^{-2}	2×10^{-2}	0.4	0.03
R1	0.002	16	1×10^{-3}	4×10^{-2}	3×10^{-2}	0.7	0.08
R2	0.02	12	9×10^{-3}	9×10^{-3}	2×10^{-2}	0.3	0.12

not penetrate the water surface despite speeds in excess of 20 cm/s. The greatest challenge in deploying R1 was maintaining its hydrophobicity. While water striders are able to dry their legs by grooming, R1 had to be dried by hand between runs in order to maintain its water-repellency and so prevent its sinking.

For locomotion of longer duration, we built another mechanical water strider, Robostrider 2 (R2) that is closer in size and weight to its natural counterpart. The body of R2 was laser micro-machined from a single piece of steel shim stock (thickness 0.04 cm), shown in Fig. 3. The legs of the machine were coated with non-wetting Teflon (AF16 Dupont), which provided a static contact angle θ of 104°, comparable to the value reported on insect cuticle by Holdgate (1955). We note, however, that the surface roughness is qualitatively different on the legs of R2 and its natural counterpart, the latter being characterized by a piliferous layer that maintains an air layer between the water and the bulk of the leg surface (Bush et al. 2007).

R2's driving legs are composed of bi-layered cantilevers, consisting of a thin and thick segments, as shown in the inset of Fig. 3 (Luo et al. 2005). When a voltage (10 V) is applied to the leg, the thin part of the cantilever heats up faster and elongates more than the thick part, which bends the cantilever 2 mm and drives the leg in a sculling motion. These actuators are seamlessly integrated into the body of

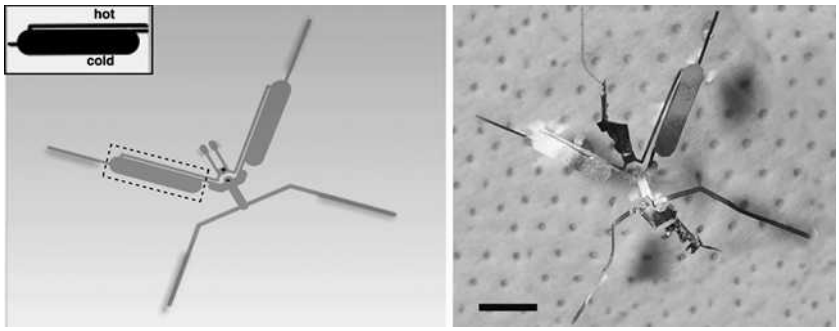

Fig. 3 R2 has built-in heat actuators to power the driving stroke. The *left inset* shows the details of the leg, which consists of a bi-layered cantilever. When a voltage is applied to the leg, the thinner layer of the cantilever heats up faster and lengthens more than the thicker layer, causing the cantilever to bend and R2 to stroke. Under an applied voltage of 10 V, the maximum deflection of the leg tip is 2 mm. *Scale bar* 1 cm

R2 in order to reduce its total weight to 0.07 g. Also, to reduce the weight, the power source for the thermal actuators was wired to an external voltage source.

The dynamics of R2, and the pros and cons over its predecessor, were assessed using high speed video of its motion. While the size of R2 is comparable to its natural counterpart, its slow body speed (2 mm/s) is two orders of magnitude lower. Unlike its predecessor, R2 has an external power supply that permits it to travel indefinitely. While R1 was hand-made, R2 was manufactured by computer-controlled machining (a similar technique as used in Fearing et al. 2000), allowing it to be made much smaller. Moreover, this production method lends itself easily to mass production and upgradability. Currently, R2's legs are wired in parallel, which makes it capable of only straight-line motion. However, by wiring each of the legs independently, R2 may be easily given turning capabilities. One disadvantage of R2's design is that there is an inherent upper limit to its maximum speed. Excessively high applied voltage results in the formation of bubbles at the leg's contact line. Insulating surface coatings would allow for the application of higher driving voltages and so higher speeds.

4 Leaping

Many water-walkers leap from the free surface (Suter and Gruenwald 2000; Suter 2003), but it was the impressive leaping ability of *Podura aquatica* that inspired our mechanical leaper. The 1 mm long *Podura* ratchets a spring-loaded forked tail called a furca at its underbelly, as shown in Fig. 4. To leap, it releases the furca which strikes the free surface, catapulting it upwards to heights of 2 cm, or 20 body lengths. High-speed video indicates that the furca is ratcheted for 100 ms and then released over a time scale of 1 ms. It is noteworthy that this is the fastest movement reported for any water-walker.

Owing to difficulties in designing on a small scale, Roboleaper (RL) was constructed to be ten times larger than its natural counterpart (Fig. 5). It consists of a curved leaf spring with a latch that is engaged by hand and released by heating with a soldering iron (Fig. 6). As the ends of the spring are released, its leaves strike the surface, catapulting RL upward. Its mass m of 4 mg makes it sufficiently light that it may be supported by surface tension; its Teflon AF16 (Dupont) coating renders it sufficiently non-wetting to detach from the free surface. We note that hydrophobicity is a critical requirement for the leaper: uncoated leaf springs were unable to detach from the free surface.

In order to leap to achieve an initial speed v, the bending energy initially stored in the spring must exceed the leaper's initial kinetic energy $\frac{1}{2}mv^2$:

$$\frac{EIL}{2R^2} > \frac{1}{2}mv^2 \tag{1}$$

where E is the the Young's modulus, I the area moment of inertia, L the length of the spring and R the radius of the circular arc (Landau and Lifshitz 1986). We were able to generate leaps of height $H \approx 10$ cm using a Kapton HN Polyimide (Dupont) sheet with density 1.4 g/cm^3, Young's modulus 2.5×10^9 dynes/cm^2, length L, width w, and thickness t listed in Table 3. The bending energy for these values is approximately 130–200 dynes cm and the initial kinetic energy only 80 dynes cm. The difference in these energies reflects the transfer of kinetic energy (KE) to the underlying fluid, the generation of surface energy (SE) in deforming the free surface, losses due to viscous dissipation (Φ), and the work done in detaching from the free surface (W_D). Rough estimates suggest characteristic values of KE of 50 dynes cm, SE and W_D less than 30 dynes cm and negligible viscous dissipation. The dominance of kinetic over surface energies is also reflected in the rupture of the interface following take-off. Note that if

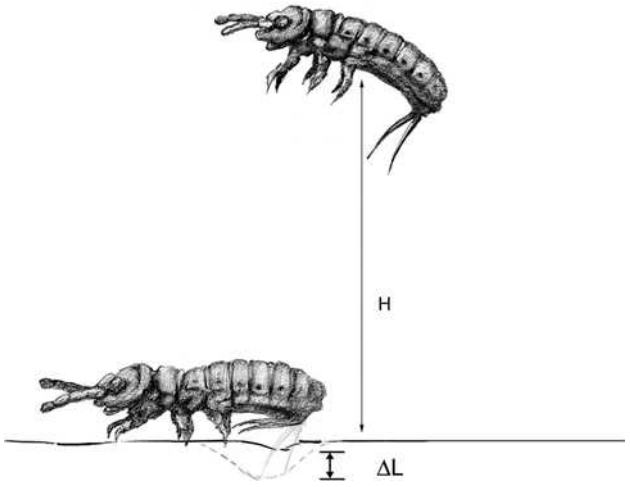

Fig. 4 The water-walking springtail *Podura aquatica* (length 2 mm) drawn from photographs. The spring-loaded forked tail swings outward, deforming the surface a distance ΔL to drive the leap of height H

the take-off is vertical, and provided aerodynamic losses are negligible, one may simply relate the initial kinetic energy of the body to the gravitational potential energy at the apex of the leap, mgH.

The motion of RL was characterized using high speed video (Fig. 6). The takeoff has a time scale of 3 ms, comparable to the 1 ms time for *Podura*. The leaf velocity of $U \sim 50$–100 cm/s resulted in vertical jumps of $H \sim 10$ cm, an order of magnitude larger than those of Podura owing to the relatively large elastic energy stored in the leaf spring. Characteristic parameters and dimensionless groups describing the device's motion are listed in Tables 3 and 4. As indicated by the large values of the Strouhal and Weber numbers, the dominant propulsive forces are associated with the added mass and inertia of the fluid, rather than the surface tension.

RL was able to leap consistently on the water surface, but the angle of departure of the leap was highly variable and difficult to control. It is noteworthy that its natural counterpart suffers the same problem. Smaller leapers such as *Podura* frequently tumble in the air and land on their backs. Since the leaps occur at such high speeds, both real and mechanical springtails are highly sensitive to their initial orientation.

5 Meniscus climbing

Water-walking insects at times cross from water to land in order to lay eggs and evade predators. In order to do so, they must contend with concave menisci at the borders of land that appear to them as frictionless mountains. While spiders and striders are capable of leaping over menisci, other relatively slow insects cannot and so are obliged to exploit the attraction between like-signed menisci in order to climb (Baudoin 1955). Non-wetting insects such as the water treader *Mesovelia* climb menisci by inserting retractable, hydrophilic claws into the free surface and pulling upwards (Hu and Bush 2005). The water lily leaf beetle larva *Pyrrhalta* is wetting and propels itself up the meniscus by arching its back, generating menisci at its head and tail (Fig. 7a) that are attracted to the background meniscus. This means of capillary propulsion provides the basis for the design of our mechanical meniscus climber.

In the first discussion of meniscus climbing, Baudoin (1955) demonstrated that millimetric bent metal strips ascend menisci. We have constructed a slightly more sophisticated mechanical climber (RC) five times larger than its natural counterpart, the larva *Pyrrhalta* (Fig. 7). RC consists of a rectangular plastic sheet with a thermally actuated Nitinol muscle wire stretched along its midline, attached to either end. Passing current through the muscle

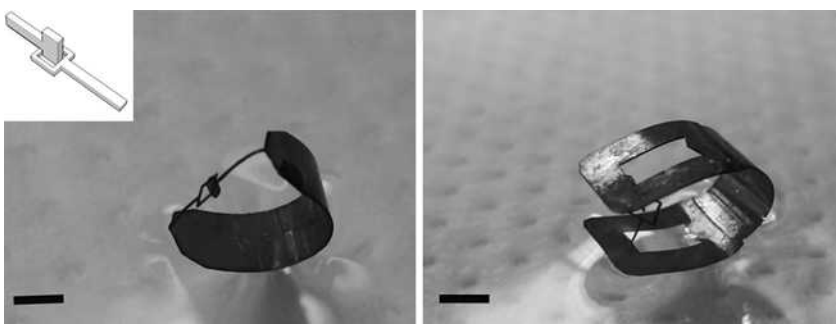

Fig. 5 Two views of the mechanical leaper floating on the water surface. The leaper is composed of a strip of metal and held in a curved posture by a micro-scale latch mechanism detailed in the *inset*. The bolt is slid into the notch; heating of the latch causes the bolt to shrink and retract from the notch. The reusable latch mechanism in the spring was cut using a pin hole steel mask (0.1 cm) and a laser (248 nm UV excimer laser from Resonetics Micromachining Systems, NH). The entire device is rendered hydrophobic with a teflon coating (static contact angle of 104°). *Scale bars* 2 mm

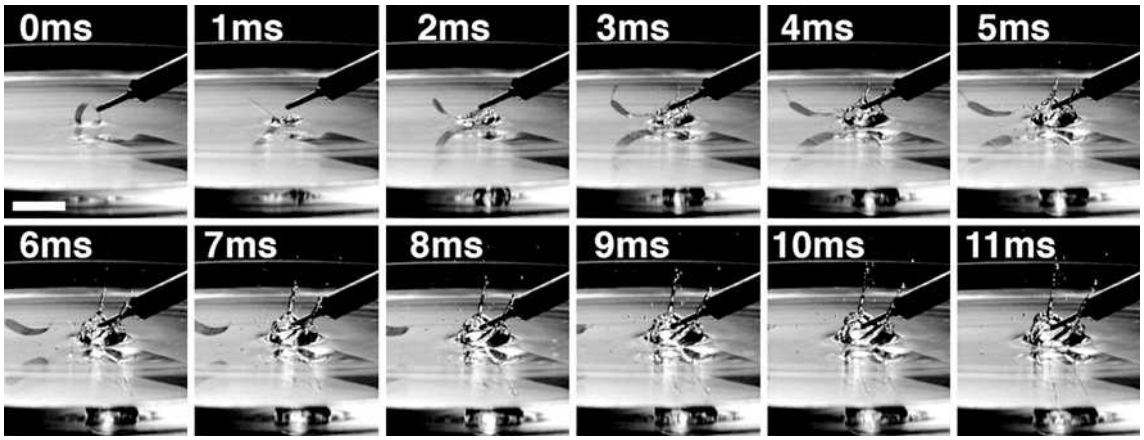

Fig. 6 High-speed video sequence of the forward jump of RL. The time-scale of the leaper's take-off is 1 ms. The mechanical leaper is actuated by heating the latch with a soldering iron (*right*) at time $t = 1$ ms. Heating releases the latch, opening the curved ends of the leaper. *Scale bar* 1 cm

Table 3 Physical parameters describing the geometry and dynamics of the mechanical leaper (RL) and its natural counterpart, the springtail *Podura aquatica*

	Body width w (cm)	Body length L (cm)	Body thickness t (cm)	Body weight Mg (dyn)	Body speed U (cm/s)	Contraction frequency f (1/s)	Body perimeter P (cm)
Springtail	0.01	0.05	0.01	0.1	50	1,000	0.1
RL	0.2	1.3	7.5×10^3	4	50–100	1,000	3

Table 4 Dimensionless groups characterizing the geometry and dynamics of the mechanical leaper (RL) and its natural counterpart

	Body aspect ratio $\lambda = \frac{w}{L}$	Reynolds $Re = \frac{Uw}{\nu}$	Bond $Bo = \frac{\rho g w^2}{\sigma}$	Weber $We = \frac{\rho U^2 w}{\sigma}$	Strouhal $St = \frac{wf}{U}$	Baudoin $Ba = \frac{\mathrm{Mg}}{\sigma P}$
Springtail	0.2	50	1.4×10^{-3}	0.4	0.2	1.2×10^{-2}
RL	0.15	10^3	0.6	7–28	2–4	1.3×10^{-2}

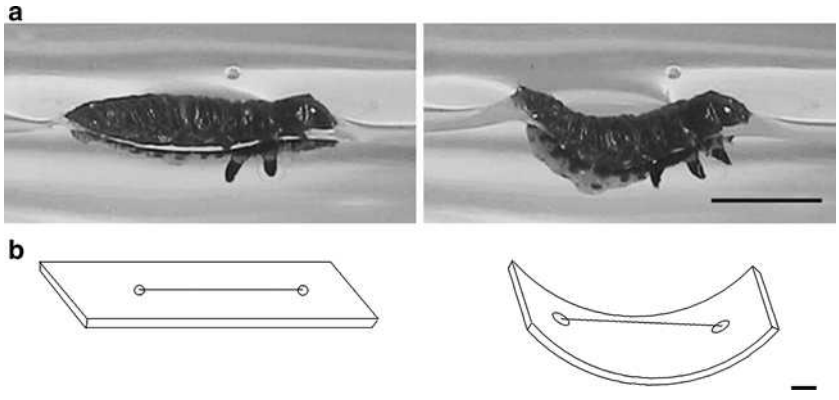

Fig. 7 Natural and mechanical mensicus climbers. **a** The beetle larva climbs the meniscus by arching its back, deforming the water surface at its head and tail. **b** For the mechanical meniscus climber, arching is prompted by the contraction of a temperature-sensitive muscle wire. *Scale bars* 3 mm

wire leads to ohmic dissipation; the resulting heating causes the wire to contract and the sheet to bend. When the wire is relaxed, the sheet's inherent stiffness provides the opposing force that returns RC to a planar state. The sheet material, lexan plastic (density 1.2 g/cm^3) was chosen so that RC would be sufficiently lightweight to be supported by surface tension. Lexan is also wetting, which allows it to deflect the free surface vertically.

The most important design parameter for RC was the size of the rectangular plastic sheet. Once the muscle wire

is contracted, a non-zero force F_{cold} is required to stretch it back to its original length. When contracting, the muscle wire exerts a maximum force F_{hot}, typically five times F_{cold} (Mondotronics, Co.). The sheet therefore must be sufficiently stiff to deform the cold relaxed wire, yet sufficiently compliant to be deformed by the hot contracted wire. This constraint may be written

$$F_{\text{hot}} > 8\frac{EI}{L^2} > F_{\text{cold}} \tag{2}$$

where E, I and L are the Young's modulus, area moment of inertia, and length of the sheet (Crandall et al. 1978). For the muscle wire used in our device, a lexan sheet with Young's modulus 2.3×10^{10} dynes/cm^2, length L, width w and thickness t listed in Table 5 was sufficient to satisfy (2).

RC is shown climbing in Fig. 8. Voltage supplied by an external power source causes RC to arch and so ascend the meniscus at an average speed of 1 cm/s. Its motion is characterized by the dimensionless groups listed in Table 6. For both RC and its natural counterpart, the dominant propulsive force is the curvature force generated by deforming the free surface.

6 Concluding remarks

We have enumerated the fundamental principles to be considered in the design of water-walking devices. Moreover, we have applied these principles in the design and construction of biomimetic mechanisms capable of rowing, leaping and meniscus climbing. We first required that our devices be sufficiently light to be supported by surface tension. This constraint was satisfied through a judicious choice of thin lightweight metals and composites. Second, we required our devices, with the exception of our mechanical meniscus climber, to be non-wetting. Our devices were made non-wetting by constructing or coating them with hydrophobic material. We also required that our devices not penetrate the surface during their driving stroke. The peak speeds and applied forces were constrained accordingly.

Much remains to be learned from water-walking arthropods. Though descended from terrestrial insects (Andersen 1982), they have since evolved several key adaptations for survival on the water surface, the most important being their water-repellency. Given the risk of entrapment by the interface, maintenance of their hydrophobicity is critical to their survival. For our mechanical water walkers, water repellency was provided by a hydrophobic coating on their legs. For water-walkers, water repellency is provided by a complex carpet of hairs; the nature of the dynamic interaction between this hair layer and the free surface is considered by Bush et al. (2007). Advances in the design and construction of water-walking devices will rely on the use of roughened hydrophobic surfaces reminiscent of insect integument, that will

Table 5 Physical parameters describing the geometry and dynamics of the mechanical climber (RC) and its natural counterpart, *Pyrrhalta*

	Body width w (cm)	Body length L (cm)	Body thickness t (cm)	Body weight Mg (dyn)	Body speed U (cm/s)	Contraction frequency f (1/s)	Body perimeter P (cm)
Beetle larva	0.3	0.6	0.3	25	10	0.3	2
RC	0.1	3.5	0.1	500	1	0.6	7

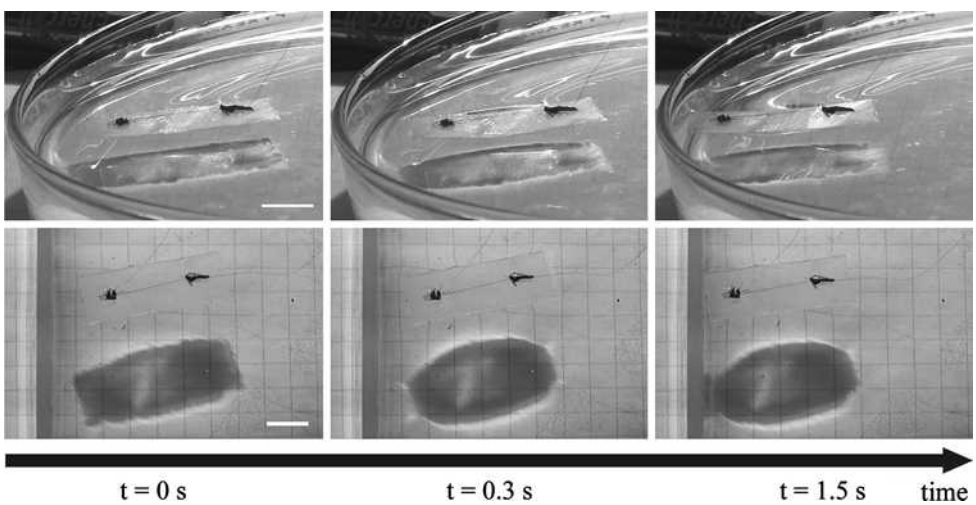

Fig. 8 Oblique views of the mechanical meniscus climber. The ascent takes roughly 1.5 s and begins when Roboclimber arches its back at $t = 0.3$ s. The deformation of the free surface due to the arching is reflected in the alteration of the underlying shadow. *Scale bars* 1 cm

Table 6 Dimensionless groups characterizing the geometry and dynamics of the mechanical climber (RC) and its natural counterpart

	Body aspect ratio $\lambda = \frac{w}{L}$	Reynolds $Re = \frac{Uw}{\nu}$	Bond $Bo = \frac{\rho g w^2}{\sigma}$	Weber $We = \frac{\rho U^2 w}{\sigma}$	Strouhal $St = wf\ U$	Baudoin $Ba = \frac{Mg}{\sigma P}$
Beetle larva	0.5	300	1.3	0.4	0.01	0.3
RC	0.4	100	22	0.02	0.8	0.9

substantially alter the nature of the interaction between the device and the free surface.

The greatest difficulty in building a reliable water-walker is preventing it from breaking the free surface during its driving stroke. The designers of micromechanical walkers, swimmers and fliers have emphasized that a control system is the way most creatures tune themselves to their environments (Dickinson et al. 2000). In the case of water-walkers, a control system could be implemented to measure the force applied by the leg to the free surface. Another means of preventing the leg from penetrating the free surface would be to increase its flexibility. Recent work on compliant bodies, such as by Alben et al. 2002, may shed light on this issue.

While the precarious nature of water-walking devices raises questions as to their practicality on the open ocean, they may yet find application in laboratory settings. Enabling water-walkers to be independent, remote-controlled devices is a step recently taken by Suhr et al. (2005) and Basso et al. (2005), who have built the next generation of water-walkers to be directed by wireless remote controllers and powered by solar energy. It should also be possible to design a water-walker that can change its wetting properties on command using recent advances in smart microfluidics (e.g. Darhuber and Troian 2005).

Acknowledgments JWMB gratefully acknowledge the financial support of the NSF through Career Grant CTS-0130465; DLH likewise through an NSF Postdoctoral Fellowship. MP acknowledge financial support of NSF Grant CCR-0122419.

References

Alben S, Shelley M, Zhang J (2002) Drag reduction through self-similar bending of a flexible body. Nature 420:479–481

Andersen NM (1976) A comparative study of locomotion on the water surface in semiaquatic bugs (Insects, Hemiptera, Gerromorpha). Vidensk Meddr Dansk Naturh Foren 139:337–396

Andersen NM (1982) The semiaquatic bugs (Hemiptera, Gerromorpha): phylogeny, adaptations, biogeography and classification. Scandinavian Science Press Ltd, Klampenborg, Denmark

Basso B, Fong A, Hurst A, Knapp M (2005) Robot using surface tension (R.U.S.T.Y). Undergraduate thesis, Columbia University

Baudoin R (1955) La physico-chimie des surfaces dans la vie des Arthropodes aeriens des miroirs d'eau, des rivages marins et lacustres et de la zone intercotidale. Bull Biol Fr Belg 89:16–164

Bush JWM, Hu DL (2006) Walking on water: biolocomotion at the interface. Ann Rev Fluid Mech 38:339–369

Bush JWM, Prakash M, Hu DL (2007) The integument of water-walking arthropods: form and function. Adv Insect Physiol (in press)

Crandall SH, Dahl NC, Lardner TJ (1978) An introduction to the mechanics of solids. McGraw-Hill, Inc., New York

Darhuber AA, Troian SM (2005) Principles of microfluidic acutation by modulation of surface stresses. Annu Rev Fluid Mech 37:425–455

Dickinson MH, Lehmann FO, Sane SP (1999) Wing rotation and the aerodynamic basis of insect flight. Science 284:1954–1960

Dickinson MH, Farley CT, Full RK, Koehl MAR, Kram R, Lehman S (2000) How animals move: an integrated view. Science 288:100–106

Fearing RS, Chiang KH, Dickinson M, Pick DL, Sitti M, Yan J (2000) Wing transmission for a micromechanical flying insect. In: Proc. of IEEE Int. Conf. Robot. Auton., pp 1509–1516

Fish FE (2006) The myth and reality of Gray's paradox: implication of dolphin drag reduction for technology. Bioinsp Biomim 1:R17–R25

Floyd S, Keegan T, Palmisano J, Sitti M (2006) A novel water running robot inspired by basilisk lizards. In: Proc. of the IEEE/RSJ intl. conf. on intell. robot. and sys, pp. 5430–5436

Gao X, Jiang L (2004) Water-repellent legs of water striders. Nature 432:436

Geim AK, Dubonos SV, Grigoreiva IV, Novoselov KS, Zhukov AA, Shapoval YS (2003) Microfabricated adhesive mimicking gecko foot-hair. Nat mater 2:461–463

Glasheen JW, McMahon TA (1996a) A hydrodynamic model of locomotion in the basilisk lizard. Nature 380:340–342

Glasheen JW, McMahon TA (1996b) Size dependence of water-running ability in basilisk lizards *Basiliscus basiliscus*. J Exp Biol 199:2611–2618

Heishichiro O, Ryutaro K, Nawa Y (1966) Ninja exhbition booklet. Iga Ninja Museum, Japan

Holdgate MW (1955) The wetting of insect cuticle by water. J. Exp. Biol 591–617

Hu DL, Bush JWM (2005) Meniscus-climbing insects. Nature 437:733–736

Hu DL, Chan B, Bush JWM (2003) The hydrodynamics of water strider locomotion. Nature 424:663–666

Landau LD, Lifshitz EM (1986) Theory of elasticity, 3rd edn. Pergamon Press, New York

Leonardo da Vinci (1478–1518) Codex atlanticus. Biblioteca Ambrosiana, Milan, p 26

Li J, Hesse M, Ziegler J, Woods AW (2005) An arbitrary Lagrangian Eulerian method for moving-boundary problems and its application to jumping over water. J Comput Phys 208:289–314

Long JH, Schumacher J, Livingston N, Kemp M (2006) Four flippers or two? Tetrapodal swimming with an aquatic robot. Bioinsp Biomim 1:2029

Luo J, He JH, Flewitt A, Spearing AM, Fleck NA, Milne WI (2005) Development of all metal electrothermal actuator and its applications. J Microlith Microfab Microsyst 4(2):1–10

McMahon TA, Bonner JT (1985) On size and life. Sci. Am. Libr., New York, p 211

Ray J (1710) Historia insectorum. Impensis/Churchill, London

Shi F, Wang Z, Zhang X (2005) Combining a layer-by-layer assembling technique with electrochemical deposition of gold aggregates to mimic the legs of water striders. Adv Mater 17:1005–1009

Song YS, Suhr SH, Sitti M (2006) Modeling of the supporting legs for designing a biomimetic water strider robot. In: Proc IEEE Int Conf Robot Auton., pp 2303– 2310

Suhr SH, Song YS, Lee SJ, Sitti M (2005) A biologically inspired miniature water strider robot. In: Proc Robot Sci Sys, pp 42–48

Suter RB (2003) Trichobothrial mediation of an aquatic escape response: directional jumps by the fishing spider. J Insect Sci 3:1–7

Suter RB, Gruenwald J (2000) Predator avoidance on the water surface? Kinematics and efficacy of vertical jumping by *Dolomedes* (Araneae, Pisauridae). J Arachnol 28(2):201–210

Triantafyllou MS, Triantafyllou GS, Yue DKP (2000) Hydrodynamics of fishlike swimming. Annu Rev Fluid Mech 32:33–53

Tseng M, Rowe L (1999) Sexual dimorphism and allometry in the giant water strider *Gigantometra gigas*. Can J Zool 77:923–929

Whitesides GM, Grzybowski B (2002) Self-assembly at all scales. Science 295:2418–2421

Flapping flexible fish

Periodic and secular body reconfigurations in swimming lamprey, *Petromyzon marinus*

Robert G. Root · Hayden-William Courtland · William Shepherd · John H. Long Jr

Received: 22 January 2007 / Revised: 5 June 2007 / Accepted: 11 June 2007 / Published online: 13 July 2007

Abstract In order to analyze and model the body kinematics used by fish in a wide range of swimming behaviors, we developed a technique to separate the periodic whole-body motions that characterize steady swimming from the secular motions that characterize changes in whole-body shape. We applied this harmonic analysis technique to the study of the forward and backward swimming of lamprey. We found that in order to vary the unsteadiness of swimming, lamprey superimpose periodic and secular components of their body motion, modulate the patterns and magnitudes of those components, and change shape. These kinematic results suggest the following hydromechanical hypothesis: steady swimming is a maneuver that requires active suppression of secular body reconfigurations.

R. G. Root (✉)
Mathematics Department, Lafayette College,
Easton, PA 18042, USA
e-mail: robroot@lafayette.edu

H.-W. Courtland
Department of Orthopaedics,
Mount Sinai School of Medicine,
New York, NY 10029, USA

W. Shepherd
Steinhart Aquarium, California Academy of Sciences,
San Francisco, CA 94118, USA

J. H. Long Jr
Biology Department and Interdisciplinary
Robotics Research Laboratory, Vassar College,
Poughkeepsie, NY 12604, USA
e-mail: jolong@vassar.edu

1 Introduction

Fish bodies are internally-actuated flapping foils that generate flexures to produce, augment, and modulate momentum transfer to and from body and water. In so doing, fish not only generate thrust, but they also create a range of mechanical behaviors, from constant-velocity cruising to high-acceleration startle responses and straight-line translation to rotational maneuvers. The dynamics of coupled internal and external forces, i.e., the hydroelastic system, reveal themselves in a body's instantaneous kinematic configuration and reconfiguration over time (Bowtell and Williams 1993; Cheng et al. 1998; Daniel and Tu 1999; Daniel and Coombes 2002). For biologists and engineers studying biological flow, accurate body kinematics are essential (1) to determine general features of locomotor kinematics across behaviors and species, (2) as input for open-loop models that estimate dynamics of the coupled hydroelastic system (Hess and Videler 1984), and (3) for validation of motions output by closed-loop hydroelastic models (Carling et al. 1998; Cheng and Blickhan 1993). The first of these pursuits, determination of general features, is the focus of this paper. In particular, our goal is to quantify body kinematics in such a way as to permit fine-scale temporal and spatial description, within a single cycle and for the whole body, respectively, and at the same time, to discover new ways of characterizing the kinematics of the whole body.

From a biological point of view, we seek to analyze, discriminate among, and generalize from a group of swimming behaviors showing high kinematic variation: translational swimming (1) at speeds determined by the animal rather than the investigator, (2) in forward and backward directions within the fish's frame of reference and using the same propulsive mechanism, and (3) of only a single or few

G.K. Taylor, M.S. Triantafyllou, and C. Tropea (Eds.): Animal Locomotion, pp. 141–159.
springerlink.com

propulsive cycles. Variation in swimming speed occurs naturally even in fish migrating upstream, a situation that might appear to demand constant-velocity swimming; individuals vary speed, by modulating the kinematic properties of cycle frequency and lateral body amplitudes, to negotiate flow obstacles inherent in natural hydrology (Castro-Santos 2005). Further, variation in swimming kinematics is higher in lake sturgeon that select their own swimming speeds compared with those for whom speed is determined by the investigator (Webb 1986). Also, kinematic variations in white sturgeon selecting their own speeds include changes in body shape, with individuals swimming at the same speeds at different times selecting different magnitudes of body curvature (Long 1995). Finally, drastic variation in swimming kinematics of European eels is seen between forward and backward undulatory swimming, where, at similar speeds, the body has different shape configurations and kinematic patterns (D'Aout and Aerts 1999).

In experimental situations, kinematic variations during swimming are often carefully minimized. For "steady" translational swimming, one such approach is to analyze only those trials in which the speed over three to five sequential tail-beat cycles varies by a small and predeterimined magnitude (D'Aout and Aerts 1999; Jayne and Lauder 1995; Tytell 2004b). For trials meeting these conditions, points along the body's midline, from snout to tail tip, are tracked through time. From the many possible metrics, tail-beat frequency (Hz) and lateral tail-beat amplitude are considered fundamental, as shown by their use in important dimensionless numbers such as the Strouhal number (Taylor et al. 2003; Triantafyllou et al. 1993), Froude efficiency (see Blickhan and Cheng 1994), and the wake vortex ratio (Dabiri 2005) for power and thrust approximations based on Lighthill's classic elongated body theory (Lighthill 1975; Wu 1977; Webb 1975). This focus on the tail-beat frequency and amplitude are justified because, in undulatory swimmers, the tail is a trailing edge and, therefore, a site of vortex shedding. At the same time, vortex production is a whole-body phenomenon, as demonstrated by oscillating pressure differentials on the flapping flexible body (Liu et al. 1996; Long et al. 2002) and direct visualization of circulation developed on the body (Tytell 2004a, b; Müller and van Leeuwen 2004). If it is the case that the whole body is a flapping foil involved in thrust production, we predict that new kinematic features of the whole body can be discovered that will help us to understand the mechanics of highly variable swimming behaviors.

Creating a method that mathematically decomposes the whole-body kinematics of lamprey swimming forward and backward at speeds of their own choosing, we address the following specific questions. First, how "steady" is steady swimming, where "steady" refers to the purely periodic nature of the undulatory motions? Second, if we measure and characterize undulatory motion as a multi-dimensional matrix of periodic and secular components, what aspects of this matrix are modulated in order to alter performance and behavior? Third, given reports, mentioned above, of fish changing body shape, what we call "reconfiguration", do fish reconfigure differently in different situations?

2 Methods

2.1 Experimental animals

We chose an elongate-body swimmer, the marine lamprey, *Petromyzon marinus*, as our study species for several reasons. First, they swim forward and backward using traveling waves of body flexure (Islam et al. 2006). While they swim forward routinely, when provoked lamprey retract their heads, as most elongate swimmers do (Ward and Azizi 2001), and swim backward with body kinematics in between the excellent backward propulsion of eels (D'Aout and Aerts 1999) and the stationary motion of ropefish (Bierman et al. 2004). Since in both swimming directions lamprey use traveling body flexures, they provide us with a wide range of swimming behaviors and body reconfigurations without the complications of comparing different species. Second, much is known about the underlying neural control of lamprey swimming, since they are used as a model organism for the neural control of vertebrate locomotion in general (Grillner et al. 1995; Grillner 1996; Ijspeert 2001; Sigvardt 1989; Guan et al. 2001) and eel-like swimming in particular (Carling et al. 1998; Ekeberg 1993; Ijspeert et al. 1999; Lighthill 1975; Williams et al. 1998). Third, lamprey have been used as the biological model for the simulation of the evolution of locomotor control systems (Ijspeert and Kodjabachian 1999; Or et al. 2002) and the design of aquatic robots (Arena et al. 2006; Crespi and Ijspeert 2006; Lachat et al. 2006).

2.2 Experimental conditions

Using high-speed video, we filmed lamprey swimming forward and backward in a still-water tank. For analysis, we biased selection of trials towards those appearing on slow-motion video to be of nearly constant velocity. We did so in order to test the ability of our methodology to detect deviations from constant velocity swimming. Since backward swimming is in part a head-retraction startle response (Ward and Azizi 2001), we also sought to measure changes in the body shape, or what we call "reconfiguration", as separate from propulsive body movements. Thus steady swimming with a constant body shape is the starting point for our analysis.

Seven metamorphosed, parasitic-phase sea lamprey, *Petromyzon marinus*, between 10 and 17 cm total length, were obtained from the Lake Huron Biological Station in Millersburg, Michigan and the Conte Anadromous Fish Research Center in Amherst, Connecticut. All lamprey were housed at 20°C in an 80 L aquarium. Swimming sequences were captured at 500 frames per second with high speed video (Kodak Ektapro model 1000 EM). The ventral surface of fish was filmed during forward and backward swimming through the glass bottom of an aquarium evenly backlit by a diffuser illuminated with a 500 W halogen light. A 10 × 10 cm square grid was placed in the video field for calibration. Swimming was initiated by gently stimulating the rostral or caudal end of the fish with a rubber tipped rod.

2.3 Digitizing and preprocessing video

Video sequences were digitized using a video deck (Sony SVO-9500MD SVHS) linked to a Macintosh IIfx computer. An *xy*-coordinate grid was overlaid upon the video screen (Image 1.51 software, Televeyes Pro video overlay board, Digital Vision, Inc.). A series of 20 points on the fish's midline was manually plotted for 20 frames per putative tailbeat cycle. These data were processed using software introduced by Jayne and Lauder (1993) to create a dataset consisting of time series of positions in two dimensions for specific points uniformly spaced on the midline of the fish. Each time series includes one pair of coordinates for each frame of the digitized video that was processed. We tracked 31 body points, extending from the rostral tip to the caudal tip. The elapsed time between successive frames was constant and is referred to as the interframe time. Since not every frame of the original video was digitized, and the number of frames skipped varies from trial to trial, the interframe time varies as well. The data form doubly indexed coordinate pairs, $\mathbf{x}_{ij} = (x_{ij}, y_{ij})$, in units of centimeters, with $1 \le i \le N$ and $0 \le j \le 30$. The index i varies over the N digitized frames, and j varies over the 31 body points.

2.4 Identifying velocity and cycle period

Following Weihs and Webb (1983), steady swimming is when the fish's undulatory motion is repetitive and the fish is moving *on average* along a straight trajectory. We regard a steadily swimming fish as having a characteristic period, p, associated with its motion. While p is traditionally measured to as the tail-beat period, taken from a single point, we define p as the *whole body cycle period*, since, for archetypal steady swimming, at the end of a cycle period the *entire* fish's body returns to its original physical configuration. This terminology is meant to signal the more balanced origin of this statistic by contrasting with the more usual tailbeat period used commonly in the biological literature.

Consider motion of a single body point of the fish. Labeling this point's position in space at one instant as $\mathbf{x}_{\text{init}}$, and the point's position after a time interval p has passed $\mathbf{x}_{\text{final}}$, the average velocity of that body point over that cycle period is

$$\mathbf{v} = \frac{\mathbf{x}_{\text{final}} - \mathbf{x}_{\text{init}}}{p}. \tag{1}$$

Steady swimming postulates that this average velocity vector, $\mathbf{v}$, and p, are constant as both the initial instant and the choice of point on the fish vary.

In current practice, tailbeat period is determined by identifying two frames in which the trailing tip is in the same relative position, for instance full extension to the fish's left, and calculating the elapsed time. While this general approach gives a good rough estimate to p, there are two important limits to its accuracy. First, it uses position information from a single point to infer a critical parameter in the kinematics of the entire fish. Given that we have position data for the entire fish, it is reasonable to seek a statistical method to use all of it to ascertain p, or equivalently its reciprocal, the *whole body cycle frequency* f. The second limitation is that determining the two frames in which the trailing tip is in the same relative position depends upon an estimation of the direction of motion of the fish, or the average velocity described above. This determination is typically done by eye, and therefore is not as accurate as a statistical technique, and this inaccuracy is particularly large in the still water situation of the data examined in this paper. Further, analysis of our kinematic data shows that both the average velocity and the period of motion display variability over the length of the fish, and so in general these quantities need to be calculated statistically. We present two techniques in this section: one based on the raw data in the time domain, and the other on data transformed to the frequency domain. The former is the natural means for estimating p, and the latter is the same for estimating f. In both cases it is essential to estimate the average velocity in conjunction with the cycle length.

2.4.1 Estimating a cycle period and velocity in the time domain

While standard techniques exist for identifying the periodic and long-term trends in time series data (see Brockwell and Davis 1996, Chap. 1), they are of limited use here because of the short duration of the times series relative to p. Few of our trials have two full cycles, whereas traditional methods work best when at least three cycles of data are available

(see Chatfield 2004, p 27), a point widely acknowledged in the literature on steady swimming (e.g., Jayne and Lauder 1995).

To overcome this difficulty, beginning with a dataset as described in Sect. 2.3, and taking all intervals of the specified length $p = k\Delta t$, where Δt is the interframe time for this dataset, we compute $31(N - k)$ sample average velocities, $(\mathbf{x}_{(i+k)j} - \mathbf{x}_{ij})/k\Delta t = \mathbf{v}_{ij}$. The sample mean $\hat{\mathbf{v}}_{\text{ave}}$ is henceforth called *composite average velocity*, to indicate that it is the mean of the average velocities of all body points, and distinguish it from the average velocity for individual body points, which will play an important role in the model constructed here. We compute a standard error under the unrealistic assumption that the estimates $\mathbf{v}_{ij}$ are independent via

$$\text{SE}(k) = \sqrt{\frac{\sum_{i,j} |\mathbf{v}_{ij} - \mathbf{v}(k)|^2}{62(N-k)[62(N-k)-1]}}. \tag{2}$$

where $\mathbf{v}(k)$ is the composite average velocity for a lag of k, a candidate for $\hat{\mathbf{v}}_{\text{ave}}$. In contrast to autocorrelation coefficients, which—as one would expect—vary erratically over body length and lag h, this standard error varies smoothly and offers a simple algorithm for finding p and $\hat{\mathbf{v}}_{\text{ave}}$. If SE($k$) achieves a local minimum at some $1 \le k \le N - 1$, then we assign $p = k\Delta t$ and $\hat{\mathbf{v}}_{\text{ave}} = \mathbf{v}(k)$. One of our trials has more than one local minimum, but this is because the trial is one of two with more than two full cycles. In this case, we use the shorter of the two intervals corresponding to a local minimum as p. If there is no local minimum, then SE(k) is monotonically decreasing for $1 \le k \le N$, and we turn to the frequency domain. In practice, this occurs in instances when p is only slightly shorter than the trial's full time interval, and the motion is not very steady, according to the criterion we develop below.

Our rationale for making the standard error rather than the sample variance our objective function is that it penalizes longer candidate p values to compensate for smaller sample sizes. Sample variance is often a monotone decreasing function unless the motion is quite steady and the trial's full interval is substantially longer than p.

2.4.2 *Estimating an average cycle frequency and velocity in the frequency domain*

To deal with instances when p is nearly as long as the trial interval in moderately to very unsteady motion, we have constructed a second technique that estimates $f = 1/p$ by applying a discrete Fourier transform that converts the data described in Sect. 2.3 to the frequency domain. The cycle frequency for each point in each dimension is then estimated, and a weighted average cycle frequency is computed. The computation involves three steps.

First, we compute a *windowed discrete Fourier transform* (henceforth FT) of the x- and y-components for the positions for each individual point. The window is a frequency bandwidth that extends from zero to twice the frequency associated with a low estimate of f. This filters out frequencies from harmonics of the estimated tailbeat frequency. The windowing serves two purposes: it aids in filtering out the displacement from the FT, and it excludes interference from the first harmonic in determination of f.

Second, we filter the net displacement of each body point out of its FT by least-squares regression. Performing this in a low-frequency window is critical for the technique's accuracy. If regression is performed in the time domain, the result is less accurate estimates of the body point's velocity, $\mathbf{v}$, and of p. From the net displacements in each coordinate an average velocity vector, $\mathbf{v}_j$ is derived for each body point. These are averaged with equal weighting to give $\hat{\mathbf{v}}_{\text{ave}}$. The residuals of this regression are a filtered FT (henceforth fFT), and this represents the frequency profile of the periodic portion of the motion of the body point. A periodogram shows the amplitude data for this frequency profile, for both spatial coordinates of all 31 body points in a representative dataset (Fig. 1).

Third, each body point offers two estimates of f, the maximum amplitude frequency in the fFT in each spatial dimension. These are denoted $f_{x,i}$ and $f_{y,i}$, where the index i varies over body points. The amplitudes at these frequencies, denoted $a_{x,i}$ and $a_{y,i}$ are used to weight the average of the frequencies over body points and directions to compute f. That is,

$$f = \frac{\sum_{\text{bodypoints}} a_{xf_x + a_y f_y}}{\sum_{\text{bodypoints}} a_x + a_y}. \tag{3}$$

Computations demonstrate that motion in the lateral direction is dominated by the fundamental frequency of the motion, with an amplitude proportional to the flexion of the spinal chord/curvature of the notochord. The motion in the axial direction is dominated by the first harmonic, with an amplitude proportional to the square of the flexion/curvature. Since flexion is less than one, this amplitude is smaller than that in the lateral direction. Thus, if the dataset happens to have the lateral and axial directions roughly aligned with the coordinate directions, it is possible the axial direction will generate false estimates of the fundamental, off by a factor of two. Hence we set the bandwidth window to exclude the first harmonic.

The estimate for p is the reciprocal of f rounded to the nearest multiple of the interframe time, so all estimates for p are integer multiples of the interframe time.

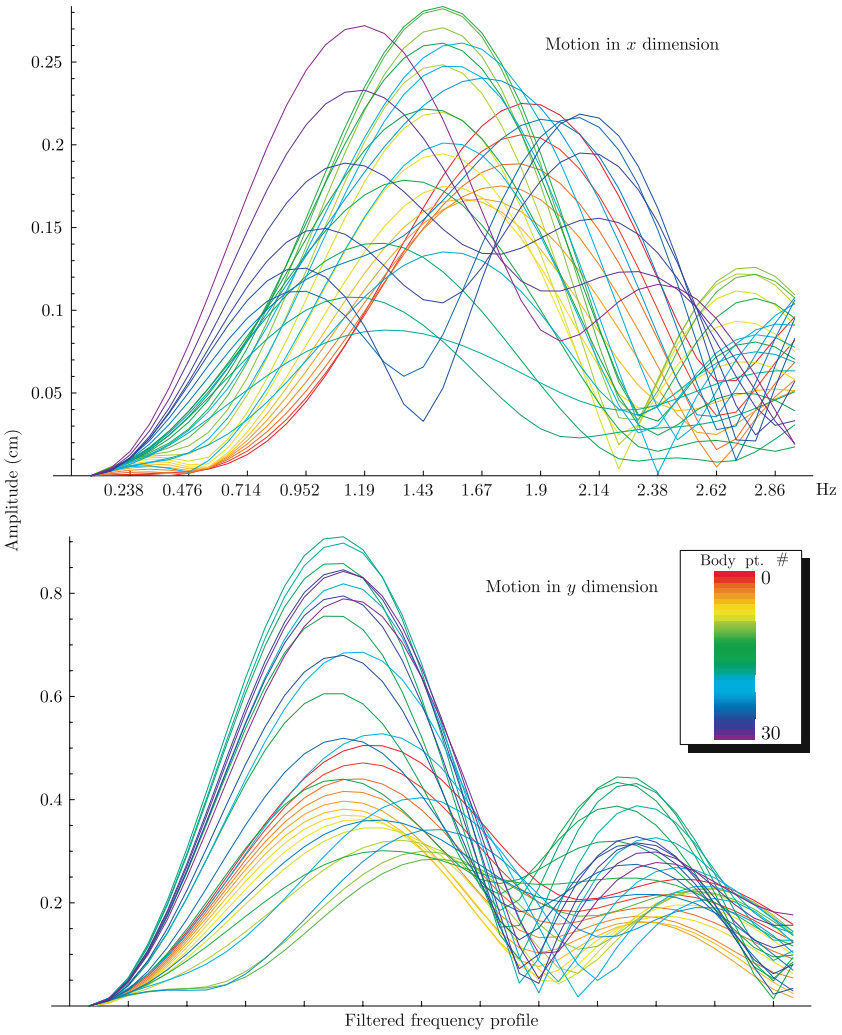

Fig. 1 Periodograms for fFT's for all body points for a representative trial where p (0.84 s or f = 1.19 Hz) was determined in the frequency domain. The frequency components due to translation, including any constant (0 Hz) component, have been eliminated from the profiles by regression. The large disparity in peaks of the various curves indicates that the different body points are displaying different fundamental frequencies. Note that while the scales in the horizontal direction are the same, the vertical scales are different, reflecting the larger amplitude of motion in the y-direction. This fish is swimming leftward in a direction roughly 20° above horizontal, as shown in Fig. 3, the trial on the *lower right*

2.5 Assessing the steadiness of swimming

Once p and $\hat{\mathbf{v}}_{\text{ave}}$ have been estimated, we can test our assumption that the swimming motion is steady. To do so, we offer an *unsteadiness index* (UI) to measure the deviation of the observed data from the ideal of steady swimming. The UI is related to, but purposely slightly different from, the standard error SE(k) minimized to find the time domain estimate of p.

The UI for a dataset with estimates of $\hat{\mathbf{v}}_{\text{ave}}$ and p is a dimensionless figure of merit quantifying the accuracy of the assumption that the dataset represents steady swimming with the specified period and velocity. Thus smaller UIs indicate more nearly steady datasets. We assume that $p = k\Delta t$ with k an integer, but this assumption can be relaxed without difficulty.

The first step in computing the UI is to compute all possible *reconfiguration errors* (RE), the relative errors between $\hat{\mathbf{v}}_{\text{ave}}$ and the average velocity of body points over a cycle. For each body point we have time series of x- and y-coordinates; a time series of position vectors for the body point, $\mathbf{x}_1, \mathbf{x}_2, \mathbf{x}_3, \ldots \mathbf{x}_N$. Compute the average velocity of the body point over the whole body cycle period that begins in frame i and ends in frame $i + k$. From Eq. 1 this gives us

$$\mathbf{v}_{\text{actual},i} = \frac{\mathbf{x}_{i+k} - \mathbf{x}_i}{p},$$

which we compare with $\hat{\mathbf{v}}_{\text{ave}}$ to get the RE

$$\text{RE}_i = \frac{\mathbf{v}_{\text{actual},i} - \hat{\mathbf{v}}_{\text{ave}}}{|\hat{\mathbf{v}}_{\text{ave}}|}. \tag{4}$$

REs are vectors that are useful in themselves in assessing the steadiness of a dataset (see Fig. 7).

Once the REs have been computed for every available cycle for every body point, we use them to compute the UI. Since the REs would all be zero for a perfectly steady swimmer, the UI is a weighted standard deviation of the REs, using the zero vector as the center value. The formula for the computation is

$$\mathrm{UI} = \sqrt{\frac{\sum_{31\ \text{points}\ \&\ 1 \le i \le N-k} |\mathrm{RE}_i|^2 \frac{|\hat{\mathbf{v}}_{\mathrm{ave}}|}{|\mathbf{v}_{\mathrm{actual},i}|}}{31(N-k)-1}}. \quad (5)$$

Note that the ratio of lengths of velocity vectors in this formula would not appear in the usual standard deviation calculation. Because the quantity $|\mathrm{RE}_i|^2$ includes a factor of $|\hat{\mathbf{v}}_{\mathrm{ave}}|^2$ in the denominator, multiplying by the ratio of lengths places the product $|\hat{\mathbf{v}}_{\mathrm{ave}}||\mathbf{v}_{\mathrm{actual},i}|$ in the denominator, giving both estimated and the computed average velocity vector weight in assessing the relative size of the error.

2.6 Modeling steady undulatory motion

The data are rotated so that the composite average velocity vector points in the positive x-direction, and each frame of the data is translated horizontally in the negative x-direction by the displacement predicted the estimated speed of the fish. That is, if $s = |\hat{\mathbf{v}}_{\mathrm{ave}}|$ in units of centimeters per interframe time, the ith frame of rotated data is translated to the left by $(i - 1)s$. The result is data that are on average stationary, assuming that $\hat{\mathbf{v}}_{\mathrm{ave}}$ is an accurate estimate. These data preserve the periodic portion of the motion, and the deviation from steadiness, including periodic axial acceleration and deceleration. The horizontal direction is now the axial direction, labeled u, and the vertical direction is now the lateral direction, labeled v.

Any function $u(t)$ with period p that is continuous and piecewise smooth (technical conditions that kinematic data always satisfy) can be written as a Fourier series (see, e.g., Tolstov 1962):

$$u(t) = u_0 + \sum_{n=0}^{\infty} A_n \cos((n+1)\omega t - \phi_n). \quad (6)$$

The quantity ω is the *fundamental angular frequency*, $\omega = 2\pi/p$. The integer multiples of the fundamental frequency $n\omega$ are the harmonics of the fundamental with the integer $n + 1$ giving the nth harmonic. Each frequency has two associated parameters that collectively characterize the function u; they are the amplitude A_n and the phase angle ϕ_n. The constant u_0 is the average value of $u(t)$.

We truncate the infinite series no later than the fourth harmonic since we can expect our discrete data to provide us with information for the first few harmonics of the full frequency spectrum. The choice of the fourth harmonic as the final term in our series is heuristic; it rarely plays a substanial role in any of our models. In practice an unmodified finite Fourier series gives a relatively poor fit to the data, even if the UI is fairly low, because, over the course of a cycle, the final configuration of the fish is never identical with its initial configuration. Even fairly steady swimmers experience changes in configuration that typically result in relative errors in their average velocity of 10% (Fig. 7). To account for this deviation from steadiness, we introduce a term that varies *secularly*. For most data sets it is sufficient to include only a constant velocity term, giving a *linearly displaced Fourier series* of this form:

$$u(t) = u_0 + \mathrm{vel}_u t + \sum_{n=1}^{n_{\max}} A_n \cos(n\omega t - \phi_n). \quad (7)$$

However, some datasets require secular acceleration as well, giving a *quadratically displaced Fourier series*:

$$u(t) = u_0 + \mathrm{vel}_u t + \frac{\mathrm{acc}_u}{2} t^2 + \sum_{n=1}^{n_{\max}} A_n \cos(n\omega t - \phi_n). \quad (8)$$

Equation 7 or, in certain instances called out below, Eq. 8, is the model we use to describe the motion of a single body point in a single dimension of uv-space, usually with $n_{\max} = 2$ to include the fundamental and first harmonic. Series expansion of relative motion caused by sinusoidally varying flexion shows that these two frequencies should include the majority of the motion of the fish. Because we have 31 body points each requiring two coordinates, a full model of the motion of the fish within its inertial frame requires 62 functions of the form given in Eq. 7 (or Eq. 8).

2.7 Summarizing the harmonic structure of swimming kinematics

To visualize the information in these models we use plots of harmonic structure (see Fig. 8). These plots consist of an array of shapes that indicate the magnitude and phase (if applicable) of the contribution of a particular term in the model (Eqs. 7, 8) at various points along the length of the fish. In these plots, the horizontal dimension represents position along the fish from rostrum on the left to caudal tip on the right. Above the central axis is data on the fit in the lateral direction, below the axial direction. For the secular velocity term, a black square is included for each body point. Sides parallel to the coordinate axes indicate the velocity is in the positive direction for its coordinate, otherwise the square has diagonal sides. A secular acceleration term, when included, is represented by a triangle, which points upward for positive acceleration.

The frequencies used in the model increase as we move outward from the central axis of the plot. The amplitude of the contribution of each frequency is indicated by the area of a disk, while the phase of the contribution is indicated by

the color of the disk, as indicated in the legend accompanying the figure.

These plots include a graphic summarizing the quality of the fit at each point in each component in a row of rectangles at the top and bottom margins of each plot. Each box conveys the R^2 value for the fit at a body point in one dimension. Values of R^2 greater than 0.5 are indicated by filling the box to a level proportional to the excess, beginning at the side closest to the central axis and using black. Values less than 0.5 are indicated by filling the box in red to a level proportional to the deficit, beginning away from the central axis.

3 Results

3.1 Comparing whole body cycle period with tailbeat period

For steady locomotion with large average speed, the visual technique commonly used by biologists to compute a tailbeat period (See Sect. 2.4) gives cycle periods generally comparable to the whole body cycle period. However, when the motion is unsteady and the average speed is small, it is much more difficult to ascertain the fundamental period for the motion. Because the backward swimming trials are generally more unsteady than the forward motion trials, as shown in Fig. 5, and they generally have lower average speeds, as shown in the first graph of Fig. 6, this means that the visual method is unsatisfactory in analyzing these trials in particular. Figure 2 shows that while the tailbeat period computed by an experienced experimenter generally agrees with those computed using the method developed here for the forward trials, there are substantial deviations between the two techniques for the backward trials.

The fact that these deviations show no systematic bias suggests that the differences in these two methods of measurement is not amenable to correction by some fixed adjustment, such as a regression formula. Rather, the statistical technique must be applied to the raw data in order to appropriately estimate the cycle period.

3.2 Unsteadiness index and steady locomotion

The UI allows us to characterize a continuum of body motions (Fig. 3). For the sake of discussion, we categorize all motions with an UI greater than one, when the fish is

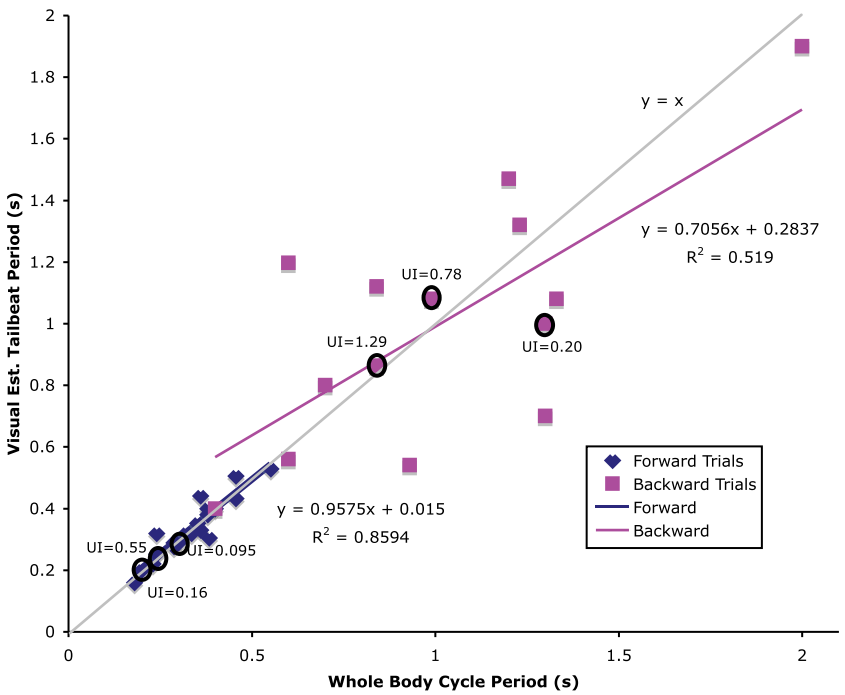

Fig. 2 Tailbeat periods for the 34 trials as found by an experienced experimenter plotted against the whole body cycle periods as computed by the technique described in Sect. 2.4. The plot shows that the two measures of the period of motion generally agree for forward trials, which characteristically have higher speeds and steadier motion. For backward trials, at slower speeds and with more unsteadiness, the measurements differ more substantially. Among backward trials, one notable exception is the only backward trial with cycle period (by either method) less than 0.5 s, where the majority of forward swimming trials lie. This trial also happens to be the fastest of the backward trials, some 40% faster than the next fastest. Although this trial is unsteady (UI = 1.30), the increased velocity seems to make it easier for the experimenter to accurately assess the direction of motion, and therefore the extremes of tail tip motion

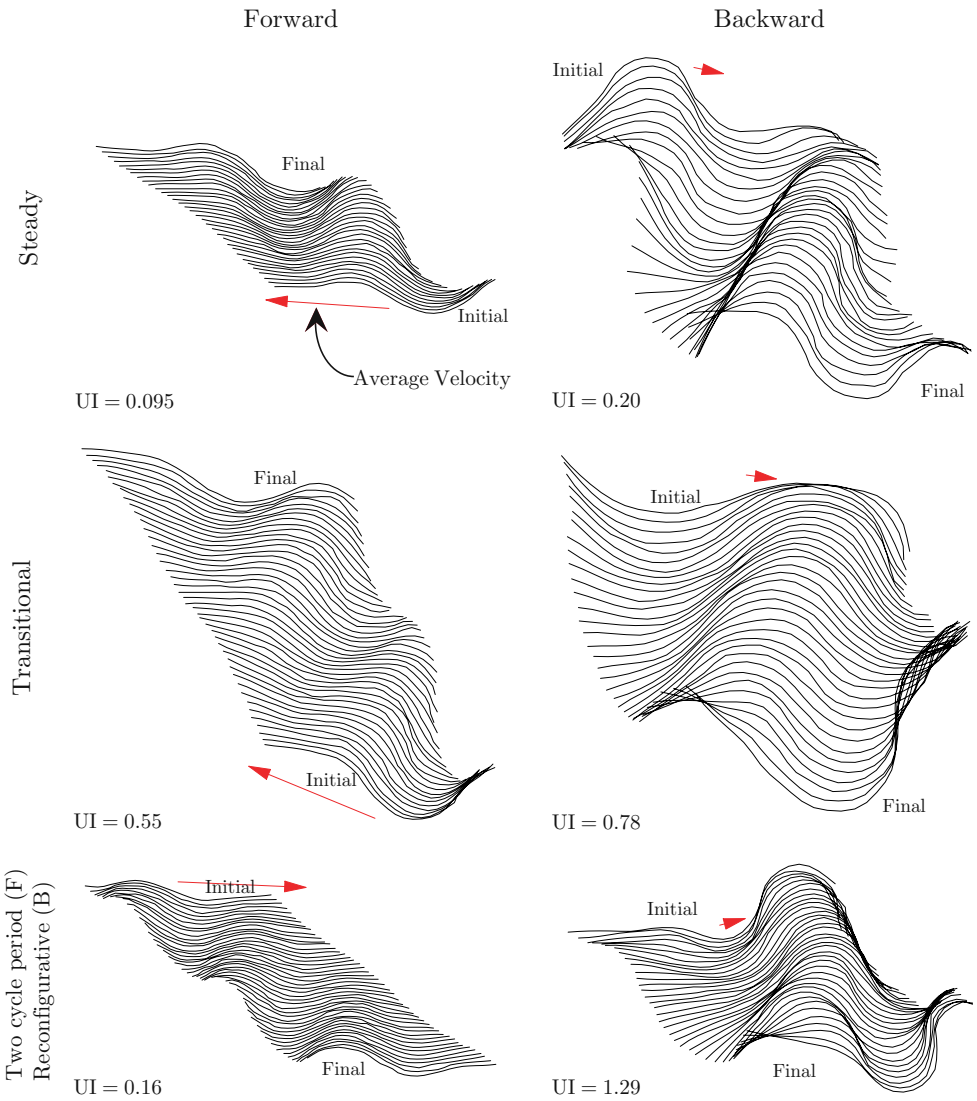

Fig. 3 Behavioral range of forward and backward volitional swimming, as measured and categorized (steady, transitional, or reconfigurative) by unsteadiness index (*UI*). Six examples. Note that *midlines*, normally superimposed, have been displaced laterally to show propagation of curvature and changes in body shape (reconfiguration). The *red arrow*, next to the initial midline in each time series, indicates the average velocity vector for that trial. Reconfigurative swimming occurs only in backward trials (see Fig. 5). The two bottom-most forward swimming trials are the only ones for which two full cycles were captured

using more than half its motion to reconfigure its body, as *reconfigurative* motion. When UI < 0.5 we call the motion *steady*. We denote motion in between reconfigurative and steady as *transitional*. The two steady trials shown as examples are moderately short extensions of a single cycle period, having eight frames (for the forward trial) and six frames (for the backward trial) more than the estimated cycle period (Fig. 3).

Unsteadiness index is sensitive to the number of available frames, since it compares the configurations of the midline in frames separated by a cycle period p (Fig. 4). The steady backward trial (Fig. 3), which has the lowest UI of any backward trial, is one of three that is quantitatively different from the rest, and more like the steady forward trials. Despite this, with 25% fewer frames, it has roughly twice as large a UI as the steady forward trial shown, which, although not the trial with the lowest UI, is still remarkable for the small UI obtained with so many frames. The two cycle forward trial (lower left, Fig. 3), is similarly remarkable for its low UI with 26 frames beyond a cycle period.

The two transitional trials illustrate lack of steadiness in backward swimming, and the importance of considering the number of frames used in the computation of the UI. The forward transitional trial is one of only two trials that contains more than two full cycle periods, having 23 frames past a cycle of 20 frames. This by itself is not enough to account for the higher UI, as the third forward trial shows (Fig. 4), but its UI is not far from the value predicted by forward trials as a whole. Compared to the other two forward trials, the transitional trial includes a reconfigurative component with motion that is otherwise fairly steady (Fig. 3).

Comparison of the two transitional trials (Fig. 3) shows the backward trial's motion is much less steady, despite being the steadiest of all the backward trials except the

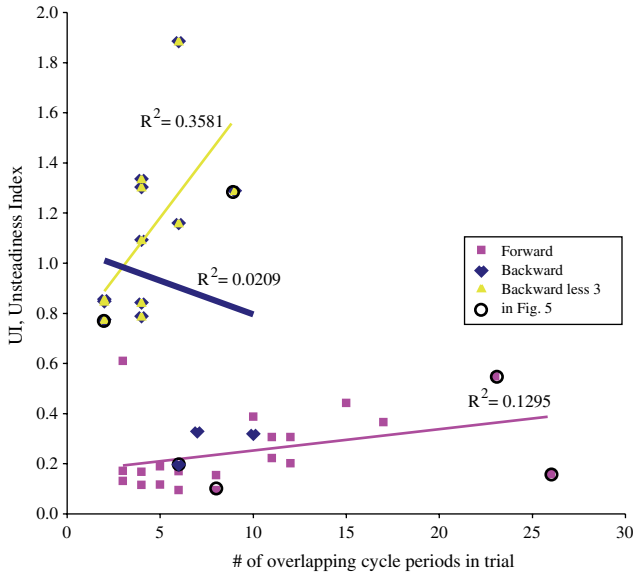

Fig. 4 The number of frames analyzed alters UI. The association for forward and most backward trials is clearly different, however, there are three backward trials (shown by *blue markers*) that follow the forward trial association. When they are included with all backward trials their effect on R is substantial, driving it to essentially 0, actually making it slightly negative. When they are excluded, however, we see that the R for both sets of trials are appreciably positive

three outliers. This trial includes only two frames more than a cycle period, and this shorter relative length is typical of backward trials (Fig. 4). This transitional trial has more in common with the third, reconfigurative, backward trial; both show substantial reconfiguration with very little displacement, as witnessed by their short average velocity vectors (shown in red, Fig. 3).

As shown in Fig. 4, the association between UI and number of frames analyzed is different for forward and backward motion. For forward trials, the association is fairly strong and linear, while for backward trials it is quite weak. In addition, the two regression lines have different slopes and more importantly different intercepts; neither of them zero. This precludes time averaging UI to obtain a parameter independent of the number of frames, as it would artificially penalize shorter trials.

While this time dependence of UI is a weakness, it displays a basic feature of this technique. Long trials, measured in terms of the cycle period rather than seconds, have more opportunity to be unsteady, and by and large are more unsteady.

3.2.1 *Steadiness and direction of locomotion*

When the UI for all 34 trials are compared (Fig. 5), we find clear separation of forward and backward swimming. Backward trials demonstrate more unsteadiness, and more variability in unsteadiness, in spite of the fact that they show less variablility in p and $\hat{\mathbf{v}}_{ave}$ than forward trials (Fig. 6). The backward and forward trials show no appreciable association between UI and either cycle period or swimming speed. If we disregard the high UI outlier trial, there is a *negative* association between UI and p (r = –0.744), suggesting that slower tail undulations and steadier motion are correlated, *only in backward swimming*.

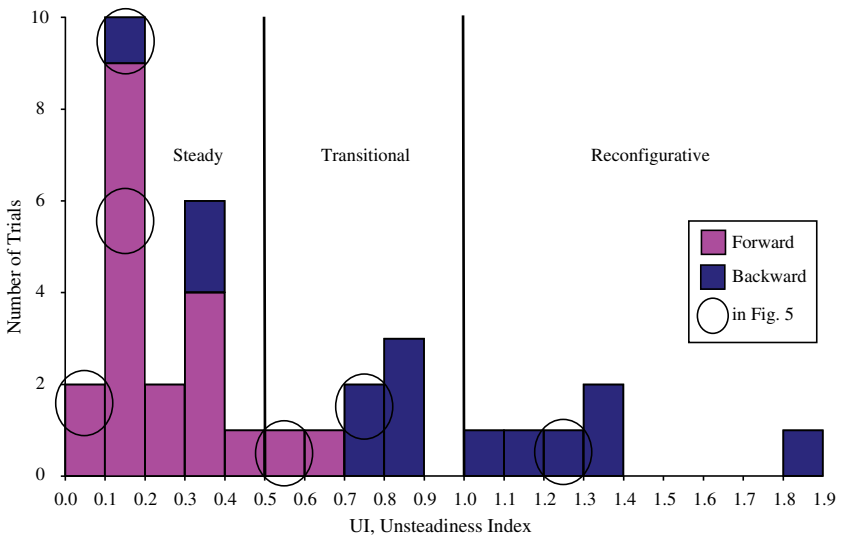

Fig. 5 Unsteadiness indexs for forward and backward swimming occupy separate modes in a biomodal distribution. The forward swimming trials form the preponderance of the primary mode within the steady category (0.1 < UI < 0.4), while the secondary mode (0.7 < UI < 1.4) is comprised entirely of backward transitional or reconfiguring trials. The largest UI is an outlier even among backward trials, which demonstrate more than twice the variability in UI of the forward trials. ($s_{backward}$ = 0.46, and even ignoring the outlier the standard deviation of the other 13 backward trials is 0.385, while $s_{forward}$ = 0.15)

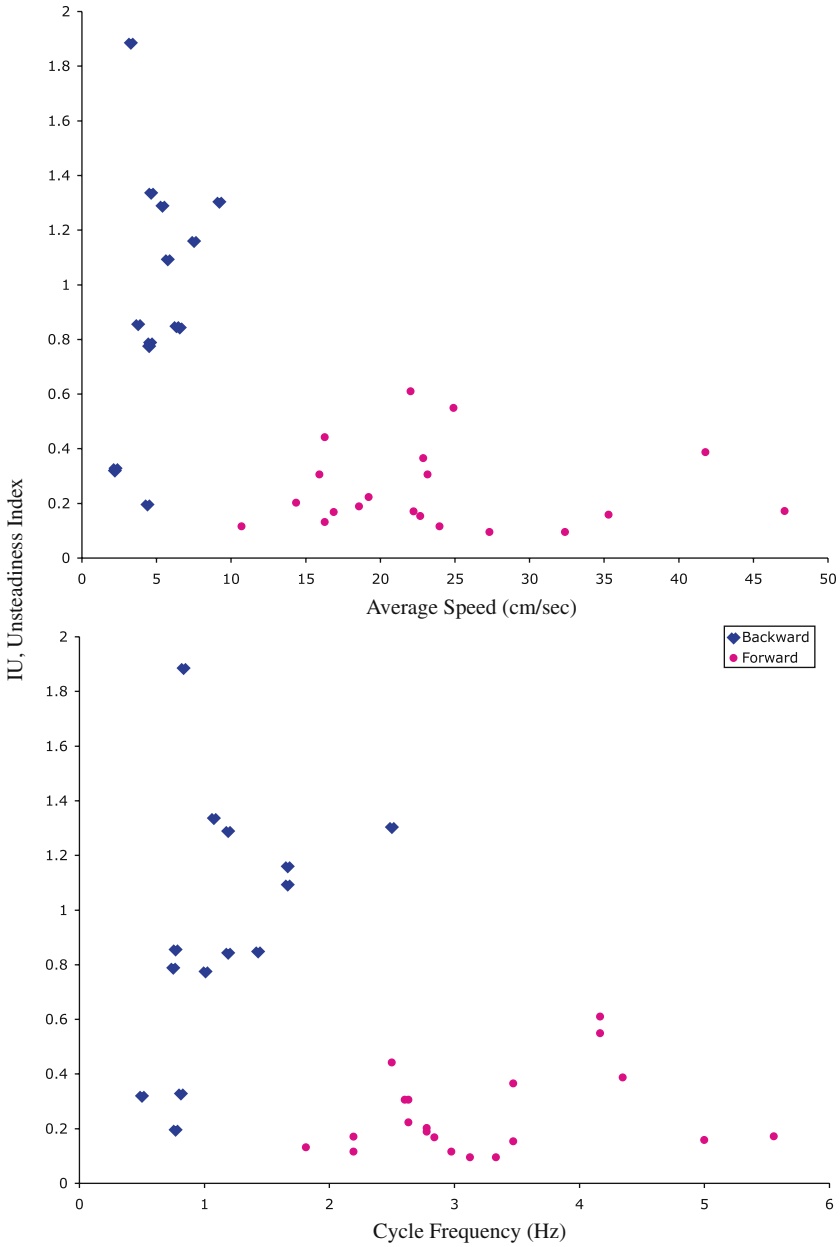

Fig. 6 When correlated with swimming speed and WBCF, the values for UI of forward and backward swimming form non-overlapping clusters. Compared to forward swimming, backward swimming is characterized by UIs with a greater range, slower speeds, and, with one exception, slower cycle frequencies

3.2.2 Reconfiguration errors and steady swimming

Differences between steady and unsteady swimming are also detected and characterized by the REs (Fig. 7). The pattern in the REs demonstrates that lamprey in the backward swimming trials (on the right) are engaged in more reconfiguration than during forward swimming. The tight cluster of the REs for forward trials is partly attributable to the greater speed, since these errors are all relative to average speed. Even allowing for this, there is substantially more reconfiguration, especially in the two least steady backward trials shown. Compare these with the transitional forward trial, where most errors are relatively tightly clumped, but the fish gradually reconfigured by sweeping its tail downward over the end of the two cycle trial.

We can see this because generally REs for later cycle period windows are larger than those for earlier windows, and, in this case, a comparison of the initial frames with the final frames (see Fig. 3), shows that the tail's upstroke is less extreme at the end of the trial. Compare this with the REs of the transitional backward trial (see Fig. 7). There are many fewer errors computed in this trial, only two frame's worth, compared with 23 for the corresponding forward trial, but the backward trial's reconfiguration errors are larger, in both absolute and relative (to speed) terms. The plot shows that, relative to the body as a whole,

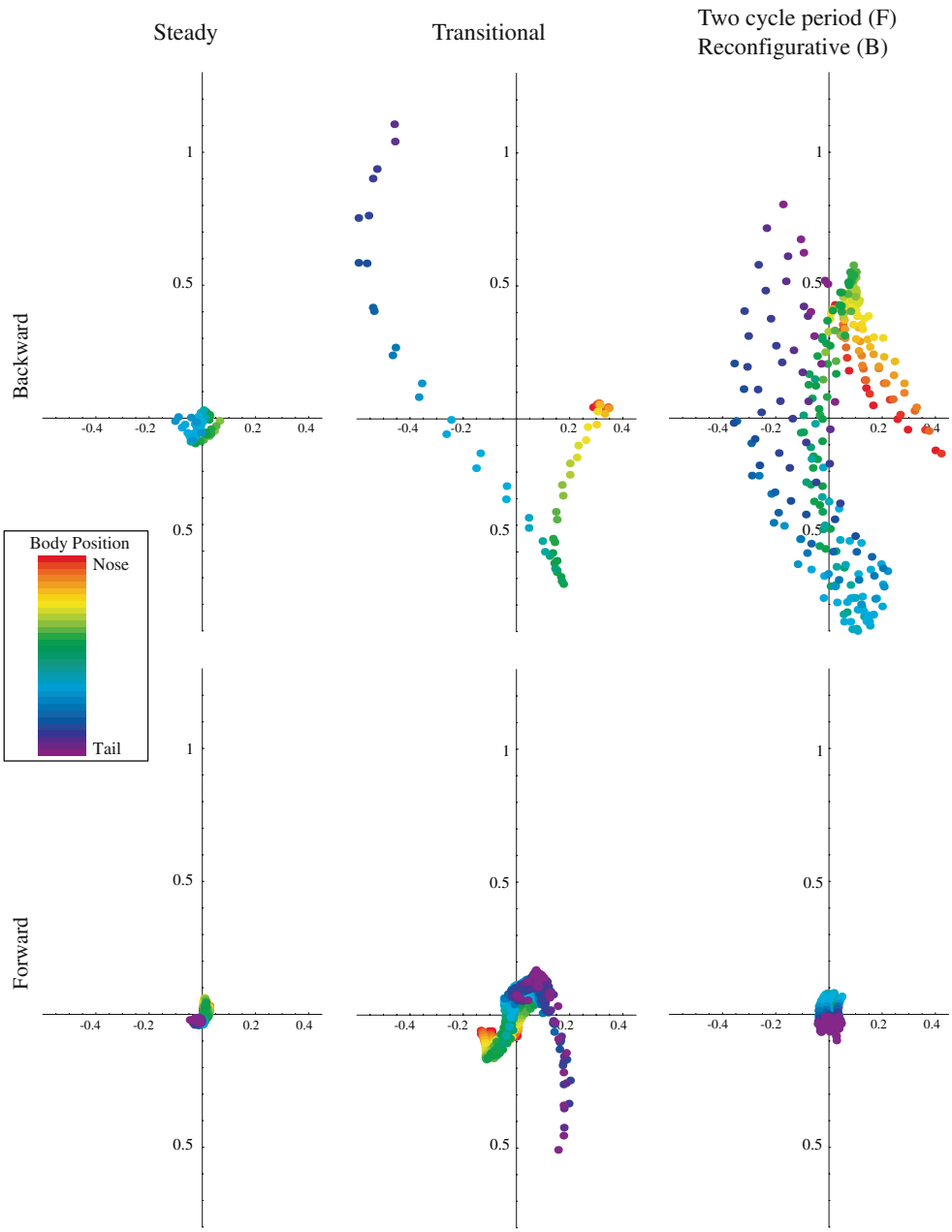

Fig. 7 Reconfiguration errors (*REs*) for the representative trials illustrated in Fig. 3 are relative errors in estimates of the average speed as defined in Eq. 4. The change in scale amongst the plots is the most important basis for comparison. These plots are transposed from the positions of the corresponding plots in Fig. 3; rotate this figure 90° clockwise to place these plots in the corresponding positions

the caudal region is reconfiguring up and to the the left, over just a little more than one cycle. Looking at the motion of the backward transitional trial (Fig. 3), we can see that this is the what has actually happened; the fish arches its leading edge (tail) up and leftward. While reconfiguration occurs in forward steady swimming, it tends to be both smaller in magnitude and more gradual in occurance than during backward swimming.

Comparing the backward transitional and reconfigurative trials, we see the latter group has no errors as large as the largest in the former; instead it has many more errors, nine frame's worth. Thus, while the reconfiguration across any individual cycle period is less for the latter, because it is longer (measured in cycle periods), it allows for more reconfiguration to occur. This is apparent from the motion (Fig. 3), where the reconfiguration from the initial to the final frame in the reconfigurative trial is more extreme than in the transitional trial. This qualitative observation is suspect because the initial and final frames of a trial are not typically at the same phase of a cycle period, and so the periodic component may appear to be reconfigurative. This idea can be made more rigorous by filtering out the periodic components of the motion as described in Sect. 3.3.2. However, the UI allows us to state that the reconfigurative trial is 65% more unsteady than the transitional trial.

3.3 Harmonic structure of undulatory swimming

The entire dataset for each of the 34 trials was analyzed. The resulting fitting functions have the form of Eq. 7 with $n_{max} = 2$. The fitting functions can be used to compute many kinematic parameters generally used to quantify motion of a swimming fish. These include not just mean velocity and tailbeat frequency, whose generalizations, $\hat{\mathbf{v}}_{ave}$ and p, have already been discussed extensively. The fitting functions also allow estimations of head-tip and tail-tip amplitude, propulsive wavelength, wavespeed, stridelength, lateral curvature, relative power, Reynolds number, Strouhal number and Froude efficiency in ways that give weight to all the data collected, rather than depending upon the measurement of a small number of points to characterize the entire motion. As an example of this, we examine these trials for the presence of an accelerating wave of curvature in Sect. 2.3 below. First, we examine the harmonic structure of the six representative trials of Fig. 3 by means of harmonic structure plots, as described in Sect. 2.7.

3.3.1 Visualizing harmonic structure

Our kinematic analysis of the whole body is summarized by harmonic structure plots (Fig. 8). Each plot displays the information contained in 62 linearly displaced Fourier series that describe the motion of one of the trials.

The plot of the forward steady trial shows basic features of steady locomotion. The secular velocity terms in both the lateral and axial dimensions are small, while the lateral fundamental frequency is large, and grows approaching the trailing edge (the caudal tip in this trial). The periodic contribution in the axial direction is small and the fundamental component has roughly constant phase. The axial first harmonic component grows in amplitude with the amplitude of the fundamental lateral component. The phase of the lateral fundamental shows that the body has roughly one and a quarter waves on it. Also, the phase decreases steadily as we move posteriorly, indicating a wave traveling down the body. Examining R^2, we see that the fit in the lateral direction is excellent, with over 90% of the motion accounted for by this model at every point on the body. The fit in the axial direction is worse, since the data have been transformed to remove the displacement due to the average velocity of the fish. Thus for a steady trial like this, there is very little axial motion left, and the error is relatively larger than in the lateral dimension.

The steady backward trial has some of the features just delineated, but also notable differences. Most obvious is more uniform amplitude of lateral fundamental components of the model. Although the smallest amplitude occurs at the leading edge (the caudal tip), that amplitude is nearer to maximum than in the forward trial. (Sizes are scaled relative to the maximum fundamental lateral component, thus relative sizes within a plot are meaningful, but comparison across trials is inappropriate.) Further, amplitudes increase moving anteriorly until roughly 30% of a fish-length from the rostral tip. Amplitudes decrease to roughly the 10% mark, and then increase to the rostral tip. Presence of a second local maximum amplitude point, as well as more nearly uniform amplitude along the whole fish, are common characteristics of backward swimming trials not shared by forward swimmers. Note that the phases of lateral fundamental components indicate both a longer wavelength (just over one wave on the body), and that the wave travels forward in this trial, since the phase decreases moving anteriorly.

The lateral fit for this trial is slightly worse than in the steady forward trial, as the REs suggest (see Fig. 7); however, the fit in the axial direction accounts for substantially more of the motion contained in the data. This is because of larger axial components; this trial has more axial motion left when displacement due to composite average velocity is accounted for. The high R^2's show that the reconfiguration taking place in this trial is occurring with roughly constant velocity at each body point, since the model, including secular velocity, yields an excellent fit to the data.

Looking at the backward transitional trial, it is clear that the model's fit to this trial is even better than either of the two trials considered to this point. The ability of a model for steady locomotion to fit so well to data that is not steady lies in the inclusion of secular velocity. Note the increase in magnitude of these components compared to the steady trials. The squares (or diamonds) symbolizing velocity are scaled so that their area is comparable to the area of a disk for a fundamental frequency component that has the same average speed over a cycle period. So, we can see that at the caudal tip, the secular velocity term is causing more displacement than the periodic motion, because it has larger average speed. If the secular dominates the periodic over the entire length of the fish, then motion would be reconfigurative. As it is, this plot agrees with its classification as transitional.

3.3.2 Excising the periodic component of motion

To remove the periodic component of the fitting functions in a model, leaving the "average" position of the fish at any moment, we set the coefficients of the cosine terms in either of Eq. 7 or 8 to zero, leaving only the secular terms. This average position can be used to identify reconfiguration of the fish independent of periodic motion.

Consider the comparison offered by Fig. 9 of the two bottom-most trials in Fig. 3. Displaying initial and final frames of the two trials with both the actual and average

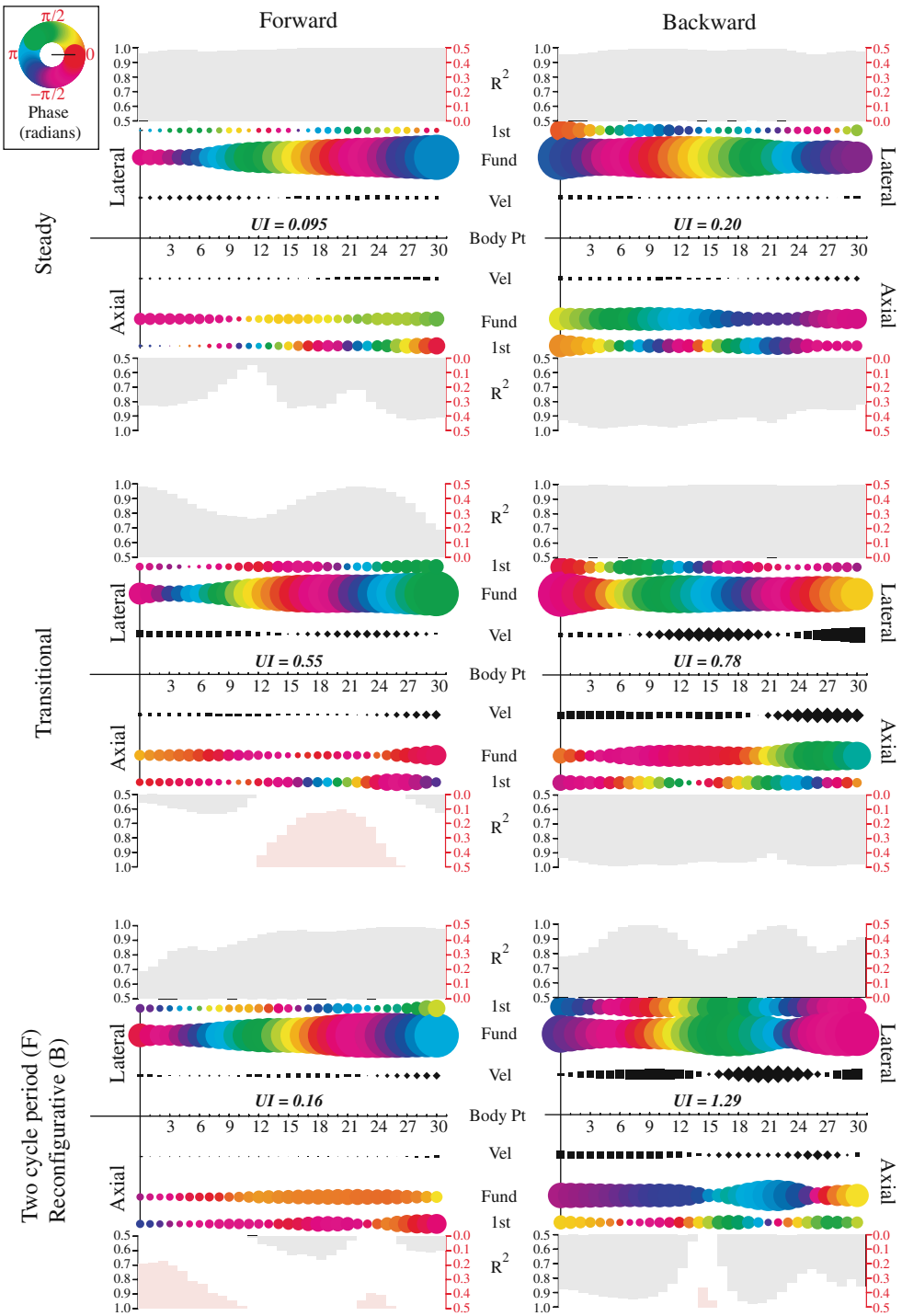

Fig. 8 Harmonic structure for the each of the six swimming trials shown in Fig. 3. Structure of the lateral and axial motion of each point is shown above and below, respectively, the horizontal axis. Harmonic structure measured as the amplitude (area of point) and phase (color of point) of the fundamental and first harmonic frequency of each point relative to the others in that trial and direction (lateral vs. axial). Secular velocities for each point in each direction is also shown. Accuracy of the harmonic model in capturing the motion of one point in one dimension indicated by the R^2 values, which are read from the scale on the left when *black*, and the scale of the right when *red*. Further description of these graphics is given in Sect. 2.7, and they are interpreted in Sect. 3.3.1

positions requires reintroducing the composite average velocity to the model (It was removed as described in Sect. 2.6.), as well as excising the periodic terms. The forward trial has very little reconfiguration, just a slight downward motion of the tail, and a compensating upward motion in the precaudal region. Over the 1.26 cycle periods of the unsteady trial, the translation in the axial direction of the fish is dwarfed by the lateral leftward (in the fish's frame of reference) motion of the midsection and corresponding rightward motion of its extremities. These results are consonant with the REs for these trials (Fig. 7), but they derive from Fourier analysis, rather than from comparison of frames separated by a cycle period. Examining Fig. 7, the REs for the forward trial shows REs of neighboring body points are necessarily grouped together, and the errors tightly clustered about the origin. The density

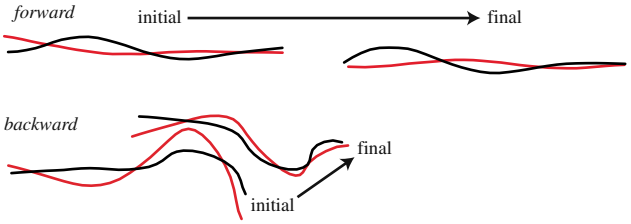

Fig. 9 Forward swimming is primarily translational while backward swimming combines translation and reconfiguration. The *black curves* represent the actual body midlines of the lampreys, while the *red curves* represent "average" positions at the same instants, as defined in Sect. 3.3.2. These average positions average out periodic undulatory motion, leaving the net positions that change aperiodically. Data from trials shown in the bottom row of Fig. 3; UI = 0.16 (*top*) and 1.29 (*bottom*). The differences in the positions of the initial and final *black curves* in the figure reflect the actual movement of the fish (as contrasted with Fig. 3). The differences in the positions of the initial and final *red curves* show the aperiodic change in the average position and configuration of the fish. Specifically, for the backward trial, the differences in the shapes of the initial and final *red curves* demonstrate the prediction of the REs shown in Fig. 7 that the fish undergoes a major displacement in the form of a U-shaped reconfiguration that dominates the translation of the fish in this trial. This deformation is not the result of periodic undulation, as this figure demonstrates. In comparison, the change in the initial and final averaged positions for the forward trial show that this trial is dominated by translation, with relatively little reconfiguration. This agrees with the REs for this trial, shown in Fig. 7

decreases roughly uniformly regardless of the direction of departure from the origin, but errors with negative y-component are for the caudal region, while those for pre-caudal to mid-fish points have positive y. The average positions in Fig. 9 confirm that reconfiguration in the raw data is not simply due to a change of phase, but rather to secular reconfiguration of the fish.

3.3.3 Number of waves on the body

By summing phase differences from one body point to the next for the fundamental frequency in the lateral direction, it is possible to compute the total phase difference from the tail to the end of the fish; dividing by 2π yields the number of traveling waves computed in a fashion that takes into account all the available data, and therefore more accurate than a visual estimate based on a single frame (Long and Nipper 1996). Based on this data we can assert that there is no important association between UI and waves on the body, but that backward swimmers have roughly one quarter fewer waves on the body than forward swimmers, since the mean for the forward trials is 1.46 with standard deviation $s_{\text{forward}} = 0.15$, while the backward trial mean is 1.20 with $s_{\text{backward}} = 0.21$. Lamprey use smaller wavelengths proportional to body size for forward swimming, as compared to backward swimming with $P = 0.0003$, $t = 3.98$, $df = 22.02$.

Linear regression of the phases of the fundamental frequency in the lateral dimension is another means to estimate the number of waves on the body; it also permits identification of acceleration of the traveling wave. The quotient $2\pi/m$ is the best estimate for the wavelength λ, assuming a traveling wave of the form $A(x)\cos(\omega t - 2\pi\, x/\lambda - \varphi)$ describes the overall motion. Here, x is distance from the rostral tip, and the other quantities are as described in Sect. 2.6. The results for five of the six trials shown in Fig. 3 are shown in Fig. 10. The wavelength is substantially constant along the length of the lamprey in all these trials. Beyond this, the plot shows a pattern in those small deviations from constancy: near the leading edge, phase is consistently underestimated by the regression line, indicating a longer wavelength in this region. Downstream there is a portion of the body, between roughly 1/6, and 1/3 fish-length from the leading edge, where phase changes are greater than predicted by the regression line, indicating a region where the wavelength is shorter. Thereafter, phase changes in the forward trials settle close to the line. In the backward trials, deviations are more pronounced, and the pattern on the more anterior portion of the fish is less clear. The steady trial seems more like the forward trials, while the two less steady trials show deviations in wavelength along the entire length of the fish.

3.3.4 The speed and amplitude of undulatory waves

In all forward swimming trials except the least steady, amplitude of the lateral wave of deflection is decreasing posteriorly at the rostral tip. While the point where minimum amplitude occurs varies from trial to trial, it is generally 10% of body length from the rostral tip. Posterior of this point, the amplitude increases roughly exponentially, but often with a stairstep appearance (Fig. 11). The three forward trials all show this profile, although the steadiest trial appears to have a change in the rate of exponential growth at a point 1/3 fish-length from the rostrum. At this point more rapid exponential growth seems to change to growth that is still exponential with a lower rate. The other two trials display stairsteps indicating a roughly constant rate of growth but with fluctuations along the length of the fish. Using the analysis of Cheng and Blickhan (1993), this suggests comparable fluctuations in the speed of the wave of curvature.

The amplitude profile of lateral deflection for backward swimmers is remarkably different. In all three trials (see Fig. 11), average amplitude is much larger, and amplitude is increasing at the leading edge, moving downstream. The amplitude reaches a peak just downstream of the leading edge and then drops to a minimum less than 1/3 fish-length from the leading edge. From there it rises to a second local maximum somewhere in the middle third, before falling to

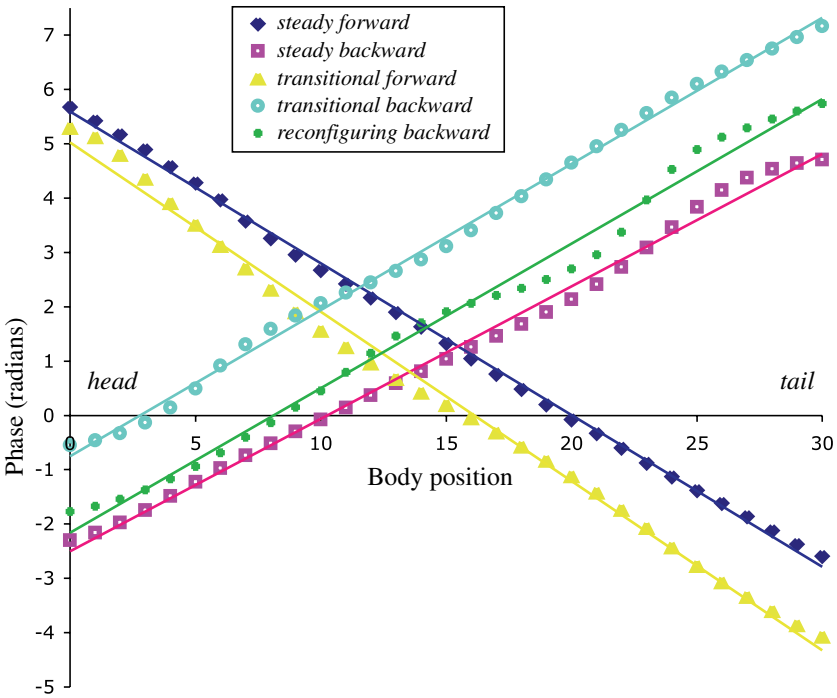

Fig. 10 Phase of the fundamental frequency in the lateral direction differs only in sign between forward and backward swimming. Data for five of the representative trials shown in Fig. 3. (The final forward trial is omitted for clarity.) In addition, the regression line in each case represents a fixed propulsive wavelength on the fish's body; each fit has a $R^2 > 0.99$

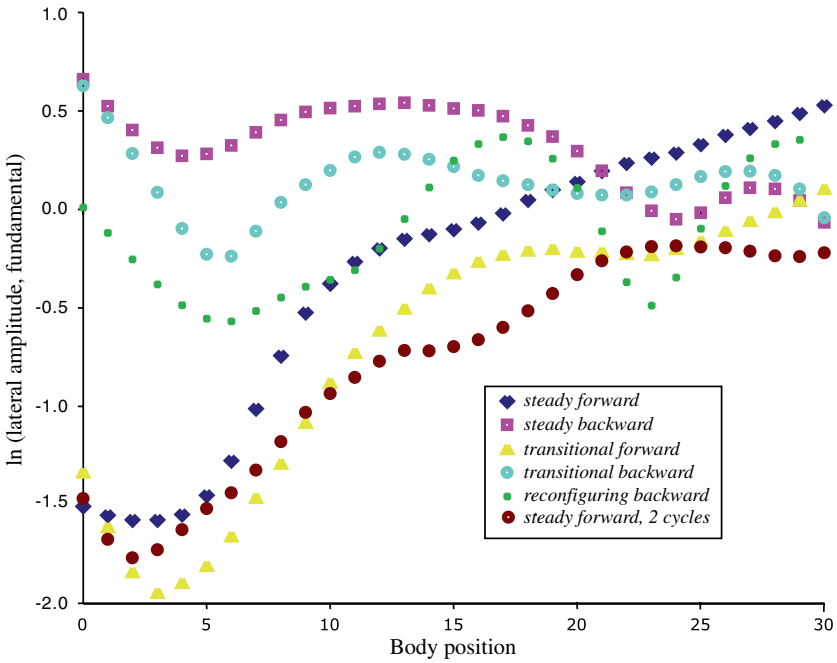

Fig. 11 Lateral amplitude profile of the fundamental frequency differs between forward and backward swimming. Data for the six representative trials shown in Fig. 3. Compare the increase in amplitude with body position for forward swimming with the relatively constant amplitudes for backward swimming

a local minimum 1/6 of a body length from the trailing edge. From that minimum, amplitude rises exponentially to the rostrum. Fluctuations near the leading edge are less pronounced in the two steadier backward trials, and the local minimum near the trailing edge is more marked in the two less steady trails. Despite these deviations, more remarkable are similarities shared by these trials, and their difference from forward swimming profiles.

3.4 Secular acceleration as a deviation from steadiness

Our technique allows us to identify secular acceleration in motion that superficially appears to be steady swimming. The utility of this technique is apparent in comparing the models of the two less steady forward trials (Fig. 8) with models incorporating a secular acceleration term (Eq. 8, see top row of Fig. 12). Inclusion of the acceleration term

offers remarkable improvement, especially for the less steady of the two trials. Perhaps more remarkable is the comparison of the fits incorporating acceleration with fits that add higher harmonics to the base model (see bottom row of Fig. 12). Despite using seven additional degrees of freedom at every body point, the higher harmonic models have lower R^2 values than the secular acceleration models, showing that secular acceleration is more important than higher harmonics in describing the motion observed in these trials.

4 Discussion

Here we present a method that analyzes, via a mathematical decomposition, whole-body kinematics of an important category of fish swimming behaviors—single propulsive cycles of translation with superimposed elements of harmonic and secular motion. After determination of the body's propulsive cycle and frequency, this method uses harmonic analysis and statistics to identify and characterize different behaviors. For example, forward and backward swimming motions in lamprey are similar in terms of the pattern of phase lag of the fundamental harmonic, but they differ in their unsteadiness. This method also makes possible analysis of kinematic changes in behavior of a single individual, a capability that, while not used in this study, should interest researchers needing detailed kinematic inputs to open-loop models or accurate tests of validation of outputs of closed-loop models.

Using this method, we found three important general conclusions about swimming lamprey: (1) they can superimpose periodic and secular components of body motion, (2) they can modulate the relative magnitudes and axial patterns of the superimposed periodic and secular components, and (3) they can change shape. We are left with a novel hypothesis—the seemingly simple act of steady swimming is a maneuver requiring active minimization of secular motion and body reconfiguration.

4.1 The whole-body kinematics of forward and backward swimming

Prior to our analysis, we had two different expectations: (1) that backward swimming in lamprey was simply forward swimming with reversed direction of body flexure propagation (Grillner 1996) and (2) that backward swimming in lamprey, based on that in eel, would involve much larger lateral displacements over more of the body than forward swimming (D'Aout and Aerts 1999). We found support for both. Even though lateral amplitudes of the fundamental frequency fits the pattern seen in eels (Fig. 11), the phase lag pattern of the lateral amplitudes of the fundamental frequency for backward swimming is equal and opposite to that of forward swimming (Fig. 10). Surprisingly, both amplitude and phase lag results for forward or backward swimming are independent of unsteadiness. In other words, the kinematic behavior of the fundamental harmonic motion of the body—arguably the basis of steady locomotion—can be analyzed and compared independently from secular components of motion, velocity and acceleration. This also suggests that neural mechanisms controlling steady locomotion can have superimposed upon them other neural mechanisms that control secular motions, including body reconfiguration. While local central pattern generators control, with feedback from stretch receptors (Sigvardt 1989), the steady kinematics, work on startle responses (Ritter et al. 2001) suggests a parallel and superimposable neural system mediated by the reticulospinal network.

Further, compared to forward swimming, backward swimming has fundamentally different kinematics: it is more reconfigurative, i.e., less steady. Backward swimming frequently also includes larger deviations in wavelength along the fish, although this is not present in the steadiest trials. This follows from a different physiology of motion: in backward swimming, points along the fish tend to follow the trajectory of points nearer the leading edge. Some of the differences between forward and backward swimming are likely to be caused by lamprey's head-retraction startle response and its associated body reconfiguration (Currie and Carlsen 1985, 1987). The startle mechanism may explain correlation between rapid cycle frequencies and high UIs in backward swimming of juvenille lampreys. Under the conditions examined here, we also see that behavioral flexibility varies with swimming direction. Forward swimming occurs over a greater range of swimming speeds and cycle frequencies than backward swimming.

4.2 Unsteady swimming and changing body shape

According to our definition, steady swimming contains unsteady elements and unsteady swimming contains steady elements. When we incorporate secular acceleration to model body kinematics, forward motion trials show rapid, small reconfigurations achieved by independent acceleration of different segments along the length of the body in the course of one or two cycle periods. In contrast, reconfiguration in backward trials, while also present, tends to be slower and steadier, and can be modeled with secular velocity alone. The ability to accurately model backward reconfigurations without secular acceleration indicates that they are achieved by steady differences in velocity of segments of the fish. The two conclusions are unexpected: (1) lamprey change shape, they reconfigure, as the swim

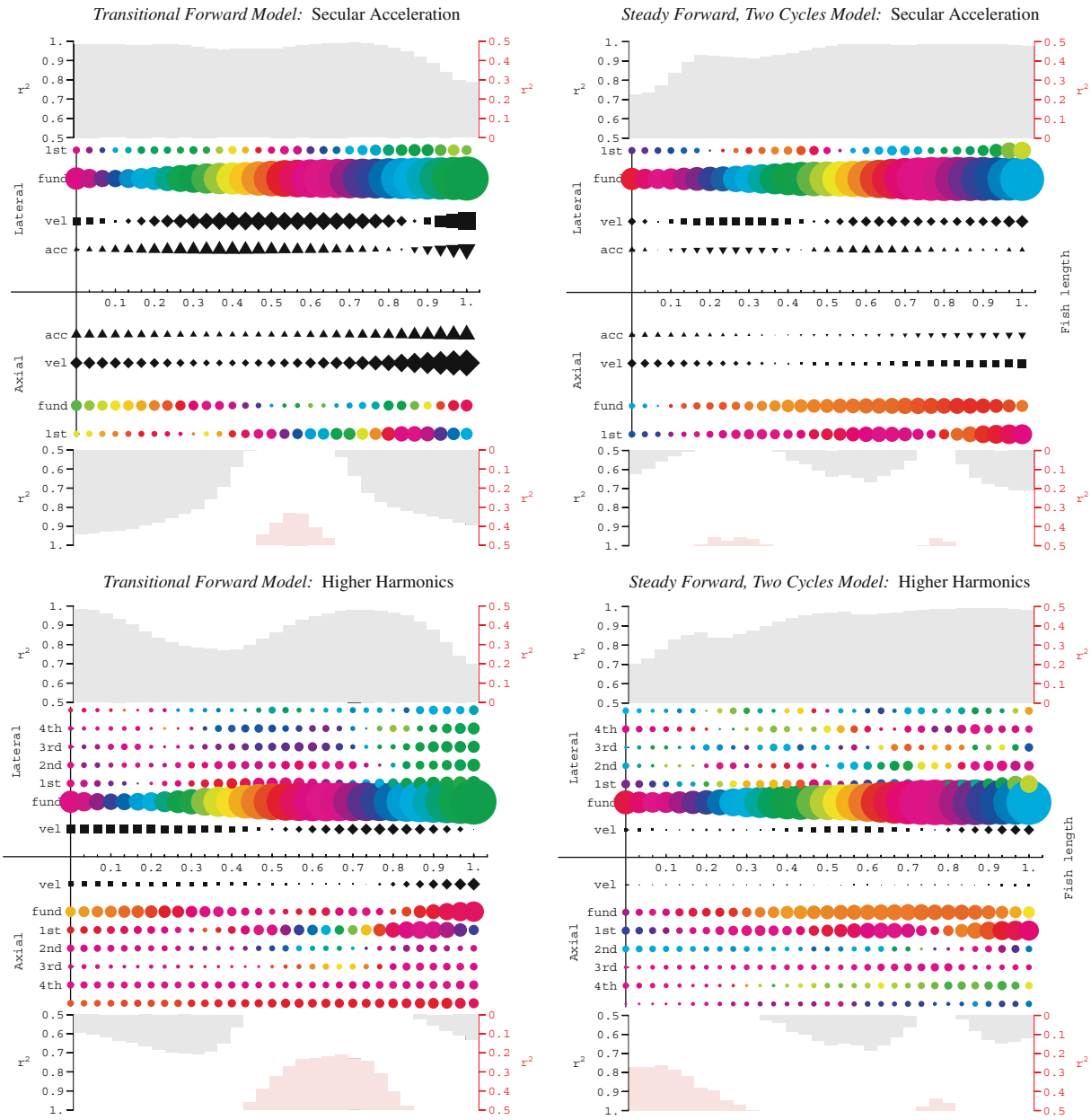

Fig. 12 Models with secular acceleration give a superior fit compared to those with just higher harmonics and no secular acceleration. Two examples are given (from Fig. 2): the transitional forward swimming and the steady two cycle forward swimming trial. Secular acceleration is included in models of the *top row* and is indicated by *triangles*. In spite of the much larger number of parameters included in the models with higher harmonics (seven more at each body point; see *bottom row*), in both cases models with secular acceleration give better fits for both axial and lateral dimensions. See Sect. 2.7 for a more detailed description, and Sect. 3.4 for a more detailed interpretation of these plots

and (2) they change shape in different ways depending on the direction of swimming.

While we have not analyzed steady swimming within the experimental paradigm of flume studies, our analysis shows that motion classified as steady in a still-water tank shows considerable variation, typically more than the 5% threshold set by Jayne and Lauder (1995). REs for the four trials with the smallest UIs all display variation greater than 5%, and for two of them, including the trial with the best UI in the dataset, the rostral tip displays errors greater than 5%. However, only the trial with the worst UI of the four has REs larger than 10%, and only near the caudal tip. Note that these REs include two dimensions, while Jayne and Lauder considered only the axial dimension.

4.3 Growth of displacement amplitude and wavespeed of curvature

Many authors have noticed that undulatory locomotion must display accelerating waves of curvature (e.g., Hess and Videler 1984; Katz and Shadwick 1998). An equivalent expression to a constant velocity wave of curvature is that the amplitude of deflection increases exponentially along the body (Cheng and Blickhan 1993). Thus a simple way to test for accelerating curvature is via amplitudes of fundamental frequency contributions to lateral motion. If logarithms of these amplitudes are concave up, indicating that the growth in amplitude is super-exponential, then the wave of curvature is accelerating. Conversely, concave down logarithms indicate decelerating curvature. Using this criterion, none of the 34 trials showed consistently accelerating waves of curvature. Instead amplitudes seem to fluctuate from concave up to concave down, indicating that curvature is changing velocity as it propagates.

4.4 Extension of the technique

The analytical technique we apply to swimming lamprey can be extended to other maneuvers. Only Eq. 1, which insists on only periodic acceleration which averages to zero, constrains the model to steady swimming. By incorporating secular acceleration constant across the extent of the fish, the model can analyze (1) linear accelerations like that associated with S-type fast starts and (2) rotational accelerations involved in turns. Moreover, if we allow secular acceleration to vary along the fish, the model applies to more intricate maneuvers, like C-type fast starts. These extensions require careful limitations on secular terms in order to maintain the model's simple form.

Acknowledgments The authors gratefully acknowledge grant support from the US Office of Naval Research, #N00014097-1-0292 and from the US National Science Foundation, #DBI-0442269 and #BCS-0320764. We thank Eamon Twohig for his work on the harmonic analysis.

References

Arena P, Fortuna L, Frasca M, Vagliasindi G (2006) A wave-based cnn generator for the control and actuation of a lamprey-like robot. Int J Bifurcat Chaos 16(1):39–46

Bierman HS, Schriefer JE, Zottoli SJ, Hale ME (2004) The effects of head and tail stimulation on the withdrawal startle response of the rope fish (*Erpetoichthys calabaricus*). J Exp Biol 207(22):3985–3997

Blickhan R, Cheng JY (1994) Energy storage by elastic mechanisms in the tail of large swimmers a re-evaluation. J Exp Biol 168:315–321

Bowtell G, Williams TL (1993) Anguilliform body dynamics: a continuous model for the interaction between muscle activation and body curvature. J Math Biol 32:83–92

Brockwell PJ, Davis RA (1996) Introduction to time series and forecasting. Springer texts in statistics. Springer, New York

Carling JC, Williams TL, Bowtell G (1998) Self-propelled anguilliform swimming: simultaneous solution of the two-dimensional navier-stokes equations and newton's laws of motion. J Exp Biol 201(23):3143–3166

Castro-Santos T (2005) Optimal swim speeds for traversing velocity barriers: an analysis of volitional high-speed swimming behavior of migratory fishes. J Exp Biol 208:421–432

Chatfield C (2004) The analysis of time series: an introduction, 6th edn. In: Texts in statistical science. Chapman & Hall/CRC, Boca Raton

Cheng JY, Blickhan R (1993) Bending moment distribution along swimming fish. J Theor Biol 168:337–348

Cheng JY, Pedley T, Altringham J (1998) A continuous dynamic beam model for swimming fish. Phil Trans R Soc Lond B 353:1–17

Crespi A, Ijspeert AJ (2006) Amphibot ii: an amphibious snake robot that crawls and swims using a central pattern generator. In: Proceedings of the 9th international conference on climbing and walking robots (CLAWAR 2006), pp 19–27

Currie SN, Carlsen RC (1985) A rapid startle response in larval lamprey. Brain Res 358:367–371

Currie SN, Carlsen RC (1987) Functional significance and neural basis of larval lamprey startle behavior. J Exp Biol 133:121–135

Dabiri JO (2005) On the estimation of swimming and flying forces from wake measurements. J Exp Biol 207(7):3519

Daniel TL, Coombes SA (2002) Flexible wings and fins: bending by inertial or fluid-dynamic forces? Integr Comp Biol 42:1044–1049

Daniel TL, Tu MS (1999) Animal movement, mechanical tuning and coupled systems. J Exp Biol 202:3415–3412

D'Aout K, Aerts P (1999) A kinematic comparison of forward and backward swimming in the eel *Anguilla anguilla*. J Exp Biol 202(11):1511

Ekeberg O (1993) A combined neuronal and mechanical model of fish swimming. Biol Cybern 1993:363–374

Grillner S (1996) Neural networks for vertebrate locomotion. Sci Am 274(1):64–69

Grillner S, Deliagina T, Ekeberg O, El Manira A, HIll RH, Lansner A, Orlovsky GN, Wallen P (1995) Neural networks that co-ordinate locomotion and body orientation in lamprey. Trends Neurosci 18(6):270–279

Guan L, Kiemel T, Cohen A (2001) mpact of movement and movement-related feedback on the lamprey central pattern generator for locomotion. J Exp Biol 204:2361–2370

Hess F, Videler J (1984) Fast continuous swimming of saithe (*Pollachius virens*): a dynamic analysis of bending moments and muscle power. J Exp Biol 109:229–251

Ijspeert AJ (2001) A connectionist central pattern generator for the aquatic and terrestrical gaits of a simulated salamander. Biol Cybern 85(5):331–348

Ijspeert AJ, Kodjabachian J (1999) Evolution and development of a central pattern generator for the swimming of a lamprey. Artif Life 5(3):247–269

Ijspeert AJ, Hallam J, Willshaw D (1999) Evolving swimming controllers for a simulated lamprey with inspiration from neurobiology. Adapt Behav 7(2):151–172

Islam SS, Zelenin PV, Orlovsky GN, Grillner S, Deliagina TG (2006) Pattern of motor coordination underlying backward swimming in the lamprey. J Neurophysiol 96(1):451–460

Jayne B, Lauder G (1993) Red and white muscle activity and kinematics of the escape response of the bluegill sunfish during swimming. J Comp Physiol A 173:495–508

Jayne B, Lauder G (1995) Speed effects on midline kinematics during steady undulatory swimming of largemouth bass, *Micropterus salmoides*. J Exp Biol 198:585–602

Katz SL, Shadwick RE (1998) Curvature of swimming fish midlines as an index of muscle strain suggests swimming muscle produces net positive work. J Theor Biol 193:243–256

Lachat D, Crespi A, Ijspeert AJ (2006) Boxybot: a swimming and crawling fish robot controlled by a central pattern generator. In: Proceedings of the first IEEE / RAS-EMBS international conference on biomedical robotics and biomechatronics (BioRob 2006)

Lighthill M (1975) Mathematical Biofluiddynamics. Res. Conf. Nat. Sci. Found., 1973, Soc. Ind. Appl. Math. (SIAM), New York

Liu H, Wassersug R, Kawachi K (1996) A computational fluid dynamics study of tadpole swimming. J Exp Biol 199:1245–1260

Long JH Jr (1995) Morphology, mechanics, and locomotion: the relation between the notochord and swimming motions in sturgeon. Environ Biol Fish 44:199–211

Long JH Jr, Nipper KS (1996) The importance of body stiffness in undulatory propulsion. Am Zool 36(6):678–693

Long JH Jr, Root RG, Watts P (2002) Is an undulating fish an oscillating wing? Integr Comp Biol 42(6):1268A

Müller UK, van Leeuwen JL (2004) Swimming of larval zebrafish: ontogeny of body waves and implications for locomotory development. J Exp Biol 207:853–868

Or H, Hallam J, Willshaw D, Ijspeert AJ (2002) Evolution of efficient swimming controllers for a simulated lamprey. In: From animals to animats: Proceedings of the 7th international conference on the simulation of adaptive behavior (SAB2002)

Ritter DA, Bhatt DH, Fetcho JR (2001) In vivo imaging of zebrafish reveals differences in the spinal networks for escape and swimming movements. J Neurosci 21(22):8956–8965

Sigvardt KA (1989) Spinal mechanisms in the control of lamprey swimming. Am Zoo 29:19–35

Taylor GK, Nudds RL, Thomas ALR (2003) Flying and swimming animals cruise at a Strouhal number tuned for high power efficiency. Nature 425:707–711

Tolstov GP (1962) Fourier series. Prentice-Hall, Englewood Cliffs (trans. by Richard A. Silverman)

Triantafyllou GS, Triantafyllou MS, Grosenbaugh MA (1993) Optimal thrust development in oscillating foils with application to fish propulsion. J Fluid Struct 7:205–224

Tytell ED (2004a) The hydrodynamics of eel swimming. ii. Effect of swimming speed. J Exp Biol 207:3265–3279

Tytell ED (2004b) Kinematics and hydrodynamics of linear acceleration in eels, *Anguilla rostrata*. Proc Roy Soc B 271:2535–2541

Ward AB, Azizi E (2001) Hydrodynamics and energetics of fish propulsion. Am Zoo 41:1620A

Webb PW (1975) Hydrodynamics and energetics of fish propulsion. Bull Fish Res Bd Can 190:1–158

Webb PW (1986) Kinematics of lake sturgeon, *Acipenser fulvescens*, at cruising speeds. Can J Zool 64:2137–2141

Weihs D, Webb PW (1983) Optimization of locomotion. In: Webb PW, Weihs D (eds) Fish biomechanics. Praeger, New York, pp 339–371

Williams TL, Bowtell G, Curtin NA (1998) Predicting force generation by lamprey muscle during applied sinusoidal movement using a simple dynamic model. J Exp Biol 201:869–875

Wu T (1977) Introduction to the scaling of aquatic animal locomotion. In: Scale effects in animal locomotion. Academic Press, New York, pp 203–232

Vortex dynamics in the wake of a mechanical fish

Christoph Brücker · Horst Bleckmann

Abstract This study focuses on the three-dimensional flow around a mechanical fish model, which reproduces the typical undulatory body and fin motion of a carangiform swimmer. The mechanical model consists of a flexible skeleton embedded in a soft transparent silicone body, which is connected with two cams to a flapping and bending hinge generating a traveling wave motion with increasing amplitude from anterior to posterior, extending to a combined heaving and pitching motion at the fin. The model is submerged in a water tank and towed at the characteristic swimming speed for the neutral swimming mode at $U/V = 1$. The method of Scanning Particle Image Velocimetry was used to analyze the three-dimensional time-dependent flow field in the axial and saggital planes. The results confirm the earlier observations that the wake develops into a chain of vortex rings which travel sidewards perpendicular to the swimming direction. However, instead of one single vortex shed at each tail beat half-cycle we observed a pair of two vortex rings being shed. Each pair consists of a larger main vortex ring corresponding to the tail beat start–stop vortex, while the second vortex ring is due to the body bending motion. The existence of the second vortex reflects the role of the body in undulatory swimming. A simplified model of the fish body comparing it to a plate with a hinged flap demonstrates the link between the sequence of kinematics and vortex shedding.

C. Brücker (✉)
Lehrstuhl für Strömungslehre und Strömungsmaschinen,
TU Bergakademie Freiberg, Lampadiusstrasse 4,
09599 Freiberg, Germany
e-mail: bruecker@imfd.tu-freiberg.de

H. Bleckmann
Zoologisches Institut Bonn, Poppelsdorfer Schloss,
53115 Bonn, Germany

1 Introduction

The propulsion of fish due to their undulatory body and fin motion is of continuous scientific interest as well as of increasing importance for unmanned underwater vehicles in developing new strategies for silent and efficient locomotion (Triantafyllou et al. 2000). This requires a detailed analysis of the unsteady flow around fish at different patterns of undulations and body kinematics. The study herein focuses on the carangiform type of fish swimming with the body as well as the fin motion contributing to the thrust generation. A detailed discussion of earlier flow studies is given in the reviews by Schultz and Webb (2002), Barett et al. (1999), Davis et al. (2000) and Liao et al. (2003). Experimental flow field measurements on live fish using modern techniques such as Particle Image Velocimetry (PIV) were presented by Stamhius and Videler (1995), Müller et al. (1997), Wolfgang et al. (1999), Videler et al. (1999), Hanke et al. (2000), Lauder et al. (2003) and Sakakibara et al. (2004). Müller et al. (1997) analyzed the wake behind a continuously swimming mullet. They concluded that the wake consists of a three-dimensional chain of vortex rings as already pointed out by Blickhan (1992). The shape of the wake and the orientation of the vortex rings depend on the ratio of the backward speed of the body wave V to the swimming speed of the fish U. Undulatory swimmers are known to generate a range of U/V ratios from 0.8–1.3 (Videler 1993). The flow structure generated by the different kinematic patterns of the tail beat of the fish confirmed the importance of the U/V

G.K. Taylor, M.S. Triantafyllou, and C. Tropea (Eds.): Animal Locomotion, pp. 161–172.
springerlink.com

ratio, as already discussed by Hertel (1966). At a *U/V* ratio above unity, the classical von Kármán vortex street is observed with a staggered row of discrete vortices of alternating sign and an axial draft flow in the wake center, which is directed in the swimming direction. At a *U/V* ratio below unity the so-called "reverse" von Kármán vortex street is formed in which the vortices rotate in opposite direction and backward momentum is added to the water.

For carangiform swimmers the undulations of the body generate additional regions of concentrated vorticity. Videler et al. (1999) observed semicircular flow patterns along the fish body that indicate a low pressure area on the concave side and a corresponding high pressure side on the convex side. They called those flow patterns along the body "proto-vortices", which travel downstream with the body wave until they reach the tail end and shed. Depending on the instant during a tail beat cycle when the proto-vortices reach the tail the wake possesses different shapes, see Müller et al. (2002a). The typical wake pattern in the axial plane consists of a single vortex pair per tail beat cycle, which they called type "A". For the uncommon type "B" wake they observed two vortex pairs being shed per tail beat cycle. They argued that each vortex pair consists of a tail vortex and a body vortex released during the tail stroke. The function of the wake with two vortex pairs per cycle is not clear yet. Videler et al. (1999) speculate that this type of wake indicates that the fish does not try to swim efficiently but uses this mode to obtain more dynamic stability.

In all PIV measurements with living fish a straight forward training of the fish is necessary to ensure that the fish swims in the desired direction. Furthermore, the position of the measuring plane is usually fixed and it hardly occurs that the fish is in a proper position within the light sheet and in an ideal orientation to the plane. In addition, the near-body flow is difficult to visualize because of shading effects and reduced contrast. Finally, it is important to have quiescent still water conditions before the fish enters the measuring area. Otherwise the recorded flow structures are disturbed by background noise or vortex structures, which have been generated before.

To overcome these difficulties the present wake studies were carried out with a mechanical fish model. The advantages are an exact repeatability of the experiments and no training of the fish. The use of the mechanical fish is considered the appropriate approach to ensure repeatability and an exact realization of experiments under different conditions. This study aims to analyze the three-dimensional structure of the flow around a swimming fish and to analyze the wake structure left by the specific kinematics of fish locomotion. A simplified mechanical model was chosen which reproduces the kinematics of living fish swimming in a carangiform mode. The fish body is a simplified geometry of a real fish since it does not have the dorsal fin, the anal fin and the paired pelvic and pectoral fins. However, our main interest is the wake in steady cruising mode in which the other fins are of less importance.

Towing tank experiments were carried out for swimming kinematics with $U/V = 1$ which is the ratio the body wave travels backwards at the same speed as the fish is traveling forward. Therefore the wake structures are not moving relative to the water in axial direction, which allows to observe the wake structures for longer time-periods within the stationary measuring window. First, the mechanical fish is described. Thereafter the experimental set-up is explained and the boundary conditions are specified. The results are discussed for horizontal and saggital cross-sections of the wake. Finally, conclusions are drawn based on the observed vortex dynamics.

2 Experimental set-up

2.1 The mechanical fish

The three dimensional surface coordinates of a goldfish were digitized and used to generate a negative mold of the body. The geometric data of the fish are shown in Fig. 1. The skeleton of the fish model is a thin transparent acrylic plate, which is held with two rods, one a short distance downstream of the nose, the other in the penduncle at the rear fin. The rear rod has a slit allowing the plate to slide within. The plate with the two rods is then positioned in the middle of a mould form and casted in soft transparent rubber, which composes the fish body (Fig. 2). Because of the soft flexible rubber, the body can be bend with a torque imposed at the rods.

2.2 Reproduction of undulatory wave motion

Body and caudal fin swimming uses the body to undulate waves towards the caudal fin (tail), thus propelling the fish.

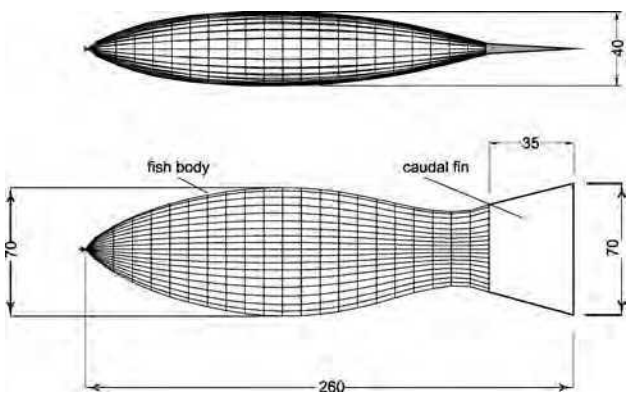

Fig. 1 Dimensions of the mechanical fish in millimeters. *Upper graph* top view. *Lower graph* side view

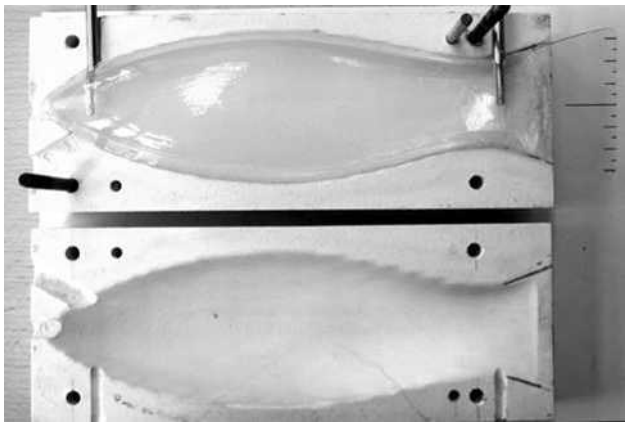

Fig. 2 The two halves of the mold used for the production of the silicon model of the fish. The model is still in the upper mold

A mechanical system was built according to Nachtigall (1998), which generates a traveling wave motion resulting in a typical undulatory body and tail motion (see Fig. 3). The two rods at the fish model are connected to a gear, the front one at the nose being free to rotate and the rear rod being fixed at a flapping hinge. In addition to the flapping motion of the rear rod a lever mechanism twists the rod around its own axis in an oscillatory manner. This imposes a time-varying torque at the rear and therefore a time-varying bending of the fish midline in addition to the flapping motion of the body. This effectively results in a combined heaving and pitching motion of the fin. The gear is adjusted such that the oscillatory heaving and pitching motion have a phase shift of 90°. The mechanical deformation of the fish body by the two rods is equivalent to a spline fixed at two positions and subjected to a torque at the rear one, thus it is mathematically described by a quadratic polynomial function with time-varying trigonometric factors:

$$x(z) = \left(\frac{2\,l\sin\alpha}{z_1} - \tan\gamma\right) \cdot z + \left(\frac{\tan\gamma}{z_1} - \frac{l\sin\alpha}{z_1^2}\right) \cdot z^2 \tag{1}$$

The angle α determines the flapping motion and the angle β the bending motion, which are defined as follows:

$$\alpha(t) = \alpha_{\max} \sin\left(\frac{2\pi t}{T_{\text{cyc}}}\right) \tag{2}$$

$$\beta(t) = \beta_{\max} \cos\left(\frac{2\pi t}{T_{\text{cyc}}}\right) \tag{3}$$

$$\gamma(t) = \alpha(t) + \beta(t) \tag{4}$$

For explanation of the variables see Fig. 3. The created motion pattern depends on the choice of the maximum

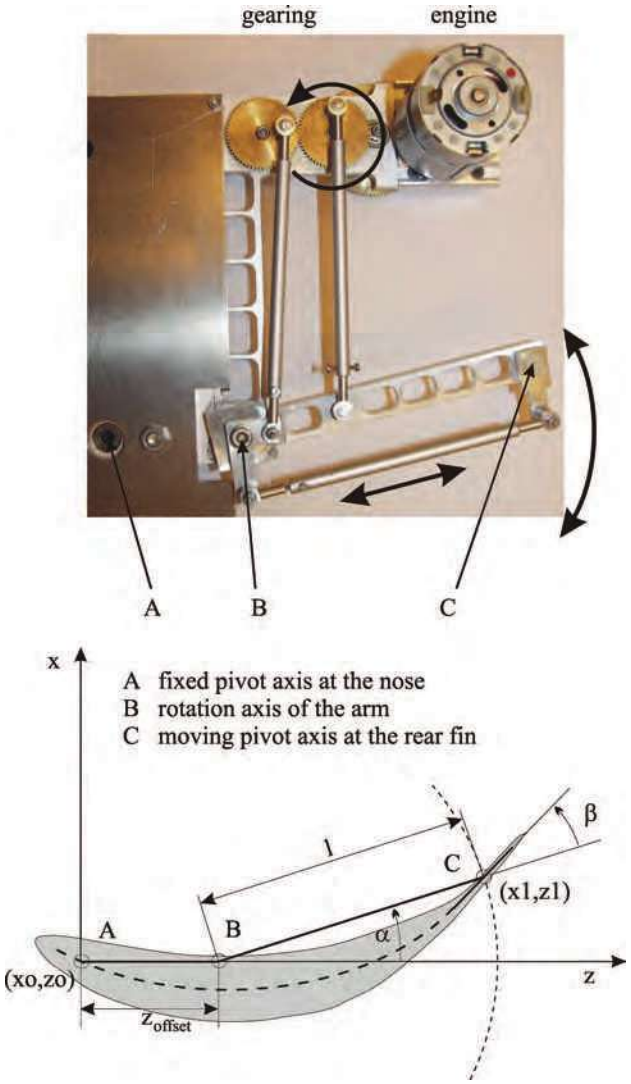

Fig. 3 Fish mechanics, developed after Nachtigall (1998); the engine activates the two gears, thereby the arm $(\overline{BC})$ completes a flapping motion ($-9° < \alpha < +9°$) with a simultaneous rotation of the lever around the pivot axis C ($-30° < \beta < +30°$), thus leading to a bending torque at the fin; the angles α and β have a phase shift of 90°; the skeleton can be approximated by a quadratic spline profile. An illustrative sequence of the generated fish motion is given in Fig. 5

flapping angle $\alpha_{\max}$ and bending angle $\beta_{\max}$: at $\alpha_{\max} = 0$ the fish model simply performs a flexing body deformation. In contrast, with $\beta_{\max} = 0$ the fish is straight and is flapping as a whole around the nose at $z = 0$. A combination of both with a phase shift of 90° of the bending deformation to the body flapping motion leads to a traveling wave motion. With a defined set of gear parameters, a typical fish-like undulatory wave can be generated, which runs as a traveling wave from head to tail with a near constant phase speed and increasing amplitude from nose to fin. Such a motion for the mechanical fish model with a length of $L = 240$ mm is obtained for values of $\alpha_{\max} = 9°$, $\beta_{\max} = 30°$, $z_{\text{offset}} = 55$ mm and

l = 125 mm. This results in a total lateral excursion of the fin of A = 80 mm and a wave length of $\bar{\lambda} = 360$ mm. Note that the wave length is longer than the fish length as typical for carangiform or subcarangiform swimmers. Figure 4 (upper graph) illustrates this type of movement in a coordinate system, which is fixed with the fish. The successive stages of the fish skeleton during the downstroke can be followed in time with the letters in alphabetic order from "a" to "i" (solid lines) and in the following upstroke in reverse order (dashed lines). The lower graph in Fig. 4 illustrates the traveling wave character during the downstroke by following the positions of the zero-crossing from the letter "a" to "e" in alphabetic order. The amplitude distribution is similar to that of a rainbow trout, where the undulations of the side to side movement in the body slightly increase from the anterior but with a significant increase in the rear half to third of the body. In addition, the snout of the fish does not travel in a straight line but tends to oscillate at small amplitudes along the mean path of the fish, see Hoar and Randall (1978).

Figure 5 shows a series of original photographs of the mechanical fish and its skeleton over 12 successive stages of the driving mechanics. The skeleton within the transparent body is seen as a bright reflection line which was visualized with a laser sheet. The lines correspond well with the theoretically derived splines in Fig. 4 proving the mechanics that reproduces the desired motion. The shadows in the background illustrate the positions of the lever and the hinge at the different stages of the cycle. With a tail beat frequency of f = 0.6 Hz the traveling wave speed results to $V \approx 0.2$ m/s ($\bar{V} = \bar{\lambda} f$; $f = 0.6$ Hz; $\bar{\lambda} = 360$ mm), which equals the towing speed U under the conditions of a U/V ratio of unity. The resulting Strouhal number is defined by the width of the wake approximated by the total lateral extension of the fin A and the swimming speed U:

$$\mathrm{St} = \frac{fA}{U} \tag{5}$$

Thus, the Strouhal number for the mechanical fish with A = 0.08 m and U = 0.2 m/s is St = 0.24, which is a typical value for efficient swimming of fish (Nudds and Thomas 2003). The Reynolds-number defined with the body length L and the swimming speed U is Re = 48,000.

2.3 Experimental set-up and flow visualization

The experiments were conducted in a 2 m water basin with a towing tank system. This principle allows a long-term observation of the development of the wake with a fixed camera and illumination system. In a flow circuit with counter-flow, the wake would immediately be washed downstream and the vortex dynamics could not be observed for a longer time span. Figure 6 shows the experimental set-up. The whole mechanics of the fish and the gear drive is moved by the towing system with wheels on rails on top of the tank. The fish moves through the water tank from right to left with a constant speed of 0.2 m/s and a tail beat frequency of 0.6 Hz.

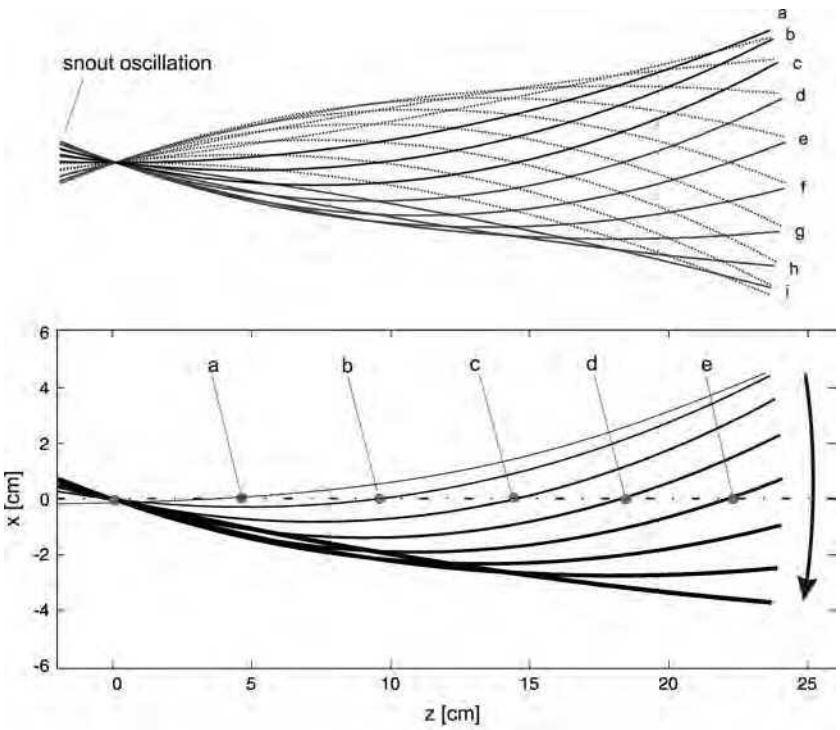

Fig. 4 *Upper graph* sequence of the fish skeleton profile in a complete up- and downstroke generated by the gear mechanics shown in Fig. 3 and calculated with Eq. (1). *Lower Graph* traveling wave character during a downstroke. In the *top* and *bottom* graph the time increases with the letters in alphabetical order

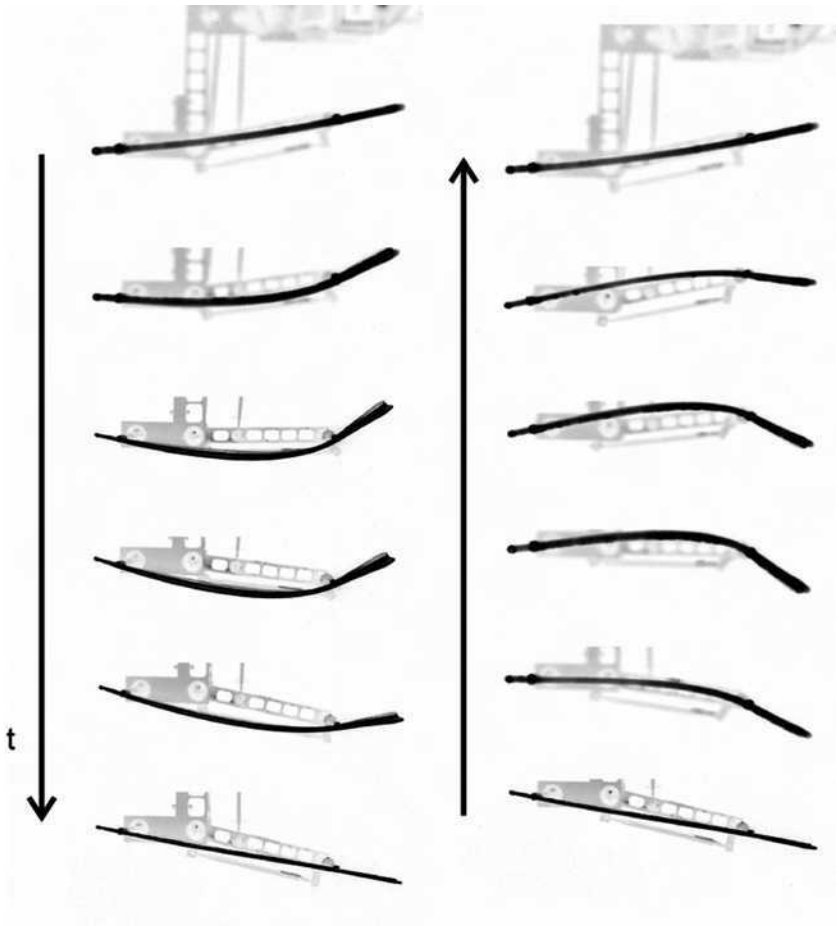

Fig. 5 Original photographs of the mechanical fish and its skeleton over 12 successive stages of a complete cycle with downstroke and upstroke. The skeleton within the transparent body is seen as a bright reflection line inverted to *black* colour which was visualized with a laser sheet. The lines correspond well with the theoretical derived spline profiles proving the mechanics reproduce the desired motion (compare Fig. 4). The *shadows* in the background illustrate the positions of the lever and the hinge at the different stages of the cycle. *Arrow t* = time

The working fluid was seeded with small fluorescent tracer particles (1.02 g/cm^3). An optical band-pass filter was placed in front of the lens to remove direct reflections of the laser light. Time-resolved digital PIV measurements were performed either in axial planes (camera position 2 in Fig. 6, *XZ*-plane) or in saggital planes (camera position 1 in Fig. 6, *XY*-plane) in the wake of the fish. For three-dimensional flow measurements the Scanning Particle-Image Velocimetry (Brücker 1995, 1997) was applied, i.e., a rotating drum scanner was used, which scanned a laser beam in successive parallel planes through the flow volume. The ten mirrors along the key slots of the scanning drum were arranged in a helical path and the drum rotated at a speed of 1,500 rpm. In total, ten laser sections were arranged within a scanning width of 45 mm with a spacing of 5 mm as shown in Fig. 7. The laser is a Coherent Innova 90C with a maximum power output of 8.5 W at a wave length of λ = 488 mm and a beam diameter of 2 mm. A digital high-speed video camera was used to record the flow at a maximum frame rate of f = 1,000 Hz with a spatial resolution of 512 × 512 pixel, synchronized with the drum scanner such that each frame corresponds to a single sweep of the laser beam and hence to a single illumination plane. The maximum number of frames within one recording period is limited to 1,000, which results from the digital memory of 256 MB in the camera control unit. Therefore, for long-term recordings of the vortex dynamics only one single plane was illuminated with reduced recording frequency, while for three-dimensional measurements we focused only on certain instances of the cycle at maximum frame rate.

In this way the flow field was recorded in single planes or scanned in up to ten parallel flow planes and the vector field was obtained by classical cross-correlation methods. A typical size of the evaluated area for the axial planes was 250 mm × 250 mm with 32 × 32 vector positions and a spacing of 7.8 mm corresponding to 16 pixel units. For the saggital planes the evaluated area was 180 mm × 180 mm with 32 × 32 vector positions and a spacing of 5.6 mm. The DPIV images were processed using the cross-correlation method with 50% overlap in an iterative procedure with the window-shifting technique and continuous window refinement. The size of the interrogation windows was reduced in three iteration steps (64, 48, 32), in which the determined vector field was used as a pre-allocator for the shift (in integer pixel units) of the second interrogation

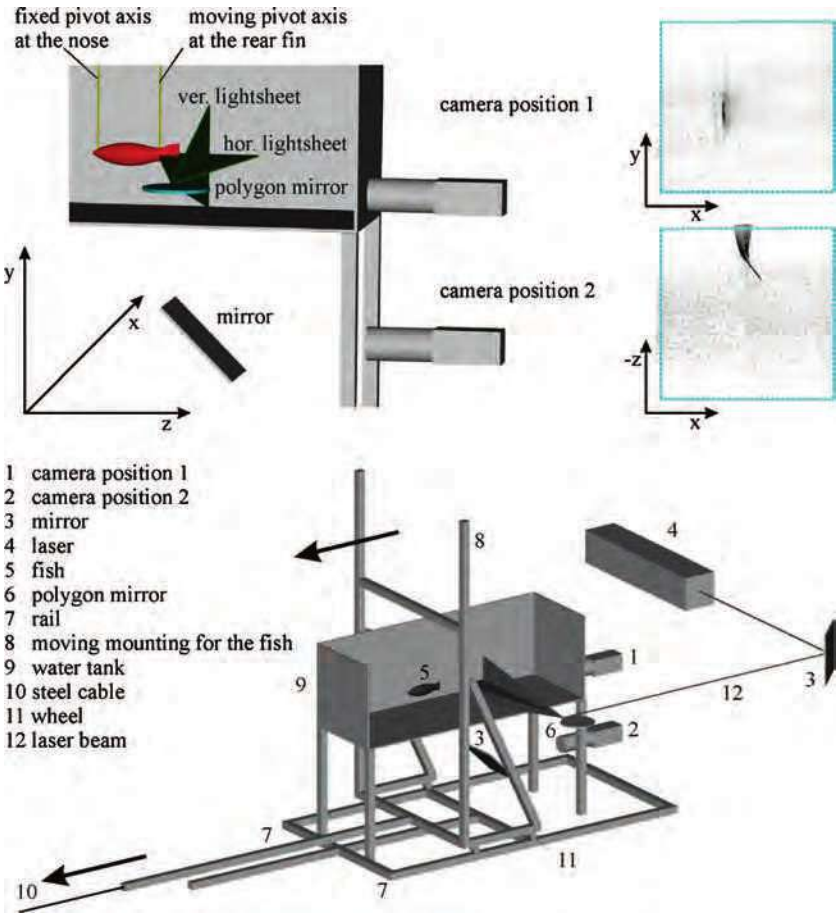

Fig. 6 Experimental set-up; the mechanical fish was towed through the water tank from right to left with a constant speed of 0.2 m/s. The tail beat frequency was 0.6 Hz. The fixed pivot axis at the nose of the fish and the moving pivot axis at the rear fin were moved by the fish mechanics. The fish mechanics is fixed at the cross-beam of the towing support. The light sheet was oriented in the horizontal (*XZ*) or vertical (*XY*) plane. Camera 1 recorded images from the vertical plane. Images of the light sheet orientated in the horizontal plane were recorded from below the tank using a front-surface mirror (Camera 2). The real images at the right-hand side outline the approximate image format analyzed using digital particle-image velocimetry

windows in the next iteration step. The correlation peak was determined with subpixel accuracy using a 2D Gaussian fit of the peak region in the correlation map. This procedure yielded a maximum subpixel error of the order of 0.1 pixel. The detectable displacement was in the range between the lower bound of 0.1 given by the subpixel error and 20 pixel, which is approximately 1/3 of the largest window size.

To prevent disturbances through small air bubbles in the water during the measurements, the water tank was filled up 2 days prior to the experiments. Approximately 5 g tracer particles were added to the water, which gave a sufficiently high particle concentration. The fish was positioned at the starting position on the right-hand side of the water tank (Fig. 6) and the fish mechanics was adjusted in the position where the skeleton of the fish is a straight line. At the beginning of the experiment the fish mechanics, the fish towing system, and the recording software were started simultaneously. At the end of the water tank the towing and the fish were stopped automatically. When the recording was finished, after approximately 7 s, the fish was positioned in the start position again. In order to have still water conditions and negligible fluctuations a waiting period of 5 min was

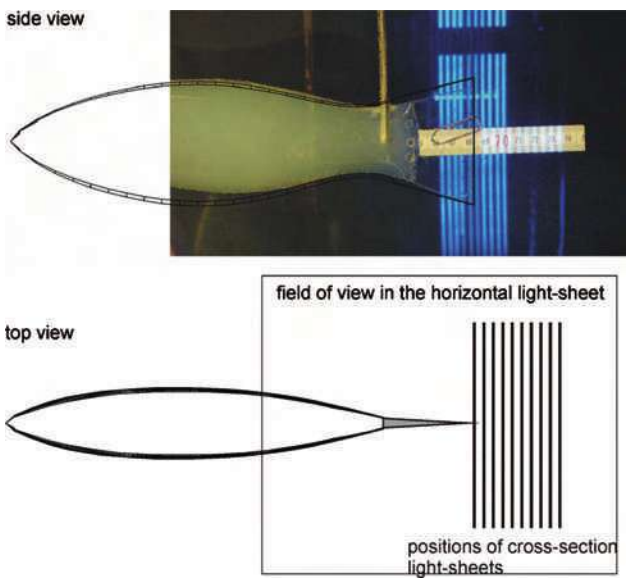

Fig. 7 Arrangement of the laser sheets in the wake of the fish illustrating the ten vertical cross-sections within a scanning distance of 45 mm and a spacing of 5 mm between the planes. The scanning process starts from the rightmost plane. The light reflections on the ruler at the fin of the fish illustrate the light-sheet positions in the plane of the fish. The reflections of the light-sheets at the back-wall of the tank are seen as *blue stripes* shifted relative to the ruler positions due to the camera perspective

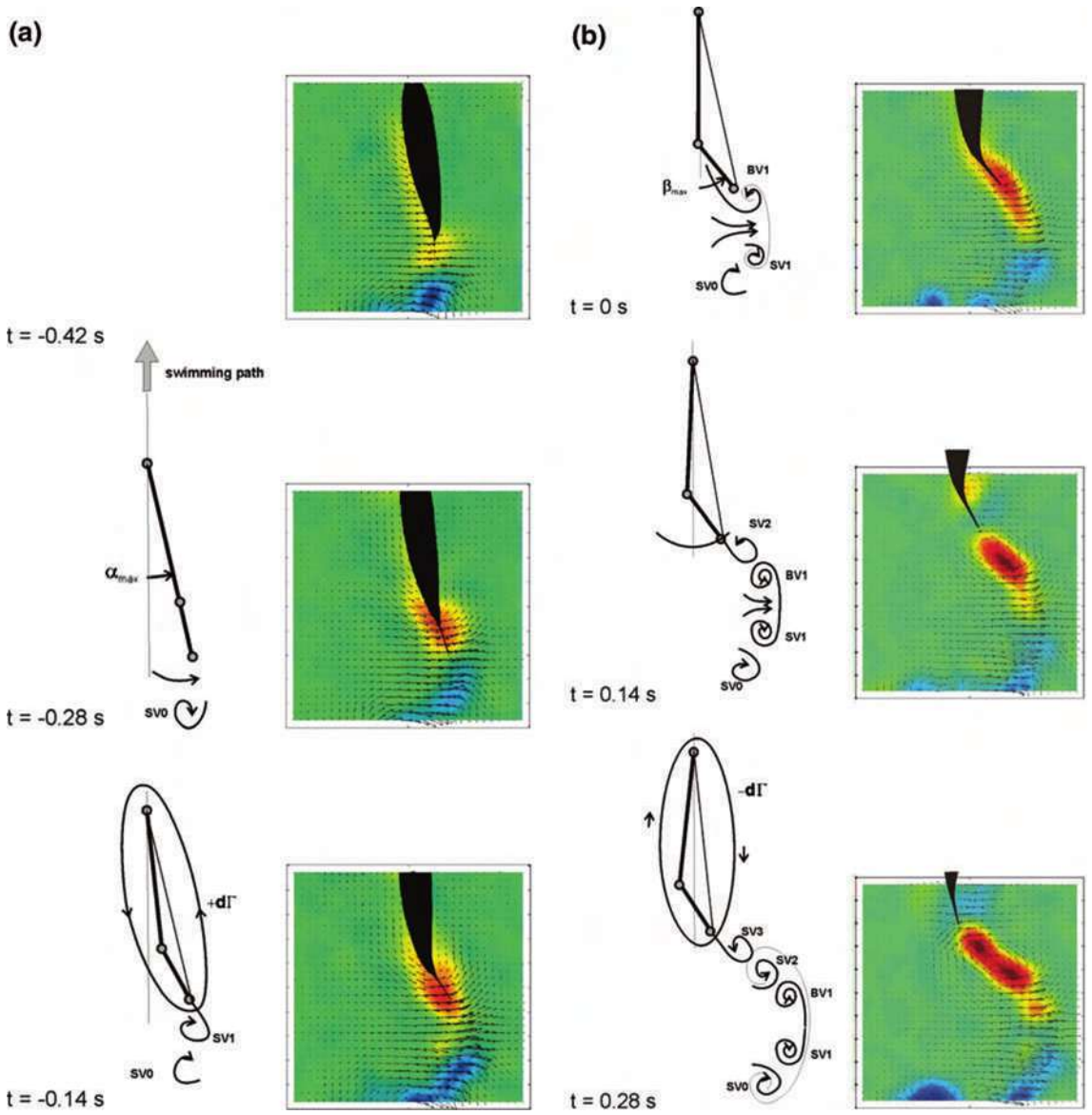

Fig. 8 Flow evolution in the wake of the fish in the horizontal midplane; (*left*) sequential steps of the fish motion explained with a simplified kinematic model and corresponding vortex dynamics; (*right*) vector plots($|v_{max}|$ = 3 cm/s) with color background indicating the value of the vorticity component normal to the horizontal plane. The moment t = 0 s is at the maximum amplitude of the caudal fin

required between the experiments. The experiments were carried out in a dark and calm environment.

3 Results

3.1 Flow evolution in the horizontal midplane (*XZ*-plane)

First, results are given for the measuring plane in the horizontal cross-section in Fig. 8. The flow velocity is represented by vectors (V_{max} = 3 cm/s) shaded by a color background indicating the value of the vorticity component normal to the plane (–6/s < ω < +6/s). The figure shows a comparison of a simplified mechanical vortex model on the left-hand side to the measured flow field on the right-hand side. To compare results from the axial and saggital light sheets to corresponding moments in the motion cycle we refer the time base t = 0 s to the moment of maximum amplitude of the caudal fin. This is the final phase of the previous stroke of the caudal fin and the initiation of the return stroke. At this moment the fish body is at the stage of maximum bending.

The bending process of the body generates a region of concentrated vorticity (positive, red) in the peduncle region between fish body and caudal fin (t = –0.42 s until

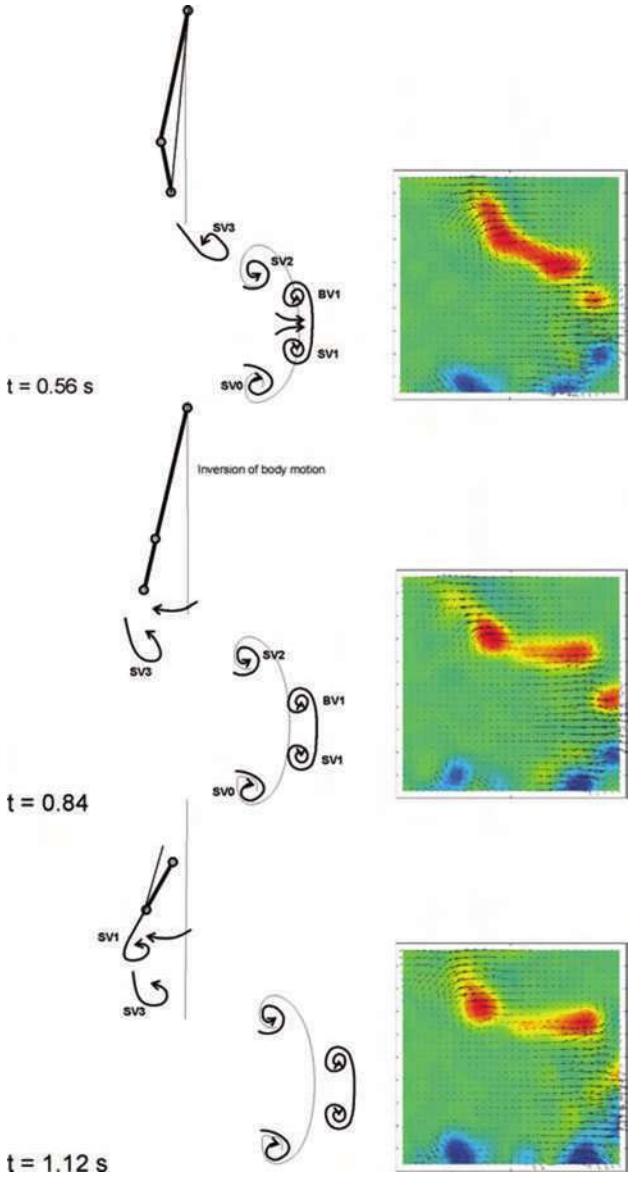

Fig. 8 continued

t = –0.14 s, Fig. 8). As a counterpart, the bending has left a starting vortex downstream, which is seen as a blue region of concentrated vorticity shed downstream of the tail fin at t = –0.42 s. A yellow colored region of vorticity extends along the left sideline of the fish body accompanied with downstream oriented velocity vectors. This flow originates from the lateral and axial fluid acceleration in the downstream direction during body pitching motion. It creates increased boundary layer vorticity on the convex side and a transversal flow around the body of the fish. In addition, it indicates an increased circulation around the body.

Note that although fluid acceleration in the backward direction is clearly present along the sidelines, there is no jet-like flow in the wake. The vorticity is swept along the sideline further downstream, feeds the peduncle region where it is redirected from the rotating tail fin and combines with the tail vorticity with the same sense of rotation. Through the stop of the tail fin motion at the end of the stroke, a stopping vortex is generated, which is of the same sense of rotation as the shed vorticity and therefore is not seen as a separate region in this early stage. At the moment t = 0 s the whole region of concentrated vorticity separates at the trailing edge of the caudal fin. Beginning from t = 0.14 s until t = 0.84 s, one can see that this region evolves into three single vortices, two of which drift in the direction of the previos stroke in positive x/L direction and one drifts with the tail fin in opposite direction. It is assumed that this vortex is the starting-vortex created during the acceleration of the caudal fin in the return stroke. The trace of this vortex can be followed over the complete period in the upper left quarter of the images. It has a blue counterpart in the lower left quarter, which seemingly is the stopping-vortex being generated in the deceleration phase of the previous stroke. Both vortices drift more or less parallel to each other to the left at similar lateral paths. The vorticity regions drifting to the right and left demonstrate a symmetrical arrangement to a transversal axis (perpendicular to the swimming direction). Parallel moving vorticity structures in the upper half of the pictures have counter-rotating counterparts in the lower half of the picture, at the mirror side of a virtual horizontal symmetry line in the middle. This strong symmetry indicates a connection of the corresponding red and blue regions as being cross sections of joint vortex rings.

The principle mechanism of the generation of the wake vortices and the typical S-form of the vortex street as observed over all experiments in the horizontal plane is displayed in the schematic sketch in Fig. 8 on the left hand side by means of a simplified mechanical model. We assumed that the fish skeleton is a 2-hinged body, the long part being the fish body representing the flapping motion and the short one the fin. This resembles a plain flap aerodynamic profile. The rear hinge position is at the peduncle region of the fish. As prescribed by the mathematically derived kinematic motion, the body and fin motion have a phase shift of 90°. Thus, when the body reaches the maximum angle of attack α_{max} relative to the swimming direction the flap has a deflection angle of β = 0 and the fish skeleton is a straight line. On the other hand, the strongest bending is at β_{max} when the body is aligned parallel to the swimming direction at α = 0 and the fin has the maximum angle β_{max} . This simplified model helps to illustrate the generation of the vortices in a stepwise evolution, which distinguishes the phase of bending and the phase of chord rotation.

The sequence starts with the body at its maximum angle of attack and the fish skeleton in straight line. The starting

vortex SV0 generated by the previous stroke is still visible. In the next step, the body starts to return back to the left while the trailing edge at the fin is still moving to the right. From an aerodynamic point of view, this increases the circulation around the flap profile and therefore requires the shed of an extra starting vortex SV1. As the tail fin motion stops and inverses, the bound vortex BV1 is shed together with a stop vortex SV2. Thereafter, in the return stroke to the left the acceleration of the tail fin generates a new start vortex SV3, which follows the fin and drifts to the left. The extra starting vortex SV1 is completed with the shed bound vortex BV1, therefore both belong to a single vortex ring. Since this vortex ring is a consequence of the bending work we call it the "bending vortex" in the following. On the other hand, the starting vortex SV0 is completed with the stop vortex SV2 and both build a large oval vortex ring. Because of the chronology of the vortex shedding, the bending vortex is nested within the larger oval start stop vortex ring. Both vortices drift in the same direction indicating the lateral momentum given to the fluid as reaction to the flapping and bending motion. The drift velocity of the vortex centers was estimated from the vector plots and is $U_d \approx 3$ cm/s which agrees with the determined drift velocity in the saggital plane that is discussed below. At later times these vortex rings interact with each other such that the smaller bending vortex is pushed further and wrapped around the main vortex ring.

3.2 Flow evolution in a single saggital plane (*XY*-plane)

The raw data in the vertical plane show a high degree of symmetry to the horizontal midplane with deviations less than 3% of the velocity data in the upper and lower half of the midplane. Because of the obvious symmetry of the results to the *XZ* plane the vector plots have been averaged on both sides. For long-term observation of the temporal vorticity evolution results are given only for a single plane. Note that the plane represents only one single cross-section in the vortex wake at a certain phase in the tail fin stroke cycle. The cross-section discussed herein represents parts of the main vortex ring.

Figure 9 shows the recorded images on the left-hand side in comparison to the flow field on the right-hand side. The caudal fin moves from the center position to the maximum left position while the trailing edge crosses the light sheet. The position of the caudal fin is indicated in the plots by the pivot axis and the edges of the fin. Again, the time base $t = 0$ s is the moment of maximum amplitude of the caudal fin. The stroke of the caudal fin to the right has generated a pair of counter-rotating vortices at the trailing edge. The region of concentrated vorticity in the cross-section of the vortex core at $t = -0.14$ s is elliptic and the main axis of the ellipse is tilted to the left and to the right for the counter-part of the pair, respectively. The average drift velocity of the vortex centers was estimated from the vector plots to be $U_d \approx 3$ cm/s equal to the value measured in the horizontal plane.

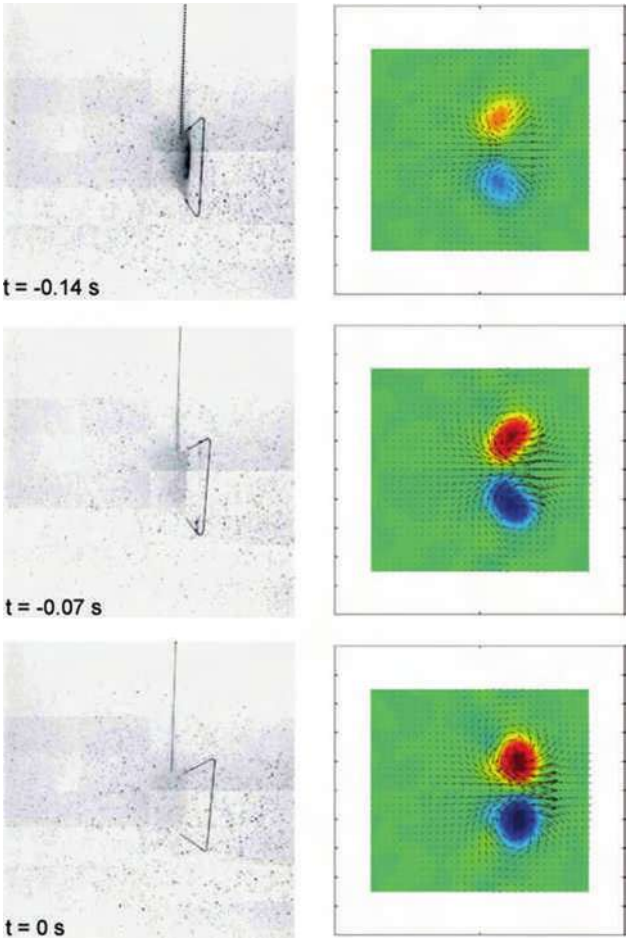

Fig. 9 Flow evolution in the wake of the fish in the saggital plane; (*left*) recorded images; (*right*) vector plots ($|v_{max}| = 3$ cm/s) with color background (from blue to red $-6 < w < +6$) indicating the value of the vorticity component normal to the saggital plane. The moment $t = 0$ s is defined to be the time of maximum amplitude of the caudal fin

3.3 3D flow structure in saggital cross-sections

Scanning PIV was applied in the wake of the caudal fin in ten vertical planes (see Fig. 7). The time between successive scans is $T_{Scan} = 0.02$ s, which is small in comparison to the characteristic time scale of the flow since the fish travels only a distance of 0.4 mm during this time interval. Therefore, the ten sections can be seen as being taken almost simultaneously. Figure 10 demonstrates the spatial structure of the streamwise vorticity in sections 1–10 at $t = 1.04$ s. Note that only the planes

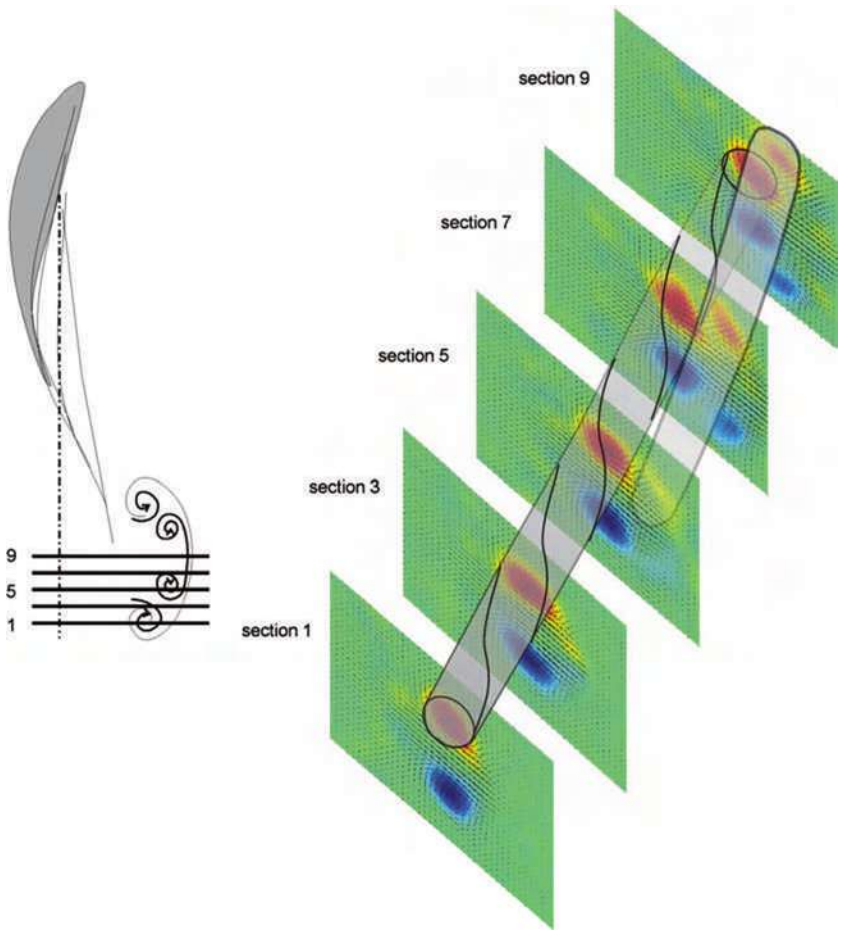

Fig. 10 Variation of the flow structure over a set of five out of ten saggital planes with a constant spacing of 5 mm and a total scanning width of 45 mm (see Fig. 7). The wake structure relative to the position and motion of the fish is illustrated at the left

with odd numbers are shown for better clarification. Although the streamwise extension of the scanning width is only 45 mm, the results indicate the variation of the flow structure between the plane nearest to the fin (9) and the most downstream plane (1). It occurs that a second pair of vortices has evolved close to the fin, which is suggested to correspond to the saggital cross-section of the streamwise parts of the bending vortex ring. The second vortex pair slightly precedes the main vortex in lateral direction as it is seen always on the right of the main vortex pair. At later times it appears that the streamwise parts of the bending vortex are stretched apart of each other and wrap around the cores of the main vortex. This interaction can be explained by the mutual induction effect of the vortices. The vortical structure in the wake is visualized in Fig. 10 by connecting the vorticity centers in the different planes by shaded regions in form of vortex cores. These regions correspond to the streamwise parts of the vortex rings. Note, that the image scaling in streamwise direction is largely overextended relative to the in-plane scales, therefore the extended vortex cores in Fig. 10 rather should be understood as curved parts of the vortex rings.

4 Conclusions

Combining the results from the horizontal and saggital planes, one can deduce the three-dimensional wake topology behind the swimming mechanical fish as given in Fig. 11. The results hold for neutral stroke conditions according to Hertel (1966), for which the kinematic parameters are a phase shift of 90° between body and fin motion and a towing speed equal to the body wave speed. The fish generates two separate ring-type vortices at each stroke, which drift in tandem to the lateral side. The main vortex ring is generated at each inflection point as a start–stop vortex ring similar to the vortex rings generated by a combined heaving and pitching foil. It has an oval shape and the jet-like flow in the center of the vortex ring is directed approximately perpendicular to the swimming direction. An additional separate vortex ring is nested within the main vortex ring, which results from the bending work. A simplified aerodynamic model of the moving fish skeleton gives an explanation of the generation and release of this additional vortex ring, which is named the “bending vortex”. This vortex ring is a result solely of the body undulations and is explained in our mechanical model by

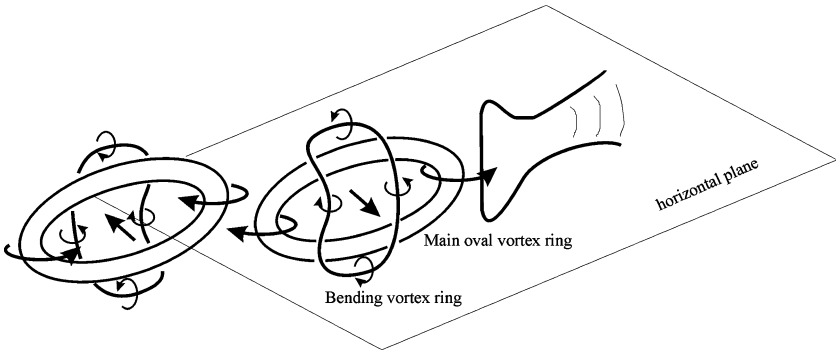

Fig. 11 Sketch of the vortex ring topology in the wake of the mechanical fish. Note that the main vortex ring is *oval*. The less intense bending vortex ring is deformed by the mutual induction effect and wrapped around the main vortex ring at its upper and lower part

the dynamic change of circulation due to the bending body deformation. The combination of a bending and successive recoil within one stroke cycle generates the extra vortex reflecting the bending action. One may speculate, that the body muscles and chords in live fish may act as an elastic system that retains energy from the stretch applied to it at one stage of the bending cycle and then pays back this energy through elastic recoil at a later stage, in a process that might improve efficiency or enhance performance.

The question remains, whether such an additional vortex ring is solely a result of the mechanical fish or whether it occurs in live fish, too, and why it has not been reported so far. The motion of the mechanical fish is indeed close to that of live fish of carangiform swimmer since the fish body is smooth and the mechanics generate a smooth traveling wave from head to tail with a near constant phase speed and increasing amplitude from nose to fin (note that the wave length is larger than the body length as typical for carangiform swimmer). In addition, the amplitude of the fin motion relative to the body length is about 0.16 and the maximum angle of attack of the fin to the path of motion reaches values of 38°, which are typical values of those type of fish (see Müller et al. 2002b). The answer to that question is possibly found in the fine tuning of the amplitude envelope and the variable phase shift between the body and tail motion that living carangiform swimmers are able to control. Müller et al. (2002b) investigated the role of the body wave in undulatory fish swimming and the importance of the slip—the ratio between swimming speed U and traveling wave speed V on the structure of the wake for living fish. For live fish swimming at slip values near to 1—the neutral swimming mode—they observed that the body and tail motion generate separate vortex cores in the wake. In addition, the jet-like flow between the vortices is directed approximately perpendicular to the swimming direction which they called the "B"-type of the wake. As slip decreases, so does the distance between the two type of vortices, until they coincide at a slip of around 0.7. An intermediate state was observed at a slip of 0.85 in which the two vortices seem to merge incompletely. These results with live fish confirm our results that the body generated bending vortex has its own cause of existence as a separate vortex structure. The mechanical fish allows to explain the additional vortex solely due to the bending motion and by the change of circulation. Therefore, no "proto"-vortices are necessary and its existence is based on lifting theory other than in the work by Videler et al. (1999).

As the results of Müller et al. (2002b) indicate, for lower slip values it is possible that the bending vortex might be integrated within the main start–stop vortex such that it is not seen as a separate vortex ring. In addition, the shape of the amplitude envelope of the fish's body wave can influence the amount of circulation and the moment of shedding. Fish seem to be able to control this process and may choose to let the body vortex enhance the tail vortex or to shed it as a separate vortex. Videler et al. (1999) speculate that the B-type of wake at the neutral swimming mode indicates that the fish does not try to swim efficiently but uses this mode to obtain more dynamic stability. This is subject of ongoing work. Future studies will focus on lower values of slip ($U/V < 1$) and different amplitude profiles by using a modified driving unit of the mechanical model.

Acknowledgments We thank Joachim Mogdans for critically reading the MS. The authors acknowledge the support of this study by the Germany Research Association (DFG).

References

Barett DS, Wolfgang MJ, Grosenbaugh MA, Yue DKP, Triantafyllou MS (1999) Drag reduction in fish-like locomotion. J Fluid Mech 392:183–212

Blickhan R (1992) Hydrodynamik der undulatorischen Lokomotion. BIONA Rep 11:331–351

Brücker Ch (1995) Digital Particle Image Velocimetry (DPIV) in a scanning light-sheet: 3D starting flow around a short cylinder. Exp Fluids 19:255–263

Brücker Ch (1997) Study of the 3D flow in a T-junction using a dual-scanning method for 3D Scanning-Particle-Image-Velocimetry (3D SPIV). Exp Therm Fluid Sci 14(1):35–44

Davies JBC, Lane DM, Sfakiotakis M (2000) Review of fish swimming modes for aquatic locomotion. IEEE J Ocean Eng 24(2):237–252

Hanke W, Brücker Ch, Bleckmann H (2000) The ageing of the low-frequency water disturbances caused by swimming goldfish and its possible relevance to prey detection. J Exp Biol 203:1193–1200

Hertel H (1966) Structure form and movement. Reinhold, New York

Hoar WS, Randall DJ (1978) Fish physiology, volume VII: locomotion. Academic, New York

Lauder GV, Drucker EG, Nauen JC, Wilga CD (2003) Experimental hydrodynamics and evolution: caudal fin locomotion in fishes. In: Bels VL et al (eds) Vertebrate biomechanics and evolution. BIOS Scientific Publishers Ltd., Oxford

Liao J, Beal DN, Lauder GV, Triantafyllou MS (2003) Fish exploiting vortices decrease muscle activity. Science 302:1566–1569

Müller UK, van den Heuveul BLE, Stammhuis EJ, Videler JJ (1997) Fish foot prints: morphology and energetics of the wake behind continuously swimming Mullet (Chelon Labrosus Risso). J Exp Biol 200:2893–2906

Müller UK , van den Heuveul BLE, Videler JJ (2002a) Aquatic vertebrate locomotion: wakes from body waves. J Exp Biol 202:3423–3430

Müller UK, Stammhius EJ, Videler JJ (2002b) Riding the waves: the role of the body wave in undulatory fish swimming. Integr Comp Biol 42:981–987

Nachtigall W (1998) Bionik, Grundlagen und Beispiele für Ingenieure und Naturwissenschaftler. Springer, Berlin

Nudds RL, Thomas ALR (2003) Flying and swimming animals cruise at a Strouhal number tuned for high power efficiency. Nature 425:707–711

Sakakibara J, Nakagawa M, Yoshida M (2004) Stereo-PIV study of flow around a maneuvering fish. Exp Fluids 36:282–293

Schultz WW, Webb PW (2002) Power requirements of swimming: do new methods resolve old questions. Integr Comp Biol 42:1018–1025

Stamhius E, Videler J (1995) Quantitave flow analysis around aquatic animals using laser sheet paricle image velocimetry. J Exp Biol 198(Pt 2):283–294

Triantafyllou MS, Triantafyllou GS, Yue DKP (2000) Hydrodynamics of fishlike swimming. Annu Rev Fluid Mech 33–53

Videler JJ (1993) Fish swimming. Chapman & Hall, London

Videler JJ, Müller UK, Stamhuis EJ (1999) Aquatic vertebrate locomotion: wakes from body waves. J Exp Biol 202:3423–3430

Wolfgang M, Anderson JM, Grosenbaugh MA, Yue DKP, Triantafyllou MS (1999) Near body flow dynamics in swimming fish. J Exp Biol 202:2303–2327

Investigation of flow mechanism of a robotic fish swimming by using flow visualization synchronized with hydrodynamic force measurement

Guang-Kun Tan · Gong-Xin Shen · Shuo-Qiao Huang · Wen-Han Su · Yu Ke

Abstract When swimming in water by flapping its tail, a fish can overcome the drag from uniform flow and propel its body. The involved flow mechanism concerns 3-D and unsteady effects. This paper presents the investigation of the flow mechanism on the basis of a 3-D robotic fish model which has the typical geometry of body and tail with periodic flapping 2-freedom kinematical motion testing in the case of $St = 0.78$, $Re = 6{,}600$ and phase delay mode ($\varphi = -75°$), in which may have a greater or maximum propulsion (without consideration of the optimal efficiency). Using a special technique of dye visualization which can clearly show vortex sheet and vortices in detail and using the inner 3-component force balance and cable supporting system with the phase-lock technique, the 3-D flow structure visualized in the wake of fish and the hydrodynamic force measurement were synchronized and obtained. Under the mentioned flapping parameters, we found the key flow structure and its evolution, a pair of complex 3-D chain-shape vortex (S–H vortex-rings, S_1–H_1 and S_2–H_2, and their legs L_1 and L_2) flow structures, which attach the leading edge and the trailing edge, then shed, move downstream and outwards and distribute two anti-symmetric staggering arrays along with the wake of the fish model in different phase stages during the flapping period. It is different with in the case of $St = 0.25$–0.35. Its typical flow structure and evolution are described and the results prove that they are different from the viewpoints based on the investigation of 2-D cases. For precision of the dynamic force measurement, in this paper it was provided with the method and techniques by subtracting the inertial forces and the forces induced by buoyancy and gravity effect in water, etc. from original data measured. The evolution of the synchronized measuring forces directly matching with the flow structure was also described in this paper.

1 Introduction

Using its tail, a real fish in nature can carry out adjustable flaps to produce highly effective or highly maneuverable hydrodynamics as main power for its locomotion, which attracts many researches on its flow mechanism and its applications to man-made marine transportation vehicles, for example robot fish (Triantafyllou and Triantafyllou 1995). The related propulsion mechanism involves 3-D flow structure and unsteady flow effect, also includes the generating, evolving, interacting and dissipating of vortex sheets or vorticity.

In previous work it was found that if a foil performs with the compound kinematical motion of heaving and pitching, it will produce the effects similar to the flap of a real fish tail fin, including the flow structure and the dynamical character in the wake (Anderson et al. 1998). But mostly it was limited in the 2-D investigation for 2-D fish model and its motion. For examples, using 2-D heaving and pitching foil model to simplify the physical fish tail fin by simulating the undulatory flap of the tail fin in water (Anderson et al. 1998; Koochesfahani 1989; Read et al. 2003; Triantafyllow et al. 2004), so-called "Reverse Karman Vortex" was showed in the tail wake structures (Triantafyllou et al. 2000), and some key parameters and conclusions have been obtained (Anderson et al. 1998).

G.-K. Tan · G.-X. Shen (✉) · S.-Q. Huang · W.-H. Su · Y. Ke
Institute of Fluid Mechanics,
Beijing University of Aeronautics and Astronautics (BUAA),
Beijing 100083, China
e-mail: gx_shen55@yahoo.com.cn

G.K. Taylor, M.S. Triantafyllou, and C. Tropea (Eds.): Animal Locomotion, pp. 173–183.
springerlink.com

However, since a real fish or even a robotic fish (the body and tail fins) bases on the 3-D geometrical form, the existence of the 3-D effect probably changes some conclusions based on the 2-D cases. Thus, some works were investigated on the heaving and the pitching of finite-span foil or the undulatory flap of 3-D tail fin model for years since 1990s. Blickhan et al. (1992) had measured the flow velocity of some spots in flow when a live fish was swimming, using the particle tracking technology and laser-Doppler anemometry, and imaged a 3-D model of the chain-shape vortex-ring produced by the fish tail. Later, Nauen and Lauder (2002) had confirmed primarily the existence of the chain-shape vortex-ring by means of measuring 2-component velocity fields in three parallel slices with digital particle image velocimetry (DPIV). In recent years, Von Ellenrieder et al. (2003), Parker et al. (2005) and Buchholz and Smits (2006) have studied the 3-D flow structures in wake produced by the heaving and pitching of finite-span foil in the experiments. Also Blondeaux et al. (2005) has put forward several 3-D structure modes of the heaving and pitching of the finite-span foil, using numerical computation under different Strouhal numbers. Also the most mentioned works were investigated in case of $St = 0.25$–0.35 for the efficiency of the flapping.

In most previous experiments, another important problem was the separated application of diversified observation and measurement tools or methods on flow structure and dynamics, for example dye visualization, PIV/SPIV measurements, hydrodynamic forces measurements etc. This has made it difficult to directly obtain the relationship between flow structure and dynamics, and might have great influence on acquiring more exact and deep understanding of such complex flow mechanism. Barret et al. (1999) had measured the drag and the power of a robot fish with a five-joint tail when it was swimming in the manner of back support. But they had not measured the flow field simultaneously and analyse the flow mechanism by combining the flow structure and the hydrodynamic forces. In the work of Drucker and Lauder (2000) and Lauder and Drucker (2002), a new method using the PIV-based data to estimate hydrodynamics was provided, which is worth under researching and developing, whereas it is still necessary to have the validation by means of other reliable conventional methods.

The research object of this paper is the flow investigation of a robotic fish model using a cable support, which has typical 3-D geometrical body and tail with 2-freedom flapping kinematical motion. The corresponding 3-component hydrodynamic force measurements (the force balance inside the body of the fish model) and special dye flow visualization of the 3-D flow structures in the wake during the flapping period for the special case of $St = 0.78$ were provided. The corresponding relationship of the 3-D flow structures and hydrodynamic force characteristics was obtained and described in different phase stages during the flapping period.

2 Experimental apparatus and technology

2.1 Robotic fish model

The experimental fish model was a self-designed robotic fish and its whole tail can perform 2-freedom special motions by driving its afterbody and tail fin, respectively. Its schematic view was shown in Fig. 1. The robotic fish was 1,155 mm long and had three parts: the head; the body; and the tail including the afterbody and the tail fin. The head had a streamline profile and the body had a cylinder shape with the outer diameter of 125 mm and the shell thickness of 5 mm. In the body there were the tandem cavities. The front cavity contained a rigid cube block fixed to a rigid frame by 12 steel cables of 1.5 mm diameter, so-called cable support, and an underwater inner strain gauge force balance. The upstream end of the balance was embedded into the block and the downstream end was mounted on the inner shell of the robotic fish body. In the

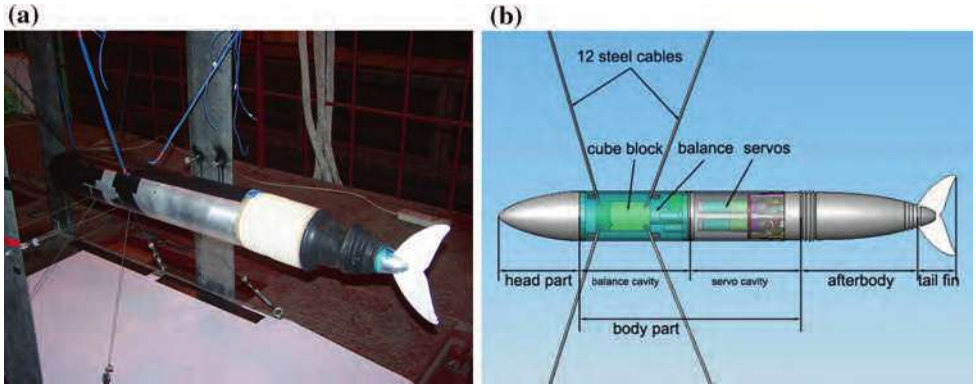

Fig. 1 **a** The robotic fish model, **b** the schematic view of the model

rear cavity two MAXON direct-current servos, RE36 (90 W) and RE30 (60 W), could drive the afterbody and the tail fin, respectively. Their power cables and signal cables enlaced with two of the mentioned 12 cables were connected to power source and servo drivers above the water. Because of the embedded servos the body was dealt with waterproof and hermetic technique.

The length of the whole tail was about 360 mm long accounting for one third of the total length of the model, which accorded with the ratio of the tail to the total length in the fish species with the thunniform mode (Sfakiotakis et al. 1999). Within the afterbody a set of parallelogram connecting rod mechanism controlled by the two servos, could make the afterbody and the tail fin flap to flap as desired. In this case, the spatial running error of the servos was not more than 1% and the temporal error not more than 0.6% under the chosen kinematical modes. Rubber cannula was used as the shell of the afterbody in order to adapt to the shell flex caused by the flap motion, and filled with air for resistance to water pressure (in Fig. 1a it has not yet been filled with air).

The lateral shape of the tail fin was similar to that of a dolphin's with a span length of 200 mm, root chord length of 66 mm and thickness of 4 mm as shown in Fig. 2. The aspect ratio was about 3. The rotation axis of the tail fin flap located at in the root and 45 mm in front of the leading-edge of the tail fin. The tail fin was made with the composite of four layers of silicone rubber–carbon fiber–film–silicone rubber. Twelve dye metal tubes with a 1-mm inner diameter were divided into two groups mounted from the afterbody to the tail fin and fixed between the layers of silicone rubber and carbon fiber in the manner of dispersing state shown as Fig. 2. In Fig. 2, the carbon fiber layer is shown and the silicone rubber layer has not yet been paved. The end of tubes traversed the carbon fiber layer at about 10 mm distance from the edges of the tail fin and opened between the layers of carbon fiber and film where the layers would form a micro-size gap which was located at the back side of the tail fin in Fig. 2.

Fig. 2 The tail fin with 12 dye tubes

The rigid steel frame was 1,198 mm high and 760 mm wide in which the model was fixed by the 12 steel cables. The stretched cable support has a greater rigidity and may produce less influence to the flow than that of the back support. The central line of the model was about 500 mm distance from both the bottom flat plate and the top water surface in the testing water channel. The reference system of the experiment was set on the central point of the balance with X positive direction upstream, Y positive direction upward and Z positive direction according with right-hand rule. During the experiment the model was fixed to have no displacement and to simulate the march of a live fish under water through changing the velocity of uniform flow of the water channel.

2.2 Flow visualization and capture devices

Two colors of ink, amaranth and brilliant blue were used as the visualizing dyes which were guided from two ink containers to the metal tubes fixed on the tail fin by 12 soft plastic tubes enlaced with other two mentioned steel cables. After flowing into the micro-size gap, the ink will overflow the gap. In order to identify the flow, which came from different edges of the tail fin, the amaranth ink was released from the trailing-edge and the brilliant blue ink from the leading-edge (this is because the blue ink will shield the visualized flow structures of the amaranth ink from the trailing-edge if the blue flows from the leading-edge). Two SONY DCR-PC350E Digital Videos (PAL standard with 25 frames per second) were employed to capture the flow visualization with the top and lateral view.

2.3 Hydrodynamic force measurement system

The hydrodynamic force measurement system consisted of the mentioned underwater inner strain gauge force balance, a signal amplifier, a data acquisition board and a data acquisition PC. The balance could measure three components of the hydrodynamic force propulsion/drag (P/D) of X direction (positive value means the propulsion and negative the drag), lateral force L of Z direction and yaw moment M_Y of Y direction, whose design loads were 12 N, 24 N and 15 Nm, respectively and relative errors were 0.48, 0.21 and 0.02% based on the steady calibration. DAS-1800 data acquisition board could collect force signals after receiving trigger signal from the following introduced signal generator, DG535. The data sampling frequency of the force measurement in the experiment was 50 Hz.

2.4 Synchronized control system

In order to obtain the synchronized relationship of the flow structure in wake and the hydrodynamic force loaded on the model when the tail was flapping, it needs to synchronize with the special motion of the flapping model tail, the capture of the flow visualization and the performance of the force measurement system. Because the tail flaps in strict periodical kinematical motion, when the motion keeps stable the flow structure also presents the stable periodic character. Therefore, the flow in wake could be observed and measured in the manner of phase sequence (instants) instead of time sequence so that the phase average algorithm will be applied to process data to discover some key features of the flow in different phase instants during the flapping period. The key device of the synchronized control system was digital delay/pulse generator DG535 with four independent signal output channels holding high degree of time accuracy up to 5 ps level. Under the control of DG535, the kinematical motion of the robotic model and the various measurement methods, such as dye visualization, force measurement, PIV measurements, etc. can proceed at the same phase instant.

2.5 Water channel

The experiments were hold in the horizontal low-velocity close-loop water channel in BUAA. The testing section was 16 m (length) × 1.2 m (high) × 1.0 m (wide). The running speed of the velocity of uniform flow can be from 0.01 to 1 m/s and 0.10 m/s were chosen in this experiment. The uniformity of the flow velocity in the testing section without the model is 0.05–0.1%. Based on the root chord length of the flapping tail and the testing flow speed in the experiments, *Re* number was about 6,600.

3 Results and analysis

3.1 The basic parameters of the kinematical mode

The following are the manipulative equations controlling the flapping kinematical motion of the afterbody and the tail fin of the robot fish:

$$\begin{cases} \theta_1 = \theta_{10} \times \sin(2\pi f t) \\ \theta_2 = \theta_{20} \times \sin(2\pi f t + \varphi) \end{cases}$$

where θ_1, θ_{10} denote the flapping angle and the flap amplitude of the afterbody, respectively and θ_2, θ_{20} denote those of the tail fin as shown in Fig. 3. The angles are relative to the central line and the starting time of a new flapping period was set at the moment that the afterbody (not the tail fin) reached the central line. f denotes the flap frequency, t denotes the running time and φ denotes the phase-delay between the afterbody and the tail fin. In this experiment, the testing values were chosen as $\theta_{10} = 13°$, $\theta_{20} = 15°$, $f = 0.5$ Hz and $\varphi = -75°$. There is not only one mode of the tail-fin flapping and the vortex structure exiting in fish's wake according to the recent numerical study of Dong et al. (2005), and due to our rough tests, we have found that it may have a greater propulsion (without consideration of the optimal efficiency) and have different flow structures with the traditional cases of $St = 0.25$–0.35. Therefore, the reduce frequency

$$k = \frac{cf}{U} = 0.33$$

and Strouhal number

$$St = \frac{A \cdot f}{U} \approx 0.78,$$

where c is the root chord length, A is the wake's width or approximate distance between the two extreme spots of the trailing-edge flapping motion, that is around 156 mm. These two basic parameters play a very important role in the flow mechanism analysis of the heaving and pitching foil (Triantafyllow et al. 2004).

3.2 Flow visualization during one flapping period

The generation and evolution of the 3-D flow structure produced by the afterbody and tail fin during the flapping period is shown in Fig. 4. The figures in the left column show the vortex structure observed from the downstream with a 45° angle to the central line in lateral view (the flapping motion starts at $\theta_1 = 0°$ from inside to outside in this sense). The right column shows the platform (top) view (the flapping motion starts at $\theta_1 = 0°$ from top to bottom) the left column. Figure 4a is at 0.04 T before the start of one flapping period (T means the period of the flapping kinematical motion) and Fig. 4b–i corresponds to eight phase instants for which every phase instant was equipartition during one flapping period. The uniform flow direction is from left to right.

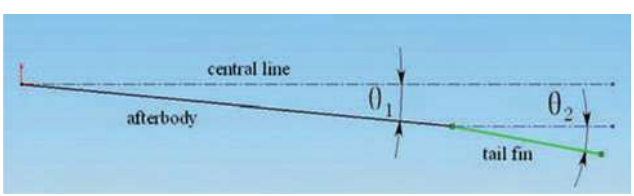

Fig. 3 The scheme of the flapping angles of the robotic fish tail

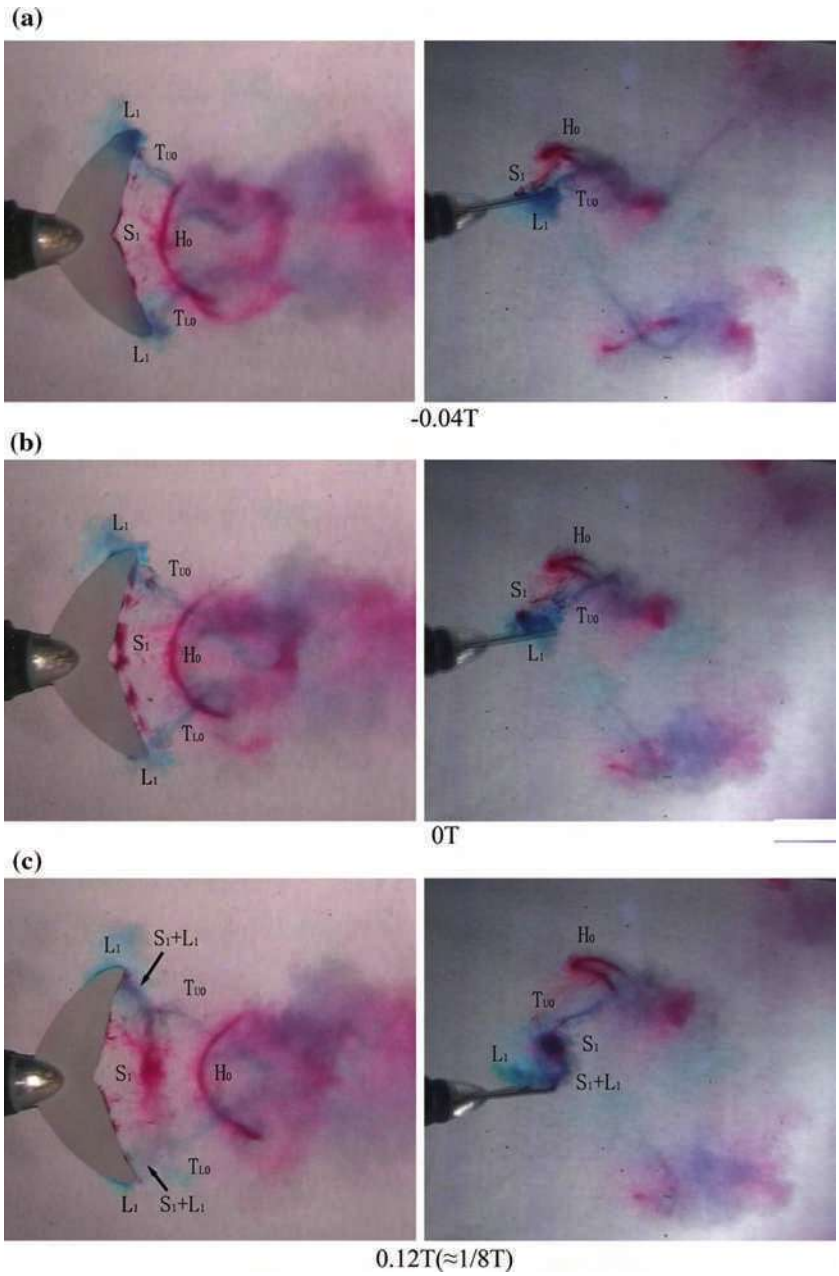

Fig. 4 The flow visualization of the evolution of the 3-D flow structures during one flapping period

From Fig. 4b–i, it can be found that a pair of vortex-rings staggering along two sides in wake are produced during one period. At each half-period, a pair of counter rotating vortices are generated and shed successively from the trailing-edge.

In Fig. 4a, when the tail fin has started from the turn point of the flap and is speeding up to the central line and the afterbody will soon reach the central line, it can be found that a vortex S_1 with a vertical upward vortex-vector along the trailing-edge and two vortices L_1 with two inclined vortex-vectors along the leading-edge begin to form. For convenience, such vortex as generated along the trailing-edge in the accelerating course of the flap is named the letter S and the subscript number of S is used to label the half-period sequence of its generation and evolution, and the vortex generated along the leading-edge is named the letter L. When the afterbody reaches the central line, a new period of the flap begins as shown in Fig. 4b. At this moment S_1 is growing up rapidly.

Then, with the shedding of S_1 firstly at its mid part, the subsequent shedding process results in two vortex legs attaching to the fin-tips of the trailing-edge and the shed part of S_1 forms a curved shape due to the greater convective velocity around the concave segment of the

Fig. 4 continued

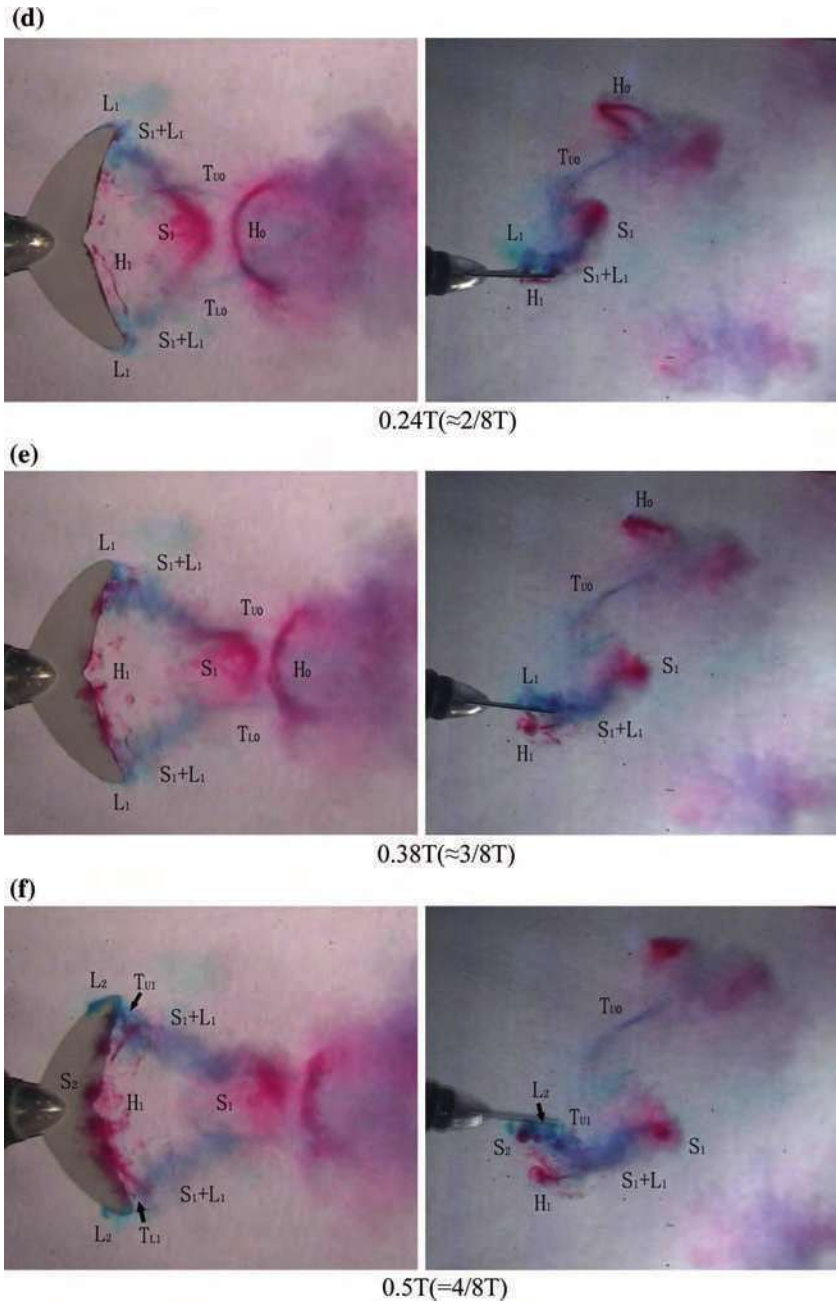

trailing-edge as shown in Fig. 4c and d when the tail fin is just flapping across the central line. In this course, the spatial pattern of S_1 is similar to a hairpin vortex with the rotations of the vortex head and the two vortex legs to induce a jet flow towards downstream at the center of the vortex ring. In other words, the flow jet induced by S_1 just produces the important part of the thrust. Considering having the hairpin vortex shape and the contrary dynamic effect relative to the traditional hairpin vortex in turbulent boundary layer, especially in complex separated flows (Johnson and Patel 1999; Lu and Su 2001), this paper herein defines it as the "reverse hairpin vortex", which is formed during the accelerating course of the flap and at the moment the afterbody and tail fin are flapping toward the center line of the fish model. Moreover, the root parts of S_1' legs, which are attaching to the trailing-edge, show the blue color. This implies that the vorticity generated from the fin-tips of the leading-edge pour into S_1. The pair of S_1' legs are named as $S_1 + L_1$ to indicate the vorticity contribution from both S_1 and L_1.

With the deceleration of the flapping afterbody as shown in Fig. 4d, another vortex H_1 with the counter rotating direction relative to S_1 appears along the trailing-edge, and sheds quickly off from the trailing-edge when the afterbody

Fig. 4 continued

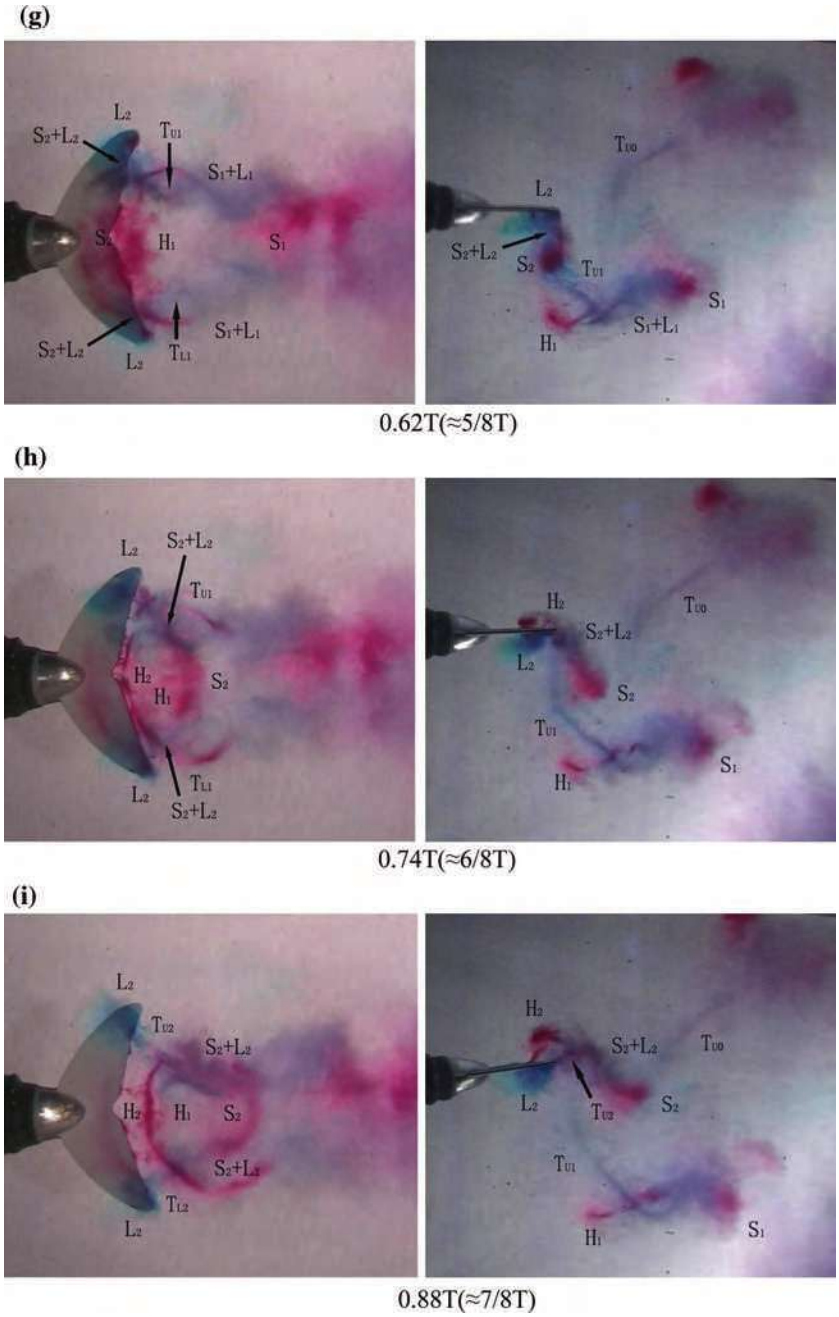

almost reaches another extreme spot and returns to the central line. For convenience, such vortex as generated in the decelerating course of the flap is named the letter H and the subscript number is also used to label the half-period sequence. The appearance of H_1 is due to the roll-up of the mentioned jet flow induced by the "reverse hairpin vortex". Because of the deceleration of the flapping afterbody the downstream velocity of the jet flow around the lee side of the tail fin is gradually greater than the downstream velocity of the flow around the windward side, which results in the generation and accumulation of the vorticity along the trailing-edge and finally produces the obvious vortex H_1. When shedding from the trailing-edge in Fig. 4e, two ends of H_1 connect with two $S_1 + L_1$ attaching to the trailing-edge to form a close vortex-ring S_1–H_1 which moves downstream and away from the central line with an oblique S pattern, as shown in Fig. 4f. This flow structure is different from that in Blondeaux et al. (2005), which had considered that a leading-edge vortex will shed off, merge with trailing-edge vorticity and constitute the upstream part of the vortex-ring, just like H_1 in this case. However, these two different mechanisms are not contradictory. In Blondeaux et al. (2005), the rectangle finite-span foils with a leading-edge normal to uniform flow will

produce shed leading-edge vortices, whereas in this paper the tail-fin-like with two inclined leading-edge, which is like the case of delta wing, will produce helical leading-edge vortices which is not easy to shed off until the flapping direction changes (Ramamuri and Sandberg 2002).

After reaching this extreme spot, the afterbody backtracks and starts to flap again. Subsequently, in Fig. 4f and h, the vortices of S_2 and H_2 are generated and the same vortex-ring forming and shedding process repeats, but S_2 (or H_2) has the opposite rotating direction with respect to S_1 (or H_1) as shown in Fig. 4f–i. Naturally, both S_1–H_1 and S_2–H_2 move downstream, outwards and distribute two anti-symmetric staggering arrays along with the center line of the fish model.

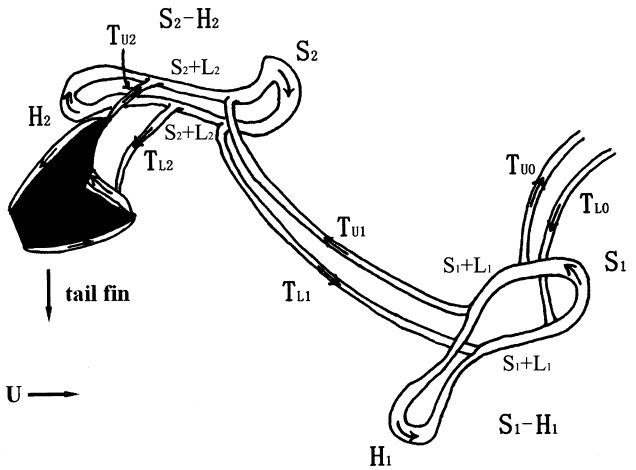

Fig. 5 3-D chain-shape vortex-ring structure after the tail fin

From Fig. 4e and f, we can also find that $S_1 + L_1$, which connected with H_1, does not shed when H_1 sheds from the trailing-edge. With S_1–H_1 moving downstream and outwards and the tail fin flapping inwards, another pair of legs connecting $S_1 + L_1$ are stretching and developing into two filament vortices aligning at the upper and lower sides of the mid-plane of the trailing-edge, namely T_{U1} and T_{L1} in Fig. 4f–i. Their blue color implies again the ceaseless import of L_1 vorticity. Owing to the opposite rotating direction of T_{U1} and T_{L1}, a flow jet heading upstream will be induced. Subsequently as shown in Fig. 4 (f) and (g), because the shedding of S_2 extends to the fin-tips, T_{U1} and T_{L1} will also shed off from the trailing-edge but still connect with S_2 of which the legs, however, do not shed off at that moment. Likewise, T_{U2} and T_{L2} will be generated in the sequent half-period as shown in Fig. 4h and i. In fact, T_{U2} and T_{L2} are just T_{U0} and T_{L0} which are generated before the first half-period and can been seen the evolution with phase instants (stages) in Fig. 4a–i.

Therefore, two pairs of the vortex-rings, namely S_1–H_1 and S_2–H_2, generated during a complete flapping period are not independent: they are connected with each other via T_{U1} and T_{L1}, and are also connected with other vortex-rings generated in the anterior and sequent periods via T_{U0}–T_{L0} and T_{U2}–T_{L2}, which all form a chain-shape vortex-ring system. According to the mapping from the figures of the left and right columns in Fig. 4, especially Fig. 4a and i, a 3-D chain-shape vortex-ring structure is obtained and sketched in Fig. 5 (the vortex vectors are denoted with arrows) during the approximate instants of the flapping period as Fig. 4a and i.

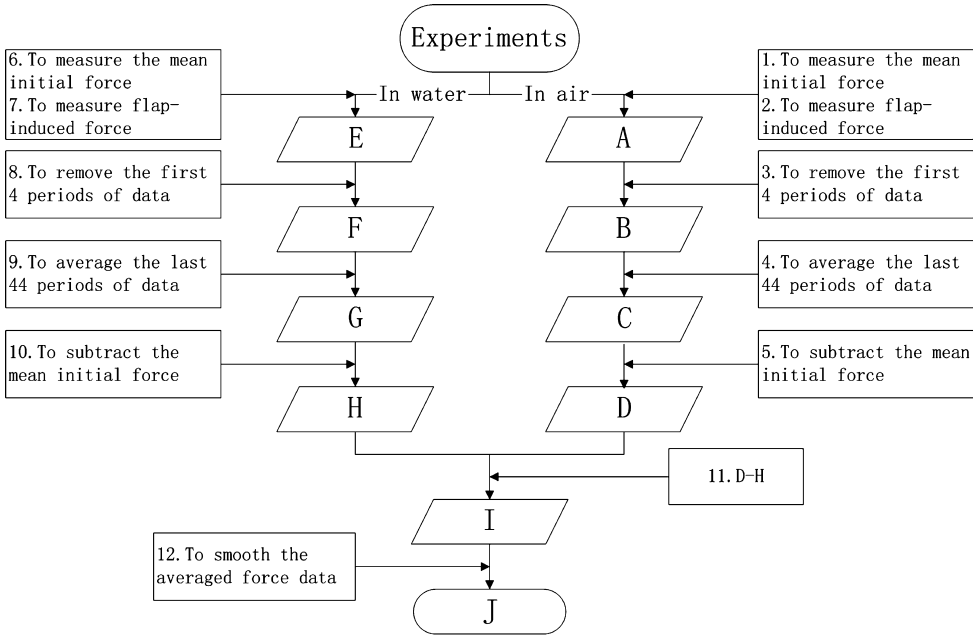

Fig. 6 The flowchart of conducting the force measurement experiments and processing the measured data. (*Note* the number *1–12* means the steps of conducting experiments and processing measured data and the capital letters *A–J* means the results corresponding to the steps.)

3.3 The analysis of the force measurement results with the flow visualization

The procedure of conducting the force measurement and processing the measured data are showed as the flowchart in Fig. 6. The force measurement experiments should be conducted twice: one in air and the other in water. Because the measured force data from the experiments in water include not only the hydrodynamic force including the adding force from virtual mass but also the inertia force of the flapping mechanism of the robotic fish and the initial force caused by initial circumstance mainly comprising water circumstance, weight-influence and preload by setting up of the model system. It needs to acquire the data of the latter two types of forces and remove them. Hence, before the experiments in water as shown from Result E to Result H of the left column of the flowchart in Fig. 6, the inertia force of the flapping mechanism should be measured in advance by the experiment in air (preciously should be in vacuum) as shown from Result A to Result D of the right column in Fig. 6.

In air, by Step 1 the mean initial force data were collected when the tail was still; and by Step 2 the measured force data was taken for 48 periods and had Result A while the tail was flapping ceaselessly. Since in the beginning of the flap the flow was not stable, the first four periods of data were removed in Step 3 and the data in the last 44 continuous periods were averaged in one period according to the condition of phase-lock in Step 4, the results of which are shown in Fig. 7. Also the accuracy of the measuring dynamic forces for data of 44 periods here were 0.98% and 1.34% for P and L full scale separately. These two steps obtained Results B and C successively. Then, Step 5 was to subtract the mean initial force from Result C and obtain Result D, which comprised the inertia force of the flapping mechanism and the aerodynamic caused by the flap. But the aerodynamic is very small relative to the force used for withstanding the inertia of the mechanism flapping. So the aerodynamic could be omitted and Result D was almost the inertia force of the flapping mechanism.

The same measurement experiment and data process were conducted in water. But it needed to pay attention that in Steps 6 and 7, the testing uniform flows were at the same speed, 0.10 m/s when collecting the force data in the cases of both measuring the mean initial force with the tail still and measuring the unsteady force with the tail flapping. In addition, the measured mean initial force included the friction drag and the static form drag, which were treated approximately as the friction drag and the dynamic form drag of the robotic fish when the tail was flapping and to be removed just as Step 10.

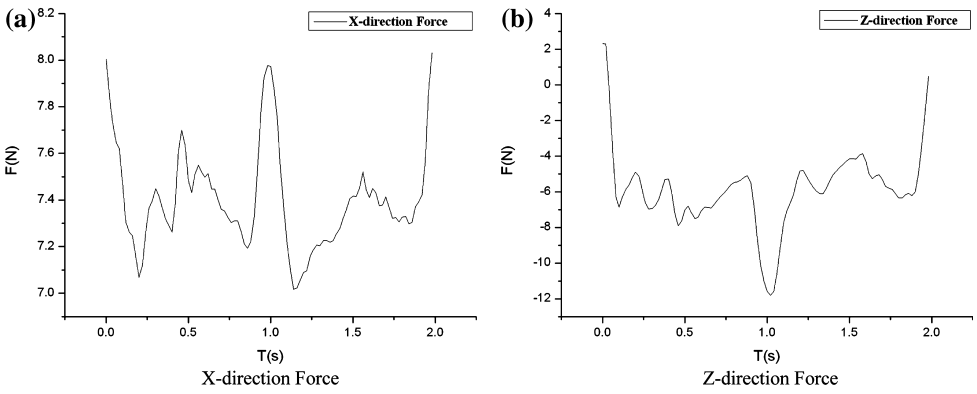

Fig. 7 The original total force during one period of the flap

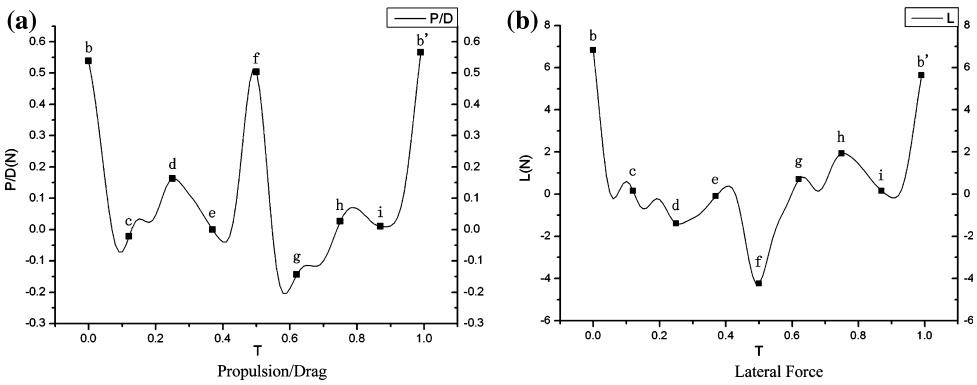

Fig. 8 The final net hydrodynamic force at the one period of flap (T is non-dimensional time)

After subtracting the mean initial force of Step 10 from Result G and the inertia force of the flapping mechanism, that is Result D, from Result H successively, Result I could be obtained with only the hydrodynamic force and the adding force caused by the unsteady flow. Through smoothing suitably Result I, Result J was the final processed force data regarded as the hydrodynamic force and the adding force. Figure 8 shows these final results, which are two change-state curves of the net P/D of X direction (left) and the net lateral force of Z direction (right). Moreover, in the P/D curve, positive force means the propulsion and negative force means the drag. In Fig. 8 the small letter (b–i–b′) marks of the curves correspond respectively with different phase instants to Fig. 4 (b–i–b′).

Figure 8 showed that the flapping afterbody reaches the central line whereas the flapping tail fin has an angle of about 15° with the central line because of the phase-difference φ, as shown in Fig. 4b, when a new period of the flap starts at the moment. The tail fin will produce the greatest propulsion (b in Fig. 8a) and the greatest value of lateral force ignoring the sign (b in Fig. 8b). In the course of the afterbody motion from the accelerating flap in Fig. 4a to the fastest speed of the flapping in Fig. 4b, the vorticity coming into being from the trailing-edge has been poured into vortex S_1 ceaselessly and as a result S_1 has quickly rolled up and strengthened. At the moment of Fig. 4b, S_1 is already very concentrated and strong and has induced a powerful jet flow pointing to downstream. A powerful jet implies a greater thrust loaded on the model by reacting from the unsteady flow. At the same time a quite great reverse circulation relative to S_1 is around the tail fin and produces a greater lift, just like flow passing a starting-up foil, which is basically the lateral force. Hence, at this moment the greatest propulsion and lateral force are produced.

When the afterbody flaps to the extreme spot on one side, e.g. Fig. 4d, vortex H_1 which is just strengthening and vortex S_1 of which the head part has shed off can jointly induce another powerful jet flow pointing to downstream. Simultaneously, the extremal offset of the afterbody produces a great form drag. The above two factors together result in another greater value of the propulsion shown as d in Fig. 8a. As for the lateral force, the value falls down to the minimum in this flapping course, shown as d in Fig. 8b, because of another great reverse circulation around the tail fin with the generation of H_1.

When the afterbody flaps from the central line to the extreme spot, e.g. from Fig. 4b to d, S_1 is partially shedding and the form drag of the afterbody is continually increasing, which make the propulsion fall down from b in Fig. 8a to the minimum c in Fig. 8a in this flapping half-period. The lateral force also falls down for the decreasing of the circulation around the tail fin with the partial shedding of S_1, shown as c in Fig. 8b.

When the afterbody returns from the extreme spot to the central line, e.g. from Fig. 4d to f, H_1 has shed off and formed vortex-ring S_1–H_1. However, the form drag of the afterbody is continually decreasing. The result of contrasting the changes of propulsion and drag makes the propulsion also fall down from d but greater than c in Fig. 8a. The lateral force rises up for the decreasing of the circulation around the tail fin with the shedding of H_1, shown as e in Fig. 8b.

From f–b′ in Fig. 8, a new flapping half-period starts just like the course of from b to f. Hence, the change-state of the propulsion of the second half-period is highly similar to that of the first half-period above mentioned and however the change-state of the later force has just an opposite trend.

4 Conclusions and Discussion

A typical robotic fish model using the cable support was designed and provided for the flow visualization and 3-component dynamic force measurements with phase-lock technique. The cable support has less interaction to the flows and gives better investigation.

For precision of the dynamic force measurement, it is necessary to subtract the inertial forces from the mass and the mass distribution of the flapping tail model and the forces from buoyancy and gravity effect in water, etc.

For this kind of typical 3-D robotic fish model and the phase delay ($\varphi = -75°$) mode of flapping tail motion in case of $Re \sim 6{,}600$ and $St \sim 0.78$, in which may have greater or maximum propulsion without consideration of the optimal efficiency of flapping, the quantitative measuring forces (P/D and Lateral force) and the spatial flow structure and its evolution in wake by flow visualization during the flapping period are examined.

In mentioned case, the flow structure and its evolution in the wake, which are complex in space and with phase instants during the flapping period, was investigated and obtained. It is different with in case of $St \sim (0.25–0.35)$ as most previous work. The key structure investigated in this paper is a pair of 3-D vortex-rings, S–H vortex structure (S_1–H_1, S_2–H_2 and its lags) during the flapping period, which attach the leading edge and backward edge, shed, move downstream, outwards and distribute two anti-symmetric staggering arrays along with the center line of the fish model.

The results also displayed that the direct relation and description between the characteristics of the forces (P/D and Lateral force) measured and the 3-D flow structures in different phase moments during the flapping period, and had understood more detail of the fluid mechanism of the locomotion of the fish.

Due to limitations of the flow visualization, probably it is necessary to continue work on using periodic 3Dt-3c DSPIV velocity field measurement technique with phase-lock techniques for more deep, detailed and better understanding of the fish flows.

Acknowledgment This work was supported by National Natural Science Foundation (Project Code: 10472011) from NNSF of China and National Education Foundation 985-1-7 from BUAA. Prof. Hui Guo and Hai-Wen Wang at Water Tunnel Lab are acknowledged for active support in conducting the experiments.

References

Anderson JM, Streitlien K, Barrett DS, Triantafyllou MS (1998) Oscillating foils of high propulsive efficiency. J Fluid Mech 360:41–72

Barret DS, Triantafyllou MS, Yue DKP, Grosenbaugh MA, Wolfgang MJ (1999) Drag reduction in fish-like locomotion. J Fluid Mech 392:183–212

Blichkhan R, Krick C, Zehren D, Nachtigall W (1992) Generation of a vortex chain in the wake of a subundulatory swimmer. Naturwissenschaften 79:220–221

Blondeaux P, Fornarelli F, Guglielminia L, Triantafyllou MS, Verzicco R (2005) Numerical experiments on flapping foils mimicking fish-like locomotion. Phys Fluids 17:113601

Buchholz JHJ, Smits AJ (2006) On the evolution of the wake structure produced by a low-aspect-ratio pitching panel. J Fluid Mech 546:433–443

Dong H, Mittal R, Bozkurttas M, Najjar F (2005) Wake structure and performance of finite aspect-ratio flapping foils. In: 43rd AIAA Aerospace Sciences Meeting and Exhibit, AIAA 2005-81, Reno, 10–13 Jan 2005

Drucker EG, Lauder GV (2000) A hydrodynamic analysis of fish swimming speed: wake structure and locomotor force in slow and fast labriform swimmers. J Exp Biol 203:2379–2393

Freymuth P (1988) Propulsive vertical signature of plunging and pitching airfoils. AIAA J 26:881–883

Johnson TA, Patel VC (1999) Flow past a sphere up to a Reynolds number of 300. J Fluid Mech 378:19–70

Koochesfahani MM (1989) Vortical patterns in the wake of an oscillating airfoil. AIAA J 27:1200–1205

Lauder GV, Drucker EG (2002) Forces, fishes, and fluids: hydrodynamic mechanisms of aquatic locomotion. News Physiol Sci 17:235–240

Lu ZR, Su WH (2001) Hairpin vortices in the wake of grid fin. Chinese J Aeronaut 14(4):200–204

Nauen JC, Lauder GV (2002) Hydrodynamics of caudal fin locomotion by chub mackerel, *Scomber japonicus*. J Exp Biol 205:1709–1724

Parker K, von Ellenrieder KD, Soria J (2005) Using stereo multigrid DPIV (SMDPIV) measurements to investigate the vertical skeleton behind a finite-span flapping wing. Exp Fluids 39:281–298

Ramamuri R, Sandberg WC (2002) A three-dimensional computational study of the aerodynamic mechanisms of insect flight. J Exp Biol 205:1507–1518

Read DA, Hover FS, Triantafyllou MS (2003) Forces on oscillating foils for propulsion and maneuvering. J Fluids Struct 17:163–183

Sfakiotakis M, Lane DM, Davies JBC (1999) Review of fish swimming modes for aquatic locomotion. IEEE J Ocean Eng 24(2):237–252

Triantafyllou MS, Triantafyllou GS (1995) An efficient swimming machine. Sci Am 272 (3):64–70

Triantafyllou MS, Triantafyllou GS, Yue DKP (2000) Hydrodynamics of fishlike swimming. Annu Rev Fluid Mech 32:33–35

Triantafyllow MS, Techet AH, Hover FS (2004) Review of experimental work in biomimetic foils. J Ocean Eng 29(3):585–594

Von Ellenrieder KD, Parker K, Soria J (2003) Flow structures behind a heaving and pitching finite-span wing. J Fluid Mech 490:129–138

PART II

The physics of flying

PIV-based investigations of animal flight

Geoffrey R. Spedding · Anders Hedenström

Abstract An overview is presented of the principles of estimation of fluid forces exerted upon solid bodies, based upon whole-field velocity measurements such as provided by PIV. The focus will be on the range of length and velocity scales characterised by the flight of large insects, birds, bats and small unmanned air vehicles, so that while viscous terms in the Navier–Stokes equations can many times be ignored in the quantitative analysis, understanding and measuring boundary-layer flows, separation and instability will ultimately be critical to predicting and controlling the fluid motions. When properly applied, PIV methods can make accurate estimates of time-averaged and unsteady forces, although even ostensibly simple cases with uncomplicated geometries can prove challenging in detail. Most PIV-based force estimates are embedded in some analytical model of the fluid–structure interaction, and examples of these with varying degrees of complexity are given. In any event, the performance and accuracy of the PIV method in use must be well understood as part of both the overall uncertainty analysis and the initial experimental design.

G. R. Spedding
Department of Aerospace and Mechanical Engineering,
University of Southern California, Los Angeles, USA

Present Address:
G. R. Spedding (✉)
Department of Mechanical and Aeronautical Engineering,
University of Pretoria, Pretoria 0002, South Africa
e-mail: geoff.spedding@up.ac.za

A. Hedenström
Department of Theoretical Ecology, Lund University,
Ecology Building, 223 62 Lund, Sweden

List of symbols

A	tip-to-tip flapping amplitude (m)
AR	aspect ratio ($AR = b/c$)
b	wingspan (m)
c	mean chord (m)
C_L, C_D	lift and drag coefficients ($C_x = F_x/qS$)
$C_{D,pro}$	profile drag coefficient of wing
$C_{D,i}$	induced drag coefficient of wing
C_F	laminar skin friction coefficient
D	image displacement (pix)
D	drag, force parallel to U_0 (N)
D'	drag per unit span (N/m)
f	flapping frequency (/s)
F_x	force component in the x direction (N)
$\mathbf{g}$	acceleration due to gravity (m/s^2)
I	impulse (kg m/s)
l	length scale (m)
L	lift, force normal to U_0 (N)
p	pressure (N/m^2)
p_0	freestream pressure (N/m^2)
q	dynamic pressure $\left(q = \frac{1}{2}\rho U^2,\ \mathrm{N/m^2}\right)$
Re	Reynolds number (Re_x based on length scale x)
r_0	vortex radius (m)
$\mathbf{R}$	general, resultant force vector (N)
R_{wv}	wake vortex ratio
S	control surface (m^2)
S	shear deformation (dx/x, dimensionless)
S	wing planform area ($S = bc$, m^2)
St	Strouhal number ($St = fA/U$)
t	time (s)
T	wingbeat period (s)
$\mathbf{u}$	velocity vector field (m/s)
u, v, w	velocity components in x, y, z (m/s)
u_1	upstream uniform streamwise velocity (m/s)
u_2	downstream,disturbed streamwise velocity (m/s)

G.K. Taylor, M.S. Triantafyllou, and C. Tropea (Eds.): Animal Locomotion, pp. 187–201.
springerlink.com

U_0	mean, undisturbed uniform streamwise velocity (m/s)
U	mean flow speed or mean flight speed (m/s)
V	control volume (m^3)
w_i	induced velocity (due to wing lift) (m/s)
W	body weight (N)
$\mathbf{x}$	position vector (m)
x, y, z	Cartesian coordinates in streamwise (flightwise), spanwise and vertical directions (m)
α	angle of attack (deg)
α_i	induced angle of attack—the decrease in α caused by w_i (deg)
δt	exposure time between two PIV images (typically μs)
ϕ	velocity potential (m^2/s)
Γ	circulation (m^2/s)
Γ_0	circulation at wing centreline (m^2/s)
μ	viscosity (kg/m/s)
ν	kinematic viscosity ($\nu = \mu/\rho$, m^2/s)
θ	momentum integral (m)
ρ	fluid density (kg/m^3)
$\boldsymbol{\omega}$	vorticity vector (/s)
ω_x	vorticity component in the x direction (normal to the yz plane) (/s)

Abbreviations

CIV	Correlation Imaging Velocimetry
DLE	Direct Lyapunov Exponent
DNS	Direct Numerical Simulation
ENOB	Effective Number of Bits
LCS	Lagrangian Coherent Structure
LEV	Leading Edge Vortex
PIV	Particle Image Velocimetry

1 Introduction

Particle image velocimetry (PIV)-based methods have been successfully used to show the airflows induced by the flapping wings of animals in free and tethered flight, and by fixed mechanical model flappers, and they feature in the majority of papers in this special issue. PIV can provide robust estimates of instantaneous velocity fields, which are often shown in conjunction with the vorticity component normal to the plane of measurement to describe complex and time-varying flows. Time-resolved PIV can also be used to estimate acceleration terms in the Navier–Stokes equations, and can then support alternative structure identification algorithms and/or compute instantaneous forces. In all of these cases, a correct quantitative analysis requires the performance characteristics of the particular method be well understood under realistic experimental conditions.

Here we give an overview of the principles of calculation of time-averaged and instantaneous forces from PIV-based measurements of the velocity field. We begin by examining the equations of motion for uniform incompressible fluids to provide a basis for quantitative analyses based on different properties of the measured flow fields. Two classes of measurement are considered—those based on integral momentum measures and those deriving from the observed structure of the vorticity field, and the strengths and limitations of PIV-based data in each will be noted. Selected examples will be given for fixed wings and for flapping animal flight. Increased sophistication may come either from reducing the number and/or scope of assumptions in the analysis, or changing their form. Improvements in analytical techniques will proceed simultaneously with predictable advances in technology, some of which are outlined.

1.1 Momentum and vorticity equations

The momentum equation for an incompressible fluid continuum of uniform density is

$$\rho \frac{D\mathbf{u}}{Dt} = \rho\mathbf{g} - \nabla p + \mu\nabla^2\mathbf{u}, \tag{1}$$

where the acceleration of a material volume of fluid is determined by the rate of generation of momentum by surface and volume forces on the right hand side. When the density, ρ, and viscosity, μ, are constant, then fluid motions, $\mathbf{u}$, are altered due to gradients in the pressure, p, and by viscous shear stresses. The Navier–Stokes equations (Eq. 1 plus a mass conservation equation) are notoriously rich in their range of possible solutions, and at the same time, experimental determination of all the terms is difficult.

The solutions of Eq. 1 can be characterised by the Reynolds number, $Re \equiv ul/\nu$, where u and l are characteristic velocity and lengthscales, and $\nu = \mu/\rho$. In many animal flight studies, Re based on a mean wing chord, c, lies between 10^3 and 10^5. This is a particularly interesting range: at the high end ($Re = 10^5$), viscous effects can almost be ignored and many classical aerodynamic theories work perfectly well. At the lower end ($Re = 10^3$), viscous effects come to predominate and ensure a degree of stability and predictability of the thick boundary layers that are formed over even quite odd-shaped bodies. In between, we pass through a regime where certain quantitative predictions of inviscid theory work very well, but where one can also find very large qualitative changes in flow fields that ultimately depend on the boundary layer behaviour. In the examples that follow, we will at times simultaneously ignore all viscous contributions to Eq. 1 and yet still seek physical explanations that depend on viscosity. The experimental domain is comparatively simple for PIV

studies—there are no significant compressibility effects and no Brownian motions at small scale to worry about. Measurement success instead usually hinges on the degree to which time-varying and/or three-dimensional flow fields can be appropriately simplified. As we shall see, this is even true for a rigid, fixed, nominally two-dimensional airfoil, which can easily be shown to induce a three-dimensional, time-varying velocity field.

While the value of *Re* determines the relative magnitude of the terms in the governing Eq. 1, and its descendents, the PIV methods and principles outlined here apply rather the same from fruit flies to geese (or models thereof).

In the search for appropriate simplifications, the momentum equation can be re-expressed in various ways. For example, Eq. 1 can be written

$$\frac{\partial}{\partial t}\int (\rho \mathbf{u})\,\mathrm{d}V + \int (\rho \mathbf{u}.dS)\,\mathbf{u} = \int \rho \mathbf{g}\,\mathrm{d}V - \int p\,\mathbf{dS} + \int \mu \nabla^2 \mathbf{u}\,\mathrm{d}V, \tag{2}$$

where the integrals are taken over a volume V enclosed by a surface S. The interest in these integral forms is that momentum fluxes in one part of the fluid can be calculated given conditions in another part, without needing to know details of the flow in between. This forms the basis for control volume methods and the force balance estimation that appears later. From an experimental point of view, we may note that integral quantities can frequently be estimated more robustly than derivatives.

Taking the curl of both sides of Eq. 1, gives the vorticity equation

$$\frac{D\boldsymbol{\omega}}{Dt} = \boldsymbol{\omega}.\nabla \mathbf{u} + \nu \nabla^2 \boldsymbol{\omega}, \tag{3}$$

where $\boldsymbol{\omega} = \nabla \times \mathbf{u}$ is the vorticity, and writing the equation in this form is interesting for at least two reasons. First, the pressure does not appear in Eq. 3, and it is only viscous shear stresses (and not the normal stresses) that can modify the angular momentum of a fluid element. Second, for moderate- to high Reynolds number, it can be convenient to describe the flow field in terms of the vorticity distribution, since in the inviscid limit there are conservation laws governing the behaviour of vortex elements. In particular, if the circulation, Γ, around a closed material curve is written

$$\Gamma(t) = \oint \mathbf{u}.\mathbf{dS}, \tag{4}$$

then Kelvin's circulation theorem shows that Γ is constant:

$$\frac{\mathrm{d}\Gamma(t)}{\mathrm{d}t} = 0. \tag{5}$$

If the closed integration curve bounds a material surface, S, then

$$\frac{\mathrm{d}}{\mathrm{d}t}\int \boldsymbol{\omega}.\mathbf{dS} = 0, \tag{6}$$

and a vortex tube within S has constant strength and moves with the fluid. The convenience of these representations encourages measurement and analysis of flow fields in terms of the vorticity field, with the added experimental advantage that once again Eq. 4 is an integral measure, which can in principle be robustly measured, provided that the appropriate surface S can be identified.

1.2 Characteristics and limits of PIV

Particle Imaging Velocimetry (PIV) methods are concerned with measuring both displacement fields and their spatial gradients, and close attention must be paid to the likely errors in estimating both in any given experiment. Here we summarize (and simplify) arguments advanced in Fincham and Spedding (1997) concerning the limits in PIV. For any PIV algorithm, there will be a fundamental lower limit in resolution of small displacements, D. This lower limit is almost always set by the severity of peak-locking errors in a given practical experiment (as opposed to an idealized numerical simulation). Peak-locking is the tendency of a correlation extremum to be resolved close to an integer number of discretisation steps. It has been discussed in Fincham and Spedding (1997), Westerweel (1997), Westerweel 2000), Prasad et al. (1992), Nogueria et al. (2001), Chen and Katz (2005) and Cholemari (2007), amongst others. A reasonable algorithm ought to be able to resolve displacements of better than 0.02 pixels. Since the algorithm error is fixed in pixels (it does not vary with D), and if the maximum tolerable (or claimed) error is 10%, then the minimum resolvable displacement $D_{\min} = 0.2$ pixels. To measure a broad range of scales, one then searches for the largest possible $D_{\max}$, set by

$$D_{\max} = u_{\max}\delta t, \tag{7}$$

where δt is the PIV exposure time between successive images. $u_{\max}$ is set by the flow and the only remaining control variable is δt. However, increasing δt also increases the local shearing deformation as

$$S = \omega \delta t. \tag{8}$$

It is for this reason that codes including box deformation (e.g. Huang et al. 1993; Scarano and Riethmuller 1999; Fincham and Delerce 2000; Scarano 2002) can offer significant practical improvements in performance (as recently confirmed by Stanislas et al. 2008). Further practical limits on δt derive partly from curvature of local pathlines which leads to significant and systematic errors in velocity estimation, and partly because very few flows are simple enough to confine their motions to a light

sheet, or light slab, for long times. (This discussion assumes simple PIV experiments, where displacements are observed within a plane. The use of 3D or stereoscopic methods modifies this latter argument.) Finally, increasing D_{max} leads inevitably to reduced spatial resolution because the result is an average over D_{max}, and reduced temporal resolution as accelerations over δt are lost.

As a very rough rule of thumb, we can suppose that the sum of these effects can be expressed conservatively as a constraint that $D_{max} = 5$ pixels. If $D_{min} = 0.2$ pixels, the bandwidth of measurable velocities within 10% uncertainty is 25. The arguments leading to this number are approximate, and numerical details can be modified by advances in technique (box deformation, multipass analysis algorithms, multiscale acquisition procedures) but the basic principles apply quite generally. In a general review, Adrian (2005) notes that due to the low dynamic range, most PIV investigations are primarily exercises in optimization.

Because the bandwidth is low (compared with LDA or hot-wire measurements, for example), and limited on the D_{min} side by algorithm errors, the strong interest in development of more sophisticated fundamental PIV algorithms persists, more than 15 years after the first digital PIV techniques were described (Utami and Blackwelder 1991; Willert and Gharib 1991). In any given system, the constraints on D_{max} and S_{max} in determining u_{max} and ω_{max} in Eqs. 7 and 8 require a very careful selection of δt. Finally, a meaningful measurement of velocity or gradient fields requires a sound quantitative knowledge of the likely measurement error and its distribution.

1.3 Objectives

The purpose of this paper is to illustrate the experimental estimation of terms in the various forms of the momentum equations, using appropriate PIV methods. Whilst all examples given will use the correlation imaging velocimetry (CIV) algorithms described in Fincham and Spedding (1997) and Fincham and Delerce (2000), the lessons and limitations are general and apply to all PIV measurement schemes. Two types of experiment/measurement are considered. The first involves an application of control volume methods suggested by Eq. 2 for an ostensibly simple flow—steady uniform flow over a flat plate, fixed at various angles of incidence. The analysis is guided by quite strong approximations from aerodynamic theory and estimated forces from PIV analysis can be compared with those measured directly by a force balance. The second example is much more complicated—in principle. We wish to make quantitative measurements of the disturbances in the wake of an animal in flapping flight. The integral momentum Eq. 2 again provides the framework for inferring average forces on the complex, time varying wing shapes by analysis of the far wake. The wake itself is described by its vorticity field, and by using circulation measures of the total strength of simple geometric approximations of the wake structure, force balance calculations can again be attempted. The results shed some light on future research strategies and on the correctness of the modeling approximations used in the analysis.

2 Control volume methods

2.1 Calculating drag from the time-averaged wake momentum defect

The calculation of the drag on a solid body immersed in a uniform flow field by estimating the momentum defect magnitude in the wake appears to have been first considered carefully by Betz (1925), which formed the basis for the treatment by Prandtl and Tietjens (1934). The principles can be found in any fluid mechanics textbook (e.g. White 2008) and are summarized here to clarify the assumptions and relation to the equations of motion given in the Introduction.

Figure 1 shows an airfoil section in a constant uniform flow, $u_1(z) = U_0$. A control volume, V, is defined by enclosing the airfoil within a streamtube with surface contour S. If viscous forces are neglected, then Eq. 2 becomes

$$\frac{\partial}{\partial t}\int (\rho \mathbf{u})\,\mathrm{d}V + \int (\rho \mathbf{u}.\mathbf{dS})\mathbf{u} = -\int p\,\mathbf{dS} - \mathbf{R}, \qquad (9)$$

where $\mathbf{R}$ is the resultant force exerted on the control surface by the normal and shear stresses acting at the airfoil surface. If the flow is further assumed to be steady, and if S is taken sufficiently far from the airfoil so that the pressure there is equal to the constant, undisturbed freestream pressure, p_0, then Eq. 9 reduces to

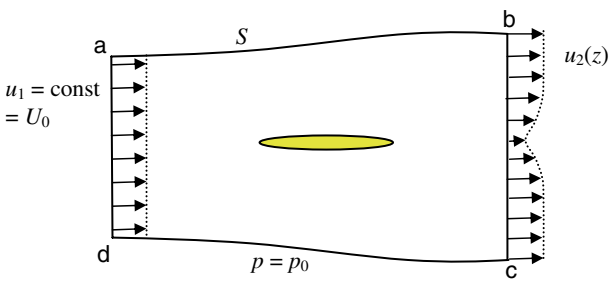

Fig. 1 Control volume around a solid body in a uniform freestream. A constant uniform flow, u_1 appears through the face *ad*, and the streamtube, *S*, that surrounds this flow is cut at face *bc* behind the body. The force on the body is equal to the change in momentum flux between $u_2(z)$ at *bc* and uniform u_1 at *ad*. The pressure, *p*, on the streamtube boundary is equal to the undisturbed pressure, p_0

$$\mathbf{R} = -\int (\rho \mathbf{u}.dS)\,\mathbf{u}. \tag{10}$$

If we consider only the streamwise component of the force, the drag per unit span (the control volume V has unit span in the out-of-plane direction), D' is

$$D' = -\int (\rho \mathbf{u}.dS)\,u. \tag{11}$$

Because S lies along streamlines in the flow, the only contribution to the momentum flux is from the flow in through the front surface and the flow out through the rear surface, and the integral in Eq. 11 is

$$\int (\rho \mathbf{u}.dS)\,u = -\int_d^a \rho_1 u_1^2 \mathrm{d}z + \int_c^b \rho_2 u_2^2 \mathrm{d}z. \tag{12}$$

When $u_1 = U_0$ and ρ are constant, the total (positive) drag of a body with span b can be expressed as

$$D = \rho U_0^2 b\theta, \tag{13}$$

where the momentum integral,

$$\theta = \int_c^b \left(\frac{u_2}{U_0} - \left(\frac{u_2}{U_0}\right)^2\right) \mathrm{d}z \tag{14}$$

has units of length. If a drag coefficient C_D is defined as D/qS, where q is the dynamic pressure, then

$$C_D = \frac{2\theta}{c} \tag{15}$$

for a wing of chord c and planform area $S = bc$. Equation 14 is simple to evaluate in an experiment, involving only the integration of profiles of the streamwise velocity.

2.2 Estimating the drag of a fixed wing at moderate *Re*

Estimating the fluid dynamic drag on objects at moderate *Re* in the range 10^4–10^5 is of particular interest because of recent developments in small-scale flying devices. The forces involved can be small ($\sim$1 mN) and the flow is easily disrupted by the presence of measuring devices. The following is an example of the simplest possible aerodynamic drag measurement, on a flat plate. The PIV-derived results can be compared with force balance data and with theoretical predictions for a laminar boundary layer.

2.2.1 Steady drag from PIV wake data

Figure 2 shows the flow behind a flat plate at $Re_\mathrm{c} = 11{,}700$ (Re_c is based on chord length, c. It is the default definition here and subscript c will be dropped unless required.), and $\alpha = 5°$ which is the angle of maximum lift to drag ratio (L/D). The flow is shown at midspan and the plate is bounded by vertical end plates aligned with the freestream. The trailing edge of the flat plate is immediately to the left of the picture. $\omega_\mathrm{y}(x, z)$ is mapped onto a discrete ten-step colorbar, which matches the likely uncertainty in its determination so measurement errors will not be seen beyond isolated single-color patches. The number of vectors per coherent structure is not large (5–10 per length scale, l_cs), and the CIV algorithms were tuned to recover the peak vorticity and velocity peaks in the wake with small deforming correlation boxes. (The correlation box size, B, was reduced in incremental steps to 12 pixels on a side. In CIV, B is independent of any search box scale, S, but B cannot be reduced without limit as the pixel information content decreases with B^2. See Fincham and Spedding (1997) for basic details and Fincham and Delerce (2000) for the removal of shear-generated box deformation as a significant source of error for small B.) The small box size comes at the expense of increased amplitude peak-locking errors in the far field, but they do not exceed the $0.1|\Delta\omega|$ colourbar stepsize (by design). The wake is not steady and uniform, but is composed of coherent patches of vorticity, which interact and decrease in amplitude with increasing downstream distance. The 5-second time average in Fig. 2b shows a smooth wake profile with significantly lower amplitude than the instantaneous field.

The box covering the right side of Fig. 2b shows a region within which mean (row-averaged) velocity profiles were made for all angles of attack and three are shown in Fig. 3, corresponding to the zero-lift ($\alpha = 0$) condition, $(L/D)_\mathrm{max}$ and $\alpha = 10°$, which is significantly beyond stall, which is abrupt for this shape at this *Re*. The profiles in Fig. 3 represent the mean momentum defect in the flow due to the presence of the airfoil. As noted in the caption, the profiles have actually been computed as difference profiles, so the far field values fluctuate around $u_\mathrm{X} = 0$. Now θ, the momentum integral can be evaluated in each to estimate the x-component of the force. The lift can be seen directly as a deflection of the profiles, which is maximum in this plot at $(L/D)_\mathrm{max}$. From the PIV processing point of view, the $\alpha = 0°$ profile has only 13 points across it, and estimating its correct magnitude is of great importance. Again, processing parameters are set so to minimising the likely error in resolving the velocity peak and its gradients, but with the side-effect that small ripples in the tails of the distribution can be observed. The tails have zero mean value however, and make no net contribution to θ.

If the flow were perfectly steady and two dimensional, then the momentum flux could be calculated at any plane through Fig. 2b, and an alternative to constructing profiles that are averaged over both space and time is to take any one of the time-averaged profiles at all x locations and calculate θ on each one. The result is shown in Fig. 4. The curves of $\theta(x)$ in Fig. 4 are flat at small α, and then as α

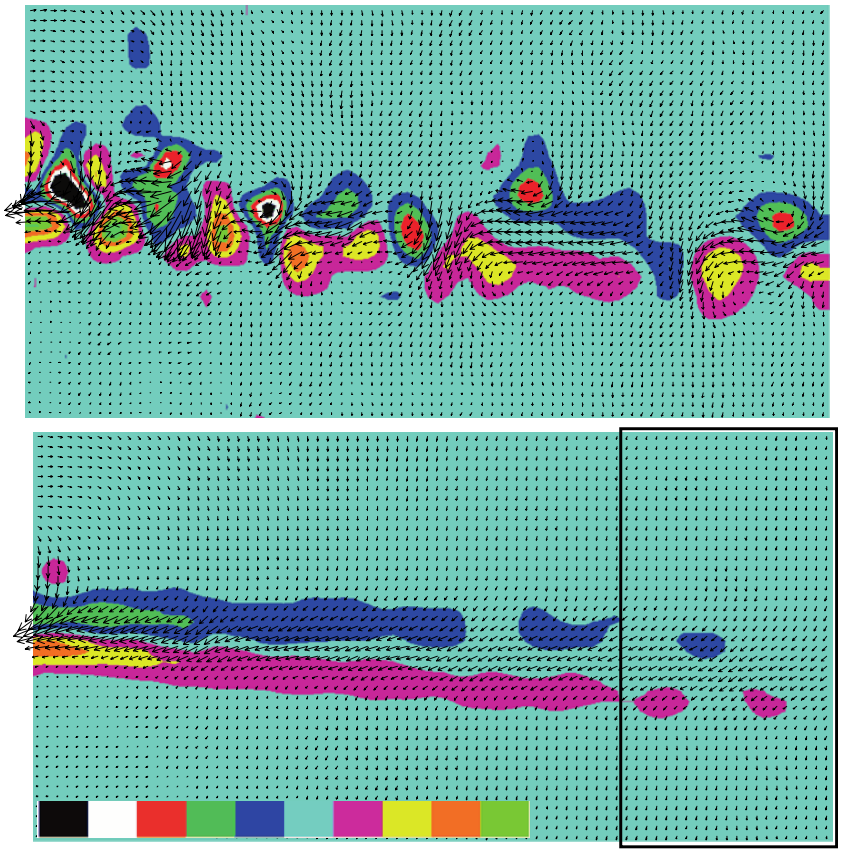

Fig. 2 Spanwise vorticity, $\omega_y(x, z)$ in the wake of a 2D flat plate. $Re = 11{,}700$, $\alpha = 5°$. The *top panel* (**a**) shows an instantaneous view, and the bottom panel (**b**) is a 5 s time-average. $\omega_y(x, z)$ is mapped onto a ten step colour bar (*inset*) from $-5U/c$ to $+5U/c$. The box covering the rightmost quarter of $\{x, z\}$ shows the region where mean profiles in Fig. 3 are calculated. The field of view, $\{\Delta X, \Delta Z\} = 3.2c \times 1.6c$. The *arrows* show the magnitude of the disturbance velocity field (with the mean inflow velocity subtracted) scaled to 16 times the displacement vector of the original CIV calculation

increases, vary significantly with x until they stabilize at $x/c \geq 2$. The systematic variations for small x/c are due to the neglect of the pressure fluctuations in the step from Eqs. 9–10 and the fluctuations on each single profile of $\theta(x/c)$ are due to the unsteadiness of the shedding at the trailing edge. Each single profile cuts through a different section of wake vorticity. Only when the pressure gradients have dropped to small values do the momentum fluxes appear exclusively as differences in the velocity. Fig. 4 suggests that consistent values of C_D require $x/c \geq 2$, and that they will be then independent of x, at least up to $x = 3.2c$. This criterion applies equally to fixed wings and flapping animal flight, as it is unlikely that pressure fluctuations in near wakes of flapping wings will be below those of fixed wings at moderate α. $C_D(\alpha)$ calculated from the PIV-derived wake defect profiles (Fig. 5) shows that the PIV-based measurements agree well with the force balance data for the same aerofoil. The standard deviations in either dataset come from the variation in repeated measurements and are usually smaller than the symbol size. $C_D(\alpha)$ close to $\alpha = 0$ is almost flat.

The analytical result for the total skin friction coefficient of a Blasius laminar profile on a two-sided flat plate is (e.g. Anderson 2001)

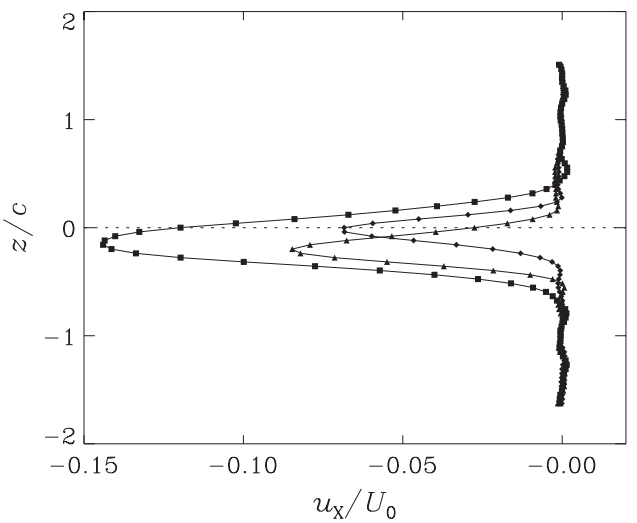

Fig. 3 Mean streamwise disturbance velocity profiles behind the flat plate of Fig. 2 for $\alpha = 0$, 5, 10° shown by *diamond*, *triangle* and *squares*. Here $u_x(z) = u_{xx}(z) - u_i(z)$, where $u_{xx}(z)$ is the row-averaged streamwise velocity, and $u_i(z)$ is interpolated from a third order polynomial derived from the tails of the distribution only ($z/c \leq -1$ and $z/c \geq +0.5$). $u_i(z)$ is therefore a smooth profile that reflects the acceleration of the mean flow due to blockage effects, and it is assumed that the defect profile rides on top of this baseline. U_0 is the uniform inflow, unaffected by the presence of the airfoil

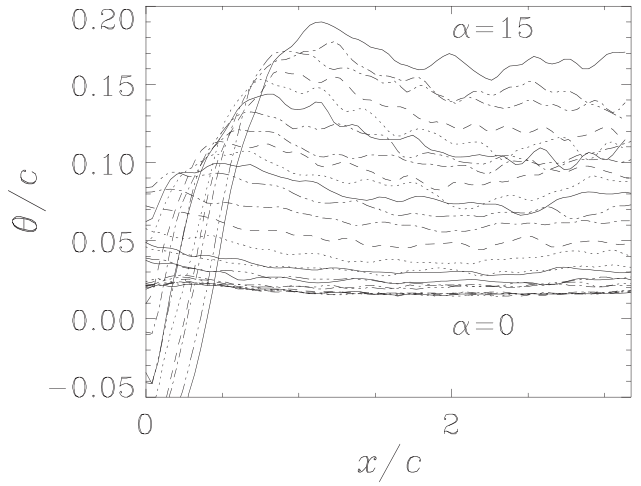

Fig. 4 Equation 14 evaluated with $u_2 = u_X$ from Fig. 3 at different downstream locations behind the flat plate for $\alpha = [-5, 20]$ in 1° increments. The inflow boundary is always assumed to have uniform speed U_0. For $x/c > 2$, θ/c increases monotonically with $|\alpha|$

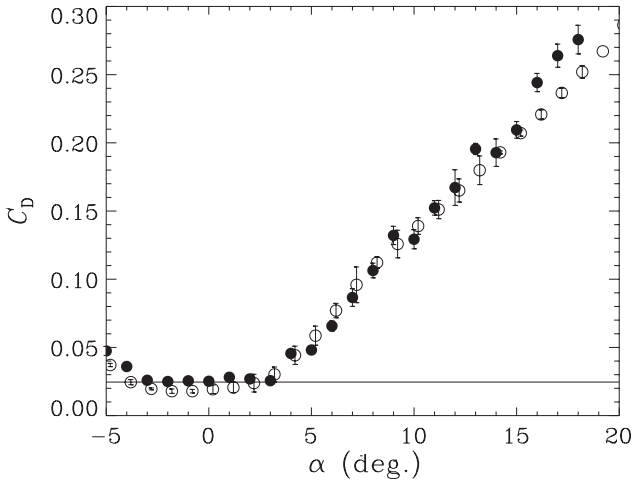

Fig. 5 Profile drag coefficient measured from PIV experiment (*filled circles*) and the total drag from force balance measurements (*open circles*) as functions of α. C_D is calculated from Eq. 15 where θ comes from a streamwise average over $x/c \in [2, 3.2]$. The horizontal line comes from Eq. 16 for the laminar skin friction over a flat plate

$$C_F = \frac{2.656}{\sqrt{Re_L}}, \tag{16}$$

where Re_L is the Reynolds number based on plate length (so Re_L is based on c). Eq. 16 evaluates to $C_F = 0.0246$ (shown by the horizontal line in Fig. 5). The measured value is $C_D(0) = 0.025 \pm 0.002$, which is the same within experimental uncertainty.

The agreement between PIV measurement and force balance data is a little surprising at large α, when the flowfield is very disorganized and the very large and fluctuating pressure drag component, together with the strongly three-dimensional motion, would combine to contradict many assumptions in deriving the simple expression for θ. Nevertheless, the time-averaged result of the unsteady force is correctly evaluated. Figure 5 shows that 3D corrections are negligible for the 2D flat plate. Strongly three-dimensional geometries and/or small aspect ratio flows may be less easy to summarise in just one measurement plane.

2.2.2 *Momentum and energy conservation in far wakes*

It is not uncommon in animal experiments for PIV data to be acquired significantly far downstream of the body, and so there is some interest in knowing how far downstream such force balance calculations can be extended. Equation 6 shows that the vorticity is a conserved quantity so it should make no difference. Similarly, Eqs. 5 and 4 show that circulation measurements will also be unaffected. These derivations assume that viscosity is unimportant, i.e. that Re is high. Saffman (1970, 1992)

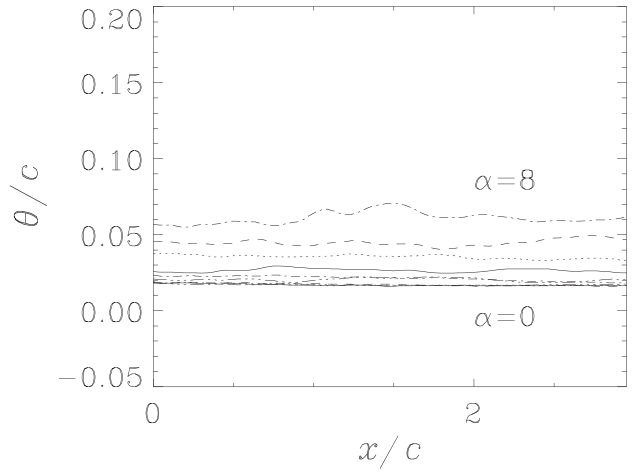

Fig. 6 Momentum integrals from profiles beginning at $x/c = 10$ for an $AR = 6$, rectangular planform flat plate wing from $\alpha = 0$ to $\alpha = 8°$

notes that viscous effects can be considered negligible in vortex rings and wing trailing vortices when the criterion $vt \ll r_0^2$ is satisfied, where r_0 is a vortex radius. Letting the time $t = x/U$, and setting an approximate length scale $r_0 = c$, we require that $x/c \ll Uc/v$. In animal flight experiments, typical x/c values (on the order of 10) are very much smaller than Re_c (on the order of 10^4), and so viscous dissipation should not be important. Indeed, Fig. 6 confirms that θ/c does not decrease significantly from $10 \leq x/c \leq 13$ and that equivalent α generate θ/c of approximately the same magnitude in both Figs. 4 and 6 (the linestyles change in the same order with increasing

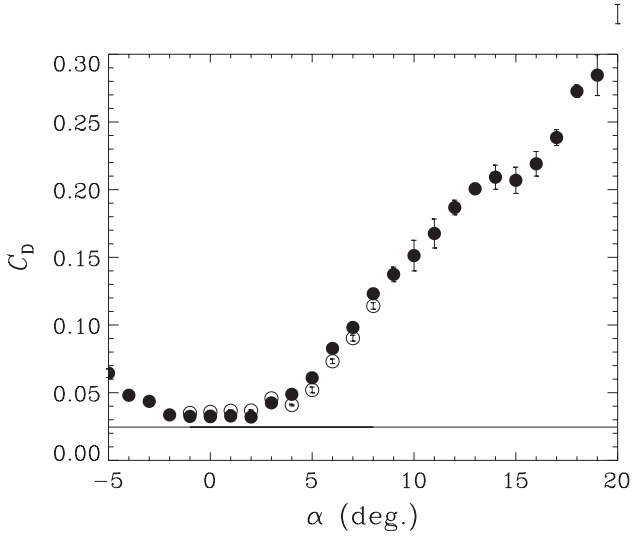

Fig. 7 Particle image velocimetry (*PIV*)-estimated profile drag from the near and far wake of the *AR*6 flat plate. The filled symbols are from streamwise-averaged velocity profiles between $2 \leq x/c \leq 3.2$. The *open symbols* come from profiles averaged over $10 \leq x/c \leq 13.2$. The *solid line* is the 2D flat plate analytical result and the experimental drag estimate is always higher (unlike in Fig. 5) because the $AR = 6$ plate has finite span. The $x = 10c$ data do not extend beyond $\alpha = 8°$

α). The equivalence is only approximate however, as the late wake data in Fig. 6 come from a finite aspect ratio plate ($AR = 6$). At high x/c the wake would be too strongly affected by growing boundary layers at either bounding walls or end-plates, and the latter would be very hard to manufacture, position and align with good accuracy. Thus the most fair comparison is for a finite wing. Figure 7 shows that the drag coefficients calculated from mean velocity profiles starting at $x/c = 10$ are the same as those calculated starting at $x/c = 2$.

2.2.3 PIV versus force balance

Provided the measurements occur sufficiently far downstream so that pressure fluctuations can be ignored, the force-balance and PIV-derived measurements agree very closely. The uncertainty in the wake measurements for C_D is approximately ± 0.002. If the effect of spanwise non-uniformity in the nominally two-dimensional flow field is included (which could be compensated for if other measurement planes were included in the analysis) then a reasonable estimate is that $\Delta C_D = 0.005$, which corresponds to $\Delta D = 0.6$ mN. The force balance is a custom-design cruciform shape with 16 strain gauge elements on the four arms to give two translations and two rotations. The six element calibration matrix was constructed using static weights. When full scale range is ± 10 N, 14-bit ADCs yield a resolution of 1.2 mN. If the data are oversampled in the presence of random additive noise, then the estimation of averages can be improved to give a larger effective number of bits (ENOB, Kester 2006). Here, an oversample rate of 8,000 times yields ENOB = 18.5, when the resolution is ± 0.05 mN.

A force balance can be constructed and carefully tuned to robustly and accurately measure the total force on the mechanical system, but the system must include the physical attachment itself. PIV methods are non-intrusive and do not disturb the low-turbulence wind tunnel ambient. They allow the resolution of the forces into different components, but because the pressure is hard to estimate directly, and thin boundary layers are also difficult to resolve, then some simplifying physical assumption (e.g. spanwise uniformity, far fields where $\nabla p = 0$) is usually required.

2.3 Advanced PIV methods for measuring forces

The force estimate for a comparatively simple 2D geometry in a steady mean flow is not complicated, and Figs. 4, 5, 6 and 7 show that the results can be reliable in practice. More sophisticated measurements can take various forms. One is the tighter integration of measurement and theoretical modeling. For example, in classical aerodynamics, one may describe the total drag on an aerofoil as the sum of a profile drag and an induced drag, so

$$C_D = C_{D,pro} + C_{D,i}. \tag{17}$$

A force balance always measures C_D. The wake measurements of Fig. 5 and 7 measure $C_{D,pro}$, and the two are equal only in the particular case where $C_{D,i} = 0$ for a two dimensional wing between endplates. If the endplates are removed, $C_{D,i}$ can be estimated by subtraction. Note that there are differing definitions of this rather benign-looking equation that can cause considerable confusion. One common variant assigns to $C_{D,i}$ all of the drag that varies with α.

$C_{D,i}$ is caused by the downwash, w_i, on the wing which, for an elliptically-loaded wing of span b, is constant, and proportional to the bound circulation, Γ_0 (e.g. Anderson 2001),

$$w_i = \frac{-\Gamma_0}{2b}. \tag{18}$$

For small values of the induced angle of attack, α_i, one can write,

$$\alpha_i = \frac{-w_i}{U} = \frac{C_L}{\pi AR}, \tag{19}$$

where $AR = b/c$ is the wing aspect ratio, and so the lift coefficient can be calculated from w_i:

$$C_{\mathrm{L}} = -\frac{w_i AR\pi}{U}. \tag{20}$$

w_i at the wing is constant for an elliptic load distribution but PIV measurements can measure w_i across the wing length. In wing theory half of the induced downwash occurs at the wing and half again behind it, so measurements in the Trefftz (y, z) plane taken in the far wake will give estimates of $2w_i$, which can in turn be used to calculate the lift on the wing through Eq. 20. Spanwise distributions of $w_i(y)$ behind the hindwing of a tethered locust derived from multiple PIV sections in streamwise planes, taken at $x \approx b/2$, are shown in Bomphrey et al. (2006), but the integrated instantaneous lift of approximately ten times the body weight was not easily reconciled.

The relationships in Eq. 15 and (17–20) show how the lift and drag components of a wing in steady flow can be calculated from quite simple wake measurements, although Eq. 17 has some subtleties that are not immediately obvious. Meheut and Bailly (2008) have shown how quite different numerical results can come from example wake surveys that were simulated through a computed direct numerical simulation (DNS) through integration of a discretised Eq. 1 flowfield, depending on details of the physical assumptions behind Eq. 17 or equivalent.

Particle image velocimetry has also been used to estimate forces in more complex geometries and in time-varying flows. Re-arranging Eq. 9, the force $\mathbf{R}$ on a body immersed in an inviscid fluid is

$$\mathbf{R} = -\frac{\partial}{\partial t}\int (\rho \mathbf{u})\,\mathrm{d}V - \int (\rho \mathbf{u}.dS)\mathbf{u} - \int p dS, \tag{21}$$

and so can be computed given a time-resolved velocity field inside a control volume and a pressure distribution at the volume surface. The pressure can be estimated from the velocity field, so neglecting viscous terms in Eq. 1 for convenience (this is not a necessary step),

$$-\nabla p = \rho \frac{\partial \mathbf{u}}{\partial t} + \rho(\mathbf{u}.\nabla)\mathbf{u} \tag{22}$$

and the pressure field is calculated by integration from some known boundary condition. Lin and Rockwell (1996) and Noca et al. (1999) have used time-resolved PIV fields using control volume methods with different techniques for estimating the pressure. The PIV requirements are quite stringent, because both velocity gradients and accelerations in Eqs. 22 and 21 must be calculated to good accuracy. We note that the examples given here have side-stepped all problems arising in resolving velocities and their gradients close to solid (possible moving and deforming) boundaries, by concentrating exclusively on far wake measurements, where the pressure gradients in Eq. 22 are small.

By contrast, Van Oudheusden et al. (2007) made time-averaged force estimates by calculating all the required terms in the momentum equation from velocity and pressure gradient fields where time-averaged pressure gradients were calculated from velocity and Reynolds stress gradients. The agreement with direct force measurement on a 2D square cylinder in a steady uniform flow was reasonable. They also measured mean lift and drag coefficients on a NACA 642A015 section at $Re = 3 \times 10^3$ and obtained better agreement in drag measurements when a single wake transect formed the basis of pressure and velocity measurements than when an exterior contour was used to calculate a form of Eq. 21.

Since animals have no rotating machinery at the macroscale (the plumbing required to support living tissue would be difficult to arrange), they have no continuously rotating propellers or turbines, and their locomotory force generators always involve reciprocal cyclical motion of propulsive elements. This means that the fluid motions and associated forces are always time varying—it is simply a question of the relative magnitude of the $\partial/\partial t.$ term in Eq. 21, for example. There are two consequences of this: first, it may be very difficult to choose an appropriate control volume in animal studies. Having highly trained, repeatable motion, without net acceleration over one periodic propulsive cycle (if such behaviour exists) certainly helps, but the far-field boundary conditions may still not be easy to verify, and one need only look at the engineering examples given in the preceding paragraphs to appreciate the complexity already offered by a fixed, non deformable bluff body in steady flow.

The second complication that comes from the unsteady motion is that although the vorticity equation (3) successfully eliminates the pressure, the nonzero unsteady term can be shown (Saffman 1992) to lead to the following relationship between the force $\mathbf{R}$, and the vorticity, $\boldsymbol{\omega}$:

$$\mathbf{R} = \rho \frac{\partial}{\partial t}\int \mathbf{x} \times \boldsymbol{\omega}\,\mathrm{d}V + \rho \frac{\partial}{\partial t}\int \phi \mathbf{n}\,\mathrm{d}\mathbf{S}. \tag{23}$$

$\mathbf{x}$ is a position vector, $\mathbf{n}$ is the surface normal to S, and ϕ is the velocity potential. The force now depends on the acceleration of a potential flow (second term on rhs of Eq. 23), as well as the strength of vortex elements in the flow (first term). If a vortex element is immersed in an unsteady potential flow field then there will be an extra force that acts like an added mass on the vortex element itself, and it is not necessarily sufficient to calculate forces from flow fields that are derived, either implicitly or explicitly, from the vorticity field alone. Dabiri (2005) first explained this in the context of animal swimming and flying and proposed a wake vortex ratio, R_{wv}, (subsequently corrected and modified in Dabiri et al 2006, Appendix) that essentially depends on the ratio of the

velocity increment of the accelerating background potential flow to the self-induced translational velocity of a vortex element. In far wake studies of bird flight R_{wv} has too small a value to merit the inclusion of vortex added mass terms (e.g. Hedenström et al. 2006), but this is likely not the case in near wakes with significant unsteadiness. The proper resolution of the fluid accelerations then will require time-resolved PIV data.

The combination of time-resolved PIV and integrated theoretical models shows great promise in accurate and non-intrusive measurement of instantaneous forces on bodies in homogeneous fluids.

3 Flight of birds and bats

We have noted above how theoretical models can guide applications of PIV measurement plans to estimate time-averaged and instantaneous forces without interference in the flow itself. Here we show two examples where such advantages are prerequisites, in the study of the free flight of birds and bats. The examples will show ways in which common aerodynamic assumptions can be used to estimate wing properties from measurements that are reasonable given the measurement uncertainty. We emphasise the PIV constraints in running such experiments to show general principles.

A number of birds and bats have been studied in the Lund University wind tunnel, and a recent review of the experiments can be found in Hedenström and Spedding (2008). Here we show two contrasting examples.

3.1 Swifts

3.1.1 The basic experiment

Swifts represent an extreme example of aerial specialization as they are thought to fly continuously, landing only to nest, from their first flight. Their flight involves flapping, gliding and sharp turns and their wings are rather rigid, with a characteristic crescent-moon planform that has long been known to be efficient in fish propulsion (Lighthill 1970). One fledgling swift was captured in its nest and made its first ever flight in the wind tunnel (Henningsson et al. 2008), learning quickly to fly reliably and repeatedly in the centre of the test section.

The closed-circuit, low turbulence wind tunnel was filled with fog particles of about 1 μm diameter, and the wake downstream of the flying bird was sampled in vertical streamwise planes at various points in the spanwise direction. The sampling rate, limited by the Nd:Yag laser, was 10 Hz, which is comparable to the wingbeat frequency of 8–9 Hz. The small phase difference between successive wake samples can thus be used to assemble contiguous sequences of images that together sample one complete wake wavelength, as shown in Fig. 8.

Figure 8 shows that spanwise vorticity is shed continuously into the wake, with positive-signed vorticity being shed at the beginning of the downstroke, and mostly negative-signed vorticity during the upstroke. The transition between the two phases is gradual and consistent with a gradually increasing bound circulation on the wing (and lift) on the downstroke followed by a decreasing circulation on the upstroke. Since the changes in wake circulation can be quantified then these can be used to infer conditions on the wing (with the necessary condition of Kelvin's circulation theorem, Eq. 5) and to calculate a wake impulse, I, that must support the weight, W, of the swift over one period, T, of the wingbeat:

$$I_z = WT, \tag{24}$$

where the subscript z denotes the vertical component of the total impulse. Taking I_z over T in this way is correct if there are no net accelerations (in any direction) over one wingbeat. Data were only used when sequences of gradually changing wake phase showed that the vertical position was steady. The other two directions are harder to verify (although the swift position was monitored in synchronised video from a downstream camera), except that anomalies in the wake structure can always be seen

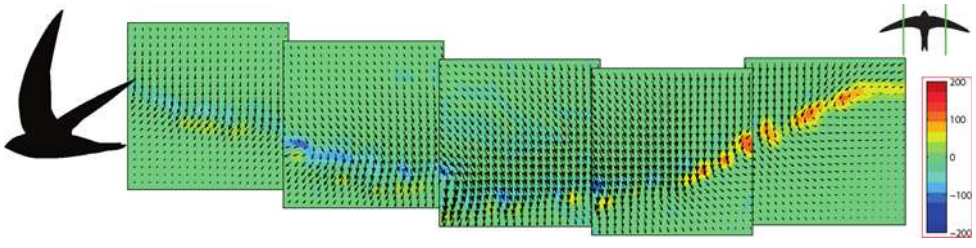

Fig. 8 A reconstruction of one wake wavelength from a swift in steady level flight at 8.4 m/s. The *colour map* shows the spanwise vorticity, which is zero, within experimental uncertainty, in most places. The thin undulating trail of nonzero vorticity approximately follows the wing trailing edge at that section (around mid-span—*inset*). The trailing vorticity does not aggregate into discrete clumps, changing only gradually from positive at the beginning of the downstroke (*upper right*) to negative at the beginning of the upstroke (*middle*). From Henningson et al. (2008)

before the signature of a significant wake/position variation is observed. Such anomalous sequences are never included in the statistics/analysis. The slow and predictable variation in wake phase over successive wingbeats acts as a very useful (and initially entirely unintentional) check on the steadiness of each flight sequence. The experiment was repeated over a number of spanwise locations, *nb*, and at each one, the wake was divided into a number of streamwise sections, $n\phi$. Then the wake impulse can be calculated from

$$I_z = \rho \sum_{i=1}^{n\phi} \sum_{j=1}^{nb} \Gamma_{ij} S_{ij}, \tag{25}$$

where the S and Γ are the projected areas and circulations of each wake panel. The time-averaged vertical force, $F_z = 0.43 \pm 0.13$ N, and the weight of the swift, $W = 0.38 \pm 0.05$ N. The two values are the same within experimental uncertainty.

3.1.2 Measurement uncertainty

The uncertainty in F_z comes from the variation of multiple wake panels from all measured flights. It includes contributions from the basic measurement uncertainty in Γ. Although the PIV processing parameters (particularly the correlation box size) were selected to correctly resolve velocity gradients, at the possible cost of incurring peak-locking errors, Γ is not affected by the peak-locking errors in low amplitude regions (like the tails of the distributions in Fig. 3) because it is a thresholded quantity. Note that an accurate estimate of the velocity gradients and derived quantities requires a careful choice of δt, within the constraints of Eqs. 7 and 8. δt is here tuned not to the mean flow, which is removed as a constant by shifting the entire correlation calculation, but to disturbance quantities about this mean. In this way the limited PIV bandwidth is used more fully. ΔF_z also depends on the variability of the bird flight patterns, and very rigorous and careful conditions are required so that these contributions do not dominate the measurement.

The PIV processing parameters together with the original experimental conditions that include δt, must be carefully chosen if distributions of $\omega_y(x, z)$ such as Fig. 8 are to be trusted. Since there is no error-free measurement, then the estimated field should be represented in discrete steps where the step size is related to the measurement uncertainty. Figure 8 does this, and it is worth enquiring whether the wake structure is similar to that expected behind more usual wing shapes at similar *Re*.

3.1.3 Comparison with fixed wings

Re_c of a swift in cruising flight is about 2.2×10^4, and Fig. 9 shows the wake behind a cambered, circular arc section for $Re = 1.2 \times 10^4$. The angle of attack, $\alpha = 5°$ where the cambered plate has a maximum $L/D = 6.8$. The near wake is composed of an ordered sequence of vortices that are more regular in appearance than for the flat plate in Fig. 2. While Fig. 9 shows the near wake up to about 1.5 chord lengths downstream of the trailing edge, the bird data are taken from $x/c = 10$ or more, and the comparatively compact regions of trailing vorticity there suggest that, like the cambered plate below stall in Fig. 9, there is most likely no large scale trailing edge separation on the wing. This would be expected, because the drag cost of having separation at the trailing edge would be high, with no obvious aerodynamic benefit.

Figure 9 shows that the steady flow past the cambered plate is attached (at least at large scale) over the entire

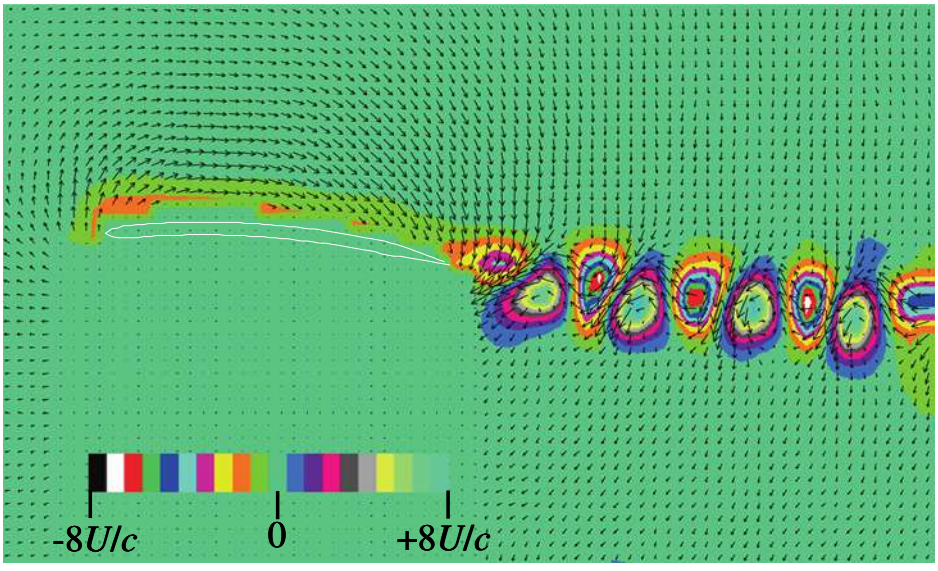

Fig. 9 The spanwise vorticity field, $\omega_y(x, z)$ around and behind a plate with 5% circular arc camber at $Re = 1.2 \times 10^4$ and $\alpha = 5°$. The mean flow, U, from left to right, has been removed. The field of view $\{\Delta X, \Delta Z\} = 2.6c \times 1.2c$

upper surface. That condition is not obvious from inspection of the free wake alone, and it is not clear either how to infer on-wing conditions from far wake measurements such as Fig. 8.

3.2 Bats

3.2.1 Measuring the instantaneous lift from the flowfield on the wing

Bats are known as specialists in manoeuvrable and slow-speed flight, and typically have lower wing loading than similar-sized birds (Norberg 1990). Their wings are composed of an elastic membrane composed of muscle fibres and a supporting collagen matrix, which is stretched between elongated bones that are derived from fingers. The aerodynamic consequences of these differences in wing shape and structure have long been of interest, both to biologists and to engineers contemplating biomimetic designs. Moreover, the role of wing flexibility is of fundamental interest in flapping flight.

Bats have also been investigated in the Lund wind tunnel and intricate patterns in the far wake have suggested (again indirectly, as for the swift) that certain details in the wing aerodynamics during the course of the wingbeat are significantly different from those seen for birds (Hedenström et al 2007). From the far-wake measurements it was unclear what the on-wing differences might be. The first measurements of the flow over the bat wing were made possible by a shroud that automatically masked the eyes of the bat when it came to feed at the nectar feeder (Muijres et al. 2008). This prevented high energy laser light from damaging the eyes. At one point in the wingbeat in slow forward flight ($\sim$1 m/s), the wing is held outstretched horizontally, roughly 2/3rd the way through the downstroke. At that moment, one can capture and analyse image pairs that show the flow field above the wing surface, much as in Fig. 9 for the cambered plate. Figure 10 shows the first image of a pair, where the bat and particle field have the PIV analysis grid superimposed. The grid is composed of calculation points, boundary points and masked points. The background bat image is reduced in amplitude by applying a high pass filter to the entire image. The CIV processing algorithms (Fincham and Spedding 1997; Fincham and Delerce 2000) calculate displacements at each grid node, and the node point is shifted by one half of the displacement. The now irregularly-spaced vector field is then re-interpolated back onto the original grid and the wing motion is used as boundary-value points for the smoothing spline interpolating functions. The objective is to resolve data as close to the moving wing boundary as possible. Details of the performance analysis are beyond the scope of this review, but an example result is shown in Fig. 11. The original data points shown by crosses are approximated by the continuous line spline functions, whose end conditions are set by the wing motion. The spanwise vorticity,

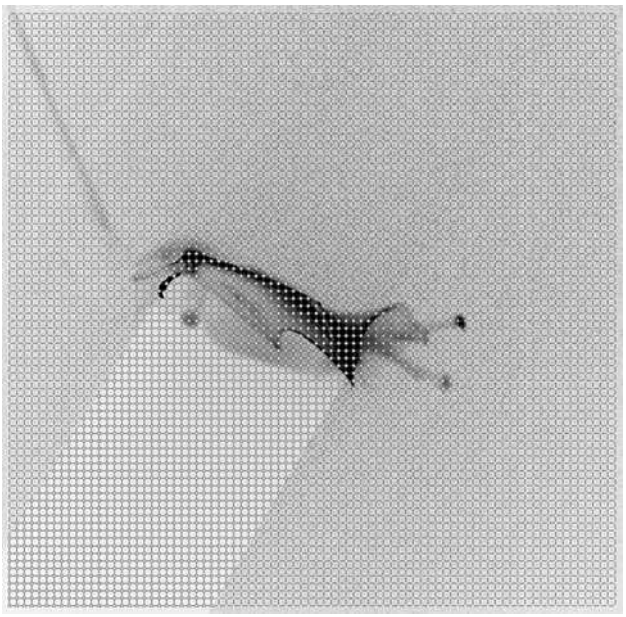

Fig. 10 Inverted grey-scale image of bat and particle field, with PIV analysis grid superimposed. Masked points are shown by *squares* at the grid nodes. Motion of the upper wing surface is calculated to provide boundary conditions to final smoothing spline interpolation back onto this analysis grid

$$\omega_y(x,z) = \partial w/\partial x - \partial u/\partial z,$$

is determined largely by the large positive values of $\partial u/\partial z$ shown in Fig. 11. A large blob of negative (clockwise rotation) spanwise vorticity lies attached to the upper wing surface (as shown by Muijres et al. 2008), and the strongest gradients in $\partial u/\partial z$ occur above the left third of the wing. The local flow above the membrane is reversed, as shown by the bold symbols. The reversal is due to the influence of the LEV, and to the motion of the wing surface itself, which sweeps from right to left in the wind-tunnel fixed reference frame. The no-slip condition causes the boundary shear profiles, which develop into the near-wake drag defects to the lower right. As the wing accelerates downwards, it also pitches clockwise by rotation about the leading edge, increasing the geometric angle of attack.

3.2.2 An aerodynamic analysis of the LEV

The aerodynamic effect of the leading edge vortex can be estimated in an approach similar to that pioneered by Polhamus (1971) for separation vortices on delta wings. In the bat experiments, the circulation of the trailing vorticity, Γ_{TEV}, is used as a measure of the total wing circulation,

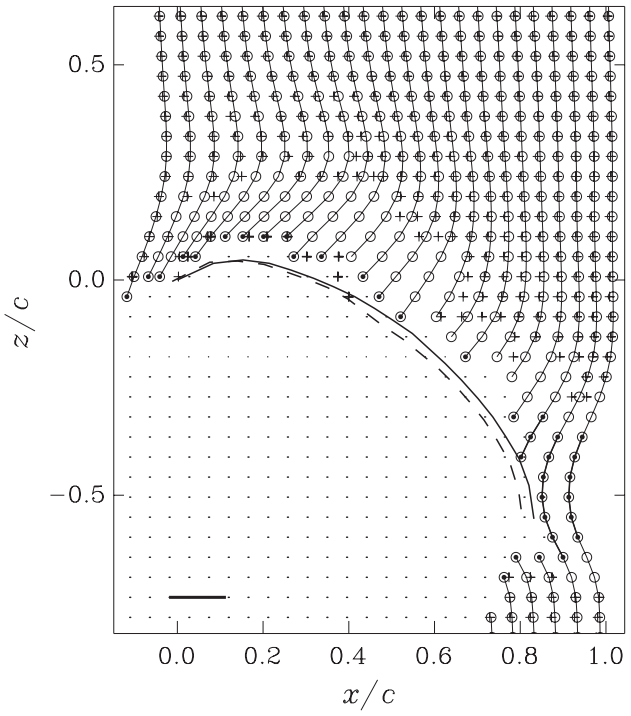

Fig. 11 Velocity profiles above the wing. The original data are shown by *crosses*. The interpolated points are shown by *circles* and *continuous lines*. *Lines* and/or *symbols* are drawn in *bold* when they denote negative velocities (from *right to left*). Displacement profiles are magnified ×5. The *horizontal scale bar at bottom left* shows a 5 m/s displacement, also magnified by ×5. The wing boundary coordinates are shown in straight-line segments for the first image and by *dashed line* for the second. The wing displacement is not magnified. All *continuous lines* are straight line segments between data points, with no curve fitting

Γ_{tot}, which is composed of two parts, the circulation of the leading edge vortex, Γ_{LEV}, which can be estimated, and the strength of the bound wing circulation Γ_{pot}, which cannot be measured directly (because it would require resolution of the velocity field and its gradients in the boundary layer all around the wing section contour), but is calculated by subtraction so that

$$\Gamma_{\text{tot}} = -\Gamma_{\text{TEV}} = \Gamma_{\text{LEV}} + \Gamma_{\text{pot}}. \tag{26}$$

The net effect, as explained in Muijres et al. (2008), is that the attached leading edge vortex increases the lift by 40%.

It was not possible to deduce this on-wing result based solely on the far-wake data of previous studies, but as Dickinson (2008) notes, the existence of a large-scale LEV on the bat wing is not that surprising given previous observations of thin wings of hawkmoths at the same *Re* (approximately 5,000) by Willmott et al (1997) and Bomphrey et al. (2005). The Strouhal number, $St = fA/U$, where f is the wingbeat frequency and A is the tip-to-tip wingbeat amplitude, lay between 0.3 and 1.3 in the hawkmoth experiments. For the bats at $U = 1$ m/s, it is 1.36. Note however, that the smoke trails of Willmott et al. and the PIV-derived results of Bomphrey et al. came from tethered animals; while there are few animal welfare requirements for invertebrates, it can also be difficult to encourage repeatable flight behaviour patterns.

4 Extensions and variations

In some respects the experiments described above are quite limited in technical ambition—they all derive from measurements of two velocity components in a plane (or rather a slab). This does not limit their application to two dimensional flows, because predictions, tests and measurements can be made in specific slices through arbitrarily complex three dimensional flows. The selection and prediction of quantities relies on the integrated theoretical models that guide the measurement strategy. Yet, as technological improvements accumulate, we may expect to see more examples of more sophisticated measurement of velocity and pressure fields and their associated forces. For example, Hedenström et al. (2008, in this volume) show time-resolved sequences of three-component stereo data that can be used to sample wake structures as they convect past a fixed measuring window in a mean flow. When such measurements can be combined with fine resolution close to solid boundaries (e.g. Fig. 11), then the previously-noted analyses of Noca et al. (1999) and van Oudheusden et al. (2007) can be extended to more complex, time-varying flows, past deformable boundaries. The application to animal flight investigations is obvious. We may also note the developments in combined computer simulations and simple experimental modelling of mechanical flapping wings, noting the recent work by Wang et al. (2004) and Kurtulus et al. (2008) as examples of a rapidly expanding literature.

The term vortex structure has been used rather loosely here as a shorthand for some clump of above-average amplitude vorticity. There are many more rigorous ways of defining an object that can be called a vortex (here we have simply referred to vorticity whenever possible). These include the various invariants of the velocity gradient tensor, such as the Q-criterion (Hunt et al. 1988) and a measure of the swirl strength (Zhou et al. 1999). Other variations have been proposed, for example by Jeong and Hussein (1995) and Chakraborty et al. (2005). Generally these methods then apply some kind of threshold criterion to state when a vortex is, or is not present. That criterion may be more or less subjective.

Although it is quite straightforward to apply these measures to PIV-generated data, the limited resolution (either in space, or in time, or both) means that the true complexity of small-scale structures is often greatly underestimated by PIV data. PIV investigations can very

usefully be combined with qualitative methods such as smoke or dye visualisation so that the particular subset of features visible in PIV can be placed in context. Bomphrey (2006) gives a comprehensive review of application of these methods in insect flight studies, and both the PIV and smoke trails illuminate different aspects.

The interpretation of smoke or dye trails is not completely straightforward, however, and in time-varying flows, they do not mark an instantaneous streamline, but represent a time history of particles that have passed the seeding point, or points. Classifications of smoke trails and instantaneous streamlines by critical points (Perry et al. 1980) and more rigorous identification in reduced forms of the velocity field (Chong et al. 1990) have been introduced, but most often smoke and dye visualisations are most useful for detailed, but qualitative information.

All of the above methods use an Eulerian description of the velocity field, and Haller (2005) has made the case that a more useful object in the flow might be the Lagrangian coherent structure (LCS), whose boundaries are determined by the rate of expansion of local fluid particles, as measured by a direct Lyapunov exponent (DLE). The DLE can be calculated quite readily from time-resolved PIV sequences, as noted in principle by Haller (2002), and the ridges or boundaries of high DLE separate significantly different parts of the flow (Shadden et al. 2005). Example descriptions of flow fields, including that of jellyfish locomotion, in these terms from time-resolved PIV data are given in Shadden et al. (2006) and Peng and Dabiri (2007). Green et al. (2007) apply the techniques to DNS of three dimensional fluid turbulence and Cardwell and Mohseni (2008) show an application to DNS data of the flow over a two dimensional Eppler 387 airfoil at fixed angle of attack at $Re = 6 \times 10^4$.

The continuing development of sophisticated analysis techniques that match the technology developments in lasers and digital cameras are signs of a very interesting near future.

5 Conclusions

The swift and bat studies reviewed above might best be regarded as combined experimental and theoretical studies, since the meaning or significance of the flowfield measurements can only be derived by combining with a theoretical model of some kind. Most PIV studies can in fact be regarded this way, as it is only when the numerous velocity vector fields can be placed in some predictive/theoretical context that they become something more than qualitative flow markers.

Particle image velocimetry measurement bandwidths are on the order of 100, which is low when compared with other velocity measurement techniques. The likely lower bound of the error in velocity measurement is usually a fixed multiple of the discrete sensor grid, and so cannot be expressed as a constant fraction of u_{obs}, but common estimates of $\pm 1\%$ in $\mathbf{u}$ and $\pm 5\%$ in gradient quantities should be regarded as target ideals in very well-controlled experiments. The art then lies in making a robust analysis that is not affected by predictable measurement error, and integral measures often achieve this.

Combinations of the integral and differential forms of the momentum equations can be used to calculate time-averaged or instantaneous forces. Estimating the pressure field is often the most difficult task, one that can be sidestepped by working far enough from the disturbance that the pressure gradients are small. Most of the examples have been for slices or slabs taken through the flow field, but extension to three dimensions is mainly constrained by the technology as the analysis principles are the same.

As time-resolved and three-dimensional data become more readily available, the volume of data will grow very fast, but special care will still have to be taken for the correct estimation of gradient quantities, particularly near moving and deformable boundaries.

Acknowledgments This work is a review based in part on work done at the University of Southern California and at Lund University. Significant contributors to this effort at USC include John McArthur and Mikael Rosen, and Florian Muijres, Christoffer Johansson and Per Henningsson at LU. We are most grateful to the Swedish Research Council and the Knut and Alice Wallenberg Foundation for support in LU. The Air Force Office of Scientific Research provided partial support for JMcA at USC.

References

Adrian RJ (2005) Twenty years of particle image velocimetry. Exp Fluids 39:159–169

Anderson JD (2001) Fundamentals of aerodynamics, 3rd edn. McGraw-Hill, New York

Betz AA (1925) A method for the direct determination of profile drag. Z Flug Motorluftschiffahrt 16:42

Bomphrey RJ (2006) Insects in flight: direct visualization and flow measurements. Bioinsp Biomim 1:S1–S9

Bomphrey RJ, Lawson NJ, Harding NJ, Taylor GK, Thomas ALR (2005) The aerodynamics of Manduca sexta: digital particle image velocimetry analysis of the leading-edge vortex. J Exp Biol 208:1079–1094

Bomphrey RJ, Taylor GK, Lawson NJ, Thomas ALR (2006) Digital particle image velocimetry measurements of the downwash distribution of a desert locust Schistocerca gregaria. J R Soc Interf 3:311–317

Cardwell BM, Mohseni C (2008) Vortex shedding over a two-dimensional airfoil: where the particles come from. AIAA J 46(3):545–547

Chakraborty P, Balachandar S, Adrian RJ (2005) On the relationships between local vortex identification schemes. J Fluid Mech 535:189–214

Chen J, Katz J (2005) Elimination of peak-locking error in PIV analysis using the correlation mapping method. Meas Sci Tech 16:1605–1618

Cholemari MR (2007) Modeling and correction of peak-locking in digital PIV. Exp Fluids 42:913–922

Chong MS, Perry AE, Cantwell BJ (1990) A general classification of three-dimensional flow fields. Phys Fluids A2(5):765–777

Dabiri JO (2005) On the estimation of swimming and flying forces from wake measurements. J Exp Biol 208:3519–3532

Dabiri JO, Colin SP, Costello JH (2006) Fast-swimming hydromedusae exploit velar kinematics to form an optimal vortex wake. J Exp Biol 209:2025–2033

Dickinson MH (2008) Animal locomotion: a new spin on bat flight. Curr Biol 18(11):R468–R470

Fincham AM, Spedding GR (1997) Low cost, high resolution DPIV for measurement of turbulent fluid flow. Exp Fluids 23:449–462

Fincham AM, Delerce G (2000) Advanced optimization of correlation imaging velocimetry algorithms. Exp Fluids 29:S13–S22

Green MA, Rowley CW, Haller G (2007) Detection of Lagrangian coherent structures in three-dimensional turbulence. J Fluid Mech 572:111–120

Haller G (2002) Lagrangian coherent structures from approximate velocity data. Phys Fluids 14(6):1851–1861

Haller G (2005) An objective definition of a vortex. J Fluid Mech 525:1–26

Hedenström A, van Griethuijsen L, Rosén M, Spedding GR (2006) Vortex wakes of birds: recent developments using digital particle image velocimetry in a wind tunnel. Anim Biol 56:535–549

Hedenström A, Johansson LC, Wolf M, von Busse R, Winter Y, Spedding GR (2007) Bat flight generates complex aerodynamic tracks. Science 316:894–897

Hedenström A, Muijres F, von Busse R, Johansson C, Winter Y, Spedding GR (2008) High-speed 3D PIV measurements of bat wakes flying freely in a wind tunnel. Exp Fluids (submitted, this volume)

Hedenström A, Spedding GR (2008) Beyond robins: aerodynamic analyses of animal flight. J R Soc Interf 5:595–601

Henningsson P, Spedding GR, Hedenström A (2008) Vortex wake and flight kinematics of a swift in cruising flight in a wind tunnel. J Exp Biol 211:717–730

Huang HT, Fiedler HE, Wang JJ (1993) Limitation and improvement of PIV. Part II: particle image distortion, a novel technique. Exp Fluids 15:263–273

Hunt JCR, Wray AA, Moin P (1988) Eddies, stream, and convergence zones in turbulent flows. Center for Turbulence Research Report CTR-S88, Stanford

Jeong J, Hussein F (1995) On the identification of a vortex. J Fluid Mech 285:69–94

Kester W (2006) ADC input noise: the good, the bad and the ugly. Is no noise good noise? Analog Dialogue 40(02):13–17

Kurtulus DF, David L, Farcy A, Alemdaroglu N (2008) Aerodynamic characteristics of flapping motion in hover. Exp Fluids 44:23–36

Lighthill MJ (1970) Aquatic animal propulsion of high hydromechanical efficiency. J Fluid Mech 44:265–301

Lin JC, Rockwell D (1996) Force identification by vorticity fields: techniques based on flow imaging. J Fluids Struct 10:663–668

Meheut M, Bailly D (2008) Drag-breakdown methods from wake measurements. AIAA J 46(4):847–863

Muijres FT, Johansson LC, Barfield R, Wolf M, Spedding GR, Hedenström A (2008) Leading-edge vortices increase lift in bat flight. Science 319:1250–1253

Noca F, Shiels D, Jeon D (1999) A comparison of methods for evaluating time-dependent fluid dynamic forces on bodies, using only velocity fields and their derivatives. J Fluids Struct 13:551–578

Nogueria J, Lecuona A, Rodriguez PA (2001) Identification of a new source of peak locking, analysis and its removal in conventional and super-resolution PIV techniques. Exp Fluids 30:309–316

Norberg UM (1990) Vertebrate flight. Springer, Berlin

Peng J, Dabiri JO (2007) A potential flow, deformable-body model for fluid structure interactions with compact vorticity: application to animal swimming measurements. Exp Fluids 43:655–664

Perry AE, Lim TT, Chong MS (1980) The instantaneous velocity fields of coherent structures in coflowing jets and wakes. J Fluid Mech 101:243–256

Polhamus EC (1971) Predictions of vortex-lift characteristics by a leading-edge suction analogy. J Aircraft 8(4):193–199

Prandtl L, Tietjens OG (1934) Applied hydro- and aeromechanics. United Engineering Trustees and Dover Publications, New York

Prasad AK, Adrian RJ, Landreth CC, Offutt PW (1992) Effect of resolution on the speed and accuracy of particle image velocimetry interrogation. Exp Fluids 13:105–116

Saffman PG (1970) The velocity of viscous vortex rings. SIAM J 49:371–380

Saffman PG (1992) Vortex dynamics. Cambridge University Press, Cambridge, UK

Scarano F (2002) Iterative image deformation methods in PIV. Meas Sci Tech 13:R1–R19

Scarano F, Riethmuller ML (1999) Iterative multigrid approach in PIV image processing with discrete window offset. Exp Fluids 26:513–523

Shadden S, Lekien F, Marsden J (2005) Definition and properties of Lagrangian coherent structures from finite-time Lyapunov exponents in two-dimensional aperiodic flows. Physica D 212:271–304

Shadden S, Dabiri J, Marsden J (2006) Lagrangian analysis of fluid transport in empirical vortex ring flows. Phys Fluids 18:047105

Stanislas M, Okamoto K, Kahler CJ, Westerweel J, Scarano F (2008) Main results of the third international PIV challenge. Exp Fluids 45:27–71

Utami T, Blackwelder RF (1991) A cross-correlation technique for velocity field extraction from particulate visualization. Exp Fluids 10:213–223

van Oudheusden BW, Scarano F, Roosenboom EWM, Casimiri EWF, Souverein LJ (2007) Evaluation of integral forces and pressure fields from planar velocimetry data for incompressible and compressible flows. Exp Fluids 43:153–162

Wang ZJ, Birch JM, Dickinson MH (2004) Unsteady forces and flows in low Reynolds number hovering flight: two-dimensional computations vs robotic wing experiments. J Exp Biol 207:449–460

Westerweel J (1997) Fundamentals of digital particle image velocimetry. Meas Sci Tech 8:1379–1392

Westerweel J (2000) Theoretical analysis of the measurement precision in particle image velocimetry. Exp Fluids 29:S3–S12

White FM (2008) Fluid mechanics, 6th edn. McGraw-Hill, New York

Willert CE, Gharib M (1991) Digital particle image velocimetry. Exp Fluids 10:181–193

Willmott AP, Ellington CP, Thomas ALR (1997) Flow visualization and unsteady aerodynamics in the flight of the hawkmoth Manduca sexta. Phil Trans R Soc Lond B 352:303–316

Zhou J, Adrian RJ, Balachandar S, Kendall TM (1999) Mechanisms for generating coherent packets of hairpin vortices in channel flow. J Fluid Mech 387:353–396

Wing–wake interaction reduces power consumption in insect tandem wings

Fritz-Olaf Lehmann

Abstract Insects are capable of a remarkable diversity of flight techniques. Dragonflies, in particular, are notable for their powerful aerial manoeuvres and endurance during prey catching or territory flights. While most insects such as flies, bees and wasps either reduced their hinds wings or mechanically coupled fore and hind wings, dragonflies have maintained two independent-controlled pairs of wings throughout their evolution. An extraordinary feature of dragonfly wing kinematics is wing phasing, the shift in flapping phase between the fore and hind wing periods. Wing phasing has previously been associated with an increase in thrust production, readiness for manoeuvrability and hunting performance. Recent studies have shown that wing phasing in tandem wings produces a twofold modulation in hind wing lift, but slightly reduces the maximum combined lift of fore and hind wings, compared to two wings flapping in isolation. Despite this disadvantage, however, wing phasing is effective in improving aerodynamic efficiency during flight by the removal of kinetic energy from the wake. Computational analyses demonstrate that this increase in flight efficiency may save up to 22% aerodynamic power expenditure compared to insects flapping only two wings. In terms of engineering, energetic benefits in four-wing flapping are of substantial interest in the field of biomimetic aircraft design, because the performance of man-made air vehicles is often limited by high-power expenditure rather than by lift production. This manuscript provides a summary on power expenditures and aerodynamic efficiency in flapping tandem wings by investigating wing phasing in a dynamically scaled robotic model of a hovering dragonfly.

F.-O. Lehmann (✉)
BioFuture Research Group, University of Ulm,
Albert-Einstein-Allee 11, 89081 Ulm, Germany
e-mail: fritz.lehmann@uni-ulm.de

1 Introduction

Flying insects are known for their impressive flight agility, manoeuvrability and endurance, including low speed hovering, effective gliding flight and sudden variation in flight speed and altitude. In the past, multiple experimental and computational studies have shown, how insects enhance their lift production to support body weight, to lift loads, and to allow manoeuvring flight (e.g. Birch and Dickinson 2003; Dickinson et al. 1999; Lan and Sun 2001; Lehmann et al. 2005; Ramamurti and Sandberg 2007; Srygley and Thomas 2002; Sun and Tang 2002; Wang et al. 2003). The discovery of the various unsteady aerodynamic mechanisms for lift enhancement such as leading edge vortex development, rotational circulation and wake capture has considerably improved our knowledge and has highlighted the complexity of flapping flight compared to fixed-wing aircraft performance.

Despite the difficulties in improving lift coefficients for flight, many insects are limited by power rather than by the ability of the flapping wings to support body weight. Aerodynamic efficiency in flapping flight is of considerable interest, because some insects such as the small fruit fly *Drosophila* may fly for several hours without food intake. Other species, such as the parasitic wasp *Nasonia*, even completely abstain from feeding as adults (King 1993; Langellotto et al. 2000). This is remarkable, because in this species the females perform elaborate and long-lasting search flights for oviposition. Comparatively few studies have addressed the potential trade-off between high-lift

G.K. Taylor, M.S. Triantafyllou, and C. Tropea (Eds.): Animal Locomotion, pp. 203–213.
springerlink.com

production and high-energetic costs during flight, and adjustments in wing kinematics have mostly been discussed in terms of maximum lift production rather than in terms of the benefits in energetic costs. Considering flapping flight from the perspective of power expenditure and aerodynamic efficiency is thus of great ecological significance in order to understand the evolution of kinematic patterns used by birds, bats and insects.

Experimental work on tethered insects suggests that most of the chemical energy stored in the food is wasted as heat in the flight musculature and as horizontal, non-weight supporting drag during wing flapping (Casey and Ellington 1989; Ellington 1984a, 1985). The efficiency with which the insect flight muscle converts chemical energy from sugar and fat into muscle mechanical power is low and typically scattered around 10% (for a review see Lehmann 2001). This value holds for the two major types of flight muscles used by flying insects: the asynchronous, indirect flight muscle (IFM) mostly found in flies, bees, and beetles, and the synchronous, direct flight muscle (SFM) of dragonflies, butterflies and many other insects. The IFM contracts in response to passive lengthening (stretch activation) during high-frequent thorax oscillations and is deactivated by fibre shortening (shortening deactivation, Moore 2006). It inserts large-scale at the thorax walls. By contrast, the SFM is closely controlled by its neural drive and attached to the wing base. This muscle moves the wing by pulling directly on the wing's lever arm. In contrast to insects, muscle efficiency of the vertebrate flight muscle in birds and bats is slightly higher and ranges from 10 to 40% (Lehmann 2001). Aerodynamic efficiency, in turn, defines how much mechanical power is required to move the wings in each flapping cycle compared to the power required to produce aerodynamic lift. In engineering terms, flight muscle mechanical power output in an insect corresponds to the shaft power of a rotating propeller. The latter efficiency is typically expressed by the ratio between the minimum power requirements for flight (Rankine–Froude power) and the aerodynamic power expenditure, and typically amounts to values scattered around 25–35% total chemical energy (Ellington 1984a). Together, this yields a relatively low total flight efficiency of not more than 3–5% in the insect species investigated so far (Lehmann 2001).

Widely neglected aspects in assessing the efficiency of flapping flight are kinematic manoeuvres in which flow conditions change due to the interference between wings. Wing–wake interaction during the dorsal stroke reversal is probably the most prominent manoeuvre in two-winged flight (Lehmann et al. 2005; Weis-Fogh 1973). In four-winged insects, such as dragonflies, the fore wing experiences change in flow conditions due to the inwash of fluid caused by the nearby hind wing, and the hind wing must cope with the downwash produced by the flapping fore wing. These dependencies, moreover, vary during manoeuvring flight, since a wide range of phase relationships has been described between fore and hind wings. High flight forces have been correlated to in-phase flapping of fore and hind wing, but in many cases dragonflies also operate with wing motion somewhat out of phase (Alexander 1984; Norberg 1975; Reavis and Luttges 1988; Rüppell 1989; Thomas et al. 2004; Wakeling and Ellington 1997a; Wang et al. 2003). A total antiphase motion in which fore and hind wings are phase-shifted by 50% of the stroke cycle might promote hunting performance, either by increasing the readiness for manoeuvrability, or by reducing the centre of body mass oscillations, thereby aiding location of targets and reducing the insect's visibility to potential prey (Grodnitsky 1999).

Computational and experimental studies on the consequences of wing phasing have demonstrated that phase has a bearing on both thrust production and power consumption (Lan 1979; Luttges 1989; Wang and Russell 2007). Moreover, flow visualizations around dragonfly model wings have shown some of the potential consequences of wing–wake interaction including the fusion of vortices, leading edge vortex destruction and wake capture effects (Maybury and Lehmann 2004, Saharon and Luttges 1987, 1988, 1989). However, the implications of these fluid dynamic effects in terms of power expenditure and aerodynamic efficiency have remained widely unclear. Lan's (1979) computational study on heaving and pitching plates predicted that interacting tandem wings may produce high thrust with high efficiency due to energy extraction by the hind wing from the wake of the fore wing. Although the latter study is not strictly applicable to hovering flight and neglects the impediments of flow separation in slow dragonfly flight (Thomas et al. 2004), it is tempting to conclude that wing kinematic patterns in four-winged insects should be shaped by both lift production and energy expenditure (Usherwood and Lehmann 2008). Moreover, measurements show that wing phasing in four wings produces higher transient forces and thus larger transient moments than in two wings (Maybury and Lehmann 2004). Depending on their temporal distribution within the stroke cycle, these extremes potentially help to improve manoeuvrability and stability of an insect.

In this paper, we analyse how dragonflies may reduce energetic costs during flight by adjusting the timing of wing motion between their two pairs of wings and discuss why efficiency of the insect flight apparatus might be a more pertinent measure for flapping flight than lift production. This is achieved by calculations of induced and aerodynamic power requirements for flapping flight at various phase shifts, estimations of the significance of wing hinge separation for the ratio of combined drag to lift production, and quantification of the wake below dragonfly model wings. The experimental force data used for these

analyses are those collected by Maybury and Lehmann (2004) who focused on force development rather than on energetic aspects during wing phasing. In sum, the present study tries to strengthen the emerging unified approach between biology and aeronautical engineering in the field of unsteady aerodynamics and energetics of flying animals.

2 The mechanical dragonfly model

The dynamically scaled, electromechanical dragonfly model mimicked wing-wake interactions during hovering flight of a generic dragonfly at intermediate Reynolds numbers (*Re*, Fig. 1). We employed an averaged kinematic pattern derived from various species, in order to demonstrate the significance of hovering for power requirements and efficiency with a range of fore-hind wing phases. Orientation of stroke planes and wing motion broadly followed the observations on free-flight hovering of *Sympetrum sanguineum*, a common species in dragonfly research (Wakeling and Ellington 1997a). The robotic fore and hind wings were stacked vertically, separated by 1.25 chord length (48 mm) between the wing hinges, and flapped with symmetrical downstroke and upstroke in a horizontal stroke plane (Fig. 1a). Flapping amplitude was 100°, flapping frequency 0.533 Hz, and feathering angle at mid-half stroke was 45° (Fig. 1b). Supination and pronation at the stroke reversals occurred during the initial and final 10% of each half-stroke, flipping the wings by 90°. Fore-hind wing phases are described as the percentage of the stroke cycle, at which the hind wing leads the fore wing: 0% indicates in-phase stroking, +25% (−25%) indicates that the hind (fore) wing leads by a quarter stroke cycle, and 50% indicates total anti-phase.

To avoid too many morphological parameters confounding the results, we used flat, non-corrugated wings made from 2 mm thick Plexiglas for both force and particle image velocimetry (PIV) measurements. Wing mass of fore and hind wing was 11.0 and 13.4 g, and mean spanwise flexural stiffness *EI* yielded 0.11 and 0.29 Nm^2 for the two wings, respectively. For comparison, spanwise flexural stiffness of insect wings ranges from approximately 10^{-6} Nm^2 in flies, to 10^{-4} Nm^2 in dragonflies and 0.5×10^{-3} Nm^2 in moths (Combes and Daniel 2003; Ganguli et al. 2008). To roughly compare these values in terms of wing deflection, we applied mean force production of the mechanical model (0.32 and 0.31 N, fore and hind wing, respectively) and one-quarter body weight of the dragonfly *Aeshna multicolor* (total weight = 754 mg) to the wing tips, respectively. According to Gordon (1978),

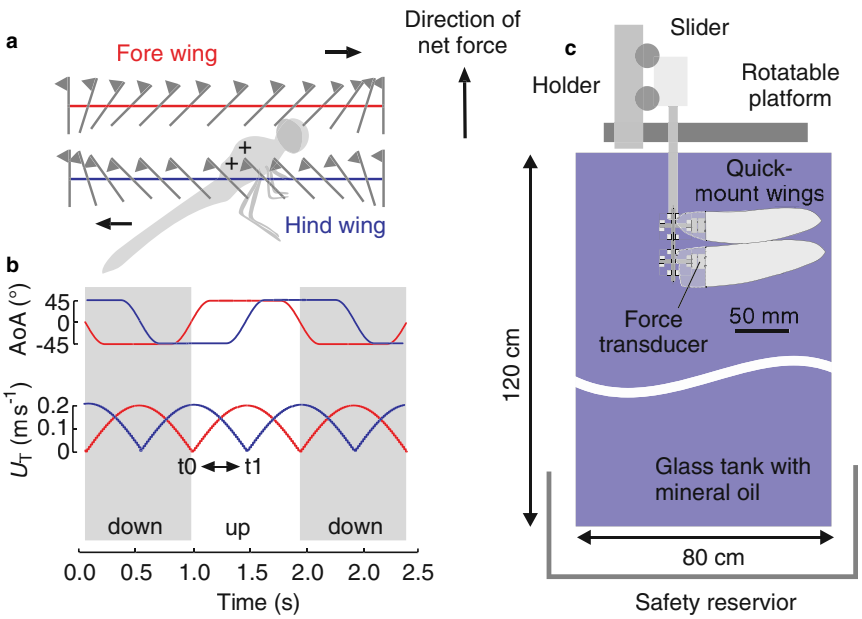

Fig. 1 Mechanical dragonfly model and wing shifting kinematics. **a** Body posture as reported for a hovering dragonfly by Wakeling and Ellington (1997a) and idealized wing tip path as used in the mechanical model of the fore- (*red*) and hind wing (*blue*). *Grey lines* show a travelling wing blade during the up (*lower wing*) and down stroke (*upper wing*). *Triangles* near the leading wing edge indicate the upper wing surface. **b** Alteration of geometric angle of attack (AoA) and translational wing velocity (U_T) based on flapping motion for both wings. The temporal difference between t_0 and t_1 indicates the kinematic phase shift between the fore- and hind wing stroke cycle. **c** Experimental setup showing gear boxes and wings of the mechanical model. The wings are stationary and immersed in a tank filled with mineral oil. Sizes of gears and wings are not to scale. *Scale bar* applies to the mechanical wings only

this resulted in a spanwise tip deflection of 1.02° (0.40°) for the model fore (hind) wing and 6.3° for the dragonfly wing. Wing planforms were based on the wings of the small dragonfly *Polycanthagyna melanictera* with low aspect ratios of 6.8 and 7.4 at spanwise lengths of 190 and 185 mm for the fore and hind wing, respectively (Fig. 1c).

Reynolds number based on the product between mean wing chord and wing tip velocity during wing flapping for the fore and hind wing was 105 and 125, respectively. Although these values are at the low end of small dragonflies (250–500, Rüppell 1989), they are considered well above the transitional Reynolds number of approximately 55 for vortex shedding (Miller and Peskin 2004; Vandenberghe et al. 2004). According to the Reynolds number of the hind wing, the flapping frequency of the mechanical model corresponds to a wing stroke frequency of approximately 40 Hz in air common for small dragonflies. Due to the sinusoidal velocity profile, the contribution of wing mass inertia to aerodynamic force at the stroke reversals is moderate and accounts for a maximum of 6% of the mean force produced by an isolated hind wing (0.21 N). According to previous calculations, the same holds for added mass inertia that produces transient force peaks at the stroke reversals of approximately 0.06 N or 30% of the measured mean force. Averaged throughout the entire stroke cycle, however, added mass inertia due to the wing's translational and rotational accelerations apparently amounts to less than 1% of the mean aerodynamic force production. We calculated added mass inertia using an analytical model for an infinitesimally thin 2D plate moving in an inviscid fluid modified towards 3D conditions (Sedov 1965; Sane and Dickinson 2001a, b; Maybury and Lehmann 2004).

Instantaneous forces such as weight-supporting lift in the vertical and drag parallel to horizontal motion were measured by 6 degrees-of-freedom force transducers (Nano 17, ATI, USA) attached to the wing bases of both wings. For each kinematic phase, we recorded a sequence of six cycles but averaged forces only from four stroke cycles (2–5) in order to avoid confounding effects from the initial downwash acceleration (Birch and Dickinson 2001). To allow 2D digital PIV, the model wings including motors, gears and force transducers were immersed in a 0.77 m^3 flow tank filled with highly viscous pharmaceutical white oil (density, 0.88×10^3 kg m^{-3}; kinematic viscosity, 120 cSt; Fig. 1c). Closest distance between wing tip and the lateral tank walls was approximately 20 cm; the fore wing stroke plane was approximately 95 cm above the bottom of the tank. Air bubbles as seeding particles reflected the light of the PIV laser (TSI, Insight 6.0) in a vertical slice situated half-way along the fore wing, highlighting flow conditions at mid down stroke. Each PIV experiment consisted of seven successive stroke cycles, but similar to the force measurements, only the flow fields from the last five cycles were recorded, averaged and analysed. In general, the aim of the mechanical model and the robotic kinematics was not to precisely copy a specific dragonfly, but to provide a reasonable test bed with which the significance of wing phasing for power requirements and aerodynamic efficiency could be investigated without too many confounding kinematics and aerodynamic factors such as changes in body position or alterations in the net flight force vector, respectively.

3 Lift and drag production in tandem wings

In the dragonfly model, the combined lift production of fore and hind wing varies with wing phasing, which widely concurs with previous computational studies on dragonfly flight (Sun and Lan 2004; Wang and Russell 2007; Fig. 2). At −25% phase shift, when the fore wing leads, fore wing lift only slightly decreases by at most 8% compared to a single wing, while hind wing lift is attenuated by more than 50% of the single wing performance (0.21 N, for combined lift see Fig. 2a). Most of this reduction in lift is due to a reduction of the aerodynamic angle of attack between each wing and the local fluid. Similar to tandem helicopters, the angle of attack is reduced by the downwash of the fore wing on the hind wing, and by the hind wing's inwash on the fore wing.

Particle image velocimetry yielded a second mechanism for lift reduction: the partial destruction of the leading edge vortex on the hind wing due to the proximity of fore wing's start vortex shed at the beginning of each half stroke. It has been shown that this vortex interaction attenuates vorticity in the leading edge vortex (LEV) of the hind wing by 31%, compared to a wing flapping in isolation (from 129 to 88.4 s^{-1}, Maybury and Lehmann 2004). Tandem wings restore *mean* lift close to the combined performance of wings flapping in isolation when the hind wing leads wing motion by +25% of the stroke cycle, although *instantaneous* lift and drag of the tandem hind wing differs from the performance of a single wing (Figs. 2a, 3). Particle image velocimetry shows that under these conditions, the leading edge vortex on the hind wing fully develops and the hind wing gains additional lift by recycling kinematic energy produced by the fore wing via a wake capture mechanism (Maybury and Lehmann 2004). In addition to the reduced lift with fore-hind wing interaction, the mean lift to mean drag ratio during wing phasing is not improved compared with wings flapping in isolation, although the ratio slightly increases with increasing drag production from 0.72 at 0.3 N to 0.85 at 0.6 N drag ($y = -0.077 + 0.98x$, $R^2 = 0.86$, $P < 0.0001$, $N = 40$, Fig. 4a). At first glance, it is thus tempting to conclude that wing phasing in dragonflies has primarily evolved to alter lift and drag for flight control rather than developed from an evolutionary pressure on power expenditure and thus flight efficiency.

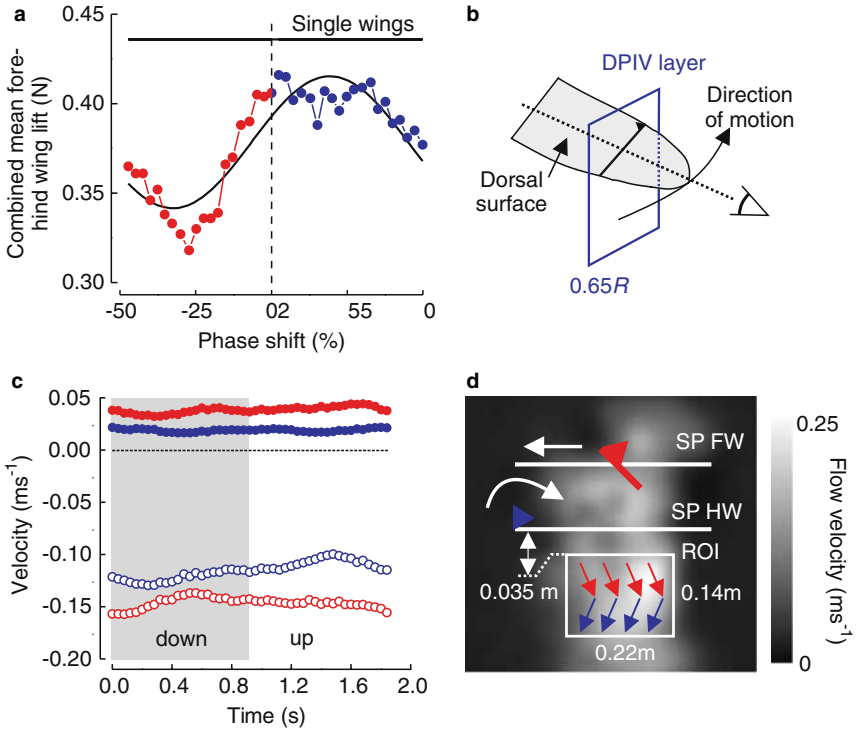

Fig. 2 Lift production and flow velocities in the wake below the hind wing averaged from 5 PIV image pairs, all recorded at mid down stroke (single point measurement at +25% stroke cycle). **a** Modulation in combined lift production during phase-shifting kinematics when either the fore wing (*red*) or the hind wing (*blue*) leads wing motion. **b** The two-dimensional layer for particle image velocimetry was orientated perpendicular to the longitudinal axis of the wing at mid half stroke. *R* wing length. **c** Vertical (*open circles*) and absolute horizontal velocity (*closed circles*) in the wake at mid half stroke, measured in a 224 mm × 140 mm (width × height) region-of-interest (ROI) below the hind wing. *Blue* (*red*) indicates +25% (−25%) phase shift when hind (fore) wing leads wing motion. **d** Fluid velocity (*grey scale*) at +25% phase shift, stroke planes of fore and hind wing, and location of the region-of-interest used for the measurements in **c**. See Fig. 7 for more detailed flow data. *SP* stroke plane, *FW* fore wing, *HW* hind wing

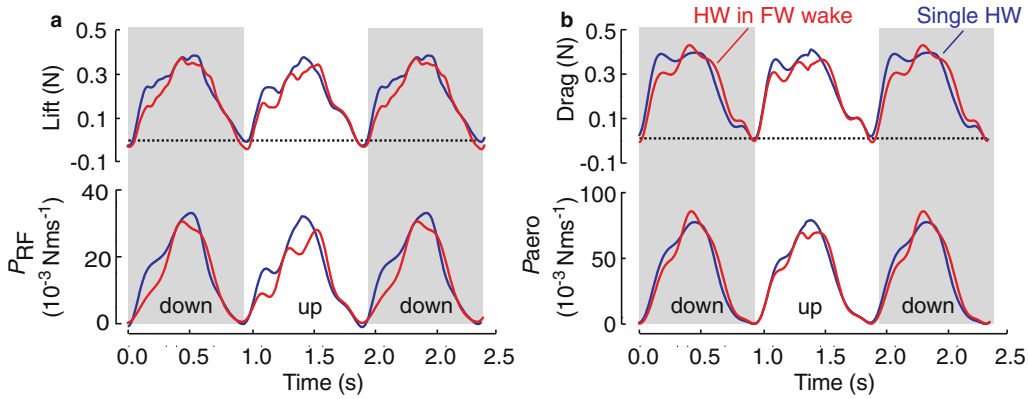

Fig. 3 Time traces of aerodynamic forces and power requirements. **a** Lift and Rankine–Froude power of a hind wing in tandem configuration (*red*) compared to forces and power of a hind wing flapping in isolation (*blue*). **b** Drag and aerodynamic power of the hind wing flapping in the downwash of the fore wing (*red*) and in a single hind wing (*blue*). P_{RF}, Rankine–Froude power; P_{aero}, aerodynamic power calculated from the product between drag and wing velocity. Wing separation between the wing hinges was 1.25 times mean chord width and wing phasing was +25% (hind wing leads by quarter stroke cycle). For abbreviations, see legend of Fig. 2

Previous work on tandem wings has shown that the modulation of combined lift and drag depends on several factors including wing size and the distance between the fore and hind wing stroke plane (Lehmann 2008). With increasing distance between both wings, phase shift for maximum lift production decreases due to vortex travel

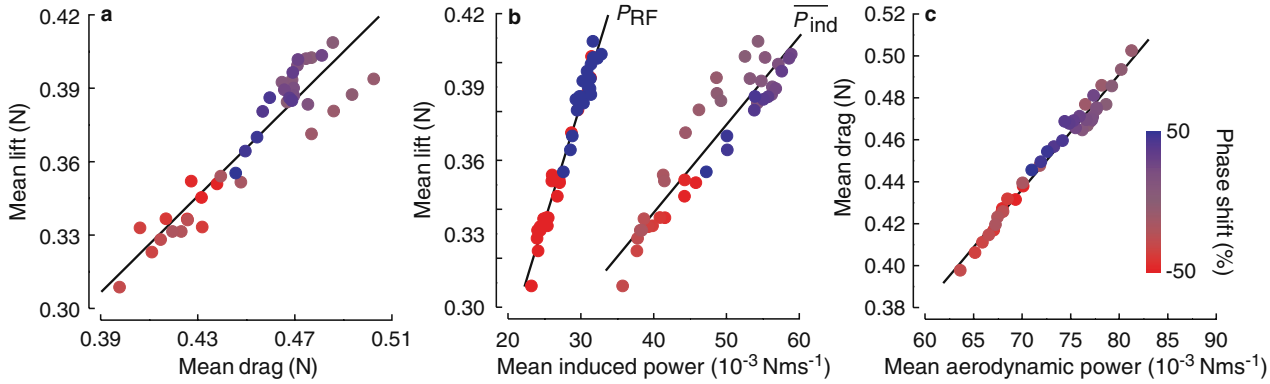

Fig. 4 Combined mean lift, drag and power requirements of both wings in dragonfly tandem wings plotted as a function of wing phasing. **a** Relationship between mean lift and mean drag. **b** Mean lift plotted against Rankine–Froude power (P_{RF}) according to Eq. 1 and mean induced power ($\overline{P_{ind}}$) calculated from the product between mean lift and mean induced velocity measured in the far wake below the hind wing. **c** Relationship between mean drag and mean aerodynamic power. Phase shift is indicated in pseudo colour (*blue* hind wing leads wing motion; *red* forewing leads wing motion). See text for more information on regression fit curves

time while the modulation of lift and drag increasingly disappears (Fig. 5). This effect is due to viscosity that smoothes out temporal and spatial fluctuation of the wake, eventually producing a downwash homogeneous in time and space. The mechanical dragonfly produces both maximum combined fore-hind wing lift at +25% phase and maximum lift modulation only when the wings are closest (Fig. 5b). Due to the increasing loss of vorticity and temporal variation in the wake with increasing wing separation, lift and drag approach the performance of wings flapping in isolation at a separation of approximately five chord lengths (Fig. 5b, c). The same holds for mean lift to mean drag ratio (Fig. 5d), together suggesting that besides other properties, the morphological distance between fore and hind wing hinge determines the animal's ability to produce and modulate lift using wing phasing kinematics.

4 Induced power during wing phasing

In his time-averaged approach towards insect flight energetics, Ellington (1984a) provided a numerical framework that allows calculations of power requirements for wing flapping based on averaged kinematics and mean lift production. Following Weis-Fogh's original work (Weis-Fogh 1972), Ellington divided the requirements for flight into

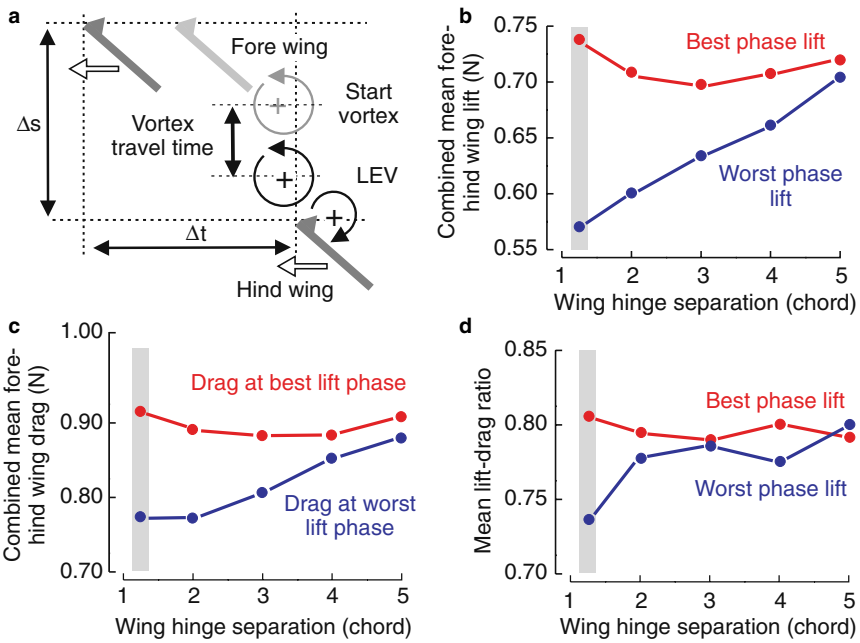

Fig. 5 Mean lift, mean drag and mean lift-to-drag ratio at best (+25%, *red*) and worst (−25%, *blue*) phase shift. **a** Schematic drawing illustrating −25% phase shift (Δt) and wing hinge separation (Δs). The phase shift for maximum lift decreases with increasing distance between both stroke planes for maximum lift production due to vortex travel time. **b** Combined fore-hind wing lift at best and worst phase shift plotted as a function of wing separation. **c** Combined drag at best and worst lift production and **d** mean lift to mean drag ratio. *Grey bar* closest distance between wing hinges; *LEV* leading edge vortex

three terms: inertial power needed to accelerate the wings in each half stroke, profile power necessary to cope with profile drag, and induced power required to produce a vertical momentum for weight support. Assuming that inertial costs are minimum due to elastic energy storage in the flight musculature, Ellington's conventional two-dimensional elementary blade approach defines total power requirements for flight as the sum of profile and induced power. The latter term represents the power associated with induced drag arising from the tilt of the relative velocity vector by the generated downwash.

Exact estimations of induced power are challenging, because this measure requires quantifications of induced velocity in the down wash of flapping wings. Figure 2c shows the temporal development of horizontal and vertical flow velocities within a flapping cycle of the mechanical model wings, measured in a region of interest, 35 mm below the hind wing stroke plane (plane covered by wing tip, Fig. 2d). These measures capture the flow regime at mid half stroke and approximately at the centre of force production of the wings (65% wing length). They should be considered as rough estimates because a three-dimensional flow field would be needed to fully quantify mean induced velocity with PIV. At minimum lift production at −25% phase shift (fore wing leads), mean vertical flow speed amounts to 0.146 ± 0.043 m s^{-1} (mean ± SD) compared to 0.115 ± 0.063 m s^{-1} (mean ± SD) at +25% phase shift (Fig. 2c). This suggests that despite higher lift production, there is less kinetic energy in the wake at best phase shift compared to worst phase conditions. Alternatively to PIV estimates, induced velocity may be derived from the velocity with which the start vortices shed by the fore wings travel downstream in the wake. A previous analysis scored this velocity using conventional video devices and derived a mean travel velocity of 0.082 m s^{-1}, which is approximately 56% of the free stream velocity of the vertical wake (Lehmann 2008).

The theoretical minimum of induced power in tandem wings of a quasi-steady jet is equal to the Rankine–Froude estimate of induced power normalized by a vortex shedding factor k_F that takes into account the periodicity of the wake due to wing flapping (Ellington 1984a). This factor is the ratio in the far wake of the Rankine–Froude velocity to the mean velocity of the periodic wake. The ideal Rankine-Froude power P_{RF} for an actuator disk produced by a hovering insect and ignoring unsteady aerodynamic mechanisms such as wake capture, is given by:

$$P_{RF} = L \cdot (\tfrac{1}{2} L \cdot \rho^{-1} A_0^{-1})^{0.5}, \quad (1)$$

with L, the mean lift force acting directly upwards, ρ, the fluid density, and A_0, the actuator disc area, the area swept by the two wings. With vertically stacked wings operating with horizontal stroke planes, just as for coaxial rotors of helicopters, the flapping fore and hind wings form a single actuator disc. Under these assumptions, the same fluid is accelerated by both sets of wings. Following Ellington, and again considering only the two wings on the right body side of the dragonfly, the area of the appropriate actuator disc A_0 may be expressed by:

$$A_0 = \tfrac{1}{2} \Phi R^2, \quad (2)$$

where Φ is the stroke amplitude and R the wing length of the longer fore wing (0.19 m). Assuming that lift is proportional to the power raised to the exponent 2/3 (cf. Eq. 1), statistical analysis suggests that lift production increases with increasing Rankine-Froude power by a slope of 4.39 ($y = -0.04 + 4.39x^{2/3}$, $R^2 = 0.97$, $\chi^2 = 97.5 \times 10^{-5}$, DOF = 38, Fig. 4b). For comparison, mean lift increases with mean induced power $\overline{P_{ind}}$ (lift × induced velocity) with a slope of 1.96 ($y = 0.11 + 1.96x^{2/3}$, $R^2 = 0.87$, $\chi^2 = 38.8 \times 10^{-4}$, DOF = 38, Fig. 4b) based on the induced velocity measurements in Fig. 2c, and with a slope of 5.62 ($y = -0.18 + 5.62x^{2/3}$, $R^2 = 0.99$, $\chi^2 = 33.3 \times 10^{-7}$, DOF = 38) based on vortex travel time. Since Rankine-Froude power is the theoretical minimum, the vortex shedding factor must be greater than unity for a periodic wake: from the above data we derived 1.69 (Fig. 4b), and 1.08 assuming a uniform vortex travel velocity of 0.082 m s^{-1}. Consequently, the mean axial wake velocity in the far wake of the mechanical dragonfly model is approximately 41% ($k_F = 1.69$) and 7% ($k_F = 1.08$) less than the Rankine-Froude estimate of axial wake velocity.

5 Aerodynamic power during wing phasing

Instantaneous aerodynamic power is given by the product between instantaneous drag and wing velocity. Time traces of aerodynamic power P_{aero} for the hind wing in tandem configuration and a hind wing flapping in isolation are shown in Fig. 3b, whereas Fig. 4c shows the relationship between mean drag and mean aerodynamic power at the various phase shifts (allometric fit: $y = -0.15 + 3.45x^{2/3}$, $R^2 = 0.98$, $\chi^2 = 57.2 \times 10^{-5}$, DOF = 38, Fig. 4c). At +25% phase shift (hind wing leads) the difference in hind wing drag between single and tandem wing configuration appears to be minor, suggesting only small changes in power due to wing-wake interference at optimal conditions (mean drag, 0.239 vs. 0.239 N; mean aerodynamic power, 37.5×10^{-3} vs. 38.2×10^{-3} Nms^{-1}; isolated hind wing vs. hind wing in tandem configuration).

To calculate aerodynamic power savings during fore-hind wing interference, we estimated the wing beat

frequency required to achieve identical mean lifts (0.404 N) for wings operating at different phases. The scaling model is independent of the aerodynamic mechanism used for lift production and simply assumes that drag scales in proportion to lift, a reasonable assumption for the expected small change in Reynolds number. From these estimates, the power requirements for hovering were scaled by adjusting stroke frequency, while constraining wing shape and all remaining kinematic parameters. The analysis shows that hovering with a phase shift of +25% requires 16% less power than with a phase shift of −25% (fore wing leads). Although this comparison ignores other potential kinematic parameters, such as adjustments in stroke amplitude or angle of attack, it shows that hovering with the appropriate phase between both wings may have a considerable energetic significance. Moreover, compared to dragonfly wings flapping in isolation, hovering with four wings at +25% phase shift requires 22% less aerodynamic power than hovering only with the two fore wings at the same mean lift production. The increase in stroke frequency required to match the lift produced by a single fore wing to the combined lift of tandem wings (at 25% phase shift) amounts to approximately 0.18 Hz or 33% of the employed flapping frequency, while Reynolds number increases from 105 to 140.

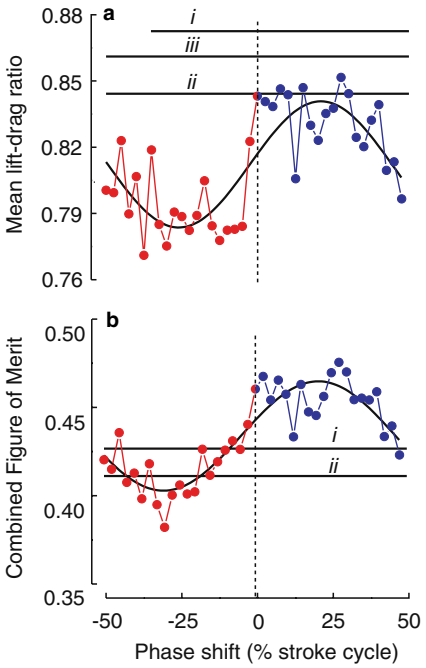

Fig. 6 **a** Ratio between mean lift and mean drag and **b** aerodynamic efficiency of total lift production expressed as Figure of Merit (FoM) during phase shifting kinematics of the mechanical dragonfly. Black solid lines show performance of isolated (*i*) fore wing, (*ii*) hind wing, and (*iii*) the cumulative effect of isolated fore and hind wings, and sine fit to the data as a function of kinematic phase

6 Aerodynamic efficiency (Figure of Merit)

Our instantaneous measurements of lift and drag circumvent Ellington's numerical framework on mean induced and mean profile power requirements in flapping wings, calculating aerodynamic power expenditure directly from the product between instantaneous drag and translational wing velocity. Aerodynamic efficiency is then represented by the Figure of Merit, FoM, a special case of propeller efficiency used for hovering helicopters. This term describes the ratio of the minimum theoretical power required to produce a vertical downward jet for hovering (Rankine–Froude power, Figs. 3a, 4b) to the measured aerodynamic power (Figs. 3b, 4c, Prouty 2005). Consequently, the Figure of Merit expresses the efficiency of flapping flight propulsion in comparison with an ideal hovering helicopter.

Similar to the mean lift and the ratio of mean lift to mean drag, aerodynamic efficiency varies with phase shift but is always below 50% of the efficiency of an ideal actuator disc or ideal helicopter (Fig. 6). Numerical predictions without flow separation (Lan 1979) and real helicopters (Prouty 2005) yield approximately twice the mean efficiency of the dragonfly tandem model. The low efficiency in the dragonfly model is due to its high aerodynamic power requirements and, therefore, consistent with the poor lift-to-drag ratio of low aspect ratio insect wings flapping at high geometrical angle of attack of approximately 30°–40° (Ellington 1984b). For comparison, wings of the fruit fly *Drosophila* produce a lift-to-drag ratio slightly above unity at best lift coefficient of 1.8 ($Re = 136$, Dickinson et al. 1999), and a continuously rotating replicate of a low aspect ratio hawkmoth wing reaches a lift-to-drag ratio of approximately 1.2 at its best lift coefficient of 1.15 ($Re = 8071$, Usherwood and Ellington 2002).

The poor lift-to-drag ratio in insects is part of a trade-off between high lift production for hovering and slow forward flight, and low energetic costs. Superficially, an insect could energetically benefit from a reduction in angle of attack during wing flapping at the cost of an increase in wing size or kinematic parameters such as stroke amplitude and stroke frequency. The latter modifications, however, potentially interfere with the limits of the flight apparatus: the mechanical limit of the thorax to move the wings at large flapping angles, the physiological limit on high-frequency muscle contraction, and the ability of flight muscle and associated proteins (e.g. resilin, Gorb 1999) to elastically store kinetic energy within each half stroke cycle. Simple numerical models on flight energetics suggest that elastic energy storage is beneficial during the wing's acceleration phases and thus in cases in which mean inertial power exceeds aerodynamic power requirements

(Dickinson and Lighton 1995). An increase in both wing mass (size) and stroke frequency would require an elevated capacity of the thorax for elastic energy recycling. Due to the difficulties in assessing metabolic rate during flight, however, it is difficult to prove such concepts in the behaving animal (e.g. Casey 1989, Feuerbacher et al. 2003; Josephson 1997; Lehmann and Dickinson 1997; Lehmann and Heymann 2006). Altogether, the numerous findings suggest that the evolution of wing kinematics and wing design in an insect depends on various aerodynamic and biological requirements and most likely reflects the best compromise between these needs.

The major reason for the poor performance—or efficiency—of an insect wing is the loss of leading edge suction force due to the development of a leading edge vortex at high angle of attack. In the dragonfly model, however, FoM clearly outscores the efficiency of wings flapping in isolation (FoM fore wing = 0.427, FoM hind wing = 0.411, Fig. 6b), significantly improving the overall energy budget during hovering in four-winged insects (Usherwood and Lehmann 2008). The apparent paradox that aerodynamic efficiency can be improved in tandem wings despite a slight reduction of lift-to-drag ratio compared to single wings can be explained by two different views describing the same physical phenomenon: a temporal shift in force production within the stroke cycle and a wake capture mechanism that removes lateral motion of the fluid by the hind wing. The periodic, non-vertical components of the wake produced by the fore wing allow, at positive phase shifts, the hind wing to produce lift when moving relatively slowly near the two stroke reversals. This view is supported by a previous study on dragonfly wings, showing that at +25% phase shift the hind wing experiences a gain in lift at 35 and 85% of the stroke cycle and thus toward the end of each half stroke, although the wing experiences maximum translational velocity at mid up and down stroke (sinusoidal velocity profile, Maybury and Lehmann 2004; Fig. 1). Thus, while the significance of lift and drag development is minor for mean lift and weight support, it may be considerable in terms of power and aerodynamic efficiency.

The second description of the mechanism causing an elevated FoM is apparent from the resultant wake structure produced by the two wings. In root flapping wings, the term 'swirl' applies to the lateral motions of the wake. Although lateral motions are useful to some degree for the control of yaw moments, the energy that resides in the swirl is mainly wasteful because it does not contribute to the weight-supporting vertical momentum. The PIV analysis in Fig. 7 suggests, that the prominent lateral motions at −25% phase shift are redirected into the vertical when the wings flap with +25% phase shift. At +25% phase shift the wake is largely vertical, producing a conventional, converting momentum jet below the hind wing stroke plane. Since within the limits of the flow measurements the fluid velocity in the wake is smaller at +25% phase shift

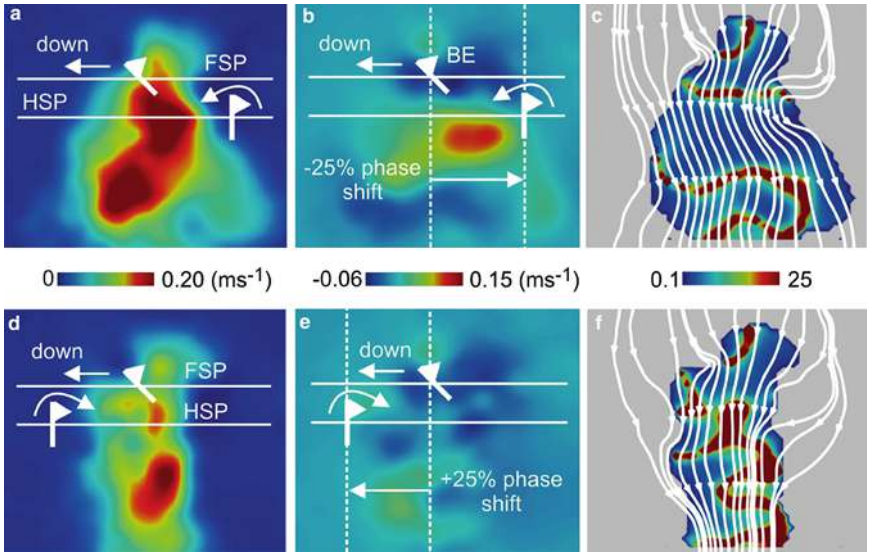

Fig. 7 Averaged wake patterns recorded at 25% forewing stroke cycle (single point measurement), at worst (−25%, fore wing leads wing motion, upper graphs) and best kinematic phase shift (+25% hind wing leads wing motion, lower graphs). See Fig. 2 for more information. **a**, **d** Vertical wake velocity for weight-supporting downwash, **b**, **e** absolute horizontal flow velocity and **c**, **f** ratio between vertical and horizontal velocity. Stream tubes, showing wake contraction in *f* compared to the wake expansion in **c**, indicate that less kinetic energy is wasted as swirl at positive, hind-wing leading phase shifts. Data are derived from two-dimensional digital particle image velocimetry in the region-of-interest shown in Fig. 2d. *Grey* indicates area in the wake at which vertical velocities are below 0.1 ms^{-1}. BE, blade element; FSP, fore wing-; HSP, hind wing stroke plane

compared to −25%, the kinetic energy put into the wake is less at the best phase shift, as already mentioned above. Thus, the power required to generate the mean lift for weight support is apparently reduced at best phase by a form of wing–wake interaction that broadly matches the prediction of Lan (1979) and also the findings by Wakeling and Ellington (1997b), who reported a +28% phase shift for dragonflies hovering freely at 0.21 advance ratio.

7 Conclusions

In this paper, we considered force production by insect tandem wings from the perspective of power expenditure and aerodynamic efficiency. Our finding that in four-winged insects, wing phasing determines both mean force production and power expenditures for flight, highlights the need of a comprehensive approach towards any explanations of how the various kinematic patterns of insect wings have evolved. Wing–wake interaction due to body motion is a common phenomenon during free-flight manoeuvring in insects and also occurs in two-winged hovering insects, for example, when the acceleration fields of the left and right wing interfere via the clap-and-fling mechanism. Detailed analyses of power expenditures and efficiency under the various flight conditions are widely missing and open a window for future research. Eventually, the finding that wing–wake interaction in root-flapping insect tandem wings is similar to the swirl removal mechanisms of contra-rotating propellers in helicopters and reconnaissance airplanes, such as the Kamov Ka-50 and the Avro Shackleton, respectively, is particularly valuable for engineers working on biomimetic aircraft design (Stafford 2007). Ellington (1999), for example, pointed out that flapping-winged aircrafts are challenged by the high power requirements for flapping flight. Any aerodynamic trick employed by insects to reduce energetic expenditures during flight should thus be of interest for both biologists and engineers.

Acknowledgments We would like to thank James Usherwood (The Royal Veterinary College, London) for his fruitful comments, Will Maybury for data collection and Ursula Seifert for critically reading the manuscript. This work was supported by grants Le905/6-1 and Le905/8-1 of the German Science Foundation (DFG).

References

Alexander DE (1984) Unusual phase relationships between the forewings and hindwings in flying dragonflies. J Exp Biol 109:379–383

Birch JM, Dickinson MH (2001) Spanwise flow and the attachment of the leading-edge vortex on insect wings. Nature 412:729–733

Birch JM, Dickinson MH (2003) The influence of wing–wake interactions on the production of aerodynamic forces in flapping flight. J Exp Biol 206:2257–2272

Casey TM (1989) Oxygen consumption during flight. In: Goldsworthy GJ, Wheeler CH (eds) Insect flight. CRC Press, Boca Raton, pp 257–272

Casey TM, Ellington CP (1989) Energetics of insect flight. In: Wieser W, Gnaiger E (eds) Energy transformations in cells and organisms. Thieme, Stuttgart, pp 200–210

Combes SA, Daniel TL (2003) Flexural stiffness in insect wings I. Scaling and the influence of wing venation. J Exp Biol 206:2979–2987

Dickinson MH, Lighton JRB (1995) Muscle efficiency and elastic storage in the flight motor of *Drosophila*. Science 268:87–89

Dickinson MH, Lehmann F-O, Sane S (1999) Wing rotation and the aerodynamic basis of insect flight. Science 284:1954–1960

Ellington CP (1984a) The aerodynamics of insect flight. VI. Lift and power requirements. Phil Trans R Soc Lond B 305:145–181

Ellington CP (1984b) The aerodynamics of insect flight. III. Kinematics. Proc R Soc Lond B 305:41–78

Ellington CP (1985) Power and efficiency of insect flight muscle. J Exp Biol 115:293–304

Ellington CP (1999) The novel aerodynamics of insect flight: applications to micro-air vehicles. J Exp Biol 202:3439–3448

Feuerbacher E, Fewell JH, Roberts SP, Smith EF, Harrison JF (2003) Effects of load type (pollen or nectar) and load mass on hovering metabolic rate and mechanical power output in the honey bee *Apis mellifera*. J Exp Biol 206:1855–1865

Ganguli R, Gorb S, Lehmann F-O (2008) Experiments on fly wing structure for biomimetic robotic flying insect design. AIAA 2008–1835

Gorb SN (1999) Serial elastic elements in the damselfly wing: mobile vein joints contain resilin. Naturwissenschaften 86:552–555

Gordon JE (1978) Structures: or why things don't fall down. Penguin Books, New York

Grodnitsky DL (1999) Form and function of insect wings: the evolution of biological structures. Johns Hopkins University Press, Baltimore

Josephson RK (1997) Power output from a flight muscle of the bumblebee Bombus terrestris: III. Power during simulated flight. J Exp Biol 200:1241–1246

King B (1993) Flight activity in the parasitoid wasp *Nasonia vitripennis* (Hymenoptera: Pteromalidae). J Insect Behav 6:313–321

Lan CE (1979) The unsteady quasi-vortex-lattice method with applications to animal propulsion. J Fluid Mech 93:747–765

Lan S, Sun M (2001) Aerodynamic force and flow structures of two airfoils in flapping motions. Acta Mech Sin 17:310–331

Langellotto GA, Denno RF, Ott JR (2000) A trade-off between flight capability and reproduction in males of a wing-dimorphic insect. Ecology 81:865–875

Lehmann F-O (2001) The efficiency of aerodynamic force production in *Drosophila*. J Comp Biochem Physiol A 131:77–88

Lehmann F-O (2008) When wings touch wakes: understanding locomotor force control by wake–wing interference in insect wings. J Exp Biol 211:224–233

Lehmann F-O, Dickinson MH (1997) The changes in power requirements and muscle efficiency during elevated force production in the fruit fly, *Drosophila melanogaster*. J Exp Biol 200:1133–1143

Lehmann F-O, Heymann N (2006) Dynamics of in vivo power output and efficiency of *Nasonia* asynchronous flight muscle. J Biotech 124:93–107

Lehmann F-O, Sane SP, Dickinson MH (2005) The aerodynamic effects of wing–wing interaction in flapping insect wings. J Exp Biol 208:2075–3092

Luttges MW (1989) Accomplished insect fliers. In: Gad-el-Hak M (ed) Frontiers in experimental fluid mechanics, Lecture Noted in Engineering. Springer, Berlin, pp 429–456

Maybury WJ, Lehmann F-O (2004) The fluid dynamics of flight control by kinematic phase lag variation between two robotic insect wings. J Exp Biol 207:4707–4726

Miller LA, Peskin CS (2004) When vortices stick: an aerodynamic transition in tiny insect flight. J Exp Biol 207:3073–3088

Moore JR (2006) Stretch activation: towards a molecular mechanism. In: Vigoreaux JO (ed) Nature's versatile engine: insect flight muscle inside and out. Landes Bioscience, Georgetown, pp 44–56

Norberg RA (1975) Hovering flight of the dragonfly *Aeschna juncea* L. In: Wu TY-T, Brokaw CJ, Brennen C (eds) Kinematics and aerodynamics, vol 2. Plenum Press, New York, pp 763–781

Prouty RW (2005) Helicopter performance, stability, and control. Kreiger, Malaba

Ramamurti R, Sandberg WC (2007) A computational investigation of the three-dimensional unsteady aerodynamics of *Drosophila* hovering and maneuvering. J Exp Biol 210:881–896

Reavis MA, Luttges MW (1988) Aerodynamic forces produced by a dragonfly. AIAA J 88-0330:1–13

Rüppell G (1989) Kinematic analysis of symmetrical flight manoeuvres of odonata. J Exp Biol 144:13–42

Saharon D, Luttges MW (1987) Three-dimensional flow produced by a pitching–plunging model dragonfly wing. AIAA J 87-0121:1–17

Saharon D, Luttges MW (1988) Visualization of unsteady separated flow produces by mechanically driven dragonfly wing kinematics model. AIAA J 88-0569:1–23

Saharon D, Luttges MW (1989) Dragonfly unsteady aerodynamics: the role of the wing phase relationship in controlling the produced flows. AIAA J 89-0832:1–19

Sane S, Dickinson MH (2001a) The control of flight force by a flapping wing: lift and drag production. J Exp Biol 204:2607–2626

Sane S, Dickinson MH (2001b) Erratum. J Exp Biol 204:3401

Sedov LI (1965) Two-dimensional problems in hydrodynamics and aerodynamics. Interscience Publishers, New York, pp 20–30

Srygley RB, Thomas ALR (2002) Unconventional lift-generating mechanisms in free-flying butterflies. Nature 420:660–664

Stafford N (2007) Spy in the sky. Nature 445:808–809

Sun M, Lan SL (2004) A computational study of the aerodynamic forces and power requirements of dragonfly (*Aeshna juncea*) hovering. J Exp Biol 207:1887–1901

Sun M, Tang J (2002) Unsteady aerodynamic force generation by a model fruit fly wing flapping motion. J Exp Biol 205:55–70

Thomas ALR, Taylor GK, Srygley RB, Nudds RL, Bomphrey RJ (2004) Dragonfly flight: free-flight and tethered flow visualizations reveal a diverse array of unsteady lift-generating mechanisms, controlled primarily via angle of attack. J Exp Biol 207:4299–4323

Usherwood JR, Ellington CP (2002) The aerodynamic of revolving wings I. Model hawkmoth wings. J Exp Biol 205:1547–1564

Usherwood JR, Lehmann F-O (2008) Phasing of dragonfly wings can improve aerodynamic efficiency by removing swirl. J R Soc Interface 1–6. doi:10.1098/rsif.2008.0124

Vandenberghe N, Zhang J, Childress S (2004) Symmetry breaking leads to forward flapping flight. J Fluid Mech 506:147–155

Wakeling JM, Ellington CP (1997a) Dragonfly Flight II. Velocities, accelerations, and kinematics of flapping flight. J Exp Biol 200:557–582

Wakeling JM, Ellington CP (1997b) Dragonfly flight III. Lift and power requirements. J Exp Biol 200:583–600

Wang ZJ, Russell D (2007) Effect of forewing and hindwing interactions on aerodynamic forces and power in hovering dragonfly flight. Phys Rev Lett 99. doi:10.1103/PhysRevLett.99.148101

Wang H, Zeng L, Liu H, Chunyong Y (2003) Measuring wing kinematics, flight trajectory and body attitude during forward flight and turning maneuvers in dragonflies. J Exp Biol 206:745–757

Weis-Fogh T (1972) Energetics of hovering flight in hummingbirds and in *Drosophila*. J Exp Biol 56:79–104

Weis-Fogh T (1973) Quick estimates of flight fitness in hovering animals, including novel mechanisms for lift production. J Exp Biol 59:169–230

Experimental investigation of some aspects of insect-like flapping flight aerodynamics for application to micro air vehicles

Salman A. Ansari · Nathan Phillips · Graham Stabler · Peter C. Wilkins · Rafał Żbikowski · Kevin Knowles

Abstract Insect-like flapping flight offers a power-efficient and highly manoeuvrable basis for micro air vehicles for indoor applications. Some aspects of the aerodynamics associated with the sweeping phase of insect wing kinematics are examined by making particle image velocimetry measurements on a rotating wing immersed in a tank of seeded water. The work is motivated by the paucity of data with quantified error on insect-like flapping flight, and aims to fill this gap by providing a detailed description of the experimental setup, quantifying the uncertainties in the measurements and explaining the results. The experiments are carried out at two Reynolds numbers—500 and 15,000—accounting for scales pertaining to many insects and future flapping-wing micro air vehicles, respectively. The results from the experiments are used to describe prominent flow features, and Reynolds number-related differences are highlighted. In particular, the behaviour of the leading-edge vortex at these Reynolds numbers is studied and the presence of Kelvin–Helmholtz instability observed at the higher Reynolds number in computational fluid dynamics calculations is also verified.

S. A. Ansari (✉)
Meggitt Avionics, 7 Whittle Avenue, Segensworth West, Fareham PO15 5SH, UK
e-mail: salman.ansari@meggitt.com

N. Phillips · G. Stabler · R. Żbikowski · K. Knowles
Cranfield University, Defence Academy of the UK, Shrivenham, Swindon SN6 8LA, UK

P. C. Wilkins
Dstl Farnborough, Ively Road, Farnborough GU14 0LX, UK

Keywords Low Reynolds number flow · Insect flight · Flapping wing · Micro air vehicles · Particle image velocimetry · Leading-edge vortex · Kelvin–Helmholtz instability

1 Introduction

Agile flight inside buildings, caves and tunnels is of significant military and civilian value because current surveillance assets (such as satellites or unmanned air vehicles) possess virtually no capabilities of information-gathering in enclosed spaces. The focus on indoor flight leads to the requirement of a distinct flight envelope. In addition, autonomy is required to enable mission-completion without the assistance of a human telepilot; this requires precise flight control. Current unmanned aerial vehicles (UAVs) are too large to achieve indoor flight and our research has concluded (Żbikowski 1999a, b, 2000; Ansari et al. 2006a) that insect-like flapping flight is the optimum way to fulfil this capability—fixed wing aircraft do not have the required low-speed agility and miniature helicopters are too inefficient and noisy. Insects, on the other hand, fly at low speeds, are extremely manoeuvrable, virtually silent and most are capable of hover. In addition, insect flapping flight offers significantly better power efficiency, particularly at low flight speeds, than both fixed-wing aircraft and rotorcraft (Woods et al. 2001; Żbikowski et al. 2003), making it ideal for our focus on flapping-wing micro air vehicles (FMAVs) for indoor flight. Insect flapping flight has been present in nature for over 300 million years and fossil evidence suggests it has changed little over this time (Dudley 1992).

FMAVs will implement insect-like wing kinematics for flight, propulsion and control. It is, therefore, of great interest to understand such kinematics and their effects in

G.K. Taylor, M.S. Triantafyllou, and C. Tropea (Eds.): Animal Locomotion, pp. 215–236.
springerlink.com

the flows they produce. In this paper, the flow around a constant-speed rotating wing at high angle of attack (emulating an insect-like flapping wing in the sweeping phase of its cycle) is studied experimentally. The inspiration for these experiments is drawn from the computational fluid dynamics (CFD) investigations of Wilkins et al. (Wilkins et al. 2006; Wilkins and Knowles 2007, 2008) who performed such studies at various Reynolds numbers (*Re*) and described their findings in terms of the development of the leading-edge vortex and occurrence of Kelvin–Helmholtz instabilities (see Sect. 1.2 below).

This paper is organised as follows. Insect wing kinematics and the associated aerodynamics are described in brief below, with emphasis on the leading-edge vortex and Kelvin–Helmholtz instability, followed by the aims and objectives of the study in Sect. 2. Section 3 describes in detail the experimental setup, noting the equipment used and explaining the methodology employed. In Sect. 4, possible sources of error in the experiments are identified and the uncertainty they introduce is quantified. The results from the study are discussed in detail in Sect. 5 and the main findings from the study are summarised in Sect. 6.

1.1 Insect wing kinematics

The insect-wing kinematics described here are found in Diptera, which are two-winged flies, as they are easy to analyse and emulate, and are excellent flyers. We are loosely inspired by the papers of Ennos (1987, 1989). A complete flapping cycle is made up of two half-strokes—downstroke and upstroke—and two stroke reversals (see Fig. 1). The downstroke describes the motion of the wing as it sweeps from its rearmost to its foremost position, relative to the insect body. The upstroke describes the return cycle. During the stroke reversals, the wing pitches up rapidly and flips over for the subsequent half-stroke so that the leading edge always leads.

In this paper, we address some aspects associated with the flow during the sweeping phase of the flapping cycle. Wing sweep typically lasts about 80–90% of the flapping cycle (Ellington 1984a) during which pitch changes are minimal. During a half-stroke, the wing accelerates to a maximum speed around the middle of the half-stroke, before slowing down to rest at the end of it. Hence, the velocity during the wing-beat cycle is non-uniform and for hover, in particular, the motion of the wing tip does not differ dramatically from a pure sinusoid (Ellington 1984a). The insect wing normally sweeps stroke lengths typically of the order of 3–5 wing chords (Ellington 1984b). The corresponding sweep angles (see Fig. 6) are of the order of 90–120°, although angles greater than 180° are not unknown (Thomas, private communications, Zoology Department, Oxford University).

1.2 Insect-like flapping flight aerodynamics

The aerodynamics of insect flapping flight is too extensive a subject to be addressed in great detail here. The non-uniform nature of insect-wing kinematics drives some salient flow features not expected from conventional aerodynamics. Amongst these are the Wagner effect, the Kramer effect, 'wake capture', effects due to apparent mass and the leading-edge vortex. Full details on these can be found in Ansari et al. (2006a). The leading-edge vortex has been found to be of great significance in insect flight and is considered in more detail below.

Recent CFD studies by the authors have revealed the presence of Kelvin–Helmholtz instability not at the low Reynolds numbers pertaining to insect flight but at the higher Reynolds numbers associated with FMAVs. Hence, a discussion on Kelvin–Helmholtz instability is also included below.

1.2.1 Leading-edge vortex

Although it had been observed in earlier experiments (Martin and Carpenter 1977; Maxworthy 1979; Brodsky 1991; Dickinson and Götz 1993; Sunada et al. 1993) it

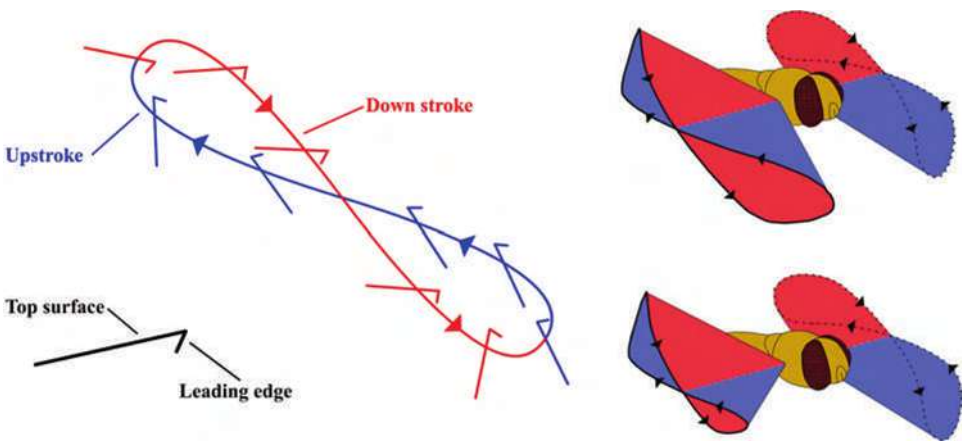

Fig. 1 Generic insect-like flapping-wing kinematics showing symmetric (*right top*) and asymmetric (*right bottom*) wing motion; colour coding: downstroke (*red*), upstroke (*blue*)

was not until the work of Ellington et al. (1996) on a scaled-up model of the hawkmoth *Manduca sexta* ($Re = 5{,}000$, based on the mean chord and rms wing tip speed) that the significance of the leading-edge vortex for insect flapping flight received proper recognition. Later experiments by Ellington et al. have further corroborated its significance (Willmott et al. 1997; van den Berg and Ellington 1997a, b).

Ellington et al. (1996) reported that the leading-edge vortex, which persisted through each half-stroke, existed on the wings and proposed that it was responsible for the high lift forces observed. The overall structure of the leading-edge vortex has been likened to that observed on low-aspect-ratio delta wings (Martin and Carpenter 1977; van den Berg and Ellington 1997a); it is produced and fed by a leading-edge separation. Birch and Dickinson (2001) suggested that spanwise transport of the leading-edge vorticity served to remove energy from it and, hence, limited its growth and shedding (see also Rossow 1978; Riddle et al. 1999). The leading-edge vortex starts close to the wing root and spirals towards the tip where it coalesces with the tip vortex and convects into the trailing wake (Ellington et al. 1996). It remains attached to the wing for most of the half-stroke and is shed at the end when the wing rapidly rotates in pitch. This is in contrast to the behaviour of a leading-edge vortex on a 2D wing, where regular break away and re-formation occur (Dickinson and Götz 1993; Wilkins et al. 2006).

Willmott et al. (1997) speculated that the leading-edge vortex was formed either due to the pitching motions prior to translation or via a dynamic stall mechanism. Although dynamic stall has been suggested by others (e.g. Ellington 1995; Dickinson 1996), this is unlikely (Żbikowski 2002) since a dynamic-stall vortex breaks away almost immediately and rapidly convects as soon as the wing translates (McCroskey, 1981). Also, a dynamic-stall vortex is formed when the wing pitches up, whereas in the rotational wing motion prior to translation the wing pitches down. A detailed account of the nature of the leading-edge vortex and its possible origins can be found in Ansari (2004).

Shyy and Liu (2007) attempted to shed light on the controversy regarding the stability of the leading-edge vortex. They used a 3D RANS CFD model to compare the flows around a thrip wing at $Re = 10$, a fruit fly wing at $Re = 120$, and a hawkmoth wing at $Re = 6{,}000$. Their results indicated that although a leading-edge vortex was formed for each case, the detailed phenomenology of the leading-edge vortex changed as Reynolds number was increased. However, it is diffcult to draw any definite conclusions from their work because when Re was changed, the wing planform was also changed. It is, therefore, not possible to isolate accurately the effect of increasing Re.

Although the leading-edge vortex may be common to most insects (Brodsky 1991; Grodnitsky and Morozov 1993; Willmott et al. 1997; Birch and Dickinson 2001), its spanwise flow characteristic seems to vary with insect size (and, hence, Reynolds number). Recent experiments by Dickinson et al. (Birch and Dickinson 2001; Sane and Dickinson 2001; Birch et al. 2004) on a dynamically scaled mechanical model of the tiny fruit fly *Drosophila melanogaster* ($Re \sim 200$) revealed the presence of a strong, bound, leading-edge vortex but they reported only weak spanwise spiralling [unlike for the hawkmoth observed by Ellington et al. (1996)], prompting them to conclude that the precise flow structure of the leading-edge vortex depends critically on Reynolds number (Birch et al. 2004). This is supported to an extent by Ellington (2006) who suggested that spanwise flow exists at all relevant speeds but its spiralling nature becomes less discernable as the Reynolds number decreases. Particle image velocimetry (PIV) measurements by Ramasamy and Leishman (2006) on a flapping wing ($Re = 15{,}500$, based on the maximum stroke velocity and mean aerodynamic chord) revealed spanwise flow within the leading-edge vortex of the same order of magnitude as the tip velocity. They also reported that the leading-edge vortex eventually broke away from the wing, but Wilkins (2008) suggests that this may have been due to wing incidence fluctuations in their experiments.

1.2.2 Kelvin–Helmholtz instability

Kelvin–Helmholtz instability is the process whereby a vortex sheet 'bunches' into smaller areas of vorticity. It can occur anywhere where there is a shear layer within the fluid or between two different fluids, i.e. a discontinuity in velocity, density, or viscosity. The susceptibility of a vortex sheet to Kelvin–Helmholtz instability depends on three factors: the ratio of densities of the fluids on either side of the sheet, the ratio of viscosities of the fluids on either side of the sheet, and the gradient of tangential velocity of the fluids across the sheet (for further details, see Drazin and Reid 1981). The formation of waves in water is attributed to Kelvin–Helmholtz instability. Kelvin–Helmholtz instability has also been observed in cloud formations (Drazin and Reid 1981, p. 21). 2D flows are particularly susceptible to this type of instability (Kim et al. 2003).

The occurrence of Kelvin–Helmholtz instability also appears to increase with Reynolds number, i.e. by increasing fluid density or chord length, or by decreasing fluid viscosity. At higher Reynolds numbers, the viscous forces are lower in proportion to the inertial forces, so that vortices develop and strengthen more readily, and velocity gradients are greater. CFD calculations by Wilkins (2008) show that it

is the gradient of velocity across a vortex sheet and not its magnitude that promotes Kelvin–Helmholtz instability. The interested reader is referred to Wilkins (2008) for for a detailed discussion on the subject.

Recent CFD calculations by Wilkins et al. (Wilkins et al. 2006; Wilkins and Knowles 2007) have shown Kelvin–Helmholtz instability not only for 2D flows but also for 3D ones. They report that Kelvin–Helmholtz instability occurs in both leading- and trailing-edge vortex sheets at higher Reynolds numbers ($Re > 1{,}000$) for both 2- and 3D flows, but does not result in the 3D leading-edge vortex detaching from the wing (Wilkins and Knowles 2007).

2 Aims and objectives

The aim of the present experiment was to study the flow associated with the sweeping phase of insect-like flapping flight at scales relating to actual insects and to FMAVs. The intention was to identify the behaviour of the leading-edge vortex and clarify the disparity that exists in the literature concerning it, and also to study the trailing-edge vortex, tip vortex and spanwise flow. Recent CFD studies by the authors have shown the existence of Kelvin–Helmholtz instability for the 3D flow around a rotating wing; a further aim of this study was to validate this

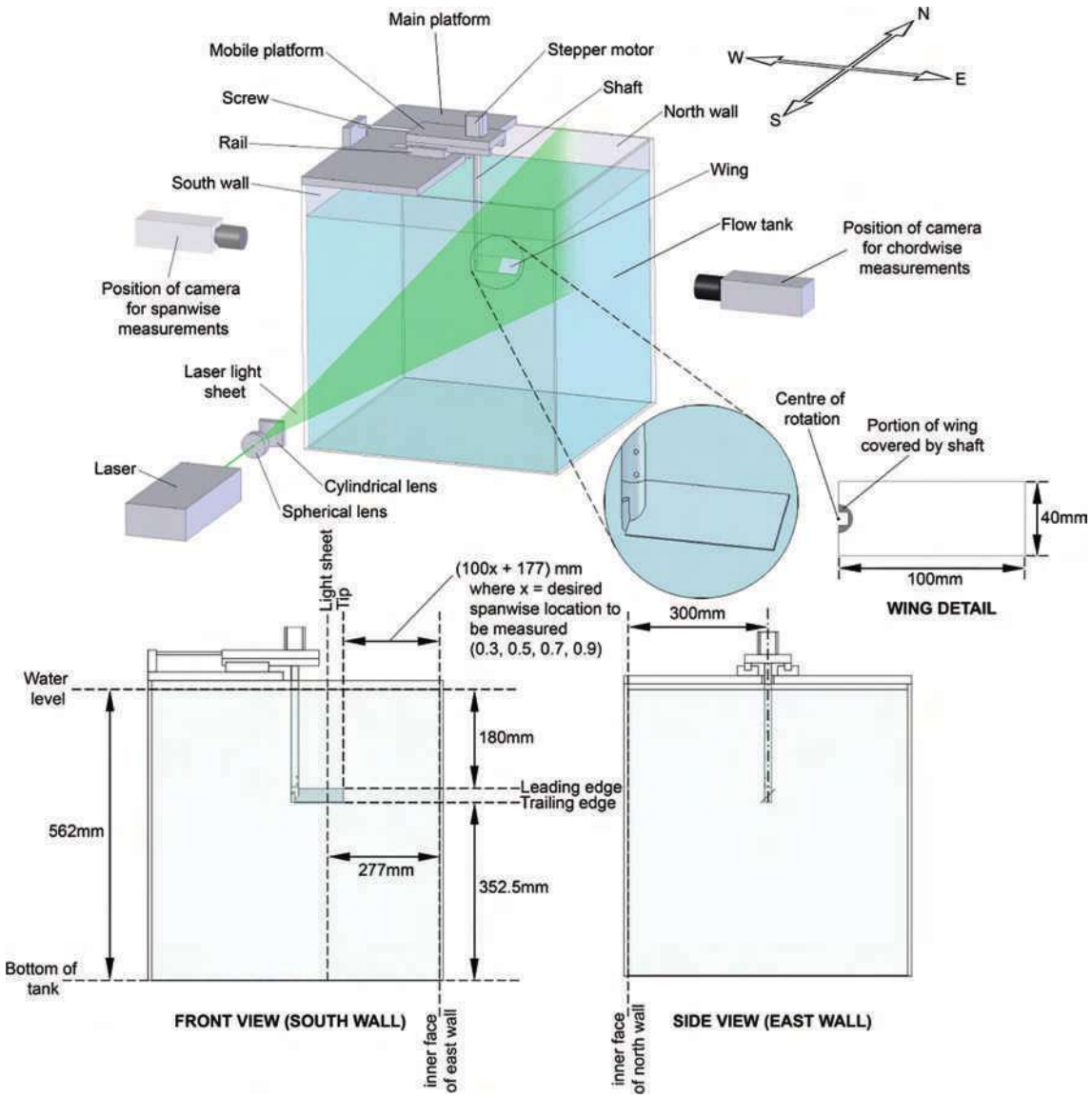

Fig. 2 Diagram of experimental setup with water tank, rotating-wing rig, laser and camera; isometric view (*top*), front view (*bottom left*), side view (*bottom right*), wing detail (*centre right*)

finding. Due to our interest in flow features only, no forces and moments, or their components (e.g. centrifugal and Coriolis forces), were measured or computed.

3 Experimental setup

The experiments were carried out on a rotating wing in a water tank and flow measurements were made using a PIV system. The data obtained were processed using off-the-shelf commercial software. Details of these three elements form the subject of the following subsections.

3.1 Water tank and rotating-wing rig

This element of the experimental setup consisted of a water tank with a rotating-wing rig mounted to it. The open-topped water tank was constructed from 8-mm-thick clear glass measured 600 × 600 × 600 mm^3 (see Fig. 2). Water was filled to a depth of 562 mm to allow for the rotating-wing rig. The tank was placed on a rigid table that provided a stable platform for measurements.

Seeding for the PIV measurements was provided by SP Micro Balloons (©RIPMax plc) because of their near-neutral buoyancy and suitable size for PIV measurements (average particle size 28 μm). The quantity of seeding was regulated by monitoring the output from the PIV system. The tank walls were mopped regularly to improve optical access that was otherwise impeded by leftover seeding on the tank walls. More seeding particles were added to compensate for those lost to cleaning. During the course of the experiments presented here, the water in the tank was replaced once.

The rotating-wing rig was mounted on top of the water tank (see Fig. 2). This mounting consisted of a platform that fitted tightly over the top of the water tank and was mounted flush with one of the tank's inner walls, covering almost half of the exposed area.

The rotating wing (taken here to mean the wing/blade and the hub) was attached by means of a 15-mm-diameter shaft to a second screw-driven mobile platform that was mounted on parallel rails running across the middle of the main platform. The horizontal position of the rotating-wing shaft in the water tank was controlled manually by adjusting the screw on the mobile platform. This position was controlled to within 0.5 mm. The vertical position of the rotating wing was fixed by the length of the shaft which placed it in the centre of the water tank. This arrangement enabled data for different spanwise and chordwise positions to be acquired without having to move the laser light sheet.

The rotating wing had only one 'blade'—an aspect ratio 4 rectangular wing with 40 mm chord and 100 mm length—made from 2 mm thick steel plate for rigidity (see wing detail in Fig. 2). The wing was embedded in the rotating-wing shaft at 45° angle-of-attack and such that rotation was about the midchord position at the wing root. The rotating-wing shaft extended 7.5 mm into the wing, thus occupying only a little over 2% of the wing area (Fig. 2).

3.2 PIV system

The PIV system used in the experiment employed a Nd:YAG laser with a wavelength of 532 nm and a pulse width of 10 ns. A set of lenses, consisting of a spherical lens with a negative focal length followed by a cylindrical lens with a positive focal length, was used to transform the beam into a light sheet. The light sheet was oriented such that it was parallel to and 277 mm away from the east wall of the water tank (see Fig. 2). Image pairs were captured using a Kodak Mega Plus ES1.0 camera which had a CCD chip measuring 9.07 mm wide by 9.14 mm tall. The CCD chip size in pixels was 1,008 × 1,016, where each pixel was 9 × 9 μm^2. The lens used on the camera was a 50 mm focal length Nikkor AFD set to a lens aperture (f#) of 2.8. Lastly, the working distances (distance from camera to light sheet) used for the spanwise (along the wing span at constant chord positions) and chordwise (along the wing chord at constant span positions) measurements were 360.5 and 560.2 mm, respectively.

Table 1 PIV acquisition parameters

	Spanwise measurements		Chordwise measurements	
	Re = 500	Re = 15,000	Re = 500	Re = 15,000
Area of interest (mm^2)	70.5 × 71	70.5 × 71	109.6 × 110.4	109.6 × 110.4
Image size (px^2)	1,008 × 1,016	1,008 × 1,016	1,008 × 1,016	1,008 × 1,016
Magnification	0.129	0.129	0.083	0.083
Lens aperture (f#)	2.8	2.8	2.8	2.8
Calibration (px/mm)	14.3	14.3	9.2	9.2
Pulse separation (ms)	30	1.2	70	1.2
Observed maximum in-plane displacement (px)	3–7.2	5.1–10.6	5.2–9.6	3.7–7

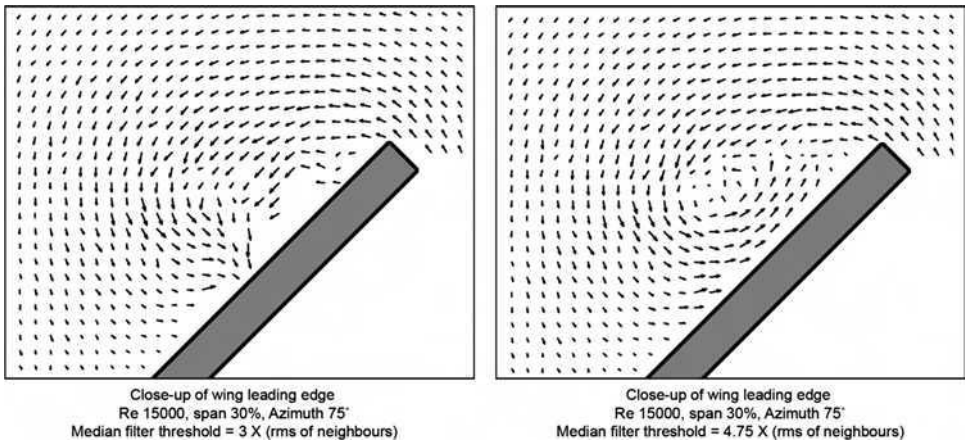

Fig. 3 Effect of median filter thresholding shown for too stringent (*left*) and adequate (*right*) thresholds

3.3 Data processing

Acquisition parameters used for both spanwise and chordwise measurements are summarised in Table 1. Listed are the areas imaged, the image sizes, magnification, lens aperture (f#), calibration, pulse separation, and the observed range of maximum in-plane displacements using the indicated pulse separations. The acquired image pairs were processed with DaVis FlowMaster software version 6.2.3 by LaVision, utilising a standard cyclic FFT-based cross-correlation algorithm. Second-order correlation, as described in Hart (1998), was also employed along with a Gaussian peak fit to locate correlation peaks to within sub-pixel resolution.

Using the cross-correlation method described, an adaptive multiple pass interrogation algorithm was employed using a coarse 'initial' grid progressing to a fine 'final' grid. Deformed interrogation windows were also used which further increases the number of matched particles and the signal-to-noise ratio. A total of four passes were utilised starting with an initial interrogation window size of 32×32 px^2 in the first pass progressing to 16×16 px^2 and 12×12 px^2 in the subsequent two passes, followed by a final interrogation window size of 8×8 px^2 in the final pass with a 0% overlap.

Between passes from the initial to final interrogation window size, the median filter proposed by Westerweel (1994) was utilised to locate spurious vectors and replace them by interpolation. Problems with this type of filter typically occur around empty areas in the vector field where there are fewer neighbours for comparison (Raffel et al. 1998). A problem of this nature was encountered at the wing leading edge where too stringent a threshold was found to alter flow structures incorrectly (Fig. 3). It was found that a threshold of 4.75 $\times$ (rms of neighbours) was suitable, as it identified spurious vectors but did not alter flow structures that were observed without the median filter.

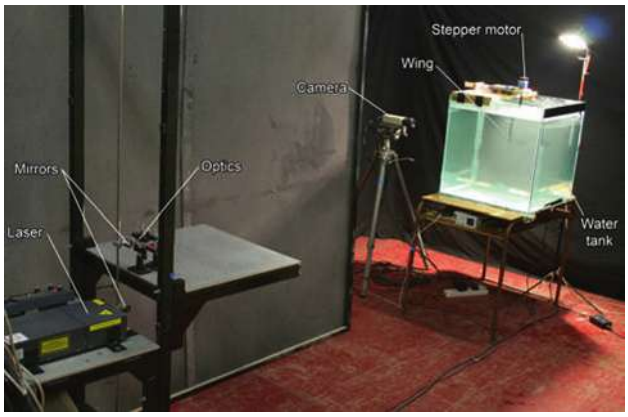

Fig. 4 Photograph of experimental setup

The number of vectors in a given vector field which had to be inserted via interpolation either due to loss of correlation in the final interrogation window from insufficient seeding or due to removal of spurious vectors was on average $\sim$2.5% with a minimum of 0.5% and maximum of 7%. The observed level of interpolated vectors was mainly a consequence of the small final interrogation window size. However, it was felt that this level of interpolated vectors was acceptable since vortex structures, such as the leading-edge vortex, were of primary interest in the present experiment, and small interrogation window sizes are better for resolving such structures. This is because they minimize biasing error and loss of correlation resulting from the velocity gradients and rotational motions associated with vortices (Willert and Gharib 1991).

3.4 Experimental procedure

The various components of the experimental setup were arranged as shown in Fig. 4. The experiments were carried out in a cool room (15 ± 5°C). Both chordwise and spanwise flow measurements were made at various wing

azimuthal positions. The wing was started from rest and moved through an azimuth angle ϕ at constant speed to reach the test position. All measurements are of the wing's first sweep without a developed wake and induced flow field. In this way, it differs from the work of Lu and Shen (2008) who allowed for the flow around their flapping wing to become reasonably periodic before taking measurements. PIV measurements were made as the wing passed through ϕ. The wing continued moving to $\phi + 5°$, then stopped and backed up to the next starting position. Settling time (see Sect. 4.3) was allowed before the next sweep from the new starting position commenced.

The test conditions are summarised in Table 2. Two wing speeds, giving Re = 500 and 15,000, were used to capture flow properties relevant to many insects and micro air vehicles, respectively. Reynolds number is defined with respect to mean wing chord (40 mm) and mean wingtip speed (100 mm $\times$ $2\pi f$), where f is rotation rate (0.126 and 3.77 Hz for Re = 500 and 15,000, respectively, in water, density ρ = 998 kg/m^3 and viscosity $\mu = 1.003 \times 10^{-3}$ Pa s). Due to the settling times required between tests (see Sect. 4.3) and in the interest of capturing the same positions for both flow speeds (to enable like-for-like comparisons), the flow was measured at 12 azimuthal positions. Except for the spanwise positions for Re = 500, all experiments were run twice and the results shown here are for the flow fields obtained by averaging the two datasets.

Table 2 Test cases

Spanwise measurement planes (% span)	30, 50, 70, 90
Chordwise measurement planes (% chord)	50
Azimuthal positions (°)	5, 10, 15, 30, 45, 60, 75, 90, 135, 180, 225, 270
Reynolds numbers	500, 15,000

To reduce errors, the laser, camera and water tank were kept stationary. Measurements at the various spanwise, chordwise and azimuthal positions of the wing were facilitated by moving the rotating wing alone. For example, for an azimuthal position of 90°, the wing was started 90° before the trigger position. Similarly, for various spanwise measurement positions, the drive shaft of the rotating wing was positioned by adjusting the screw-driven platform to which the rotating-wing drive shaft was attached. The drive shaft was started impulsively in all cases, reaching final rotational speed one motor step after start.

A typical experimental run started with stirring the tank to distribute seeding and to allow particles that had risen to the surface to descend into the tank. Ample time was allowed to let the flow settle before moving the wing and taking measurements (see Sect. 4.3 below). The experimental programme went through all azimuthal positions, firing the laser and triggering the camera at the correct

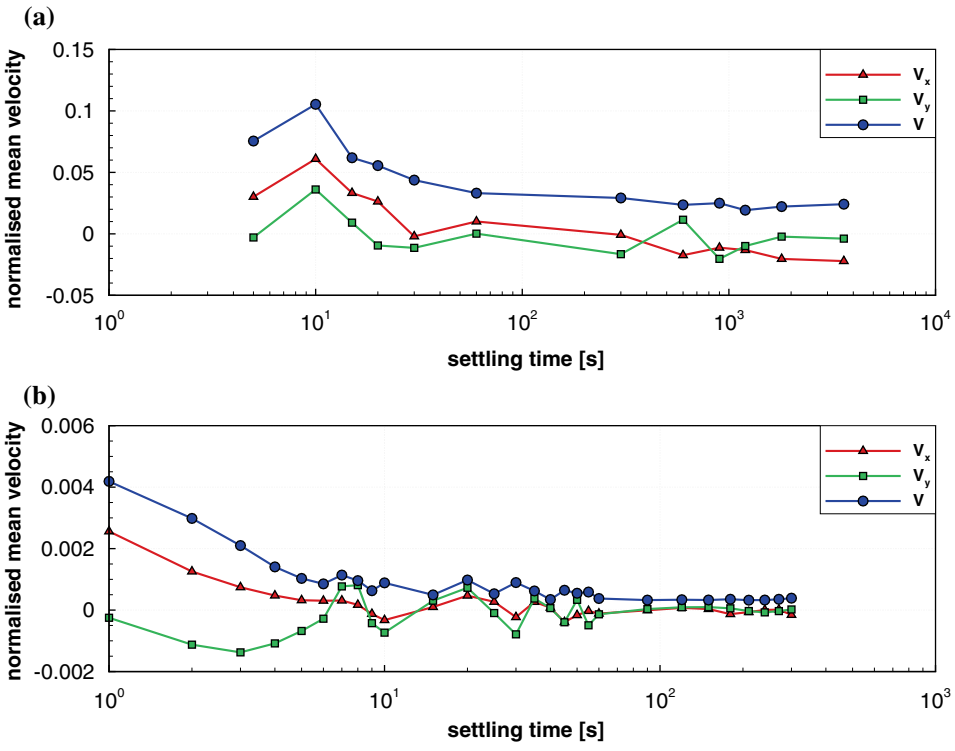

Fig. 5 Mean normalised velocities for Re = 500 and 15,000 at 90% span for various settling times (V_x is mean $x-$velocity, V_y is mean $y-$velocity and V is mean velocity magnitude; all velocities are normalised w.r.t. the wing velocity at 90% span). **a** Re = 500, **b** Re = 15,000

instances. For the case of Re = 15,000, a typical run lasted about 3 min while for Re = 500 it was of the order of 4 h.

4 Uncertainty analysis

4.1 Seeding response

The seeding response was evaluated by observing the gravitationally induced flow velocity originating from the difference in density between the seeding particles and the fluid. A 'settling time' experiment, which will be discussed in detail in Sect. 4.3 below, was performed to observe the motion of the fluid at various time intervals following a wing translation. As will be shown later, when the fluid had settled, the mean vertical velocity was observed to be essentially zero, which suggests that the difference in density between the seeding particles and the fluid was minimal. This, in conjunction with the fact that the velocity lag of a particle in an accelerating fluid is proportional to the difference in density between the particle and the fluid according to the Stokes drag law (Raffel et al. 1998), led to the assumption that the seeding response error was negligible.

4.2 PIV error

Errors in PIV measurements can be divided into three forms: outliers, mean-bias errors, and root mean square (rms) errors (Huang et al. 1997). Outliers were identified and removed using the median filter discussed in Sect. 3.3. The other two forms of error will now be discussed and evaluated.

To quantify rms error, the approach used was that of Willert and Gharib (1991), in which rms error is measured by processing particle image pairs where the particles have been displaced by an amount that is known reliably. Using this approach, the water tank was left undisturbed for 1 h and image pairs were captured using a pulse separation of 1 μs. This short pulse separation in conjunction with an undisturbed tank meant that the actual displacement of the particle images between pulses was confidently known to be zero. Therefore, any displacement that was measured was random error. Five image pairs were taken for both magnifications listed in Table 1, and were processed using the same method described in Sect. 3.3. The equation for rms error as given in (Huang et al. 1997) was then applied to each set of vector maps to calculate the rms error for each magnification. This revealed rms errors of 0.43 and 0.35 px for the magnifications used in the spanwise and chordwise measurements, respectively.

Mean-bias error is directly proportional to the particle image displacement and the velocity gradient within an interrogation window; thus, if these are minimised then mean-bias error may be made negligible (Keane and Adrian 1990). From this, it can be argued that mean-bias error in the present experiment was negligible since velocity gradients and particle image displacements were minimised through use of a small final interrogation window size and an offset, respectively.

The total error in the present experiment is dominated by rms error as all other forms of error were found to be negligible. This is in agreement with the observation that for particle image sizes $\gg$1 px, rms error will dominate (Westerweel 1997), where the particle image sizes observed were on average $\sim$1.8 and $\sim$1.6 px for the two measurement cases. Thus, with an rms error of 0.43 px for the chordwise measurements, this leads to a measurement uncertainty of $\pm$0.001 and $\pm$0.025 m/s for the Re = 500 and 15,000 cases, respectively. Similarly, for the spanwise measurements, in the Re = 500 and 15,000 cases an rms

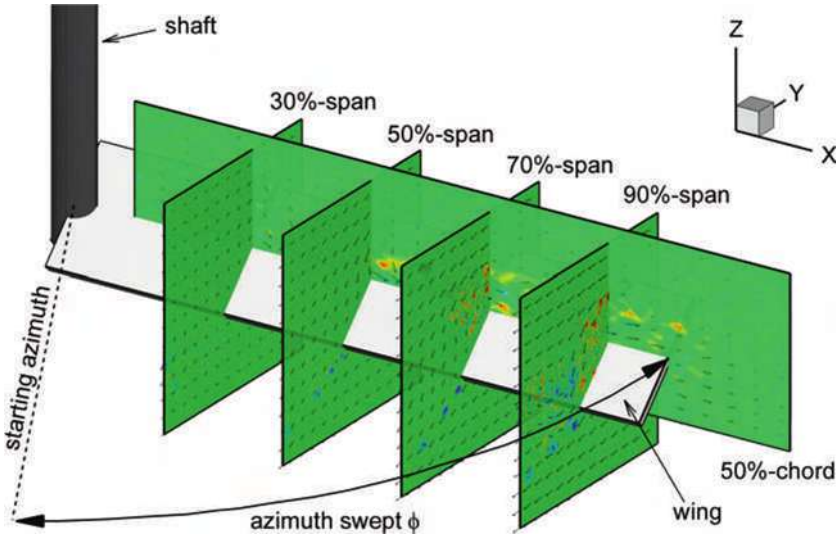

Fig. 6 Diagram showing arrangement of planes captured in the PIV experiments with the wing shown at the trigger position

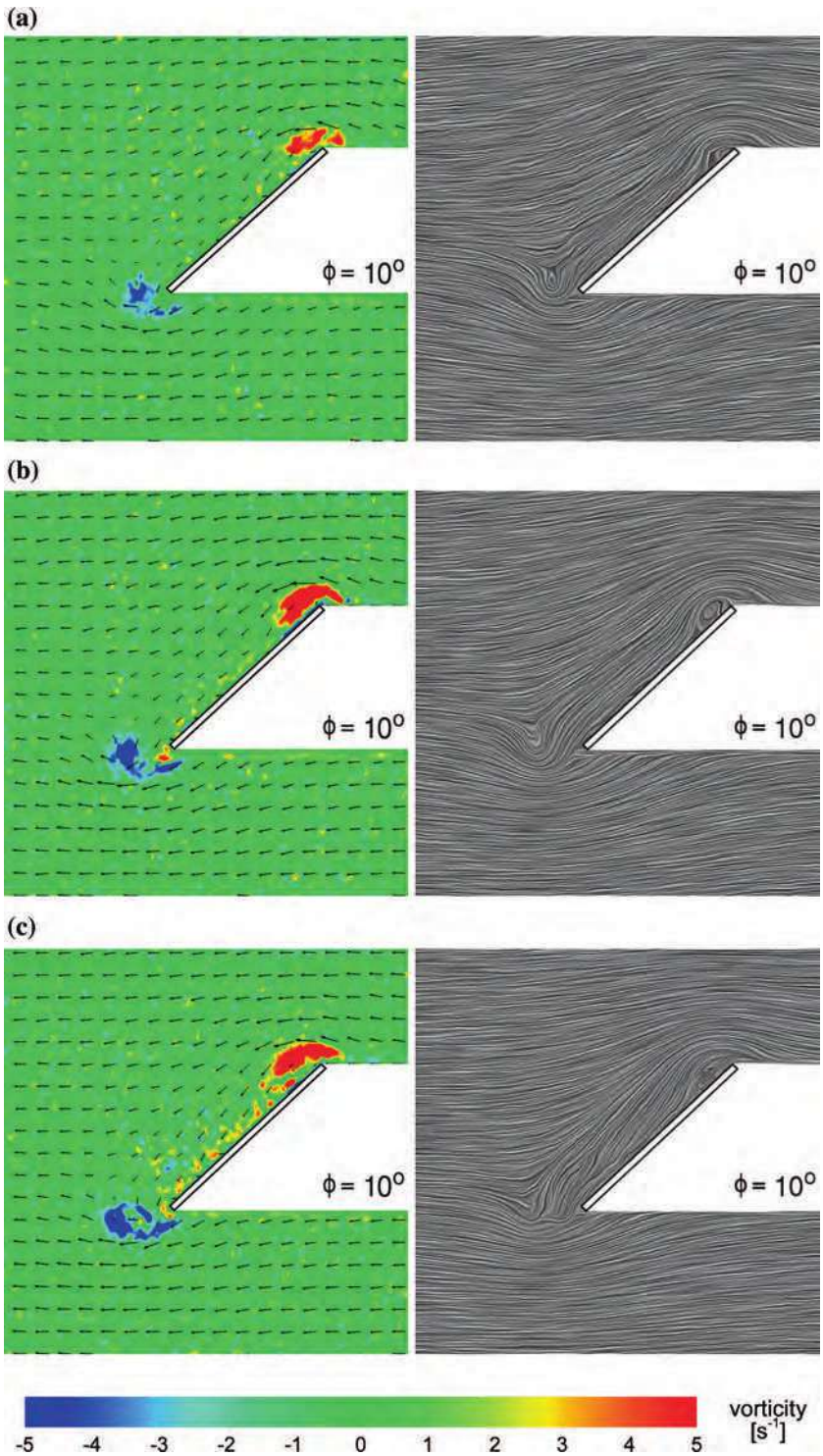

Fig. 7 Effect of spanwise position on chordwise flow for Re = 500 at 10° azimuth, shown by plots of contours of vorticity overlayed with velocity vectors (*left*) and LIC images (*right*). **a** 50% span, **b** 70% span, **c** 90% span

error of 0.35 px leads to a measurement uncertainty of 5.4×10^{-4} m/s and $\pm$ 0.032 m/s, respectively.

4.3 Other considerations

Since the wing was rotated while the measurement system was kept fixed, only one measurement could be made per pass. To make several measurements, the rotating wing was started from different starting azimuths. One of the most important considerations in the experiments, therefore, was the settling time between runs. To measure the 'stillness' of the flow in the tank, PIV measurements were made of the area of interest for various settling times after the wing motion ceased in preparation for a subsequent test

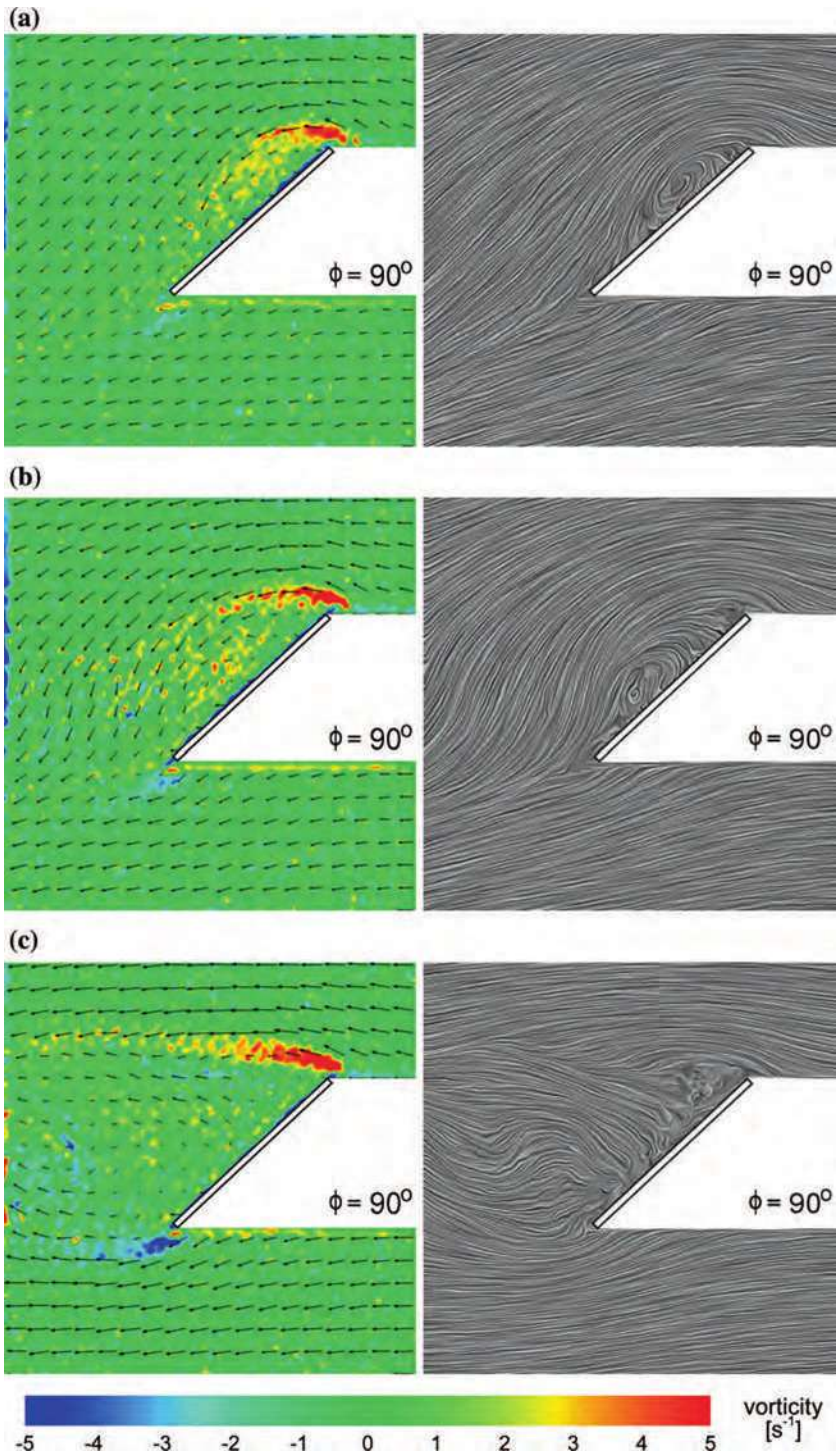

Fig. 8 Effect of spanwise position on chordwise flow for $Re = 500$ at 90° azimuth, shown by plots of contours of vorticity overlayed with velocity vectors (*left*) and LIC images (*right*). **a** 50% span, **b** 70% span, **c** 90% span

(see also Ansari et al. 2009). This was done for the largest azimuthal position ($\phi = 270°$) and the 90% span position for which the flow disturbances were envisaged to be the greatest.

The results from this study are summarised in Fig. 5, where velocities are normalised w.r.t. the wing velocity at 90% span. It is evident that there are diminishing returns for longer settling times, owing to dropping seeding levels and movement arising from the buoyancy and collision of seeding particles. On the basis of the results, at $Re = 500$, a settling time of 20 min was chosen for the wing PIV measurements, corresponding to a mean normalised flow velocity of less than 2% (see Fig. 5a). For $Re = 15{,}000$, this settling time between runs was fixed at 10 s (see Fig. 5b); mean normalised flow speeds for this interval were less than 0.1%.

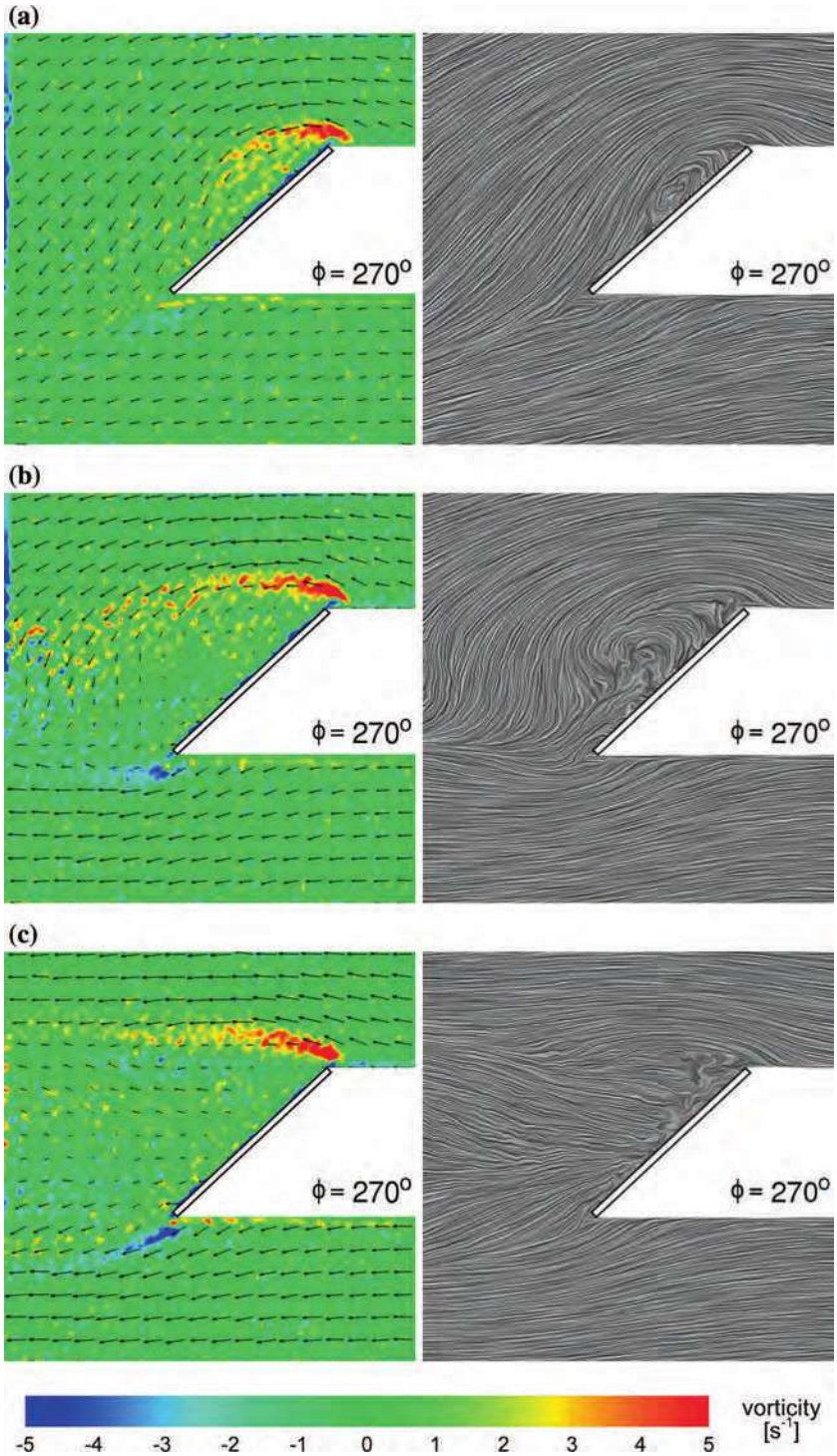

Fig. 9 Effect of spanwise position on chordwise flow for Re = 500 at 270° azimuth, shown by plots of contours of vorticity overlayed with velocity vectors (*left*) and LIC images (*right*). **a** 50% span, **b** 70% span, **c** 90% span

There are other possible sources of discrepancies that are not easily quantifiable. Because wing position in the tank was altered for each of the chordwise measurements (30–90% span), the rotating wing was not always in the middle of the tank horizontally; it was off-centre by 7–67 mm which could give rise to errors due to wall effects and asymmetry. Given the size of the wing relative to the tank, however, these effects are assumed to be minimal. There are also possible errors resulting from the recirculating flow due to wall effects; minimum wall clearance varied from 5.2 to 6.7 mean wing chords. This effect was minimised by the short run durations and the settling times between runs.

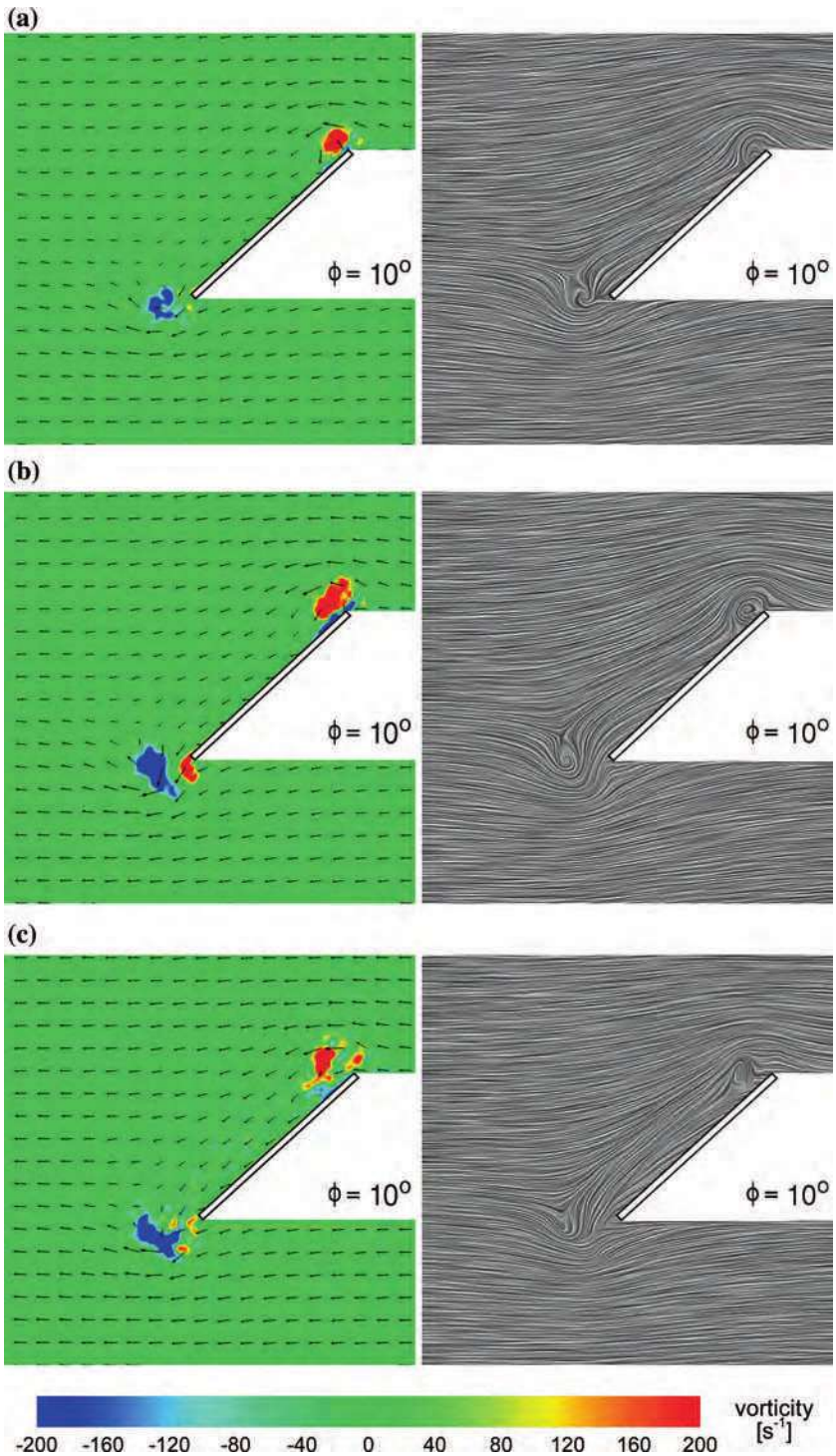

Fig. 10 Effect of spanwise position on chordwise flow for $Re = 15{,}000$ at 10° azimuth, shown by plots of contours of vorticity overlayed with velocity vectors (*left*) and LIC images (*right*). **a** 50% span, **b** 70% span, **c** 90% span

5 Results and discussion

Data were generated according to the test cases described in Table 2. They were for two Reynolds numbers (Re = 500 and $Re = 15{,}000$) in four chordwise planes (at 30, 50, 70 and 90% span positions) and 1 spanwise plane (at 50% chord position). These planes are shown in Fig. 6. The general trend is that as the rotating wing starts up, leading- and trailing-edge vortices are formed ($\phi \approx 5°$). The vortex at the leading edge begins to grow while that formed at the trailing edge is shed soon after ($\phi \approx 10°$ or 15°). At startup, the flow field around the wing is more or less horizontal but as the wing sweeps larger angles, the flow has a definite downward component. This effect

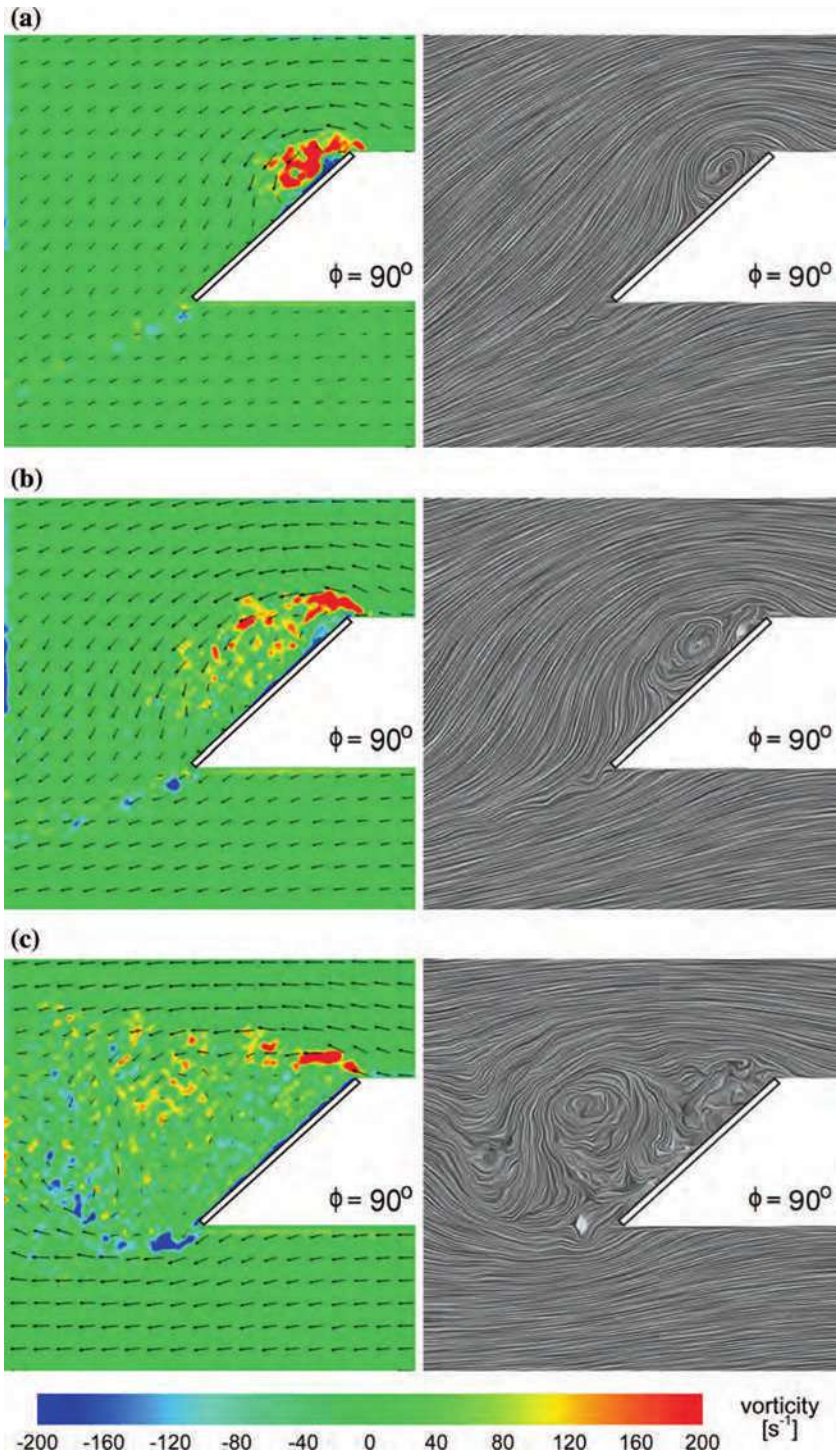

Fig. 11 Effect of spanwise position on chordwise flow for $Re = 15{,}000$ at 90° azimuth, shown by plots of contours of vorticity overlayed with velocity vectors (*left*) and LIC images (*right*). **a** 50% span, **b** 70% span, **c** 90% span

becomes less pronounced for outboard regions of the wing. As shown later (see Figs. 15, 16), immediately following startup the flow from the leading-edge vortex is predominantly chordwise, but as the wing continues to sweep, the flow vector becomes increasingly spanwise in the outboard direction. This indicates a spiralling leading-edge vortex structure that subsequently coalesces with the tip vortex, similar to that seen during the sweeping phase of the half-stroke on insect-like flapping wings (e.g. Ellington et al. 1996).

5.1 Variation with spanwise position

The effect of spanwise position on the chordwise flow field is shown in Figs. 7, 8, 9, 10, 11, 12, 13, 14, 15 and 16. Three azimuthal positions have been chosen for these

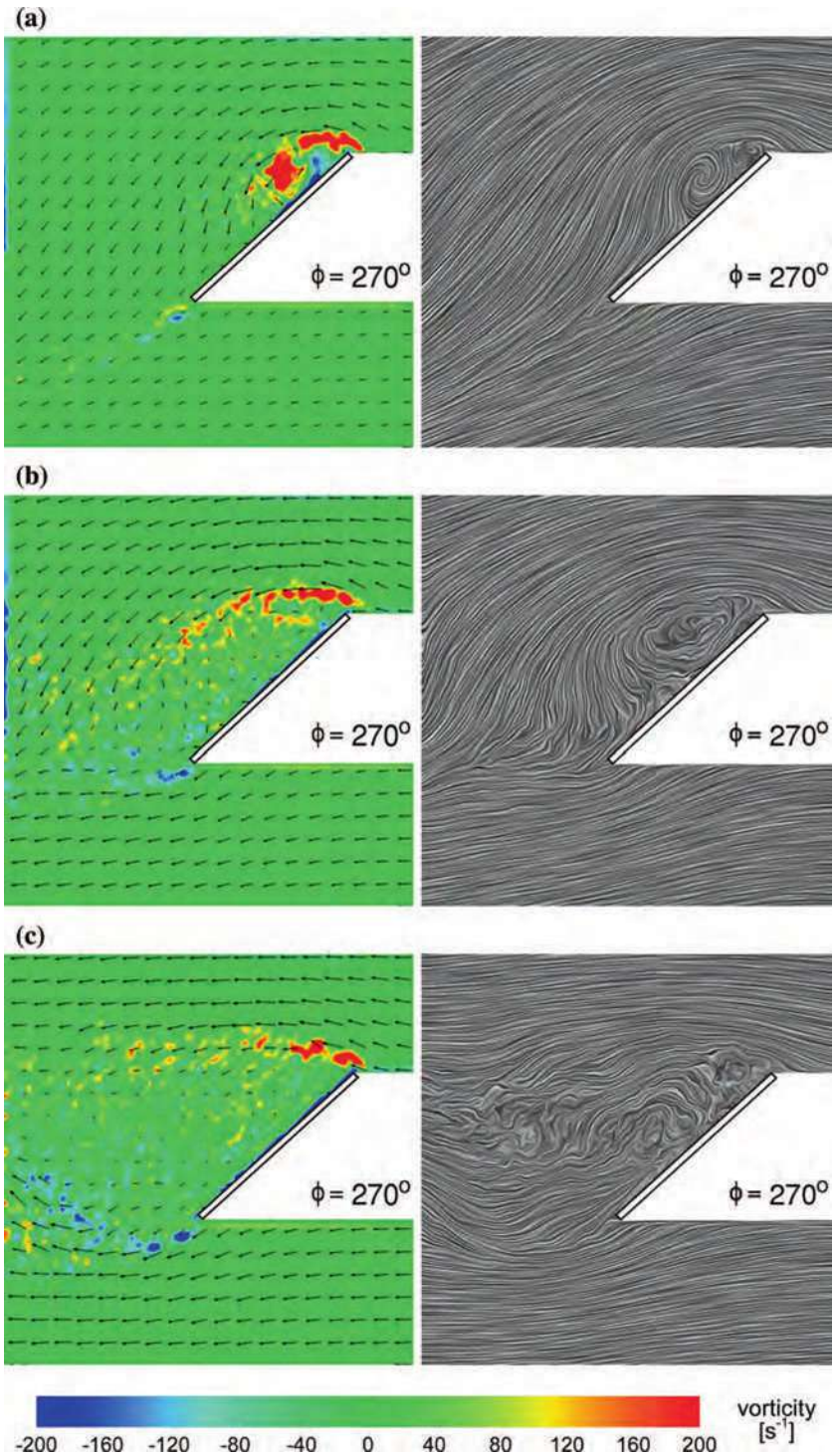

Fig. 12 Effect of spanwise position on chordwise flow for $Re = 15{,}000$ at 270° azimuth, shown by plots of contours of vorticity overlayed with velocity vectors (*left*) and LIC images (*right*). **a** 50% span, **b** 70% span,**c** 90% span

comparisons (10°, 90° and 270°) so that flow features relating to startup, mid-stroke and end of (a long) stroke may be studied. Figures 7, 8 and 9 show the chordwise flow field using vorticity contours and LIC [line integral convolution; Knowles et al. (2006)] images, and Fig. 13 contains line plots of the horizontal velocity profile through a vertical section at the midchord point of the wing, all for $Re = 500$. Figure 15 shows the spanwise flow field for the same case. For $Re = 15{,}000$, the corresponding plots are shown in Figs. 10, 11, 12, 14 and 16.

Figures 7 and 10 show that soon after startup (azimuth $\phi = 10°$), the flow field does not differ much at the various spanwise positions. Moving outboard, the leading- and trailing-edge vortices get progressively stronger due to the

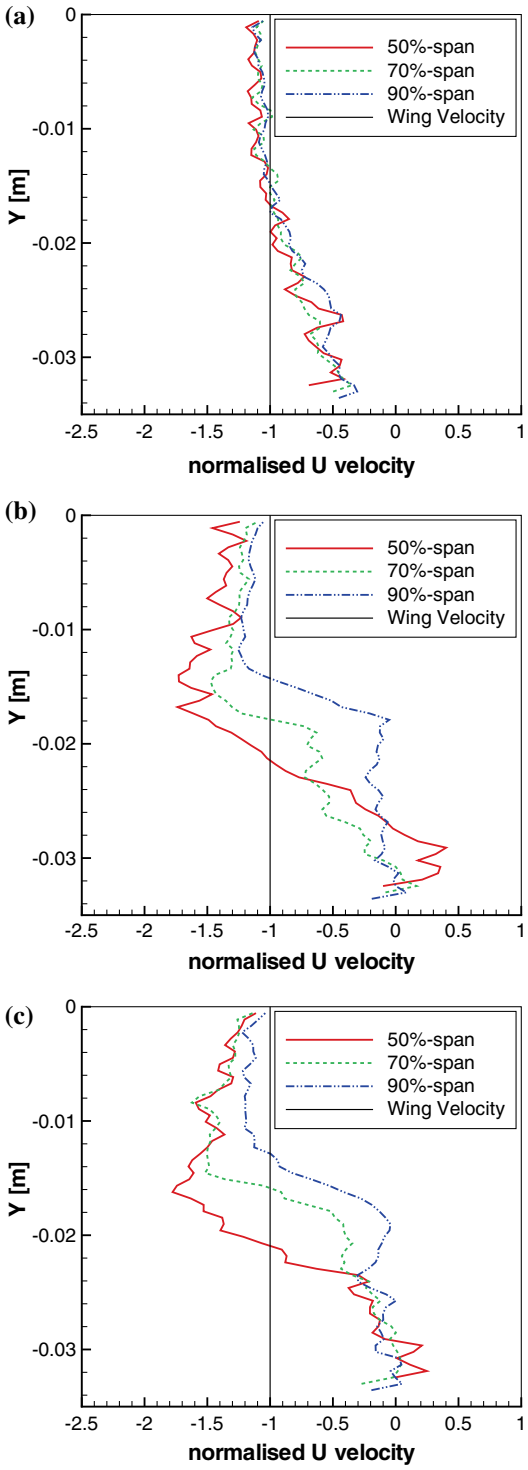

Fig. 13 Effect of spanwise position on chordwise flow for $Re = 500$ at azimuths shown (u velocity is normalised w.r.t. local wing velocity; y is measured vertically downwards from the top of the measurement domain to the midchord point on the wing). **a** 10° azimuth, **b** 90° azimuth, **c** 270° azimuth

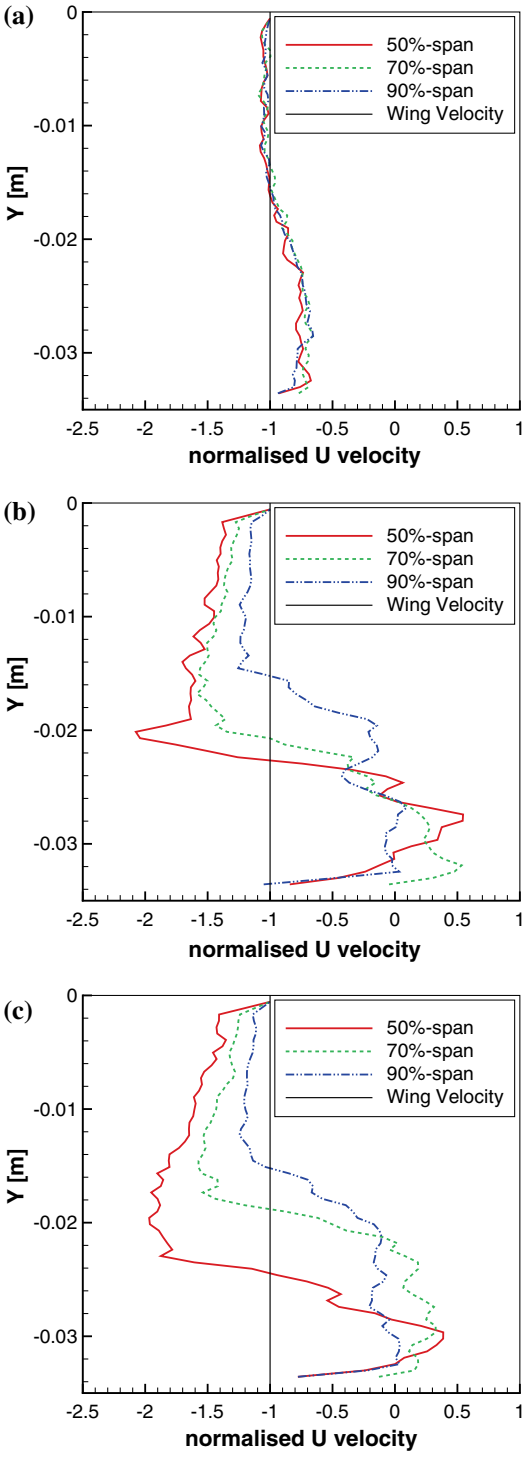

Fig. 14 Effect of spanwise position on chordwise flow for $Re = 15{,}000$ at azimuths shown (u velocity is normalised w.r.t. local wing velocity; y is measured vertically downwards from the top of the measurement domain to the midchord point on the wing). **a** 10° azimuth, **b** 90° azimuth, **c** 270° azimuth

increasing flow speeds. The leading-edge vortex structure has just begun to form at the 50% span position, is more developed at the 70% span position but then is less tightly rolled up at the 90% span position. For the later azimuthal positions ($\phi = 90°$ and 270°), the flow field at the 90% span position is significantly different from the 50 and 70%

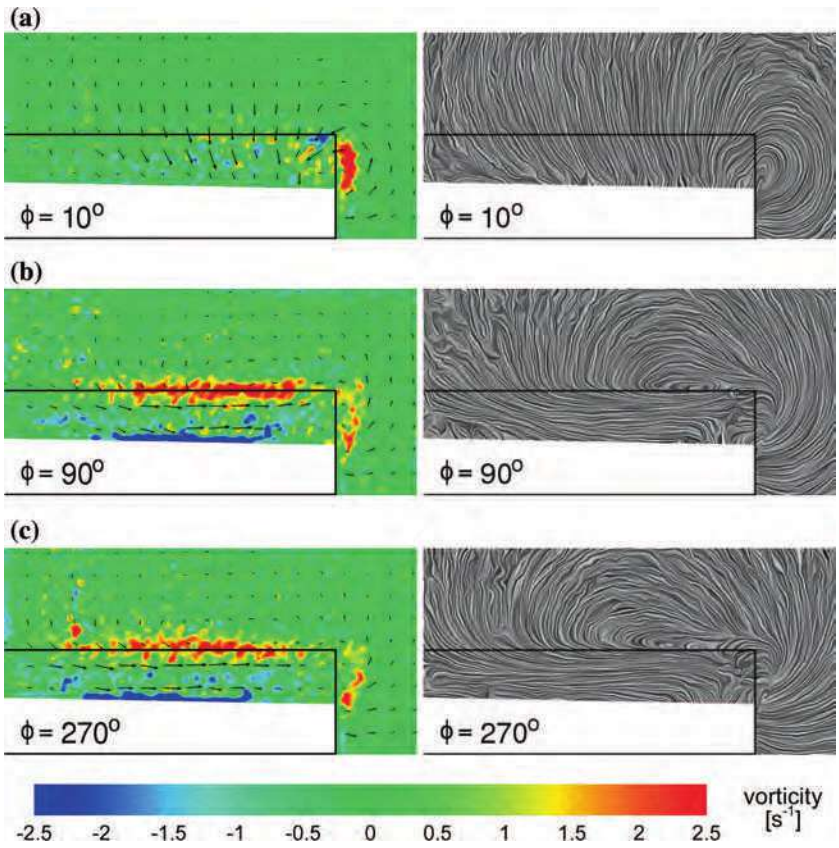

Fig. 15 Effect of azimuthal position on spanwise flow for $Re = 500$ at 50% chord, shown by plots of contours of vorticity overlayed with velocity vectors (*left*) and LIC images (*right*); velocity vectors show how flow close to the wing surface changes from chordwise to spanwise (for scale, cf. Fig. 5). **a** 10° azimuth, **b** 90° azimuth, **c** 270° azimuth

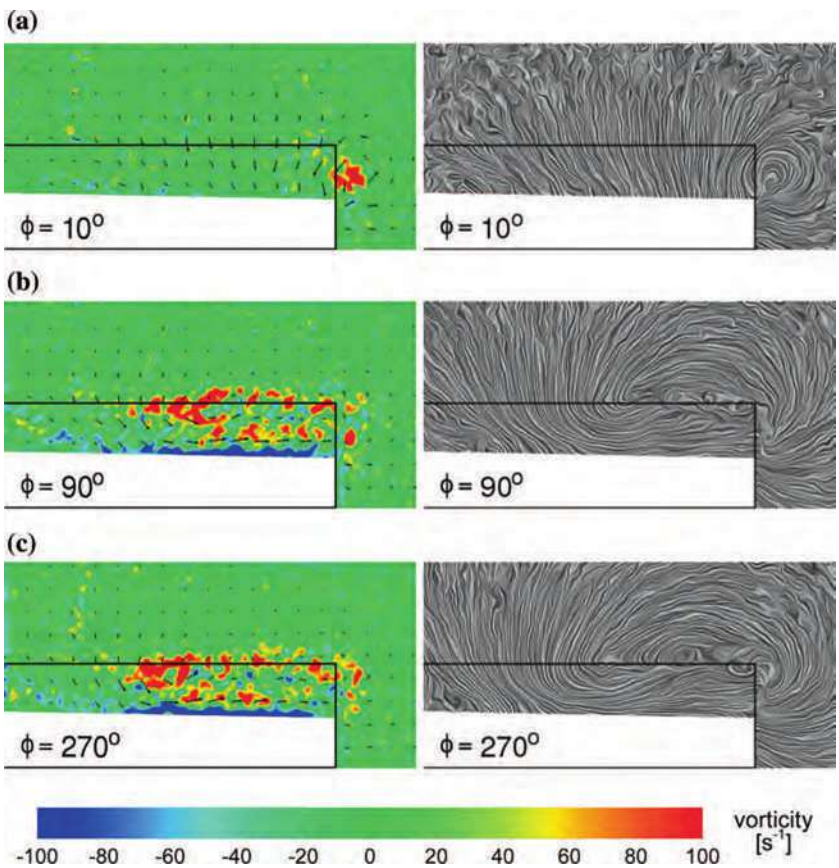

Fig. 16 Effect of azimuthal position on spanwise flow for $Re = 15{,}000$ at 50% chord, shown by plots of contours of vorticity overlayed with velocity vectors (*left*) and LIC images (*right*); velocity vectors show how flow close to the wing surface changes from chordwise to spanwise (for scale, cf. Fig. 5). **a** 10° azimuth, **b** 90° azimuth, **c** 270° azimuth

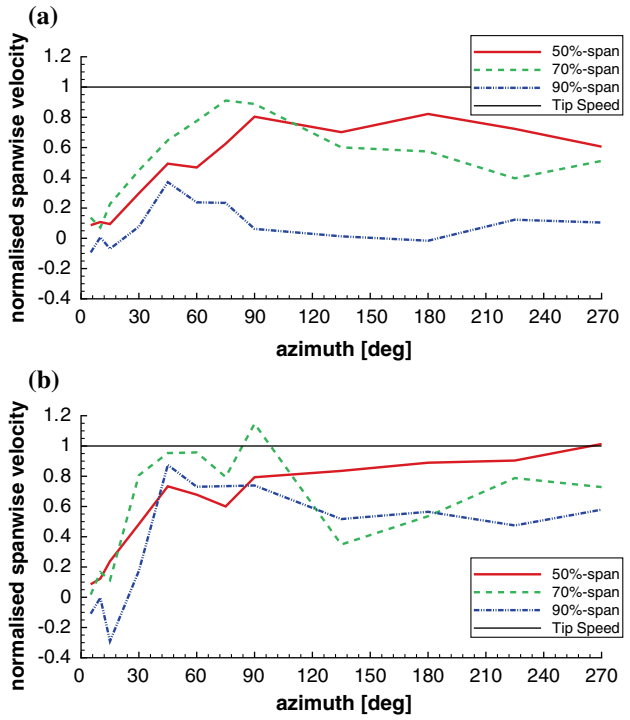

Fig. 17 Plots showing normalised spanwise flow velocity at monitor points in the spanwise measurement plane at 50% chord for $Re = 500$ and 15,000 at various spanwise positions; monitor points are at the vertical level of the wing's quarter-chord point and flow velocities are normalised w.r.t. wingtip speed. **a** $Re = 500$, **b** $Re = 15{,}000$

span positions (Figs. 8, 9, 11, 12). Although the flow rolls up clearly on the leeward side of the wing into the leading-edge vortex for the 50 and 70% span positions, the flow separates at the leading edge for the 90% span position and interference from the tip vortex is clearly visible. For the later azimuthal positions (ϕ = 90° and 270°), the flow angle at the edges of the measurement domain reduces on moving outboard.

The effect of spanwise position on the flow field can also be studied using the line plots shown in Figs. 13 and 14. These graphs show the horizontal velocity profile (normalised w.r.t. the local wing velocity) through a vertical cross-section taken at the midchord position of the wing. Only data for the flow above the wing are shown. Figures 13 and 14 correspond to Figs. 7, 8 and 9 (Re = 500) and Figs. 10, 11 and 12 (Re = 15,000), respectively. In the period immediately following startup ($\phi = 10°$), there is little difference in the flow field between the various spanwise positions. However, as wing sweep proceeds (and based on normalised velocity only), the extent of the leading-edge vortex structure appears to grow with outboard spanwise position. Yet, as wing rotation progresses beyond $\phi = 90°$ to 270°, little change is seen in the velocity profiles.

The variation in the flow field with spanwise position can also be studied in terms of the spanwise flow above the wing at these locations. This is shown in Figs. 15 and 16 for Re = 500 and 15,000, respectively. Immediately after startup, most of the flow velocity appears to be chordwise with inboard sections having a greater outboard spanwise component (cf. Figs. 15a, 16a). However, as wing sweep proceeds, the flow in proximity to the upper wing surface becomes spanwise and is nearly horizontal and directed outboard (Figs. 15b, c, 16b, c). The interference of the leading-edge vortex with the tip vortex also increases but the flow close to the wing remains spanwise and directed outboard.

To get an idea of the spanwise flow velocities, Fig. 17 shows values in the 50% chord measurement plane at various monitor points along the wing. These points coincide with the chordwise measurement planes used here and are at the vertical level of the wing's quarter-chord point. The spanwise velocity increases rapidly after startup, reaches a peak generally around $\phi = 60$–90° and then oscillates in the region of 75–85% of the wingtip velocity. Our results appear to be in agreement with those of Ramasamy and Leishman (2006) who observed spanwise velocities of the order of wingtip speed in their experiments on a model flapping wing. The current experimental results also show that flow velocity magnitudes in the chordwise and spanwise measurement planes are comparable.

5.2 Effect of Reynolds number

The effect of Reynolds number on the flow field is studied in terms of the chordwise (Figs. 8a, 11a, 18) and spanwise (Fig. 15b, 16b, 21) flow fields at $\phi = 30°$ and 90°, respectively, and the velocity profiles through the leading-edge vortex and the surrounding flow (Figs. 13, 14, 20) for the two Reynolds numbers Re = 500 and 15,000. Some of the plots discussed above are also used for this comparison (Figs. 7, 8, 9, 13, 15 for $Re = 500$ and Figs. 10, 11, 12, 14, 16 for Re = 15,000).

From Figs. 8a, 11a and 18, it can be seen that although the size of the leading-edge vortex appears to increase with Reynolds number, its structure becomes less coherent. This feature can also be seen by comparing Figs. 7, 8 and 9 for Re = 500 with Figs. 10, 11 and 12 for Re = 15,000. Close examination of these figures also shows secondary separation near the leading edge in the outboard sections of the wing for $Re = 15{,}000$ but not for the lower $Re = 500$. This is corroborated by the CFD calculations of Wilkins et al. (Wilkins et al. 2006; Wilkins and Knowles 2007) (see Fig. 19).

Another flow feature that is evident from Figs. 8a, 18 and 11a is the presence of Kelvin–Helmholtz instability at the higher Reynolds number. In the discussion in Sect. 1.2, it was noted that the onset of Kelvin–Helmholtz instability is promoted by higher Reynolds numbers and this has been

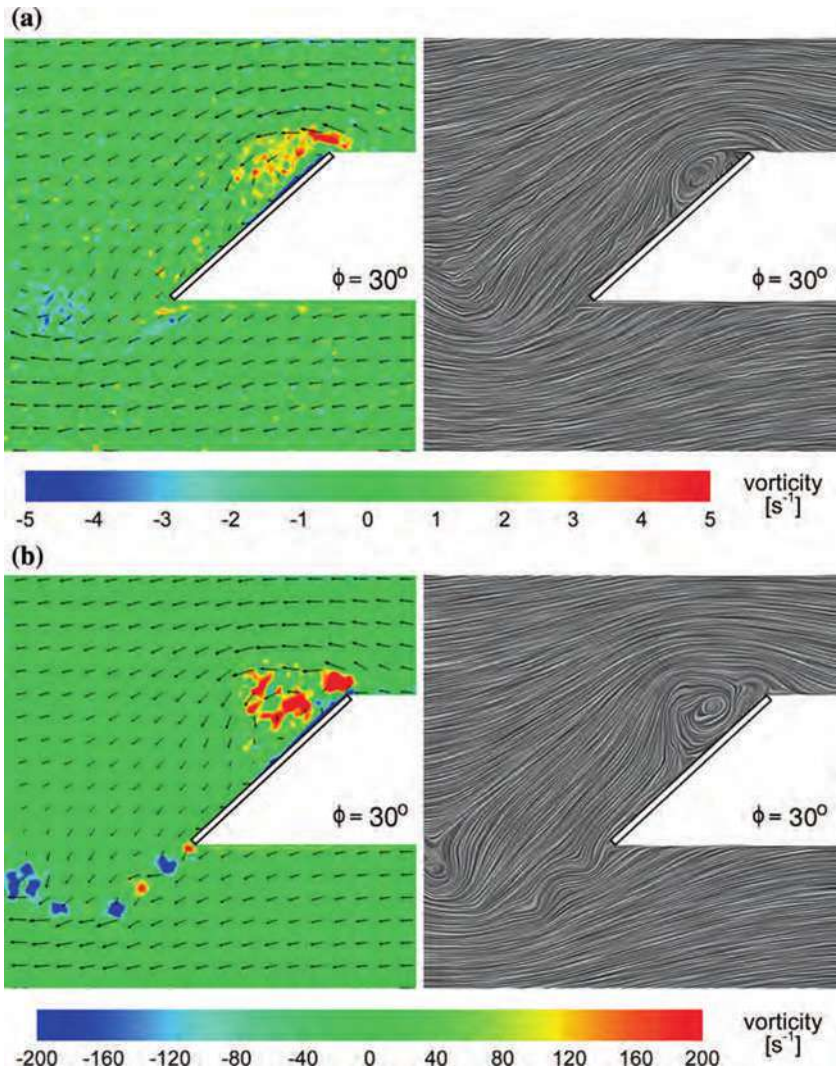

Fig. 18 Effect of Reynolds number on chordwise flow at 50% span position for 30° azimuth, shown by plots of contours of vorticity overlayed with velocity vectors (*left*) and LIC images (*right*); Kelvin–Helmholtz instability is clearly visible at Re = 15,000 in the bunching together of the trailing-edge wake into smaller vortices (for scale, cf. Fig. 5). **a** $Re = 500$, **b** $Re = 15{,}000$

shown in the experiments carried out here. This result was also predicted by the CFD calculations of Wilkins and Knowles (2007), full details in Wilkins (2008).

The effect of Reynolds number on the flow features can also be analysed by considering the profile of horizontal velocity through the leading-edge vortex. This is plotted for $\phi = 30°$ azimuth in Fig. 20 and other azimuths in Figs. 13 and 14. Although the shapes of the velocity profiles are generally similar, the velocity gradients (and, hence, vorticities) are higher for Re = 15,000 than for $Re = 500$. As noted earlier (see Sect. 1.2), one of the flow features promoting Kelvin–Helmholtz instability in a fluid is high tangential velocity gradients, which explains the occurrence of Kelvin–Helmholtz instability at the higher Reynolds number in our experiments.

The spanwise flow fields at the two Reynolds numbers (see Figs. 15b, 16b, 21) show little difference. The flow is generally spanwise in the outboard direction and the tip vortex can be seen interfering and coalescing with the leading-edge vortex. Figure 17 shows the spanwise velocities for both Reynolds numbers more clearly. Although the normalised (w.r.t. wingtip speed) spanwise flow velocity increases to more or less similar values for both Reynolds numbers (Re = 15,000 values are generally slightly higher than those at Re = 500), this 'peak' is reached earlier ($\phi \approx 45$–$60°$) by the flow at $Re = 15{,}000$ than at $Re = 500$ ($\phi \approx 75$–$90°$). This indicates that the spanwise pressure gradient grows more rapidly at the higher Reynolds number.

At $\phi = 30°$, three vortex cores (one clockwise core sandwiched between two counterclockwise cores) can be seen in the wing tip region (see Fig. 21). The left-hand counterclockwise vortex cores originates from the leading-edge vortex 'turning' through 90° while the right-hand one is the tip vortex. The fluid 'trapped' between the two cores is forced to move upwards on the left and downwards on

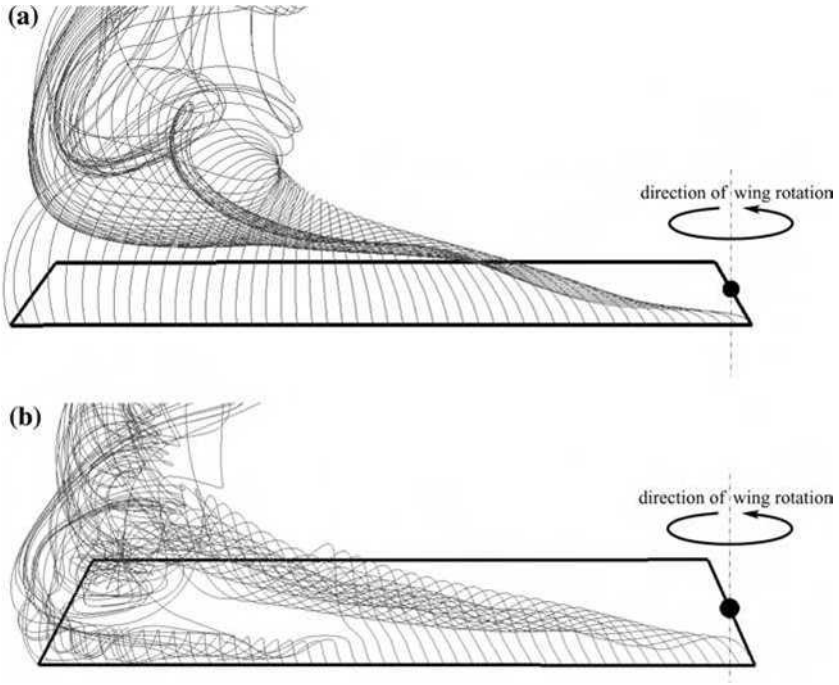

Fig. 19 CFD results of Wilkins et al. (2006) showing the effect of Reynolds number. The images show perspective views of the upper surface of the rotating wing with particle streaklines released from points along the leading edge providing flow visualisation; centre of rotation is indicated by the *filled circle*. **a** Re = 500, **b** Re = 15,000

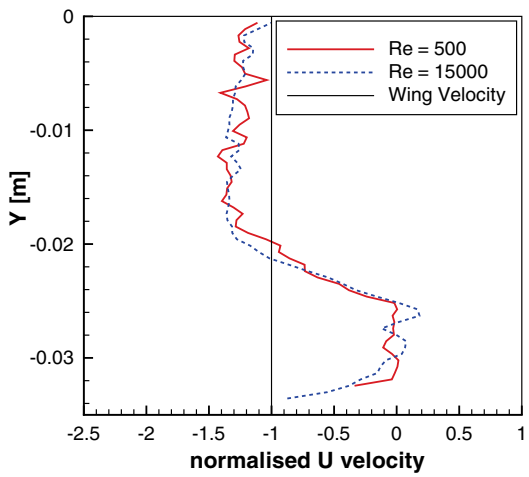

Fig. 20 Effect of Reynolds number for 30° azimuth at 50% span position (u velocity is normalised w.r.t. local wing velocity; y is measured vertically downwards from the top of the measurement domain to the midchord point on the wing)

the right, resulting in a sandwiched clockwise vortex (see Fig. 22). For $\phi = 90°$ onwards, the two counterclockwise vortex cores coalesce into one large vortex and this condition remains till the end of the experiment at ϕ = 270°. This flow feature is less pronounced at $Re = 500$ (see Fig. 15).

On the whole, however, the flow field at Re = 15,000 shows similar trends to that at $Re = 500$, most likely because the wing has travelled the same number of chord lengths. This characteristic was also highlighted by Ansari et al. (2006a, b, c).

6 Conclusions

From the experimental study presented above, a number of important inferences can be drawn. The results have shown that the leading-edge vortex is generally larger for $Re = 15{,}000$ than it is for $Re = 500$. The vorticity plots indicate that the strength of the leading-edge vortex is about 40 times greater for the same comparison, where the Reynolds number ratio is only 30.

Another important observation is the occurrence of Kelvin–Helmholtz instability. Whereas this appears to be absent for the lower Reynolds number studied here ($Re = 500$), it is prominent at $Re = 15{,}000$. This supports the CFD results of Wilkins and Knowles (2007).

Figures 15 and 16 show, for both Reynolds numbers, the presence of spanwise flow along the wing from the root to the tip. In fact, the spanwise flow appears to be almost more pronounced for the lower Re. Experiments by Dickinson et al. (Birch and Dickinson 2001; Sane and Dickinson 2001; Birch et al. 2004) revealed the presence of a strong bound leading-edge vortex but they reported only weak spanwise spiralling, prompting them to conclude that the precise flow structure of the leading-edge vortex depends critically on Reynolds number (Birch et al. 2004). This is supported by Ellington (2006) who suggested that spanwise flow exists at all relevant speeds but its spiralling nature becomes less discernable as Reynolds number decreases. Unfortunately, without stereoscopic or volumetric PIV, it is difficult to assess fully the spiralling nature of the leading-edge vortex.

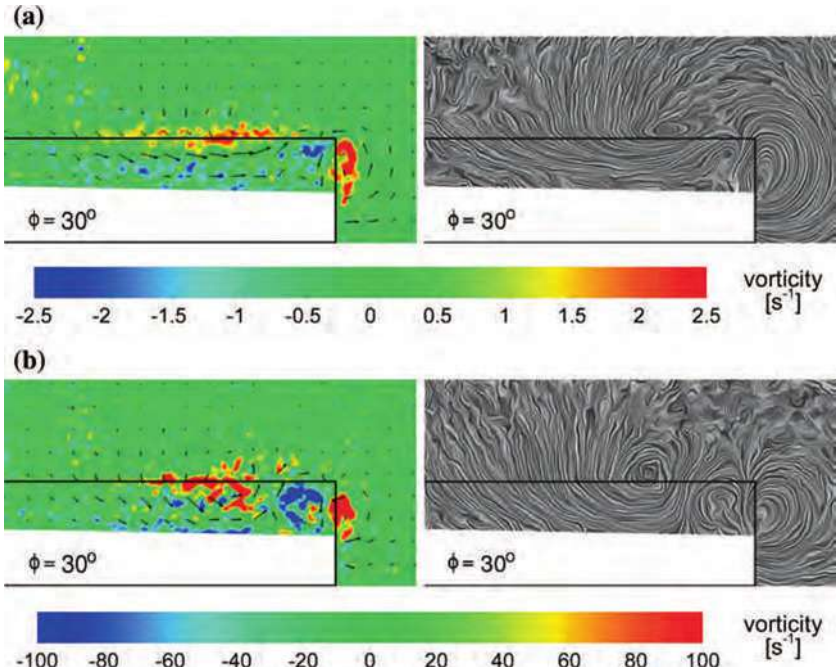

Fig. 21 Effect of Reynolds number on spanwise flow at 50% chord position for 30° azimuth, shown by plots of contours of vorticity overlayed with velocity vectors (*left*) and LIC images (*right*); spanwise flow appears to be more prominent for $Re = 500$. **a** $Re = 500$, **b** $Re = 15{,}000$

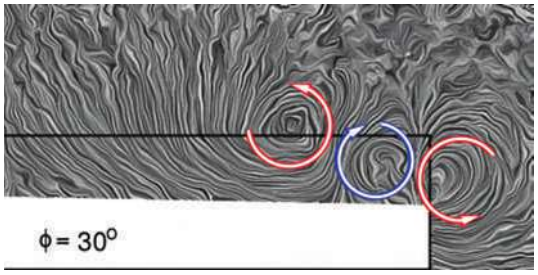

Fig. 22 LIC image showing how a third 'vortex' is formed by virtue of being sandwiched between two vortex cores in the 50% chord spanwise measurement plane at $Re = 500$ and 30° azimuth (for scale, cf. Fig. 5)

In moving outboard along the wing, the strength of the leading-edge vortex generally increases until it coalesces with the tip vortex whereupon the chordwise flow appears to break down. The leading-edge vortex structure is most coherent at the 50% and 70% span positions; at the 30% span position it is very weak due to the low speeds and at the 90% position, it has broken down due to interference from the tip vortex. Although most of the flow over the wing in the leading-edge vortex is chordwise at startup, this changes rapidly to spanwise (more so for the higher Reynolds number) and spanwise flow velocities on the order of about 80% of the wingtip speed are maintained thereafter (again, generally higher for the higher Reynolds number).

By comparing the vorticity plots for the chordwise and spanwise results, it can be seen that vorticity levels are about twice as high in the former compared with the latter (e.g. cf. Figs. 8a and 15b). This shows that more vorticity is generated in the leading-edge vortex than in the coalesced leading-edge vortex/tip vortex, probably due to destructive interference between the leading-edge vortex and the tip vortex, and energy dissipation in the process. This result is in contrast to low angle-of-attack attached flow where the dominant vorticity comes from the tip vortex. The flow velocity components in the chordwise and spanwise planes are, however, of comparable magnitudes.

In terms of future work, it will be highly useful to couple the flow field measurements obtained here with force data to relate flow features to the forces and moments they produce, and enhance understanding of the underlying flow structures. The experiments presented here have only permitted the simultaneous measurement of two velocity components. Stereoscopic or volumetric PIV measurements will produce data for three simultaneous velocity components that will enable better flow description and shed light on the elusive characteristics of the leading-edge vortex on insect-like flapping wings.

Acknowledgments The authors wish to thank Dr. Simon A. Ritchie for his help in setting up the PIV system. The authors acknowledge the partial support of the EPSRC through grant no. EP/C535278/1 (Stabler), the ORS Award Scheme (Phillips) and the Cranfield University, Department of Aerospace, Power & Sensors scholarships (Wilkins & Phillips) for this work.

References

Ansari SA (2004) A nonlinear, unsteady, aerodynamic model for insect-like flapping wings in the hover with micro air vehicle applications. PhD thesis, Cranfield University (Shrivenham)

Ansari SA, Żbikowski R, Knowles K (2006a) Aerodynamic modelling of insect-like flapping flight for micro air vehicles. Prog

Aerospace Sci 42(2):129–172. doi:10.1016/j.paerosci.2006.07.001

Ansari SA, Żbikowski R, Knowles K (2006b) Non-linear unsteady aerodynamic model for insect-like flapping wings in the hover. Part 1: methodology and analysis. Proceedings of the Institution of Mechanical Engineering. Part G J Aerospace Eng 220(2):61–83. doi:10.1243/09544100JAERO49

Ansari SA, Żbikowski R, Knowles K (2006c) Non-linear unsteady aerodynamic model for insect-like flapping wings in the hover. Part 2: implementation and validation. Proceedings of the Institution of Mechanical Engineering. Part G J Aerospace Eng 220(3):169–186. doi:10.1243/09544100JAERO50

Ansari SA, Phillips N, Stabler G, Żbikowski R, Knowles K (2009) Spanwise flow on an impulsively-started rotating wing at low Reynolds numbers. In: 39th AIAA Fluid Dynamics Conference & Exhibit AIAA. San Antonio, TX, AIAA-2009-4032, pp 1–9

Birch JM, Dickinson MH (2001) Spanwise flow and the attachment of the leading-edge vortex on insect wings. Nature 412(6848):729–733

Birch JM, Dickson WB, Dickinson MH (2004) Force production and flow structure of the leading edge vortex on flapping wings at high and low Reynolds numbers. J Exp Biol 207:1063–1072. doi:10.1242/jeb.00848

Brodsky AK (1991) Vortex formation in the tethered flight of the peacock butterfly Inachis io l. (lepidoptera, nymphalidae) and some aspects of insect flight evolution. J Exp Biol 161:77–95

Dickinson MH (1996) Unsteady mechanisms of force generation in aquatic and aerial locomotion. Am Zool 36:537–554

Dickinson MH, Götz KG (1993) Unsteady aerodynamic performance of model wings at low Reynolds numbers. J Exp Biol 174(1):45–64

Drazin PG, Reid WH (1981) Hydrodynamic stability. Cambridge monographs on mechanics. Cambridge University Press, Cambridge

Dudley R (1992) Biomechanics (structures & systems): a practical approach. Oxford University Press, Oxford

Ellington CP (1984a) The aerodynamics of hovering insect flight: III. kinematics. Philos Trans R Soc Lond Ser B 305:41–78

Ellington CP (1984b) The aerodynamics of hovering insect flight: IV. Aerodynamic mechanisms. Philos Trans R Soc Lond Ser B 305:79–113

Ellington CP (1995) Unsteady aerodynamics of insect flight. Soc Exp Biol 49:109–129

Ellington CP (2006) Insects versus birds: the great divide. In: 44th AIAA aerospace sciences meeting and exhibit, AIAA, Reno, NV, AIAA-2006-0035

Ellington CP, van den Berg C, Willmott AP, Thomas ALR (1996) Leading-edge vortices in insect flight. Nature 384:626–630

Ennos AR (1987) A comparative study of the flight mechanism of Diptera. J Exp Biol 127:355–372

Ennos AR (1989) The kinematics and aerodynamics of the free flight of some Diptera. J Exp Biol 142:49–85

Grodnitsky DL, Morozov PP (1993) Vortex formation during tethered flight of functionally and morphologically two-winged insects, including evolutionary considerations on insect flight. J Exp Biol 182:11–40

Hart D (1998) The elimination of correlation errors in PIV processing. In: 9th international symposium on applications of laser techniques to fluid mechanics. Lisbon, p 10.5

Huang H, Dabiri D, Gharib M (1997) On errors of digital particle image velocimetry. Meas Sci Technol 8(12):1427–1440

Keane RD, Adrian RJ (1990) Optimization of particle image velocimeters. Parti i: double pulsed systems. Meas Sci Technol 1(11):1202–1215

Kim SC, Lee JY, Sohn SI (2003) Long time computation of two-dimensional vortex sheet by point vortex method. J Phys Soc Jpn 72:1968–1976

Knowles RD, Finnis MV, Saddington AJ, Knowles K (2006) Planar visualization of vortical flows. Proceedings of the Institution of Mechanical Engineering. Part G J Aerospace Eng 220(6):619–627

Lu Y, Shen GX (2008) Three-dimensional flow structures and evolution of the leading-edge vortices on a flapping wing. J Exp Biol 211(8):1221–1230. doi:10.1242/jeb.010652, http://jeb.biologists.org/cgi/content/abstract/211/8/1221

Martin LJ, Carpenter PW (1977) Flow-visualisation experiments on butterflies in simulated gliding flight. Fortschritte der Zoologie 24(2/3):307–316

Maxworthy T (1979) Experiments on the Weis-Fogh mechanism of lift generation by insects in hovering flight. Part 1: dynamics of the 'fling'. J Fluid Mech 93:47–63

McCroskey WJ (1981) The phenomenon of dynamic stall. Technical Memorandum TM-81264, NASA, 1–31

Raffel M, Willert C, Kompenhans J (1998) Particle image velocimetry: a practical guide. Springer, Heidelberg

Ramasamy M, Leishman JG (2006) Phase-locked particle image velocimetry measurements of a flapping wing. J Aircr 43(6):1867–1875. doi:10.2514/1.21347

Riddle TW, Wadcock AJ, Tso J, Cummings RM (1999) An experimental analysis of vortex trapping techniques. Trans ASME J Fluids Eng 121:555–559

Rossow VJ (1978) Lift enhancement by an externally trapped vortex. J Aircr 15(9):618–625

Sane SP, Dickinson MH (2001) The control and flight force by a flapping wing: Lift and drag production. J Exp Biol 204:2607–2626

Shyy W, Liu H (2007) Flapping wings and aerodynamic lift: the role of leading-edge vortices. AIAA J 45(12):2817–2819. doi:10.2514/1.33205

Sunada S, Kawachi K, Watanabe I, Azuma A (1993) Performance of a butterfly in take-off flight. J Exp Biol 183:249–277

van den Berg C, Ellington CP (1997a) The three-dimensional leading-edge vortex of a "hovering" model hawkmoth. Philos Trans R Soc Lond Ser B 352(1351):329–340

van den Berg C, Ellington CP (1997b) The vortex wake of a "hovering" model hawkmoth. Philos Trans R Soc Lond Ser B 352(1351):317–328

Westerweel J (1994) Efficient detection of spurious vectors in particle image velocimetry data. Exp Fluids 16:236–247

Westerweel J (1997) Fundamentals of digital particle image velocimetry. Meas Sci Technol 8:1379–1392

Wilkins P, Knowles K (2007) Investigation of aerodynamics relevant to flapping-wing micro air vehicles. In: 18th AIAA computational fluid dynamics conference, AIAA-2007-4338, AIAA, Miami, FL, pp 1–13

Wilkins P, Knowles K (2008) The leading-edge vortex and aerodynamics of insect-based flapping-wing micro air vehicles. In: International powered lift conference (IPLC 2008). The Royal Aeronautical Society, London, UK, pp 1–14

Wilkins P, Knowles K, Żbikowski R (2006) CFD investigation of aerodynamics relevant to flapping-wing micro air vehicles. In: European micro air vehicle conference. EMAV, Braunschweig, Germany

Wilkins PC (2008) Some unsteady aerodynamics relevant to insect-inspired flapping-wing micro air vehicles. Ph.D. thesis, Cranfield University (Shrivenham)

Willert CE, Gharib M (1991) Digital particle image velocimetry. Exp Fluids 10:181–193

Willmott AP, Ellington CP, Thomas ALR (1997) Flow visualization and unsteady aerodynamics in the flight of the hawkmoth, Manduca sexta. Philos Trans R Soc Lond Ser B 352:303–316

Woods MI, Henderson JF, Lock GD (2001) Energy requirements for the flight of micro air vehicles. The Aeronautical Journal 105(1043):135–149, paper No. 2546

Żbikowski R (1999a) Flapping wing autonomous micro air vehicles: research programme outline. In: Fourteenth international conference on unmanned air vehicle systems, vol supplementary papers. pp 38.1–38.5

Żbikowski R (1999b) Flapping wing micro air vehicle: A guided platform for microsensors. In: Royal aeronautical society conference on nanotechnology and microengineering for future guided weapons. pp 1.1–1.11

Żbikowski R (2000) Flapping wing technology. In: European military rotorcraft symposium. Shrivenham, pp 1–7

Żbikowski R (2002) On aerodynamic modelling of an insect-like flapping wing in hover for micro air vehicles. Philos Trans R Soc Lon Ser A 360:273–290

Żbikowski R, Pedersen CB, Ansari SA, Galiński C (2003) Flapping wing micro air vehicles. Lecture series: low Reynolds number aerodynamics on aircraft including applications in emerging UAV technology RTO/AVT 104. von Kármán Institute, Belgium

Design and development considerations for biologically inspired flapping-wing micro air vehicles

Kevin D. Jones · Max F. Platzer

Abstract In this paper, the decade of numerical and experimental investigations leading to the development of the authors' unique flapping-wing micro air vehicle is summarized. Early investigations included the study of boundary layer energization by means of a small flapping foil embedded in a flat-plate boundary layer, the reduction of the recirculatory flow region behind a backward-facing step by means of a small flapping foil, and the reduction or suppression of flow separation behind blunt or cusped airfoil trailing edges by flapping a small foil located in the wake flow region. These studies were followed by systematic investigations of the aerodynamic characteristics of single flapping airfoils and airfoil combinations. These unsteady flows were described using flow visualization, laser-Doppler velocimetry in addition to panel and Navier–Stokes computations. It is then shown how this flapping-wing database was used to conceive, design and develop a micro air vehicle which has a fixed wing for lift and two flapping wings for thrust generation. While animal flight is characterized by a coupled force generation, the present design appears to separate lift and thrust. However, in fact, the performance of one surface is closely coupled to the other surfaces.

1 Introduction

The micro air vehicle (MAV) configuration shown in Fig. 1 was first flown in December 2002. Since that time variations of it have been flown many times. The third generation model shown on the right has a span of 25 cm, a length of 17 cm, a flying weight of about 13 g, and flies for about 15 min on a rechargeable lithium-polymer battery at flight speeds between 2 and 5 m/s. The MAV has a fixed wing and two flapping wings mounted downstream but very near the trailing edge of the fixed wing. The flapping wings oscillate in counterphase so that while one wing, for example, moves up the other moves down and vice versa. Therefore the joint center of gravity is essentially unaffected by the oscillations of the two wings. Furthermore, and contrary to animal flight, the amplitude of the oscillations is constant along the span.

Clearly, there is no counterpart to this vehicle in nature. Yet, one important element found in nature was adopted in its design and development, namely wing flapping. As is well known, early pioneers of aeronautical engineering, such as Lilienthal (1992) were convinced that the key to flight with heavier-than-air vehicles was to be found in emulating bird flight as closely as possible. Earlier attempts to do so are documented by Dalton (1999). Lilienthal contributed greatly to the understanding of flapping-wing aerodynamics. In particular, he correctly identified the drag reduction (or thrust generation) caused by wing flapping. However, the success of the Wright brothers in 1903 with the fixed-wing aircraft concept soon convinced the aeronautical engineering community to regard the flapping-wing aircraft concept as unpromising for further development and, indeed, throughout the whole twentieth century few attempts were made to build flapping-wing vehicles. It was only toward the end of the century that a new type of air vehicle of greatly diminished size, the micro air vehicle, triggered a re-examination of the flapping-wing aircraft concept, primarily due to the necessarily small Reynolds numbers they would experience, typically from a few thousand to a few tens of thousands.

K. D. Jones (✉) · M. F. Platzer
Naval Postgraduate School, Monterey, CA, USA
e-mail: jones@nps.edu

M. F. Platzer
e-mail: mplatzer@nps.edu

G.K. Taylor, M.S. Triantafyllou, and C. Tropea (Eds.): Animal Locomotion, pp. 237–248.
springerlink.com

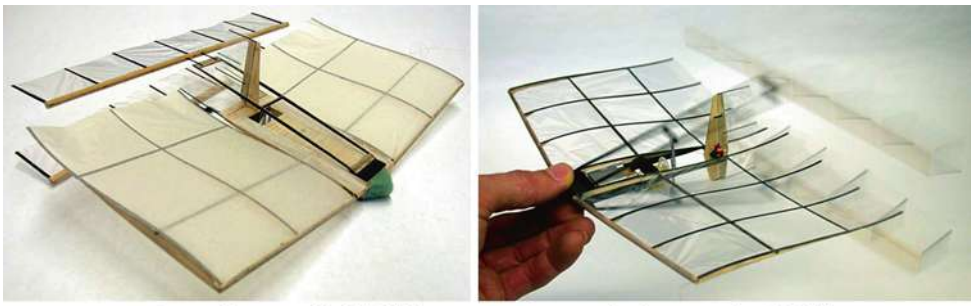

Fig. 1 The authors' unconventional fixed/flapping-wing MAV design. The large fore-wing provides most of the lift while the biplane-pair of trailing wings provide the thrust, but the interaction between them provides the necessary efficiency for flight. The first generation model had throttle control, and first flew in 2002. The third generation had two-channel control, a modular construction, 25 cm span, 17 cm length and 13 g weight, and flew for 15 min at 2–5 m/s on a rechargeable battery

In this paper, we would like to document the basic design philosophy which led us to the configuration shown in Fig. 1. This philosophy can be summarized by stating that we wanted to make maximum use of the existing knowledge about flapping wing aerodynamics. To this end, it was obvious that we should concentrate on high-aspect-ratio wings because much more was (and still is) known about two-dimensional flapping airfoil aerodynamics than about highly three-dimensional wing aerodynamics. Therefore, we first summarize the state-of-the-art in the early 1990s at the start of our MAV development effort and then proceed to the description of our experimental and computational investigations. However, in keeping with the emphasis of this journal on experiments we highlight the experimental aspects and mention the computational aspects only to the extent needed for a fuller understanding of our total approach. For additional computational details we refer to the cited references.

2 Knoller–Betz–Katzmayr effect

Although Lilienthal had already achieved a considerable understanding of the basic physics underlying flapping wings, a more definitive theory was first given independently by Knoller (1909) and Betz (1912). Their explanation is shown in Fig. 2 where an airfoil is depicted which executes harmonic plunge oscillations. As the airfoil moves through its mean position (either up or down) the airfoil "sees" an effective angle of attack, α_{eff}, due to the vectorial superposition of its flight speed, V_∞, and the plunge velocity, $z'(t)$. Neglecting viscous and three-dimensional effects a resultant aerodynamic force, N, is generated which is inclined forward. Hence a harmonically varying force component in the flight direction, T, (i.e. thrust) starts to be generated. Katzmayr (1922) verified this effect by exposing an airfoil to an oscillating wind tunnel flow. This work, in turn, stimulated a more detailed analysis by Birnbaum (1924) who applied Prandtl's unsteady thin airfoil theory to this problem. He was the first to give a quantitative prediction of thrust generation due to slowly oscillating airfoils and he was able to show that the oscillating airfoil sheds vortices from its trailing edge (an effect not yet included by Knoller and Betz). Garrick (1936) presented results valid for the complete frequency range based on Theodorsen's (1935) thin airfoil theory. At about the same time von Kármán and Burgers (1934) pointed out that the vortex shedding from a thrust-producing oscillating airfoil occurs in the form of a "reverse" Kármán vortex street.

The generation of this vortex street can be understood by recalling the basic principle of lift generation on an airfoil. To this end it is important to remember that a so-called "starting vortex" is shed from the airfoil trailing edge whenever the airfoil incidence angle is abruptly changed. A sudden increase in angle of attack produces the shedding of a counterclockwise starting vortex. A decrease produces a clockwise vortex. The trailing edge has to be reasonably sharp for this shedding to occur with sufficient strength. A rounded trailing edge greatly diminishes the shedding. Consider now the airfoil as it plunges from above through the mean position. The airfoil "sees" a maximum positive angle of attack at this moment which starts to diminish greatly as it slows down. Hence the angle of attack changes from positive to negative as it reverses and reaches the maximum negative angle of attack as it approaches the mean position from below. Therefore, during this part of the oscillation the airfoil sheds clockwise vorticity which accumulates quickly into the clockwise vortex of the lower row of the reverse Kármán vortex street. Similarly, while the airfoil moves above the mean position it sheds a counterclockwise vortex.

In the early 1990s we were able to predict this vortex shedding behavior with the panel code solutions for

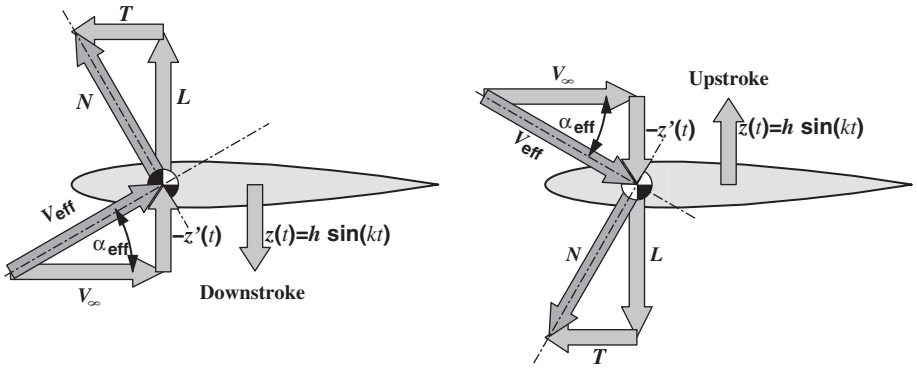

Fig. 2 Schematic illustrating thrust production by a plunging airfoil as posed by Knoller and Betz in 1909 and 1912, respectively

incompressible inviscid flow past oscillating airfoils which we had developed in preceding years for the purpose of studying low-speed airfoil flutter phenomena (Teng 1987; Platzer et al. 1993). These solutions represented a considerable advance over the linearized small amplitude solutions obtained by Birnbaum (1924) and Garrick (1936). However, they left unanswered the effect of viscosity on the thrust and propulsive efficiency predictions of the thin-airfoil and the panel codes. Therefore, we decided to perform visualizations and measurements of the flow over harmonically plunging airfoils.

3 Flow over harmonically plunging airfoils

In Fig. 3 we show a visualization of the reverse Kármán vortex street; called "reverse" because it consists of counterclockwise rotating upper row vortices and clockwise rotating vortices in the lower row. This arrangement is the exact opposite of the classical Kármán vortex street shed, for example, from a stationary cylinder in a low-speed flow where the upper row vortices are turning clockwise and lower row vortices are turning counterclockwise. These visualizations were performed in an Eidetics Model 1520 closed circuit water tunnel. The wing had a 10 mm chord with an airfoil section that approximated a NACA 0012, and was oscillated vertically with a programmable shaker. Dye was injected just upstream of the airfoil above and below the centerline. Flow speed was measured with a TSI LDV system.

The change in vortex shedding from the trailing edge of a stationary airfoil to that from a harmonically plunging airfoil as the amplitude of oscillation is increased for a given frequency of oscillation is shown in Fig. 4. The classical Kármán vortex street shed from the stationary airfoil is shown in (a). As the airfoil starts to oscillate in plunge at a relatively low reduced frequency, $k = 2\pi fc/V_\infty$, and amplitude, h (non-dimensionalized by c), the Kármán vortex street changes into the mushroom-like vortex pattern shown in (b). As the product hk (the peak non-dimensional plunge velocity) is increased, this vortex pattern changes into the pattern shown in (c). A further increase finally produces the reverse Kármán vortex street shown in (d). A comparison of the panel-code computed vortex street with the observed street of (d) shows excellent agreement. However, the panel code could not reproduce the vortex patterns shown in (a), (b) and (c). Hence these flow visualization experiments indicate the inadequacy of inviscid flow computations for low values of frequency and amplitude. On the other hand, they also show that there is a range of flow speed, frequencies and amplitudes where inviscid computations produce good agreement. In particular, when the thrust produced by flapping exceeds the viscous drag coefficient by some margin, and actually to some degree quite far into the dynamic-stall regime.

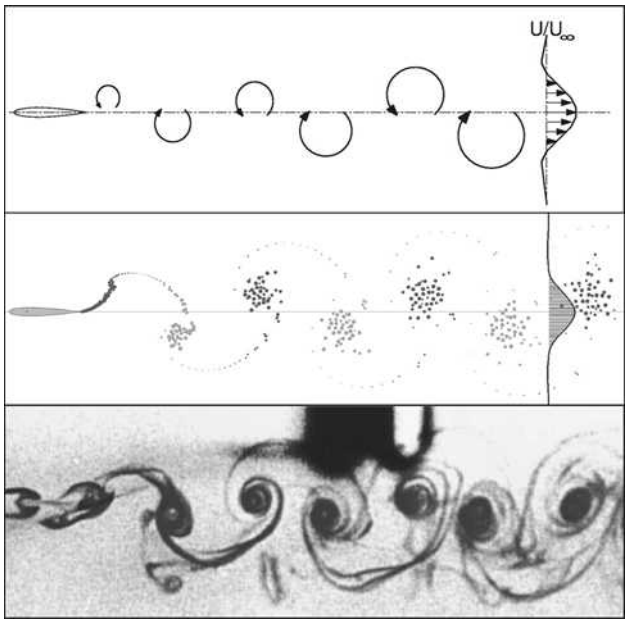

Fig. 3 Vortex arrangement in a thrust-indicative reverse Kármán vortex street: *top* schematic, *middle* panel code, *bottom* experimental. Reduced frequency, k, is 3, non-dimensional plunge amplitude, h, is 0.20, resulting in $hk = 0.60$. For the experiment, $V_\infty = 0.105$ m/s, $f = 5$ Hz, and $Re = 1{,}037$

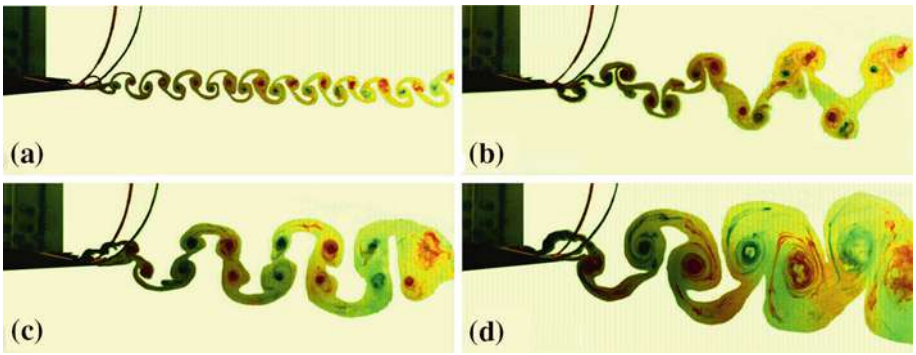

Fig. 4 Transition from normal to reverse Kármán vortex street with increasing *hk* (Lai and Platzer 1999). **a** $hk = 0.0$, **b** $hk = 0.1$, **c** $hk = 0.2$, **d** $hk = 0.4$

These flow visualizations revealed the important fact that previous conclusions drawn from inviscid flow computations can be quite wrong. For example, Garrick's inviscid linearized flow analysis showed that the propulsive efficiency of a harmonically plunging airfoil decreases from values close to 100% at very small reduced frequencies to only 50% for high frequencies. Since the amplitude of oscillation is necessarily limited to small values in linearized theory this type of analysis leads to the conclusion that propulsive efficiency of a harmonically plunging airfoil decreases from values close to 100% at very small reduced frequencies to only 50% for high frequencies. Since the amplitude of oscillation is necessarily limited to small values in linearized theory this type of analysis leads to the conclusion that good efficiencies require flapping at small frequencies. In contrast, (b) and (c) demonstrate that the transition from drag production in (a) to thrust production in (d) occurs by means of increasing the amplitude (at a given frequency). These figures also show that the transition occurs gradually by means of the changes in vortex shedding from (a) through (b) and (c) to (d). The important parameter characterizing the type of vortex shedding therefore has to contain both the frequency and amplitude, usually expressed in terms of the Strouhal number, $St = fA/U_\infty$, where f is the frequency (in Hertz), A the peak-to-peak excursion of the airfoil trailing edge ($2hc$ for a plunging wing) and U_∞ the flow or flight speed. Note that $St = hk/\pi$, and thus the product hk, the maximum non-dimensional plunge velocity, has essentially the same meaning as the Strouhal number.

As is well known, the Kármán vortex shedding from the stationary airfoil in (a) is indicative of airfoil drag. This drag is being reduced as the shedding transitions to the shedding shown in (b) and (c) until net thrust is being generated on the airfoil after transition into the reverse Kármán shedding of (d). This can be understood by realizing that the counterclockwise rotating vortices of the upper row and the clockwise rotating vortices of the lower row entrain flow from the outside so that a higher velocity flow is generated between the two vortex rows. Hence one would expect a jet-like flow to be created if one measures the time-averaged flow, as indicated in Fig. 3. This is

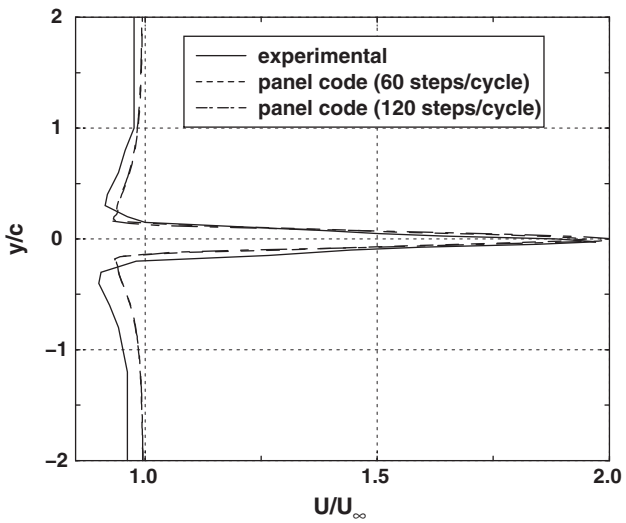

Fig. 5 Measured (LDV) and computed (panel code) time-averaged velocity profile behind the flapping wing for the case shown in Fig. 3

indeed the case. In Fig. 5 we show one of our time-averaged flow measurements (using LDV) in a plane near (but downstream) of the airfoil trailing edge (Jones et al. 1998, 2001; Lai and Platzer 1999). It is seen that the oscillating airfoil indeed generates a distinct jet. It is also seen that the panel-code computed jet profile is in good agreement with the measurement (Fig. 5), again proving that inviscid flow calculations can be quite adequate for certain parameter combinations. The oscillating airfoil therefore imparts momentum to the fluid in the streamwise direction which, in turn, generates a reaction force (thrust) in the opposite direction on the airfoil. The flapping wings of some birds and insects therefore can be considered as a "jet engine" which came into use several times many millions of years before the aircraft jet engine was invented and applied.

A more systematic variation of the amplitude and frequency of plunge oscillation, however, revealed an additional flow regime as soon as the Strouhal number exceeded a certain critical value. As shown in Fig. 6, the shedding then occurs with a finite deflection angle, accompanied by the shedding of additional secondary vorticity. Bratt (1950) shows a similar picture in his report, but makes

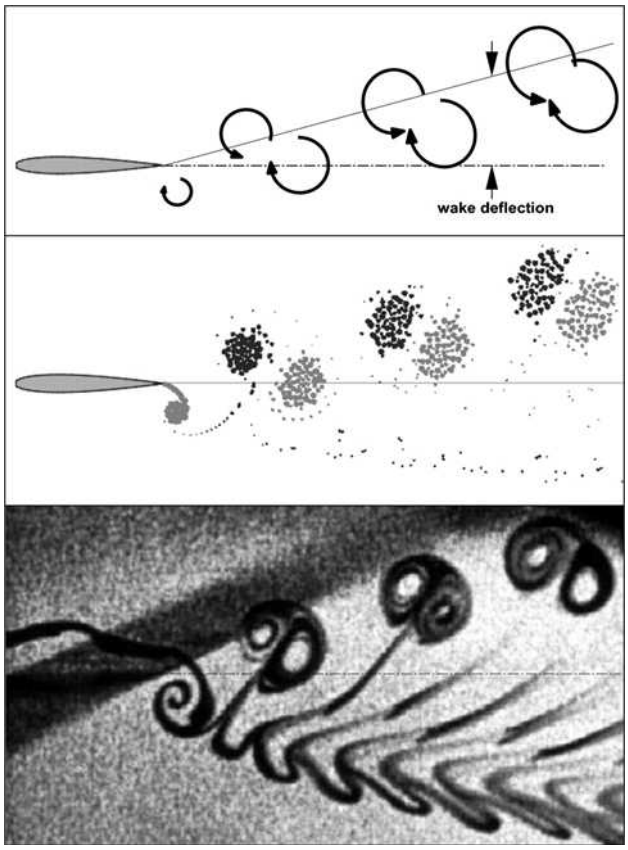

Fig. 6 Vortex arrangement for the deflected-wake vortex street: *top* schematic, *middle* panel code, *bottom* experimental. In this experiment, $k = 12.3$, $h = 0.12$, resulting in $hk = 1.48$. In the experiment, $U_\infty = 0.026$ m/s, $f = 5$ Hz, and $Re = 252$

no comments about this phenomenon. The physical reason for this type of shedding seems to be the shed vortices forming too closely spaced as the frequency is increased. As is also shown in Fig. 6, this deflected jet phenomenon (which generates both thrust and lift on the airfoil) can be predicted with the inviscid panel code. The direction of the jet deflection seemed to depend on the initial starting position of the airfoil. However, Heathcote and Gursul (2004) found in a more recent investigation that the jet switches with a period two orders of magnitude greater than the period of the plunge motion, thus triggering interesting fluid stability questions worthy of future analysis and experimentation. In the water tunnel experiments, the asymmetric wake pattern typically occurred for $hk > 1.0$, although this value is probably dependent on the Reynolds number.

4 Boundary layer and flow separation control by means of harmonically plunging airfoils

As is clear from the preceding discussion, the oscillating airfoil can be regarded as a propeller that entrains a certain

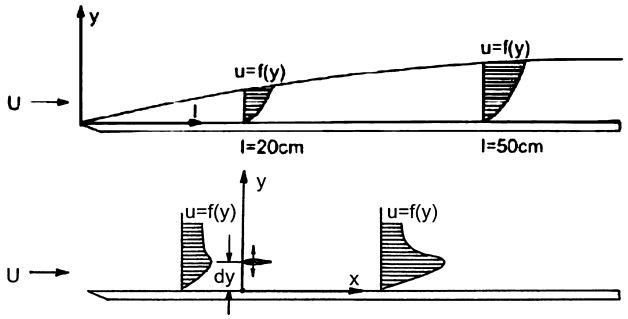

Fig. 7 In the *upper image* a typical boundary layer on a flat plate is shown. In the *lower image* a small airfoil is placed in the boundary layer and flapped. The flapping creates thrust resulting in a jet profile (Dohring 1998)

amount of flow along its span and gives it a certain amount of additional flow momentum. This fact suggested that oscillating airfoils must have potential uses for flow control purposes. Therefore, we thought it might be of interest to study the effect of a small oscillating airfoil mounted in the laminar boundary layer of a flat plate. The arrangement is shown in Fig. 7.

A NACA0012 airfoil of 20 mm chord was mounted in a laminar flat-plate boundary layer. Flow visualization and measurements were performed for different amplitudes and frequencies of the plunging foil. Also, the effect of the distance from the plate was investigated. The experiment was performed in an Eidetics water tunnel. The measurements consisted of LDV flow surveys upstream and downstream of the oscillating airfoil. A typical time-averaged flow profile at a station 0.75 chord lengths downstream of the trailing edge is shown in Fig. 8.

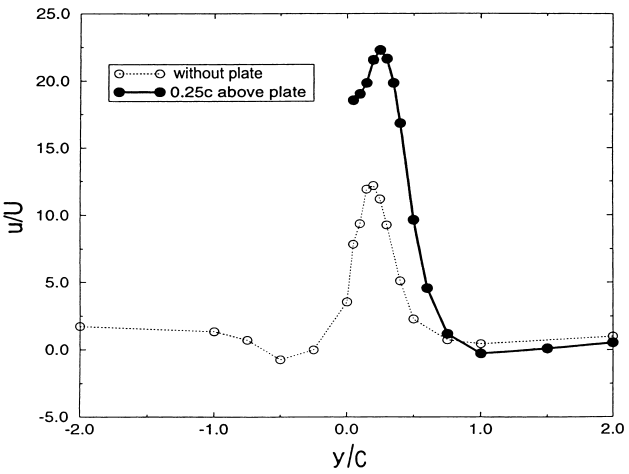

Fig. 8 Measured (LDV) time-averaged velocity profiles in free flow and in the boundary layer of a flat-plate. In the experiment, $h = 0.088c$, $k = 114$, and the Reynolds number was 220. While not shown, velocity measurements very close to the surface of the flat plate show the velocity dropping to zero quite abruptly (Dohring 1998)

It is seen that, compared to the airfoil oscillating in the outside free-stream, the airfoil oscillating in the boundary layer generates a significantly increased jet flow. The flow visualization revealed that the vortex shedding was of the deflected jet type (as discussed in the previous section). The main conclusion from this experiment was that airfoil oscillation close to a flat surface is favorable. Navier–Stokes computations were in substantial agreement with the experimental findings. Details of the Navier–Stokes solver and the results are documented in Dohring (1998).

In Fig. 9 the flow over a stationary airfoil of 28 cm chord length and a maximum thickness of 4.5 cm is shown with either a rounded or cusped trailing edge. The airfoil is at zero angle of attack. A 2 cm chord length airfoil, mounted at a small downstream distance from the trailing edge, is oscillated in plunge with varying amplitude and frequency. This experiment was again carried out in the Eidetics water tunnel. Flow visualization revealed that, depending on the chosen amplitude and frequency of oscillation, the entrainment effect of the oscillating airfoil was strong enough to suppress the flow separation. Systematic variation of the water flow speed and frequency and amplitude of plunge oscillation led to the critical boundary shown in Fig. 10 where the amplitude, h, is plotted on the ordinate and the reduced frequency, k, is plotted along the abscissa. Any combination of parameters to the right of this critical boundary produces complete flow reattachment. Again, complete details are given by Dohring (1998). Results for a range of flapping foil sizes and downstream locations were obtained, with intuitive trends, i.e., smaller flapping wings or further downstream locations required higher hk for reattachment.

In Fig. 11 the flow over a backward-facing step is shown. A harmonically plunging NACA0012 foil of 10 mm chord is mounted in the recirculating flow region caused by a step height of 30 mm. This experiment was also carried out in the Eidetics water tunnel facility of the Naval Postgraduate School. Flow visualization and single-component laser Doppler velocimetry was again used to study the effect of frequency and amplitude of plunge

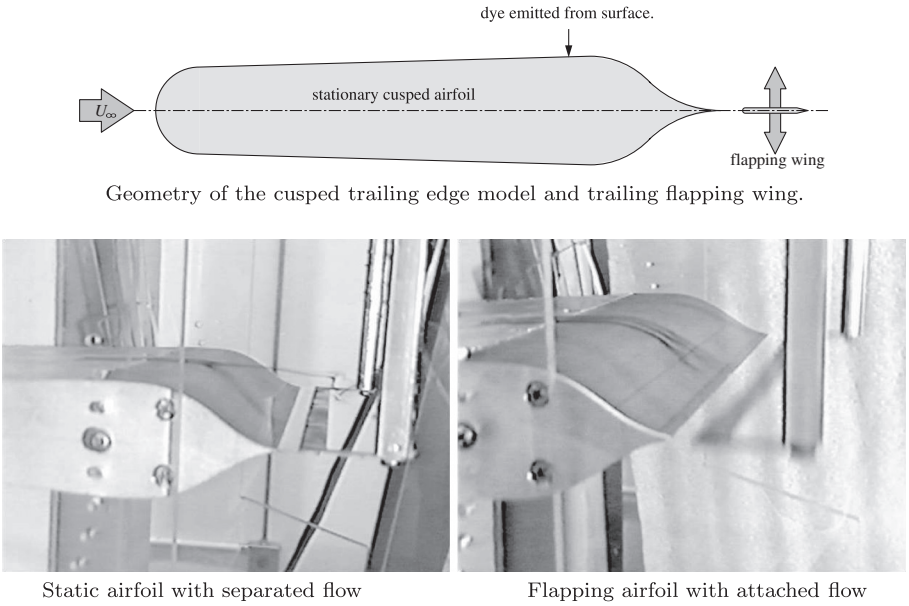

Fig. 9 In the *left image* the trailing airfoil is at rest and the injected dye illustrates massive separation. In the *right image* the trailing wing is flapped, with the entrained flow re-attaching the flow. Results for the main airfoil with rounded trailing edge are similar (Dohring 1998)

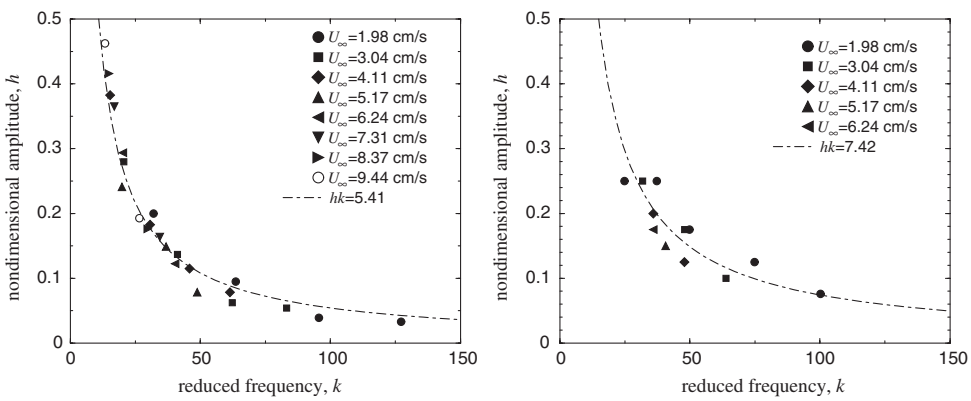

Fig. 10 Critical value of hk for flow reattachment (Dohring 1998). In the *left figure*, a 2 cm chord airfoil placed 0.2c downstream of the cusped trailing edge airfoil is flapped, and the *plotted symbols* indicate the combination of h and k that resulted in reattachment. In the *right figure* similar results are shown for the main airfoil with the round trailing edge, but with the flapping wing 0.25c downstream

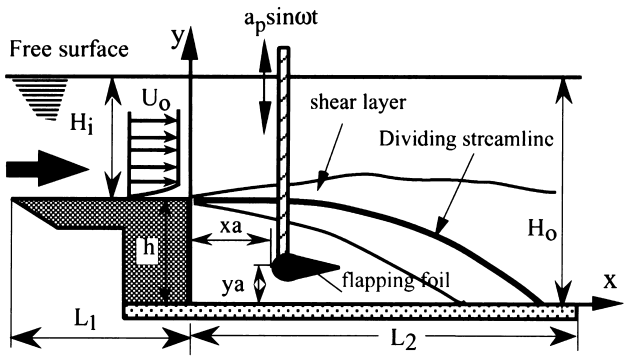

Fig. 11 Schematic of the backward-facing step experiment (Lai et al. 2002). The defining parameters are: $c = 10$ mm, $h = 3c$, $L_1 = 91c$, $L_2 = 70c$, $H_0 = 27c$, $H_i = 24c$, $V_\infty = 0.32$ m/s and *Re* based on step height was 12,700. The step width was $38c$, and the flapping wing was centered $6c$ downstream of the step

oscillation and location of the oscillating foil on the size of the recirculating flow region. This experiment revealed that the strong mixing and entrainment caused by the foil oscillation can reduce the reattachment length by as much as 70%. The measured time-averaged streamlines for the stationary foil and the foil oscillating at 20 Hz with a non-dimensional amplitude of 0.123 are shown in Fig. 12. More details are given by Lai et al. (2002).

The above three experiments led us to the insight that it might be quite beneficial to place an oscillating airfoil close to, but downstream of a stationary airfoil in order to exploit the fact that an aircraft's propulsive efficiency is improved when the air from the wake of the aircraft is used as part of the propulsive stream. Betz (1966) explains this in his book and points out that with wake ingestion the power expended can actually be less than the product of the forward speed and craft drag. At the Douglas Aircraft Company, Smith and Roberts (1947) also proposed to use the boundary layer air for propulsion and Smith (1947) of the General Electric Company quantified the potential benefits of wake ingestion.

Furthermore, the flat-plate boundary layer experiment and inviscid panel code computations for two airfoils, oscillating in counterphase in a biplane arrangement, provided the additional insight that the most promising arrangement might be the closely coupled fixed-wing/oscillating-biplane configuration. The oscillating airfoil flying near a flat surface (or the equivalent biplane airfoils oscillating in counterphase) generate a favorable ground effect (increased thrust and propulsive efficiency). Locating the oscillating biplane airfoils downstream of the fixed wing adds the favorable wake ingestion effect. These two aerodynamic benefits are greatly enhanced by the fact that oscillation in counterphase produces a dynamically balanced configuration, hence eliminates the problem of pitch oscillations induced by the use of single wings.

5 Thrust measurements of oscillating airfoils in biplane arrangement

Having recognized the advantages of the biplane arrangement it remained to select the most suitable oscillation

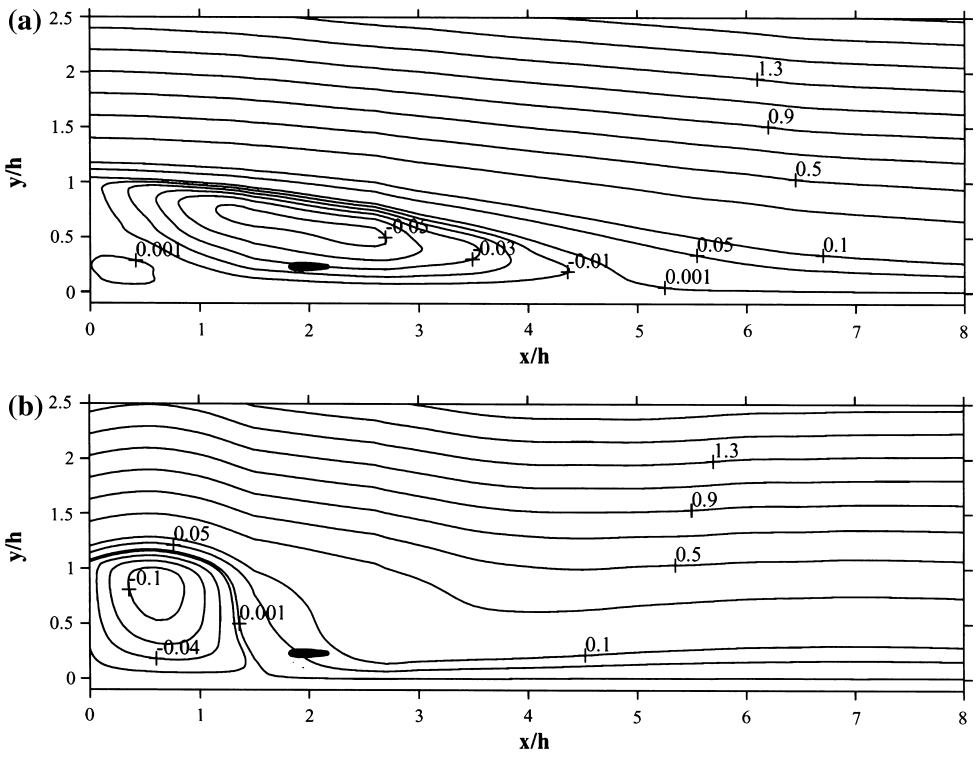

Fig. 12 Mean non-dimensional streamlines with and without flapping illustrating the reduction in the recirculation region (Lai et al. 2002). **a** Stationary foil, **b** Foil flapping at 20 Hz with amplitude $0.123c$

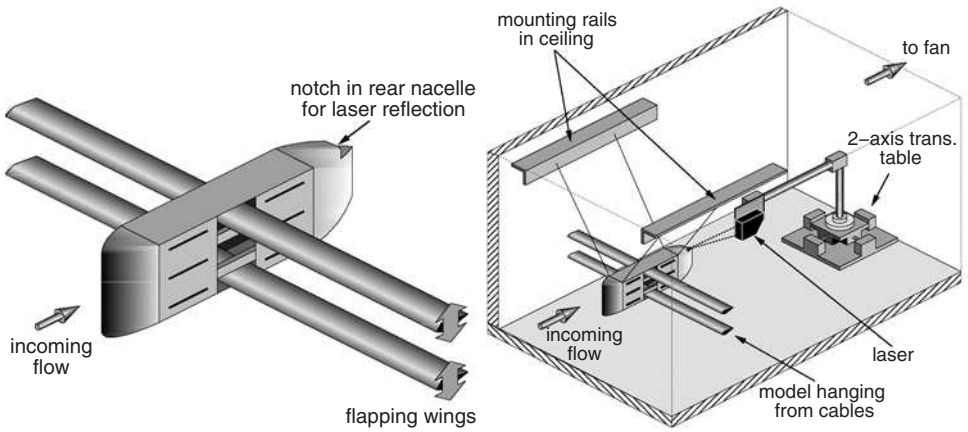

Fig. 13 Large biplane wind-tunnel test model, with 65 mm chord, 1.2 m span wings and a NACA 0014 airfoil section. The model is hung from the ceiling of the test section, and a laser range finder is used to measure its streamwise displacement to calculate thrust or drag

mode. Panel code calculations indicated that the highest propulsive efficiencies are obtained with combined pitch and plunge oscillations if the phase angle between the two modes is approximately 90°. However, experimental confirmation was needed to verify this prediction. Therefore, the model shown in Fig. 13, was built and tested. The two biplane wings could be oscillated in either pitch or plunge. The thrust could be measured quite easily by hanging the model from the wind tunnel ceiling, as shown, and by measuring the small forward movement of the model with a laser range finder as soon as the wing oscillation was turned on. Typical results are shown in Fig. 14 (Jones et al. 2001).

These thrust measurements were quite encouraging and provided the motivation to build a much smaller model (of potential MAV size) and to repeat the thrust measurements. This model is shown in Fig. 15, with a similar pendulum experimental setup (shown in Fig. 16) to measure the very small drag/thrust quantities. Typical thrust measurements are plotted in Fig. 17 (Jones et al. 2005). Another important advance was the excitation system which consists of two swing arms which are driven by a crankshaft and scotch yoke combination. This mechanism oscillates the two airfoils in plunge. Yet, as already mentioned, it is desirable to have a joint pitch/plunge oscillation with a 90° phasing between the two oscillations. This requirement was met by mounting the airfoils elastically at the ends of the swing arms, thus providing the airfoils with the desired pitch degree of freedom by properly adjusting the stiffness of the connection to the swing arms.

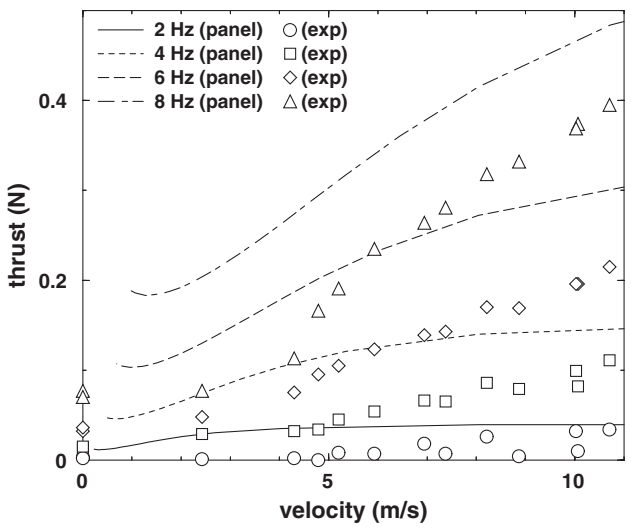

Fig. 14 Predicted and measured thrust for the large biplane model. Reynolds numbers ranged from 0 to 50,000, and the motion of each wing was pure plunge with amplitude 0.4*c*. Mean separation between the wings was 1.4*c*

6 Experimental tests of the complete micro air vehicle

Having thus solved the thrust generation problem, it remained to size the stationary wing in order to obtain sufficient lift and provide it with reflex camber and sweep or dihedral for longitudinal and lateral stability. These considerations led to the wind tunnel model shown in Fig. 18. The pendulum arrangement used in the previous studies to measure thrust/drag was not suitable for measuring both lift and thrust, so a rotating arm test stand

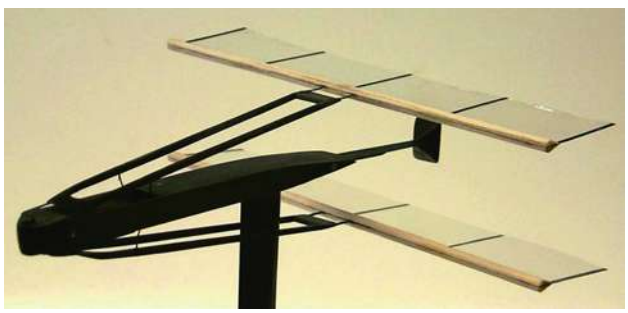

Fig. 15 MAV-sized flapping-wing propulsion model. The *small black square* behind the wings is a reflective surface for the laser range finder

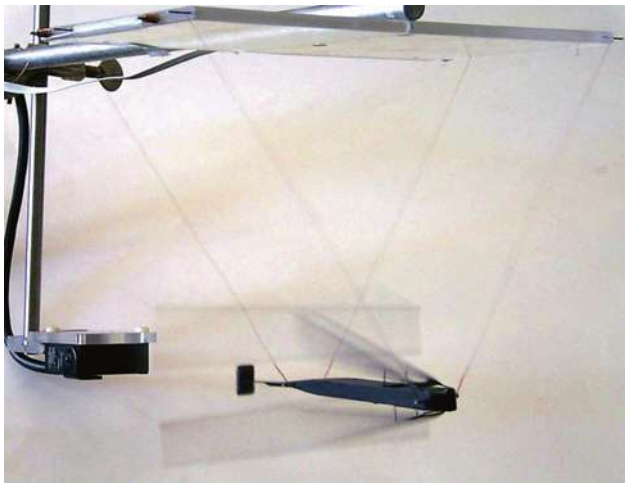

Fig. 16 Pendulum arrangement for wind-tunnel testing. The model is suspended on 0.08 mm diameter copper wires which also provide power and sensing for the stepping motor. The laser range finder is seen about 15 cm downstream

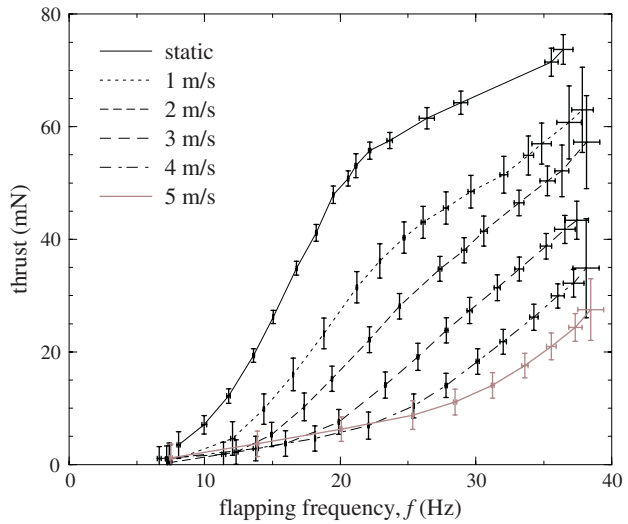

Fig. 17 Typical results from the 15 cm biplane test model. Reynolds numbers ranged from 0 to 12,000

(shown in Fig. 19) was devised. The model would propel itself around the central axis, and a hinge mount at the end of the rotating arm allowed the model to support its own weight with lift. Static thrust for this model was comparable to that shown in Fig. 17.

The results of this study provided sufficient knowledge to size a complete vehicle (shown in Fig. 1) to carry the power and control components available at the time. Having a successful free flying configuration, we then built a wind-tunnel variation, shown in Fig. 20, and performed direct force measurements, flow-visualization and LDV experiments in a low-speed wind-tunnel. Flow visualization was accomplished with a smoke wire which was constructed from 0.25 mm diameter NiCr beaded wire,

Fig. 18 First complete MAV prototype with a fixed forward wing for lift. Span length = 15 cm

heated by passing a current through it, and using Rosco Fog Juice as the smoke agent. The model was mounted at a 15° angle of attack, at a flow speed of about 2 m/s, approximating the low-speed flight conditions. In Fig. 21 we show the case when the flapping wings are at rest (left figure) or flapping at 30 Hz (right figure). The model is viewed from the left rear corner forward, providing a good view of the flow over the upper surface of the left wing. In the left figure it is clearly seen that the flow separated at the leading edge, exposing the wing to full stall. The powerful entrainment effect in suppressing stall is clearly seen in the right figure. It is also very fast acting. It took only about a tenth of a second (4 flapping strokes) to reattach the flow after activation of the flapping wings. Details of the flow visualization study are documented in Papadopoulos (2003).

Unsteady LDV measurements were made with a TSI two-channel system with a single probe and a Rosco fog generator for flow seeding. A rotary motion resolver (RMR) was used to resolve the oscillatory flow generated by the flapping wings. The measurement details are documented in Bradshaw (2003). In Fig. 22 we show the time-averaged velocity profile just in front of the flapping wings for three cases. In the first case, the main wing is removed, and the wings are flapped at 32 Hz. In the second case, the main wing is included, but the wings are not flapped. In the third case, the main wing is included and the wings are flapped at 32 Hz. In all three cases the free-stream speed is 2.75 m/s, and the model is set at a 15° angle of attack. Due to the dihedral of the main wing, a large area above the symmetry plane was inaccessible to the laser, thus yielding detailed results only for the lower flapping wing. Without wing flapping, a velocity defect is seen, whereas wing flapping generates a significant entrainment effect (with or without the presence of the main wing).

Fig. 19 Rotating-arm test stand for the MAV to measure lift and drag

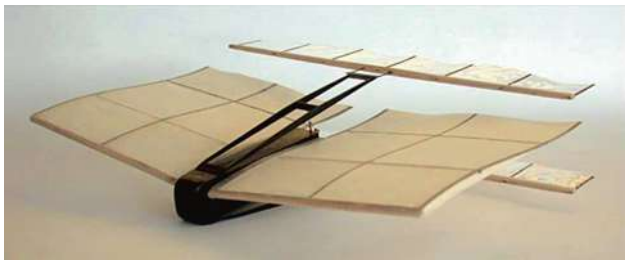

Fig. 20 Wind-tunnel variant of the first flying model with continuous-duty motor and optical encoder

7 Summary and outlook

It was the objective of this paper to describe the experiments which we conducted to develop the flapping-wing micro air vehicle shown in Fig. 1. The decision to use flapping wings rather than conventional propellers was "bio-inspired" by our belief that flapping wings might have propulsive and aerodynamic characteristics superior to conventional vehicles at the Reynolds numbers required for micro air vehicle flight. However, we resisted the temptation to "mimic" bird flight to the maximum possible extent (i.e. develop a biomimetic vehicle). Instead, we based our initial design concept on the information available in the early 1990s which was largely confined to inviscid two-dimensional flow analyses of oscillating airfoils. This state-of-the-art led us to the recognition that experiments were needed to examine the validity of ideal-flow analyses. It also led us to the conclusion that it might be advantageous to base the design on high-aspect ratio wings which are flapping with constant spanwise amplitude. This choice made it possible to limit the experiments (and additional viscous flow analyses) to two-dimensional flow studies while, at the same time, avoiding the thrust (and lift) losses incurred by birds whose flapping amplitude approaches zero toward the wing roots. Therefore, our vehicle is a biomorphic vehicle whose design is based on selecting only certain features found in nature. In fact, we deliberately adopted conventional aircraft design methods by continuing to use separate propulsion and lifting systems. We argued that it would be quite difficult to use flapping-wings for both thrust and lift

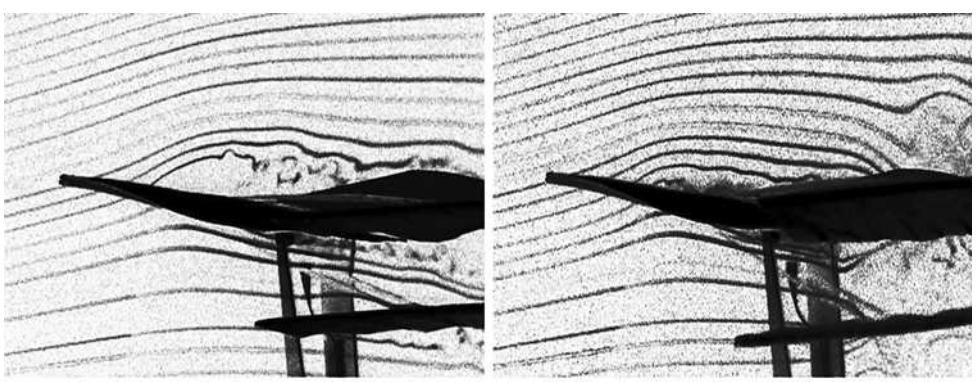

Fig. 21 View of the model in Fig. 21 from the left rear, with the flow coming from left to right. In the *left image* the aft wings are stationary, and the flow over the main wing is separated. In the *right image*, the trailing wings have started flapping and have just completed four flapping strokes, and the flow over the main wing is already reattached. For this extreme case, $\alpha = 15°$, $f = 30$ Hz and $V_\infty = 2$ m/s resulting in Reynolds numbers of 20,000 for the main wing, and 5,500 for the flapping wings

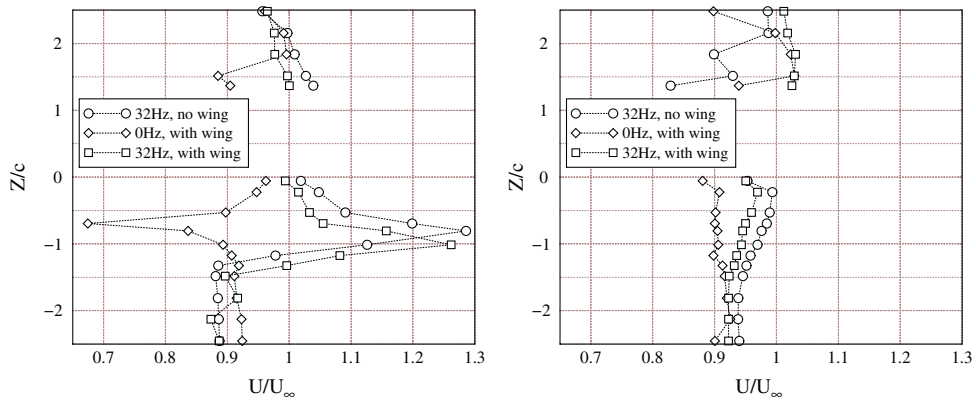

Fig. 22 Time-averaged LDV results illustrating the flow entrainment at the leading edges of the flapping wings. In the *left image*, the velocity is measured essentially at the leading edges of the flapping wings. In the *right image*, the velocity is measured a chordlength upstream of the leading edges. *Z*/*c* is the vertical distance from the centerline. Note that the region from 0 to 1.5 is masked by the main wing. Flow conditions were $V_\infty = 2.75$ m/s and $\alpha = 15°$

generation. Therefore, we concentrated on understanding the physics of thrust generation by high-aspect ratio flapping-wings and resorted to the use of fixed wings for lift generation.

The experiments described in this paper therefore focused at first on the determination of the effect of amplitude and frequency on the flow physics and on the thrust generated by two-dimensional plunging airfoils. The insight obtained from these studies then led to the exploration of the effectiveness of flapping airfoils as flow control devices. These studies revealed the advantages to be obtained from using two airfoils (flapping in counterphase) in close vicinity (but downstream) from a fixed wing.

Although the information obtained in the course of our experimental and computational studies was sufficient for the development of a successful flapping-wing micro air vehicle (Fig. 1). A number of aerodynamic aspects require further exploration. Little aerodynamic design information is available on three-dimensional flow effects for flapping-wings in forward flight. Flapping-wing micro air vehicles that can take-off and land vertically, hover, maneuver and fly forward are likely to require a detailed understanding of the complex aerodynamics of humming birds or insects. Hence, as reviewed in Platzer et al.(2008), many challenging unsteady aerodynamic flows remain to be studied experimentally and computationally in the field of low Reynolds number aerodynamics with applications to the development of micro air vehicles.

Acknowledgments We are grateful for the support received from Spiro Lekoudis of the Office of Naval Research, with project monitors Peter Majumdar and Edwin Rood, and from Richard Foch, head of the Vehicle Research Section of the Naval Research Laboratory, with project monitors Kevin Ailinger, Jill Dahlburg and James Kellogg. We would also like to acknowledge the contributions of Jiannwoei Yue, Claus Dohring, Joseph Lai, John Young, Jason Papadopoulos and Chris Bradshaw.

References

Betz A (1912) Ein beitrag zur erklaerung des segelfluges. Zeitschrift fuer Flugtechnik und Motorluftschiffahrt 3:269–270

Betz A (1966) Introduction to the theory of flow machines. Pergamon, New York

Birnbaum W (1924) Das ebene problem des schlagenden fluegels. Zeitschrift fuer Angewandte Mathematik und Mechanik 4(4):277–290

Bradshaw CJ (2003) An experimental investigation of flapping wing aerodynamics in micro air vehicles. Master's thesis, Department of Aeronautics and Astronautics, Naval Postgraduate School, Monterey

Bratt JB (1950) Flow patterns in the wake of an oscillating airfoil. Technical Report R & M 2773, Aeronautical Research Council

Dalton S (1999) The miracle of flight. Firefly Books, Westport

Dohring CM (1998) Der Schub des schlagenden Fluegels und seine Anwendung zur Grenzschichtbeeinflussung. PhD thesis, German Armed Forces University, Munich

Garrick IE (1936) Propulsion of a flapping and oscillating airfoil. Technical Report 567, NACA

Heathcote S, Gursul I (2004) Jet switching phenomenon for a plunging airfoil. AIAA-2004-2150

Jones KD, Dohring CM, Platzer MF (1998) Experimental and computational investigation of the Knoller-Betz effect. AIAA J 36(7):1240–1246

Jones KD, Lund TC, Platzer MF (2001) Fixed and flapping wing aerodynamics for micro air vehicle applications, vol 195, Progress in Astronautics and Aeronautics, Chap 16, Experimental and computational investigation of flapping wing propulsion for micro air vehicles, pP 307–339. AIAA

Jones KD, Bradshaw CJ, Papadopoulos J, Platzer MF (2005) Bio-inspired design of flapping-wing micro air vehicles. Aeronaut J Roy Aeronaut Soc 109(1098):385–392

Katzmayr R (1922) Effect of periodic changes of angle of attack on behavior of airfoils. Technical Report TM 147, NACA

Knoller R (1909) Die gesetze des luftwiderstandes. Flug- und Motortechnik 3(21):1–7

Lai JCS, Platzer MF (1999) Jet characteristics of a plunging airfoil. AIAA J 37(12):1529–1537

Lai JCS, Yue J, Platzer MF (2002) Control of backward-facing step flow using a flapping foil. Exp Fluids 32:44–54

Lilienthal O (1992) Der Vogelflug als Grundlage der Fliegekunst, 3rd edn. Harenberg Kommunikation, Dortmund

Papadopoulos JP (2003) An experimental investigation of the geometric characteristics of flapping-wing propulsion for a micro air vehicle. Master's thesis, Department of Aeronautics and Astronautics, Naval Postgraduate School, Monterey

Platzer MF, Neace KS, Pang KC (1993) Aerodynamic analysis of flapping wing propulsion. AIAA-93-0484

Platzer MF, Jones KD, Young J, Lai JCS (2008) Flapping-wing aerodynamics: progress and challenges. AIAA J 46(9):2136–2149

Smith LH (1947) Wake ingestion propulsion benefit. J Propuls Power 9(1):74–82

Smith AMO, Roberts HE (1947) The jet airplane utilizing boundary layer air for propulsion. J Aeronaut Sci

Teng NH (1987) The development of a computer code for the numerical solution of unsteady inviscid and incompressible flow over an airfoil. Master's thesis, Department of Aeronautics and Astronautics, Naval Postgraduate School

Theodorsen T (1935) General theory of aerodynamic instability and the mechanism of flutter. Technical Report 496, NACA

von Kármán T, Burgers JM (1934) General aerodynamic theory-perfect fluids, aerodynamic theory, vol II. Julius Springer, Berlin

Smoke visualization of free-flying bumblebees indicates independent leading-edge vortices on each wing pair

Richard James Bomphrey · Graham K. Taylor · Adrian L. R. Thomas

Abstract It has been known for a century that quasi-steady attached flows are insufficient to explain aerodynamic force production in bumblebees and many other insects. Most recent studies of the unsteady, separated-flow aerodynamics of insect flight have used physical, analytical or numerical modeling based upon simplified kinematic data treating the wing as a flat plate. However, despite the importance of validating such models against living subjects, few good data are available on what real insects actually do aerodynamically in free flight. Here we apply classical smoke line visualization techniques to analyze the aerodynamic mechanisms of free-flying bumblebees hovering, maneuvering and flying slowly along a windtunnel (advance ratio: −0.2 to 0.2). We find that bumblebees, in common with most other insects, exploit a leading-edge vortex. However, in contrast to most other insects studied to date, bumblebees shed both tip and root vortices, with no evidence for any flow structures linking left and right wings or their near-wakes. These flow topologies will be less efficient than those in which left and right wings are aerodynamically linked and shed only tip vortices. While these topologies might simply result from biological constraint, it is also possible that they might have been specifically evolved to enhance control by allowing left and right wings to operate substantially independently.

Electronic supplementary material The online version of this article (doi:10.1007/s00348-009-0631-8) contains supplementary material, which is available to authorized users.

R. J. Bomphrey · G. K. Taylor · A. L. R. Thomas (✉)
Department of Zoology, Oxford University, South Parks Road, Oxford OX1 3PS, UK
e-mail: adrian.thomas@zoo.ox.ac.uk

R. J. Bomphrey
e-mail: richard.bomphrey@zoo.ox.ac.uk

1 Introduction

The urban myth that aerodynamicists have proven that bumblebees cannot fly can be traced back to at least 1919, when an engineer, Hoff (1919), used data from an entomologist, Demoll (1918), to suggest that animals flew using the same attached flow aerodynamics as fixed-wing aircraft. Demoll (1919) responded, using Hoff's equations (Hoff 1919), to show that this could not be true because a bee would require a lift coefficient over twice that of any aircraft, once the speed of the beating wings was taken into account. Studies with real and model insects have since shown that they use unsteady separated flows to enhance aerodynamic force production, so in its most general sense, the "bumblebee paradox" may now be said to be solved (Bomphrey et al. 2005; Dickinson et al. 1999; Ellington et al. 1996; Maxworthy 1979; Srygley and Thomas 2002; Thomas et al. 2004) (for reviews, see Bomphrey 2006; Lehmann 2004; Sane 2003). Nevertheless, fundamental details of these aerodynamic mechanisms remain unresolved, and it is those which we address here.

The separated flows used by insects usually involve the formation of a coherent vortical structure over the suction surface of the wing. This vortex is typically generated through separation at the leading edge, and for this reason is commonly known as a leading-edge vortex (LEV). One fundamental question for aerodynamicists is whether and how LEV topology varies with wing morphology, advance ratio, and stage of stroke. This is significant, because the topology of the LEV potentially governs such key issues as

G.K. Taylor, M.S. Triantafyllou, and C. Tropea (Eds.): Animal Locomotion, pp. 249–259.
springerlink.com

aerodynamic efficiency, vortex stability and control authority (Bomphrey 2006; Thomas et al. 2004). Considering only the primary vortex, the three most basic types of flow topology are as follows, each differing fundamentally in the flow at the wing root and midline of the animal: (1) a single continuous LEV spanning from left wingtip to right wingtip, with a free-slip focus over the thorax and a tip vortex trailing from each wing (Fig. 1a); (2) separate LEVs on the left and right wings, each arising from a focus at the wing root with a tip vortex trailing from each wing (Fig. 1b); (3) separate LEVs on the left and right wings, each leading into their own root and tip vortex system (Fig. 1c). Whereas the first category is likely to come closest to developing an even downwash distribution, thereby maximizing aerodynamic efficiency, the second and third categories may offer greater potential for independent operation of the left and right wings, and hence greater control authority. Stability of the LEV in each case will depend upon the rate of transport of vorticity along the vortex core, which might be promoted by the second category of LEV flow topology, resembling as it does the stable LEV of a swept-wing aircraft. Much attention has been paid to this transport of vorticity in real insects (e.g. Bomphrey et al. 2005; Bomphrey et al. 2006a, b; Ellington et al. 1996), scale models (e.g. Birch and Dickinson 2001; Ellington et al. 1996) and computational simulations (Shyy and Liu 2007), although with varying conclusions as to its importance.

The first category of LEV flow topology (Fig. 1a) has been observed in a number of real insects, including free-flying butterflies (Srygley and Thomas 2002) and dragonflies (Thomas et al. 2004). The second category of LEV flow topology (Fig. 1b) has been observed in studies with mechanical models (Birch and Dickinson 2001; Ellington et al. 1996), and is likely also to occur in real insects—especially in the early stages of LEV formation (Bomphrey et al. 2005). The third category of LEV flow topology (Fig. 1c) is suggested by flow visualizations on mechanical models (Ramasamy and Leishman 2006). It is important to emphasize that while these topologies are strict alternatives at any given instant, there is no reason why insects should not transition between these topologies when moving between hovering and forward flight, or even at different stages of the wing stroke. Indeed, we have observed the LEV topology of free-flying insects to change from one to stroke to the next (butterflies: Srygley and Thomas 2002) and even within a stroke (dragonflies: Thomas et al. 2004). This ability to rapidly change kinematics, and thereby to control flow topology, may well be important in flight control. In this paper, we describe the flow topologies observed around bumblebees at different stages of the stroke and in a range of different free-flight conditions. No single image shows the entire wake topology at any stage of the stroke. Rather, multiple examples are presented for each of the flow elements we describe and each are grouped according to the stage of the wing stroke cycle in which they are observed. With this technique, we can conclude for different times throughout the cycle which is the most likely gross topological structure from a number of simple hypotheses using what are in fact quite coarse features of the flow.

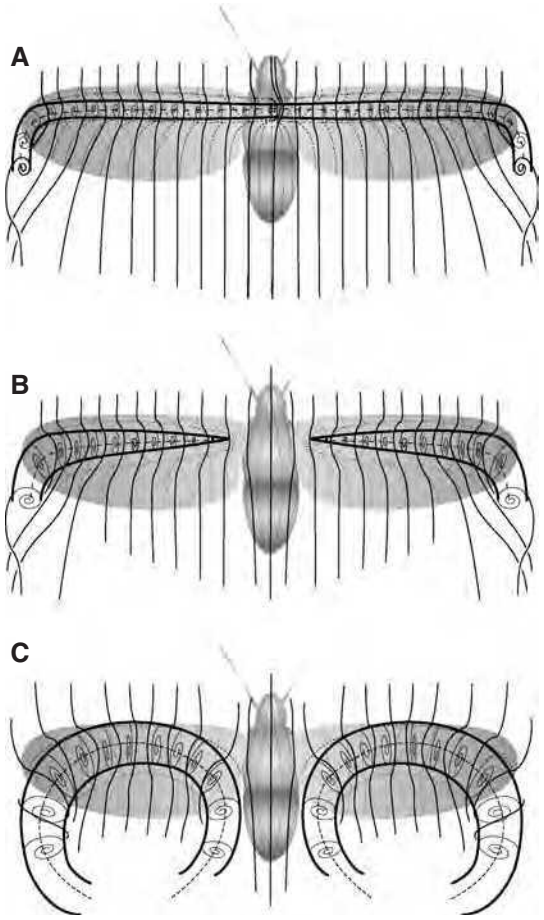

Fig. 1 Three hypotheses for separated flows over insect wings. **a** Continuous bound LEV spanning from wing tip to wing tip with free slip focus over the body. Wing tip vortices present but no root vortices. **b** A conical spiral LEV structure on each wing with a focus on each wing surface close to the root. Wing tip vortices present but no root vortices, and attached flow over the body. **c** A separate LEV on each wing with no foci on the surfaces of the wings: instead, the LEV structures inflect into the wing tip and wing root vortices

We choose to work with real bumblebees, rather than models, because we are interested in understanding the aerodynamics of real insects, and existing models are not yet able to approach the complexity revealed in studies of insect wingbeat kinematics (Walker et al. 2008, 2009). Although modelling approaches have many advantages, the paucity of high-resolution data on insect wing kinematics has meant that modelling studies to date have necessarily used highly simplified wing kinematics. In most cases, the

wing is treated as a rigid flat plate, which necessarily neglects the effects of varying camber and twist. In contrast, our high-speed digital video of real bumblebees shows that their wings not only twist but also fold through up to 90° along the hinge-like row of hooks joining the leading edge of the hindwings to the trailing edge of the forewings. In consequence, rigid flat plate models cannot necessarily be assumed to replicate the flows generated by real insects.

Simplified models of insect aerodynamics ought ideally to be tested against data from real insects. In recent years, we have successfully applied the quantitative flow visualization technique of Digital Particle Image Velocimetry (DPIV) to real insects (Bomphrey 2006; Bomphrey et al. 2005, 2006a, b). Nevertheless, we choose to use the qualitative technique of smoke visualization for this study, because it is better suited to describing the flow topologies of real, free-flying insects than DPIV or any available quantitative visualization technique. In particular, smoke visualization overcomes the practical difficulty of encouraging an insect to fly freely under the conditions of dim ambient lighting, bright laser illumination and volume seeding of the flow which DPIV requires. Moreover, although DPIV can yield precise measurements of the flow field, the difficulty of deriving forces from time-varying velocity vector fields has meant that the technique has rarely been used to its full quantitative potential in studying animal locomotion (Dabiri 2005; Noca et al. 1999). In consequence, we find that the classical technique of smoke visualization is well suited to our purpose of describing the flow topologies of insects. It is also worth noting in this context that all of the fundamental fluid dynamics work on the topology of 3D unsteady separated flows is based upon qualitative visualization techniques (Délery 2001; Perry and Chong 1987).

2 Experimental details

A colony of approximately 100 bumblebees *Bombus terrestris* was trained to forage from a nest in the laboratory to a pollen and nectar source in the working section of a low-speed wind tunnel operating at 1.2 ms^{-1}. This pollen and nectar source was removed during experiments to avoid interfering with the flow. We used a high-resolution smokewire technique (Thomas et al. 2004) to generate a vertical plane of smoke lines with approximately 1 mm spacing (one tenth of the wing length). The primary evidence provided in this paper is smoke visualizations, and while we base our conclusions on the most comprehensive set of flow visualizations of any animal to date, it must be borne in mind that smoke visualization is an inherently qualitative technique, with restricted spatial resolution. Quantitative confirmation of the results presented here are required, for example through 3D PIV with free-flying insects. A limitation with smoke-in-air visualization is that the residence time of the smoke particles can be longer than the persistence of vorticity in the wake. This effect is known to be problematic in the far wake, where smoke streaks appear to be delineating vortices long after the vorticity has diffused (Cimbala et al. 1988). Here, however, we refer only to wake structures younger than one wing beat period (1/180 s) at a Reynolds number of Re = 2,500 (based on mean wing tip speed).

Image sequences were recorded using high-speed digital video cameras aligned normal to the smoke plane acquiring data at either 1,000 fps (Hi-DCamII: NAC Image Technology, CA, USA; 1,280 × 512 px; field of view width = 85 mm; 1 px = 0.066 mm; exposure time = 1/1,000 s) or 2,100 fps (Phantom v7: Vision Research Inc, NJ, USA; 1,024 × 512 px; field of view width = 90 mm; 1 px = 0.088 mm; exposure time = 1/2,100 s).

In total, we were able to visualize 511 aerodynamically informative wingbeats from 32 separate flight sequences, in which the bees performed a variety of maneuvers. In 413 of these wingbeats, the bees were travelling approximately parallel to the long-axis of the tunnel, facing either into or away from the flow. Of the remaining 98 wingbeats we observed, 78 involved quartering flight in which the bee moved diagonal to the freestream, and a further 20 in which the bee translated sideways with respect to the freestream, at airspeeds as high as 1.4 ms^{-1}.

We were able to determine the bees' airspeed (V) while they were flying in the plane of the smoke by reference to the convection of smoke structures in the freestream of 1.2 ms^{-1}. The bees flew at a range of airspeeds from -1.5 ms^{-1} (slow backwards flight) to 1.8 ms^{-1} (slow forwards flight). Although we did not measure stroke amplitude (Φ) directly, bumblebees typically operate with a stroke amplitude of approximately 2 rad (Dudley and Ellington 1990). The mean wingbeat frequency (f) across flight sequences was 180 Hz (s.d. = 13.6 Hz, n = 32 flight sequences), so the range of airspeeds we observed corresponds approximately to advance ratios in the range $-0.2 < J < 0.2$, where $J = V/2\Phi fR$ (Ellington 1984) and wing length (R) is approximately 10 mm. Flight with an advance ratio $|J| < 0.1$ is conventionally classed as hovering, so the range of flight conditions we observed brackets hovering flight (Ellington 1984). These advance ratios are easily interpretable for forwards and backwards flight, but are of little use for the many other orientations our free-flying bumblebees adopted. For example, how should J be calculated when the bumblebee is holding station in the wind tunnel, but oriented roughly perpendicular to the incident flow? In this case, forwards–backwards velocity in the bee's frame of reference is

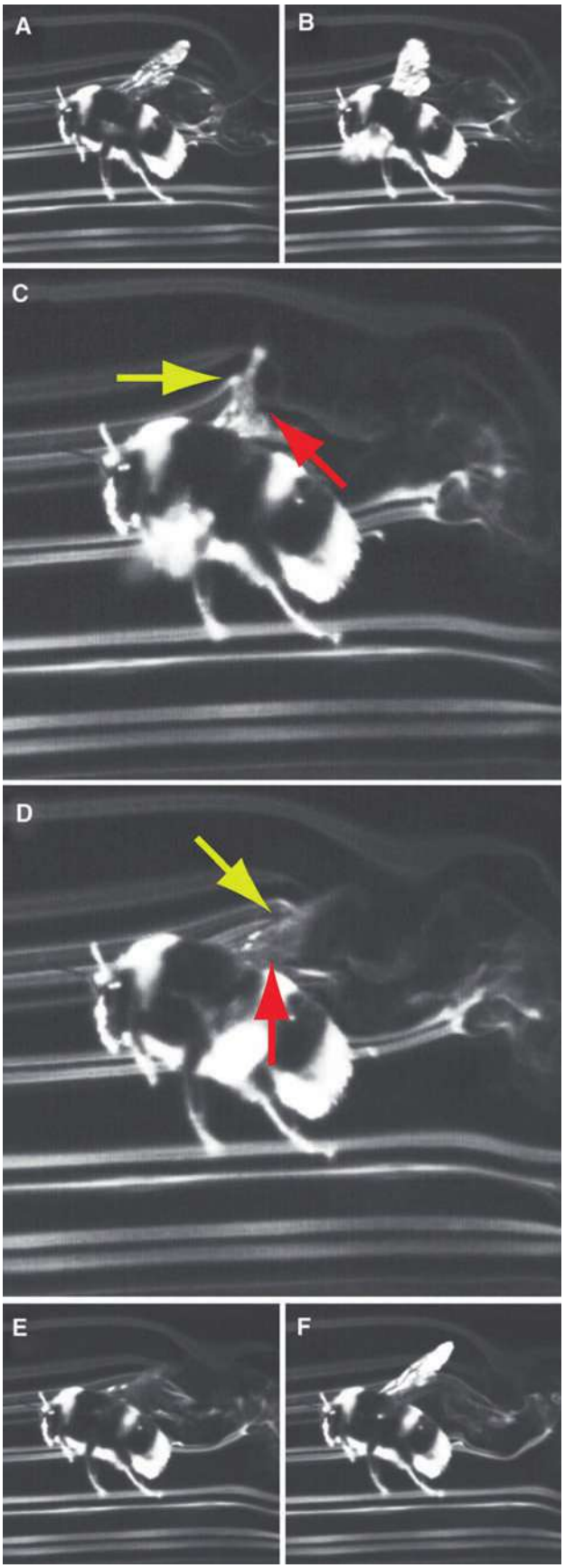

Fig. 2 Bumblebee stroke sequence in forwards flight, with arrowed ▶ smokelines visualizing points of attachment (*yellow*) and reattachment (*red*). The smokeline which reattaches delineates the extent of a LEV formed at supination. We begin the cycle with pronation occurring immediately prior to (**a**): pronation occurs again in (**f**). Overall image brightness and contrast have been increased to best visualize the smokelines—this inevitably incurs a loss of detail on the wing surface when it is angled such that the illumination reflects back into the camera lens. Frames separated by 1 ms

0 ms^{-1}, but the oncoming flow (from the side) is 1.2 ms^{-1} so a value of $J = 0$ would be misleading since it does not tell the full story about the flow physics.

3 Results

The flow topology we observed changed through the wingbeat, but did so in a rather stereotyped manner, despite the range of flight conditions. Figure 2 presents a typical wingbeat. We found no evidence of flow separation during the first part of the downstroke (Fig. 2a) in any of our recorded sequences (further evidence in Fig. 3). However, by the time of supination at the end of the downstroke, the flow over the wings had separated to form a LEV, and that LEV persisted well into the upstroke. During supination (Fig. 2c), a point along the forward line of attachment can clearly be seen on the underside of the wing, where a smokeline impacts the wing approximately halfway along its length (yellow arrow). The smokeline directly above this one bifurcates: one branch flows into the wake behind the bumblebee; the other branch flows upstream and reattaches on the wing upper surface (red arrow), delineating a LEV over half a chord in diameter. At the beginning of the upstroke (Fig. 2d), the lines of attachment (yellow arrow) and reattachment (red arrow) remain on the underside and upperside of the wings, respectively, indicating that the circulation continues to be of the same sense following stroke reversal. However, by mid-upstroke (Fig. 2e), the LEV has been shed. The timing of LEV formation is presented for a further 10 wingbeats in Fig. 3. The first frame capturing supination is highlighted in yellow and this is always concurrent with the first unambiguous appearance of the LEV (white arrows), which indicates that the LEV is formed in the latter part of the downstroke. As we now show, the topology of the LEV matches that hypothesized in Fig. 1c at this stage in the stroke cycle.

During a typical downstroke, trailing vortices are shed from both the wing tips and the wing roots. This demonstrates that the LEV is not of the form hypothesized in Fig. 1a or b. Figure 4 presents an example of quartering flight, in which the attitude of the bee makes it possible to

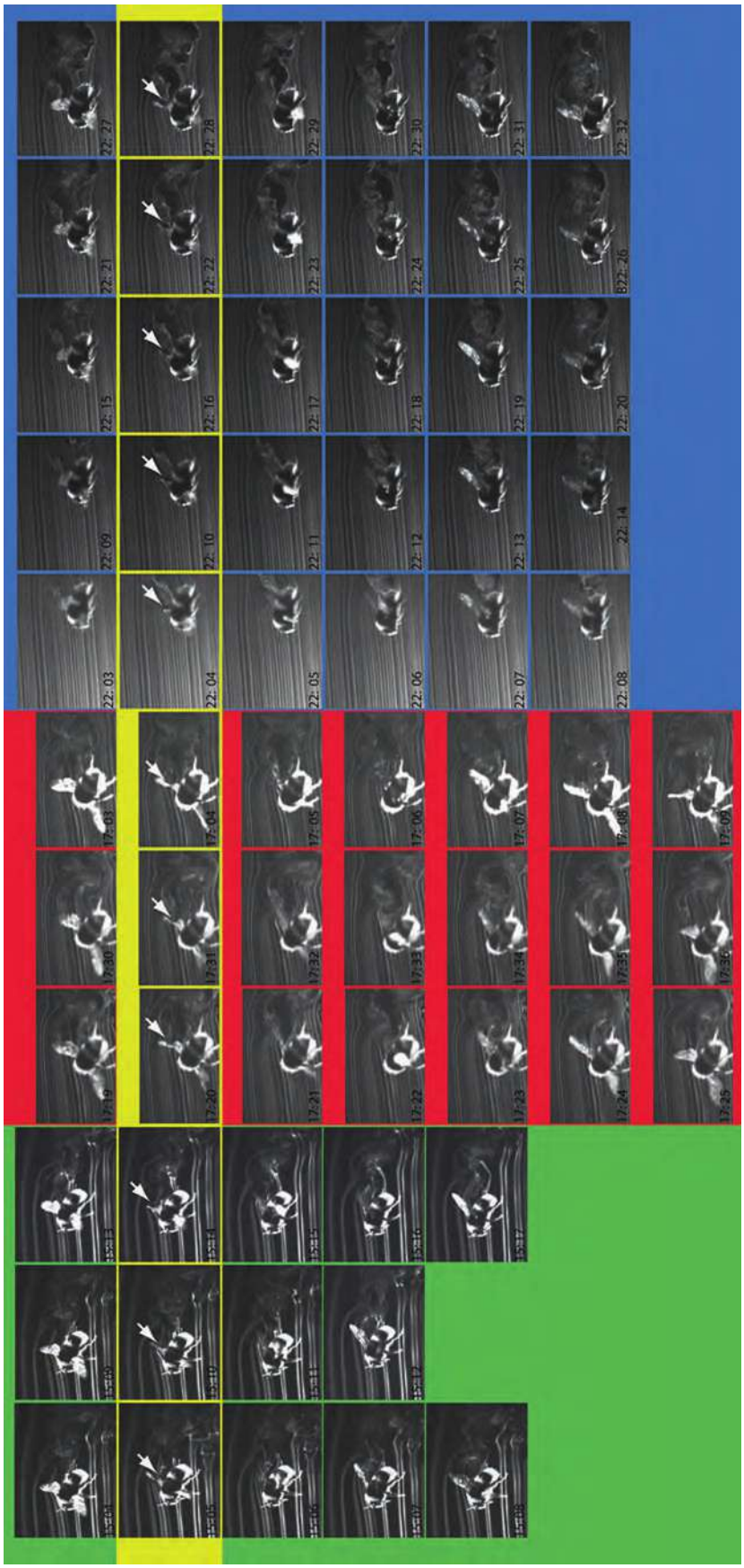

Fig. 3 Three bumblebees in quartering (*green background*), sideways (*red background*) and slow forwards (*blue background*) flight, each oriented so the formation of the LEV (*white arrow*) is visualized by smoke lines. Consecutive frames read down the columns. Individual wingbeats (*different columns*) have been arranged so that the frames showing the first evidence for supination are aligned horizontally (*yellow background*). The LEV first appears in these frames (i.e. at stroke reversal) in each wingbeat where it was visualized. The third column is the same wingbeat as shown magnified in Fig. 2

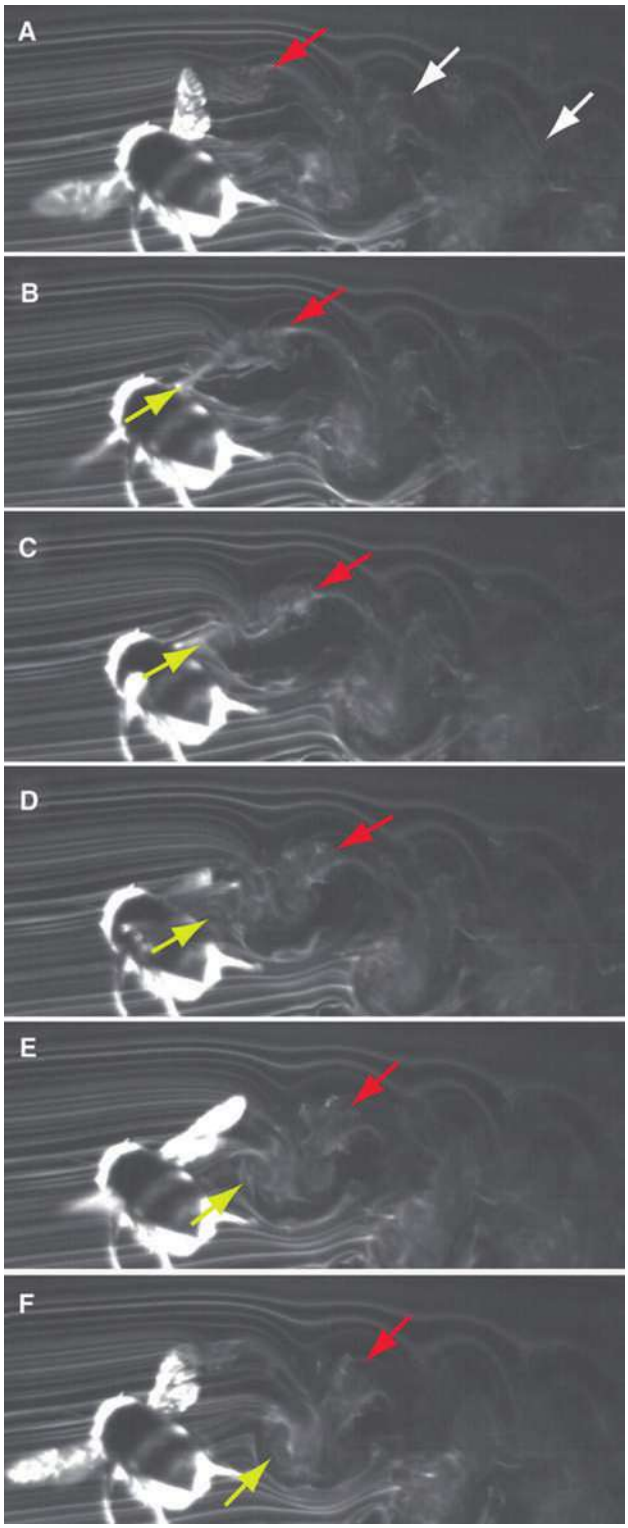

Fig. 4 Bumblebee in upwind quartering flight, showing wing tip vortices (*red arrows*, **a**–**f**) and root vortices (*yellow arrows*, **b**–**f**), which are shed into the wake as a vortex loop by the stage of the upstroke shown in panel (**e**). Wake elements shed on preceding wingbeats are arrowed in white (**a**). See main text for detailed description. Frames separated by 1 ms. Overall image brightness and contrast have been increased linearly

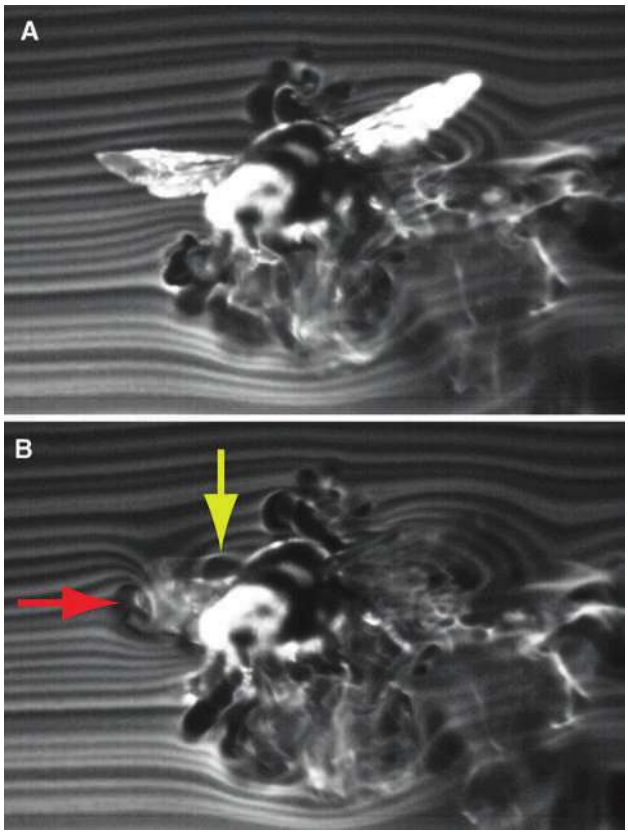

Fig. 5 Bumblebee in sideways flight, showing smokelines becoming entrained in counter-rotating wing tip vortices (*red arrow*) and wing root vortices (*yellow arrow*). Frames separated by 1 ms

visualize the structure of the vortex system along the length of the wing. A helical wing tip vortex can be seen in Fig. 4a where the right wing tip has impinged on the smokelines (red arrow); the white diagonal arrows point to vortex loop elements shed by previous wingbeats. By Fig. 4b the wing has passed further into the vertical smokeline plane and a root vortex is now visible (yellow arrow). Wing tip vortices (red arrows) and root vortices (yellow arrows) continue to trail the wing one-third of the way into the upstroke (Fig. 4c), confirming again that the circulation is of the same sense as on the downstroke. However, 1 ms later (Fig. 4d), the root and tip vortices are shed as a vortex loop in the wake behind the bumblebee, indicating a change in the circulation around the wing. The shed vortex loop distorts and rotates as it convects backwards and downwards into the wake (Fig. 4d–f). Figure 5 is another example showing a bee generating a counter-rotating pair of tip (red arrow) and root (yellow arrow) vortices while oriented sideways to the freestream. Although the orientation of the bees in Figs. 4 and 5 make it especially easy to see the 3D structure of the vortex system, root vortices were observed in the full range of flight modes we recorded (Movie S1). The stereotyped

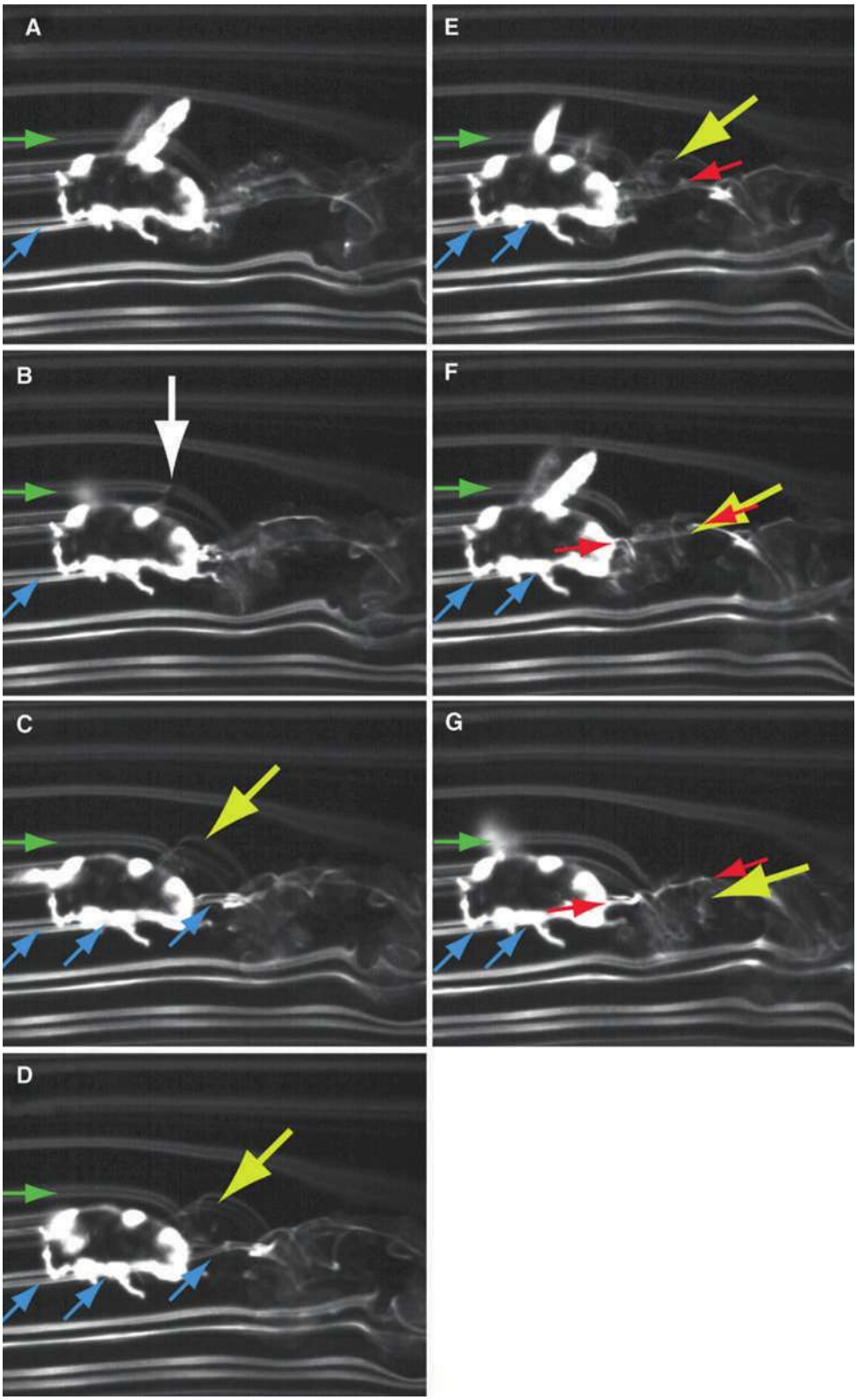

Fig. 6 Bumblebee in forward flight with smoke incident near the *midline*, showing the aerodynamic independence of contralateral wing pairs. See text for commentary on *arrowed* structure. Frames separated by 1 ms. Overall image brightness and contrast have been increased linearly. Advance ratio, $J < 0.2$

sequence of flow topologies we have described is therefore robust to large-scale changes in the direction of flow relative to the insect's body.

Further confirmation that the LEV is not of the form hypothesized in Fig. 1a is provided by the observation that smokelines running along the midline of the body pass

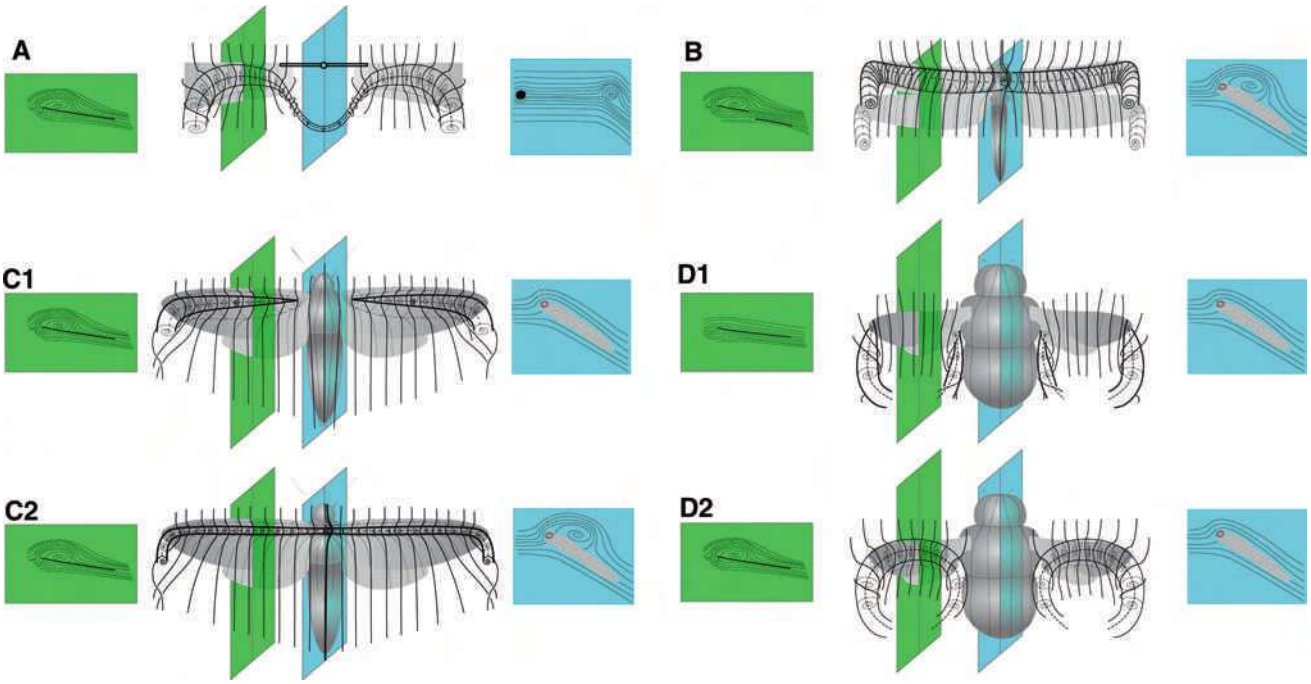

Fig. 7 Cartoon to show the qualitatively different flow topologies hypothesized for insects on the basis of mechanical models (**a**), observed in live insects (**b**, **c2**, **d1**, **d2**), and or both (**c1**). (**a**) Shows the topology described by Maxworthy (1979) for his mechanical flapper based on the clap and fling mechanism of the Chalcid wasp. (**b**) Shows the topology found over the fore and hind wings of a dragonfly for 75% of the wingbeats analysed in Thomas et al. (2004)—they found several variations, but this was considered to be the 'normal' counter-stroking topology and was not significantly different from the in-phase wingbeat topology. (**c1**) and (**c2**) shows two topologies described for hawkmoths by Ellington et al. (1996) and Bomphrey et al. (2005), the latter suggesting that (**c1**) was a transient state and (**c2**) was the topology toward the end of the downstroke once the flow over the thorax had separated too. The bumblebee flow pattern presented in (**d1**—early *downstroke*) and (**d2**—late *downstroke*) represents a novel topology with *left* and *right* wings acting independently and a LEV forming at supination (**d2**). The LEV structures are therefore clearly variable and can change throughout the course of a single wing stroke in hawkmoths, dragonflies, and bumblebees. Adapted from Bomphrey et al. 2005

smoothly into the wake, rising in the upwash between the root vortices without becoming entrained by any coherent transverse vortex structure. This is the case in Fig. 6, which shows a bee flying upwind with the smoke incident near the midline. In Fig. 6a the wings are parallel with one another at the top of the upstroke. The green arrow highlights a pair of smokelines passing to the far side of the right wing pair, which is the brighter of the visible wings; the blue arrow shows a second pair of smokelines passing nearside of the body. This distortion in the vertical alignment of the smoke plane is due to flow induced by the previous wingbeat. In Fig. 6b the right wing pair cuts the upper pair of smokelines (white arrow), which quickly roll up into a well-defined root vortex (Fig. 6c–d, yellow arrow). Crucially, the lower smokeline pair (Fig. 6d, blue arrows) passing nearside close to the tip of the abdomen remains relatively unaffected as it passes the root vortex. In Fig. 6e the same pair of smokelines rises in the upwash (red arrow) between the pair of contralateral vortex loops. Only when they are several chord lengths behind the wings do these same smokelines (red arrows) become visibly disrupted by the root vortices (Fig. 6g). Smokelines passing along the midline of the body are therefore accelerated upwards slightly at the end of the downstroke under the influence of the pair of vortex loops shed by the left and right wings, but in all other respects they pass unperturbed into the wake.

4 Conclusions

The use of a LEV has been observed in free-flying dragonflies (Thomas et al. 2004) and butterflies (Srygley and Thomas 2002), and also in tethered hawkmoths (Bomphrey et al. 2005; Ellington et al. 1996). It has been inferred in free-flying swifts (Videler et al. 2004) and hummingbirds (Warrick et al. 2005), and has been suggested by analogy with mechanical flappers of Chalcid wasps (Maxworthy 1979) and fruit flies (Birch and Dickinson 2001). A catalogue of the variation in LEV topologies observed between and within different species of insect is given in Fig. 7 (adapted from Bomphrey et al. 2005). Bumblebees' small wings are at the limit of what can be resolved with smoke visualizations. As a result, while the near wake flows were

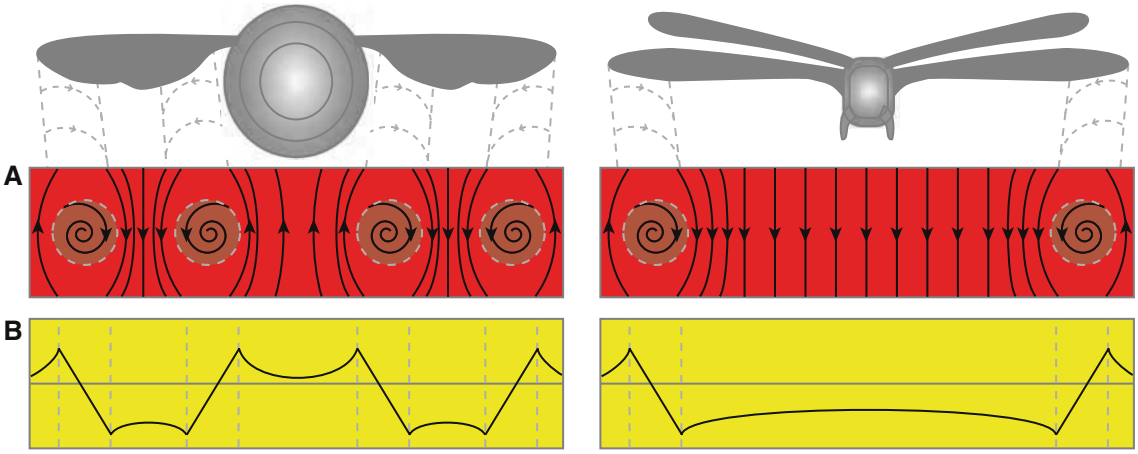

Fig. 8 Cartoon of the flow expected mid downstroke behind a bumblebee (*left*) and measured behind a desert locust (*right*). At the top the insects are depicted flying into the page. *Red boxes* (a) represent a plane aligned vertically behind the trailing edges of the insects' wings and show a 2D slice through the flow with instantaneous streamlines. *Yellow boxes* (b) show the predicted downwash distribution in the same plane behind the two insects—the locust distribution being an idealized profile based on DPIV measurement (Bomphrey et al. 2006b). *Grey dashed lines* represent the edge of the trailing vortex cores

clear, the resolution of the LEV in our flow visualizations is lower than has been achieved, for example, with dragonflies (Thomas et al. 2004). Nevertheless, the density of smoke streams was sufficient to identify the critical features of the flow topology such as bifurcations and attachment points. The bumblebee topologies we have described are shown in Fig. 7d1, d2, where d1 represents the majority of the downstroke and d2 is the topology at the end of the downstroke and beginning of the upstroke. It is apparent that bumblebees are unusual in comparison with other insects which utilize LEVs to generate lift, in that the flow appears to remain attached for the majority of the downstroke, first separating around the time of stroke reversal. This might suggest a role for wing rotation in the formation of the LEV, although we have no information as to whether this separation is the result of the angular velocity of the wing at supination or the concomitant increase in angle of attack (Walker 2002).

The ultimate structure of the bumblebee LEV (Fig. 7d2) bears some resemblance to that of Maxworthy's (1979) flapping machine (Fig. 7a) in that a LEV is present which does not terminate on the wing surface. Nevertheless, the two are distinct in that the root vortices are not linked in the bumblebee as they are in Maxworthy's (1979) flapping machine. Although our data have insufficient temporal resolution to observe transient stages in LEV development, it is quite possible that the LEV topology we have observed in bumblebees (Fig. 7d2) develops from an attached flow topology (Fig. 7d1) via a transient state like that proposed by Ellington et al. (1996) for hawkmoths (Fig. 7c1, and hypothesized in Fig. 1b).

In most other flow visualizations on birds, bats and insects to date, the left and right wing pairs are aerodynamically linked by transverse vortical structures (birds: (Kokshaysky 1979; Spedding 1986; Spedding 1987; Spedding et al. 2003; Videler et al. 2004; Warrick, Tobalske and Powers 2005); bats: (Hedenstrom et al. 2007; Norberg 1976; Swartz et al. 2005); insects: (Bomphrey 2006; Bomphrey et al. 2005, 2006b; Dickinson and Götz 1996; Grodnitsky and Morozov 1993; Lehmann et al. 2005; Maxworthy 1979; Srygley and Thomas 2002; Thomas et al. 2004; Van den Berg and Ellington 1997; Willmott et al. 1997)). In contrast, our bumblebee flow visualizations provide no evidence for such structures linking the left and right wings. The same may be true of other insect species, including crane flies, which have also been shown to generate wing root vortices in addition to the usual wing tip vortices (Brodsky 1994). This must result in a loss of efficiency, because unlike many other insects, bumblebees and crane flies are not using the full span between their wing tips to generate lift, and indeed wastefully accelerate air upwards in the vicinity of the body.

Figure 8 depicts the consequences of root vortices for the downwash distribution. Figure 8a is a cartoon depicting instantaneous streamlines in a vertical plane behind the trailing edges of a bumblebee and a locust. Figure 8b is a cartoon of the corresponding downwash distributions. In the case of the locust, we have made use of quantitative DPIV measurements of the wake to inform the figure (Bomphrey et al. 2006b); in the case of the bumblebee, we have based the expected downwash distribution on a typical velocity profile through two vortex rings. While the diagrams are idealized representations of the true flows, the root vortices which are present in the bumblebee must necessarily make the downwash distribution less even than that behind the locust. Any deviation from the ideal even

downwash distribution is a source of aerodynamic inefficiency, reinforcing our conclusion that the flow topology of bumblebees is aerodynamically inefficient at all stages of the stroke. The general conclusion over the bumblebee's inefficiency is consistent with the conclusions Altshuler et al. (2005) drew for honeybees (*Apis mellifera*). While they did not observe the aerodynamics directly and attributed enhanced lift to wake capture and rapid rotation of the wings, honeybees fill a similar ecological niche and also 'underperform' in terms of efficiency during normal flight by operating with a shallow stroke amplitude.

Why has natural selection tolerated such inefficiency? The aerodynamic independence of left and right wing-pairs in bumblebees might simply result from the biological constraint of having a wide thorax to house the massive flight motor required for their load-carrying foraging style. As a result the wing roots are widely separated in relation to the wing length, and as this ratio increases, this is bound at some point to lead to their independent operation. Alternatively, the aerodynamic independence of the wing pairs might reflect the low and negative advance ratios at which the bees flew in the sequences we have visualized. At such low airspeeds, there may simply be an insufficient flow velocity near the wing base to generate a significant circulation in comparison with that generated further out along the wing. Finally, it is also possible that the independence of left and right wing pairs might enhance control authority and could therefore represent an adaptation for manoeuvring between flowers.

Acknowledgments Research sponsored by BBSRC Studentship 00A1S06405. RJB is a PD Research Fellow at St Anne's College, Oxford. GKT is a Royal Society University Research Fellow and RCUK Academic Fellow. The authors are grateful to the BBC for loaning the Phantom high-speed digital video camera.

References

Altshuler DL, Dickson WB, Vance JT, Roberts SP, Dickinson MH (2005) Short-amplitude high-frequency wing strokes determine the aerodynamics of honeybee flight. PNAS 102:18213–18218

Birch JM, Dickinson MH (2001) Spanwise flow and the attachment of the leading-edge vortex on insect wings. Nature 412:729–733

Bomphrey RJ (2006) Insects in flight: direct visualization and flow measurements. J Bioinsp Biomim 1:S1–S9

Bomphrey RJ, Lawson NJ, Harding NJ, Taylor GK, Thomas ALR (2005) The aerodynamics of *Manduca sexta*: digital particle image velocimetry analysis of the leading-edge vortex. J Exp Biol 208:1079–1094

Bomphrey RJ, Lawson NJ, Taylor GK, Thomas ALR (2006a) Application of digital particle image velocimetry to insect aerodynamics: measurement of the leading-edge vortex and near wake of a Hawkmoth. Exp Fluids 40:546–554

Bomphrey RJ, Taylor GK, Lawson NJ, Thomas ALR (2006b) Digital particle image velocimetry measurements of the downwash distribution of a desert locust *Schistocerca gregaria*. J Roy Soc Interface 3:311–317

Brodsky AK (1994) The evolution of insect flight. Oxford University Press, Oxford

Cimbala JM, Nagib HM, Roshko A (1988) Large structure in the far wakes of two-dimensional bluff bodies. J Fluid Mech 190:265–298

Dabiri JO (2005) On the estimation of swimming and flying forces from wake measurements. J Exp Biol 208:3519–3532

Délery JM (2001) Robert Legendre and Henri Werlé: toward the elucidation of three-dimensional separation. Annu Rev Fluid Mech 33:129–154

Demoll R (1918) Der Flug der Insekten und Vögel, vol. 69. Jena, G Fischer

Demoll R (1919) Zuschriften an die Herausgeber. Der Flug der Insekten und der Vögel. Die Naturwissenschaften 27:480–482

Dickinson MH, Götz KG (1996) The wake dynamics and flight forces of the fruit fly *Drosophila* melanogaster. J Exp Biol 199:2085–2104

Dickinson MH, Lehmann F-O, Sane SP (1999) Wing rotation and the aerodynamic basis of insect flight. Science 284:1954–1960

Dudley R, Ellington CP (1990) Mechanics of forward flight in bumblebees: I. Kinematics and morphology. J Exp Biol 148:19–52

Ellington CP (1984) The aerodynamics of hovering insect flight. III. Kinematics. Phil Trans R Soc Lond B 305:41–78

Ellington CP, van den Berg C, Willmott AP, Thomas ALR (1996) Leading-edge vortices in insect flight. Nature 384:626–630

Grodnitsky DL, Morozov PP (1993) Vortex formation during tethered flight of functionally and morphologically two-winged insects, including evolutionary considerations on insect flight. J Exp Biol 182:11–40

Hedenstrom A, Johansson LC, Wolf M, von Busse R, Winter Y, Spedding GR (2007) Bat flight generates complex aerodynamic tracks. Science 316:894–897

Hoff W (1919) Der Flug der Insekten und der Vögel. Die Naturwissenschaften 10:162–169

Kokshaysky NV (1979) Tracing the wake of a flying bird. Nature 279:146–148

Lehmann FO (2004) The mechanisms of lift enhancement in insect flight. Naturwissenschaften 91:101–122

Lehmann FO, Sane SP, Dickinson M (2005) The aerodynamic effects of wing-wing interaction in flapping insect wings. J Exp Biol 208:3075–3092

Maxworthy T (1979) Experiments on the Weis-Fogh mechanism of lift generation by insects in hovering flight. Part 1. Dynamics of the 'fling'. J Fluid Mech 93:47–63

Noca F, Shiels D, Jeon D (1999) A comparison of methods for evaluating time-dependent fluid dynamic forces on bodies, using only velocity fields and their derivatives. J Fluids Struct 13:551–578

Norberg UM (1976) Aerodynamics, kinematics, and energetics of horizontal flapping flight in the long-eared bat Plecotus auritus. J Exp Biol 65:179–212

Perry AE, Chong MS (1987) A description of eddying motions and flow patterns using critical-point concepts. Annu Rev Fluid Mech 19:125–155

Ramasamy M, Leishman JG (2006) Phase-locked particle image velocimetry measurements of a flapping wing. J Aircraft 43:1867–1875

Sane SP (2003) The aerodynamics of insect flight. J Exp Biol 206:4191–4208

Shyy W, Liu H (2007) Flapping wings and aerodynamic lift: the role of leading-edge vortices. AIAA J 45:2817–2819

Spedding GR (1986) The wake of a jackdaw (Corvus-Monedula) in slow flight. J Exp Biol 125:287–307

Spedding GR (1987) The wake of a kestrel (*Falco tinnunculus*) in flapping flight. J Exp Biol 127:59–78

Spedding GR, Rosen M, Hedenstrom A (2003) A family of vortex wakes generated by a thrush nightingale in free flight in a wind tunnel over its entire natural range of flight speeds. J Exp Biol 206:2313–2344

Srygley RB, Thomas ALR (2002) Unconventional lift-generating mechanisms in free-flying butterflies. Nature 420:660–664

Swartz S, Galvao R, Iriarte-Diaz J, Israeli E, Middleton K, Roemer R, Tian X, Breuer K (2005) Unique characteristics of aerodynamics of bat flight evidence from direct visualization of patterns of airflow in the wakes of naturally flying bats. Int Comp Biol 45:1080

Thomas ALR, Taylor GK, Srygley RB, Nudds RL, Bomphrey RJ (2004) Dragonfly flight: free-flight and tethered flow visualizations reveal a diverse array of unsteady lift-generating mechanisms, controlled primarily via angle of attack. J Exp Biol 207:4299–4323

Van den Berg C, Ellington CP (1997) The vortex wake of a 'hovering' model hawkmoth. Phil Trans R Soc Lond B 352:317–328

Videler JJ, Stamhuis EJ, Povel GDE (2004) Leading-edge vortex lifts swifts. Science 306:1960–1962

Walker JA (2002) Rotational lift: something different or more of the same? J Exp Biol 205:3783–3792

Walker SM, Thomas ALR, Taylor GK (2008) Photogrammetric reconstruction of high-resolution surface topographies and deformable wing kinematics of tethered locusts and free-flying hoverflies. J Roy Soc Interface. doi:10.1098/rsif.2008.0245

Walker SM, Thomas ALR, Taylor GK (2009) Deformable wing kinematics in the desert locust: how and why do camber, twist and topography vary through the stroke? J Roy Soc Interface. doi:10.1098/rsif.2008.0435

Warrick DR, Tobalske BW, Powers DR (2005) Aerodynamics of the hovering hummingbird. Nature 435:1094–1097

Willmott AP, Ellington CP, Thomas ALR (1997) Flow visualization and unsteady aerodynamics in the flight of the hawkmoth, *Manduca sexta*. Phil Trans R Soc Lond B 352:303–316

The influence of airfoil kinematics on the formation of leading-edge vortices in bio-inspired flight

David Rival · Tim Prangemeier · Cameron Tropea

Abstract The formation process of leading-edge vortices has been investigated experimentally using Particle Image Velocimetry. Various airfoil kinematics have been tested, including asymmetric and peak-shifted plunging motions, and are evaluated for $Re = 30{,}000$ and a reduced frequency range of $0.2 \leq k \leq 0.33$. By measuring the growth in the leading-edge vortex during the dynamic-stall process, the vortex pinch-off process is examined based on the concept of an optimal vortex formation time. The various kinematics are then evaluated with respect to their associated vortex strength, timing and convection into the wake.

1 Introduction

Both natural and biomimetic flight occur predominantly at low Reynolds numbers. Mueller and Batill (1982) have shown that performance at these scales is strongly hampered by the separation-prone nature of the laminar boundary layer. Contrary to classical aerodynamics, separation becomes the norm, not the exception. Such a fundamental limitation to the aerodynamics suggests that lift must be generated through unsteady aerodynamic mechanisms such as dynamic stall, as described by McCroskey (1982), where the formation and delayed convection of a leading-edge vortex (LEV) over the downstroke can be very advantageous to lift production. This aerodynamic mechanism with regard to bio-inspired flight has been examined in detail by Ellington (1999). To date it has not yet been conclusively shown that a spanwise flow is an absolute requirement in the stabilization of the LEV. One recent study by Thomas et al. (2004) demonstrated that dragonflies produce large, quasi two-dimensional LEVs over their downstroke in cruise-flight conditions. More abstract investigations into LEV formation have been performed by Panda and Zaman (1994) and Ohmi et al. (1990) for pitching and pitching/plunging airfoils, respectively. Based on these aforementioned investigations and the inspiration from natural flight, an examination into the LEV formation process for low reduced frequencies ($0.2 \leq k \leq 0.33$) and for the quasi two-dimensional case has been performed. One major objective of this study is to better understand to what extent, if at all, the LEV can be stabilized without the help of spanwise flow.

2 Background

2.1 History effects

The reduced frequency in this study is defined in the following manner:

$$k = \frac{\pi f c}{U_\infty}, \tag{1}$$

where f is the plunging frequency, c the airfoil chord and U_∞ the freestream velocity. Thus for the value of $k = 0.25$ used in this study, a particle of fluid moving at U_∞ would convect $x/c \approx 12.5$ over one full period of the plunging motion. Panda and Zaman (1994) have shown that the actual convection speed (u_{conv}) of shed vortices varies between

D. Rival (✉) · T. Prangemeier · C. Tropea
Institute of Fluid Mechanics and Aerodynamics,
Technische Universität Darmstadt, Darmstadt, Germany
e-mail: rival@aero.tu-darmstadt.de

G.K. Taylor, M.S. Triantafyllou, and C. Tropea (Eds.): Animal Locomotion, pp. 261–271.
springerlink.com

$$0.6 < \frac{u_{\text{conv}}}{U_\infty} < 0.8 \tag{2}$$

in the vicinity of the airfoil, largely dependent on the position, size and strength of the vortex. These vortices then rapidly accelerate to the freestream velocity in the immediate wake. Therefore one can infer that a LEV shed at the bottom of the plunge stroke would travel $x/c \approx 6.25$ in the time that the airfoil would require to return back to the top of the stroke. This relatively large spacing between the LEVs suggests that the history effects in the dynamic-stall process are not strongly influenced by the previous cycle's shed vortices in the wake. Rather the history effects are expected to be more strongly influenced by the slow time scales associated with boundary-layer separation and reattachment present in the dynamic-stall process itself. In other words the state of the boundary-layer at the top of the stroke, just before the LEV formation process begins, should play a much larger role than the LEV shed from the previous cycle. A further discussion on these history effects is treated in Sect. 4.2. Measurement and comparison of these history effects are then presented in Sect. 5.2.

2.2 Optimal vortex formation

The dimensionless vortex formation time $\hat{T}$, often referred to as simply the formation time, is a measure of the state of development of a vortex. A forthcoming review paper from Dabiri (2009) suggests a level of universality among all unsteady vortical flows through the concept of an optimal vortex formation number, where the vortex stops entraining fluid from the shear layer and pinches off at a value of $\hat{T} \approx 4$. The formation time is defined in its general form in the following manner:

$$\hat{T} = \frac{C\Gamma}{D\Delta U}, \tag{3}$$

where C is a constant factor depending on the physical configuration of the vortex generator, Γ is the instantaneous vortex strength, D the characteristic length scale and ΔU the shear-layer feeding velocity. For the specific case of a two-dimensional plunging airfoil with only one LEV shed per cycle, the vortex generator constant has been set to $C = 1$ and the limiting length scale of the forming vortex set as $D = 2c$. The shear-layer feeding velocity was approximated by $\Delta U = 2\pi f h_o$, being the maximum plunge velocity of the airfoil leading edge over the downstroke. Milano and Gharib (2005) showed that maximum lift on a pitching and plunging plate was generated when $\hat{T} \approx 4$, such that the LEV would pinch off just at the end of the half stroke. A follow-up study using a translating low-aspect-ratio plate with a start-up motion was performed by Ringuette et al. (2007) to better understand the impact of the tip vortex in the start-up process. Again the LEV was found to pinch off at around $\hat{T} \approx 4$. This universal behavior in the formation of the LEV is a focus of this investigation, with close attention being given to the influence of the airfoil kinematics on this pinch-off process.

3 Experimental setup

The airfoil used in this study is the asymmetric SD7003 profile developed for transitional Reynolds numbers. The profile has a maximum thickness of approximately $0.09c$ and is rotated about the $x = c/4$ position. An attractive feature of the SD7003 profile is the substantial experimental database available in the open literature for the steady case provided in Selig et al. (1995) and Ol et al. (2005) as well as the unsteady case found in Nerger et al. (2003) and Lian et al. (2008).

The experimental rig consists of a base structure, a set of linear-motors connected with each other via a linkage system and a carbon-fibre SD7003 wall-spanning profile weighing 306 g. The profile has a chord length of 120 mm and a span of 450 mm. The profile-tip spacing at the walls is less than 2 mm on either side. Maximum static blockage in the test-section based on the frontal area was under 3%. The tunnel itself has a contraction ratio of 24:1 with five turbulence filters in the settling chamber, thus producing turbulence levels under 0.5% at these low tunnel speeds. A schematic of the test rig integrated into the Eiffel-type wind tunnel test-section at the Institute of Fluid Mechanics and Aerodynamics (TU Darmstadt) is shown in Fig. 1. The various components of the Particle Image Velocimetry (PIV) system are also included in the schematic.

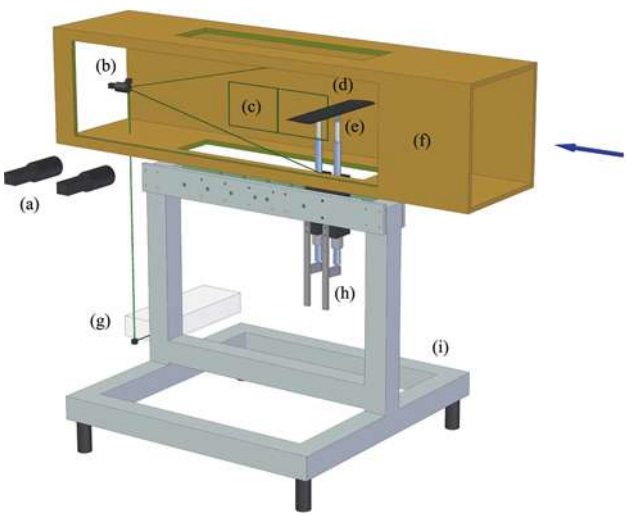

Fig. 1 Experimental setup in wind tunnel with flow direction from right-to-left: **a** CCD cameras, **b** beam expander, **c** PIV image frames, **d** wall-spanning carbon-fibre profile, **e** embedded piezo-electric force sensors, **f** test-section, **g** laser head, **h** linear motors with linkage system and **i** base structure

For the direct-force measurements a pair of one-component Kistler 9217A piezo-electric force sensors are integrated directly below the profile, one at the quarter-chord position (point of rotation) and one at the trailing edge. Together, the two sensors can measure both the profile's inertial and aerodynamic forces during the prescribed movement. The total static tare weight of the system (profile and linkage combined) totals 394 g. The analog output-charge signals from the two piezo-electric force sensors are sent through the wind-tunnel floor to a Kistler 5073A411 charge amplifier, which in turn converts the signals into an analog voltage. These voltage signals were subsequently fed into a 16-bit National Instruments 6259 A/D board. The signals are finally run through a 10 Hz low-pass filter in LabView 8.2 and are then further post-processed using MatLab 7.3.

A commercial PIV system was used in this study (Dantec Dynamics A/S) and consisted of a Nd:YAG ($\lambda = 532$ nm) Litron dual-cavity laser with a maximum power output of 135 mJ per cavity and two 10-bit FlowSense 2M CCD cameras each with a 1,600 × 1,200 pix resolution. Due to the large imaging field required, 60 mm *f*/2.8 Nikkor lenses were used. In order to reduce reflections, the profile was painted mat-black and monochromatic filters, with a corresponding wavelength of $\lambda = 532$ nm, were installed on the lenses. The laser beam was directed over three mirrors into the test-section and expanded into a sheet approximately 2 mm in thickness. This laser sheet was set parallel to the flow direction and aligned onto the airfoil quarter-span position. Due to the large imaging area of 0.0864 m^2 the laser power was set to 90% for both cavities. With the use of compressed air driven through four Laskin nozzles, DEHS seeding particles less than 1 μm in diameter were introduced into the settling chamber using a vertical rake aligned with the measurement plane.

PIV image pairs were sampled at 15 Hz allowing for 6 phases to be recorded per cycle at $k = 0.25$. In order to construct the ensemble velocity fields of 12 phases per cycle, two staggered sets with 100 images per phase were ensemble-averaged. In all cases, the first two starting cycles were removed from all ensembles. Each camera imaged a field corresponding to $x/c = 2$ and $y/c = 1.5$, with a resolution of 800 pix/*c* (6.7 pix/mm). Reflections on the model surface were strongest at the bottom of the stroke where a region 0.04*c* normal to the airfoil surface were deemed to be unreliable. Shadows and strong reflections on the pressure (lower) side required masking. Parallax effects were strongest at the top of the stroke and at this position were responsible for hiding a region 0.03*c* normal to the airfoil surface. The vector fields were calculated using an adaptive correlation with 32 × 32 pix interrogation windows and a 50% overlap. A 3 × 3 filter was used to lightly smooth the vector fields in order to more clearly define the vortical structures in the wake. The accuracy of the vector fields was estimated to lie within 2% for all cases.

Table 1 Characteristics of various test cases

Name	$f_{(downstroke)}$ (Hz)	$f_{(upstroke)}$ (Hz)	α_{eff_max} (°)	t/T (α_{eff_max})
Sinusoidal	2.5	2.5	22.1	0.25
Asymmetric	3.3	2.0	26.5	0.19
Peak-shifted	2.5	2.5	24.2	0.33
Fast-sinusoidal	3.3	3.3	26.5	0.25

4 Parameter space

4.1 Kinematics

In order to understand the effect of the airfoil kinematics on the development of the LEV, three simple and distinct

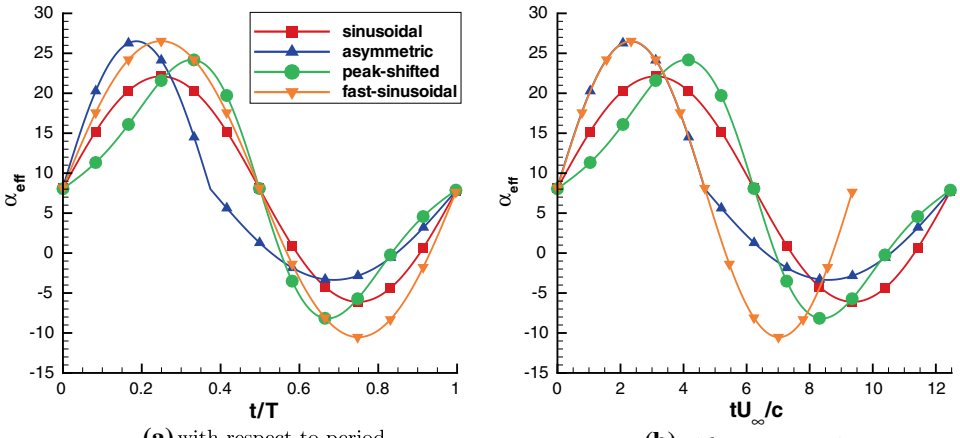

(a) with respect to period **(b)** with respect to time

Fig. 2 Effective angle-of-attack distribution for the four test cases as a function of **a** period and **b** dimensionless time; note *symbols* represent 12 measurement phases over the period

plunging motions with a constant geometric angle of attack of $\alpha_o = 8°$ and $k = 0.25$ (based on the full cycle) were selected. This incidence and frequency were chosen since they produced a well-defined LEV-TEV pair over the downstroke, as described in Rival and Tropea (2009). Once in the wake, this vortex pair has been referred to as a *mushroom-wake* structure by Panda and Zaman (1994) due to its mushroom-head shape. The plunge position (h) of the *sinusoidal* (reference) and *asymmetric* cases is based on a simple harmonic motion:

$$h(t) = h_o \cos(2\pi ft), \tag{4}$$

whereby the latter case consists of a concatenation of a fast downstroke and a slow upstroke. The *peak-shifted* case refers to a motion where the maximum plunge velocity ($\dot{h}$) and therefore the effective angle of attack (α_{eff}) occur late in the downstroke:

$$h(t) = a_1 h_o \cos\left(a_2 \sin(\pi ft) + \frac{\pi}{2}\right) - a_3, \tag{5}$$

where a_1 and a_3 are coefficients used to normalize the amplitude of the motion and $a_2 = 0.81$ is used to set the peak velocity at $t/T = 0.33$. A fourth case with $k = 0.33$ and a sinusoidal motion corresponding to the *asymmetric* downstroke was performed to access the impact of the history effects from the previous cycle. This case is referred to as the *fast-sinusoidal* case and also maintained a constant geometric angle of attack of $\alpha_o = 8°$. All cases shared a relatively large plunge amplitude of $h_o = 0.5c$. For a detailed description of the various test cases see Table 1. In Fig. 2, the variations of α_{eff} over the cycle and as a function of dimensionless time are presented for sake of clarity.

4.2 Circulatory and non-circulatory decomposition

Despite the constraints of a fully-attached flow, a planar wake and the fulfillment of the Kutta condition in classic unsteady aerodynamic theory, developed independently by Theodorsen (1935) and Kuessner (1936), such traditional models can nevertheless be useful in the estimation of the maximum attainable lift in the dynamic-stall process. At these reduced frequencies the LEV formation process is associated with a closed separation and a planar wake, and thus the basic constraints of such theoretical models are not violated. The following equation from Theodorsen decomposes the lift variation based on the assumption of superposition of the non-circulatory (added-mass) and circulatory components:

$$C_l = \frac{\pi c}{2}\left(\frac{\dot{\alpha}}{U_\infty} + \frac{\ddot{h}}{U_\infty} + \frac{c}{4}\frac{\ddot{\alpha}}{U_\infty^2}\right) + 2\pi C(k)\left(\alpha + \frac{\dot{h}}{U_\infty} + \frac{c}{2}\frac{\dot{\alpha}}{U_\infty}\right), \tag{6}$$

where a complex-valued transfer function referred to as Theodorsen's function $C(k)$ is placed in front of the circulatory component to account for the influence of the shed vorticity in the wake. All terms associated with pitching, i.e. α, $\dot{\alpha}$ and $\ddot{\alpha}$ are based on a rotation about the $c/4$ position. For the case of a pure-plunging airfoil, these pitching terms vanish leaving:

$$C_l = \frac{\pi c}{2}\frac{\ddot{h}}{U_\infty} + 2\pi C(k)\frac{\dot{h}}{U_\infty}. \tag{7}$$

In Fig. 3, the various contributions to the total lift as a function of cycle period and effective angle of attack are plotted for the reference sinusoidal case. Included in these plots are the quasi-steady curves ($2\pi\alpha$) as well as the static lift measurements from the experiment. A maximum lift of approximately $C_l \approx 1.9$ based on Theodorsen's model would be theoretically attainable if the dynamic stall process could be sustained long enough over the downstroke, i.e. the LEV would be shed at the bottom of the stroke. This is likely a reasonable estimate since it takes into consideration the negative influence of the shed

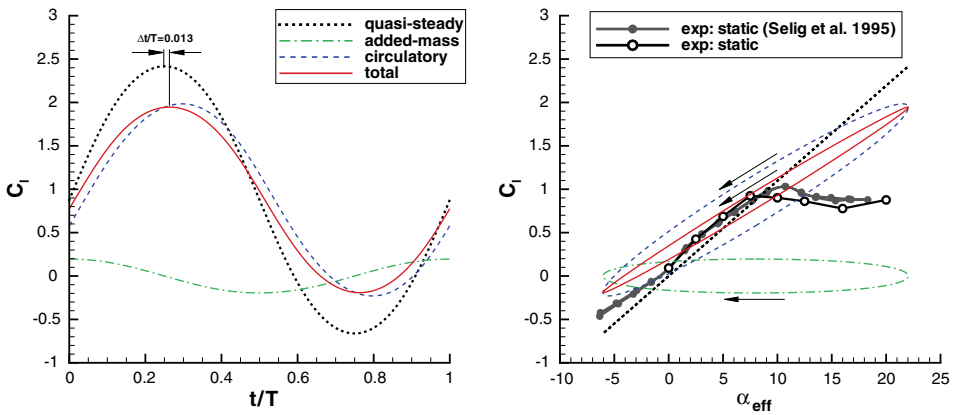

Fig. 3 Contributions of the non-circulatory (added-mass) and circulatory components to the total lift of the sinusoidal reference case based on classical theory developed by Theodorsen (1935)

(a) with respect to period

(b) with respect to effective angle of attack

vorticity at the trailing edge (circulatory component) during the climb to the lift peak. From Fig. 3a, one can infer a time lag between the peak of the quasi-steady lift and the peak predicted from Theodorsen theory of $t/T = 0.013$, corresponding to a phase lag of $\varphi = 4.7°$. At higher reduced frequencies the added-mass contribution grows, further canceling out the aerodynamic lag imposed by the circulatory contribution. However, with the onset of a fully-stalled flow after peak lift (dynamic stall), the lift variation is found to lag dramatically behind with values as high as $\varphi = 90°$, where the relatively slow viscous time scales of the boundary-layer separation and reattachment dominate the history effects from one period to the next. This phenomenon has been clearly demonstrated using force measurements at lower reduced frequencies of $0.05 \leq k \leq 0.1$, as described in Rival and Tropea (2009).

Therefore, it becomes clear that Theodorsen's circulatory approach, which assumes attached flow, is not appropriate to predict the lift variation beyond the dynamic-stall process once the airfoil is fully stalled. However, there is no immediate reason to discount the insight provided by the non-circulatory contribution. In order to test its validity, a set of so-called *added-mass* measurements were performed. In order to measure this non-circulatory component, a dummy aluminum cylinder (shown in Fig. 4), 12 mm in diameter and identical to the SD7003 profile in mass and spanwise distribution, was constructed and mounted at the airfoil center-of-mass position in the wind tunnel test-section. With the wind tunnel turned off, sinusoidal plunge motions at various mean angles of attack were measured, both for the profile and the dummy airfoil (cylinder). The measurements were based on an ensemble of 35 cycles, sampled at 1 kHz, where the first four cycles as well as the last cycle were cut away in order to remove starting and stopping effects. By taking the difference between the airfoil and cylinder force measurements, the so-called added-mass contribution could be obtained.

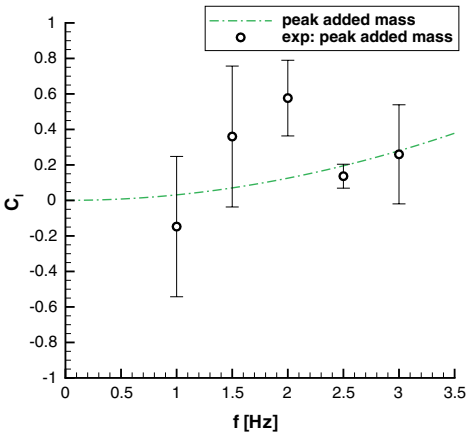

Fig. 5 Comparison of peak theoretical and measured added-mass contributions; theoretical values derived from Theodorson (1935)

In Fig. 5, the peak experimental added-mass contribution is compared with the prediction from Theodorsen's non-circulatory theory for cases of sinusoidal plunging. Despite the large variation associated with the measurements, the discrepancy between experiment and theory is pronounced, particularly at a plunge frequency of 2 Hz. When examining the flow field for such cases, clearly defined vortical structures are shed from both leading and trailing edges, as shown in the visualization of Fig. 6. These vortices, analogous to the structures found by Ringuette et al. (2007), in turn induce strong forces on the airfoil, which cannot be accounted for with Theodorson's inviscid theory.

Based on this result, it becomes clear that direct force measurements of such unsteady aerodynamic cases are limited in their accuracy since the separation of the circulatory and non-circulatory components from the inertial

Fig. 4 SD7003 carbon-fibre profile and dummy cylinder shown for comparison; note cylinder identical to profile in mass (±0.5 g) and spanwise distribution

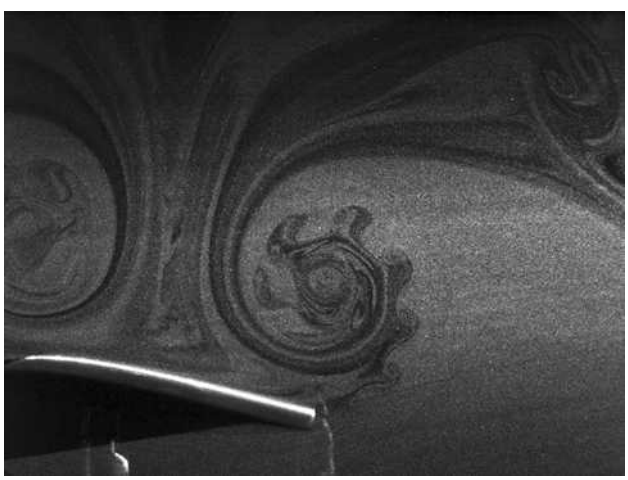

Fig. 6 Visualization depicting strong leading- and trailing-edge separation at bottom of stroke during a dynamic-tare measurement

component during the dynamic-tare cannot be performed. To confound the measurements even further, the inertial forces grow rapidly with f^2 such that at $k = 0.25$ they are approximately an order-of-magnitude larger than the aerodynamic forces, thus further deteriorating the accuracy of the measurements. In fact, for this range of reduced frequencies, the measurement error grows inversely proportional with $k^2 \propto (f/U_\infty)^2$ since the aerodynamic and inertial forces are proportional to U_∞^2 and f^2, respectively. Therefore in this investigation accurate direct force measurements were not possible. Rather the authors concentrated on PIV measurements to better understand the LEV formation process. These results will be presented in the following section.

5 Results

5.1 Reference (sinusoidal) case

Pure-plunging motions were selected for this study since the effective angle of attack distributions for such cases remain constant over the airfoil chord. This is possible since the introduction of relative leading- and trailing-edge velocities based on rotation (known as the dynamic-cambering effect) have been avoided. In Fig. 7, plots of dimensionless vorticity for 12 individual phases over the cycle are shown, where $t/T = 0$ corresponds to the top of the stroke. One can identify the clear evolution of the LEV over the downstroke, with first signs of a LEV at $t/T = 0.167$. The LEV subsequently grows in size and strength culminating in a large vortex on the order of the airfoil chord at $t/T = 0.333$. Only after this point does the separation open and vortex pinch-off occur. During the LEV formation process lift continuously increases beyond the peak static-stall value, as described in McCroskey (1982), and thus nearly continuous counter-clockwise vorticity, defined in this study as being negative, is shed from the trailing edge. This feature can be explained through Kelvin's law:

$$\frac{D\Gamma}{Dt} = 0, \tag{8}$$

such that the flux of counter-clockwise (negative) vorticity convected from the airfoil trailing edge is equal to the rate at which circulation of the leading-edge vortex grows with time:

$$\frac{D\Gamma_{\mathrm{LEV}}}{Dt} = u_{\mathrm{conv}} \int_s \omega_z \mathrm{d}s, \tag{9}$$

where s is a control surface placed normal to the freestream direction at the trailing edge. Just before the airfoil reaches the bottom of the stroke at $t/T = 0.417$, the strong counter-rotating vorticity shed at the trailing edge begins to roll-up into a trailing-edge vortex (TEV) due to the apparent interaction with the LEV passing overhead. This TEV grows very rapidly in strength and cuts apart the original LEV from the separated region above the airfoil, distinctly seen at the bottom of the stroke ($t/T = 0.5$). Thereafter the vortex pair (mushroom structure) convect rapidly downstream and the flow reattaches over the airfoil, moving from the leading edge back towards the trailing edge. By the time the airfoil reaches the middle of the upstroke ($t/T = 0.75$), the flow is again fully attached and a shear layer characteristic of static conditions is emitted from the trailing edge. As the airfoil approaches the top of the stroke a clear and repeatable instability is found in the wake such that even after 100 cycles of averaging the approximate alternating vortex position is the same, suggesting that the onset of this instability is forced by the motion and is not merely stochastic.

5.2 Effect of kinematics on LEV formation

When examining the effective angle-of-attack distribution for the various cases in Fig. 2, one can observe that the asymmetric and fast-sinusoidal cases pass through the static-stall angle at a much steeper rate when compared to the sinusoidal and peak-shifted cases. This has the effect of strengthening the shear layer feeding the LEV earlier on in the downstroke. Conversely for the peak-shifted case, the feeding only reaches its full strength in the second half of the downstroke. This variation is clearly visible when comparing the development of the LEV over the downstroke at $t/T = 0.25$ ($t/T = 0.333$ for the fast-sinusoidal case) as shown in Fig. 8.

When comparing Fig. 8b, d, one finds that the LEVs are nearly identical, albeit the asymmetric case has a more concentrated and symmetric core. The strength and shape of the planar wake are also very similar. The cause for difference between the two cases lies in the history effects, i.e. the state of the boundary layer and the surrounding flowfield at the beginning of the downstroke. At this phase ($t/T = 0$), the flow has relaxed to a quasi-steady condition for the asymmetric case since the upstroke is relatively slow ($f = 2$ Hz), whereas for the fast-sinusoidal case the boundary-layer is locally separated and the shear layer is much thicker. The comparison of the starting conditions ($t/T = 0$) in the LEV formation process for these two cases is shown in Fig. 9.

5.3 Effect of kinematics on wake formation

At a later stage in the cycle corresponding to $t/T = 0.5$, when the sinusoidal and peak-shifted cases are at the bottom of the stroke ($t/T = 0.667$ for the fast-sinusoidal case),

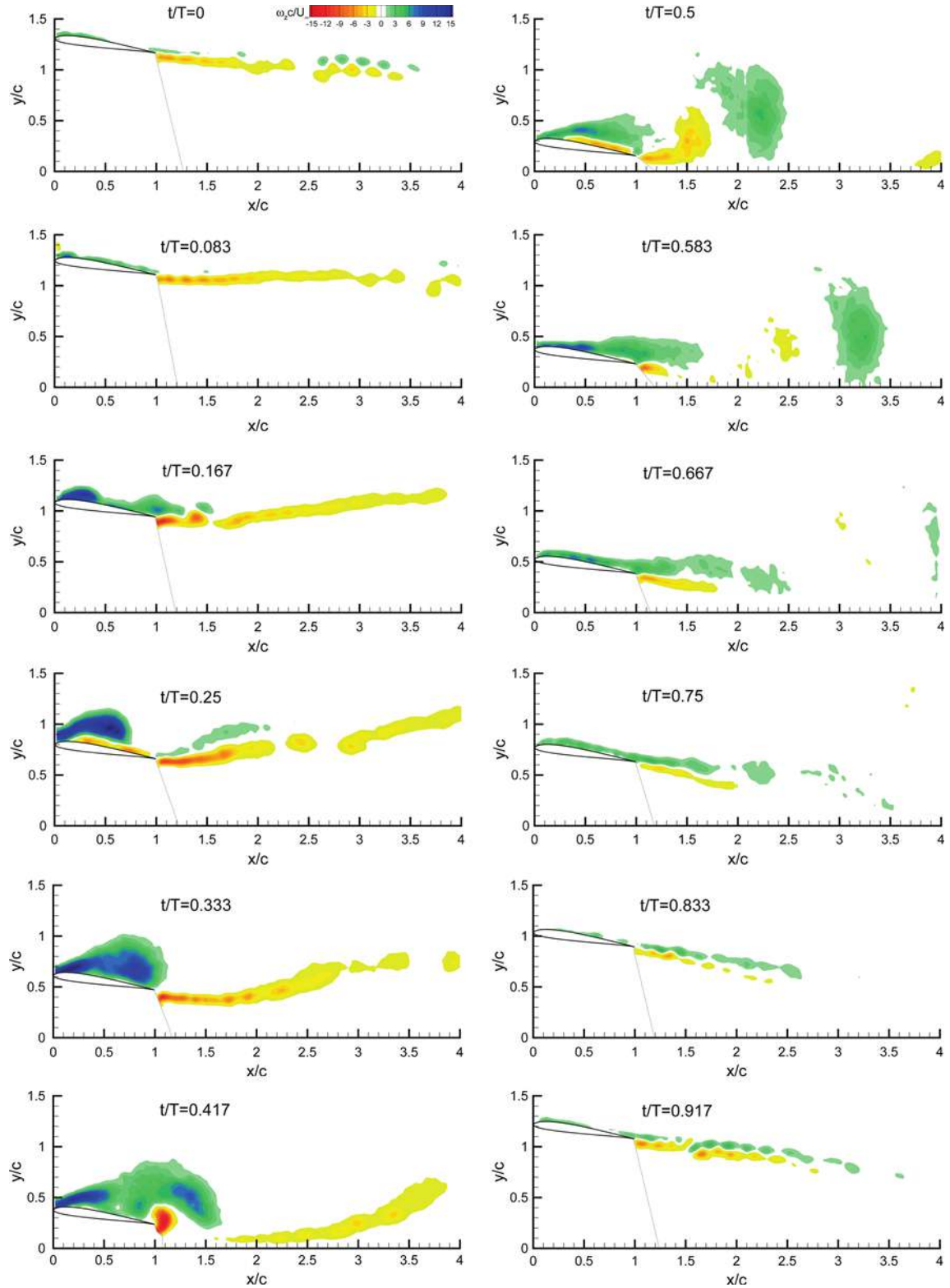

Fig. 7 Plots of dimensionless vorticity for the reference case, a sinusoidal plunging motion with a mean angle of attack of $\alpha_o = 8°$; note masking under airfoil necessary due to reflections and shadow effects

the LEV–TEV vortex pair has now begun its convection downstream. The comparison of the vortex positioning amongst the various cases is shown in Fig. 10. Again it is found that those cases with an earlier LEV formation onset time, associated with a steeper rise in the effective angle of attack slope, are also more advanced in the wake. This

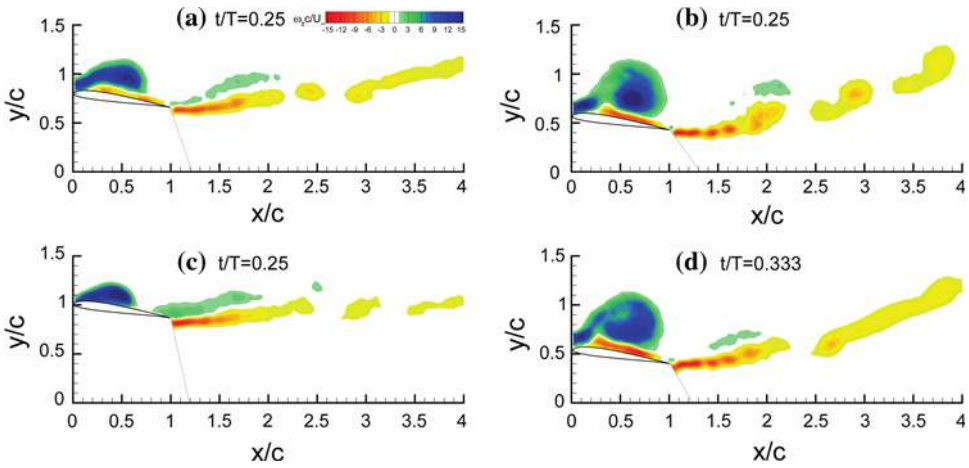

Fig. 8 Plots of dimensionless vorticity during the downstroke ($t/T = 0.25$) for **a** sinusoidal, **b** asymmetric, **c** peak-shifted and **d** fast-sinusoidal cases; note $t/T = 0.333$ used for fast-sinusoidal case to compare equivalent LEV development time

suggests that the time from onset of formation to pinch-off does not vary dramatically amongst the various cases. For the two analogous cases (Fig. 10b, d) the difference in the wakes varies very little; in both cases, the LEVs are stretched vertically and the TEVs are broken up. The peak-shifted case (Fig. 10c), as before, is much younger in its development such that the TEV has yet to pinch-off from the trailing edge. In fact, the flow at this instant shares a resemblance with the sinusoidal case but at an earlier time step ($t/T = 0.417$), as shown in Fig. 7. Thus one can infer that the timing as well as the rate at which the given motion crosses the static-stall angle is of primary importance in the LEV formation process. However, the specific kinematics after the onset of LEV roll-up impact the relative timing of the pinch-off process and will be examined in the following section.

5.4 Vortex growth and pinch-off

By tracking the development of both the LEV and TEV in each frame and extracting the respective vortex circulation from the local vorticity field using Stokes' theorem:

$$\Gamma = \iint_A \omega_z \mathrm{d}A, \tag{10}$$

where the rectangular area A was selected in each time step to encompass the vortex of interest, the dimensionless circulation of both the LEV and TEV at each phase in the cycle could be determined.

In Fig. 11, the growth and decay periods of the respective LEVs and TEVs are shown for all four motions. The maximum circulation of the LEV associated with the last time step before vortex pinch-off and maximum lift augmentation is found to occur at $t/T = 0.333$ for the sinusoidal and asymmetric motions, whereas it occurs later for the peak-shifted and fast-sinusoidal motions at $t/T = 0.417$. When comparing this result to the position of maximum effective angle of attack in Fig. 2a one can infer that a peak-circulation lag ranging between approximately $30° \leq \varphi \leq 60°$ is present in all cases, where the fast-sinusoidal motion exhibits both the largest value of circulation and delay, as would be expected. Of significance is the occurrence in all cases of pinch-off before the airfoil reaches the bottom of the stroke at $t/T = 0.5$. However, both the asymmetric and corresponding fast-sinusoidal cases, and even more noticeably the peak-shifted case demonstrate a later pinch-off and thus superior performance when compared to the reference sinusoidal motion.

When comparing the LEV timing and growth rate for the various motions as a function of dimensionless time in Fig. 11b, one finds that the asymmetric and analogous fast-sinusoidal curves are nearly identical, albeit the fast-sinusoidal motion achieves a slightly higher peak value. This again strengthens the argument that history effects do not play a dominant role in the LEV formation process. Similarly, the sinusoidal and peak-shifted cases share nearly identical LEV onset and growth periods. However, the peak-shifted case, with its maximum feeding velocity

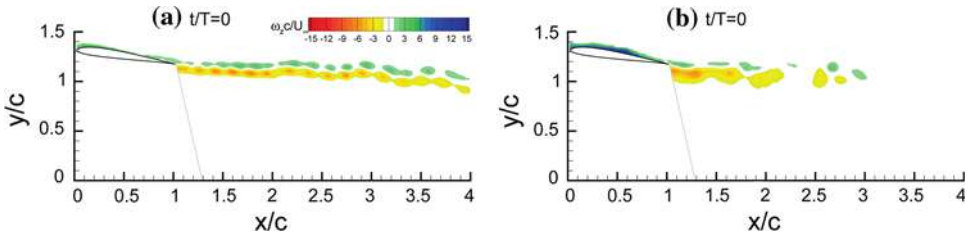

Fig. 9 Plots of dimensionless vorticity at top of stroke ($t/T = 0$) for **a** asymmetric and **b** fast-sinusoidal cases, demonstrating the importance of the history effects just before the LEV formation process begins

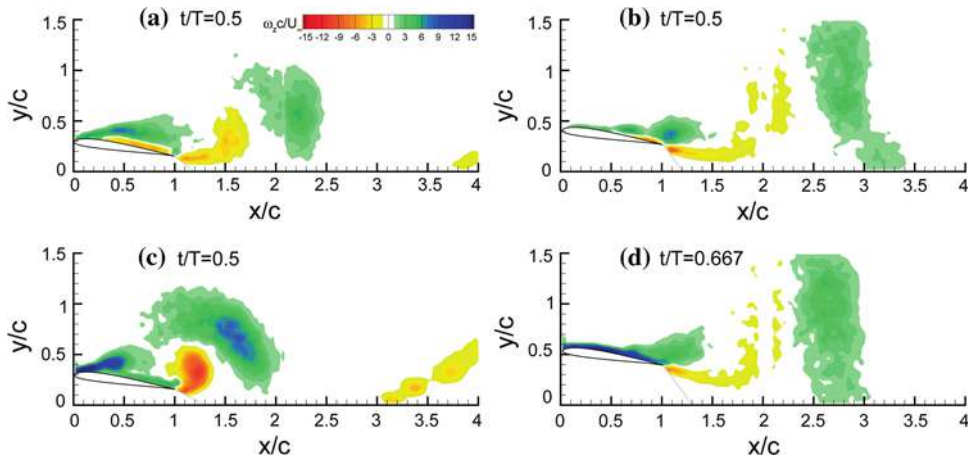

Fig. 10 Plots of dimensionless vorticity around bottom of stroke ($t/T = 0.5$) for **a** sinusoidal, **b** asymmetric, **c** peak-shifted and **d** fast-sinusoidal cases; note $t/T = 0.667$ used for fast-sinusoidal case to compare equivalent convection times of LEV and TEV in wake

occurring only later on in the downstroke, sustains LEV growth long after the sinusoidal motion's LEV has pinched-off. This is a dramatic result despite a relatively small increase in peak plunge velocity and energy expenditure.

In all cases, the TEV is found to form only once the corresponding LEV has reached its maximum strength and begins convecting downstream. In turn, the TEV rapidly loses strength in the wake due to interaction with the LEV. Again referring to Fig. 11b, one can identify that for the reference sinusoidal case the TEV forms relatively late and is weakest among the four motions. This effect can be substantiated through Kelvin's law (Eq. 8).

Based on the discussion in Sect. 2.2 regarding optimal vortex formation, the LEV and TEV formation times for the various test cases are presented in Fig. 12. When examining the peak formation time, known as the formation number, one can infer that all values reduce into a range of $4.4 < \hat{T} < 5.0$, agreeing well with the concept of an optimal vortex formation time presented by Dabiri (2009). This result suggests that in order to shed the LEV even later, i.e. at the bottom of the stroke, in order take full advantage of the dynamic-stall process, a more gradual feeding of the LEV would be necessary. This effect has been clearly demonstrated with the peak-shifted motion. However, the authors believe an additional pitching motion would be desirable late in the stroke to delay the pinch-off process even further.

5.5 Vortex convection

To complete the discussion, a study of the relative vortex positioning and convective velocity has been performed. The vortex trajectories were obtained by tracking the concentrated core whereas the convective velocities were based on a simple linear interpolation of the vortex positions with time. Shown in Figs. 13 and 14 are the respective vortex trajectories and convective velocities for both the LEVs and TEVs. In the case of the relative LEV

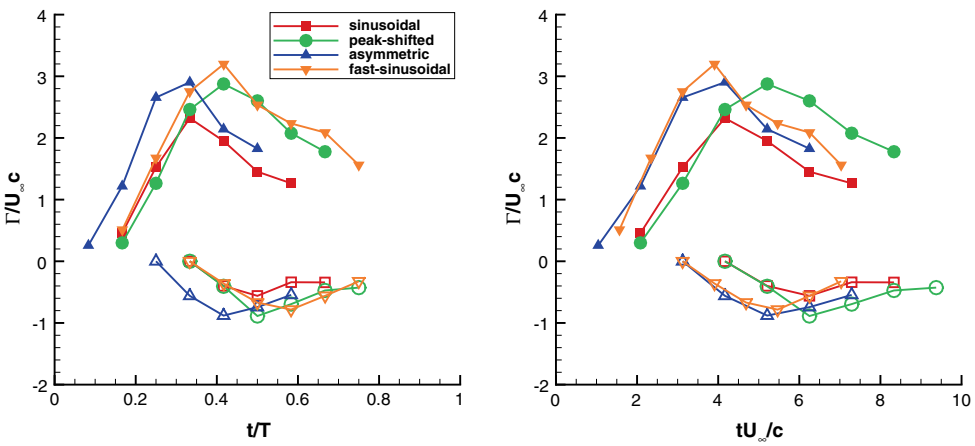

Fig. 11 Development of LEV and TEV circulation as a function of **a** period and **b** dimensionless time; note *solid* and *hollow symbols* represent LEVs and TEVs, respectively

(a) as a function of period **(b)** as a function of time

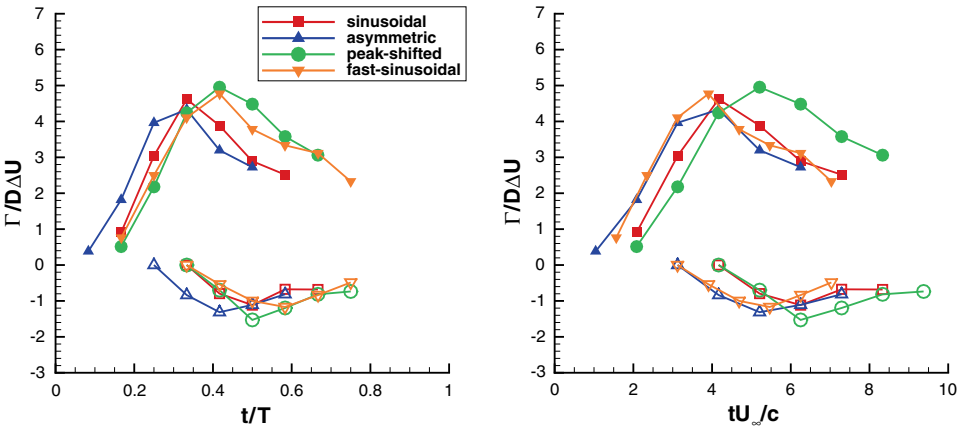

Fig. 12 Formation time as a function of **a** period and **b** dimensionless time; note *solid* and *hollow symbols* represent LEVs and TEVs, respectively

(a) as a function of period **(b)** as a function of time

position, as expected it follows the airfoil surface during the formation process. Once pinch-off takes place and the LEV convects into the wake, the vortex tends to follow a horizontal trajectory. The exception to this rule is found in the fast-sinusoidal case where the LEV shoots upwards and then later drifts back down. The corresponding TEV positions tend to curve slightly upwards for all cases due to the mutual induction of the vortex pair. The most drastic upwards movement corresponds to the TEV from the sinusoidal motion. In all cases, there exists a strong correlation between the LEV and TEV positions.

When examining the corresponding axial convection velocities, the LEV core is found to convect very slowly during the formation process but then accelerate rapidly once emitted into the wake. In fact a clear asymptotic behavior towards $u_{\mathrm{conv}}/U_\infty = 1$ is visible in Fig. 14a. This result agrees well with the measurements made by Panda and Zaman (1994) for LEVs in the wake of a pitching airfoil. Again the fast-sinusoidal case shows exceptional variation in the wake attributed to the strong interaction with the TEV. For the TEV convection velocities shown in Fig. 14b, again a clear asymptotic behavior is visible, whereby the TEV for the sinusoidal motion breaks-up rapidly as can be seen in Fig. 7 between time steps $t/T = 0.583$ and $t/T = 0.667$. Despite this outlier, it can be generalized that all vortex convection velocities approach the freestream velocity asymptotically within two chord-lengths of the trailing edge.

6 Conclusions

An investigation into the formation of LEVs for various plunging kinematics has been performed using PIV. First, a discussion on the decomposition of aerodynamic loads into circulatory and non-circulatory components is treated and compared with dynamic tares in the wind tunnel. This section demonstrates the limitations associated with the separation of inertial and aerodynamic forces through the dynamic-tare method. Subsequently the evolution of the LEV for a reference (sinusoidal) motion is examined in detail. When compared to this reference case, asymmetric and peak-shifted motions are found to impact the onset and growth in the LEV formation process. Most promising was the delayed growth and pinch-off for the peak-shifted case where the LEV convected from the airfoil just before the bottom of the stroke. When examining the growth in circulation during the LEV formation process, it was found

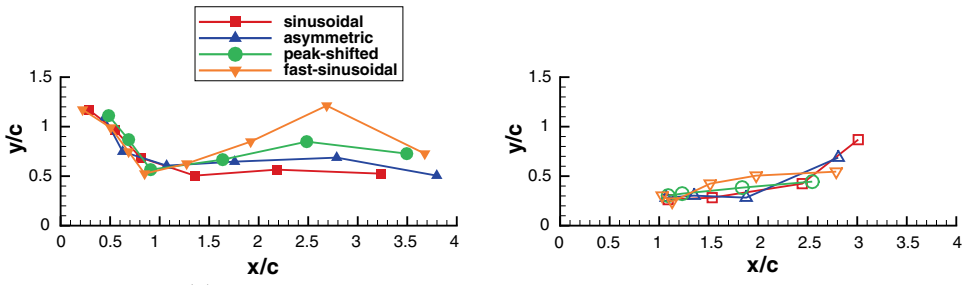

Fig. 13 Trajectories of LEV and TEV cores for the four test cases

(a) LEV position **(b)** TEV position

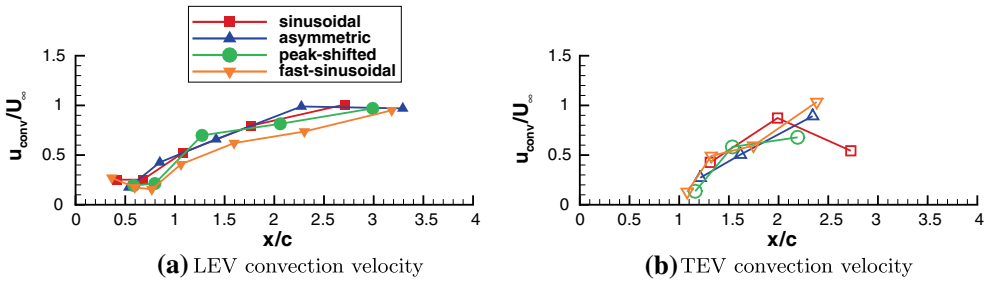

Fig. 14 Convection velocities of LEV and TEV cores for the four test cases: **a** LEV convection velocity, **b** TEV convection velocity

that all motions exhibited vortex pinch-off within $4.4 < \hat{T} < 5.0$, agreeing well with the concept of optimal vortex formation. This suggests that by carefully tuning the airfoil kinematics, thus gradually feeding the LEV over the downstroke, it is to some extent possible to stabilize the LEV without the necessity of a spanwise flow.

Acknowledgments The authors would like to thank Dr. Michael Ol from Wright-Patterson AFB for the fruitful discussions regarding Theodorsen's theory. This research was supported by the Deutsche Forschungsgemeinschaft (DFG) within the national priority program entitled *Nature-Inspired Fluid Mechanics* (SPP1207).

References

Dabiri JO (2009) Optimal vortex formation as a unifying principle in biological propulsion. Ann Rev Fluid Mech (online) 41:17–33

Ellington CP (1999) The novel aerodynamics of insect flight: applications to micro-air vehicles. J Exp Biol 202:3439–3448

Kuessner HG (1936) Zusammenfassender bericht ueber den instationaeren auftrieb von fluegeln. Luftfahrtforschung 13:410–424

Lian Y, Ol MV, Shyy W (2008) Comparative study of pitch-plunge airfoil aerodynamics at transitional reynolds number. 46th AIAA aerospace sciences meeting and exhibit, AIAA-2008-652-812, Reno, USA

McCroskey WJ (1982) Unsteady airfoils. Ann Rev Fluid Mech 14:285–311

Milano M, Gharib M (2005) Uncovering the physics of flapping flat plates with artificial evolution. J Fluid Mech 534:403–409

Mueller TJ, Batill SM (1982) Experimental studies of separation on a two-dimensional airfoil at low reynolds numbers. AIAA Journal 20 No. 4:457–463

Nerger D, Kaehler CJ, Radespiel R (2003) Zeitaufgeloeste piv-messungen an einem schwingenden sd7003-profil bei re=60000. 11 GALA Fachtagung, Braunschweig, Germany

Ohmi K, Coutanceau M, Loc TP, Dulieu A (1990) Vortex formation around an oscillating and translating airfoil at large incidences. J Fluid Mech 211:37–60

Ol MV, McAuliffe BR, Hanff ES, Scholz U, Kaehler C (2005) Comparison of laminar separation bubble measurements on a low reynolds number airfoil in three facilities. 35th AIAA fluid dynamics conference and exhibit, AIAA-2005-5149, Toronto, Canada

Panda J, Zaman KBMQ (1994) Experimental investigation of the flow field on an oscillating airfoil and estimation of lift from wake surveys. J Fluid Mech 265:65–95

Ringuette MJ, Milano M, Gharib M (2007) Role of the tip vortex in the force generation of low-aspect-ratio normal flat plates. J Fluid Mech 581:453–468

Rival D, Tropea C (2009) Characteristics of pitching and plunging airfoils under dynamic-stall conditions. 47th AIAA aerospace sciences meeting and exhibit, AIAA-2009-0537, Orlando, USA

Selig M, Guglielmo J, Broeren A, Giguere P (1995) Summary of low-speed airfoil data. SoarTech Publications, Virginia Beach, USA

Theodorsen T (1935) General theory of aerodynamic instability and the mechanisms of flutter. NACA Report No 496

Thomas ALR, Taylor GK, Srygley RB, Nudds RL, Bomphrey RJ (2004) Dragonfly flight: Free-flight and tethered flow visualizations reveal a diverse array of unsteady lift-generating mechanisms, controlled primarily via angle of attack. J Exp Biol 207:4299–4323

Wake patterns of the wings and tail of hovering hummingbirds

Douglas L. Altshuler · Marko Princevac · Hansheng Pan · Jesse Lozano

Abstract The flow fields of slowly flying bats and faster-flying birds differ in that bats produce two vortex loops during each stroke, one per wing, and birds produce a single vortex loop per stroke. In addition, the circulation at stroke transition approaches zero in bats but remains strong in birds. It is unknown if these difference derive from fundamental differences in wing morphology or are a consequence of flight speed. Here, we present an analysis of the horizontal flow field underneath hovering Anna's hummingbirds (*Calypte anna*) to describe the wake of a bird flying at zero forward velocity. We also consider how the hummingbird tail interacts with the wake generated by the wings. High-speed image recording and analysis from three orthogonal perspectives revealed that the wing tips reach peak velocities in the middle of each stroke and approach zero velocity at stroke transition. Hummingbirds use complex tail kinematic patterns ranging from in phase to antiphase cycling with respect to the wings, covering several phase shifted patterns. We employed particle image velocimetry to attain detailed horizontal flow measurements at three levels with respect to the tail: in the tail, at the tail tip, and just below the tail. The velocity patterns underneath the wings indicate that flow oscillates along the ventral–dorsal axis in response to the down- and up-strokes and that the sideways flows with respect to the bird are consistently from the lateral to medial. The region around the tail is dominated by axial flows in dorsal to ventral direction. We propose that these flows are generated by interaction between the wakes of the two wings at the end of the upstroke, and that the tail actively defects flows to generate moments that contribute to pitch stability. The flow fields images also revealed distinct vortex loops underneath each wing, which were generated during each stroke. From these data, we propose a model for the primary flow structures of hummingbirds that more strongly resembles the bat model. Thus, pairs of unconnected vortex loops may be shared features of different animals during hovering and slow forward flight.

D. L. Altshuler (✉)
Department of Biology, University of California,
Riverside, CA 92521, USA
e-mail: douga@ucr.edu

M. Princevac · H. Pan · J. Lozano
Department of Mechanical Engineering,
University of California, Riverside, CA 92521, USA

1 Introduction

Since Kokshaysky (1979) first photographed birds flying through wood and paper dust clouds, flight biologists have been working to attain higher resolution views and quantifiable features of the wakes of flying animals. Experiments have focused on vertical measurement planes with one view or two orthogonal views to characterize the momentum imparted behind and below the animal (Spedding 1986, 1987a, b; Spedding et al. 1984). Recent efforts have yielded high-resolution, three-dimensional descriptions of the wakes produced during moderate and fast forward flight in passerine birds (Hedenström et al. 2006; Rosén et al. 2007; Spedding et al. 2003), and also during slow and moderate forward flight in bats, the only other extant vertebrate lineage that has powered, flapping flight (Hedenström et al. 2007; Muijres et al. 2008). In birds, the two wings together produce a single vortex loop, whereas in bats each wing produces a separate vortex loop. In addition, birds generate considerable circulation during stroke transitions whereas circulation during bat flapping

G.K. Taylor, M.S. Triantafyllou, and C. Tropea (Eds.): Animal Locomotion, pp. 273–284.
springerlink.com

approaches zero at stroke transition. It is unknown to what extent these alternative wake structures derive from differences in flight speed versus lineage-specific differences in the morphology and neuromuscular control of the wings.

The hovering flight of hummingbirds provides an excellent opportunity to examine the wake structure produced by birds during hovering and thus with no forward velocity. The flow fields generated by hovering rufous hummingbirds (*Selasphorus rufus*) have been described from two orthogonal, vertical perspectives with the results that the wings generate a powerful wake oriented directly below the animal, which is dominated by the much stronger downstroke (Warrick et al. 2005). A horizontal view of the wakes underneath hovering hummingbirds has not been described, but this perspective should provide unique information about the wing wake structures. A horizontal perspective has the additional advantage of providing pertinent information concerning how the hummingbird tail interacts with the very strong downwards wing wakes.

Three aerodynamic functions for bird tails are known. During forward flight tails (1) function in maneuverability and stability, (2) can help control the angle of attack of the wings, and (3) during slow forward flight can produce lift (Thomas 1997; Thomas and Balmford 1995). However, the elaborated tails of some species are elongated in response to sexual selection and increase costs of parasitic drag (Balmford et al. 1993; Evans and Hatchwell 1992; Møller 1989; Norberg 1995). The aerodynamic function of the tail in hovering flight is not clear given the absence of a translational flow velocity, but it has been suggested that the tail may be generally involved in pitch control (references in Warrick et al. 2002), which should be important for maintaining stability during hovering.

Here we describe the relative motion of the hummingbird wings and tail, and the horizontal wake pattern in a two-dimensional plane. We separately considered three elevations of perspective: a plane centered within the tail, a plane at the tail tip, and a plane located just below the tail. We present velocity profiles based upon temporal sequences of wing positions. These measurements provide information about the wake structure, the tail-wake interaction, and the horizontal orientation of the velocity vectors. We use these data to propose a model of the dominant flow structures produced during hovering flight in hummingbirds.

2 Phase relationships between hummingbird wings and tail

The wing and tail kinematics of hovering hummingbirds were studied using five male Anna's hummingbirds (*Calypte anna*), which were captured in Berkeley (three birds) and Pasadena (two birds), California. These hummingbirds were housed in institutional vivaria and trained to feed from artificial feeders made from 10 ml syringes. For filming trials, the hummingbirds were moved from the vivaria to an acrylic chamber (1 m × 1 m × 1 m) constructed with three clear sides and three opaque sides. The chamber contained a single perch and a single artificial feeder, also made from a 10-ml syringe. Hovering bouts were filmed from three perspectives (top and two sides) using three digital high-speed cameras filming at 1,000 frames per second. The Institutional Animal Care and Use Committees at the University of California Berkeley and the California Institute of Technology approved these vertebrate animal procedures.

One hovering sequence for each of the five birds was analyzed via frame-by-frame digitization with custom software (Fry et al. 2003) written in Matlab (Mathworks, Inc.). The three-dimensional coordinates of the wing and tail tips were assigned for five complete wingbeats for each bird. We calculated the vector velocity of the tips of the wings and tail based upon motion through the *x*, *y*, and *z* planes. During hovering bouts, wingtip velocities were maximal during the middle of each stroke and approached 0 during stroke transitions. All five birds beat their tails in a harmonic motion, but two hummingbirds moved the tail in antiphase with the wings, one animal moved its tail in phase with the wings, and two animals exhibited a shift between phase and antiphase within the short sequence. An example of this latter category is provided in Fig. 1.

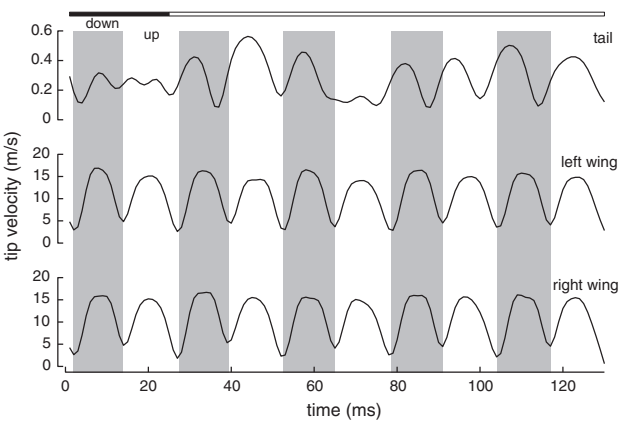

Fig. 1 The velocities of the tail and two wings of a hovering hummingbird. Five complete wingbeats are plotted with downstrokes indicated in *gray* and upstrokes in *white*. In the beginning of this sequence during the downstroke, the hummingbird moved its tail in antiphase (*top black bar*) to the wings, but used an extra tail cycle during the first upstroke to shift to in phase movement between the wings and the tail (*top white bar*)

3 Methods for recording flow features in hovering hummingbirds

We measured the flow characteristics of three male Anna's hummingbirds (*C. anna*), captured in Riverside, CA, USA and housed in the vivarium at the University of California Riverside (UCR). The Institutional Animal Care and Use Committee at UCR approved these vertebrate animal procedures.

Prior to each experiment, an individual bird was moved from the vivarium to an experimental flight chamber for 1 day of training in the new setting. The dimensions of the flight chamber were 76 cm × 76 cm × 95 cm high and it was constructed of a PVC frame with walls made of thin plastic sheeting (Fig. 2a). The chamber contained a single perch and one small feeder constructed from a 1-ml syringe. In addition to becoming accustomed to the flight chamber and feeder, we also trained the hummingbirds to feed on command by restricting access to the feeder for 15 min and then only allowing one feeding bout before again restricting access. A feeding bout was defined as a single episode of hovering at the feeder until the bird moved more than approximately two body lengths away in any direction.

Experiments began the day after training and involved the same feeding protocol. A particle image velocimetry (PIV) system was used to measure the instantaneous velocity field in the horizontal plane. The PIV technique measures the velocity in a fluid by correlating images of the particle-seeded flow (Adrian 1988). For these experiments, atomized food grade olive oil was utilized as the seeding particles. In the minute prior to providing feeder access, we filled the chamber with olive oil mist created using a pressurized oil container equipped with a perforated tube to enable oil–air mixing for adequate atomization.

As the bird approached the feeder, the olive oil particles were illuminated in a plane below the feeder using a horizontal laser sheet with a wavelength of 532 nm (with energy of 388 mJ/pulse) generated by a double-pulsed Nd:YAG laser (Big Sky Laser Technologies, Inc, model CFR400) located 0.5 m from the feeder. The Q-switch was set to 100 μs corresponding to approximately medium laser power. The laser beam was expanded into a 20° diverging light sheet using sheet-forming optics, which included a cylindrical lens (−15 mm focal length) and a spherical lens (200 mm focal length). In this way, the beam was transformed into a 200-mm wide and 0.212 mm thick sheet to illuminate seed particles in a horizontal plane close to the bird. In separate experiments, we illuminated three planes: (1) 1 cm above the middle plane, i.e., within the tail, (2) at the tail tip during its cyclical oscillation, and (3) just underneath the tail. A LASERPULSE Synchronizer (TSI Inc.) was utilized to trigger the laser pulse and the camera

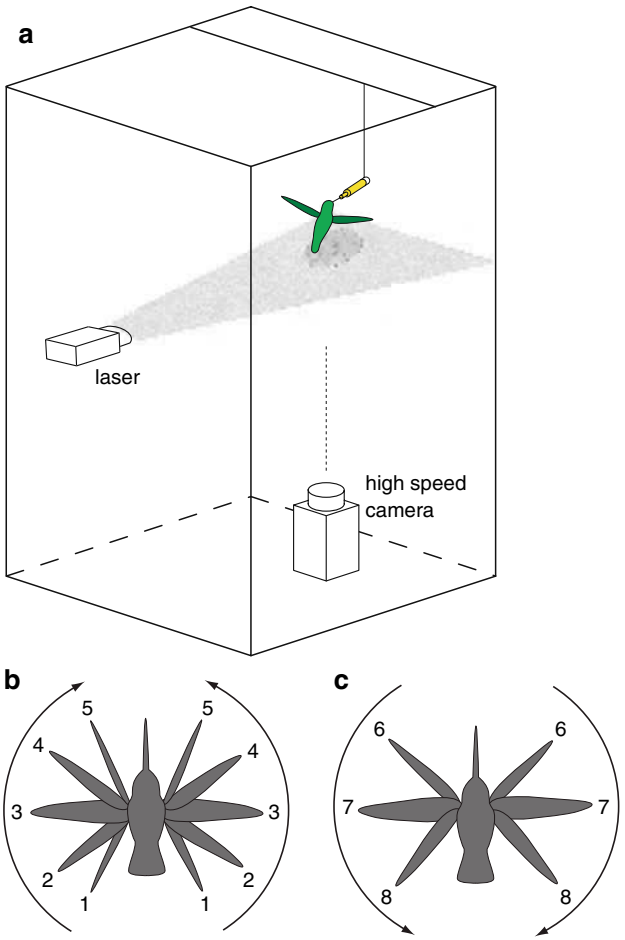

Fig. 2 **a** The experimental chamber used in hummingbird PIV experiments. During different sequences the laser sheet was moved to be either within the tail, at the tail tip, or underneath the tail (shown here). **b** The wings were visible in most of the raw images recorded from the camera located underneath the bird. The wing positions were assigned to different numbers indicating the phase within a complete wingbeat cycle. Position 1 corresponds to the wings in the rearward position in the middle of pronation. Positions 2–4 correspond to progressive movement through the downstroke, and position 5 corresponds to the forward position in the middle of supination. **c** Positions 6–8 correspond to the wings moving progressively through the upstroke

with correct sequences and timing through a 2.66-GHz dual-processor workstation (Intel® Xeon™). The laser sheet was synchronized with a high-resolution (1,600 × 1,192 pixel) POWERVIEW 2M CCD camera (TSI Inc., model 630157) with a 50-mm f/1.8 Nikkor lens and an exposure time of 260 μs. Camera aperture was set to 5.6. A total of 15 image pairs per second (15 Hz) were captured. Time difference between the two images in a pair was optimized for the best PIV quality to $\Delta t = 100$ μs. A grid for the PIV processing was formed using the Nyquist Grid Engine over 64 × 64 pixels interrogation regions. Fast Fourier transform correlation was used with the Gaussian peak engine.

4 PIV flow field analysis

We recorded at least ten hovering bouts for each of the hummingbirds, but limited our analysis to the 11 experiments during which the birds maintained constant body orientation through the trial. The instantaneous velocity fields and vorticity were calculated from all image pairs in this group of experiments. The flight chamber was sufficiently large that we could ignore wall influences to the flow because the change in lift per unit wing span due to the chamber walls (Katz and Plotkin 2001).

$$\Delta L = \frac{\pi^2}{24}\frac{c^2}{h^2} \sim 0.01 \ll 1, \quad (1)$$

where h is chamber height, and c is the wing span.

We further narrowed our analysis to the velocity measurements (i.e., image pairs) that could be grouped into one of eight wing positions within a complete wingbeat cycle (see Fig. 2b, c). This was accomplished by visual assignment of wing positions based upon each raw image. Arranging the measurements by wing position allowed us to compile a stroke sequence of velocity and vorticity profiles even though the images came from separate wingbeats. It is important to note that the wing tip velocity is greatest during mid-stroke and slowest during stroke transition (Fig. 1). Therefore the time difference between wing positions (average $\sim$3 ms) was not constant.

The different experiments yielded different perspectives of the bird and wake both due to design and behavioral variability. In the former case, we moved the camera either closer to the feeder thereby focusing on the front (ventral) half of the stroke cycle or $\sim$10 cm further away from the feeder to focus on the back (dorsal) half of the stroke cycle. In the latter case, the bird fed at different angles relative to the feeder in the horizontal plane providing either a left or right bias. To facilitate comparisons among these multiple views, we calculated velocity over specific regions of interest (ROI) and along bird-centered axes. The ROIs were constrained to one of three positions: (1) underneath either the left or right wing on the front (ventral) side of the bird, including wing positions 3–7; (2) underneath either the left or the right wing on the back (dorsal) side of the bird, including wing positions 1–3 and 7–8; (3) underneath the tail in a narrow region that covered the full range of tail movement. The original velocity vector components in the x and y axes, u and v, respectively, were rotated to along the bird component, V_s (positive from ventral to dorsal) and to a component that is perpendicular to the ventral–dorsal axis, V_n (positive when moving from the bird's lateral right to lateral left).

Within a filmed hovering bout, the velocities were averaged over all frames corresponding to the same wing position and the same ROIs were used for all frames. Because the area of the ROIs differed across experiments, we restricted our analysis to within experiment results rather than combining experiments to generate average values.

On average, the measured flow field was 5 cm below the wing stroke plane. We assumed the vertical velocity to be $U_{vert} \sim 2$ m/s based upon measurements from similarly sized rufous hummingbirds, *S. rufus* (Warrick et al. 2005). Thus, it is estimated to require an average of 25 ms for the flow structures to be advected from the wing to the measuring plane. Because the wingbeat frequency is $\sim$40 Hz (corresponding to a wingbeat period of 25 ms), the measured flow field should be lagging by the full cycle behind the actual wing stroke visible on the raw PIV image.

Another important reason why we avoided combining experiments for analytical purposes is that the vertical distance between the wings and the measuring plane—and thus the time lag—differed across experiments. Within each experiment, the hummingbirds maintained a constant body orientation and the time lag between wake generation and measurement is invariant. However, across experiments, hummingbirds used slightly different body angles, which should produce slight phase shifts in the wingbeat and PIV measurement cycles. Accordingly, we present results for individual experiments and then focus on the common features among experiments to develop a model of the wake of hovering hummingbirds.

5 Results of flow measurements

A representative trial with a perspective on the bird's ventral, right region is presented in Fig. 3. Across wing positions the along bird velocity component V_s, in the wing domain, exhibits a clear pattern of flow reversal from ventral to dorsal. The average V_s value is close to 0. The perpendicular to bird velocity component V_n, in the wing domain, indicates net flow from lateral to medial because velocity moving from the lateral right to the lateral left is indicated with positive values.

We further calculated the velocity components in the wing domain for all sequences in which the wings could be identified while the birds maintained stable positions. The along bird velocity components in the wing domain for this set of experiments is given in Fig. 4. Three measuring planes are referred as: in tail (highest), tail tip (middle) and under tail (lowest). No unique pattern was observed across different experiments, but the hummingbird used different body angles in different experiments and the ROIs were not identical between any two trials. For most of the experiments there is a similar pattern for the same measuring plane. For the highest measurement plane, velocity maxima are observed for wing positions 4–

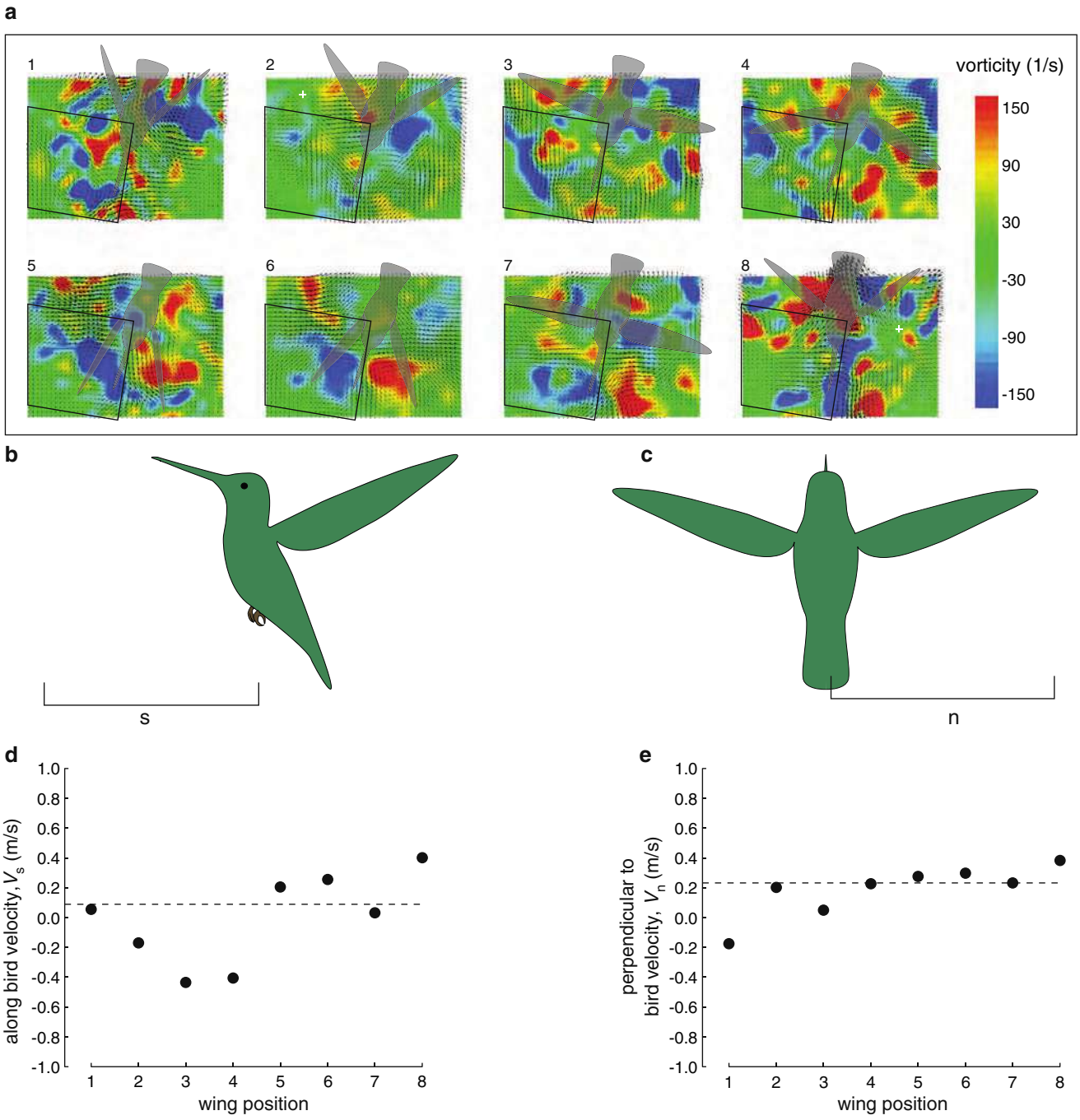

Fig. 3 Representative analysis of the wake underneath a wing, using experiment 5 as an example. **a** The raw images that contained the same wing position image were averaged to produce a color plot containing the vorticity (*colors*) and velocity vectors (*arrows*). The eight wing positions are numbered using the system described in Fig. 2b, c. Within each plot, a *black polygon* represents the region of interest over which velocity was calculated along the bird (V_s) and perpendicular to the bird (V_n). A *small white cross* indicates the center of the vortex loop if present. **b** The side view of an idealized hovering hummingbird, with the *bottom of the black bracket* indicating the planar region quantified in this dimension and the location of the laser sheet underneath the tail. **c** The backview of an idealized hummingbird, with the analogous perspective on the region of interest and level of the laser sheet. **d** The along bird velocity (V_s) across the eight wing positions. The *dashed horizontal line* indicates the mean velocity across all positions. **e** The perpendicular to bird velocity (V_n) across the eight wing positions

5, and minima are observed for positions 1–2 and 7–8. For the middle and lowest measurement planes, the overall pattern is shifted such that the velocity minima are observed for wing positions 2–3. This apparent change in phase can be attributed to different distances between wing and measuring plane. Flow reversal, from head to

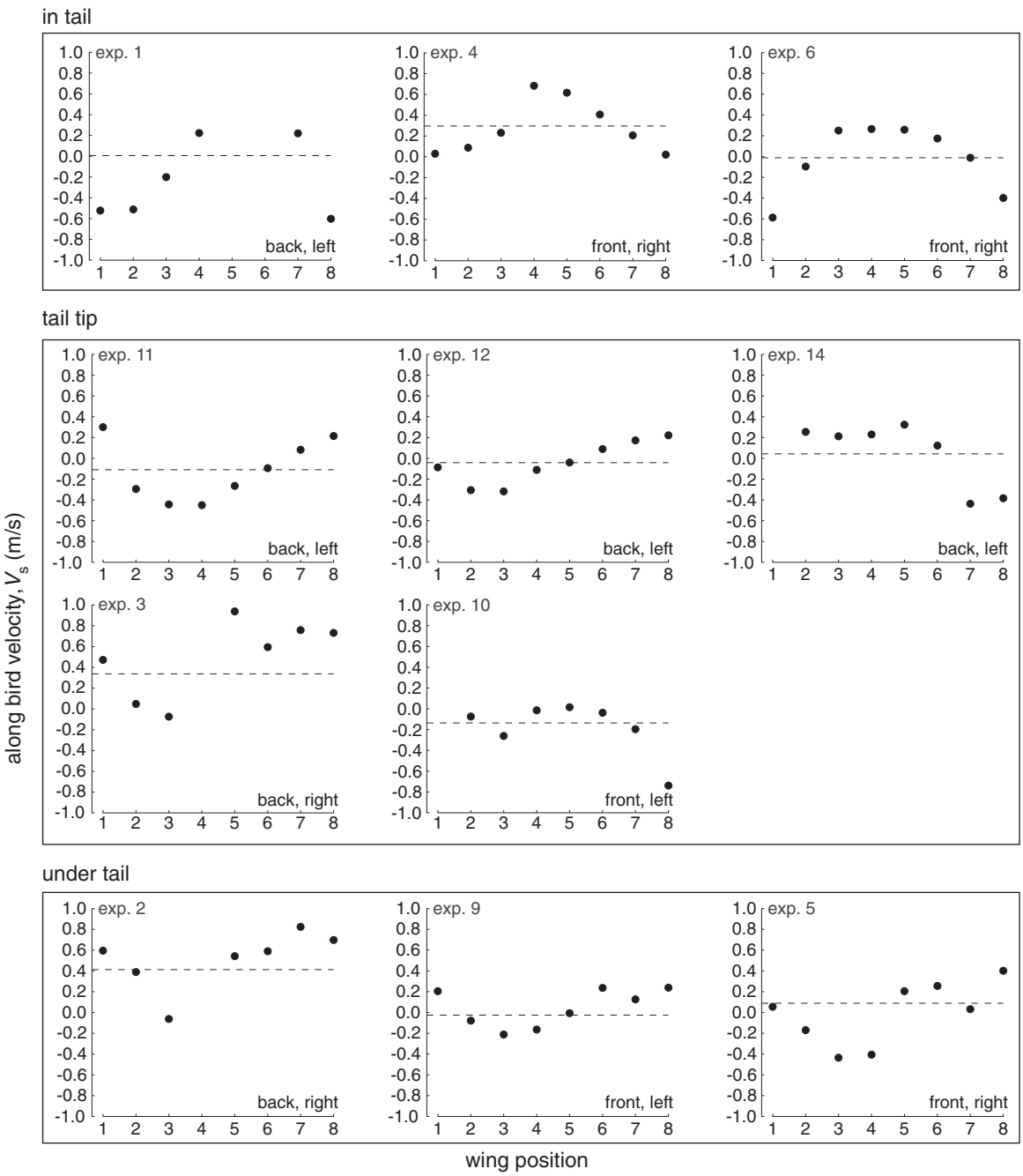

Fig. 4 Along bird velocity plots in the wing domain. The individual experiments are arranged first by tail position (*grouping boxes*), then by back to front, and lastly by left to right. Experiments 1–5 come from bird 1. Experiment 6 comes from bird 2. Experiments 9–14 come from bird 3. The wing positions are indicated on the *x*-axis. The *dashed line* indicates the mean value across all wing positions

tail and from tail to head, is observed in most but not all experiments.

The full experimental results for the normal to the bird velocity component, V_n, in the wing domain are presented in Fig. 5. Throughout all experiments, velocity is from lateral to medial, i.e., the values are consistently negative for ROIs on the left side of the birds and consistently positive for ROIs on the right side of the birds.

We further examined the subset of experiments that included complete views of the region around the tail oscillations. A representative sequence is provided in Fig. 6. The along bird velocities in the tail domain are presented in Fig. 7. Almost without exception, the velocities are positive across all wing positions, indicating that the net flow is in the ventral to dorsal direction for the region around the tail. In the majority of experiments in the

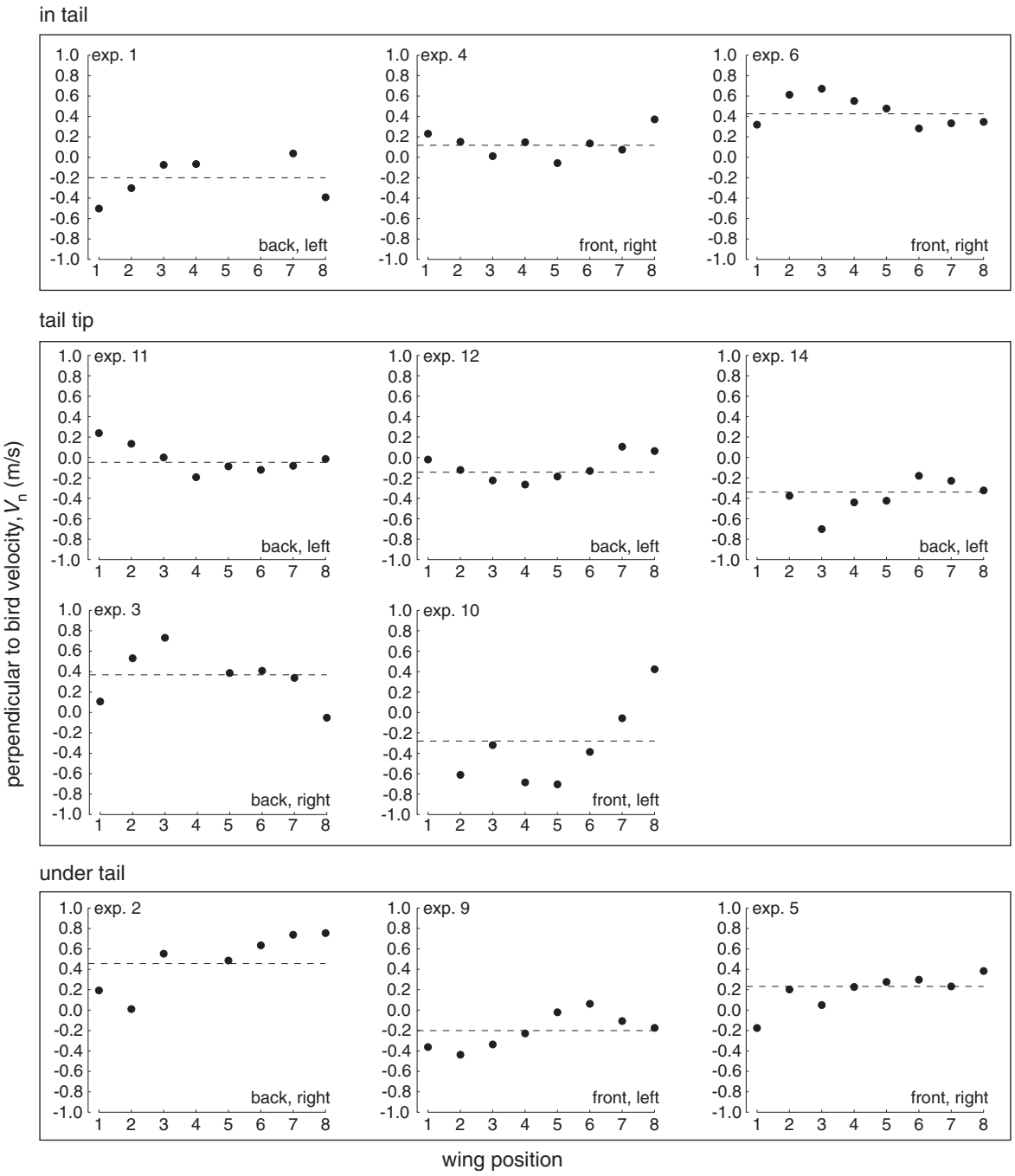

Fig. 5 Perpendicular to bird velocity plots in the wing domain. Note that all *left* perspectives have net negative velocities and all *right* perspectives have net positive velocities, indicating consistent flow from the periphery toward the bird. Details as in Fig. 4

upper and middle planes, the V_s velocity is minimal at positions 1–2 and 8. Taken together with our assumed lag of the wing wake, these data suggest that the bird is using its tail to deflect the outgoing flow caused by wings. In the lowest measuring plane for which we have only a single sample, this minimum is phase shifted.

In addition to measuring the net velocities with the ROIs, we also considered the mass flux over the entire measuring field to identify prominent sites with out of plane flow. These sites are indicated by discrete regions in which velocity emerges in all direction thereby suggesting the center of vortex ring or loop. In every experiment, we identified at least one, and usually two, wing positions in which there was evidence for vortex loops. Examples can be seen under the right wing for position 2 and under the left wing for position 8, in Fig. 3. A small white cross indicates the centers of these loops. For experiments in which both sides of the animal were visible, we identified

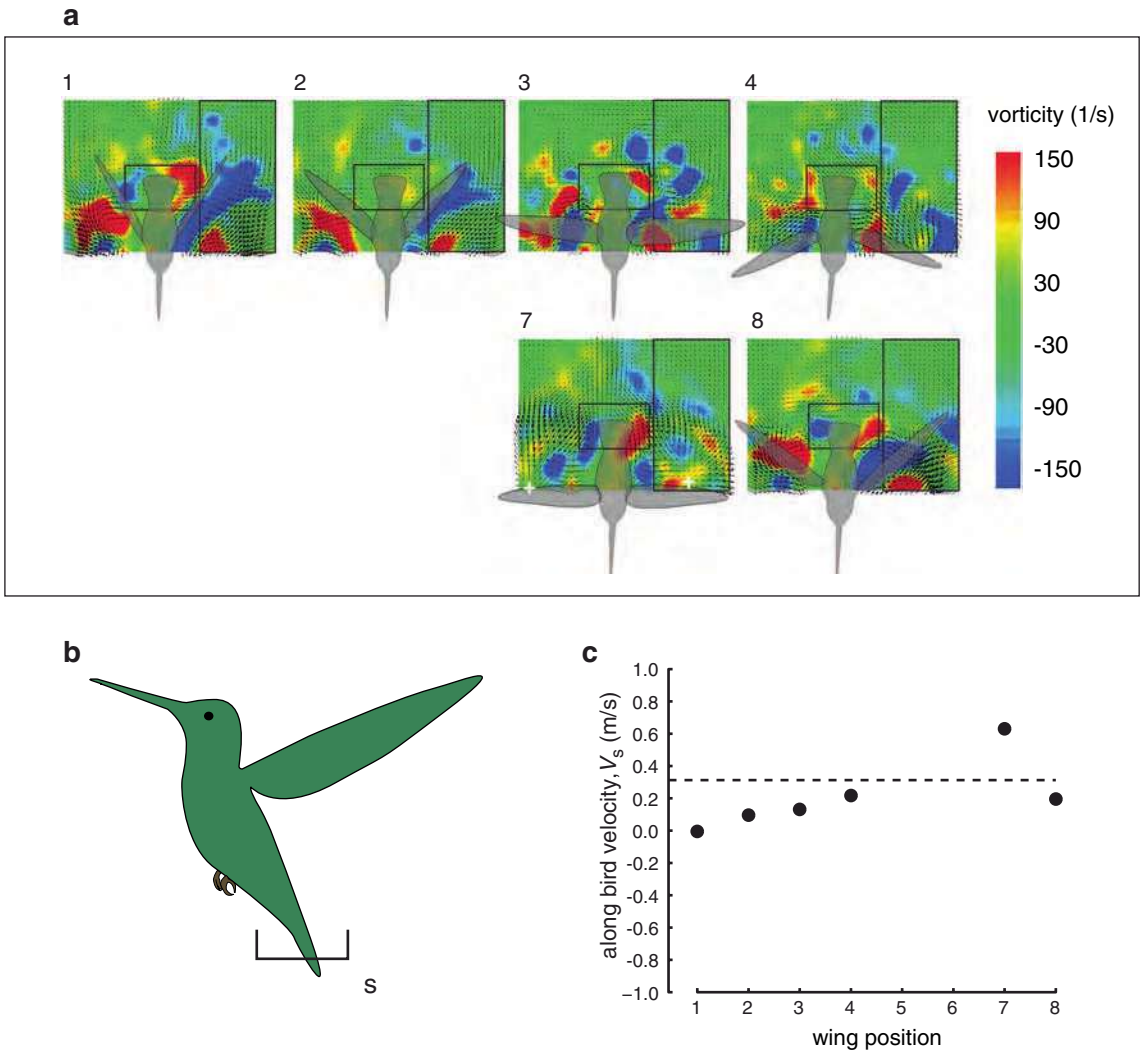

Fig. 6 Representative analysis of the wake underneath a tail, using experiment 1 as an example. **a** The color plots are configured using the same arrangement as in Fig. 3. However, these images were centered on the tail and wing positions 5 and 6 could not be identified because the both wings were out of view. Velocity was calculated only for the along bird (V_s) dimension. A small white cross indicates the center of the vortex loop if present. **b** The side view of an idealized hovering hummingbird, with the *black bracket* indicating the region quantified in this dimension and the location of the laser sheet underneath the tail. **c** The along bird velocity (V_s) across the six available wing positions. Details as in Fig. 3d, e

separate vortex loops on either side of the animal. A coarse example of this pattern can be seen in wing position 7 in Fig. 6. In Fig. 8 we present a series of representative instantaneous velocity fields from two experiments that clearly indicate the existence of vortex loops that are present during both up- and down-strokes and that are underneath both wings.

6 Discussion

Measurements of the hovering hummingbird wake in the horizontal plane near the tail revealed three general patterns of flow velocity: (1) Along the ventral–dorsal axis underneath the wings, air flow switches direction more or less sinusoidally indicating the influence of forwards (downstroke) and backwards (upstroke) movement of the wings (Fig. 4); (2) Perpendicular to this axis, underneath the wings, air flows from the periphery (lateral) in toward to the region underneath the hummingbird's body (medial) but with varying intensity (Fig. 5); (3) In a small region around the tail, the air flow is consistently oriented along the head–tail axis and away from the body (Fig. 7). In addition, we see clear evidence for separate vortex loops that are shed underneath each wing, and separate loops that are shed during down- and up-strokes.

As is the case for other PIV measurements from real flying animals, these flow fields reveal a complex wake that contains many disrupted structures and secondary flows. Furthermore, the patterns of flow reversal do not fit perfect

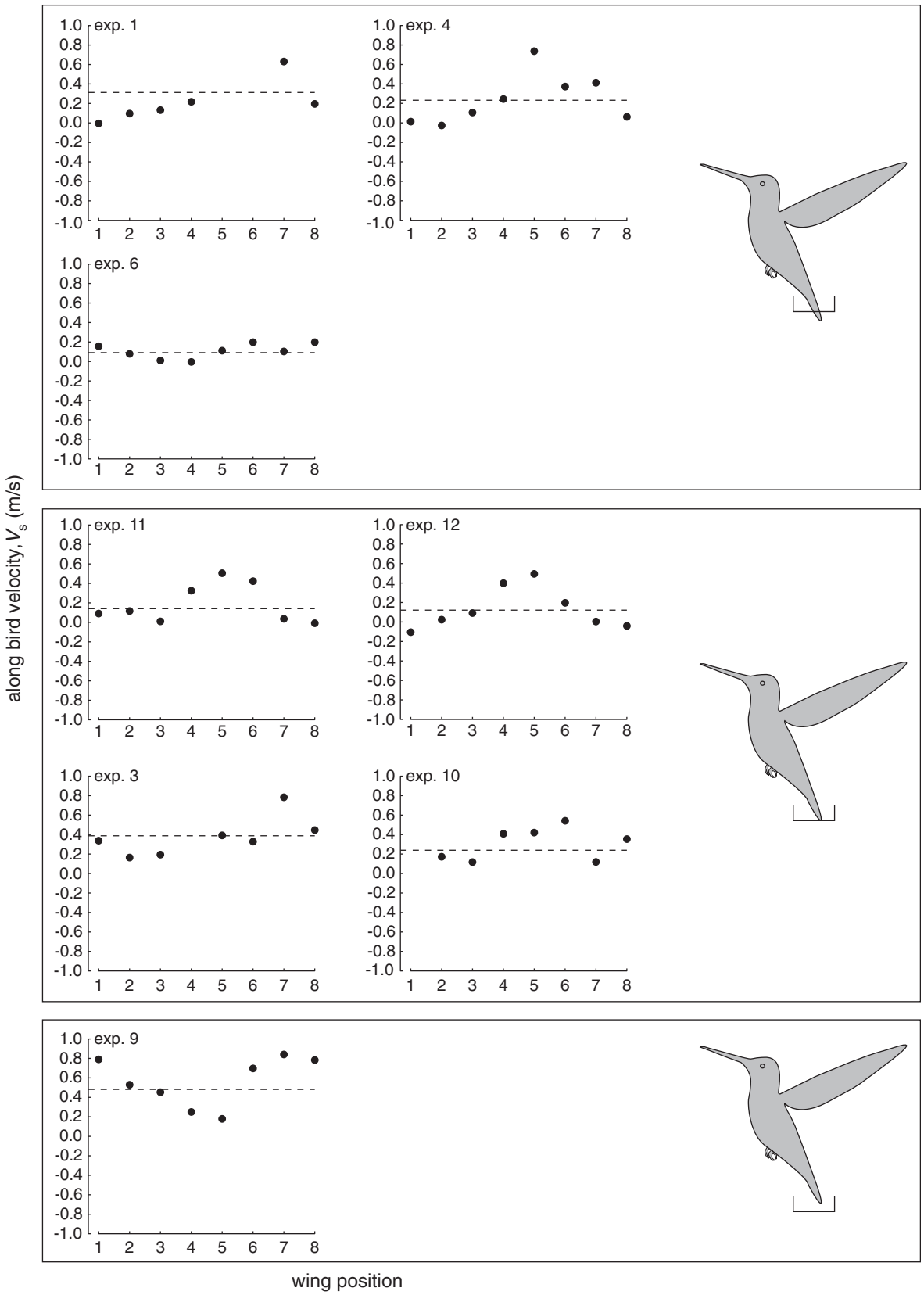

Fig. 7 Along bird velocity plots in the tail domain. Details as in Fig. 4

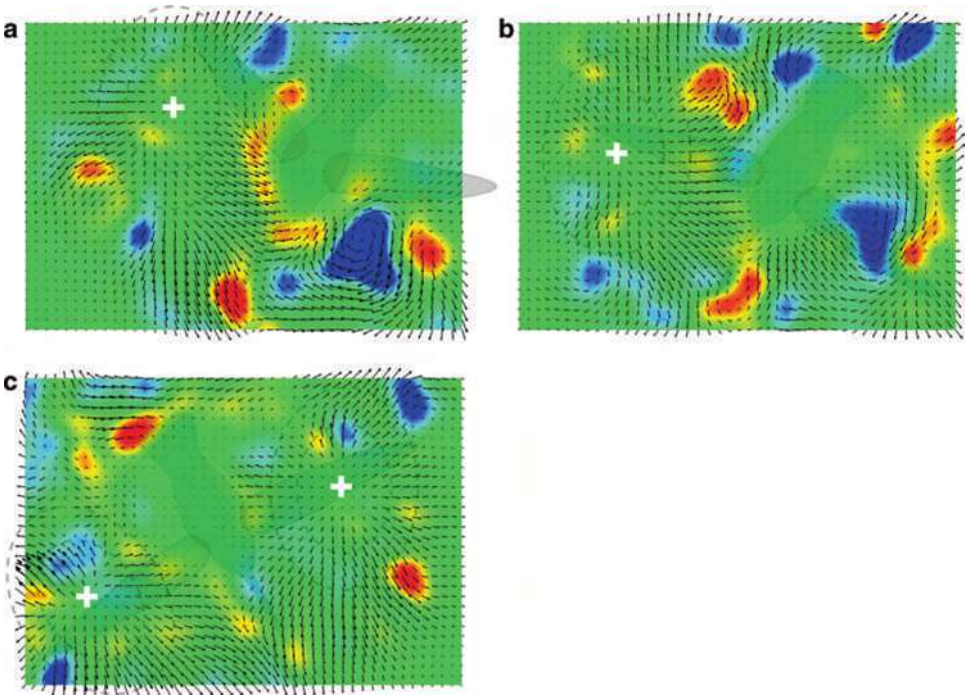

Fig. 8 Examples of prominent vortex loops. The flow fields in experiment 6 revealed prominent vortex flow structures at bird wing positions 2 (**a**) and 7 (**b**), which presumably correspond to vortices shed during down- and up-strokes respectively. The flow fields from experiment 14 where particularly illustrative of separate flow structures underneath each wing at wing position 7 (**c**). Note that these images come from single frame pairs and are not averaged across wing positions as was the case in previous flow field plots. The actual positions of the birds and their wing positions are shaded in *translucent gray* and the hypothesized vortex loops are marked by *dashed lines*. A *small white cross* indicates the center of each vortex loop

sinusoids as might be expected. However, it is unrealistic to expect invariant flow fields with perfect sinusoids because real hummingbirds exhibit differences in angle of attack, airfoil shape and stroke period between down- and up-strokes (Tobalske et al. 2007; Warrick et al. 2005; D.L. Altshuler, unpublished data). Additionally, we expect that the animals make rapid adjustments to these and other kinematic features to control stability, which will produce flow fields that vary across wingbeats.

It is not possible to infer the complete three-dimensional structure of the hummingbird's wake from the single perspective described here. Although there are relatively few measurements of the flow fields of different flying animals, we can compare our results with previous studies of forward flight in pigeons (Spedding et al. 1984), passerines (Hedenström et al. 2006; Rosén et al. 2007; Spedding et al. 2003) and bats (Hedenström et al. 2007; Muijres et al. 2008). In addition to these vertebrate fliers, the flow fields of numerous insect taxa have been measured during hovering and forward flight (Bomphrey et al. 2005, 2006; Brodsky 1991; Grodnitsky and Dudley 1996; Grodnitsky and Morozov 1992, 1993; Srygley and Thomas 2002; Willmott et al. 1997). Most of these invertebrate studies concerned single vertical perspectives oriented along the body axis and therefore do not provide information about the contributions of bilateral wings to overall flow field structures. However, Bomphrey et al. (2006) constructed a composite view from serial sections and concluded that the Tobacco Hawkmoth (*Manduca sexta*) uses its wings to produce a single vortex loop during downstroke in forward flight.

Wake descriptions from slow-flying bats and faster-flying birds differ in two fundamental aspects: (1) bat wings produce two vortex loops whereas birds produce a single vortex loop per stroke, and (2) bats do not exhibit strong circulation during stroke transitions unlike birds. Our data indicate that during hovering flight, hummingbirds more strongly resemble the bat pattern. First, we see clear evidence for separate vortex loops for each wing (Fig. 8). Second, our kinematic results indicate that wingtip velocities approach 0 at stroke transition whereas for other birds during forward flight, airstream velocity at the wing tips remains high. Because aerodynamic forces are proportional to the square of velocity, vortex generation should cease as the wings decelerate near stroke transition for hovering hummingbirds. It would be highly informative to consider the flow field patterns of hummingbirds across a wide range of flight speeds.

Combining the results from velocities and vorticity leads to a model for the principal flow structures in hovering hummingbirds (Fig. 9). The vortex loops shed during downstrokes move ventrally and loops shed during upstroke move dorsally. As air is sucked into these vortices, the principle mass comes from lateral to the bird because the bird's body acts as a boundary. Thus, the vortex loops move from lateral to medial.

With this model in mind, we can now consider the how the tail interacts with the wing wake. Although the tail

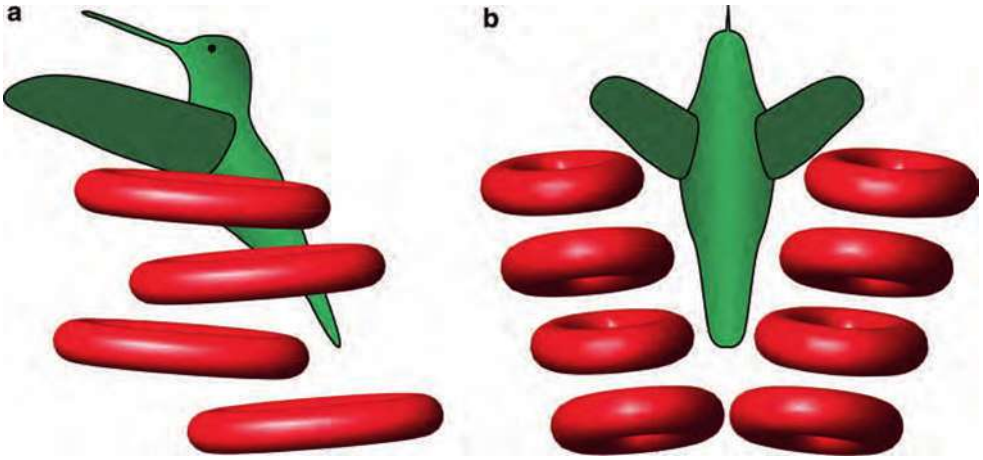

Fig. 9 Proposed model for the principal vortex wake structures of hovering Anna's hummingbirds, with left lateral (**a**) and dorsal (**b**) views. The vortex loops are elliptical in shape, being longer in the ventral–dorsal than the lateral-medial axis. Two prominent structures are produced during each wingbeat cycle when the wings reach maximum velocity during the up- and down-strokes. The vortices shed during downstrokes move ventrally and vortices shed during upstrokes move dorsally. All vortex loops move from lateral to medial positions after shedding. Other, less prominent flow structures such as cross-stream vorticity are not illustrated

oscillates with an approximately sinusoidal motion, the velocities around the actual tail are either 0 or positive, indicating net flow along the body axis but away from the bird. These velocities have high magnitudes and are almost certainly not a consequence of the wake imparted by the tail motion. Instead, these flows are likely the result of wake encounter by the two wings coming toward each other during the end of the upstroke. We hypothesize that the tail is deflecting these larger flows, although the magnitude of interference with the wake will depend upon the degree of tail spreading and the precise phasing of tail oscillation. Because the magnitude of the pressure force will be proportional to the square of the velocity, the hummingbird should have the capability of generating tail moments of sufficient size to use this structure in maintaining pitch stability.

In this communication, we focus on the analysis of the mean flow patterns for different wing and tail positions. This was done using measured horizontal velocity components in the horizontal plane. Although it is our eventual goal, at this stage we are not attempting to explain the force balance of the hovering bird through momentum or vorticity analysis because such computations would have to involve doubtful assumptions pertaining to the full three-dimensional flow field surrounding the bird. Dabiri (2005) demonstrated that the spatial velocity distribution in the wake is not sufficient for determination of locomotive forces but has to be combined with the pressure distribution. He proposed a method for accounting for the pressure contribution via wake vortex added-mass in analogy with the added-mass of fluid surrounding solid bodies.

At the present state, computational fluid dynamics and direct numerical simulation cannot be applied with confidence to bird flight. To develop and validate numerical models and to obtain information needed for analytical models (e.g., information to quantify added-mass tensor component proposed by Dabiri 2005) more detailed measurements are required. New technologies for real three-dimensional flow measurements should provide the necessary information, and can be combined with a numerical model to extract the pressure fields needed for full force balance analysis. In addition, such pressure estimates can be validated against existing, limited, pressure measurements (e.g., as in Usherwood et al. 2005). Particle tracking velocimetry can be applied directly to determine the Lagrangian properties of the flow, which can be used to determine the added-mass contributions (Dabiri 2005; Darwin 1953).

Acknowledgments We thank David Lentink for comments on an earlier version of the manuscript, and Bret Tobalske and Paolo Segre for suggestions for experimental procedures. We also gratefully acknowledge Christian Bartolome, Brian Cho, Sirish Makan, Elsa Quicazán, James Soh, and Kenneth Welch for assistance with data collection and analysis. This research was supported by a Regents Faculty Fellowship to Douglas L. Altshuler.

References

Adrian RJ (1988) Review of particle image velocimetry research. In: The symposium on optical methods in flow and particle diagnostics, 6th international congress on applications of lasers

and electro-optics, vol 9. Optics and Lasers in Engineering, San Diego, pp 317–319
Balmford A, Thomas ALR, Jones IL (1993) Aerodynamics and the evolution of long tails in birds. Nature 361:628–631
Bomphrey RJ, Lawson NJ, Harding NJ, Taylor GK, Thomas ALR (2005) The aerodynamics of *Manduca sexta*: digital particle image velocimetry analysis of the leading-edge vortex. J Exp Biol 208:1079–1094
Bomphrey RJ, Lawson NJ, Taylor GK, Thomas ALR (2006) Application of digital particle image velocimetry to insect aerodynamics: measurement of the leading-edge vortex and near wake of a Hawkmoth. Exp Fluids 40:546–554
Brodsky AK (1991) Vortex formation in the tethered flight of the peacock butterfly *Inachis io* L. (Lepidoptera, Nymphalidae) and some aspects of insect flight evolution. J Exp Biol 161:77–95
Dabiri JO (2005) On the estimation of swimming and flying forces from wake measurements. J Exp Biol 208:3519–3532
Darwin C (1953) Note on hydrodynamics. Proc Camb Philos Soc 49:342–354
Evans MR, Hatchwell BJ (1992) An experimental study of male adornment in the scarlet-tufted malachite sunbird. II. The role of elongated tail in mate choice and experimental evidence for a handicap. Behav Ecol Sociobiol 29:421–427
Fry SN, Sayaman R, Dickinson MH (2003) The aerodynamics of free-flight maneuvers in *Drosophila*. Science 300:495–498
Grodnitsky DL, Dudley R (1996) Vortex visualization during free flight of Heliconiine butterflies (Lepidoptera: Nymphalidae). J Kans Entomol Soc 69:199–203
Grodnitsky DL, Morozov PP (1992) Flow visualization experiments on tethered flying green lacewings *Chrysopa dasyptera*. J Exp Biol 169:143–163
Grodnitsky DL, Morozov PP (1993) Vortex formation during tethered flight of functionally and morphologically two-winged insects, including evolutionary considerations on insect flight. J Exp Biol 182:11–40
Hedenström A, Rosén M, Spedding GR (2006) Vortex wakes generated by robins *Erithacus rubecula* during free flight in a wind tunnel. J R Soc Interface 3:263–276
Hedenström A, Johansson LC, Wolf M, von Busse R, Winter Y, Spedding GR (2007) Bat flight generates complex aerodynamic tracks. Science 316:894–897
Katz J, Plotkin A (2001) Low speed aerodynamics, 2nd edn. Cambridge University Press, Cambridge
Kokshaysky NV (1979) Tracing the wake of a flying bird. Nature 279:146–148
Møller AP (1989) Viability costs of male tail ornaments in a swallow. Nature 339:132–135
Muijres FT, Johansson LC, Barfield R, Wolf M, Spedding GR, Hedenström A (2008) Leading-edge vortex improves lift in slow-flying bats. Science 319:1250–1253
Norberg UM (1995) How a long tail and changes in mass and wing shape affect the cost for flight in animals. Funct Ecol 9:48–54
Rosén M, Spedding GR, Hedenström A (2007) Wake structure and wingbeat kinematics of a house martin *Delichon urbica*. J R Soc Interface 4:659–668
Spedding GR (1986) The wake of a jackdaw (*Corvus monedula*) in slow flight. J Exp Biol 125:287–307
Spedding GR (1987a) The wake of a kestrel (*Falco tinnunculus*) in flapping flight. J Exp Biol 127:59–78
Spedding GR (1987b) The wake of a kestrel (*Falco tinnunculus*) in gliding flight. J Exp Biol 127:45–57
Spedding GR, Rayner JMV, Pennycuick CJ (1984) Momentum and energy in the wake of a pigeon (*Columba livia*) in slow flight. J Exp Biol 111:81–102
Spedding GR, Rosén M, Hedenström A (2003) A family of vortex wakes generated by a thrush nightingale in free flight in a wind tunnel over its entire natural range of flight speeds. J Exp Biol 206:2313–2344
Srygley RB, Thomas ALR (2002) Unconventional lift-generating mechanisms in free-flying butterflies. Nature 420:660–664
Thomas ALR (1997) On the tails of birds. Bioscience 47:215–225
Thomas ALR, Balmford A (1995) How natural selection shapes birds' tails. Am Nat 146:848–868
Tobalske BW, Warrick DR, Clark CJ, Powers DR, Hedrick TL, Hyder GA, Biewener AA (2007) Three-dimensional kinematics of hummingbird flight. J Exp Biol 210:2368–2382
Usherwood JR, Hedrick TL, McGowan CP, Biewener AA (2005) Dynamic pressure maps for wings and tails of pigeons in slow, flapping flight, and their energetic implications. J Exp Biol 208:355–369
Warrick DR, Bundle MW, Dial KP (2002) Bird maneuvering flight: blurred bodies, clear heads. Integr Comp Biol 42:141–148
Warrick DR, Tobalske BW, Powers DR (2005) Aerodynamics of the hovering hummingbird. Nature 435:1094–1097
Willmott AP, Ellington CP, Thomas ALR (1997) Flow visualization and unsteady aerodynamics in the flight of the hawkmoth, *Manduca sexta*. Phil Trans R Soc Lond B 352:303–316

Characterization of vortical structures and loads based on time-resolved PIV for asymmetric hovering flapping flight

T. Jardin · Laurent David · A. Farcy

Abstract Flight agility, resistance to gusts, capability to hover coupled with a low noise generation might have been some of the reasons why insects are among the oldest species observed in nature. Biologists and aerodynamicists focused on analyzing such flight performances for diverse purposes: understanding the essence of flapping wings aerodynamics and applying this wing concept to the development of micro-air vehicles (MAVs). In order to put into evidence the fundamentally non-linear unsteady mechanisms responsible for the amount of lift generated by a flapping wing (Dickinson et al. in Science 284:1954–1960, 1999), experimental and numerical studies were carried out on typical insect model wings and kinematics. On the other hand, in the recent context of MAVs development, it is of particular interest to study simplified non-biological flapping configurations which could lead to lift and/or efficiency enhancement. In this paper, we propose a parametrical study of a NACA0012 profile undergoing asymmetric hovering flapping motions at Reynolds 1000. On the contrary to normal hovering, which has been widely studied as being the most common configuration observed in the world of insects, asymmetric hovering is characterized by an inclined stroke plane. Besides the fact that the vertical force is hence a combination of both lift and drag (Wang in J Exp Biol 207:1137–1150, 2004), the specificity of such motions resides in the vortex dynamics which present distinct behaviours, whether the upstroke angle of attack leads to a partially attached or a strong separated flow, giving more or less importance to the wake capture phenomenon. A direct consequence of the previous remarks relies on the enhancement of aerodynamic efficiency with asymmetry. If several studies reported results based on the asymmetric flapping motion of dragonfly, only few works concentrated on parametrizing asymmetric motions (e.g. Wang in Phys Rev Lett 85:2216–2219, 2000). The present study relies on TR-PIV measurements which allow determination of the vorticity fields and provide a basis to evaluate the resulting unsteady forces through the momemtum equation approach.

1 Introduction

The aerodynamic performances of insects, in terms of lift generation, hover or flight agility, have always fascinated biologists and aerodynamicists. Pioneer works focused on explaining such performances by means of the quasi-steady approach. Walker (1925), von Holst and Kuchemann (1941) and Osborne (1951) introduced the latter (as well as the blade element theory) to flapping flight analysis but were critically reviewed by Weis-Fogh and Jensen (1956) who denoted a lack of preciseness. Jensen (1956) measured both (1) the velocities and angles of attack characterizing the wing motion of a tethered locust by means of a high-speed camera and (2) the lift and drag polar of a dissected wing; giving an evaluation of the quasi-steady aerodynamic forces in forward flight. Later, Weis-Fogh (1973) showed that the quasi-steady approach is suitable for explaining the amount of lift generated by most species of insects but may somehow fail when considering hovering flight. This observation was evidence that unsteady mechanisms are essential in insects aerodynamics. The idea was supported by Ellington (1984) who reviewed the quasi-steady studies carried out on different species in hovering

T. Jardin · L. David (✉) · A. Farcy
LEA, University of Poitiers, CNRS, ENSMA, SP2MI,
bd Marie et Pierre Curie, 86962 Futuroscope, France
e-mail: laurent.david@univ-poitiers.fr

G.K. Taylor, M.S. Triantafyllou, and C. Tropea (Eds.): Animal Locomotion, pp. 285–295.
springerlink.com

flapping flight. As a consequence, researchers then concentrated their efforts on determining the unsteady mechanisms responsible for the generation of strong aerodynamic forces. Basically, apart from the clap-and-fling mechanism (Weis-Fogh 1973) which is specific to particular species, three phenomena may be described: (1) the presence of a leading edge vortex (LEV) or dynamic stall mechanism (Walker 1931; Polhamus 1971; Maxworthy 1979; Dickinson and Götz 1993), (2) the Kramer effect analogous to the supplementary circulation generated by the combined translating and rotating motions (Kramer 1932; Bennett 1970; Dickinson et al. 1999; Sane and Dickinson 2002) and (3) the wake capture phenomenon, arising from the interaction between the wing and its own wake induced during previous strokes (Dickinson 1994; Dickinson et al. 1999; Birch and Dickinson 2003). In addition to these phenomena, one should keep in mind the concept of added mass (or virtual mass) acting as a non-circulatory reaction force due to the accelerated fluid when the wing motion is not constant.

Previous findings mainly emerged from the observation of the flow generated by three-dimensional dynamically scaled robots mimicking the flight of insects. Such configurations (i.e. revolving wings) imply the presence of a velocity gradient along the wing span which may tend to stabilize the behaviour of the leading edge vortex (Maxworthy 1979; van den Berg and Ellington 1997; Liu et al. 1998). On the other hand, two-dimensional approaches proved to be an efficient way for characterizing the flow features when considering the influence of wing kinematics.

It clearly appears that one of the inherent characteristics of unsteady phenomena relies on their dependence to wing kinematics. In order to understand the influence of the latter on the vortex dynamics, hence the generation of lift and drag forces in hovering flapping flight, parametrical numerical and experimental studies were conducted. Sane and Dickinson (2001, 2002) and Singh et al. (2005) experimentally investigated the influence of angle of attack, flip timing, stroke deviation, angular velocity and centre of rotation by means of dynamically scaled robots equipped with 2D force sensors. Similar parameters were numerically analyzed by Sun and Tang (2002) and Wu and Sun (2004). Wang et al. (2004) and Kurtulus (2005) provided a comparison of parametrical studies performed both experimentally and numerically. These previous works focused on the symmetric or "normal" hovering flapping flight configurations, known as the most common configurations in the world of insects, for which the wing translates along a horizontal stroke plane. Alternative configurations rely on the desymmetrization of the motion (e.g. different upstroke and downstroke angles of attack) resulting in an inclined stroke plane in order to maintain hovering; i.e. zero mean horizontal force. The particularity of such asymmetric motions is that the vertical force necessary to keep the insect aloft is hence a combination of both lift and drag (Wang 2004). Several studies reported results based on the flight of the dragonfly (Somps and Luttges 1985; Gustafson and Leben 1991; Wang 2000; Sun and Lan 2004; Thomas et al. 2004).

Recently, the concept of flapping wings appeared as a possible alternative to the conventional fixed and rotary wings in the development of micro air-vehicles (MAVs). This new generation of unmanned aircraft is characterized by a maximum dimension of 15 cm, which places the corresponding aerodynamic flows in the range of low Reynolds numbers (10^2–10^4), comparable to the ones found in insect flight. Thus, in order to optimize such flying devices, it is of particular interest to study simplified non-biological flapping motions which could lead to lift and/or efficiency enhancement. Platzer and Jones (2006) proposes a review of the recent works dedicated to the development of MAVs. The questions of flapping modes, amplitudes, frequencies for optimum cruise flight as well as hovering flight or wing interactions are addressed, giving rise to the authors' prototype.

In this paper, we present an experimental parametrical study of asymmetric hovering flapping motions, which, to our knowledge, has not been yet proposed in the literature. Time Resolved Particle Image Velocimetry (TR-PIV) is performed on a dynamically scaled NACA0012 profile at Reynolds 1000. The resulting flow fields allow both (1) the analysis of the spatial and temporal behaviour of the wake structure and (2) the evaluation of correlated unsteady forces determined by means of the momentum equation approach (Noca et al. 1997; Unal et al. 1997). The comparison with symmetric hovering flapping motions (Kurtulus et al. 2008) reveals significant different vortex dynamics principally arising from the absence of significant wake capture during downstroke when the upstroke angle of attack is set to a low value (e.g. 20°).

2 Experimental tools

2.1 Wing kinematics

The wing kinematics result from the combination of translating and rotating motions as shown in Fig. 1. Basically, the flapping motion may be separated into different phases whether the wing is translating at constant speed and fixed angle of attack (region T) or is subjected to both varying translation speed and rotating motion (regions R). The rotation is applied around a spanwise axis located ¼ chord away from the leading edge. Region T and regions R are, respectively 4- and 1-chord long, so that the wing travels along a total course of 6 chords during one stroke.

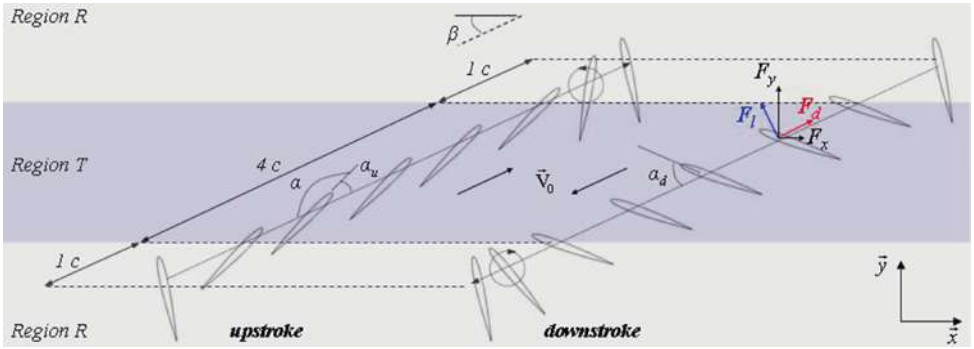

Fig. 1 Description of the flapping motion

The constant wing velocity V_0 reached during the pure translation phases (region T) is calculated with respect to the Reynolds number such that:

$$Re = \frac{cV_0}{V} \tag{1}$$

where c is the chord of the NACA0012 profile and υ the kinematic viscosity. The parametrical study relies on the corresponding downstroke and upstroke angles of attack α_d and α_u. A total of 9 configurations are investigated, α_d and α_u being set as couples to (30°, 10°), (30°, 20°), (30°, 30°), (45°, 20°), (45°, 30°), (45°, 45°) and (60°, 20°), (60°, 30°), (60°, 45°). These choices are motivated by the need to generate strong separated flow during downstroke and furthermore cover the typical values observed in nature.

The translating and rotating velocities in regions R follow fourth order polynomial motion laws, ensuring their continuity throughout the flapping period. The translating velocity V and the angle of attack α are, respectively 0 and $(180 + \alpha_d - \alpha_u)/2$ (°) at the end of a stroke. Their evolutions during a flapping period T are displayed in Fig. 2. Note that the period T, starting at the beginning of upstroke, is calculated as:

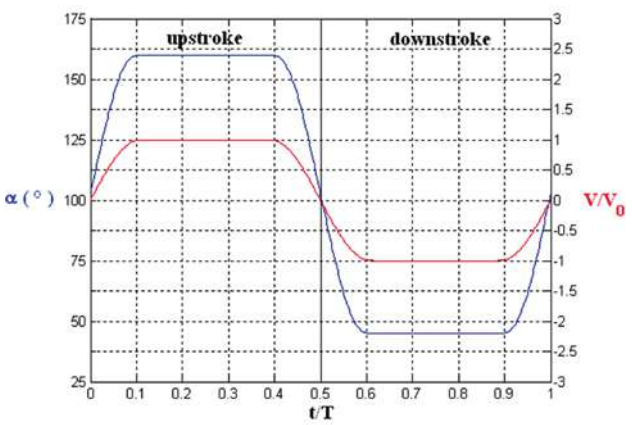

Fig. 2 Temporal evolutions of the angle of attack and translating velocity ($\alpha_d = 45°$, $\alpha_u = 20°$)

$$T = \frac{4c}{|V_0|}\left(\frac{\pi}{2} + 2\right) \tag{2}$$

leading to a flapping frequency f of approximately 10 Hz in real airflow configurations (with $c = 10$ mm). Dynamical scaling using the Reynolds similarity brings $f = 0.02$ Hz for the experimental water flow configurations described in the following section (with $c = 60$ mm).

2.2 Experimental setup

The experiments are conducted in a $1 \times 1 \times 2$-m^3 water tank made of altuglas. A NACA0012 profile of chord 60 mm and span 50 cm placed in the water tank translates and rotates according to programmed motion laws. The translational and rotational motions are driven separately through the use of two servo-controlled motors. Their respective mechanical transmissions are achieved by means of an endless screw and pulleys as shown in Fig. 3a. The airfoil is connected at both ends to Plexiglas plates which limit three-dimensional effects, i.e. spanwise flow.

Two JAI 8-bits cameras are placed side by side, focusing on the spanwise symmetry plane of the airfoil. The resolution of the sensors is 1,600 × 1,200 pixels with a pixel size of 7.4 × 7.4 µm. Each camera is equipped with a 50-mm focal length lens, $F_\#$ 2.8, for a 370 × 280-mm^2 area imaging. A continuous argon laser system (Argon Spectra-Physics of 10 W maximum power) is used to provide a 4.5-W laser. 30% of the laser is guided through spherical and cylindrical lenses, illuminating one side of the airfoil; 70% is transported by means of an optical fiber to illuminate the opposite side. This method is adopted to limit the shadow effects (Fig. 3). Hollow silver coated glass particles with a mean diameter of 15 µm are used for the seeding. The concentration is defined as $C = 1.35 \times 10^9$ (particles/m^3) in order to ensure a proper number of particles per PIV correlation interrogation window (typically between 10 and 20).

TR-PIV is performed by taking images every 1/1,000 period. The time step ($\Delta t \approx 50$ ms) allows an accurate calculation of both velocity and acceleration flow fields.

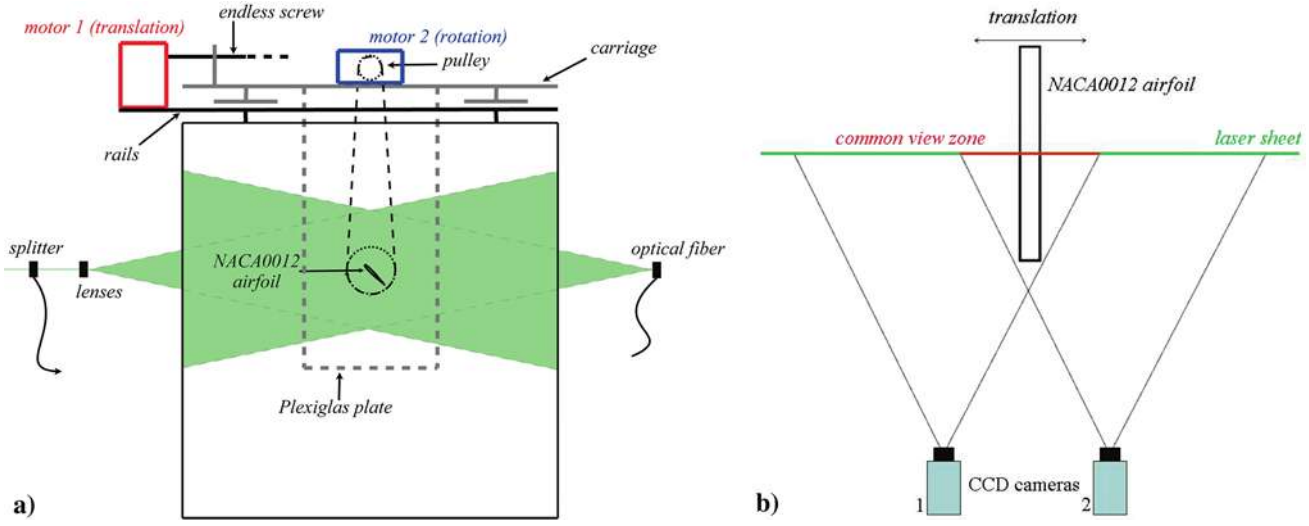

Fig. 3 Experimental setup: front view (**a**) upside view (**b**)

The acquisition is synchronised with the servo-controlled motor variators which deliver a tension signal at the beginning of the seventh period of the flapping motion for which the flow is ensured to be periodical.

2.3 Post-processing

The two-dimensional velocity flow fields for each camera are deduced from the TR-PIV images using the 7.2 LaVision software. A multipass algorithm with a final interrogation window size of 16 × 16 pixels and 50% overlapping is applied. Image deformation and round pyramidal weighting function are used. Spurious velocities are identified and replaced using both peak ratio and median filters. The average percentage of spurious vectors calculated at each instant over the whole flapping cycle (1,000 instants) is roughly 2%. The final velocity flow fields are reconstructed using kriging interpolation from the combination of both camera information and known boundary conditions on the airfoil surface (Fig. 3b). The advantages of using two cameras are (1) to increase the spatial resolution and (2) to avoid inaccessible regions due to the perspective effect. The cameras share a common view zone so that the velocity flow fields on the left and right side of the profile come from the left and right cameras, respectively. The final flow fields have an area of 570 × 280 mm^2.

2.4 Investigation methods

The flow topology is analyzed by means of the adimensional vorticity flow fields computed from the basis of TR-PIV velocity flow fields as shown in Eq. 3 for a two-dimensional flow. The vorticity criterion is here convenient since the flow is assumed to be generally laminar, exhibiting distinguished shear layers and vortical structures (Jeong and Hussain 1995).

$$\omega_z^* = \frac{c}{V_0}\left(\frac{\partial u}{\partial y} - \frac{\partial v}{\partial x}\right) \tag{3}$$

The spatial and temporal behaviours of the vortical structures are correlated with the unsteady lift and drag determined by means of the momentum equation approach. The latter relies on the integration of flow variables inside and around a control volume surrounding the airfoil (Noca et al. 1997, 1999; Unal et al. 1997) (Fig. 4). Equation 4 gives the instantaneous force $\vec{F}(t)$ experienced by the airfoil in function of four components:

$$\vec{F}(t) = -\rho \iiint_V \frac{\partial \vec{V}}{\partial t} \mathrm{d}V - \rho \iint_S (\vec{V}\cdot\vec{n})(\vec{V} - \vec{V_S})\mathrm{d}S - \iint_S P\vec{n}\,\mathrm{d}S + \iint_S \bar{\bar{\tau}}\vec{n}\,\mathrm{d}S \tag{4}$$

where $\vec{n}$ is the normal to the control surface S limiting the control volume V, ρ the fluid density, $\vec{V}$ the flow velocity

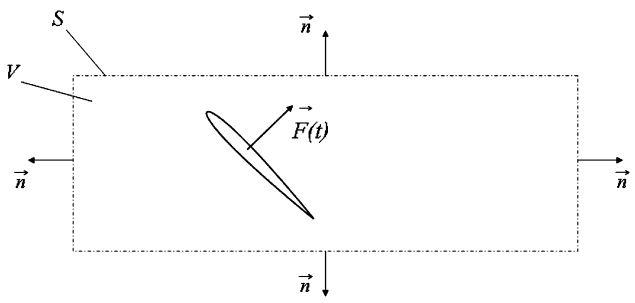

Fig. 4 Control volume definition

vector, $\vec{V}_S$ the velocity of the control volume and $\bar{\bar{\tau}}$ the viscous stress tensor. The unsteady and convective terms (the first two right hand side contributions) are directly deduced from the TR-PIV velocity flow fields and account for the rate of change of momentum due to the flow unsteadiness within the control volume and the convection across the control surface, respectively. Note that the convective term is not integrated over the airfoil surface since equals zero for a no through flow boundary condition. The third term represents the normal stresses acting on the control surface. Its deduction requires the knowledge of the pressure p, obtained through the integration of the pressure gradient along the control surface. The pressure gradient is calculated from the momentum equation:

$$\frac{\mathrm{D}\vec{V}}{\mathrm{D}t} = -\frac{1}{\rho}\nabla p + \nu\Delta\vec{V}. \tag{5}$$

The last term accounts for the viscous stresses on the control surface. It is derived from the velocity flow fields, but may be neglected for preponderant pressure force flows or if the control surface is sufficiently far away from the airfoil.

The momentum equation approach is particularly appealing since it is non-intrusive and allows an accurate correlation between flow behaviour and force mechanisms, which is not a priori the case when separate techniques are used. Furthermore, the method is convenient for measuring forces at low Reynolds numbers and on moving bodies. For such cases, the use of piezoelectric gauges introduces non-negligible relative errors caused by the range of measures (e.g. 10-g loads) as well as the presence of an inertial component (for non-constant motion), respectively. Details concerning the numerical solving methods of Eq. 4 applied on a flapping flight configuration may be found in Jardin et al. (2008). Nevertheless, we may precise that the pressure term stands as the critical point since the pressure integration by means of Eq. 5 is subjected to both (1) error emphasizing due to the presence of differential operators and (2) error propagation phenomenon. Besides, as a result to the position of the integration limits, the contribution of this pressure term is enhanced in the case of drag prediction comparatively to lift prediction, involving different level of accuracy for both components. What's more, one should expect the pressure contribution; hence, the result accuracy, to be specifically strong in large wake configurations. Previous tests on numerical data subjected to ±10% random noise on the velocity vectors revealed a mean error on the unsteady, convective and pressure contributions of 2, 3.5, 11% and 0.5, 0.5, 6% for the drag and lift predictions, respectively (David et al. 2009).

2.5 Aerodynamic indicators

The unsteady aerodynamic force $\vec{F}(t)$ is decomposed into the lift and drag components F_l and F_d, respectively perpendicular and collinear to the stroke plane as shown in Fig. 1. In the specific cases of symmetric flapping motions, the mean drag magnitude generated over a stroke is quasi-identical whether the airfoil is going downstroke or upstroke. Thus, setting the stroke plane as the horizontal axis brings $F_x = \pm F_\mathrm{d}$ and $F_y = F_\mathrm{l}$ ensuring the hovering flight condition (i.e. zero mean horizontal force). In this paper, we focus on asymmetric flapping motions, the asymmetry being introduced through non-equal downstroke and upstroke angles of attack. For such cases, the mean drag magnitude over a stroke is different whether the airfoil is going downstroke or upstroke, such that the stroke plane should be tilted to maintain hovering. The vertical and horizontal aerodynamic forces are hence a combination of both lift and drag, depending on the stroke plane incidence β (Eq. 6):

$$\begin{aligned} F_x &= \pm F_\mathrm{d}\cos(\beta) - F_\mathrm{l}\sin(\beta) \\ F_y &= F_\mathrm{l}\cos(\beta) \pm F_\mathrm{d}\sin(\beta) \end{aligned} \tag{6}$$

(+ or − signs, respectively used for downstroke or upstroke), β being computed for prescribed motion laws to satisfy the hovering flight condition:

$$\int_0^T F_x(t)\mathrm{d}t = 0 \tag{7}$$

Consequently, the common definition of the efficiency ratio $F_\mathrm{l}/F_\mathrm{d}$ loses its significance since F_l no longer represents the effective lifting force. A more suitable indicator of the aerodynamic efficiency is considered as the ratio F_y/F_d. This definition a priori suggests enhanced efficiency ratios, the harmful influence of F_d being weakened through its contribution to F_y.

The force components F_x, F_y, F_d, F_l are adimensionalized using the downstroke and upstroke translating velocity V_0 and the chord of the airfoil c. The aerodynamic coefficients are defined as:

$$C_i = \frac{2F_i}{\rho c V_0^2}. \tag{8}$$

3 Results and discussion

The aim of this section is to compare the unsteady loads resulting from different asymmetric flapping motions and to provide physical explanations by correlating them to the corresponding time dependent vorticity flow fields. In view of flapping wing concept application to MAVs, the

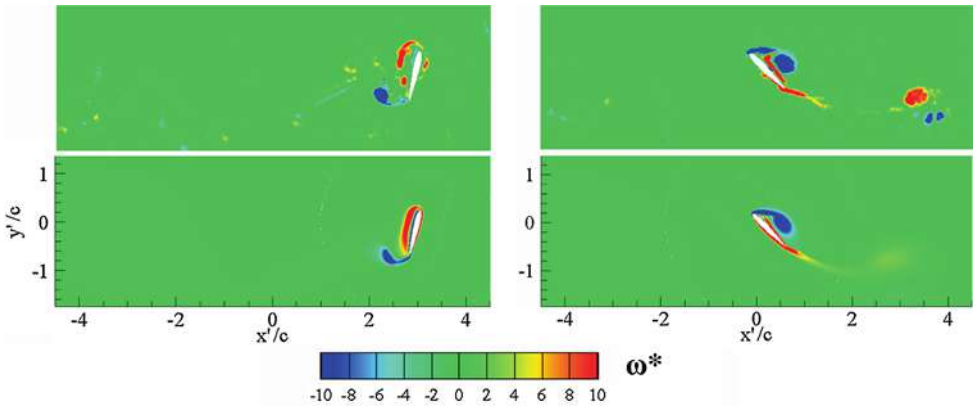

Fig. 5 Adimensional experimental (*top*) and DNS (*bottom*) vorticity flow fields at $t/T = 0.5$ (*left*) and $t/T = 0.75$ (*right*)

aerodynamic performances (e.g. lifting force, efficiency ratio) of such non-biological simplified motions are calculated and analysed. A brief confrontation with direct numerical simulation (DNS) results is first performed for both validating the momentum equation approach and demonstrate continuity with the previous complementary work of Kurtulus et al. (2008).

3.1 Experimental versus numerical results

For sake of conciseness, the comparison between experimental and numerical results is limited to the downstroke part of the asymmetric configuration $\alpha_d = 45°$, $\alpha_u = 20°$. The numerical loads and vorticity flow fields are obtained by directly solving the two-dimensional Navier–Stokes equations using a moving mesh flow solver (Kurtulus et al. 2005). Figure 5 displays the experimental and numerical adimensional vorticity flow fields at stroke reversal ($t/T = 0.5$) and in the middle of downstroke ($t/T = 0.75$). Figure 6 shows the temporal evolution of the corresponding lift and drag coefficients during the totality of downstroke.

The comparison shows good agreement between the experimental and numerical flow topologies, both in the existence of the main vortical structures and in their vorticity levels. However, the numerical solver demonstrates difficulties predicting their exact location and temporal evolution (e.g. shedding); and hence, exhibits slight discrepancies with the time-dependent experimental aerodynamic lift. We can observe from Fig. 6 that the experimental and numerical lifts match until the shedding of the leading edge vortex (represented as a negative vorticity region on the extrados at time $t/T = 0.75$, Fig. 5) which leads to a lower experimental lift at time $t/T = 0.85$. The prediction of drag is more delicate both numerically and experimentally. Indeed, the flow solver is subjected to numerical diffusivity, as observed when looking at the vorticity levels of the starting vortex at $t/T = 0.75$ (Fig. 5), which may tend to underestimate the drag. Furthermore,

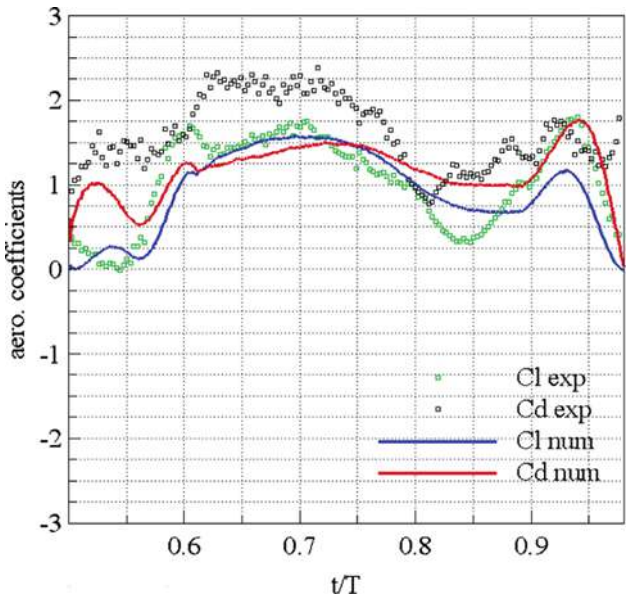

Fig. 6 Temporal evolution of the experimental and DNS downstroke aerodynamic coefficients C_l and C_d

the deduction of the experimental drag imposes to calculate the pressure in the wake, introducing non-negligible errors (Jardin et al. 2008). Thus, the comparison between numerical and experimental drags shows an offset between characteristic levels but demonstrates comparable temporal tendencies. Besides, the interesting point arising from this comparison is that similar experimental and numerical vortical flow fields lead to comparable experimental and numerical aerodynamic loads. Also, if the drag prediction may be subjected to quantitative uncertainties, the present parametrical study may accurately rely on qualitative comparisons.

3.2 Wake topology

The downstroke and upstroke angles of attack are chosen as parameters. The parametrical study is conducted fixing

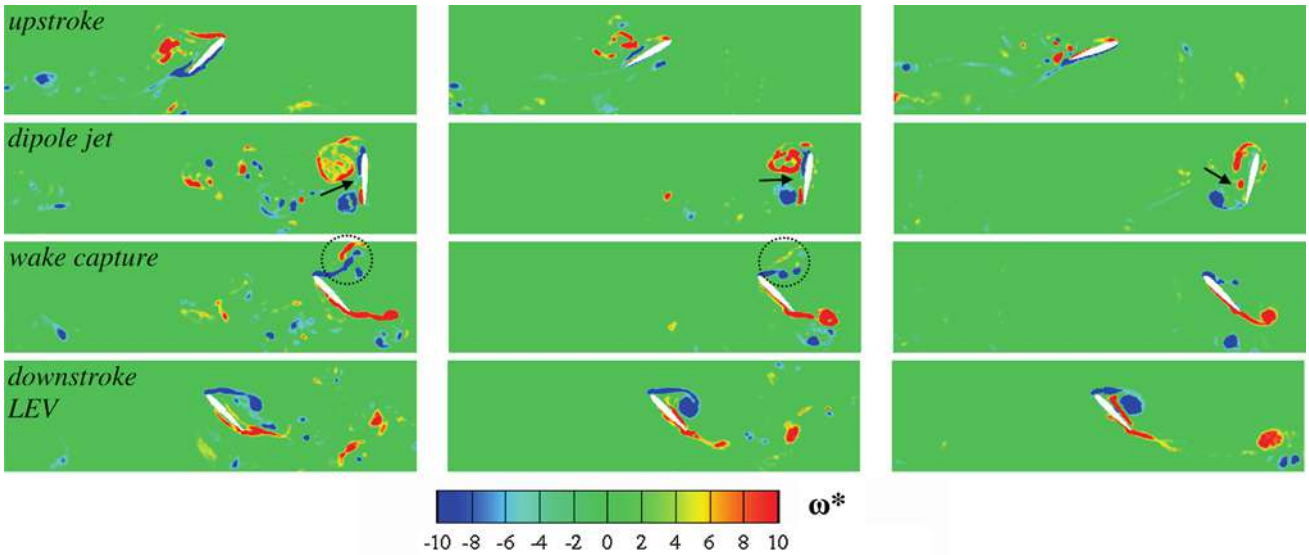

Fig. 7 Adimensional vorticity flow fields at times $t/T = 0.25, 0.5, 0.6, 0.75$ (*top to bottom*) for the configurations $\alpha_d = 45°$, $\alpha_u = 45°, 30°, 20°$ (*left to right*)

the downstroke angle of attack to either 30°, 45° or 60°; hence, distinguishing three groups. For each group, three values of the upstroke angle of attack are tested, leading to a total of nine configurations. The configurations of a similar group have quasi identical downstroke kinematics, thus differing quasi exclusively on their upstroke kinematics. As a consequence, inside a specific group, the comparison of the vortex dynamics observed during the downstroke of the different configurations directly reveals the influence of the wake capture phenomenon. The main analysis is carried out on the $\alpha_d = 45°$ group, for which the normal hovering configuration ($\alpha_u = 45°$) is described in details in Kurtulus et al. (2008). Figure 7 displays the adimensional vorticity flow fields for the three $\alpha_d = 45°$ configurations. Note that the stroke plane is represented horizontally to facilitate comparisons.

In the particular normal hovering configuration, the upstroke angle of attack is set to 45°, inducing a highly unsteady vortical wake at $t/T = 0.25$. At the end of upstroke ($t/T = 0.5$), strong leading and trailing edge vortices (LEV and TEV) are attached to the airfoil, forming a dipole which generates a fluid jet oriented towards the intrados. This jet acts as a drag enhancer and contributes to lower the aerodynamic efficiency. As the airfoil rotates and initiates the downstroke translational phase, the LEV is captured, accelerating and strengthening the leading edge separation; hence, the formation of a new counter rotating downstroke LEV ($t/T = 0.6$). The latter is carried away from the airfoil under the action of the upstroke LEV without being instantaneously shed ($t/T = 0.75$). Its consequent relative position to the airfoil extrados implies relatively weak aerodynamic forces.

Asymmetry is introduced by lowering the upstroke angle of attack, while keeping the downstroke angle of attack fixed to 45°. In the first asymmetric case, α_u is set to 30°, leading, as in the normal hovering configuration, to a strong separated flow during the upstroke translational phase. However, relatively to the normal hovering configuration, the dimensions and strengths of the vortices are here less pronounced. At stroke reversal, the vortex dipole is hence likely to produce a weaker fluid jet whose influence on aerodynamic efficiency is less penalizing though since it partially contributes to the generation of vertical aerodynamic force (the stroke plane being inclined). Furthermore, a direct consequence of reduced vortex dimensions and strengths relies on the specificity of the wing/wake interaction. At time $t/T = 0.6$, the influence of the upstroke LEV on the formation of a new downstroke LEV is lower than observed for the normal hovering case. Thus, we can remark that the downstroke LEV remains closer to the airfoil surface, presupposing enhanced lift and drag ($t/T = 0.75$). The asymmetry is pushed further in the second asymmetric case where α_u is set to 20°. In this particular configuration, the upstroke is dominated by an attached flow between time $t/T = 0.2$ and time $t/T = 0.35$, besides the fact that α_u is above the critical stall incidence for a NACA0012 profile. This attachment may be explained by the presence of a fluid downwash, resulting from the lift generation of the previous strokes, and which tends to decrease the effective angle of attack. The influence of the fluid downwash is less perceptive at the end of the strokes such that a separation still lately occurs. The growth of the resulting upstroke LEV is limited, leading to a weak vortex dipole at stroke reversal. In contrast to the

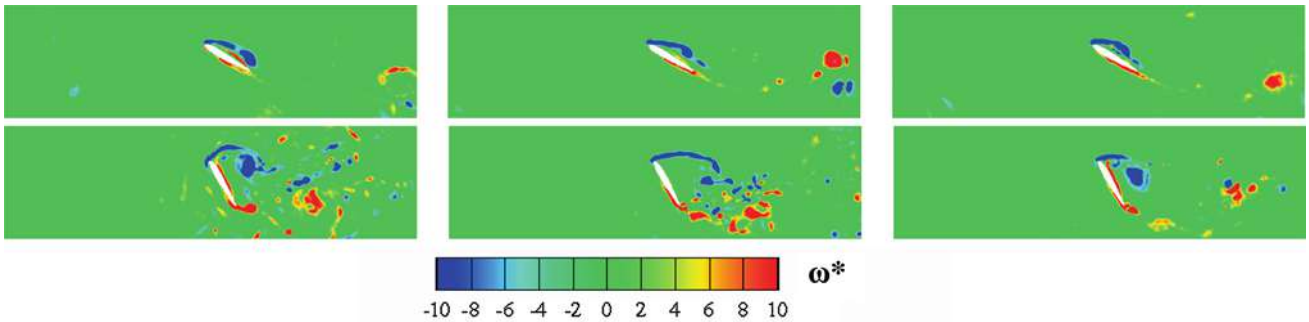

Fig. 8 Adimensional vorticity flow fields at times $t/T = 0.75$ for the configurations $\alpha_d = 30°$ (*top*), $\alpha_u = 30°$, 20°, 10° (*left to right*) and $\alpha_d = 60°$ (*bottom*), $\alpha_u = 45°$, 30°, 20° (*left to right*)

previous configurations, as the wing initiates the downstroke phase, the upstroke LEV slides under the intrados instead of being pushed above the leading edge. Therefore, the upstroke LEV has no influence on the formation of the downstroke LEV which develops smoothly on the extrados, forming a high lift generating low pressure region.

Figure 8 shows the adimensional vorticity flow fields at time $t/T = 0.75$ for the $\alpha_d = 30°$ and $\alpha_d = 60°$ groups. When $\alpha_d = 30°$, α_u is successively fixed to 30°, 20° and 10°. In the normal hovering case (30°, 30°), the position of the upstroke LEV is such that it slides under the intrados as the wing initiates the downstroke phase. On the contrary, in the first asymmetric case (30°, 20°), the upstroke LEV is split into two smaller structures, one being ejected over the leading edge, hence slightly affecting the formation of the downstroke LEV, the other sliding under the intrados. In the last asymmetric case (30°, 10°), because of the weak value of the upstroke angle of attack, the upstroke wake exhibits closely attached structures which slide under the intrados at stroke reversal. Consequently, it is denoted from Fig. 8 that the downstroke LEV is closer to the airfoil surface in the (30°, 30°) and (30°, 10°) configurations than in the (30°, 20°) one, giving additional evidences of the wake capture phenomenon. Nevertheless, despite the absence of significant wake capture in both cases, the (30°, 30°) and (30°, 10°) downstroke LEVs are not identical. This difference may arise from different rotation speed or more likely from different downwash intensity. When $\alpha_d = 60°$, the corresponding cases demonstrate more complex behaviours. The upstroke wake of the (60°, 45°) configuration is highly unsteady and vortical resulting in a severe wing/wake interaction at the beginning of upstroke. A first downstroke LEV is hence rapidly formed and shed, leaving room to a second downstroke LEV which still tends to detach from the extrados at time $t/T = 0.75$. In the (60°, 30°) configuration, the wake capture is less pronounced such that the first downstroke LEV is not promptly shed, leading to a highly stretched second downstroke LEV. In the last (60°, 20°) configuration, the upstroke LEV sweeps under the intrados as previously observed for low upstroke angles of attack. The downstroke LEV is thus not influenced by the previous wake.

3.3 Aerodynamic performances

The analysis of the vortical flow fields revealed that the desymmetrization of flapping motions reduces the effect of wake capture; hence, leading in most cases to a closely attached downstroke LEV. Consequently, the latter being assimilated to a low pressure suction region, the generation of aerodynamic loads should be enhanced during downstroke comparatively to normal hovering flapping flight configurations. Figure 9 confronts the temporal evolution of the downstroke lift component of each experimented configuration belonging to a similar α_d group. We remind that within a group, the downstroke kinematics of each configuration are roughly identical, resulting in equivalent quasi-steady forces. Notwithstanding this similarity, Fig. 9 denotes significantly different aerodynamic lift coefficients during the downstroke pure translational phase (t/T [0.61; 0.89]), consistent with the previous remarks on the attachment of the downstroke LEV. Precisely, it is shown that the highest downstroke lifts are attained for smaller upstroke angles of attack (green squares). Furthermore, noticeable different tendencies at the beginning of downstroke are exposed, supporting the evidence of dissimilar wing/wake interactions. In particular, at $t/T = 0.55$, the upstroke LEV is pushed over the leading edge for the configurations (45°, 45°) and (45°, 30°) resulting in a rapid augmentation of the lift coefficient which reaches approximately 1.5. Notice that this lift bump has been put into evidence by Birch and Dickinson (2003) and similarly attributed to the wake capture phenomenon. On the contrary, the upstroke LEV slides under the intrados for the configuration (45°, 20°), inhibiting the lift deriving from the wing acceleration ($Cl = 0$ at $t/T \approx 0.55$). Finally, the additional circulation provided by the combined translating and rotating motions (Kramer effect) implies the presence

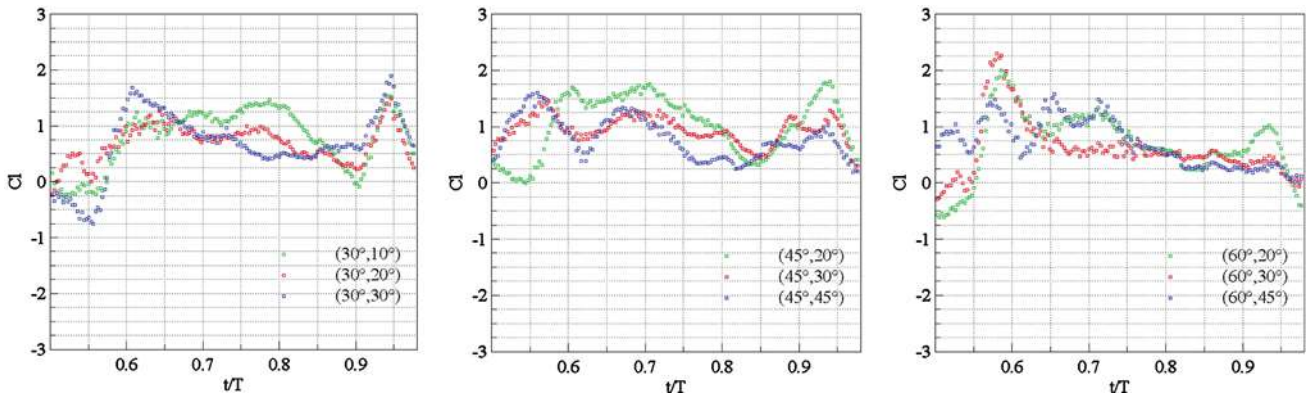

Fig. 9 Time-dependent downstroke lift coefficients of the nine configurations grouped according to α_d values ($\alpha_d = 30°$, 45° and 60° from *left to right*)

of a second lift bump at the end of downstroke as measured by Sane and Dickinson (2002). This bump is less perceptive when the difference between α_d and α_u is low (e.g. $\alpha_d = 60°$ configurations), i.e. weakened rotation speed. Consequent to these remarks, the downstroke time-averaged lift coefficients are, respectively 0.78, 0.92 and 1.02, for the configurations (45°, 45°), (45°, 30°) and (45°, 20°), proving the benefit of desymmetrization. It is not clear whether the asymmetric configurations numerically studied by Wang (2000, 2004) do benefit from such vortex dynamics (more or less significant wake capture) or not.

Despite the influence of the vortex dynamics on the production of aerodynamic forces, it is of interest to highlight the influence of tilting the stroke plane on the contributions of the lift and drag components to the resulting vertical force; hence, the efficiency ratio. Indeed, as previously expressed, the introduction of asymmetry implies an inclined stroke plane in order to verify the hovering flight condition (Eq. 7). For the $\alpha_d = 45°$ group, the calculation of the mean lift and drag coefficients leads to $\beta = -2°$, 23° and 38° for the configurations (45°, 45°), (45°, 30°) and (45°, 20°). The respective resulting mean vertical force coefficients (averaged over a flapping period T) are obtained by means of Eq. 6: $\overline{C_y} = 0.85$, 1.07 and 1.23. These results suggest that despite the harmful influence of the upstroke phase, for which the drag component tends to prevent the wing from keeping aloft, asymmetric motions generate enhanced vertical aerodynamic force. Relative to the normal hovering configuration, the increase reaches 45%. Nevertheless, one should keep in mind the difficulties linked to the experimental determination of drag through the momentum equation approach (Jardin et al. 2008), such that presented levels are likely to be slightly overestimated. Finally, the mean efficiency ratios are found to be improved: $\overline{C_{er}} = 0.53$, 0.82 and 1.02. The influence of desymmetrization on aerodynamic performances is roughly identical for the $\alpha_d = 30°$ group, the efficiency ratio coefficients being 0.90, 0.94 and 1.42 for the respective configurations (30°, 30°), (30°, 20°) and (30°, 10°). However, as previously expressed, the enhanced value of the mean downstroke lift of the asymmetric configuration (30°, 10°) compared to the normal configuration (30°, 30°) (respectively 0.78 and 0.67) does not arise from the absence of significant wake capture, but more likely from a weaker fluid downwash which may confine the LEV closer to the extrados. The configurations of the $\alpha_d = 60°$ group are characterized by large messy downstroke wakes propitious to errors on the pressure determination while predicting the loads. Precisely, the influence of specific parameters such as the dimensions and position of the control volume is amplified comparatively to the other α_d groups, which may lead to 40% discrepancies on the instantaneous values when wing/wake interactions occur. What's more, the complex fluid dynamics exhibited in such cases make the interpretation and the comparison of the resulting time-dependent coefficients particularly delicate. Nevertheless, the mean efficiency ratios obtained for the (60°, 45°), (60°, 30°) and (60°, 20°) (respectively 0.49, 0.81 and 1.31) once again corroborate the previous results, suggesting the beneficial influence of desymmetrization. As a conclusion, despite the "not so crucial" importance of the influence of the wake capture on the attachment of the downstroke LEV (the flow being strongly separated in all cases), it is probable that asymmetric configurations highly benefit from the contribution of drag to vertical force.

The previous calculations permit the representation of instantaneous aerodynamic force vectors during the flapping motions as displayed in Fig. 10 for the $\alpha_d = 45°$ group. Such representation puts into evidence the phenomenon of wake capture as well as the Kramer effect through the presence of strong vectors, respectively at the beginning and at the end of a stroke. As previously expressed, these mechanisms are also denoted by bumps in the temporal evolution of the lift coefficients (Fig. 9). Furthermore, it

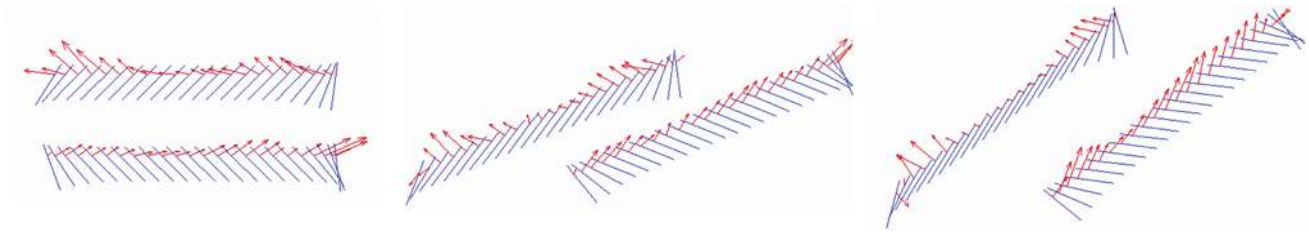

Fig. 10 Instantaneous aerodynamic force vectors for the configurations (45°, 45°), (45°, 30°) and (45°, 20°) (*left to right*)

clearly appears that the (45°, 20°) configuration fully benefits from the contribution of drag, the force vectors being nearly vertical at the beginning of downstroke.

4 Conclusion

Flapping wings recently appeared to be a high aerodynamic performance lifting device at low Reynolds numbers. In order to consider such concept as a possible alternative to the conventional fixed and rotary wings for the development of MAVs, it is of interest to investigate non-biological wing profiles and kinematics. The understanding of the influence of the latter on the aerodynamic performances of flapping wings may lead to lift/efficiency enhancement. In this paper, an experimental parametrical study of simplified two-dimensional asymmetric hovering flapping motions was carried out using 2D/2C TR-PIV measurements as a basis to evaluate both time-dependent vorticity flow fields and unsteady aerodynamic loads. Relative to normal hovering configurations, asymmetry was introduced by differentiating the downstroke and upstroke angles of attack, chosen as parameters. It is demonstrated that lowering the upstroke angle of attack while keeping a fixed downstroke angle of attack results in a reduced upstroke wake whose influence on the formation of the downstroke leading edge vortex (through the wake capture phenomenon) is hence significantly weakened. Furthermore, in some specific cases, the wake capture phenomenon no longer affects the formation of the leading edge vortex which thus develops smoothly, closely attached to the extrados. The leading edge vortex being assimilated to a low pressure suction region, such characteristics (i.e. vortex position, strengths and dimensions) lead to enhanced downstroke lift and drag. Besides, through the hovering flight condition, desymmetrization leads to an inclined stroke plane which implies that both lift and drag contribute to the production of a lifting force. Consequent to these fluid dynamics and flight mechanics considerations, asymmetric hovering flapping motions are found to be specifically efficient in comparison to normal hovering flapping motions. Such remarks support the numerical work of Wang (2004) who proposed efficient asymmetric configurations. From this point, it is of interest to introduce other parameters to asymmetric configurations in order to further increase aerodynamic performances. As an example, the augmentation of the upstroke velocity is suggested, hence minimizing the harmful influence of upstroke relative to downstroke.

References

Bennett L (1970) Insect flight: lift and the rate of change of incidence. Science 167:177–179

Birch JM, Dickinson MH (2003) The influence of wing–wake interactions on the production of aerodynamic forces in flapping flight. J Exp Biol 206:2257–2272

David L, Jardin T, Farcy A (2009) Validation of unsteady drag and lift evaluation by TR-PIV. Meas Sci Technol (in revision)

Dickinson MH (1994) The effects of wing rotation on unsteady aerodynamic performance at low Reynolds number. J Exp Biol 192:179–206

Dickinson MH, Götz KG (1993) Unsteady aerodynamic performance of model wings at low Reynolds numbers. J Exp Biol 174:45–64

Dickinson MH, Lehmann FO, Sane SP (1999) Wing rotation and the aerodynamic basis of insect flight. Science 284:1954–1960

Ellington CP (1984) The aerodynamics of hovering insect flight I–V. Philos Trans R Soc Lond B 305:1–181

Gustafson KE, Leben R (1991) Computation of dragonfly aerodynamics. Comput Phys Commun 65:121

Jardin T, David L, Farcy A, Chatellier L (2008) Correlation between vortex structures and unsteady loads for flapping motion in hover. Fourteenth international symposium on applications of laser techniques to fluid mechanics, Lisbon

Jensen M (1956) Biology and physics of locust flight. III. The aerodynamics of locust flight. Philos Trans R Soc Lond B 239:511–552

Jeong J, Hussain F (1995) On the identification of a vortex. J Fluid Mech 285:69–94

Kramer M (1932) Die zunahme des maximalauftriebes von tragflugeln bei plotzlicher anstellwinkelvergrosserung. Z Flugtech Motorluftschiff 23:185–189

Kurtulus DF (2005) Numerical and experimental analysis of flapping motion in hover. Application to micro air-vehicles. PhD Thesis, Laboratoire d'Etudes Aérodynamiques, Université de Poitiers

Kurtulus DF, Farcy A, Alemdaroglu N (2005) Unsteady aerodynamics of flapping airfoil in hovering flight at low Reynolds numbers. AIAA 2005–1356, Reno

Kurtulus DF, David L, Farcy A, Alemdaroglu N (2008) Aerodynamic characteristics of flapping motion in hover. Exp Fluids 44:23–36

Liu H, Ellington CP, Kawachi K, van den Berg C, Willmott AP (1998) A computational fluid dynamic study of hawkmoth hovering. J Exp Biol 201:461–477

Maxworthy T (1979) Experiments on the Weis–Fogh mechanism of lift generation by insects in hovering flight Part 1. Dynamics of the 'fling'. J Fluid Mech 93:47–63

Noca F, Shiels D, Jeon D (1997) Measuring instantaneous fluid dynamic forces on bodies, using only velocity fields and their derivatives. J Fluids Struct 11:345–350

Noca F, Shiels D, Jeon D (1999) A comparison of methods for evaluating time-dependent fluid dynamic forces on bodies, using only velocity fields and their derivatives. J Fluids Struct 13:551–578

Osborne MFM (1951) Aerodynamics of flapping flight with application to insects. J Exp Biol 28:221–245

Platzer MF, Jones KD (2006) Flapping wing aerodynamics—progress and challenges. AIAA 2006–500, Reno

Polhamus EC (1971) Predictions of vortex-lift characteristics by a leading-edge suction analogy. J Aircr 8:193–199

Sane SP, Dickinson MH (2001) The control of flight force by a flapping wing: lift and drag production. J Exp Biol 204:2607–2626

Sane SP, Dickinson MH (2002) The aerodynamic effects of wing rotation and a revised quasi-steady model of flapping flight. J Exp Biol 205:1087–1096

Singh B, Ramasamy M, Chopra I, Leishman J (2005) Insect-based flapping wings for micro hovering air vehicles: experimental investigations. American Helicopter Society International Specialists Meeting on Unmanned Rotorcraft, Phoenix

Somps C, Luttges M (1985) Dragonfly flight: novel uses of unsteady separated flows. Science 228:1326–1329

Sun M, Lan S (2004) A computational study of the aerodynamic forces and power requirements of dragonfly hovering. J Exp Biol 207:1887–1901

Sun M, Tang J (2002) Lift and power requirements of hovering flight in *Drosophila virilise*. J Exp Biol 205:2413–2427

Thomas ALR, Taylor GK, Srygley RB, Nudds RL, Bomphrey RJ (2004) Dragonfly flight: free-flight and tethered flow visualizations reveal a diverse array of unsteady lift-generating mechanisms, controlled primarily via angle of attack. J Exp Biol 207:4299–4323

Unal MF, Lin JC, Rockwell D (1997) Force prediction by PIV imaging: a momentum-based approach. J Fluids Struct 11:965–971

van den Berg C, Ellington CP (1997) The three-dimensional leading-edge vortex of a hovering model hawkmoth. Philos Trans R Soc Lond B 352:329–340

von Holst E, Kuchemann D (1941) Biological and aerodynamical problems of animal flight. Naturwissenschaften 46:39–58

Walker GT (1925) The flapping flight of birds. J R Aeronaut Soc 29:590–594

Walker PB (1931) Growth of circulation about a wing and an apparatus for measuring fluid motion. ARC report

Wang ZJ (2000) Two-dimensional mechanism for insect hovering. Phys Rev Lett 85:2216–2219

Wang ZJ (2004) The role of drag in insect hovering. J Exp Biol 207:4147–4155

Wang ZJ, Birch JM, Dickinson MH (2004) Unsteady forces and flows in low Reynolds number hovering flight: two-dimensional computations vs robotic wing experiments. J Exp Biol 207:449–460

Weis-Fogh T (1973) Quick estimates of flight fitness in hovering animals, including novel mechanism for lift production. J Exp Biol 59:169–230

Weis-Fogh T, Jensen M (1956) Biology and physics of locust flight. I. Basic principles in insect flight. A critical review. Philos Trans R Soc B 239:415–458

Wu J, Sun M (2004) Unsteady aerodynamic forces of a flapping wing. J Exp Biol 207:1137–1150

Unsteady fluid–structure interactions of membrane airfoils at low Reynolds numbers

P. Rojratsirikul · Z. Wang · I. Gursul

Abstract Membrane wings are used both in nature and small aircraft as lifting surfaces. Separated flows are common at low Reynolds numbers and are the main sources of unsteadiness. Yet, the unsteady aspects of the fluid–structure interactions of membrane airfoils are largely unknown. An experimental study of unsteady aerodynamics of two-dimensional membrane airfoils at low Reynolds numbers has been conducted. Measurements of membrane shape with a high-speed camera were complemented with the simultaneous measurements of unsteady velocity field with a high frame-rate particle image velocimetry system and flow visualization. Vibrations of the membrane and mode shapes were investigated as a function of angle of attack and free stream velocity. While the mean membrane shape is not very sensitive to angle of attack, the amplitude and mode of the vibrations of the membrane depend on the relative location and the magnitude of the unsteadiness of the separated shear layer. The results indicate strong coupling of unsteady flow with the membrane oscillations. There is evidence of coupling of membrane oscillations with the vortex shedding in the wake, in particular, for the post-stall incidences. Comparison of rigid (but cambered) and flexible membrane airfoils shows that the flexibility might delay the stall. Hence this is a potential passive flow control method using flexibility in nature and engineering applications.

P. Rojratsirikul · Z. Wang · I. Gursul (✉)
University of Bath, Bath, United Kingdom
e-mail: i.a.gursul@bath.ac.uk

1 Introduction

Flying mammals such as bats have thin compliant wings as lifting surfaces. These animals with flexible membranes fly at low Reynolds numbers at moderate to high angles of attack, and exhibit high maneuverability. It was suggested that bat flight might be more efficient than that of large insects or small birds of comparable size (Winter and von Helversen 1998). Flying and gliding mammals are well known for flight capabilities and agility (Bishop 2006). The skin of the bat wing is known to exhibit substantial changes in shape and camber throughout the wingbeat cycle (Swartz et al. 2007) while the effects of multiple joints and anisotropic membrane stiffness across the wing (Swartz et al. 1996) are not understood.

Membrane wings are used in many engineering applications including parachutes, microlight, paraglider and hang glider wings, yacht sails, and wings of small unmanned air vehicles known as micro air vehicles (MAVs) (Shyy et al. 1999). For the MAV applications, membrane wings are preferred because of their inherently light-weight nature as well as variable camber feature. Potential flow (Newman and Low 1984; Newman 1987; Greenhalgh et al. 1984; Jackson and Christie 1986), laminar flow (Smith and Shyy 1995), and turbulent flow (Smith and Shyy 1996) calculations were used to simulate the equilibrium shapes in steady conditions. It was found that the potential flow theory can be sufficient only for small incidences and for membrane airfoils with small excess length ratios. For larger excess lengths and incidences, viscous effects and flow separation need to be included for accurate simulations in steady flow. Unsteady aspects of the fluid–structure interaction received less attention. In many applications, unsteady aspects of membrane wings are as important as their static performance. Both in nature

G.K. Taylor, M.S. Triantafyllou, and C. Tropea (Eds.): Animal Locomotion, pp. 297–310.
springerlink.com

and small aircraft, flow separation and reattachment are typical and potential sources of unsteadiness. Yet, the unsteady aspects of the fluid–structure interactions of membrane airfoils at low Reynolds numbers are largely unknown.

The emphasis in this work is on the low Reynolds number flow over membrane airfoils. Membrane wings are often used in MAV applications, where the vehicles operate at Reynolds numbers below 10^5. Fixed-wing MAVs fly at relatively high angles of attack and close to the stall conditions due to the poor lift. Rise in unsteadiness and loss of control power are potential problems in low Reynolds number aerodynamics. Due to potentially damaging control problems, understanding of the gust response and stall conditions for fixed-wing MAVs is important. Hence, unsteady aspects of aerodynamics of membrane wings are far more important and critical for the performance and control of MAVs. For example, MAVs must be able to operate in gusts and unsteady free stream conditions (Shyy et al. 1997). They may also be subject to the instabilities caused by the fluid–structure interactions of the membrane wings. Even for membrane wings operating in steady free stream, aeroelastic instabilities may limit their operating envelope. At low incidences, the flow is mostly attached even though there might be a leading-edge separation bubble. Even these mostly attached flows may cause aeroelastic instabilities. At higher angles of attack, the flow is partially or fully separated over the membrane wings. These separated flows are expected to interact with the membrane structure.

Unsteadiness due to separation might cause buffeting of the membrane structure, and even may couple with the aeroelastic instabilities (Gordnier 2008; Visbal et al. 2008). In a recent study (Galvao et al. 2006), it was reported that standing waves with large mode numbers are observed for a membrane wing with aspect ratio of AR = 0.92. In a subsequent study (Song and Breuer 2007), similar vibrational modes were reported for $Re \geq 80{,}000$ for a rectangular wing with AR = 1.38. The flow is highly three-dimensional and tip vortices are dominant for low aspect ratio wings. It is possible that membrane vibrations can excite the separated shear layer forming the tip vortices and promote reattachment (Gursul et al. 2005). For a flexible nonslender delta wing, this mechanism delays the stall and increases the lift (Taylor et al. 2007). Hence, fluid–structure interactions on low aspect ratio wings are expected to be very complex. For this reason, we focus on two-dimensional membranes in this paper. The main objectives are to understand the unsteady aspects of these flows, membrane oscillations, and the interaction of the separated flows with the membrane. These aspects are investigated by using a high-speed camera for measurements of membrane shape and by time-accurate velocity measurements.

2 Experimental setup and methods

The experiments were carried out in the low-speed, closed-loop open-jet wind tunnel with the circular working section of the 760 mm in diameter, located in the Department of Mechanical Engineering, University of Bath. The membrane wing was placed in the test section by means of a frame and end plates as shown in Fig. 1a. Both the leading-edge and trailing-edge of the wing were fixed to circular plates at both ends to adjust the angle of attack as shown in Fig. 1b. The rigid leading- and trailing-edges run along the whole span of the test section between the two end plates. There is a small gap (1 mm) between the membrane and the end plates. The main feature of this setup is that the time-averaged membrane deformation is essentially two-dimensional, which can be seen in Fig. 1b. However fluctuating displacement might be three-dimensional due to the end effects. The wing had a span of 450 mm and chord length of $c = 150$ mm. The experiments were carried out over angles of attack from 0° to 30°, free stream velocities of 5, 7.5, and 10 m/s which correspond to Reynolds numbers, based on the chord length, of $Re = 53{,}100$, 79,700 and 106,000 respectively.

The membrane wing was made from a black latex rubber sheet with a thickness of $t = 0.2$ mm, Young's

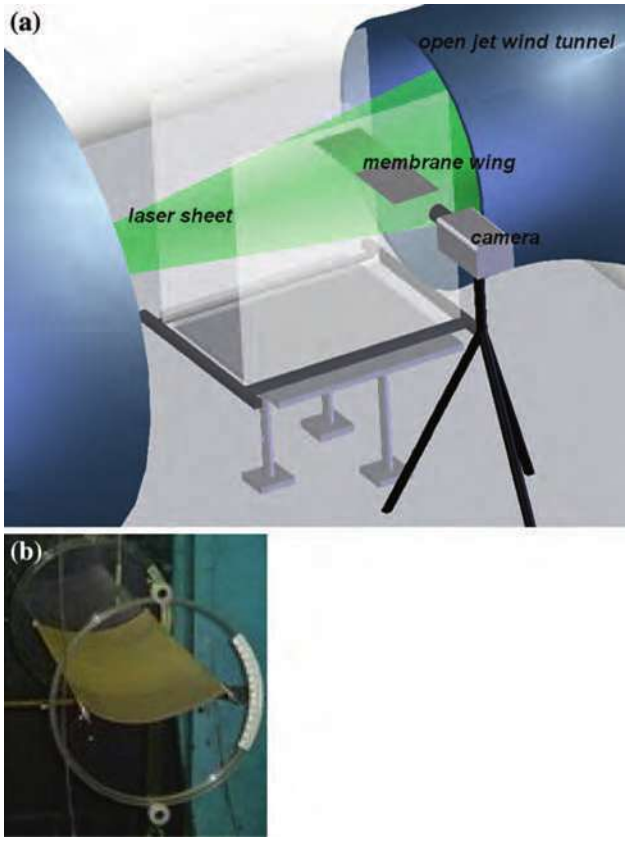

Fig. 1 **a** Schematic of experimental setup, **b** membrane airfoil in the test section

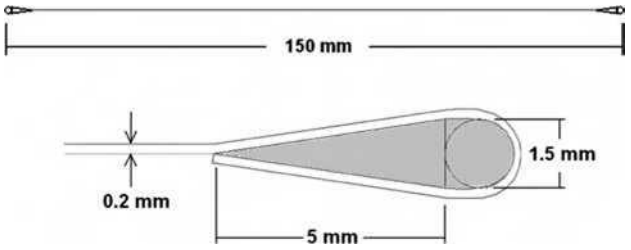

Fig. 2 Cross-section of the membrane airfoil and details of leading- and trailing-edge

modulus of $E = 2.2$ MPa, and density of $\rho_m = 1$ g/cm^3. The membrane was attached to the airfoil-shaped leading- and trailing-edges as shown in Fig. 2. The edges were designed with consideration that they must be strong enough to resist bending but small enough to produce a thin airfoil cross-section. The aeroelastic parameter used by Smith and Shyy (1996) is $\Pi = (Et/qc)^{1/3}$, where q is the free stream dynamic pressure. This parameter has a value of $\Pi = 5.77$, 4.41 and 3.64 corresponding to the free stream velocities $U_\infty = 5$, 7.5 and 10 m/s. The maximum camber took values up to around 10% of the chord length in present experiments. These values are consistent with the observations for bats (Song et al. 2008).

In addition, a rigid membrane airfoil (equivalent rigid cambered airfoil, i.e. with shape equivalent to the mean membrane deformation) was manufactured and tested in order to compare with the flexible membrane airfoil. In an effort to make a reasonable comparison over a range of incidences, the rigid wing was made of 1 mm thick stainless steel with a profile matching that of the average (over incidences) shape of the membrane wing at 5 m/s free stream velocity and at angles of attack from 10–18°. Also, the leading-edge and trailing-edge were rounded to give a similar shape to that of the flexible membrane.

In order to measure the membrane shape, a thin laser sheet from a 4-W Argon–Ion laser was used to illuminate the membrane surface in the streamwise plane located at the mid-span of the wing. A high speed camera (*Photron FASTCAM APX*) was positioned normal to the flow and images were captured at a rate of 1,500 frames per second. The resulting image appears as a white curve as shown by the example in Fig. 3. Present experimental technique can only be used to detect the chordwise modes. Spanwise modes may be present when the chordwise mode number increases, but this aspect has not been investigated with the present technique. The images with 1,024 × 1,024 pixel resolution in TIF format were obtained in 2 s, resulting in 3,000 images per each angle of attack and speed. Finally, the images were digitized through MatLab (Image Processing Toolbox) to find the coordinates. Two examples of the digitized membrane shapes at different instants are shown in Fig. 4. It is seen that the second mode and fifth

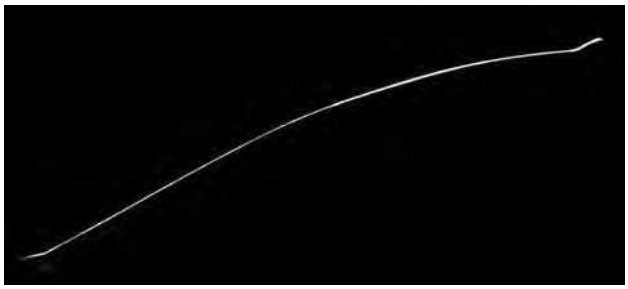

Fig. 3 Membrane shape as obtained from the laser sheet visualization, $U_\infty = 5$ m/s, $\alpha = 20°$. Flow is from *right* to *left*

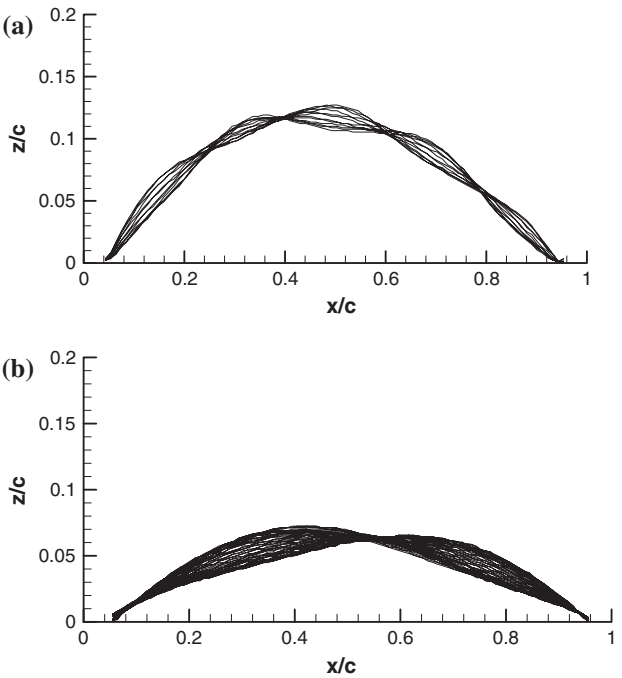

Fig. 4 Digitized membrane shape at different instants for **a** $U_\infty = 10$ m/s, $\alpha = 13°$; **b** $U_\infty = 5$ m/s, $\alpha = 28°$

mode of vibrations are captured in these examples. From the instantaneous coordinates of the membrane, the time-averaged membrane shape was calculated for each angle of attack and free stream velocity. In addition, the standard deviation of the membrane displacement was calculated as a function of the chordwise distance, which would easily indicate the mode of the vibrations. From the digitized membrane shapes as a function of time, it was also possible to study the time history of the displacement. An example of the time history of the displacement is shown in Fig. 5. The dominant frequency of the membrane oscillations can be found from the time history of membrane displacement. The dominant frequencies were found by spectral analysis using the Welch power spectral density method in MatLab.

Quantitative flow measurements were undertaken using a high frame-rate Digital Particle Image Velocimetry

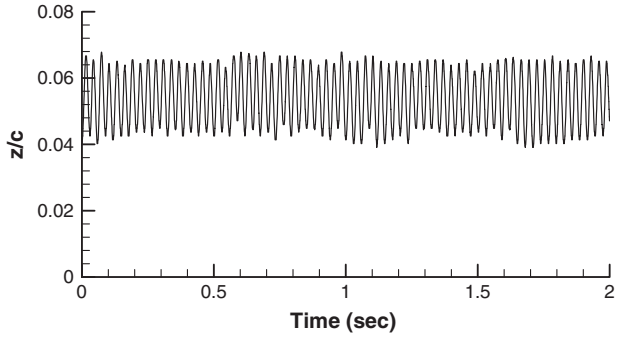

Fig. 5 Example of time history of membrane displacement as a function of time for $U_\infty = 5$ m/s, $\alpha = 28°$, $x/c = 0.32$

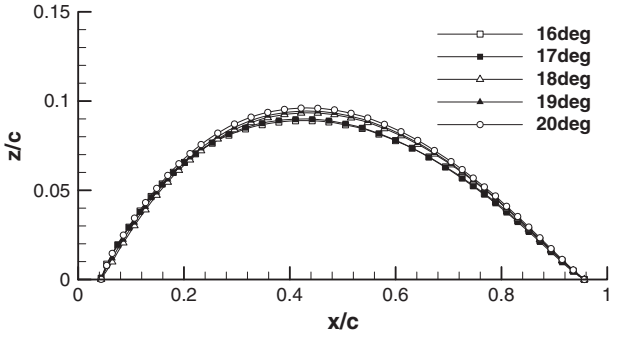

Fig. 6 Examples of time-averaged membrane shapes at different angles of attack, $U_\infty = 7.5$ m/s

(DPIV) system. Illumination of the desired plane was achieved using a New Wave Pegasus Nd:YLF double pulse high speed laser with a maximum energy of 10 mJ/pulse. The laser light sheet was placed parallel to the freestream velocity to illuminate a plane at the mid-span of the wing as shown in Fig. 1a. The PIV camera was placed normal to the flow, and the flow over the suction surface of the whole wing was imaged. In some experiments, specific areas near the leading-edge or trailing-edge were investigated. The images were captured using a TSI PowerView HS-3000 high speed CMOS camera. A TSI LaserPulse synchroniser unit was utilized to link the camera and the laser to enable the accurate capture for two frame cross-correlation analysis. For these measurements, the velocity field was captured at a rate of 1,500 frames per second, at a resolution of 1,024 by 1,024 pixels, producing sequences of 3,000 instantaneous velocity fields over 2 s. A TSI model 9307-6 multi-jet atomiser was used to produce oil droplets in order to seed the flow. The atomiser worked best using olive oil and the mean size of the droplets was 1 μm. The commercial software TSI Insight3G and a FFT cross-correlation algorithm were used for the analysis of the results obtained. The size of the interrogation window was 32 by 32 pixels. The effective grid size was around 2% of the chord length in these measurements. The measurement uncertainty for the velocity is estimated as 2% of the free stream velocity.

We also conducted flow visualization using a smoke-wire placed just upstream of the wing. In order to generate smoke, a strip of wire was clamped vertically, perpendicular to the flow at the mid-span of the wing. Oil was dropped to the wire continuously by a small valve on a dripping system. With a current applied to the wire, the oil was burnt by the heat, and the smoke was generated. The high speed camera (*Photron FASTCAM APX*) was used to capture images at a rate of 1,000 frames per second.

3 Results

3.1 Mean shape of membrane

Figure 6 shows examples of the time-averaged membrane shape for various angles of attack for $U_\infty = 7.5$ m/s. Note that the displacement is 0 in the small regions near the rigid leading-edge and trailing-edge. It is also seen in this plot that the maximum membrane displacement (also the point of maximum camber) is forward of the mid-chord point for high angles of attack, which is consistent with previous predictions and experiments (Greenhalgh et al. 1984). Figure 7a and b show the maximum camber and its

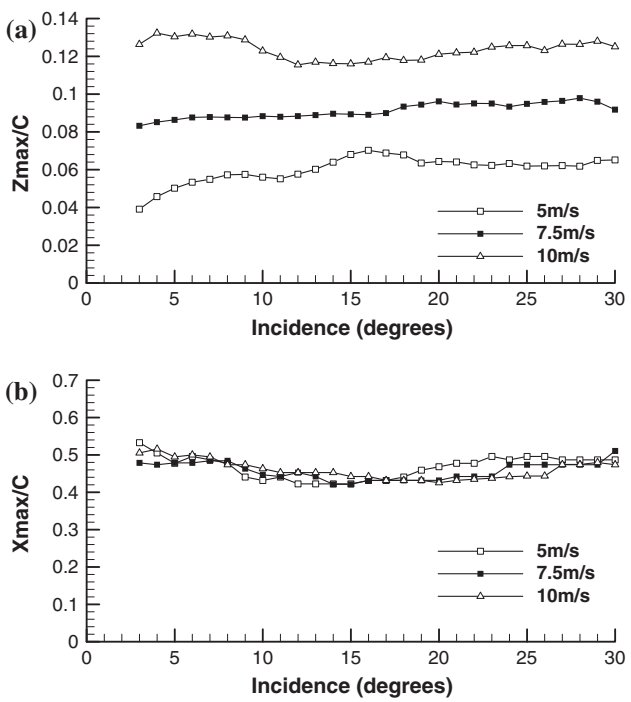

Fig. 7 Variation of **a** maximum camber, **b** chordwise location of the maximum camber as a function of angle of attack for three freestream velocities

chordwise location as a function of angle of attack for three different free stream velocities. Note that the data for $\alpha \leq 2°$ are not shown as the bistable instability known as luffing (Newman 1987) occurs in this region when the membrane is just as likely to set itself on one side as the other. The lift also experiences hysteresis (Greenhalgh et al. 1984) in this region. The maximum camber increases gradually up to for $\alpha = 16°$ for the lowest speed ($U_\infty = 5$ m/s) and then stays roughly constant. For $U_\infty = 7.5$ m/s, the maximum camber exhibits very small increase with angle of attack. For the largest free stream velocity, the variation in the maximum camber with incidence is relatively small. In general, the changes in the maximum camber are small as the angle of attack is varied for all three speeds, which is consistent with previous observations (Newman and Low 1984) and simulations (Gordnier 2008). This is different from what is expected in attached flows, and is due to the separated flows being predominant at these low Reynolds numbers.

Figure 7b shows that the location of the maximum camber is not very sensitive to the free stream velocity either. For all cases, the membrane shape is symmetrical about the mid-chord point for small incidences, which is also predicted theoretically (Newman and Low 1984). The location of maximum camber moves forward as the angle of attack is increased up to $\alpha \approx 15°$. This is also consistent with previous observations and predictions (Newman and Low 1984). There is a trend of the location of the maximum camber moving back to the mid-chord point at higher angles of attack.

3.2 Mean flow

Preliminary smoke flow visualization showed that the flow remains attached to the wing surface up to around 8° of angle attack for $U_\infty = 5$ m/s. In fact, a small leading-edge separation bubble was evident for both $U_\infty = 5$ m/s and $U_\infty = 7.5$ m/s. When the flow remains attached, oscillations of the membrane are very small. Consequently, we focus on larger angles of attack near the stall and in the post-stall regime.

Figure 8 shows the magnitude of the time-averaged velocity field superposed on the streamline pattern. For selected angles of attack, the data were taken in two

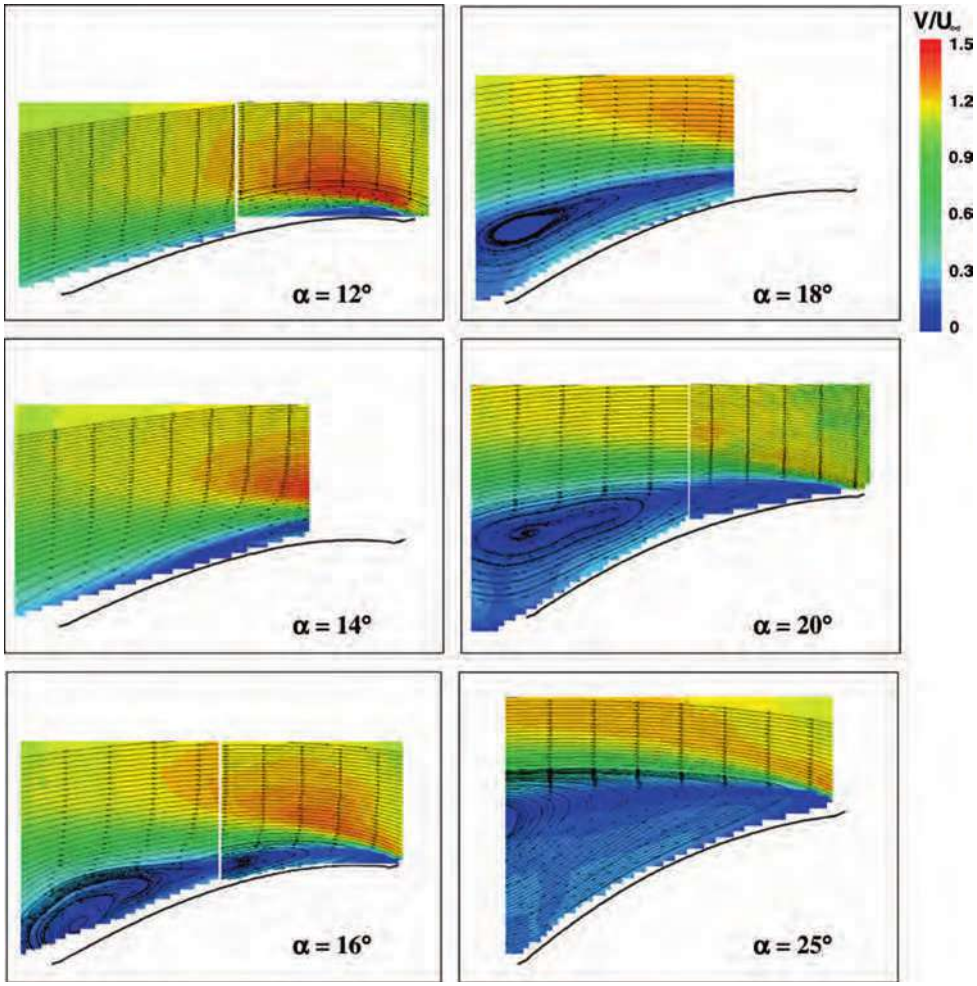

Fig. 8 Magnitude of the time-averaged velocity and streamlines at different angles of attack, $U_\infty = 5$ m/s. Flow is from *right* to *left*

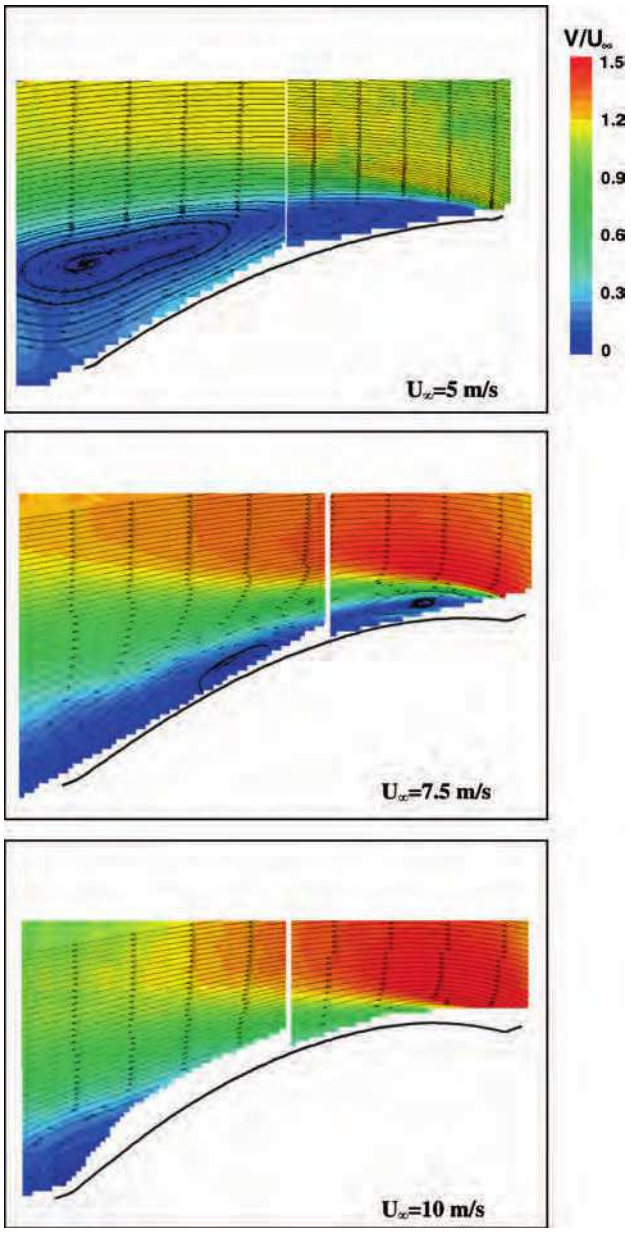

Fig. 9 Magnitude of the time-averaged velocity and streamlines at different freestream velocities, $\alpha = 20°$. Flow is from *right* to *left*

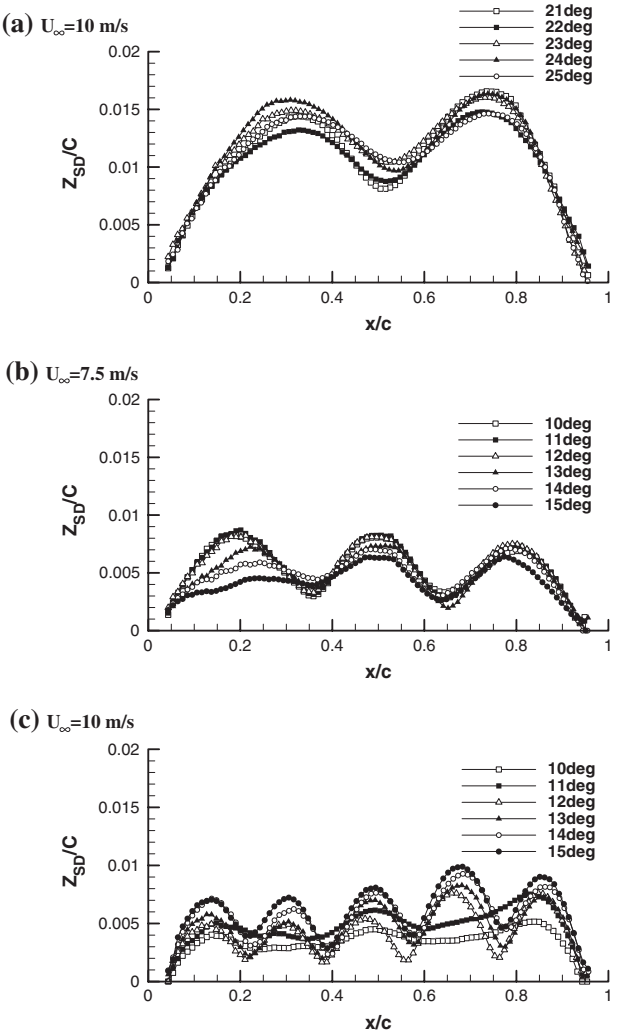

Fig. 10 Variation of the standard deviation of the membrane displacement normalized by chord length, showing examples for **a** second mode, **b** third mode and **c** fifth mode

different regions (one near the leading-edge and the other near the trailing-edge). Starting with $\alpha = 12°$, the flow is separated, but the shear layer remains very close to the membrane. With increasing angle of attack, the separated shear layer moves away from the surface. For $\alpha = 16°$, closed streamline pattern develops near the trailing-edge. The recirculation region becomes larger and moves further downstream with increasing angle of attack to $\alpha = 18°$ and 20°. For the largest angle of attack $\alpha = 25°$, the center of the closed recirculation region is no longer on the membrane wing. If the time-averaged membrane shape (Fig. 7) and the time-averaged flow (Fig. 8) are considered together, it is concluded that the changes in the mean membrane shape are much smaller than the changes in the mean flow as the angle of attack is varied for a given free stream velocity.

Figure 9 shows the magnitude of the time-averaged velocity and streamlines for different free stream velocities at $\alpha = 20°$. With increasing free stream velocity (increasing Reynolds number *Re* and decreasing aeroelastic parameter Π), there is a trend of shear layer getting closer to the wing surface while the camber of the wing increases. It will be shown later on that this affects the onset and the amplitude of the membrane oscillations. Although the effect of *Re* and Π could not be separated in these experiments, this was done in the numerical simulations by Gordnier (2008). It was shown that there was a significant reduction in the size of the separation zone with increasing Reynolds number at a fixed parameter Π.

3.3 Membrane oscillations

Figure 10 shows examples of different modes of membrane oscillations as indicated by the variation of the standard deviation with the chordwise distance. Examples of the second mode (Fig. 10a), the third mode (Fig. 10b), and the fifth mode (Fig. 10c) are shown for various free stream velocity and angle of attack combinations. Actually, it is noted for $\alpha = 10°$ and $11°$ in Fig. 10c that, the mode number appears to be three, and jumps to five for other incidences in this figure.

Figure 11 shows the variation of the mode number as a function of incidence and free stream velocity. An unambiguous identification of the second mode occurs first at the smallest angle of attack $\alpha = 11°$ for $U_\infty = 5$ m/s. With increasing free stream velocity, the smallest angle of attack at which a definite mode shape is identified decreases. This might be due to the unsteady shear layer getting closer to the wing surface (see Fig. 9). It is also noted that the mode number increases with the free stream velocity. It is interesting that, when $\alpha \geq 20°$, the second mode is observed regardless of the free stream velocity. This suggests a possible coupling of membrane with the wake flow at these post-stall incidences.

The dominant frequency as a function of angle of attack for three different free stream velocities is shown in Fig. 12. It is seen that, although the trend is similar to that of the mode number (Fig. 11), there are some differences. For example, for the same mode number of two (for $\alpha \geq 20°$), the measured frequencies are different for different free stream velocities. This is probably due to the change in the membrane shape, and therefore the tension. An attempt was made to predict the natural frequencies of the membrane, although it is not clear whether the linear elastic theory can be justified for this highly nonlinear problem. The membrane tension was estimated from the mean deformation and Young's modulus, and this was used to estimate the natural frequencies of the membrane based on the linear elastic theory. However, it should be kept in mind that this theoretical prediction is valid only for vacuum. The added mass effects as well as the effects of a mean flow are not taken into account. Substantial changes in the added mass are expected in separated flows (for an oscillating circular cylinder, the added mass may even become negative). Our prediction based on the linear elastic theory in vacuum, assuming pre-strain and two-dimensional membrane shape, provided frequencies roughly half of the experimental values. The membrane natural frequencies were predicted successfully for low aspect ratio membranes by using this approach (Song et al. 2008). However, Song et al. (2008) adjusted the value of the pre-strain (by adding additional strain of around 0.05) in order to fit to the theoretical model for the camber and argued that this value is within the fabrication uncertainty. Such a large pre-strain would correspond to nearly 7.5 mm difference in length in our setup, which we believe is not realistic. We believe that the difference between the linear theory and experiments highlight the nonlinear nature of the fluid–structure interaction.

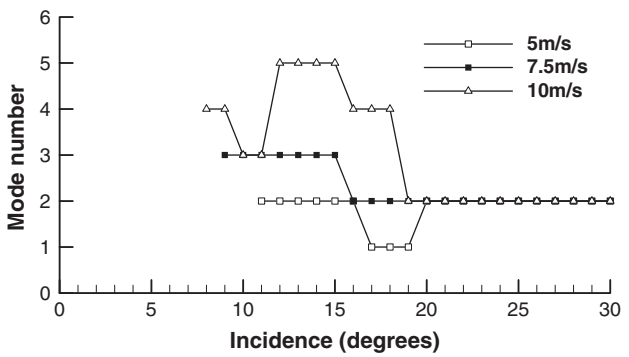

Fig. 11 Variation of the mode number as a function of incidence and freestream velocity

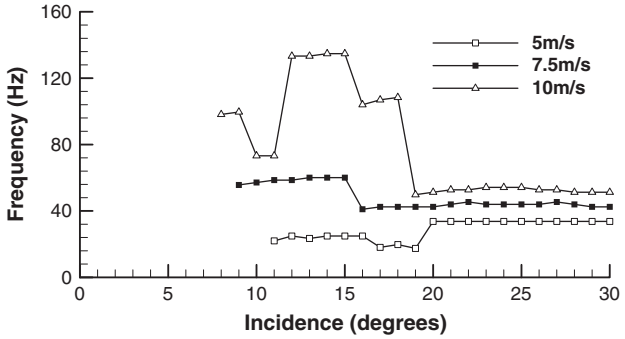

Fig. 12 Variation of the frequency of membrane oscillations as a function of incidence

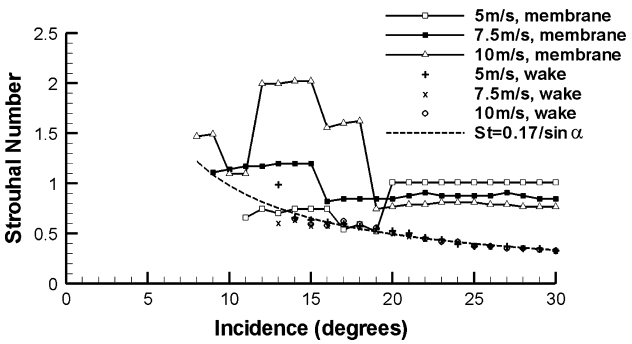

Fig. 13 Variation of Strouhal number of membrane oscillations as a function of incidence

The variation of the Strouhal number $\mathrm{St} = fc/U_\infty$ as a function of angle of attack is shown in Fig. 13. In general, the Strouhal number is in the order of unity. This is consistent with the findings of simulations for the same geometry but at much lower Reynolds number (Gordnier

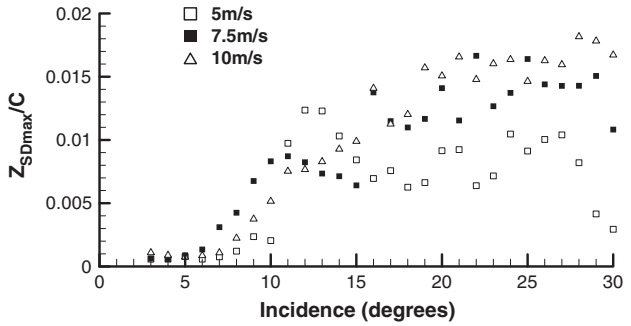

Fig. 14 Variation of the maximum standard deviation of membrane displacement normalized by chord length, as a function of incidence

2008). It is seen that, in particular, for $\alpha \geq 20°$, the Strouhal number is close to unity in Fig. 13. The Strouhal number increases with increasing free stream velocity at moderate incidences. Song et al. (2008) also reported increasing Strouhal number with free stream velocity for a low aspect ratio wing. An alternative definition of the Strouhal number, based on the vertical distance between the leading-edge and trailing-edge, is often used in the literature (Fage and Johansen 1927; Abernathy 1962):

$$\mathrm{St}_{\alpha} = \frac{fc \sin \alpha}{U_{\infty}}$$

This modified definition of the Strouhal number is reported to be constant for flat plates and thin airfoils, with the values given in the range of 0.16–0.22 (Fage and Johansen 1927; Abernathy 1962; Miranda et al. 2005). Vortex shedding frequency in the wake of the rigid membrane (equivalent rigid cambered airfoil) was measured with hot-wire anemometry and added to Fig. 13. It is seen that measured Strouhal numbers are not very different from those of flat plates and airfoils. Also, the dashed line shows $\mathrm{St}_{\alpha} = 0.17$, which agrees very well with our measurements at the three free stream velocities. This figure suggests that there might be coupling of the membrane oscillations with the vortex shedding from the membrane. In particular, for $\alpha \geq 20°$, where the second mode is always observed, the membrane oscillations might be coupled with the first harmonic of the natural frequency. In active flow control studies with rigid airfoils (Miranda et al. 2005; Wu et al. 1998), it was found that vortex shedding may lock on the first harmonic or the subharmonic of the natural frequency.

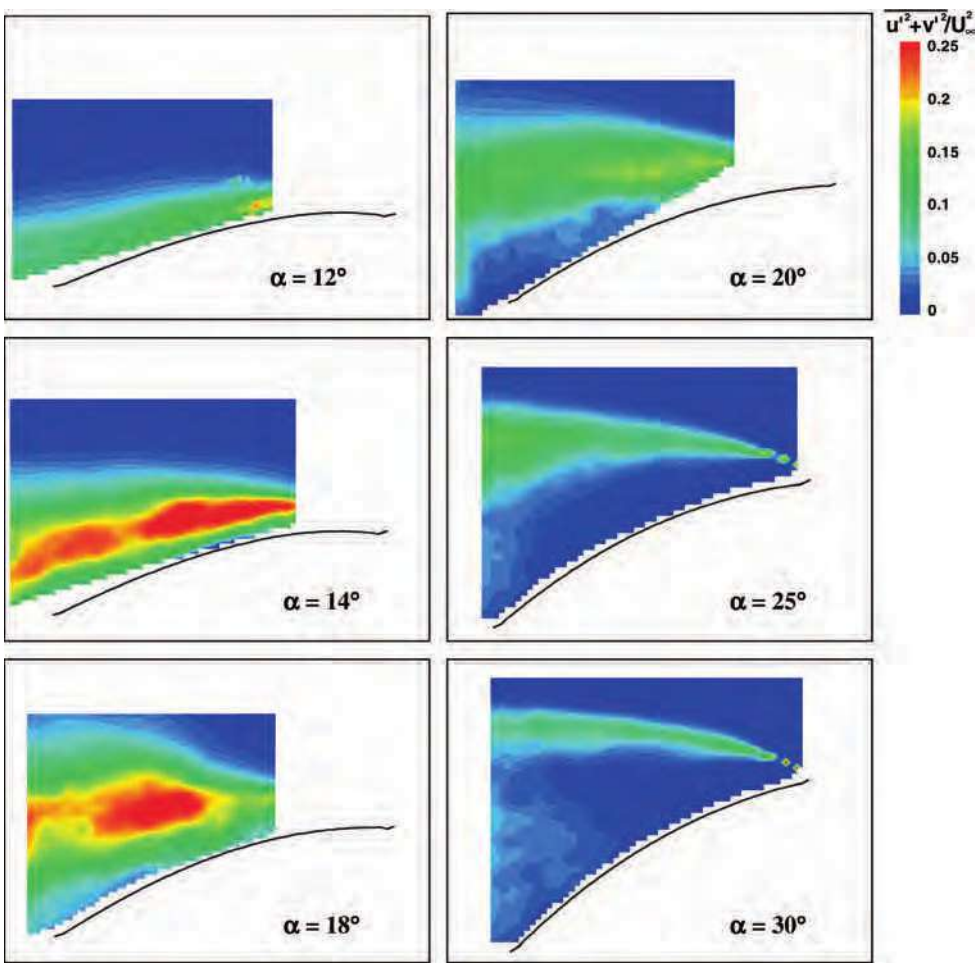

Fig. 15 Turbulence intensity at different angles of attack, $U_{\infty} = 5$ m/s. Flow is from *right* to *left*

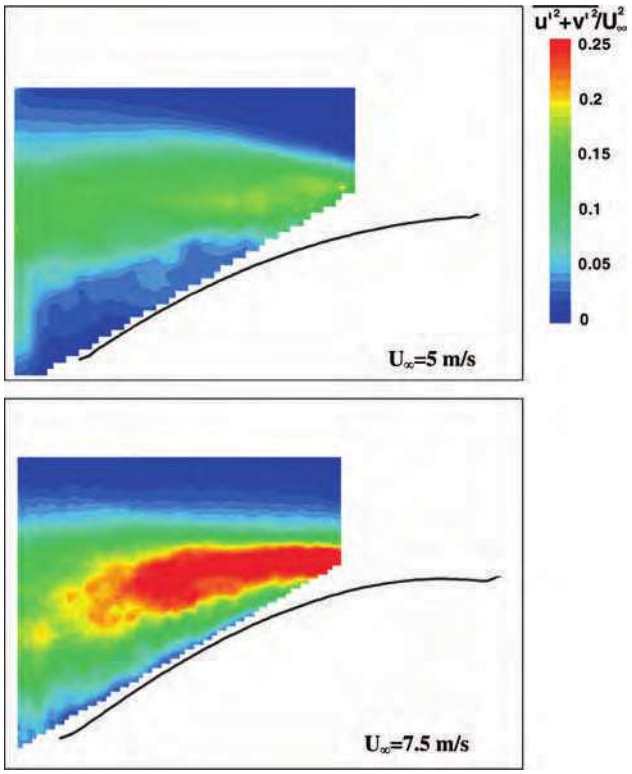

Fig. 16 Turbulence intensity at $\alpha = 20°$. Flow is from *right* to *left*

Finally, the maximum standard deviation of the membrane oscillations is shown as a function of angle of attack in Fig. 14. The amplitude of the oscillations starts to increase rapidly at a certain angle of attack and this incidence decreases with increasing free stream velocity. A local maximum is observed for $\alpha = 10$–$12°$, followed by increases or decreases depending on the free stream velocity and the mode jumps. For the lowest free stream velocity (and largest Π), the amplitude of the oscillations is somewhat smaller at high incidences. However, for the higher free stream velocities (and smaller Π), the amplitude has an increasing trend at high angles of attack. This might be partly due to the shear layer getting closer to the wing surface at higher free stream velocities.

3.4 Unsteady flow

Figure 15 shows the turbulence intensity $\overline{u'^2 + v'^2}/U_\infty^2$ in the measurement plane at different angles of attack for $U_\infty = 5$ m/s. The shear layer fluctuations move away from the surface with increasing angle of attack and also become stronger. Note that, for this free stream velocity, the largest membrane oscillations occur at $\alpha = 12°$ (see Fig. 14) for which the shear layer is closest to the surface as seen in Fig. 15. The velocity fluctuations become weaker and move away from the surface at very large incidences (see, for example, $\alpha = 30°$) and the membrane oscillations decrease.

Figure 16 shows comparison of the turbulence intensity when the free stream velocity is increased from $U_\infty = 5$–7.5 m/s for $\alpha = 20°$. It is seen that the shear layer becomes closer to the surface (which is also seen in the time-averaged flow in Fig. 9) while the magnitude of the fluctuations also increase. This explains the earlier onset of the membrane oscillations and also larger membrane oscillations at higher free stream velocities (see Fig. 14).

Figure 17 shows the Reynolds stress component as a function of angle of attack for $U_\infty = 5$ m/s. The peak in the Reynolds stress occurs along the shear layer where the time-averaged vorticity is maximum. The location of the maximum values of the Reynolds stress moves away from the membrane surface and downstream with increasing angle of attack. Peak magnitudes are observed for $\alpha = 14$–$18°$ range, then the peak value decreases at higher angles of attack. The relatively large value of the Reynolds stress observed for moderately high incidences is related to the formation of coherent structures. Examinations of the instantaneous flow fields suggest that the peak of the Reynolds stress coincides with the roll-up of the large vortices as shown in Fig. 18 for $\alpha = 18°$.

3.5 Flow–membrane coupling

Instantaneous velocity field measured by the high speed PIV system was examined to study the coupling of the instantaneous flow with the membrane deformation. In order to demonstrate the high degree of correlation between the unsteady flow and membrane shape, both the location of the shear layer (identified as the location of maximum vorticity) and the membrane displacement were analyzed for each instantaneous flow over several cycles of membrane oscillations. The inset in Fig. 19 shows the definition of the distance between the membrane surface and the shear layer, l, and the vertical displacement of the membrane from the time-averaged shape, z', measured at a chordwise location of 0.75c. Figure 19a shows the variation of the location of the shear layer and membrane displacement as a function of time for $\alpha = 13°$ and $U_\infty = 5$ m/s. It is seen that the location of the shear layer is highly correlated to the membrane oscillations. When the membrane displacement is maximum, the shear layer is farthest away from the wing at this chordwise location. Figure 19b shows instantaneous flow fields at instants corresponding to the minimum and maximum displacements of membrane at 0.75c. For this angle of attack, the shear layer flapping is significant, which might be the cause of the largest membrane oscillations for this free stream velocity.

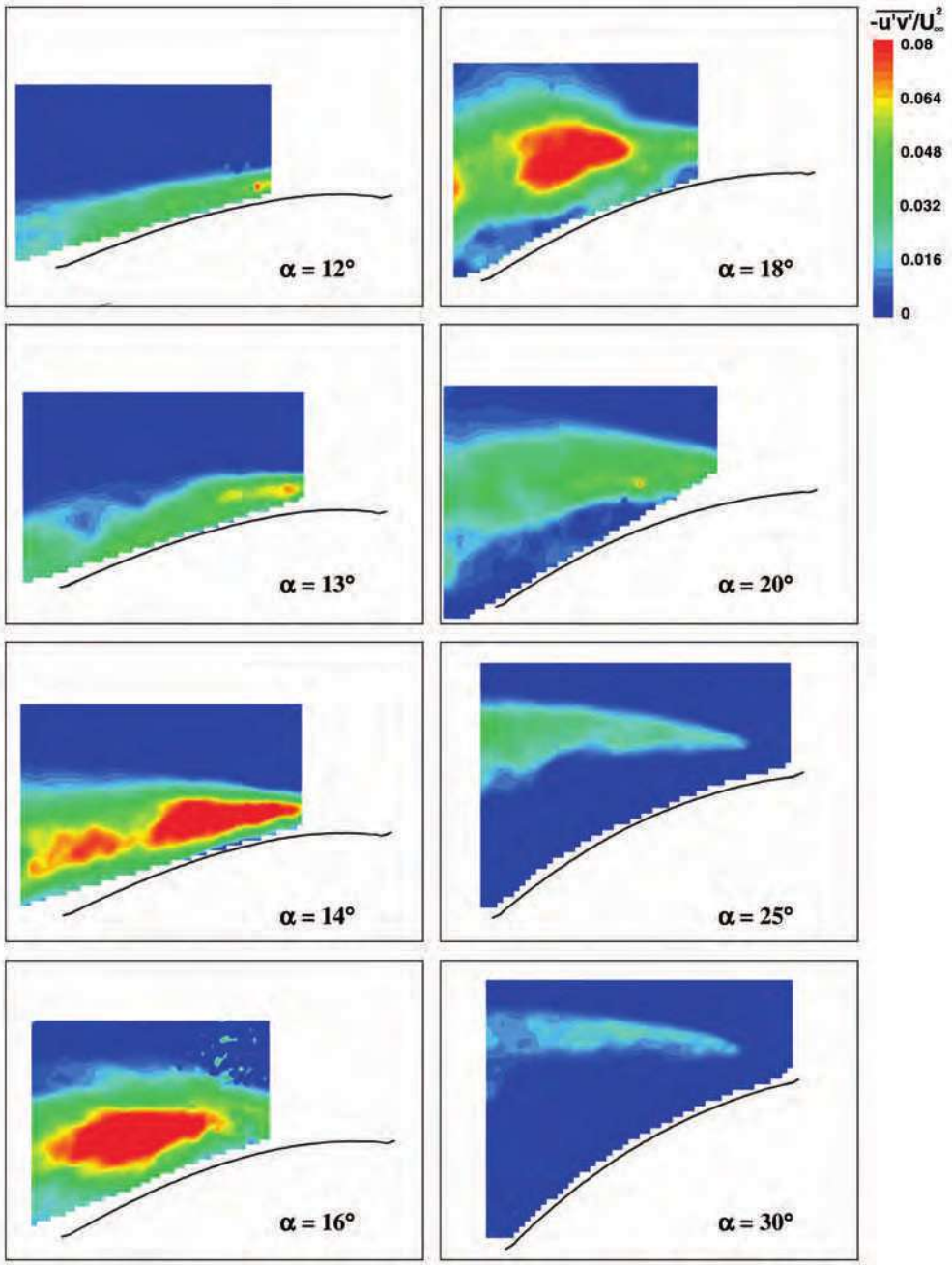

Fig. 17 Reynolds stress at different angles of attack, $U_\infty = 5$ m/s. Flow is from *right* to *left*

Figure 20 shows similar data for a higher angle of attack ($\alpha = 18°$) and $U_\infty = 5$ m/s. Positive correlation between the shear layer location and membrane displacement at 0.75c is similar to the case of $\alpha = 13°$. Figure 20b shows two instantaneous flow fields at instants of minimum and maximum membrane displacements. At this angle of attack, the roll-up of large vortices is more evident (see also Fig. 18).

3.6 Comparison of rigid and flexible membranes

Figure 21 shows smoke flow visualization with a high speed camera for the flexible membrane (left column) and the rigid membrane (right column). For the rigid membrane (a curved metal sheet), the mean camber is the same as for the flexible membrane, but of course there is no vibration. This presence or absence of membrane vibrations affects

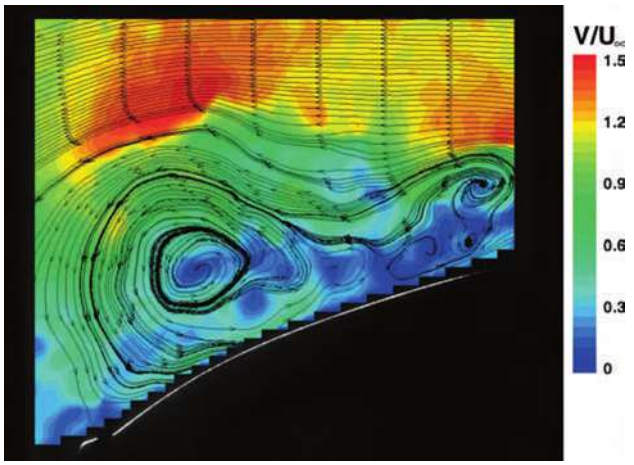

Fig. 18 Instantaneous velocity magnitude and streamlines for $U_\infty = 5$ m/s and $\alpha = 18°$. Flow is from *right* to *left*

the separated flow significantly. It is seen that for all incidences, the size of the separation and recirculation region is smaller for the flexible membrane. Also, at higher incidences ($\alpha = 18°$ and 20°), the roll-up of large vortices is evident over the flexible membrane whereas the shear layer does not exhibit large vortices for the rigid membrane. The oscillations of the membrane excite the shear layer, resulting in the roll-up of the large vortices. As the location of the shear layer (distance from the wing surface) is smaller for the flexible membrane, this suggests that drag might be smaller and stall might be delayed compared to the rigid membrane. Figure 22 shows the magnitude of the Reynolds stress for the flexible and rigid membrane wing for $\alpha = 18°$ and 20°. It is seen that the Reynolds stress is much larger for the flexible membrane due to the membrane vibrations, which excite the shear layer and promote the roll up of the vortices.

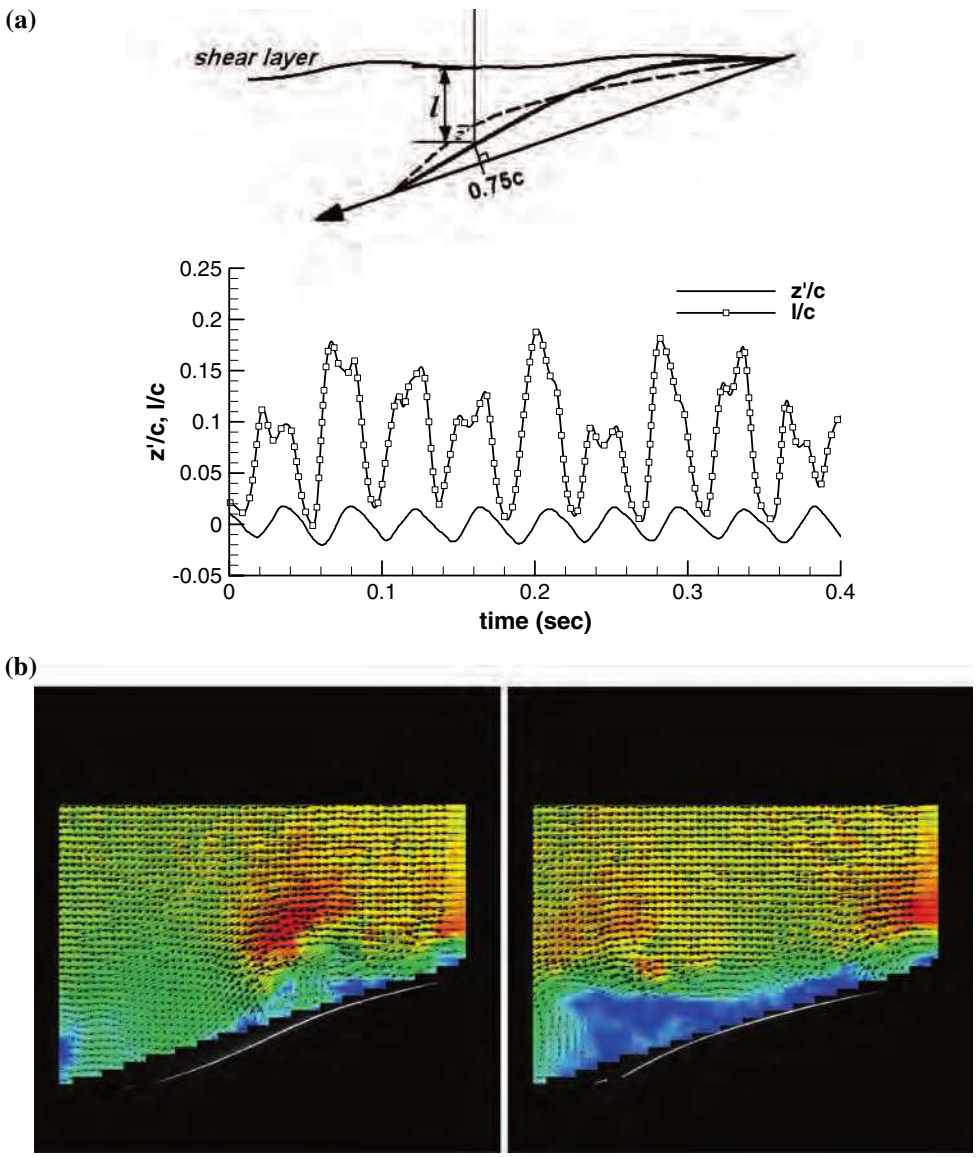

Fig. 19 **a** Time history of the locations of the shear layer and membrane as measured at 0.75c (the inset shows the definition of these quantities), **b** instantaneous flow field at minimum (*left*) and maximum (*right*) values of membrane displacement, $U_\infty = 5$ m/s, $\alpha = 13°$. Flow is from *right* to *left*

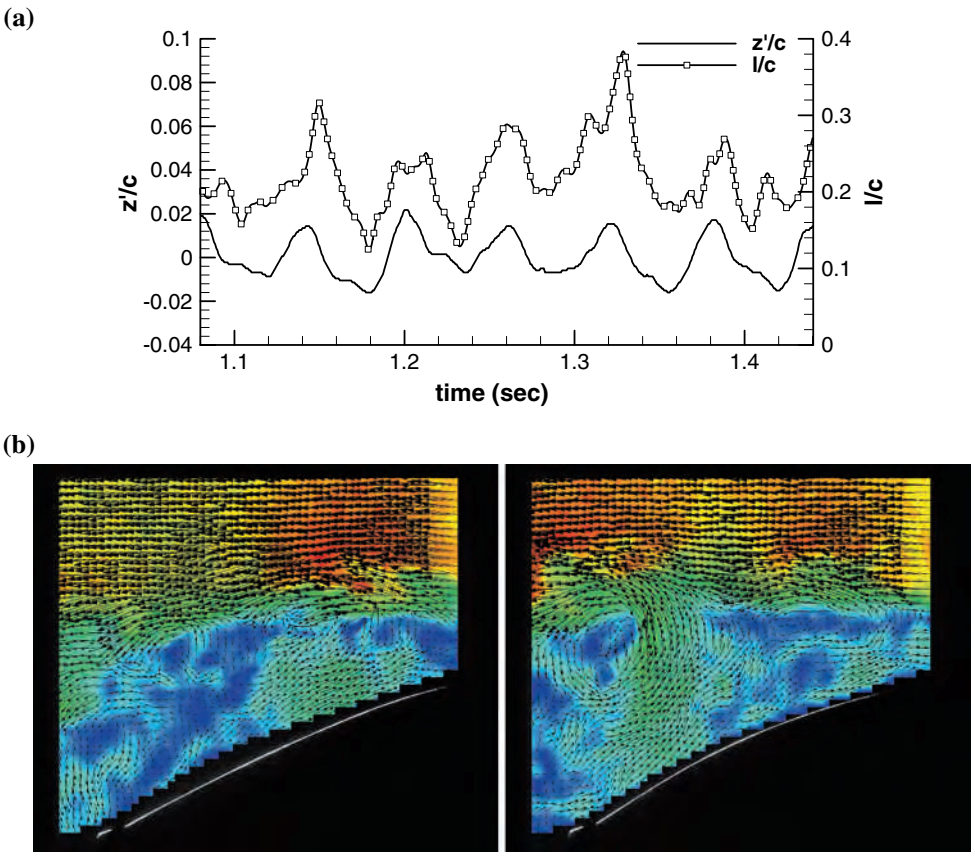

Fig. 20 **a** Time history of the locations of the shear layer and membrane as measured at 0.75c, **b** instantaneous flow field at minimum (*left*) and maximum (*right*) values of membrane displacement, $U_\infty = 5$ m/s, $\alpha = 18°$. Flow is from *right* to *left*

A similar comparison of flexible and rigid membranes was made in the simulations by Gordnier (2008) at $Re = 2{,}500$. It was shown that the dynamic motion of the membrane excites the shear layer causing it to roll up sooner and to form a series of vortices. This resulted in an increase in lift and decrease in drag.

4 Conclusions

Unsteady aerodynamics and fluid-structure interaction of a nominally two-dimensional membrane airfoil were investigated experimentally. Measurements of membrane shape, measurements of velocity field with a high speed PIV system, and flow visualization were performed. Experiments were conducted for three different values of the aeroelastic parameter $\Pi = (Et/qc)^{1/3}$ and in a Reynolds number range of $Re = 53{,}100$–$106{,}000$.

Mean membrane shape is not very sensitive to the changes in angle of attack, even though the time-averaged flow differs considerably: attached flow at small incidences, weakly separated flow at moderate incidences with the shear layer remaining close to the surface, and massively separated flows with large recirculation regions at high incidences. When the flow remains attached, the membrane oscillations are negligibly small. With increasing angle of attack, the amplitude of the oscillations increases rapidly around $\alpha = 10°$ for the lowest Reynolds number. The largest membrane oscillations occur when the separated shear layer remains close to the surface. With increasing angle of attack, the shear layer moves away from the surface. With increasing free stream velocity (increasing Reynolds number and decreasing aeroelastic parameter Π), the camber of the wing increases while the separated shear layer becomes more energetic and closer to the surface. This affects the onset of the vibrations and increases the amplitude.

Membrane oscillations with mode numbers of up to five were observed in the present experiments. The mode number increases with the free stream velocity at moderate incidences, whereas the second mode is always observed regardless of the free stream velocity for $\alpha \geq 20°$. The variation of the Strouhal number suggests a possible coupling of membrane oscillations with the Karman vortex shedding phenomenon in the wake. In particular, for $\alpha \geq 20°$, the data suggest possibility of the membrane oscillations locking on the first harmonic of the natural frequency.

Coupling of the membrane oscillations and separated shear layer has been demonstrated with the high degree of correlation between the membrane displacement and location of the shear layer from the analysis of instantaneous

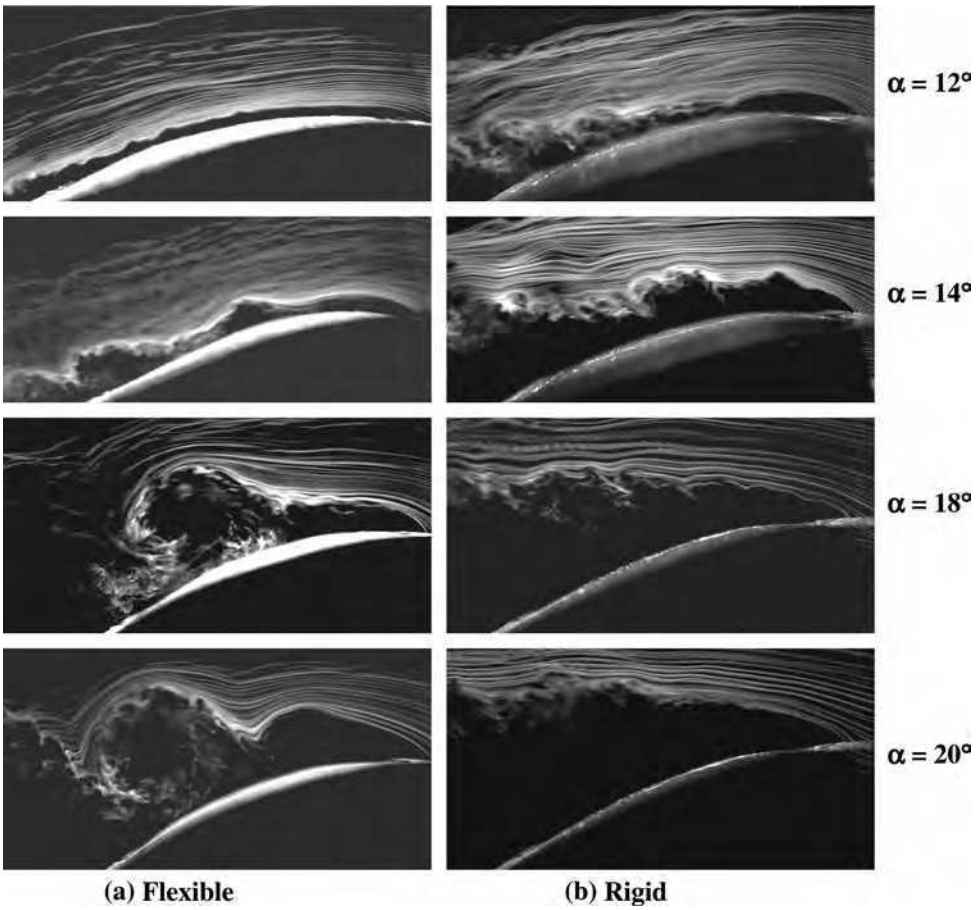

Fig. 21 Smoke flow visualization with a high speed camera at different incidences for **a** flexible, **b** rigid membrane, $U_\infty = 5$ m/s. Flow is from *right* to *left*

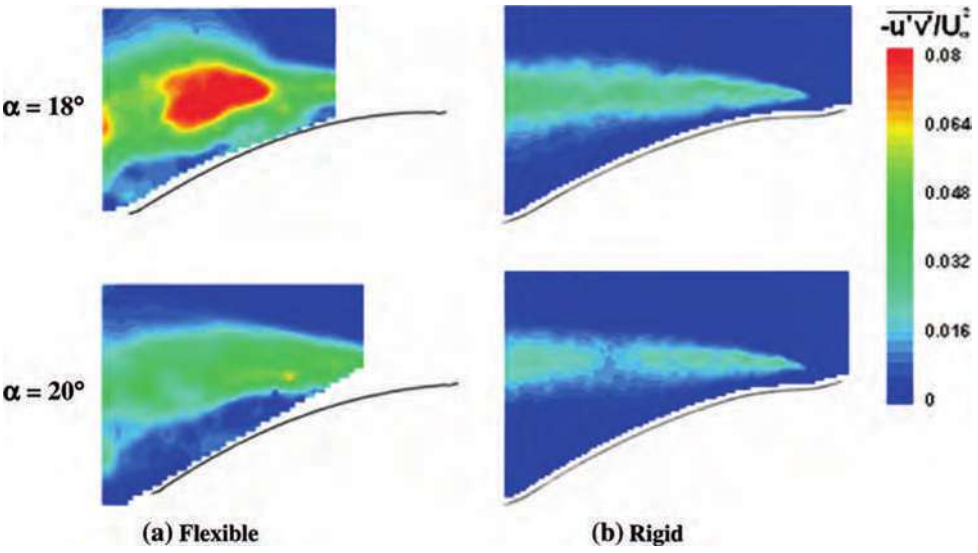

Fig. 22 Magnitude of the Reynolds stress for **a** flexible and **b** rigid membranes, $U_\infty = 5$ m/s. Flow is from *right* to *left*

flow fields. At moderate incidences, the flapping of the shear layer is more dominant, whereas at larger incidences ($\alpha = 16$–$20°$), the roll-up of large vortices is more characteristic of the flow. At even higher angles of attack ($\alpha = 25°$ and $30°$), the shear layer has relatively low level of fluctuations and does not exhibit the roll-up of the large vortices over the wing.

Comparison of the rigid and flexible membranes indicates that the size of the separation region is smaller for the flexible membrane. The oscillations of membrane excite

the shear layer, resulting in the roll-up of the large vortices over the wing. This suggests that membrane flexibility might decrease the drag and delay the stall.

Acknowledgments The authors would like to acknowledge funding from the US Air Force Office of Scientific Research (AFOSR), the Research Councils UK Academic Fellowship in Unmanned Air Vehicles, and the Royal Thai Government Scholarship. The authors would like to thank the EPSRC Engineering Instrument Pool.

References

Abernathy FH (1962) Flow over an inclined plate. Trans ASME J Basic Eng 84:380–388

Bishop KL (2006) The relationship between 3-D kinematics and gliding performance in the southern flying squirrel, Glaucomys volans. J Exp Biol 209(4):689–701

Fage A, Johansen FC (1927) On the flow of air behind an inclined flat plate of infinite span. Proc R Soc Lond A 116:170–197

Galvao R, Israeli E, Song A, Tian X, Bishop K, Swartz S, Breuer K (2006) The aerodynamics of compliant membrane wings modelled on mammalian flight mechanics. In: Proceedings of the 36th AIAA fluid dynamics conference and exhibit, 5–8 June 2006, San Francisco, AIAA-2006-2866

Gordnier R (2008) High fidelity computational simulation of a membrane wing airfoil. In: Proceedings of the 46th AIAA aerospace sciences meeting and exhibit, 7–10 January, Reno, AIAA-2008-614

Greenhalgh S, Curtiss HC, Smith B (1984) Aerodynamic properties of a two-dimensional inextensible airfoil. AIAA J 22(7):865–870

Gursul I, Gordnier R, Visbal M (2005) Unsteady aerodynamics of nonslender delta wings. Prog Aerosp Sci 41(7):515–557

Jackson PS, Christie GW (1986) Numerical analysis of three-dimensional elastic membrane wings. AIAA J 25(5):676–681

Miranda S, Vlachos PP, Telionis DP, Zeiger MD (2005) Flow control of a sharp-edged airfoil. AIAA J 43(4):716–726

Newman BG (1987) Aerodynamic theory for membranes and sails. Prog Aerosp Sci 24:1–27

Newman BG, Low HT (1984) Two-dimensional impervious sails: experimental results compared with theory. J Fluid Mech 144:445–462

Shyy W, Jenkins DA, Smith RW (1997) Study of adaptive shape airfoils at low Reynolds number in oscillatory flows. AIAA J 35(9):1545–1548

Shyy W, Berg M, Ljungqvist D (1999) Flapping and flexible wings for biological and micro air vehicles. Prog Aerosp Sci 35:455–505

Smith R, Shyy W (1995) Computational model of flexible membrane wings in steady laminar flow. AIAA J 33(10):1769–1777

Smith R, Shyy W (1996) Computation of aerodynamic coefficients for a flexible membrane airfoil in turbulent flow: a comparison with classical theory. Phys Fluids 8(12):3346–3353

Song AJ, Breuer KS (2007) Dynamics of a compliant membrane as related to mammalian flight. In: Proceedings of the 45th aerospace science meeting and exhibit, 8–11 January 2007, Reno, AIAA-2007-665

Song A, Tian X, Israeli E, Galvao R, Bishop K, Swartz S, Breuer K (2008) Aeromechanics of membrane wings with implications for animal flight. AIAA J 46(8):2096–2106

Swartz SM, Groves MS, Kim HD, Walsh WR (1996) Mechanical properties of bat wing membrane skin. J Zool 239:357–378

Swartz SM, Iriarte-Diaz J, Riskin DK, Song A, Tian X, Willis D, Breuer KS (2007) Wing structure and the aerodynamic basis of flight in bats. In: Proceedings of the 45th AIAA aerospace sciences meeting and exhibit, 8–11 January, Reno, AIAA-2007-42

Taylor G, Wang Z, Vardaki E, Gursul I (2007) Lift enhancement over flexible nonslender delta wings. AIAA J 45(12):2979–2993

Visbal M, Gordnier R, Galbraith M (2008) High-fidelity simulations of moving and flexible airfoils at low Reynolds numbers. Animal locomotion: aerodynamics of flying (special issue of experiments in fluids)

Winter Y, von Helversen O (1998) The energy cost of flight: do small bats fly more cheaply than birds? J Comp Physiol B Biochem Syst Environ Physiol 168(2):105–111

Wu JZ, Lu X, Denny AG, Fan M, Wu JM (1998) Post-stall flow control on an airfoil by local unsteady forcing. J Fluid Mech 37:21–58

Aerodynamic and functional consequences of wing compliance

Andrew M. Mountcastle · Thomas L. Daniel

Abstract A growing body of evidence indicates that a majority of insects experience some degree of wing deformation during flight. With no musculature distal to the wing base, the instantaneous shape of an insect wing is dictated by the interaction of aerodynamic forces with the inertial and elastic forces that arise from periodic accelerations of the wing. Passive wing deformation is an unavoidable feature of flapping flight for many insects due to the inertial loads that accompany rapid stroke reversals—loads that well exceed the mean aerodynamic force. Although wing compliance has been implicated in a few lift-enhancing mechanisms (e.g., favorable camber), the direct aerodynamic consequences of wing deformation remain generally unresolved. In this paper, we present new experimental data on how wing compliance may affect the overall induced flow in the hawkmoth, *Manduca sexta*. Real moth wings were subjected to robotic actuation in their dominant plane of rotation at a natural wing beat frequency of 25 Hz. We used digital particle image velocimetry at exceptionally high temporal resolution (2,100 fps) to assess the influence of wing compliance on the mean advective flows, relying on a natural variation in wing stiffness to alter the amount of emergent deformation (freshly extracted wings are flexible and exhibit greater compliance than those that are desiccated). We find that flexible wings yield mean advective flows with substantially greater magnitudes and orientations more beneficial to lift than those of stiff wings. Our results confirm that wing compliance plays a critical role in the production of flight forces.

Electronic supplementary material The online version of this article (doi:10.1007/s00348-008-0607-0) contains supplementary material, which is available to authorized users.

A. M. Mountcastle (✉) · T. L. Daniel
Department of Biology, University of Washington, Seattle, WA 98195-1800, USA
e-mail: mtcastle@u.washington.edu

T. L. Daniel
e-mail: danielt@u.washington.edu

1 Introduction

During flight, wings deform—sometimes dramatically—as they propel animals through the air (see, for example, Wootton 1992 for insects; Biewener and Dial 1995 for birds; Swartz et al. 1992 for mammals; Fig. 1). While the functional consequences of such complex, three-dimensional patterns of deformation is key to our understanding of wing design for locomotion, there are few studies that relate wing compliance to any measure of aerodynamic performance. Recent work has shown that subtle kinematic details of wings (e.g., rotations and supinations, wing–body interactions) can have dramatic consequences to the fluid forces associated with flight (Carruthers et al. 2007; Ellington 1995; Hedenstrom et al. 2007; Sane and Dickinson 2002). Associated with all of these dynamical processes are a host of issues surrounding the inertial and elastic mechanisms that determine the instantaneous shape of wings and how the dynamic deformation of wings may influence flight. The challenge we have faced over the years is how to approach this potential coupling between fluid dynamic loading and wing shape.

The deformations experienced by a flapping insect wing most often involve some combination of spanwise bending and torsion (Wootton 1981; Wootton et al. 2003). Because the center of aerodynamic pressure is located behind the center of torsion, some deformation patterns are inevitable

G.K. Taylor, M.S. Triantafyllou, and C. Tropea (Eds.): Animal Locomotion, pp. 311–320.
springerlink.com

Fig. 1 *Manduca sexta* wings exhibit pronounced deformations during flight, shown here at ventral stroke reversal (photo by Armin Hinterwirth). Note the torsional deformation of the wing facing the camera

(Ennos 1988; Norberg 1972; Wootton 1981; Wootton 1992). For example, Ennos (1988) showed that favorable camber is automatically generated during wing translation in both odonates and dipterans as a consequence of the structural support of wing veins. Dynamic deformation patterns may also be dominated by purely inertial and elastic processes, remaining largely independent of the pressure distribution resulting from aerodynamic forces. Recent results for robotically actuated wings of the hawkmoth, *Manduca sexta*, show that these wings deform nearly identically in air as they do in a low-pressure helium-filled chamber (15% of air density; Combes and Daniel 2003c). Thus, we can predict that the pattern of deformation one observes in these wings is somewhat decoupled from the pressure distribution to which wings are normally exposed.

Dynamically scaled robotic models (e.g., matched Reynolds and Strouhal numbers, reviewed by Sane 2003) are powerful tools for unraveling the complex aerodynamic forces and flows associated with model wings moving with complex kinematics. However, such dynamically scaled models are limited as biological proxies because structural dynamics do not scale in the same manner as fluid dynamics. It is thus a significant challenge to fabricate a dynamically scaled airfoil that faithfully recreates the emergent deformation patterns observed in flying insects.

Robotically actuated natural wings in air (as in Combes and Daniel 2003c) provide unique opportunities for examining the interaction between dynamic deformations and the emergent flow patterns (e.g., momentum flux, vorticity). In such cases, we avoid the challenge of scaling structural elastic and inertial forces with fluid forces. We face, however, the other technical challenge of providing kinematics at biologically relevant frequencies and amplitudes while measuring flows with very high temporal resolution. For large flying insects with relatively slow wing beat frequencies, we are able to resolve flows and deformation patterns with high-speed digital videography.

This study uses robotically actuated wings from *M. sexta*, a large moth that flaps its wings at 25 Hz. Due to the technological challenges of multi-axis actuation at such high frequencies, and in contrast to prior studies using scaled robotic models of insect wings (e.g., Sane 2003), we use a single axis rotation to yield natural deformations that reasonably well approximate wing kinematics observed in flight. We rely on natural changes in wing stiffness combined with exceptionally high temporal resolution digital particle image velocimetry to quantify the flow consequences of wing deformation.

2 Materials and methods

2.1 Overview

We measured the flexural stiffness and induced flow fields of 3 ipsilateral wing pairs of *M. sexta*, each in both a fresh state and dry state. Wings extracted from freshly enclosed moths are more flexible than those allowed to dry and stiffen over time, permitting us to examine the consequences of wing stiffness to the flow field induced by their motion. Wings that undergo desiccation also lose mass, however, so we controlled for mass by applying spray paint to the dry wings until they regained their original weight.

To quantify the overall difference in stiffness between fresh wings and dry wings, we used a proxy measurement of spanwise flexural stiffness, calculated using an applied ventral force and resulting wing deflection. Although the wings of insects have inhomogeneous, anisotropic distributions of flexural stiffness that differ not only in their spanwise–chordwise directions but also in their ventral–dorsal loading (Combes and Daniel 2003a, b), we did not focus on the details of wing structural properties in this study.

Each wing pair was robotically actuated at its natural wingbeat frequency of 25 Hz, and we employed digital particle image velocimetry (PIV) to explore the consequences of wing stiffness to the emergent fluid dynamics at ventral stroke reversal. We computed a representative velocity vector, the mean advective flow, for each flow field and used it to make general comparisons between the induced flows of different wing types.

In order to evaluate the biological significance of the deformations exhibited by our robotically actuated wings, and thus their flow field results, we quantified the wing deformations of a robotically actuated sample wing unit (in both its fresh and dry state) as well as the natural deformations observed in free flight hovering for comparison. Our quantification method consisted of finding an average flat plate that best fit the deformed wing surface at each

consecutive time step throughout a complete ventral stroke reversal, and calculating the overall deviation of the wing surface from the flat plate.

Finally, we needed to rotate our robotic wing data into a biologically relevant configuration. Thus, we performed a principal components analysis on the wing trajectory of a hovering moth to determine its average stroke plane in global coordinates, onto which we mapped the stroke plane of our robotically actuated wing and rotated the PIV flow fields accordingly.

2.2 Flexible wing preparation

We extracted and prepared wings from *M. sexta* moths obtained from a captive-bred colony at the University of Washington. We selected individuals within 24 h of eclosion and cold-anesthetized them at 0 C for 12–15 min. We removed each right forewing and hindwing pair at the thorax and fastened the wing bases adjacent to each other on the top edge of ca. 5 cm^2 sheet metal mounting plate using cyanoacrylate glue cured with sodium bicarbonate. We mounted the forewing directly in front of the hindwing so that the trailing edge of the forewing slightly overlapped the leading edge of the hindwing, approximating their arrangement during natural flight. A small drop of cyanoacrylate glue applied between the dorsal side leading edge of the hindwing and the ventral side trailing edge of the forewing, approximately 2 cm distal to the hindwing base, adhered the two wings together where they overlapped. We weighed the mounted wing unit before proceeding with flexural stiffness measurements and PIV trials.

2.3 Dry wing preparation

Following each fresh wing PIV trial, we let the wing unit dry at room temperature for 12–24 h, during which time it both lost mass and gained stiffness. After recording the weight of the dried wing unit, we applied a series of thin coats of evenly distributed spray enamel to both ventral and dorsal sides, periodically weighing the wing unit until we approximately reached its original weight when freshly mounted. Each of our three painted wing units deviated less than 1.5% from their original mass. We then repeated our flexural stiffness measurements and PIV trials on these dry, painted wing units.

2.4 Flexural stiffness measurements

We calculated the flexural stiffness of each wing unit by applying a series of point forces on the ventral wing surface, along the wingspan, and measuring the resulting wing displacements in photographed images in a method similar to that used by Combes and Daniel (2003a, b). We fastened

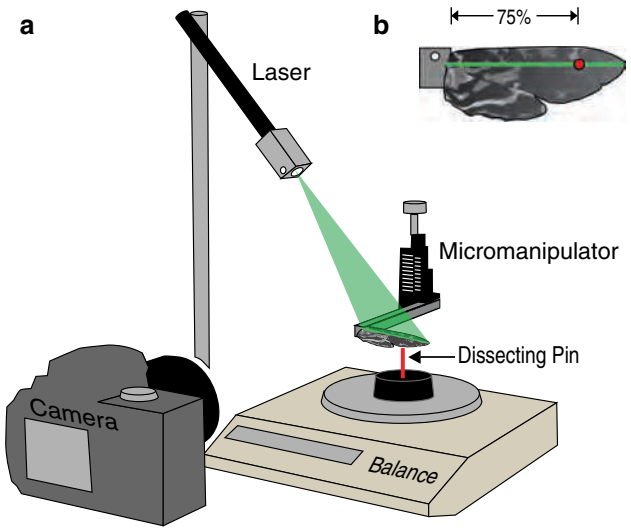

Fig. 2 Apparatus used to measure wing flexural stiffness. **a** Wings were fixed to a micromanipulator and lowered onto the head of a dissecting pin resting on a digital balance. **b** A laser light sheet illuminated a spanwise line along the dorsal wing surface and a point force was applied via the pinhead at 75% wing span along the illuminated line. Wing deflection was captured in a photographed image for subsequent analysis

the wing unit, by the mounting plate, to an aluminum beam connected to a micromanipulator and positioned the wing above a dissecting pin vertically mounted on a digital balance (Sartorius L610D; Fig. 2a). A 5 mm diameter quartz cylindrical rod was affixed to the front of a 100 mW red laser pointer (Pulsar P100, Wicked Lasers) to create a vertical light sheet that projected obliquely onto the dorsal wing surface. The light sheet illuminated a line running spanwise from the forewing base to the tip (Fig. 2b). Images were captured with a Nikon D40 digital camera and 60 mm micro lens positioned posterior to the wing and orthogonal to the laser light sheet.

Using the micromanipulator we lowered the wing unit onto the pinhead at approximately 75% of the wingspan along the illuminated line (Fig. 2b). An initial photograph of the wing was taken at its unloaded reference location, where its ventral surface only just made contact with the pinhead with no applied force measured by the scale. We then applied a series of point loads of varying magnitudes, photographing the deflected wing unit in each case and returning the wing to its unloaded state after each trial. We performed five to ten flexural stiffness trials on each wing unit. Lastly, we removed the wing unit and inserted a metric ruler at the same location, taking a final photograph for image calibration.

We analyzed each image of the deflected wing unit to determine its effective beam length and deflection. We used custom Matlab software (Hedrick 2008) to digitize our calibration and wing images. Digitizing the ruler

calibration image enabled us to convert image coordinates from pixels to meters. Beam length (L) was measured as the distance along the illuminated line from the base of the wing where it left the mounting plate to the point of applied force at the pinhead. Since the point of applied force was constant, deflection (δ) was measured as the vertical distance traveled by the micromanipulator from its initial reference location. We used these two measured values and the applied force (F), the product of mass reported on the balance readout and gravitational acceleration, to calculate the wing's overall spanwise flexural stiffness (EI) for each trial (Combes and Daniel 2003a, b):

$$EI = \frac{FL^3}{3\delta}$$

All wing deflection magnitudes in our trials were less than 5% of the effective beam length, as in Combes and Daniel (2003a).

2.5 Particle image velocimetry

By combining continuous laser light and high speed digital videography with short exposure times, we were able to compute induced flow fields at extremely high temporal resolution, exceeding 2,000 images/s at 0.6 megapixels per image.

Each wing unit was fastened to a brass rod attached to a pen motor from a Gould chart recorder and flapped sinusoidally around a dorsoventral axis of rotation at a frequency of 25 Hz and amplitude of 125°, typical of hovering *M. sexta* (Willmott and Ellington 1997). The motor was mounted to a platform in the center of a glass chamber (42 cm × 27 cm × 31 cm; Fig. 3a). A 5 mm diameter quartz cylindrical rod was affixed to the front of a 200 mW, 532 nm continuous green laser pointer (Spyder II GX, Wicked Lasers) to create a vertical light sheet projecting down the length of the chamber, parallel to the axis of wing rotation. The flapping wing intersected the light sheet at ventral stroke reversal, illuminating a chordwise wing section at 75% wingspan during supination (Fig. 3b). The laser rode on a mini optical rail (Newport), allowing us to position the light sheet at the proper spanwise location for each wing. We seeded the chamber with *Lycopodium* spores (mean diameter 30 μm) as tracer particles (as in Dickinson and Gotz 1996).

A Phantom v5.1 high speed digital camera (Vision Research) with a 50 mm Nikon lens imaged the induced *Lycopodium* flow patterns illuminated by the orthogonal laser light sheet. We used a camera frame rate of 2,100 frames/s, a shutter speed of 200 ms, and a lens aperture of 1.2 to capture images with a pixel resolution of 768 × 768. Both camera and motor were simultaneously controlled by a custom signal-generating Matlab program (Mathworks) via a National Instruments USB-6229 data acquisition board, and were phase-locked at 84 images per wing stroke.

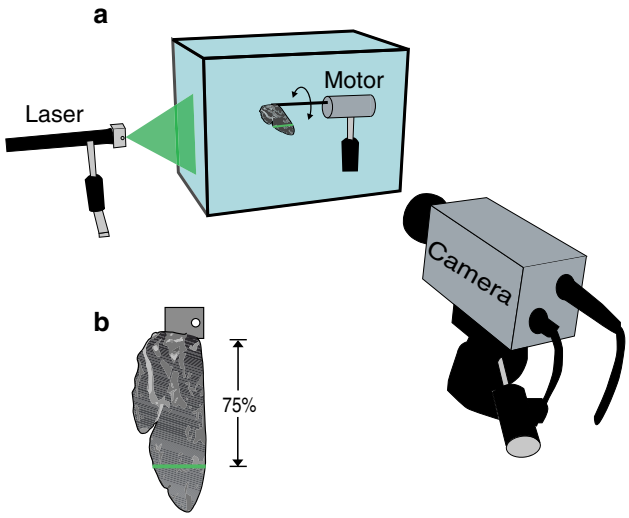

Fig. 3 Apparatus used to image induced flows around a robotically actuated moth wing for PIV analysis. **a** A right ipsilateral wing pair was fixed to a motor within a glass chamber and oscillated at 25 Hz. A 200 mW continuous laser light sheet was projected down the center of the chamber, **b** illuminating a chordwise wing section at 75% wingspan during ventral stroke reversal. The chamber was seeded with *Lycopodium* spores as tracer particles and flows were imaged at 2,100 frames/s with a high-speed digital camera

Prior to each trial we introduced a 5 s burst of compressed air into the chamber through a flexible hose to suspend a majority of the *Lycopodium* spores, then waited 10 s for the injected turbulence from the air hose to dissipate before beginning our trial. The wing unit was driven for 25 strokes (1 s total duration) for each trial, and we recorded the final 10 strokes for subsequent PIV analysis.

Particle image velocimetry analysis was performed with MatPIV 1.6.1, an open-source toolbox for Matlab (Sveen 2004). Velocity fields were computed for every frame advance through nine complete wing strokes for Wing 1, totaling 757 interrogated image pairs, and 10 complete wing strokes for Wings 2 and 3, totaling 841 interrogated image pairs each. A two-frame cross-correlation was performed with 50% window overlap, proceeding through 6 iterations of consecutively smaller window sizes from 64 × 64 to 16 × 16 pixels. This resulted in 9,025 velocity vectors per frame.

We applied a series of data filters available in the MatPIV package to remove spurious vectors and ultimately replace them using a nearest-neighbor interpolation. The vector field was validated with both a signal-to-noise ratio filter using a threshold value of 1.3, and a local filter that operated on the squared difference between each velocity vector and the medians and means of its surrounding neighbors (Sveen 2004). A combination of hardware and image interrogation algorithm produced a small region of no data in every vector field, which we ignored.

We phase-averaged our velocity fields across nine wing strokes for Wing 1 and 10 wing strokes for each of Wings 2 and 3, and computed a mean velocity vector for each phase by spatially averaging all vectors in each phase-averaged field. Finally, we averaged these 84 phase vectors to find a single velocity vector that represents the average flow magnitude and direction through our control region throughout a complete (phase-averaged) wing stroke. We found this representative velocity vector—the mean advective flow (MAF)—to be a useful metric for comparing the overall induced flows of different wing types.

2.6 Wing deformation measurements

We quantified the overall wing deformations at ventral stroke reversal of a robotically actuated fresh and stiff wing, and the natural deformations exhibited by a wing during hovering flight for comparison. A sample wing unit was extracted, prepared and mounted to the PIV motor assembly, as above, and subjected—in both its fresh and dry states—to the following treatment. Three synchronized high-speed digital cameras (Phantom v5.1, Vision Research) were used to film the oscillating wing from various directions at 1,000 frames/s. We used custom Matlab software (Hedrick 2008) to track and digitize an array of 12 points evenly distributed around the entire wing margin. The moth's natural wing pigmentation pattern provided landmarks that served as tracking points, and we used the same 12 tracking points for every deformation trial analyzed. We digitized the wing margin points through 14 consecutive video frame images (14 ms) encompassing each ventral stroke reversal. Five ventral stoke reversals were mapped and analyzed for each of the fresh and stiff wings.

The deformed surface of the wing was approximated at each time interval by linearly interpolating the 12 wing margin data points onto an intervening regularly spaced fine grid of 870 points. We then found an average flat plate that best fit the deformed wing surface at every instant by minimizing the sum squared distances from the plate to all 870 interpolated wing surface points. We defined *deformation* as the spatial (across the entire wing surface) and temporal (throughout all 14 frames of stroke reversal) average distance from an interpolated wing point to the best-fit flat plate. Thus, we distilled from surface coordinate data a single value for deformation that summarizes the detailed wing kinematics of each ventral stroke reversal. We calculated the mean deformation and standard deviation for our five fresh wing stroke reversals, and also for our five stiff wing stroke reversals.

Notably, our deformation value reflects only the gross extent of wing deformation and captures nothing of the spatial or temporal details of the deformation pattern. Nevertheless, it provides a useful metric for making general comparisons in deformation between wing strokes.

Wing deformation was equivalently measured in natural hovering flight for comparison. An adult male *M. sexta* moth was obtained from the captive bred colony at the University of Washington approximately 5 days after eclosion, and placed in a flight chamber (86 cm × 53 cm × 87 cm). Four synchronized high speed digital cameras (Phantom v5.1, Vision Research) mounted to a frame (80/20 Inc.) surrounding the infrared-illuminated chamber were used to film the nectarivorous moth hovering steadily in front of a freshly cut flower at 1,000 frames/s. We quantified wing deformation for five consecutive ventral stroke reversals (14 images each, as before), and also calculated the mean deformation and standard deviation of these five deformation values.

2.7 Principal components analysis

We performed a principal components analysis (PCA) on the wing trajectory of a moth during free flight hovering to determine its average stroke plane. We chose to use a PCA rather than a more commonly used linear regression method (Ellington 1984) because observations of wing position have variance in every spatial dimension. Thus, we avoid making an arbitrary choice for any particular dimension to be regressed upon another. The results of a PCA on a given data set are often similar to a linear regression, however, and they take the same form of mutually orthogonal eigenvectors (reported as principal components) and their associated eigenvalues.

Analyzing another multi-camera video sequence of hovering flight with custom Matlab software (Hedrick 2008), we digitized two points on the rigid leading edge of the right forewing throughout five complete wing strokes: one point at the wing base and the other at 60% of the wingspan. A PCA on a two-dimensional lateral projection of this data set in global coordinates yielded two principal components. The principal component with the highest eigenvalue defines the dominant plane of motion swept out by the flapping wing, or the average stroke plane. This enabled us to rotate the coordinate system of our flow field data such that the stroke plane of our robotically actuated wing matched the moth's natural stroke plane.

3 Results

3.1 Principal components analysis

A PCA on a lateral view projection of the leading edge wing kinematics produced a first principal component of [−0.94 0.33] with an eigenvalue of 0.40 and a second

principal component of [−0.33 –0.94] with an eigenvalue of 0.02. The first principal component defines the dominant plane of motion (the average stroke plane) and lies at 19° relative to the *x*-axis in global coordinates, within the range of stroke plane angles previously identified in hovering *Manduca* (Willmott and Ellington 1997). The default stroke plane of our robotic wing was exactly vertical, so we applied a 71° counter-clockwise rotation to our robotic wing coordinate system after PIV analysis. All flow field results and images described hereafter account for this rotation into a biologically relevant configuration, and are therefore presented in the moth's global coordinates.

3.2 Flexural stiffness measurements

Overall flexural stiffness *EI* increased from the fresh wing state to the dry wing state for all three wings and these increases were significant, based on a Student's *t* test performed on each data pair. Wing 1 *EI* increased from a mean of 9.79×10^{-6} Nm^2 for the fresh wing to a mean of 2.04×10^{-5} Nm^2 for the dry wing, $t = 6.29$, $P < 0.001$. Wing 2 *EI* increased from a mean of 2.84×10^{-5} Nm^2 to 7.06×10^{-5} Nm^2, $t = 13.68$, $P < 0.001$, and Wing 3 *EI* increased from a mean of 1.73×10^{-5} Nm^2 to 3.45×10^{-5} Nm^2, $t = 13.64$, $P < 0.001$. These data are consistent with those in prior studies; using a similar methodology, Combes and Daniel (2003b) reported overall spanwise *EI* values for *M. sexta* in the range of 10^{-6}–10^{-5} Nm^2.

3.3 Wing deformation measurements

We computed a mean wing deformation value of 1.60 mm for five stroke reversals of our sample robotically actuated fresh wing, with a standard deviation of 0.0544 mm. Our sample dry wing yielded a mean deformation of 1.15 mm, with a standard deviation of 0.0449. By comparison, five consecutive wing stroke reversals of a freely hovering hawkmoth yielded deformations ranging from 1.45 to 1.68 mm, with a mean deformation of 1.52 mm and a standard deviation of 0.0954 mm. Thus, our mean fresh wing deformation was within 1 standard deviation above the natural mean and our mean dry wing deformation was within 4 standard deviations below the natural mean. Further, the variance in deformation of the five natural wingstrokes was greater than that of either the fresh or dry robotically actuated wing.

Our wing actuation method had fundamental limitations that prevented exact replication of a natural wing stroke. First (as previously discussed), our motor had only one degree of active rotational freedom, versus three degrees of freedom on the moth. Second, in affixing the forewing and hindwing bases on a flat mounting plate, the degree of camber of the wing unit may not have matched that occurring in the natural wing pair. Camber significantly affects the extent of wing deformation (Ennos 1995). These important differences must be considered when comparing the deformation values of our robotically actuated wings with those from free flight. Yet despite these differences, the deformation patterns of the robotically actuated wings nevertheless approximated the patterns observed in natural flight reasonably well due to the wing's natural elastic properties, especially with respect to torsion (Fig. 4; Movie 1; Movie 2). This indicates that the need for multi-axis actuation is actually diminished by the presence of passive elastic processes. Indeed prior work has established that torsional wing deformation is critical for flight in many insects, enabling the production of positive lift during both the upstroke and downstroke, despite having wings that are doubly hinged at the thorax (Wootton 1993; Ennos 1995).

3.4 Particle image velocimetry

All fresh wings produced flow fields with greater local velocities and more pronounced downward orientations throughout the stroke cycle than those of their stiff wing counterparts (Fig. 5). The MAF for each fresh wing had a greater magnitude and a greater angle relative to the $-x$-axis than the MAF for each dry wing (Fig. 6). The MAF for Wing 1 decreased from a magnitude of 19.7 cm/s at −65° for the fresh state to 4.7 cm/s at −18° for the dry state. For Wing 2 the MAF decreased from 44.5 cm/s at −66° to 17.2 cm/s at 4°, and for Wing 3 it decreased from 49.3 cm/s at −78° to 18.1 cm/s at −24°.

A hovering moth accelerates air downward, creating sufficient average vertical force to support its weight. Of particular interest, then, is the extent to which the vertical component of the MAF comprises the total MAF magnitude and how the vertical component changes from the fresh wing state to the dry wing state. The vertical component of the fresh Wing 1 MAF was −17.9 cm/s, or 91% of its total magnitude. By comparison, the vertical component of the dry Wing 1 MAF was −1.5 cm/s, or 32% of its magnitude. The vertical component of the Wing 2 MAF changed from −40.6 cm/s at 91% magnitude for the fresh state to 1.3 cm/s at 8% magnitude for the dry state. The vertical component of the Wing 3 MAF changed from −48.4 cm/s at 98% magnitude for the fresh state to −7.3 cm/s at 40% magnitude for the dry state.

4 Discussion

We found that flexible (fresh) wings produced mean advective flows with substantially greater magnitudes and orientations more beneficial to lift than those produced by

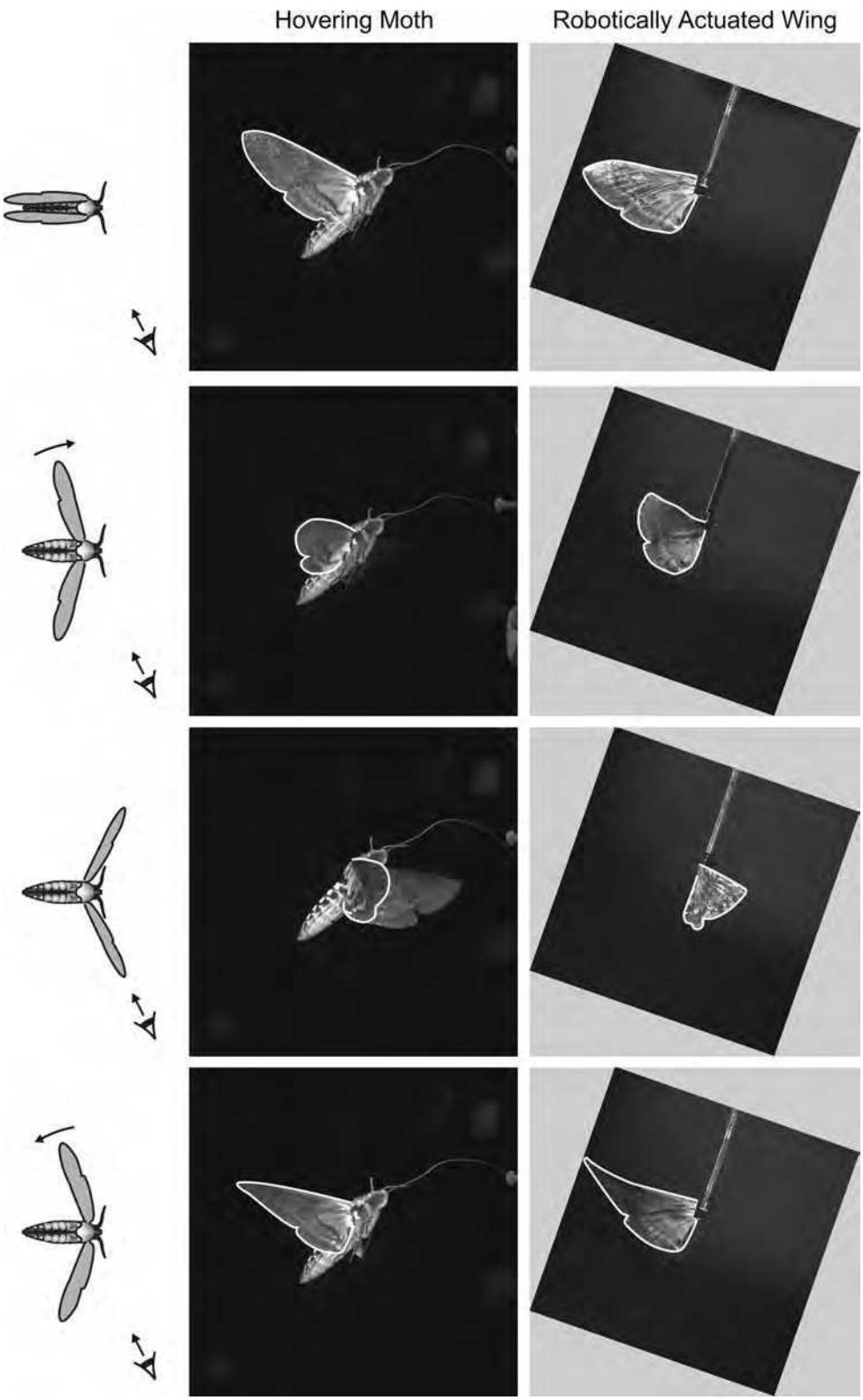

Fig. 4 A freshly extracted wing robotically flapped along a single axis of rotation approximates natural wing motion during hovering flight, illustrated in synchronized phases of a wing stroke at quarterly intervals. The collective tilt of the robotically actuated wing images is the result of a coordinate rotation to match the robotic wing stroke plane with the average stroke plane in hovering flight. The wings have been outlined to highlight their overall similarities in shape. The moth planform diagrams in the left column provide positional reference of the wing stroke phase relative to the viewpoint

stiff (dry) wings. We also showed that wing deformations exhibited by our robotically actuated fresh and dry wings are similar to those measured in hovering flight, straddling the naturally occurring values. These results were made possible by using high temporal resolution particle image velocimetry (2,100 frames/s) combined with real wings flapped at natural wing beat frequency, rather than dynamically scaled models. We are unaware of any other

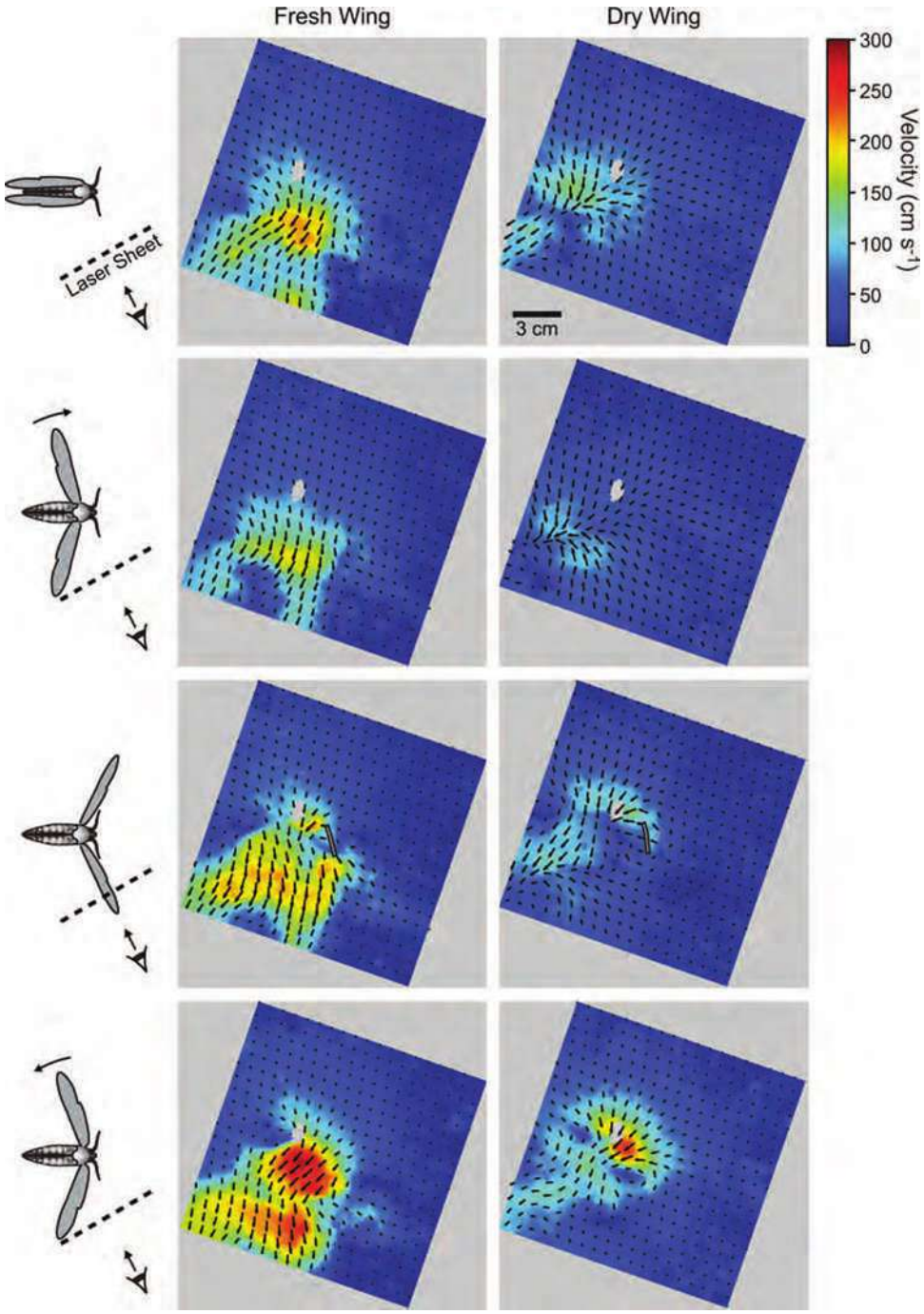

Fig. 5 A robotically actuated fresh wing induces flows with greater overall velocities and more pronounced downward orientations than a dry wing, illustrated in phase-averaged velocity fields at synchronized quarterly wing stroke intervals for Wing 3. *Arrow lengths and direction* indicate magnitude and orientation of local fluid velocity, computed with PIV. Velocity magnitude is also represented in the pseudo-color background. The collective tilt of the control regions is the result of a coordinate rotation to match the robotic wing stroke plane with the average stroke plane in hovering flight. A cross-section of each wing appears in the third row of images, where the wing intersects the light sheet at ventral stroke reversal. A *small gray region* containing no data can be seen at the same location in every image, resulting from the combined affect of hardware and the PIV algorithm employed. The moth planform diagrams in the left column provide positional reference of the wing stroke phase relative to the laser light sheet and viewpoint

flow visualization studies of animal locomotion using standard particle image velocimetry techniques that have reached such high a frame rate.

Passive wing deformation may lead to a number of aerodynamic mechanisms that may affect induced flows and thus aerodynamic forces. For example, during supination in natural flight a moth wing undergoes inertial-driven pitch reversal about a spanwise axis, manifest as a torsional wave that propagates from the tip to the base, thereby establishing a positive angle of attack for the subsequent upstroke (Bergou et al. 2007; Willmott and Ellington 1997). We observed a more pronounced and significant pitch reversal—a torsional wave with greater amplitude—accompanying ventral stroke reversal in our highly deforming fresh wings than in our lesser deforming dry wings. Wootton (1992) noted that, in general, the greater torsion an insect wing experiences on the upstroke, the closer the aerodynamic force vector will approach the vertical. He suggested that highly twistable wings that develop vertical force during both the downstroke and

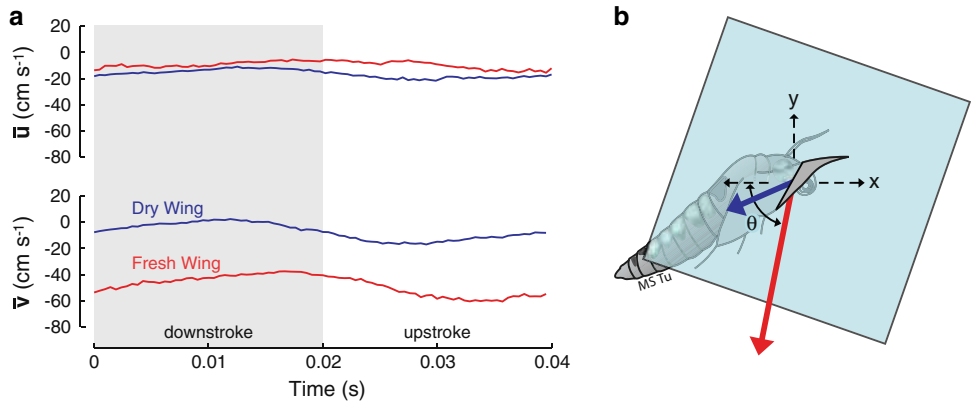

Fig. 6 Fresh wing mean flow velocities have greater magnitudes and greater downward components than dry wing mean flow velocities, shown here for Wing 3. **a** Each phase-averaged velocity field is spatially averaged over the entire field to yield a single representative velocity vector per time step. The components of all such field-averaged vectors are plotted for an entire phase-averaged stroke for both wing types, with $\bar{u}$ representing the *x*-component and $\bar{v}$ representing the *y*-component in global coordinates (*red* fresh wing, *blue* dry wing). **b** The stroke average of all field-averaged velocity vectors is the MAF, plotted relative to the control region and a hovering moth in global coordinates (*red* flexible wing, *blue* dry wing)

upstroke permit slow, maneuverable flight, while less twistable wings can only accommodate fast flight (Wootton 1992). Although Wootton addressed torsional consequences during the translational stages of the wing stroke where we did not focus our attention, ventral stroke reversal by definition captures something of the end of the downstroke and the beginning of the upstroke, and its fluid dynamics are not independent of those manifest throughout the stroke cycle. Our fresh wings with more pronounced pitch reversals during supination presumably maintained greater torsion throughout both the downstroke and upstroke than their dry wing counterparts, thereby contributing to the more vertically oriented MAF appearing at stroke reversal.

The markedly greater pitch reversal in our fresh wings may also generate greater circulation via the Kramer effect. A flat, rigid wing undergoing rotation about a spanwise axis while translating develops extra circulation proportional to the angular velocity of rotation, causing rotational forces that either augment or reduce the net force due to translation (Sane 2003; Sane and Dickinson 2002). Wing rotation in advance of translational reversal augments translational forces, delayed rotation reduces them, and rotation that is symmetrical about reversal has no net effect (Sane and Dickinson 2002). The extent to which wing deformation contributes to the Kramer effect has not been explored. It is reasonable, however, to propose passive chordwise bending as one component of effective wing rotation.

Chordwise bending waves may also contribute to fluid dynamic forces in much the same way as fin waves contribute to thrust in fish (Combes and Daniel 2001; Wu 1971). At ventral stroke reversal, when the wing chord is oriented vertically, a rapid, large amplitude wave propagating from the leading to trailing edge of the wing could lead to a vertical force. To our knowledge, this mechanism has not been considered in studies of animal flight.

Spanwise bending was observed in both our robotically actuated wings and in natural flight. Investigations of *Manduca* flight kinematics offer qualitative descriptions of spanwise wing bending and how it varies with different flight modes and steering maneuvers (Weis-Fogh 1973; Willmott and Ellington 1997). Few studies, however, have explored the aerodynamic consequences of transverse bending. Although we observe greater transverse bending in our fresh wings than our dry wings, consistent with their greater overall deformation, the extent to which this mode of deformation may be contributing to the induced flow fields is unknown.

We relied upon a natural material stiffening process of extracted moth wings to modify emergent deformation. The mechanisms by which wing deformation may be altered during flight, however, remain unknown. Here we briefly offer several possible mechanisms that may contribute to deformation changes. As a passive, inertial-driven process, the pattern and extent of deformation likely depend on overall wing trajectory, which is itself controlled by the powerful flight muscles in the thorax as well as the steering muscles. For example, for moths flying in a wind tunnel, an increase in flight speed was accompanied by both a posterior shift in the wingtip path and an increase in wing rigidity (Willmott and Ellington 1997). Although the observed increase in wing rigidity (measured by torsion and thus related to deformation in this study) may indeed be a byproduct of the changes in wing trajectory associated with flight speed, emergent deformation in this example may also be affected by other processes. For example, it

may be affected to some extent by the changes in external airflow that accompany changes in flight speed or by a change in the structural properties of the wing unit itself, resulting from the posterior shift in wingtip trajectory. If such a kinematic adjustment involved an increase in overlap between the forewing and hindwing, for example, the overall wing geometry would be modified and possibly the flexural stiffness distribution of the entire wing unit as well. Further, there is the possibility that flight muscles may have some degree of direct control of wing deformation, aside from the secondary effects associated with changes in wing trajectory. It is unclear how the flight muscles might achieve such a task, however.

Although stroke-to-stroke kinematic variations during steady hovering flight are smaller than those arising between different modes of flight (Willmott and Ellington 1997), one or more of the mechanisms proposed above might nevertheless be contributing to more subtle changes in wing deformation, possibly accounting for the variation measured in our free-flight analysis. The induced flow results presented in this study suggest that such changes in deformation may in turn affect important changes in the fluid dynamics and forces relevant to the flight of insects.

Acknowledgments The authors would like to thank Dr. Dana Dabiri (University of Washington) for his assistance with PIV methods, and two anonymous reviewers for providing helpful comments on this paper. This work was supported by DARPA and the Komen Endowed Chair to T.D., and a National Science Foundation Graduate Research Fellowship to A.M.

References

Bergou A, Xu S, Wang Z (2007) Passive wing pitch reversal in insect flight. J Fluid Mech 591:321–337

Biewener A, Dial K (1995) In-vivo strain in the humerus of pigeons (*Columba livia*) during flight. J Morphol 225:61–75

Carruthers A, Thomas A, Taylor G (2007) Automatic aeroelastic devices in the wings of a steppe eagle *Aquila nipalensis*. J Exp Biol 210:4136–4149

Combes SA, Daniel TL (2001) Shape, flapping and flexion: wing and fin design for forward flight. J Exp Biol 204:2073–2085

Combes S, Daniel T (2003a) Flexural stiffness in insect wings I. Scaling and the influence of wing venation. J Exp Biol 206:2979–2987

Combes S, Daniel T (2003b) Flexural stiffness in insect wings II. Spatial distribution and dynamic wing bending. J Exp Biol 206:2989–2997

Combes S, Daniel T (2003c) Into thin air: contributions of aerodynamic and inertial-elastic forces to wing bending in the hawkmoth *Manduca sexta*. J Exp Biol 206:2999–3006

Dickinson M, Gotz K (1996) The wake dynamics and flight forces of the fruit fly *Drosophila melanogaster*. J Exp Biol 199:2085–2104

Ellington CP (1984) The aerodynamics of hovering insect flight. III. Kinematics. Philos T R Soc B 305:41–78

Ellington CP (1995) Unsteady aerodynamics of insect flight. In: Ellington CP, Pedley TJ (eds) Unsteady aerodynamics of insect flight. The Company of Biologists, Cambridge, pp 109–129

Ennos AR (1988) The inertial cause of wing rotation in Diptera. J Exp Biol 140:161–169

Ennos AR (1995) Mechanical-behavior in torsion of insect wings, blades of grass and other cambered structures. Proc Roy Soc Lond B Biol 259:15–18

Hedenstrom A, Johansson L, Wolf M, Von BR, Winter Y, Spedding G (2007) Bat flight generates complex aerodynamic tracks. Science 316:894–897

Hedrick TL (2008) Software techniques for two- and three-dimensional kinematic measurements of biological and biomimetic systems. Bioinspir Biomim 3:034001

Norberg R (1972) Evolution of flight in insects. Zoologica Scripta 1:247–250

Sane SP (2003) The aerodynamics of insect flight. J Exp Biol 206:4191–4208

Sane S, Dickinson M (2002) The aerodynamic effects of wing rotation and a revised quasi-steady model of flapping flight. J Exp Biol 205:1087–1096

Sveen JK (2004) An introduction to MatPIV v. 1.6.1, Eprint No. 2, Department of Mathematics, University of Oslo. http://www.math.uio.no/~jks/matpiv

Swartz S, Bennett M, Carrier D (1992) Wing bone stresses in free flying bats and the evolution of skeletal design for flight. Nature 359:726–729

Weis-Fogh T (1973) Quick estimates of flight fitness in hovering animals, including novel mechanisms for lift production. J Exp Biol 59:169–230

Willmott A, Ellington C (1997) The mechanics of flight in the hawkmoth *Manduca sexta*.1. Kinematics of hovering and forward flight. J Exp Biol 200:2705–2722

Wootton RJ (1981) Support and deformability in insect wings. J Zool 193:447–468

Wootton RJ (1992) Functional morphology of insect wings. Annu Rev Entomol 37:113–140

Wootton RJ (1993) Leading-edge section and asymmetric twisting in the wings of flying butterflies (*Insecta*, *Papilionoidea*). J Exp Biol 180:105–117

Wootton RJ, Herbert RC, Young PG, Evans KE (2003) Approaches to the structural modelling of insect wings. Philos T R Soc B 358:1577–1587

Wu TY (1971) Hydrodynamics of swimming propulsion. Part 1. Swimming of a two-dimensional flexible plate at variable forward speeds in an inviscid fluid. Part 2. Some optimum shape problems. Part 3. Swimming and optimum motions of slender fish with side fins. J Fluid Mech 46:337–355

Shallow and deep dynamic stall for flapping low Reynolds number airfoils

Michael V. Ol · Luis Bernal · Chang-Kwon Kang · Wei Shyy

Abstract We consider a combined experimental (based on flow visualization, direct force measurement and phase-averaged 2D particle image velocimetry in a water tunnel), computational (2D Reynolds-averaged Navier–Stokes) and theoretical (Theodorsen's formula) approach to study the fluid physics of rigid-airfoil pitch–plunge in nominally two-dimensional conditions. Shallow-stall (combined pitch–plunge) and deep-stall (pure-plunge) are compared at a reduced frequency commensurate with flapping-flight in cruise in nature. Objectives include assessment of how well attached-flow theory can predict lift coefficient even in the presence of significant separation, and how well 2D velocimetry and 2D computation can mutually validate one another. The shallow-stall case shows promising agreement between computation and experiment, while in the deep-stall case, the computation's prediction of flow separation lags that of the experiment, but eventually evinces qualitatively similar leading edge vortex size. Dye injection was found to give good qualitative match with particle image velocimetry in describing leading edge vortex formation and return to flow reattachment, and also gave evidence of strong spanwise growth of flow separation after leading-edge vortex formation. Reynolds number effects, in the range of 10,000–60,000, were found to influence the size of laminar separation in those phases of motion where instantaneous angle of attack was well below stall, but have limited effect on post-stall flowfield behavior. Discrepancy in lift coefficient time history between experiment, theory and computation was mutually comparable, with no clear failure of Theodorsen's formula. This is surprising and encouraging, especially for the deep-stall case, because the theory's assumptions are clearly violated, while its prediction of lift coefficient remains useful for capturing general trends.

M. V. Ol (✉)
Air Force Research Lab, Wright-Patterson AFB,
Dayton, OH, USA
e-mail: Michael.Ol@wpafb.af.mil

L. Bernal · C.-K. Kang · W. Shyy
Department of Aerospace Engineering, University of Michigan,
Ann Arbor, MI, USA
e-mail: lpb@umich.edu

C.-K. Kang
e-mail: kangck@umich.edu

W. Shyy
e-mail: weishyy@umich.edu

List of symbols

C_L	Airfoil lift coefficient per unit span
c	Airfoil chord (= 152.4 mm)
f	Airfoil oscillation pitch–plunge frequency
ω	Pitch–plunge circular frequency
h	Plunge position as function of time
h_0	Nondimensional plunge amplitude
k	Reduced frequency of pitch or plunge, $k = \omega c/2U_{\infty:} = \pi fc/U_\infty$
St	Strouhal number, $2fch_0/U_{\infty:} = 0.08$
U_∞	Freestream (reference) velocity (cm/s)
Re	Reynolds number, $Re = c\ U_\infty/v$, v taken as 0.93×10^{-6} in SI units for water at 23°C
α	Kinematic angle of incidence due to pitch
A	Pitch amplitude (in degrees)
α_0	Mean angle of attack (i.e., the constant pitch angle offset from zero)
α_e	Total angle of attack from trigonometric combination of pitch and plunge

G.K. Taylor, M.S. Triantafyllou, and C. Tropea (Eds.): Animal Locomotion, pp. 321–339.
springerlink.com

x_p Pitch pivot point: fraction of chord downstream from airfoil leading edge (= 0.25)
t/T Dimensionless time, in fractions of one oscillation period
φ Phase difference between pitching and plunging; positive → pitch leads
λ Ratio of pitch-amplitude to plunge-induced angle of attack

1 Introduction

We present comparisons between experimental, computational and theoretical results of a nominally two-dimensional airfoil undergoing synchronized pitching and plunging sinusoidal motion of large amplitude at Reynolds numbers in the transitional range. A fundamental question in the aerodynamics of flapping-wing flight, (Ellington 1984; Dickinson and Götz 1993; Lehmann 2004; Liu and Kawachi 1998; Shyy et al. 2008) is to quantitatively ascertain the role of two-dimensional effects such as leading edge vortex formation and vortex shedding, and three-dimensional effects such as spanwise relief in leading edge vortices (Usherwood and Ellington 2002) and leading–trailing edge vortex interaction was made possible through wingtip interactions (Poelma and Dickinson 2006). For all of the complexities of 3D effects, fundamental features of vorticity dynamics and time-dependent aerodynamic loads must be accurately predicted in two dimensions before more complex three dimensional effects can be adequately understood. Further, nominally two-dimensional problems remain useful as validation cases for computations, as means of addressing large parameter studies with comparative simplicity, and as explorations of how classical unsteady aerodynamics could still capture some of the salient features of flapping-wing flight in nature and in man-made micro unmanned flight vehicle applications.

The combination of low Reynolds number ($Re < 10^5$) phenomena and large topological changes in flow structure encountered in flapping wing flows suggests departure from classical unsteady airfoil theory (von Karman and Sears 1938). Crucial issues include the interaction of the time-dependent wing pressure distribution with shed vortices and the effect of concentrations of shed vorticity on the aerodynamic loads time history, and the role of transition in shear layers bounding regions of laminar separation.

Prior to current interest in flapping wing aerodynamics, dynamic stall of helicopter blades was perhaps the main application for high-rate unsteady airfoil aerodynamics, but the difference in Reynolds number is a factor of order 100. The quintessential feature of dynamic stall is the formation, shedding and downstream convection of a strong vortex-like disturbance emanating from near the leading-edge. McCroskey et al. (1976) pointed out that as this vortex passes over the airfoil surface, it significantly changes the chordwise pressure distribution and produces transient forces and moments fundamentally different from those in static stall. Comprehensive reviews of dynamic stall are given by McCroskey (1982), Carr (1988) and Carr and McCroskey 1992).

Ohmi et al. (1990, 1991), considered a sinusoidally-pitching NACA0012 airfoil with impulsive-start to steady translation in a water tow tank. Both the reduced frequency and amplitude were found to affect the structure of the vortex wake. However, they also demonstrated that as the pitching frequency increases, the patterns of the vortex wake are dependant on both the reduced frequency and the amplitude. Visbal and Shang (1989) studied the high-rate high-angle of attack linear pitch-ramp of a NACA0015 airfoil at $Re = 10^4$ by solving the full 2D Navier–Stokes equations, finding that lags between evolution of leading-edge flow separation and the airfoil motion kinematics should increase with increasing reduced frequency. Ghosh Choudhuri and Knight (1996) examined the effects of compressibility, pitch rate, and Reynolds number on the initial stages of 2D unsteady separation of laminar subsonic flow over a pitching airfoil in the Reynolds number ranging from 10^4 to 10^5, finding that increasing the Reynolds number hastens the appearance of the primary recirculating region.

The aforementioned studies focus mostly on transients following the initiation of the airfoil motion from rest. Others considered the periodic or phase-averaged behavior of pitch–plunge motions after initial transients have relaxed, typically with a focus on motion kinematics for optimal thrust efficiency. Platzer and Jones (2006) discussed theoretical prediction of thrust efficiency versus flow visualization and thrust measurements for an airfoil in pure-plunge, over a range of reduced frequencies and reduced amplitudes. Koochesfahani studied high-frequency low-amplitude airfoil pitch oscillations with quantitative and qualitative visualization, identifying vortex shedding patterns versus motion kinematic parameters (Koochesfahani 1989). Anderson et al. (1998) used particle image velocimetry and direct force measurement to study the combined pitch–plunge parameter space for propulsive efficiency optimization. Young and Lai (2004) used a 2D Reynolds-Averaged Navier–Stokes (RANS) approach to study the frequency–amplitude parameter space for optimal thrust efficiency for a plunging NACA 0012 airfoil at $Re = \mathrm{O}(10^4)$, and Jones et al. (1996) demonstrated good agreement in wake vortex structure between dye injection in a water tunnel, 2D laminar Navier–Stokes computation, and a 2D vortex-particle method. Lian and Shyy (2007)

showed similar agreement using a RANS solver run fully-turbulent. Here, we seek to extend these results to more complex kinematics of motion, to a range of Reynolds numbers bracketing transition-dominated effects evinced in the static case and in lower-amplitude pitch–plunge cases (Radespiel et al. 2007), and to include effects of leading-edge separation.

One important issue in periodic oscillatory airfoil flows is the lag between the aerodynamic response and the airfoil motion kinematics in 2-degree-of-freedom pitch–plunge. As a natural extension of the strictly quasi-steady model, one seeks to construct an explicit relation of the lag of putatively sinusoidal force response to sinusoidal motion kinematics, as a function of reduced frequency, of amplitudes of pitch and plunge, of phase difference between pitch and plunge, of Reynolds number and so forth. This could then form a model for the lift response to more general motions and in more general configurations, serving as an engineering tool for parameter studies. Perhaps the simplest generalization beyond the quasi-steady approximation is the Theodorsen model (Leishman 2000), where for harmonic motions in pitch and plunge, the lift coefficient is given by

$$C_{\mathrm{L}}(t) = 2\pi\alpha_0 + \frac{\pi c}{2}\left(\frac{\dot{\alpha}}{U_\infty} + \frac{\ddot{h}}{U_\infty^2} - \frac{c\left(2x_{\mathrm{p}} - 1\right)\ddot{\alpha}}{2U_\infty^2}\right) + 2\pi\left(\frac{\dot{h}}{U_\infty} + \alpha - \alpha_0 + c\left(1.5 - 2x_{\mathrm{p}}\right)\frac{\dot{\alpha}}{2U_\infty}\right)C(k) \tag{1}$$

The pitch and plunge are input as complex exponentials, $\alpha(t) = \alpha_0 + A\mathrm{e}^{i(\omega t + 2\pi\phi)}$ and $h(t) = h_0\mathrm{e}^{i\omega t}$. The phase lead of pitch versus plunge, in fractions of motion period, is φ. The reduced frequency, k, is defined as $k \equiv \omega c/2U_\infty = \pi f c/U_\infty$. The first term in Eq. 1 is the steady-state lift. The second term is the "apparent mass" or noncirculatory lift, due to acceleration effects. It is progressively larger for larger k. The third term models circulatory effects. $C(k)$ is the complex-valued "Theodorsen function", with magnitude ≤ 1. It is essentially a transfer function, accounting for attenuation of lift amplitude and phase lag in lift response, from its real and imaginary parts, respectively. Setting $C(k) = 1$ $(k = 0)$ and ignoring noncirculatory effects recovers quasi-steady thin airfoil theory. The noncirculatory term follows instantaneously the kinematics of motion, but evolution of vorticity in the wake yields phase lag relative to the kinematics of airfoil motion in the circulatory term, which is predicted to peak for $k \sim 0.3$.

Equation 1 assumes a planar wake and a trailing-edge Kutta condition, thus excluding wake rollup and vortex streets, vortex shedding, convection of large separations over the airfoil, open separations, large laminar separation bubbles (LSB), leading edge and trialing edge vortices and so forth. But the simplicity of such a model obviously makes it attractive as an engineering tool. Thus, we consider to what extent this model is useful for kinematics where the flow separation in portions of the airfoil oscillation ranges from moderate to severe. Using quite conventional particle image velocimetry, we present phase-averaged data on velocity and vorticity. These are compared with 2D RANS computations, which are similarly treated as an engineering tool to evince general trends. Lag in flow separation time-history is contrasted with lift coefficient time-history data from experiment and computation, versus Eq. 1. The overall philosophy is that if a simple attached-flow model is reasonably successful in predicting lift time history for a broad range of motion kinematics, even in the presence of large separation, then this would be useful for engineering purposes, in flapping-wing aircraft flight control, and in rapid searches through parameter space for aerodynamic and aeroelastic optimization studies.

We consider the following kinematics for combined pitch and plunge:

$$\begin{aligned}\text{plunge}: h(t) &= h_0\, c\cos(2\pi f t) = 0.5c\cos(0.5U_\infty t/c)\\ \text{pitch}: \alpha(t) &= \alpha_0 + A\cos(2\pi(ft + \phi))\\ &= 8^\circ + 8.42^\circ\cos(0.5U_\infty t/c + \pi/2)\end{aligned} \tag{2}$$

The parameters describing the airfoil motion are illustrated in Fig. 1.

Here the choice of reduced frequency, $k = 0.25$, was motivated in part by cruise-type conditions for flapping flight of birds. Although the Strouhal number, $St = 0.08$, is below the range for maximum propulsive efficiency for most flyers in nature (Taylor et al. 2003), the present flow conditions are on the upper-end of the dynamic-stall literature for helicopter blade applications (McCroskey 1982; Liiva 1969), for which the traditional analytical or phenomenological models in aeronautics tend to focus. As is often taken in applications motivated by propulsive efficiency of pitch–plunge (Anderson et al. 1998), pitch leads plunge by one quarter of phase ($\varphi = 0.25$) and thus the airfoil "feathers", with the geometric pitch angle partially cancelling the plunge-induced angle of attack, $\arctan(\dot{h}/U_\infty)$. The amplitude of pitch, $A = 8.42^\circ$, was chosen from the expression

$$\lambda \equiv \frac{A}{\arctan(\dot{h}_{\max}/U_\infty)}.$$

λ is the ratio of pitch angle amplitude to the peak angle of attack induced by the plunge motion; we chose $\lambda = 0.6$, which as will be shown below, leads to shallow dynamic stall. $\lambda = 0$, on the other hand, is a pure plunge, which produces a strong leading edge vortex, and is more akin to deep dynamic stall.

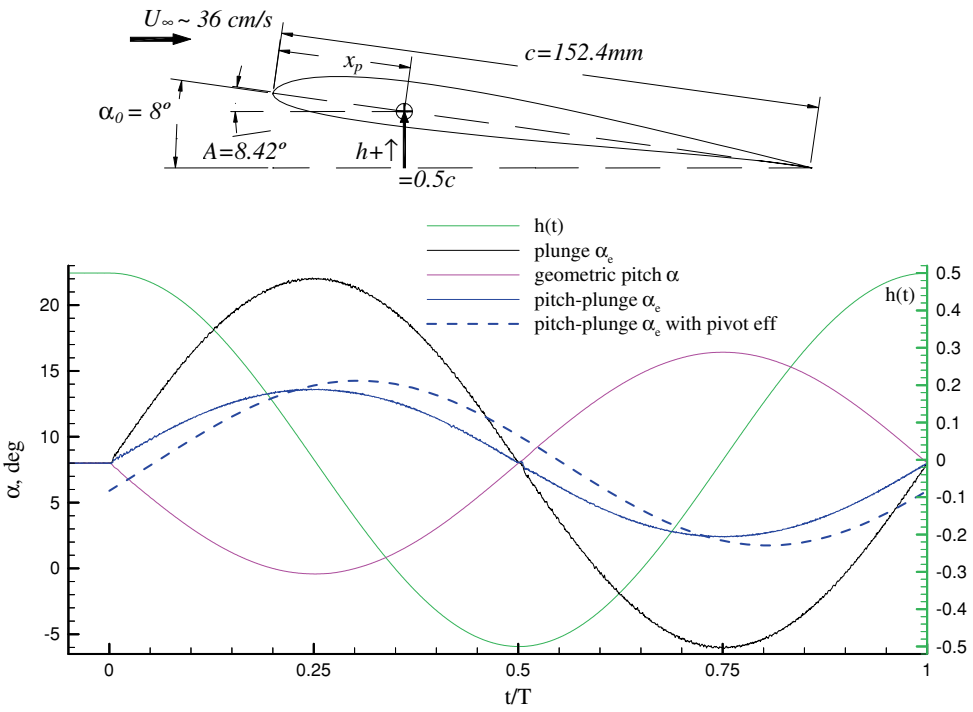

Fig. 1 Schematic of airfoil and parameters of motion (*top*); time-traces of prescribed and recorded angle of attack over one motion period, including start-up, for pure-plunge and pitch–plunge, $k = 0.25$

Figure 1 shows the plunge trajectory (green curve), total effective angle of attack in pure-plunge (black curve), pitch geometric angle of attack (purple curve) and total effective total angle of attack for combined pitch–plunge (blue curves). For pitch–plunge, the total effective angle of attack time-trace, α_e, straddles the static stall value of $\sim 11°$ (Ol et al. 2005); this is just the sum of the pitch and plunge cosines with appropriate phase shift. But α_e, can be taken to include the effect of pivot point location by summing all of the components inside the brackets in the third term of Eq. 1; this is the dashed blue curve in Fig. 1. The difference, versus disregarding the effect of pitch pivot point location (solid blue curve) is a phase shift of ~ 0.05 t/T. With inclusion of the pivot effect, the limits on α_e become $2.03° < \alpha_e < 14.03°$, whereas for pure-plunge they are $-6.0° < \alpha_e < 22.0°$.

We also consider the extent to which the nominally 2D flow is truly 2D in a realizable experiment, with a wing extending from wall to wall in a tunnel test section, with sidewall gaps comparable to the local boundary layer thickness. In a computation, "2D" is taken to mean a grid with zero out-of-plane depth. For the question of computational validation, one is interested both in whether the 2D computation is sufficient to capture a representative slice of a separated flowfield as measured in the experiment, and in whether the flowfield in the experiment is itself approximately 2D. In other words, installation-effects, blockage and so forth can conceivably produce irreducible 3D effects. Also 3D effects arise naturally in the form of spanwise flow in shed vortices and tend to dominate the vortex shedding process at increased reduced frequency (Koochesfahani 1989). For parameter studies, the simplification of 2D flows—if borne out by validation—is an obvious advantage in both computational cost and in simplicity of velocimetry approaches. Likewise, justifiability of simplification to 2D is useful in invoking application of classical results in unsteady aerodynamics, which in relying on manipulation of complex-valued functions are explicitly 2D.

2 Experimental and computational setup

2.1 Facility and motion-rig

Experiments were conducted in the U.S. Air Force Research Laboratory's Horizontal Free-surface Water Tunnel, with a 46 cm wide by 61 cm high test section and speed range of 3–45 cm/s. The water tunnel, schematic of the pitch–plunge rig and installation of the model in the tunnel are shown in Fig. 2. In the photograph, the model is inside the test section, but the test section glass sidewalls are not visible. Turbulence intensity (u and v components) as determined from PIV free-stream data is estimated at 0.5% at $U_\infty = 30$–40 cm/s. A surface skimmer plate at the entrance to the test section and a sealed lid of the intake plenum (visible as plywood cover in Fig. 2) damp sloshing in the tunnel, that could otherwise have been be excited as a first-mode shallow water wave, and would have resulted in low-frequency (~ 0.16 Hz) sinusoidal variation in U_∞.

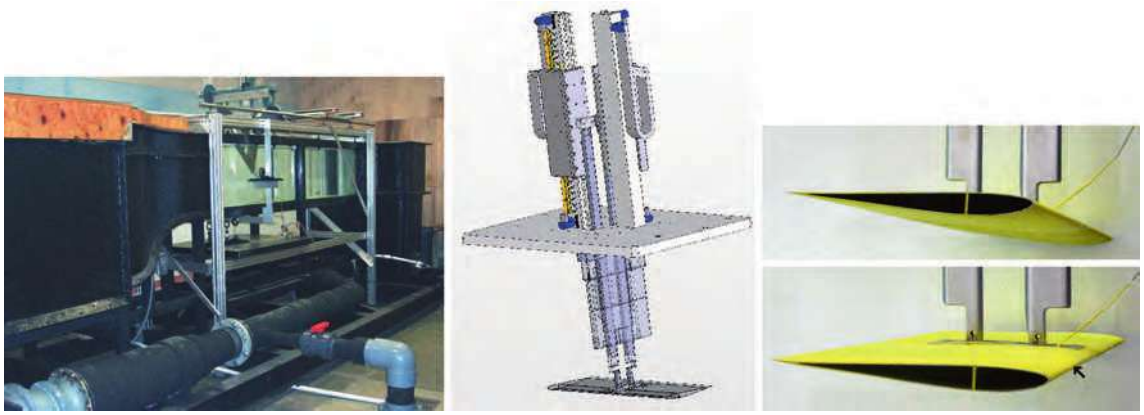

Fig. 2 AFRL Horizontal Free-surface Water Tunnel (*left*); schematic of pitch–plunge rig and airfoil model (*middle*); SD7003 airfoil installed inside test section, showing smooth suction-side of airfoil (*top right*) and plunge rod coupling on pressure-side of airfoil (*bottom right*). *Black arrow* in *bottom-right* points to dye injection exit port location

A second skimmer plate mounted $\sim$1 m downstream of the oscillation rig damps motion-induced free surface oscillations, which were $\leq$1 mm at the leading edge of the downstream plate. More detail on the facility is given in Ol et al (2005).

The pitch–plunge rig consists of a pair of electric linear motors mounted vertically on a plate above the tunnel test section. Each motor actuates a vertical "plunge rod", which connects via a bushing to the airfoil at a fixed pivot point on the airfoil chord, in the test section vertical plane of symmetry. The upstream plunge rod is constrained to move purely vertically, whereas the downstream plunge rod is allowed to pivot in the test section vertical plane of symmetry. Motion trajectory of each rod is programmed independently, such that the desired angle of attack and vertical position time history of the airfoil are converted to position commands for each linear motor. This allows for single degree-of-freedom motions such as pure-pitch about a prescribed fixed pivot point, or pure-plunge. Pitch and plunge can be combined, and the pitch pivot point can be varied by suitable choice of phase and amplitude difference in trajectory of front or rear plunge rod. For all cases, where the pitch pivot point is not coincident with the bushed end of the front plunge rod, there will be a small parasitic streamwise displacement of the model, which would be unavoidable unless the front plunge rod were to be allowed to pivot similarly to the downstream one.

A SD7003 airfoil model (http://www.ae.uiuc.edu/m-selig/ads/coord_database.html) with 152.4 mm chord and 458 mm span was mounted horizontally in the test section and was driven by a 2-degree-of-freedom pitch–plunge rig. The model was wire-cut from five 10-cm-thick blocks of 316-series stainless steel to a shell thickness of 0.89 mm, and the blocks were welded edge-to-edge to form the full model, resulting in a weight of approximately 1 kg.

The airfoil model is mounted upside down, with access for the PIV light sheet through the test section bottom, and keeping the suction-side of the airfoil clear of plunge rods. While the installation is relatively intrusive, the rig was designed to support aggressive motions with minimal elastic deflection or vibration, such as could have been the case with a cantilever aft-mount sting, or a vertical orientation of the airfoil supported above the tunnel free-surface from one of its wingtips. More details of the pitch–plunge rig are given in Ol (2007).

The total effective angle of attack time histories in Fig. 1 are calculated from plunge rod position measurements from the rig's linear motors, and thus include plunge-rod vibrations, motion tracking errors in the rig controller servo loop, and startup effects. Motion control consists of piecewise approximation to a sinusoid in increments of 4 ms, or 1315 segments per period for $k = 0.25$ at $Re = 60$ K. At $Re = 60{,}000$ a reduced frequency of $k = 0.25$ corresponds to a physical frequency of 0.190 Hz and tunnel flow speed of 36.4 cm/s, in 23°C water. Water temperature was monitored to $\pm$0.5°C. Static blockage based on projected frontal area of the model at maximum pitch amplitude is 7%. Gaps between the model tips and the tunnel walls were approximately 1.0 mm, or $0.007c$.

2.2 Particle image velocimetry

A PCO 4000 11Mpix camera (http://www.cookecorp.com/cooke/php/products/technical_1-en__01030) run in single A–D mode was triggered off of an external pulse train derived from the position encoder of the motion rig, thus allowing for selection of motion phase at which to acquire data, and for phase averaging. Velocity data were acquired once per period of oscillation, for a sequence of 120 periods. These were repeated for 7 phases of airfoil

motion: $t/T = 0$ (top of the plunge stroke), 0.25, 0.333, 0.417, 0.5, 0.583, and 0.75 (or 0, 90, 120, 150, 180, 210 and 270°, respectively). Prior results with dye injection and PIV for pure-pitch at $k = 3.93$ and $Re = 40{,}000$ (Liiva 1969) showed that startup transients relax and the flow attains periodicity in two periods of oscillation after startup, where the startup is continuous in velocity and bound by 5 m/s^2 in acceleration in the controller software. The first 5 periods were removed from each data set, and the remaining 115 velocity data sets were ensemble averaged for each phase of motion. Vorticity was calculated by explicit differentiation of cubic spline fits to the velocity field [as discussed by Willert and Gharib (1991), and implemented by Jeon (2000)].

PIV resolution was 156 pixels/cm, which for 32 × 32-pixel windows with 16 × 16 overlap gives 148 vectors per chord length. Because of laser reflections from the model surface (polished stainless steel, spray-painted flat-black) and lack of corrections for PIV windows which at least partially intersect with the model surface, data in the first row of PIV windows adjacent to the airfoil surface are not reliable. Data near the leading edge are also not reliable, because of parallax: the wingtip of the model nearest to the camera blocks the camera's view of the leading-edge region in the plane of the light sheet. Light sheet thickness was approximately 2 mm max, though the large field of coverage (up to 45 cm across) makes precise collimation of the light sheet difficult. To obtain the "most 2-dimensional" flowfield, the PIV light sheet was placed at the 3/4 span location; i.e., approximately halfway between the plunge rods and the tunnel wall, and $0.05c$ inboard of the dye injection slot.

There are two main causes of error in the model motion (and hence, in the flow measurements): noise or other disturbances in the physical motion of the airfoil, and deviation between the assumed and actual position of the airfoil at every instance when PIV images are taken. Airfoil jitter will introduce "turbulence" in the flowfield response, and if severe, could trigger shedding of vortices at jumps in airfoil angle of attack. This was not observed. Disturbances in the airfoil angle of attack time history are inherited from overshoots and noise in the motors' position time history. By adjusting the proportional–integral–derivative constants of the controller feedback loop, one can trade between two competing undesirables: high-frequency instabilities and position overshoot during instances of high acceleration. From data such as in Fig. 1, jitter of the actual motor position relative to the commanded position is results in jitter in angle of attack of <0.15°.

The second source of error is uncertainty in the position of the airfoil with respect to the phase of motion when a PIV image pair is captured, for e.g., if the laser triggering pulse is slightly off in phase. The estimated drift period-to-period in airfoil position as recorded in the raw PIV images is <0.1° in pitch and $<0.002c$ in vertical position. DC bias error, due mostly to the layer of saturated pixels adjacent to the airfoil surface, is estimated for sinusoidal oscillations as <0.2° in angle of attack and $0.007c$ in vertical position, or about ½ of a PIV window height. These account not only for errors in the linear motor positioning but also for possible deformations in the plunge rods, structural vibration of the airfoil model, and accretion of air bubbles on the model surface. The latter are insidious reflectors of laser light, saturating the CCD camera and invalidating the PIV cross-correlation scheme. The resulting overall error bounds are of concern if studying in detail the physics of attached boundary layers, but are arguably of secondary importance in the present work.

2.3 Dye injection

We assume that the passive scalar of dye concentration is an adequate surrogate for the out-of-plane component of vorticity, at least for qualitative assessment of attached versus separated flow. A 1 k × 1 k-pix digital camera (UniqVision UP-1830) at 30 frames/s was used for imaging, operating unshuttered. For $k = 0.25$ oscillation at $Re = 60$ K, one motion period corresponds approximately to 158 frames at 30 frames/s, giving temporal resolution of ~2.3° of motion phase per video frame.

A wand with 0.5 mm internal diameter, injecting concentrated blue food coloring, was fitted inside the model and exits flush with the outer mold lines on the airfoil pressure-side, at $x/c \sim 0.01$ downstream of the leading edge, firing approximately wall-normal. The dye exit location is not visible in Fig. 2, but is marked by the black arrowhead in the bottom-right-hand portion of Fig. 2. Dye is entrained toward the suction side at those phases of airfoil motion where the leading edge stagnation point is downstream of the wand placement point. Dye is injected by a "New Era" NE-1000 syringe pump (http://www.syringepump.com/NE-1000), with infusion volumetric flow rate programmed to attain $\sim 0.25U_\infty$ at the probe exit. Dye flow streaklines were found to be independent of dye exit rate for rates less than $\sim 0.5U_\infty$, and the value of $0.25U_\infty$ was selected to attain reasonable flow visualization image contrast while further reducing likelihood of flowfield disturbance.

2.4 Force measurement

In an effort to circumvent difficulties associated with electrical strain gauges in water—waterproofing, routing of wires, drift, gauge delamination and so forth—an optical approach, using fiber-Bragg gratings (FBGs) (Rao 1997), was used. Coherent light is sent through the fiber and through gratings written onto the fiber. Each grating

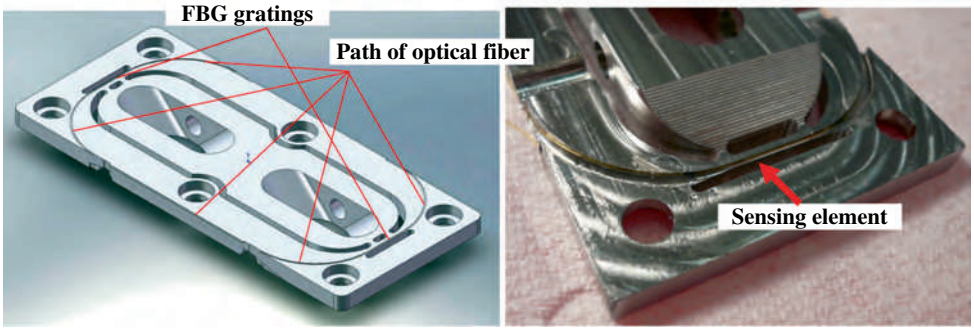

Fig. 3 Three-component force balance based on Fiber Bragg grating (*FBG*) sensors, integrated with airfoil mount; schematic (*left*) and photograph from underside, with detail of a flexure joint (*right*); installed-view is given in Fig. 2

reflects light of very narrow bandwidth. If the segment of the fiber containing a grating is strained, the reflected light wavelength shifts proportionately. Strain of the fiber could be due to mechanical strain of the underlying substrate (the flexure joint in the force balance) and to thermal effects, which must be removed though appropriate compensation. In the present application, a single fiber with 4 grating elements was integrated into a two-flexure-joint airfoil mount, thus serving as an integrated force balance (Fig. 3). The balance can resolve axial force, normal force and pitching moment, though only the lift is reported here.

The FBG signal was interrogated via a Micron Optics sm130 instrument (http://www.micronoptics.com/sensing_instruments.php), with sampling at 250 Hz phase-averaged over 200 periods of oscillation and low-pass filtered at 6.5 Hz, with the first 5 periods removed from the sample. Inertial tares were conducted by draining the water tunnel and repeating the airfoil motion. This simplicity of such tares is an important advantage for dynamic testing in water (Kramer 2002).

Zhang et al. (2002) discuss signal-to-noise and other operational issues of FBG sensors and interrogation techniques. For the present measurements, the balance was calibrated in benchtop tests with loads applied at 0° and ±45°. These data were used to compute the load cell calibration matrix. The standard error of the calibration matrix for the lift force is 0.16 N, which corresponds to a lift coefficient standard error of 0.03. To characterize measurement error, the standard deviation was computed at each measurement point using phase averages for the unsteady measurements or time averages for the steady data, and is shown in all the force plots below as an error bar. For the sample size/duration used in these tests and considering conservative estimates of the number of independent samples, the ±1 standard deviations shown in the plots are an upper bound of the 95% confidence interval.

2.5 Computations

The unsteady, incompressible Navier–Stokes equations with constant transport properties are solved on a 2D unstructured grid with the Reynolds-Averaged (RANS) solver Loci-STREAM (Kamakoti et al. 2006) and Menter's shear stress transport (SST) turbulence model (Menter 1993). Mindful of its limitations, we nevertheless pursue a RANS approach because of its relative simplicity and desirability for parameter studies. Loci-STREAM is a parallelized unstructured curvilinear pressure-based finite volume code with moving grid capabilities. The present calculations use implicit first order time stepping. The convection terms are treated using the second-order upwind scheme (Shyy 1985; 1994) while pressure and viscous terms are treated using second-order central differencing schemes. The geometric conservation law (Thomas and Lombard 1978; Shyy et al. 2007), a necessary consideration in domains with moving boundaries, is satisfied.

Computations were on an open domain of 50 chords, which of course does not capture the water tunnel test section walls or the free-surface. The grid, with 46,281 mixed elements, is shown in Fig. 4. Choice of grid size arose from the grid refinement study of Kang et al. (2009). No-slip was imposed on the airfoil surface, and the outer boundary was incompressible-inlet. Computations were run fully turbulent, with no attempt to model transition or to prescribe the chordwise location of when to turn on the production term in the turbulence model.

Clearly there are limitations for how well eddy-viscosity models, especially in a 2D implementation, can handle complex unsteady 3D flows. The ideal counterpart to experiment would be true direct numerical simulation. Any turbulence model, eddy-viscosity model or large-eddy simulation would likely not be without its challenges. The present objective is to baseline the acuity of the 2D eddy-viscosity method for prediction of onset of dynamic stall, the return from stall and the lift coefficient time history, for flows dominated by laminar separation and transition in free shear layers. Comparison with PIV not only helps to ascertain the performance of the numerical model, but also sheds light on the relation between flowfield phenomena and aerodynamic force time history.

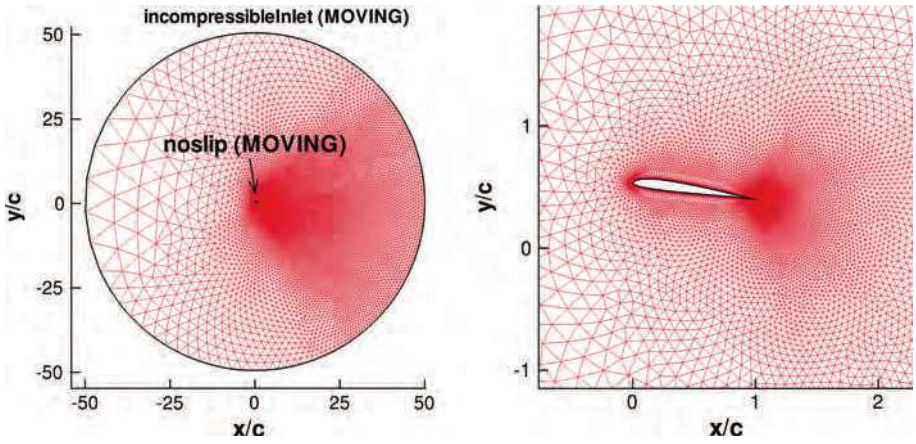

Fig. 4 Unstructured grid in (*left*) and its distribution near the SD7003 airfoil (*right*)

3 Results

3.1 Static lift coefficient

We begin with a conventional static lift sweep versus angle of attack, as a scheme for baselining the force balance and for notional assessment of how static blockage, wingtip gap effects, free-surface effects etc. may detract from nominal 2D conditions in the water tunnel. This of course also allows comparison of $C_L(t)$ versus $\alpha_e(t)$ in the dynamic cases, with the $C_L(t)$ measured at the "equivalent" static angle of attack, in the traditional sense of dynamic stall measurements (McCroskey 1982). Figure 5 compares the presently measured values of lift coefficient (with the usual decomposition from normal and axial force) in the range $-12° < \alpha < 22°$, together with a XFOIL calculation at N-factor = 9 and wind tunnel data from Selig et al. (http://www.ae.uiuc.edu/m-selig/ads/coord_database.html). The latter two do not include deep-stall, whence it is not possible to directly compare static blockage effects at the extremes of airfoil position. Where data from all three sources are available, mutual agreement is encouraging. Static stall in the present data set occurs at $\sim 11°$, confirming prior results in the same facility with a larger model with a conventional static aft-mount static sting (Ol et al. 2005). Error bars in the present data set represent the 95% confidence interval.

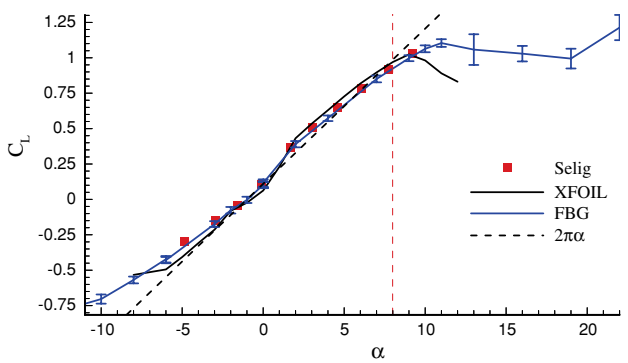

Fig. 5 Static lift coefficient vs. angle of attack for the SD7003 airfoil at $Re = 60$ K: XFOIL results at $N = 9$ (*black line*), wind tunnel data of Selig et al. (http://www.ae.uiuc.edu/m-selig/ads/coord_database.html), and water tunnel data (*blue line*), with error bars at 95% confidence intervals. Mean angle of attack for pitch–plunge and pure-plunge, α_0, is labeled by the *dashed red line*

The slope of the lift curve, as compared to $2\pi\alpha$, can be considered as a surrogate for the extent to which the static configuration is 2D, but care is required to avoid conflating boundary layer growth, which can effectively decamber the airfoil with increasing angle of attack, with effective aspect ratio. The lift curve slope of the pre-stall portion of the measured lift curve is $0.87 \times 2\pi\alpha$, as compared to $0.905 \times 2\pi\alpha$ in the wind tunnel data of Selig et al. (http://www.ae.uiuc.edu/m-selig/ads/coord_database.html). One may speculate that blockage effects are responsible for the higher stall angle and higher maximum lift coefficient in the present experiment, but these do not appear to be severe.

3.2 Pitch–plunge: flowfield evolution and *Re*-effects

The pitch–plunge case can be considered as weak dynamic stall. Dye injection results for seven phases of motion are shown in Fig. 6, for $Re = 10$, 20, 30, 40, 60 and 75 K. To vary Reynolds number, the tunnel speed and model physical oscillation speed were changed proportionately. PIV and CFD u-component velocity contours for $Re = 60$ K are compared in Fig. 7, together with velocity profiles in the near-wake at $x/c = 0.25$ downstream of the airfoil trailing edge. Contours of out-of-plane vorticity are compared in Fig. 8. Contour levels for all velocity plots and vorticity plots are respectively the same. For vorticity, the near-zero contours are removed for clarity. Dimensions are normalized by airfoil chord, with the trailing edge placed at the origin in all cases. The region underneath the airfoil, in the shadow of the PIV laser light sheet, is blanked off. For

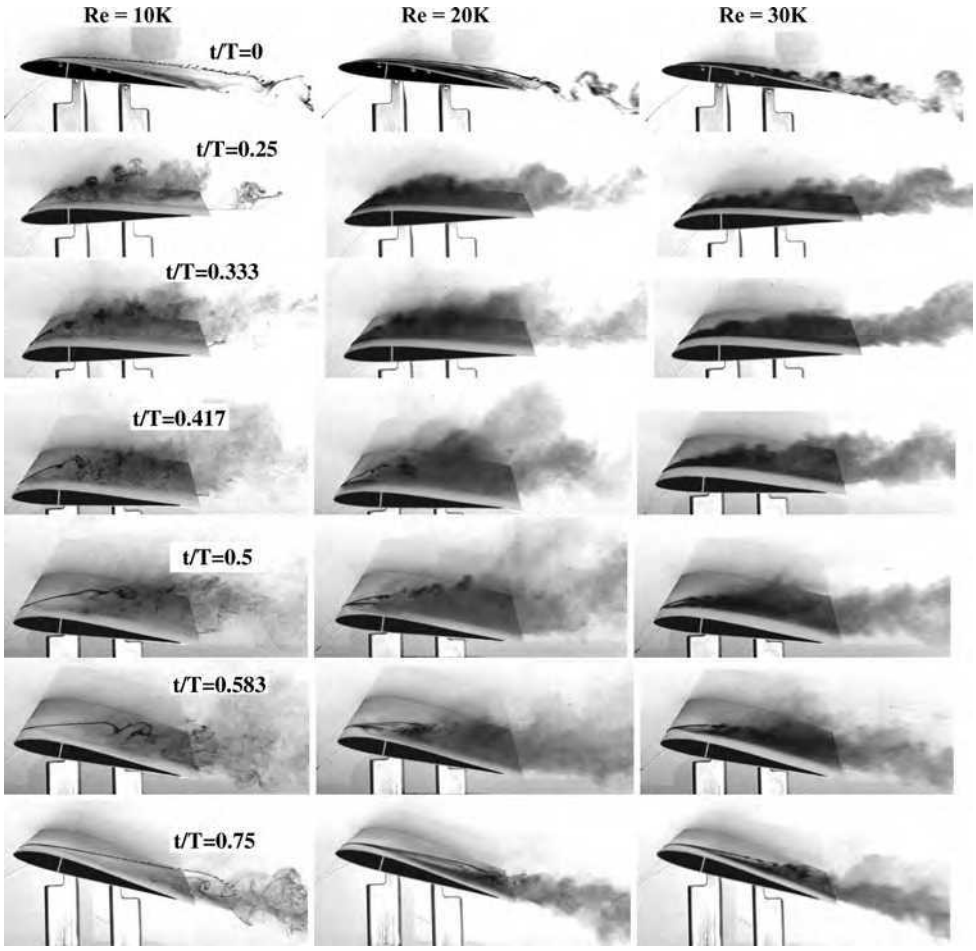

Fig. 6 Dye injection for pitch–plunge at seven phases of motion; $Re = 10$, 20, 30, 40, 60, and 75 K

reasons of aesthetic sensibility, the same region is blocked off in the computation. In comparing dye injection, PIV and CFD, the dye injection is by definition "instantaneous", the PIV is phase-averaged, and the CFD is from one period of motion (not phase-averaged) but shows essentially zero period-to-period variation.

At $Re = 10$ K the flow over the airfoil suction side is never fully attached at any time. Toward the top of the plunge stroke, the dye streakline smoothly bounds an open region of separation, as opposed to a LSB. By $t/T = 0.25$, where effective angle of attack is maximum, large disturbances akin to Kelvin-Helmholtz rollers are visible, bounding a broad separated region. By $t/T = 0.5$ the loss of coherence of such structures suggests shear-layer transition. By $t/T = 0.58$ there is visible return to smooth boundary of the separated region, and by $t/T = 0.75$ a well-organized streakline bounds the separation region all to way to the trailing edge. At $Re = 20$ K, the suction-side flow separation is thinner and the aforementioned rollers at $t/T = 0.25$ are no longer discrete, but fully attached flow is still not present at any time. By $Re = 30$ K, the separation at $0.75 < t/T < 0$ (or 1.0) closes into what might be termed a LSB. The LSB is much smaller but still present at $Re = 60$ K, and no longer discernable at $Re = 75$ K.

The $Re = 30$–40 K range is a qualitative divide in the size of the separated region, in particular at $t/T \sim 0.33$, and the structure of the near-wake. Above this divide, the near-wake is "planar" for $0.75 < t/T < 0.25$; not in the strict sense of being negligibly thin and parallel to the free-stream direction, but more precisely, in following a linear trajectory nearly tangent to the airfoil chord line at each of the respective cited phases of motion, and in being apparently free of large coherent vortical structures. Below this divide, the wake consists of discrete vortical structures, vaguely akin to bluff-body shedding. We also note that in the far-wake, the dye trace has a sinusoidal undulatory shape with spatial period of ~ 5 chords (not shown), but that on the scale of one airfoil chord the wake appears linear. Even based on this very generous definition of "planar wake", the assumptions of Theodorsen's formula are clearly violated toward the bottom of the plunge stroke.

The combination of dye injection, velocity and vorticity contours allows one to consider how the flowfield response lags the angle of attack time history. By this one can mean

Fig. 6 continued

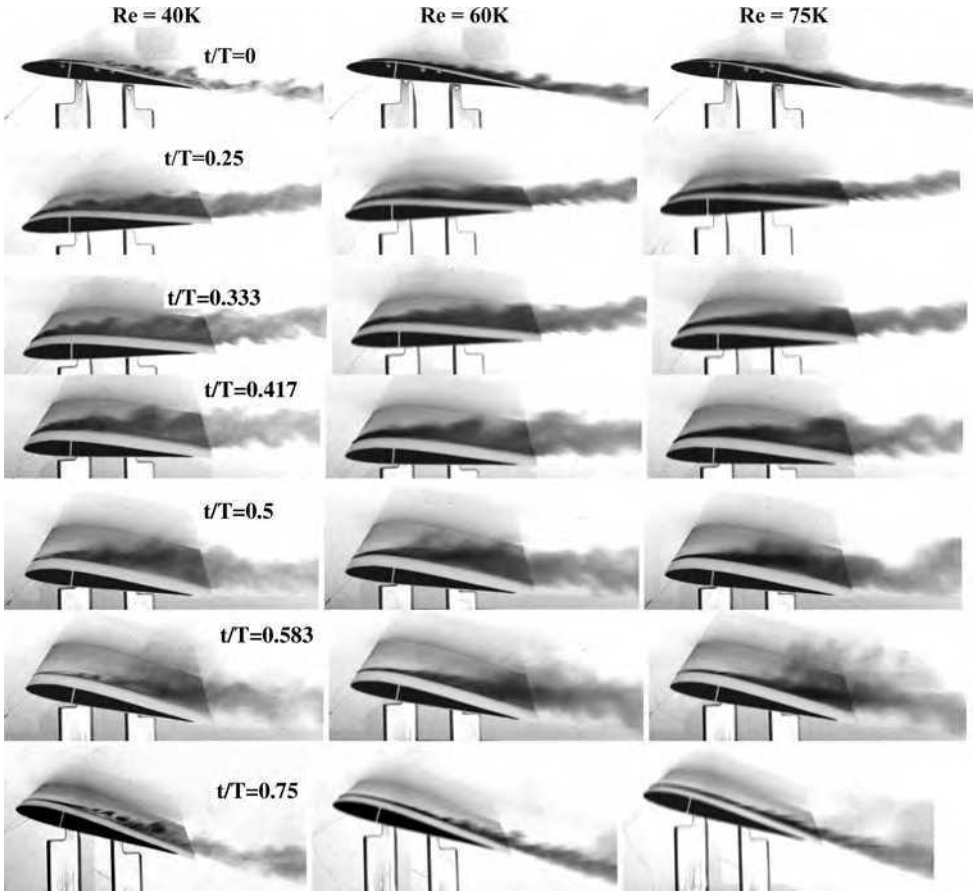

assessment of the rough size of the suction-side separated region, intensity of peak shed vorticity, or momentum deficit in the near wake, for example. $\alpha_e(t)$ reaches its maximum at $t/T = 0.25$ if pitch pivot-point effects are ignored, and at $t/T \sim 0.30$ if they are included. If the growth of separated flowfield structures were quasi-steady, they would reach their largest spatial extent—as judged, for e.g., by the size of the phase-averaged reverse-flow region in Fig. 7—at the same t/T as the $\alpha_e(t)$ maximum. Qualitatively, the height of the dye-tagged flowfield region above the airfoil suction-side reaches maximum extent just before $t/T = 0.5$. Phase-averaged vorticity contours reach their largest spatial extent at $t/T \sim 0.4$–0.5. The near-wake momentum deficit at $x/c = 0.25$ aft of the trailing edge is largest somewhat later, at the $t/T = 0.583$. Thus, while there is ambiguity in how one assesses the response of flow separation to variation in effective angle of attack, there is clearly a phase lag—on the order of 0.2 t/T.

3.3 Pure-plunge: flowfield evolution and *Re*-effects

Dye injection images for nine phases of motion at $Re = 20$, 30 and 60 K are shown in Fig. 9; PIV and CFD u-component velocity contours for $Re = 60$ K are compared in Fig. 10, together with velocity profiles at $x/c = 0.25$ downstream of the airfoil trailing edge. Contours of out-of-plane vorticity component for $Re = 60$ K are given in Fig. 11.

The distinguishing feature of the pure-plunge case, relative to the pitch–plunge, is the presence of a strong vortical structure at the leading edge—to which we will refer as the leading edge vortex—at $t/T = 0.25$. The formation process, size and shape, and subsequent downstream progression of the LEV does not differ significantly from $Re = 20$–60 K in Fig. 9. Comparing Fig. 9 and the PIV in Fig. 11, the dye concentration is a tenable surrogate for the phase-averaged vorticity contours. By $t/T = 0.333$, the LEV has broadened or diffused over the entire airfoil chord, and PIV shows in the phase-average a region of reversed flow blanketing the airfoil suction side. This is, strictly speaking, a figment of phase-averaging, as otherwise one would have expected to see a rotation in the flowfield associable with this region. Nevertheless, the salient point of the phase average, consistent with the corresponding dye injection image, is that the suction-side flow is fully separated. At $t/T \sim 0.4$, the dye-tagged region of fluid has reached its maximum vertical extent above the airfoil suction-side. The instantaneous effective angle of

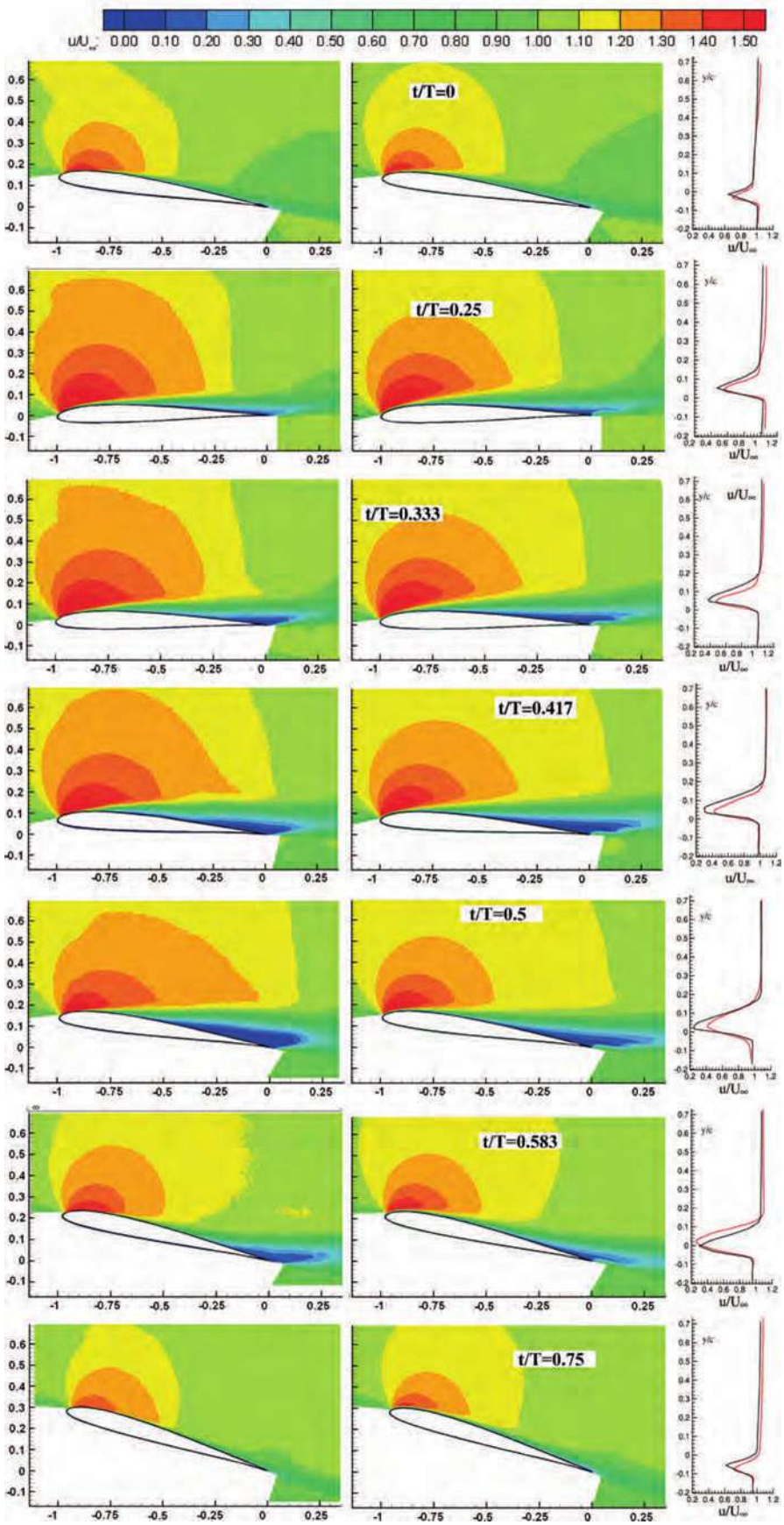

Fig. 7 Normalized u-component velocity contours from experiment (*left column*) and computation (*middle column*) for pitch–plunge, and u-component velocity profiles at $x/c = 0.25$ downstream of the trailing edge (*right column*; *black curve* is CFD, *red curve* is PIV). Data shown for seven phases of airfoil motion (motion $t/T = 0$, 0.25, 0.333, 0.417, 0.5, 0.583, and 0.75)

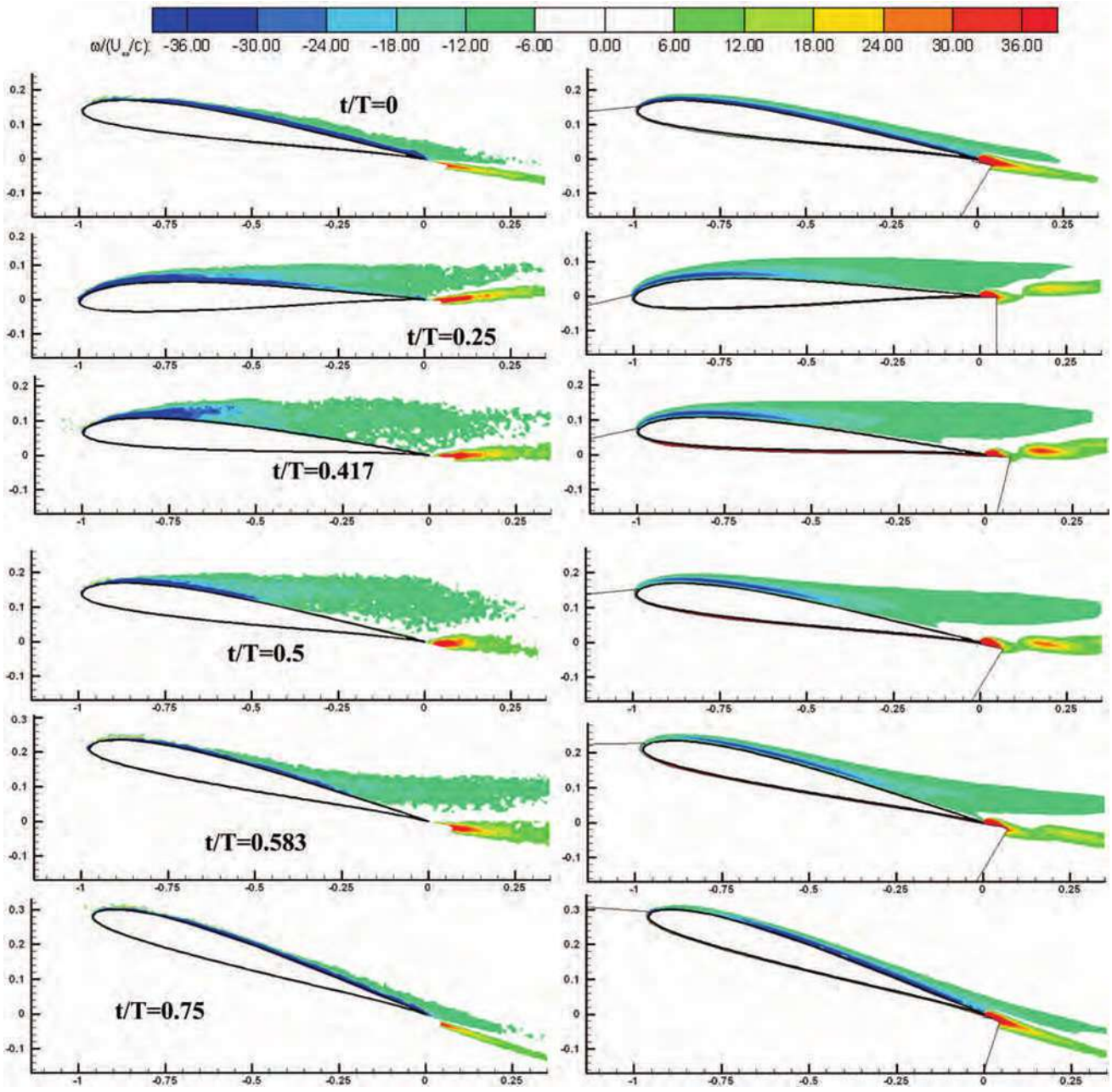

Fig. 8 Contours of out-of-plane component of vorticity for pitch–plunge, $Re = 60$ K: PIV (*left column*) and CFD (*right column*); phases of motion $t/T = 0$, 0.25, 0.417, 0.5, 0.583 and 0.75

attack is $\sim 16°$. Also at $t/T \sim 0.4$, a thin and organized dye streak has reemerged in the vicinity of the leading edge. It can be identified as bounding a laminar separated region (dye injection) and the remaining concentration of vorticity after LEV ejection (Fig. 11), and precedes the route to flow reattachment, which is essentially complete by $t/T = 0.75$.

Reynolds number effects, as evinced by the dye injection results, are associable with flowfield events at both the leading and trailing edge. At the trailing edge, at $Re = 30$ K and especially at $Re = 20$ K there is a discernable trialing edge vortex at $t/T = 0.375$–0.417 in the dye injection, and indeed there is a region of reverse flow just ahead of the trailing edge. At $Re = 60$ K, no TEV is clearly visible in the dye injection, but it is strongly apparent at $t/T = 0.417$ in the PIV, and at $t/T = 0.5$ in the CFD. The near-wake at the top of the plunge stroke also shows a discernable *Re*-effect, with coherent vortices seen for $Re = 20$ K. In going from $t/T = 0$ to 0.125 to 0.25, the suction-side dye concentrations splits, as

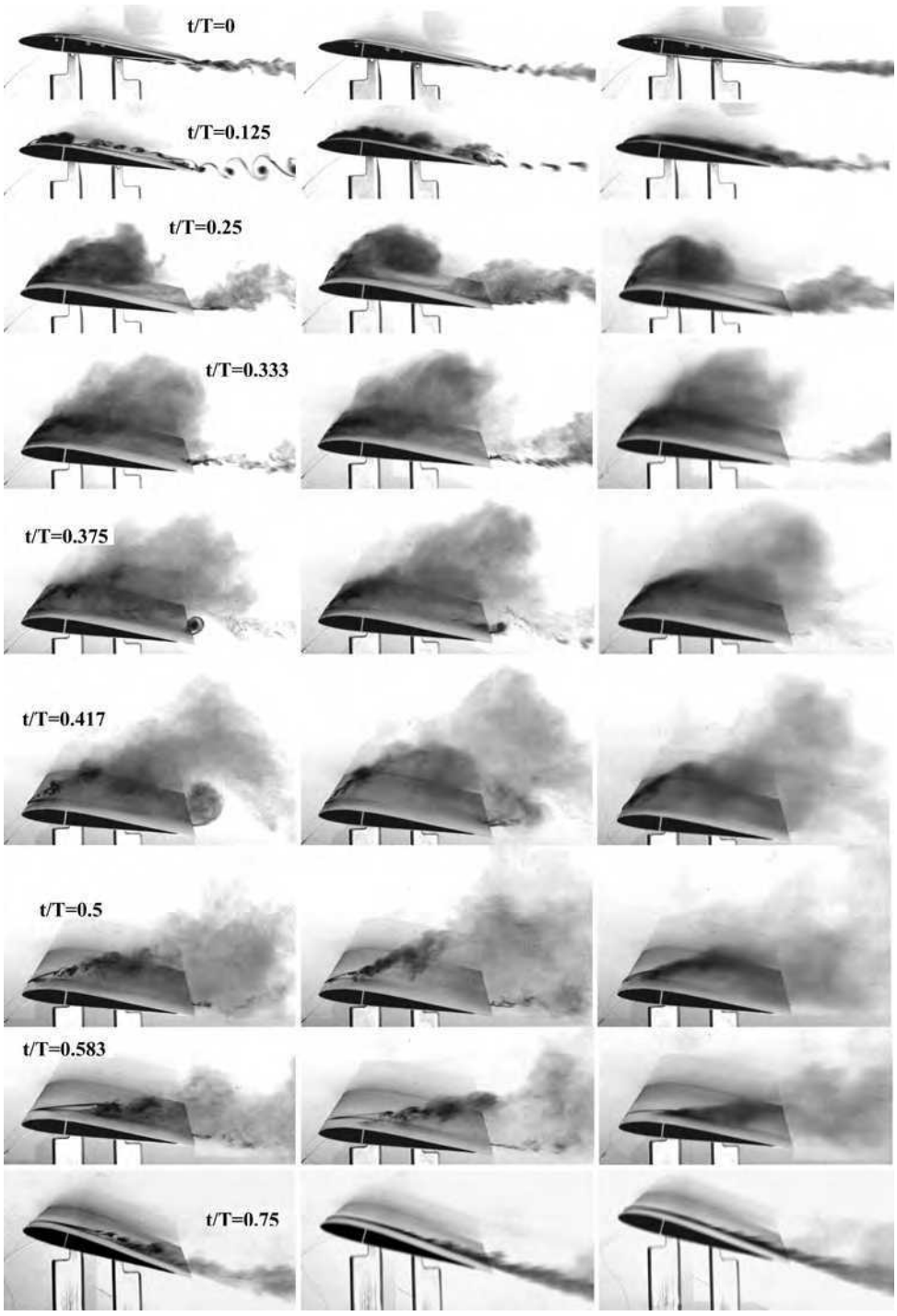

Fig. 9 Dye injection for pure-plunge, $Re = 20$ K (*left column*), 30 K (*middle column*) and 60 K (*right*)

it were, into a leading-edge and trailing-edge portion, the former coagulating into the LEV at $t/T = 0.25$. Toward the bottom of the plunge stroke, the pocket of dye lacuna just aft of the leading edge is smaller for higher Re, further suggesting that this region can be thought of as a LSB.

Experimental-computational comparison in Fig. 11 shows reasonable agreement on the upstroke, $\sim 0.6 < t/T < 1.0$. On the downstroke the computational result lags, as it were, the experimental: the $t/T = 0.333$ computation is qualitatively similar to the $t/T = 0.25$ experiment, t/T 0.417 computation is similar to $t/T = 0.333$ experiment, $t/T = 0.5$ computation is similar to $t/T = 0.417$ experiment. The large, flat region of vorticity covering the airfoil suction side at $t/T = 0.25$ in the computation was not observed in the experiment. Thus the computation misses the details of the LEV formation process, but evinces the eventual shedding of vorticity and the process of reattachment—in other words, of return from dynamic stall.

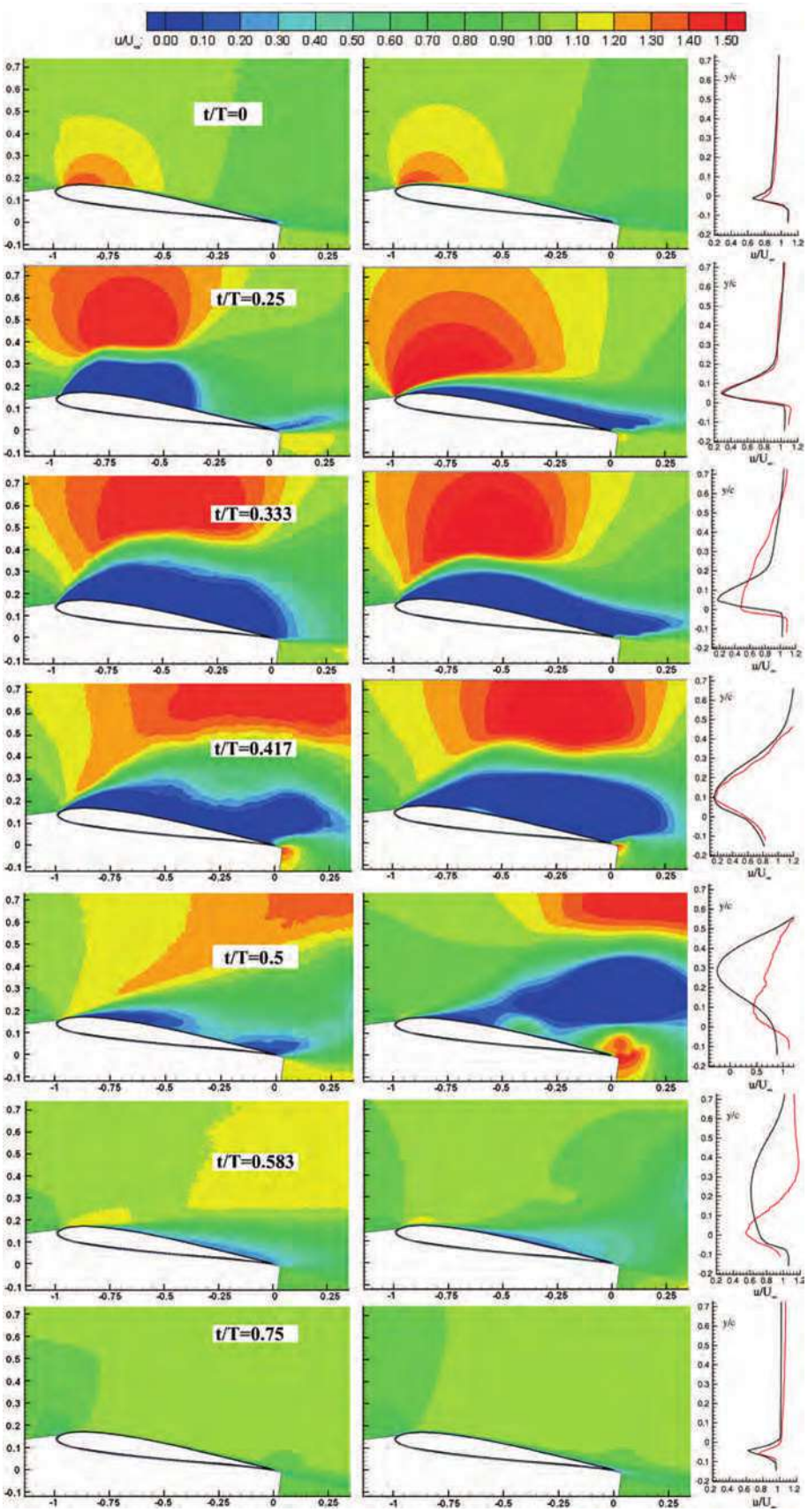

Fig. 10 Normalized u-component velocity contours from experiment (*left column*) and computation (*middle column*) for pure-plunge, and u-component velocity profiles at $x/c = 0.25$ downstream of the trailing edge (*right column*; *black curve* is CFD, *red curve* is PIV). Data shown for seven phases of airfoil motion (motion $t/T = 0$, 0.25, 0.333, 0.417, 0.5, 0.583, and 0.75)

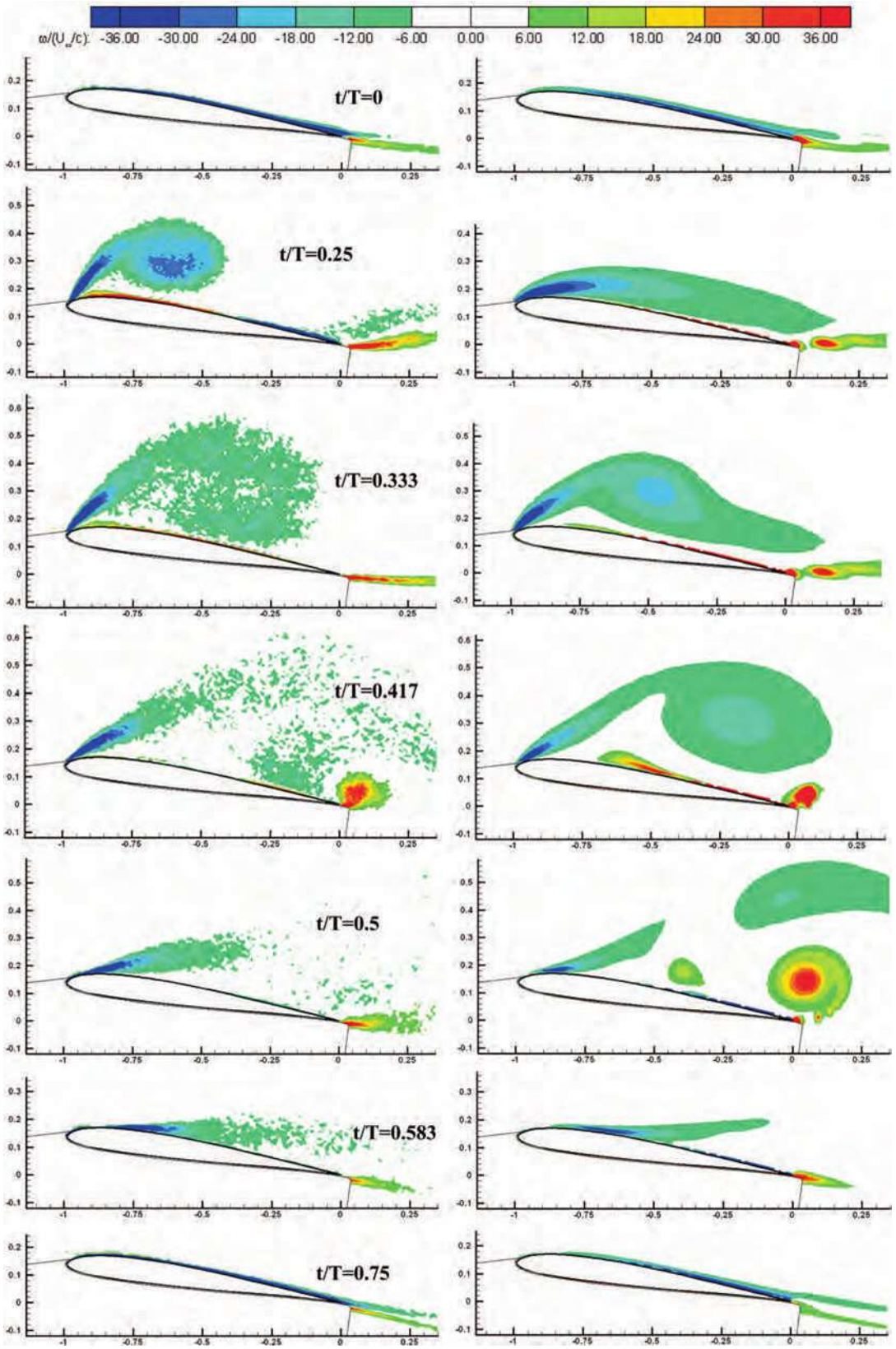

Fig. 11 Contours of out-of-plane component of vorticity for pure-plunge, $Re = 60$ K: PIV (*left column*) and CFD (*right column*)

In the near-wake u/U_∞ velocity profiles (Fig. 10), PIV and CFD agree well, except for phases $t/T = 5$ and 0.583, and to a lesser extent $t/T = 0.333$. At $t/T = 0.5$, CFD predicts a strong momentum deficit in the wake. Qualitatively, this is consistent with CFD-predicted formation of flowfield structures "lagging" the experiment. In other words, lags in earlier phases have by this time convected into the near-wake. The overall question of lag of flowfield response relative to $\alpha_e(t)$ is more complicated than in the pitch–plunge case. Formation of leading-edge vorticity appears to be quasi-steady: from Fig. 11, the strength of the LEV peaks nearly at $t/T = 0.25$. But from the dye injection, the height of the near-wake is qualitatively maximum at $t/T \sim 0.4$.

The pitch–plunge case has what might be termed a wall-bounded separation of moderate extent, while the pure-plunge case is at least qualitatively more akin to traditional dynamic stall, evidently because its angle of attack time history is deeper past the static stall value. Next, we consider the issue of spanwise broadening of the dye-tagged region, connecting the advent of strong leading edge separation with subsequent 3D effects.

3.4 Qualitative assessment of three-dimensional effects

Both the particle image velocimetry and computations in the present study are limited to two dimensions. By way of preliminary investigation of three-dimensionality of flow separation, we consider planform-views of the dye-identified flows, taken by imaging from underneath the test section (Fig. 12). In Fig. 12, the apparent "gaps" at the tips of the airfoil are just an image of twice the thickness of the test section sidewall glass. The model support linkages are visible near the airfoil trailing edge, at the image centerline. Results are presented for $Re = 60$ K, for pitch–plunge and pure-plunge.

Proceeding from the top of the plunge stroke, $t/T = 0$, for pitch–plunge, the dye streakline and subsequent evolution remain nominally two-dimensional until approximately $t/T = 0.375$. Toward the extreme bottom of the plunge stroke there is an abrupt spanwise broadening of the dye-tagged flow, from $x/c \sim 0.5$ aft. The broadened flowfield structure convects at essentially free-stream velocity downstream, and is well aft of the trailing edge by $t/T = 0.75$, by which time the flow over the airfoil suction-side has fully reattached. The extent of the spanwise broadening is weakly periodic, and indeed has some variability from one realization of the experiment to another. A smaller spanwise broadening is associable with a concomitant apparent increase in the dye-tagged region of flow separation in the sideways view.

For the pure-plunge case, the spanwise broadening is significantly larger in spatial extent and in prevalence over the duration of the motion period. At $t/T = 0$ the dye streak is again thin and of minimal spanwise extent, but spanwise eruption accompanies formation of the LEV at $t/T = 0.25$, broadening further as the LEV loses coherence and convects downstream. At $t/T = 0.5$ the spanwise structure is again larger aft of $x/c = 0.5$ than closer to the leading edge, but even at the leading edge the flow has appreciable spanwise extent, in contrast with the pitch–plunge case. Reattachment at the leading edge brings return to nominal two-dimensionality upon commencement of the upstroke. By $t/T = 0.75$, the dye-tagged flowfield region over the suction side is again nominally 2D. Flow over the pressure side of the airfoil remains essentially 2D throughout the entire motion period.

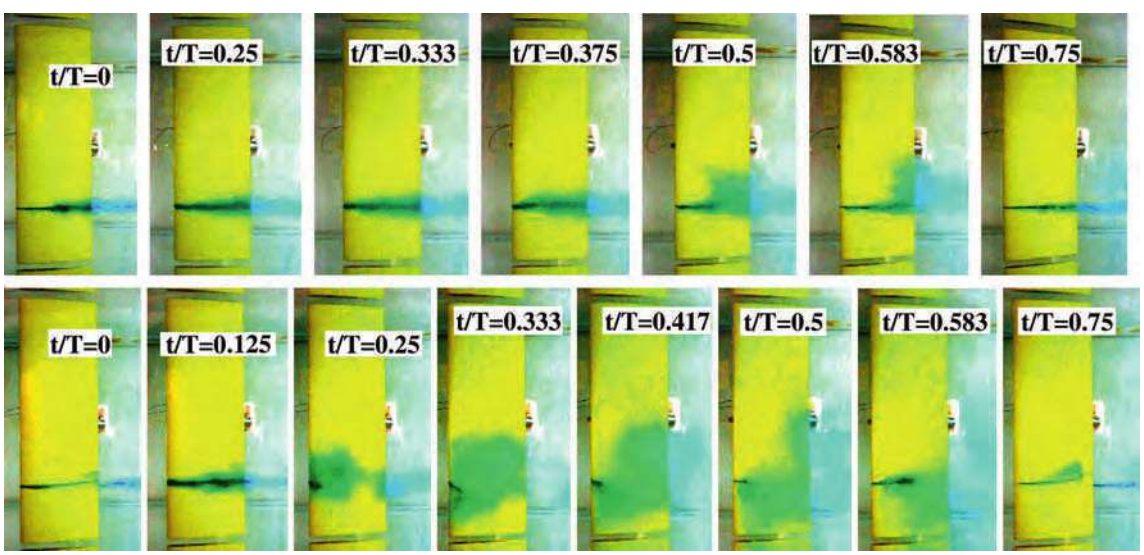

Fig. 12 Planform view of dye streaks, over one period of motion; pitch–plunge case (*top row*) and pure-plunge case (*bottom row*), $Re = 60$ K

For experimental studies, the practical consequence of the large extent of spanwise flow, especially for the pure-plunge case, is a requirement on small time step in the 2D PIV, to preclude out-of-plane particle loss and consequent reduction of cross-correlation peak height. It is not possible to infer conclusively if the spanwise eruption is specific to a wall-bounded wing, or to what extent the plunge rig actuator rods affect three-dimensionality; or, in the alternative case, to what extent LEV formation and bulk flow separation are irreducibly 3D. Nevertheless, as shown in the next section, the apparent impact on lift-coefficient time history of the sum total of these three-dimensional effects is not large.

The invalidation of 2D assumptions suggested by the planform-view flow visualization (Fig. 12) can be expected to suggest that a 2D computation should fail to agree with experiment for at least two reasons. First, the experiment is not truly 2D, in the sense of results departing from those expected for a high physical aspect ratio wing undergoing the same motion at the same Reynolds number. And second, a 3D structure in the turbulent flow separation could be expected even for a high physical aspect ratio wing, which would be absent in the computation. We next consider how the various approaches perform in prediction of the lift coefficient time history.

3.5 Lift coefficient versus motion time history

One can consider two kinds of lag in aerodynamic response: between onset/growth/attenuation of separated structures in the flowfield versus effective angle of attack time history; and between $C_L(t)$ and the angle of attack time history. It is quite possible that there are large lags in the flowfield time history, without necessarily large lags in the force time history, whence for purposes of force prediction, relatively crude methods may be acceptable.

Figure 13 compares time-traces of quasisteady $C_L(t) = 2\pi\alpha_e(t)$, computed $C_L(t)$, measured $C_L(t)$, and $C_L(t)$ from

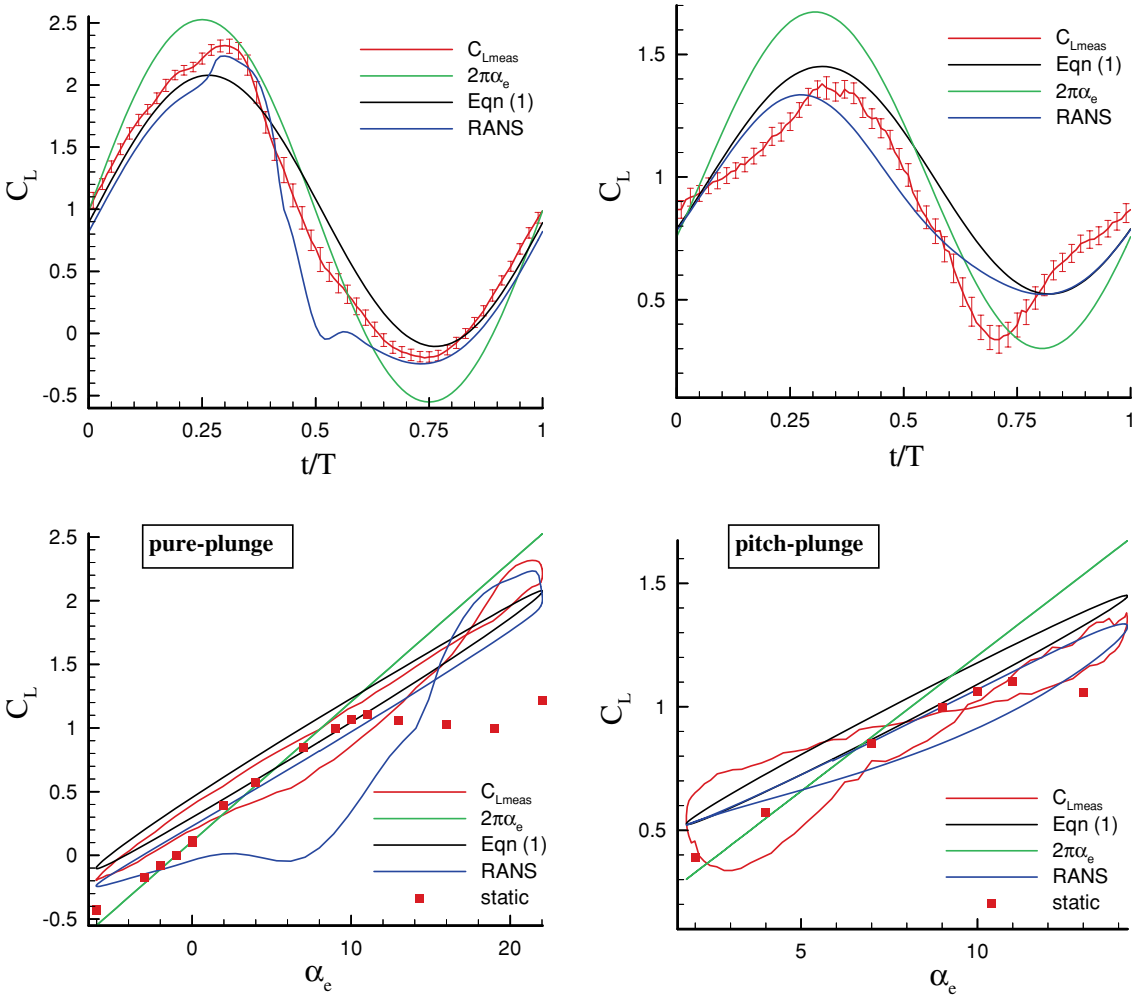

Fig. 13 Computed, measured and theoretical lift coefficient: pure-plunge $C_L(t)$ versus t/T (*top left*), pitch–plunge $C_L(t)$ versus t/T (*top right*); pure-plunge $C_L(t)$ versus $\alpha_e(t)$ (*bottom left*) and pitch–plunge $C_L(t)$ versus $\alpha_e(t)$ (*bottom right*)

Eq. 1, all plotted versus t/T and vs. $\alpha_e(t)$. Static measured $C_L(t)$, from Fig. 5 is also superimposed on the plots with respect to $\alpha_e(t)$. Broadly speaking, no two curves are very close to one another, with the other two being outliers; however, several trends are discernable. The quasi-steady solution for $C_L(t)$ is larger in peak-to-trough variation than the other three, but all four curves show lift response well in access of static stall, suggesting that positive lift increment due to dynamic stall is present in both pitch–plunge and pure-plunge cases. For both pitch–plunge and pure-plunge, the Theodorsen solution agrees best with the computed $C_L(t)$ for those t/T where flow separation is least. At those phases of motion where separation is large, the assumptions behind the Theodorsen solution are inconsistent with the flowfield structure evinced by dye injection, PIV or computation.

For the deep-stall case, experiment and computation both pick up a lift coefficient peak, evidently due to the LEV, at $t/T \sim 0.3$. This is of course not contained in Eq. 1. But the computation predicts a strong stall in the pure-plunge case at $t/T = 0.5$, evidently attributable to an unloading of the airfoil due to downstream convection and dissipation of the LEV. This is not present in the measured $C_L(t)$.

For the shallow-stall case, experiment and computation differ the most at $t/T \sim 0.7$, near the region of maximum geometric angle of attack ($\alpha = 16.42°$ at $t/T = 0.75$), where the experiment evinces a lift trough. Curiously, agreement between the Theodorsen prediction and computation is not appreciably worse in the deep-stall (pure plunge) case than the shallow-stall (pitch–plunge) case, suggesting that the LEV formation and subsequent reverse-flow region just above the airfoil suction side are not principal contributors to lift coefficient time history.

Since the $C_L(t) = 2\pi\alpha_e(t)$ curve is just a surrogate for effective angle of attack, broadly it is clear from Fig. 13 that the lag in computed–measured–theoretical $C_L(t)$ versus alpha is smaller than that between qualitative size of flow separation and $\alpha_e(t)$. In other words, the lift response is more quasi-steady than is the flowfield response. This suggests that the evinced flow separation does not have a dominant effect on the integrated lift, except possibly at narrow intervals of t/T. It remains to explore the limits of validity of this result across the range of parameter space: reduced frequency, reduced amplitude, pitch pivot point location, Reynolds number and angle of attack time history.

4 Conclusion

We consider, primarily at $Re = 60$ K, airfoil pitch–plunge and pure-plunge sinusoidal oscillations, representative of shallow and deep dynamic stall, respectively. Comparison of classical unsteady aerodynamic theory, a 2D fully-turbulent RANS computation, and water tunnel measurements for an airfoil spanning the test section seek to elucidate the impact of flow separation on the validity of the various approaches and on prediction of lift coefficient time history.

The experimental–computational–theoretical comparison begins to answer questions about the two-dimensionality of the flow. Static lift data in the experiment is consistent with 2D expectations, but spanwise eruption in separated flowfield regions in the dynamic cases brings 2D methods—in computation and experiment alike—into question. The computed flowfield agrees well with PIV in the shallow-stall case, in velocity/vorticity phase averages, even in phases of motion where flow separation is significant. For the deep-stall case, which has a strong leading edge vortex and complicated and highly-3D process of return to flow reattachment, PIV-CFD agreement in vorticity is worse; the numerical prediction lags the experiment, in that the CFD shows a LEV and TEV qualitatively similar to the PIV, but at a later phase of motion. This suggests that while the computation does not capture the onset of separation fully, shows promise in capturing the return from stall and the overall extent of separation. Further improvement of computational–experimental agreement is contingent upon two important extensions: (1) a 3D computation to further probe assertions about spanwise variation in the experiment, perhaps including modeling of tunnel side walls; and (2) 3D velocimetry methods in the water tunnel, to measure both the out-of-plane velocity component and variations in the velocity field in going along the model span.

Theodorsen's formula, which assumes fully attached flow and a planar wake, gives lift coefficient time history prediction that is not an outlier relative to the computed and measured results, even in the deep-stall (pure-plunge) case. Indeed, mutual discrepancies between theory, experiment and computation in lift coefficient time history are comparable. Thus there is evidence to broaden the possibility of applying Theodorsen's formula to cases where intuitively it should fail, to parameter studies of different educed frequency, Strouhal Number and so forth.

References

Anderson JM, Streitlien K, Barrett DS, Triantafyllou MS (1998) Oscillating foils of high propulsive efficiency. J Fluid Mech 360:41–72

Carr L (1988) Progress in analysis and prediction of dynamic stall. J. Aircraft 25:6–17

Carr L, McCroskey WJ (1992) A review of recent advances in computational and experimental analysis of dynamic stall. In: IUTAM symposium on fluid dynamics of high angle of attack

Dickinson MH, Götz KG (1993) Unsteady aerodynamic performance of model wings at low Reynolds numbers. J Exp Biol 174:45–64

Ellington CP (1984) The aerodynamics of hovering insect flight. I. The quasi-steady analysis. Philos Trans R Soc Lond B Biol Sci B 305:1–15

Choudhuri PG, Knight DD (1996) "Effects of compressibility, pitch rate, and Reynolds number on unsteady incipient leading-edge boundary layer separation over a pitching airfoil. J Fluid Mech 308:195–217

Jeon D (2000) Dissertation, Caltech

Jones KD, Dohring CM, Platzer MF (1996) Wake structures behind plunging airfoils: a comparison of numerical and experimental results. AIAA Paper 96-0078

Kamakoti R, Thakur S, Wright J, Shyy W (2006) Validation of a new parallel all-speed CFD code in a rule-based framework for multidisciplinary applications. AIAA-3063

Kang C-K, Baik YS, Bernal LP, Ol MV, Shyy W (2009) Fluid dynamics of pitching and plunging airfoils of Reynolds number between 1 × 10^4 and 6 × 10^4. AIAA-0536

Koochesfahani MM (1989) Vortical patterns in the wake of an oscillating airfoil. AIAA J. 27(9):1200–1205

Kramer B (2002) Experimental evaluation of superposition techniques applied to dynamic aerodynamics. AIAA-0700

Lehmann F-O (2004) The mechanisms of lift enhancement in insect flight. Naturwissenschaften 91:101–122

Leishman JG (2000) Principles of helicopter aerodynamics. Cambridge University Press, London

Lian Y, Shyy W (2007) Aerodynamics of low reynolds number plunging airfoil under gusty environment. AIAA Paper-0071

Liiva J (1969) Unsteady aerodynamic and stall effects on helicopter rotor blade airfoil sections. J Aircraft 6(1):46–51

Liu H, Kawachi K (1998) A numerical study of insect flight. J Comput Phys 146:124–156

McCroskey WJ (1982) Unsteady airfoils. Ann Rev Fluid Mech 14:285–311

McCroskey WJ, Carr LW, McAlister KW (1976) Dynamic stall experiments on oscillating airfoils. AIAA J. 14(1):57–63

Menter FR (1993) Zonal two equation k-ω turbulence models for aerodynamic flows. AIAA-2906

Ohmi K, Coutanceau M, Loc TP, Dulieu A (1990) Vortex formation around an oscillating and translating airfoil at large incidences. J Fluid Mech 211:37–60

Ohmi K, Coutanceau M, Daube O, Loc TP (1991) Further experiments on vortex formation around an oscillating and translating airfoil at large incidences. J Fluid Mech 225:607–630

Ol M (2007) Vortical structures in high frequency pitch and plunge at low Reynolds number. AIAA-4233

Ol M, McAuliffe BR, Hanff ES, Scholz U, Kaehler Ch (2005) Comparison of laminar separation bubble measurements on a low Reynolds number airfoil in three facilities. AIAA-5149

Platzer M, Jones K (2006) Flapping wing aerodynamics—progress and challenges AIAA-0500

Poelma C, Dickinson MH (2006) Time-resolved reconstruction of the full velocity field around a dynamically-scaled flapping wing. Exp Fluids 41:213–225

Radespiel R, Windte J, Scholz U (2007) Numerical and experimental flow analysis of moving airfoils with laminar separation bubbles. AIAA J 45(6):1346–1356

Rao Y-J (1997) In-fibre bragg grating sensors. Meas Sci Tech 8(4):355–375

Shyy W (1985) A study of finite difference approximations to steady-state, convection-dominated flow problems. J Comput Phys 57(3):415–438

Shyy W (1994) Computational modeling for fluid flow and interfacial transport. Elsevier, Amsterdam

Shyy W, Udaykumar HS, Rao MM, Smith RW (2007) Computational fluid dynamics with moving boundaries. Taylor & Francis, Washington DC (1996, rev. printing 1997, 1998 & 2001); Dover, New York

Shyy W, Lian Y, Tang J, Viieru D, Liu H (2008) Aerodynamics of low Reynolds number flyers. Cambridge University Press,

Taylor GK, Nudds RL, Thomas ALR (2003) Flying and swimming animals cruise at a Strouhal number tuned for high power efficiency. Nature (London) 425:707–711

Thomas PD, Lombard K (1978) The geometric conservation law—a link between finite-difference and finite-volume methods of flow computation on moving grids. AIAA-1208

Usherwood JR, Ellington CP (2002) The aerodynamics of revolving wings I. Model hawkmoth wings. J Exp Biol 205:1547–1564

Visbal M, Shang JS (1989) Investigation of the flow structure around a rapidly pitching airfoil. AIAA J. 27(8):1044–1051

von Karman T, Sears WR (1938) Airfoil theory for nonuniform motion. J Aeronaut Sci 5(10):379–390

Willert CE, Gharib M (1991) Digital particle image velocimetry. Exp Fluids 10(4)

Young J, Lai JCS (2004) Oscillation frequency and amplitude effects on the wake of a plunging airfoil. AIAA J 42(10):2042–2052

Zhang L, Zhang W, Bennion I (2002) In-fiber grating optic sensors. In: Yu FTS, Yin S (eds) Fiber optic sensors. Marcel Dekker, NY, pp 123–181

High-fidelity simulations of moving and flexible airfoils at low Reynolds numbers

Miguel R. Visbal · Raymond E. Gordnier · Marshall C. Galbraith

Abstract The present paper highlights results derived from the application of a high-fidelity simulation technique to the analysis of low-Reynolds-number transitional flows over moving and flexible canonical configurations motivated by small natural and man-made flyers. This effort addresses three separate fluid dynamic phenomena relevant to small fliers, including: laminar separation and transition over a stationary airfoil, transition effects on the dynamic stall vortex generated by a plunging airfoil, and the effect of flexibility on the flow structure above a membrane airfoil. The specific cases were also selected to permit comparison with available experimental measurements. First, the process of transition on a stationary SD7003 airfoil section over a range of Reynolds numbers and angles of attack is considered. Prior to stall, the flow exhibits a separated shear layer which rolls up into spanwise vortices. These vortices subsequently undergo spanwise instabilities, and ultimately breakdown into fine-scale turbulent structures as the boundary layer reattaches to the airfoil surface. In a time-averaged sense, the flow displays a closed laminar separation bubble which moves upstream and contracts in size with increasing angle of attack for a fixed Reynolds number. For a fixed angle of attack, as the Reynolds number decreases, the laminar separation bubble grows in vertical extent producing a significant increase in drag. For the lowest Reynolds number considered ($Re_c = 10^4$), transition does not occur over the airfoil at moderate angles of attack prior to stall. Next, the impact of a prescribed high-frequency small-amplitude plunging motion on the transitional flow over the SD7003 airfoil is investigated. The motion-induced high angle of attack results in unsteady separation in the leading edge and in the formation of dynamic-stall-like vortices which convect downstream close to the airfoil. At the lowest value of Reynolds number ($Re_c = 10^4$), transition effects are observed to be minor and the dynamic stall vortex system remains fairly coherent. For $Re_c = 4 \times 10^4$, the dynamic-stall vortex system is laminar at is inception, however shortly afterwards, it experiences an abrupt breakdown associated with the onset of spanwise instability effects. The computed phased-averaged structures for both values of Reynolds number are found to be in good agreement with the experimental data. Finally, the effect of structural compliance on the unsteady flow past a membrane airfoil is investigated. The membrane deformation results in mean camber and large fluctuations which improve aerodynamic performance. Larger values of lift and a delay in stall are achieved relative to a rigid airfoil configuration. For $Re_c = 4.85 \times 10^4$, it is shown that correct prediction of the transitional process is critical to capturing the proper membrane structural response.

1 Introduction

Unsteady low-Reynolds-number flows are found in natural flyers, as well as in small unmanned air vehicles and micro air vehicles (or MAV's) due to the relatively small size and low flying speeds involved (Mueller 1985; Shyy 2008; Ellington et al. 1996). Depending upon the specific conditions, these flow fields may be characterized by extensive regions of laminar flow, by the onset of laminar separation bubbles (even at moderate incidence), and by laminar-turbulent transition zones. For the case of flapping wings, as

M. R. Visbal (✉) · R. E. Gordnier · M. C. Galbraith
Computational Sciences Branch, Air Vehicles Directorate,
Air Force Research Laboratory, Wright-Patterson AFB,
OH 45433, USA
e-mail: miguel.visbal@wpafb.af.mil

G.K. Taylor, M.S. Triantafyllou, and C. Tropea (Eds.): Animal Locomotion, pp. 341–360.
springerlink.com

well as for severe gusts, the highly unsteady forcing induces the formation of dynamic-stall and leading-edge vortices whose evolution and interaction with the aerodynamic surfaces have a significant impact on flight stability and performance. Although much has been studied and learned about these unsteady vortical flow features, challenges still remain in understanding fully their structure, scaling and implications on flight efficiency, in particular over the broad range of parameters encountered.

Vehicle weight considerations in MAV design dictate the use of lightweight and highly flexible or compliant structures. These characteristics create additional complexities due to the rich fluid-structure interactions generated by coupling of aerodynamic, inertial and elastic forces. There is growing recognition that wing deformation may be beneficial to flight performance including stall delay (Smith and Shyy 1995; Shyy and Smith 1997; Song and Breuer 2007; Rojratsirikul et al. 2008; Waszak et al. 2001). However, harnessing these passive effects through aeroelastic tailoring clearly demands further investigation.

From the perspective of analysis and simulation, this non-traditional low-Reynolds-number aerodynamic regime over flexible or flapping surfaces poses a severe challenge due to the following key factors. Difficulties arise due to the presence of highly unsteady flows which defy standard quasi-steady characterization. The flow fields are of a mixed laminar-transitional-turbulent type which high-Reynolds-number analysis tools are not particularly well-suited to handle. Both in nature and in MAV applications, an extensive range of parameters and configurations are encountered. Lastly, there exists a strong coupling of the unsteady aerodynamics and structural response which requires advanced multidisciplinary approaches.

Given the aforementioned difficulties, a heirarchy of increasingly more complex canonical model problems can be considered in order to facilitate progress in the improved understanding and prediction of the multi-disciplinary physics relevant to small flyers. The simplest of these configurations is a maneuvering or flexible airfoil section as a model for flapping flight. In that spirit, the present effort addresses the application of a high-fidelity simulation technique for the analysis of low-Reynolds-number transitional flows over stationary, plunging and flexible airfoils. The methodology, summarized in Sect. 2 and described in more detail elsewhere (Visbal and Rizzetta 2002; Visbal et al. 2003), is based on a 6th-order accurate implicit large-eddy simulation (ILES) procedure incorporating a low-pass spatial numerical filtering technique. The high order algorithm facilitates the proper representation of the transition process whereas the low-pass filter provides regularization in turbulent flow regions in lieu of a standard sub-grid-scale model. This method is particularly attractive for low-Reynolds-number applications since it permits a seamless treatment of the mixed laminar, transitional and turbulent flow features previously noted.

The first problem considered (Sect. 3) is the detailed structure of the transitional flow over a rigid stationary SD7003 airfoil section. Several experimental and computational studies of this configuration have been performed recently (Ol et al. 2005; Radespiel et al. 2006; Yuan et al. 2005; Lian and Shyy 2006). Although this canonical problem represents perhaps the simple abstraction of low Reynolds number aerodynamics, it exhibits a complex flow physics. Of particular interest here is the process of laminar–turbulent transition over the airfoil associated with the separated shear layer which is present even at modest incidence. In the classical time-averaged representation, this leads to the formation of the so-called laminar separation bubble (LSB) which eventually bursts leading to airfoil stall. The effects of Reynolds number ($10^4 < Re_c = \rho c U_\infty/\mu < 9 \times 10^4$) and angle of attack ($2^\circ < \alpha < 14^\circ$) on the transition process are investigated.

Of more interest to biological and MAV flight, is the aerodynamics of maneuvering airfoils as a tractable model of flapping flight. As a point of departure in this direction, we consider in Sect. 4 the unsteady transitional flow over a plunging SD7003 airfoil. The specific flow and motion parameters correspond to the recent experimental and computational study of McGowan et al. (2008). The airfoil is set at a static angle of attack $\alpha_o = 4^\circ$, and the reduced frequency and plunging amplitude are $k = \pi fc/U_\infty = 3.93$ and $h/c = 0.05$, respectively. These parameters result in a maximum excursion in motion-induced angle of attack of 21.5° which promotes through unsteady separation the generation of dynamic-stall-like vortices near the airfoil leading edge. The transitional behavior of these vortices, as they propagate along the airfoil, is investigated for two values of the Reynolds number ($Re_c = 10^4$ and 4×10^4).

Finally, in Sect. 5, we study the impact of structural compliance on the unsteady flow past a stationary flexible airfoil at low Reynolds number. The configuration employed consists of a latex sheet attached to two rigid mounts located at the leading- and trailing-edge of the membrane, and corresponds to the experimental arrangement of Rojratsirikul et al. (2008). The effect of increasing angle of attack on the fluid–structure interaction is examined for a fixed low Reynolds number ($Re_c = 2.5 \times 10^3$). As the membrane deforms due to the aerodynamic load, a cambered geometry is achieved which modifies the stall characteristics of the airfoil. For high incidence, large fluctuations in membrane shape occur which can be viewed as forcing of the separated vortical flow. Limited results on the effect of transition on the flow plast the flexible membrane are also considered for $Re_c = 4.85 \times 10^4$.

2 Methodology

2.1 Governing equations

In the present moving or flexible airfoil simulations, the governing equations are taken to be the full unsteady Navier–Stokes equations cast in strong conservative form and incorporating a general time-dependent curvilinear coordinate transformation $(x, y, z, t) \rightarrow (\xi, \eta, \zeta, \tau)$ (Vinokur 1974; Steger 1978) from physical to computational space. In terms of non-dimensional variables, these equations can be written in vector notation as:

$$\frac{\partial}{\partial\tau}\left(\frac{\vec{U}}{J}\right)+\frac{\partial\hat{F}}{\partial\xi}+\frac{\partial\hat{G}}{\partial\eta}+\frac{\partial\hat{H}}{\partial\zeta}=\frac{1}{Re}\left[\frac{\partial\hat{F}_v}{\partial\xi}+\frac{\partial\hat{G}_v}{\partial\eta}+\frac{\partial\hat{H}_v}{\partial\zeta}\right] \quad (1)$$

where $\vec{U}=\{\rho,\rho u,\rho v,\rho w,\rho E\}$ denotes the solution vector, $J=\partial(\xi,\eta,\zeta,\tau)/\partial(x,y,z,t)$ is the transformation Jacobian, $\hat{F},\hat{G}$ and $\hat{H}$ are the inviscid fluxes, and $\hat{F}_v,\hat{G}_v$ and $\hat{H}_v$ represent the viscous terms. The full form of these terms can be found, for instance, in Anderson et al. (1984).

It should be noted that the above governing equations correspond to the original *unfiltered* Navier–Stokes equations, and are used without change in laminar, transitional or fully turbulent regions of the flow. Unlike the standard LES approach, no additional sub-grid stress (SGS) and heat flux terms are appended. Instead, a high-order low-pass filter operator (Visbal and Gaitonde 1999; Gaitonde et al. 1999) is applied to the conserved dependent variables during the solution of the standard Navier–Stokes equations. This highly-discriminating filter selectively damps only the evolving poorly resolved high-frequency content of the solution (Visbal and Rizzetta 2002; Visbal et al. 2003). This filtering regularization procedure provides an attractive alternative to the use of standard sub-grid-scale (SGS) models, and has been found to yield suitable results for several turbulent flows on LES level grids. A re-interpretation of this implicit LES (ILES) approach in the context of an approximate deconvolution model (Stolz and Adams 1999) has been provided by Mathew et al. (2003). The ILES approach is very attractive for the present applications involving mixed laminar, transitional and turbulent flow regions.

The structural model for the membrane airfoil is based on the approach of Smith and Shyy (1995) for a two dimensional elastic membrane subjected to a normal force. The governing equation in nondimensional form is

$$\rho_s h\frac{\mathrm{d}^2z}{\mathrm{d}t^2}+\rho_s C_d\frac{\mathrm{d}z}{dt}-T\frac{\mathrm{d}^2z}{\mathrm{d}x^2}\left[1+\left(\frac{\mathrm{d}z}{\mathrm{d}x}\right)^2\right]^{-\frac{3}{2}}=\Delta p \quad (2)$$

where

$$T=Eh(\delta_o+\bar{\delta}) \quad (3)$$

$$\bar{\delta}=L-1 \quad (4)$$

and

$$L=\int_0^1\sqrt{1+\left(\frac{\mathrm{d}z}{\mathrm{d}x}\right)^2}\,\mathrm{d}x. \quad (5)$$

In these equations ρ_s, h, C_d, T, E and δ_o are the membrane density, thickness, damping, tension, modulus of elasticity and the length increase of the pretensed membrane, respectively.

2.2 Numerical procedure

All simulations are performed employing the extensively validated high-order Navier–Stokes solver *FDL3DI* (Visbal and Gaitonde 1999; Gaitonde and Visbal 1998). In this code, a finite-difference approach is employed to discretize the governing equations, and all spatial derivatives are obtained using a sixth-order compact-differencing scheme (Lele 1992).

In order to eliminate spurious components, a high-order low-pass spatial filtering technique (Visbal and Gaitonde 1999; Gaitonde et al. 1999) is incorporated. The filter is applied to the conserved variables along each transformed coordinate direction once after each time step or sub-iteration. For transitional and turbulent flows, the previous high-fidelity spatial algorithmic components provide an effective implicit LES approach in lieu of traditional SGS models, as demonstrated in Visbal and Rizzetta (2002) and Visbal et al. (2003).

For the case of a maneuvering airfoil, the grid is moved in a rigid fashion following the prescribed kinematics which provides the position and velocity of the mesh at every instant in time. For the flexible membrane airfoil computations, the aerodynamic mesh is allowed to deform in accordance with the motion of membrane. A simple algebraic method, described in Melville et al. (1997), is used to deform the grid in order to accommodate the instantaneous shape of the membrane. In both situations, great care must be exercised to avoid grid-motion-induced errors. In order to ensure that the geometric conservation law (GCL) is satisfied, the time metric terms are evaluated as described in detail in Visbal and Gaitonde (2002).

The membrane structural equation is solved numerically employing the procedure discussed in Gordnier (2008). Pinned conditions are prescribed at the membrane leading- and trailing-edges. Coupling of the aerodynamics with the membrane response occurs through the imposed pressure force, Δp, in Eq. 2 and by the resulting deflection of the

membrane, which is returned to the aerodynamic grid. A complete synchronization of the aerodynamic and structural systems is achieved through an implicit global subiteration strategy (Gordnier 2008). During each subiteration, the aerodynamic loading in the membrane equations is updated, and the new surface displacements are then provided to the aerodynamic solver. Using this approach, the temporal lag between the aerodynamic and structural solutions, as well as numerical linearization errors may be effectively eliminated.

3 Transitional flow over stationary SD7003 airfoil

In this section, we consider the effect of transition on the flow structure over an airfoil at Reynolds numbers relevant to MAV applications. At low Reynolds numbers ($Re_c = \rho c U_\infty/\mu < 10^5$), the flow may remain laminar over a significant portion of the airfoil, and is unable to sustain even mild adverse pressure gradients. For moderate incidence, separation leads to the formation of a laminar separation bubble (LSB) which breakdowns into turbulence prior to reattachment. The dynamics of this laminar separation bubble, as it moves towards the leading edge with increasing angle of attack and eventually bursts, has a significant impact on airfoil performance.

Results from large-eddy simulations for an SD7003 airfoil are presented. This airfoil geometry was selected since it exhibits a relatively large LSB on the suction side of the airfoil, and since it has been the subject of recent experimental and computational investigations (Shyy 2008; Ol et al. 2005; Radespiel et al. 2006; Yuan et al. 2005; Galbraith and Visbal 2008). Details of the present computations can be found in Galbraith and Visbal (2008) and Galbraith (2009) wherein the effects of grid resolution, Mach number and computational spanwise extent have been explored. Computations were performed for a Reynolds number range $10^4 < Re_c < 9 \times 10^4$, and for angles of attack $2^\circ < \alpha < 14^\circ$.

3.1 Effect of angle of attack

The evolution of the time-averaged flow structure with increasing incidence is examined at a fixed Reynolds number ($Re_c = 6 \times 10^4$). Shown in Fig. 1 are the mean streamline patterns and the Reynolds stress ($u'v'$) contours for several angles of attack. The corresponding mean surface pressure distributions are given in Fig. 2. In addition, Table 1 provides a summary of the locations of laminar separation and turbulent reattachment, as well as the maximum bubble height (defined in terms of the distance from the airfoil surface to the maximum velocity location at the edge of the shear layer). Further information such as skin-friction coefficient distribution and aerodynamic loads can be found in Galbraith and Visbal (2008).

At $\alpha = 2^\circ$, a long region of laminar separation is observed over the airfoil which closes just upstream of the trailing edge ($x/c = 0.92$). Relatively small values of Reynolds stress magnitude are seen near the reattachment zone. As the angle of attack increases to $\alpha = 4^\circ$, the laminar separation point moves upstream due to the higher adverse pressure gradient it encounters. The reattachment location is also displaced upstream due to the more intense process of transition to turbulence, as reflected in the increased magnitude of Reynolds stress. As a result, the mean separation bubble contracts both in height and in streamwise extent. This overall behavior of the LSB continues as the angle of attack increases up to $\alpha = 11^\circ$. Over this range of incidence, the C_p (Fig. 2) distributions display several well-defined characteristics, including a suction peak, a plateau associated with laminar separation, and a fairly rapid recovery following transition. All of these features are found to become sharper with increasing airfoil incidence. At $\alpha = 14^\circ$, the laminar separation bubble fails to close resulting in so-called bubble bursting. Airfoil stall is evident in the collapse of the suction peak and in an essentially flat pressure distribution over the entire suction surface. A large mean region of recirculation (which extends far away from the airfoil), as well as a reduction in the maximum magnitude of the Reynolds stress are also observed (Fig. 1).

Comparison of the computed time-averaged flow structure with high-resolution experimental measurements is shown in Fig. 3 for $\alpha = 4^\circ$. The measurements denoted as TU-BS correspond to the experiments of Radespiel et al. (2006), whereas the data referred to as HFWT was obtained by Ol et al. (2005). A comparison with experiments in terms of the mean separation bubble characteristics is also provided in Table 2. Good overall agreement is observed between the experimental and computational flow structures. Some discrepancies in specific details exist between the computations and experiment, as well as between the experimental data sets themselves. In particular, the LSB and the region of significant Reynolds stress appear to be larger in the computation relative to experiment. Also, the reported separation locations differ between the two experiments, due in part to the difficulties associated with obtaining the precise separation point from near-wall PIV measurements for a very shallow separation region. It should be noted, that the LSB transition process is expected to be quite sensitive to several factors including freestream turbulence and precise experimental setup (e.g., aspect ratio, interference effects). In the present calculations, no attempt has been made to duplicate any such factors which in general are not well characterized. For instance, no freestream turbulence is imposed on the incoming

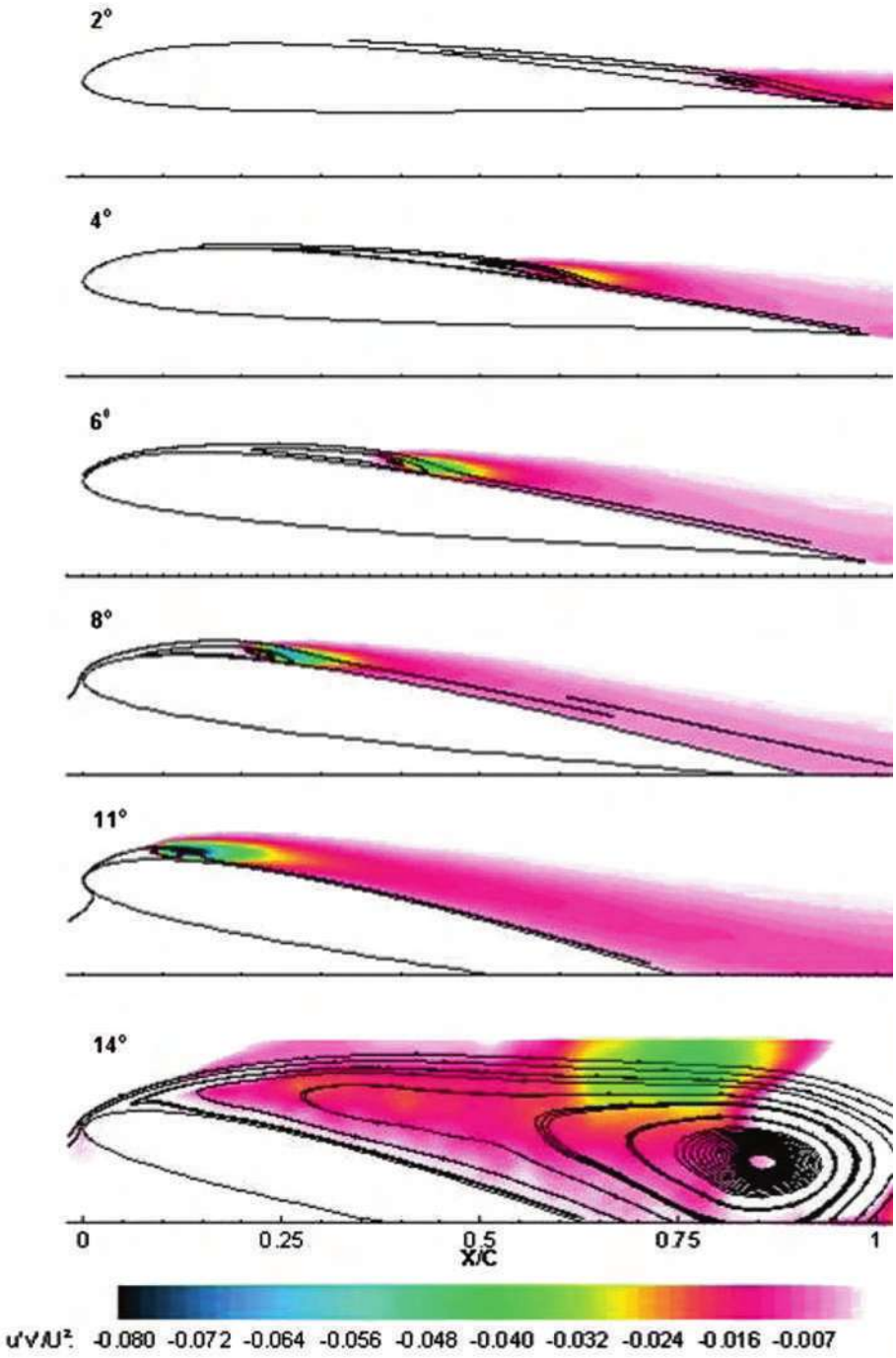

Fig. 1 Mean streamline pattern and Reynolds stress as a function of angle of attack for $Re_c = 6 \times 10^4$

computed flow fields, which may account for differences in the LSB size. Elucidation of these effects would require additional computational and experimental studies wherein these factors could be varied in a systematic fashion. Nonetheless, given all the sources of uncertainty, the level of agreement observed is found to be encouraging. Additional comparison with experiments, including different angles of attack and aerodynamic loads is provided in Galbraith and Visbal (2008).

The present high-fidelity simulations permit a characterization of the complex three-dimensional flow structure which is more difficult to obtain from experimental measurements. The evolution of the computed three-dimensional instantaneous flow structure with increasing angle of attack

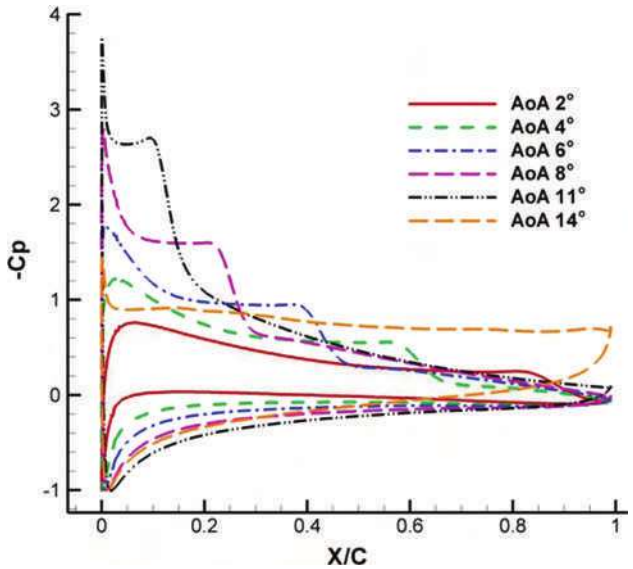

Fig. 2 Effect of angle of attack on mean surface pressure distribution, $Re_c = 6 \times 10^4$

Table 1 Effect of angle of attack on computed LSB properties

α (degrees)	Separation (x_s/c)	Reattachment (x_r/c)	Max bubble height (h_b/c)
2	0.45	0.92	0.036
4	0.23	0.65	0.030
6	0.11	0.45	0.028
8	0.04	0.28	0.027
11	0.007	0.16	0.025
14	0.01	–	–

$Re_c = 6 \times 10^4$

is shown in Fig. 4. This figure displays iso-surfaces of the Q-criterion (Dubeif and Delcayre 2000) which provides a means of visualizing vortical structures. At the lowest incidence ($\alpha = 2°$), the breakdown of the separated shear layer begins to emerge just upstream of the trailing edge. Significant changes occur with a small increase in angle of attack to $\alpha = 4°$. Coherent vortices form in the separated shear layer and rapidly breakdown due to spanwise instability effects. Nonetheless, the original coherent spanwise structures, surrounded by fine-scale features, are still discernable. With further increase in angle of attack (up to $\alpha = 11°$), the shear-layer vortices form closer to the leading edge, and the viscous flow region above the airfoil is characterized by progressively less coherent fine-scale features associated with the earlier transition to turbulence. Finally, for $\alpha = 14°$, the shear layer fails to reattach following separation from the leading edge and large scale vortex shedding ensues. These results demonstrate that the ILES approach is capable of capturing without change in parameters the entire process of laminar boundary layer separation, shear-layer transition, reattachment of the LSB, and eventually the passage into full airfoil stall.

The present high-fidelity 3-D simulations indicate that the dynamics of the flow remains qualitatively unchanged prior to stall ($2° < \alpha < 11°$). In all cases, the flow stays fairly aligned with the airfoil surface, and transition takes place through the formation of a closed separation bubble in a time-averaged interpretation. In an unsteady sense, coherent vortices form in the separated shear layer and exhibit spanwise instabilities and subsequent breakdown into fine-scale turbulent structures. High magnitudes of Reynolds stresses are generated which promote reattachment to the surface. This process becomes more abrupt as the angle of attack and the corresponding adverse pressure gradient increases, resulting in a shorter mean LSB. This consistent flow evolution for a stationary airfoil prior to stall therefore appears amenable to being captured by 2-D Reynolds-averaged simulations employing simplified transition models (Shyy 2008; Radespiel et al. 2006; Yuan et al. 2005). Significant challenges however are anticipated when using those approaches for stalled flows or for highly maneuvering and flexible airfoils involving the generation of dynamic-stall-like vortices.

3.2 Effect of Reynolds number

In order to explore the effect of Reynolds number on the transition process, several computations were performed for a fixed angle of attack ($\alpha = 8°$) over the Reynolds number range $10^4 < Re_c < 9 \times 10^4$. Results for the time-averaged flow fields are shown in Figs. 5, 6, as well as in Table 3.

For the lowest Reynolds number considered ($Re_c = 10^4$), the time-averaged flow exhibits a large recirculation zone above the airfoil. The corresponding surface pressure distribution displays a very weak suction peak and a fairly flat distribution over the suction side. Only small values of Reynolds stress are observed near the trailing-edge region. For $Re_c = 3 \times 10^4$, a better defined LSB begins to emerge, and there is a significant increase in the magnitude of the Reynolds stress. However, the LSB is still fairly large and produces significant boundary-layer displacement. The corresponding C_p distribution shows a stronger suction peak followed by a plateau and a mild recovery. As Reynolds number increases further, the separation location remains effectively unchanged while the LSB shrinks considerably in size. This is also accompanied by a more effective recovery in the surface pressure distribution. The variation of the mean drag with Reynolds number for a fixed angle of attack is given in Table 3. It is apparent that with decreasing Re_c there is a significant

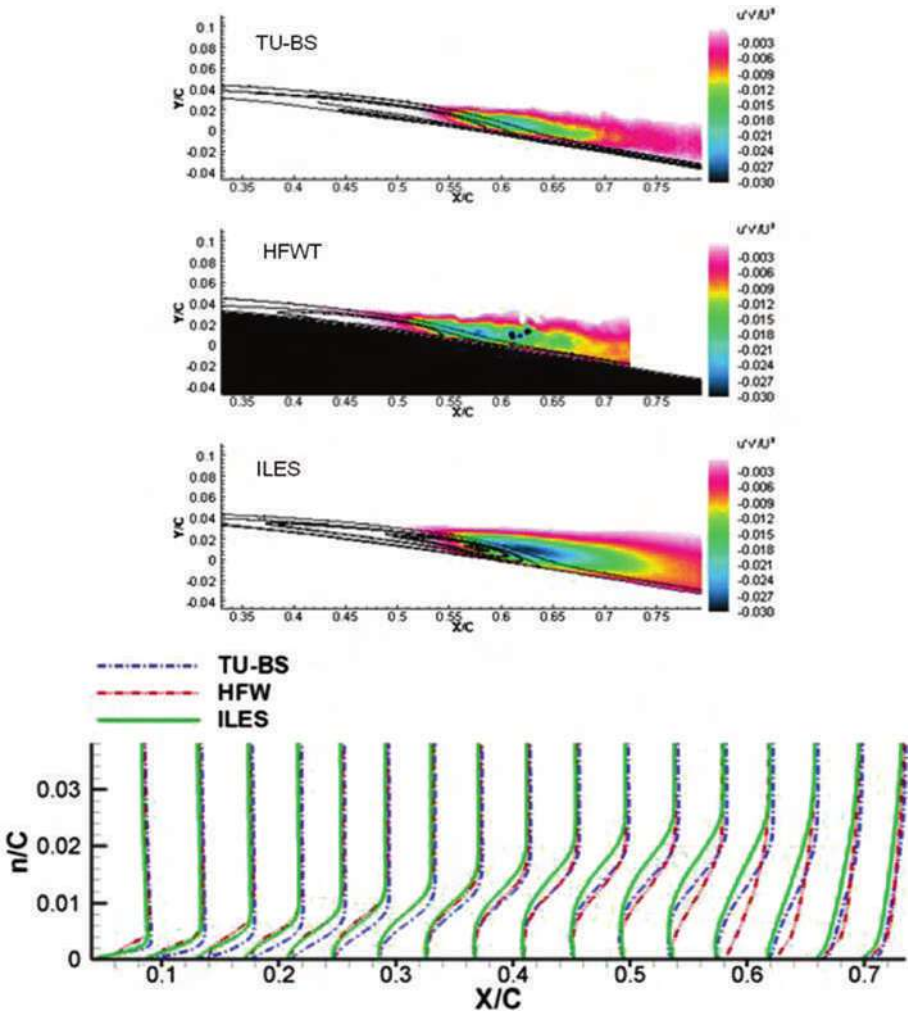

Fig. 3 Comparison of computed and experimental mean streamline pattern, Reynolds stress and velocity profiles for $Re_c = 6 \times 10^4$ and $\alpha = 4°$

Table 2 Comparison of experimental and computed LSB properties

Data set	Freestream turbulence (%)	Separation (x_s/c)	Reattachment (x_r/c)	Max bubble height (h_b/c)
TU-BS	0.08	0.30	0.62	0.028
HFWT	0.1	0.18	0.58	0.029
ILES	0	0.23	0.65	0.030

$\alpha = 4°$, $Re_c = 6 \times 10^4$

increase in the mean drag coefficient. This reduction in aerodynamic performance is a direct consequence of the significant vertical displacement effect created by the larger LSB at lower Reynolds number (Fig. 5).

The evolution of the instantaneous three-dimensional flow structure is shown in Fig. 7, using again an iso-surface of the Q-criterion. For $Re_c > 3 \times 10^4$, the process of boundary layer transition is clearly observed. In addition, finer scale turbulent flow features are generated with increasing Reynolds number. At the lowest Reynolds number considered ($Re_c = 10^4$), shear layer transition does not occur above the airfoil. Instead, the flow is characterized by the formation of large-scale coherent vortices which are shed from the leading edge and which only exhibit mild spanwise instabilities in the aft-region of the airfoil. It is expected that the effect of Reynolds number on the transition process depends also on angle of attack. Additional results showing Reynolds number effects for $\alpha = 4°$ and $\alpha = 14°$ are presented in Galbraith (2009) and Visbal (2009). At the lower incidence the flow failed to transition for $Re_c = 10^4$. In the stalled regime ($\alpha = 14°$), transition of the separated shear layer takes place in the aft-portion of the airfoil for $Re_c = 10^4$.

4 Transitional flow over plunging SD7003 airfoil

In this section, the influence of a prescribed motion on the transitional low-Reynolds-number airfoil flow is examined. Computations were performed for a plunging SD7003 airfoil section for which recent PIV measurements (McGowan

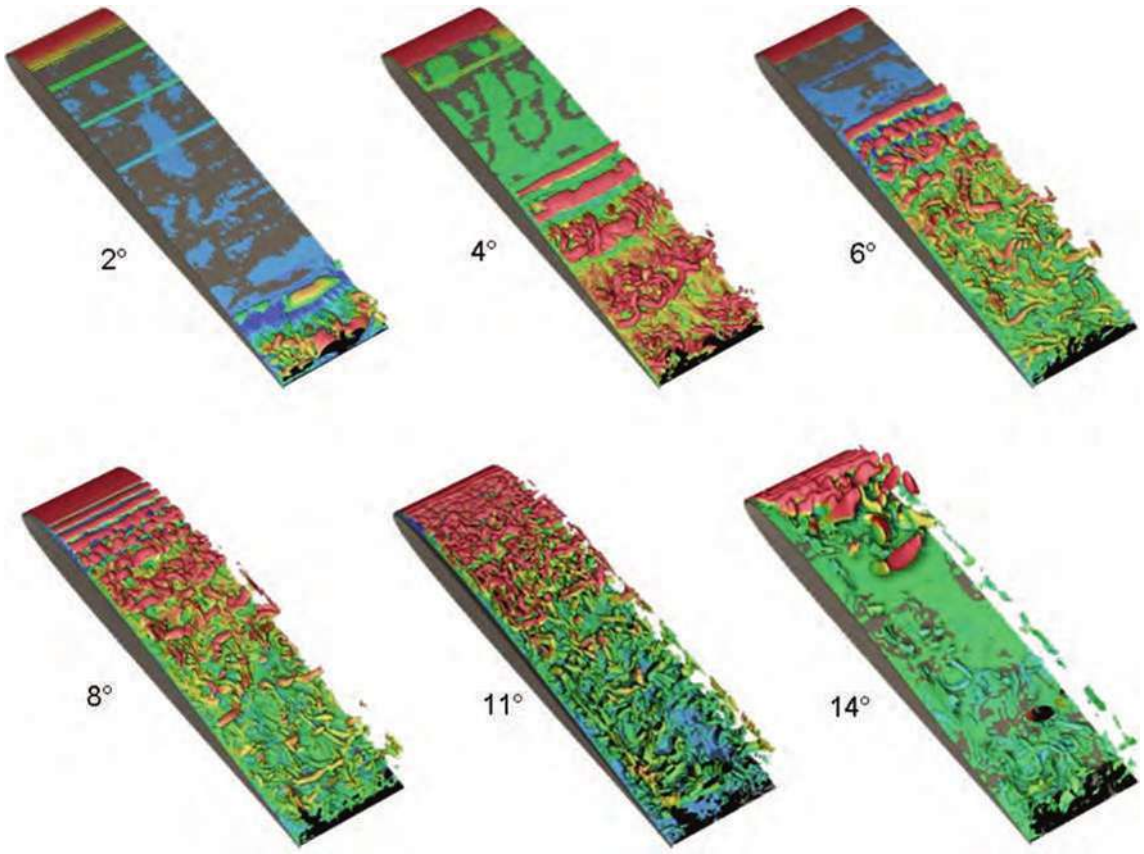

Fig. 4 Evolution of instantaneous three-dimensional flow structure with angle of attack, $Re_c = 6 \times 10^4$

et al. 2008) have been conducted. The airfoil is set at a static angle of attack $\alpha_o = 4°$, and the reduced frequency and plunging amplitude are $k = \pi fc/U_\infty = 3.93$ and $h/c = 0.05$, respectively. These motion parameters result in a maximum excursion in induced angle of attack of 21.5° which should promote leading-edge separation and the generation of dynamic-stall-like vortices. Two different Reynolds numbers ($Re_c = 10^4$ and 4×10^4) are considered in order to explore the impact of transition on the flow structure over the plunging airfoil.

Details of the computational mesh generated around the SD7003 airfoil are described elsewhere (Visbal 2009). Grid points were concentrated near the airfoil in order to capture the transition process. Therefore, description of the wake is limited to the region just downstream of the airfoil trailing edge (up to $x/c = 2.0$). Study of the downstream evolution of the wake far away from the airfoil is not considered since a larger grid would be needed. Both 2-D and 3-D simulations were performed in order to explore the suitability of the much more efficient 2-D approach for low-Reynolds-number applications, as well as to compare with previous computations (McGowan et al. 2008). For the 3-D calculations, the flows were assumed to be periodic in the spanwise direction with an extent $s/c = 0.2$. This value of s was selected based on a previous investigation of the effect of spanwise extent on the transitional flow past the same airfoil geometry at fixed angle of attack (Galbraith and Visbal 2008).

Comparison of the instantaneous spanwise vorticity component obtained from both 2-D and 3-D computations is shown at a given phase of the plunging motion in Fig. 8. For $Re_c = 10^4$, the 2-D and 3-D results are in close agreement with each other over a significant portion of the airfoil. Some discrepancies exist in the aft-portion near the trailing edge, as well as in the near wake due to incipient 3-D effects. However, the leading-edge vortex formation in particular exhibits a two dimensional character. This behavior appears to be consistent with the previous stationary airfoil (Sect. 3) for which transition was not observed at this low Reynolds number. As the Reynolds number is increased to 4×10^4, significant differences emerge between 2-D and 3-D results. The coherent vortices observed in the 2-D simulations breakdown in the spanwise direction, as described in more detail later. Given the importance of spanwise effects, only results from 3-D computations are discussed below.

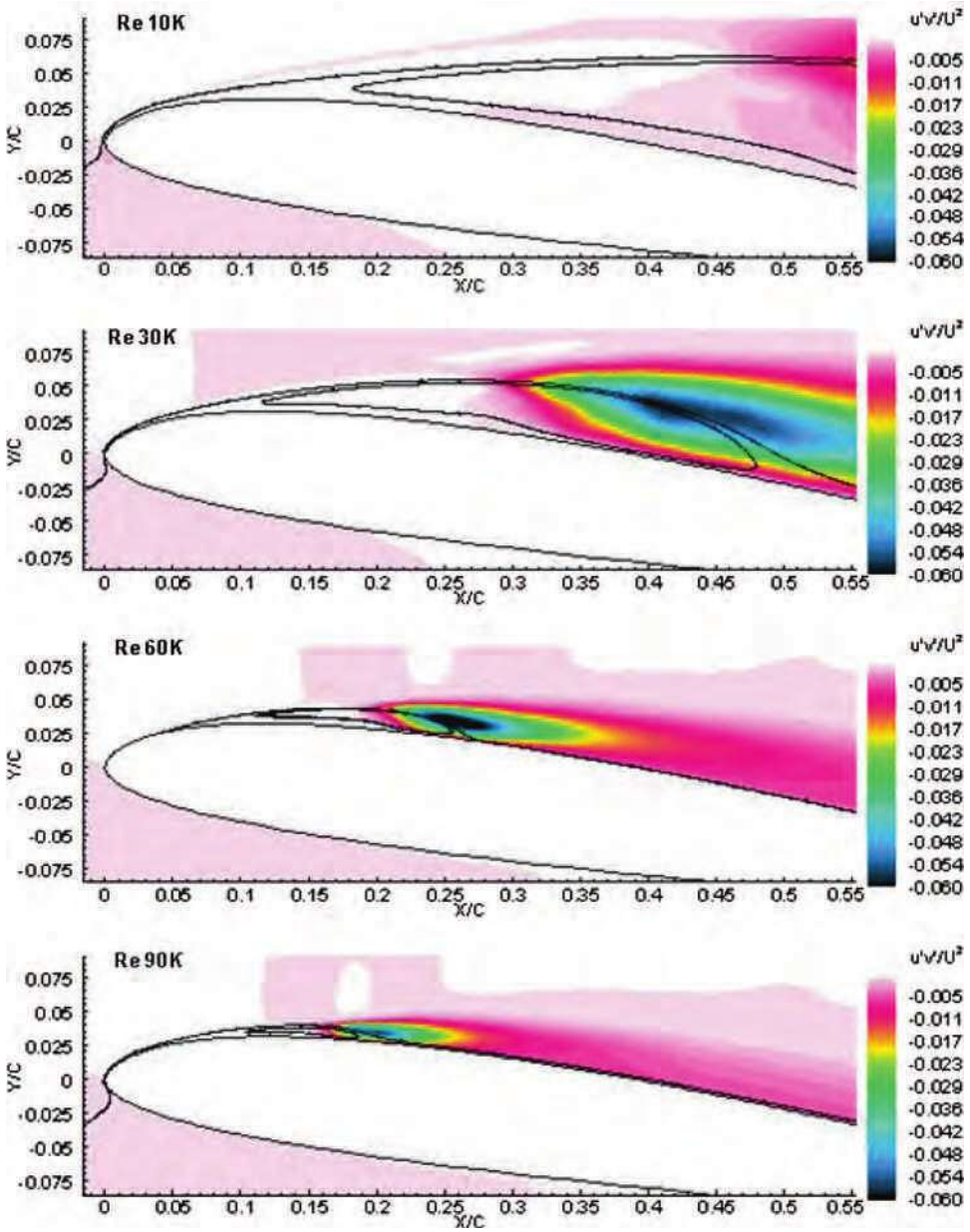

Fig. 5 Effect of Reynolds number on time-averaged flow structure, $\alpha = 8°$

The computed instantaneous flow structure over the plunging airfoil for $Re_c = 10^4$ is shown in Fig. 9. The selected motion phases correspond to the positions of maximum upward displacement ($\Phi = 0$), maximum downward velocity ($\Phi = 1/4$), maximum downward displacement ($\Phi = 1/2$) and maximum upward velocity ($\Phi = 3/4$). Although not included here, at this lower Reynolds number, the overall instantaneous and phase-averaged flow structures are found to be in reasonable agreement with each other due to the limited impact of transition (Visbal 2009). A fairly good comparison between experimental and phase-averaged vorticity is also shown in Visbal (2009).

Due to the large angle attack induced by the plunging motion during the downstroke, leading-edge separation occurs on the upper surface of the airfoil, and coherent dynamic-stall-like vortices are generated. Two distinct leading-edge vortices (denoted as '1' and '2' in Fig. 9c) are formed by the time the airfoil reaches its bottom dead center. During the upstroke, these vortices propagate close to the airfoil surface thereby precluding massive stall for this high value of reduced frequency. Given the short period of the motion ($T = \pi/k = 0.8$), the dynamic stall vortices emerge before the pair of vortices generated in the previous cycle (denoted as '3' and '4' in Fig. 9d) have reached the airfoil trailing edge. In addition to the primary

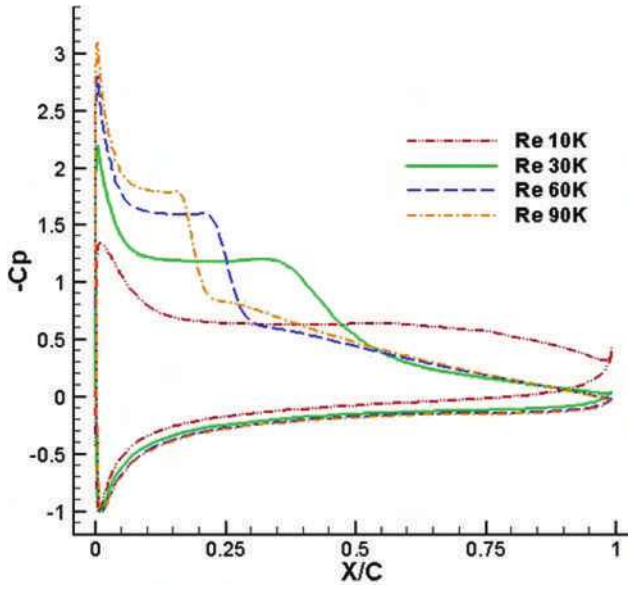

Fig. 6 Effect of Reynolds number on mean surface pressure distribution, $\alpha = 8°$

Table 3 Effect of Reynolds number on computed LSB propreties and mean drag coefficient

Re_c	Separation (x_s/c)	Reattachment (x_r/c)	Max bubble height (h_b/c)	Mean drag ($C_{D_{\text{mean}}}$)
1×10^4	0.09	0.98	0.217	0.082
3×10^4	0.05	0.53	0.073	0.070
6×10^4	0.04	0.28	0.027	0.043
9×10^4	0.04	0.20	0.014	0.035

$\alpha = 8°$

leading-edge vortical structures, another distinct feature is the ejection of vorticity of the opposite sign due to the ensuing vortex surface interaction. This ejected vorticity is quite prominent between the two primary dynamic-stall vortices (Fig. 9d), and eventually surrounds completely the leading vortex (denoted as '1'). Further downstream, this secondary vorticity becomes less apparent due to spanwise instability effects, as discussed below. Separation and formation of a single dynamic-stall vortex is also observed on the airfoil lower surface (Fig. 9b) as a result of the large negative angle of attack induced during the upstroke.

The present implicit large-eddy simulations permit a detailed description of the 3-D instantaneous flow structure which complements experimental planar observations. The overall instantaneous 3-D flow features for $Re_c = 10^4$ are displayed for several phases in Fig. 10. These plots show an iso-surface of vorticity magnitude colored by density in order to enhance contrast. At all phases of the plunging motion shown, one can observe coherent spanwise vortical structures or rollers which exhibit a fairly 2-D character. These vortices are surrounded by complex 3-D flow features resulting from spanwise instabilities. In particular, the dynamic stall vortex forming near the leading edge retains its spanwise coherence; however, the vorticity ejected from the airfoil surface (as a result of the strong vortex–surface interaction) rapidly breakdowns giving rise to the appearance of longitudinal vortical structures. Therefore, for this high reduced frequency and low Reynolds number, transitional effects over the airfoil appear to be minor, and are associated with the ejected secondary vorticity. However, as discussed next, this situation changes significantly with increasing Reynolds number.

Results for $Re_c = 4 \times 10^4$ are considered next. Figure 11 displays a comparison of the experimental and computed phase-averaged streamwise velocity and spanwise vorticity contours at the end of the upstroke. The computed results are found to be in reasonable qualitative agreement with the experimental measurements. A more quantitative comparison is shown in Fig. 12 in terms of the streamwise velocity profiles in the near wake at $x/c = 1.5$. The agreement between the measured and computed profiles is in general quite good. The velocity profile corresponding to the phase of maximum vertical displacement ($\Phi = 0$) exhibits a well-defined jet character. This jet-like behavior is consistent with the fact that the trailing-edge vortex shed from the airfoil lower surface is above the vortex shed from the upper surface boundary layer (see Fig. 11c, d). As it will be discussed later, this inverted vortex street results in a net mean thrust.

The computed instantaneous and phased-averaged spanwise vorticity fields are shown in Fig. 13. Significant differences are observed between the instantaneous and phased-averaged representations which reflect the fully 3-D transitional nature of the flow. The instantaneous vorticity exhibits fine-scale flow features within the dynamic stall vortices, as well as in the near wake. These features are essentially eliminated in the phase-averaging process. Increasing the Reynolds number has clearly modified the details of the phase-averaged vortical structure emerging from the unsteady separation process near the airfoil leading edge. As discussed earlier, for $Re_c = 10^4$ (Fig. 9c, d), the leading-edge vortex system exhibited a pair of dynamic-stall-like vortices which retained their identity as they propagated downstream in the absence of significant spanwise transitional effects. By contrast, for $Re_c = 4 \times 10^4$ (Fig. 13), a single and more diffused leading-edge vortex is observed in the phased-averaged representation.

The computed instantaneous 3-D flow structure above the plunging airfoil for $Re_c = 4 \times 10^4$ is displayed in Fig. 14. The most prominent overall flow features are the leading-edge vortices and their breakdown into fine-scale turbulence due to spanwise instability effects. At the end of

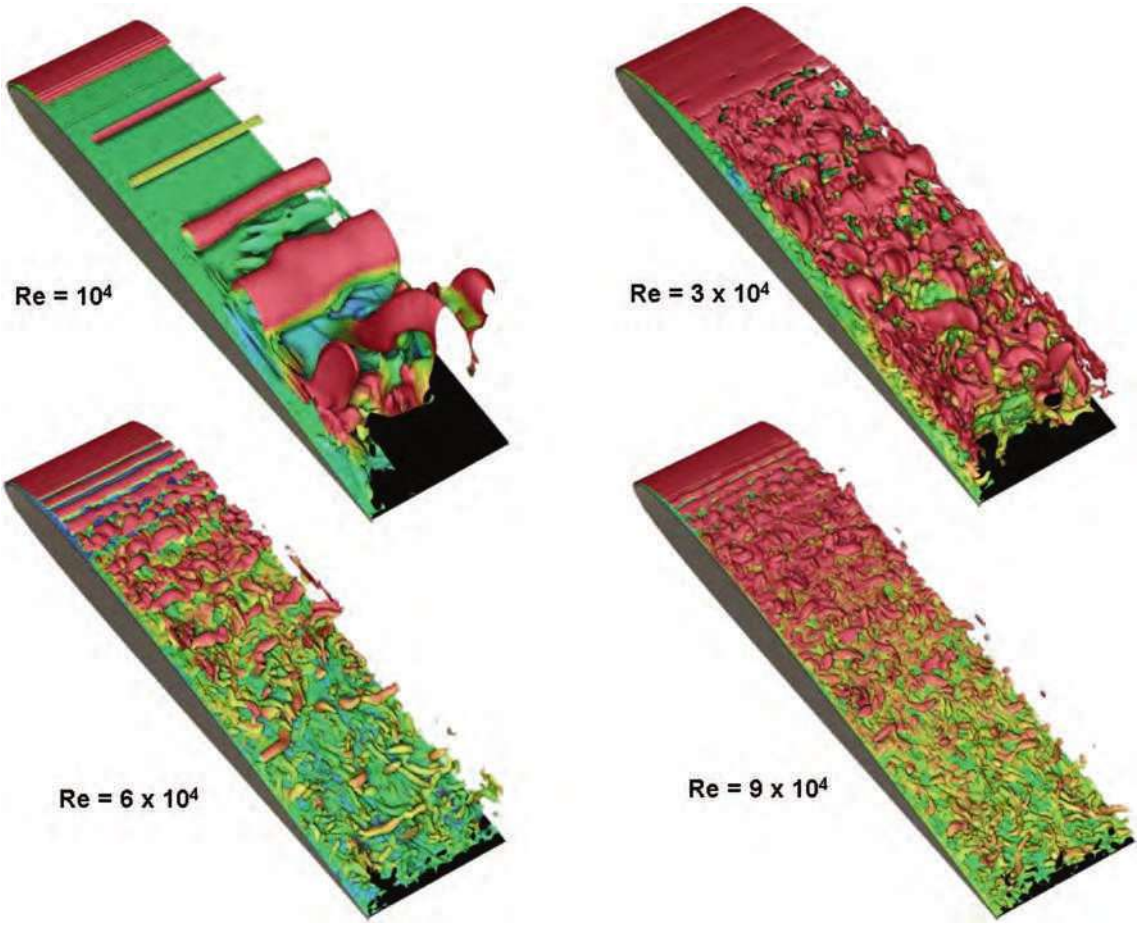

Fig. 7 Effect of Reynolds number on three-dimensional instantaneous flow structure, $\alpha = 8°$

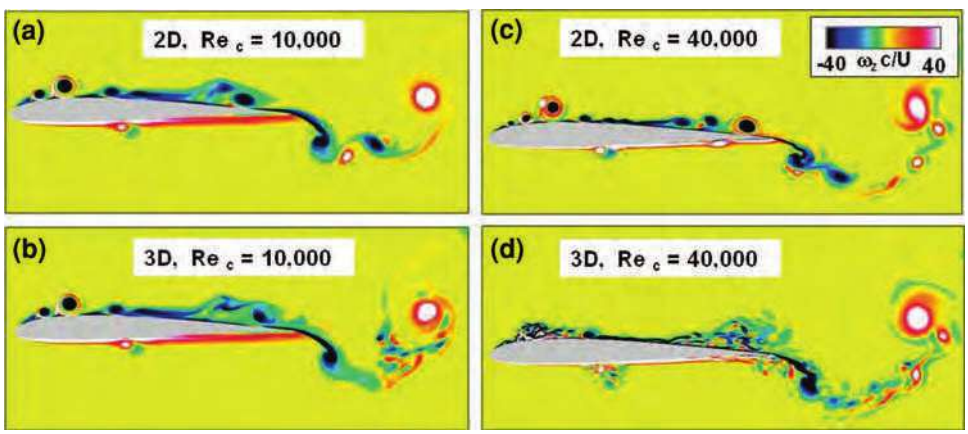

Fig. 8 Comparison of instantaneous spanwise vorticity for 2-D and 3-D plunging airfoil simulations

the upstroke ($\Phi = 0$), the boundary layer near the leading edge remains laminar and attached to the airfoil surface. By the time the airfoil has reached its maximum downward velocity ($\Phi = 1/4$), a small region of laminar separation has emerged near the leading edge. Between $\Phi = 1/4$ and $\Phi = 1/2$, this separation region evolves into a coherent dynamic-stall-like vortex which subsequently breakdowns into fine-scale structures. This transitional leading-edge vortex propagates downstream close to the airfoil surface, as seen in Fig. 13. Given the relatively high value of reduced frequency, the dynamic-stall-like vortex generated in the previous cycle (denoted as V_1 in Fig. 14c) has not reached the airfoil trailing edge before a new leading-edge vortex (V_2) is generated.

The transition of the dynamic stall vortex near the leading edge is described in detail in Visbal (2009). This

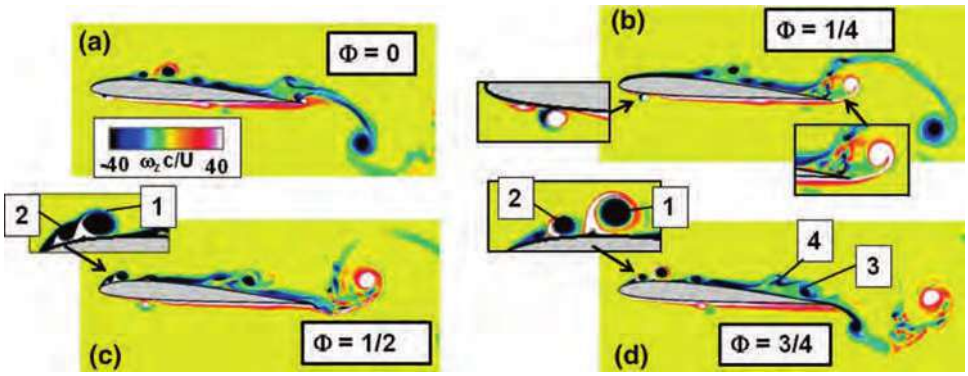

Fig. 9 Instantaneous spanwise vorticity at selected phases of the plunging motion for $Re_c = 10^4$

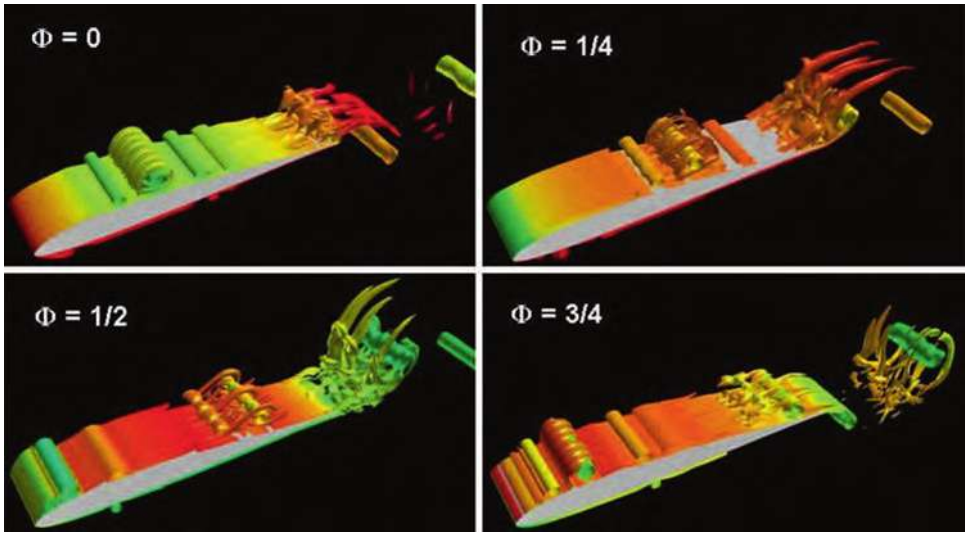

Fig. 10 Iso-surface of instantaneous vorticity magnitude at selected phases of the plunging motion for $Re_c = 10^4$

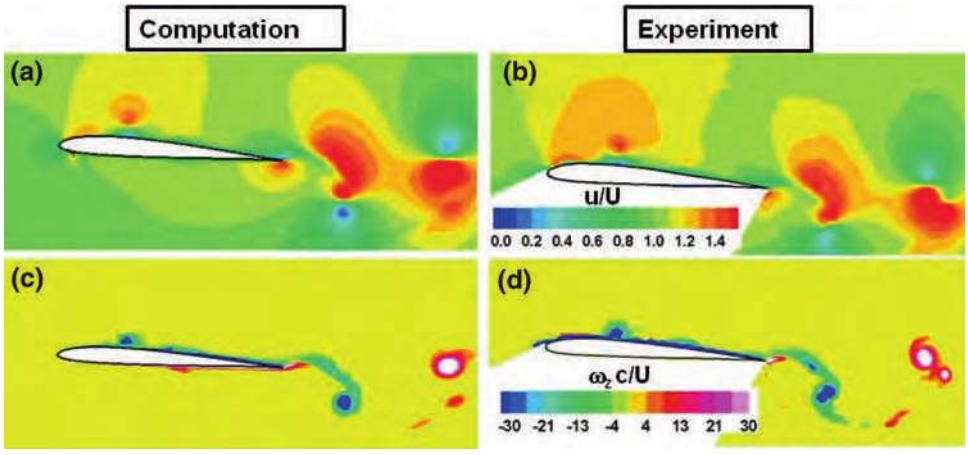

Fig. 11 Comparison of computed and experimental phased-averaged streamwise velocity (**a**, **b**) and spanwise vorticity (**c**, **d**) at the end of the upstroke for $Re_c = 4 \times 10^4$

transition process is found to be rather abrupt and takes place over a short non-dimensional time interval of order $\Delta t U_\infty / c \leq 0.04$. This represents a fast onset compared to either the plunging motion or the vortex convection time scales. If remains to be seen whether this process can be duplicated by standard Reynolds-averaged eddy-viscosity models which rely on dissipation-like terms. In addition, the mixed laminar-transitional character of this highly unsteady flow is quite apparent. For instance, the vortex structure of Fig. 14c displays an extensive region of fairly laminar flow between the two transitional leading-edge vortices generated in consecutive cycles of the plunging motion. This mixed flow structure, although amenable to simulation with the present high-fidelity ILES approach,

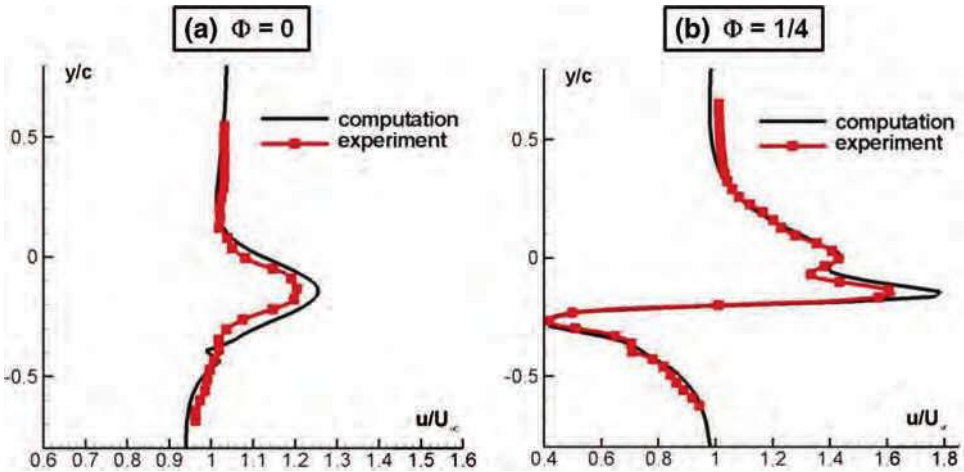

Fig. 12 Comparison of computed and experimental phased-averaged streamwise velocity profiles in the near wake ($x/c = 1.5$) of the plunging airfoil for $Re_c = 4 \times 10^4$

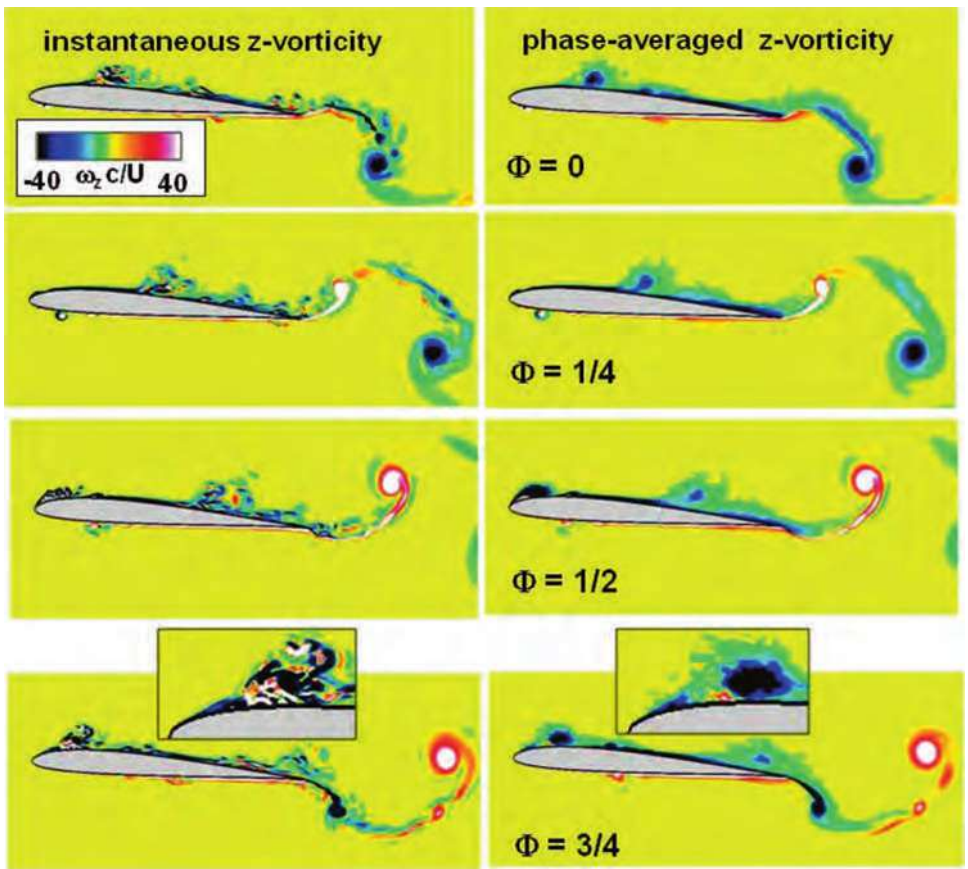

Fig. 13 Comparison of computed instantaneous and phased-averaged spanwise vorticity at selected phases of the plunging motion for $Re_c = 4 \times 10^4$

will remain a significant challenge for more efficient Reynolds-averaged methods incorporating simplified transition models.

The time histories of the lift coefficient for both Reynolds numbers are shown in Fig. 15a. Clearly, C_L appears to be essentially independent of Reynolds number and of the 3-D transitional aspects of the flow field. The insensitivity of the aerodynamic lift is due to the fact that at this high value of reduced frequency, C_L is dominated by the acceleration of the airfoil which scales with k^2. Indeed, the computed lift is found to be in close agreement with the prediction given by the inviscid theory (Fung 1993) (Fig. 15b) which in turn is shown to be dominated by non-circulatory effects. The computed mean drag coefficients for $Re_c = 10^4$ and $Re_c = 4 \times 10^4$ were found to be -0.055 and -0.083, respectively, where negative C_D values correspond to net thrust on the airfoil. As it is perhaps to be expected, the drag coefficient shows a significant dependence on Reynolds number and on the transitional aspects of the flow.

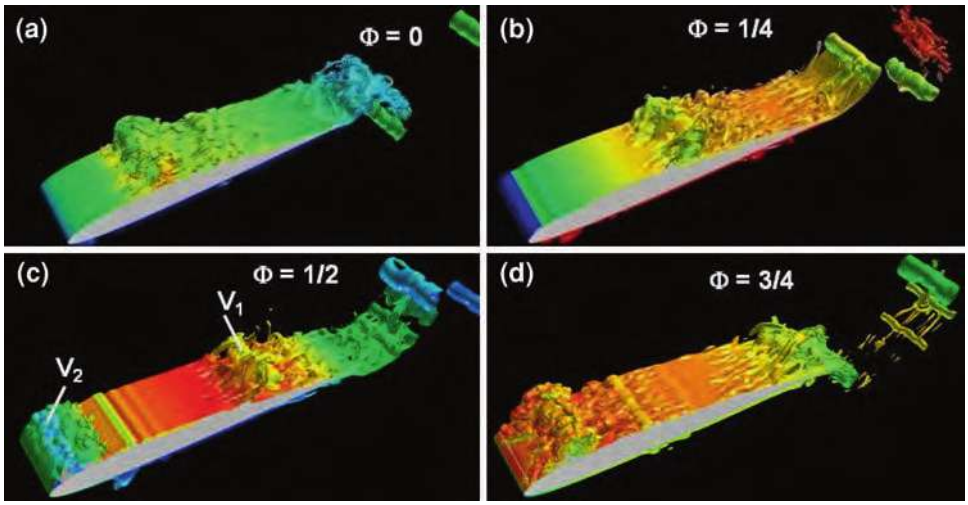

Fig. 14 Iso-surface of instantaneous vorticity magnitude showing flow structure above plunging airfoil at selected phases of the plunging motion for $Re_c = 4 \times 10^4$

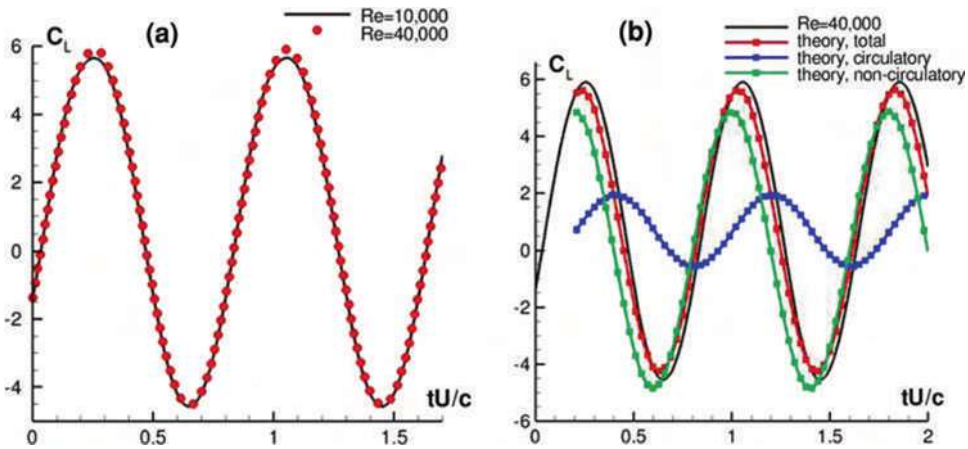

Fig. 15 Computed lift coefficient histories for plunging airfoil

5 Flexible membrane airfoil

In this section, the impact of fluid–structure interaction on the low-Reynolds-number flow past a flexible airfoil is investigated. The membrane airfoil configuration considered is based on the experimental model of Rojratsirikul, Wang, and Gursul (Rojratsirikul et al. 2008). In these experiments, the membrane wing consists of a thin latex sheet stretched between two small, aerodynamically-shaped, rigid mounts. The sheet is glued to the mounts resulting in pinned boundary conditions for the flexible membrane. Experimental observations (Rojratsirikul et al. 2008) indicate that the membrane deformation is essentially uniform in the spanwise direction. This observation justifies the initial assumption of 2-D deformation, at least for low Reynolds number simulations.

For the present computations, a freestream Mach number $M_\infty = 0.05$ is prescribed in order to approach the incompressible situation. Unless otherwise noted, the results presented are for a Reynolds number based on airfoil chord of $Re_c = 2{,}500$. The static angle of attack ranged from $\alpha = 4°$ to $\alpha = 20°$. The membrane structural parameters in Eq. 2 are specified as follows: mass ratio, $\rho_s h = 0.589$, membrane rigidity, $Eh = 50$, no structural damping, $C_d = 0$, and no membrane pretension, $\delta_o = 0$. To explore the impact of transition an additional computation at a higher Reynolds number ($Re_c = 4.85 \times 10^4$), and with structural parameters $Eh = 14.48$ and $\rho_s h = 1.2$ is also presented. Further simulations for higher Reynolds numbers and for other values of the structural parameters are described in Gordnier (2008) and Gordnier and Attar (2009) wherein additional details of the computations can also be found.

The evolution of the time-averaged flow structure with increasing angle of attack is shown in Figs. 16, 17, and 18 in terms of the mean vorticity and streamline patterns, the membrane shape and pressure distributions, as well as the mean aerodynamic lift coefficient. The most obvious effect of flexibility is the development of significant camber in the mean shape of the membrane due to the differences in pressure between the upper and lower sides of the airfoil. The maximum deflection (Fig. 17a) grows over the

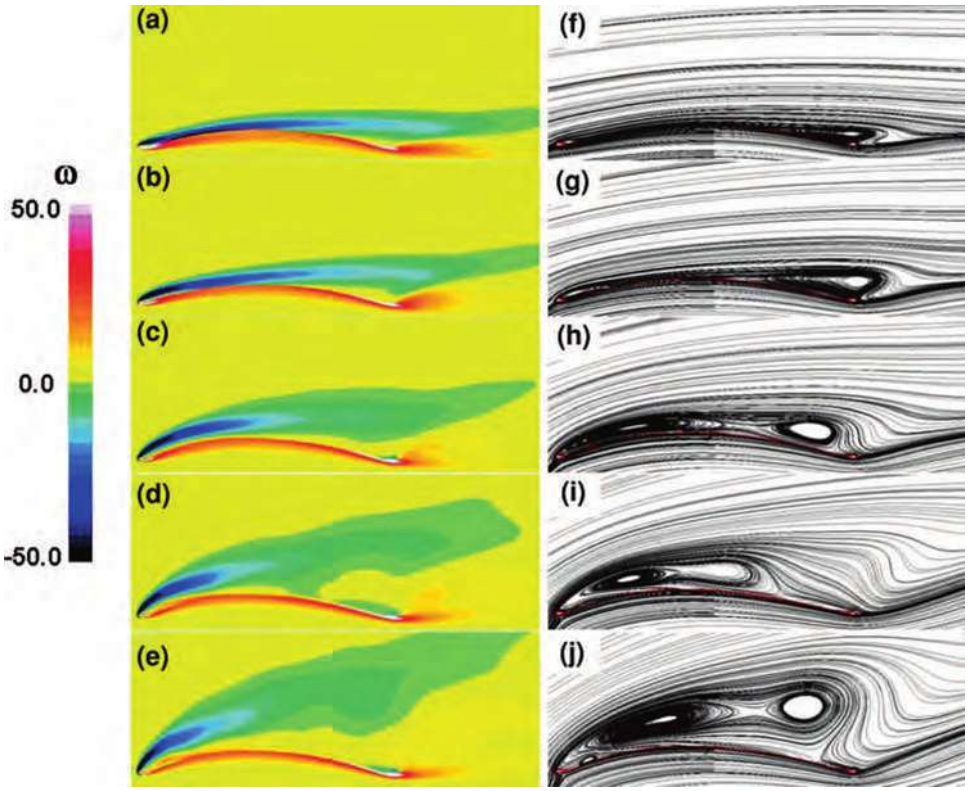

Fig. 16 Mean vorticity and streamline patterns for membrane airfoil at selected angles of attack: **a**, **f** $\alpha = 4°$; **b**, **g** $\alpha = 8°$; **c**, **h** $\alpha = 12°$; (**d**, **i**) $\alpha = 16°$; and (**e**, **j**) $\alpha = 20°$

incidence range considered from $z_{max}/c = 0.0724$ at $\alpha = 4°$ to $z_{max}/c = 0.0899$ at $\alpha = 20°$. For $\alpha = 4°$ the membrane shape is nearly symmetric. However, it becomes progressively more asymmetric with increasing incidence. For $\alpha = 16°$, the point of maximum deflection reaches $x/c = 0.426$ before it starts moving back downstream with further increase in angle of attack.

The impact of increasing angle of attack (and correspondingly mean camber) on the overall mean flowfield is shown in Fig. 16. At $\alpha = 4°$, the flow detaches at $x/c = 0.738$ resulting in a narrow separation bubble which extends to the trailing edge (Fig. 16f). A very small separation bubble is present near the leading edge associated with the rigid membrane mount. It should be noted that separation was always found to occur at the rigid mount. This fact suggests that how the underlying support structure for a membrane is designed may have direct influence on the flexible airfoil performance. As the angle of attack is raised to $\alpha = 8°$, the downstream separation point moves forward to $x = 0.57$, and the normal extent of the separation bubble increases. The leading-edge separation bubble also increases in size with attachment occurring at $x = 0.161$. By $\alpha = 12°$ the two separation zones have merged creating one large separation region that is narrow in vertical extent and covers nearly the full length of the airfoil. At $\alpha = 16°$, the separation zone has shrunk with attachment at $x = 0.774$, but the normal extent of the separated region has grown. Finally, by $\alpha = 20°$, a massively separated flow region exists over the airfoil. A small secondary separation zone is also observed near the leading edge of the membrane.

The corresponding evolution of the mean vorticity field is shown in Fig. 16a–e. At the lowest angle of attack (Fig. 16a), the shear layer separates from the upstream mount but rapidly attaches to the membrane airfoil. It subsequently departs from the membrane surface downstream at the previously noted separation location. By $\alpha = 12°$ (Fig. 16c), the shear layer separates from the upstream mount and fails to reattach to the membrane surface. A significant thickening of the shear layer is also observed. At the higher angles of attack, the departure angle of the shear layer from the leading edge mount grows and the shear layer moves increasingly away from the membrane. At $\alpha = 20°$ (Fig. 16e), a small region of vorticity of the opposite sign is located under the shear layer near the leading edge associated with the development of secondary separation.

The resulting mean surface pressure distributions on the membrane are plotted in Fig. 17b. As the incidence angle increases, a well-defined suction peak develops on the upper surface in the leading edge region. On the lower surface, the pressure progressively increases with angle of attack.

Shown in Fig. 18 is a comparison of the mean lift coefficient for the flexible membrane airfoil, as well as for a rigid flat airfoil. The C_L distribution for a symmetric

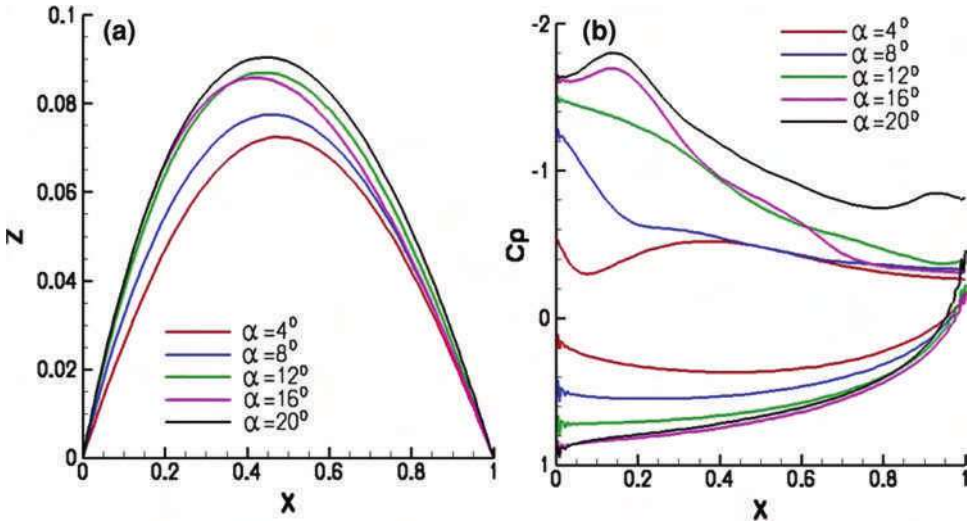

Fig. 17 Mean membrane deflection (**a**) and surface pressure coefficient (**b**) for various angles of attack

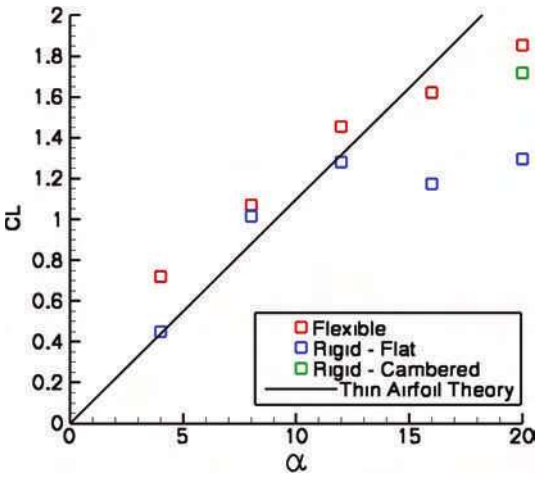

Fig. 18 Comparison of mean lift coefficient for flexible membrane and for rigid symmetric and cambered wing configurations

airfoil based on thin-airfoil theory is also shown for reference purposes. The rigid airfoil lift coefficient increases approximately in a linear fashion with a slope which is close to the theoretical value. A maximum C_L is achieved for $\alpha = 12°$. Beyond this angle of attack, the lift distribution displays the characteristics of a stalled flow. The flexible membrane airfoil exhibits a lift variation which differs significantly from its rigid counterpart. If one extrapolates the lift coefficient to zero incidence, a significant lift is achieved due to the camber effect induced by flexibility. When the angle of attack is increased up to $\alpha = 12°$, C_L increases in an approximate linear fashion albeit with a reduced slope relative to either the rigid case or the theoretical distribution. For higher incidence ($12° < \alpha < 20°$), the flexible airfoil lift coefficient continues to rise, although there is a further reduction in the lift-curve slope. Therefore, at high angles of attack, airfoil flexibility results in substantial lift enhancement relative to the rigid case. For the range of α considered, there appears to be no evidence of stall for the membrane airfoil, at least in terms of the aerodynamic lift coefficient. Lift enhancement due to wing flexibility at high angles of attack has also been demonstrated in wind tunnel tests by Waszak et al. (2001) and is due to both the effect of the induced mean camber, as well as the dynamic surface motion to be described next.

Instantaneous snapshots of the vorticity field (Fig. 19) illustrate the evolving unsteady flow structure with increasing angle of attack. At $\alpha = 4°$, the flow separates just past the midpoint of the airfoil. The separated shear layer does not become unstable or roll up until it passes the trailing edge and interacts with the separating flow from the lower surface. Therefore, the flow over the airfoil is predominantly steady. As the angle of attack is increased, the onset of the shear layer rollup moves progressively upstream and the flow becomes increasingly unsteady over the airfoil. Up to $\alpha = 12°$, the vortices remain close to the airfoil surface as they propagate downstream. At $\alpha = 16°$, the vortex train begins to depart from the membrane. The convecting shear-layer vortices interact with the surface boundary layer resulting in the development of secondary vortical structures, and the eventual eruption of vorticity of the opposite sign from the surface. Pairing of the shear-layer vortices is also observed in computed animations for the higher angles of incidence.

The unsteady structural response of the membrane airfoil is shown in Fig. 20. This figure displays the membrane oscillations by means of $x-t$ diagrams showing the difference between the instantaneous and mean membrane deflections. The membrane is nominally stationary at $\alpha = 4°$ since, as noted earlier, the flow is steady over the major portion of the airfoil (Fig. 19a). At $\alpha = 8.0°$, a third mode standing wave response develops with a

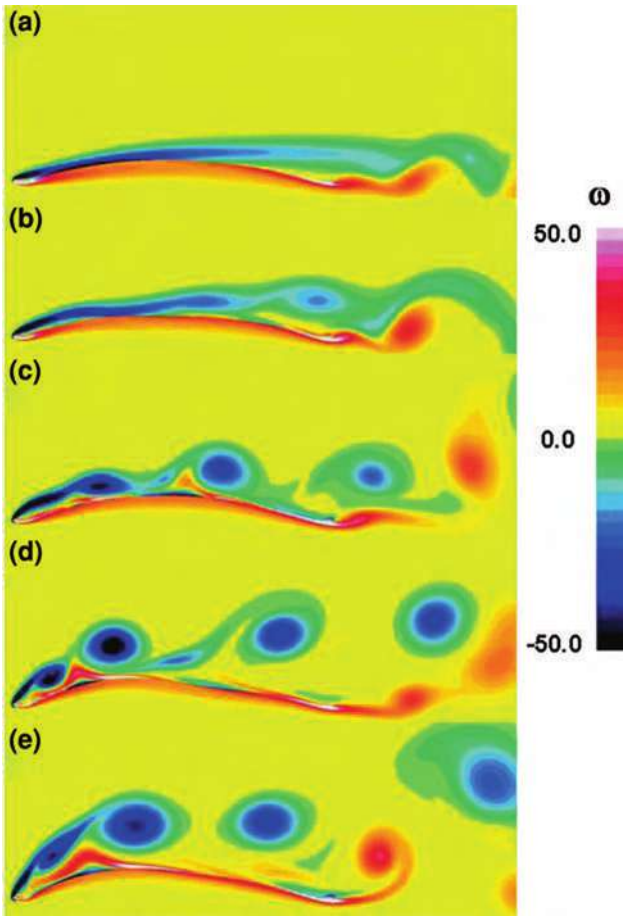

Fig. 19 Instantaneous vorticity for membrane airfoil at selected angles of attack: **a** $\alpha = 4°$, **b** $\alpha = 8°$, **c** $\alpha = 12°$, **d** $\alpha = 16°$, and **e** $\alpha = 20°$

nondimensional frequency, $St = fc/u_\infty = 1.43$. This frequency correlates within the tolerance of the Fourier analysis to the vortex shedding frequency $St \approx 1.45$ as measured at a point above the airfoil by which the shed vortices are passing. At the higher angles of attack $\alpha = 12°$ to $\alpha = 20°$ the membrane structural response exhibits a less regular behavior resulting from a combination of structural modes. Multiple frequency peaks are found in the Fourier analysis of the structural response. By $\alpha = 20°$ three peaks emerge in the spectral analysis of the structural response with the dominant frequency being $St = 0.59$. This corresponds to the computed vortex shedding frequency, $St = 0.6$, which correlates with the standard value for the wake shedding frequency when rescaled by angle of attack, $St \sin(\alpha) = 0.2$. The maximum peak-to-peak amplitude of the deflection reached values of order $0.07\ c$ which is of the same order as the maximum mean deflection (Fig. 17a). Therefore, in addition to the mean camber effect previously discussed, flexibility provides a significant forcing of the unsteady separated flow over the membrane.

In order to separate the effects of the dynamic motion of the membrane from the mean induced camber at higher angles of attack, a computation was run at $\alpha = 20°$ for a rigid cambered airfoil with its shape prescribed by the previously computed mean membrane deflection. A comparison of the mean and unsteady solutions for these two cases is shown in Fig. 21. The mean streamline patterns (Figs. 21a, b) show that the rigid airfoil flowfield exhibits a larger recirculation region, as well as a larger secondary separation bubble located further downstream on the airfoil. These significant differences between the time-averaged flows for the rigid and flexible airfoils result from a distinct change in the instantaneous vortical structure (Fig. 21c, d). The dynamic motion of the membrane excites the shear layer separating at the leading edge causing it to roll up sooner and to form a series of more coherent vortices which convect closer to the airfoil surface. The trailing edge vortex in the dynamic case is also reduced in strength and forms farther downstream and away from the airfoil. A similar comparison between a rigid cambered airfoil and a flexible membrane has been investigated experimentally by Rojratsirikul et al. (2008). Their flow visualizations (Rojratsirikul et al. 2008) also demonstrate a reduction of the separation zone due to the dynamic motion of the membrane. The overall impact of flexibility, through the combined effects of induced mean camber and dynamic motion, is a significant delay in the stall of the airfoil with a corresponding increase in lift coefficient in the post-stall region (Fig. 18). This enhanced lift arises predominantly from the effect of mean camber with additional lift enhancement resulting from the membrane motion. Further investigation of the impact of flexibility on the overall aerodynamics is warranted as it may provide a means for passively controlling the flow in order to achieve improved airfoil performance through judicious aeroelastic tailoring.

As the Reynolds number is increased from the low values considered to this point to more moderate values, the impact of transition on the flow becomes important. Figure 22 compares a laminar, 2-D simulation with a 3-D implicit LES simulation for $Re_c = 4.85 \times 10^4$ and $\alpha = 8°$. For the 2-D laminar simulation where transition of the flow cannot be captured directly (Fig. 22a), strong vortices are formed and shed from the leading edge. As these vortices convect downstream, they engender a very dynamic interaction with the flexible membrane resulting in large higher-mode fluctuations. The results of the 3-D computation using the implicit LES approach (Fig. 22b), exhibit rapid transition of the flow separating from the leading edge, and the subsequent development of large-scale coherent turbulent structures with embedded fine scale features. A more regular second-mode oscillation of the membrane results for this transitional flow. It is therefore apparent that correct prediction of the transitional behavior

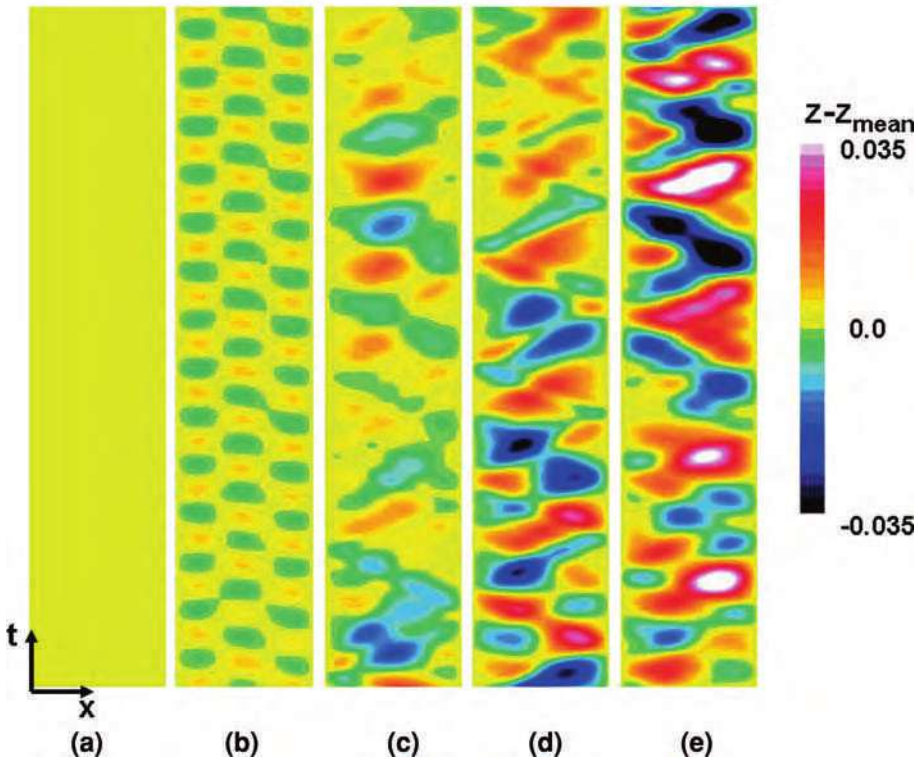

Fig. 20 $x-t$ diagram of instantaneous membrane deflection for selected angles of attack: **a** $\alpha = 4°$, **b** $\alpha = 8°$, **c** $\alpha = 12°$, **d** $\alpha = 16°$, and **e** $\alpha = 20°$

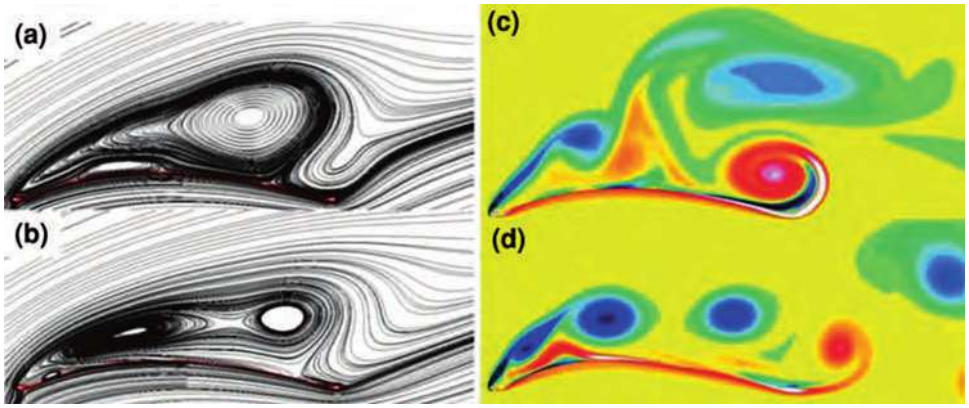

Fig. 21 Comparison of rigid cambered airfoil (**a**, **c**) and flexible membrane (**b**, **d**) flow fields for $\alpha = 20°$: **a**, **b** mean streamlines, and **c**, **d** instantaneous spanwise vorticity

is critical in order to capture the proper membrane structural response. Therefore, computational approaches that are capable of treating these unsteady, mixed transitional flows are required at these moderate Reynolds numbers. Further discussions of the ILES simulations for membrane airfoils may be found in Gordnier and Attar (2009).

6 Summary and conclusions

A high-fidelity implicit large-eddy simulation approach has been employed to investigate several aspects of the complex unsteady flow physics encountered by small-scale vehicles in low-speed flight. This regime is characterized by highly unsteady mixed laminar-transitional-turbulent flows over moving and flexible surfaces. Three separate fluid dynamic phenomena are considered, including: laminar separation and transition over a stationary airfoil, transition effects on the dynamic stall vortex generated by a plunging airfoil, and the effect of flexibility on the flow structure above a membrane airfoil. Comparison with high-resolution PIV experiments has been provided whenever possible.

The process of boundary-layer transition over a stationary SD7003 airfoil has been examined for a range of Reynolds number ($10^4 < Re_c < 9 \times 10^4$) and angle of attack ($2° < \alpha < 14°$). Prior to stall, the flow is characterized by a separated shear layer which exhibits the

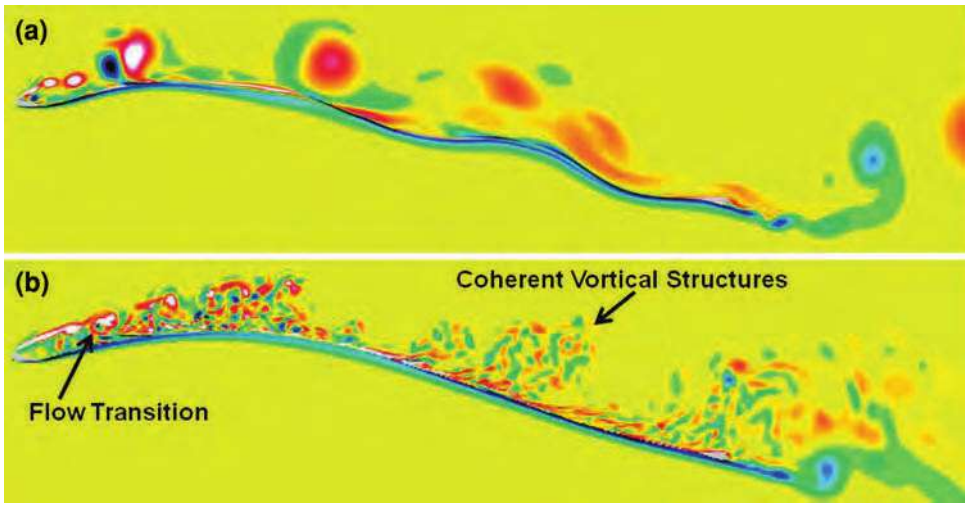

Fig. 22 Effect of transition at Reynolds number, $Re_c = 48{,}500$: **a** 2-D laminar flow simulation, **b** 3-D transitional flow simulation

formation of spanwise coherent vortical structures. These vortices breakdown due to spanwise instability mechanisms and promote the reattachment of the boundary layer. In a time-averaged representation, a laminar separation bubble (LSB) is formed which diminishes both in streamwise and vertical extent with increasing angle of attack. At fixed incidence, decreasing Reynolds number promotes the formation of a larger LSB. By $Re_c = 10^4$, transition fails to occur over the airfoil with an accompanying significant increase in drag coefficient. The sensitivity of these transitional flows to freestream turbulence or other imposed disturbances needs to be elucidated.

The unsteady low-Reynolds-number ($Re_c = 10^4$ and 4×10^4) flow past a SD7003 airfoil plunging at a relatively high reduced frequency ($k = 3.93$) was investigated. Comparison was made with recent PIV measurements. For the parameters chosen, the large motion-induced angle of attack generates dynamic-stall-like vortices in the leading-edge region both above and underneath the airfoil. Due to the high value of k and small plunging amplitude ($h/c = 0.05$), these vortices convect downstream close to airfoil surface precluding massive stall. For $Re_c = 10^4$, the computed instantaneous and phased-averaged flow structures are in fairly good agreement with each other. This is due to the incipient process of transition which is mainly limited to the secondary vorticity ejected from the airfoil surface. When the Reynolds number is increased to 4×10^4, the dynamic-stall vortices breakdown shortly after their onset due to spanwise instability effects. The instantaneous flow exhibits fine-scale structures which are eliminated in the phase-averaged representation. At this intermediate Reynolds number, a quite complex mixed transitional-turbulent flow field exists which would pose a formidable challenge for its simulation employing simplified approaches.

The effect of structural compliance on the unsteady flow past a membrane airfoil at low Reynolds number ($Re_c = 2.5 \times 10^3$) has been explored by solving the coupled fluid-structural system. The most notable effect of membrane flexibility is the introduction of a mean camber due to the fluid forces acting on both sides of the airfoil. At high incidence, large membrane fluctuations are also established with peak-to-peak amplitudes commensurate with the mean deflection. This dynamic behavior provides an aeroelastically induced excitation of the separated shear layer which rolls up more readily and remains closer to the membrane. These combined effects result in an increase in lift and in a delay in the onset of stall. At a higher Reynolds number ($Re_c = 4.85 \times 10^4$), the inclusion of transition effects is required to capture the correct membrane structural response.

Acknowledgments The authors are grateful for AFOSR sponsorship under tasks monitored by Dr. J. Schmisseur. This work was also supported in part by a grant of HPC time from the DoD HPC Major Shared Resource Center at AFRL, WPAFB. The authors are grateful to M. OL, R. Radespiel and J. Windte for their kind assistance with their experimental data sets.

References

Anderson DA, Tannehill JC, Pletcher RH (1984) Computational fluid mechanics and heat transfer. McGraw-Hill Book Company

Dubeif Y, Delcayre F (2000) On coherent-vortex identification in turbulence. J Turbul 1(11):1–22

Ellington C, van den Berg C, Willmott A, Thomas A (1996) Leading-edge vortices in insect flight. Nature 384:626–630

Fung YC (1993) An introduction to the theory of aeroelasticity. Dover, New York

Galbraith M (2009) Implicit large-eddy simulation of low-Reynolds-number transitional flow past the SD7003 airfoil. MS Thesis, Dept of Aerospace Engineering, University of Cincinnati, Cincinnati, OH, March 2009

Galbraith M, Visbal M (2008) Implicit large eddy simulation of low Reynolds number flow past the SD7003 airfoil. AIAA Paper 2008-0225, 2008

Gaitonde DV, Visbal MR (1998) High-order schemes for Navier–Stokes equations: algorithm and implementation into FDL3DI. Technical report AFRL-VA-WP-TR-1998-3060, Air Force Research Laboratory, Wright-Patterson AFB

Gaitonde DV, Shang JS, Young JL (1999) Practical aspects of higher-order numerical schemes for wave propagation phenomena. Int J Numer Methods in Eng 45:1849–1869

Gordnier RE (2008) High fidelity computational simulation of a membrane wing airfoil. AIAA-2008-0614, January 2008

Gordnier RE, Attar PJ (2009) Implicit LES simulations of a low Reynolds number flexible membrane airfoil. AIAA-2009-0579, January 2009

Lele SK (1992) Compact finite difference schemes with spectral-like resolution. J Comput Phys 103:16–42

Lian Y, Shyy W (2006) Laminar-turbulent transition of a low-Reynolds-number rigid or flexible airfoil. AIAA-2006-3051, June 2006

Mathew J, Lechner R, Foysi H, Sesterhenn J, Friedrich R (2003) An explicit filtering method for LES of compressible flows. Phys Fluids 15(8):2279–2289

McGowan G, Gopalarathnam A, OL M, Edwards J, Fredberg D (2008) Computation vs. experiment for high-frequency low-Reynolds-number airfoil in pitch and plunge. AIAA Paper 2008-0653, 2008

Melville RB, Morton SA, Rizzetta DP (1997) Implementation of a fully-implicit, aeroelastic Navier–Stokes solver. AIAA 97-2039, June 1997

Mueller TJ (1985) Low Reynolds number vehicles. AGARDograph No. 288

Ol MV, McAuliffe BR, Hanff ES, Scholz U, Khler C (2005) Comparison of laminar separation bubble measurements on a low Reynolds number airfoil in three facilities. AIAA Paper 2005-5149, 2005

Radespiel R, Windte J, Scholz U (2006) Numerical and experimental flow analysis of moving airfoils with laminar separation bubbles. AIAA Paper 2006-501, 2006

Rojratsirikul P, Wang Z, Gursul I (2008) Unsteady aerodynamics of membrane airfoils. AIAA-2008-0613, January 2008

Shyy W (2008) Aerodynamics of low Reynolds number flyers. Cambridge University Press, New York

Shyy W, Smith R (1997) A study of flexible airfoil aerodynamics with application to micro aerial vehicles. AIAA-1997-1933, June 1997

Smith R, Shyy W (1995) Computation of unsteady laminar flow over a flexible two-dimensional membrane wing. Phys Fluids 7(9):2175–2184

Song AJ, Breuer KS (2007) Dynamics of a compliant membrane as related to mammalian flight. AIAA-2007-0665, January 2007

Steger JL (1978) Implicit finite-difference simulation of flow about arbitrary two-dimensional geometries. AIAA J 16(7):679–686

Stolz S, Adams N (1999) An approximate deconvolution procedure for large-eddy simulation. Phys Fluids 11(7):1699–1701

Vinokur M (1974) Conservation equations of gasdynamics in curvilinear coordinate systems. J Comput Phys 14:105–125

Visbal M (2009) High-fidelity simulation of transitional flows past a plunging airfoil. AIAA Paper 2009-391, 2009

Visbal MR, Gaitonde DV (1999) High-order accurate methods for complex unsteady subsonic flows. AIAA J 37(10):1231–1239

Visbal MR, Gaitonde DV (2002) On the use of high-order finite-difference schemes on curvilinear and deforming meshes. J Comput Phys 181:155–185

Visbal MR, Rizzetta DP (2002) Large-eddy simulation on curvilinear grids using compact differencing and filtering schemes. J Fluids Eng 124:836–847

Visbal MR, Morgan PE, Rizzetta DP (2003) An Implicit LES approach based on high-order compact differencing and filtering schemes. AIAA Paper 2003-4098, June 2003

Waszak MR, Jenkins LN, Ifju P (2001) Stability and control properties of an aeroelastic fixed wing micro aerial vehicle. AIAA-2001-4005, August 2001

Yuan W, Khalid M, Windte J, Scholz U, Radespiel R (2005) An investigation of low-Reynolds-number flows past airfoils. AIAA Paper 2005-4607, 2005

High-speed stereo DPIV measurement of wakes of two bat species flying freely in a wind tunnel

Anders Hedenström · F. T. Muijres · R. von Busse · L. C. Johansson · Y. Winter · G. R. Spedding

Abstract Previous studies on wake flow visualization of live animals using DPIV have typically used low repetition rate lasers and 2D imaging. Repetition rates of around 10 Hz allow ~ 1 image per wingbeat in small birds and bats, and even fewer in insects. To accumulate data representing an entire wingbeat therefore requires the stitching-together of images captured from different wingbeats, and at different locations along the wing span for 3D-construction of wake topologies. A 200 Hz stereo DPIV system has recently been installed in the Lund University wind tunnel facility and the high-frame rate can be used to calculate all three velocity components in a cube, whose third dimension is constructed using the Taylor hypothesis. We studied two bat species differing in body size, *Glossophaga soricina* and *Leptonycteris curasoa.* Both species shed a tip vortex during the downstroke that was present well into the upstroke, and a vortex of opposite sign to the tip vortex was shed from the wing root. At the transition between upstroke/downstroke, a vortex loop was shed from each wing, inducing an upwash. Vorticity iso-surfaces confirmed the overall wake topology derived in a previous study. The measured dimensionless circulation, Γ/Uc, which is proportional to a wing section lift coefficient, suggests that unsteady phenomena play a role in the aerodynamics of both species.

A. Hedenström (✉) · F. T. Muijres · L. C. Johansson
Department of Theoretical Ecology, Lund University,
Ecology Building, 223 62 Lund, Sweden
e-mail: Anders.Hedenstrom@teorekol.lu.se

R. von Busse · Y. Winter
Department of Biology, Bielefeld University,
33501 Bielefeld, Germany

G. R. Spedding
Department of Aerospace and Mechanical Engineering,
University of Southern California, Los Angeles,
CA 90089-1191, USA

Present Address:
G. R. Spedding
Department of Mechanical and Aeronautical Engineering,
University of Pretoria, Pretoria 0002, South Africa

1 Introduction

Flapping flight in vertebrates has resisted simple analysis, because of the time-varying shape of elastic actuators and their complex interaction with the surrounding fluid. Early models therefore discarded these facts altogether by representing the animal, bird or bat, by mass and wing span alone (Pennycuick 1968, 1975; Norberg 1990). Even though this approach allows predictions for cruising flight performance (Pennycuick 1989; Hedenström 2002), it does not capture any details of the kinematics and associated time-varying force production and cannot be used to predict performance during maneuvering or hovering flight. On the other hand, the early vortex wake theory of bird flight was based upon a minimum of kinematic details, even if the assumptions about the wake geometry itself were more realistic than the actuator disk and momentum jet models (Rayner 1979a, b). Experiments originally focused upon kinematic analyses of wing motions (Brown 1948; Norberg 1976; Aldridge 1986). Eventually, with improved experimental techniques for quantitative wake flow visualization (Spedding et al. 1984; Spedding 1987a, b), the conceptual image of the wake structure began to improve (if not always simplify), now that it was based on actual evidence. Digital particle image velocimetry (DPIV) techniques have been applied to freely flying birds in wind

G.K. Taylor, M.S. Triantafyllou, and C. Tropea (Eds.): Animal Locomotion, pp. 361–370.
springerlink.com

tunnels (Spedding et al. 2003a, b; Warrick et al. 2005; Hedenström and Spedding 2008) to yield more refined models of the wake geometry and its variation with forward flight speed, wing geometry and kinematics. The same techniques have also been applied to the small Glossophagine bats, and reveal some notable differences in wake geometry compared with birds (Hedenström et al. 2007).

To date, quantitative wake data of flying vertebrates have come from rather low repetition rates lasers (5–10 Hz), and the three-dimensional wake structure over one wingbeat cycle is assembled from large numbers of separate images, obtained from large numbers of separate wingbeats. Previous studies have also derived primarily from stacks (in space or time) of 2D data, with two out of three velocity components available in any one plane. Nevertheless, the use of DPIV methods has considerably strengthened our understanding of wake topology and aerodynamics of vertebrate flapping flight in recent years (e.g. Hedenström and Spedding 2008), and continued rapid technological advances are likely to propel the scientific progress further still (see Spedding and Hedenström 2009, this issue). Here we report on the first high-speed stereo-3D DPIV measurements, and thus 3D velocity profiles, of bat flight in the Lund University wind tunnel using two species of Glossophagine bats. The main objective was to investigate whether the wake topology derived from high-speed wake sampling conforms to previous conclusions derived from low-speed sampling (Hedenström et al. 2007). A second objective was to compare the scaling of wake properties from two species of bats with different body weight, aspect ratio and wing loading.

2 Materials and methods

2.1 Experimental animals

Two species of nectarivorous bats, *Glossophaga soricina* and *Leptonycteris curasoae*, were trained to fly in front of a thin metal tube (feeder) providing honey water in the test section of a low-turbulence wind tunnel. For these experiments, two individuals each of *G. soricina* and *L. curasoae* were used. The morphology of the four bats is summarised in Table 1. Wing span and wing area were measured from top-view images obtained at flight speeds 5–6 m/s captured, when the wings are positioned horizontally during the downstroke. At this flight speed, the body angle is near horizontal. Wing span and wing area were measured using ImageJ (http://rsb.info.nih.gov/ij/) with the length of the radius as reference length (Table 1). Body mass was measured with an electronic balance before and after each experimental session, and the mean values are shown in Table 1.

Since bats are nocturnal and mainly active in the dark, they were clock-shifted by 12 h, so their active feeding period coincided with researchers' working schedule. Before experiments, the bats were released into the wind tunnel, where they roosted on a net inside the settling chamber 6 m upstream from the test section. When a bat decided to feed, it would fly with the wind towards the test section, increasing the speed between the settling chamber and the test section through the contraction, and would then make a U-turn inside the test section to approach the feeder from the downstream direction. The requirement of making this U-turn inside the test section area (1.22 × 1.08 m) limits the maximum flight speed range that can be studied to approximately 7–8 m/s.

2.2 Wind tunnel

The Lund University wind tunnel is a closed-loop, low-speed, low-turbulence wind tunnel crafted for studies of animal flight. The overall design and baseline characteristics are described in Pennycuick et al. (1997). The background turbulence is about 0.03% (Spedding et al. 2009), which makes this tunnel suitable for repeatable quantitative measurements at the moderate values of wing chord-based Reynolds number that are characteristic of small birds and bats (see below). All airspeeds (U) refer to the equivalent airspeed defined as

$$U_{\mathrm{eq}} = \sqrt{2q/\rho_0},$$

Table 1 Morphological properties of the four bats used in this study, body mass (m), wing span (b), wing area (S), mean wing chord (c), aspect ratio (AR = b^2/S), wing loading ($Q = mg/S$), and f is wing beat frequency

Bat	m (kg)	Femur length (mm)[a]	Wing length (m)	b (m)	S (m^2)	c (m)	AR	Q (N)	f (Hz)
Glossophaga soricina, male (#1)	0.0101	34.6	0.101	0.233	0.00879	0.038	6.2	11.3	14.9
Glossophaga soricina, female (#5)	0.0095	34.9	0.097	0.230	0.00860	0.037	6.2	10.9	14.9
Leptonycteris curasoae, male (#97)	0.0216	50.3	0.149	0.335	0.01576	0.047	7.1	13.4	10.4
Leptonycteris curasoae, female (#18)	0.0236	51.0	0.144	0.323	0.01529	0.047	6.8	15.1	9.9

[a] Used as reference length on images for estimating wing length, wing span and wing area

where ρ_0 is the assumed air density at sea level in the International Standard Atmosphere (1.225 kg/m^3) and q ($=\rho U^2/2$) is the dynamic pressure at the measured air density during an experiment. During this study, ρ varied between 1.16 and 1.20 kg/m^3, and the temperature was 19–24°C. The bats were studied at forward flight speeds 1–7 m/s, but the main results in this paper are based on observations at 4 m/s. The Reynolds number based on airspeed ($Re = Uc/v$, where c is the mean chord length of the wing and v is the kinematic viscosity) ranged from $Re = 0.26–1.81 \times 10^4$ in *G. soricina* to $Re = 0.32–2.27 \times 10^4$ in *L. curasoae*. At $U = 4$ m/s, the speed for which we present most of the data in this paper, $Re = 1.03 \times 10^4$ and 1.30×10^4, respectively. This difference in Re is aerodynamically not significant. The bats are small in comparison with the test section [wing span (b)/tunnel diameter (B): $b/B < 0.28$) and so interactions with the side walls are ignored.

2.3 Stereo DPIV

The flow field was measured over an approximately 20×20 cm^2 area using two CMOS-cameras (HiSpeedStar3; 1,024 × 1,024 pixels) and frame grabber PCI boards in the host computer. The cameras were equipped with 60 mm lenses (Micro Nikkor, f2.8) on Scheimpflug mounts. Two alignments of the light sheet were used: (1) the vertical [xz] plane is aligned with the free-stream, with the cameras mounted on opposite sides outside the test section (Fig. 1a), and (2) the [yz] plane is normal to U, and the cameras are mounted in the open part of the test section (Fig. 1b), viewing obliquely from above and behind onto

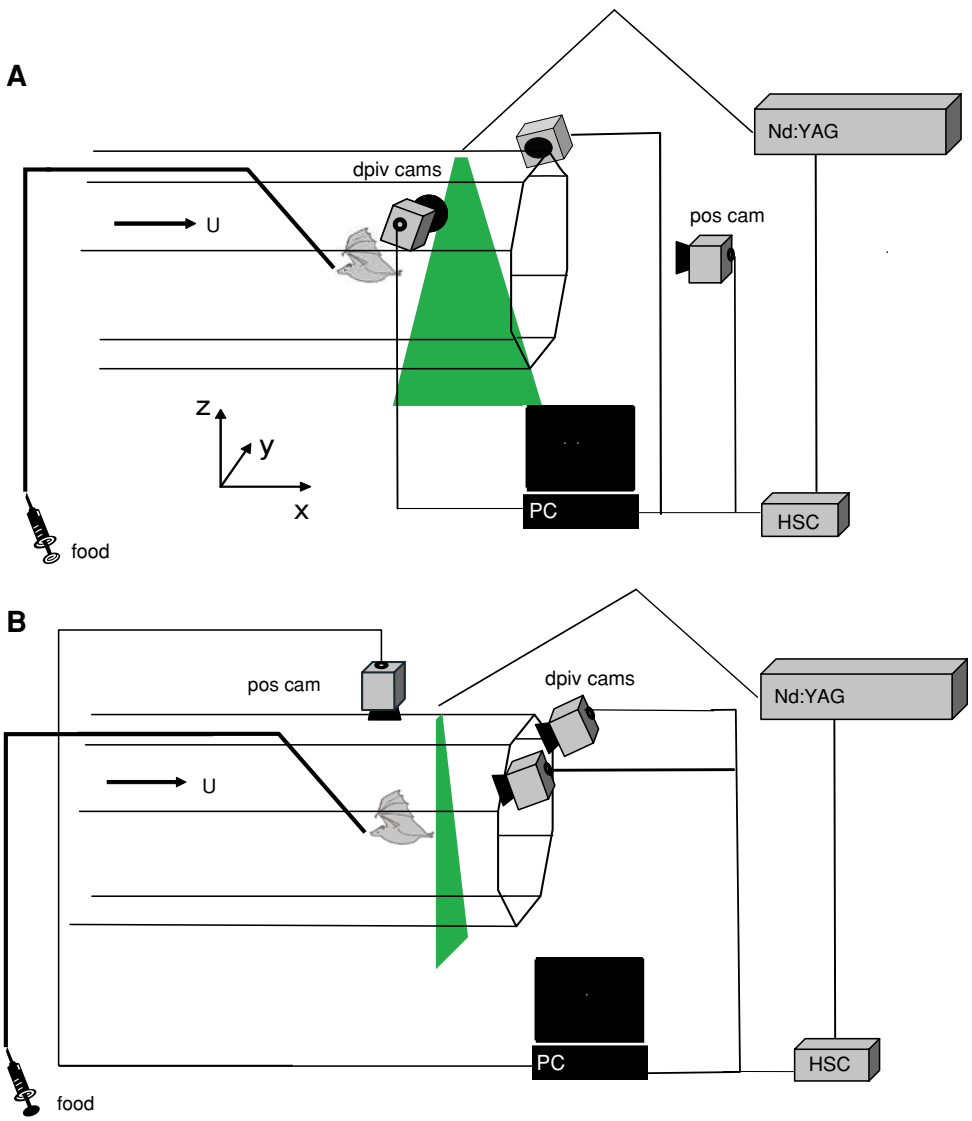

Fig. 1 Experimental set-up for visualizing wakes of bats flying in the Lund University wind tunnel. The pulsed laser (Nd:YAG) generates a light sheet in the wind tunnel test section. Image pairs of densely-distributed fog particles, illuminated by the light sheet, are captured by the two CMOS cameras (DPIV cam) and stored on the host PC. The light sheet is positioned by the use of an optical arm and either aligned parallel to U (**a**) or perpendicular to U (**b**). The position camera monitors the flight behaviour and position of the bat with respect to the light sheet. The triggering of image acquisition and laser pulses is synchronized by a high speed controller box (HSC). Honey water is provided through a syringe and thin plastic tubing to a metal tube of 3 mm diameter

the light sheet. The feeder was about 20 cm upstream of the center of the light sheet, and the distance from the wing tip to the imaging plane varied between 16 and 18 cm, which is 3.4–4.7c, or 0.5–0.8b. At $U = 4$ m/s, the vortex travel time from the wing tip to the imaging plane was about 0.04 s, which is 0.4–0.6T_w, where T_w is the time for one wingbeat cycle. The whole tunnel was filled with a thin fog (particle size 1 μm), which was illuminated in slices by a pulsed 50 mJ Laser (Litron LPY732 series, Nd:YAG, 532 nm) at 200 Hz repetition rate. The PIV cameras have band pass filters (530 ± 5 nm) to minimize stray light from other sources. An independent camera monitored the position and flight behaviour of the bat in relation to the light sheet. This position-monitor camera was positioned on the top of the test section in the transverse light sheet configuration (Fig. 1b), and in the first diffuser downstream from the test section in the streamwise light sheet configuration (Fig. 1a). For both transverse [yz] and streamwise [xz] data, the left wing and body were imaged.

2.4 DPIV analysis

2.4.1 The DPIV system and calibration

The DPIV data are captured and analyzed using the DaVis software package from LaVision (Davis 7.2.2.110). It is calibrated using a calibration plate (20 × 20 cm^2, type 22), in combination with the DaVis Stereo PIV self-calibration algorithms to compensate for misalignments between the laser sheet and the calibration plate. Background flow DPIV measurements were performed for monitoring the pixel displacement magnitudes and possible peak-locking errors, and the time difference between the laser pulses was adjusted to optimise the available velocity bandwidth. The background flow was also used to determine the flight speed at low wind tunnel speed settings ($U \leq 2$ m/s), since at these low speeds, the conventional wind tunnel monitor system (using the static pressure difference before and after the contraction immediately upstream from the test section) is inaccurate. At low speeds, the spatial variation (RMS within the 20 × 20 cm^2 measurement area) was less than 2.5% of the mean velocity ($n = 6$). The temporal velocity variations are on average of 2.25% of the mean velocity ($n = 3$), with a maximum time difference between the measurements of 1 h.

2.4.2 Data acquisition

The bat flight data were captured by manual triggering. When a bat was flying steadily in front of the feeder, the laser shutter was opened and a sequence of 50 frames was captured by the DPIV cameras. Simultaneously (using a synchronization signal), a 1 s video sequence of the flying bat and laser pulses was recorded using a 250 Hz frame-rate digital video camera (Fig. 1). If the bat continues to fly behind the feeder, the triggering routine can be repeated. This procedure typically generates DPIV data for up to two (*L. curasoae*) and three (*G. soricina*) consecutive wingbeats per trigger event.

2.4.3 Analysis

The DPIV data were analyzed using the DaVis software. The images were pre-processed to reduce systematic errors due to background noise, for example, when a bat is visible in the background. A multi-pass stereo cross-correlation was used (64 × 64 and 32 × 32, 50% overlap), and the results were post processed using a correlation peak ratio deletion scheme (peak ratio < 1.01), a median vector field filter, and a false vector rejection criterion of vector magnitudes, $|v| > 1.5$ times the neighbourhood RMS, and recalculation for $|v| > 2$ times the local RMS, and a single 3 × 3 smoothing average.

The computed $\{u, v, w\}$ velocity components in x- (streamwise), y- (spanwise) and z- (vertical) directions were used to calculate the vorticity components, $\{\omega_x, \omega_y, \omega_z\}$ normal to the planes [yz, zx, xy], respectively. For example, the streamwise vorticity, $\omega_x = \partial w/\partial y - \partial v/\partial z$, is determined by the $\{v, w\}$ velocity gradients in the [yz] plane. The circulation of identified vortex structures was also measured in selected planes using procedures described in Spedding et al. (2003b).

The DPIV data were compiled into a 3D spatial matrix (x, y, z), by concatenating the results from consecutive DPIV frames, and converting the time difference between the frame pairs into a streamwise displacement ($\Delta x = U\Delta t$). When doing this, one assumes that wake displacements are dominated by mean flow convection, and that no strong vortex wake evolution/kinematics occurs at and after the measurement point.

Although the data are assembled into a single 3D cube, the original data acquisition planes (where the in-plane velocity estimation errors are smaller than the out-of-plane components) have some particular interest in the analysis. The streamwise [xz] planes are parallel to U, and to g. The drag is defined as the aerodynamic force component parallel to U, and the lift is defined as normal to U, which is parallel to g here. The u and w disturbance velocities are therefore the leading contributors to estimates of D and L. Invoking quite reasonable assumptions for far-field flows shows that they are the only components of significance (see Spedding and Hedenström 2009, this volume). These points were noted in the original bird flight DPIV studies (Spedding et al. 2003b) and the [xz] plane data can be compared directly with them.

The [yz] plane, normal to U, is where the v and w components of velocity can be most accurately estimated

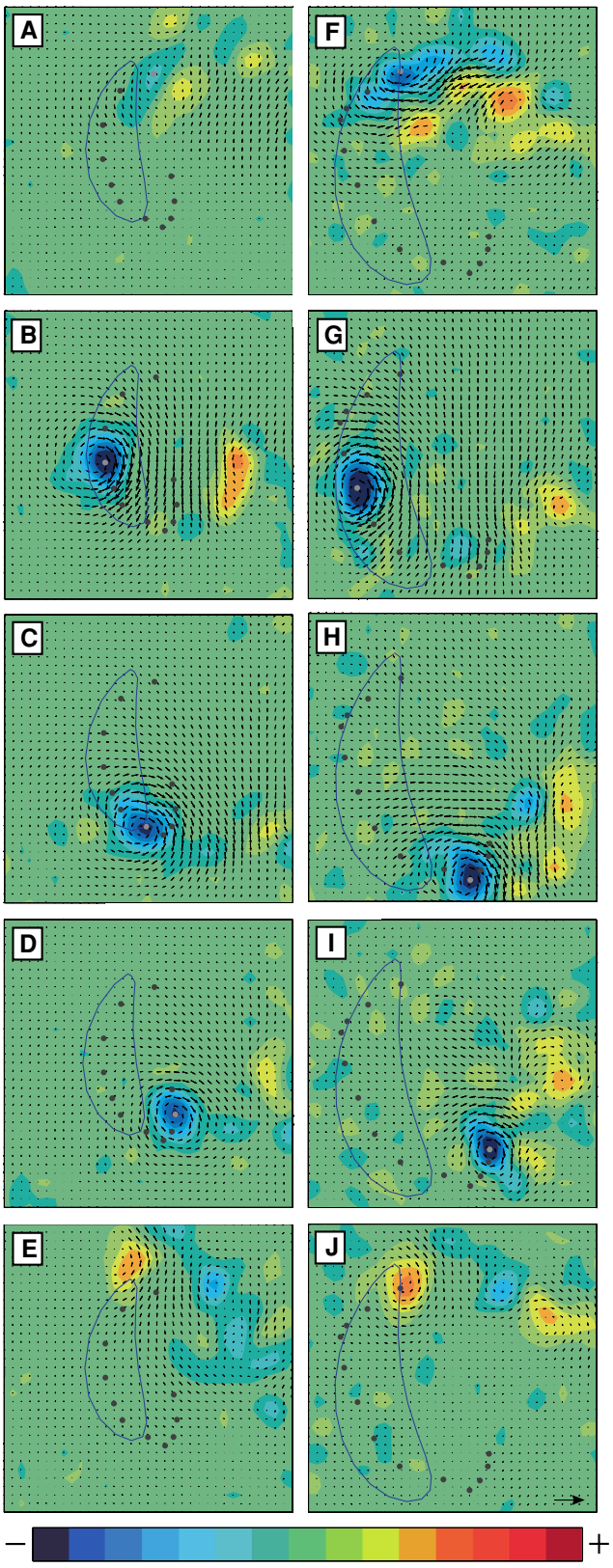

Fig. 2 Colour-coded vorticity fields and velocity vector fields from two bats flying in a wind tunnel. The images show the [*yz*] plane of the left wing and body for one *Glossophaga soricina* (**a**–**e**) and one *Leptonycteris curasoae* (**f**–**j**), both flying at $U = 4$ m/s. The individual bats are the males (#1 and #97) of Table 1. The distance from the bat to the [yz] imaging plane varied between 3.4 and 4.7 chord lengths. The *panels* represent sub-periods of a wing stroke as follows (*top–bottom*): beginning of downstroke, mid downstroke, end of downstroke, mid upstroke and end of upstroke. The colour scale symmetrically maps the streamwise vorticity, ω_x, (s^{-1}) from −280 (*blue*) to +280 (*red*) in steps of 40 s^{-1}. The {*v*,*w*}-component velocity vectors are scaled to the reference at 5 m/s at *bottom right*. The *closed curves* show the path of the wing tip for an average wingbeat and the *dots* show the centers of the wing tip vortices with the *grey dot* showing the current frame. The *panels* represent a real area of 17.5 × 17.5 cm

together. When this plane is far from the disturbance source, then the only significant disturbance velocities will be the *v* and *w* components in the wake itself (*u* will be much smaller), and inviscid theory can be used to estimate the induced drag of a wake oriented parallel to *U* and passing through this plane. This plane is called the Trefftz plane in aeronautics. If all the three components of velocity are available in this plane, then both the lift and drag can be computed, using only this information. It is tempting to invoke all [*yz*] planes as Trefftz planes, but they must be large, far from the body and the wake must be normal to them for the original analysis to hold.

3 Results

3.1 Wake structure and implications for aerodynamic force generation on the wing

Figure 2 shows a time sequence of [*yz*] planes at $x/c \approx 5$ (from set-up in Fig. 1b), behind the body and left wing through one complete wing stroke at $U = 4$ m/s, for one individual each of *G. soricina* and *L. curasoae* (hereafter *G. s.* and *L. c.*). The path of the wingtip is shown by a continuous line and the centers of the tip vortices are shown as black dots with the current centre of the wing tip vortex shown in grey. At the beginning of the downstroke, some weak streamwise vorticity is seen in *G. s.* (Fig. 2a), while in *L. c.*, the tip vortex is already visible (blue patch, Fig. 2f), together with a counter-rotating vortex shed from the wing root (yellow patch, Fig. 2f). By mid downstroke, there are prominent wing tip vortices as well as wing root vortices in both species (Fig. 2b, g). At this stage, there is a clear downwash between the opposite-signed shed vortices, with magnitude (mean ± SD) 1.47 ± 0.63 m/s ($n = 18$) and 1.27 ± 0.47 m/s ($n = 25$) in *G. s.* and *L. c.*, respectively (*n* is the number of vectors between tip- and toot-vortices). The larger sample size in *L. c.* is due to the longer wingspan compared with *G. c.* At mid downstroke, the wing span has its maximum horizontal extent, and the horizontal distance, l_y, between tip and root vortices for

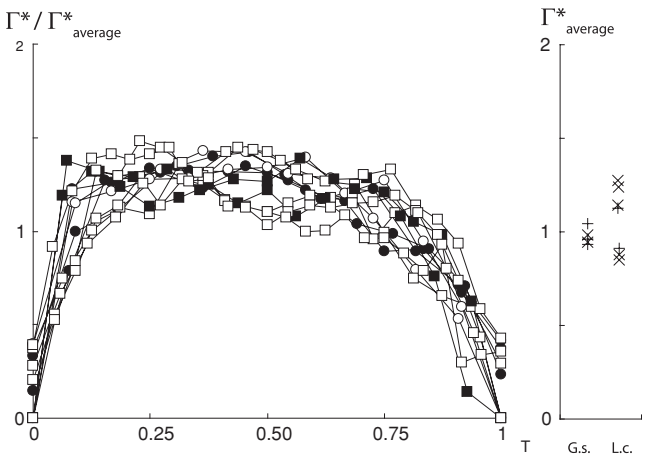

Fig. 3 Normalised circulation, $\Gamma^*_{\text{average}} = \Gamma/Uc$, of the wingtip trailing vortex, realtive to the mean value of the sequence. Mean values for individual wingbeats are given in the *panel* to the *right*. The *symbols* represent *Glossophaga soricina* (*circles*; *open* and *filled symbols* denote different individuals) and *Leptonycteris curasoae* (*squares*) followed over a number of wing strokes. The wingbeat period was 0.067 and 0.099 s for *Glossophaga soricina* and *Leptonycteris curasoae*, respectively

G. s. and *L. c*. is 7.9 and 12.2 cm, respectively. Normalised by the wing semispan, $2l_y/b = 0.69$ and 0.74, respectively.

At the end of the downstroke, the tip vortex has the same circulation magnitude as at mid downstroke, but it is now shed from a position closer to the body midline as the wing tips are moved towards each other below the body (Fig. 2c, h). At the beginning of the upstroke, the wing is being flexed and at mid upstroke, the tip vortex is still present, although it is closer to the body midline than it was at mid downstroke. Notice that there is still an induced downwash about halfway into the upstroke (Fig. 2d, i), indicating that the wing is generating lift also during the upstroke up to this point. Towards the end of the upstroke, the tip vortex vanishes, but instead, there is shedding of a vortex dipole inducing an upwash and hence an associated negative lift (Fig. 2e, j). The root vortex appears weaker during the upstroke in *G. s*. than in *L. c*. (Fig. 2c, d vs. h, i). In most cases, the centre of the tip vortex is inboard of the wing-tip trace, except for about one quarter into the downstroke in *L. c.* (Fig. 2).

The circulation, Γ is a measure of the integrated vorticity magnitude in a region. The normalised circulation of the tip vortices, $\Gamma^* = \Gamma/Uc$, is plotted as a function of T ($T = t/T_{\text{w}}$, where T_{w} is the wing beat period, and t is counted from the beginning of each downstroke) stroke at $U = 4$ m/s in Fig. 3. Γ^* increases rapidly after the beginning of the downstroke ($T < 0.1$), and then varies only little between 1.2–1.8 well into the upstroke ($T \approx 0.75$), after which it drops to almost zero at the end ($T = 1$) of the upstroke. The pattern and magnitude of the circulation variation throughout a wing stroke are very similar between the two species, although one individual *L. c.* (the female) appears to show somewhat larger variation.

3.2 Three-dimensional wake topology

As the wake is sampled at 200 Hz, the $[yz](t)$ image sequence can be used to generate iso-surfaces of constant streamwise vorticity (ω_x) over one wing stroke. $\omega_x(x, y, z)$ was assembled from time sequences of data, such as Fig. 2, using the previously-noted transform rule $\Delta x = U\Delta t$, and ω_x iso-surfaces are shown in Fig 4. The iso-values of ω_x are $\pm$mean $|\omega_x|$ (red positive, blue negative). The bat is flying from left to right and obliquely towards the observer, and the iso-surfaces show the streamwise vorticity that trails the bat wing and body during the course of a little over one wingbeat. The tip vortex shed by the right wing is blue, circulating clockwise when viewed downstream from the bat, and the root vortex is red, rotating in the opposite, anti-clockwise direction. Their counterparts in mirror image behind the left wing are opposite in direction of rotation and colour. The downstroke generates a prominent tip vortex in both *G. s.* and *L. c.* A wing root vortex of opposite sign is also present during the downstroke in both species. At the end of the upstroke, an inverted vortex dipole, whose cross-section was shown in Fig. 2e and j, can be seen in the top right of both Fig. 4a and b. The wingtip trailing vortex gradually loses strength and falls below the visualization threshold towards the end of the upstroke, but we should remember that the visualized component is ω_x (and not $|\omega|$), so although the connecting start and stop vortices, which are primarily ω_y, are not visible, their presence (as required by Helmholtz's conservation laws) is known from the full vorticity vector data, and from plots of ω_y (x, z). Here, however, the vortex loops appear as disconnected vortex strands of ω_x.

3.3 Wake defect maps

Figure 5 shows the normalized streamwise velocity, $(u - U)/U$. Since drag and thrust are associated with deceleration and acceleration of the mean streamwise velocity, U, then a region of $(u - U)/U < 0$ might be interpreted to contribute a net drag and $(u - U)/U > 0$, a net thrust. Then the integrated sum of these regions, taken over a suitable control volume, will be zero for any self-propelled body in steady motion. This is a rather over-simplified picture, especially for such a complex flow, and so close to the wings and body (see Spedding and Hedenström 2009, this volume, for conditions for estimating mean forces from wake velocity distributions), but as a first order approximation, we may assert that maps of $(u - U)/U$ show where the major contributors to thrust and drag are located on the bat, through their imprint in the cross-plane wake. The trailing tip vortex has a velocity defect towards its centre in both species. This

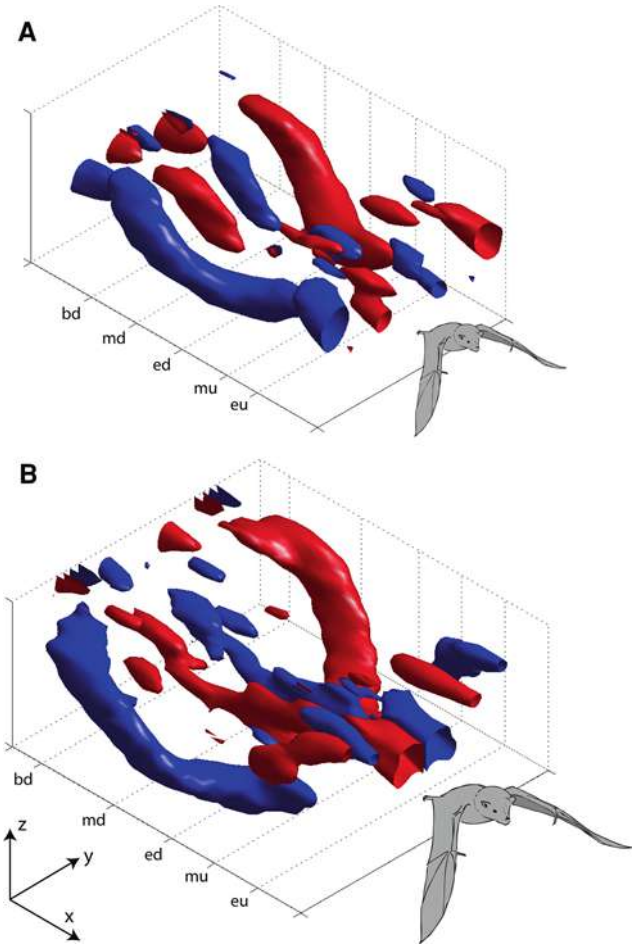

Fig. 4 Iso-surfaces of normalized constant streamwise vorticity ($\omega_x^* = \omega_x/|\varpi_x|$) during just over one wing stroke of (**a**) *Glossophaga soricina* (#1) and (**b**) *Leptonycteris curasoae* (#97). The iso-values are normalized of $\omega_x^* = \pm 1.0$ (*red* is positive; *blue* is negative). The data cubes are oriented, so the bat is flying obliquely to the right and towards the viewer. The larger centrally trailing tubes therefore mark the streamwise vorticity shed at the wing root. Approximate time-marks are: *bd* (beginning of downstroke), *md* (mid downstroke), *ed* (end of downstroke), *mu* (mid upstroke), *eu* (end of upstroke). The *data boxes* are scaled as (x, y, z) = (400, 260, 180) mm in (**a**) and (x, y, z) = (400, 345, 180) mm in (**b**)

is consistent with an axial flow along the vortex core towards the wing, as also noted in the kestrel wake by Spedding (1987b), and based also on 3D velocity fields. The strongest accelerated wake flow appears inboard of the tip vortex, between it and the wing root. At the body, the flow is again decelerated in this cut, at this stage of the wingbeat. Figure 6 shows that this is true for most of the wingbeat, for both bats.

4 Discussion

4.1 Aerodynamically-equivalent flight speeds

This paper describes the wakes of two species of bats flying at the same speed, $U = 4$ m/s, which is in the middle of the

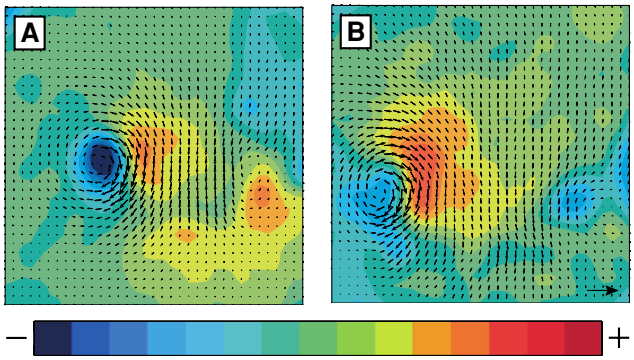

Fig. 5 $(u - U)/U$ at mid downstroke of (**a**) *Glossophaga soricina* (#1)and (**b**) *Leptonycteris curasoae* (#97). The *colour bar* runs from $(u - U)/U = -0.35$ to 0.35 in steps of 0.05 m/s. The $\{v,w\}$-component velocity vectors are scaled to the reference at 5 m/s at *bottom right*. The *panels* represent a real area of 17.5 × 17.5 cm

speed range of small bats (Lindhe Norberg and Winter 2006). In a comprehensive study of insect flight, Ellington (1984) used the advance ratio $J = U/2\Phi fR$, where Φ is stroke angle (in radians), f is wingbeat frequency and R is wing length, to describe the force asymmetry between downstroke and upstroke and defined hovering as including slow forward speed with $J < 0.1$. Here $J = 1.08$ for both for *G. s.* and *L. c.* The related Strouhal number, $St = fA/U$, where A is the vertical peak-to-peak amplitude of the wingtip, evaluates to 0.47 and 0.43 for *G. s.* and *L. c.*, respectively. The similar values of both J and St show that the flight speeds are aerodynamically-equivalent for the two bat species, even though they are of different size.

St measures the mean wingtip speed relative to the forward speed (it is one half of this ratio; Spedding et al. 2008) and so at $U = 4$ m/s, the tip and forward speeds have a similar magnitude. Since the wingtip speed fluctuates considerably during each wingbeat cycle, then we may expect time-varying aerodynamic force components to be non-negligible, simply based on such values of St.

4.2 The loading and unloading wing cycle

The circulation of the wingtip trailing vortex varies smoothly through the downstroke/upstroke transition and continues to be measurable, with the same sign, until close to the end of the upstroke. At the same time, a downwash induced between the wingtip and wing root sections supports the notion that the upstroke is aerodynamically active for about half its duration, at which point, the circulation falls to zero and the wing is aerodynamically unloaded. This cycle of wing loading and unloading through the wingbeat is quite consistent with previous interpretations (Hedenström et al. 2007) based on multiple 2D DPIV planes. The agreement of the 3D data with multiple 2D slices from hundreds of different wingbeats is gratifying.

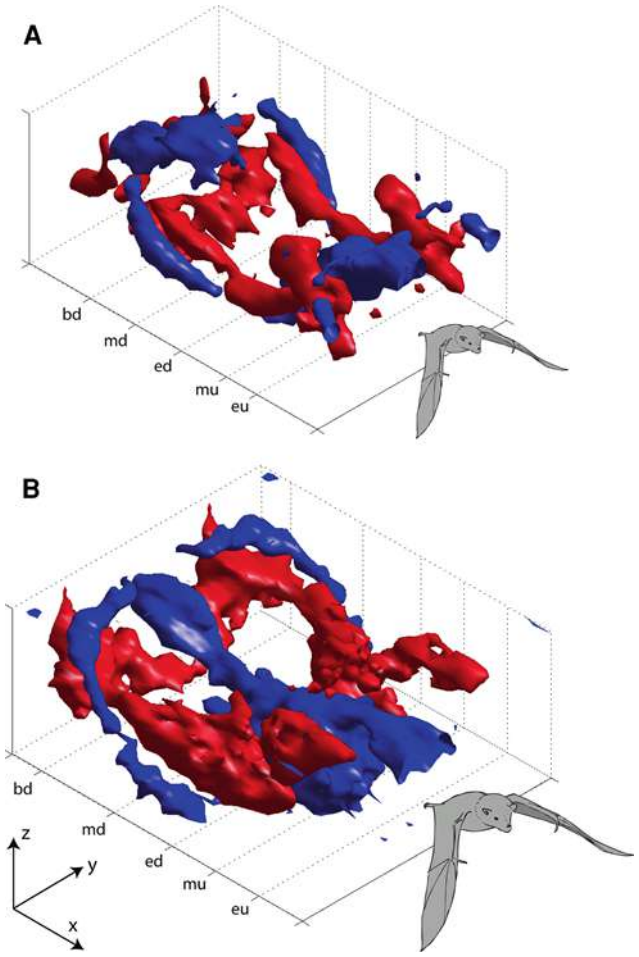

Fig. 6 $(u - U)/U$ (x, y, z) for one wing beat of (**a**) *Glossophaga soricina* (#1) and (**b**) *Leptonycteris curasoae* (#97). Orientation and time-marks as in Fig. 4.The threshold values used were $(u - U)/U = \pm 0.25$ in (**a**) and ± 0.3 in (**b**). The *data boxes* are scaled as $(x, y, z) = (400, 260, 180)$ mm in (**a**) and $(x, y, z) = (400, 345, 180)$ in (**b**)

4.3 Pseudo-3D data

It is not only the wing loading/unloading cycle that can be confirmed in the 3D data, but also the observations of wing root vortices and of the shedding of inverted vortex loops at the end of the upstroke. These phenomena were newly observed in bats and make their wake signatures qualitatively different from those of birds (Hedenström et al. 2007). The 3D reconstructions in Figs. 4 and 6 are reasonable if the transformation $\Delta x = U\Delta t$ is reasonable. The wake evolves in both space and time, and one can only substitute one for the other provided the intervals are short compared with spatial or temporal evolution time-scales. This is often known as the 'frozen-flow' hypothesis: would the wake really be frozen in place as it convects through the measurement volume? The streamwise extent of the reconstructed wake, $X_w = UT_w$, where T_w is the wingbeat period, and here $X_w/c = 7.2$ for *G. s.* and 8.3 for *L. c.*

A comparison of near and far wakes in *G. s.* at $x = 3.2c$ and $19c$ (Johansson et al. 2008) shows that the qualitative and quantitative wake properties vary rather little with x and so the frozen flow assumption is tenable.

4.4 Drag, thrust and power

The power required to move at steady speed U is just DU, where D is the total drag that must be overcome to move through the surrounding fluid. In steady, unaccelerated flight, the total drag is balanced by the total thrust and the net horizontal momentum flux in the wake is zero. Although the wake is often touted as the footprint of the flying animal, which must contain a record of all the forces experienced by the wings and body, the causes and traces of drag and thrust are not necessarily separable. There are two major contributors to drag in a three-dimensional lifting system—the induced drag due to the downwash induced by the trailing vortices, and the viscous drag due to friction and pressure drag on all exposed surfaces. The induced drag is an inviscid component, and will be non-zero on all parts of the flyer that generate lift (and hence shed trailing vortices). The largest part of that, by far, can be expected to be from the wings, but especially in light of the complex root vortex shedding, it will be interesting to see how and when body lift makes a contribution to the induced drag.

The viscous drag is not predicted by any tractable theory, so it is always estimated from empirical performance curves, usually from polar plots of lift coefficient versus drag coefficient. There is a very significant uncertainty in its estimation, especially for complex systems like flapping bat wings. Given this practical problem, it is tempting to look to the wake structure for alternative measures of drag. Thus far, animal wake analyses have assumed that the total drag of the flying animal is balanced by a thrust that can be calculated from the geometry of the vortex wake (e.g. Spedding et al. 2003b; Hedenström et al. 2006; Henningsson et al. 2008). Thus the wake geometry, which is essentially an inviscid construct of line vortices in a potential flow, can be estimated to give a certain net forward impulse. This is then assumed to balance a viscous drag over one wingbeat, whose signature has not been explicitly measured, but which is assumed to trail behind the wings and body without disrupting the primary trailing vortex system.

It may be reasonable to further localize these forces. The wake directly downstream of the body presumably contains the drag signature of the body, and the measurement of a three-dimensional, mean streamwise velocity defect could be used to estimate the body drag. It is tempting therefore to look to data such as Fig. 6, which contains the velocity defect map for one wingbeat, for a complete solution to the

drag estimation problem. Indeed, blue and red blobs of momentum excess or deficit seem to be located in separate regions, and so while their sum must be zero, the different parts might be countable. It seems plausible that most thrust comes from the outer part of the wing, and that most drag comes from the body, as deduced from Fig. 6. However, it is far from clear that the pressure fluctuations can be ignored at $x = 3$–$5c$ in this highly unsteady wake, and it is also not clear whether appropriate far-field boundary conditions can be assumed. Furthermore, there is a uniqueness problem when the propulsor is a source of both thrust and drag, because there are an infinite number of combinations of negative and positive momentum flux that could have given rise to any given positive or negative net result. Teasing out these force components will be a significant challenge, but at least the data that one requires (such as Figs. 4, 6) are now becoming available.

4.5 Unsteady aerodynamics

Based on values of the Strouhal number alone ($St \approx 0.4$–0.5), we expect that unsteady aerodynamic forces are likely to be non-negligible. Wake measurements here show that $\Gamma/Uc \approx 1$ for both bat species and if this is interpreted as one half of a local lift coefficient (Rosén et al. 2007), then the wings apparently have time-averaged $C_L \approx 2$. A local wing section sees the vector sum of U and its local flapping speed, and not just U, and if the tip speed and mean speed have the same magnitude, then the corrected speed will be $\sqrt{2}U$ and the implied average C_L becomes 1.4. This is close to the upper limit that could be expected from moderate aspect ratio wings at this Re (Laitone 1997; Lyon et al. 1997; Spedding et al. 2008). *G. s.* has been shown to develop a significant fraction of its lift in near hovering flight from an unsteady leading-edge vortex (LEV) that appears and is stable due to wing accelerations (Muijres et al. 2008). It is possible that some form of LEV persists into higher speed conditions for *G. s.*, and since it appears to be flying in a very similar regime, the same extrapolation is as likely to hold for *L. c.* also.

5 Conclusion

The higher temporal resolution and availability of the third velocity component allows wake reconstructions for flying animals of greater detail and reliability than before. Nevertheless, it is notable how the new wake data are very consistent with previous reconstructions based on the painstaking assembly of multiple, separately-acquired data planes. We look forward to make new flight models based on these more comprehensive data, and to explore the challenges in estimating force coefficients from the 3D, unsteady wake.

Acknowledgments The manuscript benefited from the comments by two anonymous referees. The 3D high-speed PIV system was acquired through a generous grant from the Knut and Alice Wallenberg foundation. The research was funded by the Swedish Research Council to A.H.

References

Aldridge HDJN (1986) Kinematics and aerodynamics of the greater horseshoe bat, *Rhinolophus ferrumequinum*, in horizontal flight at various flight speeds. J Exp Biol 126:479–497

Brown RHJ (1948) The flight of birds. The flapping cycle of the pigeon. J Exp Biol 25:322–333

Ellington CP (1984) The aerodynamics of hovering insect flight. III. Kinematics. Phil Trans R Soc B 305:41–78

Hedenström A (2002) Aerodynamics, evolution and ecology of bird flight. Trends. Ecol Evol 17:415–422

Hedenström A, Spedding GR (2008) Beyond robins: aerodynamic analyses of animal flight. J R Soc Interface 5:595–601

Hedenström A, Rosén M, Spedding GR (2006) Vortex wakes generated by robins *Erithacus rubecula* during free flight in a wind tunnel. J R Soc Interface 3:263–276

Hedenström A, Johansson LC, Wolf M, von Busse R, Winter Y, Spedding GR (2007) Bat flight generates complex aerodynamic tracks. Science 316:894–897

Henningsson P, Spedding GR, Hedenström A (2008) Vortex wake and flight kinematics of a swift in cruising flight in a wind tunnel. J Exp Biol 211:717–730

Johansson LC, Wolf M, von Busse R, Winter Y, Spedding GR, Hedenström A (2008) The near and far wake of Pallas' long tongued bat (*Glossophaga soricina*). J Exp Biol 211:2909–2918

Laitone EV (1997) Wind tunnel tests of wings at Reynolds numbers below 70 000. Exp Fluids 23:405–409

Lindhe Norberg UM, Winter Y (2006) Wing beat kinematics of a nectar-feeding bat, *Glossophaga soricina*, flying at different flight speeds and Strouhal numbers. J Exp Biol 209:3887–3897

Lyon CA, Broeren AP, Giguere P, Gopalarathnam A, Selig MS (1997) Summary of low-speed airfoil data, vol 3. Soartech, Virginia Beach

Muijres FT, Johansson LC, Barfield R, Wolf M, Spedding GR, Hedenström A (2008) Leading-edge vortex improves lift in slow-flying bats. Science 319:1250–1253

Norberg UM (1976) Aerodynamics, kinematics, and energetics of horizontal flapping flight in the long-eared bat *Plecotus auritus*. J Exp Biol 65:179–212

Norberg UM (1990) Vertebrate flight. Springer, Berlin

Pennycuick CJ (1968) Power requirements for horizontal flight in the pigeon *Columba livia*. J Exp Biol 49:527–555

Pennycuick CJ (1975) Mechanics of flight. In: Farner DS, King JR, Parkes KC (eds) Avian Biology, vol 5. Academic Press, New York, pp 1–75

Pennycuick CJ (1989) Bird flight performance: a practical calculation manual. Oxford University Press, Oxford

Pennycuick CJ, Alerstam T, Hedenström A (1997) A new low-turbulence wind tunnel for bird flight experiments at Lund University, Sweden. J Exp Biol 200:1441–1449

Rayner JMV (1979a) A vortex theory of animal flight. Part 2. The forward flight of birds. J Fluid Mech 91:731–763

Rayner JMV (1979b) A new approach to animal flight mechanics. J Exp Biol 80:17–54

Rosén M, Spedding GR, Hedenström A (2007) Wake structure and wingbeat kinematics of a house-martin *Delichon urbica*. J R Soc Interface 4:659–668

Spedding GR (1987a) The wake of a kestrel (*Falco tinnunculus*) in gliding flight. J Exp Biol 127:45–57

Spedding GR (1987b) The wake of a kestrel (*Falco tinnunculus*) in flapping flight. J Exp Biol 127:59–78

Spedding GR, Hedenström A (2009) PIV-based investigations of animal flight. Exp Fluids. doi:10.1007/s00348-008-0597-y

Spedding GR, Rayner JMV, Pennycuick CJ (1984) Momentum and energy in the wake of the a pigeon (*Columba livia*) in slow flight. J Exp Biol 111:81–102

Spedding GR, Hedenström A, Rosén M (2003a) Quantitative studies of the wakes of freely flying birds in a low turbulence wind tunnel. Exp Fluids 34:291–303

Spedding GR, Rosén M, Hedenström A (2003b) A family of vortex wakes generated by a thrush nightingale in free flight in a wind tunnel over its entire natural range of flight speeds. J Exp Biol 206:2313–2344

Spedding GR, Hedenström A, McArthur J, Rosén M (2008) The implications of low-speed fixed-wing aerofoil measurements on the analysis and performance of flapping bird wings. J Exp Biol 211:215–223

Spedding GR, Hedenström A, Johansson C (2009) A note on wind-tunnel turbulence measurements with DPIV. Exp Fluids 46:527–537. doi:10.1007/s00348-008-0578-1

Warrick DR, Tobalske BW, Powers DP (2005) Aerodynamics of the hovering hummingbird. Nature 435:1094–1097

Time-resolved wake structure and kinematics of bat flight

Tatjana Y. Hubel · Nickolay I. Hristov · Sharon M. Swartz · Kenneth S. Breuer

Received: 20 June 2008 / Revised: 12 December 2008 / Accepted: 23 January 2009 / Published online: 22 February 2009

Abstract We present synchronized time-resolved measurements of the wing kinematics and wake velocities for a medium sized bat, *Cynopterus brachyotis*, flying at low-medium speed in a closed-return wind tunnel. Measurements of the motion of the body and wing joints, as well as the resultant wake velocities in the Trefftz plane are recorded at 200 Hz (approximately 28–31 measurements per wing beat). Circulation profiles are found to be quite repeatable although variations in the flight profile are visible in the wake vortex structures. The circulation has almost constant strength over the middle half of the wing beat (defined according the vertical motion of the wrist, beginning with the downstroke). A strong streamwise vortex is observed to be shed from the wingtip, growing in strength during the downstroke, and persisting during much of the upstroke. At relatively low flight speeds (4.3 m/s), a closed vortex structure behind the bat is postulated.

1 Introduction

Humans have long been fascinated with the movement of animals through the air, and observations of nature's fliers' seemingly effortless defiance of gravity first inspired our dreams of taking to the air. In the centuries it took to achieve this goal, animal flight has not only aroused passion, but also served the more utilitarian function of inspiring design innovations, particularly during the earliest stages of aeronautic history. For example, observations of the wings of flying storks provided the first insight into the role of camber in the functional architecture of airfoils (Lilienthal 1889). Nonetheless, the early attempts to use flapping wings for propulsion were bound to fail, and consequently, research concerning flapping flight has been overshadowed by the study of fixed and rotating wings for almost 100 years, particularly outside of the communities of zoologists with particular interests in insects, birds, pterosaurs, or bats. Interest in bio-inspired flight among diverse groups of engineers has resurfaced in recent years, however, and both the desire to develop highly efficient and maneuverable MAVs, and the greatly improved capabilities of modern equipment to image animal motion at high speed and visualize complex fluid flows have returned attention to animal flight research. Over the last two decades, knowledge about insect and bird flight has advanced tremendously, and we have gained greatly improved understanding about a host of issues in animal flight, such as the scaling of flight performance and the importance of unsteady effects (Ellington 1999; Ellington et al. 1996; Hedenström et al. 2006; Sane 2003; Spedding et al. 2003).

Although bats are the only mammals that have achieved powered flight, their flight has received relatively little attention until recently (Hedenström et al. 2007; Muijres et al. 2008; Tian et al. 2006), in part due to their nocturnal lifestyle which has kept them, literally, out of the spotlight. These astonishingly accomplished flyers number over 1,200 species, making up about one quarter of the diversity of all extant mammals. Unlike birds and insects, which regularly employ many forms of terrestrial locomotion, the vast majority of bats rarely move more than a few meters by any form of locomotion other than flight. Their tremendous ecological diversity, however, encompasses most of the earth's habitats, and their dietary specializations include not only insects, but also fruit, flowers, pollen, fish

T. Y. Hubel (✉) · N. I. Hristov · S. M. Swartz · K. S. Breuer
Brown University, Providence, RI 02912, USA
e-mail: tatjana_hubel@brown.edu

G.K. Taylor, M.S. Triantafyllou, and C. Tropea (Eds.): Animal Locomotion, pp. 371–381.
springerlink.com

and other small vertebrates, and even mammal and bird blood (Neuweiler 2000). They are able to land and roost on myriad substrates, can eat almost half of their body weight in a single night, and during pregnancy carry fetuses as large as a third of the mother's weight (Nowak 1994).

The flight of bats, much like that of birds has often been modeled to a first approximation as quasi-steady, with wings treated as rigid plates (Pennycuick 1968; Rayner 1979; Tobalske et al. 2003a). The assumption of steady flight was largely necessitated by the lack of analytical and experimental tools to analyze more complex flows, but this situation has changed considerably in the past few years. Similarly, the treatment of wings as rigid plates was initially one of simplicity, and has proved quite reasonable for some aspects of the flight of insects and even birds (Tobalske et al. 2003b). Bat wings are, however, anything but rigid, and are characterized by structural design that embodies a unique amount of flexibility (Swartz et al. 2006). In particular, bat wings possess more than two dozen joints, highly deforming bones, and anisotropic wing membrane skin with variable stiffness (Swartz et al. 1996). Even in level flight at constant speed, bat wings differ from those of birds and insects in their large and dynamically changing camber, and complex kinematics. As a consequence, aerodynamic models of bat flight that do not account for the dynamic aspects of the bat wing architecture can provide a starting point for understanding the mechanistic basis of bat flight, but are ultimately limited in explaining the ways that bats produce the aerodynamic forces required for flight. We can therefore expect that studies that account for the dynamic conformation of bat wings will substantially improve understanding of the aeromechanics of bat flight. Because of the distinctive anatomy of the bat wing, and the particular evolutionary history of bats, descendents of mammalian ancestors with highly complex and flexible locomotion, bats may represent the extreme among flying animals in this regard (Fig. 1).

In this paper, we describe aspects of the flight mechanics of a non-echolocating bat of intermediate body size, the Lesser dog-faced fruit bat, *Cynopterus brachyotis*. To better understand bat aerodynamics in the context of the time-varying three-dimensional structure and posture of the wing, we have simultaneously captured detailed wing kinematics and wake structure by using multiple camera high speed videography synchronized with time-resolved particle image velocimetry (PIV). Attempts to gain insight into the mechanistic basis of flight from PIV independent of wing kinematics will achieve limited success compared to analyses that link the development and evolution of wake structure to the dynamically changing shape of the wing. PIV is a powerful tool to enable researchers to better understand the aerodynamics of animal flight, but is most valuable when coupled directly to detailed kinematics, particularly for animals whose wings employ a large range of motion and dramatic modulations of three-dimensional conformation and stiffness.

The approach we use here, employing a 200 Hz PIV system, allows us to observe the details of wake development over multiple wing beat cycles, avoiding the necessity of building a composite picture of wake development by concatenating results obtained from multiple trials or wing beats at low sampling rates. We demonstrate that this coupling enables the exploration of relatively fine-scale variation in wing kinematics, wake structure, and kinematic/aerodynamic interrelationship. Understanding the significance of kinematics and aerodynamics at a fine-scale is critical to understanding flight variation within individuals and individual variation within-species for a given flight condition, such as level flight at constant speed. Also, importantly, the variation observed during other flight behaviors, such as changing speed, maneuvering, or changing altitude must be analyzed. Furthermore, the explicit coupling of kinematic and wake structure analysis can provide a fruitful framework for evaluating the possibility of aerodynamically distinctive flight gaits in bats.

As a crucial early step toward achieving the long-term goal of fully integrated analyses of complex kinematics and aerodynamics, our specific focus in this paper is time-resolved wake structure, and its spatial and temporal

Fig. 1 Complex wing kinematics, shape change, and bending in bat flight. **a** *Cynopterus brachyotis*, the Lesser dog-faced fruit bat, in steady flight ($Re = 27{,}000$) in the Brown University wind tunnel, illustrating multiple stages in the upstroke. **b** *Cynopterus brachyotis* maneuvering in wind tunnel test section

relationships with the motions of the wing tip and wrist. Future reports will build on these fundamental relationships by providing a more comprehensive analysis of the joint motion, membrane dynamics, and their detailed connections with the wake flow structures.

2 Experimental methods

2.1 Bats

We trained Lesser dog-faced fruit bats, *Cynopterus brachyotis*, to fly in the low-speed wind tunnel in the Division of Engineering at Brown University. These captive-bred female bats, on loan from the Lubee Bat Conservancy (Gainsville, Florida) received a 15–20 min wind tunnel training two to four times a week over a period of 2 months prior to the experiments reported here.

2.2 Wind tunnel

The low speed wind tunnel we employed has a closed-circuit design and has a test section measuring 3.8 m in length, with a cross-section of 0.60 by 0.82 m (height × width). Although the free stream turbulence level of the tunnel is quite low (0.29% at 2.81 m/s), a fine-mesh net is placed at the upstream entrance to the test section to restrict the bats, and this results in a turbulence level of 0.5% at 2.8 m/s at the location of the PIV observation area. Antireflective glass plates on bottom, top, and portions of the side of the test section, and Plexiglas windows on the walls allow almost unhindered visibility (Fig. 2). The bats are introduced to the flow by a member of the research team at a station approximately 0.5 m downstream of the measurement section. They fly into the oncoming air stream, moving slowly up the test section towards the settling chamber. Having flown sufficiently upstream and beyond the measurement volume, they are "retrieved" from the test section by a second research team member. The test section is sufficiently long (3.8 m) such that the measurement area is far from the points of introduction and retrieval, and during measurements, Plexiglass doors were closed to prevent the generation of any additional turbulence in the test section. We define a right-handed coordinate system with positive x defined in the direction of the wind (negative in the flight direction of the bat). The z-coordinate is positive in the vertical upward direction, and y is positive from center of the bat towards the tip of the right wing. Our results are usually presented in a bat-centered coordinate system, but depending on the specific goal of the analysis, sometimes in a combination of wind tunnel and bat-centered coordinate systems, with y and z in bat-centered coordinate system, with the origin located between the shoulder blades (along the midline of the back, roughly 1.5 cm posterior to the neck) and with the origin of the x-axis fixed at the plane where PIV measurements were acquired.

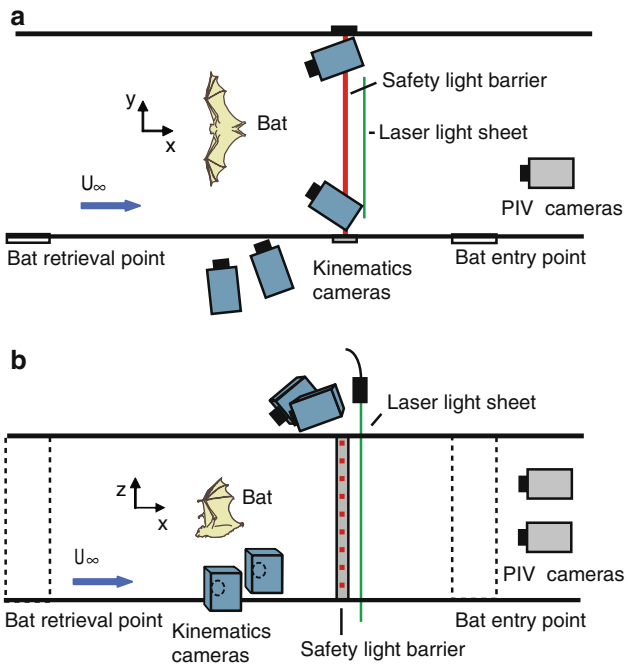

Fig. 2 Top (**a**) and Side (**b**) schematic views of the experimental setup in the wind tunnel for measurements in the transverse plane, perpendicular to the flow stream (Trefftz plane). The kinematics cameras are positioned above and beside the test section, out of the air stream, while the PIV cameras are in the test section, oriented perpendicular to the flow stream. The safety light-curtain is positioned 5 cm upstream of the laser light sheet. The locations of the introduction and retrieval of the animal are windows on the side of the test section

2.3 PIV

To obtain the wake velocity components, we performed time-resolved PIV using a 200 Hz double-pulse Nd:YAG laser (Litron LPY 703-200) to illuminate the observation area (pulse duration 6 ns, energy 60 mJ). The wind tunnel was seeded with di-ethyl-hexyl-sebacate (DEHS) using a custom built Laskin-type nozzle fog generator.

Two high-resolution CMOS cameras (Photron 1,024 PCI, resolution 1,024 × 1,024 pixels, lens 85 mm, f/1.4) captured the motion of the DEHS particles in the observation area. The two PIV cameras were located at the downstream end of the test section, and positioned perpendicular to the flow stream so as to capture the wake structure in the Trefftz (y–z) plane. The two cameras imaged overlapping but separate fields of view to maximize the size of the observation area. A single calibration

plate and the coordinate system origin were visible in both cameras, with an overlap of approximately 0.05 m, and the resulting image size was 0.23 m × 0.41 m. This field of view was sufficient to image the complete wake of the right wing; in our analyses, we mirrored this wake structure to visualize the entire wake for ease of viewing, using the assumption that left and right wing motions differ little in straight, steady flight.

We recorded PIV data using a buffer loop function to record the data in an endless loop triggered by an END signal (DaVis 7.13 software, LaVision). The calibration parameters are achieved by using the pinhole calibration, and the two camera images stitched together within the software. Vector fields were calculated using cross-correlation with multi-pass iterations with decreasing size (128 × 128, 2 iterations to 64 × 64, 2 iterations, 50% overlap) resulting in a 32 × 56 vector field. Vectors with peak ratio $Q < 1.2$ and variations to the average neighborhood >1.5 × r.m.s. of neighbor vectors were replaced via interpolation (average replacement 1.7%, average Q-value 2.96) and a simple 3 × 3 smoothing filter was applied. The vector field was exported and subsequently processed in Matlab®.

Circulation (Γ) was obtained by integration of the vorticity (ω_x) over the area to the right of the body marker. The measured velocity and vorticity fields are typically noisy and for this reason, there are several viable methods for estimating the circulation. One method is to integrate only the vorticity that rises above an arbitrary threshold, and subsequently to add back an analytical estimate for the neglected vorticity (Spedding et al. 2003). Another method is to calculate the swirl from the velocity field (i.e. the rotational part of the local two-dimensional rate-of-strain tensor) and to use this as a mask for the circulation calculation (thus filtering out vorticity due to local shear). Our approach was to integrate the entire measurement area to the right of the body, assuming that positive and negative vorticity due to turbulence will cancel out, leaving only the coherent circulation generated by the bat. The resulting average circulation generated over one wing beat cycle can differ up to 30% depending on the chosen method, however the primary vortex structure and its temporal development (if not the absolute value) was found to be very consistent between different methods.

The circulation was normalized by average wing chord (c) and the true flight velocity, such that $\gamma = \Gamma/(U_t)c$. The true flight speed (U_t) combines the wind speed with any additional flight speed of the bat (U_b). Since the bat was usually moving up the test section, flying towards the front screen (in the negative x-direction in the wind tunnel coordinate system), the velocity of the bat was actually negative and the true flight speed is $U_t = U_\infty - U_b$. We calculated local circulation maxima and minima and defined the wing beat cycle as the period between two minima.

The flapping frequency based on the wake measurements (f_{PIV}) was calculated according to the period. However, due to the movement of the bat in the test section, the wake frequency can be different from the true flapping frequency due to a Doppler shift:

$$f_t = \frac{U_t}{U_\infty} f_{PIV}$$

where f_t is the true flapping frequency. We have also assumed that the wake vortex structure travels at the free stream velocity. The actual flapping frequency was also extracted directly from the kinematics (f_K) and compared with the wake-based flapping frequency (f_{PIV}) and the corrected true flapping frequency (f_t). Subsequently, the true flapping frequency (f_t) and true flight speed (U_t) are used to calculate Reynolds number ($Re = (U_t c)/\nu$, reduced frequency ($k = (\pi f_t c)/U_t$) and Strouhal number ($Sr = (f_t A)/U_t$) (ν is the kinematic viscosity, A is the wingtip excursion, the vertical distance traveled by the tip of the wing during the flapping stroke).

Small variations in the flapping frequency of consecutive wing beat cycles led to a variable number of computed values of the velocity field and circulation during each cycle (approximately 28–31), and to address this, we partitioned each wing beat cycle into 35 segments and used interpolation to compute the circulation for 35 time increments per wing beat cycle. We estimated a moving average over three values, and then computed the mean and standard deviation of the circulation over six consecutive wing beat cycles. Six cycles were chosen because this was the maximum number of consecutive wing beat cycles available for all trials.

To visualize the development of the wake structure over time, we first convert time to streamwise distance (assuming that the wake structures advect with the freestream velocity) and plot an isosurface of the swirl (Adrian et al. 2000), therefore taking only the rotational part of the vorticity from PIV measurements in the Trefftz (y–z, or transverse) plane into account. While visualization of the vorticity field requires additional smoothing and a high threshold (±50% of maximum vorticity value) to enable a clear visualization of the main vortex, the swirl is effectively seen using a very low threshold (we use isosurfaces of 2.5% of the maximum swirl value), and requires no additional smoothing. This also allows us to show the development of small, but coherent, vortex structures that appear during the wing beat cycle, but are difficult to see using vorticity visualization. Swirl does not differentiate between counter- and clockwise rotating vortices and so the vorticity field was used to determine the local rotational direction, and a color was assigned, based on the circulation at that particular time.

2.4 Kinematics

Kinematic data were recorded using four cameras (Photron 1,024 PCI, resolution 1,024 × 1,024 pixels, 200 fps) positioned above and alongside the test section (Fig. 2). The cameras were synchronized with the PIV recordings by using a laser flash lamp sync signal to trigger a digital delay-pulse generator (Model 555 Berkeley Nucleonics Corporation). Kinematic and PIV cameras shared a single origin and coordinate system; calibration was achieved with the direct linear transformation (DLT) method (Abdel-Aziz and Karara 1971) following videographic recording of a calibration plate mounted on a linear traverse, moved through the control volume by successive displacements of 0.1 m. Seventeen white circles marked the joints and other important anatomical positions on the dorsal surface of the bat (Fig. 3). The kinematic measurements were sub-sampled by a factor of ten using a spline interpolation to fill gaps in the data due to obstruction of markers. This method ensured the accuracy of the correlation between the PIV and kinematic measurements, as well as during the correction of the PIV data to account for the Doppler shift described above.

2.5 Light

To minimize light pollution, the PIV cameras were equipped with 532 nm band-pass filters transmitting light in the range of 511–548 nm. Narrower filters darkened videographic images significantly and were not usable. The kinematics volume was illuminated by three Xenon strobe lights (Nova-Strobe dax, Monarch Instrument) operating at 200 Hz, and synchronized with the kinematics cameras. The strobe lights emit short (10–25 μs) intense light pulses which provide sufficient illumination for the kinematic recordings, eliminate motion-induced blurring while maintaining a low average light level, which is preferred by the nocturnal bats. By pointing the strobes away from the PIV cameras, we kept reflections to a minimum. This approach also allows us to interlace the PIV lasers with the strobe lights, thus further reducing light pollution during image capture for PIV. However, this was not found to be necessary and was not used in the experiments reported here.

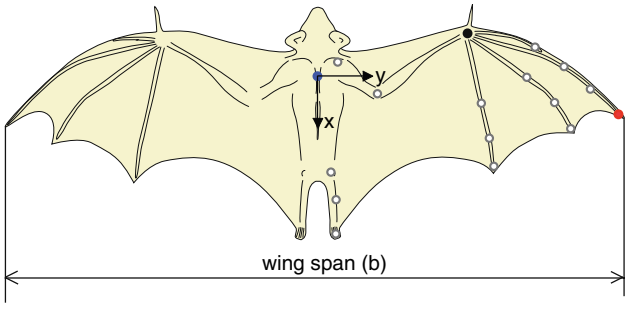

Fig. 3 Positions of kinematics markers on the dorsal surface of the bat. Body (*blue circle*) and wrist (*black circle*) and wing tip (*red circle*) position of the bat, *x* and *y* indicate the body fixed coordinate system

2.6 Light curtain

The intense energy in the PIV laser light sheet is capable of injuring bats in several ways, particularly their eyes, so the operation of the PIV system was gated by a laser light safety curtain, positioned 0.05 m upstream of the laser light sheet. The safety curtain consisted of an array of 21 low-power red diode lasers spanning the entire test section, each aimed at a complementary photo-diode. After the bat was released and had safely advanced upstream of the light curtain, the system was activated. If the bat moved downstream for any reason, it would interrupt one of the safety beams, at which point the laser system automatically shut down.

3 Results and discussion

We present results collected in four trials of three bats. The original data collection included measurements using three individuals flying at freestream velocities ranging from 3.5 to 5.5 m/s. Measurements such as these, using un-tethered live animals, are difficult, and for this reason, the present manuscript only reports on four trials obtained using three bats (Table 1).

Wing beat kinematics for bat flight are extremely complex (Riskin et al. 2008) and beyond the scope of this paper. Because the wing changes shape continuously as it flaps, it cannot be viewed as a flapping plate, or even as a flapping plate with one or two simple hinges. Many of the joints of the handwing are extended during the downstroke until the lower reversal point, at which point they begin to flex, and the wingtip moves closer to the body in horizontal direction. At the same time, early in the upstroke, the wingtip moves simultaneously upwards and outwards. At the end of the upstroke, the wing has adopted a rather extended posture. Moreover, the motion of the wingtip is not primarily vertical with respect to either gravity or the animal's body. The wings sweep forward as they move downward, increasing the relative forward velocity during downstroke, and decreasing angle of attack and backwards sweep during upstroke.

A sample trace of the vertical motion of the wrist and wingtip with respect to the body (Fig. 4), illustrates the phase and position difference between the wingtip and the wrist. Although the wingtip motion has larger amplitude,

Table 1 Physical characteristics of the three bats

Individual	Mass (kg)	Average chord (m)	Maximum span (m)	Maximum wing area (m^2)	Aspect ratio (-)	Wing loading (N/m^2)
Bat 1	0.033	0.061	0.406	0.025	6.59	13.20
Bat 2	0.029	0.059	0.376	0.022	6.43	13.18
Bat 3	0.030	0.058	0.399	0.023	6.92	13.04

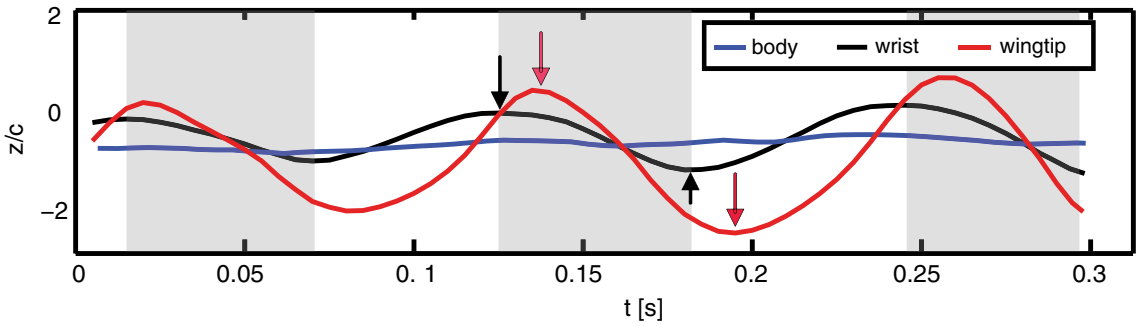

Fig. 4 Lateral view of the trace of body, wrist and wingtip motion. The *shaded areas* represent the downstroke (as defined by the wrist motion). The body motion is usually quite steady, although does show some periodic variation associated with the wing beat cycle. The *arrows* marking the beginning and end of the downstroke of the wrist (*black*) and wing tip (*red*) and reveal the fact that the phase of the wingtip motion lags that of the wrist

we choose to define the upstroke and downstroke according the wrist motion because it has a more purely sinusoidal motion, and the movement of the wrist is more directly controlled by the primary flight musculature.

Many flights are highly regular, with stereotyped kinematic patterning and hence aerodynamics. However, some trials display substantial variation in the observed patterns of circulation from one wing beat cycle to the next. For example, in one flight (Fig. 5), the wing beat cycles early in the flight are very consistent, with little variation in either flapping frequency (f_{PIV} = 7.7 Hz ± 0.4) or mean normalized circulation (0.132 ± 0.015); later in the same flight, both wing beat frequency and normalized circulation decrease temporarily as the subject slowed, then accelerated. Such variation among wingbeats within a single flight sequence of a single individual highlights the benefits of high frequency PIV experiments. Using a low-frequency PIV system in which the laser repetition rate is low relative to wing beat frequency, it is necessary to piece together records from multiple wing beats to create a single composite wing beat cycle, and such inconsistencies and variation among wing beats are more likely to lead to errors than to new insights. Similar difficulties might also arise from PIV without synchronized and detailed kinematic measurements.

The bat flies upstream in the wind tunnel, away from the laser light sheet, and therefore the distance between the vortex generation and the measurement plane increases (up to 2 m) as the measurement sequence progresses. If there

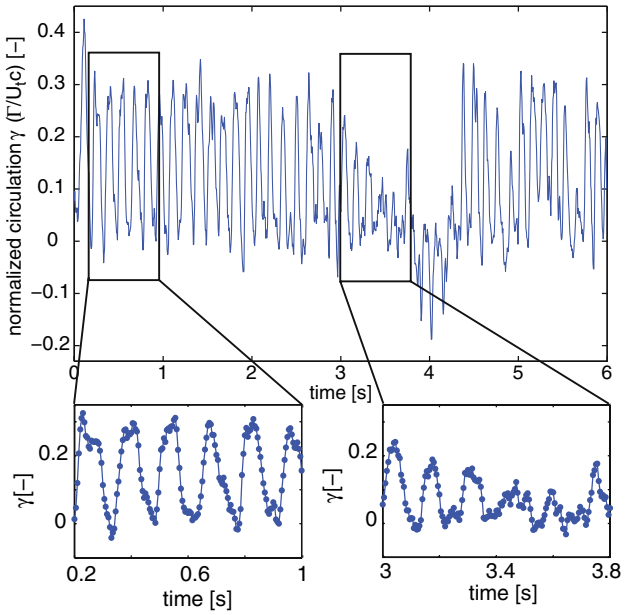

Fig. 5 Normalized circulation versus time at Re = 20,000, k = 0.28 (bat 2) derived from the wake PIV measurements. For this particular trial, PIV data was obtained for over 6-s and approx. 45 wing beats. At the beginning of the trial there is a good uniformity in the flapping frequency, amplitude and shape of the circulation cycle. However, differences are observed in the middle of the record, corresponding to observed deceleration and manoeuvring by the bat

were a significant influence of the vortex convection time, one would expect to see this reflected in a change in the measured vortex structure over the duration of the sequence.

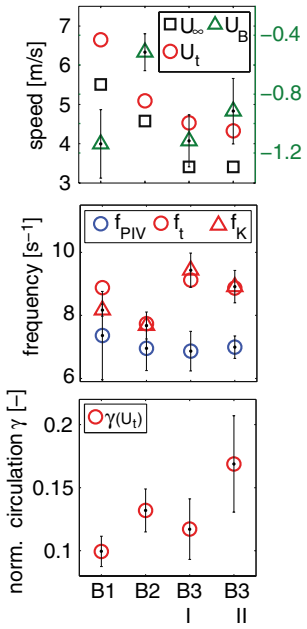

Fig. 6 Flight speed, flapping frequency and circulation from four trials with three individuals. *Top frame*: wind speed (U_∞), bat speed relative to the wind speed and in opposite direction and therefore negative (U_B) and the true flight speed ($U_t = U_\infty - U_B$); *Middle frame*: flapping frequency derived from (1) PIV (f_{PIV}) (2) PIV, adjusted for Doppler shift (f_t), and (3) derived from kinematics (f_K); Lower frame: normalized circulation (based on the true flight speed) (γ)

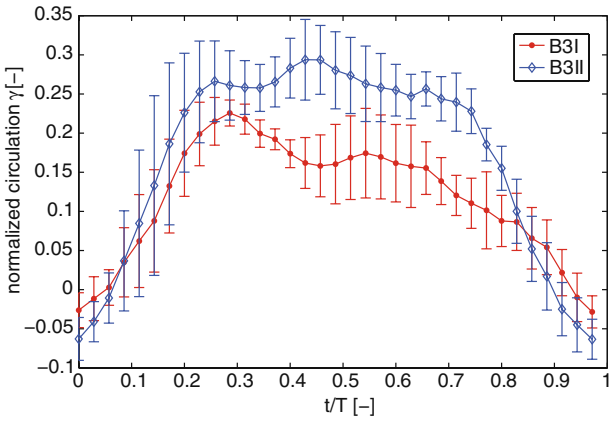

Fig. 7 Development of the normalized circulation over one wing beat cycle, averaged over six wing beats. Two trials are shown from the same individual flying at $Re = 17{,}500$ and 16,700 with $k = 0.38$ in both cases. The variation in the circulation appears to be related changes in altitude during the measurement window

However, although small flow structures that are visible in the first couple of wing beat cycles do seem to disappear with time (Fig. 10), the overall structure and amplitude of the circulation over the wing beat cycles (Fig. 5) and the average circulation do not decrease in any significant manner, and we therefore assume that dissipation and flow unsteadiness, at least of the large-scale structures, are not of primary importance and can be neglected.

The circulation and flapping frequency was averaged over six wing beat cycles for four trials of three different bats (Fig. 6). The frequency of the circulation signature measured in the wake (f_{PIV}) varies very little, typically around 7 Hz. However, U_B, the motion of the bat relative to the test section, was typically between -0.5 and -1.1 m/s (negative due to the bats upstream motion), and when wingbeat frequency is corrected for the Doppler shift due to this relative motion, the wake frequency closely matches the frequency measured directly from the kinematic record. Reynolds number, reduced frequency and Strouhal number vary among the bats, but are consistent between the two trials of the same bat (Table 2).

Although it is not surprising that the normalized circulation varies from bat to bat, in part because no two bats possess identical body mass, there is also a marked difference between consecutive trials of the same individual (bat 3) flying at the same reduced frequency (Fig. 6). Figure 7 presents a view into the development of the circulation over the wingbeat cycle for this case and emphasizes the difference, with trial no. 2 exhibiting a consistently higher circulation than trial no. 1 over the central core of the wingbeat, $t/T = 0.2$–0.8. Examination of the kinematics results reveals that the two trials are characterized by different vertical histories, with the bat in trial no. 1 moving downwards 13% of the horizontal travel distance and moving upwards 8% in trial no. 2. It is important to account for these changes in altitude in detailed aerodynamic analyses, and we will explore these specifics in more detail in future work.

The average circulation is only about one half the value that one would expect to see based on weight support at the observed flight speed. This is, of course, a serious concern, and we have explored the issue quite thoroughly. We are confident that the measurements presented are not dependant on PIV acquisition or processing parameters (e.g. time between laser pulses, interrogation window area, overlap, filtering, etc.). We speculate that two issues are primarily responsible for the discrepancy. Firstly, it is possible that a portion of the tip vortex structure is destroyed by background turbulence and other unsteady vortex structures shed by the bat. Secondly, it is possible that a significant fraction

Table 2 Reynolds number (Re), reduced frequency (k) and Strouhal number (Sr) for three different bats and four trials based on the true flapping frequency and flight speed

	Bat 1	Bat 2	Bat 3 trial I	Bat 3 trial II
U_∞ (m/s)	5.51	4.58	3.41	3.41
Re	27,000	20,000	17,500	16,700
k	0.24	0.28	0.38	0.38
Sr	0.25	0.28	0.42	0.41

of the vortex sheet shed by the wing may be lost due to diffusion before it is gathered up into the primary tip vortex. This idea is supported by recent experiments (Gerontakos and Lee 2006) conducted using both swept and rectangular wings at $Re = 181{,}000$, which found similarly small fractions of the total shed circulation present in the tip vortex structure. We also explored this by measuring the tip vortex behind a rigid rectangular wing at several Reynolds numbers, including those comparable to the bats' flight conditions (Table 2). We found that the measured circulation was only about 50% of that predicted by thin airfoil theory, and measured directly using a load cell, thus supporting the idea that, while the vortex structure accurately reflects the nature of the lifting body, at these low Reynolds numbers, the tip vortex might not capture the total circulation associated with the bound vorticity on the lifting surface. This is an ongoing investigation.

In *C. brachyotis* at moderate flight speed, circulation is generated continually during a large part of the downstroke and part of the upstroke (Fig. 7). At the beginning of the downstroke, the streamwise vorticity field in the wake shows no presence of a distinct vortex structure (Fig. 8a). At the end of the first third of the downstroke the wake measurements indicate the development of a single streamwise vortex structure that starts at a point 1.5 half-spans above the center-plane. The structure continues to gain strength while moving downwards and outwards (Fig. 8b), reaching maximum strength 1.5 half-spans below the center-plane at the end of the downstroke. This maximum strength remains approximately constant during transition between downstroke and upstroke, although the vortex moves upward and inboard as the upstroke begins (Fig. 8c). The vortex structure remains during most parts of the upstroke, and begins to weaken during the middle of the upstroke. At the end of the upstroke and beginning of the downstroke, little or no circulation is generated. The development of the wingtip vortices shows some similarities to the pattern identified in previous measurements made at lower temporal resolution (Tian et al. 2006), but

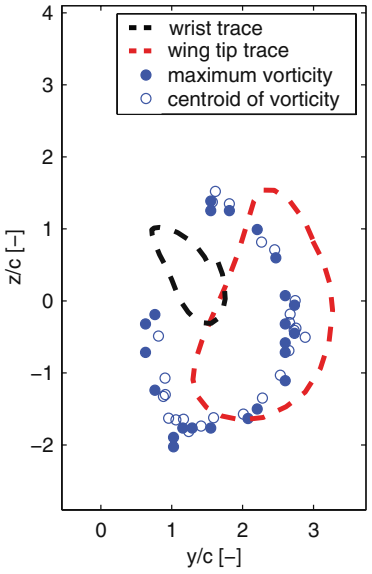

Fig. 9 Correlation between the wrist and wing tip locations and the tip vortex location, calculated from both the maximum vorticity and the centroid of vorticity ($Re = 16{,}700$, $k = 0.38$). The vortex core tracks the wing tip motion very closely, lying inboard by approximately $0.5c$, consistent with the location of the tip vortex shed from stationary fixed wings (Betz 1932; Devenport et al. 1996)

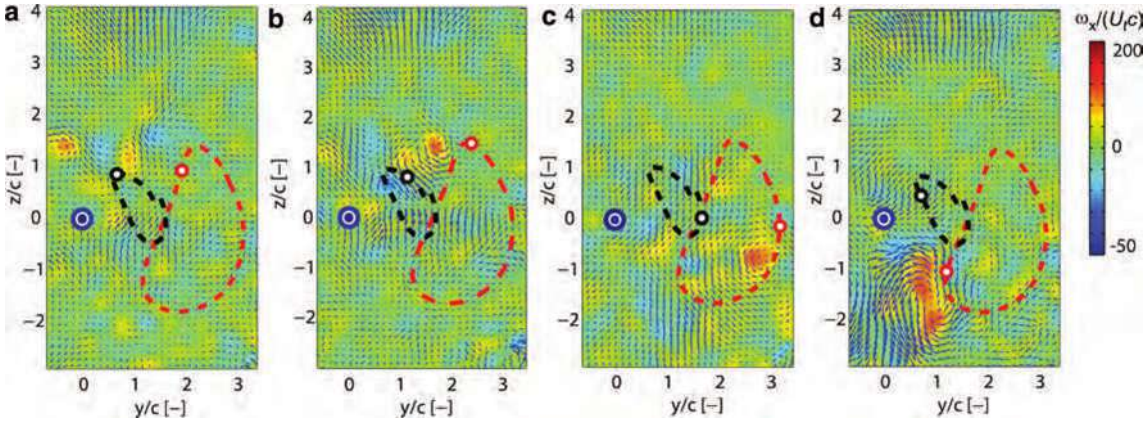

Fig. 8 Vector velocity field and streamwise vorticity at $Re = 16{,}700$, $k = 0.38$ in the plane perpendicular to the flow stream. The vorticity is shown behind the right wing of the bat in the coordinate system, where z and y coordinates are body-centered and normalized by the average wing chord. No distinct vortex structure at the beginning of the downstroke (**a**). Formation of the tip vortex during the first third of the downstroke (**b**) gaining strength while moving downwards and outwards during the second third of the downstroke (**c**). The tip vortex gains maximum strength at the end of the downstroke, keeping it while moving in and upward (**d**) and stays present till almost the end of the upstroke—Body (*large blue double circle*) and wrist (*black circle*) and wing tip (*red circle*) position of the bat are computed from kinematics. The motion of the wrist and wingtip over one wing beat cycle, projected on the *y*–*z* plane, is indicated by the *dashed black and red line*, showing the phase difference between wrist and tip position

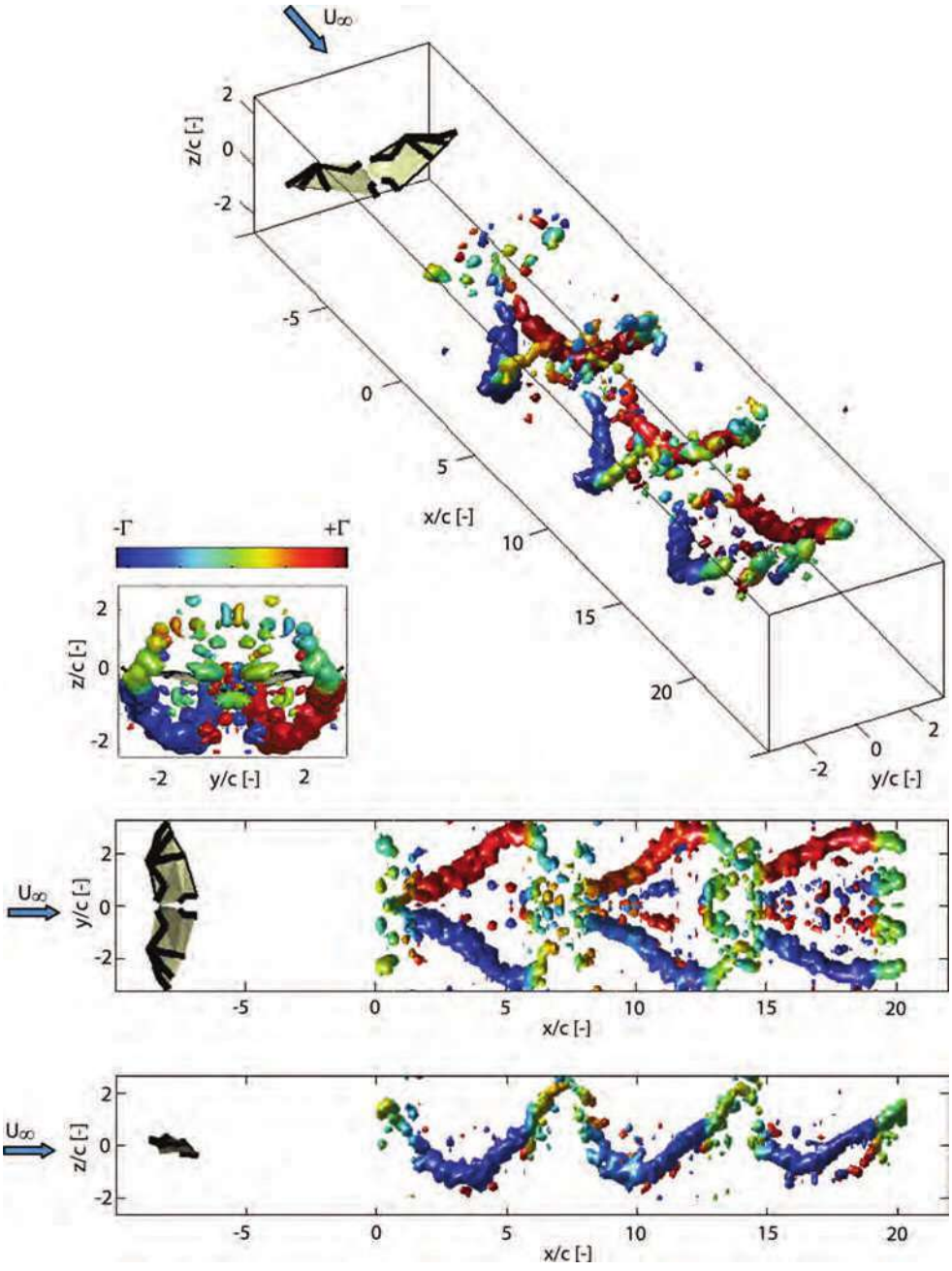

Fig. 10 Reconstruction of the wake of *C. brachyotis* flying at $Re = 16{,}700$, $k = 0.38$. Isosurfaces of the streamwise swirl from the right wing tip vortex are shown (and mirrored on the left side for ease of viewing). The y and z axis are as defined in Fig. 8. The origin of the x-axis is the position of the laser light sheet. The streamwise coordinate is derived from the time series using $x(t) = (U_\infty^2/U_t)(t_0 - t)$, where t_0 is the duration of the measurement sequence. At every instant in time, each vortex structure is assigned a rotational direction using the sign of the local vorticity, and is colored based on the magnitude of the total circulation at that time. This accurately reflects the changes in the circulation over the wing beat cycle, but does not allow for a quantitative comparison between clockwise and counter-clockwise vortices at any given time

also distinct differences, especially in terms of the correlation between kinematics and wake structure. These differences likely derive from the difficulties associated with the low-frequency of data acquisition in the previous work, and emphasize the importance of the simultaneous time-resolved measurements of wake and motion.

There are at least two ways to identify the center of the tip vortex: as the location of maximum vorticity in the observation area, or as the location of the centroid of the vortex, based on a threshold of 20 s^{-1} to avoid identifying maxima at times were no defined tip vortex was present. The spatial geometry of the tip vortex motion does not depend on the method (Fig. 9), and in both cases the vortex core tracks the wing motion very closely, lying inboard by approximately $0.5c$. This is consistent with predicted location of the tip vortex shed from a stationary fixed wing (Betz 1932; Devenport et al. 1996).

The observation of the streamwise vorticity, as well as the calculated circulation, suggests a wake structure of closed vortex loops similar to that observed during the slow flight of some birds (Spedding 1986; Spedding et al. 1984), rather than a constant circulation wake, as postulated for birds in cruising flight (Spedding 1987; Spedding et al. 2003). A ring vortex wake structure is also consistent with

aerodynamic interpretations based on calculations derived from kinematic modeling of displacements of the center of mass of the body plus flapping wings (Iriarte-Diaz et al. 2009a). However, large parts of the upstroke are aerodynamically active and contribute a considerable portion of the overall wing beat circulation. The aerodynamically inactive phase is limited to the portion over the wingbeat cycle close to the upper reversal point. The streamwise swirl topology (Fig. 10) demonstrates a characteristic "wishbone" structure, but shows a more complex vortex structure than that observed in bird flight; this pattern is consistent with observations made from flights of a smaller, nectar-feeding bat, *Glossophaga soricina* (Hedenstrom et al. 2007). Our reconstruction reveals a secondary vortex structure close to the body, similar to one observed for *G. soricina* in medium and slow flight. However, in the present case, the secondary structure is considerably weaker. While the one visualized for *G. soricina* was reported to have approximately 50% of the strength of the tip vortex, for *C. brachyotis,* maximum secondary vortex strength is only 8% of the maximum tip vorticity present in the wing beat cycle. The vortex structure close to the body rotates in the opposite direction to that of the tip vortex, and is present over the whole wing beat cycle. Due to its low amplitude, it can only be visualized from wing beat cycles in which the bat flew very close to the measurement plane. When the bat is further upstream, the weak structure has probably decayed by the time it advects to the PIV measurement plane, and thus it cannot be detected. The three displayed wing beats indicate a very repeatable wake structure during the consecutive wing beat cycles. Although the tip vortex was present during most of the upstroke, we have a more frequent occurence of weak vortices, both positive and negative, at the end of the upstroke and beginning of the downstroke.

These likely are shed from the body and the highly folded wing, but thus far no clear structure has been identified in the measurements (Fig. 8a) and additional data from further investigations will be required to fully resolve this issue. The slow formation of the streamwise vortex during the downstroke and its rather abrupt disappearance at the end of the upstroke suggests that slow flight in these bats is characterized by a number of relatively weak starting vortices, and in contrast, a single, strong stopping vortex at the end of the wing beat cycle.

4 Concluding remarks

Although these results do not provide a complete description of the complexity of mechanics of flight of even a single species of bat, the demonstration of high-resolution kinematics synchronized with time-resolved wake velocity measurements represents an important advance in experimental capabilities for the study of animal flight, and greatly advance our understanding of bat aeromechanics. Unlike previous methods which have relied on the assembly of a "typical" wake structures to form a composite view, the current methods allow for the full variability of the wake structure to be directly assessed and indentified with changes in wing and body kinematics. Wingbeat to wingbeat, flight-to-flight, and individual variability are increasingly recognized as important issues in natural animal flight, and are only recently being quantified (Iriarte-Diaz et al. 2009b) The techniques we employ here will provide the necessary framework to explore the aerodynamic aspect of variability in animal flight in significantly more detail than has previously been possible.

Despite the limited nature of the current data set, we can draw some important conclusions. A closed loop vortex structure is dominant at these relatively slow forward flight speeds, and there is evidence for additional small vortex structures shed from other appendages. In the future, a larger data set will allow us to make more general statements about the vortex structure at different flight speeds, and measurements in the parasaggital (x–z) plane as well as three-component PIV will provide more detail on these structures. It will also be possible to make direct comparisons between experimental, PIV measured wake structures and numerical simulations based on kinematics of the same bat species (Willis et al. 2007) Continuing advances in experimental approaches thus promise greatly improved understanding of the complex mechanisms of the flapping flight of bats in the coming years.

Acknowledgments We thank A. Song, R. Waldman and D. Riskin for helpful discussions, and A. Sullivan, L. Macayeal and A. Robb for handling and training of animals and their help with data collection. We are very thankful for the support provided by D. Riskin regarding kinematic analysis and data flow issues. We also thank R. Waldman for the construction of the safety light barrier. We thank the Lubee Bat Conservancy, especially A. Walsh, for the long term access to the bats. This work was supported by the Air Force Office of Scientific Research, monitored by Drs. Rhett Jeffries, John Schmisser and Willard Larkin, and the National Science Foundation. All experiments were conducted with the authorization of the Institutional Animal Care and Use Committees of Brown University, the Lubee Bat Conservancy and the Division of Biomedical Research and Regulatory Compliance of the Office of the Surgeon General of the United States Air Force.

References

Abdel-Aziz YI, Karara HM (1971) Direct linear transformation from comparator coordinates into object space coordinates in close-range photogrammetry. In: Proceedings of the symposium on close-range photogrammetry, American Society of Photogrammetry, Falls Church, pp 1–18

Adrian RJ, Christensen KT, Liu ZC (2000) Analysis and interpretation of instantaneous turbulent velocity fields. Exp Fluids 29:275–290

Betz A (1932) Verhalten von Wirbelsystemen. Zeitschrift fur angewandte Mathematikund Mechanik 12:164–174 (Also published as NACA TM 713)

Devenport WJ, Rife MC, Liapis SI, Follin GJ (1996) The structure and development of a wing-tip vortex. J Fluid Mech 312:67–106

Ellington CP (1999) The novel aerodynamics of insect flight: applications to micro-air vehicles. J Exp Biol 202:3439–3448

Ellington CP, van den Berg C, Willmott AP, Thomas ALR (1996) Leading-edge vortices in insect flight. Nature 384:626–630

Gerontakos P, Lee T (2006) Near-field tip vortex behind a swept wing model. Exp Fluids 40:141–155

Hedenström A, Johansson LC, Wolf M, von Busse R, Winter Y, Spedding GR (2007) Bat flight generates complex aerodynamic tracks. Science 316:894–897

Hedenström A, Rosén M, Spedding GR (2006) Vortex wakes generated by robins *Erithacus rubecula* during free flight in a wind tunnel. J Royal Soc Interface 3:263–276

Iriarte-Diaz J, Riskin DK, Willis DJ, Breuer KS, Swartz SM (2009a) No net thrust on the upstroke: whole-body kinematics of a fruit bat reveal the influence of wing inertia on body accelerations (in review)

Iriarte-Diaz J, Riskin DK, Swartz SM (2009b) Modulation of wingbeat kinematics with flight speed in the fruit bat *Cynopterus brachyotis* (in prep.)

Lilienthal O (1889) Der Vogelflug als Grundlage der. Fliegekunst Leipzig: Gaertuer

Muijres FT, Johansson LC, Barfield R, Wolf M, Spedding GR, Hedenstrom A (2008) Leading-edge vortex improves lift in slow-flying bats. Science 319:1250–1253

Neuweiler G (2000) The biology of bats. Oxford University Press, Oxford

Nowak RN (1994) Walker's bats of the world. Johns Hopkins University Press, Baltimore

Pennycuick CJ (1968) Power requirements for horizontal flight in the pigeon Columba Livia. J Exp Biol 49:527–555

Rayner JMV (1979) A vortex theory of animal flight. Part 2: the forward flight of birds. J Fluid Mech 91:731–763

Riskin DK, Willis DJ, Iriarte-Díaz J, Hedrick TL, Kostandov M, Chen J, Laidlaw DH, Breuer KS, Swartz SM (2008) Quantifying the complexity of bat wing kinematics. J Theor Biol 254:604–615

Sane SP (2003) The aerodynamics of insect flight. J Exp Biol 206:4191–4208. doi:10.1242/jeb.00663

Spedding GR (1986) The wake of a jackdaw (*Corvus Monedula*) in slow flight. J Exp Biol 125:287–307

Spedding GR (1987) The wake of a kestrel (Falco Tinnunculus) in flapping flight. J Exp Biol 127:59–78

Spedding GR, Rayner JMV, Pennycuick CJ (1984) Momentum and energy in the wake of a pigeon (Columba Livia) in slow flight. J Exp Biol 111:81–102

Spedding GR, Rosen M, Hedenström A (2003) A family of vortex wakes generated by a thrush nightingale in free flight in a wind tunnel over its entire natural range of flight speeds. J Exp Biol 206:2313–2344. doi:10.1242/jeb.00423

Swartz SM, Groves MS, Kim HD, Walsh WR (1996) Mechanical properties of bat wing membrane skin. J Zool 239:357–378

Swartz SM, Bishop KL, Ismael-Aguirre M-F (2006) Dynamic complexity of wing form in bats: implications for flight performance. In: Akbar Z, McCracken G, Kunz T (eds) Functional and evolutionary ecology of bats. Oxford University Press, Oxford

Tian X, Iriarte-Diaz J, Middleton K, Galvao R, Israeli E, Roemer A, Sullivan A, Song A, Swartz S, Breuer K (2006) Direct measurements of the kinematics and dynamics of bat flight. Bioinspir Biomim 1:10–18

Tobalske BW, Hedrick TL, Dial KP, Biewener AA (2003a) Comparative power curves in bird flight. Nature 421:363–366

Tobalske BW, Hedrick TL, Biewener AA (2003b) Wing kinematics of avian flight across speeds. J Avian Biol 34:177–184

Willis DJ, Israeli ER, Persson P-O, Drela M, Peraire J, Swartz SM, Breuer KS (2007) A computational framework for fluid structure interaction in biologically inspired flapping flight. In: AIAA applied aerodynamics meeting, vol 1, pp 38–59, American Institute of Aeronautics and Astronautics Inc, Miami, United States, Reston, VA 20191–4344, United States

Experimental investigation of a flapping wing model

Tatjana Y. Hubel · Cameron Tropea

Abstract The main objective of this research study was to investigate the aerodynamic forces of an avian flapping wing model system. The model size and the flow conditions were chosen to approximate the flight of a goose. Direct force measurements, using a three-component balance, and PIV flow field measurements parallel and perpendicular to the oncoming flow, were performed in a wind tunnel at Reynolds numbers between 28,000 and 141,000 (3–15 m/s), throughout a range of reduced frequencies between 0.04 and 0.20. The appropriateness of quasi-steady assumptions used to compare 2D, time-averaged particle image velocimetry (PIV) measurements in the wake with direct force measurements was evaluated. The vertical force coefficient for flapping wings was typically significantly higher than the maximum coefficient of the fixed wing, implying the influence of unsteady effects, such as delayed stall, even at low reduced frequencies. This puts the validity of the quasi-steady assumption into question. The (local) change in circulation over the wing beat cycle and the circulation distribution along the wingspan were obtained from the measurements in the tip and transverse vortex planes. Flow separation could be observed in the distribution of the circulation, and while the circulation derived from the wake measurements failed to agree exactly with the absolute value of the circulation, the change in circulation over the wing beat cycle was in excellent agreement for low and moderate reduced frequencies. The comparison between the PIV measurements in the two perpendicular planes and the direct force balance measurements, show that within certain limitations the wake visualization is a powerful tool to gain insight into force generation and the flow behavior on flapping wings over the wing beat cycle.

T. Y. Hubel (✉) · C. Tropea
Fachgebiet Strömungslehre und Aerodynamik,
Technische Universität Darmstadt, Darmstadt, Germany
e-mail: tatjana_hubel@brown.edu

1 Introduction

Recent interest in the development of micro air vehicles (MAVs) has brought attention to the fundamental aerodynamics of flapping flight (Mueller 2001). In order to gain a better understanding of the flow behavior on moving wings at low Reynolds numbers, aerodynamics, kinematics, morphology and energy consumption of animal flight have been recently studied with renewed interest (Dickinson et al. 1999; Ellington 1999; Rayner and Gordon 1998; Sane 2003; Spedding et al. 2003b). In spite of the increasing research in flapping flight over the last decade, many questions are still unresolved in order for flapping flight to be used in engineering applications. Not only is the unsteady aerodynamic research field at these Reynolds numbers and reduced frequencies comparatively new, but also the flow behavior in the MAV Reynolds number range (<100,000) is quite distinct from the performance at higher Reynolds numbers more characteristic of aircraft.

The challenge to better understand the aerodynamic and kinematic aspects of flapping flight and the correlation between them is accompanied by additional laboratory challenges posed by moving test objects. Direct force measurements on swimming and flying animals are difficult to perform and analyze, especially in untethered conditions A small number of successful measurements on tethered insects such as locusts (Cloupeau et al. 1979; Wilkin 1990; Zarnack 1969), moths (Bomphrey et al. 2005; Wilkin 1991; Wilkin and Williams 1993), fruit flies

G.K. Taylor, M.S. Triantafyllou, and C. Tropea (Eds.): Animal Locomotion, pp. 383–399.
springerlink.com

(Dickinson and Gotz 1996) and dragonflies (Thomas et al. 2004) have been conducted. Vertebrates generally refuse to fly or swim under tethered conditions; therefore, direct force and drag measurements are limited to dead animals and body parts (Maybury and Rayner 2001, Webb 1975). Similarly, pressure measurements on animals are difficult; hence even fewer examples of successful force measurements have been collected (Usherwood et al. 2003, 2005).

Contrary to former visualization tools such as smoke that provided only qualitative (Thomas et al. 2004; Willmott et al. 1997) or helium bubbles with limited quantitative insight into the flow behavior (Spedding 1986, 1987a, b; Spedding et al. 1984), current optical measurement techniques, such as particle image velocimetry (PIV), are often used for quantitative investigations of the wake flow field in terms of the instantaneous velocity and vorticity fields (Drucker and Lauder 1999; Spedding et al. 2003a, b; Warrick et al. 2005).

This present study was conducted by applying Helmholtz's vortex laws, to estimate the generated forces from a 2-D plane perpendicular to the flow stream. Accordingly, the circulation in a closed vortex ring is equal throughout. Therefore the tip-vortex circulation of a single wing should be equal to that of the bound vortex circulation from which the lift is obtained by applying the Kutta-Joukowsky theorem. While the measurements in the tip vortex plane contain the information about the total circulation of the bound vortex and the change in circulation over the wing beat cycle, measurements parallel to the flow in the transverse vortex plane contain information about the local change in circulation across the span.

The comparison with direct force measurements was used to assess how suitable simple 2D PIV measurements are to estimate the time-resolved generated lift forces on the wing using the Kutta-Joukowsky theorem.

2 Methods and materials

The flapping-wing model was investigated in the low-speed wind tunnel (test section 2.90 width × 2.20 height × 4.90 m length, turbulence level < 1%) at the Technische Universität Darmstadt. Flow visualization using PIV and direct force measurements using a three-component balance were performed on fixed wings as well as flapping wings. Vertical force, horizontal force, and pitching moment coefficients were calculated from the balance, after taking into consideration the inertial forces and added mass effect in the case of the flapping wings. For the comparison between fixed wing and flapping wing measurements the effective angle of attack was calculated at mid wing-span.

Vorticity, circulation, the distribution of the circulation, and the lift coefficient were calculated based on visualization perpendicular to the flow stream. Due to the distance separating the measurement plane in the wake from the wing itself (distance 2.2 chord lengths (c)), a time lag between wing position and wake characteristics can be expected. This was compensated by delaying the comparison times by the separation distance divided by the free-stream velocity (Hubel 2006).

2.1 Flapping wing model

The model was about the size of a goose (wingspan 1.13 m; average wing chord (c) 0.141 m; Fig. 1). The

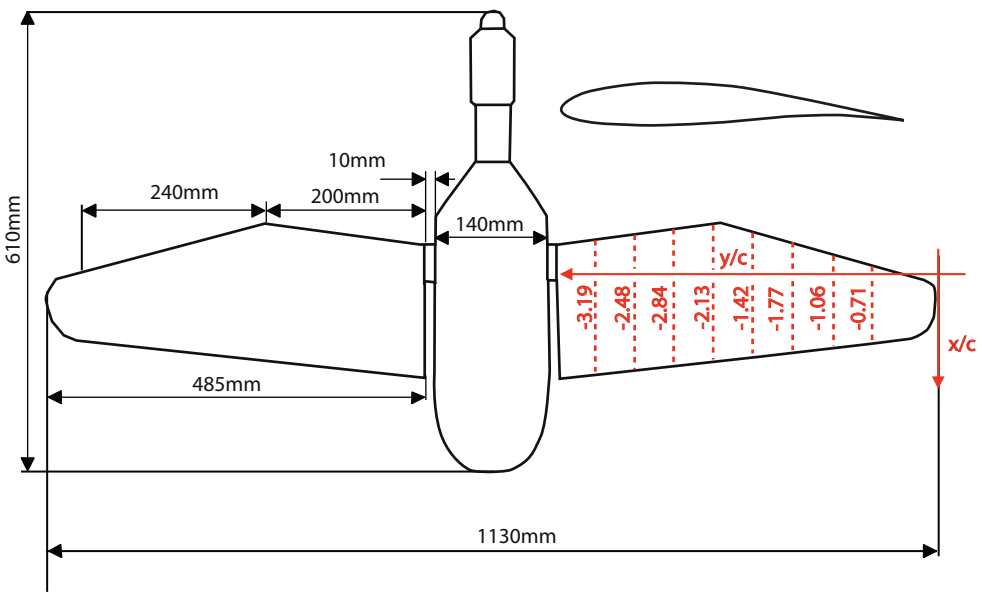

Fig. 1 Flapping wing model and wing profile

wings were made of fiberglass and epoxy resin. The model was powered by a direct current motor with a maximum flapping frequency of 2.2 Hz, controlled by a 4-Q-EC Servoamplifier. The body covered the driving mechanics and the three-component balance inside the model.

The static angle of attack (α_0) was adjusted at the shoulder joint. The flapping motion was asymmetrical, where the typical deflection below horizontal was 17° and above horizontal 27°. Depending on wind speed, the Reynolds number was between 28,000 and 141,000 (3–15 m/s) and the reduced frequency between 0.04 and 0.20, where the reduced frequency was defined as $k = (\pi fc)/U_\infty$ (f is wingbeat frequency, U_∞ the free-stream velocity, and c the average wing chord). *Re* and k were therefore typical of bird and large insect flight; however, similar to animal flight not independent from each other. The variation in Reynolds number and reduced frequency was accomplished by changes in wind speed, so that the highest reduced frequencies were accompanied by the lowest Reynolds numbers. Due to the large discrepancy between the wing profiles of resting versus flying birds, a realistic goose-like wing profile under loading was not available and a profile comparable to the proximal wing section of a gliding bird (cambered profile with rounded leading edge); a Wortmann Fx-60-126 was used across the entire wingspan.

2.2 Direct force measurements

Vertical force, horizontal force, and pitching moment were recorded as a function of time using an internal three-component balance, which was located between the model and the holder. The three-component balance was built of 4 force transducers: three vertical and one horizontal, mounted between two plates. Forces and moment were obtained by using the calibration matrix generated under single and combination loads. The measurement range (r) and precision (p) of the balance was as follows: vertical force ($r = \pm 115$ N, $p = 0.02\%$), horizontal force ($r = \pm 40.5$ N, $p = 0.6\%$) and pitching moment ($r = \pm 5.3$ Nm, $p = 1.5\%$).

Measurements under steady flow conditions with horizontally fixed wings, as well as under unsteady conditions with flapping wings, were performed. The measurement rate was between 300 and 600 Hz, depending on the flapping frequency. Up and downstroke were separated and the forces were interpolated over the amplitude angle and averaged over 10–15 wing beat cycles. A Butterworth low-pass filter was used to eliminate noise, such as the natural frequency of the wings (22 Hz) and balance (11 Hz), in the force measurements above 10 Hz.

Vertical-, horizontal and pitching coefficients were calculated from the averaged forces and moment in the following manner and referenced to a constant wing area, where the body area between the wings was included.

Vertical force coefficient (C_z)

$$C_z = \frac{2Fz}{\rho U_\infty^2 A} \tag{1}$$

Horizontal force coefficient (C_x)

$$C_x = \frac{2Fx}{\rho U_\infty^2 A} \tag{2}$$

Pitching moment coefficient (C_m)

$$C_m = \frac{2My}{\rho U_\infty^2 Ac} \tag{3}$$

where F_z is the vertical force, F_x is the horizontal force, M_y is the pitching moment, U_∞ the free-stream velocity, A the wing area, ρ the density, and c the average wing chord.

The average standard deviation for balance measurements over a wing beat cycle was typically in the range of 0.004–0.009 for the vertical force coefficient and in a range of 0.0007–0.003 for the horizontal force coefficient. The magnitude depended on the reduced frequency, increasing slightly with decreasing Re and higher flapping frequency, but exhibiting no correlation for different angles of attacks.

2.2.1 *Fixed wing*

In case of the measurements under steady flow conditions, the wings were fixed in the horizontal position and the static angle of attack was adjusted at the shoulder joint. Measurements at different static angles of attack ($\alpha_0 = 0°$–12°) and Reynolds numbers ($U_\infty = 28{,}000$, 56,000, 85,000, 113,000, 141,000) were performed. The lift coefficient versus angle of attack of a 2-D Wortmann Fx-60-126 Profile at $Re = 100{,}000$, published in (Althaus 1981) was taken as a reference. The 2D coefficients were transferred into 3D wing coefficients by using Prandtl's lifting line theory:

$$C_{\mathrm{L3D}} = C_{\mathrm{l2D}}\left(\frac{1}{1 + a_0/\pi \mathrm{eAR}}\right) \quad \text{with} \quad a_0 = \frac{\Delta C_{\mathrm{l2D}}}{\Delta \alpha^\circ}\frac{180}{\pi} \tag{4}$$

where AR is the aspect ratio of the wing and e the Oswald efficiency factor that was assumed to be 1, although the lift distribution on the model was presumably not perfectly elliptical.

2.2.2 *Dynamic forces and added mass effects on flapping wings*

Contrary to measurements under steady conditions, the results of force measurements on flapping wings comprise

not only the aerodynamic forces, but are a combination of the aerodynamic forces, dynamic forces and added mass effect. Therefore, in order to eliminate the contributions of the dynamics forces and added mass, each test case was performed twice, once with and once without wind. The test results without wind were then subtracted from the test results with wind. This was performed with the assumption that the inertial forces generated under wind load conditions were the same as when testing without wind. To determine the added mass effect additional measurements were performed using appropriately weighted tars in place of the wings. Here the assumption is made that these tars provide the same inertial forces as when testing with the actual wings themselves, the difference between the measurements with wings and rods (both performed without wind) being taken to represent the added mass force.

As a comparison to the measurements, the added mass force was calculated for a sinusoidal movement with a flapping frequency of 2 Hz. The centre of the added mass was assumed to be located at half of the wing chord and according to Walker 2002, the added mass force F_{add} can be calculated using the following equation:

$$F_{\text{add}}(r,t) = \frac{\pi}{4}\rho c^2(r)\dot{v}_n(r,t)\beta_n \mathrm{d}R \tag{5}$$

where R is the wingspan, r the position along the wingspan and β_n the added mass coefficient ($\beta_n = 1$).

For a flapping wing without a pitching movement the acceleration normal to the surface $\dot{v}_n$ is:

$$\dot{v}_n(r,t) = r\ddot{\theta}(t) \tag{6}$$

$$\theta(t) = \theta_1 \sin(\omega t) \tag{7}$$

$$\dot{\theta}(t) = \omega\theta_1 \cos(\omega t) \tag{8}$$

$$\ddot{\theta}(t) = -\omega^2\theta_1 \sin(\omega t) \tag{9}$$

where θ is the amplitude angle, θ_1 the maximum amplitude of 22° (neglecting the difference in deflection below and above horizontal) and ω the angular velocity.

2.2.3 *Flapping wings*

In order to obtain the difference between measurements under static conditions and measurements with flapping wings the results were shown as force coefficient versus angle of attack. For flapping wings the effective flow direction is a result of the horizontal free-stream velocity U_∞ and the vertical velocity component (v_z) caused by the flapping movement. For an infinite span 2D airfoil with only a plunge motion the effective angle of attack (α_{eff}) is:

$$\alpha_{\text{eff}}(t) = \alpha_0 + \arctan\frac{v_z(t)}{U_\infty} \tag{10}$$

where α_0 is the angle of attack under static conditions. However, because the wings pivot about the shoulder joint the local velocity changes along the span. If the wing bending is negligible there is a linear increase of the vertical velocity towards the wing tip. The increasing influence of the vertical velocity towards the tip results in an increasing effective angle of attack as shown in Fig. 2.

The effective angle of attack of the flapping wing was calculated at the mid-span position of the wing. The vertical velocity was calculated in following manner:

$$v_z(t) = \frac{h(t_2) - h(t_1)}{t_2 - t_1} \tag{11}$$

where t is time and h is the local horizontal position of the wing:

$$h(t) = r\sin\theta(t) \tag{12}$$

θ is the amplitude angle and r the distance from the wing root.

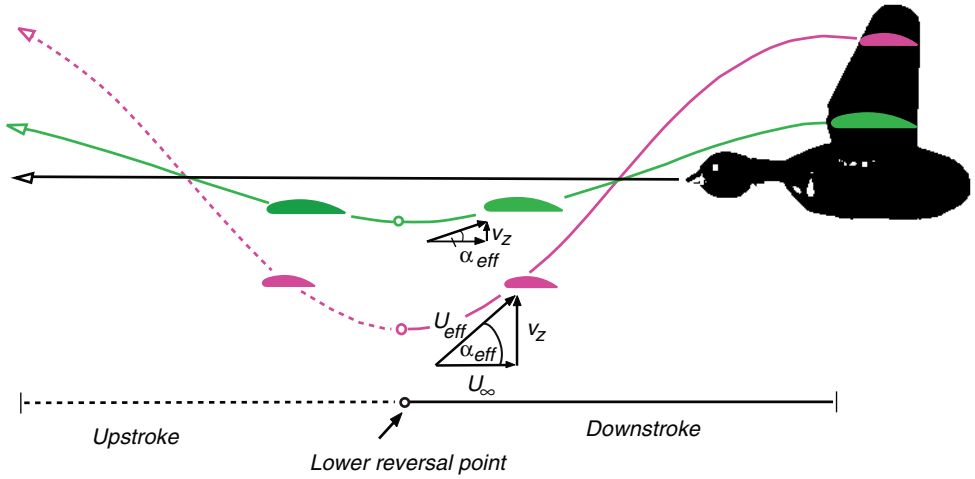

Fig. 2 Path of the proximal and distal wing areas, showing the increasing influence of the vertical velocity towards the wing tip

2.3 Flow visualization perpendicular to the flow stream (tip-vortex plane)

Particle image velocimetry (PIV) was used to capture the instantaneous velocity-field in the plane perpendicular to the flow stream The observation area was positioned 2.2 wing chords downstream of the trailing edge and was patched together using multiple camera positions due to the large flapping amplitude. The area was illuminated with a 200 mJ Nd:YAG double-pulse laser (New Wave Gemini 200), producing a pulse width of 10 ns and a variable duration between pulses. Images were taken with two CCD cameras (PCO SensiCam, 1,024 × 1,280 Pixels) mounted on a traversing system at the end of the test section. The vector field was calculated by using the adaptive correlation function in the standard two-dimensional PIV software system from Dantec Dynamics (Flow Manager®). The Interrogation area was 32 × 32 pixels with a 50% overlap, and a validation area that included 3 × 3 pixels. All further processing was carried out in Matlab® (MathWorks, Inc., Natick MA, USA). The first image in the wing-beat cycle was triggered via a rotational potentiometer in the model, while all subsequent images were triggered via pre-set time stepping. Because of the low pulse frequency of the laser (10 Hz), the wing-beat cycle was reconstructed from measurements over many wing beat cycles (25–50) to obtain sufficient resolution of the wing beat cycle. For each wing-beat cycle, 50–70 positions were sampled, depending on the wing-beat frequency. For the static wing measurements, in which the wings were fixed in the horizontal position, 500 image pairs were sampled and averaged. The standard deviation depended on the measurement position along the span, showing significant higher values for the area close to the body and increased with increasing reduced frequency.

The vorticity (ω) in the observation area was calculated from the vector field in the following manner:

$$\begin{aligned} \omega_x &= \frac{\partial w}{\partial y} - \frac{\partial v}{\partial z} \quad \text{(streamwise)} \\ \omega_y &= \frac{\partial u}{\partial z} - \frac{\partial w}{\partial x} \quad \text{(transverse)} \end{aligned} \tag{13}$$

Subsequently, the circulation (Γ) over the measurement plane was calculated through integration of the vorticity over the observation area in the following manner:

$$\Gamma = \iint_A \omega \mathrm{d}A \tag{14}$$

The circulation measured in the longitudinal tip vortices can be related to the lift (L) production via the Kutta-Joukowsky relation:

$$L = \rho U_\infty \int_{-b/2}^{b/2} \Gamma(y)\mathrm{d}y \tag{15}$$

Subsequently the lift coefficient (C_L) is given by:

$$C_\mathrm{L} = \frac{2L}{\rho U_\infty^2 A} = \frac{2}{U_\infty A} \int_{-b/2}^{b/2} \Gamma(y)\mathrm{d}y \tag{16}$$

In order to calculate the total circulation on the wings, the vorticity was integrated over the entire observation area. However, information about the distribution of the circulation can be obtained by separating the observation area in small strips (Fig. 3). The circulation of each strip was calculated in order to obtain the variation in circulation in spanwise direction.

The circulation was calculated from the vorticity field by integration over the strip area (A_i):

$$\Delta\Gamma_i = \iint_A \omega_{x,i}\mathrm{d}A_i \tag{17}$$

Subsequently, the change in circulation was normalized with the free-stream velocity (U_∞) and the average wing chord (c):

$$\Delta\gamma_i = \frac{\Delta\Gamma_i}{U_\infty c} \tag{18}$$

In order to obtain the distribution of the circulation rather than the local circulation itself, the change in circulation was summed over the wingspan, in the following manner:

$$\gamma_i = \sum_{j=1}^{i} \Delta\gamma_j \tag{19}$$

The distribution was compared to analytic calculations based on Multhopp's methode of solving Prandtl's lifting line theory by using linear equations at specific locations along the span (Multhopp 1938). Multhopp's methode is a quasi-steady estimation, which includes neither boundary effects, unsteady effects, body wing interactions, nor Reynolds number influence.

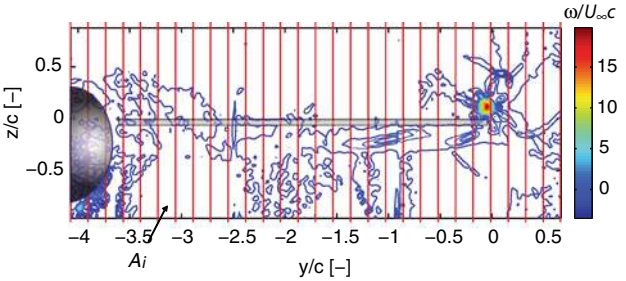

Fig. 3 Contours of normalized vorticity illustrated over partitioned observation areas (A_i) behind the wing (Trefftz plane)

2.4 Flow visualization parallel to the flow stream (transverse vortex plane)

In order obtain the change in circulation in the transverse vortex plane, PIV measurements in the vertical plane parallel to the flow direction were performed at several wingspan positions (Fig. 1).

The change of circulation in the spanwise direction was obtained by calculating the vorticity contained in the start/stop vortices leaving the trailing edge. The change of bound circulation on the wing in a time interval $\Delta t = t_{i+1} - t_i$ can be calculated in following manner:

$$\Delta\Gamma = \oint_{C_{i+1}} \vec{v}\vec{dl} = \iint_{A_{i+1}} \omega_y \mathrm{d}A \tag{20}$$

where the contour C_{i+1} or area A_{i+1} are given by the material lines of the fluid elements starting from a fixed line located immediately downstream of the trailing edge.

This method requires in theory the time-resolved acquisition of the wake-velocity field and a corresponding Lagrangian particle tracking but was simplified by using the streamwise velocity component to define the downstream contour of the area, i.e.

$$\mathrm{d}(z) = \frac{[u_i(z) + u_{i+1}(z)]}{2} \Delta t \tag{21}$$

where u_i and u_{i+1} are the velocities at the upstream and downstream end of the integration area and $\Delta t = T/N$, with N number of images over one wing-beat period T.

2.5 Comparison of PIV results (Tip and transverse vortex plane)

To compare the results from the tip-vortex plane and the transverse vortex plane, the change of circulation in the observation area perpendicular to the flow stream was calculated close to the same spanwise location where the transverse vortices were visualized. However, while the transverse vortex plane showed the vortex generation in a narrow plane, limited by the laser-light sheet thickness to approximately 3 mm, observations in the tip vortex plane require a certain size for the integration area (see A_i in Fig. 3) and consider the vortex development over a larger area along the span ($y/c = 0.22$).

2.6 Comparison of balance and PIV results (Tip vortex plane)

The comparison between PIV and balance results was complicated due to the fact that vertical and horizontal forces measured by the balance equal lift and drag only under horizontal fixed wing conditions. On flapping wings the incident flow direction changes constantly due to the changing influence of the vertical velocity along the span and during the wing beat cycle, leading to a constant change in lift direction. A direct comparison between balance results (C_z) and PIV results (C_L), would require a transformation of either C_z or C_L, which requires detailed information about the lift distribution on the wing over the whole wing beat cycle. Although the tip vortex measurements provided a good insight into this distribution (as can be seen later) it did not provide the information on the wing itself. Direct comparisons between the results of the two investigation methods were therefore not strictly possible, but assuming that the lift force dominated the vertical force component, the comparison of the vertical component value to the wake lift measurement was felt to be justified.

3 Results

3.1 Direct force measurements

3.1.1 Fixed wing

The comparison of the fixed wing measurements with the calculated 3D results based on (Althaus 1981) exhibits good agreement (Fig. 4a).

The lift coefficients at higher Reynolds numbers match well the literature based 3D calculation in the linear range of the wing. At higher angles of attack the stall induced decrease of the lift coefficient was slightly smoother in the case of the model. The differences were likely caused by the interference between body and wings of the model. The lift coefficients clearly showed a Reynolds number dependency: the results of measurements at $Re = 28{,}000$, were drastically lower. At such low Reynolds numbers there were apparently large areas of laminar flow while at higher Reynolds numbers the flow was predominantly turbulent. The dependence of the flow condition on the Reynolds number can also be seen in the drag polars (Fig. 4b) and the pitching coefficient in (Fig. 4c).

3.1.2 Dynamic forces and added mass effects on flapping wings

Following the procedure outlined above, example measurements are presented to indicate the magnitude of the corrections for inertial forces and added mass effects. In Fig. 5a and b the total measured force and the force measured without wind are shown. The subtraction of the results measured without wind reveals that the vertical force generation over the upstroke was considerably lower than during the downstroke (Fig. 5c). Furthermore, the results of the vertical force generated without wind showed

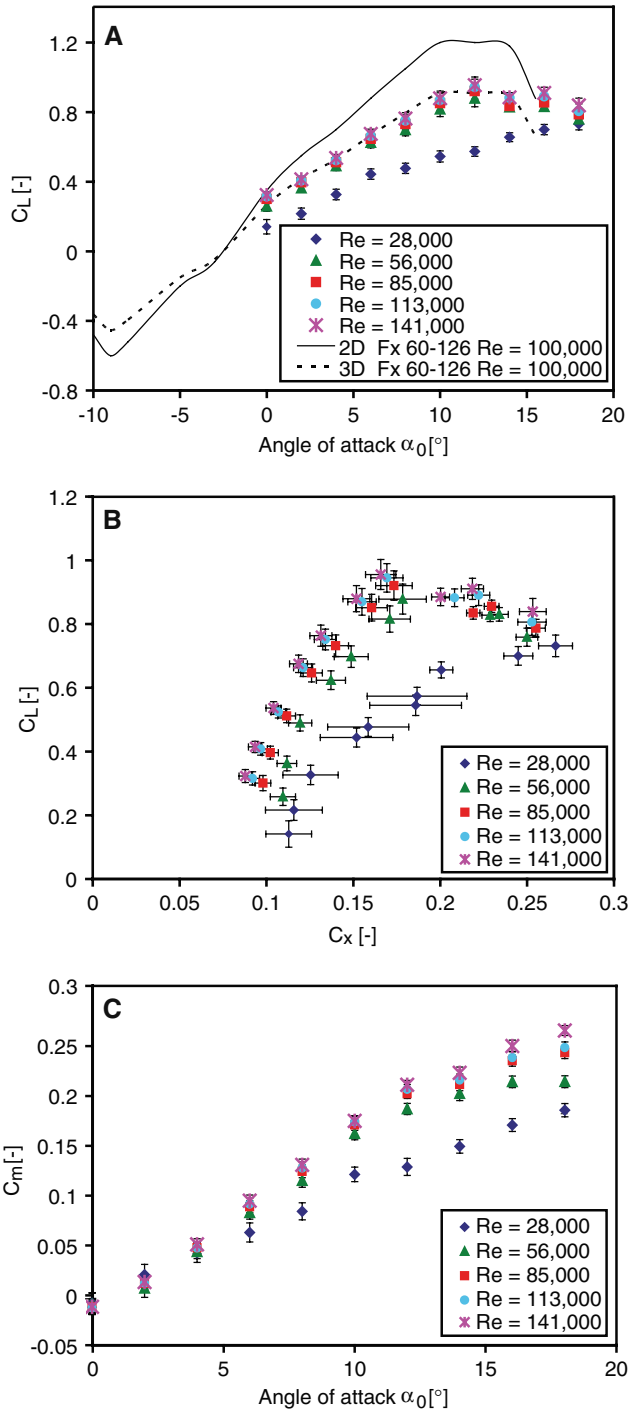

Fig. 4 **a** Lift coefficient (C_L) versus angle of attack (α_0) of the fixed wings at different Reynolds numbers compared to the lift performance of a Wortmann Fx 60-126 Profile (from Althaus 1981). The 3D results are derived from the 2D data using lifting line theory. **b** Lift coefficient (C_L) versus drag coefficient (C_D) of the fixed wings at different Reynolds numbers. **c** Pitching moment coefficient (C_m) versus angle of attack (α_0) of the fixed wings at different Reynolds numbers

that the inertial forces and added mass effects combined were of the same magnitude as the aerodynamic forces. The inertial forces were provided by the replacement of the wings with rods (Fig. 5d). The added mass was obtained by subtracting these results from the results from measurements with wings but without wind. According to these measurements the added mass force was less than 10% of the aerodynamic force in this particular example. Added mass forces are highly dependent on the acceleration of the wings, which do not always perform a sinusoidal movement, but recent studies in bird and insect flight show that values around 10% are very reasonable (Hedrick et al. 2004; Dickson and Dickinson 2004).

The comparison between the result of the added mass calculation and the measured added mass effect showed values of the same order of magnitude (Fig. 6). The effect of the non-sinusoidal movement was clearly visible in the phase difference to the sinusoidal results and the strong acceleration at the lower reversal point was reflected in the quickly increasing added mass force during this wing beat phase.

3.1.3 Aerodynamic forces and moments on flapping wings

The force generation on the wings changes over the wing beat cycle as well as with the spanwise position. While the balance results do not give insight into the events along the wingspan the change of the total force can be illustrated in relation to the phase of the wing beat cycle, indicated by the amplitude angle of the wing. The development of C_z during the wing beat cycle is correlated with the reduced frequencies, whereas the variation of k was either obtained through a change in the free-stream velocity (Fig. 7a) or the flapping frequency.

C_z during the downstroke was considerably higher than during the upstroke for all k. The flow conditions close to the reversal points were the most similar to steady flow conditions due to the minimum of vertical velocity. Nevertheless there was still a considerable influence of the aerodynamic phase lag, causing slightly different C_z values for the upper and lower reversal points. The Re dependency, known from the fixed-wing measurements, can also be seen at the reversal points, especially for the results at $Re = 28{,}000$, which are significantly lower than at higher Re.

For $k < 0.14$ a positive vertical force (C_z) was generated during both the downstroke and upstroke. However, for increasing k the difference of C_z during the downstroke and upstroke became larger to the point of generating negative C_z values during the middle parts of the upstroke. The increasing contribution of the vertical velocity component to the effective angle of attack at high k contained also the risk of flow separation. At $k = 0.20$ the effective angle of attack exceeded 48° at the wing tip (without consideration of the induced angle of attack). In this case, flow separation occurred on distal wing areas, which is indicated by

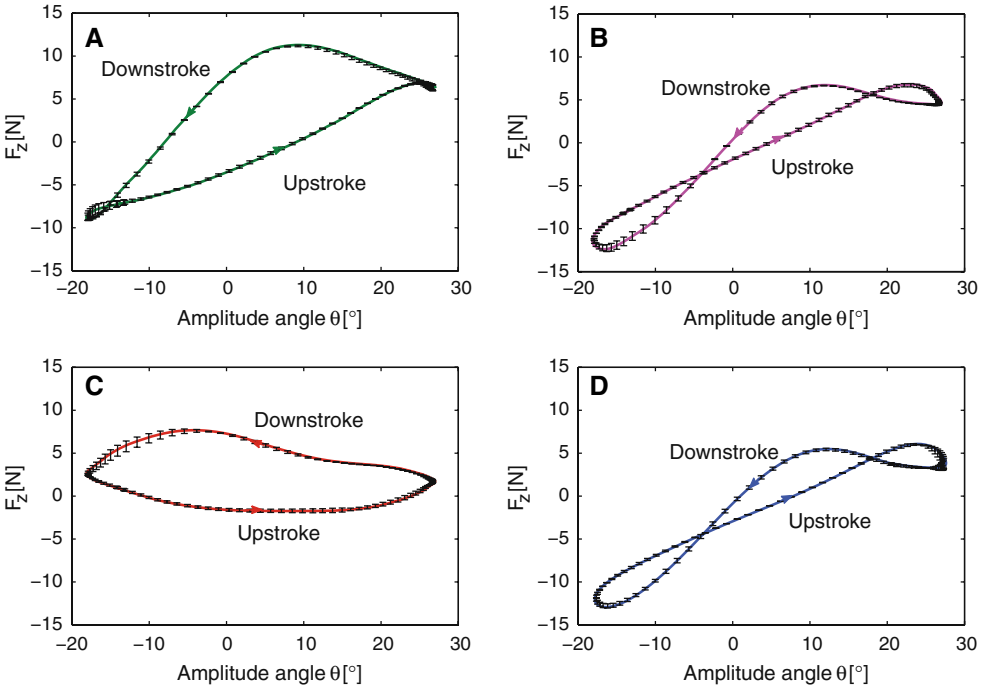

Fig. 5 Vertical force (F_z) versus amplitude angle (θ) for flapping wings at $\alpha_0 = 0°$ and $f = 2$ Hz including the standard deviation (displayed only for every third value). **a** Total vertical force at $U_\infty = 9$ m/s. **b** Vertical force (F_z) representing the inertial and added mass effects at $U_\infty = 0$ m/s. **c** Vertical aerodynamic force after the subtraction of the inertial and added mass effects at $U_\infty = 9$ m/s. **d** Measurement of inertial effects using rods instead of wings at $U_\infty = 0$ m/s)

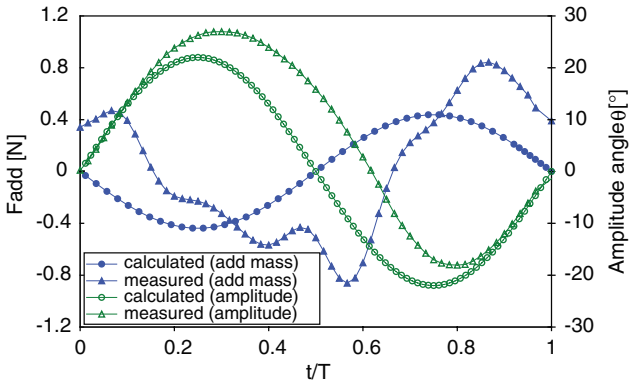

Fig. 6 Comparison of the measured added mass force (F_{add}) and calculated added mass force (based on Walker 2002) at $\alpha_0 = 0°$ and $f = 2$ Hz

reaching C_{z_max} (maximum lift) before reaching the maximum effective angle of attack, while otherwise at low k C_{z_max} occurred after reaching the maximum angle of attack due to the aerodynamic phase lag.

Not only C_z but also the C_x generation changed during the wing beat cycle (Fig. 7b). The deviations of drag generation at the reversal points from static conditions was indicated by lower and higher C_x values in relation to the C_x values at the reversal points. There was a considerable decrease in the C_x generation during the downstroke at all k. However, while the C_x generation during the upstroke was higher than at the reversal points for low k, there was an additional thrust generation during the upstroke at $k = 0.07$ due to the negative C_z generation at distal positions of the wings.

The static angle of attack was not only changed for the fixed wings but also varied in the case of the flapping wings, increasing the α_{eff} over the wing beat cycle at given k. C_z values increased with increasing α_0 during the downstroke as well as during the upstroke. While the change of C_z over the wing beat cycle for low α_0 was very similar, and the increasing α_0 acted comparable to an offset (Fig. 8a), effects such as flow separation changed the shape of the curve at higher α_0 especially at high k (Fig. 8b).

3.1.4 *Comparison between fixed and flapping wings*

A direct comparison between the results of the flapping wings and static measurements was obtained by showing C_z versus the (effective) angle of attack, which also allowed new insights into the C_z development over the wing beat cycle. At low k and relatively high Reynolds number ($k = 0.04$, $Re = 141{,}000$), through which the flow conditions tend to be more quasi-steady, the C_z values at the reversal points were close to the results of the static measurements (Fig. 9a). However, the maximum C_z value of the flapping wings at $\alpha_0 > 6°$ was significantly higher as C_{z_crit} for fixed wings. Therefore the C_z enhancement was considered as an unsteady effect, which occurs even at relatively low k. The influence of this unsteady effect increased at higher k, as can be seen in Fig. 9b. In addition, the consequence of flow separation is also clearly recognizable in the rapid decrease of the C_z values around the maximum effective angles of attack.

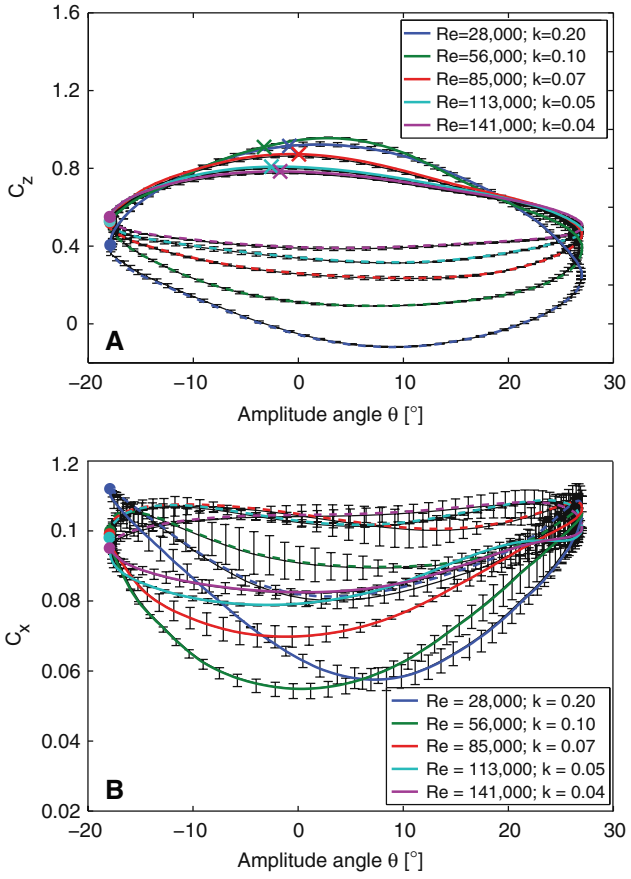

Fig. 7 **a** Vertical force coefficient (C_z) and **b** horizontal force coefficient (C_x) versus amplitude angle (θ) at different Reynolds numbers (Re) for $\alpha_0 = 4°$ and $f = 1.28$ Hz, including the standard deviation (displayed only for every third value). Upstroke (*dashed line*); downstroke (*continuous line*); lower reversal point (*circle*); maximum effective angle of attack (*cross*)

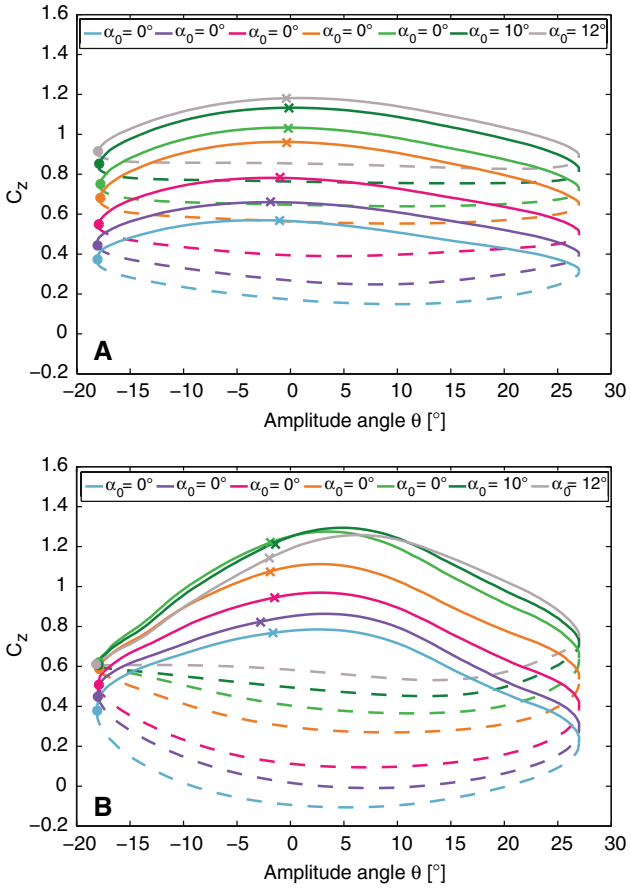

Fig. 8 **a** Vertical force coefficient (C_z) versus amplitude (θ) at different α_0 for $k = 0.04$ ($f = 1.28$ Hz, $Re = 141{,}000$). **b** Vertical force coefficient (C_z) versus amplitude (θ) at different α_0 for $k = 0.10$ ($f = 1.28$ Hz, $Re = 56{,}000$). Upstroke (*dashed line*); downstroke (*continuous line*); lower reversal point (*circle*); maximum effective angle of attack (*cross*)

But not only C_z values can yield insight into the flow conditions on the wings. Thrust generation and flow separation are visible in the comparison between the C_x values under fixed-wing conditions and those generated by flapping wings. At relative low reduced frequencies the C_x values increase during the upstroke but decrease remarkable during the downstroke because of the high thrust generation (Fig. 9c). The non-linear increase in drag generation increased the inclination of the curves and the aerodynamic phase shift with increasing α_0.

At higher k flow separation effects have dramatic influences at higher α_0 (Fig. 9d). There was a sudden increase in the C_x values at high α_{eff} during the downstroke, due to the flow separation over large parts of the wings. The dominant stall influence was also recognizable in the C_m values. While the curve shape at low α_0 was nearly linear the flow separation caused a significant bend in the curve progression (Fig. 9e).

3.2 Flow visualization perpendicular to the flow stream

The circulation (Fig. 10a) and the distribution of the circulation (Fig. 10b) behind fixed wings showed that the roll-up process behind the wing was not completed $2.2c$ downstream of the wing. The circulation was highest close to the wing tip region where the tip-vortex was located. In addition, there was a significant amount of the circulation distributed along the span. There was a considerable amount of negative circulation near the body, where the standard deviation was significantly higher than in other parts of the observation area.

The comparison with simple quasi-steady calculations according to Multhopp (Fig. 11) showed that the values based on the Multhopp calculation at high Re are of the same magnitude as the PIV based calculations and take a similar course apart from the area near the body. The change in the distribution of the circulation over the wing beat cycle was clearly visible at all reduced frequencies

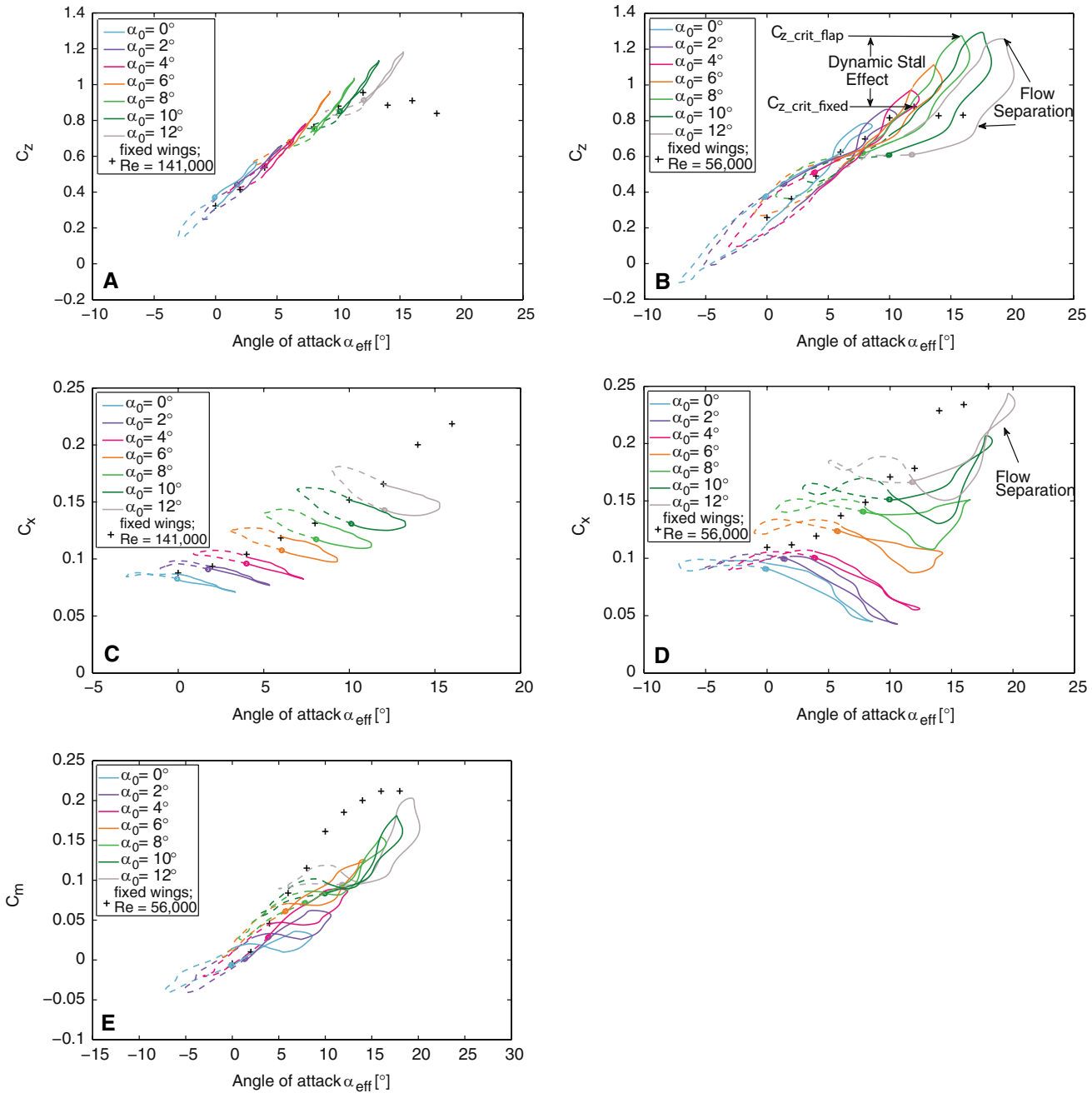

Fig. 9 Force coefficient versus effective angle of attack (α_{eff}) at different static angle of attacks (α_0). **a** C_z for $k = 0.04$ ($f = 1.28$ Hz, $Re = 141{,}000$). **b** C_z for $k = 0.10$ ($f = 1.28$ Hz, $Re = 56{,}000$). The flapping wing results show the following unsteady effects: the critical vertical force coefficient (C_{z_crit}) for flapping wings is distinct higher than for fixed wings (indicating dynamic stall); different C_z values at identical α_{eff} (indicating aerodynamic phase lag) and a rapid drop in C_z at high α_{eff} (indicating flow separation) with long delays in reattachment (hysteresis). **c** C_x for $k = 0.04$ ($f = 1.28$ Hz, $Re = 141{,}000$). **d** C_x for $k = 0.10$ ($f = 1.28$ Hz, $Re = 56{,}000$). Flow separation indicated by the sudden increase of C_x at $\alpha_0 \geq 6°$. **d** Pitching moment coefficient (C_m) versus effective angle of attack (α_{eff}) at different static angle of attacks (α_0) for $k = 0.10$ ($f = 1.28$ Hz, $Re = 56{,}000$). Upstroke (*dashed line*); Downstroke (*continuous line*); lower reversal point (*circle*)

(Fig. 12a, b). In agreement to the quasi-steady assumption the highest lift was generated during the downstroke whereas the lowest lift was produced during the upstroke. At the reversal points the distribution was quite similar to one another in case of a relatively low reduced frequency (Fig. 12a). However, there was a location shift in the onset of the circulation due to the asymmetrical amplitude of the flapping motion. At a considerably higher k (Fig. 12b) the

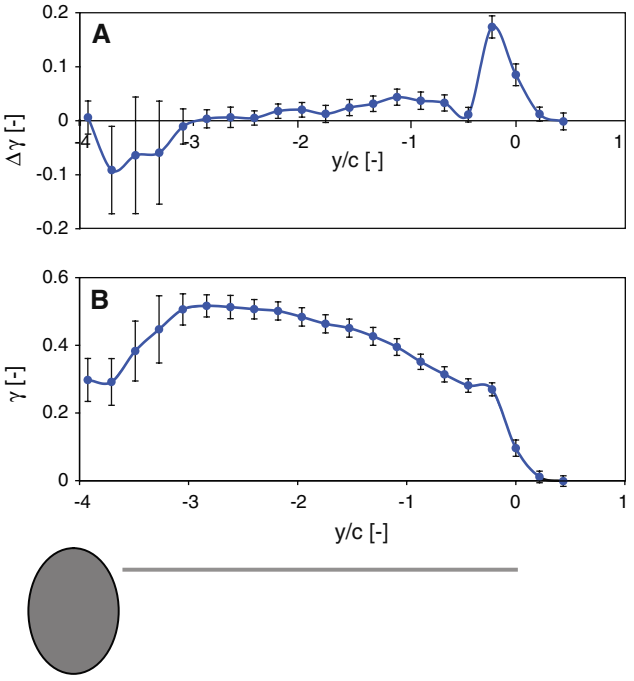

Fig. 10 **a** Normalized circulation ($\Delta\gamma$) and **b** distribution of the normalized circulation (γ) over the span (y/c) in the wake of the model with fixed wings (tip-vortex plane) at $\alpha_0 = 8°$ for $Re = 113{,}000$, averaged over 500 image pairs

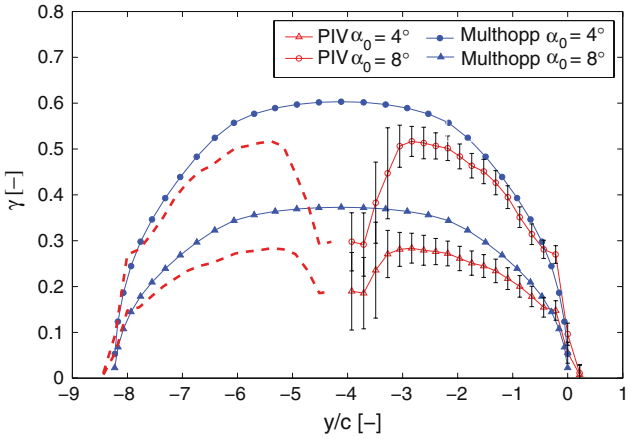

Fig. 11 Distribution of normalized circulation (γ) over the span (y/c) in the wake of the model with fixed wings at $\alpha_0 = 4°$ and $\alpha_0 = 8°$ in comparison with calculated values (based on Multhopp) at $Re = 113{,}000$, averaged over 500 image pairs

aerodynamic phase lag caused a distinct difference in the distribution at the reversal points. While at a low reduced frequency ($k = 0.05$) positive lift was generated over the entire wing-beat cycle, negative lift was generated in the phase close to the horizontal position during the upstroke at high reduced frequencies ($k = 0.16$). A closer view at the change in the distribution at high k over the downstroke with elimination of the shift in the onset of the circulation

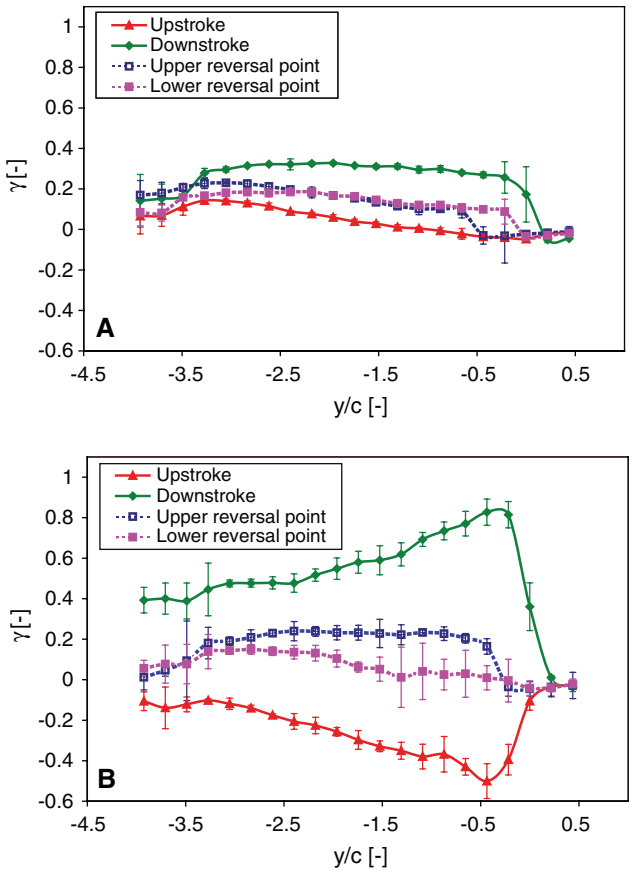

Fig. 12 Distribution of normalized circulation (γ) over the span (y/c) in the wake of the model (tip-vortex plane) at the upper and lower reversal points as well as for the instant when the wing pass through the horizontal position during the upstroke and downstroke: **a** at $k = 0.05$ ($f = 1.28$ Hz, $Re = 113{,}000$, $\alpha_0 = 4°$); **b** at $k = 0.16$ ($f = 2.02$ Hz, $Re = 56{,}000$, $\alpha_0 = 4°$)

due to wing motion showed that the peak in circulation shifted from the tip towards the root (Fig. 13). This is a clear indication of flow separation which then proceeded from the tip to the root. The flow separation during the downstroke also explains the large difference between the circulation distribution at the upper and lower reversal points compared to the results at lower k.

3.3 Comparison of balance and PIV results (Tip vortex plane)

The comparison between the C_L and C_z values showed a constant offset in the coefficients between the balance and PIV results (Fig. 14a–c). The offset was calculated by using unconstrained nonlinear optimization to determinate the optimal match of the PIV and balance results at different Re, k and α_0; resulting in an average offset value of 0.29 ± 0.019. To permit a comparison of the relative changes during the wing beat cycle the minimum on the

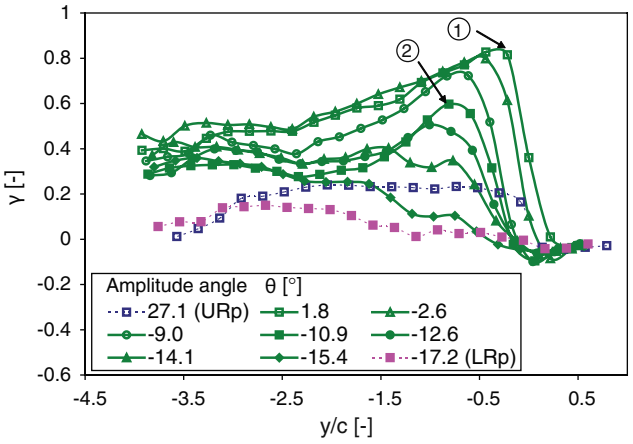

Fig. 13 Distribution of normalized circulation (γ) over the span (y'/c) in the wake of the model for part of the downstroke at $k = 0.16$ ($f = 2.02$ Hz, $Re = 56{,}000$, $\alpha_0 = 4°$, tip-vortex plane, wing-fixed coordinate system y', *URp* upper reversal point, *LRp* lower reversal point

vertical scale was shifted while the scaling of both axes remained the same. The change in the circulation during the wing beat cycle calculated from the PIV results complied well with the balance results. The maximum change in circulation over the wing beat cycle was used to define the discrepancy between PIV and balance results, comparing the difference between maximum and minimum of C_z and C_L within the wing beat cycle at different k. At $k = 0.05$ and $k = 0.08$ discrepancy was 3.29 and 3.48% referring to the balance results. At $k = 0.16$ the discrepancy was much higher (26.6%), due to the high differences during the second phase of the downstroke, when α_{eff} is high above α_{crit} and unsteady effects and flow separation occurred. The reason for the necessary offset has not been resolved.

3.4 Comparison of PIV results (Tip and transverse vortex plane)

The comparison of the change of circulation calculated from the different planes showed a similar magnitude and shape (Fig. 15a). The agreement depends on the Reynolds number and the reduced frequency. High Reynolds numbers and low reduced frequency measurements showed a better agreement than at highly unsteady conditions. However, the turbulence and influence of the pressure equalization due to the wing/body gap increased with increasing Reynolds number and reduced frequency in the area close to the body (Fig. 15b). The fluctuation and turbulence level in the area near the body is significantly higher than in the distal regions, which is in agreement with the high standard deviation of the circulation in this area for fixed wings (Fig. 10). In addition, the change in

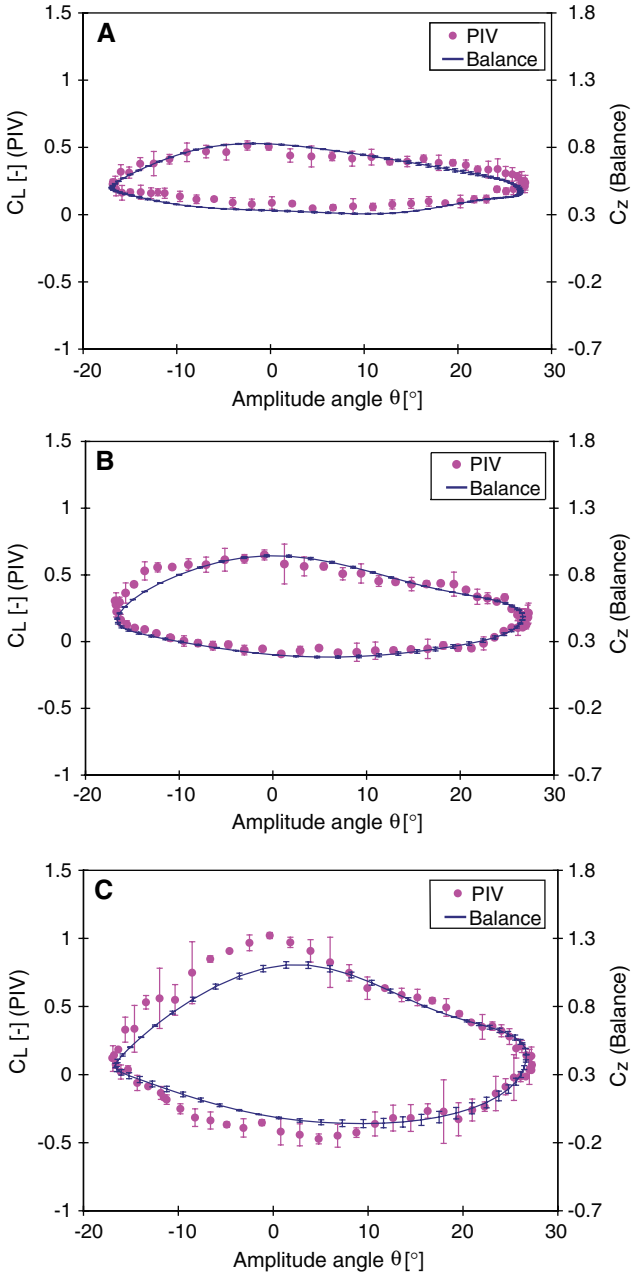

Fig. 14 Comparison of lift coefficient (C_L), calculated from the visualized circulation, and vertical force coefficient (C_z) measured with the balance over the wing beat cycle at different k: **a** at k = 0.05 ($f = 1.28$ Hz, $Re = 113{,}000$, $\alpha_0 = 4°$); **b** at $k = 0.08$ ($f = 2.02$ Hz, $Re = 113{,}000$, $\alpha_0 = 4°$); **c** at $k = 0.16$ ($f = 2.02$ Hz, $Re = 56{,}000$, $\alpha_0 = 4°$). The PIV coefficients are averaged over 25 image pairs, the balance results were displayed on a second y axis due to the constant offset of 0.3 in the force coefficients, while the scaling was the same, the standard deviation is included for both PIV and balance measurements (displayed only for every third value for the balance)

circulation at this position was asymmetric and the positive and negative circulation was not equalized at the end of the wing-beat cycle, showing the three-dimensional nature of the wake.

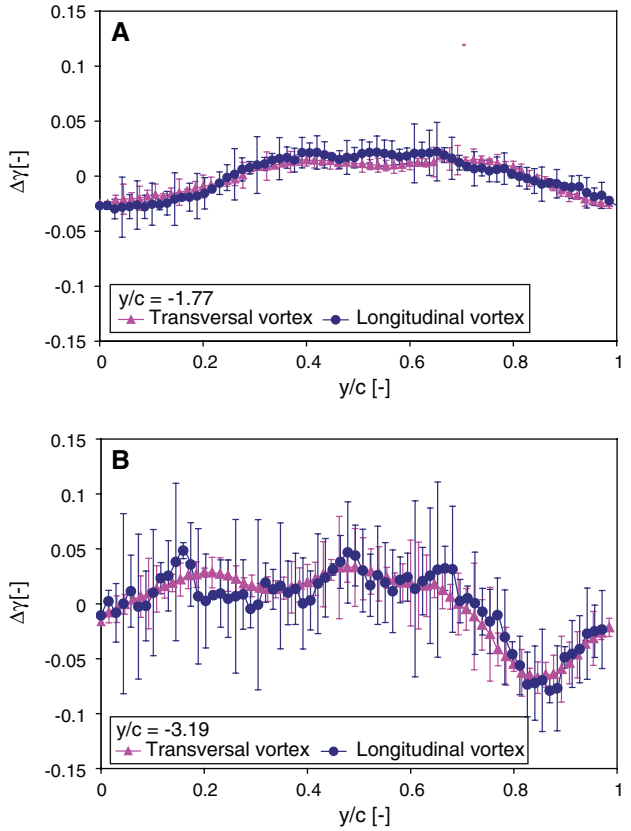

Fig. 15 Change in circulation ($\Delta\gamma$) over the wing-beat cycle calculated from the tip-vortex plane (longitudinal vortex) perpendicular to the flow stream and the transverse-vortex plane (transversal vortex) parallel to the flow stream at $k = 0.08$ ($f = 2.02$ Hz, $Re = 113{,}000$, $\alpha_0 = 4°$). **a** At a distal wingspan position ($y/c = -1.77$), **b** at a proximal wingspan position ($y/c = -3.19$)

4 Discussion

4.1 Direct force measurement

The results of the fixed wings measurements with the balance, which were used for reference purposes, showed good agreement with the results of the 2D Wortmann profile (Althaus 1981) after applying lifting line theory to account for the finite wingspan.

Consideration of inertial forces and the added mass effect, revealed that the vertical force generation over the upstroke was considerably lower than during the downstroke, agreeing with the expectation based on quasi-steady assumptions. At moderate k and Re the inertial forces were slightly lower then the aerodynamic forces and the added mass effect was about 10%, agreeing in magnitude with calculations based on a sinusoidal movement.

Lift was produced mainly by the wings since the body itself generated very little lift ($C_{L\_Body} \approx 0.02$–0.03). In contrast to the lift, the body was the main source of drag ($C_{D\_Body} \approx 0.08$).

Increasing the static angle of attack α_0 for flapping wings resulted in a change in C_z, similar to the that of an oscillating airfoil described by McCroskey (1981). According to McCroskey the high α_{eff} in combination with the wing movement induce a high fluctuating pressure field which is related to the delayed stall phenomena.

Provided that the flapping frequency, angle of attack and amplitude is high enough, a well-structured leading edge vortex (LEV) is formed. As long as the LEV remains stable it leads to a high lift coefficient. However, as soon as the vortex is shed at the trailing edge, stall sets in and the reattachment of the flow with decreasing α_{eff} is delayed, clearly expressed by a large hysteresis loop. This hysteresis loop was clearly seen in the flapping wing results, when α_{eff} was high enough due to high k and high α_0. At the same time the onset of stall is related to an abrupt increase in drag and pitching moment, likewise clearly visible in the balance results. Contrary to insect flight, where additional lift generation due to unsteady effects, such as wake capture, rotational lift and delayed stall, has been substantially documented during the last decade (Bomphrey et al. 2005; Dickinson et al. 1999; Lehmann 2004), Vertebrate flight has often been treated as quasi-steady, and only recently has it been questioned whether or not the delayed stall effect also plays a role in bird and bat flight. Investigations on small birds like hummingbirds and swifts are in progress. A leading-edge vortex was found so far on static swift wings (Videler et al. 2004), which are characterized through sharp leading edges and high swept-back configurations (delta wing like), both features supporting the development of a leading edge vortex. In the case of hummingbirds, whose flight style shows similarities to large insect flight, a dynamically scaled flapping flat plate ($Re \sim 4{,}000$) clearly showed the development of a LEV during mid upstroke and downstroke but could not be visualized on the bird itself (Tobalske et al. 2008). The occurrence of LEVs in bat flight (<10 g, $U_\infty = 1$ m/s) was recently discovered (Muijres et al. 2008). The present observations of high vertical force coefficients of the flapping goose model at higher α_{eff} leads to the assumption that there were phases in the wing beat cycle when a leading edge vortex developed, in spite of round leading edges and the lack of similarity to insect flight. However, due to the 3D wing movement, the balance results gave no information about the stability of the LEV. According to Ellington (1999) and Liu et al. (1998) the lateral flow, as a result of the flapping movement, is responsible for the stabilization of the leading edge vortex. However, Birch and Dickinson (Birch et al. 2004) claimed that the importance of the lateral flow depends on the Reynolds number. To what extent the lateral flow played a role in the present case is unknown; a lateral flow component could not be visualized behind the wing and probably requires

measurements on the surface of the wing itself. Measurements on the wing could also confirm the assumption that the delayed stall effect was responsible for the enhanced lift generation, by detecting the LEV. Of course measurements on a flapping wing introduce other, rather difficult obstacles to the experimental configuration.

4.2 Flow visualization perpendicular to the flow stream (tip-vortex plane)

One of the goals of the investigation was to obtain an answer to the question of whether 2D PIV measurements can be used to obtain the forces on flapping wings, based on the Helmholtz vorticity laws and lifting line theory. One has to be aware of the limitation of the 2D measurement procedure. The aerodynamic forces on an object can be obtained by using the control-volume approach and applying the momentum equation and taking into account the total surface forces over the entire control volume. However, even in steady locomotion such as in cruising flight, the propulsion area and actually the whole body of the animal is subjected to a periodic acceleration and deceleration. These unsteady flow conditions around the body lead to the problem that an exact determination of aerodynamic or hydrodynamic forces requires measurement of the net flow of momentum out of the control volume surface as well as the time rate of change due to the unsteady fluctuations inside the control volume itself (Dabiri 2005). So, to obtain the actual forces, the whole volume of the flow field has to be recorded by time-resolved tomographic PIV (Arroyo and Hinsch 2008), to fulfill the requirements of the momentum equation, which up to now has only been possible for very limited volumes. 2D measurements by nature can therefore only provide an approximation of the actual forces.

Measurements downstream of the trailing edge require the consideration of the time delay between the visualization and the events on the wing itself. However, even if the comparison of the change in circulation obtained by PIV and balance measurements confirm the usability of the free-stream velocity to relate the visualization in the observation plane with the wing position, one should keep in mind that due to the spanwise dependency of the roll up process, the vorticity information contained in the observation plane at any particular instant originates at different times across the wingspan.

Nevertheless, the distribution of the circulation estimated from the visualization in the tip-vortex plane $2.2c$ behind the wings agreed well with the distribution based on simple quasi-steady assumptions, except for the near-body region. Negative circulation was generated close to the body due to the pressure equalization in the gap between body and wing and high turbulence and laser light sheet reflections led to high standard deviations of the velocity measurements. The total circulation based on the Multhopp calculation was significant higher that the PIV based results due to the poor modeling of the near-body region.

The circulation distribution over the wing beat cycle exhibited, in addition to an increasing aerodynamic phase lag, an increasing difference between upstroke and downstroke with increasing k. At higher k negative circulation were observed at the distal areas of the wing during the upstroke. Flow separation can be observed over the downstroke, indicated by the change in location of the peak in circulation towards the body, which also provides the explanation for the increasing difference in circulation at the two reversal points.

4.3 Comparison of balance and PIV results (tip vortex plane)

PIV and balance results showed good agreement in the change of circulation over the wing beat cycle. However, the degree of accuracy was related to the flow conditions and decreases with increasing k. This can be explained partly due to the comparison of C_L and C_z, while at low k ($k = 0.05$) the difference between the two coefficients was estimated to reach a maximum of about 1.6% of C_L: there is a significant increase in the difference with increasing k ($k = 0.16$, 4.2%; $k = 0.25$, 8.6%). However, the main source of the difference is the increasing influence of flow separation and unsteady effects, as is evident from the agreement at high k in wing beat phases of low α_{eff}, but less accuracy in phases of extraordinary high α_{eff}.

Independent of Re, k and α_0 there was constant offset of 0.29 ± 0.019 in the absolute value of the lift and vertical force coefficient of the PIV and balance. There are two possible explanations for this offset. One is an error in the measurements technique itself either in the balance or PIV measurements. Another possibility was that significant information was missing in the force calculations based on the flow visualization due to the limitation to 2D measurements and the downstream position of the observation area.

To eliminate any mistake in the direct force measurements, additional fixed wing measurements were performed using an external balance and different software. Apart from the results at $Re = 28{,}000$, the discrepancy between external and internal balance results was lower than 5%. The discrepancy was most likely the result of the interference between model and support and due to the external balance range of $\pm 6{,}000$ N, which limited the resolution. Furthermore the balance results at $Re = 56{,}000$ matched the expected literature results of the Wortmann FX 60-126 profile at $Re = 100{,}000$.

A mistake in the PIV calculation was dismissed due to the fit in the change of circulation in the balance and PIV

results as well as with the results in the transverse vortex plane.

Important evidence was that the offset was constant for the non-dimensional coefficient therefore the offset of the force itself depended on the free stream velocity which made it unlikely to be an offset in the measurement equipment itself.

The observation area was considered as appropriately large to avoid the loss in circulation, especially because the vector fields showed that the circulation was located close to the wing tip. A loss of information caused by the slight change in orientation of the vortex with respect to the observation plane was considered; however, it was ruled out as an explanation because the offset did not change significantly for different static angles of attack.

The obstruction based on the frontal area was less the 0.4% and the distance to each wind tunnel wall > 0.8 m, eliminating any influence of vortex wall interaction under consideration of the magnitude of the generated forces.

In the hummingbird related investigations of the flat plate robotic wing (Tobalske et al. 2008) the calculated force from the circulation of the tip vortex matched the measured forces within one chord length but showed only 50% of the measured forces at $2c$, which was explained by the instability of the shed vortices. However, any instability and dissipation should be influenced by the change in flow speed and should increase for low speed due to the constant distance between observation area and trailing edge.

Wake vortex added mass effects can lead to an underestimation of the necessary forces in swimming and flying using wake measurement (Dabiri 2005). However, while they represent an additional force that contributes to the necessary power input, vortex added mass effects went undiscovered for a long time because they cannot be noticed in the time averaged forces. Only recently, with increasing time resolved measurements, have they been examined more closely. However, the magnitude of the vortex added mass effect for these measurements can be assumed to be small and the offset is still present in the time averaged forces for balance and PIV results, therefore the vortex added mass effect does not provide a sufficient explanation for the difference in PIV and balance results.

Up to now none of these effects offered a satisfying explanation for the observed offset. While influences of dissipation, added mass and loss off information due to the limited 2D measurements certainly are a source of possible errors, the loss would be assumed to be much smaller than the observed 100%. Any explanation so far is in contradiction to the fact that while the absolute value differed of a constant value of 0.29 (independent of Reynolds number and reduced frequency) the relative change in circulation was in agreement with the results of the direct force measurements.

The body wing area was a source of high turbulence and the gap between wing and body, which was mechanically necessary, was an additional complication. The gap allowed a considerably pressure equalization between the upper and lower surfaces of the wing, as could be seen in the decline in circulation in the near-body region. In addition, the laser light reflections off the body made the flow measurements more difficult and increased the standard deviation of the velocity values in this region. The comparison between quasi-steady calculations (Multhopp) and experimentally acquired distributions supports the theory of a wing/body gap explanation due to the good agreement in circulation in the distal areas, but significantly different absolute values due to the negative circulation in proximal areas (Fig. 13). The Multhopp based calculation for the absolute force generated were in the range of the results from the direct force measurements, while the PIV results were considerably lower, which might be an additional indication that the difference is due to the drop in circulation in the near body area. However, there is no satisfying explanation to why this drop in circulation should not be reflected in the force measurements.

After careful consideration of possible fluid dynamic explanations as well as errors in the measurement techniques itself, the authors have yet to find a sufficient explanation for the extremely high value of the offset.

4.4 Comparison of PIV results (Tip and transverse vortex plane)

The comparison of the change in circulation over the wing beat calculated from the two perpendicular planes (tip and transverse) showed very good agreement. Differences can be explained by the fact that the distribution in the wake differ from the distribution on the wing itself due to the roll-up process and a highly three-dimensional flow field. The turbulence and highly three-dimensional flow conditions close to the body caused significantly higher disturbances in the results of the transverse vortex plane than the tip vortex plane.

5 Conclusions

Wake PIV measurements in two planes perpendicular to each other (tip and traverse vortex plane) were performed in addition to direct force measurements with a three-component balance, with the goal to verify the appropriateness of quasi-steady assumptions in the range of bird flight and the qualification of simple 2D PIV measurements to obtain the generated forces on flapping wings.

The results of the direct force measurements were qualified to give good insight into the flow conditions on

the wings. Even if the measurements on flapping wings are difficult to perform and require certain assumptions and simplifications, unsteady effects and flow separation could clearly be recognized.

Typically the balance results showed a significantly higher vertical force coefficient for flapping wings compared to the maximum coefficient of the fixed-wing results. It is postulated that this was caused by the delayed stall effect, a phenomenon which occurs on plunging or pitching airfoils. This indicates that the flow around the wing cannot be simplified as a quasi-steady flow.

When flow separation occurs over large parts of the wing, the influence could be seen in a hysteresis loop in the vertical force coefficient and a sudden increase in horizontal force generation.

One should keep in mind that due to the movement around a shoulder joint, the flow conditions are entirely three dimensional and the flow conditions change along the span. While the flow can be still attached at proximal wing positions, unsteady effects such as delayed stall, can be developed at distal positions and flow separation occurs in the outward direction. The results of the balance showed only the net result of different conditions along the wingspan and different effects as flow separation and delayed stall could even be compensating.

It was assumed that the measurements in the tip vortex plane provide the absolute value of the circulation on the wing itself as well as the change in circulation and the distribution along the span over the wing beat cycle. While the absolute value of the circulation was not reliable, the change in circulation over the wing beat cycle agreed well with the balance results and with the calculations from the transverse vortex plane measurements. The agreement is typically higher at high Reynolds numbers and low reduced frequencies and tended to decline under highly unsteady conditions and highly three-dimensional flow conditions.

The measurements in the tip vortex plane and the transverse vortex plane at different positions along the wingspan provided insight into the distribution of the circulation. However, measurements close to the body were more difficult to perform. The change in distribution over the wing beat cycle obtained through the measurements in the tip vortex plane showed clear indications of flow separation, but further measurements on the wing itself would be necessary to show the separation and assumed delayed stall effect conclusively. The agreement in the distribution of the circulation obtained by wake measurements with the circulation distribution on the wing itself depends on the proximity of the measurements to the wing as well as the flow velocity, reduced frequency and the spanwise position. Nevertheless, with due consideration of the factors influencing the PIV accuracy, this method can be used to provide useful insights into the flow conditions on a model with flapping wings.

References

Althaus D (1981) Wortmann, F.X.: Stuttgarter Profilkatalog Braunschweig

Arroyo M, Hinsch K (2008) Recent developments of PIV towards 3D measurements. In: Particle image velocimetry, vol 112. Springer, Berlin, pp 127–154

Birch JM, Dickson WB, Dickinson MH (2004) Force production and flow structure of the leading edge vortex on flapping wings at high and low Reynolds numbers. J Exp Biol 207:1063–1072

Bomphrey RJ, Lawson NJ, Harding NJ, Taylor GK, Thomas ALR (2005) The aerodynamics of *Manduca sexta*: digital particle image velocimetry analysis of the leading-edge vortex. J Exp Biol 208:1079–1094

Cloupeau M, Devillers JF, Devezeaux D (1979) Direct measurements of instantaneous lift in Desert Locust; comparison with Jensen's experiments on detached wings. J Exp Biol 80:1–15

Dabiri JO (2005) On the estimation of swimming and flying forces from wake measurements. J Exp Biol 208:3519–3532

Dickinson MH, Gotz KG (1996) The wake dynamics and flight forces of the fruit fly *Drosophila melanogaster*. J Exp Biol 199:2085–2104

Dickinson MH, Lehmann F, Sane SP (1999) Wing rotation and the aerodynamic basis of insect flight. Science 284:1954–1960

Dickson WB, Dickinson MH (2004) The effect of advance ratio on the aerodynamics of revolving wings. J Exp Biol 207:4269–4281

Drucker EG, Lauder GV (1999) Locomotor forces on a swimming fish: three-dimensional vortex wake dynamics quantified using digital particle image velocimetry. J Exp Biol 202:2393–2412

Ellington CP (1999) The novel aerodynamics of insect flight: applications to micro-air vehicles. J Exp Biol 202:3439–3448

Hedrick TL, Usherwood JR, Biewener AA (2004) Wing inertia and whole-body acceleration: an analysis of instantaneous aerodynamic force production in cockatiels (*Nymphicus hollandicus*) flying across a range of speeds. J Exp Biol 207:1689–1702

Hubel T (2006) Untersuchungen zur instationären Aerodynamik an einem vogelähnlichen Flügelschlagmodell In: Department of Biology. PhD, Darmstadt University of Technology, Darmstadt, p 194

Lehmann F-O (2004) The mechanisms of lift enhancement in insect flight. Naturwissenschaften 91:101–122

Liu H, Ellington CP, Kawachi K, Van Den Berg C, Willmott AP (1998) A computational fluid dynamic study of hawkmoth hovering. J Exp Biol 201:461–477

Maybury WJ, Rayner JMV (2001) The avian tail reduces body parasite drag by controlling flow separation and vortex shedding. Proc R Soc B Biol Sci 268:1405–1410

McCroskey WJ (1981) The phenomenon of dynamic stall. NASA TM-81264

Mueller TJ (2001) Fixed and flapping wing aerodynamics for micro air vehicle applications. Progress in astronautics and aeronautics, vol 195, AIAA, New York

Muijres FT, Johansson LC, Barfield R, Wolf M, Spedding GR, Hedenstrom A (2008) Leading-edge vortex improves lift in slow-flying bats. Science 319:1250–1253

Multhopp H (1938) Die Berechnung der Auftriebsverteilung von Tragflügeln. Luftfahrt-Forschung 4:153–169

Rayner JMV, Gordon R (1998) Visualization and modelling of the wakes of flying birds, vol 13. Gustav Fischer Verlag, Jena

Sane SP (2003) The aerodynamics of insect flight. J Exp Biol 206:4191–4208

Spedding GR (1987a) The wake of a Kestrel (*Falco tinnunculus*) in flapping flight. J Exp Biol 127:59–78

Spedding GR (1987b) The wake of a Kestrel (*Falco tinnunculus*) in gliding flight. J Exp Biol 127:45–57

Spedding GR (1986) The wake of a Jackdaw (*Corvus monedula*) in slow flight. J Exp Biol 125:287–307

Spedding GR, Hedenström A, Rosén M (2003a) Quantitative studies of the wakes of freely flying birds in a low-turbulence wind tunnel. Exp Fluids 34:291–303

Spedding GR, Rayner JMV, Pennycuick CJ (1984) Momentum and energy in the wake of a pigeon (*Columba livia*) in slow flight. J Exp Biol 111:81–102

Spedding GR, Rosen M, Hedenstrom A (2003b) A family of vortex wakes generated by a thrush nightingale in free flight in a wind tunnel over its entire natural range of flight speeds. J Exp Biol 206:2313–2344

Thomas ALR, Taylor GK, Srygley RB, Nudds RL, Bomphrey RJ (2004) Dragonfly flight: free-flight and tethered flow visualizations reveal a diverse array of unsteady lift-generating mechanisms, controlled primarily via angle of attack. J Exp Biol 207:4299–4323

Tobalske BW, Warrick DR, Dickson WB, Altshuler DA, Dickinson MH (2008) Hovering aerodynamics in hummingbirds: comparing a dynamically-scaled robot with live birds. In: Society for Integrative and Comparative Biology, 2008 Annual Meeting, San Antonio

Usherwood JR, Hedrick TL, Biewener AA (2003) The aerodynamics of avian take-off from direct pressure measurements in Canada geese (*Branta canadensis*). J Exp Biol 206:4051–4056

Usherwood JR, Hedrick TL, McGowan CP, Biewener AA (2005) Dynamic pressure maps for wings and tails of pigeons in slow, flapping flight, and their energetic implications. J Exp Biol 208:355–369

Videler J, Stamhuis E, Povel D (2004) Leading-edge vortex lifts swifts. Science 306:1960–1962

Walker JA (2002) Rotational lift: something different or more of the same? J Exp Biol 205:3783–3792

Warrick DR, Tobalske BW, Powers DR (2005) Aerodynamics of the hovering hummingbird. Nature 435:1094–1097

Webb PW (1975) Hydrodynamics and energetics of fish propulsion. Bull Fish Res Bd Can 190:1–158

Wilkin PJ (1990) The instantaneous force on a desert locust, *Schistocerca gregaria* (Orthoptera: Acrididae), flying in a wind tunnel. J Kansas Ent Soc 63:316–328

Wilkin PJ (1991) Instantaneous aerodynamic forces developed by an Indian Moon Moth, *Actias selene*, in near hovering flight. Physiol Zool 64:193–211

Wilkin PJ, Williams MH (1993) Comparison of the instantaneous aerodynamic forces on a sphingid moth with those predicted by quasi-steady aerodynamic theory. Physiol Zool 66:1015–1044

Willmott AP, Ellington CP, Thomas ALR (1997) Flow visualization and unsteady aerodynamics in the flight of the hawkmoth, *Manduca sexta*. Philos Trans Biol Sci 352:303–316

Zarnack W (1969) Kinematik der Flügelbewegungen bei Locusta migratoria L. Math-Nat-Fak. Dissertation, Munich: Universitaet Muenchen

Aerodynamics of intermittent bounds in flying birds

Bret W. Tobalske · Jason W. D. Hearn · Douglas R. Warrick

Abstract Flap-bounding is a common flight style in small birds in which flapping phases alternate with flexed-wing bounds. Body lift is predicted to be essential to making this flight style an aerodynamically attractive flight strategy. To elucidate the contributions of the body and tail to lift and drag during the flexed-wing bound phase, we used particle image velocimetry (PIV) and measured properties of the wake of zebra finch (*Taeniopygia guttata*, $N = 5$), flying at 6–10 m s^{-1} in a variable speed wind tunnel as well as flow around taxidermically prepared specimens ($N = 4$) mounted on a sting instrumented with force transducers. For the specimens, we varied air velocity from 2 to 12 m s^{-1} and body angle from −15° to 50°. The wake of bounding birds and mounted specimens consisted of a pair of counter-rotating vortices shed into the wake from the tail, with induced downwash in the sagittal plane and upwash in parasagittal planes lateral to the bird. This wake structure was present even when the tail was entirely removed. We observed good agreement between force measures derived from PIV and force transducers over the range of body angles typically used by zebra finch during forward flight. Body lift:drag (*L*:*D*) ratios averaged 1.4 in live birds and varied between 1 and 1.5 in specimens at body angles from 10° to 30°. Peak (*L*:*D*) ratio was the same in live birds and specimens (1.5) and was exhibited in specimens at body angles of 15° or 20°, consistent with the lower end of body angles utilized during bounds. Increasing flight velocity in live birds caused a decrease in C_L and C_D from maximum values of 1.19 and 0.95 during flight at 6 m s^{-1} to minimum values of 0.70 and 0.54 during flight at 10 m s^{-1}. Consistent with delta-wing theory as applied to birds with a graduated-tail shape, trimming the tail to 0 and 50% of normal length reduced *L*:*D* ratios and extending tail length to 150% of normal increased *L*:*D* ratio. As downward induced velocity is present in the sagittal plane during upstroke of flapping flight, we hypothesize that body lift is produced during flapping phases. Future efforts to model the mechanics of intermittent flight should take into account that flap-bounding birds may support up to 20% of their weight even with their wings fully flexed.

B. W. Tobalske (✉)
Division of Biological Sciences, Field Research Station at Fort Missoula, University of Montana, Missoula, MT 59812, USA
e-mail: bret.tobalske@mso.umt.edu

J. W. D. Hearn
Harvard Medical School, 25 Shattuck Street, Boston, MA 02115, USA

D. R. Warrick
Department of Zoology, Oregon State University, 2002 Cordley Hall, Corvallis, OR 97331, USA

1 Introduction

Probably the most common style of flight in small birds is a form of intermittent flight that consists of flapping phases interrupted by flexed-wing bounds during which the wings are held motionless and flexed against the body (Rayner 1985; Tobalske 2001). Small birds with rounded, low-aspect ratio wings use intermittent bounds, and small birds with pointed, high-aspect ratio wings use both intermittent bounds and glides in which the wings are extended (Tobalske 2001). The use of intermittent bounds declines with increasing mass among bird species, and the pileated woodpecker (*Dryocopus pileatus*; 0.26 kg) is the largest species for which the flight style has been described (Tobalske 1996, 2001). An adverse scaling of

G.K. Taylor, M.S. Triantafyllou, and C. Tropea (Eds.): Animal Locomotion, pp. 401–411.
springerlink.com

the mass-specific power available from the flight muscles (or lift per unit power output; Marden 1994) has been hypothesized to account for an upper size limit for this behavior (Rayner 1977, 1985; Tobalske 1996, 2001). Flap-bounding flight may offer a reduction in the mechanical power required for fast forward flight (Rayner 1977; 1985; DeJong 1983; Ward-Smith 1984a, b). However, for flap-bounding to offer an advantage at moderate speeds such as the maximum-range speed considered to be optimal for migration, a dominant model suggests that a bird must support some of its weight during bounds using body lift (Rayner 1985). The aerodynamics of this vertical force are largely unknown.

Working with plaster-cast models of zebra finch (*Taeniopygia guttata*) and an instrumented sting in a wind tunnel, Csicsáky (1977a, b) first demonstrated that a bird in a bound posture can produce body lift (vertical force) of magnitude equal to body drag (horizontal force), with an optimal lift to drag (*L*:*D*) ratio exhibited when the body angle (β) relative to horizontal is approximately 20°. More recently, Tobalske et al. (1999) measured accelerations using kinematics of live birds flying in a wind tunnel and observed that zebra finch generate body lift that supports up to 16% of their body weight and provides *L*:*D* ratios >1 during flight at velocities from 4 to 10 m s^{-1}. These levels of weight support may make flap-bounding an aerodynamically attractive flight strategy at velocities >6 m s^{-1} (Rayner 1985; Tobalske et al. 1999).

Despite considerable effort, there remains uncertainty about the magnitude of body (parasite) drag that birds experience during flight. It is vital to refine the current understanding of body drag, because drag is predicted to affect the magnitude and shape of curves that predict the way power varies with velocity during forward flight. Such curves are necessary for modeling flight behavior, ecology and physiology (Pennycuick 1975; Hedenström and Alerstam 1995; Rayner 1999; Thomas and Hedenström 1998; Tobalske 2007).

Generally, body drag is measured by mounting prepared specimens upon a sting that is instrumented with force transducers. Using such methods, parasite drag coefficients (C_D) of up to 0.5 have been measured (Tucker 1973, 1990; Pennycuick et al. 1988; Maybury 2000; Maybury and Rayner 2001). It is thought that a C_D of this magnitude is likely an overestimate due to the difficulty of preparing specimens to match in vivo feather arrangement and boundary-layer conditions. Streamlined objects prepared to minimize drag should have a $C_D \leq 0.05$ (Hoerner 1965; Pennycuick et al. 1996). One potential constraint to proper feather arrangement in studies using carcasses is that the wings are typically removed with the explicit goal of accounting for parasite drag on the body independently of profile drag on the wings. The lowest C_D yet reported for a carcass is 0.13, and this was measured in European starling (*Sturnus vulgaris*) specimens that were footless and prepared with a coating of paraffin (Maybury 2000).

In contrast, in vivo measures of body C_D during flight are greater than 0.12. Decelerations during bounds in zebra finch suggest a C_D of approximately 0.31 (Tobalske et al. 1999). Rates of steady descent when diving from high altitude during migration give a C_D of 0.37 in other passerine species (Hedenström and Liechti 2001).

Depending upon its shape and how it is spread, the tail may function to provide lift and reduce drag. Delta-wing theory predicts that all surface area cranial to the maximum width of a tail contributes lift and drag, whereas area caudal to the maximum width contributes only drag (Thomas 1993). Some evidence suggests that birds do not always use their tail as predicted according to this theory (Evans et al. 2002). However, other work with tail models indicates that the theory accurately accounts for flow dynamics, at least over a range of tail postures that may commonly be used in flight (Evans 2003). Working with wingless specimens, Maybury (2000) and Maybury et al. (2001) demonstrated that the tail of European starlings sheds a pair of vortices into the wake, consistent with delta-wing theory (Thomas 1993). The tail in starlings also functions as a splitter that helps maintain attached flow via static pressure recovery in the caudal region of the body (Maybury and Rayner 2001).

Because living birds can control their own feather arrangement, intermittent bounds offer a useful model for furthering our understanding of the aerodynamics of body lift and drag in birds. Our first objective in the present study was to test the estimate from Csicsáky (1977a, b) and Tobalske et al. (1999) that zebra finch can generate body lift sufficient for *L*:*D* ratios >1 during intermittent bounds. Our second objective was to test the relative contribution of the body versus the tail to the production of body lift and drag during bounds. To test the relationship between data obtained in vivo versus data obtained from mounted carcasses, we coupled measurements of airflow in the wake of live birds flying in wind tunnel with force-transducer and wake measurements of mounted specimens.

2 Methods

2.1 Animals and wind tunnel

We used five live zebra finch (*T. guttata*, four male, one female, body mass = 17 ± 3 g, length 11.5 ± 0.5 cm, width 3.4 ± 0.2 cm, tail length 3.7 ± 0.3 cm) and four taxidermically prepared specimens (two of each sex, 14 ± 3 g, length 11.0 ± 0.3 cm, width 3.1 ± 0.2 cm, tail length 3.7 ± 0.1 cm). All experiments were performed

using a variable-speed wind tunnel previously described in Tobalske et al. (2005). The live birds flew at 6, 8, and 10 m s^{-1}, their preferred range of flight velocity. The specimens were exposed to velocities from 2 to 12 m s^{-1} at increments of 2 m s^{-1}. This is the full range of forward flight speeds over which zebra finch will fly in our tunnel. We prepared the specimens to be in a bound posture with the tail spread so that the maximum tail span was 75% of the body width (b). The postures and tail spread were informed by film and video images from previous studies (Tobalske et al. 1999; 2005). Given conventional usage of the symbol "b" in the animal-flight literature to represent wing span or half span, it should be noted that when wings are fully flexed during a bound, b also represents wing span.

2.2 Measuring lift and drag

For live birds and specimens, we measured lift (L) and drag (D) using 2D particle image velocimetry (PIV) and also by mounting specimens on a sting instrumented with force transducers. During all experiments with live birds, we verified the location of the bird and the motion of its wings relative to the illumination field using a synchronized high-speed video camera (Redlake PCI-2000) sampling at 250 Hz and located dorsal to the bird. Bounds were identified as intervals with the wings held motionless and fully flexed against the body (Tobalske et al. 1999).

For PIV, we used a LaVision GmBH system with DaVis 7.1 software, a Flowmaster 1,376 × 1,040 pixel digital camera sampling at 5 Hz and a 50-mJ dual-cavity pulsed NdYAG laser. We seeded the air with particles of olive oil (<1 μm in diameter) generated at a rate of 7×10^{10} particles s^{-1} using a vaporizer fitted with a Laskin nozzle. We placed the camera perpendicular to the planar (~3 mm thick) illumination field. For most of our analysis, we used sagittal and parasagittal illumination fields that were 0–3 body lengths caudal to the live birds and specimens. For a subset of the samples of the specimens, we mounted a mirror inside the windtunnel and used it to view a transverse illumination plane 7.5 cm caudal to the shoulder of the specimen (≤0.5 body lengths caudal to the tip of the tail). We accomplished quantitative analysis of 90 PIV samples of bounds from live birds and 3,720 images from specimens. We also performed PIV and visually inspected well over 1,000 images of the wake sampled during flapping phases of flight.

To calculate particle velocity, we used cross-correlation of paired images with an elapsed time between images (Δt) of 250–400 μs to give ~10-pixel particle separation in the regions of greatest velocity. We employed an adaptive multipass with an initial interrogation area of 64 × 64 pixels and final area of 16 × 16 pixels with 50% overlap. Vector fields were post-processed using a median filter (strong removal if difference relative to average >2 * r.m.s. of neighbors and iterative reinsertion if <3 * r.m.s of neighbors), removal of groups with <5 vectors, fill of all empty spaces by interpolation, and one pass of 3 × 3 smoothing. All measures of live birds were from individual (instantaneous) samples. For specimens, we computed an average velocity field from ten images. We estimate minimum error in velocity measurements to be 5.0 ± 0.5% including contributions due to a correlation peak of 0.1 pixels, optical distortion and particle-fluid infidelity (Raffel et al. 2000; Spedding et al. 2003a).

We calculated L using a simplified form of closed-loop integration of velocity about the core of a vortex (Batchelor 1967). We sampled sagittal (±5 mm) illumination planes that bisected a pair of counter-rotating trailing vortices that were always present in the wake of the birds and specimens. Circulation (Γ) was obtained using a line integral of the vertical component of velocity (w) along the Z axis (see Fig. 3a for orientation of axes), with the sample line extended approximately into free-stream flow where $w = 0$ (Spedding et al. 1984; Stamhuis and Nauwelaerts 2005):

$$\Gamma = \int_{-\infty}^{+\infty} w\mathrm{d}Z = \int_{-z(w\approx 0)}^{+z(w\approx 0)} w\mathrm{d}Z. \quad (1)$$

We then estimated L using the Kutta–Joukowski theorem:

$$L = \rho \Gamma u b \quad (2)$$

where ρ = air density, u = horizontal component of velocity, in this case free stream, and b = body width.

Drag was measured using a control-volume with height (h) and width (b) through which we calculated rate change of momentum flow (Batchelor 1967; Vogel 1994):

$$D = b\left(h\rho u_1^2 - \rho \int_0^h u_2^2 \mathrm{d}Z\right). \quad (3)$$

We sampled horizontal velocity in the wake (u_2) along a line on the sagittal plane, and we assumed $u_1 = u_2$ = free-stream u at the upper and lower edges of the control volume. We also assumed static pressure was the same upstream and at our sampling location in the wake. In a subsample of the measurements on specimens, we estimated D by traversing the wake at 5-mm increments from the sagittal plane to the lateral edge on one side of the body (~15 mm). In these instances, Eq. 3 was modified:

$$D = 2\int_0^{b/2}\left(h\rho u_1^2 - \rho\int_0^h u_2^2 \mathrm{d}Z\right)\mathrm{d}Y. \quad (4)$$

Our approach to the control-volume method assumed that there was no sideways (Y-axis) flow in or out of the volume, and we were unable to evaluate this assumption using 2D visualization of flow.

Measures of L and D were obtained for the mounted specimens using a custom-made, calibrated sting that featured an aluminum base instrumented with two dual-element strain gauges per axis (Vishay Measurements Group EA-250PD, 120 Ω) that were in a full-bridge configuration. The resonant frequency of the sting was 15 Hz, and crosstalk between axes was 2%. Signals were conditioned and amplified 2,000× using Vishay Measurements Group 2120B amplifiers, and the voltages from the amplifiers were input to computer using a 16-bit data acquisition system (Digidata 1320A; Axon Instruments). Subsequent low-pass filtering and measurement of the data was performed using Igor (v4) software.

Both L and D were converted to coefficients of lift (C_L) and drag (C_D):

$$C_L = 2L/\rho S u^2 \quad (5)$$

and

$$C_D = 2D/\rho S u^2 \quad (6)$$

where S = frontal projected area of the body. We measured S in live birds as they perched in the wind tunnel with u set at 8 m s^{-1}, the middle of the range of the experiment. We took digital photographs of the birds and imported the images to ImageJ v1.4 software (National Institutes of Health) for calibration to metric coordinates and measurement of S. Similar methods were employed for the mounted specimens, but we measured S at body angles (β) relative to horizontal that varied from −15° to 50° in increments of 5° so that C_L and C_D were calculated using S specific to each β (Fig. 1).

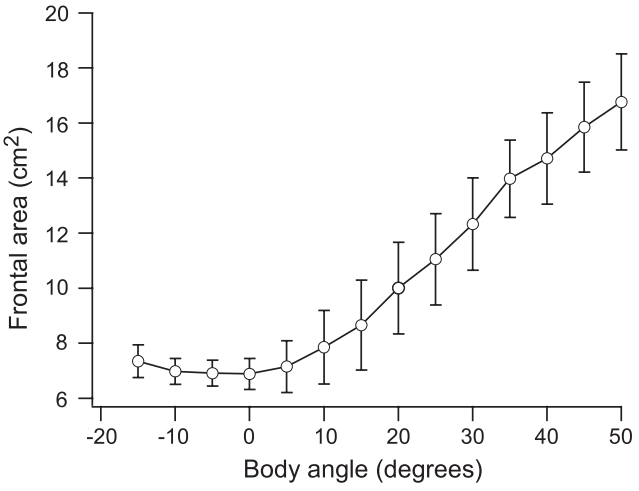

Fig. 1 Effect of body angle (β) upon projected frontal surface area (cm^2) of zebra finch specimens. Projected surface area was used for computing coefficients of lift and drag (C_L and C_D). Shown are mean ± SD (n = 4 specimens)

2.3 Tail manipulation

We altered the tails of mounted specimens to measure the relative contribution of the tail to L and D (Fig. 2). Tails were extended to 150% of initial length by gluing apical extensions obtained from other zebra finch to each of the retrices (Cuervo et al. 2003). We also cut the tail feathers to give a tail length of 50% of normal without apical replacement, and we plucked the feathers (all retrices and tail coverts) to give 0% of normal (Maybury 2000; Maybury and Rayner 2001). We did not vary the tail spread. With the specimens at β = 15°, S was decreased by 9% with no tail, decreased by 4% with the tail length at 50%, and increased by 14% with tail length at 150%. Zebra finch have a graduated tail (Fig. 2), so most of the experimental variation in length caused an increase in tail area cranial to the point of maximum span (Thomas, 1993). For example, comparing 150% to normal (100%) tail length, area cranial to maximum span increased by a factor of 2.2 ± 0.2 while area caudal increased by 1.3 ± 0.2.

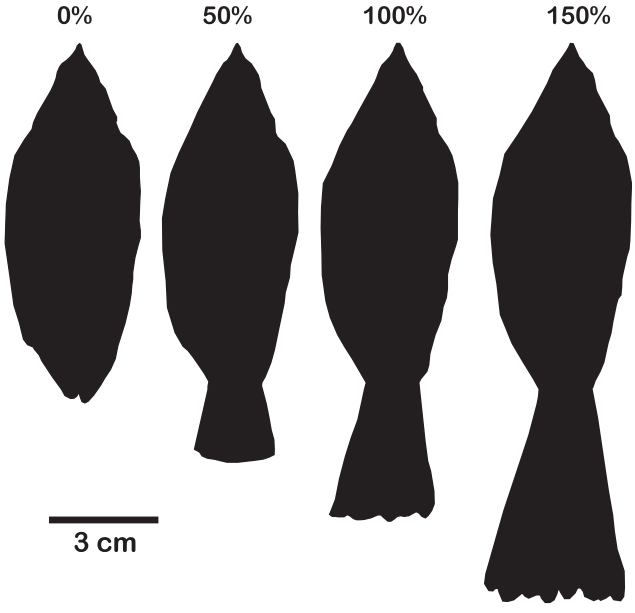

Fig. 2 Body outlines of a zebra finch specimen prepared to be in a bound posture with wings flexed against the body and the tail spread so that its maximum width was 75% of body width. Percentages indicate tail length relative to normal. We glued feathers to specimens to increase tail length and cut feathers to reduce tail length

2.4 Statistical analysis

For each variable, we computed a mean per live bird or specimen and treatment (velocity and/or body angle). We report mean ± SD. Subsequent statistical analyses were performed using StatView v. 5.0.1. To test for differences in the mean values of variables measured in live birds versus the mounted specimens, we used unpaired *t*-tests. We used repeated measures analysis of variance to test for the effects of velocity upon C_L, C_D and $L{:}D$ ratio in live birds and the effects of tail length on these variables in mounted specimens.

3 Results

3.1 Wake geometry

The wake of live birds during bounds and mounted specimens consisted of a continuously shed pair of counter-rotating vortices with filaments oriented approximately parallel with free-stream flow but convected downward with distance due to downward induced velocity in the middle of the wake (Fig. 3). Parasagittal traverses of the wake at 5-mm intervals showed that the bird's body induced downwash in the middle of the vortex pair out to 10 mm from the midline and upwash on the lateral side of the body and tail at 15 and 20 mm from the midline (Fig. 3a, b). These patterns indicated that the vortex cores were separated by a distance of between 60 and 100% of *b*. Instances of a bounding bird moving along the *Y*-axis through the interrogation plane provided confirmation that the wake consisted of downwash medially and upwash laterally (Fig. 3c).

Profiles of vertical (*w*) and horizontal (*u*) velocity sampled on the sagittal plane of the wake were consistent with predictions for a counter-rotating pair of vortices and a momentum deficit due to drag (Batchelor 1967, Fig. 4). Peak *w* in the center of the wake varied from 2 to 3 m s^{-1} (Fig. 4a), while peak *u* varied from 2 to 4 m s^{-1} less than free-stream *u* (Fig. 4b).

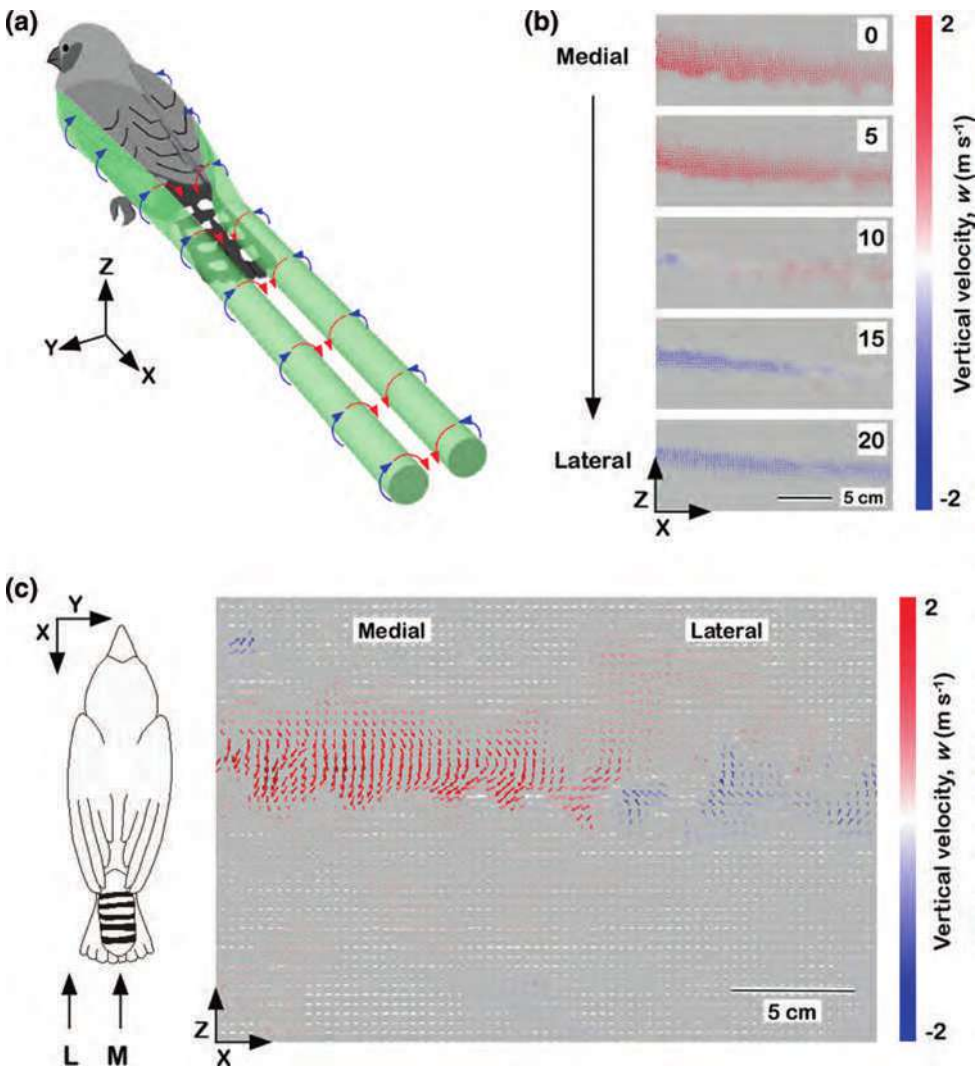

Fig. 3 When in a bound posture, mounted specimens (**a**, **b**) as well as live birds (**c**) shed a pair of counter-rotating vortices into the wake. *Colors* indicate the direction of vertical velocity (*w*) induced by the bird: *red* downwash, *blue* upwash. A cartoon (**a**) indicates the geometry of the flow surrounding the bird and shed into the wake. Three-dimensional axes are provided as orientation for PIV images. Sagittal and parasagittal traverses of the wake (**b**) of a zebra finch specimen mounted with body angle (β) = 15° and horizontal velocity (u) = 8 m s^{-1} (flow from *left* to *right*). A live bird flying at 10 m s^{-1} (**c**) moved through the interrogation plane so that the lateral portion of its wake was sampled first (*blue* upwash at *right*) and then the *middle* of its wake was sampled (*red* downwash at *left*). *Arrows* pointing to the bird outline indicate the location of the lateral (*L*) and medial (*M*) planes sampled in the PIV image. Bird outline from Tobalske et al. (1999)

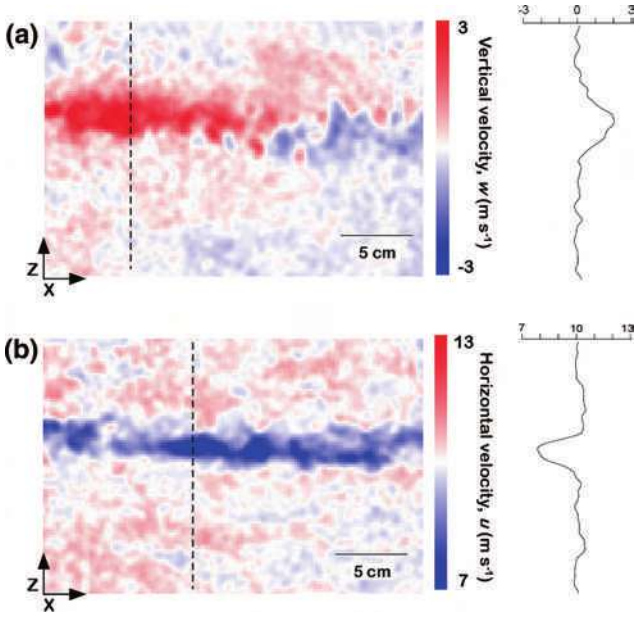

Fig. 4 Profiles of (**a**) vertical velocity (w) and (**b**) horizontal velocity (u) in the wake of a zebra finch engaged in a bound during flight at 10 m s^{-1}. The velocity panels are from the sagittal plane and correspond to the bound shown in Fig. 3c. The *dashed lines* on panels indicate the location from which the profiles were sampled, and the resulting profiles are at *right*. We integrated velocity along these profile lines to estimate body lift and drag. In this instance, L:D ratio was 1.15

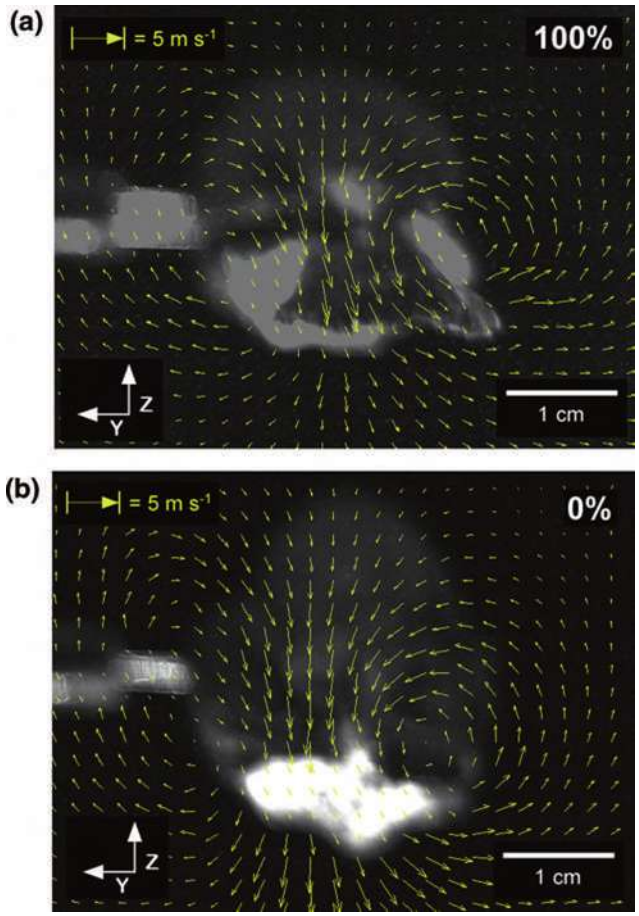

Fig. 5 Caudal views of the pair of vortices shed from a zebra finch specimen mounted with body angle (β) = 15° and horizontal velocity (u) = 8 m s^{-1}. Vectors indicate velocity. The specimen and transducer sting are visible in the background. In a specimen with an intact tail (**a** 100% normal tail length), the vortices in the wake were located dorsal to the tail. The same wake structure was apparent when the tail was removed (**b** 0% of normal tail length), but the presence of the sting consistently distorted the wake so that the midpoint between the counter-rotating vortices was offset laterally from the saggital plane of the body

Transverse views of the wake of specimens mounted at $\beta = 15°$ further clarified that two symmetrical, counter-rotating vortices were shed into the wake (Fig. 5). In birds with intact tails, these vortices were positioned symmetrically about the sagittal plane, dorsal to the tail and with cores spaced approximately = b (Fig. 5a). With removal of the tail length (0%), a counter-rotating pair of vortices was still observed, but drag on the sting caused a distortion of the wake on the side of the sting (Fig. 5b). Traverses providing lateral views of the wake as well as the transverse view in Fig. 5b revealed that the tail was not necessary to the production of induced downwash and the pair of shed vortices. In three specimens (75%) that lacked a tail, drag on the sting pulled the wake along the Y-axis so that, by the time they were fully developed several centimeters into the wake, the counter-rotating pair of vortices were symmetrical about the point of sting attachment rather than the sagittal plane of the bird. In the bird shown in Fig. 5b, the wake was approximately symmetrical about the sagittal plane, but the presence of the sting appeared to distort the shape of the vortex core on that side of the body.

Smaller-scale transverse or cross-stream vorticity in the wake was observed in the lateral view of the wake when sampled at the sagittal plane (Fig. 6). Positive-signed vorticity was shed from the ventral surface of the body and negative-signed vorticity was shed from the dorsal surface. Considerable distortion of the organization of this vorticity was apparent within 20 cm (~2 body lengths) into the wake (Fig. 6).

The wake structure produced during bounds was different from that produced during flapping flight (Fig. 7). Samples from mid-wing, parasagittal plane indicated that the flapping wake was dominated by a vortex ring produced during downstroke (Fig. 7a). However, sagittal samples revealed that vortex cores corresponding to starting and stopping vortices were less evident, perhaps distorted by the wake of the bird's body, and that w was induced downward by the bird during both downstroke and upstroke (Fig. 7b).

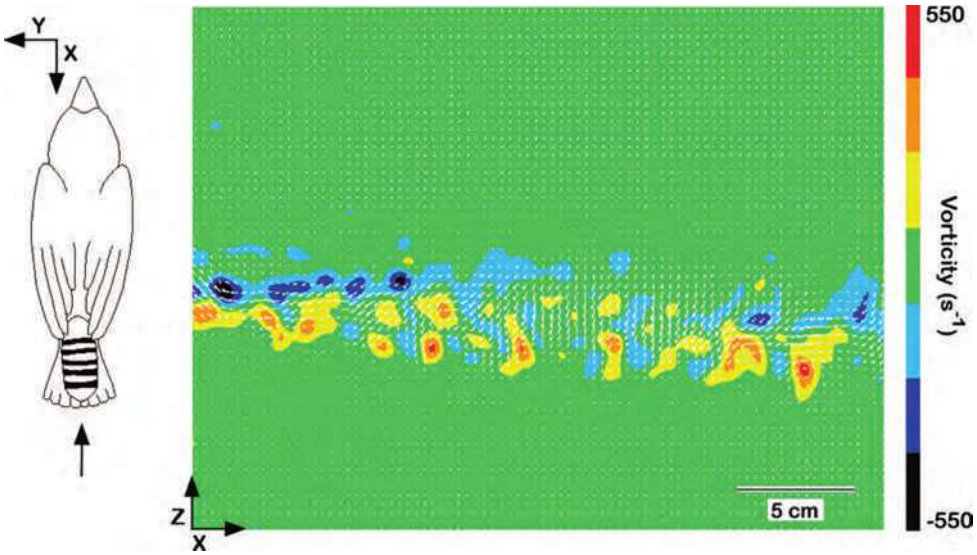

Fig. 6 Velocity and vorticity in the wake of a zebra finch engaged in a bound during flight at 8 m s^{-1}. These data were from a sagittal interrogation plane with *y*-axis location as indicated by the position of the arrow relative to the bird outline (outline from Tobalske et al. 1999). Vectors indicate velocity with free-stream velocity subtracted

3.2 Body lift and drag

Live birds generated *L*:*D* ratios of 1.36 ± 0.03 during bounds while flying at 6–10 m s^{-1} (Fig. 8a). Velocity did not have an effect upon *L*:*D* ratio in live birds (repeated-measures ANOVA, $P = 0.1$, $df = 3, 2$), but there was greater variation in *L*:*D* ratio among birds during flight at 6 m s^{-1} than at the other velocities. The coefficient of variance for *L*:*D* ratio was 38% at 6 m s^{-1} versus 17% at 8 m s^{-1} and 11% at 10 m s^{-1} (Fig. 8a). Lift and drag coefficients (C_L and C_D) varied significantly with flight velocity (repeated-measures ANOVA, $P = 0.0094$ and $P = 0.0021$, respectively, df 3, 2 per test), decreasing with each increase in velocity from 6 to 10 m s^{-1} (Fig. 8b). Specifically, between 6 and 10 m s^{-1}, C_L varied from 1.2 ± 0.4 to 0.7 ± 0.1 and C_D varied from 0.9 ± 0.1 to 0.5 ± 0.1.

Also in live birds, the forces associated with our computed C_L and C_D increased with increasing velocity. Lift varied from 24 ± 8 mN (14.3% of body weight) at 6 m s^{-1} to 39 ± 8 mN (23.5% of body weight) at 10 m s^{-1}. Over the same range of velocity, drag varied from 19 ± 1.9 mN (11.5% of body weight) to 31 ± 4 mN (18.3% of body weight). Over all flight velocities, the percentage of weight supported by body lift during bounds was 20 ± 5%, and body drag was 15 ± 3% of weight.

For mounted specimens, our measures of lift and drag using PIV were in reasonable agreement with our measures using a sting instrumented with force transducers, particularly over the range of β typically used by zebra finch during forward flight (5–30°, Tobalske et al. 1999; Fig. 9). Velocity did not have an effect upon *L*:*D* ratio, but over a range of β from −15° to 50°, *L*:*D* ratio varied from −1 to 1.5 based upon PIV measurements and from −0.8 to 1.2 based upon transducer measurements. *L*:*D* ratios >1 were measured over the range of β from 5° to 25° using PIV and from 10° to 35° using the force sting (Fig. 9a). The polars for C_L as a function of C_D were similar in shape over the range of β up to 35°, although greater scatter was apparent among the polars generated using PIV due primarily to large variation in C_D among velocities within any given body angle (Fig. 9b). For $\beta \geq 35°$, C_D measured using PIV exceeded C_D measured using the force sting, but the large variation in the PIV measures, and relatively small sample size, rendered statistically insignificant the observed differences between mean measurement values. As an example, at 8 m s^{-1}, with $\beta = 40°$ average C_D was 1.0 ± 0.1 using the transducer sting and 1.2 ± 0.3 using PIV (paired *t*-test, $P = 0.1$).

Comparing results from the specimens versus live birds, peak *L*:*D*, averaged among velocities of 6-10 m s^{-1} in the specimens was 1.5 ± 0.3, which was not different from the peak *L*:*D* of 1.5 ± 0.4 in the live birds (*t*-test, $P = 0.9$, $df = 7$).

3.3 Tail manipulation

Although tail length in the specimens mounted at $\beta = 15°$ did not alter the basic wake structure (see Sect. 3.1, above), it did affect *L*:*D* ratio (Fig. 10) as measured using the force sting. Average *L*:*D* ratio among velocities increased with increasing tail length from 1.13 ± 0.04 with no tail (0%) to 1.40 ± 0.04 with tail length at 150% of normal. The effect upon *L*:*D* ratio was statistically significant. For example, at 8 m s^{-1}, the observed differences among the treatment means were significant at $P = 0.003$ (repeated measures ANOVA, $df = 3, 9$). Both C_L and C_D increased with increasing tail length, but the effects of any tail trimming (0 or 50% tail length) were similar, and the most obvious effect among treatments was a relatively greater increase in

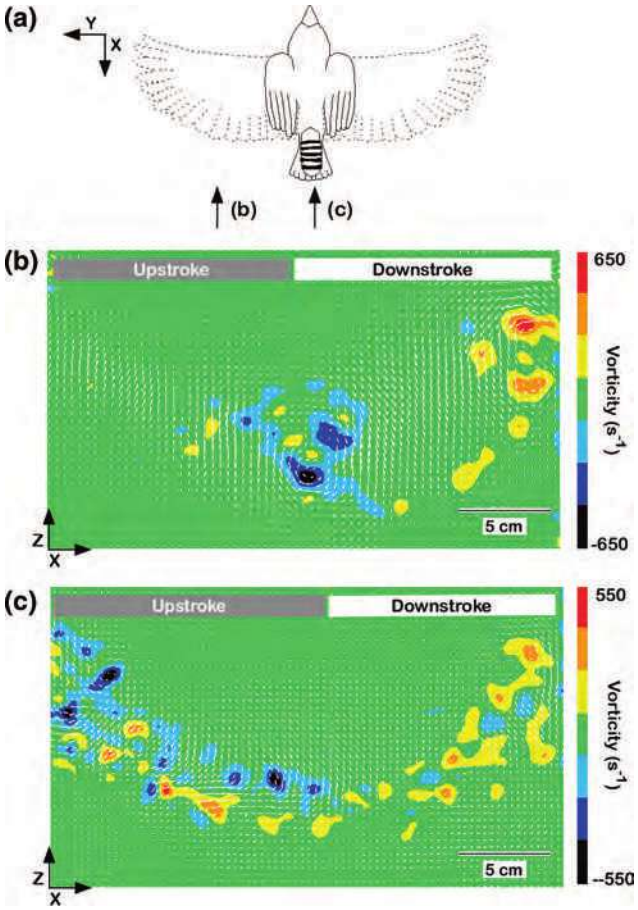

Fig. 7 Velocity and vorticity in the wake of a zebra finch engaged in flapping during flight at 8 m s^{-1}. The bird outline (**a**) shows a dorsal view of wing posture at mid-downstroke (*dashed lines*) and mid-upstroke (*solid lines*), and the arrows indicate the *Y*-axis location of the mid-wing, parasagittal plane (**b**) and saggital plane (**c**). A vortex ring was produced during downstroke, and cross-sectional views of the starting (+) and ending (−) vortices are present in **b**. Although the wings are flexed close to the body during upstroke, downwash is present throughout the wingbeat cycle. We hypothesize that body and tail lift may have contributed to this downwash

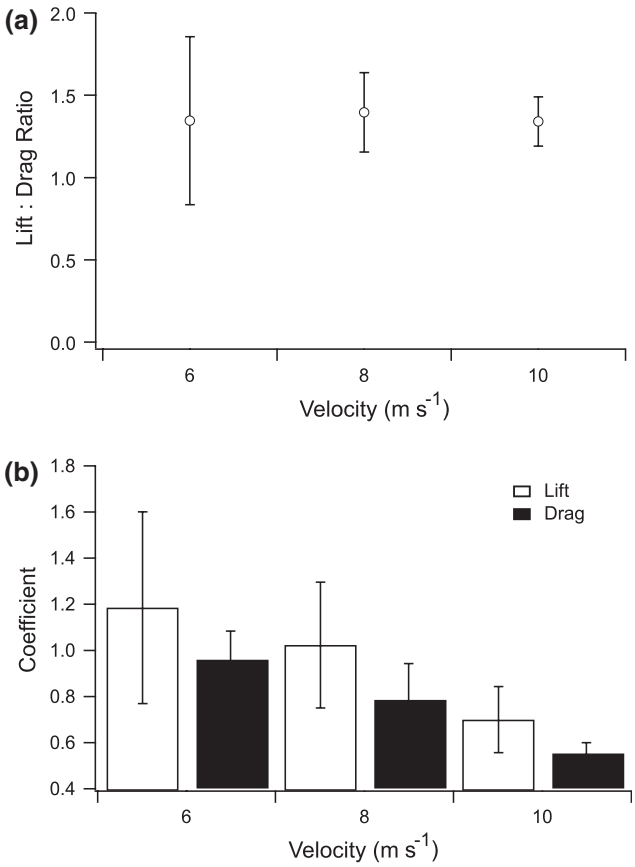

Fig. 8 Lift and drag as estimated from the wake of zebra finch engaged in bounds during flight at 6, 8 and 10 m s^{-1}. **a** Lift:drag (*L*:*D*) ratio. **b** Lift and drag coefficients (C_L and C_D). Shown are mean ± SD, $n = 5$ birds

C_L compared with C_D between 100 and 150% of length. As an example, again at 8 m s^{-1}, intact specimens (100% tail) had a C_L of 0.8 ± 0.1 while C_D was 0.67 ± 0.06. Tail trimming reduced C_L by 38% and C_D by 36% for both the 0% and 50% treatments. Increasing tail length to 150% of normal caused C_L to increase by 42% while C_D increased by only 19%.

4 Discussion

Our measurements showed body lift functions during bounds to support 20% of the bird's body weight (Figs. 3c, 4a, 8). This amount of weight support is slightly higher than the 16% estimate obtained from measures of whole-body acceleration in zebra finch (Tobalske et al. 1999). These levels of body lift are predicted to be sufficient to make flap-bounding an aerodynamically attractive flight strategy compared with continuous flapping at flight speeds greater than 6 m s^{-1} (Rayner 1985; Tobalske et al. 1999). This helps to explain the widespread use of this behavior during flight in small birds up to the size of large woodpeckers (Danielson 1988; Tobalske 1996).

As the zebra finch completely flexes its wings during bounds, it is likely that species that use partial bounds, with wings slightly extended, will achieve comparatively greater levels of weight support during pauses in flapping. Such species include the budgerigar (*Melopsittacus undulatus*; Tobalske and Dial 1994), European starling (Tobalske 1995) and barn swallow (*Hirundo rustica*; Bruderer et al. 2001). Moreover, we predict that downward induced velocity present in the sagittal plane of the wake during upstroke (Fig. 7c) was due in part to body lift during the flapping phases of intermittent flight. Similar wake patterns from flapping phases of flap-bounding flight are evident in the robin (*Erithacus rubecula*; Hedenström et al. 2005). The partially extended wings that are characteristic of mid-

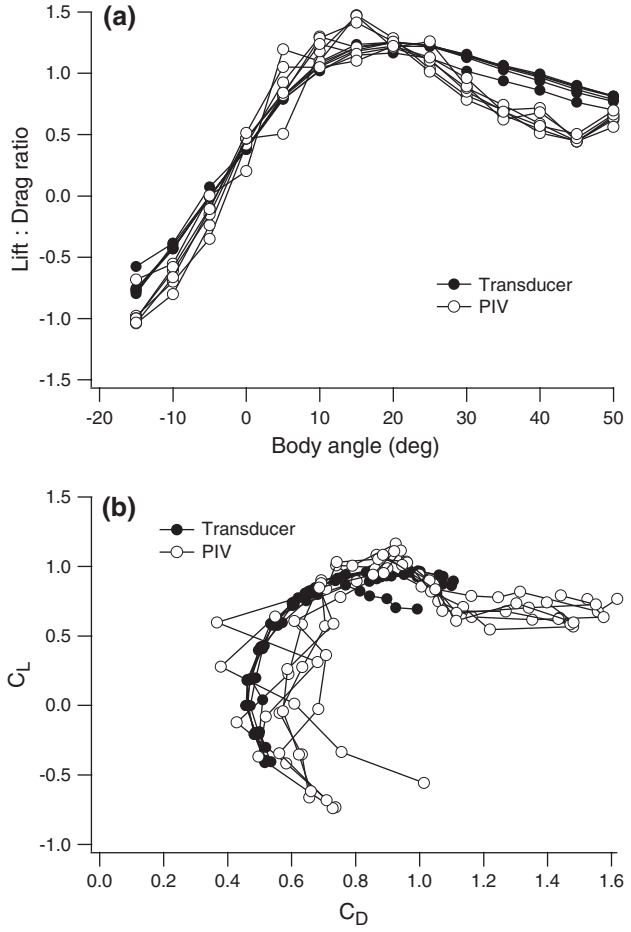

Fig. 9 Lift:drag (L:D) ratio as a function of body angle (β) in zebra finch specimens with traces included for each air velocity from 2 to 12 m s^{-1}. Shown are means ($n = 4$ specimens). *Filled circles* data from sting instrumented with force transducers. *Open circles* data from analysis of the wake using PIV

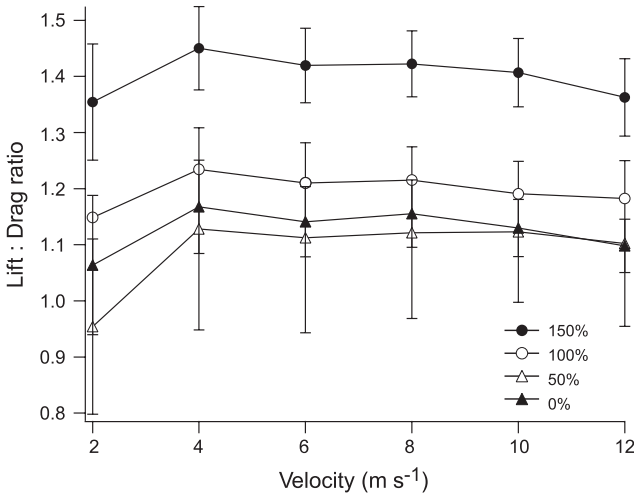

Fig. 10 Effects of tail manipulation on lift:drag (L:D) ratio of zebra finch specimens mounted in a bound posture with body angle (β) = 15°. Percentages indicate tail length relative to normal. Shown are mean ± SD ($n = 4$ specimens)

upstroke in the zebra finch (Fig. 7a) and robin likely also contribute to lift during upstroke. (Tobalske et al. 1999; Spedding et al. 2003b; Hedenström et al. 2005). Testing the relative contribution of the wings versus the body will help refine models of mechanical power output during flap-bounding (Rayner 1985).

Using L:D ratio as a criterion, optimal β during bounds was 15° based on PIV data and 20° based on data from our force sting (Fig. 5). Csicsáky (1977a, b) similarly reports an optimum of 20° for plaster-cast models of zebra finch. The L:D ratio for the plaster cast models in Csicsáky (1977a, b) is 1.18, lower than the average value of 1.4 we measured in live birds (Fig. 8a) and peak values of 1.5 that we measured in mounted specimens (Fig. 9a). Live zebra finch exhibit average β from 20° to 30° (range 12°–37°) during bounds at flight velocities from 6 to 10 m s^{-1} (Tobalske et al. 1999). Thus, zebra finch adopt a body posture during bounds that appears to either maximize body L:D ratio or, at least, keep L:D ratio >1.

Our present experiments are the first efforts applied to bird flight in which force transducers independently confirm that PIV is a reasonably accurate method for measuring in vivo L and D (Figs. 8, 9). However, a force balance against a null hypothesis of weight support in flapping flight is well established using PIV and impulse-based wake analysis (Spedding et al. 2003b; Warrick et al. 2005; Hedenström et al. 2005, 2006). For an animal in steady horizontal flight or hovering, L from flapping wings simultaneously provides both weight support against gravity and thrust to match D, including parasite drag from the body as well as profile drag from the wings. When an animal's mass is known, the vertical component is a known force given gravitational acceleration. Likewise, the net horizontal component of the wake impulse can provide an estimate of the average D due to the body and wings (Hedenström et al. 2005).

The flexed-wing bound posture (Fig. 3) was simple compared with the complex kinematics of the avian wing stroke and rendered adequate a taxidermically prepared model. In contrast, providing transducer-based measures of force during wing flapping may ultimately require the use of dynamically scaled robots (Birch et al. 2004), in vivo implantation of strain gauges (Dial et al. 1997; Biewener et al. 1998; Tobalske et al. 2003) or external mounting of pressure transducers (Usherwood et al. 2005).

Both force sting and PIV measurements confirmed that body lift comes with a substantial cost in the form of body drag (Figs. 4b, 8b, 9). Our measurements of C_D up to 0.9 in live birds is approximately 3 times greater than the average C_D reported for diving passerines (Hedenström and Liechti 2001) and almost 10× the C_D measured in carefully prepared, wingless starling carcasses (Maybury 2000;

Maybury and Rayner 2001). Without doubt, C_D during intermittent bounds was much greater than expected values for streamlined bodies such as airfoils ($\leq$0.05; Hoerner 1965; Pennycuick et al. 1996). It would be worthwhile to test whether body drag during flapping phases is as high as it is during bounds. Using impulse and incline angle of vortices in the wake of flapping phases, Hedenström et al. (2005) report a *L*:*D* ratio of 7.5 for the robin. They do not report body and wing area for calculation of C_D, but the weight balance derived for L implies that D represents approximately 13% of body weight during flapping in the robin. This is only slightly less than our measurement of D at 17% of body weight in live zebra finch, but it is important to note that the wing contribution to D must be greater during flapping than during a bound.

An effect of Reynolds number (*Re*) could potentially account for the unexpectedly high values of C_D we measured in zebra finch. C_L and C_D both decreased as a function of increasing flight speed and, hence, *Re* (Fig. 8b). For diving passerines, Hedenström and Liechti (2001) observed that C_D decreased from 0.77 to 0.17 as *Re* increased from 35,000 to 85,000, and the highest *Re* corresponds to a velocity of 53.7 m s^{-1}. The regression formula for their data is $C_D = 0.82 - 7.5 \times 10^{-6}Re$. Using b as a characteristic length as in Hedenström and Liechti (2001), our measurements at 6, 8 and 10 m s^{-1} in live birds correspond to *Re* values of 9,900, 13,300 and 16,000. Since the range of *Re* during experiments in the wind tunnel was less than half the minimum *Re* measured by Hedenström and Liechti (2001), extreme caution is warranted in extrapolation of their regression equation. Nonetheless, their equation predicts C_D values of 0.75, 0.72 and 0.70 at flight speeds of 6, 8 and 10 m s^{-1}. These predicted values are within 1 standard deviation of our observed C_D at 8 and 10 m s^{-1} (Fig. 8b).

Tail manipulations showed that the tail is not required to produce the pair of counter-rotating trailing vortices associated with body lift (Figs. 3a, 5). With a tail, the vortices appeared to be shed from the edges of the tail and were oriented on the upper surface (Fig. 5). Maybury et al. (2001) observed the same form of vortex production in wingless starling carcasses. Although a counter-rotating pair of vortices shed into the wake by the tail is consistent with predicted function of a tail performing as a delta wing (Thomas 1993), a variety of bluff bodies without tails are known to produce streamwise vortices. Examples include motor vehicles (Hucho and Sovran 1993) and tilted cylinders with an upswept aft section (Zhang et al. 2004). Likewise, specimens with 0% tails at $\beta = 15°$ shed a trailing vortex pair (Fig. 5b) with separation between vortex cores approximately the same as when the tail was present. Since the wingless specimens used by Maybury et al. (2001) and the tailless specimens in our experiments generated the same wake structure, it is apparent that the approximately fusiform shape of a bird's body is sufficient to generate body lift when it is placed at optimal angles relative to horizontal (Figs. 5b, 10).

Lengthening the tail to 150% of normal significantly increased *L*:*D* ratio (Fig. 10), so an obvious question emerges: why have not zebra finch and other flap-bounding birds evolved long tails to help maximize their *L*:*D* ratio during bounds? There are several alternatives that may constrain tail length in these birds. Given their wing morphology, an increase in tail length may compromise stability or maneuverability (Thomas 1993; Thomas and Taylor 2001; Taylor and Thomas 2002). It may also be subject to relatively higher rates of breakage or wear (Thomas 1993; Barbosa et al. 2003). Additionally, as the birds that use intermittent bounds are relatively small, living at comparatively low Reynolds numbers, it is feasible that tail drag disproportionately limits their ability to fly fast. To the extent that flying fast is necessary, for example to minimize exposure to predators or to migrate in a timely fashion, minimizing tail drag may as important as maximizing lift.

Acknowledgments All procedures involving the animals were approved by the Institutional Animal Care and Use Committee of the University of Portland. This research was supported by National Science Foundation Grants IBN-0327380 and IOB-0615648.

References

Barbosa A, Merino S, Cuervo JJ, De Lope F, Møller AP (2003) Feather damage of long tails in barn swallows. Ardea 91:85–90

Batchelor GK (1967) An introduction to fluid dynamics. Cambridge University Press, Cambridge

Biewener AA, Corning WR, Tobalske BW (1998) In vivo pectoralis muscle force–length behavior during level flight in pigeons (*Columba livia*). J Exp Biol 201:3293–3307

Birch JM, Dickson WB, Dickinson MH (2004) Force production and flow structure of the leading edge vortex on flapping wings at high and low Reynolds numbers. J Exp Biol 207:1063–1072

Bruderer L, Liechti F, Bilo D (2001) Flexibility in flight behaviour of barn swallows (*Hirundo rustica*) and house martins (*Delichon urbica*) tested in a wind tunnel. J Exp Biol 204:1473–1484

Csicsáky M (1977a) Aerodynamische und Ballistische Untersuchungen an Kleinvögeln. PhD thesis, University of Hamburg, Germany

Csicsáky MJ (1977b) Body-gliding in the zebra finch. Fortschr Zool 24:275–286

Cuervo JJ, Møller AP, de Lope F (2003) Experimental manipulation of tail length in female barn swallows (*Hirundo rustica*) affects their future reproductive success. Behav Ecol 14:451–456

Danielson R (1988) Parametre for fritflyvende småfugles flugt. Dan Orn Foren Tidsskr 82:59–60

DeJong MJ (1983) Bounding flight in birds. PhD thesis, University of Wisconsin, Madison, USA

Dial KP, Biewener AA, Tobalske BW, Warrick DR (1997) Mechanical power output of bird flight. Nature 390:67–70

Evans MR (2003) Birds' tails do act like delta wings but delta-wing theory does not always predict the forces they generate. Proc Biol Sci 270:1379–1385

Evans MR, Rosén M, Park K, Hedenström A (2002) How do birds' tails work? Delta-wing theory fails to predict tail shape during flight. Proc Biol Sci 269:1053–1057

Hedenström A, Alerstam T (1995) Optimal flight speed of birds. Philos Trans R Soc Lond B Biol Sci 348:471–487

Hedenström A, Liechti L (2001) Field estimates of body drag coefficient on the basis of dives in passerine birds. J Exp Biol 204:1167–1175

Hedenström A, Rosén M, Spedding GR (2005) Vortex wakes generated by robins *Erithracus rubecula* during free flight in a wind tunnel. J R Soc Interface 3:263–276

Hedenström A, Griethuijsen LV, Rosén M, Spedding GR (2006) Vortex wakes of birds: recent developments using digital particle image velocimetry in a wind tunnel. Anim Biol 56:535–549

Hoerner SF (1965) Fluid-dynamic drag. Hoerner fluid dynamics. Bricktown, New Jersey

Hucho W, Sovran G (1993) Aerodynamics of vehicles. Annu Rev Fluid Mech 25:485–537

Marden JH (1994) From damselflights to pterosaurs: How burst and sustainable flight performance scale with size. Am J Physiol 266:R1077–R1084

Maybury WJ (2000) The aerodynamics of bird bodies. PhD thesis, University of Bristol, UK

Maybury WJ, Rayner JMV (2001) The avian tail reduces body parasite drag by controlling flow separation and vortex shedding. Proc Biol Sci 1474:1405–1410

Maybury WJ, Rayner JMV, Couldrick LB (2001) Lift generation by the avian tail. Proc Biol Sci 268:1443–1448

Pennycuick CJ (1975) Mechanics of flight. In: Farner DS, King JR (eds) Avian biology, vol 5. Academic Press, New York, pp 1–75

Pennycuick CJ, Obrecht HHIII, Fuller MR (1988) Empirical estimates of body drag of large waterfowl and raptors. J Exp Biol 135:253–264

Pennycuick CJ, Klaassen M, Kvist A, Lindström AK (1996) Wingbeat frequency and the body drag anomaly: wind tunnel observations on a thrush nightingale (*Luscinia luscinia*) and a teal (*Anas crecca*). J Exp Biol 199:2757–2765

Raffel M, Willert C, Kompenhans J (2000) Particle image velocimetry: a practical guide. Springer, Berlin

Rayner JMV (1977) The intermittent flight of birds. In: Pedley TJ (ed) Scale effects in animal locomotion. Academic Press, New York, pp 37–55

Rayner JMV (1985) Bounding and undulating flight in birds. J Theor Biol 117:47–77

Rayner JMV (1999) Estimating power curves for flying vertebrates. J Exp Biol 202:3449–3461

Spedding GR, Rayner JMV, Pennycuick CJ (1984) Momentum and energy in the wake of a pigeon (*Columba livia*) in slow flight. J Exp Biol 111:81–102

Spedding GR, Hedenström A, Rosén M (2003a) Quantitative studies of the wakes of freely flying birds in a low-turbulence wind tunnel. Exp Fluids 34:291–303

Spedding GR, Rosén M, Hedenström A (2003b) A family of vortex wakes generated by a thrush nightingale in free flight in a wind tunnel over its entire natural range of flight speeds. J Exp Biol 206:2313–2344

Stamhuis EJ, Nauwelaerts S (2005) Propulsive force calculations in swimming frogs. II. Application of a vortex ring model to PIV data. J Exp Biol 208:1445–1451

Taylor GK, Thomas ALR (2002) Animal flight dynamics. II. Longitudinal stability in flapping flight. J Theor Biol 214:351–370

Thomas ALR (1993) On the aerodynamics of birds' tails. Philos Trans R Soc Lond B Biol Sci 340:361–380

Thomas ALR, Hedenström A (1998) The optimum flight speeds of flying animals. J Avian Biol 29:469–477

Thomas ALR, Taylor GK (2001) Animal flight dynamics. I. Stability in gliding fight. J Theor Biol 212:399–424

Tobalske BW (1995) Neuromuscular control and kinematics of intermittent flight in the European starling (*Sturnus vulgaris*). J Exp Biol 198:1259–1273

Tobalske BW (1996) Scaling of muscle composition, wing morphology, and intermittent flight behavior in woodpeckers. Auk 113:151–177

Tobalske BW (2001) Morphology, velocity, and intermittent flight in birds. Am Zool 41:177–187

Tobalske BW (2007) Biomechanics of bird flight. J Exp Biol 210:3135–3146

Tobalske BW, Dial KP (1994) Neuromuscular control and kinematics of intermittent flight in budgerigars (*Melopsittacus undulatus*). J Exp Biol 187:1–18

Tobalske BW, Peacock WL, Dial KP (1999) Kinematics of flap-bounding flight in the zebra finch over a wide range of speeds. J Exp Biol 202:1725–1739

Tobalske BW, Hedrick TL, Dial KP, Biewener AA (2003) Comparative power curves in bird flight. Nature 421:363–366

Tobalske BW, Puccinelli LA, Sheridan DC (2005) Contractile activity of the pectoralis in the zebra finch according to mode and velocity of flap-bounding flight. J Exp Biol 208:2895–2901

Tucker VA (1973) Bird metabolism during flight: evaluation of a theory. J Exp Biol 58:689–709

Tucker VA (1990) Body drag, feather drag and interference drag of the mounting strut in a peregrine falcon, *Falco peregrinus*. J Exp Biol 149:449–468

Usherwood JR, Hedrick TL, McGowan CP, Biewener AA (2005) Dynamic pressure maps for wings and tails of pigeons in slow, flapping flight, and their energetic implications. J Exp Biol 208:355–369

Vogel S (1994) Life in moving fluids. Princeton University Press, Princeton

Ward-Smith AJ (1984a) Analysis of the aerodynamic performance of birds during bounding flight. Math Biosci 68:137–147

Ward-Smith AJ (1984b) Aerodynamic and energetic considerations relating to undulating and bounding flight in birds. J Theor Biol 111:407–417

Warrick DR, Tobalske BW, Powers DP (2005) Aerodynamics of the hovering hummingbird. Nature 435:1094–1097

Zhang X, Senior A, Ruhrmann A (2004) Vortices behind a bluff body with an upswept aft section in ground effect. Int J Heat Fluid Flow 25:1–9

Experimental analysis of the flow field over a novel owl based airfoil

Stephan Klän · Thomas Bachmann · Michael Klaas · Hermann Wagner · Wolfgang Schröder

Abstract The aerodynamics of a newly constructed wing model the geometry of which is related to the wing of a barn owl is experimentally investigated. Several barn owl wings are scanned to obtain three-dimensional surface models of natural wings. A rectangular wing model with the general geometry of the barn owl but without any owl-specific structure being the reference case for all subsequent measurements is investigated using pressure tabs, oil flow pattern technique, and particle-image velocimetry. The main flow feature of the clean wing is a transitional separation bubble on the suction side. The size of the bubble depends on the Reynolds number and the angle of attack, whereas the location is mainly influenced by the angle of attack. Next, a second model with a modified surface is considered and its influence on the flow field is analyzed. Applying a velvet onto the suction side drastically reduces the size of this separation at moderate angles of attack and higher Reynolds numbers.

1 Introduction

In the last couple of decades air traffic has continuously increased. The number of starting and landing airplanes and the size of airports has rapidly grown to manage the vast number of passengers. In other words, more and more people live in the direct neighborhood of airports and suffer from air traffic noise. Nowadays, air traffic is so dense that take-off and landing have been extended even into the night leading to an increase of the disturbance to airport residents. However, it is a must to decrease the noise level and as such the noisy plight of airport neighbors. Thus, noise emission of airplanes is one major issue to airports and the design of future aircraft (Lilley 2004). To minimize the disturbance of the environment surrounding the airport, it will be necessary to develop new strategies to sufficiently reduce the emission of noise by airplanes (Hileman et al. 2007).

It is well known that silent flight can be found in nature. Most owl species have evolved a hunting strategy which requires to fly quietly (Lilley 1998). Owls localize their prey with their very accurate acuesthesia. On the one hand, it is necessary to suppress any kind of noise disturbing the localization of prey and on the other hand, to be inaudible to the prey. Hence, owls have evolved special features on their wings to fly silently. Three characteristics have been identified by Graham (1934), namely the velvet-like surface, the leading edge serrations, and the trailing edge fringes. Additionally, the airfoil geometry of the owl wing has an exceptional shape.

However, the aeroacoustic field is always determined by the flow field over any kind of configuration. It is the interaction between the flow and the surface which defines the noise emitted by wings. In other words, first the flow physics has to be understood in detail before a clear relation between various geometric features and the acoustic field can be derived. For this reason, this study focuses only on the aerodynamics of a novel airfoil the shape of which is related to that of an owl.

S. Klän (✉) · M. Klaas · W. Schröder
Institute of Aerodynamics, Wüllnerstr. 5a,
52062 Aachen, Germany
e-mail: s.klaen@aia.rwth-aachen.de

T. Bachmann · H. Wagner
Institute of Biology II, Kopernikusstr. 16,
52074 Aachen, Germany
e-mail: bachmann@bio2.rwth-aachen.de

G.K. Taylor, M.S. Triantafyllou, and C. Tropea (Eds.): Animal Locomotion, pp. 413–427.
springerlink.com

To be more precise, it is the main interest of this study to understand the aerodynamics of the owl wing and the influence of the velvet surface structure on the flow field. The velvet surface of the owl wing is similar to a fur. The drag reducing function of seal fur has been investigated by Itoh et al. (2006). The maximum drag reduction ($\sim 12\%$) was even higher and the Reynolds number range of remarkable drag reduction was larger than for a riblet surface. An increase of drag caused by the surface roughness was not observed. The influence of a soft coating consisting of filaments upon a technical airfoil (RAF-6E) was studied by Vad et al. (2006). The flow field was investigated by oil flow visualization, laser–doppler anemometry, and static pressure measurements. Measurements of the sound pressure revealed a reduction in the hearing range of humans due to the coating. However, the sound pressure level was increased at higher and lower frequencies. At the same time, the coating reduced the lift, increased the drag, and the turbulence level in the wake and the boundary layer was intensified. At high angles of attack, the coating even caused separation on the suction side of the wing, which resulted in a strong loss of aerodynamic performance. Those results seem to indicate that it is not just one feature but the interaction of the special characteristics of the owl wing that is responsible for the silent but also highly maneuverable flight of the owl in its special habitat, i.e. trees and bushes.

Investigations on the influence of surface structure and roughness have been discussed in the literature before. Bechert et al. (1997), for instance, performed experiments on riblet surfaces and on slit surfaces inserted into the side of an oil channel at zero pressure gradient and Reynolds numbers based on the width of the test section ranging from $Re_w = 8{,}200$ to 26,800. Using a shear stress balance they measured the drag reduction of several surface geometries. The highest value of drag reduction was 9.9%.

Furthermore, numerous numerical simulations of turbulent flow over riblets exist in the literature. Among other authors, Choi et al. (1993) compared the flow statistics over riblets to those of a flat plate. They found that the influence of the riblets on the mean velocity profiles was limited to the inner region of the boundary layer. Velocity fluctuations, vorticity fluctuations, and the Reynolds shear stresses could be reduced with an adequate riblet structure.

In a joint project of the Institute of Aerodynamics and the Institute of Biology II of the RWTH Aachen University, an attempt is made firstly, to understand the details of the aerodynamics of the owl wing under gliding flight conditions. That is, no flapping motion of the owl wing is considered. An artificial three-dimensional and a quasi-two-dimensional wing is constructed on the basis of the natural owl wing and those owl-specific structures influencing the flow are identified. The knowledge gathered on the wing models with and without owl-specific structures will be transfered to a technical airfoil and secondly, those results will be used to design a silent owl based wing. That is, the findings discussed in this study focus on understanding the aerodynamics of a newly developed owl-related airfoil, which is essential to understand the suppression of noise. As a first step, special interest is put on the airfoil geometry and the velvet-like surface in the frame of this work. The measurements were performed in the low-speed wind tunnel of the Institute of Aerodynamics. Different measurement techniques are used to characterize the flow field of the novel airfoil including pressure tabs, the oil flow technique, and the particle-image velocimetry.

In the following, the construction of a fully three-dimensional and a quasi-two-dimensional artificial wing based on the geometry of an owl wing will be discussed. Subsequently, the measurement technique to record the flow field of the quasi-two-dimensional wing is described. Next, the results are presented and analyzed in Sect. 4, before a concise summary of the findings is given in Sect. 5.

2 Construction of an artificial owl based wing

Measurements of the airfoil geometry of different bird species have been performed by Nachtigall and Klimbingat (1985) and Biesel et al. (1985). Their measurements show the airfoil geometry of the owl wing to differ from that of other birds or technical airfoils regarding, e.g., the planform and the thickness. A reconstruction of wings of several bird species for the purpose of numerical simulation has been performed by Liu et al. (2006). Their results also point out the significant differences in the geometry between the wings of owls and other species.

As mentioned above, the specific structures of the owl wing have been identified by Graham (1934). To understand their impact on the aerodynamics of a technical model it is necessary to build a clean wing model, which will be later equipped with those structures. That is, first the basic wing geometry has to be obtained and then, the owl-specific structures have to be rebuild. Unfortunately, deriving the geometry from natural wings obtained from dead or narcotized specimen does not give the correct wing form during flight (Biesel et al. 1985). That is, the natural wing is formed by feathers resulting in a non-uniform surface structure and it also is twisted due to drying processes of skin, tendons, and feathers and due to the relaxation of muscles. Feathers that are not aligned in their natural position can lead to an increased thickness, camber, or chord.

An empirical approach to correct the chord length and to estimate the deviation of the chord length of an individual

from the mean distribution of its species has been introduced by Oehme and Kitzler (1975). However, the result of this approach was not satisfying in respect to the spanwise distribution of the chord length and the shape of the wing tip (Fig. 1). The extraction of the airfoil geometry has also been performed by Liu et al. (2006). Their algorithms do not take care of some of the major problems such as the deformation of the natural wing due to drying. Therefore, a different strategy had to be found.

2.1 Digitizing natural wings

The Institute of Biology II considered several owls (*Tyto alba pratincola*) to determine the deviation between different animals. A natural owl wing with its main dimensions is depicted in Fig. 2. The comparison of Figs. 1 and 2 shows the differences of the details of the geometry of the original and the technical wing. However, it can also be stated that the basic features are alike. That is, the wings had a rather elliptic planform, the thickness of the inner half (arm) was mainly located close to the leading edge, whereas the outer half (hand) possessed the shape of a slightly cambered plate.

Surface scans of dead owls were performed to obtain three-dimensional digital models of the wings. The wings were placed in a position resembling gliding flight. The wing position during gliding flight was chosen based on photographs and videos. It was decided that a proper gliding position would be a fully stretched, untwisted wing. Since the natural wing twist is less than 3° (Liu et al. 2006) and since it is a very unsteady parameter with a high dependence on the current flight conditions varying in a limited range, it was neglected for the construction of the artificial wing models. According to photographs of gliding barn owls, the leading edge of the arm region was placed normal to the flight direction. The position of the wing was fixed by a metal frame, which was positioned such that it could be removed from the digital image of the owl wing. To avoid changes in the geometry of the inner part, all wings were scanned together with the body.

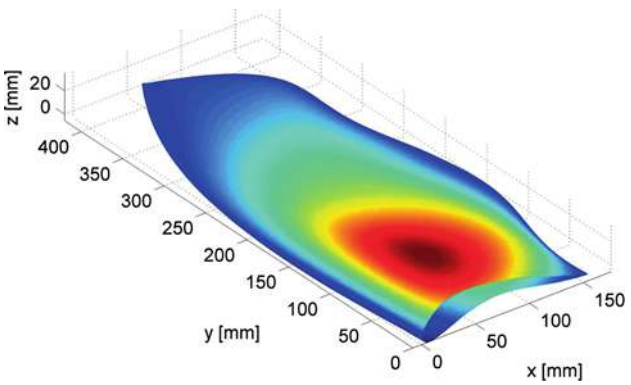

Fig. 1 Reconstruction of the a natural wing using the approach of Oehme and Kitzler (1975) to correct the distribution of the chord. The z coordinate is color coded

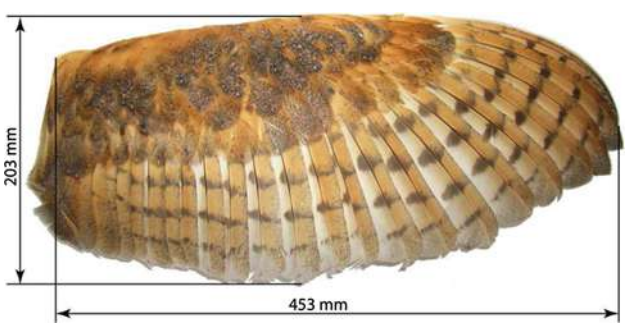

Fig. 2 Main dimensions of a natural barn owl wing

The scan was performed using an optical digitizer (ATOS I, GOM Optical Measuring Techniques, Braunschweig, Germany). The resulting digital models were polygon meshes. Scans of several wings were considered, but only the digital models of two selected wings were used to calculate the final three-dimensional model, which was also used to design the quasi-two-dimensional wing model.

It is well known that the shape, especially the camber and the twist of living and dead bird wings are different (Biesel et al. 1985). The reason for this modification is the drying and contracting of muscles, tendons, and tissue. To minimize the effects of drying the birds were frozen directly after their death. Shortly before scanning the birds were defrosted and prepared as mentioned above. Additionally to the deformation due to drying, all active (e.g. turning of the wrist) and some of the passive mechanisms (e.g. flexibility of skin and feathers) to control the in-flight geometry of the wing are not present if a dead wing is investigated. Both effects have a great impact on the camber line. In contrast to the camber line, Biesel et al. (1985) showed the thickness distribution to be not affected by the drying process and the ineffectiveness of in-flight control mechanisms.

An increase of the camber can also be observed in narcotized birds. This has been demonstrated by Biesel et al. (1985) on pigeons (*Columbia livia var domestica*). Note, using narcotized birds the effects of drying are not taken into account. Since the owls used for scanning have been frozen directly after decease and were defrosted just before they were prepared for the scan the impact of drying is assumed to be much smaller than that due to the relaxation of muscles. That is, the deformation of the wings used here is similar to the deformation of narcotized birds.

2.2 Aerodynamic postprocessing

After scanning, the wings were first divided into several cross sections, each consisting of a number of points,

which depended on the spanwise position of the cross section. The upper and lower surface of the final profiles, which were used to construct the three-dimensional wing model, consisted of 5,000 points. The spatial distance between two adjacent cross sections was 2 mm. Tests with a smaller spatial resolution did not show any improvement. Two hundred and eleven separate cross sections were extracted from each wing. The innermost cross section was placed on the border of the scapulars. Scapulars are feathers that overlie the scapula bone and resemble a link between body and wing. The outermost cross section was placed at approximately $y/2b \approx 0.95$, where y is the spanwise coordinate and $b/2$ the half span. Since the wing tip only consists of a few feathers, which do not overlap, it was not possible to describe this region in terms of an airfoil. That is, the formulae given by Liu et al. (2006) to calculate the camber line and the thickness distribution could not be applied at the wing tip.

Naturally, the cross section extracted from the three-dimensional scan did not meet the requirements of a wind tunnel model. The surface was not smooth and although the wings were fixed onto a frame they did not comply with the requirement of being not twisted. Therefore, for the final model, the surface of each cross section had to be smoothed and the twist of the wing had to be removed. This was achieved by rotating every cross section separately around its own leading edge to remove the twist. The angle of rotation was calculated as the angle between the chord of the cross section and the chord of the wing root. Thereafter, the cross sections were decomposed into a camber line and a thickness distribution. Other parameters to describe the three-dimensional wing were the local chord length and the position of the leading edge.

The mathematical formulation for the camber line and for the thickness distribution was based on algorithms given by Liu et al. (2006). The camber line was described by a Birnbaum–Glauert function

$$\frac{z_{(c)}}{c} = \frac{z_{c(\max)}}{c} \cdot \eta(1-\eta) \sum_{n=1}^{3} S_n \cdot (2\eta - 1)^{n-1} \tag{1}$$

and the thickness distribution by

$$\frac{z_{(t)}}{c} = \frac{z_{t(\max)}}{c} \cdot \sum_{n=1}^{4} A_n \cdot (\eta^{n+1} - \sqrt{\eta}), \tag{2}$$

where $\eta = x/c$ is the normalized chordwise coordinate. The quantities S_n and A_n are the coefficients of the resulting polynomials describing the considered profile. Liu et al. used the aforementioned empirical estimate by Oehme and Kitzler (1975) (Fig. 1) for the local chord length. However, this approach resulted in a non-realistic configuration since the wing tip of this was sharp and the planform was not elliptic. The result achieved when the leading edge and the chord length were extracted from the surface scans agreed well with the natural wing.

The model constructed from the profiles described by the solution of Eqs. 1 and 2 together with the distribution of the chord length and the position of the leading edge showed severe deficiencies. At several positions the discrepancy of the maximum camber and the maximum thickness between adjacent profiles was very high as exemplarily depicted in Fig. 3 for the maximum camber of one scan. That is, the surface was not smooth in the spanwise direction. Even the leading edge and the chord length did not show a smooth distribution due to feathers sticking out of the wing at the leading edge or damaged feathers at the trailing edge. Using a least square fit the coefficients of the camber line and the thickness distribution, the leading edge and the chord length were adjusted in spanwise direction yielding a smooth wing surface.

As mentioned above, the camber of the wings considered here is increased compared to the camber of flying birds. For this reason, the results of Biesel et al. (1985) were used to correct the camber of the scanned owl wings, even though their results were obtained on pigeons. The range and the spanwise distribution of the maximum camber are similar for *Tyto alba pratincola* and *Columbia livia var domestica* (Bachmann et al. 2007). Biesel et al. (1985) measured the profile at nine spanwise locations and determined the chord length, maximum camber, location of maximum camber, maximum thickness, and location of maximum thickness. The ratio of maximum camber of living and dead birds are presented in Fig. 4. These values were used to estimate a spanwise correction factor for the maximum camber. A fourth-order polynomial was

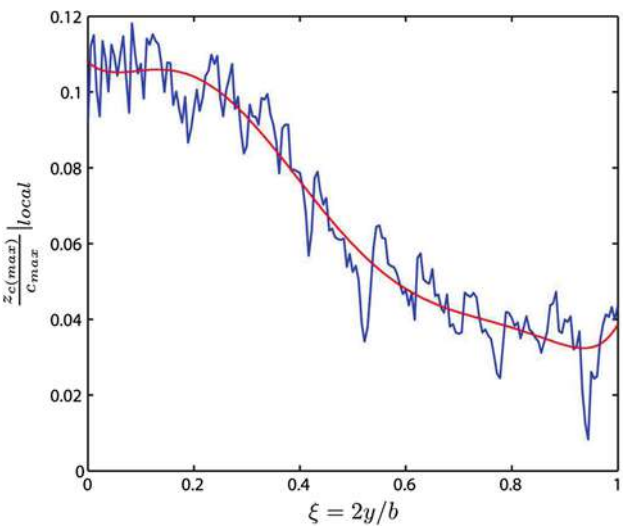

Fig. 3 Distribution of the maximum camber of one scan at spanwise positions (*blue*) and the polynomial fit to obtain a smooth surface (*red*)

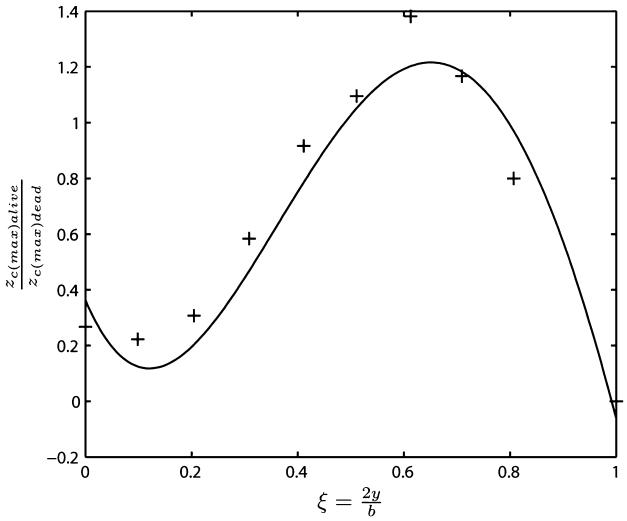

Fig. 4 Spanwise distribution of the maximum camber of a pigeon wing; *symbols* Biesel et al. (1985), *solid line* distribution of the polynomial for the correction factor

determined using a least square fit. The tenth value at $\xi = 1.0$ was added.

Using this distribution to correct the camber line, the geometry of the resulting model resembled the natural wing much better. The very high camber of the three-dimensional wing model with uncorrected camber line becomes obvious in Fig. 5. The correction of the camber line leads to a wing model that matches the natural geometry much better (Fig. 6). Note, the wing tip could not be extracted for reasons mentioned above. It was subsequently constructed using a CAD program and added to the wing model. The contour of the wing tip was determined to be an arc tangent to the leading and to the trailing edge. The upper and lower surface were extended to form a smooth surface.

The first measurements were intended to be performed with a two-dimensional reference wing, i.e., a wing without

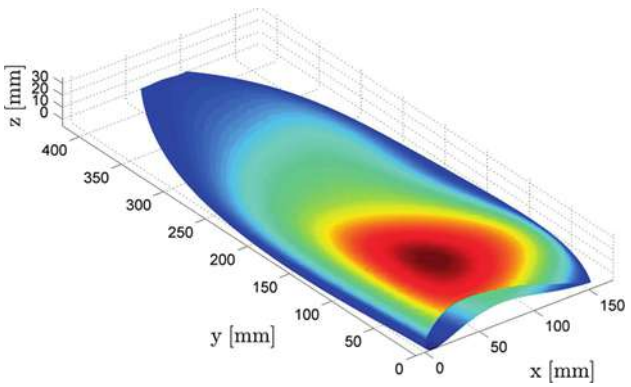

Fig. 5 Three-dimensional model of the wing without the correction of the distribution of the maximum camber. The z coordinate is color coded

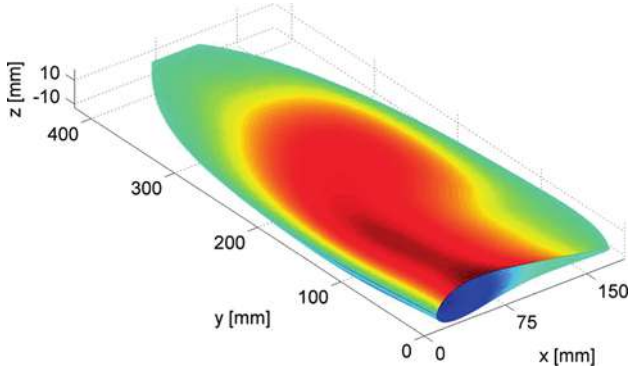

Fig. 6 Three-dimensional geometry of the final wing model

serrations and with a clean surface. That is, the low-speed flow field is only characterized by the freestream, the angle of attack, and the geometry. This wing model was to resemble an owl wing without any special structure or individual characteristics such as the velvet surface or position and alignment of feathers.

Assuming the owl wing to be perfectly adopted to its flight condition and to possess an elliptic lift distribution, 50% of the lift of one wing is approximately provided by the inner 40% of the wing. Therefore, this range is averaged and the resulting profile is used for the quasi-two-dimensional wing. The coefficients of the polynomials describing the camber line and the thickness distribution (Eqs. 1 and 2) are given in Table 1. To obtain a flow field which is not dominated by the averaging it must be ensured that the averaged profile does not show significant differences in the flow field compared with a single profile from the three-dimensional wing. This issue will be discussed in Sect. 4.

Figures 7 and 8 show the camber line and the thickness distribution of the quasi-two-dimensional owl based wing model. The data is juxtaposed with the camber line and the thickness distributions of an owl wing published by Liu et al. (2006). The camber line is nearly symmetric in both cases. The maximum camber of the profile measured by Liu et al. is located at $x/c = 0.47$, for the owl based profile it is located slightly downstream at $x/c = 0.50$. Unlike the camber line distribution the thickness distribution differs somewhat. Again, the maximum of the profile of Liu et al. is located slightly upstream, i.e., $x/c_{\mathrm{Liu}} = 0.11$ and

Table 1 Coefficients S_n and A_n of Eqs. 1 and 2 for the geometry of the quasi-two-dimensional aifoil

	1	2	3	4
S_n	1.503×10^{-1}	-2.841×10^{-3}	1.188×10^{-3}	–
A_n	−1.912	4.005	−3.451	1.091

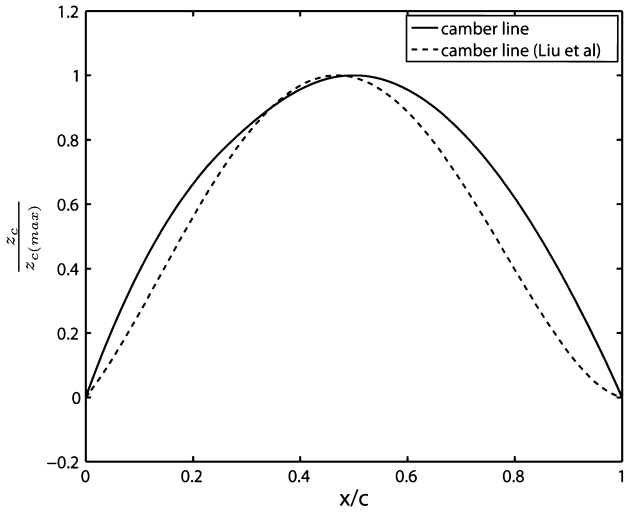

Fig. 7 Camber line of the quasi-two-dimensional wing model $z_c/z_{c(\max)}$ vs. x/c compared with that by Liu et al. (2006)

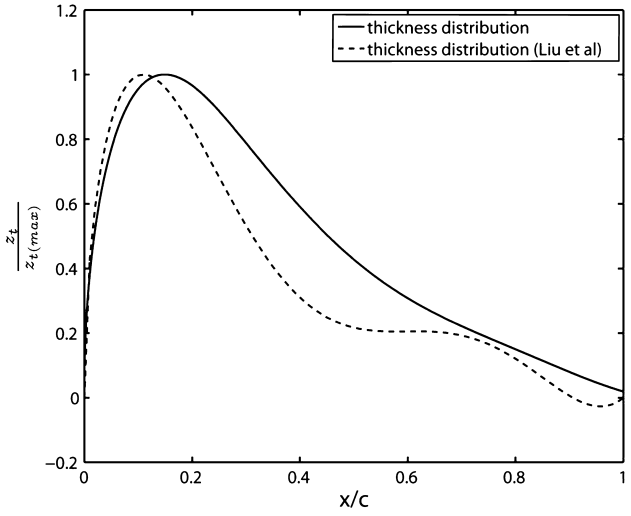

Fig. 8 Thickness distribution of the quasi-two-dimensional wing model $z_t/z_{t(\max)}$ vs. x/c compared with that by Liu et al. (2006)

$x/c_{\text{owl}} = 0.15$. The thickness distributions show the same features, i.e., a high maximum close to the leading edge, a strong decrease downstream of the maximum thickness, and low values in the region close to the trailing edge. Downstream of the maximum thickness, the profile investigated by Liu et al. is thinner than the novel owl based shape ($z_{t\,\text{owl}} > z_{t\,\text{Liu}}$ for $x/c > x/c_{z_{c(\max)}}$). The former geometry also shows a constant thickness in the region of $0.5 \leq x/c \leq 0.7$ and negative values for $x/c \geq 0.9$. In this region, the natural wing is very thin, since it consists of only one single layer of feathers. The novel thickness distribution derived here decreases monotonically and shows no negative values at the trailing edge.

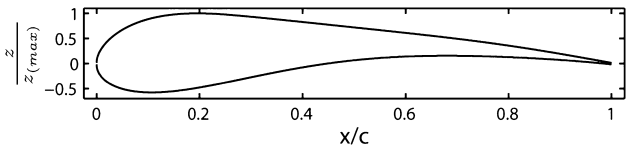

Fig. 9 Profile of the quasi-two-dimensional wing model

Table 2 Characteristics of the quasi-two-dimensional owl based profile

Description	Abbreviation	
Chord length	c	0.178 m
Span	l	0.5 m
Wing area	A	0.089 m^2
Max. thickness	$z_{t(\max)}$	14.77%
Location of $z_{t(\max)}$	$x_{zt(\max)}$	15.00%
Max. camber	$z_{c(\max)}$	3.80%
Location of $z_{c(\max)}$	$x_{zc(\max)}$	50.40%
Nose radius	r_n	11.35%
Trailing-edge angle	α_{tr}	4.53%

The upper and the lower surfaces of the profile are calculated by $z_{\text{upper}} = z_c + z_t$ and $z_{\text{lower}} = z_c - z_t$. The resulting profile is depicted in Fig. 9. Table 2 summarizes the basic geometric characteristics of the owl based quasi-two-dimensional airfoil.

The three-dimensional and the quasi-two-dimensional wing model were manufactured by rapid prototyping. From both wing models a casting mold was created to be able to reproduce a series of models, which can be equipped with the owl-specific structures. Table 3 lists several versions of the three-dimensional and quasi-two-dimensional wings equipped with different structures that have been manufactured. In the following, the notation of Table 3 will be

Table 3 Versions of the wing models which have been manufactured

	Geometry		Equipped with	
	Two dimension	Three dimension	Velvet surface	Serrations
Wing 1a	•			
Wing 1b	•		•	
Wing 1c	•			•
Wing 1d	•		•	•
Wing 2a		•		
Wing 2b		•	•	
Wing 2c		•		•
Wing 2d		•	•	•

used, e.g. the quasi-two-dimensional wing model with the velvet surface will be denoted "wing 1b".

Note, only the models of wing 1a and 1b will be considered in this paper since it is the purpose of this investigation to clearly show the impact of the velvet-like surface on the near-wall flow field. The influence of the serrations and the three-dimensionality will be analyzed in future experiments.

3 Experimental setup and measurement techniques

The flow fields of the wings 1a and 1b were measured in the low speed wind tunnel of the Institute of Aerodynamics (Fig. 10). It is a closed circuit wind tunnel with a test section possessing a cross section of 500×500 mm^2 and a length of 1,200 mm. The side walls of the test section are made of plexiglass. On each side a transparent round plate exists to adjust the angel of attack. To provide optical access the top wall of the test section is made of transparent material. The measurement equipment such as probes or other sensors was installed on the bottom wall. The power unit is water-cooled to stabilize the temperature.

The flow field of the artificial owl based airfoil was analyzed and characterized using several measurement techniques. All measurements were performed at angles of attack of $\alpha = -3°$, 0°, 3°, and 6°. Chord based Reynolds numbers of $Re_c = 20{,}000$, 40,000, and 60,000 were investigated, i.e., freestream velocities of approximately 1.8, 3.5, and 5.3 m/s were considered. Pressure measurements were performed on the upper and lower surface. A special wing model was built to integrate brass pipes into the interior of the wing. The position of the pressure holes is depicted in Fig. 11. The brass pipes were connected to the side wall of the test section. The pressure measurements were conducted using a micro-manometer.

The oil-flow pattern technique was used to visualize the flow immediately adjacent to the surface and as such to identify major flow phenomena such as separation, reattachment, and a possible transition from laminar to turbulent flow. The wing model was coated with an oil film which was mixed with a fine grained pigment. The shear

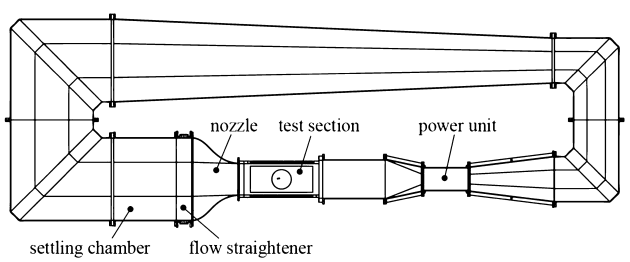

Fig. 10 Schematic of the closed circuit low-speed wind tunnel

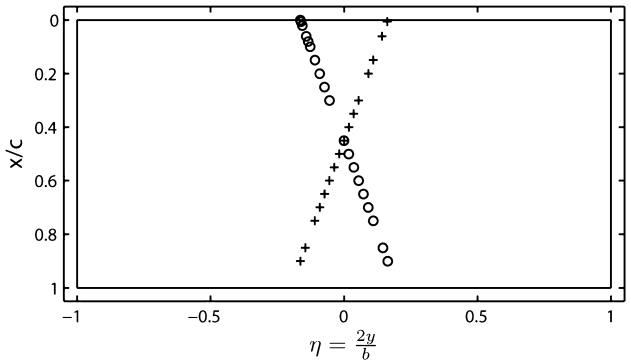

Fig. 11 Distribution of the pressure holes of the suction side (*circle*) and the pressure side (*plus*)

stress of the air flow directs the oil, which evaporates leaving the deposit of the pigment on the surface. The structures of the deposit indicate the flow direction or the flow conditions, e.g. laminar or turbulent flow. It is essential to match the viscosity of the oil to the shear stress of the flow. Otherwise, no flow structures can be observed because the oil and the pigments are not transported by the flow. Good results at transonic and supersonic conditions have been obtained using solvent petroleum. The viscosity varies with the mixing ratio of petroleum and pigment. At the low velocities considered here, it was impossible to obtain satisfying flow structures with petroleum due to its high viscosity whereas using a mixing ratio of petroleum and lamp oil of 1:2 to lower the viscosity flow structures could be observed. However, the runtime of the wind tunnel had to be increased to ensure that enough oil evaporates such that the flow structures do not vanish after turning off the wind tunnel.

To obtain two-dimensional data of the velocity field, particle-image velocimetry (PIV) measurements were performed. The measurement plane was oriented in flow direction and normal to the wing surface. Only the velocity field of the suction side was recorded. A standard PIV system with a double-pulse Nd:YAG laser (*New Wave SoloXT 200*) and a double-shutter camera (*PCO SensiCam*) was used. A light arm connected the laser with the light sheet optics. The laser and camera were triggered at 3 Hz by a synchronizer (*ILA mini PIV-Synchronizer*). The pulse distance was 100 μs for $Re_c = 40{,}000$ and 60,000, respectively, and 150 μs for $Re_c = 20{,}000$.

At an angle of attack of 3° the entire flow field of the upper side was recorded at $Re_c = 40{,}000$ and 60,000 using up to 3,000 images to determine the average velocity field and to identify separation and reattachment. Since the main interest was on the influence of Reynolds number and angle of attack on the occurring separation bubble, it was decided to limit the recorded area to that of the approximate size of the bubble, i.e., for each flow condition the measurement plane ranged from the leading edge to $\sim$65% chord length.

Table 4 Measurements performed on wing 1a using oil flow pattern (OFP), pressure tabs (PD), and particle-image velocimetry (PIV)

Re	α (°)	Wing 1a			Wing 1b
		OFP	PD	PIV	PIV
20,000	−3			•	•
	0			•	•
	3			•	•
	6			•	•
40,000	−3	•	•	•	•
	0	•	•	•	•
	3	•	•	•	•
	6	•	•	•	•
60,000	−3	•	•	•	•
	0	•	•	•	•
	3	•	•	•	•
	6	•	•	•	•

Additionally, for all test cases the measurement plane was divided into three sections resulting in a spatial resolution of 0.4 mm between each vector, i.e., 0.0022 chord length. To determine the position of the measured field relative to the wing a calibration grid was used. The shape of this calibration grid perfectly matched the wing to achieve a high repeatability.

Table 4 summarizes the measurements that have been performed. The flow over wing 1a has been analyzed using the oil flow technique, pressure tabs, and particle-image velocimetry. The flow structure and the details of the separation and reattachment of wing 1b has only been measured using PIV because it is not possible to perform the oil flow technique and the pressure measurements on the velvet surface.

4 Results and discussion

The characteristics of the flow field and its dependence on the Reynolds number and angle of attack were investigated using the aforementioned measurement techniques. The flow fields for several flow parameters will be discussed. Note, however, the variations in the flow structure will be evidenced for the $Re_c = 40{,}000$ and $\alpha = 0°$ problem. First, the results of the pressure measurements will be presented and compared with pressure distributions calculated by the software XFoil. Next, these findings will be compared with the flow field visualized by the oil flow pattern. Subsequently, PIV measurements will provide quantitative data on the two-dimensional flow field. This data will be used to estimate the transition onset and to calculate the spatial two-point correlations. To investigate the impact of the owl-specific surface structure of the owl wing, the suction side of the quasi-two-dimensional wing was equipped with a velvet surface structure. The leading edge serration are not considered here, but will be subject to future investigations.

4.1 Pressure distribution

The pressure distribution was measured for the flow conditions mentioned in Table 4 and also calculated with the software XFoil. Figure 12 depicts exemplarily the distributions at $Re_c = 40{,}000$ and $\alpha = 0°$ for wing 1a, i.e., the configuration with a clean surface. It evidences a fairly low suction peak and a plateau just downstream of the peak extending from approximately $x/c = 0.25$ to 0.55. The plateau is followed by a monotonous increase in pressure towards the trailing edge. The experimental distribution is in close agreement with the pressure distribution computed by XFoil at the same flow conditions. According to Thwaites (1960), this distribution indicates the presence of a leading edge separation and a so-called "long bubble". It is characteristic for this kind of separation that its chord wise extent on formation is very small at low angles of attack, approximately 2–3% chord (Thwaites 1960), and that it grows rapidly at increasing angles such that at high angles of attack the flow does not reattach anymore. Interestingly, the same pressure distribution is found on the lower side indicating a separated flow. This detachment is caused by the high thickness close to the leading edge resulting in a high curvature of the lower side of the airfoil.

Due to the increase of the bubble length at increasing angle of attack, the gradient of the lift coefficient c_l decreases. Figure 13 shows the distributions of the experimentally and numerically determined lift coefficient c_l at $Re_c = 40{,}000$ and 60,000, respectively, calculated by $c_l = \frac{1}{A}\int_A (c_{p,\text{lower}} - c_{p,\text{upper}})\mathrm{d}A$ from the pressure measurements

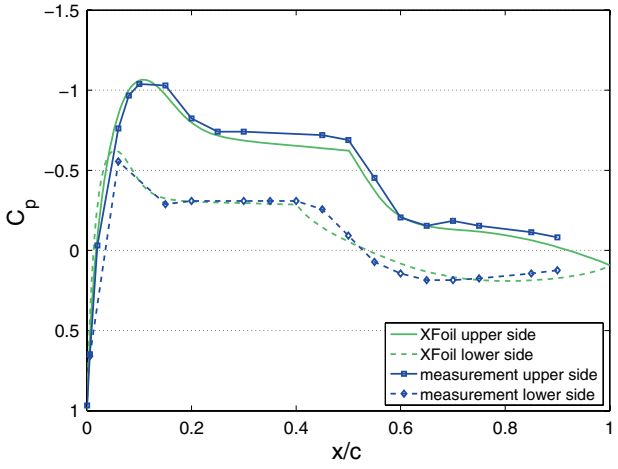

Fig. 12 Measured and computed pressure coefficient distribution $c_p = (p - p_\infty)/(\frac{\rho}{2}u_\infty)$ at $Re_c = 40{,}000$ and $\alpha = 0°$

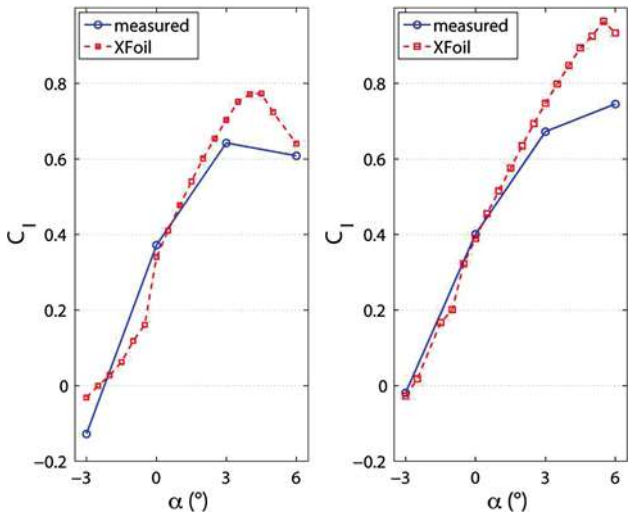

Fig. 13 Distribution of the lift coefficient C_l over α for $Re_c = 40{,}000$ (*left*) and $Re_c = 60{,}000$ (*right*)

and also by XFoil. The graphs clearly depict that the higher the Reynolds number, the larger is the maximum lift coefficient. The maximum lift is reached when the bubble extends to the trailing edge of the wing (Thwaites 1960). In the case of $Re_c = 40{,}000$, this occurs at $\alpha = 4°$ and in the case of $Re_c = 60{,}000$ between $\alpha = 5°$ and 6°, respectively. Note, the PIV data discussed further below confirm the close correlation indicated by the pressure measurements between the size of the separation and the lift coefficient. At high angles of attack the flow separates completely. XFoil, however, is not capable of computing separated flows since it is based on solutions of the boundary layer conditions plus the Euler equations. That is, only incipient separation can be computed. This explains the high discrepancy at angles of attack $3° \leq \alpha \leq 6°$. The rate of change of the lift coefficient with respect to the angle of attack at $\alpha \leq 3°$ does match in the numerical and experimental distribution.

To verify whether the separation observed in the pressure distribution is a result of the averaged geometry, the pressure distributions of several profiles from the three-dimensional wing were calculated using XFoil. Ten pressure distributions at locations between $0 \leq 2y/b \leq 0.4$, which corresponds to the range that was used to determine the averaged quasi-two-dimensional geometry, were computed. In all cases, the distributions indicated the presence of a separation bubble on the suction side. This suggests that it is not only a geometry effect that leads to the formation of a separation bubble, but rather the removal of the owl-specific structures of the wing. In other words, those structures seem to have a great impact on the overall flow field and on the flight capabilities of the owl.

4.2 Oil flow pattern

To further substantiate the analysis of the flow field and to verify the findings of the pressure measurements oil flow visualization was applied. The results of the oil flow pattern technique indicate the flow around the leading edge to be attached and laminar as it is exemplarily shown in Fig. 14 for the parameter combination $Re_c = 40{,}000$ and $\alpha = 0°$. The point of separation can be determined to be approximately located at the maximum thickness ($x/c = 0.15$) and becomes evident in the distinct alteration in the oil flow pattern. At increasing angle of attack the point of separation moves upstream. In the separated region, the oil pattern does not show any structure. In the depicted test case, this region extends to $x/c = 0.5$, which agrees well with the pressure distribution shown in Fig. 12. In most cases this region can easily be identified.

4.3 Particle-image velocimetry

The flow has also been investigated using PIV to detect the separation bubble. Considering the raw PIV data, i.e., the particle images, the contour streamline of the bubble is determined to be the line the highest velocity gradient occurs. Extrapolating this streamline to the surface of the wing the point of separation is determined. The results of this analysis corroborate the findings of the oil flow pattern measurements. The data is summarized in Table 5. It shows the point of separation to hardly depend on the Reynolds number, but primarily on the angle of attack and agrees well with the findings of Burgmann and Schröder (2008) on the SD7003 airfoil.

The identification of the separation bubble using PIV was based on averaging 1,500 instantaneous images. Figure 15 shows the average velocity field at $Re_c = 40{,}000$ and $\alpha = 0°$. This averaged analysis suggests a clearly

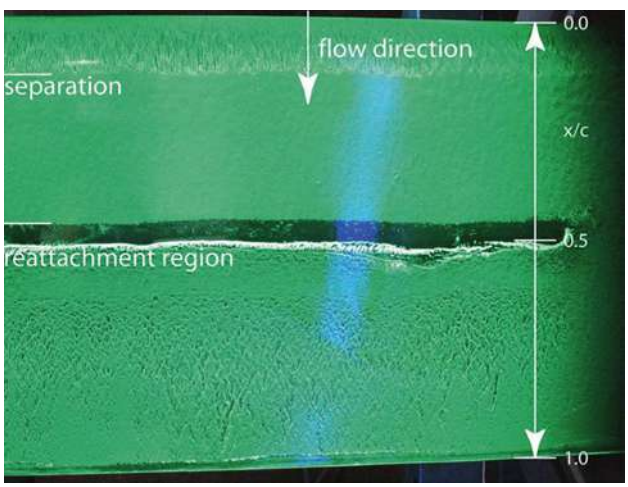

Fig. 14 Result of the oil flow pattern at $Re_c = 40{,}000$ and $\alpha = 0°$

Table 5 Separation points $(x/c)_{sep}$ based on PIV data

Angle of attack	x/c		
α (°)	Reynolds number		
	20,000	40,000	60,000
−3	0.26	0.26	0.25
0	0.19	0.19	0.20
3	0.16	0.16	0.17
6	0.15	0.15	0.15

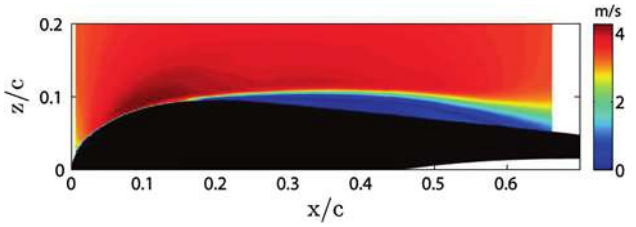

Fig. 15 Magnitude of averaged velocity field for a clean wing (wing 1a) at Re_c = 40,000 and $\alpha = 0°$

defined end of the separation in those cases where the bubble is closed. However, a closer look reveals that this is not the case. Reattachment does not occur at a fixed location. In fact, it is a highly unsteady and spatially oscillating process. At the downstream end of the separation bubble, the shear layer rolls up forming a vortex that eventually detaches from the bubble and moves downstream. This is illustrated in Fig. 16 at $Re_c = 40{,}000$ and $\alpha = 0°$. The unsteadiness of the bubble length also becomes evident in the oil flow pattern as the black band, which is clearly visible in Fig. 14. Its size is approximately $x/c \approx 0.06$ and, thus, is consistent with the vortex size depicted in Fig. 16. In other words, the black band marks rather a reattachment region than a reattachment line.

The size of the separation bubble grows at increasing angle of attack. At $Re_c = 40{,}000$ and $\alpha = 3°$ the average flow field evidences a reattachment at $x/c \approx 0.65$. However, at $\alpha = 6°$ a total separation occurs. This means that the maximum bubble length, i.e. when the bubble extends to the trailing edge, is reached between $\alpha = 3°$ and 6°. Thus, the maximum lift is also reached in that interval, which complies with the assumption made by the distribution of the lift coefficient in Fig. 13.

An investigation of the vortex structure detaching from a separation bubble on a SD7003 airfoil has been performed by Burgmann et al. (2007). Time resolved PIV as well as stereo scanning PIV was used to record and analyze the vortex roll-up at $Re_c \leq 100{,}000$ and $\alpha > 4°$. Initially, the separated shear layer rolls up forming a vortex. The vortex drifts downstream and detaches from the bubble. Immediately after the detachment of the vortex, the bubble closes and the process starts again. Moving further downstream it

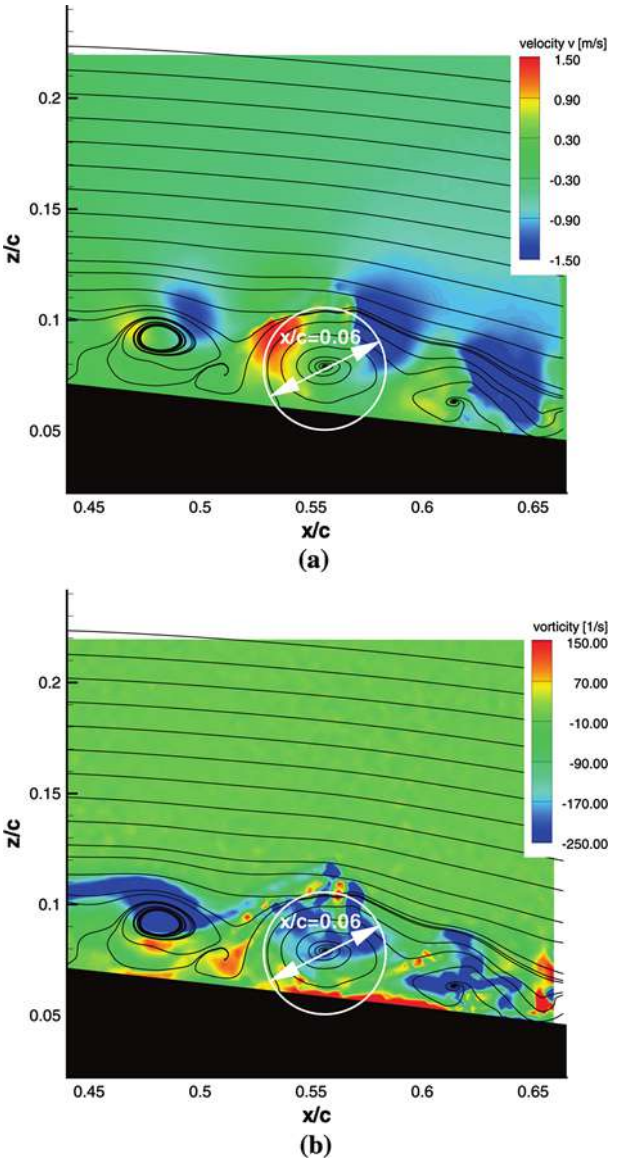

Fig. 16 Instantaneous PIV image of vortices at the end of the separation bubble at $Re = 40{,}000$ and $\alpha = 0°$. **a** The color defines the distribution of the normal velocitycomponent; **b** the color defines the distribution of the vorticity

finally breaks down and dissipates. The PIV measurements over the owl based wing did not reveal a similar evolution of the vortex. In fact, the vortices being formed at the downstream end of the separation bubble are shed, but their size relative to the bubble is small. That is, most vortices do not reach the surface of the wing. This seems to destabilize the vortices and they break down immediately after having detached from the bubble.

4.4 Velvet surface

It goes without saying that such a flow field, which is highly susceptible to changes in the flow conditions, cannot

be characteristic for the owl. Note, for the experiments mentioned above, all of those specific owl features were removed to have a clean technical reference flow (wing 1a). Therefore, the owl-specific structures of the owl wing must have a considerable influence on the development of the flow field on the wing and hence on the outstanding flight performance of the owl. Applying those structures to this wing it is possible to investigate their influence in detail. In a first step, the special surface structure of the owl wing was investigated. Therefore, the suction side of the wing was covered with velvet (wing 1b). The velvet was chosen to match the geometric characteristics of the real surface structure of the owl wing, i.e., the length and the density of the hairs (Bachmann et al. 2007). Figure 17 shows a comparison of the natural and the artificial surface structure. The material properties were only checked manually. That is, the Youngs-modulus has not been investigated but the feel of the natural and the artificial surface is alike. A detailed comparison of the biological and the technical material will be presented elsewhere.

PIV measurements were performed to analyze the impact of the velvet surface on the overall flow field. The comparison of the velocity distributions of wing 1a and wing 1b is shown in Figs. 18 and 19. The slight discontinuities in Figs. 18 and 19 are due to the decomposition of the measurement plane into three sections to enhance the spatial resolution. Before each measurement the calibration grid was placed on the wing to determine the position of the measurement plane relative to the wing and using the chord based Reynolds number Re_c and the temperature the corresponding freestream velocity was calculated. Minor errors in placing the calibration grid or in calculating the Reynolds number and the freestream velocity caused the observed discontinuities.

The velocity distributions illustrated in Figs. 18 and 19 evidence the influence of the surface structure on the separation bubble. The effect seems to be a combination of an increased roughness and something similar to a riblet structure due to the alignment of the hairs (Itoh et al. 2006). Both, the roughness and the riblets, have a significant impact on the aerodynamic performance since they influence the separation, consequently the transition onset, and thus, the reattachment (Roberts and Yaras 2006). For all flow conditions shown in Figs. 18 and 19 the point of separation moves upstream at increasing angle of attack on wing 1a as well as on wing 1b. At $Re_c = 20{,}000$ and $\alpha = 6°$ the velvet has no influence on the reattachment. That is, the perturbations excited by the velvet surface are in neither case strong enough to increase the momentum exchange in the near-wall layers such that separation can be avoided or the flow can be forced to reattach. At higher Reynolds numbers, i.e., $Re_c = 40{,}000$, the influence does depend on the angle of attack. At $\alpha = 6°$ the flow over the suction side of the clean wing completely separates. The PIV image in Fig. 19c also shows the flow over the velvet surface to be detached. At lower angles of attack, however, the size of the separation bubble decreases due to the velvet surface. That is the separation bubbles at $Re_c = 40{,}000$ and $\alpha = 0°$ and 3° in Fig. 19a, b are smaller than in Fig. 18a, b.

The reattachment of the flow occurs due to laminar-turbulent transition, which is excited by the inflection in the

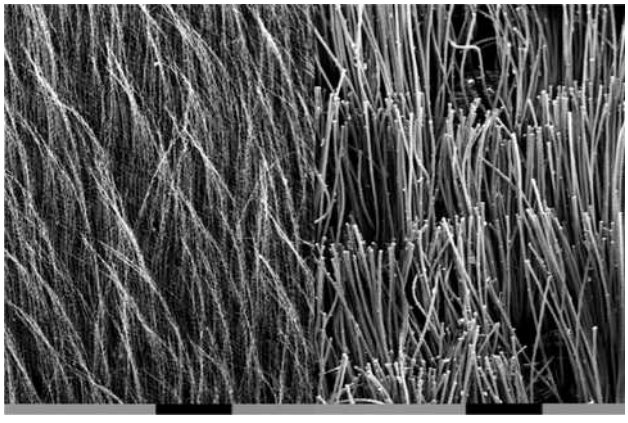

Fig. 17 Surface structure of the natural owl wing (*left*) and the applied velvet (*right*). The *black bar* at the bottom represents a length of 400 μm

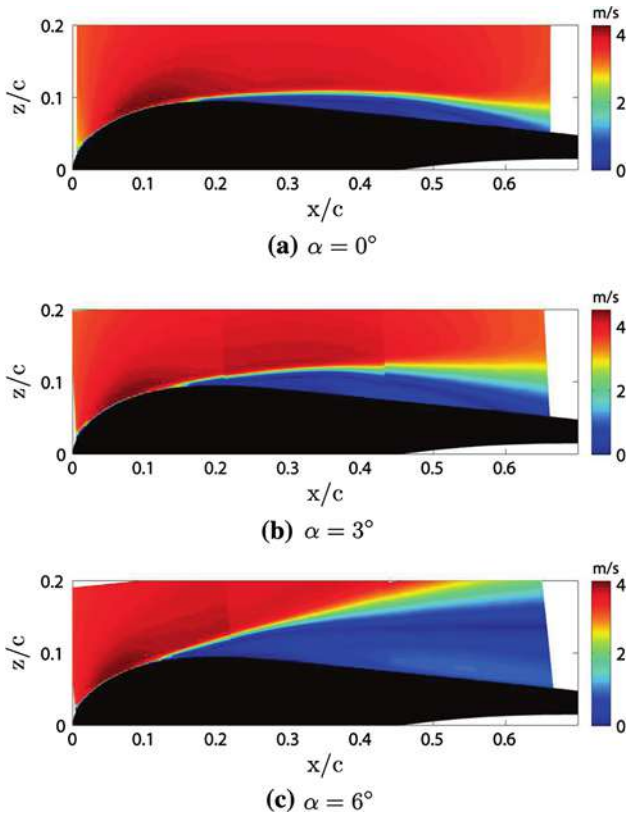

Fig. 18 Averaged velocity fields for a clean wing (wing 1a) at Re_c = 40,000 and $\alpha = 0°$, 3°, and 6°

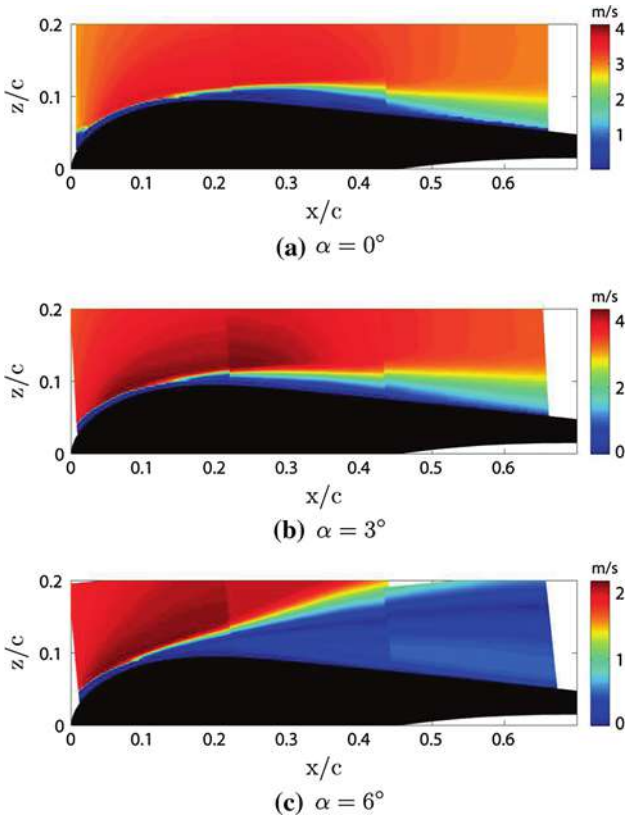

Fig. 19 Averaged velocity fields for a velvet wing (wing 1b) at Re_c = 40,000 and $\alpha = 0°$, 3°, and 6°

velocity distribution in the separated flow regime. To identify the transition region the $u'v'$-correlation of the Reynolds shear stress tensor is analyzed. The process of separation and reattachment is dominated by vortex structures which form in the separation bubble, drift downstream, and finally detach from the bubble effecting the location of the transition onset. Therefore, it is not one definite position where transition sets in but rather a zone in freestream direction where an increase of the Reynolds shear stress can be observed as shown by Burgmann et al. (2007) on a SD7003 airfoil. Therefore, the location of a strong increase of the Reynolds shear stresses, i.e., a pronounced change in the streamwise gradient of the shear stresses can be used to indicate and define the position for the onset of transition. The Reynolds shear stress grows in streamwise direction. An exponential growth is observed, which can be predicted by linear stability theory as it has been done by, e.g., Lang et al. (2004). McAuliff and Yaras (2005) suggested the transition onset to occur where the increase of the normalized Reynolds shear stress rate deviates from the exponential growth.

A strong increase of the Reynolds shear stresses is also observed in the flow field over the owl based wing independent of the clean or the velvet surface. The methods of Burgmann and Schröder (2008) and McAuliff and Yaras (2005) are used to determine the point of transition onset. Since the streamwise gradient of the shear stresses undergoes an evident change already in the regime of exponential growth, the transition onset listed in Table 6 according to Burgmann and Schröder (2008) are closer to the leading edge. The distributions of the normalized Reynolds shear stresses are shown in Fig. 20 for wing 1a and 21 for wing 1b, respectively. It is obvious that the increase in the Reynolds shear stresses occurs closer to the leading edge for wing 1b.

Table 6 Point of transition onset $(x/c)_{tr}$ according to McAuliff and Yaras (2005) [MY] and Burgmann and Schröder (2008) [BS] for the clean (wing 1a) and the velvet surface (wing 1b)

α (°)	Reynolds number					
	20,000		40,000		60,000	
	MY	BS	MY	BS	MY	BS
Clean surface (wing 1a)						
0	–	0.53	0.55	0.39	0.46	0.34
3	0.59	0.42	0.42	0.32	0.38	0.28
6	0.48	0.38	0.34	0.25	0.28	0.19
Velvet surface (wing 1b)						
0	0.55	0.44	0.33	0.24	0.28	0.17
3	0.47	0.38	0.24	0.22	0.24	0.21
6	0.45	0.33	0.22	0.18	0.16	0.10

The rise in the values of the maximum Reynolds shear stress occurs slowly. At higher angles of attack as well as at higher Reynolds numbers the beginning of the increase moves further upstream, which corresponds with the shift of the separation point. The more upstream occurring transition due to an increased Reynolds number leads to an earlier reattachment, which is evident in the averaged velocity fields shown in Figs. 18 and 19. That is, unlike the separation point, which is hardly influenced by the Reynolds number, the transition onset and thus the reattachment depends on the Reynolds number.

Based on the PIV data, the spatial two-points correlations are calculated. As pointed out above for the PIV images, the images of the spatial two-point correlations show the same discontinuities. Since the two-point correlations are not computed across the borders of the sections of the measurement plane the values differ and the structures possess a pronounced alteration.

Using spatial two-point correlations it is possible to estimate the size of the vortices and the location where they emanate. The distribution of the local maxima and minima indicates the average streamwise extent of a shed vortex and the distance between two consecutive vortices (Kim et al. 1987). Furthermore, the regions of strong correlation also describe where the vortices arise and how their size develops downstream. The contours of the spatial two-point correlation of the normal velocity component are

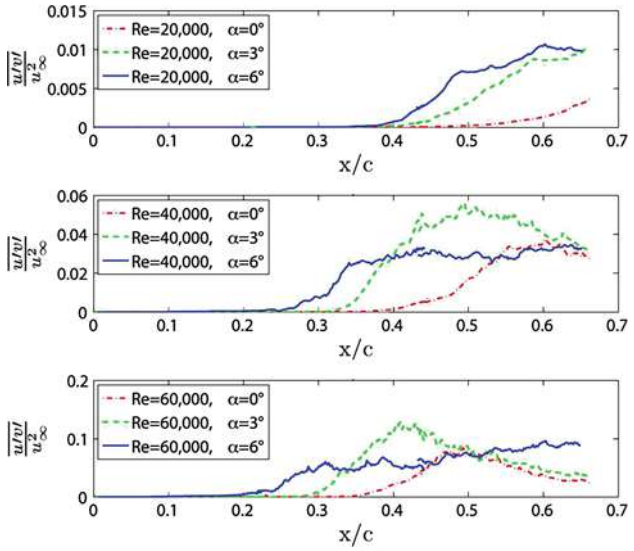

Fig. 20 Distributions of the maximum normalized Reynolds shear stress $u'v'/u_\infty^2$ at $Re_c = 20{,}000$, 40,000, and 60,000 and $\alpha = 0°$, 3°, and 6° for the wing with clean surface (wing 1a)

shown in Fig. 21 for $Re_c = 40{,}000$ and $\alpha = 0°$ for wing 1a and wing 1b, respectively. The correlations reveal significant differences in the location where the correlations are highest and the size of the structures.

Cal et al. (2007) investigated the development of a boundary layer over a rough surface under a favorable pressure gradient. They stated the surface roughness to destroy the near-wall coherent structures. This implies that the size of those flow structures, which eventually dissipate downstream, would be rather small, or at least smaller than that for the clean surface.

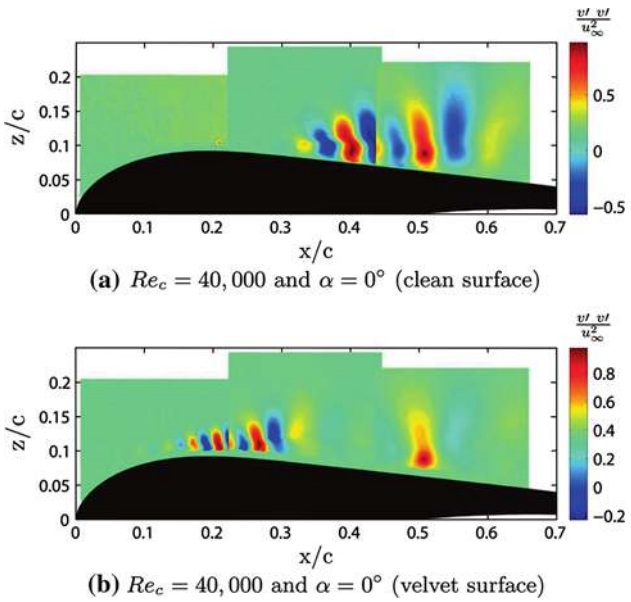

(a) $Re_c = 40,000$ and $\alpha = 0°$ (clean surface)

(b) $Re_c = 40,000$ and $\alpha = 0°$ (velvet surface)

Fig. 21 $v'v'$-correlation at Re_c = 40,000 and $\alpha = 0°$ for a clean (**a**) and a velvet wing (**b**)

These findings are corroborated by comparing the structures of the spatial two-point correlations of wing 1a and wing 1b. The spatial two-point correlation of the normal velocity component for wing 1a in Fig. 21a indicates the location from where vortices start to shed to be approximately located at $x/c \approx 0.31$. The distance between the maximum and the minimum, which approximates the radius of a vortex, is approx. 0.03 c. Consequently, the size of a vortex, i.e., the distance between two adjacent minima is approx. 0.06 c which agrees well with the size of the black band in the oil flow pattern (Fig. 14) and in the instantaneous PIV image (Fig. 16). The velvet surface (wing 1b) shifts the point, where the vortices start to shed, closer to the leading edge $x/c \approx 0.13$ and diminishes the radius of the vortices to roughly 0.02 c and the distance between them to approximately 0.04 c.

Note, the smaller vortex size and the occurrence of vortices further upstream for wing 1b substantiates the above statement visualized in Figs. 20 and 22 that changing the surface structure moves the transition onset further upstream and decreases the size of the separation bubble.

5 Conclusion and outlook

The wings of several barn owls were investigated. Using three-dimensional surface scans an artificial wing for wind tunnel tests was constructed. The surface scans were divided into approximately 200 cross sections. Mathematical algorithms based on a Birnbaum–Glauert distribution were used to extract the camber line and the thickness distribution.

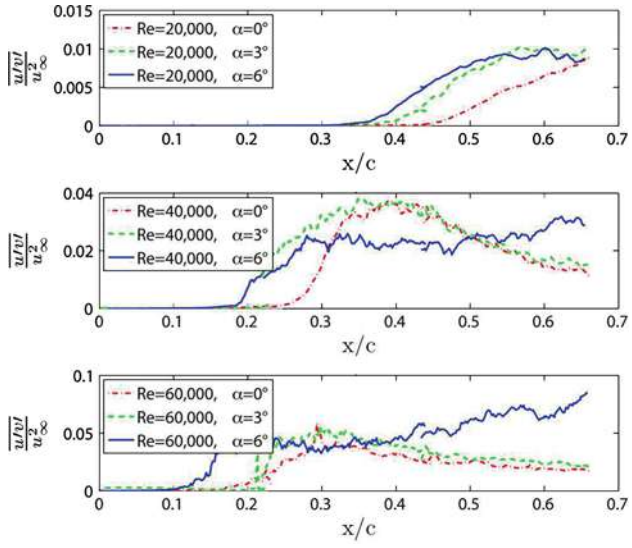

Fig. 22 Distributions of the maximum normalized Reynolds shear stress $u'v'/u_\infty^2$ at $Re_c = 20{,}000$, 40,000, and 60,000 and $\alpha = 0°$, 3°, and 6° for the wing with velvet surface (wing 1b)

Together with the local chord length and the position of the leading edge these profiles were reassembled to a three-dimensional artificial wing with a clean surface.

The resulting shape showed the characteristics which are special for owls. The owl wing's planform is rather elliptical having an area which exceeds by far the area of similar sized birds (e.g. pigeons, Bachmann et al. 2007). In the inner half of the wing the thickness is mainly concentrated close to the leading edge ($x/c \leq 0.25$). Downstream of the location of maximum thickness, the thickness decreases drastically resulting in a very thin trailing edge of the wing. The camber line is symmetrical and the position of the maximum camber is located at approximately $x/c = 0.50$. Consisting of only one layer of feathers with small overlap and almost no camber, the outer half of the wing resembles rather a flat plate.

The three-dimensional model was used to derive a quasi-two-dimensional wing model by averaging a certain interval of the span. Assuming the owl wing to be perfectly adapted to its flight conditions and to possess an elliptical lift distribution, the chosen interval ($0.0 \leq x/c \leq 0.4$) would provide half of the total lift of a single wing.

Three different measurement techniques were used to record and analyze the flow field of the novel owl based quasi-two-dimensional airfoil. Pressure distributions revealed a separation bubble on the suction side of the clean wing model. The existence of the separation bubble and its dependence on the Reynolds number and the angle of attack were also verified by the oil flow pattern technique and particle-image velocimetry.

Next, the wing was equipped with a velvet surface resembling the velvety soft surface of an barn owl's feather to investigate its influence on the flow field. At higher Reynolds numbers and at moderate angles of attack, the size of the separation bubble was reduced significantly. It is assumed that the impact of the velvet surface is a combination of an increased surface roughness and some kind of riblet structure due to the alignment of the hairs.

Since the reattachment is forced by the transition from laminar to turbulent, a decrease in the size of the separation bubble and, hence, a reattachment further upstream, corresponds to a transition onset further upstream. It is obvious that the velvet surface shifts the point of transition onset upstream in all test cases.

The influence of the velvet surface is also evident in spatial two-point correlations of the normal velocity component. In all test cases, the size of the vortices and their distance are diminished by the velvet surface. At the same time, the point where the vortices develop moves further upstream.

The experiments for the velvet surface emphasize the special structures of the owl wing, i.e. the velvet surface and the leading edge serrations, to be essential for the flow field. An understanding of the aerodynamics of the owl wing and how it is influenced by the different structures is necessary to come up with ideas how to transfer those effects to the much higher Reynolds number range of aircraft and how those mechanisms can be used to design a silent airfoil. Further experiments will be conducted with the fully three-dimensional wing to investigate the impact of the serrations and of the material properties, i.e., Youngs modulus, of the surface structure on the three-dimensional flow field.

Acknowledgments This work has been funded by the Deutsche Forschungsgemeinschaft in the priority research program "SPP 1207 Strömungsbeeinflussung in der Natur und Technik" under grant number SCHR 309/35.

References

Bachmann T, Klän S, Baumgartner W, Klaas M, Schröder W, Wagner H (2007) Morphometric characterisation of wing feathers of the barn owl *tyto alba pratincola* and the pigeon *columbia livia*. Front Zool 4:23, doi:10.1186/1742-9994-4-23

Bechert DW, Bruse M, Hage W, von der Hoeven JGT, Hoppe G (1997) Experiments on drag-reducing surfaces and their optimization with an adjustable geometry. J Fluid Mech 338:59–87

Biesel W, Butz H, Nachtigall W (1985) Erste Messungen der Flügelgeometrie bei frei gleitfliegenden Haustauben (*columbia livia var. domestica*) unter Benutzung neu ausgearbeiteter Verfahren der Windkanaltechnik und der Stereophotogrammetrie. Biona-report 3, pp 139–160

Burgmann S, Schröder W (2008) Investigation of the vortex induce unsteadiness of separation bubble via time-resolved and scanning PIV measurement. Exp Fluids 45(4):675–691. doi: 10.1007/s00348-008-0548-7

Burgmann S, Dannemann J, Schröder W (2007) Time-resolved and volumetric PIV measurements of a transitional separation bubble on an SD7003 airfoil. Exp Fluids (online). doi:10.1007/s00348-007-0421-0

Cal RB, Brzek B, Castillo L, Johannsson G (2007) Anisotropy of the rough turbulent boundary layer subject to a favorable pressure gradient. In: Proceedings of TFSP-5, vol 1, pp 157–162

Choi H, Moin P, Kim J (1993) Direct numerical simulation of turbulent flow over riblets. J Fluid Mech 255:503–539

Graham RR (1934) The silent flight of owls. J R Aeronaut Soc 38:837–843

Hileman J, Spakovszky Z, Drela M, Sargant M (2007) Airframe design for "silent aircraft". In: 45th AIAA aerospace sciences meeting and exhibit, AIAA 2007-453

Itoh M, Tamano S, Iguchi R, Yokota K, Akino N, Hino R, Kubo S (2006) Turbulent drag reduction by the seal fur surface. Phys Fluids 18(065102). doi: 10.1063/1.2204849

Kim J, Moin P, Moser R (1987) Turbulence statistics in fully developed channel flow at low Reynolds number. J Fluid Mech 177:133–166

Lang M, Rist U, Wagner S (2004) Investigations on controlled transition development in a laminar separation bubble by means of lda and piv. Exp Fluids 36:43–52. doi:10.1007/S00348-003-0625-X

Lilley GM (1998) A study of the silent flight of the owl. In: 4th AIAA/CEAS aeroacoustics conference, AIAA 98-2340

Lilley GM (2004) A quest for quiet commercial passenger transport aircraft for take-off and landing. In: 10th AIAA/CEAS aeroacoustics conference, AIAA 2004-2922

Liu T, Kuykendoll K, Rhew R, Jones S (2006) Avian wing geometry and kinematics. AIAA J 44(5):954–963

McAuliff BR, Yaras MI (2005) Separation-bubble-transition measurements on a low-Re airfoil using particle image velocimetry. In: Proceedings of GT2005 ASME Turbo Expo 2005: power for land, sea and air

Nachtigall W, Klimbingat A (1985) Messung der Flügelgeometrie mit der Profilkamm-Methode und geometrische Flügelkennzeichnung einheimischer Eulen. Biona-report 3, pp 45–86

Oehme H, Kitzler U (1975) On the geometry of the avian wing (studies on the biophysics and physiology of avian flight II). NASA-TT-F-16901

Roberts SK, Yaras MI (2006) Effects of surface-roughness geometry on separation-bubble transition. J Turbomach Trans ASME 128:349–356

Thwaites B (ed) (1960) Incompressible aerodynamics. Oxford University Press, London

Vad J, Koscsó G, Gutermuth M, Kasza Z, Tábi T, Csörgö T (2006) Study of the aero-acoustic and aerodynamic effects of soft coating upon airfoil. JSME Int J 49(3):648–656

The aerodynamic forces and pressure distribution of a revolving pigeon wing

James R. Usherwood

Abstract The aerodynamic forces acting on a revolving dried pigeon wing and a flat card replica were measured with a propeller rig, effectively simulating a wing in continual downstroke. Two methods were adopted: direct measurement of the reaction vertical force and torque via a forceplate, and a map of the pressures along and across the wing measured with differential pressure sensors. Wings were tested at Reynolds numbers up to 108,000, typical for slow-flying pigeons, and considerably above previous similar measurements applied to insect and hummingbird wing and wing models. The pigeon wing out-performed the flat card replica, reaching lift coefficients of 1.64 compared with 1.44. Both real and model wings achieved much higher maximum lift coefficients, and at much higher geometric angles of attack (43°), than would be expected from wings tested in a windtunnel simulating translating flight. It therefore appears that some high-lift mechanisms, possibly analogous to those of slow-flying insects, may be available for birds flapping with wings at high angles of attack. The net magnitude and orientation of aerodynamic forces acting on a revolving pigeon wing can be determined from the differential pressure maps with a moderate degree of precision. With increasing angle of attack, variability in the pressure signals suddenly increases at an angle of attack between 33° and 38°, close to the angle of highest vertical force coefficient or lift coefficient; stall appears to be delayed compared with measurements from wings in windtunnels.

J. R. Usherwood (✉)
Structure and Motion Lab, The Royal Veterinary College,
North Mymms, Hatfield, Herts AL9 7TA, UK
e-mail: jusherwood@rvc.ac.uk

List of symbols

C	coefficient
c	chord
dP	differential pressure
F	force
K	average wing pressure normalised by density and angular velocity
k	point pressure normalised by density and angular velocity
M_2	second moment of wing mass (moment of inertia)
Q	torque
R	wing length
r	radius from centre of rotation
S	area
S_2	second moment of wing area
S_3	third moment of wing area
V	speed
α	geometric angle of attack
ρ	air density
Ω	angular velocity

Subscripts

5areas	relating to the average values in each of five areas
5points	relating to the values of five sites near the midline
D	pro, profile drag
h	horizontal
i	relating to one of many small wing sections
j	relating to one of five sections
L	lift
max	maximum
P	pressure
R	resultant
v	vertical

G.K. Taylor, M.S. Triantafyllou, and C. Tropea (Eds.): Animal Locomotion, pp. 429–441.
springerlink.com

1 Introduction

The physics of low-speed bird flight is of fundamental aerodynamic, physiological and behavioural interest: do the higher Reynolds numbers experienced by birds preclude insect-like aerodynamics? Exactly how much power does slow, and particularly ascending, flight require from muscle? How do these power requirements relate to foraging and display?

It has recently been suggested that the high force coefficients of flapping insect wings (Ellington et al. 1996; Dickinson et al. 1999; Usherwood and Ellington 2002a, b) may not be maintained at Reynolds numbers appropriate for bird flight, and that hummingbirds might experience some form of aerodynamic transitional regime between insects and the majority of birds (Ellington 2006). Preliminary measurements of a revolving quail wing (Usherwood and Ellington 2002b) at a Reynolds number $Re \approx 26{,}000$, and those of hummingbird wings (Altshuler et al. 2004) at $Re \approx 5{,}000$ indicate that lift coefficients above 1.5 can be achieved at angles of attack around 45°. Are these high force coefficients at high angles of attack, reminiscent of those found in flapping or revolving insect wing models, also achieved at higher (though still, in engineering terms, far from high) Reynolds numbers? In this study, a dried wing and a flat card model pigeon wing was tested on a propeller rig (following Usherwood and Ellington 2002a, b; Altshuler et al. 2004), effectively simulating an extended downstroke, at Reynolds numbers up to 108,000, appropriate for slow, flapping pigeon flight.

Slow, flapping flight, whether during take-off and ascent, hovering or landing, demands a large amount of power from muscle. Indeed, the mass-specific power of quail in ascending flight is currently the highest recorded multi-cycle vertebrate muscle power (Askew et al. 2001). Such high power performances are informative both in terms of muscle physiology (e.g. Askew and Marsh 2001) and behaviour such as display (Usherwood 2008). However, conventional approaches to calculating the power requirements of bird flight (Pennycuick 1975, 1989; Rayner 1979a, b), based on modifications of aeroplane theory, are only valid for medium and fast flight, as profile drag coefficients vary strongly at the high lift coefficients characteristic of low-speed flight (Pennycuick et al. 1992). Modified profile drag coefficients derived from revolving propeller experiments give results, at insect scales at least, equivalent to more sophisticated flapping robot models (though the propeller values can take no account of pronation/supination). Such coefficients can be adopted successfully (e.g. Hedrick and Daniel 2006), but their application into the conventional power calculation framework must be approached with caution.

An alternative approach to calculating the power requirements of flight is to measure the pressures acting along and across the wings (Usherwood et al. 2003, 2005). This sidesteps many of the difficulties inherent in conventional aeroplane- or helicopter-like (blade-element) analyses. Specifically, assumptions need not be made concerning the appropriate lift and drag coefficients, or the influence of the locally induced and unsteady air movements. However, such a technique is reliant on two key assumptions. These are that point differential pressure measurements can be related to the net aerodynamic forces acting on a region, and that the resultant force acts predominantly perpendicular to the local wing chord. In order both to test the validity of these assumptions (and the soundness of the findings of Usherwood et al. 2005) and to provide insight into the local flow behaviour of a revolving pigeon wing, a 16-point pressure map is presented.

2 Methods

2.1 Overview

The inertial and aerodynamic properties of a dead racing pigeon's wings were measured by slicing and weighing the left wing while fresh, and drying and mounting the right wing on to a DC motor. This formed a one-bladed propeller; the pair of wings from a single bird are mirror images of each other, so cannot form a two-winged, balanced propeller. Slow flight, including take-off, involves relatively low advance ratios: at the midpoint of the first downstroke of a pigeon taking off from a perch (measured at 500 Hz with the motion analysis system described below) the advance ratio (body speed/wingtip speed) was 0.10 ± 0.05 (mean $\pm$ SD, $N = 5$ flights). The propeller setup, therefore, provides a crude simulation of a downstroke during slow or hovering flight. While unsteady, inter- and intra- wing–wing and wing–body aerodynamic interactions are poorly replicated, the propeller system does provide an interesting alternative to the traditional wind-tunnel measurements, and has the potential to include more realistic three-dimensional aerodynamic effects associated with low advance ratio flapping.

In order to measure the net aerodynamic thrust ($\approx$lift) force and torque of the revolving wing, the propeller was mounted on a forceplate. For comparison, the aerodynamic forces acting on a card (3-mm corrugated packing cardboard with edges sealed with insulating tape) model of the dried wing were also measured. Force coefficients for two further pigeon wings are also presented. The aim of this work was to describe one real pigeon wing in as thorough detail as possible; neither cardboard cut-out force nor pressure measurements were taken for the two additional wings. A pressure map of a single, real dried wing was measured by placing a pair of differential pressure transducers through

the wing feathers. This was repeated eight times, resulting in 16 point pressure measurements distributed along and across the wing.

2.2 Morphometrics

A recently killed racing pigeon was dissected, and the wings and flight muscles weighed. The fresh left wing was sliced into 18 strips at 2-cm intervals with a sharp paper guillotine to determine the second moment of wing mass (moment of inertia), M_2 (see Van Den Berg and Rayner 1995). The right wing was sutured to card board in an outstretched position with the ventral surface flat against the card, and allowed to dry until stiff. This wing was then sutured to a 2.5-mm metal rod, which acted as a sting, connecting the wing to a custom-made aluminium motor head (Fig. 1a). When in situ, mounted on the motor, the dried right wing and its cardboard cut-out replica were photographed, and the relevant wing area moments calculated (Table 1).

The surface topography of each of the three wings was measured with a laser scanner (Polyhemus FastScan, Colchester, Vermont, USA), and are available from the author on request. In order to quantify the degree to which a wing deforms under the aerodynamic and inertial loads of revolving at a range of speeds, reflective tape markers were placed on points on leading and trailing edges and the wingtip (Fig. 1c), and recorded with a high speed (500 Hz) infra-red 3-D motion analysis system (Qualisys, Gothenburg, Sweden). Deflections are reported at the angle of attack resulting in highest vertical force coefficients.

2.3 Propeller and forceplate setup

The 2.5-mm rod connecting the dried wing, or the flat card cut-out wing, was connected through the centre of 72-tooth gear cog (Fig. 1a). This allowed precise 5° increments in wing angle, and also ensured that the wing was held at a consistent distance from the propeller head throughout the range of geometric angles of attack. The centre of rotation was 34 mm from the humerus, allowing the full range of angles of attack to be measured. This, in effect, reduced the geometric advance ratio from 0 to 0.09. While having some aerodynamic effect, this is likely to be minor (see Dickson and Dickinson 2004). An initial geometric angle of attack was measured in situ at the wing tip marked in Fig. 1 using a digital inclinometer. This site is convenient because it is relatively flat and thin, and relevant because this portion of the wing moves relatively fast, producing disproportionately high aerodynamic forces. A counter-balance mass was connected to the same rod on the other side of the propeller head. The 12-V high-torque DC motor was mounted vertically in a 1-m card tube, which was mounted directly on to a Kistler 9287B forceplate, and stabilised by four tensioning wires running to each corner of the forceplate (Fig. 1b). The wing was mounted such that the 'thrust', 'weight-supporting' or 'lifting' force was orientated directly downwards; the propeller downwash was directed upwards. The ceiling and walls were at least 2.5 m from the wing; aerodynamic wall- and ground-effects were considered negligible. The effect of in-wash to the propeller at the level of the forceplate was minimal; propeller-induced drafts did not affect a small down feather placed

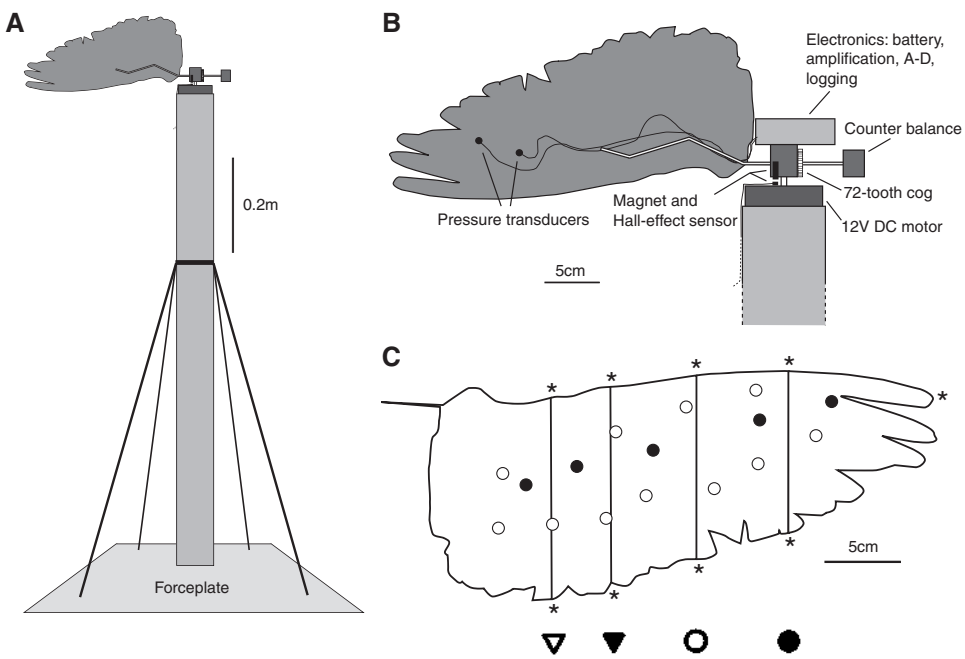

Fig. 1 Experimental setup of a one-winged propeller formed by a dried or card replica pigeon wing. When mounted on a forceplate (**a**, here shown at a +90° angle of attack), reaction forces indicate the aerodynamic forces acting on the wing as it revolves. Pressure transducers mounted through feather shafts (**b**) were powered, amplified and logged by a unit revolving with the propeller head. Eight repeats (two sites each time) result in a pressure map of 16 sites (**c**) along the wing. *Black circles* indicate sites near the midline of the wing. *Stars* indicate later positioning of motion analysis markers; the *symbols* underneath the wing relate to wing positions from base to tip, matching the symbols in Fig. 2b

Table 1 Relevant morphometrics of the dried right pigeon wing and its cardboard model calculated from photographs taken once mounted on to the motor

	Right wing	Right wing on sting	Card wing	Card wing on sting
R (m)	0.326	0.364	0.343	0.375
S (m^2)	3.22×10^{-2}	3.22×10^{-2}	3.66×10^{-2}	3.66×10^{-2}
S_2 (m^4)	9.53×10^{-4}	1.42×10^{-3}	1.13×10^{-3}	1.57×10^{-3}
S_3 (m^5)	2.09×10^{-4}	3.52×10^{-4}	2.61×10^{-4}	4.03×10^{-4}

on the forceplate, so cowling of the forceplate was considered unnecessary.

In order to measure rotational frequency, a small bar magnet was mounted on the propeller head, which triggered a Hall-effect sensor mounted on the top of the propeller body once a cycle. In order to drive the propeller at set speeds despite radically differing aerodynamic loads, this magnetometer signal was measured and used to determine the power output of a power supply (N5743A, Agilent Technologies, Wokingham, Berks, UK) [analogue in and out signals were received/emitted at 500 Hz through a National Instruments (Austin, TX) 6024E PCMCIA card]. Actual measured rotational frequencies for each trial were used in subsequent calculations; while they differed only slightly from the intended frequencies (coefficient of variation <2%), aerodynamic forces are broadly proportional to the square of velocity, so it is worth using the most accurate measure of rotational frequency in calculating coefficients.

2.4 Reynolds number

The chord-based Reynolds number (using Ellington's (1984c) formulation) for a pigeon in slow flight (Usherwood et al. 2005) is of the order of 92,000 [wing span of 0.302 m, wing area 0.0296 m^2, wingbeat frequency 7.98 Hz (downstroke period 0.0673 s), downstroke amplitude approximately 180°] and the aerodynamic power derived from direct pressure measurements was 12.8 W (single wing). Therefore, a rotational frequency of 8 Hz for a 12 V, 7.2-A motor provides a suitable comparison to the slow-flying pigeon (providing $Re \approx 108{,}000$). However, at high angles of attack—potentially of relevance during take-off, hovering and landing—the power demands on the motor operating at 8 Hz were excessive. Therefore, to provide aerodynamic coefficients covering the complete range of potentially relevant angles of attack, the propeller was also driven at 4 Hz ($Re \approx 54{,}000$, a quarter of the aerodynamic forces and an eighth of the power requirements). At extreme angles of attack (90° ± 10°), the power requirements at even 4 Hz were too much for the motor, and the rotational frequency was further reduced, down to 3.6 Hz ($Re \approx 49{,}000$).

2.5 Presentation of forceplate results

Real dried and model card wings were tested at 8 Hz (for 10 angles around zero angle of attack) and at 4–3.6 Hz (for 24 angles, ranging from below zero to above 90°). The reaction forces measured by the forceplate at 500 Hz were used to determine aerodynamic forces. The thrust force F_v, coaxial with the propeller, acted vertically. Using the blade-element analysis (e.g. Osborne 1951; Weis-Fogh 1973; Ellington 1984a, b, c; Usherwood and Ellington 2002a) for revolving wings, a mean vertical force coefficient C_v can be derived, as

$$F_v = \int_0^R \frac{\rho}{2} C_{v,i}\, c_i\, V_i^2 \mathrm{d}r = \frac{\rho}{2} C_v\, \Omega^2 S_2, \quad (1)$$

where ρ is the density of air (taken as 1.2 kg/m^3), $C_{v,i}$ the vertical force coefficient, c_i the chord and V_i the velocity, each for element i along the entire length (R) of the wing. Ω is the angular velocity, and S_2 the second moment of a single wing's area. Thus,

$$C_v = \frac{2F_v}{\Omega^2 S_2}. \quad (2)$$

While variations in horizontal reaction forces experienced by the forceplate could, in theory, be used to determine the average aerodynamic drag and position of the centre of drag directly, this requires a very high frequency response: mechanical smoothing of forces transmitted between the wing and the forceplate would result in an under-calculation of drag (as mean horizontal force experienced by the forceplate is zero) and miss-calculation of the centre of drag towards the centre of rotation. Instead, drag is derived from the net torque (Q) measurements about the vertical axis following the standard blade-element formulation:

$$Q = \int_0^R \frac{\rho}{2} C_{h,i}\, c_i\, r_i\, V_i^2 dr = \frac{\rho}{2} C_h\, \Omega^2 S_3, \quad (3)$$

where C_h is the mean horizontal force coefficient taken to act across the wing, and S_3 is the third moment of a single wing's area. Thus,

$$C_{\mathrm{h}} = \frac{2Q}{\Omega^2 S_3}. \tag{4}$$

Note that, in this study, a distinction is made between horizontal and vertical force coefficients, and drag and lift coefficients. Aerodynamic drag and lift coefficients relate to forces parallel and perpendicular to the airflow, respectively; in the case of a static but revolving propeller, the induced flow at the blade (or wing) may be considerable. Drag and lift coefficients are calculated using the large-angle formulation of Usherwood and Ellington (2002a), which takes account of the changes in geometry associated with a downwash calculated as a conventional Rankine-Froude momentum jet and a triangular downwash distribution. However, the effect to the main points of this study of the distinction between C_{h} and $C_{D,\mathrm{pro}}$, and C_{v} and C_{L} is minor. This blade-element approach is based on the 2-D assumption that the aerodynamic consequences (lift, drag) of conditions at each element (angle of attack, velocity, chord width and profile) can be combined as a simple summation; aerodynamic interaction between elements is not accounted for. However, using this terminology even for cases where strong spanwise flows are suspected allows comparisons between wing properties to be made despite very different motions (translating, rotating, flapping, etc.), and indeed can indicate where 3-D flows are likely to be important.

2.6 Pressure measurements

Differential pressures between lower and upper wing surfaces were measured at 16 sites (8 sets of experiments, 2 pressure sites each set) across the wing operating at 4 Hz (down to 3.6 Hz as before), over 24 angles of attack ranging from $-17°$ to $+98°$ at the wingtip. Hollowed pen nibs glued over the gauge hole of the pressure sensors (EPE-EO1-2P, Measurement Specialties, Hampton, VA USA) were pushed through feather shafts and, where necessary, held in place by hot glue (see Usherwood et al. 2005). At central portions of the wing, covert feathers were prevented from obstructing the ports by the application of a small tab of cloth tape. The nibs projected from the upper wing surface by approximately 1% of wing chord width. The pressure sensors and op-amps were powered from the stabilised supply provided by the data logger (Logomatic, Sparkfun Electronics, Boulder, CO, USA). Pressure signals were logged at 10 bits at 500 Hz per channel and written to an SD card. Each pressure sensor was calibrated directly after the experiments by raising a column of water in 5-mm intervals. This was achieved by pushing the pen nib through a latex glove tightly stretched over a stiff, vertical tube filled with water, with the open end of the tube in water.

The pressure sensors have a rated frequency response within ±½ dB to 5 kHz, so sampling at 0.5 kHz allows recording of real aerodynamic phenomena; signal variability may have some value, potentially indicating the chaotic flow usually associated with stall.

Results from pressure measurements are presented in two ways. The first uses the coefficient of pressure C_{P}, formulated to be directly comparable with the propeller force coefficients:

$$\frac{\text{Aerodynamic force}}{\text{area}} = \mathrm{d}P = \frac{\rho}{2} C_{\mathrm{P}} V^2 \tag{5}$$

where $\mathrm{d}P$ is the differential pressure measured at a point and V the velocity at that point. So, for a revolving wing, and a pressure site at distance r from the propeller axis,

$$C_{\mathrm{P}} = \frac{2\,\mathrm{d}P}{\rho\,\Omega^2 r^2}. \tag{6}$$

The second way of presenting the data keeps the relative magnitudes of the various sites, maintaining the relative importance of outer (faster) wing sections. In this case, the term r is removed:

$$k_{\mathrm{p}} = \frac{2\,\mathrm{d}P}{\rho\,\Omega^2} \tag{7}$$

This, taken over the whole wing using a resultant force coefficient $\left(C_{\mathrm{R}} = \sqrt{C_{\mathrm{h}}^2 + C_{\mathrm{v}}^2}\right)$, is equivalent to

$$K_{\mathrm{p}} = C_{\mathrm{R}} \frac{S_2}{S} \tag{8}$$

from the forceplate measurements.

2.7 Signal analysis

Each test, for each wing, angle of attack, pressure positioning or forceplate measurement, started with the wing at rest for 9 s, followed by an impulsive start up to the required rotational frequency, which was maintained for 4 s. After this the propeller came to a halt for 7 s, and started and stopped two further times. For both forceplate and pressure measurements, a linear drift was removed from just before to just after each period of rotation. The values from N-10 to N-2 (where $N = 0$ is the last revolution), as indicated by the magnetometer, were assessed. This period was after the downwash had fully developed, and before the wing had started to slow. The average rotational frequency, vertical force and torque or differential pressures for these three periods were calculated. For the pressure measurements, the standard deviation during each of the three periods was calculated and averaged.

2.8 Derivation of coefficients from differential pressure measurements

The areas of five regions (Fig. 1C) down the wing were measured from photograph. Also, the twist of the chord relative to the wingtip chord was measured with a digital inclinometer so that the geometric angle of attack could be determined for each section at each set angle of attack. The average resultant force coefficient derived from the differential pressure measurements was derived in two ways: first, the average differential pressure for all of the sensors within an area was multiplied by the section area to provide the section force; second, only those pressure sensors near the midline of the wing (Fig. 1C) were taken as representative for the pressure across the whole wing section. The purpose of the midline-only contributions was to determine whether a reduced set of measurements—far more realisable with free-flying, live, flapping birds—might be sufficient to provide informative values. The contribution of each section j to the resultant aerodynamic force $F_{R,j}$ is

$$F_{\mathrm{R},j} = \mathrm{d}P_j S_j, \tag{9}$$

where $\mathrm{d}P_j$ is the representative differential pressure for the section (either the average or that of the mid-line sensor) and S_j the area of the section. If this resultant aerodynamic force acts perpendicular to the wing section—an assumption shown to be broadly valid for model insect wings at high angles of attack (Dickinson 1996; Dickinson et al. 1999; Usherwood and Ellington 2002a), and only likely to be incorrect by a few degrees for fully attached flow with leading-edge suction (typical of low angles of attack)—then the contribution of each section to horizontal and vertical force coefficients is a simple matter of geometry:

$$C_{\mathrm{h}} = \frac{2}{\rho \Omega^2 S_2} \sum F_{\mathrm{R},j} \sin(\alpha_j), \tag{10}$$

and

$$C_{\mathrm{v}} = \frac{2}{\rho \Omega^2 S_2} \sum F_{\mathrm{R},j} \cos(\alpha_j) \tag{11}$$

where α_j is the geometric angle of attack of section j.

3 Results and discussion

3.1 Morphometrics

The racing pigeon had the following morphometry: mass, 507.4 g; total pectoralis, 149.7 g; total supracoracoideous, 16.1 g; total wing mass, 73.2 g. The left wing, while still fresh, had a second moment of mass of 3.28×10^{-4} kg m^2. The wing lengths, areas, and moments of areas for the dried right wing and the cardboard model are shown in Table 1.

High speed motion analysis of this wing revolving at the angle of attack resulting in the maximum vertical force coefficient, at a range of rotational frequencies, demonstrates that wings can undergo considerable passive deflections due to life-like aerodynamic forces (Fig. 2): the wing tip deflected 'upwards' (in the aerodynamic sense) by around 100 mm; the angle of attack decreased towards the wing base, but increased slightly at the wingtip.

3.2 Force coefficients

Force coefficients for stiff, flat model pigeon wings operating at $Re \approx 108{,}000$ and 54,000 match those of simple hawkmoth wing models operating at $Re \approx 8{,}000$ (Fig. 3), which have been shown to be largely indistinguishable—except for a lesser minimum drag coefficient—from *Drosophila* wings operating at $Re \approx 200$ (Dickinson et al. 1999; Usherwood and Ellington 2002b). It is therefore difficult to support the notion of a critical Reynolds number above which the high-lift mechanisms of revolving insect wings fail (see Ellington 2006). Whether the

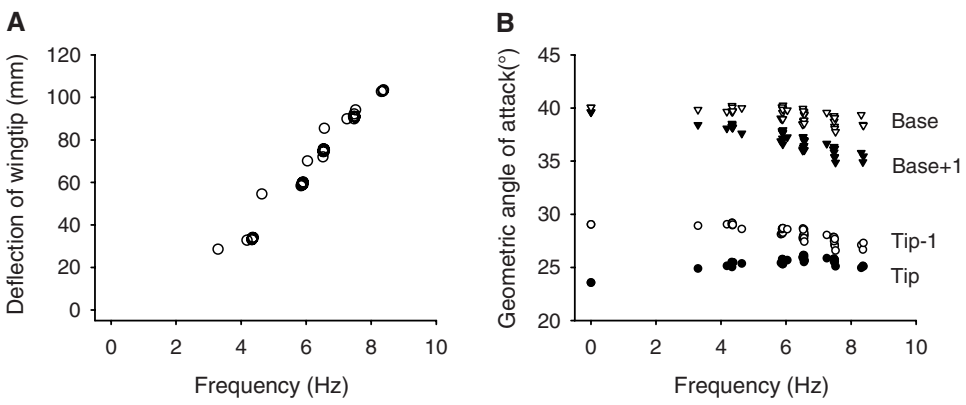

Fig. 2 Deflections of wing tips 'upwards' (in the aerodynamic sense) (**a**) and wing sections, influencing the angles of attack (**b**), for a dried pigeon wing for a range of rotational frequencies, at the angle of attack resulting in the highest vertical force coefficients (initially set at 38°)

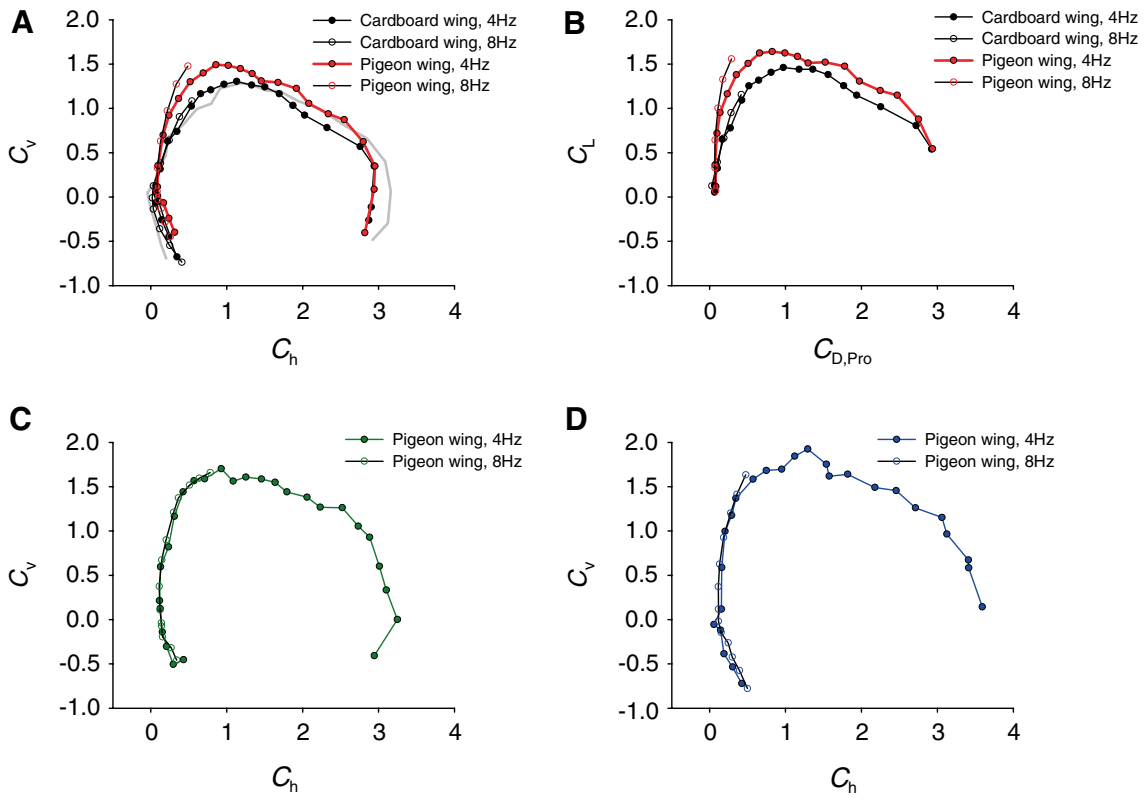

Fig. 3 Aerodynamic force coefficients for revolving real, dried (coloured, **a**–**d**) and flat card (*blacklines*, *black circles*) pigeon wings. *Open circles* indicate values with a rotational frequency of 8 Hz ($Re \approx 108{,}000$); *filled circles* at approximately 4 Hz ($Re \approx 54{,}000$). The underlying grey plot (**a**) indicates values from flat model hawkmoth wings at $Re \approx 8{,}100$ from Usherwood and Ellington 2002b. Horizontal and vertical force coefficients (from **a**) are transformed to lift and profile drag coefficients (**b**) avoiding small angle assumptions following Usherwood and Ellington 2002a. **c** and **d** show force coefficients for two further pigeon wings

aerodynamic mechanisms behind the high forces are identical is doubtful; whether they are broadly similar remains controversial (is spanwise flow present or required at all Reynolds numbers?), but such issues motivate future DPIV investigations.

The real, dried wing performs considerably better than the card replica wing (Fig. 3a, b), with the maximum lift coefficient for the dried wing of 1.64, and for its card replica of 1.44. Whereas attempts at improving upon flat-winged performance of model hawkmoth wings by introducing camber and twist largely failed (Usherwood and Ellington 2002a), some attributes of the real bird wing clearly makes a notable difference. The salient differences between the flat, card wing and the real, dried pigeon wing is not yet clear. Therefore, an attractive line of future research to tease apart which factors contribute to this difference, parallel to that of Ellington's for hummingbird wings, would involve: imaging and reconstructing the wing, varying the aerofoil and whole-wing properties, and rapid prototyping and aerodynamic propeller-testing.

In the case of the main real, dried wing of this study, but much less so (if at all) the other dried wings or the card replica, vertical or lift coefficient increases far more rapidly with angle of attack at high rotational frequencies than low (Fig. 3). While an increase in maximum vertical or lift coefficients are not observed (potentially because the motor was unable to power the wing at sufficiently high angles of attack at 8 Hz), performance is improved at high speeds as the high lifts occur at relatively low drags: $C_L/C_{D,pro}$ at maximum lift coefficient were 5.4 and 2.0 for fast and slower real wings, respectively. One account for this phenomenon, and possibly its inconsistency between real wings and absence in the card wing, might be aeroelastic deflection. The pigeon wings were dried fully outstretched, tied with their ventral surfaces flattened; this somewhat arbitrary and inconsistent wing form may benefit from the deflections, particularly the twist, imposed by aerodynamic (and, potentially, 'centrifugal' inertial) loads (Fig. 2).

Lift coefficients, derived by transforming horizontal and vertical force coefficients to take account of the flow induced at the level of the wing, are, as expected, somewhat higher than C_v (apparently contradicting Altshuler et al. 2004); the performance of the wing would be somewhat higher for the first flap of take-off, before the wake had fully formed. Whether considering C_L, which requires a range of simplifying assumptions, or accepting

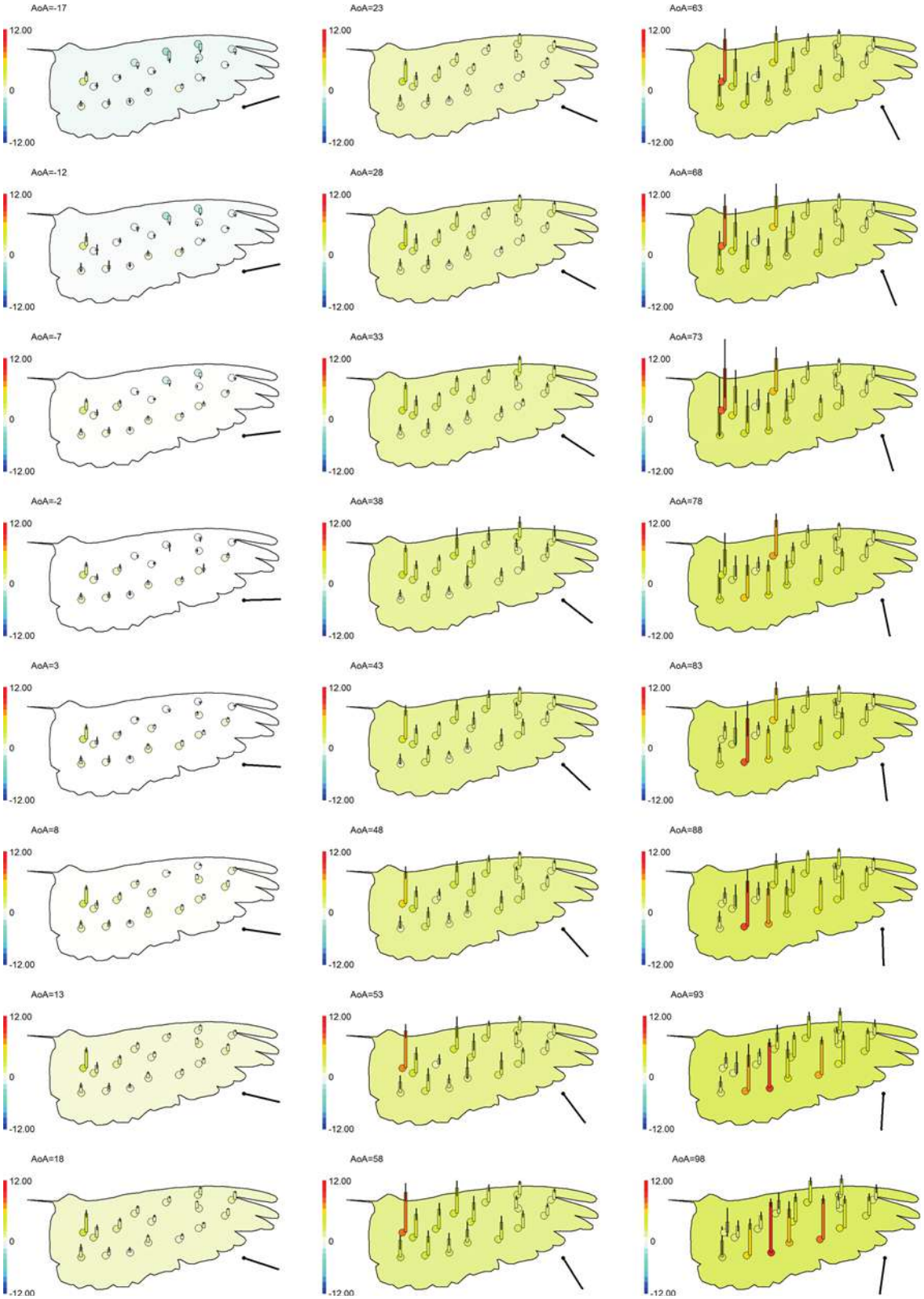

Fig. 4 Coefficients of pressure C_P from point pressure measurements, and for the whole wing derived from forceplate measurements (*background colours*). *Black vertical bars* show ±6 SD of the pressure-derived signals. The *scale bars to the left* relate pressure coefficients to both colour and column (and *error bar*) height

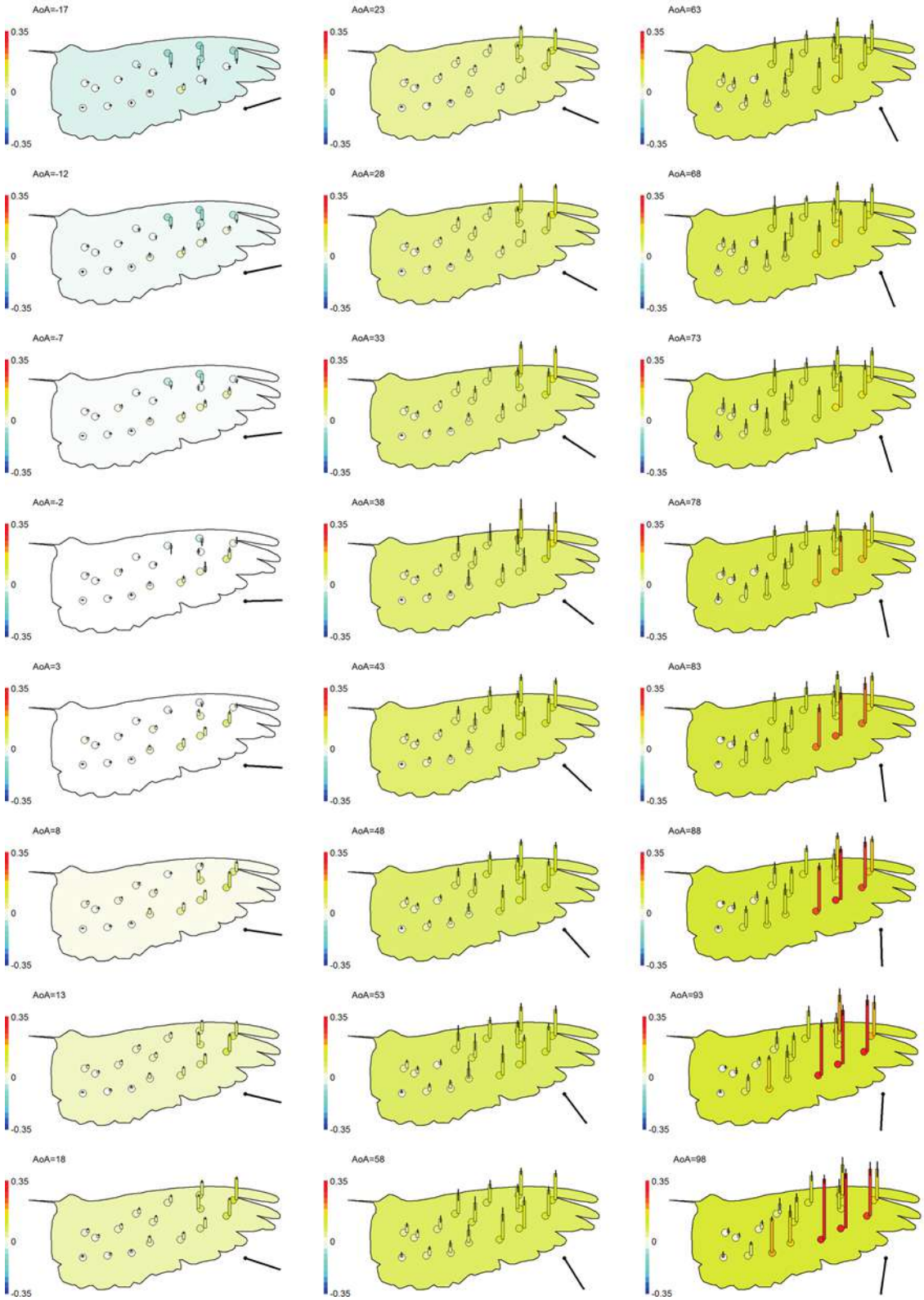

Fig. 5 Point (k_p) and whole wing (K_p, *background wing colours*) differential pressures normalised by air density and the square of angular velocity, but not (unlike the coefficients in Fig. 4) by distance from the centre of rotation. Therefore, values show true relative magnitudes: larger differential pressures occur at the (faster moving) wingtip. *Black vertical bars* show ±6 SD of the pressure-derived signals. The *scale bars* to the left relate pressure coefficients to both colour and column (and *error bar*) height

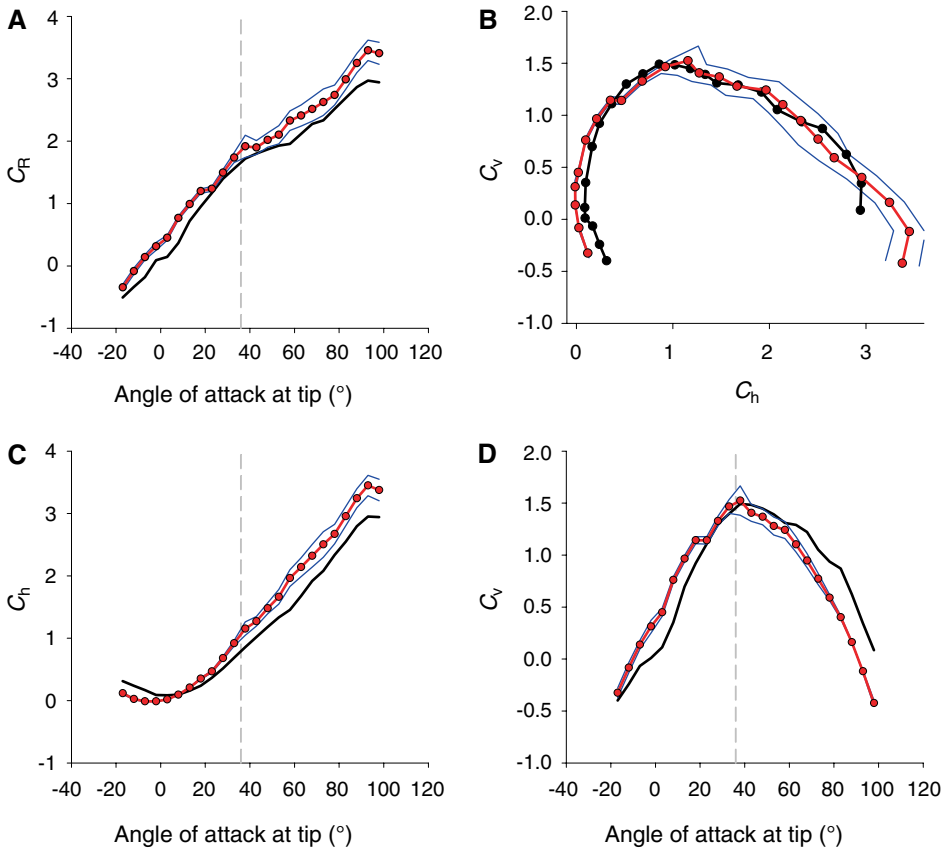

Fig. 6 Force coefficients derived from forceplate measurements (*bold black*), and differential pressure measurements (*red*), using averages of all the pressure measurements for each section, and assuming the resultant aerodynamic force acts perpendicular to each wing chord. *Blue lines* bounding the pressure-derived values show coefficients derived with ±2 SD of the measured pressure signals. The *vertical dashed lines* indicate the angle at which stall is postulated

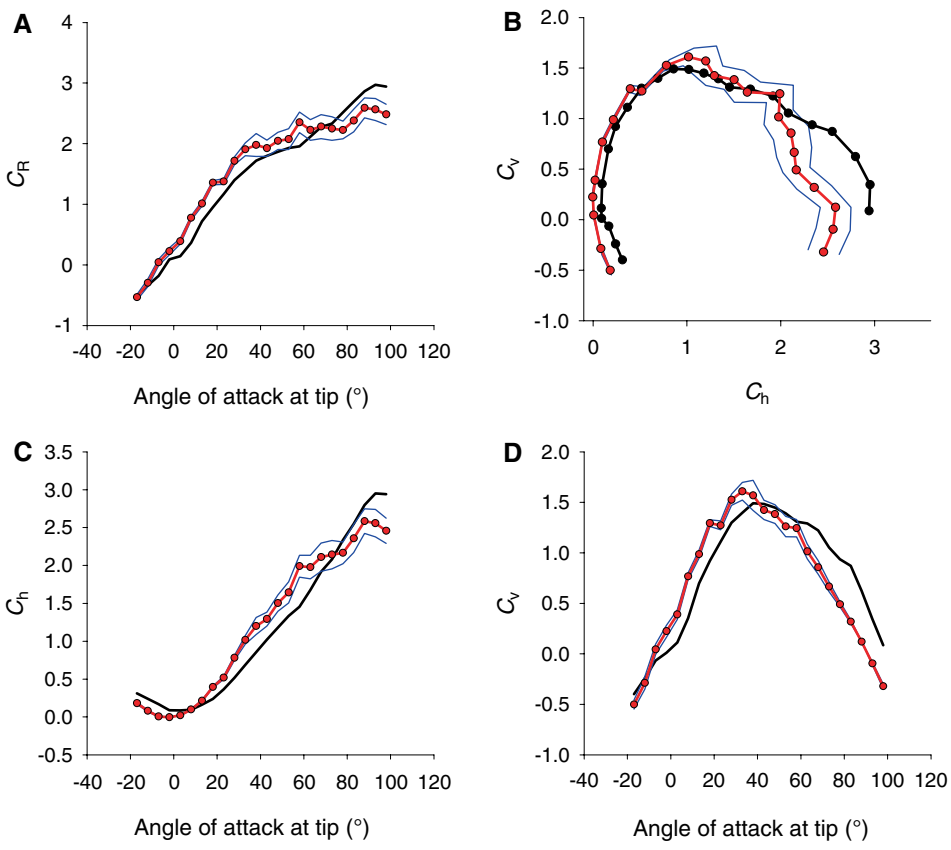

Fig. 7 Force coefficients derived from forceplate measurements (*bold black*), and differential pressure measurements (*red*), using only mid-line pressure measurements for each section (in contrast to Fig. 6) indicated in Fig. 1c. *Blue lines* bounding the pressure-derived values show coefficients derived with ±2 SD of the measured pressure signals

Table 2 Linear regression coefficients for resultant, horizontal and vertical force coefficients (C_R, C_h and C_v) derived from forceplate measurements (subscript FP) predicted from pressure measurements across five areas (subscript 5areas) or five points along the wing midline (subscript 5points)

Dependent variable	Independent variable	Gradient (95% CI)	Intercept (95% CI)	R^2	Angle of attack range
$C_{R,FP}$	$C_{R,5areas}$	0.964 (0.924 to 1.005)	−0.196 (−0.280 to −0.113)	0.991	Full
$C_{R,FP}$	$C_{R,5points}$	0.945 (0.877 to 1.014)	−0.158 (−0.262 to −0.055)	0.983	−17° to 63°
$C_{R,FP}$	$C_{R,5points}$	1.688 (0.695 to 2.681)	−1.389 (−3.772 to 0.995)	0.793	68° to 98°
$C_{h,FP}$	$C_{R,5areas}$	0.826 (0.788 to 0.864)	−0.031 (−0.039 to 0.101)	0.989	Full
$C_{v,FP}$	$C_{R,5areas}$	0.901 (0.704 to 1.098)	0.122 (−0.063 to 0.308)	0.803	Full
$C_{h,FP}$	$C_{R,5points}$	1.022 (0.902 to 1.142)	−0.079 (−0.263 to 0.106)	0.934	Full
$C_{v,FP}$	$C_{R,5points}$	0.818 (0.634 to 1.002)	0.193 (0.015 to 0.371)	0.795	Full

C_v as a conservative, somewhat underestimating proxy to C_L, the maximum lift of the revolving pigeon wing exceeds that of bird wings measured in the steady, translating flow of windtunnels. Maximum lift coefficients for a range of bird wings (Withers 1981) and a model pigeon wing (Nachtigall 1979) measured in windtunnels only achieve 1.2. Withers' bird wings achieve their maximum lift at angles of attack (at mid-wing) at 8°–25°. These measurements contrast with the C_v of 1.49 or $C_{L,max}$ of 1.64 (or even higher, Fig. 3c, d) reported here for the revolving pigeon wing, at angles of attack of 38–43° at the wingtip. The most parsimonious explanation for this, at least until near-field flow modelling or visualisation can be performed on pigeon wings, is that some aspect of 3-D flow is present in the revolving (propeller) case and absent in translating (windtunnel) case; and that this spanwise flow disrupts the process of conventional stall, resulting in high force coefficients at high angles of attack.

3.3 Pressure maps

The pressure map data for the real, dried pigeon wing revolving at 4 Hz is presented in two forms (Fig. 4, 5): as coefficients of pressure, which normalises point pressures by air density and local velocity (Fig. 4), and k_p, that normalises by density and angular velocity (Fig. 5). Higher than wing-average coefficients of pressure are observed towards the base of the wing, consistent with their relatively thick and highly cambered aerofoil sections. In contrast, coefficients towards the wingtip are close to the average for the wing area. This is consistent with the dominant contribution of the aerodynamic forces of the distal wing to the overall wing (despite their lower coefficients) due to their much higher absolute velocities (Fig. 5).

Integrating the pressure maps over the wing area by two techniques appears largely effective in predicting net forces (Figs. 6, 7). By taking the average pressure as representative, or the pressure at the sensor near the midline of the wing (Fig. 1c), for each of five wing sections, the resultant aerodynamic force coefficients ($C_{R,5areas}$ and $C_{R,5points}$ respectively) correlates well with that measured in the forceplate experiments $C_{R,FP}$, albeit with a slight offset in angle of attack. Linear regressions (Table 2) show that the areas method is reasonably accurate over the whole range of angles of attack, and the midline, five-points method for angles between −17° and 63°. At higher angles, midline-only measurements start to undervalue the resultant forces. Also, resolving the resultant force into vertical and horizontal components by assuming that the force on each section acts perpendicular to the wing chord is largely successful (Figs. 6c, d; 7c, d). Over all angles of attack, the linear regressions for horizontal and vertical force coefficient measurements derived from either pressure-based technique provide, depending on the level of accuracy required, a reasonable match with those calculated from the forceplate measurements (Table 2). These findings provide some support for the techniques of Usherwood et al. (2005), indicating that direct, local pressure measurements can be effective in determining the whole-wing lift and drag for slow, flapping flight. In that the midline-only measurements were, within limits, effective for determining wing forces, the feasibility of using a reduced array of pressure measurements to determine aerodynamic power requirements in flapping, free-flying birds is encouraging. Whether this technique is appropriate for higher speed flight, where attached flow and leading-edge suction are presumably maintained, and the assumption that the resultant force acts perpendicular to the wing chord potentially less valid, remains uncertain.

3.4 Stall and mechanisms of high resultant forces

The flow structure about a revolving pigeon wing cannot be determined without some form of flow visualisation. However, the pressure map, notably the variability in the

measured signal, can be highly informative. A band of low pressure running lengthways along the wing near the leading edge, that would be consistent with the presence of a stable leading-edge vortex (e.g. Liu et al. 1998), is not observed. Whether this is due to the absence of a stable leading-edge vortex structure, or the limited spatial resolution of the sensors is unclear. However, given the success in determining net aerodynamic forces from summing the local pressures, it appears that invoking an unmeasured region of very high differential pressure due to a tight, stable leading-edge vortex is unnecessary. What is clear is that, at an angle of attack between 33° and 38°, there is a dramatic increase in variability of the pressure signal across the wing (Figs. 4, 5). This occurs at approximately the angle of attack leading to maximum vertical force (or lift) (Figs. 6, 7), and is good evidence either for some form of stall, or aeroelastic ringing, or both. Given the higher lift coefficients, and higher angles of attack for maximum lift, of the revolving wings described here than the windtunnel measurements of Withers (1981), it appears reasonable to suppose that some aspect of revolution delays full, conventional stall.

3.5 Limitations and relevance of propeller measurements to bird flight

The process of removal, drying, mounting and spinning a dead bird wing clearly departs from the reality of live, dynamically (both actively and passively) controlled flapping wings in myriad ways, and the motivation behind developing direct pressure measurement techniques is to advance the study of birds in free, near-natural flight. While the main focus of this paper is in validating such techniques, it is worthwhile considering whether the measurements made might provide insight into the aerodynamics of real pigeon flight. Recent kinematic measurements of pigeons in slow flight (Berg and Biewener 2008) demonstrate that some of the conditions experienced by a real pigeon may be more closely simulated with a propeller setup than traditional windtunnel setup. Very high angles of attack (in the conventional pre-stall sense) were observed during mid downstroke: at the wrist during level flight, the angle of attack was $40° \pm 1°$(SE). In addition, the lift and drag coefficients estimated from kinematics were 1.44 ± 0.29 and 1.01 ± 0.08, respectively. While such measurements are not in exact agreement with propeller-based measurements—at a tip angle of attack of 40°, the forceplate-derived C_v coefficient was between 1.49 and 1.48, and C_h between 0.86 and 1.02—they provide a considerably closer match than windtunnel measurements on real bird wings.

3.6 Profile drag and power calculations in slow bird flight

It is worth commenting here on the apparent discrepancy between the values of $C_{D,pro}$ reported here for bird wings, and those reported elsewhere for bird wings (e.g. Rayner 1979b; Pennycuick et al. 1992). Historically, analyses of bird flight performance have made the convenient, and perhaps not unreasonable when considering flight at medium and high air speeds, assumption that profile drag coefficient should approximate the minimum or no-lift drag coefficient. At lower flight speeds, requiring higher angles of incidence, this is certainly not the case (e.g. Withers 1981; Pennycuick et al. 1992). Under these conditions, $C_{D,pro}$ derived from low-drag configurations—$C_{D,pro} = 0.02$ appears a widely accepted rule of thumb (e.g. Askew et al. 2001; Askew and Ellerby 2007)—must be inappropriate. Therefore, just as methods for calculating aerodynamic power in hovering insects have had to be revised (Ellington 1999) (resulting in dramatically higher values; see, for instance Fry et al. 2005) following flapper and propeller experiments leading to the rejection of Ellington's (though reasonable at the time) approximation for low Reynolds numbers of $C_{D,pro} = 7/\sqrt{Re}$ (Ellington 1984c), so may calculations of power in low-speed bird flight. One further note of caution is worthwhile: when considering flight with strongly inclined stroke planes [typical of slow bird flight other than hummingbirds (see Norberg 1975; Berg and Biewener 2008)], profile drag will contribute to weight support, and so the traditional distinctions between induced and profile powers become confounded.

Acknowledgments This work was funded by The Wellcome Trust. Bret Tobalske and Ty Hedrick provided valuable criticism throughout this project.

References

Altshuler DL, Dudley R, Ellington CP (2004) Aerodynamic forces of revolving hummingbird wings and wing models. J Zool Lond 264:145–181

Askew GN, Ellerby DJ (2007) The mechanical power requirements of avian flight. Biol Lett 3:445–448

Askew GN, Marsh RL (2001) The mechanical power output of the pectoralis muscle of blue-breasted quail (*Coturnix chinensis*): the in vivo length cycle and its implications for muscle performance. J Exp Biol 204:3587–3600

Askew GN, Marsh RL, Ellington CP (2001) The mechanical power output of the flight muscles of the blue-breasted quail (*Coturnis chinensis*) during take-off. J Exp Biol 204:3601–3619

Berg AM, Biewener AA (2008) Kinematics and power requirements of ascending and descending flight in the pigeon (*Columba livia*). J Exp Biol 211:1120–1130

Dickinson MH (1996) Unsteady mechanisms of force generation in aquatic and aerial locomotion. Am Zool 36:536–554

Dickson WB, Dickinson MH (2004) The effect of advance ratio on the aerodynamics of revolving wings. J Exp Biol 207:4269–4281

Dickinson MH, Lehmann F-O, Sane SP (1999) Wing rotation and the aerodynamic basis of insect flight. Science 284:1954–1960

Ellington CP (1984a) The aerodynamics of hovering insect flight. I. The quasi-steady analysis. Phil Trans R Soc Lond B 305:1–15

Ellington CP (1984b) The aerodynamics of hovering insect flight. II. Morphological parameters. Phil Trans R Soc Lond B 305:17–40

Ellington CP (1984c) The aerodynamics of hovering insect flight. VI. Lift and power requirements. Phil Trans R Soc Lond B 305:145–181

Ellington CP (1999) The novel aerodynamics of insect flight: applications to micro-air vehicles. J Exp Biol 202:3439–3448

Ellington CP (2006) Insects versus birds: the great divide (invited). In: Charles Ellington, 44th AIAA Aerospace Sciences Meeting and Exhibit, Reno, Nevada, 9–12 Jan 2006. AIAA-2006-35, University of Cambridge, Cambridge http://www.aiaa.org/content.cfm?pageid=406&gTable=Paper&gID=47786

Ellington CP, Van den Berg C, Willmott AP, Thomas ALR (1996) Leading-edge vortices in insect flight. Nature 384:626–630

Fry SN, Sayaman R, Dickinson MH (2005) The aerodynamics of hovering flight in *Drosophila*. J Exp Biol 208:2303–2318

Hedrick TL, Daniel TL (2006) Flight control in the hawkmoth *Manduca sexta*: the inverse problem of hovering. J Exp Biol 209:3114–3130

Liu H, Ellington CP, Kawachi K, Van Den Berg C, Willmott A (1998) A computational fluid dynamic study of hawkmoth hovering. J Exp Biol 201:461–477

Nachtigall W (1979) Der Taubenflugel in Gleitflugstellung; Geometrische Kenngroflen der Flugelprofile und Luftkrafterzeugung. J Ornithol iao, 30–40

Norberg UM (1975) Hovering flight of the pied flycatcher (*Ficedula hypoleuca*) In: Wu TY, Brokaw CJ, Brennen C (eds) Swimming and flying in nature, vol 2. Plenum Press, New York, pp 869–881

Osborne MFM (1951) Aerodynamics of flapping flight with application to insects. J Exp Biol 28:221–245

Pennycuick CJ (1975) Mechanics of flight. In: Farner DS, King JR (eds) Avian biology, vol 5. Academic Press, London, pp 1–75

Pennycuick CJ (1989) Bird flight performance: a practical calculation manual. Oxford University Press, Oxford

Pennycuick CJ, Heine CE, Kirkpatrick SJ, Fuller MR (1992) The profile drag coefficient of a Harris' hawk wing, measured by wake sampling in a wind tunnel. J Exp Biol 165:1–19

Rayner JMV (1979a) A vortex theory of animal flight. Part 2. The forward flight of birds. J Fluid Mech 91:731–763

Rayner JMV (1979b) A new approach to animal flight mechanics. J Exp Biol 80:17–54

Usherwood JR (2008) Collared doves *Streptopelia decaocto* display with high, near-maximal muscle powers, but at low energetic cost. J Avian Biol 39:19–23. doi:10.1111/j.2007.0908-8857.04347.x

Usherwood JR, Ellington CP (2002a) The aerodynamics of revolving wings. I. Model hawkmoth wings. J Exp Biol 205:1547–1564

Usherwood JR, Ellington CP (2002b) The aerodynamics of revolving wings. II. Propeller force coefficients from mayfly to quail. J Exp Biol 205:1565–1576

Usherwood JR, Hedrick TL, Biewener AA (2003) The aerodynamics of avian take-off from direct pressure measurements in Canada geese (*Branta canadensis*). J Exp Biol 206:4051–4056

Usherwood JR, Hedrick TL, McGowan CP, Biewener AA (2005) Dynamic pressure maps for wings and tails of pigeons in slow, flapping flight, and their energetic implications. J Exp Biol 208:355–369

Van den Berg C, Rayner JMV (1995) The moment of inertia of bird wings and the inertial power requirement for flapping flight. J Exp Biol 198:1655–1664

Weis-Fogh T (1973) Quick estimates of flight fitness in hovering animals, including novel mechanisms for lift production. J Exp Biol 59:169–230

Withers PC (1981) An aerodynamic analysis of bird wings as fixed aerofoils. J Exp Biol 90:143–162

Author Index